

Lecture Notes in Civil Engineering

Tung Nguyen-Xuan ·
Thanh Nguyen-Viet · Thanh Bui-Tien ·
Tuan Nguyen-Quang ·
Guido De Roeck *Editors*

Proceedings of the 4th International Conference on Sustainability in Civil Engineering

ICSCE 2022, 25–27 November, Hanoi,
Vietnam

 Springer

Lecture Notes in Civil Engineering

Volume 344

Series Editors

Marco di Prisco, Politecnico di Milano, Milano, Italy

Sheng-Hong Chen, School of Water Resources and Hydropower Engineering,
Wuhan University, Wuhan, China

Ioannis Vayas, Institute of Steel Structures, National Technical University of
Athens, Athens, Greece

Sanjay Kumar Shukla, School of Engineering, Edith Cowan University, Joondalup,
WA, Australia

Anuj Sharma, Iowa State University, Ames, IA, USA

Nagesh Kumar, Department of Civil Engineering, Indian Institute of Science
Bangalore, Bengaluru, Karnataka, India

Chien Ming Wang, School of Civil Engineering, The University of Queensland,
Brisbane, QLD, Australia

Lecture Notes in Civil Engineering (LNCE) publishes the latest developments in Civil Engineering—quickly, informally and in top quality. Though original research reported in proceedings and post-proceedings represents the core of LNCE, edited volumes of exceptionally high quality and interest may also be considered for publication. Volumes published in LNCE embrace all aspects and subfields of, as well as new challenges in, Civil Engineering. Topics in the series include:

- Construction and Structural Mechanics
- Building Materials
- Concrete, Steel and Timber Structures
- Geotechnical Engineering
- Earthquake Engineering
- Coastal Engineering
- Ocean and Offshore Engineering; Ships and Floating Structures
- Hydraulics, Hydrology and Water Resources Engineering
- Environmental Engineering and Sustainability
- Structural Health and Monitoring
- Surveying and Geographical Information Systems
- Indoor Environments
- Transportation and Traffic
- Risk Analysis
- Safety and Security

To submit a proposal or request further information, please contact the appropriate Springer Editor:

- Pierpaolo Riva at pierpaolo.riva@springer.com (Europe and Americas);
- Swati Meherishi at swati.meherishi@springer.com (Asia—except China, Australia, and New Zealand);
- Wayne Hu at wayne.hu@springer.com (China).

All books in the series now indexed by Scopus and EI Compendex database!

Tung Nguyen-Xuan · Thanh Nguyen-Viet ·
Thanh Bui-Tien · Tuan Nguyen-Quang ·
Guido De Roeck
Editors

Proceedings of the 4th International Conference on Sustainability in Civil Engineering

ICSCE 2022, 25–27 November, Hanoi,
Vietnam

 Springer

Editors

Tung Nguyen-Xuan
University of Transport
and Communications (UTC)
Hanoi, Vietnam

Thanh Nguyen-Viet
University of Transport
and Communications (UTC)
Hanoi, Vietnam

Thanh Bui-Tien
University of Transport
and Communications (UTC)
Hanoi, Vietnam

Tuan Nguyen-Quang
University of Transport
and Communications (UTC)
Hanoi, Vietnam

Guido De Roeck
Department of Civil Engineering,
KU Leuven
Leuven, Belgium

ISSN 2366-2557

ISSN 2366-2565 (electronic)

Lecture Notes in Civil Engineering

ISBN 978-981-99-2344-1

ISBN 978-981-99-2345-8 (eBook)

<https://doi.org/10.1007/978-981-99-2345-8>

© The Editor(s) (if applicable) and The Author(s), under exclusive license to Springer Nature Singapore Pte Ltd. 2024, corrected publication 2024

This work is subject to copyright. All rights are solely and exclusively licensed by the Publisher, whether the whole or part of the material is concerned, specifically the rights of translation, reprinting, reuse of illustrations, recitation, broadcasting, reproduction on microfilms or in any other physical way, and transmission or information storage and retrieval, electronic adaptation, computer software, or by similar or dissimilar methodology now known or hereafter developed.

The use of general descriptive names, registered names, trademarks, service marks, etc. in this publication does not imply, even in the absence of a specific statement, that such names are exempt from the relevant protective laws and regulations and therefore free for general use.

The publisher, the authors, and the editors are safe to assume that the advice and information in this book are believed to be true and accurate at the date of publication. Neither the publisher nor the authors or the editors give a warranty, expressed or implied, with respect to the material contained herein or for any errors or omissions that may have been made. The publisher remains neutral with regard to jurisdictional claims in published maps and institutional affiliations.

This Springer imprint is published by the registered company Springer Nature Singapore Pte Ltd. The registered company address is: 152 Beach Road, #21-01/04 Gateway East, Singapore 189721, Singapore

Organization

Organizer and Sponsors

Organizer



Sponsors



ICSCE 2022 International Scientific Committee

Chairs and Co-chairs

Prof. Nguyen Ngoc Long, University of Transport and Communications, Vietnam
Prof. Guido De Roeck, KU Leuven, Belgium
Prof. Jinhai Zheng, Hohai University, China
Prof. Magd Abdel Wahab, Ghent University, Belgium
Prof. Yasuhiro Dosho, Meijo University, Japan
Prof. Matt Evans, Oregon State University, USA
Prof. Jose Campos e Matos, Universidade do Minho, Portugal

Scientific Members

Prof. Anand J. Puppala, Texas A&M University, USA
Prof. Günther Meschke, Ruhr University Bochum, Germany
Prof. Hajime Mase, Kyoto University, Japan
Prof. Farid Asma, Mouloud Mammeri University of Tizi-Ouzou, Algeria
Prof. Hocine Hammoum, Civil Engineering Department, Mouloud Mammeri University, Algeria
Prof. Young-sang Kim, Chonnam National University, Korea
Prof. Cheong Siew Ann, Nanyang Technological University, Singapore
Prof. Nasser Khalili, University of New South Wales, Australia
Prof. Osamu Kiyomia, Waseda University, Japan
Prof. Shimizu Norikazu, Yamaguchi University, Japan
Prof. Tatsunori Matsumoto, Kanazawa University, Japan
Prof. Torsten Schlurmann, Leibniz University Hannover, Germany
Prof. Watabe Yoichi, Hokkaido University, Japan
Prof. Yakun Guo, University of Bradford, UK
Prof. Zhang Jisheng, Hohai University, China

Prof. Zoubir Mehdi Sbartai, Université de Bordeaux, France
Prof. Takeshi Katsumi, Kyoto University, Japan
Prof. Zhang Chi, Hohai University, China
Prof. Yasuyuki Nakagawa, Port and Airport Research Institute, Japan
Prof. Magd Abdel Wahab, Faculty of Engineering and Architecture, Gent University, Belgium
Prof. Tran Hoai Nam, National Center for Asphalt Technology, Auburn University, USA
Assoc. Prof. Pham Huy Giao, Asian Institute of Technology, Thailand
Assoc. Prof. Javed Mallick, King Khalid University, King of Saudi Arabia
Dr. Nguyen Mai Lan, IFSTTAR, Nantes, France
Dr. Nguyen Minh Hai, University of Texas at Arlington, USA
Dr. Samir Khatir, Faculty of Engineering and Architecture, Ghent University, Belgium
Dr. Tang Anh Minh, Ecole des Ponts ParisTech, France
Assoc. Prof. Dr. Liu Pei, Feng Chia University, Taiwan.

ICSCE 2022 Organizing Committee

Local Organizing Committee

Assoc. Prof. Thanh Bui-Tien, University of Transport and Communications, Vietnam (Chair)
Assoc. Prof. Thanh Nguyen-Viet, University of Transport and Communications, Vietnam, (Co-chair)
Dr. Tung Nguyen-Xuan, University of Transport and Communications, Vietnam, (Co-chair)
Assoc. Prof. Tuan Nguyen-Quang, University of Transport and Communications, Vietnam (Co-chair)
Dr. Samir Khatir, Faculty of Engineering and Architecture, Gent University, Belgium
Assoc. Prof. Ngo Van Minh, University of Transport and Communications, Vietnam
Assoc. Prof. Nguyen Thi Tuyet Trinh, University of Transport and Communications, Vietnam
Assoc. Prof. Do Anh Tu, University of Transport and Communications, Vietnam
Assoc. Prof. Nguyen Chau Lan, University of Transport and Communications, Vietnam
Dr. Bui Ngoc Dung, University of Transport and Communications, Vietnam
Dr. Dang Minh Tan, University of Transport and Communications, Vietnam

Secretariat

Assoc. Prof. Tran Thu Hang, University of Transport and Communications (Chair)
Dr. Pham Van Phe, University of Transport and Communications (Co-chair)
Dr. Ta Duy Hien, University of Transport and Communications
Dr. Le Van Hien, University of Transport and Communications
Dr. Chu Tien Dung, University of Transport and Communications, Vietnam
Dr. Le Vinh An, University of Transport and Communications
Dr. Tran Ngoc Hoa, University of Transport and Communications
Msc. Nguyen Ngoc Lan, University of Transport and Communications

Advisory Committee Members

Prof. Bui Xuan Cay, Department of Highway and Traffic Engineering, University of Transport and Communications (UTC)
Prof. Pham Huy Khang, Department of Highway and Airport Engineering, UTC
Prof. Pham Van Ky, Department of Railway Engineering, UTC
Prof. Tran Duc Nhiem, Department of Bridge Engineering and Underground Infrastructure, UTC
Assoc. Prof. La Van Cham, Department of Highway and Traffic Engineering, UTC
Assoc. Prof. Le Hai Ha, Department of Railway Engineering, UTC
Assoc. Prof. Nguyen Quang Phuc, Department of Highway and Traffic Engineering, UTC
Assoc. Prof. Hoang Ha, Department of Urban Transport and Marine-Coastal Engineering, UTC
Assoc. Prof. Tran The Truyen, Department of Bridge Engineering and Underground Infrastructure, UTC
Assoc. Prof. Ho Anh Cuong, Department of Public Transport Works and Environment Engineering, UTC
Assoc. Prof. Ho Lan Huong, Department of Surveying, UTC
Assoc. Prof. Nguyen Trung Kien, Department of Structural Engineering, UTC
Assoc. Prof. Pham Hoang Kien, Department of Informatics in Civil Engineering, UTC
Dr. Tong Anh Tuan, Department of Hydraulics and Hydrology, UTC
Dr. Phung Duc Long, VSSMGE

Preface

The construction industry has experienced fundamental changes in facilitating environmental-friendly infrastructure toward the sustainable development goals (SDGs) in recent years. Since the 1973 oil crisis, the green structures have ever improved and gained momentum across all industries. Green construction has become a popular norm in many new construction projects. Promoting green building principles in infrastructure is globally challenging for all stakeholders.

Green building is still in its infancy and constantly evolving. There are numerous principles applied to green projects: efficiency of structural design, energy distribution, water supply, material selection, waste, pollutant reduction, and so forth. Nowadays, the combination of economic development and advanced environmental management technology has paved the way for a sustainable built environment. At the country level, construction projects should be built to meet the green building standards, focusing on a priority for customers and communities.

The 4th International Conference on Sustainability in Civil Engineering—ICSCE 2022 was successfully held on November 25–27, 2022, in Hanoi, Vietnam. The local organizing committee (LOC) would like to greatly appreciate to all of you. Your participation contributes not only to the success of the conference itself but also to the innovation in green technologies. The ICSCE 2022 received 262 abstracts and 167 full papers from 15 countries and regions, including Algeria, Australia, Belgium, Brazil, Bulgaria, China, France, Japan, South Korea, Portugal, Russia, Taiwan, Myanmar, Cambodia, and Vietnam. The International Scientific Committee selected 81 papers for this proceedings, which is divided into eleven parts. These papers were presented at the conference and played an important role in promoting sustainable civil engineering infrastructures toward a green future.

The LOC would like to sincerely thank the International Scientific Committee, keynote speakers, session chairs, and reviewers for your support and cooperation for the success of the ICSCE 2022. We also gratefully acknowledge the sponsors for their valuable time and support.

Assoc. Prof. Thanh Bui-Tien
Chairman of the LOC—ICSCE 2022
Dean of the Faculty of Civil
Engineering
University of Transport
and Communications (UTC)
Hanoi, Vietnam

Contents

Keynotes

The Use of New Tools and Technologies for the Management of Existing Infrastructures. Worldwide Perspective	3
José C. Matos, Ngoc-Son Dang, Mário Coelho, and Sérgio Fernandes	

Development and Characterization of Controlled Low-strength Materials as a Heat Transfer Medium for Horizontal Ground-Source Heat Pump System	23
Young-Sang Kim and Ba Huu Dinh	

Materials for Construction

Experimental Investigation of Cs of Reinforced Concrete Structures in Sea Island Regions of Khanh Hoa (Viet Nam) Application on Service Life Prediction	37
Thi Thu Hien Dang, Duy Huu Pham, Thi Bach Duong Nguyen, and Trong Chuc Nguyen	

Performance Evaluation and Mix Proportion Design of Concrete Using Low-quality Recycled Aggregate in Vietnam	45
Huynh Nguyen Van, Yasuhiro Dosho, Duc Nguyen Anh, and Sang Nguyen Thanh	

Effects of Rejuvenators on Cracking Resistance of High RAP Asphalt Mixtures	59
Van Quyet Truong, Ngoc-Lan Nguyen, Dong Van Dao, Kim Youngik, and Duc Trung Tran	

Using Paper Production Industry Waste as Soil Stabilizer for Pavement Construction in Vietnam	69
Nguyen Trong Hiep and Pham Huy Khang	

Experimental Investigation of Silica Fume Effect on Durability of High Performance Concrete (HPC)	79
Thi Thu Hien Dang, Thi Bach Duong Nguyen, Thi Hong Bui, and Quang Trung Dinh	
Leaching Mechanism of Metals from Recycled Concrete Aggregates (RCA) and Potentially Environmental Issues	89
Vu Quoc Hung, Prasanna Egodawatta, Chaminda Gallage, and Les Dawes	
Effect of Shape Memory Alloy Fibers on Volumetric Strain and Moduli of Concrete in Cyclic Compression	99
Vinh-Ha Ho, Van-Minh Ngo, Eunsoo Choi, and Ngoc-Long Nguyen	
Construction Engineering and Management	
Framework for Measuring Controlling Function Management of Vietnam’s Public Construction Works	113
Ngo Anh Tuan and Nguyen Luong Hai	
The Impact of Project Organizational Culture on Cost Performance of Construction Projects	121
Do Van Thuan and Nguyen Luong Hai	
Propose the Construction Orientation of Two Airports in Hanoi After Forecasting Airport Passenger Demand	131
Quoc Van Nguyen, Trung Tien Trinh, and Thuy Anh Vu	
An Overview of the Legislation on Sustainability and Strategy Accessing the Sustainability Performance of Road Construction Projects in Vietnam	141
Ngoc Minh La, Trong Hung Dinh, and Thi Tuyet Pham	
Constraints in Implementing Public–Private Partnerships (PPPs) in Vietnam: Private Sector’s Perspective	151
Hang Vu and Quynh-Huong Pham-Nguyen	
Assessing the Accuracy of Lidar UAV Technology Along with the Lidar Camera in Establishing the Terrain Map for Construction in Vietnam	159
Tran Quang Hoc, Tran Duc Cong, and Do Van Manh	
Bridge and Highway Engineering, Railway Engineering	
A Review of Methods for Protecting Highway Embankments from Overtopping Flow	169
Huy Quang Mai, Tuan Anh Tong, and Phong Dang Nguyen	

Applied Technology of Stay Cable with Saddle System in Song Hieu Bridge 177
 Nguyen Dac Duc and Nguyen Tuan Ngoc

Weight Evaluation of Criteria Influencing Road Flooding Using Multi-criteria Analysis 185
 Thai Thi Kim Chi and T. T. K. Chung

Equilibrium Local Scour Depth Under Live-Bed Scour for Cylindrical Piers with Their Width Greater Than Three Meters Based on Field Data 193
 T. N. Doan and D. N. Tran

Study on the Effect of Corrugated Webs in Steel I-Girder Bridge 201
 Tran Viet Hung

Evaluation of Dynamic Behaviors of Girders in High-Speed Railway Bridges Under Dynamic Impact of Electric Multiple Unit and Push–Pull Trains 209
 Nguyen Duc Thi Thu Dinh

Application of Mobile Road Profiler for International Roughness Index Monitoring in Hanoi 223
 Hoang Kien Pham and Kazunari Hirakawa

River, Estuary and Coastal Hydrodynamic Engineering

Numerical Simulation of Submarine Landslide-Induced Tsunami Using Two-Layer Extended Boussinesq Equations 235
 Van Khoi Pham, Van Nghi Vu, and Changhoon Lee

Selecting Optimal Marina Configuration with Regard to Mooring Safety and Port Area Water Exchange 243
 Izmail Kantarzhi, Alexander Gogin, and L. G. Tran

Wave Reflection from Typical Sloping Dike in the North of Vietnam 253
 Thi Phuong Thao Nguyen

The Mechanism of Large-Scale Flow Circulation at Asymmetric Sand Spit Inlet: A Case Study in Degi Estuary, Binh Dinh Province 263
 Vu Van Ngoc, Tran Thanh Tung, and Nguyen Quang Duc Anh

A Mathematical Model of Two-Dimensional Vertical Flow Based on the Dual Approach 271
 The Hung Nguyen

Analysis on Feasibility Study of PE Material Buoys for Vietnam Inland Waterways and Maritime Channels 287
 Nguyen Xuan Thinh and Bui Minh Thu

Research on Verification of the Pile Types of a Port Structure by Using Impact Vibration Test in Vietnam 295
 Thi Bach Duong Nguyen and Thanh Dat Pham

Prediction of Water Setup and Wave Crest Heights on Submerged Coral Reefs with Steep Slopes 305
 Tao Nguyen Quang, Ha Thi Thu Nguyen, Bau Nguyen Van, and Cuong Dinh Quang

A Study of Wave Attenuation Through Vegetation 313
 Phan Khanh Linh, Pham Lan Anh, Truong Hong Son, and Le Hai Trung

Effects of Beach Slope on Wave Characteristics in the Surf Zone Over Fringing Reef 321
 Pham Lan Anh, Phan Khanh Linh, and Truong Hong Son

A New Framework for Estuarine and Coastal Modeling to Monitor Water Security in a Changing Climate 329
 Truong Hong Son and Phan Khanh Linh

Hydrodynamic Modelling of New Segment Channel to Navigation Channel in Hau River, Vietnam 337
 Nguyen Viet Thanh, Le Vinh An, Thai Thi Kim Chi, Nguyen Dang Phong, Hoang Nam Binh, Nguyen Duy Tien, Bui Vinh Phuc, and Trinh Dinh Lai

Numerical Model of the Impact of Submerged Breakwater on Shoreline Evolution of Bona Beach, France 347
 Vu Minh Tuan and Yves Lacroix

Wave Transmission Through Pile–Rock Breakwater to Protect the Mekong Delta Coastal and Develop an Empirical Formula 357
 Nguyen Hai Duong, Dinh Cong San, Nguyen Nguyet Minh, Vu Van Nghi, and Le Duy Tu

An Empirical Prediction of $T_{m-1,0}$ on the Reef Flat of Atolls 369
 Thi Thuy Pham, Hai Trung Le, and Thanh Tung Tran

Overview of Coastal Protection Structures in the Mekong River Delta 377
 Le Vinh An, Nguyen Viet Thanh, Pham Van Hai, and Trinh Dinh Lai

Geotechnical Engineering

Thermo-Hydro-Mechanical Behavior of the Rock Mass Surrounding Wellbore in Deep Saturated Geological Layer 399
 Nam Hung Tran, Thi Thu Nga Nguyen, Duc Tiep Pham, and Duc Tho Pham

Numerical Study on Behaviors of EPS Geofom Embankment on Soft Ground 409
 Quoc-Bao Truong, Anh-Tuan Vu, Hoang-Kien Pham, and Duy-Canh Nguyen

Investigation of Slope Protection Using Vegetation: A Case Study in Ninh Thuan Province, Vietnam 417
 Tuan-Nghia Do and Lan Chau Nguyen

Rockfall Mitigation for Highway in Vietnam: A Case Study on the Hoang Sa Road, Da Nang City 427
 Cho Thu Thu Naing, Lan Chau Nguyen, and Tien Dung Nguyen

Volume Loss During the TBM Construction of Metro Line 1, Ho Chi Minh City, Monitoring Data Assessment and New Analytical Model for Prediction 439
 Nguyen Phuong Duy, Nguyen Thach Bich, and Tran Duc Nhiem

Proposing an Analytical Equation to Evaluate the Maximum Surface Settlement Due to TBM Construction Based on the Monitoring Data from Ho Chi Minh City Metro Construction ... 447
 Nguyen Thach Bich, Nguyen Phuong Duy, and Tran Duc Nhiem

EPS Geofom Embankment on Soft Ground—A Full-Scale Test 455
 Quoc-Bao Truong, Hoang-Kien Pham, Anh-Tuan Vu, Satoshi Kobayashi, and Duy-Canh Nguyen

Earthquake Resistance of Caisson-Type Quay Wall Renovated by Grouting and Deepening: Geo-Centrifuge Test 463
 Anh-Dan Nguyen and Young-Sang Kim

Remedy Solutions for a Deep-Seated Landslide on Road No. 155, Section Km 12 + 667.85–Km 12 + 711.57, Sapa Town, Lao Cai Province, Vietnam 473
 Thu Zar Aung, Lan Chau Nguyen, and Tien Dung Nguyen

Water Resource and Environment Engineering

Uses Field-Scale Data to Modify the HEC-18 Scour Model 487
 Huy Quang Mai and Nghien Dinh Tran

Identifying the Reasonable Rainfall Intensity Formula and Intensity–Duration–Frequency Curve for Tan Son Hoa Station, Ho Chi Minh City 495
 Dong Nguyen Dang and Thi Hoa Binh Le

Use of Disdrometer Dataset to Detect Kinetic Energy Expenditure and Rainfall Intensity Relationships 503
 Linh Nguyen Van, Xuan-Hien Le, Giang V. Nguyen, Minho Yeon, Younghoon Kim, and Giha Lee

Evaluating the Performance of Light Gradient Boosting Machine in Merging Multiple Satellite Precipitation Products Over South Korea 513
 Giang V. Nguyen, Xuan-Hien Le, Linh Nguyen Van, Sungho Jung, Chanul Choi, and Giha Lee

Multiple Methods for Homogeneity Analysis of Precipitation Series in Vinh Phuc Province 523
 Phan Manh Hung and Chien Pham Van

Impacts of the Threshold Value of the Enhanced Vegetation Index on Surface Water Area and Extent in MODIS Imagery 535
 Chien Pham Van

Extracting Water Depth from Landsat-8 Multispectral Satellite Imagery in Coastal Waters 545
 Tran Duc Phu

The Novelty of Extreme Natural Drought Trend Using the Statistical Approach 553
 Tuong Vo

Proposed Adaptation Measures for Saltwater Intrusion in the Vietnamese Mekong Delta 563
 Nguyen Phuong Mai, Sameh Kantoush, Sumi Tetsuya, and Tang Duc Thang

Structural Modelling and Analysis

Evaluation of Partial Safety Coefficients in the Concrete Tank Design by a Semi-Probabilistic Approach 575
 Hocine Hammoum, Karima Bouzelha, and Amar Aliche

Multi-Criteria Optimization of the Quality Indicators of Steel Foundry Ladles, Based on Priorities and Weighting Coefficients of the Indicators 583
 Dimitar Borisov

Research on Construction of Prefabricated Precast Concrete Columns Combined with S-VRO Foam Core Slab 593
 Thang Hoang Duc

Influence of Cohesive Interface on the Flexural Behavior of Textile-Reinforced Concrete 605
 Nguyen Thi Thu Nga, Dang Thi Thu Hien, and Tran Nam Hung

Nondestructive Mechanical Characterization by Small Punch Test and Statistical Fractography for the Determination of the Residual Lifetime of Old Steel Bridges 615
 Bholah Bhimal, Delgado Julien, Depale Bruno, Auvray Nicolas, and Ponson Laurent

Evaluating Damping Model Applied for Cable Tension of Cable-Stayed Bridge 623
 An Huynh-Thai, Toan Pham-Bao, Hung Nguyen-Quoc, and Luan Vuong-Cong

Investigating Seismic Response of Container Crane Subjected to Near-Field Ground Motions 631
 Van Bac Nguyen and Van Hung Nguyen

Structural Damage Detection and Health Monitoring

Mechanical Reliability Analysis of an RC Storage Tank Considering Pitting and Uniform Corrosion 641
 Karima Bouzelha, Nassima Miloudi, Hocine Hammoum, Lysa Benaddache, and Serine Bennabi

Study to Apply Artificial Neural Network for Establishing Displacement Models of a Cable-Stayed Bridge 649
 Thuy Linh Nguyen and Van Hien Le

Filtering Outliers in GNSS Time Series Data in Real-Time Bridge Monitoring 657
 Ngoc Quang Vu and Van Hien Le

Safety Warnings for Technical Status of Port Structure by Automatic Monitoring in Vietnam 665
 Thi Bach Duong Nguyen, Van Hien Le, and Duc Cong Tran

Opportunities and Challenges of Digital Twins in Structural Health Monitoring 673
 Minh Quang Tran, Hélder S. Sousa, Nhung Thi Cam Nguyen, Quyet Huu Nguyen, and José Campos e Matos

Damage Detection in Structural Health Monitoring Using a One-Dimensional Convolutional Neural Network—The Z24 Bridge Case Study 683
 Hieu Nguyen-Tran, Dung Bui-Ngoc, Dung Pham-Tuan, Lan Ngoc-Nguyen, Hoa Tran-Ngoc, and Thanh Bui-Tien

The Effect of the Cut on the Power Spectral Density of the Beam 693
 Toan Pham-Bao and Luan Vuong-Cong

Building Information Modelling and AI in Civil Engineering	
Application of FARO Focus 3D S350 Terrestrial Laser Scanner in Building 3D Models of Potential Areas of Landslides and Rocks—Case Study in Ha Giang Province, Vietnam	703
Hanh Hong Tran, Hung Quoc Vu, and Anh Van Tran	
Risk Identification and Prediction for Highway Bridge Projects Using an Artificial Intelligence Model	711
Dao Duy Lam, Le Duc Anh, Luu Truong Giang, and Hoang Ha	
Integrating Terrestrial Laser Scanning Technology and Unmanned Aerial Vehicles in Establishing a Database for the Preservation of Ancient Constructions	721
Do Van Manh, Le Quang, and Vu Ngoc Phuong	
Pavement Crack Segmentation Using an Attention-Based Deep Learning Model	727
Hieu Dao, Tung Khuc, Quan Truong, Cang Dinh, and Andy Nguyen	
Hindrances to the Application of Building Information Modeling (BIM) in the Construction Field in Vietnam	739
Nguyen Tai Duy	
AI Solutions for Innovation of Pavement Crack Analysis on Images Taken from Specialized Road Surface Survey Vehicles in Vietnam	747
Thao Dinh Nguyen and Nhung Thi Hong Nguyen	
Traffic Engineering, Transportation and Logistics Engineering	
An Investigation of Cargo Handling Equipment Performance in Vietnam Container Terminals	757
Pham Huy Tung and Nguyen Luong Hai	
Assessment of Traffic Safety Between Pedestrians and Vehicles Using Traffic Conflict Technique	763
Tuan Thanh Nguyen and Phuong Thao Cao	
Vehicle Speed Analysis Toward Traffic Safety at School Zones Considering Roadside Activities—Case Study in Vietnam	771
Dang Minh Tan and Vu Quang Huy	
Impact of COVID-19 on the Inland Waterways and Review Recovery Solutions	781
Nguyen Viet Thanh, Nguyen Dinh Thao, Dang Tuyet Ly, and Pham Van Hai	
COVID-19 Impact on the Operations of Road Transport Enterprises and Green Recovery Solutions	793
Thao Dinh Nguyen, Ly Tuyet Dang, and Quyen Van Nguyen	

**Correction to: Proceedings of the 4th International Conference
on Sustainability in Civil Engineering** C1
Tung Nguyen Xuan, Thanh Nguyen Viet, Thanh Bui Tien,
Tuan Nguyen Quang, and Guido De Roeck

About the Editors

Dr. Tung Nguyen-Xuan has been working at Civil Engineering Faculty, University of Transport and Communications (UTC), Vietnam, since 2008. He got Bachelor's and Master's degrees at UTC and Ph.D. degree at Tokyo Metropolitan University, Japan, with his main research topic about corrosion monitoring on steel truss bridges. Dr. Tung's research interests are concrete structure including concrete using recycled aggregates, structure engineering, advanced material, and structural health monitoring. Dr. Tung has published 20 scientific papers (in national and international journals) and 4 scientific books and is a principle investigator for 3 research projects.

Dr. Thanh Nguyen-Viet obtained his engineering and master's degrees from the National University of Civil Engineering (Vietnam) in 2001 and 2006 and his Ph.D. degree from Hohai University (China) in 2012, respectively. He joined the University of Transport and Communications in 2005 as a lecturer and is now a vice dean and an associate professor in the Faculty of Civil Engineering at the University of Transport and Communications, Hanoi, Vietnam. Dr. Viet Thanh Nguyen is a specialist working in the field of the harbor, coastal, and offshore engineering. Practical knowledge and experience help a lot in his research as well as inspire students and researchers. Dr. Nguyen's research areas are hydrodynamics, sediment transport, port, coastal and offshore engineering, and inland waterways. He has 26 publications in Web of Science and Scopus. He has obtained an Outstanding Ph.D. Candidate Award at Hohai University in 2013.

Assoc. Prof. Dr. Thanh Bui-Tien is an expert in Civil Engineering, specializing in structural health monitoring, AI, digital twin, intelligent transportation, and structural damage diagnosis of bridges. He is currently the dean of the Faculty in Civil Engineering at the University of Transport and Communications in Vietnam. He obtained his Bachelor of Engineering degree in Bridge Engineering from the University of Transport and Communications (UTC) in Vietnam in 2000 and his Ph.D. in Civil Engineering from the University of New South Wales (UNSW), Australia, in 2007. He has held academic positions at various institutions, including lecturing at UNSW and UTC and postdoctoral research at Université de Liège and KU Leuven. Assoc.

Prof. Dr. Bui Tien Thanh has published numerous papers in peer-reviewed prestigious journals and has contributed to many conferences and seminars around the world. He has a citation count of 1048, an h-index of 18, and an i10-index of 26. His current work involves developing new methods based on optimization and AI for structural health monitoring and structural damage detection.

Assoc. Prof. Tuan Nguyen-Quang is currently the vice dean of Faculty at Civil Engineering, University of Transport and Communications in Vietnam. His research domain is on the behavior of materials and structures, new materials, and technologies in construction. He graduated from University of Transport and Communications, Vietnam, in 2006. Then, he received a master's degree in 2007 and a Ph.D. in 2011 from Ecole Nationale des Travaux Publics de l'Etat (ENTPE) in France. Until now, he has more than 10 years of research in the field of materials in transport construction, especially asphalt materials. He is a member of the editorial board of Road Materials and Pavement Design Journal since 2016. He has published 60 scientific papers (in national and international journal) and 2 scientific books. His total number of citations is 750 (according to Google scholar). His h-index is 13 (according to Google scholar) and is 10 (according to Scopus). He chaired and participated in more than 10 ministerial and state-level projects in Vietnam as well as participated in the international RILEM project (RILEM TC 237 SIB, Testing and characterization of sustainable innovative bituminous materials and systems).

Emeritus Prof. Dr. Guido De Roeck is a highly respected figure in the field of civil engineering, with a distinguished career spanning several decades. He is currently affiliated with the Department of Civil Engineering, Section Structural Mechanics at Katholieke Universiteit Leuven (KU Leuven), Belgium. With expertise in fuzzy finite element method, dynamic analysis, soil mechanics, and fracture mechanics of composite materials, he has contributed extensively to research in these areas. Professor De Roeck obtained his Bachelor of Engineering Science in 1968, followed by his Master of Science in Civil Engineering in 1971, both from KU Leuven. He earned his Ph.D. in Structural Mechanics from the same institution in 1975 and his Doctor of Science degree in 1981. As a top professor at KU Leuven, Prof. De Roeck has published thousands of international articles, with a citation count of 22609, an h-index of 74, and an i10-index of 220. His notable achievements include being a senior specialist in the field of structural health monitoring with the output-only method of determining damage from vibration measurement. Professor De Roeck leads multiple research activities, covering a broad spectrum of domains such as static and dynamic analysis of mechanical structures, damage detection by vibration monitoring, dynamic system identification, soil-structure interaction, non-linear constitutive soil models, fracture mechanics of composite materials, fuzzy finite element method, and so on.

Keynotes

The Use of New Tools and Technologies for the Management of Existing Infrastructures. Worldwide Perspective



José C. Matos, Ngoc-Son Dang, Mário Coelho, and Sérgio Fernandes

Abstract The development of modern society heavily relies on existing infrastructures. In particular, transport infrastructures are crucial to moving people and goods around the world, thus materializing globalization. In recent years, awareness has been raised on the necessity to maintain the existing infrastructures and aspects such as sustainability are nowadays the top priorities of infrastructures' stakeholders. Accordingly, the future infrastructures will be those already existing and properly maintained rather than new ones to be built to replace them. The success of this huge compromise on maintaining existing infrastructure depends on the development of more accurate, efficient, cost-effective and sustainable tools and technologies to support all the lifecycle management. The present work provides an overview of some relevant efforts that are being conducted worldwide in this regard, highlighting the current trends of technological development, identifying some existing opportunities, and anticipating some of the most relevant tools that will be used in the near future to support transport infrastructures' management.

Keywords Transport infrastructures · Management · Technology

1 Introduction

During the last decades of the twentieth century and the start of the twenty-first century, significant investments were made in the transport industry in most developed nations. In the past, the main emphasis was on finding a design that would result in the lowest investment cost for various assets, including bridges, viaducts, and highways, while merely considering the functional requirements. This strategy

J. C. Matos (✉) · N.-S. Dang · M. Coelho · S. Fernandes
ISISE, University of Minho, Guimarães, Portugal
e-mail: jmatos@civil.uminho.pt

N.-S. Dang
e-mail: sondn@civil.uminho.pt

produced an infrastructure design with high maintenance costs. An innovative life-cycle cost analysis (LCCA) method was developed to buck this tendency and seek the best balance between maintenance and investment [1].

The fact that a portion of Portugal's transportation system traverses several geological and environmental concerns enhances its sensitivity to climatic risks. Due to their crucial role in socioeconomic growth, one of the difficulties for transport decision-makers is ensuring the transportation networks' resilience to extreme events and climate change [2]. The Strengthening Infrastructure Risk Management in the Atlantic Area (SIRMA) project was suggested to create, validate, and implement a comprehensive framework for effectively managing and mitigating natural hazards in terrestrial transportation modes. According to the Transport White Paper (2011), SIRMA significantly increases the resilience of transportation infrastructure. The SIRMA idea, which uses multiplatform remote sensing and crowdsourcing to monitor big data, is at the forefront of the adoption of predictive maintenance [3, 4]. The primary goals of SIRMA are to lower maintenance and retrofitting costs through long-term recovery and risk mitigation. To achieve this goal, existing deterministic models of infrastructure resilience under the current climate will be modified to incorporate probabilistic models that take into account the uncertainties of future climate and change on land use and how it affects the impact of hazards on specific mode components [5, 6].

On the other hand, recently, the bridge management system (BMS, hereafter used by the acronym GOA—Gestão de Obras de Arte in Portuguese) has evolved to meet the needs of various clients and to reflect the features of their bridges. GOA has been modified into a product owned by Betar, Lda. Betar discovered a void in the domestic market and began developing the first Portuguese bridge management system in 1997, 29 years after establishing the first bridge management system in the USA [7]. Estradas de Portugal, a public transportation company, was also acquired and used the GOA system in 2004. By establishing GOA as a national standard, these facts helped private and public transportation agencies in Portugal, and practically, all bridge owners create a consistent language and framework. Continuous advancements in GOA have been made possible by more than 20 years of research and experience. It led to expansion outside the Portuguese market, specifically in Mozambique and China. More recently, opportunities to implement it in other countries have also arisen. The specification of the fundamental modules that allow storing various data types has mostly undergone revisions during the past few years (LABSE Symposium Report 91). In this sense, GOA.BI is a project built on modern technology and digital trends that focuses its efforts on addressing the issues with the highway and railroad infrastructures that were previously mentioned. Due to the large number of assets involved, this project seeks to develop a smart interface to assist stakeholders (owners, transportation authorities, and inspectors, among others) in the lifecycle management of complex systems, such as transportation infrastructures (bridges, viaducts, tunnels, acoustic barriers, buildings, retaining walls, slopes, pavements, rail tracks, telematics equipment, sign gantries, high mast columns, among others). The first step is to create an integrated asset management system framework based on the

bridge management system (BMS), which offers flexibility to apply and extrapolate its concepts for different types of infrastructure.

Building information modelling (BIM), which can cover integrated management of entire asset networks like motorways, railways, or bridges, has recently assumed a crucial position in the infrastructure sector. The state of the art of BIM implementation in this field, including an overview of the BIM domains, BIM applications, data schemas, and BIM uses, has been presented through the thorough review and critical analysis of 198 publications in the field of building information modelling for transportation infrastructure [8]. For transportation infrastructure in general, and particularly for highways and bridges, it demonstrates better BIM research and application development. Additionally, it draws attention to the state of research at the moment, how emerging technologies are being used, and the considerable research gaps that still need to be filled.

Depending on the originator's source, the 3D geometrical model for an existing infrastructure can be generated in various ways. The IFC model, which aims to link the geometric representations with the semantic objects in a flexible manner, is the geometric representation of each structural member. In this context, several types of bridge structures have lately been widely launched using the bridge digital information model (BIM method) [9–14]. An improved version of the alignment-based object-oriented design philosophy appears to be the key to building a bridge information model. The entire bridge model can be delivered without discontinuity using a set of parameter definitions and suitable algorithms. Because of the flexibility afforded by the parametric design idea, the model's creator can alter any input variables to satisfy the desired objectives. The digital bridge model greatly aids the engineer in effectively controlling the flow of information for various goals throughout the project's lifecycle. Collaboration between multiple project stakeholders and stages is made possible by the design platform's interoperability.

2 Methodology and Framework

Managing the existing infrastructure is challenging regarding interoperability among different BIM solutions, different BIM uses, or difficulties in integrating other BIM models. Therefore, the prototyping methodology and case study are strongly recommended. This method includes the prototype creation, application and curating to a specific infrastructure asset, then reworking when needed until an acceptable prototype is achieved. It allows engineers to deal with any project when the requirements come from multiple disciplines and aspects, a crucial challenge that needs to be overcome.

During the prototyping research, the expertise and methods from different disciplines will be integrated into pursuing objectives. According to the management purposes for existing infrastructure, the following concept and framework works can be introduced:

2.1 Risk and Resilience-Based Decision-Making

Extreme natural occurrences and the robust corrosion processes brought on by closeness to the water directly impact how well railway and transportation infrastructure performs in the service, particularly in the Atlantic Area. To increase the resilience of transportation infrastructure, a robust framework for managing and mitigating extreme natural occurrences must be developed and put into place. Figure 1 suggests a framework for risk- and resilience-based decision-making intended to lessen the effects of extreme natural hazards, such as floods and fires, on people and local and global economies.

The main actions and deliverables following the proposed framework can be considered as follows:

- Risk-based predictive model (algorithm) for transportation infrastructures (includes climate change effects on the impact and return period of extreme events).
- Relational database with risk mitigation measures for transportation infrastructures, their effects, and costs.
- Framework (user-friendly software) for multi-criteria decision-making, i.e. by maximizing resilience and minimizing the risk mitigation costs.

Noteworthy, the risk definition here is associated with the consequences of an asset’s failure in case of a hazard’s occurrence. While a holistic methodology was defined, its implementation was only done for specific parameters. Risk management involves monitoring the factors that influence these three risk components and defining mitigation actions to keep the network risk within acceptable levels. This framework enables forecasting transportation infrastructure performance to multiple hazards, comprising the likelihood of such extreme events and their impact on the infrastructures. Moreover, it is expected to create the premise for the creation of a database with the most relevant risk mitigation measures, including their description, when they should be used, and with what time frequency, effects, and costs (direct and indirect).



Fig. 1 Configuration for the risk and resilience-based decision-making framework

2.2 BIM-Based Bridge Management System

A desktop web-based and intelligent interface platform should be available and supported by the new bridge management system (GOA.BI). The earlier system is a full version with all its modules because it is designed for the central management team. In situ inspectors will use this GOA.BI, which they will access through mobile devices. There should be a lighter version with less functionality in fewer modules.

Figure 2—Flowchart of the new system architecture summarizes the new system architecture. On top and bottom extremities are represented the two main ways to access the new system referred to before. In the middle, the significant modules to be developed are shown. They are beginning with the system’s core, GOA. BI module will be essentially based on the existing GOA system, which will be upgraded considering the interoperability between the current system and the new modules. Remark that this is the central module through which all other modules communicate.

Besides the objectives directly related to developing a new bridge management system, other important goals are associated with the recent acquisition tools and the exchange of information between all modules. The following list summarizes all the main objectives of the project:

- Development of a new web-based platform, modular, and scalable that can be continuously upgraded with new features and modules.
- Development of an intelligent interface platform to be used in the field by the in situ inspectors’ team.
- Development of new inspecting equipment taking advantage of existing commercial tools (e.g. commercial drones, cameras, etc.) and algorithms/methods in the computer vision and deep learning field.
- Development of mixed reality tools to manage bridges information with visual analytics and augmented reality techniques.

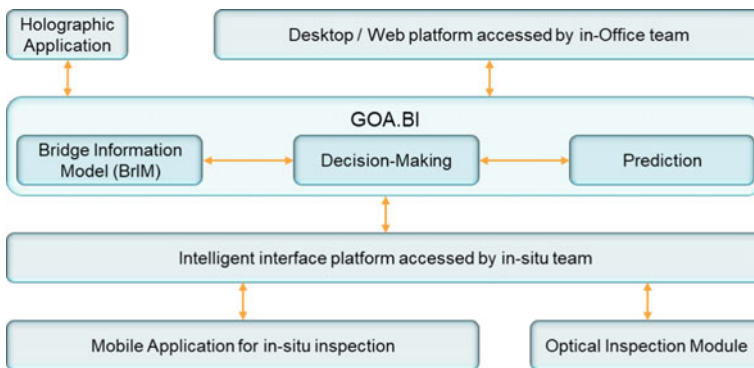


Fig. 2 Flowchart of the new BIM-based bridge management system architecture

- Development of algorithms to be used in information exchange between new inspecting equipment sensors and BrIM models.
- Development of digital image correlation algorithms to post-process inspection measurements.
- Development of a predictive maintenance management module, which will help in defining priorities for maintenance works.
- Development of a decision-making module will help define the type of intervention to be taken, considering the associated cost–benefit ratio.

3 Case Study 1: Strengthening Infrastructure Risk Management (SIRMA)

To achieve the project’s aims, the distribution of different Work Packages (WPs) was proposed and subdivided into specific actions that interact with each other (see Fig. 3). The technical WPs are listed: WP4—Climate change and natural hazards in Atlantic Area; WP5—Instrumenting transportation infrastructure for extreme natural hazards; WP6—Risk and resilience-based decision-making procedure for transportation infrastructure; WP7—Testbed.

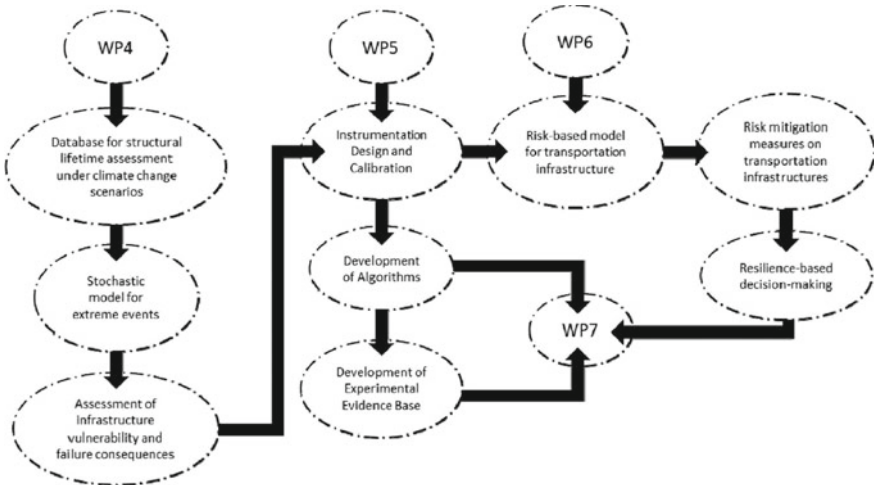


Fig. 3 Interaction graph between WPs

3.1 WP4: Climate Change and Natural Hazards in Atlantic Area

The primary goal will be to determine how vulnerable transportation infrastructure is to events that can be intercepted (such as deterioration from chloride ingress) and cannot be intercepted (such as scour) under various climate change scenarios. This working package will be divided into three primary tasks connected to the infrastructure vulnerability assessment technique, stochastic modelling, and the database for structural lifespan evaluation.

- (1) *Database for structural lifetime assessment under climate change scenarios:* This action intends to create a database that is appropriate for an infrastructure scale on the weather and climate factors, such as temperature, relative humidity, precipitation, rainfall, annual flow, sea level rise, that could affect the structure's dependability. This database will take into account scenarios from the Intergovernmental Panel on Climate Change's (IPCC) Representative Concentrations Pathways (RCP) (IPCC).
- (2) *Stochastic model for extreme events:* To create a stochastic model that may be used to calculate the impact on global transportation infrastructure and the vulnerability it faces. The method will be based on a Markov-switching autoregressive model to represent the temporal evolution of the maximum yearly flow. The information from the previous action will be needed as input and will be updated as soon as new information becomes available. The outcomes can be entered into a tool for making decisions.
- (3) *Methodology for assessment of infrastructure vulnerability and failure consequences:* To create a stochastic framework capable of simulating the combined effects of interceptable events and those that are not. A deterministic function will initially represent progressive deterioration. Randomness will be incorporated as a shock process, with appropriate deterministic functions used to describe the intervals between random degradation jumps. Sudden events will follow a compound point process with independent, symmetrically distributed random variables for the shock magnitude and interarrival times.

3.2 WP5: Instrumenting Transportation Infrastructure for Extreme Natural Hazards

The primary goal of this WP is to validate the damage pathologies chosen in WP4 using numerical and experimental evidence. As a result, this WP's actions concern the definition and use of monitoring and sensor equipment, algorithms' numerical validation, and laboratory tests' experimental validation.

- (1) *Instrumentation Design and Calibration:* From WP4, sensors and monitoring requirements with damage pathologies (e.g. timespan, frequency, data transfer,

power) will be chosen. The ideal sensor placement will be mathematically determined using deployment scenarios from WP4 and WP7 and risk-driven decisions from WP6. An electrodynamic shaker will calibrate the sensors using historical benchmark data, both synthetic and real. Geometric and radiometric sensors will be calibrated, put together, synchronized, and integrated with sensor platforms.

- (2) *Development of Algorithms*: The data gathered above will create algorithms for multimodal transportation networks. The use of custom climate-aware indicators of scour, floods, stiffness degradation, and durability using machine learning, heuristics, and time series will be the focus of output-only, near-real-time monitoring. The applicability of algorithms will be determined by a specific numerical benchmark that considers synthetic, real, and big geographic data, parameter calibration, sensitivity, and measurement noise/uncertainty effects.
- (3) *Development of Experimental Evidence Base*: By implementing the algorithms for various synthetic and historical, real data utilizing an electrodynamic shaker containing data communications, the numerical benchmark from the previous part will be empirically tested in a lab. It will be possible to see examples of near-real-time detection and model update, and WP7 implementation problems will be researched in a lab setting.

3.3 WP6: Risk and Resilience-Based Decision-Making Procedure for Transportation Infrastructure

This WP intends to create a resilience-based decision-making tool for the Atlantic region's transportation infrastructure. It consists of three tasks:

- (1) *Risk-based model for transportation infrastructure*: This work will construct a risk-based forecasting model that uses measured data from WP5. The chance of interceptable and noninterceptable events, as well as their effect on infrastructure performance, will be predicted by this model, together with the accompanying direct and indirect consequences. This model will also consider how climate change may affect the frequency and duration of such events, as determined by WP4.
- (2) *Risk mitigation measures on transportation infrastructures*: With the help of a questionnaire, which will ask experts in transportation infrastructure management about the impacts, costs (direct and indirect), and recurrence rates of the most prevalent risk mitigation techniques, the most appropriate risk mitigation strategies will be identified. The computation of such results is subsequently done using a hierarchical analytical process. Additionally, the framework created in the preceding section will describe these measures.
- (3) *Resilience-based decision-making*: In this work, an optimization model is built to minimize risks and increase rewards within a set of predetermined restrictions. This will be accomplished by taking into account a global optimization

technique that will maximize the resilience of the infrastructure to a specific incident. The outcomes include creating risk mitigation strategies for transportation infrastructures and considering the most pertinent risks in the Atlantic region.

3.4 WP7: Testbed

The primary goal will be to deploy the SIRMA risk assessment system and decision-making in two multimodal case studies affected by climate change events, one in Portugal and the other in Ireland/Northern Ireland, to test and validate it (transborder).

A portion of National Road 6 (EN6) and the Cascais Train Line will serve as the Portuguese test bed (Fig. 4a). There are parts of both infrastructures that practically sit atop the Atlantic Ocean. Every winter, the water surges over the road due to floods alone or in conjunction with sea storms, resulting in significant traffic accidents and protracted blockages.

The primary rail line (Fig. 4b) between Ireland and Northern Ireland (UK) will also serve as the test bed. More than 200 train crossings will be employed for a chosen 10-km length of track to evaluate the track’s state, the strength of its bridges, and the capability to spot water damage to the road’s pavement.

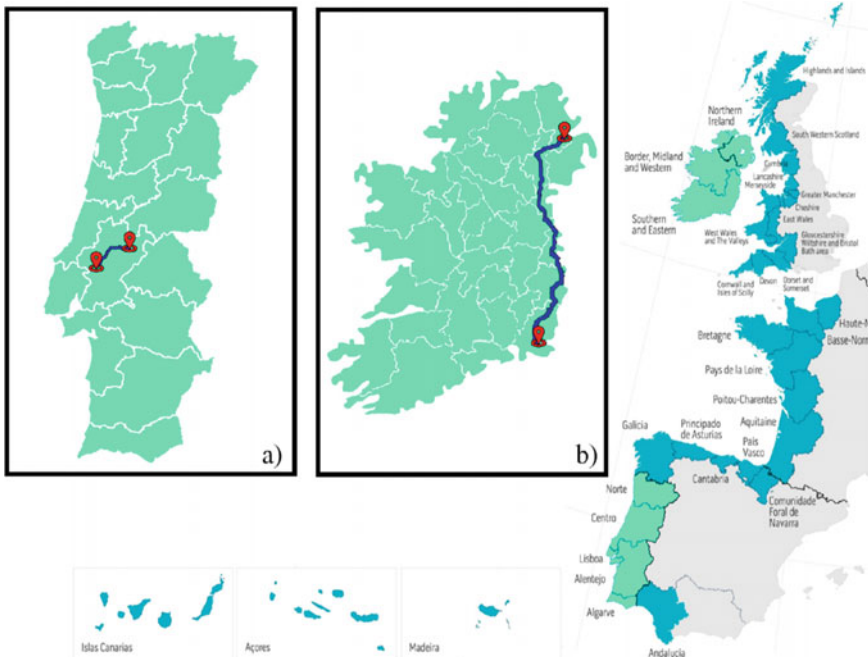


Fig. 4 Tentative test bed location. a Portugal, b Northern Ireland

The two case studies will test the sensing system created by WP5. From that system, a list of indicators about the performance of the infrastructure will be incorporated into the risk-based model and later into the decision-making framework created by WP6. Additionally, the risk-based model will include WP4 research on the effects of climate change. As a result, WP7 will calibrate this model and test the decision-making algorithm to determine the best course of action for risk minimization.

4 Case Study 2: GOA Bridge Management System—Bridge Intelligence (GOA.BI)

The project's success depends on all intervening co-promoters working well together. In this regard, the actions listed in the following table were created to get the best out of each promoter and more effectively pursue the project's goals. Eight different activities, ranging from industrial research to experimental development, were anticipated:

- (1) *Preliminary studies*
- (2) *GOA.BI platform architecture*
- (3) *GOA.BI platform development*
- (4) *Prototype development*
- (5) *Tests*
- (6) *Integration and validation*
- (7) *Dissemination, promotion and capitalization*
- (8) *Project coordination and technical management.*

It is significant to note that, even if each task has a designated responsible promoter, the work will be carried out with all consortium partners' assistance, input, and recommendations. The preliminary investigation was conducted, and comprehensive reports emphasized the state-of-the-art prediction and decision-making models and benefits for BrIM applications. On the other hand, next-generation mixed reality technologies and the state-of-the-art upgrading of intelligent sensor systems are also synthesized. The following can be used to introduce the critical technical actions:

4.1 GOA.BI Platform Architecture

The solution's architecture is being developed piecemeal, taking a staged approach to various aspects of the platform. Concerning the interaction of the GOA platform with mixed reality tools, mobile 3D representation, and intelligent image processing platform, the architectural design is further advanced at this stage. The initial iteration of this component of the solution, which is still in an iterative phase of assessing the architecture, begins from a sketch that is depicted in the following image (Fig. 5):

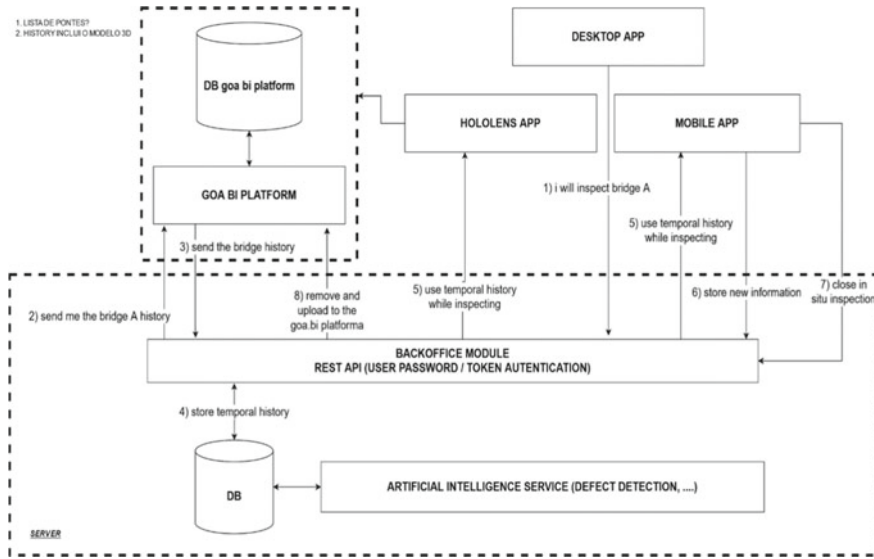


Fig. 5 GOA.BI platform architecture

According to the smart sensor system specification for optical inspection, Django and Tensorflow are advanced web programming and artificial intelligence frameworks that will be used to implement the optical inspection system. This will guarantee interoperability between the various parts to integrate the new platform. It is anticipated that the artificial intelligence-powered optical inspection system would use algorithms for object detection and classification to find flaws in photos that auditors have taken. A back office module based on rest requests (verified by user/password and tokens) will be used to manage the use of artificial intelligence algorithms and approaches. Access to the mixed reality tools and the data related to each inspection will be made possible via this module.

There are two different supports and solutions to be recognized in terms of the mixed reality tools definition, the holographic and portable versions. In the mobile version, which will be utilized on-site, users can access various information about the bridge and take pictures to be analysed later. The holographic version gives you more freedom to access the history, expand elements, and compare flaws while allowing you to examine and edit the details in a controlled environment. Reconciling two functioning versions with different supports and capabilities will be the most challenging hurdle. Suppose our ability to interact with the elements is constrained when using a mobile device, such as a smartphone or tablet. In that case, we can interact and control the elements more immersive and detailedly when using a holographic device like the HoloLens 2. A desktop/web version with the primary goal of managing the data that the other versions will consume was defined in addition to the mobile and

holographic versions. With this update, users can examine inspections, amend or add to the related data, upload 3D models to the system, and associate those models with existing bridges or components.

4.2 *GOA.BI Platform Development*

The application group, the GOA.BI platform group, and the server and BackOffice group are the three groups that make up the system architecture, as shown in Fig. 4. The application group includes desktop/web, HoloLens, and mobile applications. It also consists of the GOA.BI platform group houses all of the original user, inspection, and other data, as well as the server and BackOffice groups, which act as a bridge between the GOA.BI group and the applications group. Additionally, this group will permit the temporary storage of data produced by applications.

Initial versions of the applications have already been developed and evaluated in terms of implementation, using created data and content to ensure their functionality. The database's foundations have also been established, as seen from the primary architecture displayed in Fig. 6. Other tables make the system more comprehensive in addition to the fundamental tables depicted in the figure. This data structure was created to supplement the one that already exists in the GOA.BI platform.

Figure 6 depicts the database's overall layout, with the inspection table's centre of attention. This table will hold the fundamental inspection data, and its primary connections are made to the component classification table (process inspection-component classification), the view table (process view), the anomaly table (process anomaly), and the bridge table (process bridge).

Starting with the bridge table will link to other tables that allow you to describe the bridge in more detail. It will have all the essential information, such as name and location. One such connection is made to the component table, which essentially enables the division of a bridge into numerous components. Each of these elements will possess specific characteristics that allow them to be connected to a 3D model and a spatial position. This is crucial so that the bridge can be created in a virtual setting with the appropriate position and scale comparable to or similar to the actual bridge. The anomalies and views tables will be utilized here so that many peculiarities and perspectives are connected with each inspection, each with unique data and attributes. During an examination, the inspector can record several abnormalities and views.

Since anomalies are one of the most crucial components of inspections, it is essential to be as thorough as possible when capturing them. Anomalies are deformations, damages, or other problems that the bridge structure may show. Information as likely to have these abnormalities fixed as soon as possible. Due to this, tables that allow for the detailed description of each anomaly, as well as tables that allow for the assignment of multimedia assets to each anomaly, were constructed. The most crucial of these multimedia assets will be the on-site images, which will be examined using an artificial intelligence system to automatically find the anomaly in the photo and make its treatment easier.

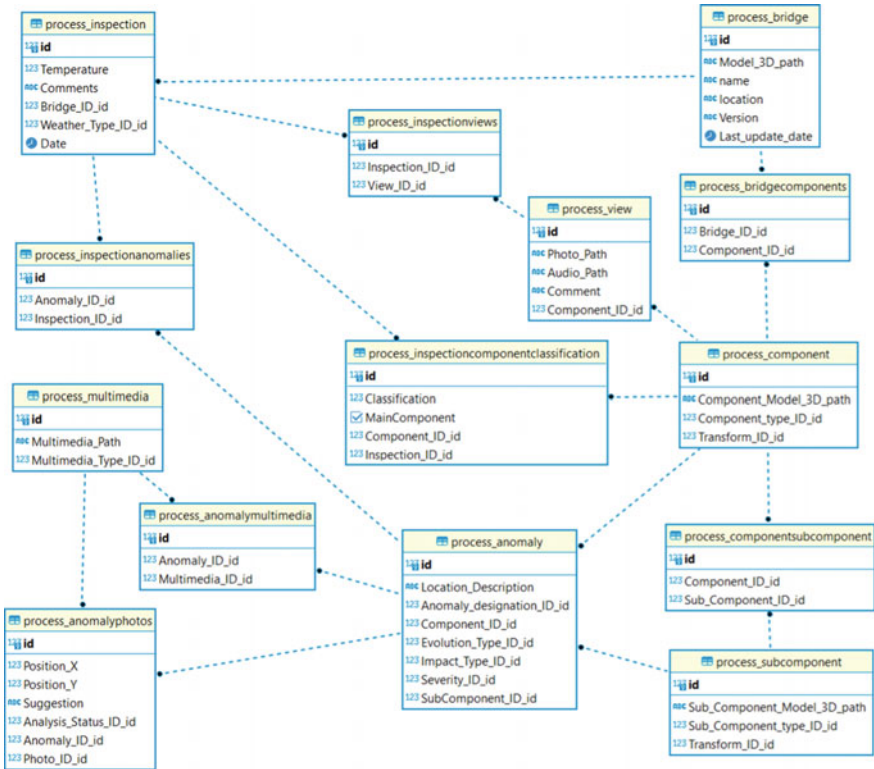


Fig. 6 Database for the GOA.BI platform

4.3 Prototype Development

The algorithm-based coding in algorithmic tools is mainly used to create the BrIM module. The coordinates and size of the primary structural members served as the basis for producing a 3D geometric model. An example of a typical spreadsheet file (.xls) containing a data template for the concrete part of a standard 1-pier PSC bridge is shown in Fig. 7, with information about the alignment of the bridge, the measurements of each structural element, and any restrictions. Considerations for various LOD dimensions are required. The algorithmic tool directly imports the template. This modelling tool’s algorithm can be divided into two categories: one for reading input data and the other for modelling three-dimensional objects (which includes parameter definition, geometric generation, and model export). The 3D geometric model of the bridge is constructed by first creating each structural part separately as a solid member, including the pier, abutments, bearings, girders, crossbeam, slab, and pavement.

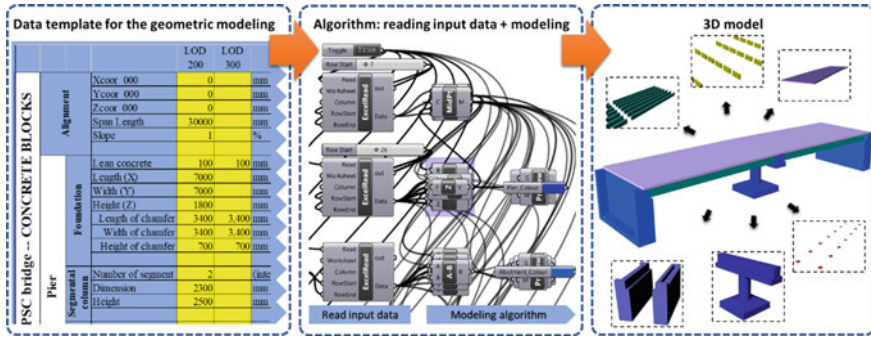


Fig. 7 Algorithm-based coding for a PSC bridge in an algorithmic tool

The reference coordinates data, dimension table data, and modelling algorithm data can be embedded into a web-based modelling platform by an open-source cloud application scripting tool or even some commercial ones. Figure 8 introduces the cloud application for the GOA.BI modelling platform. The BIM users can join with the originator to modify any parameters and algorithm. The model can be flexibly changed according to different BIM uses. Along with that, the users also can export the 3D model to a neutral format.

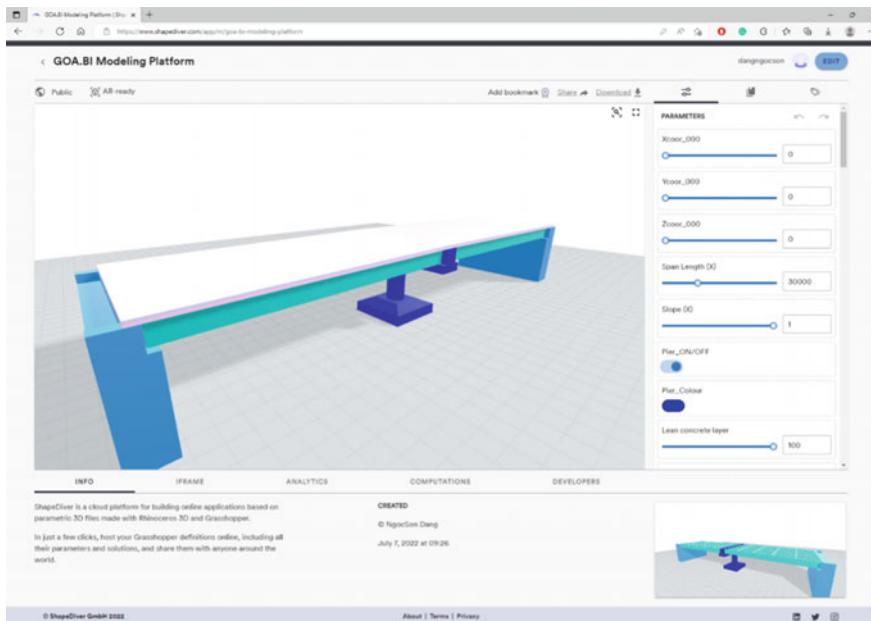


Fig. 8 Cloud applications for the GOA.BI modelling platform

The IFC Spatial Structure for the GOA.BI project and process of parsing data in existing IFC from the current GOA platform can be introduced in Fig. 9. IfcOpenShell is an open-source (LGPL) software library that helps users and software developers to work with the IFC file format. The IFC file format can be used to describe building and construction data. The form is commonly used for BIM/BrIM. IfcOpenShell helps engineers build digital platforms and tools for the built environment. Read, write, and modify BrIM using IFC, a diverse digital language from design to construction and beyond.

IfcOpenShell is unique in its extensive Python API, which includes hundreds of functions for common IFC manipulation operations. This API supports many aspects of IFC not usually kept in other tools, including cascading geometric coordinate changes, subgraph purging, appending elements, and extensive support for 4D and 5D BIM operations like cost formulas, critical path analysis, and calendar-based scheduling propagation. It is also unique in its support for HDF5 caching, voxel analysis for dealing with less-than-precise BIM geometry, and semantic SVG-based drawing generation.

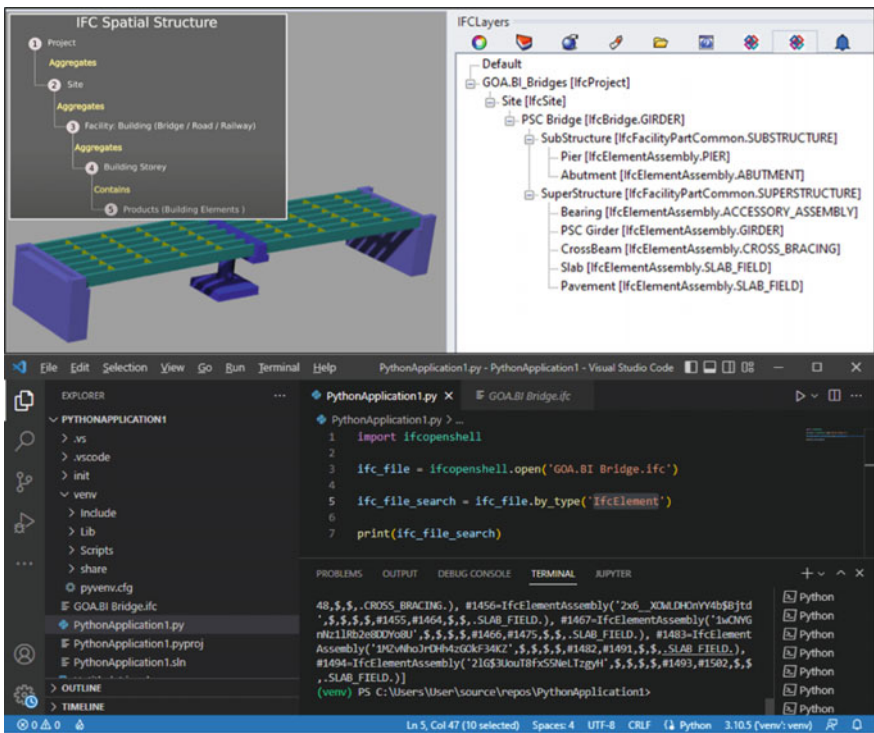


Fig. 9 IFC spatial structure and parsing IFC data by IfcOpenShell-python

Comes with many utility functions for geolocation, data extraction, IFC query filtering, and more. Figure 1 shows an example of the use of IfcOpenShell-python to parse the data from GOA.BI exported. It is possible to read the data from the input IFC file, find the appropriate information, and export that individual information for further BIM uses. In contrast, any information can be imported into the inputted IFC by the predefined template, then directly changed and exported to the new IFC model.

The android application's primary focus is to allow it to be easy to use and for the recording of anomalies and views during inspection to be done. For this, it is foreseen that most of the data to be registered does not require the user to write a lot of text, or none, depending on the field to be filled in. For this to be possible, during the anomaly registration form, the use of dropdown boxes and the provision of pre-filled content, where the user only needs to choose the appropriate option. It will also be possible to take photos and draw on them during registration to facilitate the visualization of the problem in the photo. This form will follow an order of contents to be filled in to make the experience more uniform and guided for the user. It will also be necessary for the application to have an internet connection, not only for the user authentication part but also to access data from previous inspections so that the recorded inspection information is stored and accessible to all system users. For the development of the augmented reality application, the objective is to use a 3D model of the bridge in question. You can easily see which parts' anomalies were registered and visualize more information about them. During the visualization of the holographic model of the bridge, the user must also be able to manipulate certain aspects that facilitate the visualization, such as zooming, rotating, and positioning the model in any position in space. Suppose the user wants to see more information about an anomaly in question. In that case, he should also have access to more details on that anomaly without the data obstructing or disturbing the experience. The augmented reality application must have a network connection to access all the information (Fig. 10).

Finally, the desktop/web application will include most of the features of the mobile application, such as accessing and editing data already existing in the system. The advantage of this module is that it allows for an easier way, using a physical keyboard, to add denser written content, which will help clarify certain aspects that were not detailed in the field. It will also allow you to improve specific parts of the information that may not have been explained during the inspection with the mobile application (Fig. 11).

5 Discussion

A successful framework to increase resilience in the most critical transportation infrastructure in the Atlantic Area is anticipated following the development of the SIRMA project, taking into account the database gathered from the implemented monitoring and the impact of extreme events under the effects of climate change. Additionally, this project's long-term benefits will include decreasing the risk of

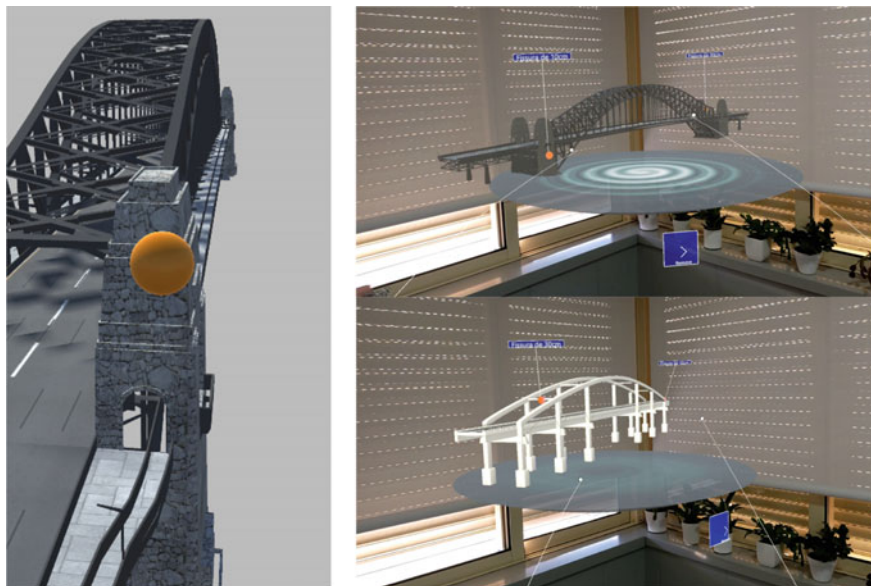


Fig. 10 Mobile application versus mixed reality application for GOA.BI project

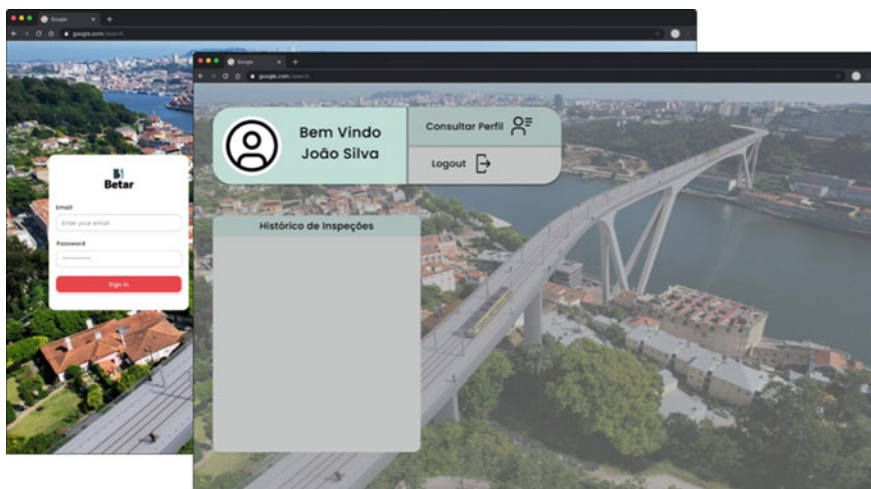


Fig. 11 Web/desktop application

extreme natural calamities, including floods and fires, on transportation infrastructure and improving population readiness for such hazards. Two public operators will test and use the proposed framework and make it available to other public and commercial operators in and outside the Atlantic Area. These organizations will

ensure such effects in conjunction with assisting partners (such as the government, municipalities). The scientific outcomes from this initiative will also be integrated with academic institutions, with some of the findings used in current or future courses (e.g. asset management, risk analysis, etc.).

Concerning the GOA.BI project, the digital revolution, has led to the design and management of numerous new and existing transportation infrastructures utilizing what is known as bridge information models (BrIM). Although BrIM models are primarily used in the design phase, they are a beneficial tool for infrastructure management during the operational stages. Therefore, it is critical to reconsider how maintenance has been carried out and how it should change to meet today's difficulties and prepare for the future. Due to this, two significant changes will be made to the current project. The first has to do with the required maintenance paradigm. A predictive maintenance paradigm will be used instead of the current preventive maintenance paradigm, which calls for several maintenance inspections and preventative treatments. The objective is to allocate resources more effectively while also being able to predict how the infrastructure's conditions will change over time. The second change concerns the new maintenance management tools' incorporation of digital elements. This modification will change two things: first, the management platform will be developed to be completely compatible with BrIM standards. On the other hand, modern inspection tools will be improved in terms of the inspector's equipment (such as a mobile tablet), the equipment utilized for the inspection (such as drones), and the features of both (e.g. digital image correlation). Mixed reality tools for information analysis and visualization will also be created to support the maintenance process.

After completing those projects, the largest Portuguese owner of transportation infrastructure, the project's partner (Infraestruturas de Portugal), will offer actual data for the new web-based platform's testing.

References

1. Hammervold J, Reenaas M, Brattebø H (2013) *J Bridg Eng* 18:153–161
2. Demirel H (2012) Impacts of climate change on transport: a focus on road and rail transport infrastructures. Françoise Nemry, Hande Demirel
3. Campo L, Caparrini F, Castelli F (2006) Use of multiplatform, multi-temporal remote-sensing data for calibration of a distributed hydrological model: an application in the Arno basin, Italy. *Hydrol Process* 20(13):2693–2712
4. Sy B, Frischknecht C, Dao H, Consuegra D, Giuliani G (2019) Flood hazard assessment and the role of citizen science. *J Flood Risk Manage* :1–14 (Dec 2018)
5. Alderson DL, Brown GG, Carlyle WM (2015) Operational models of infrastructure resilience. *Risk Anal* 35(4):562–586
6. Barber R (2015) MMO climate change adaptation report, 20
7. Costa S, Brito V, Mendonça T (2019) Transport infrastructures and asset management in Portugal: past, present and future. In: IABSE symposium 2019 Guimarães towards a resilient built environment—risk and asset management, pp 1750–1757

8. Costin A, Adibfar A, Hu H, Chen SS (2018) Building Information Modeling (BIM) for transportation infrastructure—literature review, applications, challenges, and recommendations. *Autom Constr* 94:257–281
9. Dang NS, Shim CS (2020) BIM-based innovative bridge maintenance system using augmented reality technology. *Lect Notes Civil Eng* 54:1217–1222
10. Dang NS, Shim CS (2020) Bridge assessment for PSC girder bridge using digital twins model. *Lect Notes Civil Eng* 54:1241–1246
11. Dang NS, Shim CS (2018) BIM authoring for an image-based bridge maintenance system of existing cable-supported bridges. *IOP Conf Ser: Earth Environ Sci* 143(1):012032
12. Kim D, Chung D, Shim C (2012) Development of 3D parametric models for modular bridge substructures. *Undefined*
13. Shim CS, Lee KM, Kang LS, Hwang J, Kim Y (2018) Three-dimensional information model-based bridge engineering in Korea 22(1):8–13
14. Shim CS, Kim SW, Song H-H, Yun NR (2011) Development of BIM for a maintenance system of subway infrastructures. *J KIBIM* 1(1):6–12

Development and Characterization of Controlled Low-strength Materials as a Heat Transfer Medium for Horizontal Ground-Source Heat Pump System



Young-Sang Kim and Ba Huu Dinh

Abstract In a horizontal ground-source heat pump system, thermal properties of the material backfilling the ground heat exchanger are the key factor that affects the performance of the system. The aim of this study is to evaluate the feasibility of steel-making slag-based controlled low-strength materials (CLSM) as a heat transfer medium for horizontal ground-source heat pump systems. Firstly, the engineering properties of CLSM mixtures were evaluated with different steel-making slag contents and steel-making slag types. Secondly, the effects of the GWT level drop on the thermal–hydraulic properties of different backfill materials and the performance of the system was investigated using a numerical analysis model of COMSOL Multiphysics based on measured water retention characteristics. The in-door thermal response test was conducted to validate the numerical analysis model and access the heat exchange rate of spiral-coil GHE backfilled with CLSM and natural sand. Finally, to access and compare the beneficial use of the CLSM over the typical soil, an economic analysis of 50 case studies for the horizontal GHE was performed. The results indicate that the suggested steel-making slag-based CLSM satisfied all requirements of common backfill material. Furthermore, using ground steel-making slag to replace the sand in the CLSM mixture can enhance the thermal conductivity up to 2.35 W/(mK), which is double that of the conventional grout (bentonite). Another advantage of CLSM is a high air-entry value, which can limit the influence of the GWT drop. Finally, as expected, the GHE backfilled with the CLSM shows a better economic performance compared to that of the GHE backfilled with an ordinary soil owing to its high heat transfer performance.

Keywords Steel-making slag · Ground-source heat pump system · Ground heat exchanger · Thermal conductivity · CLSM

Y.-S. Kim (✉) · B. H. Dinh

Department of Architecture and Civil Engineering, Chonnam National University, Yongbong-Ro 77, Buk-Gu, Gwangju 61186, South Korea

e-mail: geoyskim@jnu.ac.kr

1 Introduction

The ground-source heat pump (GSHP) system is a well-known environmentally clean and energy-efficient technology for the cooling and heating of buildings with ground energy sources. The horizontal GSHP system is expected to widely use in Korea since it is easy to install and has low construction cost compared to that of vertical GSHP system; however, its low heat transfer efficiency results in the large installation area required. By-product-based controlled low-strength material (CLSM), with a relatively high thermal conductivity and good workability, is expected to utilize in the horizontal GSHP in order to increase the heat transfer efficiency of the system [1]. Therefore, this study conducted a novel performance evaluation of the horizontal GSHP system backfilled with CLSM through experimental, numerical, and economic approaches. It should be noted that horizontal GHE is generally embedded at a shallow depth above the GWT, where unsaturated soil exists [2, 3]. The change in the GWT strongly affects the thermal properties of the soil and therefore influences the heat transfer efficiency of the HGHEs. Thus, the effect of the GWT level drop on the heat transfer performances of HGHEs should be considered. Besides increasing the thermal conductivity of backfill materials, another solution to increase the heat transfer performance of the horizontal GSHP system is using the new ground heat exchanger type to increase heat exchanger length (i.e., slinky, spiral-coil types). Yoon et al. [4] found that using spiral-coil and slinky-type pipes increased the total heat exchange nearly twice that of the conventional GHEs (U-type). The results presented above demonstrated that using the CLSM and spiral-coil type is a potential solution to enhance the performance of the horizontal GSHP system; however, it may cause an increase in the initial investment cost [1, 4]. The economic analysis is, therefore, necessary to answer the question: “Whether the high heat transfer performance of the spiral-coil GHE and CLSM can offset its high installation cost?”.

2 Experimental Programs

2.1 *Engineering Properties of Controlled Low-strength Materials*

The CLSM mixture typically contains cement, fly ash, fine aggregate, and water. This study used different steel slag sizes (raw steel slag and ground steel-making slag) and content (10%, 20%, and 30%) to replace the natural sand in the control mixture. The engineering properties of mixtures, such as flowability, unconfined compressive strength (UCS), and thermal conductivity, were tested in accordance with applicable ASTM Standards (2004): D 6103, D 4832, and D 5334, respectively.

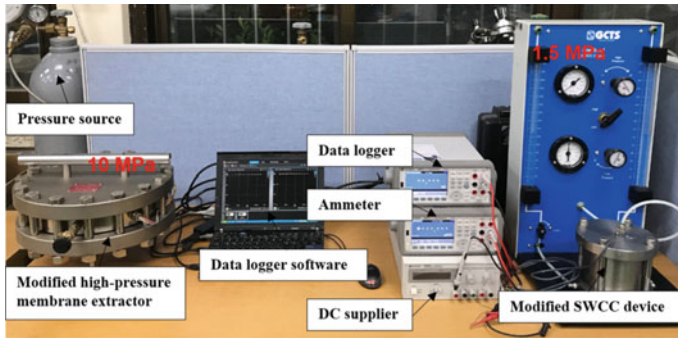


Fig. 1 Modified SWCC device and modified high-pressure membrane extractor

2.2 Performance Evaluation of Horizontal GSHP System Considering Hydraulic-Thermal Characteristics of Backfill Material and Groundwater Table Level Drop

In the experimental study, the soil–water characteristic curves and unsaturated thermal properties of backfill materials (natural sand (NS), weathered granite soil (WGS), and controlled low-strength materials (CLSM)) were defined using modified 150-SWCC devices and a high-pressure membrane extractor, coupled with a thermal conductivity measurement system (Fig. 1). Subsequently, the influence of the GWT level change on the moisture content of the backfill materials was investigated using a seepage analysis (SEEP/W) [2]. Furthermore, the thermal performance analysis of the HGHEs with different backfill materials was conducted using a commercial finite element code program (COMSOL Multiphysics) (Fig. 2). The experimental program and numerical model were presented in detail in [2, 5].

2.3 In-Door Thermal Response Test and Economic Analysis

The TRT test set-up is shown in Fig. 3. A spiral-coil type heat exchanger was buried in a steel box ($5 \times 1 \times 1$ m) and backfilled with CLSM. The inlet and outlet fluid temperature were measured by resistance temperature detector (RTD) sensors connected with a data logger program (Fig. 3). Then, a finite element model was created using COMSOL Multiphysics to validate the experiment model (Fig. 4) [3].

After validation, the model was scaled up to calculate the annual heat exchange of a full-size horizontal ground heat exchanger. The AHE value and the total construction costs of the 50 cases study (see Table 1 in Fig. 15) (various with installation depth and flow rate of fluid) were used to access the beneficial use of CLSM by using economic parameters such as simple payback period (SPP) and internal rate of return (IRR).

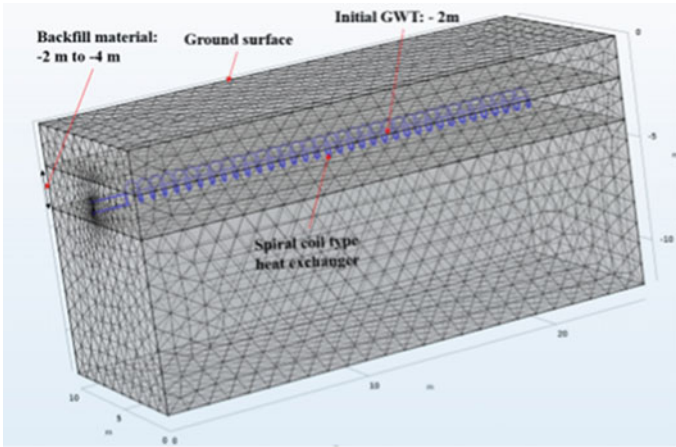


Fig. 2 Numerical model

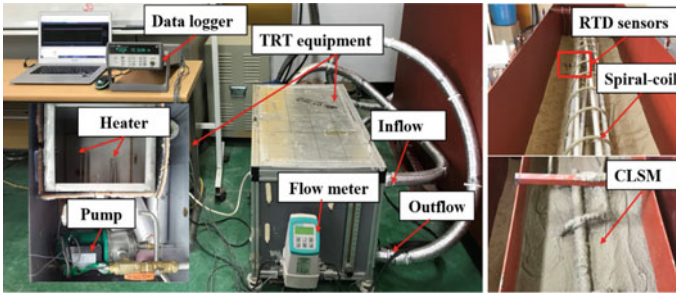
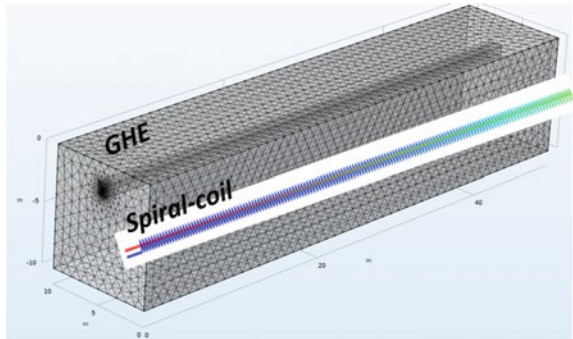


Fig. 3 Thermal response test set-up

Fig. 4 Full-size numerical model



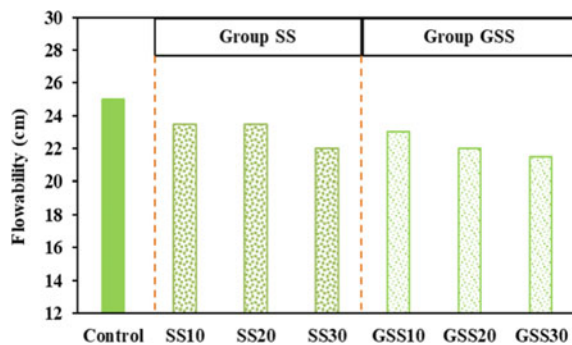
3 Results and Discussion

3.1 Engineering Properties of Proposed CLSMs

Flowability is a very important factor for the investigation of self-leveling ability of CLSM. A high flowability is necessary to completely fill a GHE without any compaction effort. Figure 5 presents the flowability test results of the CLSM mixtures. The flowability decreases with increasing steel-making slag content. This is probably due to the strong water absorption property of the steel-making slag. However, flowability of all CLSM mixtures in this study ranged from 21.5 to 25.0 cm and can be classified as high flowability (from 20 to 30 cm) according to ACI. The unconfined compressive strengths of all CLSM mixtures are presented in Fig. 6. The UCS increases with increasing curing time, and all mixtures with steel-making slag have higher UCS than the controlled mixture with natural sand. Using raw steel-making slag (>10%) causes a decrease in the UCS due to the inherent voids inside the slag particles, while UCS significantly increases with the increase of ground steel-making slag content (Fig. 6). Because grinding slag can (1) reduce the voids and (2) increase the specific surface area resulting in the improving pozzolanic reaction ability between slag and fly ash [1].

The thermal conductivities of all CLSM mixtures considered in this study and those taken from the literature are presented in Figs. 7 and 8, respectively. In a saturated condition, the thermal conductivities of the CLSM mixtures in this study range from 2.00 to 2.35 W/mK. The thermal conductivity of the CLSM proposed in this study is significantly higher than those of conventional grout materials such as cement grout (0.80 W/mK), high-solids bentonite (0.87 W/mK), and thermally enhanced bentonite (1.46 W/mK) [1]. Moreover, the thermal conductivity of steel-making slag-based CLSM is higher than pond ash-based CLSM (1.6 W/mK) [1].

Fig. 5 Flowability



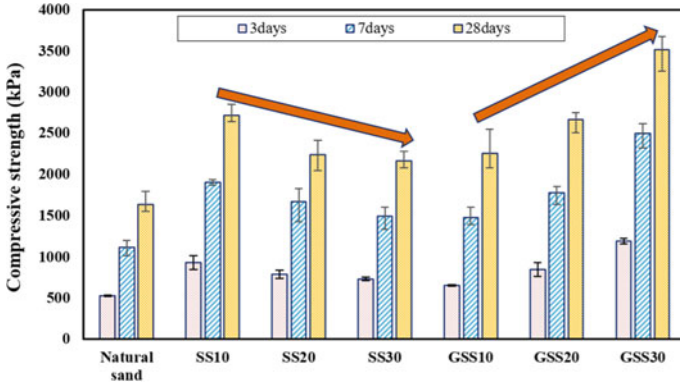


Fig. 6 Unconfined compressive strength

Fig. 7 Thermal conductivity of proposed CLSM

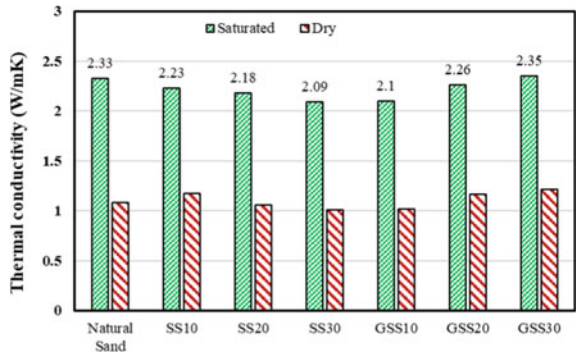
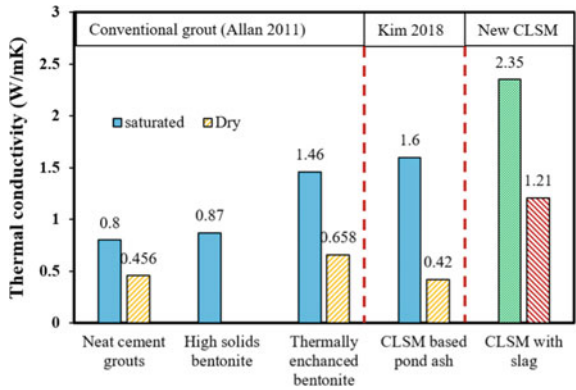


Fig. 8 Thermal conductivity of different backfill materials



3.2 Water Retention Curves and Thermal Conductivity-Water Content Relationship

The water retention curves the backfill materials are presented in Fig. 9. The air-entry value (AEV) of the proposed CLSM mixture, which represents the water retention ability, was significantly greater than that of the natural sand and weathered granite soil. The AEV of the CLSM was 1000 kPa, whereas the AEVs of natural sand and WGS were 4 kPa and 16 kPa, respectively. The relationships between the normalized thermal conductivity and volumetric water content of the backfill materials are shown in Fig. 10. The thermal conductivity significantly decreases with the decrease in the volumetric water content. A linear relationship is observed for all backfill materials.

Fig. 9 Water retention curves

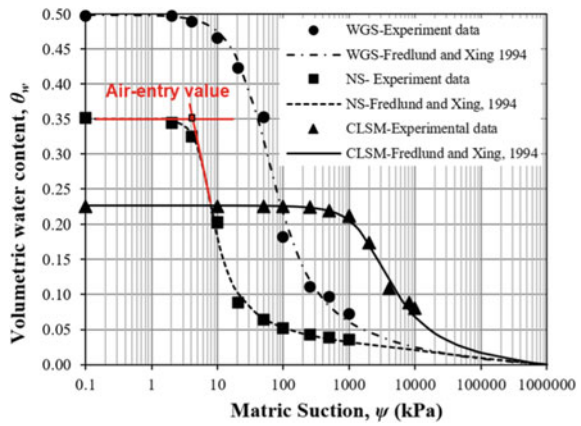
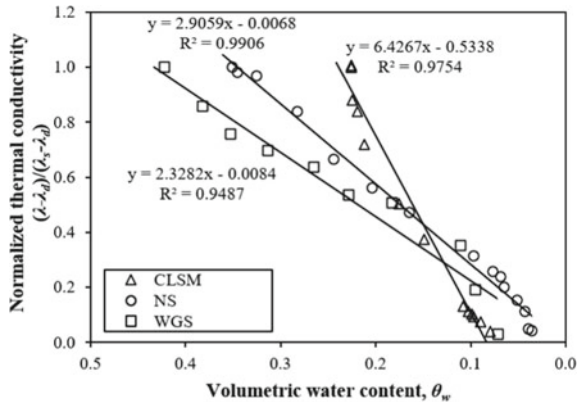


Fig. 10 Normalized thermal conductivity and volumetric water content



3.3 Effect of GWT Level Drop on Thermal Conductivity of Backfill Materials

Figure 11 presents the thermal conductivity variations in the unsaturated WGS caused by the GWT level drop. The pore-water pressure versus depth, as a result of the SEEP/W analysis, is displayed in Fig. 11a. When the GWT level drops, the pore-water pressure decreases, leading to an increase in the suction and a decrease in the volumetric water content. In this case, the SWCC from the experimental results (Fig. 9), which provides the relationship between the matric suction and volumetric water content, can be used to convert the pore-water pressure versus depth (Fig. 11a) to a volumetric water content versus depth (Fig. 11b). To determine the thermal conductivity profile (Fig. 11c), the thermal conductivity–volumetric water content relationship (Fig. 10) and the volumetric water content profile (Fig. 11b) are employed. Using the same analysis method presented above, the thermal conductivity profiles of the NS and CLSM are shown in Figs. 12c and 13c, respectively.

When the GWT decreases from -2 m to -12 m, the thermal conductivities of the WGS and NS at the middle of GHE (depth = -3 m) are significantly reduced, as presented in Figs. 11c and 12c, respectively. This is owing to the high volumetric water content and low AEV of the WGS and NS, causing sensitivity to the thermal conductivity. In contrast, the thermal conductivity of the CLSM is insignificantly

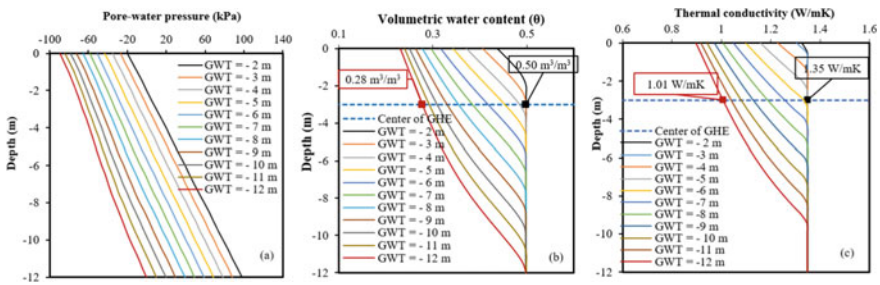


Fig. 11 WGS: a Pore-water pressure, b volumetric water content, c thermal conductivity

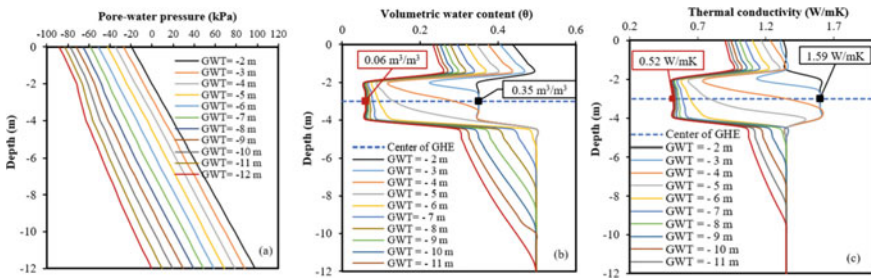


Fig. 12 Natural sand: a Pore-water pressure, b volumetric water content, c thermal conductivity

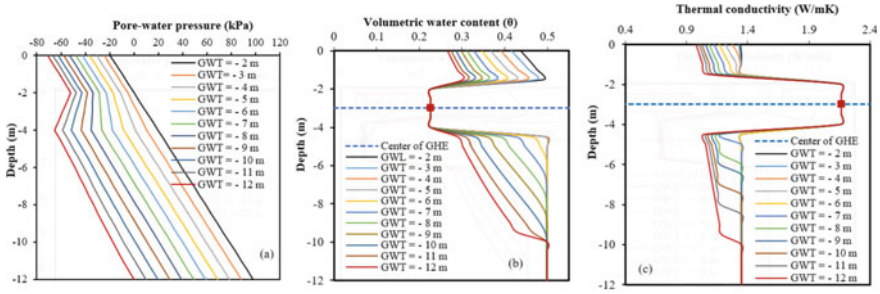


Fig. 13 CLSM: **a** Pore-water pressure, **b** volumetric water content, **c** thermal conductivity

affected by the GWT reduction owing to its low volumetric water content and very high AEV. The AEV of CLSM is 1000 kPa, i.e., 250 times and 166 times higher than that of NS (4 kPa) and WGS (16 kPa), respectively. However, when the GWT level drops from -2 m to -12 m, the maximum suction caused by the decrease in the pore-water pressure is 70 kPa (Fig. 13a), which is much lower than that of the AEV of the CLSM. Consequently, the volumetric water content (Fig. 13b) and the thermal conductivity (Fig. 13c) of CLSM are not affected by the GWT level drop. The results presented in Figs. 11c and 13c can be utilized as input data for heat transfer simulations.

Figure 14 shows the heat exchanger performances of the HGHEs with reference to the decrease in the GWT. The HGHE backfilled with NS is the most influenced by the decrease in the GWT (63% decrease) (Fig. 14b). This is owing to the high volumetric water content and the low water storage capability (AEV of 4 kPa) of the NS; thus, the drop in the GWT level has the most significant effect on the thermal conductivity of the NS (see Fig. 12c). Regarding the WGS (Fig. 14a), the reduction in the GWT causes a 42% decrease in the heat exchange rate at the quasi-steady-state conditions. Interestingly, when the GWT changes from -2 m to -4 m, the heat exchange rate slightly decreases; however, when the reduction is beyond 2 m, a significant reduction in the heat exchange rate is observed. This result implies that if the change in the GWT causes the suction to exceed the AEV, the water in the largest pore size will be replaced by air leading to a dramatic reduction in the thermal conductivity; consequently, the heat exchange rate of the system will be significantly reduced. Concerning the CLSM, with the highest AEV and strong water storage ability, the effect of the GWT level drop is not noticeable. The results presented above imply that the GWT level drop should be considered when evaluating and designing HGHEs systems to avoid overestimations, especially in the areas with a high GWT level drop, or where the soil has a weak water storage ability (low AEV) (e.g., sand and sandy soil).

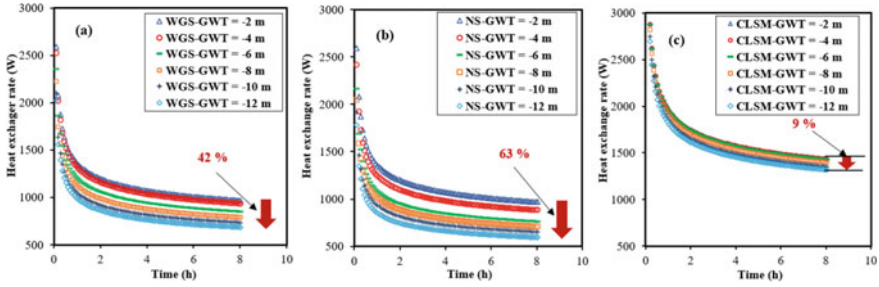


Fig. 14 Heat exchange rate of GHE backfilled with **a** WGS, **b** NS, and **c** CLSM

3.4 TRT and Economic Analysis Results

A very well agreement in the experimental (TRT) and numerical results (COMSOL) (Fig. 15a outlet fluid temperature, (b) soil temperature) demonstrated that the model proposed in Fig. 4 and the parameters used for analysis are suitable to simulate the heat transfer in the horizontal GSHP system. With the same installation depth, the total construction cost of the Spiral-CLSM type is about 22% higher than that of the Spiral-Soil (Fig. 15c) since the CLSM costs about 40 USD/m³ [1] while the soil is free to use. However, above the groundwater table level, where the horizontal GSHP system is located, the unsaturated thermal conductivity of CLSM is 1.68 W/(mK), which is about 52% higher than that of the unsaturated soil (1.16 W/(mK)). As a result, the annual heat exchange rate of the Spiral-CLSM is significantly higher than that of the Spiral-Soil (39% higher); thus, the net cash inflow of the Spiral-CLSM is considerably higher than the Spiral-Soil one. Consequently, the Spiral-CLSM has a lower simple payback period and higher IRR, compared to that of the Spiral-Soil one. Note that the annual heat exchange increases with an increase in the installation depth and fluid velocity (Fig. 16a); however, it causes a significant increase in the total construction cost (Fig. 15c) (i.e., excavation cost) and operation cost (i.e., the electrical power consumption of the pump). The Spiral-CLSM type with a buried pump depth of 2.5 m and a fluid velocity of 10 l/min has the lowest SPP and highest IRR (case 44); thus, it is the most beneficial use case from the standpoint of the economic analysis.

4 Conclusions

This study comprehensively evaluated the feasibility of steel-making slag-based CLSM as a heat transfer medium for horizontal ground-source heat pump systems through engineering properties, thermal performance, and economic aspects. The advantages of CLSM were found as follows: (1) CLSM has a high flowability; thus, it can fill the GHE without compaction; it is especially appropriate for spiral-coil

Fig. 15 a Outlet fluid temperature, b soil temperature, c total initial costs

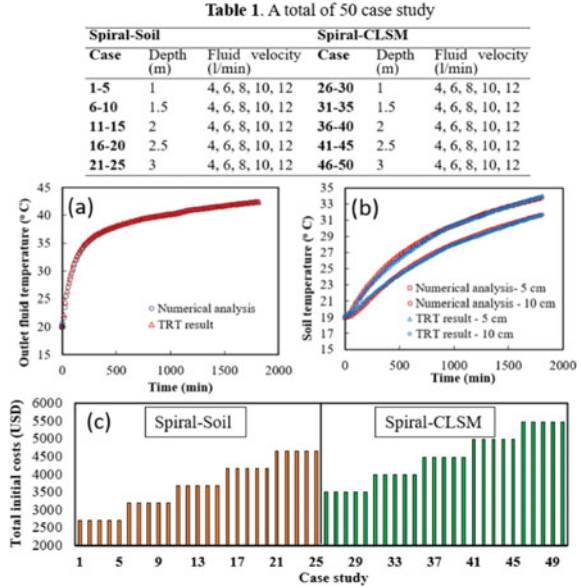
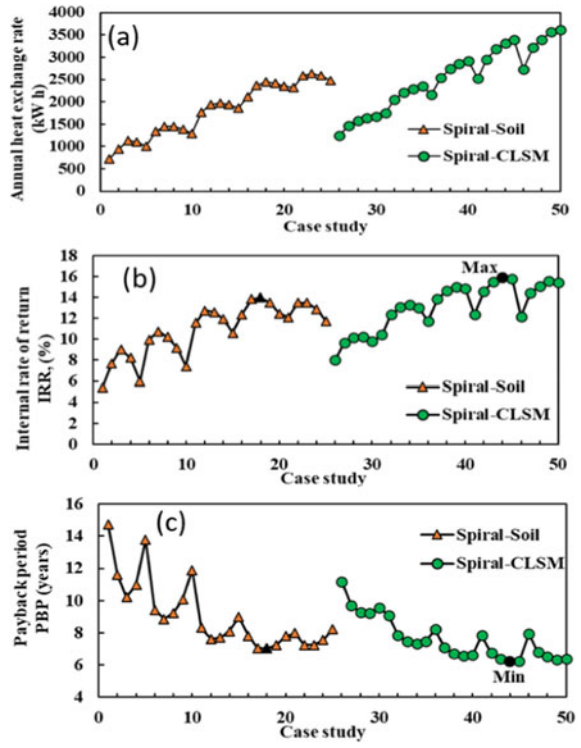


Fig. 16 a Annual heat exchange rate, b internal rate of return, c payback period



GHE. (2) CLSM has a high thermal conductivity at both saturated and unsaturated conditions; thus, it can improve the heat transfer performance of the horizontal GHE. (3) Especially for spiral-coil GHE, the CLSM has a UCS of 2.0 MPa (or higher); thus, it can protect the coil pipe from broken and shaped deformation. (4) The GWT level reduction caused an adverse effect on the heat transfer performance of horizontal GHE, especially where the soil has a weak water storage ability (low AEV) (e.g., sand and sandy soil). As a solution, using CLSM with a strong water retention ability (AEV = 1000 kPa) can limit the influence of GWT level drop. (5) CLSM can incorporate many kinds of waste materials and by-products (i.e., pond ash, bottom ash, steel-making slag); therefore, the use of CLSM is not only economically beneficial but also has a good impact on waste treatment and environmental protection.

Acknowledgements This work was supported by a National Research Foundation of Korea (NRF) grant funded by the Korean Government (MSIT) (No. NRF-2021R1A2B5B01002809) and Korea Agency for Infrastructure Technology Advancement (KAIA) (No. 22RITD-C162545-0240982119420002).

References

1. Kim YS, Dinh BH, Do TM, Kang GO (2020) Development of thermally enhanced controlled low-strength material incorporating different types of steel-making slag for ground-source heat pump system. *Renew Energy* 150:116–127. <https://doi.org/10.1016/j.renene.2019.12.129>
2. Dinh BH, Go GH, Kim YS (2021) Performance of a horizontal heat exchanger for ground heat pump system: effects of groundwater level drop with soil–water thermal characteristics. *Appl Therm Eng* 195:117203. <https://doi.org/10.1016/j.applthermaleng.2021.117203>
3. Dinh BH, Kim YS, Yoon S (2022) Experimental and numerical studies on the performance of horizontal U-type and spiral-coil-type ground heat exchangers considering economic aspects. *Renew Energy* 186:505–516. <https://doi.org/10.1016/j.renene.2022.01.001>
4. Yoon S, Lee S, Go G (2015) Evaluation of thermal efficiency in different types of horizontal ground heat exchangers. *Energy Build* 105:100–105. <https://doi.org/10.1016/j.enbuild.2015.07.054>
5. Dinh BH, Kim YS, Kang GO (2020) Thermal conductivity of steel-making slag-based controlled low-strength materials over entire range of degree of saturation: a study for ground source heat pump systems. *Geothermics* 88:101910. <https://doi.org/10.1016/j.geothermics.2020.101910>

Materials for Construction

Experimental Investigation of Cs of Reinforced Concrete Structures in Sea Island Regions of Khanh Hoa (Viet Nam) Application on Service Life Prediction



Thi Thu Hien Dang, Duy Huu Pham, Thi Bach Duong Nguyen, and Trong Chuc Nguyen

Abstract Corrosion of steel rebar's in reinforced concrete (RC) structures, known as main cause reducing their service life, could be significantly accelerated in maritime regions where environmental chlorine ions (Cl^-) content is very high. The crucial phrase of corrosion phenomenon, initial corrosion phrase concerning the penetration of Cl^- through concrete cover, depends deeply on the surface chlorine ions content (Cs). The Cs data should be gathered from in-situ structures. For this motivation, in this paper, experimental investigation on Cs is performed. The surface chlorine ions (Cs) content of RC structure is obtained by extrapolating experimental data gathered from in-situ RC samples in the tide zones of sea island regions of Khanh Hoa (Viet Nam). Then, using these estimated Cs at different ages, it is possible to establish empiric evolution of surface chlorine ions content versus the concrete age. Unlikely to constant value of Cs versus concrete age as practical routine, results of this paper show non-negligible time-dependence of Cs. And, based on experimental results in this paper, prediction of service life of constructions is performed by durability method. It is concluded that service life estimated by durability method is 4 times smaller than design working life of studied structures.

Keywords Chloride surface content · Empiric time evolution · Practice · Life service · Durability

D. H. Pham · T. B. D. Nguyen
University of Transport and Communications, Hanoi, Vietnam

T. T. H. Dang (✉) · T. C. Nguyen
Le Quy Don Technical University, Hanoi, Vietnam
e-mail: thuhien118v2@gmail.com

1 Introduction

It is shared by many authors that the corrosion of steel reinforcement due to chloride ions (Cl^-) penetration is the major cause to reduce durability capacity of RC structure. In fact, chloride ions ingress in contact with steel rebar's (reinforcement) cause corrosion with chemical reaction which continue to produce Cl^- as summarized in [1]. For corrosion phenomenon, the crucial phrase is initial corrosion which consists in the penetration of Cl^- from surface of structure toward steel rebar through concrete cover. In general, to prevent the penetration of Cl^- , a "good" cover concrete as corrosion shield against initial chlorine ions penetration must be ensured for RC structures.

Since the first instance of corrosion (initial corrosion) is very important, the time necessary for Cl^- to penetrate from the surface concrete to rebar contact is the key element to determine service time of RC structures. The diffusive of chlorine ions in concrete is described by Fick equation:

$$\frac{\partial C(x, t)}{\partial t} = D \frac{\partial^2 C(x, t)}{\partial x^2} \quad (1)$$

where D is diffusive coefficient in concrete, which may lightly depend on time and depth (in practice, a constant value of D is used). To solve this "Eq. (1)", it is necessary to determine initial and boundary conditions, such as chlorine content at initial instant $C(x, t = 0) = 0$ and chlorine surface content $C(x = 0, t = t_i) = C_{si}$, where C_{si} is surface chlorine ions content at time i . Therefore, information on C_s is necessary to predict Cl^- penetration duration.

It is known that the surface chlorine ions content depends on the environmental chlorine ions content, maintenance conditions, structure shapes, etc. Summarized in [2], C_s is supposed to be independent of time and can be determined by experimental data. For example, in tide zones, C_s is varied from 0.75% to 0.9% of concrete masse. In this case where C_s is time- constant, the solution of "Eq. (1)" is known

$$C(x, t) = C_{s,cl} \left(1 - \text{erf} \left(\frac{x^d}{\sqrt{4D(t) \cdot t}} \right) \right) \quad (2)$$

However, more recent researches have demonstrated that C_s depends significantly on time as concluded in [3] based on laboratory tests in under shallow immersion conditions. Then, the solution "Eq. (2)" is not valuable for shallow immersion such as in the tide zones of sea island regions of Khanh Hoa (Viet Nam).

In practice, experimental data for chlorine ion content in the depth of RC structure can be gathered by testing samples from in-situ RC structures to determine surface chlorine ions content of RC structure (C_s) as seen in [2, 4, 5].

Consequently, it is necessary to perform gathering data for Cs from in-situ structure for tide zones of sea island region of Khanh Hoa to estimate lifetime of RC structure in this region. That motivation leads us to perform in this paper experimental studies of the chloride surface content of concrete structures in the tide zone of Khanh Hoa regions (Viet Nam) by extrapolating experimental data gathered from in-situ concrete samples. Then, using these estimated Cs at different ages, it is possible to establish empiric evolution of surface chlorine ions content versus the concrete age. Unlike to constant values of Cs versus concrete age as practically used value, results of this paper show non-negligible time-dependence of Cs. And, based on experimental results in this paper, prediction of service life of constructions is performed by durability method. It is concluded that service life estimated by durability method is 4 times smaller than design working life of studied structures.

2 Empiric Evolutions of C_s of RC Structures in Khanh Hoa Regions

2.1 Method of Estimation of Chlorine Ion Content at Surface (C_s)

According to [6, 7], the content of chlorine ion at surface is varied as function of time and can be expressed as following:

$$C_s(t) = C_1 \cdot t^n \quad (3)$$

Coefficients C_1 and n can be easily obtained from fitting experimental data to this curve of "Eq. (3)". However, when gathering experimental data from in-situ samples, it is impossible to directly determine the value of C_s at given age (t) because each sample has a certain thickness, and its measured value is associated to mean depth of this sample. Therefore, it is necessary to extrapolate from chlorine ions content in the depth of concrete to obtain C_s at the surface of concrete. According to [5], evolution of chlorine ion content can be expressed as natural logarithm as following:

$$C_{CL}(x) = C_s \cdot e^{-mx} \quad (4)$$

where C_s and m can be obtained by fitting experimental data at different depth of concrete $C_{CL}(x)$ from in-situ samples.

2.2 Experimental Data of Chlorine Ion Content in Depth of Concrete

The extraction of in-situ concrete samples is processed according to the Vietnamese standard 7572-15-2006 [8] (Fig. 1).

In this region, mean value of environmental temperature is about 28.2 °C with min–max values of 24.5–34.2 °C. Humidity (amount of water vapor in air) is varied from 75 to 80%. During gathering RC samples, the sea water composition is also examined and presented in Table 1.

In-situ concrete samples are extracted from tide zones of sea island regions of Khanh Hoa at different ages of concrete and different depths, then analyzed at the laboratory of Da Nang University of Technology. The experimental data are presented in Table 2.



Fig. 1 Example of existing concrete structure (left) and extraction of sample (right)

Table 1 Composition of sea water in extraction site

Composition	Unit	Measure
pH	–	6.68
DO	mg/l	6.0
Cl ⁻	mg/l	19,312
Na ⁺	mg/l	13,685
Ca ²⁺	mg/l	415
SO ₄ ²⁻	mg/l	4449
Mg ²⁺	mg/l	984

Table 2 Experimental data from in-situ concrete samples gathered from tide zones of sea island regions of Khanh Hoa

N°	ID	Age (years)	Chlorine ion content (% of concrete mass)					
		Depth	0-1 cm	1-2 cm	2-3 cm	3-4 cm	4-5 cm	5-6 cm
1	K11-7 year	7	0.6023	0.3985	0.2976	0.2124	0.1332	0.0887
2	K12-7 year	7	0.5981	0.4106	0.3076	0.2348	0.1657	0.1045
3	K21-12 year	12	0.8089	0.6202	0.4923	0.3732	0.2889	0.2112
4	K22-12 year	12	0.8223	0.5923	0.4378	0.3156	0.2445	0.1965
5	K31-18 year	18	0.9962	0.7979	0.6834	0.5123	0.4129	0.4389
6	K32-18 year	18	0.9201	0.7312	0.7012	0.5678	0.4121	0.3878
7	K41-22 year	22	1.0980	0.6923	0.7256	0.5021	0.4272	0.3123
8	K42-22 year	22	1.0623	0.7135	0.6923	0.4870	0.4240	0.3340

2.3 Estimation of Surface Chlorine Ions Content C_s

The surface chlorine ions content is obtained by fitting the “Eq. (4)” to the experimental data at Table 2. The results of C_s are presented in Table 3 where C_s is varied as function of concrete age.

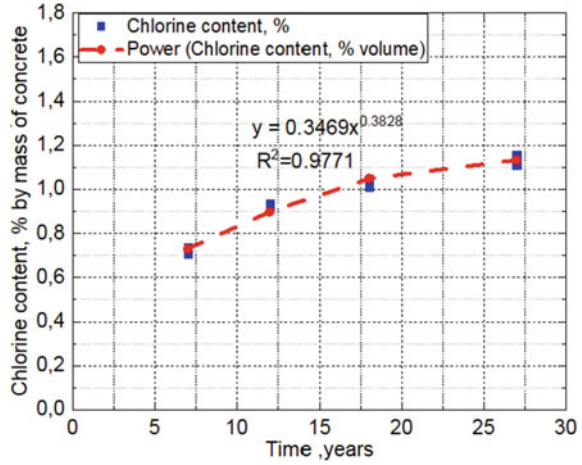
According to the “Eq. (3)”, the evolution of surface chlorine ions content is obtained by fitting data in Table 3 the “Eq. (3)”. Then, empirical values of coefficient C_1 and n are obtained as following (Fig. 2):

$$C_s(t) = 0.3469t^{0.3828} \quad (5)$$

Table 3 Estimation of surface chlorine ions content from experimental data

ID	Age (years)	Chlorine ion content at surface C_s (% of concrete mass)	m	Coefficient of goodness
K11-7 year	07	0.7363	-0.3377	0.9953
K12-7 year	07	0.7090	-0.3350	0.9926
K21-12 year	12	0.9345	-0.2659	0.9983
K22-12 year	12	0.917	-0.2900	0.9950
K31-18 year	18	1.0487	-0.1820	0.9379
K32-18 year	18	1.0107	-0.1790	0.9632
K41-27 year	22	1.1558	-0.2320	0.9511
K42-27 year	22	1.1126	-0.2200	0.9695

Fig. 2 Empiric time evolution of Cs in tide zones of Khanh Hoa regions



3 Estimation of Service Life Based on Experimental Data of Cs

3.1 Method of Service Life Prediction

As mentioned, the durability of concrete (T_d) can be obtained by sum of initial corrosion (phrase 1: T_{ini}) and propagation corrosion (Phrase 2: T_p):

$$T_d = T_{ini} + T_p \tag{6}$$

The mean value estimated for phrase 2 for RC of grade C30 with water/cement ratio of 0.45 is about 6 years (recommended value $T_p = 6$ years according to [9]). Duracrete [10] has proposed a simplified equation to determine the initial corrosion time (T_{bd}) as follows:

$$T_{ini} = \left[\frac{(x - \Delta x)^2}{4D_{28}k_c k_e t_{28}^m \left(\operatorname{erf}^{-1} \left(1 - \frac{C_{CR}}{C_s} \right) \right)^2} \right]^{\frac{1}{1-m}} \tag{7}$$

where

- x is depth of designed concrete cover (m); $x = x^d = 0.075$ m;
- Δx tolerance of concrete cover thickness (m); $\Delta x = 0.008$ m, according to [2];
- k_c coefficient of maintenance condition, $k_c = 0.79$, according to [2];
- k_e coefficient of environmental condition; $k_e = 0.92$ for tide zones, according to [2];

- D_{28} coefficient of diffusive of chlorine ion at 28 days old [9]; for W/C ratio = 0.40; ($N/X = 0.40$).

$$D_{28} = 1 \times 10^{(-12.06+2.4N/X)}$$

$$\rightarrow D_{28} = 7.943E - 12(\text{m}^2/\text{s}) = 0.000255(\text{m}^2/\text{year})$$

- $t_{28} = 28 \text{ days} = 0.0767 \text{ year}$.
- m coefficient taking account the age of concrete, $m = 0.2$ for ordinary concrete.
- erf is error function.
- C_{CR} yielding value of corrosion on steel surface, $C_{CR} = 0.8\%$ of concrete mass = 0.15% of binder mass [2].
- Surface chlorine ion content C_s depends also in time (T_{ini}), denoted $C_s(T_{ini})$.

By replacing the empiric time-dependence of $C_s(T_{ini})$ previously established in “Eq. (5)”, the “Eq. (6)” can be solved with T_{ini} as unknown, the penetration of Cl^- is then obtained.

3.2 Numerical Application of Service Life Prediction

By using the semi-empirical procedure to obtain C_s , the time necessary of initial corrosion (T_{ini}) is obtained by replacing the C_s from Eq. (5) to the “Eq. (7)”. The estimation time (T_{ini}) of 16.8 years is then found.

Finally, the durability capacity time estimated according to corrosion time “Eq. (6)” is equal to $16.8 + 6 = 22.8$ years. This capacity is much smaller than Esperance age of concrete designed according to ordinary concrete (normally at 100 years).

4 Conclusions

In this study, experimental data of chlorine ions content are gathered from in-situ concrete samples extracted from tide zones of sea island regions of Khanh Hoa, at different ages and different depths. Extrapolation in function of depth can be processed and lead us to estimations of surface chlorine ions content (with depth $x = 0$) (C_s). From these estimated values of C_s at surface of concrete at different ages (t), empirical time evolution law of chlorine ions content is established and allows us to estimate the time necessary for Cl^- to penetrate from the surface to the steel rebar contact. For ordinary concrete in tide zones of sea island regions of Khanh Hoa, the corrosion time estimated is about 23 years, which is much less than design lifetime normally estimated at 100 years. Therefore, it is necessary to consider the Cl^- penetration to evaluation durability capacity of concrete in tide zones of sea island regions of Khanh Hoa. Even experimental data given in this paper is numerous,

more gathering of in-situ samples may be recommended in the future work to map all data of Cs representative for island regions of Khanh Hoa.

References

1. Gladis C, Paulo Sérgio B, Denise CB (2013) Chloride penetration depth in Silica Fume concrete. *IACSIT Int J Eng Technol* 5(6)
2. Phạm DH, Trần TT, Thái KC, Đào VD, Nguyễn TS (2016) Theory of corrosion. Design for durability (Language Vietnamese). Nhà xuất bản Giao thông vận tải, Hà Nội
3. Jun L, Kaifeng T, Dong P, Zongru L, Weilu W, Feng X (2014) Surface chloride concentration of concrete under shallow immersion conditions. *Materials*
4. Chuanqing F, Xianyu J, Nanguo J (2010) A modeling of chloride ions diffusion in cracked concrete. In: *Engineering, science, construction, and operations in challenging environments*, pp 3579–3589
5. Ho VQ (2016) Research on durability of sulfate and chlorine of concrete of coastal regions in Central-North regions in Viet Nam, Thesis dissertation. (Language Vietnamese)
6. Uji K, Matsuoka Y, Maruya T (1990) Formulation of an equation for surface chloride content of concrete due permeation of chloride. In: *Corrosion of reinforcement in concrete*, society of chemical industry, London, UK, pp 258–267
7. Stewart M, Rosowsky DV (1998) Structural safety and serviceability of concrete bridges subject to corrosion. *J Infrastruct Syst* 4(4):146–155
8. TCVN 7572-15:2006 (2016) Vietnamese standard for concrete and mixture—experimental process
9. Ehlen MA, Michael DT, Evan CB (2009) Life-365 service life prediction model™ version 2.0. *Concr Int* 31(5):41–46
10. DuraCrete (2000) Probabilistic performance based durability design of concrete structures, The European Union-Brite EuRam III

Performance Evaluation and Mix Proportion Design of Concrete Using Low-quality Recycled Aggregate in Vietnam



Huynh Nguyen Van, Yasuhiro Dosho, Duc Nguyen Anh,
and Sang Nguyen Thanh

Abstract In Vietnam, the amount of generated construction waste is rapidly increasing along with economic and social development. According to a report from the World Bank, the amount of treated construction waste was 1.8 million tons in 2018, but the amount of untreated construction waste was considerably larger. If the construction waste is not recycled, it will become a huge environmental problem. According to the World Bank, the Vietnamese government envisions a construction waste recycle rate of 60% by 2025, most of which will be used as leveling material, roadbed material and non-fired brick. To improve the recycle rate of construction waste, a measurement for disseminating the use of low-quality recycled aggregate (recycled aggregate class L) in concrete is necessary. In this study, by mixing low-quality recycled and normal aggregates in a suitable replacement ratio, a relative quality index method was used for evaluating the concrete's performance. Accordingly, a mix proportion of concrete using low-quality recycled aggregate can be designed that satisfies Vietnam's required performance.

Keywords Low-quality recycled aggregate · Recycled aggregate concrete · Relative quality index method · Vietnam

H. N. Van (✉) · Y. Dosho · D. N. Anh
Meijo University, Nagoya, Japan
e-mail: 213434002@cmailg.meijo-u.ac.jp

S. N. Thanh
University of Transport and Communications, Hanoi, Vietnam

1 Introduction

If low-quality recycled and normal aggregates are combined, then it is possible to apply for structural concrete in Vietnam [1]; however, there was no study on mix proportion design for recycle aggregate concrete (RAC). In this study, by mixing low-quality recycled and normal aggregates in a suitable replacement ratio, a relative quality index method was used for the evaluation of the concrete's performance. Accordingly, a mix proportion of concrete using low-quality recycled aggregate can be designed that satisfies Vietnam's required performance.

2 Outline of Experiment

2.1 Materials

In Table 1, cement, water and chemical admixtures used in this study were selected by comparing Vietnam Standards (TCVN) and Japanese Industrial Standards (JIS). Thus, the materials in Japan satisfied both TCVN and JIS.

As shown in Table 2, materials in Japan, normal fine aggregates were river sand (NS) and crushed sand (CS) and two types of crushed stone 2005 (NG₁, NG₂) were used as normal coarse aggregates. These normal aggregates satisfied TCVN 7570:2006, JIS A 5038 and JIS A 5005. Four types of recycled coarse aggregate class L 2005 (RLG₁₋₄) and two types of recycled fine aggregate class L (RLS₁, RLS₂) were used. In which, RLG₁₋₄ was accordance with recycled coarse aggregate type II in TCVN 11969:2018 [2].

Table 1 TCVN and JIS used for material selection

Material	TCVN	JIS
Ordinary Portland cement	TCVN 2682:2009	JIS R 5210
Water	TCVN 4506:2012	JIS A 5308
Chemical admixtures	TCVN 8826:2011 and TCVN 12300:2018	JIS A 6204

Table 2 Quality of aggregate*1

Item	Test method	NS*2	CS*3	NG ₁₋₂ *4	RLS ₁₋₂ *5	RLG ₁₋₄ *5
Density in oven-dry condition (g/cm ³)	JIS A 1109	2.55–2.60	2.52	2.61–2.68	2.06–2.14	2.22–2.30
Water absorption (%)	JIS A 1110	1.42–1.92	1.60	0.60–1.21	8.45–10.25	5.33–6.84
Fineness modulus (F.M.)	JIS A 1102	2.50–2.73	2.63	6.65–6.66	3.09–3.37	6.39–6.73
Materials finer than 75 μm sieve (%)	JIS A 1103	1.9–4.6	4.5	0.8–1.8	5.5–7.0	0.2–1.4
Solid content (%)	JIS A 1104	62.8–67.2	67.1	58.6–62.8	65.2–69.8	59.2–62.2
Solid content in aggregate (%)	JIS A 5005	–	58.2	58.3–62.3	60.3–66.1	59.5–63.2
Aggregate crushing value (ACV) (%)	BS 812-110	–	–	14.5	–	23.3–27.0
Ten percent fines value (TFV) (kN)	BS 812-111	–	–	294	–	134–152
Freezing–thawing damage index	JIS A 5022	–	–	0	–	0.03–0.05
Alkali-silica reactivity	JIS A 1804	–	–	Harmless	–	–
	JIS A 5021	–	–	–	–	Harmless

*1 Those shown in range were taken in multiple lots. *2 Ibi river sand. *3 Shinshiro crushed sand. *4 Crushed sandstone from Kasugai and Shinshiro. *5 The total amount of contained impurities was from 0.1 to 2.2 mass%

2.2 Mix Proportion

Table 3 shows the mix proportions in this study. Experimental and test methods are shown in Table 4. The water-cement ratios (W/C) were 35%, 45%, 55% and 65%. Further, the replacement ratios of RLG and RLS were 0%, 30% (only for RLS), 50% and 100% in volume. In total, there were 22 specimen groups.

In this study, the relative quality index was employed to evaluate the relationship between the relative water absorption (Q_{at}) and concrete performance using Eq. (1)

$$Q_{at} = \frac{Q_{vaG} \times a + Q_{vaN} \times b + Q_{raG} \times c + Q_{raN} \times d}{a + b + c + d} \quad (1)$$

where Q_{at} : relative water absorption (%);

Q_{vaG} : water absorption of normal coarse aggregate (%);

Q_{vaN} : water absorption of normal fine aggregate (%);

Q_{raG} : water absorption of recycled coarse aggregate (%);

Q_{raN} : water absorption of recycled fine aggregate (%);

a , b , c and d : absolute volumes of aggregates, respectively (L/m³).

Table 3 Mix proportion of concrete and test results of fresh concrete

Type	Mix proportion of concrete*1										Test results of fresh concrete				
	Replacement ratio (%) RLS	W/C (%)	s/a (%)	Unit weight (kg/m ³)		AL*2 content (kg/m ³)	Chloride content (kg/m ³)*3	Qat (%)	Slump (cm)	Air content*4 (%)	Density (kg/m ³)	Temperature(°C)	Chloride content (kg/m ³)*3		
				W	C										
NG ₂ NS-35	0	35	39.8	170	486	2.7	0.07	1.24	18.5	4.2(0.1)	2310	28.2	0.04		
RLG ₄ 50NS-35	50		39.8	170	486	3.7	0.07	2.78	20.5	5.3(0.3)	2206	26.0	0.18		
RLG ₄ 50RLS ₂ 30-35	50	30	39.8	170	486	4.4	0.07	3.83	20.5	5.7(0.3)	2199	26.0	0.17		
RLG ₄ 100NS-35	100	0	39.8	170	486	4.8	0.07	4.32	20.0	4.9(0.5)	2276	25.1	0.18		
NG ₂ NS-45	0	45	43.5	183	407	2.1	0.04	1.30	19.5	4.4(0.2)	2299	28.0	0.03		
NG ₂ RLS ₁ 100-45	0		43.5	183	407	4.3	0.12	4.34	16.5	3.9(1.6)	2250	25.8	0.12		
NG ₁ RLG ₂ 50NS-45	50	0	42.1	185	411	3.0	0.09	2.74	19.0	5.0(0.4)	2230	17.4	0.03		
NG ₂ RLG ₄ 50RLS ₂ 30-45	50	30	45.4	183	407	4.0	0.12	4.10	20.5	3.6(0.4)	2250	27.6	0.14		
NG ₂ RLG ₃ 50RLS ₁ 50-45	50	50	43.5	183	407	4.1	0.14	4.08	18.0	4.4(0.6)	2226	24.8	0.11		
RLG ₃ 100NS-45	100	0	43.5	183	407	4.0	0.15	3.83	20.0	5.0(0.5)	2184	28.0	0.06		
NG ₂ NS-55	0	55	45.8	180	327	1.7	0.04	1.30	18.0	4.1(0.2)	2336	28.4	0.02		
NG ₂ RLS ₁ 100-55	0	100	45.8	180	327	4.1	0.12	4.51	19.0	5.2(0.9)	2084	30.1	0.09		
NG ₁ RLG ₂ 50NS-55	50	0	44.9	180	327	2.6	0.08	2.68	20.5	4.9(0.5)	2260	18.8	0.03		
NG ₂ RLG ₄ 50RLS ₂ 30-55	50	30	43.9	180	327	3.5	0.14	3.90	20.0	4.9(0.4)	2141	16.8	0.13		
NG ₂ RLG ₃ 50RLS ₁ 50-55	50	50	45.8	180	327	3.8	0.13	4.12	19.5	4.1(0.3)	2099	29.2	0.08		
RLG ₃ 100NS-55	100	0	45.8	180	327	3.6	0.14	3.74	16.5	4.6(0.5)	2208	27.7	0.09		
NG ₂ NS-65	0	65	47.4	177	272	1.4	0.03	1.31	18.0	4.6(0.2)	2288	24.6	0.02		
NG ₂ RLS ₁ 100-65	0	100	47.4	177	272	4.0	0.12	4.62	18.0	4.5(1.5)	2142	22.8	0.12		

(continued)

Table 3 (continued)

Type	Mix proportion of concrete*1						Test results of fresh concrete						
	Replacement ratio (%) RLG RLS	W/C (%)	s/a (%)	Unit weight (kg/m ³)		AL*2 content (kg/m ³)	Chloride content (kg/m ³)*3	Q _{air} (%)	Slump (cm)	Air content*4 (%)	Density (kg/m ³)	Temperature(°C)	Chloride content (kg/m ³)*3
				W	C								
NG ₁ RLG ₂ 50NS-65	50	0	47.6	176	271	2.4	0.08	2.63	17.5	5.2(0.4)	2180	18.6	0.02
NG ₂ RLG ₄ 50RLS ₂ 30-65	50	30	49.2	177	272	3.6	0.13	4.11	19.5	5.3(0.5)	2161	24.3	0.11
NG ₂ RLG ₃ 50RLS ₁ 50-65	50	50	47.4	177	272	3.4	0.11	4.14	18.0	4.5(1.2)	2163	23.5	0.11
RLG ₃ 100NS-65	100	0	47.4	177	272	3.3	0.14	3.67	16.0	4.2(0.5)	2189	22.0	0.10

*1 The AE water-reducing admixture (high-performance type) was used with 1.0% of the cement mass and air-entraining admixture was used at 0.05%-0.10% of the cement mass. *2 Total alkali content. *3 Chloride content of RAC was higher than the calculated values due to the influence of the calculation method in JIS A 5023. *4 In the round brackets () is aggregate correction factor

Table 4 Test items and method

Type	Experiment	Test method	Reference method	Remark
Fresh concrete	Slump	JIS A 1101	TCVN 3106:1993	–
	Air content	JIS A 1128	TCVN 3111:1993	–
	Density	JIS A 1116	TCVN 3108:1993	–
	Temperature	JIS A 1156	TCVN 9340:2012	–
	Chloride content	JIS A 5308; JIS A 5023 JASS 5 T-502	–	–
Hardened concrete	Compressive strength	JIS A 1108	TCVN 3118:1993	Standard curing method 4 weeks (6 samples), 13 weeks (6 samples)
	Static modulus of elasticity	JIS A 1149	TCVN 5276:1993	
	Drying shrinkage	JIS A 1129-3	ASTM C157	At 26 weeks
	Accelerated carbonation depth	JIS A 1153	–	–

3 Experimental Result

3.1 Experimental Result of Fresh Concrete

Slump and Air Content: In Table 3, the target slump of 18 ± 2.5 cm and target air content of $4.5 \pm 1.5\%$ was satisfied in all specimens.

Density and Chloride Content: In Table 3, the density of concrete tended to be lower when the RLG and RLS replacement ratios increased. Further, the target value of chloride content in JIS A 5308 (≤ 0.30 kg/m³) was satisfied for all specimens. The chloride content of RAC was higher than the calculated values in Table 3. This was due to the influence of the calculation method in JIS A 5023.

3.2 Experimental Result of Hardened Concrete

Compressive Strength and Static Modulus of Elasticity: From Fig. 1, the compressive strength and the static modulus of elasticity were lower when the recycled aggregate replacement ratio increased.

Drying Shrinkage: Comparing TCVN and JIS, 8×10^{-4} was set as the target quality [1]. In Fig. 2, drying shrinkage was higher when RLG and RLS replacement ratios were $\geq 50\%$. However, the target quality threshold value of $\leq 8 \times 10^{-4}$ for drying shrinkage was satisfied in almost all specimens.

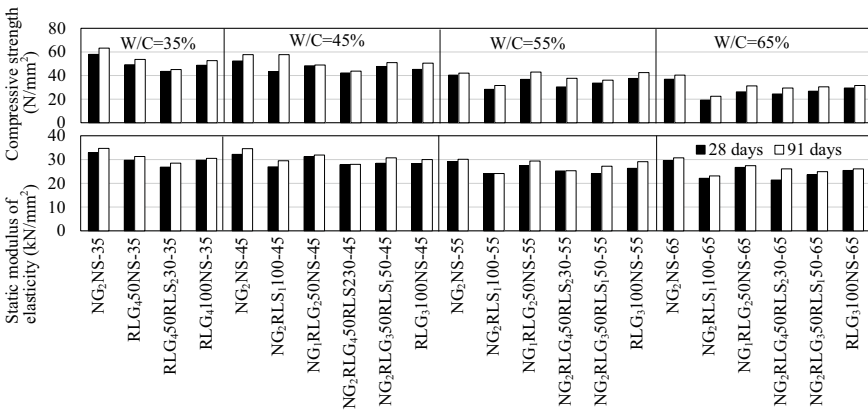


Fig. 1 Compressive strength and static modulus of elasticity

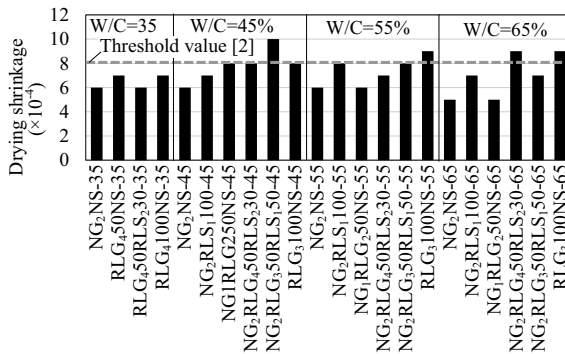
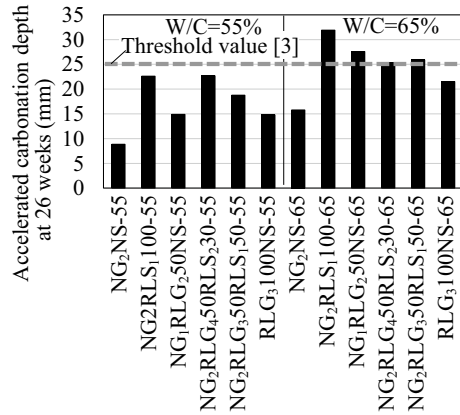


Fig. 2 Drying shrinkage

Fig. 3 Accelerated carbonation depth

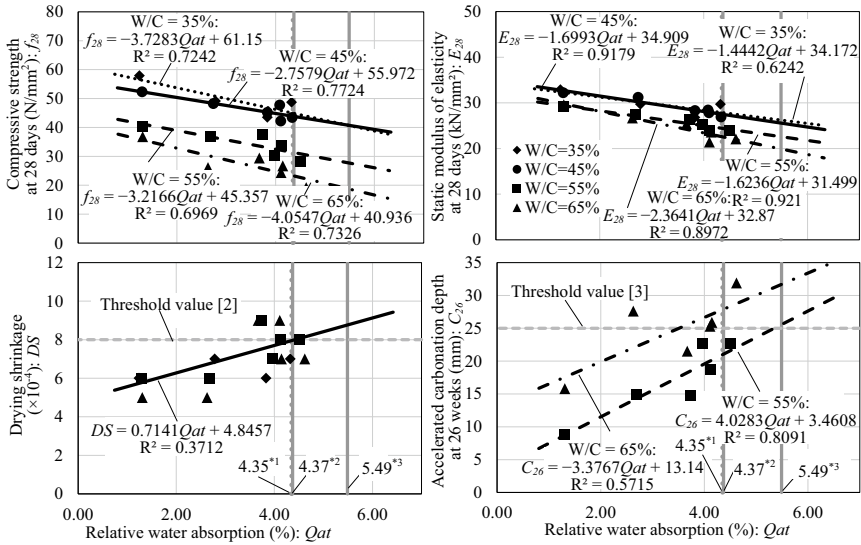


Accelerated Carbonation Depth: Comparing TCVN and JIS, the target quality of ≤ 25 mm was selected in this study [1]. In Fig. 3, when RLG and RLS replacement ratios were $\geq 50\%$, the carbonation depths tended to be larger. The 25-mm target quality was satisfied in almost all specimens.

3.3 Concrete Performance Evaluation by Relative Quality Index

Figure 4 shows that the primary performance of concrete decreased when Q_{at} increased. Some variations were observed, but in general, a relationship was obtained. The threshold values of Q_{at} were calculated based on the upper limit of water absorptions for RLG, RLS and normal aggregate specified in JIS and TCVN. The threshold values were $Q_{at} = 4.35\%$ for recycled coarse aggregate type I with 100% replacement ratio according to TCVN 11969: 2018 [2], $Q_{at} = 4.37\%$ for RAC-Class M1 with 50% RLG replacement ratio and $Q_{at} = 5.49\%$ for RAC-Class M2 with 50% RLG and 30% RLS replacement ratios, respectively.

The compressive strength (f_{28}) and static modulus of elasticity (E_{28}) at 28 days tended to decrease when Q_{at} increased. Moreover, Fig. 4 shows that many specimens exceed the target quality when Q_{at} was 3.50%–4.37%. In contrast, when $Q_{at} \leq 3.50\%$, the target value of 8×10^{-4} [3] was satisfied in all specimens. For accelerated carbonation depth, when W/C was 65%, some specimens exceeded the target quality of 25 mm [4], even when $Q_{at} \leq 4.35\%$. The accelerated carbonation depth is significantly affected by W/C; therefore, it can be suppressed by reducing W/C.



*1 100% RLG type 1 based on TCVN 11969:2018 [4] *2 RAC-Class M1 based on JIS A 5022 *3 RAC-Class M2 based on JIS A 5022

Fig. 4 Relationship between the relative water absorption and concrete performance

4 Mix Proportion Design

In Vietnam, TCVN 5574:2018 [5] and ACI 211.1-91 [6], which do not specify the design method for RAC, were used for concrete mix proportion design. In this study, the compressive strength of RAC was compared with that of normal-weight concrete to examine the effect of strength reduction on the mix proportion design.

4.1 Mix Proportion Design Flow

First, the materials were confirmed; then, the strength equation was examined on the basis of the theory of cement–water ratio. The target slump and air content were set as 18 ± 2.5 cm and 4.5 ± 1.5%, respectively. After examining the mix proportion strength, the alkali and chloride contents were confirmed in material design; then, an assumed mix proportion was decided. RAC was manufactured and evaluated by the relative quality index method. Finally, the strength equation for RAC was proposed and the mix proportion was decided.

Table 5 Calculation result of mix proportion strength

Cement type	F_q^* (N/mm ²)	Range of θ (°C)	$28S_{91}$ (N/mm ²)	$F_m = F_q + 28S_{91}$ (N/mm ²)	σ (N/mm ²)	F (N/mm ²)		
						$F \geq F_m + 1.73\sigma$	$F \geq 0.85F_m + 3\sigma$	Set up value
Ordinary Portland cement	22.0	$8 \leq \theta$	3	25	2.5	29.3	28.8	29.3
		$0 \leq \theta < 8$	6	28	2.8	32.8	32.2	32.8
	18.5	$8 \leq \theta$	3	21.5	2.5	25.8	25.8	25.8
		$0 \leq \theta < 8$	6	24.5	2.5	28.8	28.3	28.8
	15.0	$8 \leq \theta$	3	18.0	2.5	22.3	22.8	22.8
		$0 \leq \theta < 8$	6	21.0	2.5	25.3	25.4	25.4
	11.0	$8 \leq \theta$	3	14.0	2.5	18.3	19.4	19.4
		$0 \leq \theta < 8$	6	17.0	2.5	21.3	22.0	22.0

* Based on standard design strength (F_q) in TCVN 5574:2018[5]

4.2 Mix Proportion Strength

In this study, mix proportion strength (F) was calculated based on JASS 5 (2018) [3], where the standard design strength was based on TCVN 5574:2018 [5]. The calculation results are shown in Table 5.

4.3 Material Design

As shown in Table 3, the chloride content of RAC satisfied $\leq 0.3 \text{ kg/m}^3$ in accordance with JIS A 5308. For the alkali content, it satisfied $\leq 3.0 \text{ kg/m}^3$ in accordance with JIS A 5022 when RLG replacement ratio $\leq 50\%$, except for $W/C = 35\%$.

4.4 Strength Equation of RAC

Q_{at} was calculated for all RAC and normal-weight concrete in Table 3. The relationship between F and Q_{at} is shown in Eq. (2).

$$F = l + m \times Qat \quad (2)$$

where l and m : experimental constants (intercept and slope of compressive strength equation in 28 days in Fig. 4)

Using the Qat of all specimens, F can be calculated for each of them. From these results, the reduction rate (R) of mix proportion strength can be calculated by Eq. (3) as follows:

$$R = F_{28R}/F_{28N} \quad (3)$$

where R : reduction rate of mix proportion strength;

F_{28R} : mix proportion strength at 28 days of RAC (N/mm²);

F_{28N} : mix proportion strength at 28 days of normal-weight concrete (N/mm²).

The results of R were multiplied with constants of normal-weight concrete's strength equation in Eq. (4) to obtain RAC's strength equation. By applying these strength equations, RAC can be manufactured in accordance with TCVN and JIS.

$$F_{28R} = R \times (a + b \times C/W) \quad (4)$$

where C/W : cement–water ratio and a and b : constant (Table 6).

5 Conclusion

The fresh concrete satisfied the target value by adjusting chemical admixtures, even when the replacement ratios of RLG and RLS were high. In hardened concrete, when the recycled aggregate replacement ratio increased, the concrete performance became lower. Further, when mixing low-quality recycled and normal aggregates, based on the concrete performance evaluation results using the relative quality index and material design, the mix proportion strength equation of RAC can be determined. Therefore, as the research results in Japan, RAC can be manufactured in accordance with TCVN.

Table 6 Calculation result of strength equation's constant for recycled aggregate concrete

F_q^{*1}	W/C (%)	NGNS			NGRLS100			RLG50NS				
		F_{28N}^{*1}	Constant	b	F_{28R}^{*1}	R^{*2}	Constant	$b \times R$	F_{28R}^{*1}	R^{*2}	Constant	$a \times R$
22.0	35	56.5	12.26	16.20	-	-	-	-	48.7	0.88	10.79	14.26
18.5	45	52.3			43.9	0.74	9.07	11.99	48.4	(0.03)		
15.0	55	41.2			30.9	(0.11)			36.7			
11.0	65	35.6			22.2				30.3			
F_q^{*1}	W/C (%)	RLG50RLS30			RLG50RLS50			RLG100NS				
		F_{28R}^{*1}	R^{*2}	Constant	F_{28R}^{*1}	R^{*2}	Constant	F_{28R}^{*1}	R^{*2}	Constant	$a \times R$	$b \times R$
22.0	35	46.9	0.79	9.69	12.80	-	-	-	45.0	0.80	9.81	12.96
18.5	45	44.7	(0.08)			44.7	0.77	9.44	45.4	(0.06)		
15.0	55	32.1				32.1	(0.09)		33.3			
11.0	65	24.3				24.1			26.1			

* 1 Unit: N/mm². * 2 In the round brackets () is standard deviation

References

1. Dinh VL, Nguyen AD, Tao YZ, Nishikigi K, Dosho Y (2020) Application of recycled aggregate concrete technology for construction work in Vietnam. *Meijo Asian Res J* 10(1):5–19
2. Vietnam Standards (2018) TCVN 11969: 2018, Recycled coarse aggregate for concrete, Vietnam
3. Architectural Institute of Japan (2018) Japanese architectural standard specification JASS 5 Reinforced concrete work 2018, Japan
4. Architectural Institute of Japan (1991) Recommendations for design and construction practice of high durable concrete, Japan
5. Vietnam Standards (2018) TCVN 5574:2018, Design of concrete and reinforced concrete structures, Vietnam
6. American Concrete Institute (2009) ACI 211.1-91, Standard practice for selecting proportions for normal, heavyweight, and mass concrete, America

Effects of Rejuvenators on Cracking Resistance of High RAP Asphalt Mixtures



Van Quyet Truong, Ngoc-Lan Nguyen, Dong Van Dao, Kim Youngik, and Duc Trung Tran

Abstract Incorporating recycled asphalt mixture with reclaimed asphalt pavement (RAP) is becoming popular because of its economic and environmental benefits. However, using high RAP contents is often prone to cracking. To address the problem, recycling agents (rejuvenators) are often used to reduce the hardness of the mixture and, therefore, improve the cracking resistance. In this paper, two types of petroleum-based rejuvenators (aromatic extracts—A rejuvenator) and vegetable-based (V rejuvenator) are used at different contents (0%, 4%, 8%, and 12% by the weight of recycled bitumen). IDEAL-CT test (ASTM D8225) is used to evaluate the impact of these rejuvenators on the cracking resistance of asphalt mixtures. Laboratory test results indicated that the use of the rejuvenators improves the cracking resistance of asphalt mixtures, in which using petroleum-based rejuvenator is more effective against cracking than vegetable-based rejuvenator.

Keywords Reclaimed asphalt pavement (RAP) · Rejuvenator · Cracking resistance · Cracking tolerance index (CT_{Index})

V. Q. Truong (✉) · N.-L. Nguyen · D. V. Dao
University of Transport and Communications/UTC, Hanoi, Vietnam
e-mail: quyet.tv@utc.edu.vn

D. V. Dao
Hoa Binh University, Hanoi, Vietnam

K. Youngik
Hansoo Road Industry Co., Ltd, Daejeon, Korea

D. T. Tran
National Center for Asphalt Technology, Auburn University, Alabama, USA

1 Introduction

The application of RAP produces hot or warm mix asphalt is becoming increasingly popular over the world. 95% of RAP materials were reused to make asphalt mixtures in the United States, with a volume of up to 76.4 million tons [1]. Using RAP will reduce the dependence on non-renewable resources (virgin aggregates and virgin bitumen), save construction costs, and ensure economic and environmental efficiency. However, mixtures with high RAP content are stiffer and more brittle than conventional ones. Therefore, these mixtures are often difficult to compact in the field, prone to cracking, and have lower durability properties than those of asphalt mixtures without RAP [2]. The problems can be resolved by recycling agents that increase RAP content without losing durability performance.

Recycling agents (rejuvenators) help to reinstate the rheological properties of aged bitumen in RAP. It helps to decrease viscosity, hardness and increase the ductility of the aged bitumen. Several studies showed that using rejuvenators decreased the hardness of the RAP mixture [3–6]. Besides the effect on the stiffness, the use of rejuvenators effectively improved the cracking resistance based on test methods such as overlay test (OT), semi-circular bend (SCB) test, four-point bending test, Illinois Flexibility Index Test (I-FIT), and indirect tensile asphalt cracking test (IDEAL-CT) [7–10]. Among the cracking test models, SCB, IDEAL-CT, and OT have the highest correlation with actual cracking in asphalt pavement [11]. Recently, IDEAL-CT test has been widely applied for quality control because of its simplicity, practicality, and low coefficient of variance [11, 12].

The project was conducted to evaluate the effect of rejuvenator on cracking resistance of recycled asphalt mixtures. The IDEAL-CT method was used to determine the index CT_{Index} of mixture with a ratio of 30% RAP and the control asphalt mixture (without RAP). The mixtures were mixed with two types of commercially available rejuvenators, including petroleum-based (aromatic extracts) and vegetable-based (vegetable oils) at different contents (0%, 4%, 8%, and 12% by the weight of recycled bitumen).

2 Experimental Research

2.1 Materials

Asphalt mixtures with type 12.5 (AC 12.5) were selected for this research. Aggregates used in this study are crushed stone with the nominal maximum aggregate size (NMAS) of 12.5, 9.5, and 4.75 mm, respectively. RAP with (NMAS) is 12.5 mm. All materials were collected from Tan Cang 3 Plant of BMT Company, Bien Hoa, Dong Nai, Vietnam. The two rejuvenators, petroleum-based (aromatic extracts—A rejuvenator) and vegetable-based (V rejuvenator), were used at 0%; 4%; 8%, and 12% by the weight of recycled bitumen in RAP. Table 1 shows the particle gradation

of the different aggregates and the RAP. Properties of RAP and bitumen types are presented in Tables 2 and 3. Figure 1 shows the aggregate gradation of mixtures, satisfying the TCVN 13567-2022 requirements.

Table 1 Particle gradation of the aggregates

Sieve size, mm	Passing percentage of the aggregates at sieve sizes, %				
	Agg. D_{max} 12.5	Agg. D_{max} 9.5	Agg. D_{max} 4.75	Mineral filler	RAP 12.5
16	100	100	100	100	100
12.5	64.6	100	100	100	87.6
9.5	8.6	88.9	100	100	77.3
4.75	0.4	7.2	84.4	100	46.9
2.36	0.0	0.9	49.7	100	28.0
1.18	0.0	0.0	31.2	100	20.9
0.6	0.0	0.0	21.0	100	15.0
0.3	0.0	0.0	13.8	100	11.5
0.15	0.0	0.0	9.4	97.9	8.2
0.075	0.0	0.0	3.7	95.8	5.6

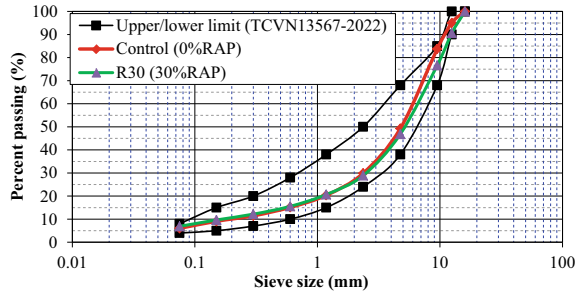
Table 2 Properties of RAP

Property	Result	Criteria
Bitumen content in RAP, %	3.0	–
Los Angeles, %	21	≤ 28
Durability, %	2.3	≤ 10

Table 3 Properties of virgin binder (Pen 60/70) and binder extracted from RAP

Property	Virgin bitumen (Pen 60/70)	Bitumen extracted from RAP
Penetration at 25 °C (0.1 mm)	67.8	22.0
Softening point (°C)	49.6	64.1
$G^*/\sin\delta$ at 64 °C, kPa	1.38	–
$G^*/\sin\delta$ at 82 °C, kPa	–	1.11

Fig. 1 Gradation plot for mixtures



2.2 Preparation of Test Specimens

The mixtures were designed according to the Marshall method, and the results are presented in Table 4. Eight mixtures were prepared, as shown in Table 5. For each mixture, three specimens of 150 mm diameter and 62 ± 1 mm thickness with an air void content of $7 \pm 0.5\%$ were prepared using the Superpave Gyrotory Compactor (Figs. 2 and 3). The mixtures were conditioned for 4 h at $135 \text{ }^\circ\text{C}$ before the compaction.

Table 4 Properties of the mixture

Property	Values at the optimal content		Requirements TCVN 13567-2022
	Control (0% RAP)	R30 (30% RAP)	
Bitumen content of mixture, P_b , %	5.0	5.0	–
Bitumen content of RAP, P_b (RAP), %	0.0	0.9	–
Virgin bitumen, P_b (virgin), %	5.0	4.1	–
Air void, V_a , %	4.0	4.2	4–6
Voids in the mineral aggregate, VMA, %	14.7	14.1	Min 14
Voids filled with asphalt, VFA, %	71.5	70.6	65–75
Marshall stability, MS, kN	11.3	12.1	Min 8
Marshall flow, MF, mm	3.0	2.3	1.5–4

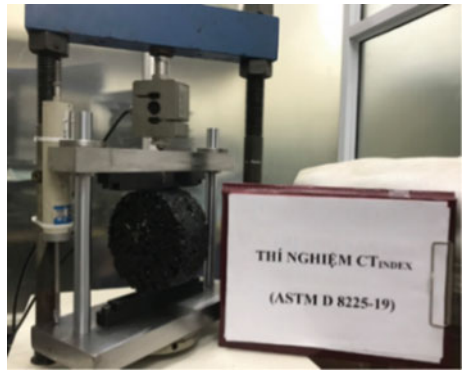
Table 5 Information of mixtures

ID mixture	Rejuvenation method	Rejuvenator content (%)	Types of rejuvenator
Control	–	–	–
R30	No rejuvenator added	0	–
R30.A.4	Blended with the virgin bitumen	4	Aromatic extracts
R30.A.8	Blended with the virgin bitumen	8	Aromatic extracts
R30.A.12	Blended with the virgin bitumen	12	Aromatic extracts
R30.V.4	Added directly on the RAP	4	Vegetable oil
R30.V.8	Added directly on the RAP	8	Vegetable oil
R30.V.12	Added directly on the RAP	12	Vegetable oil

Fig. 2 Superpave gyratory compactor

2.3 Testing Method

The IDEAL-CT evaluates the cracking resistance of asphalt mixtures according to ASTM D8225 [13]. Before testing, the specimens were cured at 25 °C in the environmental chamber. Specimens were loaded monotonically at the 50 ± 2 mm/min rate until failure (final displacement at 0.1 kN) (Fig. 4). A load and displacement curve were then used to calculate CT_{Index} (Fig. 5), using following equation:

Fig. 3 Specimens test**Fig. 4** CT_{Index} test

$$CT_{\text{index}} = \frac{t}{62} \times \frac{G_f}{|m_{75}|} \times \left(\frac{l_{75}}{D} \right) \quad (1)$$

where

G_f —fracture energy (J/m^2);

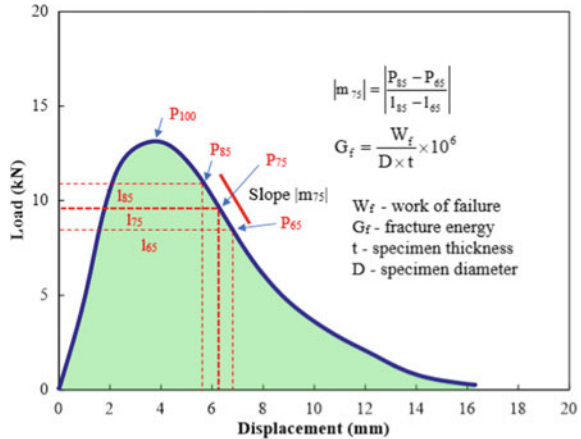
l_{75} —displacement corresponding to load equal to 75% of maximum load (mm);

D —specimen diameter (mm); t —specimen thickness (mm);

$|m_{75}|$ —absolute value of the load–displacement curve slope after the maximum load value (N/m);

$|m_{75}| = \left| \frac{P_{85} - P_{65}}{l_{85} - l_{65}} \right|$, P_{85} and P_{65} values are determined as shown in Fig. 5.

Fig. 5 Recorded load versus load-line displacement curve



3 Results and Discussion

The CT_{Index} results are shown by load–displacement curves in Fig. 6 in which the load–displacement curves of the 30%RAP mixture using rejuvenators were different from each other, especially for the mixture using petroleum-based rejuvenator (aromatic extract). The maximum load value increased significantly, and the slope before achieving the maximum load value (pre-peak slope) became steeper than for asphalt mixtures without rejuvenator (Figs. 6 and 7). Figure 8 shows the result of CT_{Index} values of different asphalt mixtures. A higher CT_{Index} value indicates better crack resistance performance. The minimum CT_{Index} value of 80 was recommended to ensure cracking resistance for asphalt mixtures [14]. The results show that CT_{Index} of 30%RAP mixture (without rejuvenator) was smaller than that of the control mixture (0%RAP). However, the addition of rejuvenators increased the CT_{Index} of the mixtures. Therefore, to ensure a minimum cracking resistance index of 80, the rejuvenator content should be at least 4% for the mixture containing 30%RAP. The results also indicated that using a petroleum-based rejuvenator provided higher cracking resistance than a vegetable-based rejuvenator. This result is consistent with the study of Nabizadeh et al. [15], in which they compared the effectiveness of three types of rejuvenators (soybean oil, aromatic extract, and tall oil). This study concluded that using aromatic extract provided the most effective in increasing the cracking resistance of the asphalt mixtures.

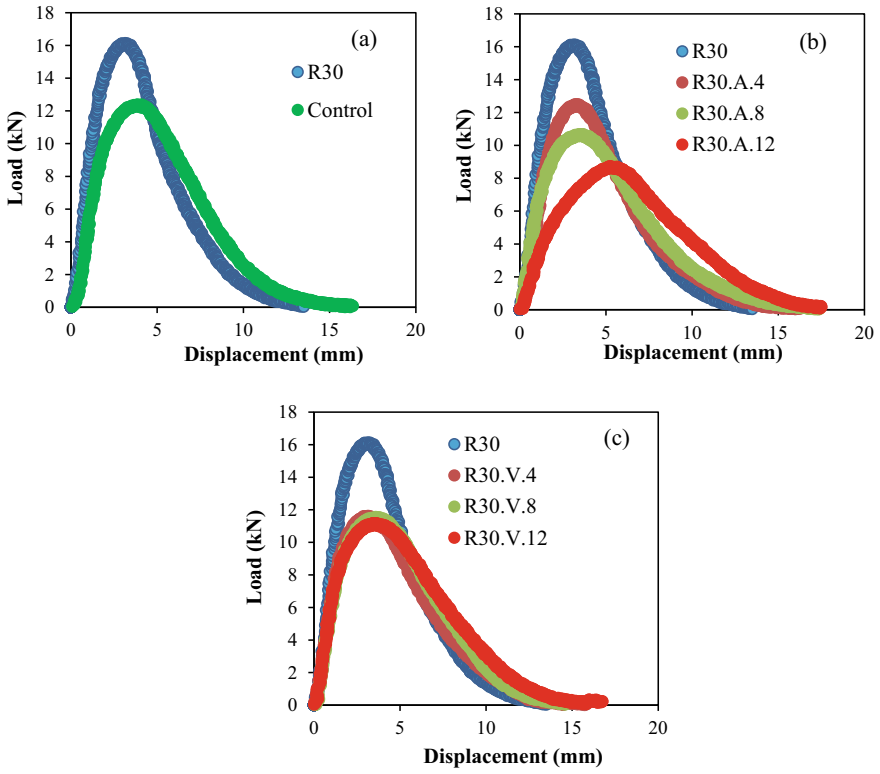


Fig. 6 Load–displacement curve of the different mixtures

Fig. 7 Maximum load value (P_{100}) of the mixtures

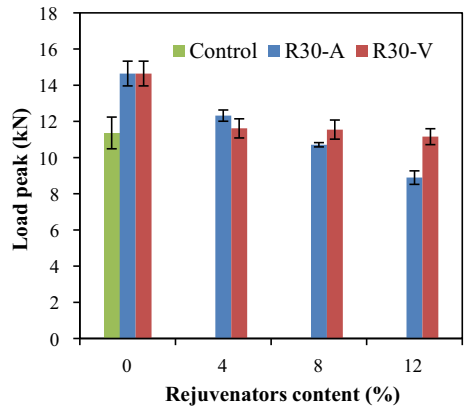
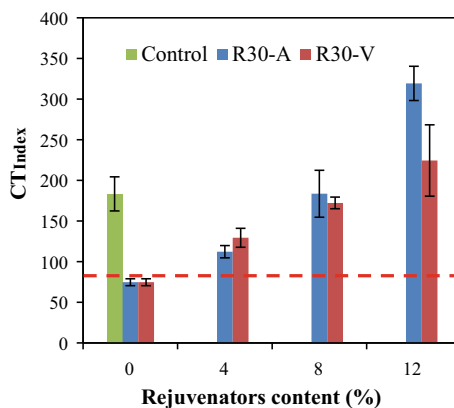


Fig. 8 CT_{Index} of the mixtures



4 Conclusion

Based on two types of rejuvenators used in the study, recycled asphalt mixture using petroleum-based rejuvenators is more effective against cracking than vegetable-based rejuvenators. Moreover, increasing the rejuvenator's content will increase the mixture's cracking resistance. However, it can impact the rutting resistance of rejuvenated asphalt mixture. Therefore, the content of rejuvenators must be selected to ensure the asphalt mixture's resistance to rutting. Further work will study to determine the optimal rejuvenator content to balance cracking and rutting resistance in asphalt mixtures.

Acknowledgements Van Quyet Truong was funded by the Master, Ph.D. Scholarship Programme of Vingroup Innovation Foundation (VINIF), code [VINIF.2022.TS099]

References

1. NAPA (2018) Annual Asphalt pavement industry survey on recycled materials
2. Tran HN, Ga L, Taylor A, Willis PER (2012) Effect of rejuvenator on performance properties of HMA mixtures with high RAP and RAS contents. NCAT Report 12-05
3. Wang F, Wang Z, Li C, Xiao Y, Wu S, Pan P (2017) The rejuvenating effect in hot asphalt recycling by mortar transfer ratio and image analysis. *Materials* 10(6):574–590
4. Zaumanis M, Mallick RB, Frank R (2014) Evaluation of different recycling agents for restoring aged asphalt binder and performance of 100% recycled asphalt. *Mater Struct* 48(8):2475–2488
5. Dong VD, Ngoc-Lan N, May HN, Hai-Bang L, Van Quyet T (2022) Evaluation of cracking resistance of warm mix asphalt incorporating high reclaimed asphalt pavement content. *J Mater: Des Appl*
6. Kaseer F, Yin F (2017) Stiffness characterization of asphalt mixtures with high recycled material content and recycling agents. *J Transp Res Board* 2633:58–68
7. Yin F, Kaseer F, Arámula-Mercado E, Epps Martin A (2017) Characterising the long-term rejuvenating effectiveness of recycling agents on asphalt blends and mixtures with high RAP and RAS contents. *Road Mater Pavement Des* 18(4):273–292

8. Yan J, Zhang Z, Zhu H, Li F, Liu Q (2014) Experimental study of Hot recycled asphalt mixtures with high percentages of reclaimed asphalt pavement and different recycling agents. *J Testing Eval* 42(5)
9. Espinoza-Luque AF, Al-Qadi IL, Ozer H (2018) Optimizing rejuvenator content in asphalt concrete to enhance its durability. *Constr Build Mater* 179:642–648
10. Mogawer WS, Booshehrian A, Vahidi S, Austerman AJ (2013) Evaluating the effect of rejuvenators on the degree of blending and performance of high RAP, RAS, and RAP/RAS mixtures. *Road Mater Pavement Des* 14:193–213
11. Bennert T, Haas E, Wass E (2018) Indirect tensile test (IDT) to determine asphalt mixture performance indicators during quality control testing in New Jersey. *Transp Res Board* 2672(28):394–403
12. NCAT Report PHASE VII (2018–2021) (2021) NCAT test track findings. National Center for Asphalt Technology at Auburn University, Alabama, US
13. ASTM D8225-19 (2019) Standard test method for determination of cracking tolerance index of asphalt mixture using the indirect tensile cracking test at intermediate temperature. ASTM International
14. Diefenderfer SD, Boz I, Habbouche J (2021) Balanced mix design for surface asphalt mixtures: phase I: initial roadmap development and specification verification. Virginia Transportation Research Council (VTRC)
15. Nabizadeh H, Haghshenas HF, Kim Y-R, Aragão FT (2017) Effects of rejuvenators on high-RAP mixtures based on laboratory tests of asphalt concrete (AC) mixtures and fine aggregate matrix (FAM) mixtures. *Constr Build Mater* 152:65–73

Using Paper Production Industry Waste as Soil Stabilizer for Pavement Construction in Vietnam



Nguyen Trong Hiep and Pham Huy Khang

Abstract The solution of using organic and inorganic chemical agents to strengthen soil for base, subbase or surface layers in road pavement has been applied for a long time in the world. In Vietnam, the method has been initially researched, but still very limited in practical application. Chemical waste from the paper industry has been studied and used around the world as a soil stabilizer in construction. The paper presents the research results from the use of lignosulfonate, which is derived from the waste of paper production process, collected from the paper factory located in Ky Son District, Hoa Binh Province, as the soil stabilizer, namely DBS-06, to strengthen the soil used as base, subbase or surface layers in road pavement. The research also proved that the DBS-06 agent is not only a good achievement on technical or economic sides, but also a fruitful outcome for environmental problem treatment in the paper industry.

Keywords Soil stabilizer · Paper industry · Waste · Pavement · Construction material · DBS-06

1 Introduction

In road construction, the use of local or in-situ materials is the most fundamental and important principle, which allows us to utilize favorable conditions to minimize construction cost. The common rule is worldwide applied not only in developing or new emerging economies, but in the developed world. The in-situ available soil is always a good material resource for pavement construction. One of the main directions for utilization of the material is to use the chemical admixtures (organic or inorganic) to improve the soil properties to increase its strength, durability, stability to satisfying the requirements for using in base, subbase or even surface courses of pavement structure [1].

N. T. Hiep (✉) · P. H. Khang
University of Transport and Communications/UTC, Hanoi, Vietnam
e-mail: nguyentronghiep@utc.edu.vn

© The Author(s), under exclusive license to Springer Nature Singapore Pte Ltd. 2024
T. Nguyen-Xuan et al. (eds.), *Proceedings of the 4th International Conference on Sustainability in Civil Engineering*, Lecture Notes in Civil Engineering 344,
https://doi.org/10.1007/978-981-99-2345-8_6

Since the 1940s of the last century, the issue of soil stabilization has been studied by scholars and scientists worldwide. Since then, many types of soil admixture have been researched and developed, and millions of square meters of road pavement have been constructed all over the world. In Vietnam, due to various economic and technological barriers, this method has just been applied in recent years.

There are some kinds of soil admixtures which have been introduced in Vietnam such as Con-Aid (South Africa) CONSOLID (Switzerland); Dustex (Australia), however, only two brands have been used in small scale pilot projects. The first one is Reynolds Roadpacker 2-3-5 Special RRP-S, denoted RRP, and developed from Germany. When mixed RRP, a liquid (sulfurized oil) soluble in water, soil will change the physicochemical properties, as the result, it has higher density and strength after compaction, and not being an expensive underwater effect. RRR has been applied for some rural road pilot projects in the countryside and road of the military barracks, the efficiency of the new agent is under monitoring. However, the main disadvantage of this admixture is high price, which leads to the construction cost nearly equal to that of the crushed aggregate.

The second admixture is SA44/LS40, the soil stabilizer supplied by the manufacturer Dallas Roadway, from the United State of America. The product was licensed by the US Department of Transportation since 1990, and has been used in over 50 countries around the world. SA44/LS40 is considered as a new technology used to stabilize soils for subgrade of roadway, an alternative for conventional materials. In Vietnam, this is the first chemical soil stabilizer approved by the Ministry of Transport for pilot application.

The research results from pilot projects proved that SA44/LS40 has advantages over the others because the soil is treated in terms of composites, then it is not only high strength but more stable in adverse conditions of water saturated. The application results in practice in many provinces and cities of Vietnam, with many types of soil, with a certain percentage added lime, SA44/LS40 has performed very well. Therefore, it has been approved by the Ministry of Transport for application. However, the high price is still the biggest disadvantage of the agent (equivalent to RRP-S) [2].

The initial applications of using new admixtures for soil stabilization in Vietnam revealed that the stabilizers, especially SA44/LS40, can be completely used for roadway pavement construction. The current conditions of construction technology also allow the stabilizers to be widely used. However, the high price is a barrier widely applied in the conditions of Vietnam. Therefore, the problem is how to make use of domestic materials and favorable conditions to produce a soil admixture which has equivalent features, at a reasonable price for Vietnam conditions. The paper presents the research results of soil stabilizer DBS-06 production in Vietnam condition, a new domestic option for admixture in road pavement construction.

2 Soil Stabilization Methods

2.1 Soil Stabilization

Soil stabilization means implementing a series of successive technological procedures to give the soil high strength and long-term stability, not only in the dry condition but in the state of water saturation or other adverse natural condition, by the effect of soil and admixtures.

The in-situ clay, loam are usually types of soil with high strength and cohesiveness in the dry state, but it is very weak in the water saturated condition. The low workability, low bearing capacity, and unfavorable properties such as high water content, shrinkage, compressibility are the limits for the in-situ soil in wet condition utilized in road construction.

It is because of the high specific surface, leading to the common important characteristics of clays, despite their different formation processes, particle, mineral and chemical compositions (clay sand, loam, and especially clays) are in wet condition, they exhibit some properties of colloidal particle systems. There are common methods for soil stabilization which can be applied in practice:

- (1) The mechanical method: Using compaction equipment to arrange and change the position of particles close to each other to increase the density, thereby improving the physical and mechanical properties of the material. This method is usually used in combination with other methods to increase the density and flatness of the layer of material mixture. [1, 3–5];
- (2) Particle size adjustment method: In this method, two or more kinds of soils which have different grain size compositions are mixed together to improve the grain composition of the mixture, thereby effectively improving densification through the compaction process. [4, 5];
- (3) Chemical methods: This is a method of using inorganic or organic chemical compounds (including lime, cement, fly ash, bitumen, bottom ash and sodium hydroxide, steel furnace slag) that are blended with the in-situ soil at certain proportions. These chemicals will usually react with water through a hydration reaction, or react with soil components, thereby binding soil particles together and increasing the strength of the mixture. During chemical reactions, mechanical compaction processes are carried out to increase the density and smoothness of the material mixture [6–9].
- (4) Electro-chemical method: This is a commonly used method to improve the physical and mechanical properties of clay soil. Water, existing as moisture in the soil, acts as a carrier of chemical ions which affects the electro-static bonding of the soil. The stabilizing principle of the method is that the stabilizer can break the water membrane of the clay content of the soil, then creating the convenient condition for soil hydration [10–14].
- (5) Microbiological method: Using microorganisms or enzymes to increase the adhesion of clay. The advantages of biotechnology over the chemical method,

which is considered as an economical solution but toxic and may cause pollution on soil and groundwater, is that it does not induce adverse impacts to the environment [15–17].

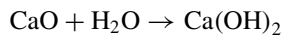
Among these mentioned methods, the electro-chemical methods and microbiological methods are considered as new methods compared to other traditional methods and are still being researched and developed.

2.2 *Lignosulfonate and Stabilization Mechanism*

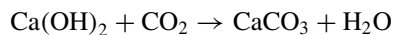
The lignosulfonate is a lignin-based polymeric compound/soil admixture, which can be collected and synthesized from the waste of the paper production industry. The content of the compound comprises two chemical groups: the hydrophilic groups of sulphonate, alcoholic hydroxyl, and phenolic hydroxyl, the other one is the carbon chain. The prominent properties of lingo-sulfonate compared to the conventional stabilizers is that it is not toxic, corrosive and biodegradable hydrocarbon (fungi, yeast or bacteria) [11, 13, 14].

The stabilization mechanism starts with the hydrolysis reaction between water and lingo-sulfonate which generates the positively charged ions, then, the ion reacts with negatively charged clay minerals. The ionic or electro-static reaction of the admixture will thin the membrane surrounding clay particles, then forming stronger links and more stable aggregates [3]. The chargeability of the stabilizer and the surface charge of clay minerals are the basic conditions for electro-static reactions to occur [12, 13, 18].

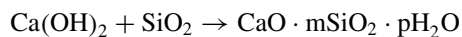
In practice, lignosulfonate is recommended to combine with lime for increasing the effectiveness of soil stabilization [3, 19, 20]. When lime is mixed with the soil, the chemical and physical processes will occur at the same time. With the main content of CaO, lime will absorb water to form lime mortar.



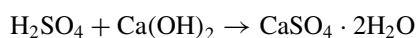
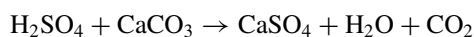
In the air, the lime mortar will solidify, there will be 2 main processes: (1) The dehydration of the mortar makes Ca(OH)₂ change from colloidal state to crystallized state, the crystals move closely and then bond together. The calcium hydroxide Ca(OH)₂ reacts carbon dioxide in the air:



The CaCO₃ and Ca(OH)₂ crystals alternately existed, making the soil in solid state. There is also the silicate reaction:



After mixing the soil with lime, lignosulfonate is added with suitable ratio and well blended at appropriate moisture. The concentrated sulfuric acid, second content of stabilizer compound (SA44), reacts with fine particles, creating a suitable environment for ion exchange in the soil. In addition, it is easy to see that SA44 also makes soil hardens faster by the release of CO_2 and forming salts, which increase the volume of $\text{CaSO}_4 \cdot 2\text{H}_2\text{O}$.



In the clay, there are mainly kaolinite substances $\text{Al}_2\text{O}_3 \cdot 2\text{SiO}_2 \cdot 2\text{H}_2\text{O}$. The strong expansive clay also includes much monmoriolite $2\text{MgO} \cdot \text{Al}_2\text{O}_3 \cdot 4\text{SiO}_2 \cdot n\text{H}_2\text{O}$ content, therefore, when mixed with water will expand, the volume increases up to 20 times. In addition, in the clay composition, there are many ions such as Na^+ , Ca^{++} , Mg^{++} . Therefore, when mixed with lime and the lignosulfonate compound (like SA44/LS40), it will form large insoluble substances such as $\text{CaO} \cdot \text{Al}_2\text{O}_3 \cdot 3\text{CaSO}_4 \cdot 32\text{H}_2\text{O}$, CaCO_3 , $\text{CaO} \cdot \text{Fe}_2\text{O}_3 \cdot n\text{H}_2\text{O}$, and the remaining cations.

According to the experiment result, when lime is added with soil, then mixing the lignosulfonate (e.g., SA44/LS40) with the mixture, the loading capacity increases from 25 to 30%, depending on the type of soil.

3 Production of Soil Stabilizer DBS-06 from Paper Industrial Waste

3.1 Production Technology

Similar to SA44/LS40, DBS-06 is a lignosulfonate, a lignin-based polymeric compound. DBS-06 is produced from paper production process from the paper factory located in Ky Son District, Hoa Binh Province, as common procedure as follows [21]:

In the paper production process, at first, the raw materials (bamboo, wood...) will be debarked and chipped to get small size pieces, which go into the tempering stage. After being hydrated by acid to get raw cellulose pulp, which in turn is bleached and filtered to get pure material for paper production (Fig. 1).

In order to produce the lignin sulfonate, main content of DBS-06, the chemical waste from the paper production process is partially collected to a storage tank for preliminary processing by removing the waste, and then going into another tank for distilling at 100–110 °C. The time for the stage is 12–16 h, which allows the light substances to be evaporated. The remaining concentration liquid is checked by hydrometer, pre-filtered by sedimentation method for 10 days. The obtained substance will be purified through two stages, centrifugal filtering for increasing the concentration, and then adjusting to the pH of 12.

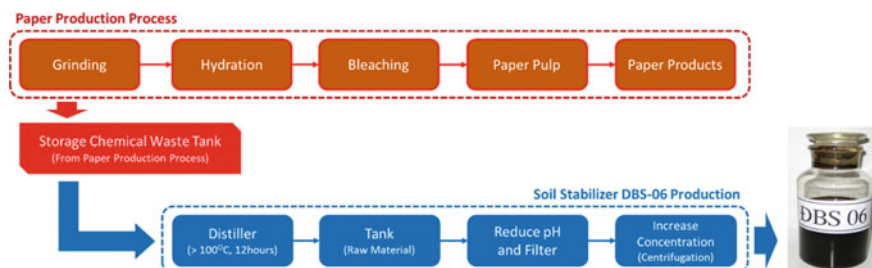


Fig. 1 Flow chart of soil stabilizer DBS-06 production

Table 1 Main characteristics of DBS-06

DBS-06 feature	Description	Note
Color	Glossary black	
Odor	Pungent aroma	
Density	1104 (g/l)	
pH	11–12	Adjusted by sulfuric acid 95–99%

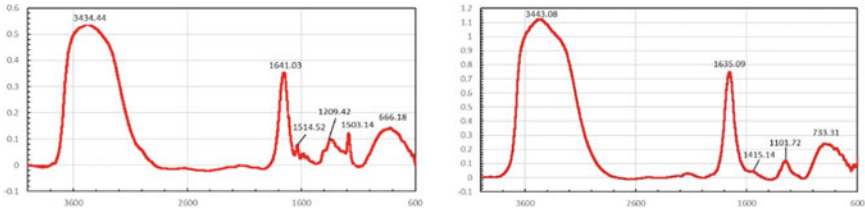
3.2 Characteristics of DBS-06

DBS-06 has some typical characteristics: the color is glossy black, specific density is of 1104 g per liter. Typical odor is pungent aroma (due to cellulose) which is represented for alkali still existing in the form of a light evaporation. The pH of DBS-06 ranges in 11–12, controlled by concentration sulfuric acid 95–99%, which can be collected as waste from chemical plants. The main properties of DBS-06 are shown in Table 1.

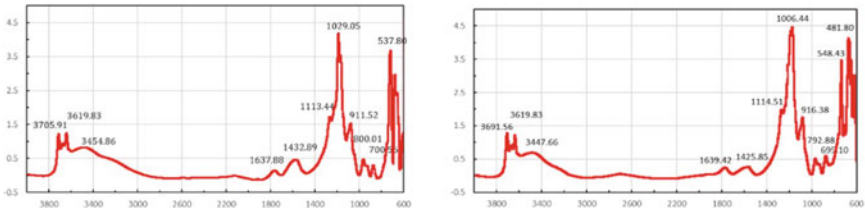
3.3 Comparison of DBS-06 to the Other Commercial Product

In order to give a comprehensive evaluation about the quality of DBS-06, spectral analysis is conducted to compare between the research product soil stabilizer DBS-06 and the well-known commercial SA44/LS40, the benchmarking compound.

The general shapes of the wavenumber graphs of the two soil stabilizer compounds DBS-06 and SA44/LS40 are very similar, with small value differences at the peak points of the two pairs of graphs. There are only two obvious differences when comparing the composition spectral graph of the two pairs. The first one is shown in Fig. 2a DBS-06-TP01 versus SA44. On the graph of DBS-06-TP01, at wavenumber of 1053.15, there is a peak of absorbance at 0.13, while on the corresponding graph



(a) Spectral of DBS-06-TP01 and SA44



(b) Spectral of DBS-06-TP02 and LS40

Fig. 2 Comparison of the spectral of DBS-06 and SA44/LS40 [2]

of SA44, the value is only 0.05; the second difference is expressed in Fig. 2b DBS-06-TP02 versus LS40. At the position of wavenumber of 548.34 cm^{-1} on the graph of DBS-06-TP02, there is a peak of absorbance of 3.5, while the corresponding value on the LS40 graph is 2.3.

From a chemical expert viewpoint, the differences between DBS-06 and SA44/LS40 are minor and can be explained by slight differences in the chemical waste composition, derived from input material and applied technology in paper production. The quality, environmental impact and soil stabilization function of the two compounds are nearly equivalent.

4 Potential Application DBS-06 in Practice

In general, the soil stabilizer compound DBS-06 is studied to enhance the properties of clay, ensuring that the soil after treatment can be used as the construction material for the subgrade, or pavement layers (base/subbase or surface courses, depending on the type of road category). This is a very good solution, helping to make use of in-situ or local materials in the construction of roadway, for example, rural roads (alley and inter-commune roads, agricultural roads, etc.), or roadway constructions in areas with extremely difficult conditions in terms of material supply such as border patrol roads, road in remote islands, remote mountainous areas. It also can be used for protection or strengthening the other elements of roadway such as shoulders, slopes [3, 13].

In addition to roadway construction, the DBS-06 has high potential to be used in the other fields of construction such as unfired clay brick, trench wall, partition panel; in the field of bottom of lake, dyke, etc.

Regarding the economic aspect, DBS-06 has proved to be a very promising soil stabilizer in application. The price of DBS-06 is \$15 USD per liter, about 25% of the corresponding SA44/LS40 price. The construction cost is about 5000–8000 VND/m² standard road base/subbase pavement, equivalent to 25% construction cost of road base with standard crushed aggregate material. Evidently, the reasonable price and construction cost of DBS-06 is high potential for applications in practice.

5 Conclusion

The paper introduces soil stabilization methodology and present condition of soil admixture and its difficulties for practical application in Vietnam. The potential of lignosulfonate as a soil admixture for stabilizing clay soils is highlighted with many advanced features. The availability of waste from the paper production industry can be used for the DBS-06 product, a lignosulfonate-based product.

The reasonable price of DBS-06, a product from a research project, is an initial good condition to promote a new sustainable method into practical application.

References

1. Chieu NQ, Khang PH (2006) Highway pavement construction, 2nd edn. Transport Publishing House, Hanoi
2. Khang PH et al (2007) Research on production of soil stabilizer agent using for base and subbase of road pavement from waste of paper production industry, Research Project (Code B2005-35-TĐ), 2005–2007, Final Report
3. Afrin H (2017) A review on different types soil stabilization techniques. *Int J Transp Eng Technol* 3(2):19–24. <https://doi.org/10.11648/j.ijtet.20170302.12>
4. McLeod NW (1943) The fundamental principles of mechanical stabilization. Department of Asphalt Technology, Imperial Oil Limited, Sarnia, Ontario, Canada
5. Yoder EJ (1957) Principles of soil stabilization. Joint Highway Research Project, Purdue University
6. Brand AS, Singhvi P, Fanijo EO, Tutumluer E (2020) Stabilization of a clayey soil with ladle metallurgy furnace slag fines. *Materials* 13:4251. <https://doi.org/10.3390/ma13194251>
7. Kang G, Kim Y, Tran TQ, Nguyen AD (2019) Strength monitoring of dredged marine clay stabilized with basic oxygen furnace steel slag using non-destructive method. In: The 29th international Ocean and polar engineering conference, Honolulu, Hawaii, USA
8. Thien QT, Amir B, Alexander SB (2022) Heat of hydration in clays stabilized by a high-alumina steel furnace slag. *Cleaner Mater* 5:100105, ISSN 2772-3976. <https://doi.org/10.1016/j.clema.2022.100105>
9. Kim Y, Thien QT, Kang G, Tan MD (2019) Stabilization of a residual granitic soil using various new green binders. *Constr Build Mater* 22:724–735. ISSN 0950-0618. <https://doi.org/10.1016/j.conbuildmat.2019.07.019>

10. Trushinskii MY (1993) Electrochemical soil stabilization method. *Soil Mech Found Eng* 30:61–65. <https://doi.org/10.1007/BF01782910>
11. Vinod JS, Mahamud MAA, Indraratna B (2012) Elastic modulus of soils treated with lignosulfonate. In: ANZ 2012 conference proceedings, Australia
12. Vinod JS, Indraratna B, Mahamud MA (2010) Stabilisation of an erodible soil using a chemical admixture. In: Faculty of engineering and information sciences—papers: Part A, 715. <https://ro.uow.edu.au/eispapers/715>
13. Alazigha DP, Vinod JS, Indraratna B, Heitor A (2018) Potential use of lignosulfonate for expansive soil stabilization. *Environ Geotech* 6(7):480–488
14. Vaiana R, Oliviero Rossi C, Perri G (2021) An eco-sustainable stabilization of clayey road subgrades by lignin treatment: an overview and a comparative experimental investigation. *Appl Sci* 11:11720. <https://doi.org/10.3390/app112411720>
15. Balu S, Ponnusamy K, Subramaniam N, Venkatasalpathi S (2020) A critical review on soil stabilization using bacteria. *IOP Conf Ser: Mater Sci Eng* 955(1):12–65. <https://doi.org/10.1088/1757-899X/955/1/012065>
16. Baveye P, Vandevivere P, Hoyle BL, DeLeo PC, de Lozada DS (1998) Environmental impact and mechanisms of the biological clogging of saturated soils and aquifer materials. *Critical Rev Environ Sci Technol* 28: 123–91
17. Mitchell JK, Santamarina JC (2005) Biological considerations in geotechnical engineering. *J Geotech Geoenviron Eng* 131:1222–1233
18. Chen Q, Indraratna B, Carter J, Rujikiatkamjorn C (2014) A theoretical and experimental study on the behavior of lignosulfonate-treated sandy silt. *Comp Geotech* 61:316–327
19. Li C, Pan Q, Zhang J, Qin X, Wang Z, Liu L, Pei M (2007) The modification of calcium lignosulfonate and its applications in cementitious materials. *J Disper Sci Technol* 28(8):1205–1208
20. Colombo A, Geiker M, Justnes H, Lauten RA, De Weerd K (2017) On the mechanisms of consumption of calcium lignosulfonate by cement paste. *Cement Concrete Res* 98:1–9
21. Aro T, Fatehi P (2017) Production and application of lignosulfonates and sulfonated lignin. *Chemoschem* 10(9):1861–1877

Experimental Investigation of Silica Fume Effect on Durability of High Performance Concrete (HPC)



Thi Thu Hien Dang, Thi Bach Duong Nguyen, Thi Hong Bui,
and Quang Trung Dinh

Abstract Chloride ions penetration in reinforced concrete (RC) structures causes serious problems linked to steel rebar corrosion, especially in maritime regions in Vietnam where environmental chloride ions content is much higher than standard value regarding corrosion problems. In this study, experimental investigation to determine durability capacity of HPC, regarding chlorine ion penetration, is performed in different conditions of chloride ion content in environmental water: laboratory condition, Ha Long Bay and Khanh Hoa region. Different doses of silica fume additive (5%, 10% and 15% replacing cement in concrete) are consequently examined on three HPC grades (C50, C60 and C70). Service life or durability capacity by mean of rapid chloride ions permeability measures, according to ASTM C1202 standard, at 365 days are analyzed. Experimental results show that 15% of silica fume additive replacing cement is the best dose to reduce chloride ions penetration for all studied maritime regions in Vietnam. Among three grades of HPC, C70 is more suitable in high environmental chlorine ions content regions and capable to stand against chlorine ions penetration much more than C50 and C60 HPC.

Keywords Rapid chloride ion permeability · Silica fume additive · Experimental investigation · Durability or service life capacity · HPC

1 Introduction

As a country with very long coastline, high performance concrete (HPC) for RC infrastructure application in maritime regions in Vietnam is recently developed within various types of civil structure such as seaports, breakwaters, ship locks, drilling rigs. Concrete used in these areas should be capable to stand against chlorine ions

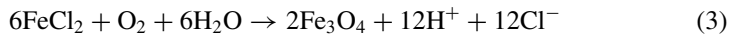
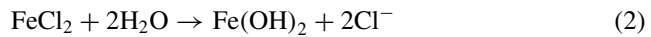
T. B. D. Nguyen · T. H. Bui
University of Transport and Communications, Hanoi, Vietnam

T. T. H. Dang (✉) · Q. T. Dinh
Le Quy Don Technical University, Hanoi, Vietnam
e-mail: thuhen118v2@gmail.com

© The Author(s), under exclusive license to Springer Nature Singapore Pte Ltd. 2024
T. Nguyen-Xuan et al. (eds.), *Proceedings of the 4th International Conference on Sustainability in Civil Engineering*, Lecture Notes in Civil Engineering 344,
https://doi.org/10.1007/978-981-99-2345-8_7

penetration because its content in seawater is usually much higher than yielding value according to the corrosion problems, which may cause serious damages for HPC structures. Therefore, durability capacity of HPC in maritime regions in VietNam is particularly considered while designing HPC infrastructure in these regions.

It is shared by many authors that the corrosion of steel reinforcement due to chloride ions penetration is the major cause reducing durability capacity of concrete. In fact, chloride ions ingress in contact with steel rebar's (reinforcement) can produce corrosion with chemical reaction as following:



As we can see, the chemical reaction chain reproduces chlorine ions (Cl^{-}), therefore, even with a very small amount of chlorine ions penetrating through concrete and being in contact with steel reinforcement, the corrosion is continuous and cause serious damages for RC structures.

In order to prevent this mechanism of corrosion, engineer must to design RC concrete with a "good" cover concrete as corrosion shield against initial chlorine ions penetration and reduce concrete pores in order to minimize water and oxygen inside concrete structure. A very comprehensive explanation of corrosion with chlorine ions penetration is presented in [1].

Recent works by many authors share common interest in additive to cementitious material such as silica fume (MS) in [2–6], in order to increase concrete strength in compression, shear and tension capacities. In [6], authors have studied the influence of silica fume for concrete used in hot coastal conditions. Not only increasing concrete strength, these studies lead us to the conclusion that silica fume can increase concrete surface protection against chlorine ion penetration and also reduce concrete pores. The double effect of MS additive is the main reason to explain the trend of using silica fume as additive to replace cementitious materials.

Regarding standards and norms related to prevent corrosion phenomenon, it is practical to limit upper water/binder ratio (or water/cementitious materials ratio). For concrete structures in marine environments, the current European concrete code EN 206-1 [7] allows concrete quality based on water/binder ratios up to 0.45. In the national appendix to this code, the current Norwegian concrete specification, NS-EN 206-1 [8], has reduced the upper limit for a water/binder ratio of 0.40. After extensive experience with durability problems with all coastal concrete bridges, the Norwegian Public Transport Authority (NPRA) in 1988 requires a water/binder limit ratio for such structure (e.g., for bridge, limit ratio is 0.40). Since 1996, this upper limit has been reduced to 0.38 for RC parts in contact with sea water. However, there is a lack in standard about silica fume additive in concrete to prevent the corrosion phenomenon, especially in Vietnamese maritime regions.

The question on optimal ratio of silica fume additive used in HPC is the main motivation of this study in which experimental investigation to determine durability capacity of HPC is performed in different conditions of chloride ions content in environmental water: laboratory condition, Ha Long Bay and Khanh Hoa region. Different doses of silica fume additive (5%, 10% and 15% replacing cement) are consequently examined on three HPC grades (C50, C60 and C70). Durability capacity, in other world, service life capacity by mean of rapid chloride ion permeability measures, according to ASTM C1202 standard, at 365 days are analyzed. Experimental results show that 15% of silica fume additive replacing cement is best dose to reduce chloride ion penetration for all studied far-coastal regions in Vietnam. Among three grades of HPC, C70 is more suitable in high environmental chlorine content regions and capable to stand against chlorine ion penetration more than C50 and C60.

2 Material and Methodology

2.1 Material

Cement PC40 Vicem of Ha Tien Company, fabricated according to the TCVN 2682:2009, is used with details of chemical composition presented in Table 1.

Silica fume sikacrete PP1 of Sika Company is used with chemical composition presented in Table 2.

Coarse aggregate of 5×10 mm and fine aggregate (natural yellow sand and crushed sand) extracted from Hon Ngang–Dien Khanh quarry were used for all mixtures. Coarse and fine aggregate size distribution are presented in Fig. 1.

In addition, additive GPS-5000 is also used according to TCVN 4506-2012 [9]. Concrete mixtures were cast using 5, 10 and 15% of silica fume (MS) as additive to ordinary concrete mixture. In total, 9 types of HPC are built, mixing of 3 concrete grades (C50, C60 and C70) with 3 doses of silica fume (5%, 10% and 15%). The composition of concrete mix design is presented in Table 3.

Table 1 Chemical composition of Ha Tien Cement

SiO ₂	Al ₂ O ₃	Fe ₂ O ₃	CaO	MgO	SO ₃	Na ₂ O	K ₂ O	MKN
21.49	5.40	3.49	63.56	1.40	1.65	0.15	0.70	1.20

Table 2 Chemical composition of silica fume

SiO ₂	Al ₂ O ₃	Fe ₂ O ₃	CaO	MKN
93.45	0.92	0.52	1.57	4.20

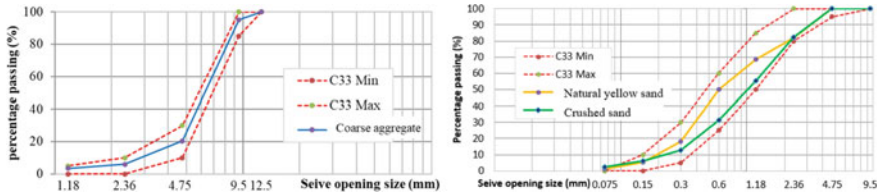


Fig. 1 Coarse (upper) and fine (lower) aggregate size distribution

There are 09 types of HPC, mixing of 03 doses of Silica Fume (5%, 10% and 15%) and 03 HPC grades (C50, C60 and C70). For each type of HPC, certain identical samples are built in the laboratory which serve two measurements: strength measurement and chlorine ions penetrability measurement.

2.2 Methodology

The experimental investigation consists in two stages:

- Stage 1: In laboratory

In this stage, all samples of concrete up to 28 days old are conserved in the laboratory. Concrete strength is measured at 3, 7 and 28 days old according to ASTM C39.

- Stage 2: In sea island conditions

Certain concrete samples are conserved in the laboratory. For these samples, the rapid chlorine ion permeability is measured according to ASTM C1202 standard at 28, 180 and 365 days old.

Certain 28 days old concretes are transported to Khanh Hoa and Ha Long Sea zones and immersed in water until 365 days. Then, the rapid chlorine ion permeability is measured according to ASTM C1202 at 365 days.

3 Experimental Investigation Results

3.1 Concrete Strength Measurement

Compressive strengths are measured at 3rd, 7th and 28th day and presented in Fig. 2. As we can see that all concrete samples have their compressive strength satisfactory to the designed concrete grades. In addition, the silica fume increases compressive strength of concrete.

Table 3 Concrete mix design

Comp	HPC grades	W/B	B = cement + MS (kg)	W = Water (l)	Cement (kg)	MS = silica fume (kg)	Coarse 5 × 10 (kg)	Total sand (kg)	Crushed sand (kg)	Yellow sand (kg)	GPS-5000 additive (l)
1	5%	0.39	400	155	380	20	1085	833	292	541	7.5
2		0.33	470	155	446.5	23.5	1085	746	261	485	7.5
3		0.29	530	155	503.5	26.5	1085	693	243	451	7.5
4	10%	0.4	390	155	351	39	1085	809	283	526	7
5		0.34	460	155	414	46	1085	747	261	485	7
6		0.3	520	155	468	52	1085	694	243	451	7
7	15%	0.37	420	155	357	63	1085	776	271	504	7.5
8		0.32	490	155	416.5	73.5	1085	712	249	463	7.5
9		0.28	560	155	476	84	1085	649	227	422	7.5

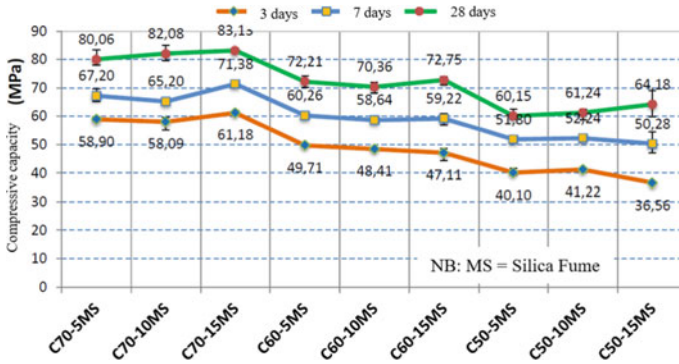


Fig. 2 Compressive strength concrete measurement

3.2 Measure of Chlorine Ions Penetrability in Laboratory

The electrical current was measured according to the ASTM C1202 standard. A D.C. external voltage of 60 V was applied to a 50 mm of diameter and 50 mm of height concrete sample. This concrete specimen was in contact with a solution of sodium hydroxide in the anode and with a solution of sodium chloride in the cathode. The samples were saturated in water before the test according to the standard. During the test, the main parameter measured was the current flow (in coulombs) through the concrete for a period of 6 h. The total charge passed (coulombs) is determined by calculating the area under the plot of current (A) versus time (S) (Fig. 3).

According to the chlorine ions penetrability in laboratory condition regarding yielding values in Table 4, HPC with MS additive is qualified as very low (Q between 100 and 1000C) and impermeable (Q < 100C) to chlorine ions. This excellent impermeability of concrete sample ensures durability capacity in HPC. In addition, the

Fig. 3 Experimental set-up for chlorine ion penetration test in UTC Lab



Table 4 Chloride ion penetrability based on charged passed ASTM C1202

Charge passed (coulombs)	Chloride ion penetrability
> 4000	High
2000–4000	Moderate
1000–2000	Low
100–1000	Very low
< 100	Negligible (impermeable)

more important HPC grade is, the less penetrable HPC concrete is. For 5% MS, the charge passing of C70 at 28 days old (227C) is almost the half of C50’s one (475C).

As increasing MS additive in concrete mixture, the penetrability of chlorine ions decreases. For all HPC grades tested in this study, with 15% MS, the concrete is qualified “impermeable”.

The penetrability is decreasing as function of days old measurement ($D_{28} > D_{180} > D_{365}$). This can be explained by the fact that after 28 days, chemical reaction in concrete still happens and made surface concrete shield harder against chlorine ions penetration (Fig. 4).

Fig. 4 Chlorine ion penetrability of HPC at 28th, 180th and 365th day

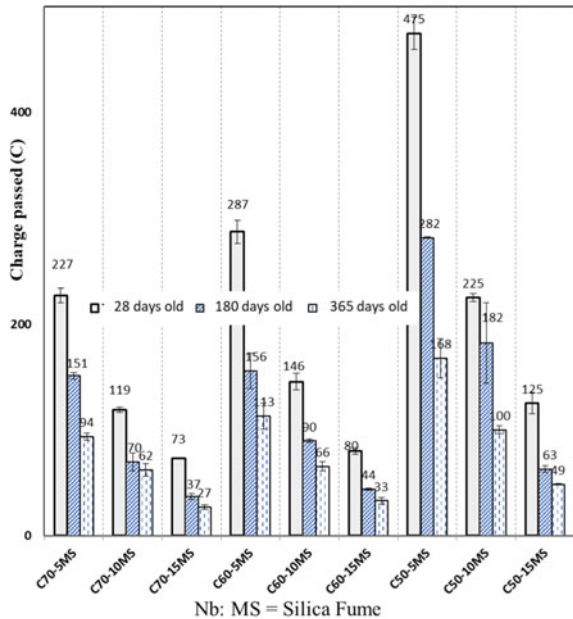




Fig. 5 Photos of immersed sampled in tides zones of Khanh Hoa region (left) and Ha Long Bay (right)

3.3 Measure of Chlorine Ion Penetrability at 365 days Old for Ha Long Bay, Khanh Hoa Region

The 28-day-old concrete in laboratory condition is then transported and immersed in tides zones of Ha Long and Khanh Hoa regions, until their 365 days old (Fig. 5).

The 365-day-old samples are then used to measure chlorine ions penetrability such as ASTM 1202. The charge passing is presented in Fig. 6. The 365-day-old measures of chlorine ions penetrability show the impact of chlorine content in environmental water. The richer environmental chlorine ions content (in Khanh Hoa region and Ha Long Bay seawater) is, the more penetrable chlorine ion of concrete is. However, with more than 10% of MS additive in C70 grade, HPC is qualified as impermeable for chlorine ion ($Q < 100C$) for all studied regions in Vietnam in this study. As recommendation for studied regions in Vietnam, 10% of silica fume additive is sufficient for all HPC grades to protect against chlorine ions penetration in laboratory condition ($Q < 100C$) but HPC of C70 with 10% is necessary for maritime regions.

4 Conclusions

In this study, experimental investigation of silica fume on durability is carried out with concrete sampled immersed in different environmental conditions of chlorine ion content. Different doses of MS are examined such as 5%, 10% and 15% replacing cementitious materials in three HPC grades (C50, C60 and C70). As expected, strength capacity in compression of all concrete sample is ensured within their grades. According to durability capacity, the more silica fume additive is added, the less penetrable chlorine ion is. Higher grade is more suitable for high chlorine content in environmental conditions. And the charge passing of chlorine ion penetrability for C70 with 10% of MS is less than 100 C in maritime regions, therefore,

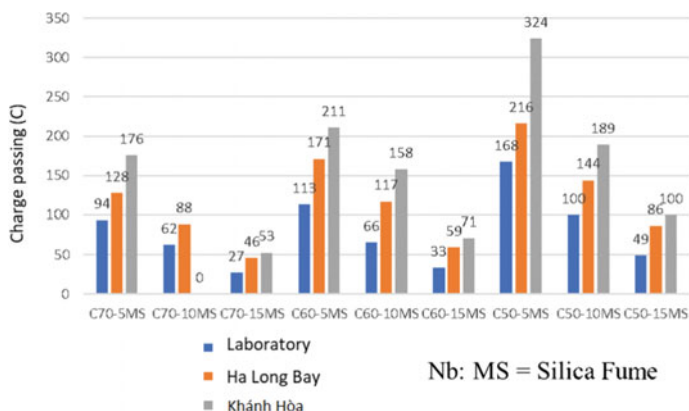


Fig. 6 Chlorine ion penetrability at different condition of environmental chlorine content

this HPC is recommended for concrete infrastructure in studied maritime regions in Vietnam while HPC C50 with 10% is sufficient for laboratory condition.

References

1. Gladis C, Paulo Sérgio B Denise CB (2013) Chloride penetration depth in silica fume concrete. *IACSIT Int J Eng Technol* 5(6)
2. Hooton RD, Pun P, Kojundic T, Fidjestol P (1997) Influence of silica fume on chloride resistance of concrete. In: *Proceeding international symposium of high performance concrete*, Chicago (P. Johal, Precast Prestressed Concrete Institute), pp 245–249
3. Lizarazo-Marriaga J, Lucio Guillermo L (2012) Effect of silica fume addition on the chloride-related transport properties of high-performance concrete, *Dyna* (Medellin, Colombia)
4. Mansor Am, Ahmed h, Ruben PB (2016) Effect of silica fume on high performance concrete strength
5. Pun PCH (1999) Influence of silica fume on chloride resistance of concrete
6. Smith BG (2001) Durability of silica fume concrete exposed to chloride in hot climates. *J Mater Civil Eng* 13(1):41–48
7. CEN EN 206-1 (2000) Concrete—Part 1: specification, performance, production and conformity, Brussels, Belgium
8. NS-EN 206-1 (2013) Concrete—specification, performance, production and conformity
9. 4506 TCVN (2012) Water for concrete and mixture—technical specification

Leaching Mechanism of Metals from Recycled Concrete Aggregates (RCA) and Potentially Environmental Issues



Vu Quoc Hung, Prasanna Egodawatta, Chaminda Gallage, and Les Dawes

Abstract Recycled concrete aggregates (RCA) is one of the most prevalent construction waste products what is regularly used in the road construction industry. Besides many advantages, substances leaching from RCA are emphasised as the most involving the environmental problem. The research investigated metals leaching characteristics from RCA by carrying out a detailed experimental method with many influential factors to grasp the most influencing factors on the metal leaching regime. Research outcomes disclosed that the integrated influences of factors are changed to RCA, while individual metals released are also influenced following to varied ways. Liquid-to-solid ratios (L/S) significantly affect leaching metals from RCA controlling saturated conditions, facilitating high metal concentrations in the leachate. Interestingly, the larger degree of compaction leading to increasing density of materials displayed the highest negative influence on metal leachability, suggesting that the metal release can considerably decrease, especially when the RCA is used for the sub-base road layers with a high degree of compaction. However, the use of recycled construction materials under field conditions should be further studied as there is an increasing concern of metal leaching from RCA with respect to recreational and drinking water thresholds.

Keywords Recycled materials · Recycled concrete aggregates · Roads construction · Metal leaching · Leaching · Metal pollution · Recycled waste products

V. Q. Hung (✉)
Ha Noi University of Civil Engineering/HUCE, Hanoi, Vietnam
e-mail: hungvq@huce.edu.vn

P. Egodawatta · C. Gallage · L. Dawes
Queensland University of Technology/QUT, Brisbane, QLD, Australia

© The Author(s), under exclusive license to Springer Nature Singapore Pte Ltd. 2024
T. Nguyen-Xuan et al. (eds.), *Proceedings of the 4th International Conference on Sustainability in Civil Engineering*, Lecture Notes in Civil Engineering 344,
https://doi.org/10.1007/978-981-99-2345-8_8

1 Introduction

Recycled concrete aggregates (RCA) has been considered as an optimal solution to management of concrete wastes. This product is mostly used in road construction and low grade concrete productions [1]. There are plenty of reasons for the raising popularity of using RCA. Firstly, the natural aggregates are limited due to restrictions in mining and harvesting. Secondly, recycled construction material is regularly regarded as a sustainable waste management practice. However, many problems are also emphasised including lack of awareness, unsuitable technologies and insufficient control and guidelines [2]. Particularly, the environmental problems associating with using RCA. In which, substances leaching, have been the most critical matter. Sakanakura et al. [3] revealed that high-pH and high concentration of heavy metals released from RCA could cause die-off of vegetation. Moreover, pollutants from RCA used in road construction are able to leach into groundwater and thus could cause human health via direct exposure or consumption drinking water [4].

Leaching mechanism of metals has complicated process with a range of factors, which can be categorised as physical, chemical and external [5]. Fundamentally, these factors are not independent and exhibit an interactive influence. These five factors were selected due to their practical relevance in geotechnical engineering in terms of road sub-base and backfill designs. The relationship of such influential factors is described as Fig. 1.

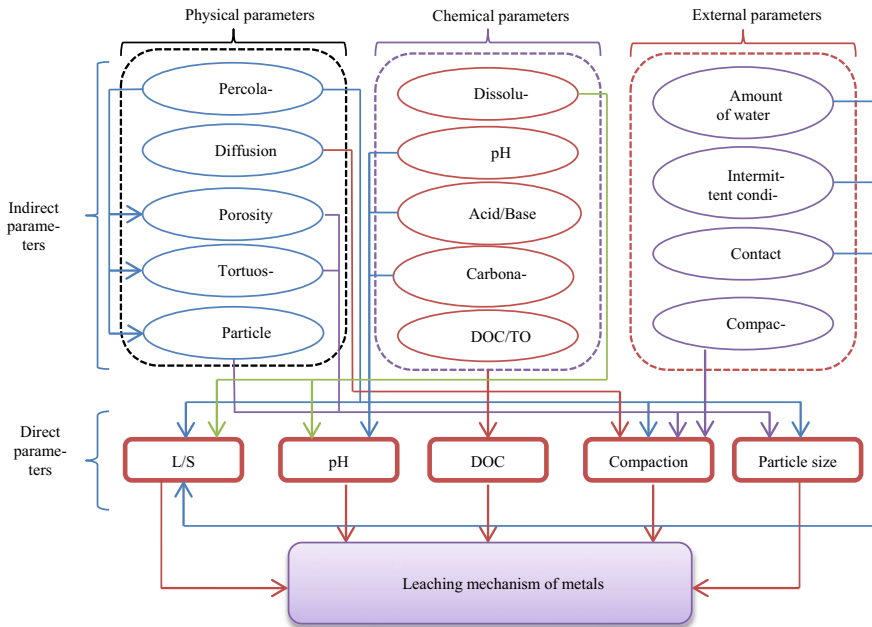


Fig. 1 Relation of influential factors on leaching mechanism

The main objective of the study is to identify the extent of individual key factors impacting on the leaching mechanism of metals from RCA in comparison with the standard leachate. The studying outcomes are expected to develop more understanding of leaching regime relating to the rank of primary influential factors, as well as metals released characteristics and mineralogical composition in RCA. The relations of metals leached into water resources and water quality management was also evaluated as fundamental knowledge to stipulate popular guidance for using RCA in practice.

2 Material and Methods

2.1 Sample Collection

Concrete waste were classified and crushed at a production plant according to a variety of aggregate sizes before using road construction. RCA samples were collected by one of leading producer of recycled materials for civil construction industry in Australia.

2.2 Laboratory Analysis

The collected samples of RCA were split into six portions to conduct the tests as in Table 1. Particle sizes distribution of RCA was performed using dry sieve analysis grain size. Mineralogy in RCA was determined by X-ray diffraction (XRD). Standard leaching test was carried out is to identify the largest amount of metals leaching controlled by extreme conditions. Leaching test under control of individual conditions including L/S, compaction, DOC and pH were carried out separately. Concentration of metals in leachate was identified by using inductively coupled plasma mass spectrometry (ICP-MS).

2.3 Data Analysis

The factors influencing metals leaching from RCA were identified using multivariate data analysis techniques of principal component analysis (PCA) and the Preference Ranking Organisation Method for Enrichment Evaluations (PROMETHEE).

Table 1 Leaching parameters and testing methods

Parameters	Test method
Particle size distribution	Test by sieving
Mineralogy	X-ray diffraction
Standard leaching	Leaching characteristic
Leaching test as a function of L/S	Compliance test for leaching
Leaching test as a function of pH	Leaching behaviour test-Influence of pH
Leaching test as a function of compaction	Leaching test and compacted bulk density
Leaching test as a function of DOC	Compliance test for leaching and method 5310C
Metals	ICP-MS, method 200.8

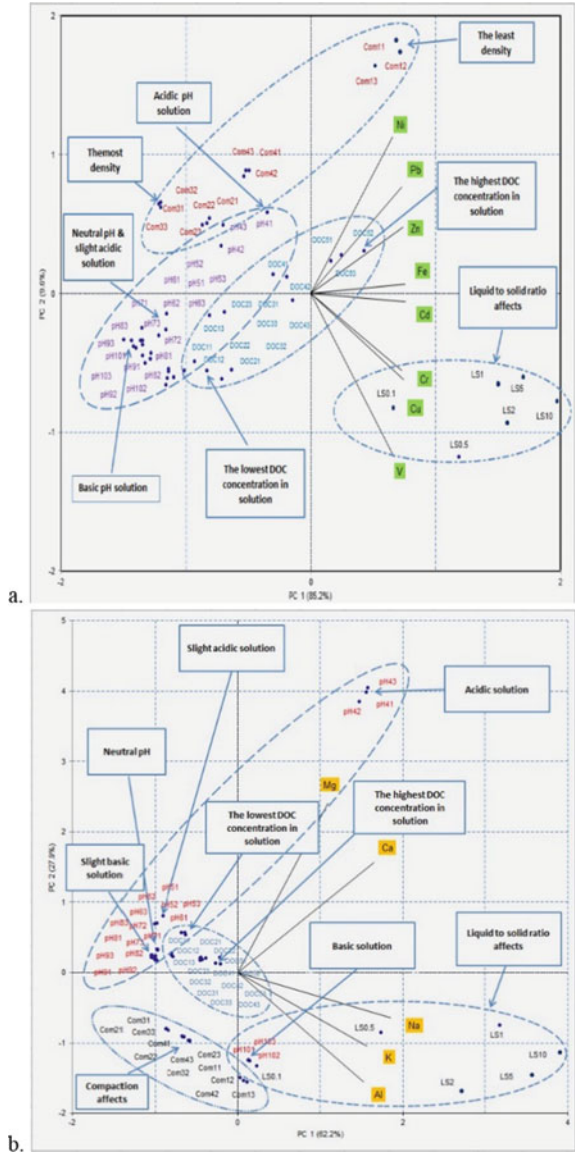
3 Results and Discussion

3.1 Leaching Characteristics of Metals from RCA

A general assessment of many influential factors of metal leaching from RCA enables the duplicate realistic field conditions. Accordingly, PROMETHEE and PCA analyses were performed to provide a more understanding evaluation and ranking of the influential factors. The assessment was conducted to major metals (Na, K, Al, Ca and Mg) and trace metals (Ni, Cd, Cr, Pb, Zn, Fe, Cu and V) separately for selected recycled materials. Data for pH above 10 and less than 5 were disregarded for this analysis to prevent obscured outcomes. The data matrix consisted of major/trace metals concentrations and 54 objects representing changes to pH (ranging from 5 to 10), DOC, L/S ratio and compaction experiments.


As evident from the PCA biplot for major elements leached from RCA (see Fig. 2), L/S ratios changed supply the highest variance where Na, Al and K are shown. This point demonstrated that these metals release is highly influenced by the L/S ratio. It is also noted that alkaline environment can grow up the leaching of the metals. Particularly, Mg and Ca, are indicated that the general direction where the objects pointed pH changes, while the influence of other factors can be considered minimal. For trace metals, Ni, Pb and Zn are influenced by the different compaction and DOC and for a lesser extent by L/S ratio. The other group including Cr, Cu and V points a negative relationship with different compaction, pH and DOC, but a positive relationship with varying L/S ratio. This implies that the leaching of Cr, Cu and V from RCA is strongly influenced by the L/S ratio, while the degree of influence by pH, DOC and compaction is minor. These observations point the differences in leaching mechanism and change in the degree of influence by factors on different metal elements.

Fig. 2 PCA biplots representing the factors influencing the leaching of **a** Major metals and **b** trace metals from recycled concrete aggregates (RCA)



As observed in Table 2, the most positive influence on metal leaching from RCA is L/S ratios ≥ 1 condition, while high-pH values (alkalinity) and high compaction exert the most negative influence. This implies that metals are likely to be leached from recycled waste materials under high L/S ratios, while highly compacted materials have provided limited opportunities for water contact and hence potential leaching of metals. Based on this, it can be proposed that the leaching metal from RCA is considerably influenced by L/S ratio, compaction and pH variations. Having DOC

Table 2 General rank of specific factors influence on leaching regime

Ranking	Factors	ϕ^+	ϕ^-	ϕ	Comments
1	L/S10	0.668	0.0444	0.6236	<p style="text-align: center;"><i>The most influence</i> (High positive influence on leaching)</p>  <p style="text-align: center;"><i>The least influence</i> (High negative influence on leaching)</p>
2	L/S5	0.6395	0.0547	0.5848	
3	L/S2	0.5399	0.0979	0.442	
4	L/S1	0.3792	0.1435	0.2357	
5	Com1	0.2578	0.1918	0.066	
6	L/S0.5	0.2377	0.1826	0.0551	
7	DOC5	0.2018	0.1656	0.0363	
8	pH4	0.2063	0.2001	0.0062	
9	DOC1	0.1463	0.1908	-0.0445	
10	DOC4	0.1395	0.1917	-0.0522	
11	pH10	0.1701	0.2254	-0.0553	
12	DOC3	0.131	0.1922	-0.0612	
13	DOC2	0.114	0.2067	-0.0927	
14	L/S0.1	0.1163	0.229	-0.1127	
15	Com4	0.0952	0.2561	-0.161	
16	Com2	0.0805	0.2612	-0.1806	
17	pH6	0.0517	0.2426	-0.1909	
18	pH9	0.0438	0.2456	-0.2017	
19	pH8	0.0432	0.253	-0.2098	
20	pH5	0.0514	0.2695	-0.2182	
21	pH7	0.0406	0.2607	-0.2201	
22	Com3	0.0335	0.2823	-0.2489	

concentrations close together in the mid-range of ranking suggests that its influence on metal leaching is minimal.

3.2 Variability in Metal Leaching with Respect to Threshold Concentrations

A comparison between metals leached from RCA because of variation in the major influential factors with heavy metal threshold concentrations in form of drinking water monitoring, recreational water monitoring and industrial waste effluent monitoring and metals leached during standard leaching tests are shown in Fig. 3. Based on the available thresholds, the metals including Al, Fe, Zn, Ni, Cu, Cd and Pb are discussed. The threshold concentrations for water quality and public health risk are specified based on a range of guidelines [6]. Further, thresholds metals from solid

wastes into the environment is mainly governed by the guideline relating to industrial waste management.

As shown in Fig. 3, Zn and Cd concentrations release from RCA because of primary factors are lower than the industrial waste disposal, recreational and drinking water thresholds except during extreme pH values. Moreover, Al and Fe leaching from RCA can be concerned as critical for water sources in recreational purposes as their concentrations are well above the threshold for most of the conditions. Even though low level exposure to Al and Fe does not cause adverse effects on human, chronic exposure to Al may cause nerve damage, kidney damage and allergies [7, 8] and genetic and metabolic diseases by Fe [9]. On the other hand, water insoluble Fe (3+) can cause undesirable tastes and colour, preventing usage of water for drinking and recreation purposes. Also, metals concentrations leached out (Ni, Cu and Pb) are greater than the drinking water thresholds and position close to recreational water thresholds. A high level of Cu usually leaves a metallic or unpleasant bitter taste in the drinking water [9], whereas Pb exposure for young children via ingestion can impair mental function [8]. Furthermore, chronic exposure to Ni via drinking water can cause carcinogenic effects. Thus, it can be postulated that Ni, Cu and Pb leaching from RCA can potentially cause human health impacts when RCA is used close to drinking or recreational water resources.

4 Conclusion

This study analysed the metal leaching characteristics from RCA due to the variations in key influential factors of compaction, pH, DOC and L/S ratio. The study found Al and Fe leaching from RCA is critical and above the thresholds stipulated for recreational water use. Furthermore, leaching of Ni, Cu and Pb from RCA lies close to the threshold concentrations for recreational water use, implying that they can potentially cause harmful effects to human health and to the environment when used close to water resources and sensitive environments. Leachate from RCA can be an added source of metals. Though high concentration can be diluted in large water sources, long term exposure and bioaccumulation can influence environmental and human health risks.

About leaching conditions, high L/S ratios and high alkalinity present the highest influence on leaching of metals such as Na, Al and K from RCA. Metals such as Mg and Ca are influenced by acidic pH ranges while Fe, Ni, Pb, Zn and Cd are influenced by different degree of compaction and DOC content. Leaching of Cr, Cu and V are strongly influenced by changes to L/S ratio. Based on the PROMETHEE raking, L/S ratios with saturated conditions present the highest positive influence on metal leaching from RCA, while high-pH values and high compaction exert the most negative influence. Overall, it can be concluded that the influence of L/S ratio, pH and compaction on metal leaching is significant. Therefore, it is important to consider these factors critical variables in modelling practices and field scale monitoring for better environmental protection.

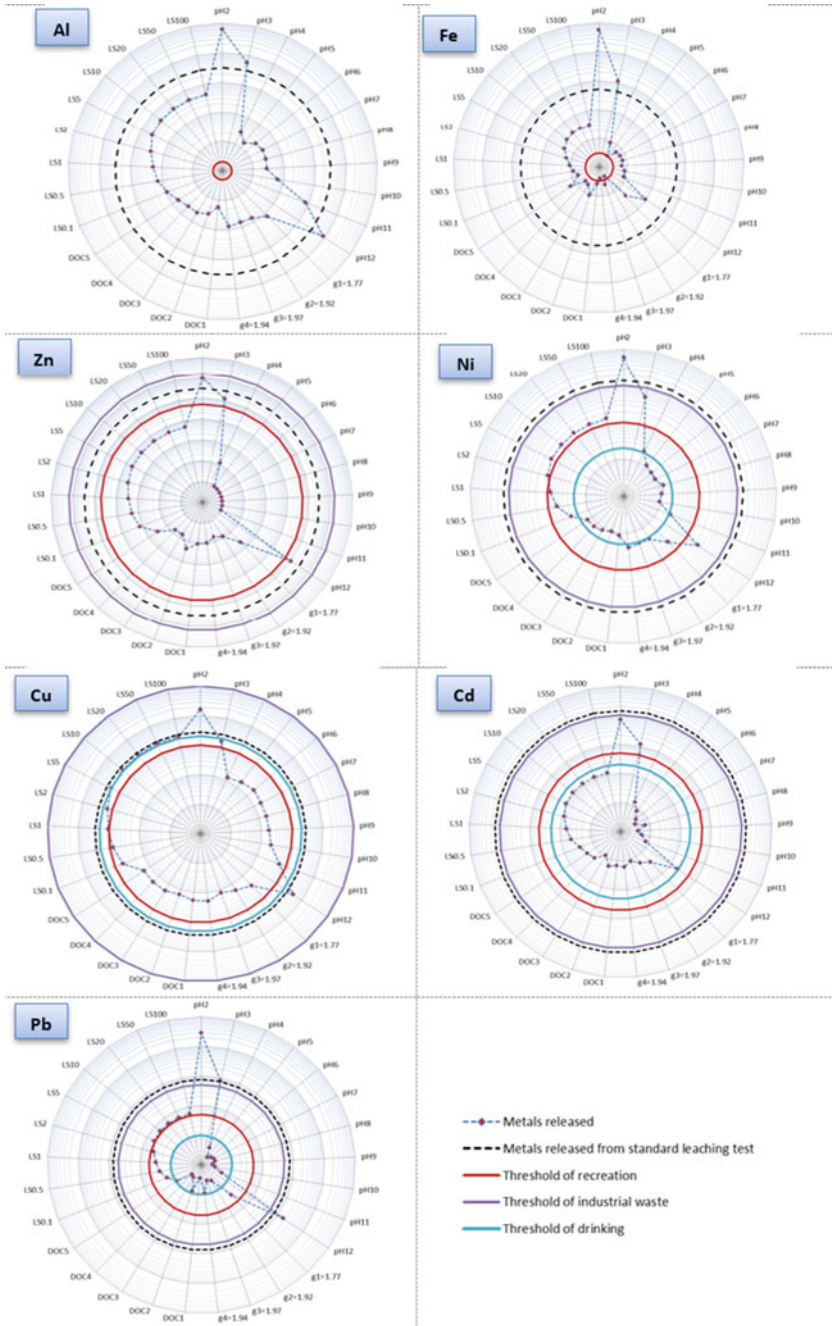


Fig. 3 Concentrations of metals leaching from recycled concrete aggregates (RCA) in comparison to standard leaching test and water quality thresholds

References

1. Vieira CS, Pereira PM (2015) Use of recycled construction and demolition materials in geotechnical applications: A review. *Resour Conserv Recycl* 103:192–204
2. Rao A, Jha KN, Misra S (2007) Use of aggregates from recycled construction and demolition waste in concrete. *Resour Conserv Recycl* 50:71–81
3. Sakanakura H, Osako M, Kida A (2009) Effect of exposure test conditions on leaching behavior of inorganic contaminants from recycled materials for roadbeds. *Waste Manage* 29:1658–1665
4. Butera S, Christensen TH, Astrup TF (2014) Composition and leaching of construction and demolition waste: inorganic elements and organic compounds. *J Hazard Mater* 276:302–311
5. Van der Sloot H, Dijkstra J (2004) Development of horizontally standardized leaching tests for construction materials: a material based or release based approach?: Identical leaching mechanisms for different materials, ECN
6. A. ANZECC (2000) Australian and New Zealand Environment and Conservation Council and Agriculture and Resource Management Council of Australia and New Zealand, Australian and New Zealand guidelines for fresh and marine water quality, Canberra, pp 1–103
7. Exley C (2016) The toxicity of aluminium in humans. *Morphologie* 100:51–55
8. Ritter KS, Sibley P, Hall K, Keen P, Mattu G, Linton BL (2002) Sources, pathways, and relative risks of contaminants in surface water and groundwater: a perspective prepared for the Walkerton inquiry. *J Toxicol Environ Health Part A* 65:1–142
9. Fraga CG, Oteiza PI (2002) Iron toxicity and antioxidant nutrients. *Toxicology* 180:23–32

Effect of Shape Memory Alloy Fibers on Volumetric Strain and Moduli of Concrete in Cyclic Compression



Vinh-Ha Ho, Van-Minh Ngo, Eunsoo Choi, and Ngoc-Long Nguyen

Abstract This study investigated the impact of dog-boned and crimped shape memory alloy (SMA) fibers on the volumetric strain and moduli of concrete. The SMA fibers were produced via cold drawing and shaping through crimping or heating. Cyclic compression tests were conducted on plain and 1.0–1.5% fiber content concrete under heating and non-heating conditions. Results showed that adding SMA fibers decreases volumetric strain and increases ductility of concrete. However, heating led to an increase in volumetric strain due to recovery stress. The presence of SMA fibers also increased secant and tangent moduli, with dog-boned fibers proving more effective than crimped fibers. The recovery stress caused a factor of 2 and 1.6 increase in secant and tangent moduli, respectively, enhancing the stiffness of the SMA fiber-reinforced concrete. The study provides valuable insights into the potential use of SMA fibers in improving the ductility and stiffness of reinforced concrete structures.

Keywords Cyclic behaviors · Compression · Volumetric strain · Shape memory alloy · Cementitious materials

V.-H. Ho (✉)

Campus in Ho Chi Minh City, University of Transport and Communications, No 450-451 Le Van Viet Street, Ho Chi Minh City, Vietnam
e-mail: hahv_ph@utc.edu.vn

V.-M. Ngo · N.-L. Nguyen

University of Transport and Communications, No 3 Cau Giay Street, Hanoi, Vietnam

E. Choi

Department of Civil and Environmental Engineering, Hongik University, Seoul 04066, Republic of Korea

1 Introduction

In recent decades, fibers have gained popularity as an additive in cementitious materials due to their ability to enhance mechanical properties [1–3]. Their potential for improving civil and infrastructure structures has led to increased usage [4–6]. However, cyclic loads can cause fatigue failure in these structures, yet limited studies have investigated the cyclic behavior of reinforced concrete [7, 8]. Kesner et al. [9] found that polymer fibers improved the ductile behavior of concrete under cyclic compression. Another study showed that steel fiber content affects plastic strains but not fiber aspect ratio, resulting in stiffness degradation and linear unloading behavior [10]. Nonetheless, the behavior of fiber-reinforced concrete under cyclic loads remains largely unexplored and requires further research.

In recent years, shape memory alloy (SMA) fibers have become a subject of interest among researchers for their superior properties, including high modulus, high yield stress, shape memory effect, and superelasticity, making them a desirable addition to cementitious materials. Potential applications of SMA fibers in concrete include crack-closing, prestressing, crack-repairing, and self-healing, with significant implications for infrastructure durability and sustainability [11–15]. Researchers have explored various shapes for SMA fibers to optimize their performance in concrete, with crimped and 5D hooked-end shapes providing higher resistance through the anchoring effect [16–18]. Despite the potential of SMA fiber-reinforced concrete, research into its compression behavior has been limited due to the novelty of the material. While previous studies have focused on the monotonic compression behavior of SMA fiber-reinforced concrete, such as the studies by Aslani et al. [19] and Naidu et al. [20], which found that the strength of the material was influenced by the volumetric ratios of the SMA fibers, further investigation is required to explore its cyclic behavior. In particular, a study by Naidu et al. [20] revealed that SMA fibers were unable to demonstrate their smart performance of shape memory effect in comparison with steel fiber-reinforced concrete.

Recently, Choi et al. [21, 22] investigated the compression behaviors of cold-drawn shape memory alloy (SMA) fiber-reinforced concrete. Their study revealed that heating SMA fibers with a 1.0% volume fraction induced recovery stress, which was effective in controlling expansion after cracking. However, the influence of SMA fibers on the strain behavior and moduli of concrete under cyclic compression remains unexplored. This study aims to investigate the cyclic compressive behavior of SMA fiber-reinforced concrete, including volumetric strain, and modulus increment, with dog-boned and crimped shaped SMA fibers and plain, 1.0%, and 1.5% volume fraction SMA fiber-reinforced specimens. The study will be conducted under both heating and non-heating conditions. The research findings will contribute to the development of sustainable and resilient infrastructure systems by enhancing our understanding of the cyclic behavior of cementitious materials reinforced with SMA fibers.

2 Cyclic Compression Test

2.1 Properties of SMA Fibers

Cold drawing and producing fibers

A 0.955 mm cold-drawn NiTi shape memory alloy (SMA) fiber was created by annealing, straightening, removing dislocations, heating to 500 °C, and cooling to 25 °C. The cold-drawing process induces a prestrain that generates recovery stress when heated, making the fiber useful in embedding in cement concrete for cyclic compression tests. The dog-boned and crimped fibers used in the study are depicted in Fig. 1 [22].

Recovery stress

Figure 2 [22] depicts the recovery stress curves of SMA fibers, showing that the fibers exhibited the shape memory effect by generating recovery stress upon heating. The curves indicated a decreasing trend in slopes when heated at 200 and 300 °C, with the thermal effect being more pronounced at temperatures above 200 °C. Therefore, to optimize the reinforced concrete, it is recommended that the heating temperature range should be between 100 and 200 °C. Accordingly, a temperature of 150 °C was selected for the cyclic compression test, as it produced the maximum recovery stress ratio of 1.67 times between the dog-boned and crimped fibers.

Deformation recovery

Table 1 summarizes the changes in dimensions of SMA fibers following heat treatment. The study found that the shape memory effect induced a larger reduction in length compared to the combined effect of thermal and stretching on the fibers. Specifically, the diameter of the dog-boned fiber increased from 0.955 to 0.971 mm, resulting in a significant increase in frictional resistance but a decline in anchoring bond to zero value. Conversely, the thickness of the crimped fiber increased by

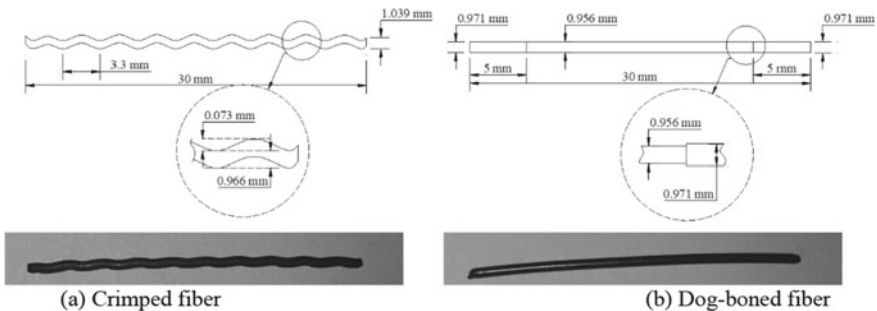


Fig. 1 Dimensions of fibers [22]

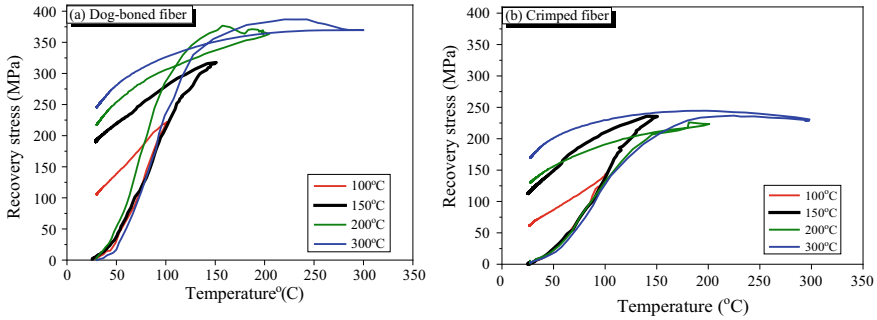


Fig. 2 Relationship between recovery stress and temperature of SMA fibers [22]

Table 1 Dimensions of SMA fibers (unit: mm)

Type	Parameter	Non-heating	Heating	Changing (%)
Crimped fiber	Thickness	0.966	0.974	1.0
	Wave depth	0.073	0.040	-45.2
	Wave height	1.039	1.014	
Dog-boned fiber	Thickness in middle parts	0.955	0.971	
	Thickness in end parts	0.971	0.971	

approximately 1.0%, which led to a slight improvement in the frictional resistance. However, the wave depth of the crimped fiber decreased by 45.2%, causing a declining trend in the anchoring bond. The heat treatment had both favorable and unfavorable impacts on the bond resistance of the dog-boned and crimped fibers.

2.2 Fabricating Specimens

The cylindrical specimens had a diameter of 100 mm and a height of 200 mm [22]. The mixture proportions, including cement, fly ash, silica sand, and water, were designed with a weight ratio of 1:1:1:1 and a water-cement ratio of 0.7. During the casting process, crimped and dog-boned fibers were mixed into the cementitious concrete. Prior research conducted by Choi et al. [21] examined the impact of 0.5% and 1.0% volume fractions of SMA fiber content in a monotonic compression test. The results showed that the compressive strength of the fiber-reinforced specimens increased with a 1.0% volume fraction, while 0.5% had no significant effect. To ensure that the cyclic compression behavior was impacted by the SMA fiber, the study employed 1.0% and 1.5% fiber content.

A total of thirty specimens were fabricated, with six specimens in each group, as illustrated in Fig. 3. Three specimens from each group were subjected to testing at room temperature, while the remaining three were heated to a temperature of 150 °C

Fig. 3 Testing specimens [22]



Table 2 Specimens' matrix

Specimens	Volume fraction	Non-heating	Heating
Plain cylinder	0	P-N	P-H
Crimped fiber cylinder	1.0%	CR10-N	CR10-H
	1.5%	CR15-N	CR15-H
Dog-boned fiber cylinder	1.0%	DG10-N	DG10-H
	1.5%	DG15-N	DG15-H

before testing. The specimens were marked according to the fiber shape, volume fraction, and heating condition, as outlined in Table 2.

2.3 Cyclic Compression Test

The study conducted a cyclic compression test on cylindrical specimens using a material testing system with a maximum capacity of 2000 kN. Three linear variable differential transformers (LVDT#1,#2,#3) were positioned in the vertical direction to accurately measure the vertical displacement, while an extensometer (E#1) was placed at the center of the cylinder height to measure lateral displacement. The compressive load was recorded using a computer system. The specimens underwent cyclic loading with a step displacement increment of 0.4 mm and unloading stopped when the load reached a value close to zero. Despite a limited displacement value of 4.8 mm, most specimens failed at a displacement of less than 2.0 mm. The experimental setup and equipment are shown in Fig. 4, while the cyclic loading process is illustrated in Fig. 5.

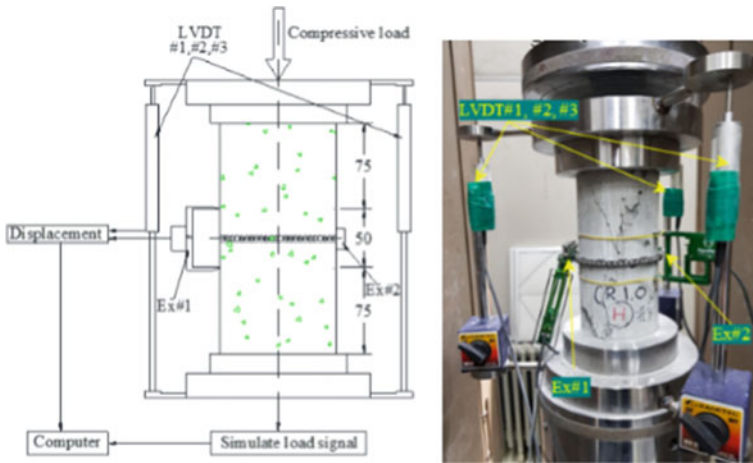
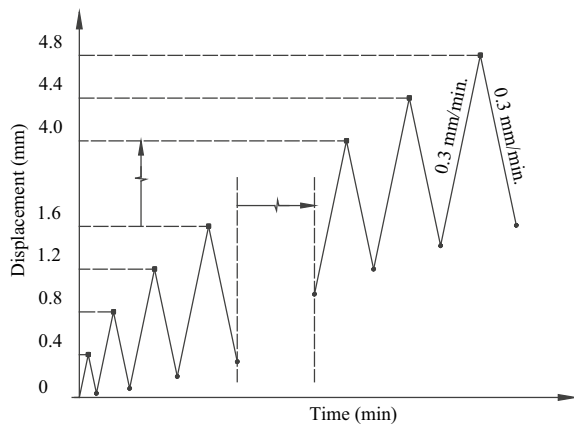


Fig. 4 Cyclic compression test [22]

Fig. 5 Load scheme of cyclic compression [22]

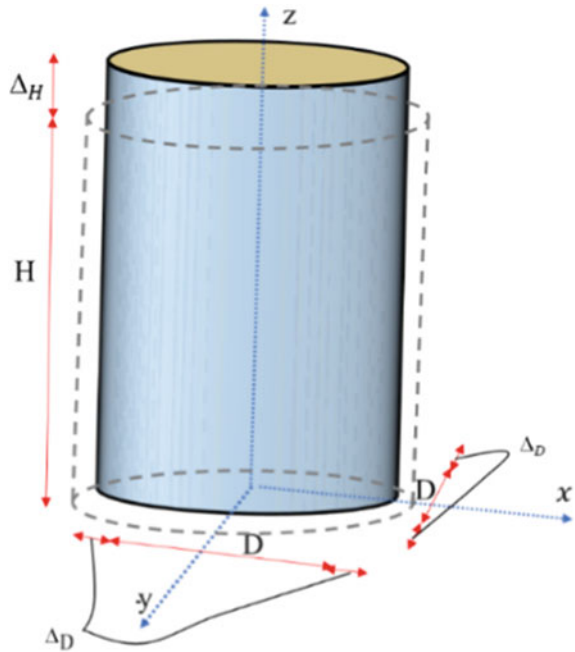


3 Outcomes and Discussion

3.1 Volumetric Strain

The volumetric strain is a critical metric in evaluating the behavior of a compressive cylinder under cyclic loading. By measuring the ratio of volume change to the original volume, volumetric strain provides insight into the material's deformation and aids in predicting future behavior. In this study, axial strain represented compression (positive), while lateral strain indicated bulging (negative) (Fig. 6). Using Eq. (1) and changes in dimensions along the x , y , and z axes, volumetric strain was calculated for the cylinder. This comprehensive analysis allowed for a more in-depth understanding

Fig. 6 Change in volume



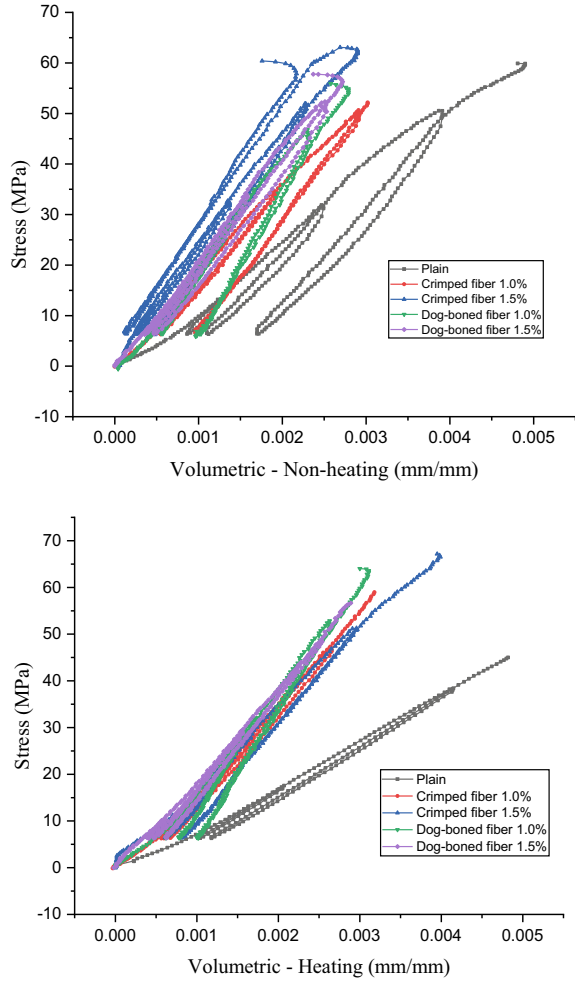
of specimen behavior under loading. In Eq. (1), ϵ refers volumetric strain; Δ_H , Δ_D are the change of dimension in the axial direction and in the lateral directions; H and D refer to the fabricating height and diameter of the cylinder, respectively.

$$\epsilon = \Delta_H/H - 2(\Delta_D/D) \tag{1}$$

Figure 7 displays the volumetric strain of the compressive cylinders. Typically, the cylinders experienced cracking at around 70% of their peak compressive strength, leading to a significant increase in lateral strain due to the opening of crack width. As a result, the non-heated cylinders exhibited a small reversal in the volumetric strain toward the end of the curve. In contrast, the heating treatment did not show any reversal in the cylinders. The chemical reaction of cement in concrete was facilitated by heating, resulting in an increase in the adhesion between the elements in the concrete matrix and a reduction in the softening behavior of the cylinders. The increased brittleness of concrete due to heating resulted in less pronounced lateral strain compared to non-heated concrete.

Furthermore, the addition of SMA fibers has been shown to enhance the ductility of concrete. SMA fibers can undergo significant deformation before failure, resulting in lower volumetric strain in the reinforced cylinder compared to the plain cylinder, both in heating and non-heating scenarios. The addition of SMA fibers reduces volumetric strain by approximately 38–63%, irrespective of fiber shape. In heating scenarios, the volumetric strain of the plain cylinder remains nearly unchanged, whereas reinforced

Fig. 7 Volumetric strain of the cylinders



cylinders exhibit greater volumetric strain values than non-heated reinforced cylinders. This suggests that SMA fibers contribute to the prestressing effect in reinforced concrete, resulting in pre-compaction of heated reinforced concrete before external compressive load application. The recovery stress of SMA fibers creates prestressing in embedded fibers and affects volumetric strain. Previous studies have shown that the prestress caused by SMA fibers enhances the tensile strength of reinforced concrete, making it a desirable construction material [23, 24]. Hence, the inclusion of SMA fibers has a significant impact on the behavior and properties of reinforced concrete.

3.2 Increment of Modulus Due to SMA Fiber

Previous studies have shown that the mechanical properties of cementitious materials can be greatly affected by cyclic loading due to the occurrence of microcracks [25, 26]. These microcracks tend to propagate when stress levels exceed around 70% of the ultimate stress, usually forming at the interface between aggregates and mortar [27]. As load increases, the width of these cracks also tends to increase, resulting in a curved stress–strain relationship with decreasing tangent modulus until failure, known as softening behavior. In our research, we calculated the secant modulus for cylinders that experienced stress levels below 70% of the ultimate stress, while the tangent modulus was calculated for stress levels ranging from 70% up to ultimate stress (Fig. 8). The values of secant and tangent moduli are provided in Table 3 and Fig. 9.

The results showed that the moduli of reinforced cylinders were higher than those of plain cylinders, and that they increased as the fiber content increased. Specifically, the moduli of cylinders with 1.0% fiber content were found to be 1.1–1.2 times

Fig. 8 Definition of secant modulus and tangent modulus

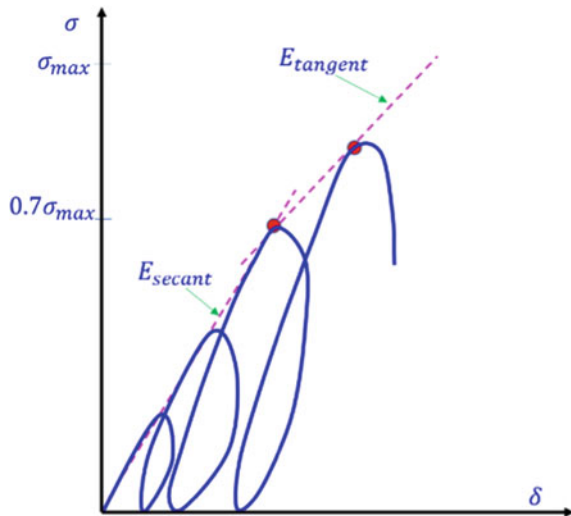


Table 3 Modulus of cylinders (unit: GPa)

Type	Secant modulus	Tangent modulus	Type	Secant modulus	Tangent modulus
P-N	12.3	6.3	P-H	7.9	7.1
CR10-N	14.5	7.3	CR10-H	15.4	10.8
CR15-N	18.3	7.4	CR15-H	15.5	10.9
DG10-N	14.7	7.7	DG10-H	16.0	11.1
DG15-N	19.7	10.3	DG15-H	16.4	11.7

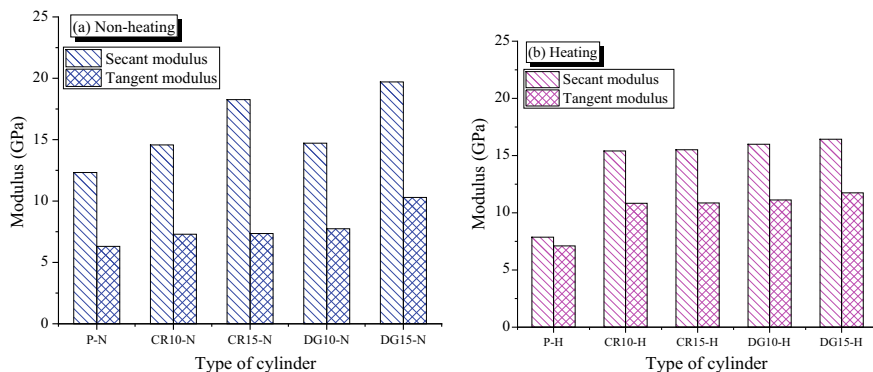


Fig. 9 Modulus of cylinders

higher than those of plain cylinders. Meanwhile, cylinders with 1.5% fiber content demonstrated an increment of 1.5–1.6 times. The addition of fibers to the concrete matrix can reduce the propagation of microcracks because they create a network of reinforcing elements within the concrete that can limit the growth and spread of cracks under load. Moreover, the embedded fibers can create frictional resistance within the concrete, which increases the stiffness of the material [1].

Dog-boned fibers were found to be more advantageous than crimped fibers, with dog-boned cylinders at the same 1.5% fiber content having secant and tangent moduli 1.07 and 1.39 times higher, respectively, than crimped cylinders. The resistance created dowel action for the fibers, allowing them to bridge across cracks. However, crimped fibers were stretched during cyclic compression loads, while dog-boned fibers were not. As a result, crimped fiber cylinders had lower secant and tangent moduli than dog-boned fiber cylinders.

In the case of heating, the P-H cylinder decreased the secant modulus, consistent with some previous studies [28]. The high temperature had a negative impact on the secant modulus of cementitious materials, and the effect of SMA fibers on the modulus was evident in this case. The secant modulus of reinforced cylinders increased about double, while the tangent modulus was 1.6 times higher than that of the P-H cylinder. In the case of heating, the increase in modulus was not significantly affected by the fiber content. The secant and tangent moduli of CR-H cylinders were estimated to be about 15.5 GPa and 10.8 GPa, respectively, while those of DG-H cylinders were approximately 16.2 and 11.4 GPa. Dog-boned fibers also presented more advantages in terms of the secant and tangent moduli of heated cylinders compared to crimped fibers. The recovery stress of SMA fibers played a critical role in confining the cylinder before cracking, leading to an increasing trend in the secant modulus. The recovery stress also reduced the crack width, resulting in a higher tangent modulus for the cementitious composite with heated SMA fibers.

4 Conclusions

This study aimed to provide a comprehensive understanding of the cyclic compression behavior of concrete reinforced with shape memory alloy (SMA) fibers. Two types of SMA fibers, crimped and dog-boned, were used to reinforce the concrete, and their effects on the concrete's behavior were examined. To assess the performance of the reinforced concrete, cyclic compression tests were carried out on plain concrete and concrete with 1.0 and 1.5% fiber content under both heating and non-heating conditions. The results of the investigation indicate that the inclusion of SMA fibers reduced the volumetric strain of the concrete, making it more ductile. However, the recovery stress of SMA fibers increased the volumetric strain of the concrete. Moreover, the addition of SMA fibers in the concrete increased the secant and tangent moduli, with the dog-boned fiber exhibiting superior performance to the crimped fiber. Although the fiber content did not significantly affect the moduli, the recovery stress of SMA fibers increased the secant and tangent moduli of reinforced concrete by a factor of 2 and 1.6, respectively, emphasizing the importance of considering the shape memory effect in structural design.

Acknowledgements This research is funded by the Ministry of Education and Training (MoET), Vietnam under the grant number B2022-GHA-04.

References

1. Abbass W, Khan MI, Mourad S (2018) Evaluation of mechanical properties of steel fiber reinforced concrete with different strengths of concrete. *Constr Build Mater* 168:556–569
2. Choi E, Ho HV, Seo J (2021) Dynamic behaviors of mortar reinforced with NiTi SMA fibers under impact compressive loading. *Materials* 14(17):4933
3. Chen H, Xu Q, Chen S, Zhang Z (2009) Evaluation and design of fiber-reinforced asphalt mixtures. *Mater Des* 30(7):2595–2603
4. Zia A, Ali M (2017) Behavior of fiber reinforced concrete for controlling the rate of cracking in canal-lining. *Constr Build Mater* 155:726–739
5. Xu Q, Chen H, Prozzi JA (2010) Performance of fiber reinforced asphalt concrete under environmental temperature and water effects. *Constr Build Mater* 24(10):2003–2010
6. Maekawa K, El-Kashif KF (2004) Cyclic cumulative damaging of reinforced concrete in post-peak regions. *J Adv Concr Technol* 2(2):257–271
7. Osorio E, Bairán JM, Marí AR (2013) Lateral behavior of concrete under uniaxial compressive cyclic loading. *Mater Struct* 46(5):709–724
8. Breccolotti M, Bonfigli MF, D'Alessandro A, Materazzi AL (2015) Constitutive modeling of plain concrete subjected to cyclic uniaxial compressive loading. *Constr Build Mater* 94:172–180
9. Kesner KE, Billington SL, Douglas KS (2003) Cyclic response of highly ductile fiber-reinforced cement-based composites. *Mater J* 100(5):381–390
10. Li B, Xu L, Chi Y, Huang B, Li C (2017) Experimental investigation on the stress-strain behavior of steel fiber reinforced concrete subjected to uniaxial cyclic compression. *Constr Build Mater* 140:109–118
11. Choi E, Ho HV, Jeon JS (2020) Active reinforcing fiber of cementitious materials using crimped NiTi SMA fiber for crack-bridging and pullout resistance. *Materials* 13(17):3845

12. Rojob H, El-Hacha R (2017) Self-prestressing using iron-based shape memory alloy for flexural strengthening of reinforced concrete beams. *ACI Struct J* 114(2):523
13. Choi E, Kim DJ, Youn H, Nam TH (2015) Repairing cracks developed in mortar beams reinforced by cold-drawn NiTi or NiTiNb SMA fibers. *Smart Mater Struct* 24(12):125010
14. Chen W, Lin B, Feng K, Cui S, Zhang D (2022) Effect of shape memory alloy fiber content and preloading level on the self-healing properties of smart cementitious composite (SMA-ECC). *Constr Build Mater* 341:127797
15. Raza S, Shafei B, Saiidi MS, Motavalli M, Shahverdi M (2022) Shape memory alloy reinforcement for strengthening and self-centering of concrete structures—state of the art. *Constr Build Mater* 324:126628
16. Ho HV, Choi E, Kim D, Kang J (2021) Straining behavior of mortar reinforced by cold drawn crimped and dog-bone-shaped fibers under monotonic and cyclic compressions. *Materials* 14(6):1522
17. Dehghani A, Aslani F (2021) Effect of 3D, 4D, and 5D hooked-end type and loading rate on the pullout performance of shape memory alloy fibres embedded in cementitious composites. *Constr Build Mater* 273:121742
18. Ho HV, Choi E, Kang JW (2021) Analytical bond behavior of cold drawn SMA crimped fibers considering embedded length and fiber wave depth. *Rev Adv Mater Sci* 60(1):862–883
19. Dehghani A, Aslani F (2020) The effect of shape memory alloy, steel, and carbon fibres on fresh, mechanical, and electrical properties of self-compacting cementitious composites. *Cement Concr Compos* 112:103659
20. Naidu GG, Prasad MSDV, Mani E (2019) Mechanical behaviour of fibre reinforced concrete using shape memory alloys. *Int J Innov Technol Exploring Eng* 9(1):230–232
21. Choi E, Kim D, Kang J (2022) Uniaxial compressive behaviour of mortar cylinders reinforced with crimped NiTi shape memory alloy fibres. *Mag Concr Res* 1–19
22. Choi E, Kim WJ, Kim T (2021) Uniaxial compressive cyclic behavior of mortar reinforced with crimped or dog-bone-shaped SMA fibers. *Compos Struct* 262:113600
23. Kim MK, Kim DJ, Chung YS, Choi E (2016) Direct tensile behavior of shape-memory-alloy fiber-reinforced cement composites. *Constr Build Mater* 102:462–470
24. Choi E, Jeon JS, Lee JH (2022) Active action of prestressing on direct tensile behavior of mortar reinforced with NiTi SMA crimped fibers. *Compos Struct* 281:115119
25. Sturman GM, Shah SP, Winter G (1965) Microcracking and inelastic behavior of concrete. *Special Publication* 12:473–499
26. Shah SP, Winter G (1966) Inelastic behavior and fracture of concrete. *Journal Proceedings* 63(9):925–930
27. Shah SP, Chandra S (1970) Fracture of concrete subjected to cyclic and sustained loading. *Journal Proceedings* 67(10):816–827
28. Xiao J, König G (2004) Study on concrete at high temperature in China—an overview. *Fire Saf J* 39(1):89–103

Construction Engineering and Management

Framework for Measuring Controlling Function Management of Vietnam's Public Construction Works



Ngo Anh Tuan and Nguyen Luong Hai

Abstract The controlling function plays a vital role in successfully managing public construction works. Several studies have focused on the area of construction project management, but the results have rarely emphasized investigating controlling behaviors, which are critical factor for measuring management effectiveness within public construction works. To fulfill this research objective, a regression research design was performed based on data from questionnaires answered by professionals involved in public construction works in Vietnam. The structural equation modeling (SEM) technique with partial least-squares estimation (PLS) was applied to analyze the data. The results confirmed six behavioral dimensions (i.e., legal monitoring (CT1), plan monitoring (CT2), evaluating (CT3), corrective action (CT4), inspection implementation (CT5), and punishing action (CT6)) to asses controlling function. The behaviors related to legal monitoring (CT1) and corrective action (CT4) were revealed to have significant impacts on management performance (ME). In addition, corrective action (CT4) was found to mediate between evaluating (CT3) and plan monitoring (CT2); while punishing action (CT6) was noted as the mediator of inspection implementation (CT5).

Keywords Public construction works · Controlling function · Plan monitoring · Legal monitoring · Management effectiveness

N. A. Tuan
Institute for Transport Administration and Management Cadres, Hanoi, Vietnam

N. L. Hai (✉)
University of Transport and Communications, Hanoi, Vietnam
e-mail: hainl@utc.edu.vn

1 Introduction

For years, considerable work has emphasized the managerial behaviors that are considered key elements of the successful performance of construction organizations. Chua et al. [1] clarified the relevant managerial behaviors as aspects of teams' behaviors, and they noted that behavioral management reflects the way project members deliver their commitment, coordination, and competence to achieve the project organization's goals [2]. However, public works are not as relevant to the conventional management of construction projects. In particular, controlling management must ensure that public expenditure and investment conform to several related laws and regulations. The development of management behaviors has rarely examined the nature and degree of controlling functions' impacts. The literature has still noted critical problems in terms of poor construction work performance, such as low quality, budget overrun, and time delay [3–5]. Thus, it is a matter of which specific managerial behavior, in terms of controlling function, could appropriately explain management performance. Hence, it is essential to clarify each controlling behavior and examine the way each interrelates to management performance.

2 Research Methods

2.1 *Developing Controlling function's Attributes*

The successful control function reflects behavior and work procedures that conform to standards and accomplish goals [6]. To develop controlling behavior's attributes, focus group studies (FGSs) and focal interviews were used. The FGSs and focal interviews aimed to obtain collective issues regarding controlling management within the course of public work implementation, explaining the traits of the controlling function's attributes. The participants and interviewees were primarily familiarized with the previous works on the notions of controlling function to determine controlling behavioral attributes. They were then asked to answer questions related to the study's attention. The discussions emphasized the following areas: principles of controlling management, common difficulties in terms of controlling management functions, description of controlling management behavior, and measurement of controlling behaviors, measurement of management performance within public construction works. In short, six behaviors were identified and recommended for assessment of controlling function (Table 1).

The following hypotheses are suggested:

H1—Legal monitoring has a constructive impact on the management performance.

H2—Plan monitoring has a constructive impact on the management performance.

H3—Evaluating has a constructive impact on the management performance.

H4—Corrective action has a constructive impact on the management performance.

Table 1 Attributes of controlling function

Function	Attributes	Code	Descriptions
Controlling (CT)	• Legal monitoring	CT1	• The degree of legal documents is set and used to control tasks and goals during the plan implementation
	• Plan monitoring	CT2	• The degree of monitoring plan' clarification is set for the management of public construction works
	• Evaluating	CT3	• Managers evaluate the plan implemented, ensuring accomplishment of investment objectives
	• Corrective action	CT4	• Corrective actions are delivered to solve any deviations over the course of the investment plan implementing
	• Inspection implementation	CT5	• Managers always inspect their subordinates' activities over the course of the investment plan implementation
	• Punishing action	CT6	• Punishing actions are delivered appropriately when mistakes are recorded

H5—Inspection implementation has a constructive impact on the management performance.

H6—Punishing action has a constructive impact on the management performance.

2.2 Data Collection

A total of 139 valid questionnaires were distributed to qualified professionals for the official analysis. Of these valid samples, 59 respondents were officials, 53 was public clients, and the remaining 27 were state auditors. In terms of the background of respondents, 81% of them had over ten years of experience working in the industry.

2.3 Measures

Structural equation modeling (SEM) was employed as the main techniques to examine the research hypotheses. The SEM method is the widely employed to test the

relationships among controlling behaviors on management performance in regression analyses. Although, covariance-based SEM (CB-SEM) and partial least-squares SEM (PLS-SEM) are known as the two types of SEM. The PLS-SEM approach was appropriately nominated for this study due to of smaller sample sizes required [7] and less convergence problems [8], compared with the CB-SEM technique.

3 Results and Discussion

The influences of controlling behaviors and management performance were tested using SEM. The findings indicate significant relationships between following variables (Table 2):

- (1) legal monitoring (CT1) and ME ($\beta = 0.384, p < 0.000$) (Table 3),

Table 2 Comparison of AVE and correlation coefficients between constructs

Latent constructs		AVE	Latent constructs					
			CT4	CT3	CT5	CT1	CT2	CT6
Corrective action	(CT4)	1.000	1.000					
Evaluating	(CT3)	1.000	0.575	1.000				
Inspection implementation	(CT5)	1.000	0.590	0.516	1.000			
Legal monitoring	(CT1)	1.000	0.433	0.535	0.370	1.000		
Plan monitoring	(CT2)	1.000	0.523	0.703	0.566	0.556	1.000	
Punishing action	(CT6)	1.000	0.537	0.507	0.516	0.390	0.381	1.000

Table 3 Results of regression analyses

Hypotheses	Coef	VIF	R square	R square Adjusted	f Square	T values	P Values	Interpretation
CT1 → ME	0.384	1.593	0.606	0.588	0.235	4.393	0.000	Supported
CT2 → ME	0.147	2.456			0.022	1.594	0.111	Not supported
CT3 → ME	0.037	2.457			0.001	0.430	0.667	Not supported
CT4 → ME	0.167	1.956			0.040	2.088	0.037	Supported
CT5 → ME	-0.015	1.920			0.000	0.197	0.844	Not supported
CT6 → ME	0.266	1.667			1.108	3.499	0.000	Supported
CT2 → CT3	0.703	1.000			0.978	13.441	0.000	Supported
CT3 → CT4	0.575	1.000			0.495	7.774	0.000	Supported
CT5 → CT6	0.516	1.000			0.363	7.392	0.000	Supported

- (2) corrective action (CT4) and ME ($\beta = 0.176, p < 0.05$) (Table 3),
- (3) punishing action (CT6) and ME ($\beta = 0.266, p < 0.000$) (Table 3),
- (4) planning monitoring (CT2) and evaluating (CT3) ($\beta = 0.703, p < 0.000$) (Table 3),
- (5) evaluating (CT3) and corrective action (CT4) ($\beta = 0.575, p < 0.000$) (Table 3),
- (6) inspection implementation (CT5) and punishing action (CT6) ($\beta = 0.516, p < 0.000$) (Table 3).

The outcomes are relevant to Hypotheses H1, H4, and H6. Table 3 and Fig. 1 show that the three controlling behaviors (i.e., CT1, CT4, and CT6) have direct impacts on the management performance (ME), which can infer 58,8% of the modification in ME ($p < 0.000$). However, the findings also indicated no straight significant effects of planning monitoring (CT2) on ME (H2) ($\beta = 0.147, p > 5%$) (Table 3), evaluating (CT3) and on ME (H3) ($\beta = 0.037, p > 0.05$) (Table 3), and inspection implementation (CT5) on ME (H5) ($\beta = -0.015, p > 5%$) (Table 3).

In addition, the indicators of variance inflation factors (VIFs) were analyzed for the potential multicollinearity within the predictor variables. The results indicated the maximum value (2.457) of the VIF is much lower than the suggested threshold (i.e., 10) by Hair et al. [9], which reflects no multicollinearity or minor standard errors of the examined data [10]. The results of the discriminant validity examination also indicate no violation by comparing the square root of the average variance extracted

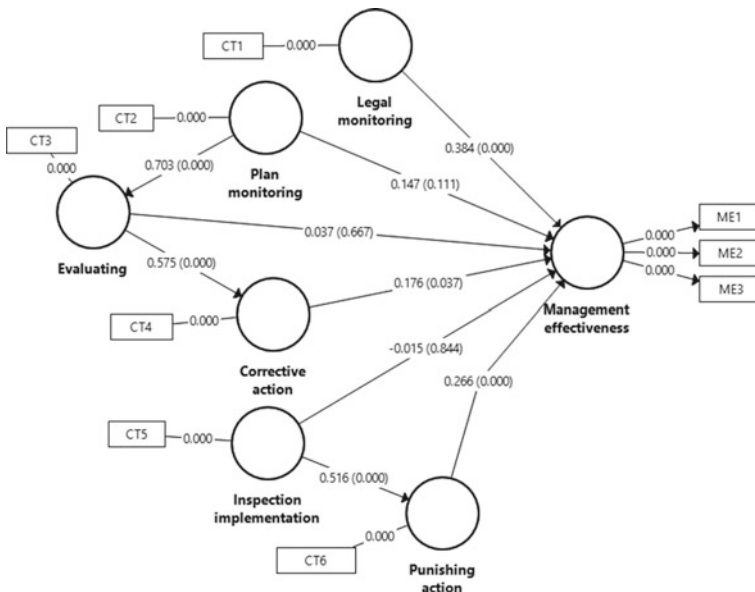


Fig. 1 Controlling behaviors and management effectiveness

(AVE) and the correlation between latent constructs (Table 2), which indicates that each of the six controlling behaviors is unique.

As mentioned in the statements of H1, H4, and H6, the results show that controlling behaviors related to legal monitoring, corrective action, and punishing action have a positive impact on the ME of public construction works. This finding clarifies that direct improvement in the three controlling behaviors (i.e., CT1, CT4, and CT6) could enhance the performance of public construction work management. The findings are explained. Firstly, the legal monitoring (CT1) behavior reflects the managers' concern about delivering public works legally. It addresses questions such as: what are the limits and rules that the work implementation needs to follow up? how do stakeholders behave legally in terms of delivering their decision-making? Secondly, proposing corrective actions that can solve deviations or problems during the plan implementation is crucial. This result is explained by the fact that the construction industry is natural complex and uncertain, making it prone to risk. Thus, closely monitoring corrective actions is essential to mitigate the risks and get the plan back on track. In addition, promoting a punishing mechanism is significant to ensure that the workforce follows rules and regulations during the plan's implementation. However, the findings were not relevant to the hypothetical importance of the controlling behaviors related to plan monitoring (CT2), evaluating (CT3), and inspection implementation (CT5). This redundancy can be explained by the mediators of corrective action (CT4) and punishing action (CT6), where these behaviors could have an authorized impact on management efficiency.

4 Conclusions

This work developed a theoretical framework for controlling management functions within the public construction works. In this respect, six functional behaviors of controlling functions were first developed through FGSs with practitioners in public work management. The attributes measurements were collected in the case of Vietnam and then used in SEM to confirm these attributes' association with management performance.

The controlling function notes the significant effect of legal monitoring, plan monitoring, evaluating, corrective action, inspection implementation, and punishing action, which are followed by all units and stakeholders to examine the actual performance of works against the established standard performance, discover the causes of deviations and deliver corrective actions. The regression model was then analyzed to clarify the hypothetical associations between each predictor and management performance. The findings indicate that CT1, CT4, and CT6 contribute to better management performance.

References

1. Chua DKH, Kog YC, Loh PK (1999) Critical success factors for different project objectives. *J Constr Eng Manag* 125(3):142–150
2. Jha KN, Iyer KC (2007) Commitment, coordination, competence and the iron triangle. *Int J Project Manage* 25(5):527–540
3. Ibrahim A et al (2010) An investigation of the status of the Malaysian construction industry. *Benchmarking* 17(2):294–308
4. Kashiwagi D et al (2012) The source of degradation of the construction industry performance. *J Advancement Performance Inf Value* 4(2):206–222
5. Xiong B et al (2014) Examining the influence of participant performance factors on contractor satisfaction: a structural equation model. *Int J Proj Manag* 32(3):482–491
6. Leifer R, Mills PK (1996) An information processing approach for deciding upon control strategies and reducing control loss in emerging organizations. *J Manage Stud* 22(1):113–137
7. Hair J et al (2021) *A primer on partial least squares structural equation modeling (PLS-SEM)*. Sage Publications
8. Henseler J (2010) On the convergence of the partial least squares path modeling algorithm. *Comput Statistics* 25(1):107–120
9. Hair JF et al (1998) *Multivariate data analysis, vol 5*. Prentice Hall, Upper Saddle River, NJ
10. Field AP (2000) *Discovering statistics using SPSS for windows: advanced techniques for the beginner*. Sage Publications, London

The Impact of Project Organizational Culture on Cost Performance of Construction Projects



Do Van Thuan and Nguyen Luong Hai

Abstract The culture within project organizations has been acknowledged as a determinant of successful organizations. Previous works in this domain has emphasized the development of organizational culture models. However, little attention has been paid to determining the relationships between culture and cost performance within construction project organizations. This study aimed to address this gap. Project organizational culture artifacts were employed in a developed model and validated using a data survey conducted on 199 completed construction projects. Through a principal component factor analysis and the structural equation model (SEM) technique, the cultural behaviors were organized into a framework of four-factor culture dimensions. The findings reveal that commitment orientation and shared understanding contribute to improved cost performance. In addition, commitment orientation plays the role of mediator of the potential effects of the leadership orientation and supportive orientation culture on cost performance. The findings of this study reinforce the cultural effects and provide a useful project management tool that can contribute to the successful management of construction project organizations.

Keywords Project organizational culture · Cultural effect · Project cost · Project performance

1 Introduction

For years, several works have emphasized examining critical success factors (CSFs) that contributed to the successful project [1, 2]. Among these factors, project organizational culture (POC) has been identified as an essential contributor to a successful project organization [3–7]. A construction project organization involves participants

D. Van Thuan
Institute for Transport Administration and Management Cadres, Hanoi, Vietnam

N. L. Hai (✉)
University of Transport and Communications, Hanoi, Vietnam
e-mail: hainl@utc.edu.vn

from diverse backgrounds, which can result in varying perspectives and expectations. Consequently, the behaviors and attitudes of the individuals involved in a project organization can have a complicated influence on the project organization's performance. Earlier, Chua et al. [4] classified cultural behaviors into five teams' behaviors in terms of competency, active involvement, commitment, contribution and collaboration among project members. Chan et al. [3] classified team factors that concern the client's behaviors and other project teams' behaviors. The client's behaviors emphasize the experience, capability, nature, focus and contribution, while the project teams' behaviors emphasize leadership experience and skills, leaders' commitment, the project team leaders' contribution and flexibility. However, the development of modeling organizational culture has rarely addressed the relationships between cultural dimensions and the project's cost, which has been reported as critical problems in terms of cost overrun and client dissatisfaction [8–10]. Hence, it deserves to examine how each cultural behavior interacts with project cost performance, which is the study's hypothesis. This study aims to define the attributes of POCs within construction project management and examine the relationships between POCs and project cost performance.

2 Project Organizational Culture

This study employed the project organizational culture framework that had been developed in the work of Nguyen and Watanabe [11], who developed the organizational culture attributes by examining the problems that members must overcome or for which they must propose strategies during the construction project delivery (Table 1).

3 Research Methods

Data were collected from professionals who were project manager and senior engineer within construction project organizations. In total, 416 official samples were sent to respondents to collect the level of specific cultural artifacts based on their experience within participated construction project organizations. 199 valid responses were obtained from this survey for the study analyses, whereby 169 respondents were from contractors and 30 ones were from clients.

To analyze the research models, the main approaches are confirmatory factor analysis (CFA) and structural equation modeling (SEM). The CFA method was first applied to examine the reliability and fitness of the factor structure of cultural artifacts. Additionally, Cronbach's alpha values were checked to verify the reliability of the factorized artifacts [12], in which the alpha value should be >0.7 as suggested in the literature [12, 13]. The SEM technique was then employed to examine the

Table 1 Dimensions of POC

No	Dimensions	Code	Cultural behaviors [11]
1	Supportive orientation (POC1)	C1	Open attitude and shared admiration
		C2	Ideas exchange and collaboration
		C3	Accountability assignment
		C4	Availability of training course
		C5	Subordinates appreciation
		C6	Subordinates apprehension
2	Shared understanding (POC2)	C7	Goal understanding
		C8	Responsibilities and duties of contractor
		C9	Responsibilities and duties of client
		C10	Mutual sympathetic
		C11	Working relationship
		C12	Information exchange

(continued)

Table 1 (continued)

No	Dimensions	Code	Cultural behaviors [11]
3	Commitment orientation (POC3)	C13	Commitment to quality
		C14	Commitment to schedule
		C15	Commitment to budget
4	Leadership orientation (POC4)	C16	Empowerment
		C17	Inspiration of delivering decision making
		C18	Direction promotion

relationships between organizational dimensions and project cost performance in the regression analyses.

4 Results and Discussion

4.1 Validity and Reliability Analysis

SmartPLS 3.0 software was used to examine individual item reliability and standardization. The factor loadings exceeding the 0.4 thresholds were accepted [5, 14]. The findings indicate that individual loadings (Table 2) are all above the threshold, showing the acceptance of indicator reliability. In addition, Cronbach’s alpha values, composite reliability scores and average variance extracted (AVE) analyses were performed to examine the convergent validity of measured constructs [15]. The

Table 2 Measurement model evaluation

Construct	Indicator	Loading	Cronbach's alpha	Composite reliability	AVE
Supportive orientation (POC1)	C1	0.729	0.875	0.905	0.615
	C2	0.749			
	C3	0.717			
	C4	0.821			
	C5	0.850			
	C6	0.838			
Shared understanding (POC2)	C7	0.783	0.821	0.868	0.524
	C8	0.769			
	C9	0.691			
	C10	0.640			
	C11	0.688			
	C12	0.763			
Commitment orientation (POC3)	C13	0.869	0.871	0.921	0.796
	C14	0.931			
	C15	0.875			
Leadership orientation (POC4)	C16	0.770	0.664	0.816	0.598
	C17	0.807			
	C18	0.741			

outcomes of the convergent validity test are presented in Table 2. The results indicate that Cronbach's alpha values and composite reliability scores all exceeded 0.7, except for POC4, which shows that the internal consistency reliability of all the components was not violated [14, 16]; and AVE values were relatively higher than the accepted threshold of 0.50 [14]. Discriminant validity was also tested by analyzing cross-loadings (Table 3) to verify if the various items in the same construct were located with high loadings on their construct (Table 4).

4.2 Structural Model Analysis

The correlations between cultural dimensions and project cost performance (PC) were tested using SEM. The four cultural dimension are the predictors in the SEM model, in which the measurement items of each predictor were derived from validity and reliability analysis in the previous section. The results clarify significant and positive relationships between:

- (1) Shared understanding (POC2) and cost performance (PC) ($\beta = 0.163$, $p < 0.05$) (Table 5),

Table 3 Cross loadings

Items	POC3	POC4	POC2	POC1
C10	0.259	0.317	0.640	0.385
C11	0.230	0.344	0.688	0.328
C12	0.372	0.281	0.763	0.393
C13	0.869	0.436	0.489	0.548
C14	0.931	0.376	0.501	0.500
C15	0.875	0.400	0.476	0.498
C16	0.309	0.770	0.364	0.352
C17	0.399	0.807	0.435	0.478
C18	0.337	0.741	0.359	0.442
C1	0.367	0.466	0.610	0.729
C2	0.361	0.384	0.577	0.749
C3	0.384	0.426	0.531	0.717
C4	0.573	0.399	0.437	0.812
C5	0.485	0.488	0.457	0.850
C6	0.489	0.454	0.450	0.838
C7	0.547	0.403	0.783	0.625
C8	0.390	0.459	0.769	0.534
C9	0.510	0.322	0.691	0.403

Table 4 Comparison of square root of AVE and correlation coefficients between constructs

Latent constructs	AVE	Latent constructs			
		POC3	POC4	POC2	POC1
Commitment orientation	0.796	0.892			
Leadership orientation	0.598	0.454	0.773		
Shared understanding	0.524	0.548	0.502	0.724	
Supportive orientation	0.615	0.578	0.552	0.634	0.784

Table 5 Results of regression analyses

Hypotheses	Coef	VIF	R square	R square adjusted	f Square	T values	P Values	Interpretation
POC1 → PC	0.134	2.091	0.309	0.294	0.012	1.524	0.128	Not supported
POC2 → PC	0.163	1.891			0.020	2.291	0.022	Supported
POC3 → PC	0.292	1.671			0.074	3.785	0.000	Supported
POC4 → PC	0.082	1.553			0.006	0.951	0.342	Not supported
POC1 → POC3	0.471	1.438			0.242	6.104	0.000	Supported
POC4 → POC3	0.194	1.438			0.041	2.216	0.027	Supported

- (2) Commitment orientation (POC3) and cost performance (PC) ($\beta = 0.292, p < 0.000$) (Table 5),
- (3) Supportive orientation (POC1) and commitment orientation (POC3) ($\beta = 0.471, p < 0.000$) (Table 5),
- (4) Leadership orientation (POC4) and commitment orientation (POC3) ($\beta = 0.194, p < 0.05$) (Table 5).

The results support H2 and H3. However, no significant direct relationships were found between supportive orientation (POC1) and cost performance (PC) (H1) ($\beta = 0.134, p > 0.05$) (Table 5); and leadership orientation (POC4) and cost performance (PC) (H4) ($\beta = 0.082, p > 0.05$) (Table 5). The indirect relationships were explained by the mediator of commitment orientation (POC3) as mentioned. Table 5 and Fig. 1 show that the cultural dimensions are conducive to enhancing the cost performance (PC), in which the suggested models explained 29.4% of the variation in PC ($p < 0.000$). Additionally, variance inflation factor (VIF) values were analyzed to predict the multicollinearity among the predictors within the regression analyses. The outcomes indicated all the VIF values, with the maximum value of 2.091, are substantially lower than the threshold of 10 [17], which indicates no significant amount multicollinearity [16]. Also, the distribution of path coefficients (Fig. 2) between the predictors and project cost was created to follow normal distributions, which appear to have exact means of the true population means.

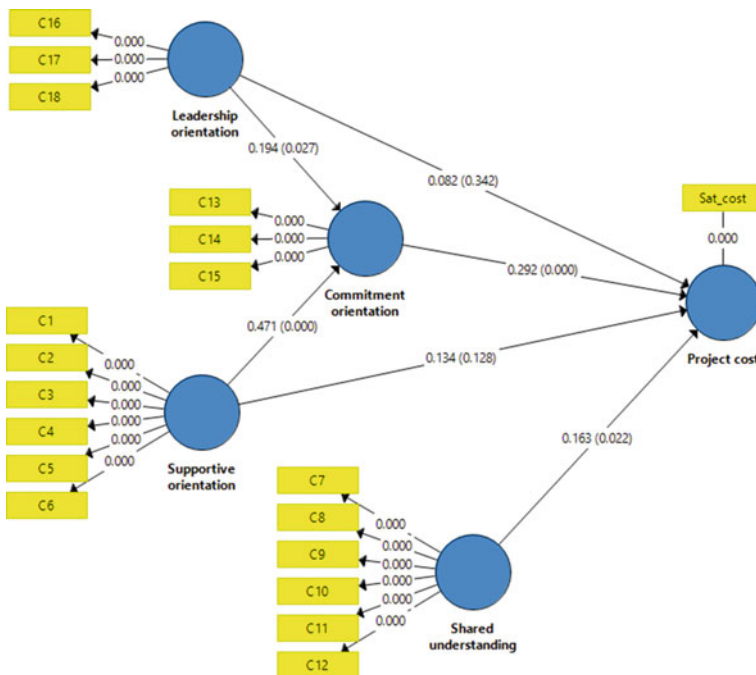


Fig. 1 Project organizational culture and project cost

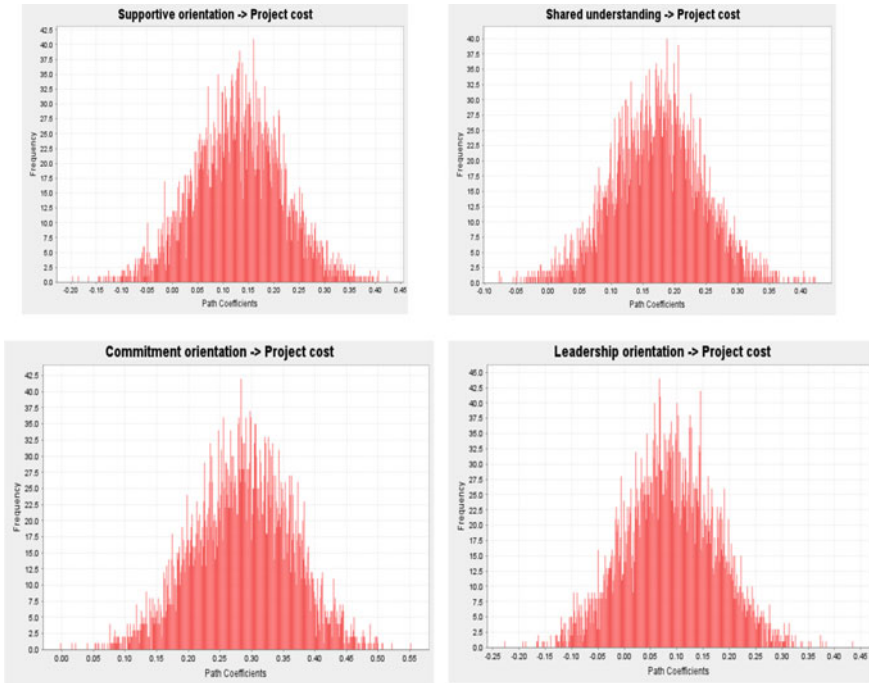


Fig. 2 Path coefficient distribution

Calculation method: two-stage; product term generation: standardized

It is noted from the findings that the cultural behaviors of a shared understanding (POC2) and commitment orientation (POC3) have a positive impact on the project cost performance. This suggests that direct improvement in these two project organizational culture dimensions could increase the cost performance of construction projects. However, the findings do not support the theoretical relationship between supportive orientation (POC1) and leadership orientation (POC4). In temporary organizations like a construction project organization, supportive behavior between project members and leadership promotion are important to ensure successful organization in an environment of complexity and uncertainty of the construction industry. This conventional perception was found to vary in this study within the CPO. However, this can be logically explained by the mediator of the commitment behavior (POC3). This result is not surprising, as when project members receive support and direction from other members and top management, they are more likely to commit to the project goals.

5 Conclusions

This study aimed to examine the relationships between POC and cost performance within the context of construction project organizations. In this aim, four cultural dimensions with 18 attributes of POCs were first derived based on previous works. A case study was conducted in the Vietnamese construction industry to measure, which were then analyzed in the confirmatory factor analysis to validate the four cultural dimensions. The four valid cultural dimensions were analyzed in a robust regression model that validated significant relationships between each cultural dimension and cost performance. The revelations note that POC2 and POC3 have a direct positive impact on cost performance, while POC3 acts as a mediator of the indirect influence of POC1 and POC4 on cost performance. The judgments suggest that POCs should be promoted as an effective management tool for the success of construction project organizations, and positive behavior among project members is expected to drive successful project management.

References

1. Fortune J, White D (2006) Framing of project critical success factors by a systems model. *Int J Proj Manag* 24(1):53–65
2. Kandelousi NS (2011) Key success factors for managing projects. *World Acad Sci Eng Technol Int J Soc Behav Educ Econ Bus Ind Eng* 5(11):1541–1545
3. Chan APC, Scott D, Chan APL (2004) Factors affecting the success of a construction project. *J Constr Eng M* 130(1):153–155
4. Chua DKH, Kog YC, Loh PK (1999) Critical success factors for different project objectives. *J Constr Eng M* 125(3):142–150
5. Cserhádi G, Szabó L (2014) The relationship between success criteria and success factors in organisational event projects. *Int J Proj Manag* 32(4):613–624
6. Fong PS, Kwok CW (2009) Organizational culture and knowledge management success at project and organizational levels in contracting firms. *J Constr Eng M* 135(12):1348–1356
7. Todorović ML et al (2015) Project success analysis framework: a knowledge-based approach in project management. *Int J Proj Manag* 33(4):772–783
8. Ibrahim A et al (2010) An investigation of the status of the Malaysian construction industry. *Benchmarking* 17(2):294–308
9. Kashiwagi D et al (2012) The source of degradation of the construction industry performance. *J Adv Perform Inform Value* 4(2):206–222
10. Xiong B et al (2014) Examining the influence of participant performance factors on contractor satisfaction: a structural equation model. *Int J Proj Manag* 32(3):482–491
11. Nguyen LH, Watanabe T (2017) The impact of project organizational culture on the performance of construction projects. *Sustainability* 9(5):781
12. Sharma S (1996) *Applied multivariate techniques*
13. Pallant J (2020) *SPSS survival manual: a step by step guide to data analysis using IBM SPSS*. Routledge, London
14. Hair J et al (2021) *A primer on partial least squares structural equation modeling (PLS-SEM)*. Sage publications, London
15. Fornell C, Larcker DF (1981) Evaluating structural equation models with unobservable variables and measurement error. *J Mark Res* 18(1):39–50

16. Field AP (2000) *Discovering statistics using SPSS for windows: advanced techniques for the beginner*. Sage Publications, London
17. Hair JF et al (1998) *Multivariate data analysis, vol 5*. Prentice Hall, Upper Saddle River, NJ

Propose the Construction Orientation of Two Airports in Hanoi After Forecasting Airport Passenger Demand



Quoc Van Nguyen, Trung Tien Trinh, and Thuy Anh Vu

Abstract In recent years, air transport passenger (pax) demand through Noi Bai International Airport (NBIA) has increased rapidly, requiring us to have a plan to supplement, upgrade and expand NBIA accordingly. Recently, the several airport experts have proposed to build the second airport in Hanoi area which is different from the accepted airport planning in 2019 by ADP Ingénierie Company (ADPi). Our forecasting using logarithmic function with parameters in form of time functions for regression method to predict the pax demand for Hanoi then propose the options to upgrade NBIA and build the second airport in Hanoi area.

Keywords Pax demand · Hanoi airport · Forecasting · Regression method

1 Introduction

In recent years, the Civil Aviation Industry of Vietnam has made good progress and many innovations on the path of modernization. Many runways, taxiways, terminals, platforms, aprons, etc. in the airports have been upgraded and expanded.

Q. V. Nguyen · T. T. Trinh (✉)
Le Quy Don Technical University, Hanoi, Vietnam
e-mail: trungtienmta@gmail.com

T. A. Vu
Hanoi Institute for Socio-Economic Development Studies, Hanoi, Vietnam

© The Author(s), under exclusive license to Springer Nature Singapore Pte Ltd. 2024
T. Nguyen-Xuan et al. (eds.), *Proceedings of the 4th International Conference on Sustainability in Civil Engineering*, Lecture Notes in Civil Engineering 344,
https://doi.org/10.1007/978-981-99-2345-8_12

In 2019, Noi Bai International Airport (NBIA) has an operating passenger traffic of 29 million passengers and the comparison between 2019 and 2014 (Table 2) shows that after 06 years, the number of passenger traffic has doubled. In this paper we would like to propose the estimation of pax demand for the Hanoi area to propose directions for the planning and construction of the 2nd international airport in Hanoi Capital.

2 Literature Review

Economic is main factor to determine the pax demand at a particular airport, region or city. During the past five decades, forecasting and modeling the pax demand in order to open or expand the airport has attracted the attention of many academics' scholars and engineers. The input data can be simple like the traveling numbers in past years, but in complication it can contain several variables and parameters. Among they are GDP, GDP per capita, population, income, income per capita, frequency [1], flight time, flight distance, catchment area, nearby airports, pax flow, nodal attraction, fares [2–5].

There is a number of forecasting methods like Exponential Smoothing [6, 7]; Holt-Winters [7, 8], ARIMA, SARIMA [7]; Gray Model [1, 9], Markov chain [9, 10].

The gravity model for forecasting passenger patronage in a new airport in Bangladesh using aggregated data of time series technique by [11].

In Vietnam, there have been many methods of forecasting pax demand for airports. Currently, the forecasting of pax demand for each airport usually applies the following methods: expert judgment, extrapolation, statistical testing, similar model method, derivative analysis, vehicle competition model and integrated economic model method [12].

The expert judgment method is based on the judgment of experts with in-depth knowledge of the forecasting field. At first, a group of experts prepare a number of polls on the fields to be forecasted, and then send the opinion forms to experts and managers of that field. After each receiving the opposite information, the inconsistent points will be discussed and the consultation form is continued like the above process, the process is repeated many times until the end, the results will be correct gradually [12].

The extrapolation method is based on analyzing and evaluating the performance of the aviation industry in the past and assuming the operation of the aviation industry in the future. This method proves to be very effective when conducting short-term forecasts but for long-term forecasts this approach appears to be unsatisfactory [12, 13].

The derivative analysis method is often used to forecast the pax demand of each airport from the total national demand. It assumes that portion of the pax demand for that airport and the total demand in the country is unchanged over time, so once the pax demand forecasting for the whole country is known, the pax demand of each airport can be found.

This method is often applied when the air passenger demand forecast for airports that have been in stable operation. The mathematical model of derivative analysis:

$$T_i = M_{i,J} M_{J/s} E_s \quad (1)$$

where T_i = shipping volume of the airport i th; $M_{i,J}$ = portion of shipping volume in the i th airport and total shipping volume in zone J (cluster); $M_{J/s}$ = portion of shipping volume of cluster airport and total shipping volume of the whole country (E_s).

Another forecasting method using in Vietnam is method of economic models. Actually, it is regression method with many economic factors. When forecasting the pax demand at airport i , it is necessary to consider many other socio-economic factors affecting aviation activities such as population, living standards, tourism, industry, GDP:

$$T_i = a_0 + a_1 X_1 + a_2 X_2 + \dots + a_n X_n \quad (2)$$

where T_i = pax demand in the i th airport; a_0, \dots, a_n - regression coefficients, determined on the basis of analyzing the statistical series; X_0, \dots, X_n - influencing factors.

The economic modeling method is often applied in cases where the statistical series is relatively complete, allowing the analysis to accurately determine the regression coefficients and other influencing factors. An example applied in the state of Florida [10]:

$$\ln \frac{T_i}{P_i} = 10.8 - 1.72 F_i + 1.41 \ln I_i \quad (3)$$

where: T_i - demand for passenger forecast at the airport i ; P_i - the number of residents in that area; F_i - average airfare for 1 mile; I_i - local per capita income; \ln - natural logarithms.

Recently, Vietnam Association of Science and Technology proposed a forecasting of pax demand using integrated economic model combined with expert judgment method [12]:

$$G_{HK} = 3.09 + (0.13 \times \%GDP) + (0.02 \times \%XK) + (0.36 \times \%DL) + (k \times 0.39 \times \%HK) \quad (4)$$

where $\%GDP$, $\%XK$, $\%DL$ and $\%HK$ = annual growth rate of GDP, export turnover, tourism industry and aviation, respectively; k = coefficient after appropriate adjustments.

3 Forecasting Method Using the Integrated Economic Model to Determine the Air Transport Passenger Demand for the Area of Hanoi City

3.1 Propose Forecasting Methodology

In this section, author used theory of method of economic models based on Eq. (2) but the variables X_1, X_2, X_3, X_4 using logarithmic function and parameters in form of a time function, so as the Hanoi airport pax demand function can be:

$$\log(\text{Pax}_{1t}) = \beta_t + a_0 \log(\text{Pax}_{1t-1}) + \sum_{i=1}^4 a_i \log(X_{it}) \quad (5)$$

$$\log(\text{Pax}_{1t}) = \beta_t + a_0 \log(\text{Pax}_{1t-1}) + \sum_{i=1}^4 a_i \log\left(\frac{M_{it} - M_{it-1}}{M_{it-1}}\right) \quad (6)$$

$X_1, X_2, X_3, X_4, M_1, M_2, M_3, M_4$ = annual growth rate and monetary value of GDP, export and import, tourism and aviation sectors for Hanoi, respectively;

$\beta_t, a_0, a_1, a_2, a_3, a_4$ = regression coefficients for the pax demand, annual growth rate of GDP, export and import, tourism and aviation sectors for of Hanoi, respectively.

$t, t - 1$ = denote for the year t and year $t - 1$, respectively.

The regression coefficients were determined from the collected data in year period 2010–2019 since Hanoi city expanded the city area in year 2008 and before the COVID-19 pandemic in year 2020. Taking into account the weight of above four factors X_1, X_2, X_3, X_4 on the pax demand rate, assuming that 100% the weight comes from 5 factors, we have:

$$a_1 + a_2 + a_3 + a_4 = 1 - a_0 \quad (7)$$

$$a_{it} = (1 - a_0) \frac{\log(M_{it})}{M_1(t) + M_2(t) + M_3(t) + M_4(t)}; i = 1, 2, 3 \text{ and } 4 \quad (8)$$

$$a_i = \text{average}(a_{it}); i = 1, 2, 3 \text{ and } 4 \quad (9)$$

According to statistics data from [14], the figures of monetary value of GDP, export and import, tourism and aviation sectors for Hanoi is in Table 1.

In addition, the statistics data from Civil Aviation Authority of Vietnam (CAAV) for period 2010–2019 as shown in Table 2.

Run a MATLAB code to solve the system of Eqs. (5), (6), (7), (8) and (9) with the data from Tables 1, 2, for the running variable a_0 with condition that $0 < a_0 < 1$ and with every interval of 0.001 to get the best agreement between the solved result and actual pax demand in period 2010–2019, we have:

Table 1 Monetary value of GDP, export and import, tourism and aviation sectors for Hanoi [14]

Year	Sector monetary value (Billion USD)			
	GDP	Export and import	Tourism	Aviation
2010	2.384	24.955	1.115	2.588
2011	2.681	26.577	1.289	2.718
2012	2.955	29.128	1.487	2.837
2013	3.291	31.197	1.670	3.027
2014	3.707	33.193	1.966	3.242
2015	4.198	35.450	2.265	3.447
2016	4.701	36.727	2.574	3.671
2017	5.267	38.159	2.957	3.840
2018	5.963	40.792	3.228	4.101
2019	6.711	43.933	3.909	4.191

Table 2 Pax demand through Noi Bai International Airport

Year	Pax demand (million/year)	Actual growth rate (%)	Year	Pax demand (million/year)	Actual growth rate (%)
2010	9.5	10.5	2015	17.2	21.13
2011	10.3	8.42	2016	20.6	19.77
2012	11.4	10.68	2017	23.2	12.62
2013	13.1	14.91	2018	26.0	12.07
2014	14.2	8.40	2019	29.0	11.54

$$\log(\text{Pax}_{1t}) = 0.124 + 0.89 \log(\text{Pax}_{1t-1}) + 0.022 \log(X_{1t}) + 0.058 \log(X_{2t}) + 0.011 \log(X_{3t}) + 0.019 \log(X_{4t}) \quad (10)$$

3.2 Forecast the Pax Demand for Noi Bai International Airport in 2022–2050

In order to forecast the pax demand for Noi Bai International Airport in 2022–2050, it is required the growth rate of GDP, export and import, tourism and aviation sectors for Hanoi. They are determined and forecasted from Hanoi city council and the headquarters of these four sectors. The growth rates are in Tables 3, 4, 5, 6.

Applying the Eq. (10) with the data from Tables 3, 4, 5, 6, we have the pax demand forecasting in three scenarios for Hanoi airports from 2022 to 2050 in Table 7 or Fig. 1.

Table 3 GDP growth data of Hanoi City area (X_1) [15]

Year	Scenario			Source or note
	Low	Basic	High	
2021–2030	9	9.5	10	The socio-economic development strategy of Hanoi City to 2030, with a vision to 2050
2031–2040	4.5	5	5.5	The draft strategy for Vietnam's socio-economic development to 2030, the 2045 orientation of the Party Central Committee
2041–2050	3.5	4	4.5	The draft strategy for Vietnam's socio-economic development to 2030, the 2045 orientation of the Party Central Committee

Table 4 Growth rate in the period 2021–2050 of Hanoi's the import and export industry [15]

Year	Scenario			Source or note
	Low	Basic	High	
2021–2025	17	18	19	Import and export industry development strategy to 2030 vision 2050
2026–2030	16	17	18	
2031–2050	12	12.5	13	

Table 5 Growth rate in the period 2021–2050 of Hanoi's tourism industry [15]

Year	Scenario			Source or note
	Low	Basic	High	
2021–2025	13	13.5	14	Hanoi tourism development strategy to 2021–2025
2026–2030	11	11.5	12	Hanoi tourism development strategy to 2030, vision 2050
2031–2050	9	9.5	10	Hanoi tourism development strategy to 2030, vision 2050

Table 6 Growth rate in the period 2021–2050 of Hanoi's aviation sector [15]

Year	Scenario			Source or note
	Low	Basic	High	
2021–2025	10	11	12	Strategy for development of Aviation sector of Vietnam
2026–2030	9	10	11	
2031–2050	8	9	10	

4 Proposing Some Initial Ideas for Airport Planning for Hanoi City Area

According to forecast data as presented in Table 7, by 2030, the pax demand through NBIA will reach 83.84; 87.41; 90.89 million passengers/year and by 2050 it will reach 111.68; 119.76; 127.67 million passengers/year corresponding to 3 scenarios (low, base and high scenario). From the figures of the pax demand, the NBIA should

Table 7 The pax demand forecasting for Hanoi airports to 2050 (unit: million passengers)

Year	Scenario (million passengers)		
	Low	Basic	High
2022	28.36	28.55	28.73
2023	34.71	35.15	35.58
2024	41.54	42.30	43.03
2025	48.75	49.88	50.96
2026	55.80	57.36	58.86
2027	62.93	64.96	66.92
2028	70.03	72.56	75.01
2029	77.03	80.07	83.03
2030	83.84	87.41	90.89
2031	87.18	91.17	95.05
2032	90.27	94.65	98.91
2033	93.12	97.86	102.48
2034	95.72	100.80	105.77
2035	98.10	103.50	108.78
2036	100.27	105.96	111.53
Year	Scenario (million passengers)		
	Low	Basic	High
2037	102.24	108.20	114.04
2038	104.02	110.24	116.32
2039	105.64	112.08	118.39
2040	107.10	113.74	120.26
2041	107.82	114.68	121.42
2042	108.46	115.53	122.45
2043	109.04	116.28	123.38
2044	109.55	116.96	124.22
2045	110.02	117.57	124.97
2046	110.43	118.11	125.64
2047	110.80	118.59	126.23
2048	111.13	119.03	126.77
2049	111.42	119.41	127.25
2050	111.68	119.76	127.67

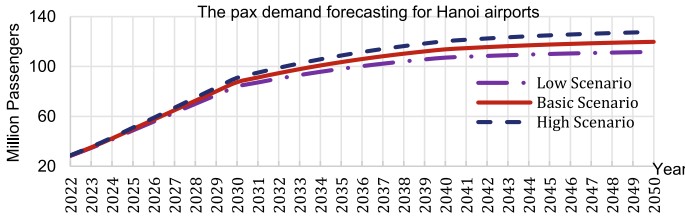


Fig. 1 The pax demand forecasting for Hanoi airports to 2050

plan in particular and determine whether Hanoi City needs a second airport and what is appropriate time.

4.1 Propose the Implementation of the Project Development for NBIA from Now to 2030, with a Vision to 2050

Currently, the two runways and accompanied system of aprons, taxiways and terminals in NBIA can handle for up to 40–42 million passengers per year, however according to our forecasting, this figure of passengers will reach in year 2025. As a result, the requirement of upgrading the NBIA needs to start as soon as possible in order to have three runways and their accompanied system. The progress of implementing should be as follows:

- In 2022–2023, survey, prepare site clearance and project technical document for the construction of runway No. 3 and its accompanied system for NBIA.
- Then, in 2023–2024 this job can immediately start to build and hopefully the third runways in NBIA can start using for commercial operation by 2025–2026.

4.2 Propose the Hanoi Airport Development for the Years from 2030 to 2050

With three runways in NBIA by 2025–2026, its capacity can handle around 65–70 million passengers per year. According to our forecasting using Fig. 1, the airport configuration is capable for air travel and freight cargo going through up to year 2033. As the result, after the third runway has been operated commercially in NBIA. For the next period plan, in our opinion, there are two options below:

- **Option 1:** The progress of construction for the 4th runway NBIA is similar to project idea of ADP Ingénierie (ADPi) from 2019. Although so far this option has not been started yet, thus in our opinion, Ha Noi city should commence to build the 4th runway and its accompany systems (terminal, aprons, taxiways) as soon as possible.

- **Option 2:** Hanoi should start to plan the second airport somewhere to the south or the south west of the city so in the near future the project can handle the large amount of passengers using flights.

5 Conclusion

The paper proposed the economic model forecasting for pax demand for Hanoi based on 4 selected economic factors then propose the options for Hanoi to upgrade or new build the second airport to satisfy the demand of air transport passengers.

References

1. Hsu CI, Wen YH (2000) Application of grey theory and multiobjective programming towards airline network design. *Eur J Oper Res* 127(1):44–68
2. Grosche T, Rothlauf F, Heinzl A (2007) Gravity models for airline passenger volume estimation. *J Air Transp Manag* 13:175–183
3. Hwang C, Shiao G (2011) Analyzing air cargo flows of international routes: an empirical study of Taoyuan. *Int Airport J Transp Geogr* 19:738–744
4. Shen G (2004) Reverse-fitting the gravity model to inter-city airline passenger flows by an algebraic simplification. *J Transp Geogr* 16(4):213–217
5. Srinidhi S (2009) Development of an airline traffic forecasting model on international sector. In: *The 2009 IEEE international conference on automation science and engineering*, IEEE computer society Washington, pp 322–327
6. Gardner E, McKenzie E (1989) Seasonal exponential smoothing with damped trends. *Manag Sci* 35:372–376
7. Samagio A, Wolters M (2010) Comparative analysis of government forecasts for Lisbon airport. *J Air Transp Manag* 16(4):213–217
8. Grubb H, Mason A (2001) Long lead-time forecasting of UK air passengers by Holt-Winters methods with damped trend. *Int J Forecast* 17:71–82
9. Wei Z, Jinfu Z (2009) Passenger traffic forecast based on the Grey-Markov method. In: *IEEE international conference on grey systems*, pp 630–633
10. Carmona-Benitez RB, Carmona-Paredes RB, Lodewijks G (2013) Damp trend grey model forecasting method for airline industry. *Exp Syst Appl* 40:4915–4921
11. Wadud Z (2011) Modeling and forecasting passenger demand for a new domestic airport with limited data. *Transp Res Rec J Transp Res Board* 2214:59–68
12. Ha CH, Đông ND, Toi PV, Minh TQ, Tam PT, Vinh NT (2013) Airport planning. Hanoi
13. Chau CN (1997) Forecasting methods. University of Transportation and Communication, Hanoi
14. Department of statistic of Vietnam (2020) Hanoi socio-economics in recent years. Hanoi
15. Anh VT (2020) Summary of socio-economics planning and target of Hanoi in vision to 2050. Report for city council, Hanoi

An Overview of the Legislation on Sustainability and Strategy Accessing the Sustainability Performance of Road Construction Projects in Vietnam



Ngoc Minh La, Trong Hung Dinh, and Thi Tuyet Pham

Abstract Road construction projects require a large amount of resources, labor, and equipment, which has significant negative effects on sustainability, such as carbon emissions, resource depletion, and forced labor. This paper aims to conduct a review of current policies and regulations concerning the sustainability of road construction projects. According to the results, policies are primarily aimed at achieving economic and environmental objectives, while social issues are barely considered. Accordingly, a systematic strategy is developed to assess the sustainability performance of road construction projects in Vietnam. The strategy sets a foundation for comparing systematically projects toward sustainable development. Additionally, supporting activities, such as improving stakeholder understanding, enforcing mandatory requirements, and ensuring consistency of laws, are proposed to adopt the proposed strategy.

Keywords Sustainability · Road construction projects · Strategy · Legislation

1 Introduction

Construction of roads plays an important role in every country's growth [1]. It is expected that there will be 25 million kilometers of new roads built worldwide by 2050, a 60% increase from 2010 [2, 3]. Besides, numerous resources, labor, and equipment are required for road construction projects, which creates significant negative impacts on sustainability, such as carbon emission, resource depletion, and forced labor [4]. Because of these circumstances, the world faces a range of inevitable consequences, including limited resources, climate change, rising populations, and construction-related health hazards [5, 6]. Therefore, road construction projects must take into account three pillars of sustainable development, consisting of economic, environmental, and social aspects.

N. M. La (✉) · T. H. Dinh · T. T. Pham
University of Transport and Communications, Hanoi, Vietnam
e-mail: lnminh@utc.edu.vn

© The Author(s), under exclusive license to Springer Nature Singapore Pte Ltd. 2024
T. Nguyen-Xuan et al. (eds.), *Proceedings of the 4th International Conference on Sustainability in Civil Engineering*, Lecture Notes in Civil Engineering 344,
https://doi.org/10.1007/978-981-99-2345-8_13

Vietnam is a developing country that has experienced rapid economic growth since the 1990s [7] and a substantial increase in new construction projects [8]. In comparison to developed countries, Vietnam is relatively new to the concept of sustainable practices [8]. According to Nguyen et al. [9], incorporating sustainable practices in Vietnam is very necessary because it can reduce pollution and energy consumption, decrease long-term costs, and improve living standards.

Accordingly, the current legislation concerning sustainability in the construction industry and road construction projects in Vietnam is analyzed in the next section to find out whether the policies support sustainability comprehensively or not.

2 Status of Legislation System Concerning Sustainability in the Construction Industry and Road Construction Projects

Similar to many countries in the world, Vietnam is always aiming for the goal of sustainable development. Several laws concerning sustainability and the construction industry were promulgated. Table 1 illustrates the system of policies, legal regulations, and standards concerning sustainable development and road construction projects in Vietnam.

After a few years of implementing the goals of Agenda 30, Vietnam's ranking in the results of the implementation of the Sustainable Development Goals has continuously increased globally in the period 2016–2020 (49/166 in 2020). However, the system of policies, regulations, laws, and standards relevant to sustainable development is not numerous and exhaustive in the construction industry and especially in road construction projects. According to Table 1, most of the policies mainly focus on economic and environmental goals, while social problems are barely considered. In addition, the integration of economic, social, and environmental dimensions in road construction projects is not yet specified in laws.

3 Developing a Systematic Strategy for Assessing the Sustainability Performance of Road Construction Projects in Vietnam

Sustainable construction practices in Vietnam face some potential challenges. Pham et al. [8] conducted a survey to point out primary challenges which must be addressed in the integration of sustainable development into the road construction projects, such as lack of legislation, guidelines, and a well-defined set of sustainable construction practices. Accordingly, a systematic strategy is proposed for integrating sustainable development into road construction projects in Vietnam (see Fig. 1).

Table 1 The system of policies, legal regulations and standards concerning sustainable development and road construction projects in Vietnam

Year	Type of legislation	Legislative documents	Information related to sustainability and road construction projects	Limitation or drawback of legislative documents
2004	Decision No.153/2004/QĐ-TTg	Strategic orientations for sustainable development in Vietnam (Vietnam's Agenda 21 in 2004)	Developing an orientated strategy for sustainable development (Vietnam's Agenda 21) in order to develop the country sustainably by combining economic development, social development, and environmental protection closely, rationally, and harmoniously	Only basic orientations for sustainable development have been given, but specific goals have not been set
2017	Decision 622/QĐ-TTg	The National action Plan to implement the 2030 Agenda for Sustainable development	The 2030 Agenda for sustainable development with 17 common goals and 115 specific goals and has been implemented in many sectors and regions. The Ministry of Construction and the Ministry of Transport and Communications are responsible for some sustainable targets, such as introducing land-use criteria for centralized wastewater treatment construction projects	Sustainable development criteria groups such as economic, social, and environmental dimensions are not specified
2019	Directives No. 25/CT-TTg	Solution for promoting growth and sustainable development in the key northern economic region	Enhancing the growth and sustainability of the key northern economic region by proposing management solutions	There are no specific solutions to the construction industry's problems, including road construction projects

(continued)

Table 1 (continued)

Year	Type of legislation	Legislative documents	Information related to sustainability and road construction projects	Limitation or drawback of legislative documents
2019	Directives No. 27/CT-TTg	Solution for promoting growth and sustainable development in the central	Enhancing the growth and sustainability of the central region by proposing management solutions	There are no specific solutions to the construction industry's problems, including road construction projects
2019	Directives No. 19/CT-TTg	Solution for promoting growth and sustainable development in the key southern economic region	Enhancing the growth and sustainability of the key southern economic region by proposing management solutions	There are no specific solutions to the construction industry's problems, including road construction projects
2019	Decision 681/QĐ-TTg	Promulgating a roadmap for the implementation of Vietnam's sustainable development goals to 2030	Promulgating criteria for Vietnam's sustainable development targets for 2020, 2025, and 2030	There is no roadmap for sustainable development related to the construction industry and road construction projects
2020	Decision no. 889/QĐ-TTg	The National action program on sustainable production and consumption in the 2021–2030 period	The decision was issued with the purpose of promoting the management, exploitation, and efficient and sustainable use of natural resources, fuels, and raw materials; promoting sustainable production and consumption on the basis of innovation	No specific tasks have been set for the construction industry in general and road construction projects in particular

(continued)

Table 1 (continued)

Year	Type of legislation	Legislative documents	Information related to sustainability and road construction projects	Limitation or drawback of legislative documents
2020	Resolution No136/NQ-CP	Sustainable development	Maintain sustainable economic growth in connection with the advancement of social progress and equality, environmental protection, efficient use and management of natural resources, and proactive response to climate change	The resolution has only provided the main tasks and solutions related to the management field of the ministries and management agencies. No specific criteria have been given
2021	Decision No 1658/QĐ-TTg	National strategy on Green Growth for the period 2011–2020, vision to 2050	This contributes to the achievement of economic prosperity, environmental sustainability, and social justice in the direction of a green and carbon-neutral economy and the reduction of the global temperature	The decision has not set specific targets for the construction industry as well as road construction projects. In addition, the task assignments to the Ministry of Construction and the Ministry of Transport are not detailed
2022	Resolution No. 06-NQ/TW	Planning, construction, management, and sustainable development of urban areas in Vietnam till 2030, with a vision toward 2045	Institutions and policies on planning, construction, management, and sustainable urban development are basically completed. Urban infrastructure, especially framework technical infrastructure and essential social infrastructure, is constructed and developed in a synchronous and modern manner. Economic growth in urban infrastructure is fast, efficient, and sustainable	The resolution only sets general tasks for the construction and development of the urban system

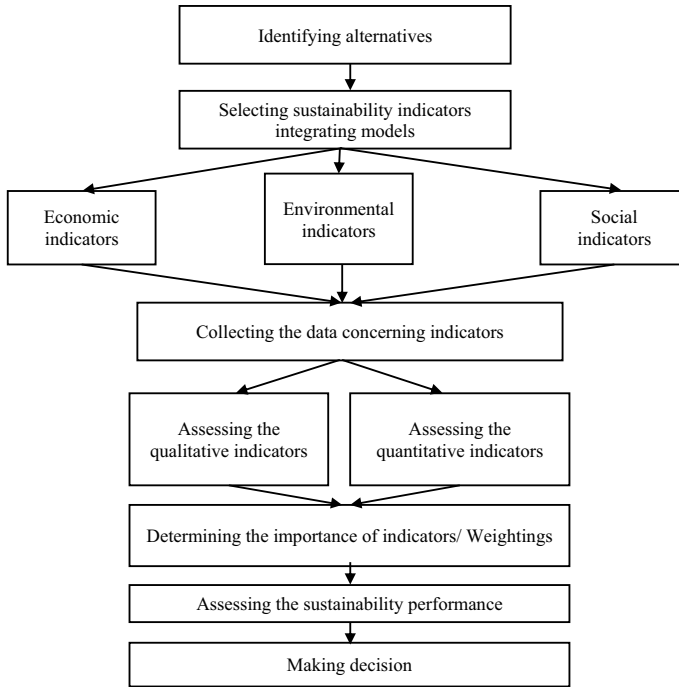


Fig. 1 A systematic strategy for assessing the sustainability performance of road construction projects

- *Step 1: Identifying alternatives*

In the first step, alternatives are identified based on pre-determined technical criteria. All available options are compared to the technical criteria, and those that do not meet the criteria are eliminated. The remaining alternatives are selected to conduct the sustainable assessment.

- *Step 2: Selecting sustainability indicators and integrating models*

Sustainability indicators play an important role in comparing alternatives. The indicator can be categorized into three groups, including economic, environmental, and social indicators. The economic indicators may include the fixed cost, variable cost, and total cost. Climate change, acidification, and energy consumption can be used to measure environmental performance, while the social indicators focus on social problems like child labor, forced labor, and local employment. There are some studies analyzing sustainability indicators, but there are few ones conducted in Vietnam

[8]. In addition, integrating models are also selected to integrate the economic, environmental, and social indicators.

- *Step 3: Collecting the data concerning indicators*

The data must be collected from a variety of sources and ideally be clear, transparent, and trustworthy. In this stage, the data must be examined and analyzed for consistency, accuracy, validity, and completeness. The consistency check determines if the data contains inconsistencies. The accuracy check indicates whether the input data values are accurate. The validation check is performed to verify and provide evidence that the data requirements have been met. The completeness check determines whether the information from the data is sufficient to draw conclusions.

- *Step 4: Assessing the qualitative indicators/quantitative data*

In this step, all relevant data are classified into qualitative indicators and quantitative indicators. The qualitative data can be assessed by the Likert scale or ranking scale to convert qualitative values to quantitative numbers.

- *Step 5: Determining the importance of indicators/Weightings*

There may be trade-offs between the environmental, economic, and social dimensions of sustainable development. The trade-offs are represented as the importance weightings evaluated by some methods, such as the Analytic Hierarchy Process (AHP) method and the Likert scale.

- *Step 6: Assessing the sustainability performance*

The weightings and the results of evaluating environmental, economic, and social performance are integrated into the integrating models to assess the sustainability performance of alternatives.

- *Step 7: Making decisions*

According to the results of step 6, the alternative performing the most sustainable results are selected.

4 Discussion

The adoption of legislation is a significant obstacle in many countries, specially in developing countries. The lack of legislation and policies concerning sustainable development, the construction industry and road construction projects is a critical problem in Vietnam. Since 2008, the United Kingdom (UK) has implemented regulatory and financial actions that help to reduce the amount of construction waste. Besides, these activities are also strongly attributable to the rising landfill tax, the increasing costs of waste disposal, and compliance obligations with site

waste management laws [10]. Moreover, the construction industry's waste management in Europe is affected by the Waste Framework Directive (2008/98/EC), one of the European Union regulations. It requires that waste must be managed without impacting human life, environment and risks to air, water, soil, animals, and plants. The regulations put into effect the polluter-pays principle, which specifies that the polluter or previous waste owners are accountable for the costs of waste management. In addition, penalties, fines, and other fiscal provisions are effective methods for supporting the treatment of construction waste [11].

Besides of UK, China is a country that has made great achievements in promoting sustainability in the construction sector. In order to enable the transition to sustainable construction, the Chinese administration has issued a total of 27 important policies categorized into three groups, namely policies, framework, specific instructions, and supporting regulations from 1998 to 2012 [12]. In 2017, the research of Chang et al. [12] not only systematically examined the development of the policy structure that the Chinese administration has evolved to promote sustainability but also recommended that more social indicators and criteria should be involved in future policy formulation.

The proposed strategy in Fig. 1 is developed for assessing the sustainability performance of road construction projects. Accordingly, some activities can be conducted to support the strategy's implementation. The activities are presented below.

- It may be problematic for laws be enforced without adequate emphasis on the awareness of the law. So, it is necessary to improve the understanding of sponsors, contractors, as well as other stakeholders in sustainable development. For example, they can participate in training courses and review historical data of previous projects.
- The sustainable assessment and its criteria (economic, environmental, and social criteria) must become compulsory requirements in all road construction projects. By complying with the proposed systematic strategy (Fig. 1), all the sustainable criteria are evaluated.
- The legislation system can support the proposed systematic strategy. At first, the required sustainable criteria focusing on economic, environmental, and social issues must be established. The criteria should be referred from global standards, such as UNEP-SETAC guideline [13] and ReCiPe [14]. Then, criteria assessment methods must be provided to ensure that all road construction projects are comprehensively analyzed, such as life cycle analysis. Accordingly, benchmarks (or standards) for all criteria are published to help experts compare and make decisions.
- A specialized organization should be established to supervise sustainable compliance from the initiation phase to the disposal phase of road construction projects. The organization may have responsibility for assessing the sustainability reports, the compliance of the proposed systematic strategy, and improving sustainable performance.

- Tools and software can be applied to assess sustainable criteria, such as SimaPro, Gabi, or Umberto. Besides, data from previous road construction projects must be gathered to build sustainable databases.

5 Conclusion

Reviewing the most recent legal documents reveals that the Vietnamese government's laws consider sustainability in economic, ecological and social goals, but specific criteria, frameworks, and guidelines are not provided, particularly in the field of sustainable development in road construction projects. It is necessary to develop a strategy for incorporating sustainable development into road construction projects.

Accordingly, a seven-step strategy is developed for assessing the sustainability performance of road construction projects. In the first step, alternatives must be identified according to technical requirements. Next, sustainability indicators and integrating models are selected, containing economic, environmental, and social indicators. The indicators can be defined based on a literature review or survey. Then, the data must be collected from a variety of sources and ideally be clear, transparent, and trustworthy. The data must fulfill the requirements concerning consistency, accuracy, validity, and completeness. In the fourth step, all relevant data are classified into qualitative and quantitative indicators and then analyzed. Subsequently, the weightings are estimated to compare trade-offs between the ecological, economic, and social aspects of sustainability. Lastly, the decisions are made after assessing the sustainability performance based on the selected integrating models. However, the paper only provides a systematic strategy for judging the sustainability performance of road construction projects. A detailed guideline involving sustainability criteria, their assessment methods and integrating models must be developed. Accordingly, future works may focus on setting up the main sustainable criteria in Vietnam and proposing a detailed methodology for assessing the criteria in the context of Vietnam.

References

1. Balaguera A, Carvajal GI, Alberti J, Fullana-i-Palmer P (2018) Life cycle assessment of road construction alternative materials: a literature review. *Resour Conserv Recycl* 132:37–48
2. Chen J, Zhao F, Liu Z, Ou X, Hao H (2017) Greenhouse gas emissions from road construction in China: a province-level analysis. *J Clean Prod* 168:1039–1047
3. Alamgir M, Campbell MJ, Sloan S, Goosem M, Clements GR, Mahmoud MI, Laurance WF (2017) Economic, socio-political and environmental risks of road development in the tropics. *Curr Biol* 27:R1130–R1140
4. Dinh TH, Dinh TH (2021) Building a comprehensive conceptual framework for material selection in terms of sustainability in the construction preliminary design phase. *Int J Sust Constr Eng Technol* 12:73–84
5. Al Hazaimeh IA, Alnsour M (2022) Developing an assessment model for measuring roads infrastructure sustainability in Jordan. *Innov Infrastruct Solut* 7:287

6. Shafiq A, Arun K, Les D (2018) Sustainability assessment of road infrastructure using sustainability index. *Infrastruct Asset Manag* 5:3–13
7. World Bank (2016) Vietnam 2035: toward prosperity, creativity, equity, and democracy
8. Pham H, Kim S-Y, Luu T-V (2020) Managerial perceptions on barriers to sustainable construction in developing countries: Vietnam case. *Environ Dev Sust* 22:2979–3003
9. Nguyen H-T, Skitmore M, Gray M, Zhang X, Olanipekun AO (2017) Will green building development take off? An exploratory study of barriers to green building in Vietnam. *Resour Conser Recycl* 127:8–20
10. Al-Otaibi A, Bowan PA, Abdel Daiem MM, Said N, Ebohon JO, Alabdullatief A, Al-Enazi E, Watts G (2022) Identifying the barriers to sustainable management of construction and demolition waste in developed and developing countries. *Sustainability* 14:7532
11. Ajayi SO, Oyedele LO (2017) Policy imperatives for diverting construction waste from landfill: experts' recommendations for UK policy expansion. *J Clean Prod* 147:57–65
12. Chang R-D, Soebarto V, Zhao Z-Y, Zillante G (2016) Facilitating the transition to sustainable construction: China's policies. *J Clean Prod* 131:534–544
13. UNEP, SLCA, SLA (2020) Guidelines for social life cycle assessment of products and organizations
14. RIVM (2020) RIVM national institute for public health and the environment: ReCiPe 2016

Constraints in Implementing Public–Private Partnerships (PPPs) in Vietnam: Private Sector’s Perspective



Hang Vu and Quynh-Huong Pham-Nguyen

Abstract The role of the private sector in the successful implementation of PPPs projects is critical; however, little effort has been made to explore the constraints of implementing PPPs. The purpose of this study is first to explore the current situation of PPPs in Vietnam and then to investigate the point of view and assessment of the private sector on the constraints of PPPs implementation. Methods included semi-structured interviews and content analysis of the findings of the semi-structured interviews carried out with PPPs practitioners of senior management level. The complete picture of current PPPs implementation practice in infrastructure in Vietnam was then obtained. The findings include three main categories: “legal and regulatory issues”, “institutional and capacity issues”, and “financial issues”. These results offer a better understanding of current PPP practice projects in Vietnam and are expected to help the public sector and lawmakers to develop strategies and improve the efficiency of the process of applying PPP in Vietnam.

Keywords Public–private partnerships · Private sector · Constraints · Vietnam

1 Introduction

Public–Private Partnership (PPP) is acknowledged all over the world as a procurement strategy that governments use to mobilize essential resources such as capital, skills, and expertise of the private sector to deliver key infrastructures. PPPs involve the participation of the public sector, the private sector and members of the community for win–win-win solutions [1]. In a typical PPP structure, there are contractual

H. Vu (✉)

University of Transport and Communications, Hanoi, Vietnam
e-mail: vmhang@utc.edu.vn

Q.-H. Pham-Nguyen

University of Transport and Communications, Ho Chi Minh City, Vietnam
e-mail: huongpnq_ph@utc.edu.vn

arrangements between parties including clients, sponsors and financiers, construction contractors, project operators, facilities management contractors, contractors, suppliers, and users or community members [2]. The public sector consists of any public administrators, and the private sector includes different private participants, mainly landowners, financiers, constructors, operators, and consultant firms. The users are either directly or indirectly involved in the payment of the PPPs project.

The private sector, by joining the PPPs contract, aims to achieve a return on investment in generating sufficient revenue to cover initial capital investment and finance charges, thus providing enough profit to pay shareholder dividends and then invest in future projects. The private sector plays a crucial role in the success of the project; however, little effort has been made to explore the constraints of implementing PPPs from the private sector's perspective. Therefore, there is a need for a thorough analysis of the private sector's views on PPPs implementation practices. This study is expected to offer a better understanding of current PPPs practice projects in Vietnam based on the private sector's perspective.

2 Constraints in Implementation of PPP: Literature Review

Besides numerous successful PPPs projects, some have failed as well. Thus, much research has recently focused on studying the obstacles in implementing PPPs projects. The list of constraints below was derived from the comprehensive and robust research of Osei-Kyei and Chan [3] and ABD [4] (Table 1).

Constraints in implementing PPPs vary from country to country, and PPPs in Vietnam will share some of the constraints as in other developing countries. Thus, it is expected that the obstacles to implementing PPP in Vietnam can represent many developing countries.

3 Current Situation of PPPs in Vietnam

Every year, the Government of Vietnam (GoV) invests millions of dollars in developing critical large-scale infrastructure. As a lower-middle-income country, the level of Official Development Assistance (ODA) will be lower in the future; hence, private investment is crucial to fill the public budget shortage [4].

As shown in Fig. 1, out of the total 336 signed PPP contracts prior to January 2020, 220 are transportation projects, which implies the importance of road infrastructure projects in Vietnam, thirty-two projects are resettlement houses and dormitories, 11 projects are health, culture, and sports projects. To date, the majority of privately invested infrastructure projects in Vietnam have been developed under the BOT model.

Table 1 Constraints in implementing PPP

Name of constraints	Author(s)
Corruption	Demuijnck and Ngondjom, 2011; Chan and Ameyaw, 2013 [as cited in 3]
Weak public institutional structure	Pessoa, 2010; Loxley, 2013 [as cited in 3]
High-end user charge	Amadi et al., 2014; Ismail and Haris, 2014, Osei-Kyei and Chan, 2015b [as cited in 3]
The lack of competition in the procurement process	Loxley, 2013; Pessoa, 2010; Marin, 2009; Abdul-Aziz and Kassim, 2011; Askar and Gab-Allah, 2002; World Bank, 2012 [as cited in 3]; ADB [as cited in 4]
Unstable macroeconomic indicators	
Immature financial market	
Incomplete risk transfer	
High use of unsolicited proposals	
Lengthy nature of the bidding process of PPP	Cheung and Chan, 2011 [as cited in 3]
Delay in finalizing negotiations	
Dispute resolution and arbitration	ADB [as cited in 4]
A lack of government capacity	
The lack of financial viability	
Low levels of tariff	

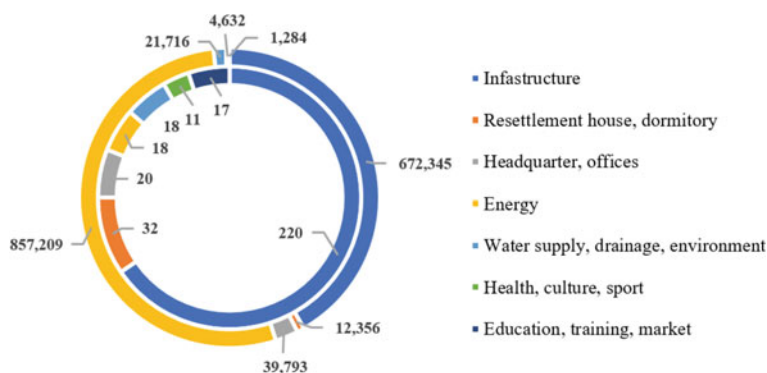


Fig. 1 Number of PPP projects and the total amount of investment by sector (January 2020) [5]

Regardless of the government's effort to attract private and foreign investment, many local investors still hesitate to take risks. And even though Vietnam has been one of the region's most attractive destinations for foreign investors, there have been very limited records of PPP infrastructure projects involving international investors [6]. According to Nguyen [7], the main reason is that Vietnam lacks a mature legislation system, inadequate regulations, and a missing buy-out clause. Despite the Law on Public-Private Partnership (PPP) being issued and running for almost two years, according to experts, it has made little to little difference to domestic investment [8]. At the same time, many risks have been embedded during the implementation of PPPs in Vietnam; hence, investors are reluctant to invest. Therefore, this study provides a comprehensive review and assessment of the current implementation practices of PPP in Vietnam, and the results are believed to offer a better understanding of PPP implementation in Vietnam.

4 Constraints in Implementing PPPs in Vietnam

4.1 Interview Process

Since the focus of this research is on exploring the private sector's perspective on the implementation of PPP in Vietnam, semi-structured interviews were conducted to obtain an in-depth understanding of the implementation practices of PPPs. Interviews were adopted because this facilitates a deeper investigation of problems. This qualitative technique was widely used and considered suitable to gain more valuable and insightful information under the study. The interviews were carried out with experienced PPP experts from private sectors in Vietnam in the interviewees' offices, with a duration of 45 min to 1 h. The main question is: "What are the main constraints your organization is facing while doing PPP projects in Vietnam?" The qualitative data were transcribed and investigated manually by using the content analysis technique. Experts are knowledgeable about PPPs implementation in Vietnam. All the private sector interviewees have different expertise, from both economic and social infrastructure, large-scale (e.g., expressway and tunnel) and smaller-scale projects (e.g., water systems and school). Generally, all interviewees demonstrated their in-depth knowledge, and their responses were considered reliable and satisfactory for analysis.

4.2 Findings from Interviews

All interviewees agreed that PPP projects in Vietnam are executed mainly in numerous key areas: energy, transportation, wastewater, and waste treatment, and have not been applied successfully in education, agriculture, health care, culture,

and sports. Although PPP is an inevitable trend to develop infrastructure and public services when the state budget is limited; however, the failure of numerous PPP projects, especially in the infrastructure, showed that achieving the designed outcomes of PPPs is not as easy as expected. To support their opinions, the interviewees provided many examples of problematic PPP projects: inadequate legal system, lack of guidelines, financial issues, and superficial investment preparation work and weak in forecasting. Other issues related to inexperienced staff with adequate skills in human resources.

4.3 Legal and Regulatory Issues

All private sector interviewees agreed that PPP regulations in Vietnam are complicated, even though some positive changes have been observed. In Vietnam, projects are administered by laws, decrees and circulars, and legal instruments of local governments. Private parties are suffering from risks in the procedure of implementing PPP projects as they are the primary source of delays. Another issue is that lengthy procedures for granting investment registration certificates are, hence, deceleration the project schedule. Interviewees proposed that the development of a fit-for-purpose legal framework is crucial and can provide consistency and clarity to all parties related to PPP projects.

The private sector interviewees also highlighted that toll road fees and service charges are other issues. These charges are currently under the control of by the government and are not entirely consistent with the market-based mechanism. Thus, the projects then become non-bankable, and the project revenue is less reliable. Many BOT highway projects, namely BOT North Thang Long, BOT An Suong-An Lac, and BOT Cai Lay, faced public opposition due to high toll rates and unreasonable toll booth locations. Many PPP projects around the world have experienced public opposition on this issue.

Despite risk sharing is one of the advantages and drivers of adopting a PPP, the current Vietnamese regulation system does not offer guidance on the allocation of risks among parties. These findings are consistent with the results from the questionnaire survey, as the criteria 'mature legal system required to support PPP procurement' was recorded as the second most important consideration for a PPP project in Vietnam [9].

4.4 Institutional and Capacity Issues

The application of direct appointment has affected the transparency and competitiveness of the investment environment, reducing the ability to select high-quality investors with financial capacity and expertise in project management. By using this

means of procurement, the government will lose the opportunity to assess, evaluate, and select the most suitable investor to carry out the project.

Furthering discussion on this, interviewees insisted that there was a lack of transparency over PPPs, which is a well-recognized constraint in literature. The information about the project has not been published, is not transparent, and access to information is limited. The PPP agreements were normally considered confidential. Many investors have not felt confident to invest in the Vietnamese market, even though the political and economic system is stable.

On the other hand, the capability in PPP still needs to improve, though a lot of training and education have been carried out. The management and supervision of the project quality were still weak, almost entrusted to investors from the stage of project formulation, project approval, and project implementation. Other challenges include poorly defined duties and tasks, lack of communication and commitment from various partners, difficulties in member coordination, and a lack of leadership skills.

There were also concerns that the capacity of many local investors is still inadequate, and the development of supporting industries is underdeveloped. The weak financial capacity of investors is also one of the reasons leading to delays, even cancelation of the projects. Some projects were sold to other investors or reverted from PPP to traditional procurement. This also aligned with the findings from ADB [4].

4.5 Financing Issues

Some respondents agreed that the financial market in Vietnam is still immature and unable to provide sufficient long-term capital needed by investors. GoV has utilized many incentives, including exemption of land tax and land use levy, tax-deductible or enterprise income tax, import tax, or VAT incentives [10]. These can significantly reduce the construction and operational risks of the project company. Another issue related to PPPs in Vietnam is funding. Some participants believed that the size of domestic banks is small while most PPP investments in infrastructure are being financed by the banks; therefore, this can generate colossal risk.

As the revenue generated from PPPs project is in the local currency, projects involving foreign investors will assume the exchange risk. Interviewees that have experiences in PPPs expressway and highway projects highlighted that foreign investors have not been interested in PPPs in Vietnam because it is still believed that there are many risks related to exchange rates. Despite great efforts to promote, in Vietnam, there is not yet any PPP infrastructure project with the participation of foreign investors successfully deployed.

Interviewees also argued that if the mechanism for guarantee should be issued soon, it will increase the economic significance and social implications. This is because if the project is delayed during implementation, say for a few years, the cost would increase significantly, especially the cost of land acquisition and resettlement.

Table 2 Summary of existing obstacles in doing PPPs in Vietnam

What is/are the current constraints in implementing PPPs in Vietnam?
<i>Legal and regulatory issues</i>
<ul style="list-style-type: none"> • Regulations were complicated and overlapped • Lack of guidelines or unclear guidelines
<i>Institutional and capacity issues</i>
<ul style="list-style-type: none"> • Lack of transparency • Lack of competitive bidding • Human resources lack experience and appropriate skill
<i>Financing issues</i>
<ul style="list-style-type: none"> • Lack of government guarantee • Funding difficulties • The size of domestic banks is small

Table 2 represents the summary extracted from interviews regarding the existing issues in doing PPPs in Vietnam.

5 Conclusion

Through in-depth interviews with experts, the complete picture of PPP implementation practice in Vietnam is obtained. Most interviewees highlighted that the implementation constraints in Vietnamese PPPs can be categorized into three groups: “legal and regulatory issues”, “institutional and capacity issues”, and “financial issues”. Interview results observed that regardless of government efforts, private sectors still believe that undertaking PPP in Vietnam is quite risky, and they lack confidence in investing. Issues related to legal and regulations, including complicated and overlapped PPP regulations. Lack of guidelines or unclear guidelines was frequently mentioned by private sector interviewees. The immaturity of the legal system, lack of competitive bidding, and transparency and capability are the major PPP implementation barriers. The other issues observed by the interviewees are related to financing problems in which lack of government guarantee, funding difficulties, and the size of domestic banks is small were the most frequently mentioned responses. The outputs of this study are consistent with previous studies, including Osei-Kyei and Chan [3] and ADB [4]. The result will help the public sector, and lawmakers to develop strategies and improve the efficiency of PPP implementation in Vietnam.

References

1. Grimsey D, Lewis MK (2009) Developing a framework for procurement options analysis. Policy, finance and management for public-private partnerships. Wiley-Blackwell, Chichester, pp 398–413
2. Rouboutsos A, Macário MR (2013) Public-private partnerships in transport: theory and practice. *Built Environ Proj Asset Manag* 3(2):160–164
3. Osei-Kyei R, Chan AP (2017) Implementation constraints in public-private partnership: empirical comparison between developing and developed economies/countries. *J Facil Manag* 15(1):90–106
4. Asian Development Bank (2012) Assessment of public-private partnerships in Viet Nam: constraints and opportunities. Asian Development Bank, Philippines
5. Nguyen TKV (2020) Public-private partnership (PPP) investment policy in infrastructure development in Vietnam. *Const Econ J*
6. Breu M, et al (2012) Sustaining Vietnam's growth: the productivity challenge. McKinsey Global Institute
7. Nguyen HV (2017) Making public-private partnerships in infrastructure successful in Vietnam: a need for a better procurement legal mechanism. Queensland University of Technology
8. VNA (2022) Public-private partnership law offers little benefit to public projects. <https://en.vietnamplus.vn/publicprivate-partnership-law-offers-little-benefit-to-public-projects/234649.vnp>
9. Vu H, et al (2018) Selection criteria for implementation of public-private partnerships in infrastructure projects: a case of Vietnam. In Vietnam symposium on leadership and public policy: policy innovation and leadership in the digital age. Hanoi
10. Tran HD (2019) Public sector management of revenue risk in public-private partnerships: Vietnam's north-south expressway project. Harvard Kennedy School of Government

Assessing the Accuracy of Lidar UAV Technology Along with the Lidar Camera in Establishing the Terrain Map for Construction in Vietnam



Tran Quang Hoc, Tran Duc Cong, and Do Van Manh

Abstract LiDAR technology has been a few developments in recent years, but they are applied to the recently released Matrice M300 which can use many different types of cameras. In this study, the authors conducted a survey to assess the accuracy of Lidar UAV technology on Matrice 300 flying devices with Lidar camera L1 in different terrain projects. From there, make comments on the accuracy of this technology and its applicability in topographic surveying in Vietnam.

Keywords Light detecting and ranging (LiDAR) · Unmanned aerial vehicle (UAV) · Global navigation satellite system (GNSS)

1 Introduction

Now a day, with the development of unmanned aerial vehicles and digital image processing techniques, the method of creating topographic maps using images taken from UAV devices is being widely applied in the world and Vietnam. According to recent studies [1–3], using images taken from unmanned aerial vehicles allows the creation of a 1:1000 scale topographic map with open terrain with little real cover. However, for areas with a vegetal layer, the use of images cannot accurately determine the height under the vegetal layer.

T. Q. Hoc (✉) · T. D. Cong · D. Van Manh
University of Transport and Communications/UTC, Hanoi, Vietnam
e-mail: hoctq@utc.edu.vn

© The Author(s), under exclusive license to Springer Nature Singapore Pte Ltd. 2024
T. Nguyen-Xuan et al. (eds.), *Proceedings of the 4th International Conference on Sustainability in Civil Engineering*, Lecture Notes in Civil Engineering 344,
https://doi.org/10.1007/978-981-99-2345-8_15

159

A new step in the development of Lidar technology mounted on unmanned aerial vehicles (UAV Lidar technology) has brought high efficiency in topographic survey work, especially for medium and small areas. The advantage of Lidar UAV technology, it allows the removal of the vegetal layers, from which it is possible to determine the accuracy of evaluation. Therefore, in this study, the authors conducted a study to investigate the accuracy of Lidar UAV technology with Matrice 300 flying device, and Lidar camera L1 in some of the projects in Vietnam. Studies on the accuracy of coordinate position have been available, so in this study, only the survey and accuracy of the elevation.

2 Overview of Lidar Technology and the UAV DJI MATRICE 300 with LIDAR CAMERA L1

2.1 Overview of Lidar Technology

Light Detecting And Ranging (LiDAR) technology, also known as Airborne Laser Ranging (ALR) laser measuring technology, for topographic research started in the 1990s. XX. Laser technology itself has been invented and applied in engineering fields since the 60 s, 70 s, and 80 s of the previous era. In the early 90s, laser technology was applied by NASA (USA) in topographic research. ALR technique is increasingly improved in both equipment and technology. Therefore, the cost of laser technology is decreasing.

LiDAR consists of many interconnected systems, first of all, a laser measuring device (T/B) placed on an aircraft, which allows measuring the distance D from the aircraft to a feature or terrain point. The laser device can scan the terrain with a width of several tens of meters to several hundred meters, thanks to the rotating mirror. The mirror mounted at the top of the scanner bends the laser beam toward the terrain surface.

Lasers operate on the principle of electrical pulses (with wave principle types) with frequencies as high as several kHz emitted from a laser light source. The energy reflected from the surface of the terrain or feature through the optical system is recorded. Based on knowing the time (t) of the response of the signal from the terrain surface to the recording device and the frequency of the electrical pulse (ν), this study will determine the distance D from the topographical or feature point aircraft at the time of scanning. The laser rangefinder operates in infrared and near-infrared spectral ranges with wavelengths up to 1540 nm. Laser distance measurement accuracy can be achieved with an error of $m_D = \pm 1$ cm (Fig. 1).

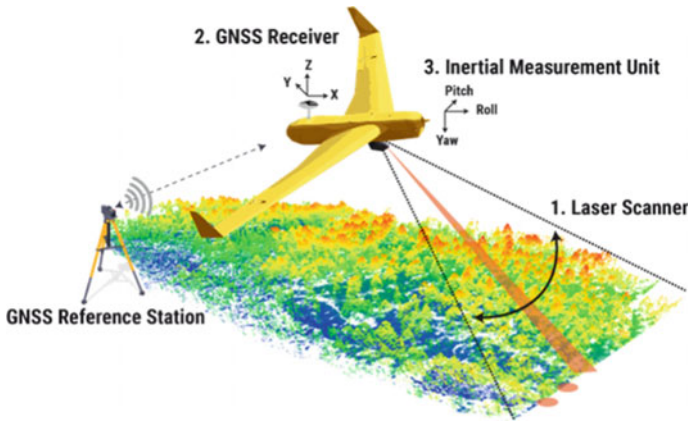


Fig. 1 Introduces the working principle of the LiDAR system

2.2 Introduction DJI MATRICE 300 with Lidar Camera L1



Matrice 300 RTK is an unmanned aircraft device researched and produced by DJI. With many innovative new features, it is a useful tool for measuring and surveying with accuracy up to cm

- Weight (excluding battery) 3600 g
- Maximum horizontal speed 23 m/s
- Maximum flight time (sea level) 55 mi
- Highest flight range above sea level: 7000 m
- Wind resistance: 15 m/s

Specifications of Lidar camera L1:

- Weight: 930 ± 10 g
 - Dimensions $152 \times 110 \times 169$ mm
 - Moisture resistant: IP54
 - System performance:
- Detection range: 450 m @ 80% reflectance, 0 klx, 190 m @ 10% reflectivity, 100 klx
 System Accuracy (RMS 1σ) * Horizontal: 10 cm @ 50 m Stand: 5 cm @ 50 m
- Lidar:
- Accuracy Range (RMS 1σ) * 3 cm @ 100 m
 Integrated Camera Mapping RGB: 20 Mp

3 Survey and Assess Experimental Results in Some Projects

3.1 Method of Survey and Accuracy

To survey and accuracy, the author compares results measured by GNSS-RTK technology at DC2 benchmarks, and points on the field, and measured these points respectively on the model built from Lidar scan data. Calculate the height difference from these two results according to formula (1) and the mean error to evaluate the accuracy according to formula (2).

$$\Delta h = H_{MH} - H_{RTK} \quad (1)$$

$$m_{\Delta h} = \pm \sqrt{\frac{[\Delta h \Delta h]}{n - 1}} \quad (2)$$

where: H_{RTK} —elevation measured by GNSS-RTK technology, H_{MH} —elevation measured on the model.

The survey project has been done with three projects in different terrain, plain area, and area with many trees.

3.2 Trieu Phu Multi-industrial Park Project, Quang Tri Province

The survey area belongs to Trieu Thach, Trieu Son, and Trieu Lang communes in Southeast Quang Tri economic zone, Quang Tri province. Scope of detailed planning map survey scale 1:500, total area 631.6 ha. The topography of this area is relatively flat and less hidden by trees and other features (Fig. 2).

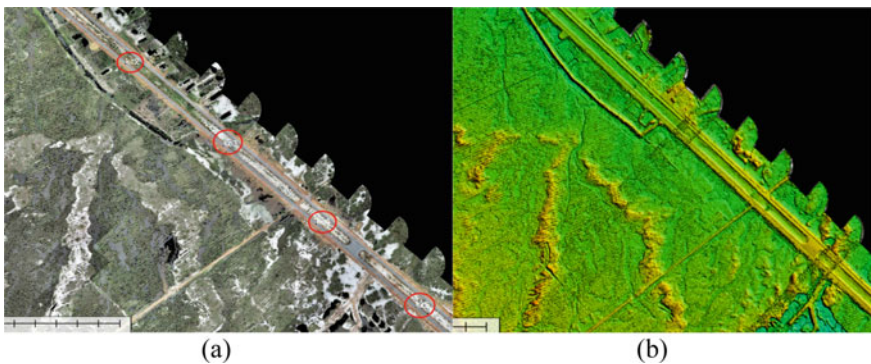


Fig. 2 a Image map and b digital elevation model of the experimental area in

Table 1 Coordinates and heights of test measuring points

Points name	Coordinates VN-2000		Elevation Lidar (m)	Elevation RTK (m)	Difference Δh (m)
	X (m)	Y (m)			
KT1	1,862,800.881	605,681.212	4.516	4.532	0.016
KT2	1,862,594.414	605,905.452	4.393	4.420	0.027
KT3	1,862,380.722	606,137.552	4.635	4.655	0.020
KT4	1,862,177.928	606,357.839	5.026	5.047	0.021
KT5	1,861,961.518	606,592.989	5.364	5.399	0.035
KT6	1,861,755.532	606,816.791	5.276	5.299	0.023
KT7	1,861,543.851	607,046.603	5.067	5.079	0.012
KT8	1,861,314.033	607,293.257	5.293	5.330	0.037
KT9	1,861,115.087	607,512.286	5.475	5.506	0.031
KT10	1,860,918.473	607,725.865	5.428	5.449	0.021
KT11	1,860,680.625	607,984.203	6.469	6.465	-0.004

Trieu Phu Industrial Park.

The total number of test points in the field and on the model built from Lidar scan data is 11, coordinate data and elevation are shown in Table 1.

Calculate the mean square error by formula (2): $m_H = \pm 0.026$ m.

3.3 Detailed Planning Project of Quan Chu Urban Area and Golf Course

The project's survey area is in Quan Chu town, Dai Tu district, Thai Nguyen province. Scope of investigation, measurement, and topographic mapping at scale 1:500 for detailed planning, total area: 500 ha. The topography of this area is mainly hilly, with many shrubs covering the terrain surface (Fig. 3).

The total number of test points in the field and on the model built from Lidar scan data is 10, the coordinate and elevation data are shown in Table 2.

Calculate the mean square error by formula (2): $m_H = \pm 0.066$ m.

3.4 Khanh Hoa–Buon Ma Thuot Expressway Project

The section of the surveyed Bay route is located in Dak Lak province under the Khanh Hoa–Buon Me Thuot expressway project. This is a new road, and the location of the pilot survey route is mountainous terrain, the design consultant is expected to design the tunnel through this location (Fig. 4).

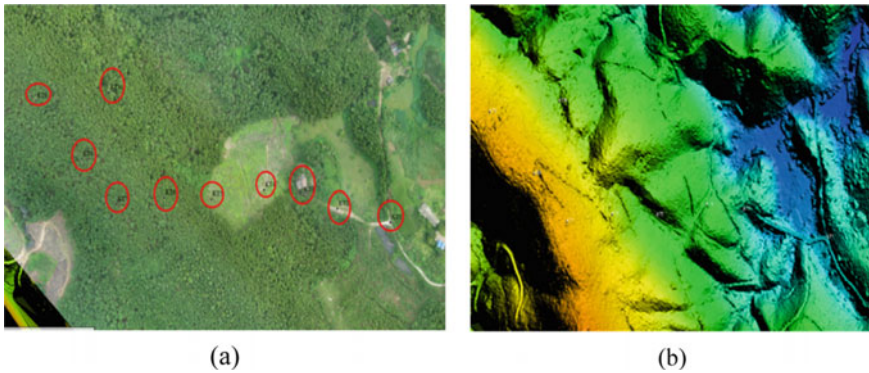


Fig. 3 a Image map and b digital elevation model of an experimental area at Quan Chu golf course

Table 2 Coordinates and heights of test measuring points

Points name	Coordinates VN-2000		Elevation Lidar (m)	Elevation RTK (m)	Difference Δh (m)
	X (m)	Y (m)			
KT1	2,379,412.461	237,913.845	51.312	51.283	0.029
KT2	2,379,427.811	237,845.318	51.957	51.920	0.037
KT3	2,379,442.613	237,800.913	55.862	55.892	- 0.030
KT4	2,379,448.095	237,750.477	66.491	66.449	0.042
KT5	2,379,438.227	237,682.498	75.452	75.405	0.047
KT6	2,379,439.872	237,621.647	96.804	96.860	- 0.056
KT7	2,379,432.745	237,559.698	115.715	115.802	- 0.087
KT8	2,379,482.632	237,515.293	116.404	116.493	- 0.089
KT9	2,379,547.87	237,456.086	113.508	113.540	- 0.032
KT10	2,379,557.189	237,550.379	86.024	86.134	- 0.110

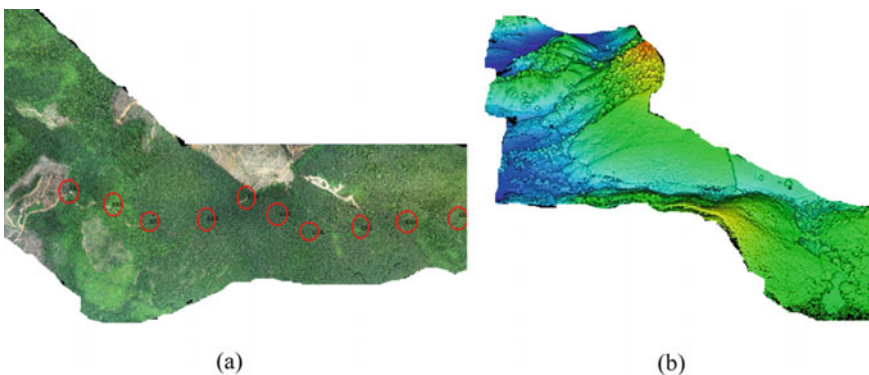


Fig. 4 a Image map and b digital elevation model of the experimental area at the expressway Khanh Hoa–Buon Ma Thuot

Table 3 Coordinates and heights of test measuring points

Points name	Coordinate VN-2000		Elevation lidar (m)	Elevation RTK (m)	Difference Δh (m)
	X (m)	Y (m)			
KT1	1,383,434.339	567,551.190	491.267	491.305	- 0.038
KT2	1,383,378.835	567,384.679	498.388	498.444	- 0.056
KT3	1,383,351.924	567,179.484	435.088	435.208	- 0.120
KT4	1,383,330.059	567,009.610	367.561	367.599	- 0.038
KT5	1,383,311.558	566,821.234	362.814	362.880	- 0.066
KT6	1,383,382.199	566,695.089	369.378	369.409	- 0.031
KT7	1,383,451.158	566,572.308	306.471	306.463	0.008
KT8	1,383,365.380	566,414.207	297.309	297.414	- 0.105
KT9	1,383,353.606	566,190.511	290.838	290.994	- 0.156
KT10	1,383,419.201	566,047.547	283.989	284.113	- 0.124
KT11	1,383,479.751	565,881.036	286.750	286.850	- 0.100

The total number of test points in the field and on the model built from Lidar scan data is 11, coordinate and elevation data is shown in Table 3.

Calculate the mean square error by formula (2): $m_H = \pm 0.093$ m.

4 Conclusion

Based on the actual experimental survey results in Vietnam, with different terrains, some comments can be made as follows.

The accuracy of Lidar UAV technology depends on the degree of occlusion of the terrain. With the project in Trieu Phu industrial park, the terrain is relatively flat, the test points are not obscured by the vegetation, and the accuracy obtained is very high 0.026 m. At the Khanh Hoa–Buon Ma Thuot highway project, the topography of this area is mainly forests and mountains, trees with thick foliage, and an average height of 15–20 m, greatly affecting the accuracy of identifying terrain. The error received is 0.093 m.

According to the circulars and standards currently being applied [4, 5], the error in the elevation of topographic features does not exceed 1/3 of the basic elevation range (contour lines). If you take a topographic map with a contour line of 0.5 m, the allowed error does not exceed 0.167 m.

- With the survey and evaluation results in the above projects, the received errors are all smaller than the allowed errors. Thus, the Lidar UAV technology on the Matrice 300 flying device with the L1 scanner meets the accuracy requirements of the topographic survey in construction.

References

1. Hoc TQ, et al (2017) Investigation of the accuracy of horizontal points of unmanned aerial vehicle in establishing of large scale Terrain maps. In: Hanoi CSMI 2017 November, proceedings of international conference on smart management of infrastructures
2. Quang L et al (2022) Research on the application of ground laser scanners and images taken from unmanned aerial vehicles (UAVs) in building 3D ground models. *J Natl Resour Environ* 4:148
3. Tung DT et al (2012) Artistic Lidar application to establish 3D terrain map in Bac Giang city. *J Hanoi Univ Natl Resour Environ* 3:11–17
4. Circular No. 68/2015/TT-BTNMT (2015) Circular No. 68/2015/TT-BTNMT dated December 22, 2015, of the Minister of Natural Resources and Environment providing technical regulations for direct topographic measurement to serve the establishment of topographic maps and geospatial database scale 1:500, 1:1000, 1:2000, 1:5000
5. Basic standard TCCS 31:2020/TCDBVN, Highway - Specifications for a survey

Bridge and Highway Engineering, Railway Engineering

A Review of Methods for Protecting Highway Embankments from Overtopping Flow



Huy Quang Mai, Tuan Anh Tong, and Phong Dang Nguyen

Abstract Highway overtopping due to floods is one of the critical causes of road damage in Central Vietnam because of the potential for rapid soil erosion and mass wasting resulting in partial or complete failure of the roadway embankment. This paper focuses on feature analysis of the hydraulic characteristics of water flowing over an embankment providing a basis for understanding the erosion process. The effectiveness and application conditions of several modern methods to protect road embankments from overtopping flow are also presented.

Keywords Highway embankments · Overtopping flow · Broad-crested weir · Erosion

1 Introduction

One of the nations with the highest risk of natural disasters is Vietnam. Vietnam experiences a wide range of natural hazards due to its 3440 km of coastline and its varied and complex topography, especially typhoon, floods, and heavy rainfalls [1]. During flood events, flood water could flow over highway embankments, resulting in not only traffic disruption between communities, but also damage to the embankment and pavement. Figure 1 shows the flow through the pavement during flood and pavement damage after the flood at some roads in Central Vietnam. During floods, roadway embankments can fail in a variety of ways, including erosion owing to river overtopping, piping and liquefaction, and perhaps mass wasting due to slip ring fracture.

Various hydraulic situations, such as sub-critical and super-critical flow as well as hydraulic leaps, may occur on an overtopped road and embankment, as shown in Fig. 2. Erosion and/or embankment failure are more likely to happen if the instantaneous shear forces of the running water are greater than the materials that make

H. Q. Mai (✉) · T. A. Tong · P. D. Nguyen
University of Transport and Communications/UTC, Hanoi, Vietnam
e-mail: mqhuy@utc.edu.vn



Fig. 1 **a** Overtopping event on National Highway 1A, Ha-Tinh Province, Vietnam; **b** Pavement damage due to overtopping event on National Highway 49B, Hue City, Vietnam, October 2020 (Photo from Internet)

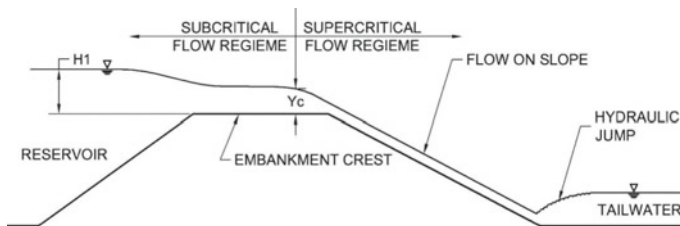


Fig. 2 Hydraulic flow regimes and overtopping flow zones [2]

up the road or the embankment's resisting forces. There is a chance that the entire roadway might be breached or washed out when overtopping occurrences persist for a long time (i.e., hours to days).

Currently in Vietnam, the road surface elevation is determined through the flood stage corresponding to the design frequency in accordance with the grade of the road [3]. Therefore, it is not possible to assess the unusual floods due to the effects of climate change that may cause irregular floods the road in the future. This paper presents the unfavorable hydraulic characteristics of the overflow flow over the road surface, the erosion phenomenon on the road embankment. Some current design solutions commonly used to minimize the adverse effects of overflow are also presented.

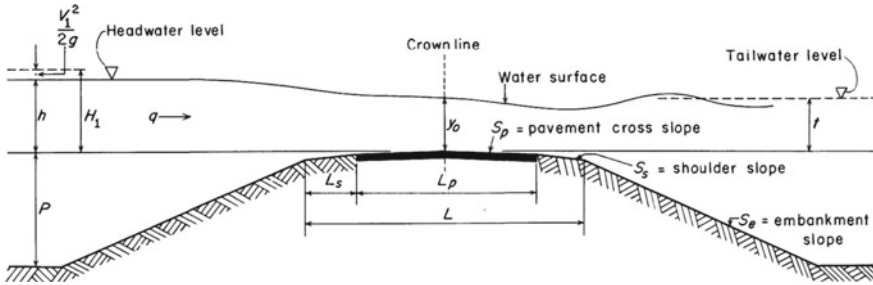


Fig. 3 A principal variable needed to describe flow over an embankment [4]

2 Characteristics of Flow Over a Highway Embankment

2.1 Flow Types

The hydraulics of water flowing over an embankment give a foundation for understanding the erosion process. Different flow types were seen as the water flowed over the embankment. In the research of Kindsvater [4], three flow patterns were identified when water runs over an embankment: free-plunging flow, free surface flow, and submerged flow. When the jet plunges beneath the tailwater surface, it creates a submerged hydraulic leap on the downstream slope. Surface runoff arises when the jet detaches from the roadway surface at the downstream shoulder and “riding” over the tailwater’s surface. Submerged flow is usually surface flow, whereas free flow can be either submerged or surface flow. Submersible runoff is more likely than surface runoff to cause roadway bed erosion.

Kindsvater depicted flow types across embankments using charts based on the variables defined in the Fig. 3 [4].

2.2 Determination of Discharge for Flow Overtopping Roadway Embankment

The widely recognized equation that is used for calculating discharge over an embankment under free flow situations is

$$q = CH_1^{3/2} \tag{1}$$

where: q —unit discharge; C —a coefficient of discharge, and H_1 —total head over the embankment crest as specified in Fig. 2.

Bradley provided Fig. 4 to calculate the discharge coefficient using Kindsvater’s data for a flat highway surface [5]. To calculate the discharge flowing over a roadway, first calculate the free flow coefficient of discharge (C) in relation to the ratio $H_1/$

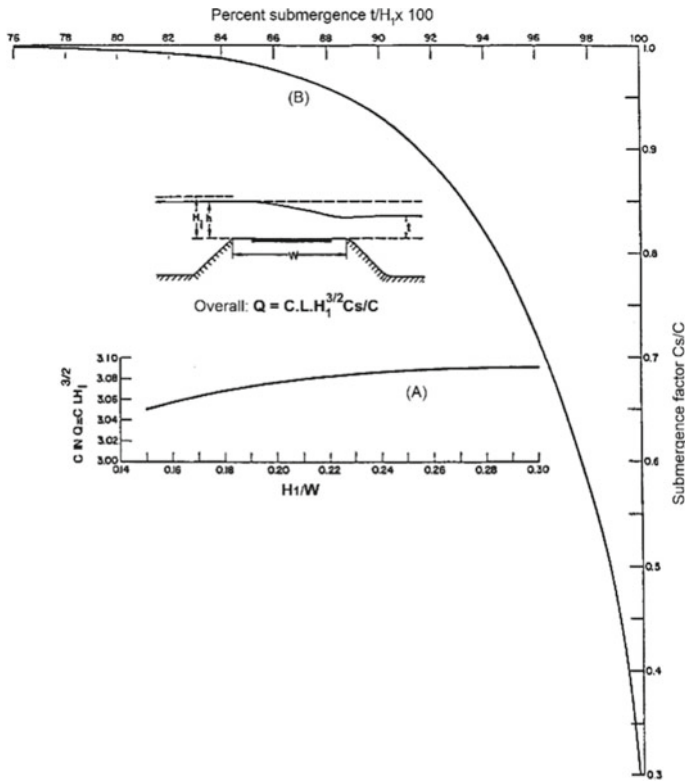


Fig. 4 Coefficients of discharge for flow over roadway embankment [5]

W , then input Curve B with the appropriate amount of submergence in percent and calculate the submergence factor (C_s/C). The following equation is used to compute the resulting discharge:

$$Q = CLH_1^{3/2}(C_s/C) \tag{2}$$

where: L —flooded roadway embankment length; C_s —a coefficient of discharge for condition of submerged flow.

If the water depth changes throughout the route, it is best to divide the flooded roadway into tiny fragments and calculate each independently.

2.3 Determination of Roadway Embankment Erosion

Because of the high velocities on the downstream side of the embankment when embankments are overtopped by flood waters, erosion damage can be significant.

When the flow's shear stress surpasses the soil's critical shear stress, erosion occurs. The tensile strain increases as the velocity increases. The velocity is determined by the headwater and tailwater conditions. A further critical factor is the soil's erodibility. When opposed to non-cohesive, fine-grained soils, cohesive soil or soil with bigger particles is more resistant to erosion. Finally, the quantity of damage is affected by the time of overtopping.

According to the study of Chen and Anderson [9], there are 02 erosion mechanisms occurring for the road embankment, depending on the flow regime as follows:

- Freefall situation: Erosion tends to begin at the embankment toe and progress upstream as a head-cut in a freefall state.
- Submerged situation: in this case, erosion often begins in the downstream shoulder and spreads up and downstream over time.

The critical or permitted shear stress and velocity are defined as the highest shear stress and velocity of flow that will not produce erosion. To calculate the critical shear stress in non-cohesive materials, use the following equation [6]:

$$\tau_c = 0.05(\gamma_s - \gamma)d_{50} \quad (3)$$

here γ_s and γ are the specific weights of soil and water, respectively; d_{50} —the corresponding particle size when the cumulative percentage reaches 50%.

For cohesive soil, many formulae for estimating critical shear stress have been devised. According to Smerdon and Beasley [7], the critical shear stress of cohesive soil is significantly connected to the plasticity index. Chen and Anderson suggested the following equation to compute the critical shear stress for the highway embankment [9] using data from McWhorter et al. [8] and their own results:

$$\tau_c = 0.019(\text{PI})^{0.58} \quad (4)$$

where PI is the plasticity index.

A comprehensive literature review of previous studies of embankment erosion and several equations which relate embankment erosion rates to shear stress. The general equation for estimating the embankment erosion rate is:

$$E = K(\tau - \tau_c)^a \quad (5)$$

where E is the rate of erosion per unit area; τ and τ_c are effective shear and critical shear stress, respectively; K and a are empirical coefficients dependent on soil properties. For highly cohesive soil such as clay ($\text{PI} \geq 10$), $K = 0.000086$ and $a = 0.91$; For low cohesive soil such as sandy clay ($\text{PI} \leq 5$), $K = 0.00022$ and $a = 0.43$; For non-cohesive soil such as gravel and sand $K = 0.00324$ and $a = 1.3$.

3 Highway Embankment Protection Measures

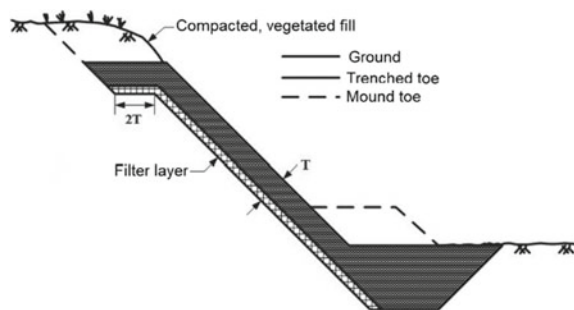
The use of protection measures to highway embankment against erosion induced by overtopping flow is an important issue for highway safety. Various erosion prevention techniques have been offered based on the erosion mechanisms. These methods can be divided in to three categories including (a) mitigation measures, (b) countermeasures and (c) a combination of both. Mitigation strategies include the installation of culverts to avoid overtopping, raising the level of the roadway embankment crest, and installing fuse plugs. Countermeasures include employing plant, riprap and geotextile, precast articulated concrete block matrices, gabions, and concrete slope lining to protect the downstream slope against back erosion and, eventually, embankment failure. This section discusses several erosion control strategies against overtopping.

3.1 Riprap

Riprap has been used successfully to prevent erosion in both coastal and riverine situations. The idea behind this strategy is to employ heavier stones than river bed grains to enhance resistance to hydraulic shear stress and hence avoid erosion. The size of riprap is dictated by the shear stress induced by the flow and the location of the riprap stones, as illustrated in Fig. 5 [10, 11].

Many studies show that a filter must be placed between the soil and the riprap layer once applied on slopes to prevent areas of the riprap from damage caused by soil particles flowing through the pores of the riprap preventing soil erosion. Even without filters, underlying soil beneath the riprap may erode via big holes in the riprap. Lastly, the riprap might not even move further away, but it may shift dramatically if the underlying soil is degraded. The filter might be sand or geosynthetic [12, 13].

Fig. 5 Typical sketch of riprap installation [10]



3.2 Gabion Mattress

Gabion mattress, also named as Reno mattress or Mac mattress, is formed of metal hexagonal wire mesh and loaded on-site with stones or even other comparable substances to make a flexible, permeability, rigid frame. The rocks used to fill the containers could be angular rock or huge cobblestone, however angular rock is favored due to the increased degree of interlocking between the rocks [12]. Following the failure of several installations, a recent appraisal of their field use in New York State is fairly negative. Simon et al. [14] present a research on the usage of gabions in the fluvial region. They discovered that the critical shields stress necessary to move a rock within a Reno mattress' steel cage is more than double that required to move the same rock just outside of the mattress. Gabions may outperform ripraps of the same size in terms of scour reduction, or equal sizing of gabions may result in more cost-effective scour reduction solutions [15].

3.3 Blankets Made of Precast Articulating Concrete Blocks

Blankets made of precast articulating concrete blocks consist of precast blocks tied together to make a mat. Currently, two different types of blocks are typically used: open blocks and closed blocks. The open blocks feature open cells that allow grass to grow, increasing abrasion resistance. On a cohesive subsoil, these structures may endure high-velocity flows of up to 7.9 m/s without failing [16]. Figure 6 depicts a typical portion.

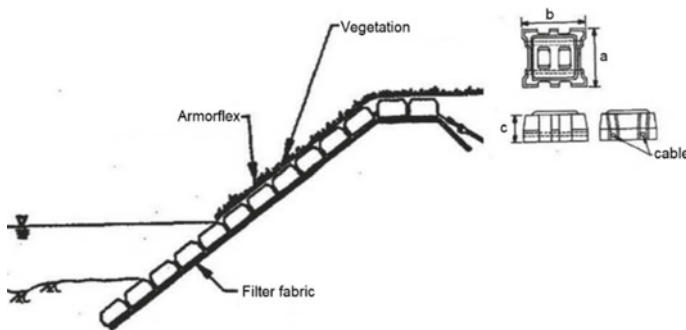


Fig. 6 A typical precast concrete block arrangement in section [10]

4 Conclusion

An overview focusing on unfavorable hydraulic characteristics of the overflow flow over the road surface, the erosion phenomenon on the road embankment as well as some current design solutions to minimize the adverse effects of overflow is presented in this paper. The research results show that the roadbed must work in very unfavorable hydraulic conditions, when designing roads that are likely to be flooded in the future, the designer needs to evaluate the technical–economic efficiency between the plan of raising the road surface elevation to avoid flooding or keep the road surface elevation in combination with measures to strengthen the roadbed to prevent erosion.

References

1. IMHEN and UNDP (2015) Vietnam special report on managing the risks of extreme events and disasters to advance climate change adaptation. In: Publishing house of natural resources, environment and cartography, Hanoi
2. Clopper PE, Chen Y (1988) Minimizing embankment damage during overtopping flow. In: FHWA report: FHWA-RD-88-181. Federal Highway Administration, McLean
3. TCVN (2005) Highway: specifications for design—TCVN4054:2005
4. Kindsvater CE (1964) Discharge characteristics of embankment shaped weirs. USGS water-supply paper 1617-A. Study of Flow of water over weirs and dams, U.S. Geological Survey
5. Bradley JN (1973) Hydraulics of bridge waterways, hydraulic design series No.1. U.S. Department of Transportation, Federal Highway Administration
6. Gessler J (1971) Beginning and ceasing of sediment motion. In: Shen HW (ed) River mechanics, Chapter 7. Fort Collins, Colo
7. Smerdon ET, Beasley RP (1959) Relation of compaction and other soil properties to erosion resistance of soils. *Trans ASCE* 8:199
8. McWhoeter JC, Carpenter TG, Clark RN (1968) Erosion control criteria for drainage channel. Mississippi State Highway Department, Jackson. FHWA, U.S. Department of Transportation Agricultural Experiment Station, Mississippi State university, State College
9. Chen YH, Anderson BA (1987) Development of a methodology for estimating embankment damage due to flood overtopping. In: FHWA report: FHWA/RD-86/126. Federal Highway Administration, McLean
10. Brown SA, Clyde ES (1989) Design of riprap revetment, hydraulic engineering circular No. 11, FHWA-IP-89-016. Federal Highway Administration, Washington, DC
11. Lauchlan CS, Melville BW (2001) Riprap protection at bridge piers. *J Hydraul Eng* 127:412–418
12. Huy MQ (2021) An overview: modern countermeasures against local scour at bridge piers—applicability in Vietnam. In: Ha-Minh C, Tang AM, Bui TQ, Vu XH, Huynh DVK (eds) CIGOS 2021, emerging technologies and applications for green infrastr
13. National Academies of Sciences, Engineering, and Medicine (2016) Minimizing roadway embankment damage from flooding. The National Academies Press, Washington, DC
14. Simon DB, Chen YH, Swenson LJ (1984) Hydraulic test to develop design criteria for the use of Reno mattresses. Report, Colorado State University, Colorado
15. Yoon T (2005) Wire gabion for protecting bridge piers. *J Hydraul Eng* 131:942–949
16. Powledge G, Ralston D, Miller P, Chen Y, Clopper P, Temple D (1989) Mechanics of overflow erosion on embankments. *J Hydraul Eng ASCE* 115(8):1056–1075

Applied Technology of Stay Cable with Saddle System in Song Hieu Bridge



Nguyen Dac Duc and Nguyen Tuan Ngoc

Abstract Cable stayed bridges are often chosen because of its long span and esthetics. However, this type of structure requires high level of corrosion protection of stay cable and components. Improved continuously since the mid-1970s, Freyssinet stay cable technology is the world reference in terms of fatigue resistance, protection against corrosion, ease of inspection and replaceability. High strength galvanized strand is selected to use along with active adjustable anchorage at girder level and saddle at tower to allow each strand goes through saddle and keep their protective HDPE sheath. Fatigue test of stay cable system is carried out as projects reference. Strand can resist 300 MPa stress amplitude at 45% of ultimate strength for 2 million cycles. Thank to high friction between strand and saddle that made by UHPC, unbalanced force between two sides of bridge will be assured not only during construction but also in service stage. This type of stay cable and friction saddle allow to minimize work of maintenance in time of service. The pylon is also more compact because of no space require for cable anchorage inside. Internal Hydraulic Dampers (IHD) is also used to limit vibration of stay cable due to traffic and wind and rain effect. To get accurate require tensile force in stay cable, iso-tension technology is used by special equipment. This is the first cable stayed bridge with friction saddle in Vietnam.

Keywords Stay cable · Saddle · Corrosion protection · Fatigue resistance

N. D. Duc
University of Transport and Communications/UTC, Hanoi, Vietnam
e-mail: ngdacduc@utc.edu.vn

N. T. Ngoc (✉)
Freyssinet Viet Nam Company Limited, Hanoi, Vietnam
e-mail: ntngoc@freyssinet.com.vn

1 Introduction

Concrete cable stayed bridges are economical structure type within main span of 200–500 m. For shorter span, cable stayed bridge could be chosen because of its esthetic. This is case of Sông Hiếu bridge that is located in Đông Hà city, not far from sea, Quảng Trị province. With one pylon, two spans of 100 m, the design of Sông Hiếu bridge requires high level of technology of stay cable. Firstly, stay cable need comply to all requirement of most updated international specification and recommendation such as Fib bulletin 30–Acceptance of stay cable systems using prestressing steels (which is now replaced by Fib bulletin 89), CIP-Recommendations of French inter-ministerial commission on prestressing, PTI-Recommendations for stay cable design, testing and installation. The stay cable system must comply with requirement of tensile strength, fatigue and water proofing. Secondly, most cable stayed bridge use anchorage at both deck side and tower side while the design of Sông Hiếu bridge requires active anchorage at deck side only and saddle at tower side. Stay cable will thread through saddle and protective layer of strand must remain continuously. High friction between stay cable and saddle is calculated base on difference external force applied in two side of bridge.

2 Technical Requirement of Stay Cable System

Stay cable is sensitive to corrosion and need to replace after some years in service as indicated in studies [1, 2]. Bare strand with cement grout is not good enough to use as stay cable. Other types of stay cable such as thread bar used in Penang bridge [3] and locked coil cables in Ewijk bridge [4] are also replaced. The technical requirement of stay cable for Sông Hiếu bridge will be described as below.

The design of stay cable bases on parallel strands consisting of 15.7 mm galvanized, wax or soft resin filling material and individually sheathed strands. The anchorage and saddle capacity shall be greater than the cable breaking load and fatigue test shall be required. Strand will be manufactured in accordance to requirement of EN 10138 (Table 1).

The corrosion protection barriers for the strand shall comprises of the following:

- The internal barrier shall be hot dip galvanizing of the individual steel wires. It must cover the full length of cable without a break. The mass of zinc coating per area shall be between 190 and 350 g/m².
- The second barrier (external barrier) shall be a water tight HDPE sheathing extruded on the individual strand. The space between strand wires and the sheathing shall be filled with corrosion protective filler as wax or soft resin that provides airtight and watertight encapsulation to the strand (Table 2).

Table 1 Strand characteristics

Description	Value
Nominal diameter (mm)	15.7
Nominal tensile strength (N/mm ²)	1860
Nominal mass (g/m)	1172
Specified permitted deviation on mass (g/m)	±24
Specified cross-sectional area (mm ²)	150
Specified permitted deviation on cross-sectional area (mm ²)	±2%
Specified characteristic breaking load (kN)	279
Modulus of elasticity (N/mm ²)	195,000 ± 5%
Max relaxation after 1000 h at 20 °C and 70% breaking load	2.5%
Fatigue stress range, 2 million cycles with maximum stress of 45% UTS (Mpa)	300

Table 2 HDPE sheathing characteristics

Property	Requirement HDPE	Test method
Melt index	≥0.1 g and ≤1.0 g per 10 min under 5 kg	ISO 1133
Specified weight, density	≥0.94 g/cm ³	ISO 1183
Carbon black	2.3 ± 0.3%	ISO 6964
Dispersion of the carbon black	Index is max 3	ISO 18553
Distribution of the carbon black	Index is max C2	ISO 18553
Tensile strength	≥22 Mpa on raw material	ISO 527-2
	≥18 Mpa on sheathing	
Elongation at break at 23 °C	≥600% on raw material	ISO 527-2 test speed 50 mm/min
	≥350% on sheathing	
Thermal stability under O ₂	≥20 min at 210 °C without degradation	ISO/TR 10837

Anchorage of stay cable shall be designed to individually anchor each strand. The anchorage head shall be capable of transmitting the full ultimate tensile force of the cable. Fatigue test is required for anchorage.

Saddle shall be designed to resist the differential cable forces by friction. Friction coefficient developed between strand and the saddle shall equal or greater than 0.5 during service and construction. The friction value shall be obtained from proven test results before applying safety factors. The HDPE sheathing of strand shall be continuous without interruption.

Technical requirements to anti vibration of stay cable:

- Modified surface of pipe to reduce the effect of vibration due to wind and rain. The surface of pipe will have helical ribs.
- Damper devices shall provide an additional effective damping of 3% (logarithmic decrement) if stay cable is longer than 80 m.

3 Applied Technology of Stay Cable System with Saddle of Freyssinet

General view of stay cable system with saddle described in Fig. 1 for anchorage block at girder side and Fig. 2 for saddle at tower side. The use of saddles as an alternative to cable anchors in bridge towers has become commonplace over recent decades. Such components can be beneficial as they allow bridge towers to be slimmed down and reduce the amount of working at height that is required during construction. The Freyssinet saddle system consists of a multitube saddle based on the use of the cohestrand or local cohestrand (LCS) in order to take up the asymmetric frictional loads through the strand sheath to the pylon. Each strand is threaded individually through saddle hole, giving the following advantages:

- Corrosion protection without discontinuity of HDPE sheath.
- Ability of individual replacement of strands.
- Fatigue resistance equal to a standard stay cable anchor.

The LCS strands used in Sông Hiếu bridge has 1860 MPa ultimate tensile strength capacity.

Friction test

Without anchors to actively secure the cables at the tower tops, a suitably high friction coefficient in the saddle is crucial to prevent stay cables from slipping when

Fig. 1 Stay cable of Freyssinet

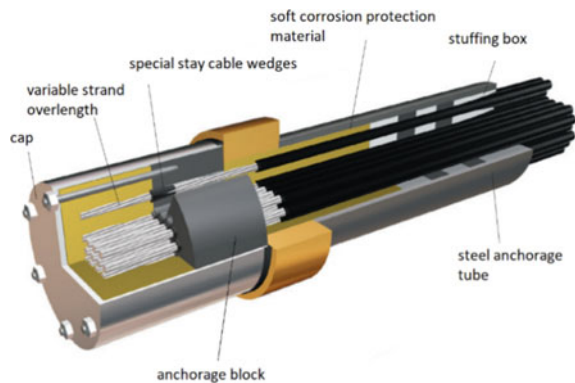


Fig. 2 Saddle made from ultra-high performance concrete (UHPC)



adjacent spans experience unbalanced live loads, and to efficiently transfer loads to the structure. The durability of the saddle and the cables within it are also key considerations that impact on the longevity of this arrangement. The minimum friction test coefficient in the whole campaign is 0.65 so that Freyssinet can guarantee this minimum value for all its project (Fig. 3).

Fatigue test

Fatigue test of 55 strands multitube saddle starts on 27/01/2020 and finishes on 08/02/2020. The tensile test carries out on 11/02/2020. Radius of the tested saddle is 1500 mm (Table 3).

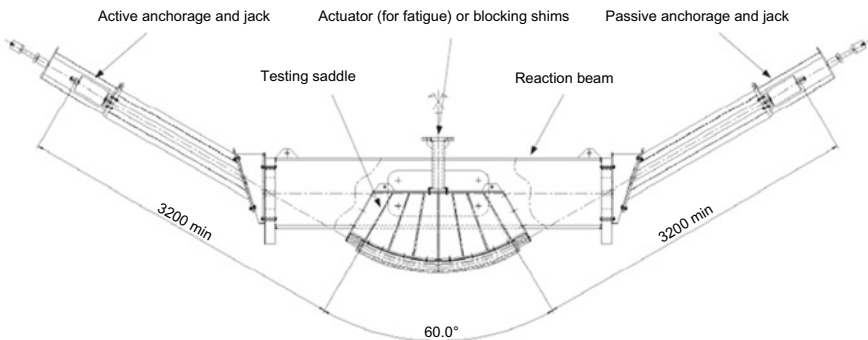


Fig. 3 Friction test setup

Table 3 Fatigue test parameters

Type	Nominal steel area of strand (mm ²)	Minimum breaking strength of a strand (kN)	Nominal steel area of stay cable (mm ²)	Minimum ultimate tensile strength GUTS (kN)	Actual ultimate tensile strength AUTS (kN)
55 strands multitube saddle	150	279	8250	15,345	15,939

For the fatigue test, two million load cycles with an upper load F_{up} of 0.45 GUTS and lower load F_{lo} which follows the stay test fatigue stress range of $\Delta\sigma = 200$ Mpa was applied to the stay cable system with a frequency 2.0 Hz. Multitube saddle pass the required 2.0 million load cycles without specimen failure. After the fatigue test the lower anchorage, the saddle and the HDPE sheath of the outer strands were visual examined and no abnormalities and hints on any wire breakage could be observed.

Water tightness test

Water tightness test of stay cable system of Freyssinet were carried out from 22/08/2002 to 10/10/2002. Some verification steps as described below:

24 September	VERITAS control Heating sequence cycle 8 Realization of 250 transversal movement cycles Stop heating cycle8 after 24 h at 70 °C
26 September	End of cycle 8 after 24 h at cool temperature
27 September	VERITAS control
3 October	End of the waiting week with no water movement Empty of the water
4 October	Detension of cable Check the cable force
10 October	Removing the block to check internal part of the anchorage stuffing box

After water tightness test finish, no sign of water or color inside the injection room. Its efficiency as a waterproofing barrier is therefore demonstrated (Fig. 4).

Iso-tension

The stay cable system of Freyssinet applied in Sông Hiếu bridge allows tension strand by strand using special equipment as described in Fig. 5.

Damper

To reduce vibration of stay cable that is longer than 80 m, internal hydraulic damper will be installed for Sông Hiếu bridge. Site test of vibration will be carried out to measure the logarithmic damping of system (Fig. 6).

Fig. 4 Water tightness test setup



Fig. 5 Iso-tension equipment



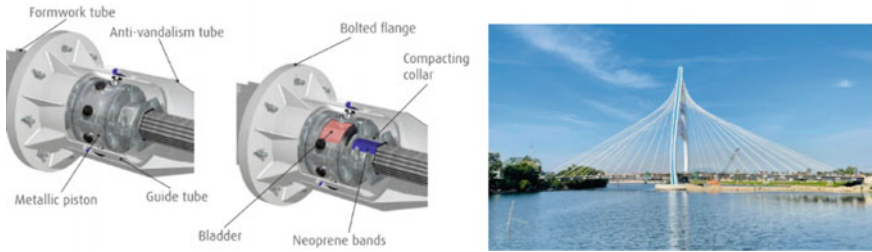


Fig. 6 Internal hydraulic damper applied for Sông Hiếu bridge and Sông Hiếu bridge during construction

4 Conclusion

Stay cable requires high level of fatigue resistance and corrosion resistance according to international specification and recommendation like FIB, PTI, CIP. Particularly for bridge using saddle at tower, applied technology could be different from each supplier but they must pass the required tests such as fatigue test, tensile test and friction test. The system of stay cable with a saddle of Freyssinet complies all these requirements. Sông Hiếu cable stayed bridge is the first one in Viet Nam that Freyssinet provide this technology beside some other extradosed bridges.

References

1. Li HJ (2020) Replacement of cable stays in Yonghe Bridge in Tianjin, China. *Adv Civil Eng* 2020:6650393
2. Li HJ (2012) Technologies on replacement of structural members in prestressed concrete cable-stayed bridges. *Adv Mater Res* 446–449:1158–1166
3. Lavery C, Moore P, Vonk E, Nagtegaal G (2020) Replacement of the cable stays at Ewijk Bridge, the Netherlands
4. Mehrabi AB, Ligozio CA, Ciolko AT, Wyatt ST (2020) Evaluation, rehabilitation planning, and stay-cable replacement design for the Hale Boggs Bridge in Luling, Louisiana

Weight Evaluation of Criteria Influencing Road Flooding Using Multi-criteria Analysis



Thai Thi Kim Chi and T. T. K. Chung

Abstract Vietnam is in the top five countries most vulnerable to climate change. Vietnam is ranked fourth among countries worldwide with the highest number of people exposed to flood risk. Floods often cause damage to the transportation infrastructure in Vietnam. The assessment of flood risk in road networks should be considered as the problem of multi-index evaluation. Vulnerability analysis of roads that are exposed to flood is an important part of risk assessment and management. Thus, index weight evaluation is the critical issue when quantifying flood vulnerability. In the present paper, the causes and major factors influencing the road flooding in the Red River Delta were investigated. Both subjective and objective weights are studied. In addition, the methodology for determining the weighting factors will be presented in detail.

Keywords Flood risk · Road flooding · Subjective weight · Objective weight · Weight evaluation

1 Introduction

Under climate change scenarios, the frequency and intensity of natural disasters are altered and need to be examined at all scales, including global, regional and local scales. Among natural disasters, flooding is considered as the most devastating and frequent disaster in the world. For over 20 years, the frequency of floods has increased by over 40% [1]. The occurrence of floods impacts both socioeconomic and environmental attributes of the affected area [2].

Vietnam is also in the top four countries with the highest number of people exposed to river flood risk worldwide [3]. There have been more than 400 flood events for

T. T. K. Chi (✉)
University of Transport and Communications/UTC, Hanoi, Vietnam
e-mail: chitk@utc.edu.vn

T. T. K. Chung
University of Transport Technology, Hanoi, Vietnam

the period 2006–2016. More than 14,900 people have been killed and 16,800 people have been injured by floods in the period from 1989 to 2015. Floods are responsible not only for the significant loss of lives but for the extensive damage to infrastructures as well [4].

In particular, the transportation infrastructure (roads, highways, railways, dykes) in Vietnam was extensively affected by the flooding. For example, in October–December 2016 floods caused serious damage to the transportation infrastructure in eighteen provinces in central Vietnam with total damage of US\$70 million. Flood flows inundated roads, washed away part of roads in many places, eroded the road pavement and embankments, caused inaccessibility of road pavements and damaged many bridges.

Hence, risk evaluation of road flooding disaster plays important roles in guidance of the prevention and mitigation of road flooding disasters, the protection of the people living in vulnerable areas and risk management in general.

In order to perform the evaluation, the main contributing factors of road flooding disasters need to be identified and its relative weight must be considered. The obtained result in this phase strongly affects the accuracy of the further phases and the whole modeling process.



Inundated road in Quang Ninh, 2020

In this study, the factors that would affect the road flood risk in the Red River Delta of Vietnam are defined. The multi-criteria analysis based on the analytic hierarchy process (AHP) is used to assess the influence of each factor on the flood risk in this case and determine its weights.

2 Methodology

2.1 Case Study

The Red River Delta covers 5 coastal provinces (Ninh Binh, Thai Binh, Nam Dinh, Hai Phong and Quang Ninh) and 6 plainland provinces (Ha Nam, Ha Noi, Vinh Phuc, Bac Ninh, Hung Yen and Hai Duong) with the area of 21.051 km² and a total population of over 20 million people. The Red River Delta consists of two main river systems (Thai Binh River and Red River system) with the total catchment area of 86.660 km² and over 200 km of coastline.



Red River Delta (MARD, 2011)

The Red River Delta is located in the strong monsoonal climate. The monsoon is from approximately late May to early November with about 80% of the total annual rainfall [5]. The average precipitation rate is about 1800–1900 mm/year [6]. The annual mean temperature ranges from 16 to 20 °C [7]. In the coastal provinces, the typhoon season is usually from June to October. Floods in the Red River Delta often occur in July, August and cause serious losses.

2.2 Methods

Because the natural and anthropogenic factors must be considered for the flood risk occurrence, multi-criteria analysis (MCA) approach has been used extensively to solve complex problems such as flood risk assessment. MCA is a method that supports the decision-making process, including qualitative and/or quantitative aspects of the problem [8]. The multi-criteria decision analysis (MCDA) approach uses different mechanisms to define the contributing criteria and then determine the weight of each criterion.

At present, there are two weight calculation methods including the subjective and objective methods. The subjective weighting method determines weights simply based on the judgments of decision-makers. The main disadvantage of this method is its uncertainty. The weight in the objective weighting method is calculated in accordance with the actual observations. This method does not consider the decision-maker’s propensity or take advantage of the experience and knowledge of decision-makers.

The most commonly used MCDA methods are Analytical hierarchy process (AHP), Data envelopment analysis (DEA), Analytic network process (ANP), Weighted sum model (WSM), Goal programming (GP), Multi-attribute utility theory (MAUT), Weighted product model (WPM), Simple multi-attribute rating technique (SMART), Technique for order preferences by similarity to ideal solutions (TOPSIS), etc. [9].

Analytic hierarchy process (AHP) established by Saaty [10] is one of the most widely used MCA methods. In this method, the qualitative preference among indicators is quantified, and the importance of factors is evaluated according to weight values. AHP can check consistency in decision-makers’ judgment so it is possible to identify and improve the accuracy of the assessment. Thus, AHP is a well-known method of determining these weights with high accuracy.

The process of AHP includes the following steps: Break a complex problem down into small elements or component factors; Develop the AHP hierarchy; Determine the paired compare matrix among the elements or factors by established judgments; Assign values to subjective judgments; Estimate the relative weights of each elements/criterion; Determine important variables by synthesizing judgments; Analyze the consistency of the assessments and judgments.

The scale proposed by Saaty [10] is used to perform the binary combination. For each pairing within each criterion, the score in range 1–9 is given (Table 1).

The judgment matrix X for the case of m decision-makers is:

$$X = \begin{bmatrix} x_{11} & x_{12} & \dots & x_{1m} \\ x_{21} & x_{22} & \dots & x_{2m} \\ \vdots & \vdots & \ddots & \vdots \\ x_{m1} & x_{m2} & \dots & x_{mm} \end{bmatrix} \tag{1}$$

Table 1 Pair-wise comparison scheme for data collection

Scale	Description
1	Two parameters contribute equally to the objective
3	Moderate importance
5	Strong importance
7	Very strong importance
9	Extremely strong importance
2, 4, 6, 8	Interval values between two adjacent choices

where: m is the number of criteria; x_{ij} is the pairwise comparison ($1 \leq i, j \leq m$), which is the importance of criterion i according to criterion j .

The weighting coefficient of the i -th index w_i is calculated according to the formula as below:

$$w_i = \frac{Z_i}{\sum_{i=1}^m Z_i} \tag{2}$$

where: Z_i is normalized vector.

The maximum Eigen value is defined as:

$$\lambda_{\max} = \sum_{i=1}^m \frac{(Xw)_i}{nw_i} \tag{3}$$

The total ordering can be calculated from top level to bottom level.

$$W_i = \frac{1}{m} \sum_{j=1}^m w_{ij} \tag{4}$$

where: W_i is weighting factors of criteria i ; n is number of criteria.

The consistency ratio (CR) should be calculated to examine the discordances of the pairwise comparisons and the reliability of the obtained results. The value must be in the required range to be accepted, otherwise the weight calculation must be processed again.

$$CR = \frac{CI}{RI} \tag{5}$$

where:

CR is the consistency ratio, if the consistency ratio is <0.1 for $n \geq 5$, then the mentioned matrix is considered acceptable;

RI is the random index that describe the consistency of the pairwise comparison matrix (Table 2).

CI is the consistency index. When $CI = 0$, the judgment matrix has completion consistency, the larger the CI value, the worse the degree of consistency,

$$CI = \frac{\lambda_{\max} - n}{n - 1} \tag{6}$$

Results of the multi-criteria analysis based on the AHP method to identify the important criteria and determine the weighting factors for each cause of the road flood in the Red River Delta are presented in the section below.

Table 2 Random consistency index

<i>n</i>	1	2	3	4	5	6	7	8
RI	0	0	0.58	0.9	1.12	1.24	1.32	1.41

3 Results

In this study, four criteria including road characteristics, hydro-meteorological factors, geological conditions and human activities are selected based on the formation mechanism of road flood in the Red River Delta in order to perform the weight evaluation.

The survey was conducted by four experts working in the field of road engineering and flood risk management. Experts provided their judgements of the relative importance of one factor against another. The scores were varied from 1 to 9. The higher the score is, the more important the criterion.

The weights given by one of our experts to the criteria influencing the road flooding risk in the Red River Delta is presented below. The order of criteria is road characteristics, hydro-meteorological factors, geological conditions and human activities.

The pairwise comparison matrix given by 1st expert is obtained as follows:

$$X_1 = \begin{bmatrix} x_{11} & x_{12} & x_{13} & x_{14} \\ x_{21} & x_{22} & x_{23} & x_{24} \\ x_{31} & x_{32} & x_{33} & x_{34} \\ x_{41} & x_{42} & x_{43} & x_{44} \end{bmatrix} = \begin{bmatrix} 1 & 1/3 & 1 & 2 \\ 3 & 1 & 3 & 4 \\ 1 & 1/3 & 1 & 2 \\ 1/2 & 1/4 & 1/2 & 1 \end{bmatrix} \tag{7}$$

This expert considered that the hydro-meteorological conditions are slightly more important than road characteristics and geological conditions (level of importance is 3). The geological conditions and road characteristics contribute equally to the road flood risk. The hydro-meteorological factors are strongly more important than human activities (level of importance is 3) and slightly more important than geological conditions (level of importance is 3).

The normalized matrix of road flood criteria:

$$Z_1 = \begin{bmatrix} 0.18 & 0.17 & 0.18 & 0.22 \\ 0.55 & 0.52 & 0.55 & 0.44 \\ 0.18 & 0.17 & 0.18 & 0.22 \\ 0.09 & 0.13 & 0.09 & 0.11 \end{bmatrix} \tag{8}$$

The final weight vector matrix given by the 1st expert is: [0.19 0.51 0.19 0.11]. The consistency index is calculated by using Eq. (9):

$$CI = \frac{\lambda_{\max} - n}{n - 1} = 0.009 \tag{9}$$

As the random consistency index for the case of 4 indicators RI equals 0.9, the consistency ratio is determined as follows:

$$CR = \frac{CI}{RI} = \frac{0.009}{0.9} = 0.01 \tag{10}$$

As $CR = 0.01 \leq 0.1$, the consistency ratio is in the acceptable range. These weights of the road flood causing criteria are consistent and no more information of the decision-makers or repeated procedure is required.

As a result, according to this expert’s opinion, road characteristics, hydro-meteorological factors, geological conditions and human activities were weighted as 19, 51, 19 and 11%, respectively.

Similar to the above-mentioned process, the weights of criteria influencing the road flood given by remain experts. In the final step, the weights of the criteria influencing the road flood risk in the Red River Delta were calculated by using the average values of normalized weights of criteria obtained from all experts. All the judgment matrix has passed the consistency test. Thus, the weights are acceptable. The obtained weights are presented in Table 3.

It can be seen that the hydro-meteorological factors are the most influencing factors to the road flood risk in the Red River Delta with the weight of 0.45. Road characteristics and human activities contribute almost the same to the road flood risk with the weights of 0.17 and 0.15, respectively. The geological conditions are more important than road characteristics and human activities but less important than hydro-meteorological factors.

These criteria are very important information for further research. Stakeholders can take more reasonable measures to control the road flood risk. Based on the obtained weights of criteria influencing the road flooding, the classification of road flood disaster can be provided that can be used as the foundation for road flood risk assessment and management.

Table 3 The results of weights given to the criteria influencing the road flood

Criteria	Experts				Average
	1st	2nd	3rd	4th	
Road characteristics	0.19	0.13	0.19	0.18	0.17
Hydro-meteorological factors	0.51	0.48	0.43	0.37	0.45
Geological conditions	0.19	0.22	0.23	0.28	0.23
Human activities	0.11	0.17	0.15	0.16	0.15

4 Conclusions

In this study, the weights of criteria influencing the road flooding risk in the Red River Delta were identified and determined using the multi-criteria analysis based on analytic hierarchy process (AHP). It has been found that the major criteria influencing the road flood risk in the Red River Delta are road characteristics, hydro-meteorological factors, geological conditions and human activities. Among them, the hydro-meteorological factors were the most significant influencing criteria. The weights of hydro-meteorological factors, geological conditions, road characteristics and human activities were 0.45, 0.23, 0.17 and 0.15, respectively.

The obtained weights can be used to classify the degree of road flood disaster, estimate the road flood vulnerability and provide the basis for decision-making in the road flood management in hazardous areas such as the Red River Delta.

References

1. Hirabayashi Y, Mahendran R, Koirala S et al (2013) Global flood risk under climate change. *Nat Clim Change* 3:816–821
2. Meyer V et al (2013) Review article: assessing the costs of natural hazards – state of the art and knowledge gaps. *Nat Hazards Earth Syst Sci* 13:1351–1373
3. Luo P, Mu D, Xue H et al (2018) Flood inundation assessment for the Hanoi Central Area, Vietnam under historical and extreme rainfall conditions. *Sci Rep* 8:12623
4. Merz B, Kreibich H, Schwarze R, Thielen A (2010) Review article: assessment of economic flood damage. *Nat Hazards Earth Syst Sci* 10:1697–1724
5. Tinh D (2011) Participatory planning and management for flood mitigation and preparedness and trends in the Red River Basin, Vietnam. In: UN Economic and Social Commission for Asia and the Pacific, Bangkok
6. Tuan PA, Shannon K (2010) Water management in Vietnam: indigenous knowledge and international practices: the case of the Red River Delta, Conference of Network-Association of European Researchers on Urbanization in the South (N-AREUS XI)
7. Pilarczyk K, Nuoi NS (2005) Experience and practices on flood control in Vietnam. *Water Int* 30:114–122
8. Mendoza GA, Prabhu R (2000) Development of a methodology for selecting criteria and indicators of sustainable forest management: a case study on participatory assessment. *Environ Manag* 26(6):659–673
9. Abdullah MF et al (2013) An overview of multi-criteria decision analysis (MCDA) application in managing water-related disaster events: analyzing 20 years of literature for flood and drought events. *Water* 13:1358
10. Satty T (1980) *The analytical hierarchy process*. McGraw Hill, New York

Equilibrium Local Scour Depth Under Live-Bed Scour for Cylindrical Piers with Their Width Greater Than Three Meters Based on Field Data



T. N. Doan and D. N. Tran

Abstract Despite the numerous studies on local scour at piers conducted, very few of them applied pier local scour formulas based on field data, but mainly on the laboratory experimental data. Consequently, the scour depth is often biased larger than the actual one. This paper proposes a formula (UTCwp20-University of Transport and Communications for wide pier 2020) for piers 3 m wider (b or D) and field data set or live-bed scour from 68 publications in the USA, China and Russia, and recorded the best results compared to eight published formulas using the same data set.

Keywords Local scour depth · Field data · Wide piers · Local scour equation · Live-bed local scour formula

1 Introduction

For a long time, there are many researchers about local scour at bridges (see [1–8]). However, in several cases when extreme flooding conditions, the equilibrium scour depths are lesser than the actual leading to bridge failure is not properly evaluated. Therefore, this paper presents a formula (Equation) for local scour with pier width greater than and equal to ($D \geq 3$ m), the ratio of the depth to the width ($0.25 \leq (h/D) \leq 3.31$) under live-bed scour directly using field data set. This type of cylinder diameter is often used by bridge construction engineers.

T. N. Doan (✉) · D. N. Tran
University of Transport and Communications/UTC, Hanoi, Vietnam
e-mail: dtnoi@utc.edu.vn

© The Author(s), under exclusive license to Springer Nature Singapore Pte Ltd. 2024
T. Nguyen-Xuan et al. (eds.), *Proceedings of the 4th International Conference on Sustainability in Civil Engineering*, Lecture Notes in Civil Engineering 344,
https://doi.org/10.1007/978-981-99-2345-8_19

193

Table 1 Field data basic statistical parameters

Descri	h_s	h_o	D	(h_s/h_0)	(D/h_0)	(h_s/D)	d_{50}	(D/d_{50})	V
	(m)	(m)	(m)				(mm)		
Max	5.6	16.55	5.03	0.52	4.0	1.8	1.53	23,300	3.2
Min	1.62	0.9	3.05	0.145	0.30	0.37	0.165	3268	1.02

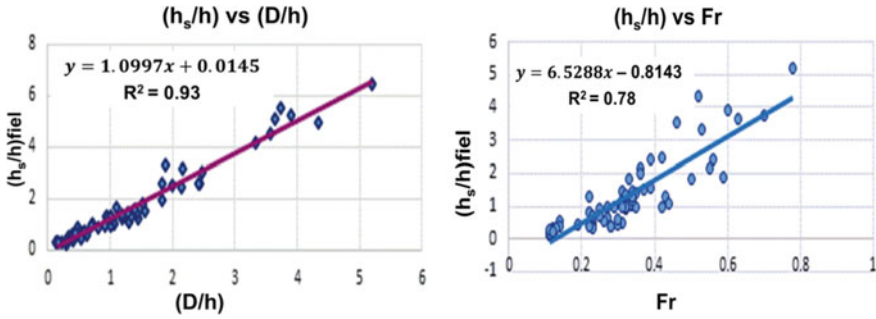


Fig. 1 (h_s/h) versus (D/h) and (h_s/h) versus Fr

2 Materials and Methods

2.1 Materials

There are 68 field data points for the cylindrical pier in the rivers, including Mueller and Wagner/US (9 field data points), Gao et al./China (13 field data points) and Juravlev/Russia (46 field data points). The range of these field data for local scour characterization is given in Table 1 and the graphs show their basic relation of Fig. 1 for calculation.

2.2 Methods

Dimensional analysis

The relationship between the local scour depth at a bridge pier and parameters can be written:

$$h_s = f[(V, h, g, \nu, \rho), (D, Sh, Al), (V_c, d_{50}, \sigma_g, \rho_s)] \tag{1}$$

where h_s = local scour depth, V = mean approach flow velocity, h = flow depth, g = acceleration of gravity, ν and ρ = kinematic viscosity and fluid density, respectively, D = pier diameter, Sh and Al = parameters describing the pier shape (including

floating debris) and the alignment of the pier shape, respectively, V_c = critical mean approach flow velocity for entrainment of bed sediment, d_{50} , and σ_g = median size and geometric standard deviation of the sediment particle size distribution, respectively, ρ_s = sediment density. Assuming $(\rho_s - \rho)/\rho = \Delta = 1.65$, the theorem of Vaschy-Buckingham allows one to write non-dimensional parameters, the effect on local scour depth h_s of each of the parameters in Eq. (1) at the cylindrical pier under live-bed scour is now considered as in Eq. (2).

$$\frac{h_s}{h} = f\left(\frac{D}{h}, \frac{v}{\sqrt{gh}}, \frac{V_e}{V_d}, \frac{D}{d_{50}}\right) \tag{2}$$

where h_s/h shows the influence of flow depth on scour depth; D/h = relative flow depth or flow shallowness; $Fr = V/\sqrt{gh}$ = Froude number representing the strength of the flow intensity; D/d_{50} = relative roughness or sediment coarseness, expressing the effect of the sediment size; V_e/V_d represents the impact of the normalized effectiveness of flow intensity to the sediment velocity $V_d = \sqrt{\Delta g d_{50}}$ for live-bed scour; where $V_e = (V - V_c)$ = excess velocity above the incipient scour condition, critical Shields' parameter calculated using Soulsby and Whitehouse's improved empirical Eq. (3).

$$\theta_{cr} = \frac{0.3}{1 + 1.2d_*} + 0.055[1 - \exp(-0.020d_*)] \tag{3}$$

where d_* = non-dimensional particle size, $d_* = \left[\frac{\Delta g}{\vartheta^2}\right]^{1/3} \times d_{50}$ with $(\vartheta = 1 \times 10^{-6} \text{ m}^2/\text{s})$ = kinematic viscosity of water, $\Delta = ((\rho_s - \rho)/\rho)$.

$$V_c = 5.75[\log(12h/6d_{50})] \times \sqrt{\theta_{cr}\Delta g d_{50}} \tag{4}$$

Effect of flow depth in field data and development of local scour formula

Field data in dimensionless groups that represent ratios of the pertinent physical phenomena are given in Table 2 and Fig. 1.

The correlation relationship between the relative local scour depth (h_s/h) with (D/h) and Fr in Fig. 1 is quite tight with the correlation coefficient $R^2 = 0.93$ for (D/h) and $R^2 = 0.78$ for Fr . These variables (D/h) and Fr shall be combined to find the relative local scour depth expression (h_s/h) at circular cylinder through multivariate relations according to Eq. (2). Using the Excel Solver with the data in Tables 1, 2,

Table 2 Statistics of calculated values

Descri	h/D	D/d_{50}	θ_c	V_c	V/V_c	Fr	h_s/h	h_s/D	V_e
Max	3.31	23,300.0	0.0543	0.744	8.675	0.782	5.2	1.803	0.157
Min	0.25	3267.97	0.0306	0.28	1.946	0.109	0.14	0.368	0.052

Fig. 2 Predicted (h_s/h) versus observed (h_s/h) based on field data

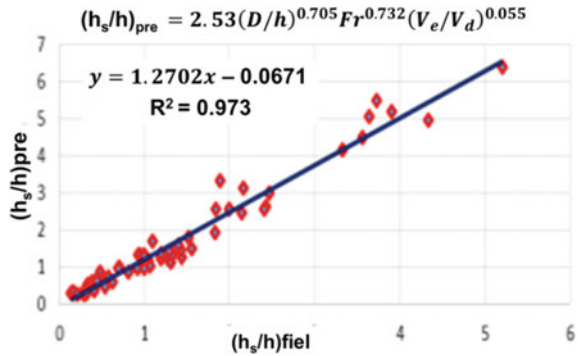


Table 3 Calculated values in multivariate relation

Description	Intercept	(D/h)	Fr	$(V_e)/\sqrt{\Delta g d_{50}}$	Multiple R
Value	0.4023	0.705	0.732	0.055	0.973

the terms in Eq. (1) give Eq. (5) (UTCwp20) as pier scour equation for wide piers in cohesiveness soil based on field data to predict the relative local scour depth (h_s/h) of the cylindrical under live-bed conditions with $R^2 = 0.973$ in Fig. 2.

$$\frac{h_s}{h} = 2.53(D/h)^{0.705} Fr^{0.732} \left(V_e / \sqrt{\Delta g d_{50}} \right)^{0.055} \tag{5}$$

The dimensional scour depth is deduced from the proposed formula (5) as:

$$h_s = 2.53h(D/h)^{0.705} Fr^{0.732} \left(V_e / \sqrt{\Delta g d_{50}} \right)^{0.055} \tag{6}$$

Scatter and statistical evaluation criteria for Eq. (5) are given in Table 3

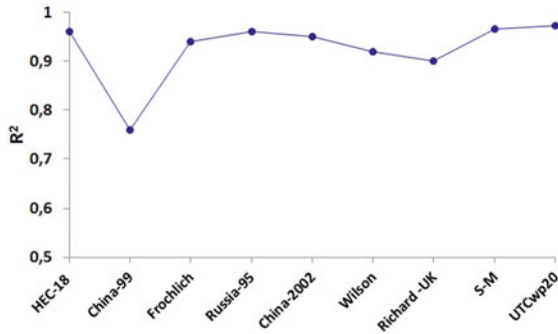
The computed equilibrium relative local scour depth (h_s^p/h) versus measured equilibrium relative scour depths (h_s^0/h) based on field data is given in Fig. 2 with correlation coefficient $R = 0.98$.

3 Results

The proposed Eq. (5) is assessed according to the following criteria: Scatter index: $SI = 0.382$. Sum of the squared error of the dispersion: $SSE =$ similarly, the same criteria are computed for dimensional scour depths Eq. (6): $SI = 0.296$. Sum of the squared error of the dispersion-SSE, $SSE = 0.0828 = 8.28\%$.

The evaluation results in Table 3 and Fig. 3 show that the proposed formula has high accuracy. The evaluation results according to the criteria allow the suggested

Fig. 3 Plot of the correlation coefficient R^2 of $Y = (h_s^p/h)$ versus $X = (h_s^0/h)$



relation Eqs. (5) and (6) to be used for exploratory calculation and comparison with eight well-known design formulae to predict the equilibrium scour depth at bridge piers. The HEC-18, FHWA-HIF-12-003 and China’s Specification (1999) formulas for live-bed based on experimental and field data. The Russia’s Specification (1995), China (2002) and Wilson (1995) formulas are based on field data. In this research Soulsby’s critical velocity is applied [10].

Results of scour prediction according to Eq. (5) and eight well-known design formulae were chosen for evaluation using field data based on their performances listed in Table 4.

The fit of the proposed models of prediction (h_s^p/h) , versus observation (h_s^0/h) , (Eq. (5)) and prediction, (h_s^p/h) versus observation, (h_s^0/h) of eight formulae in Tables 5, 6 shows that the regression equations for the relative local scour depth, $Y = (h_s^p/h)$ versus $X = (h_s^0/h)$ has a fairly high correlation coefficient, R^2 increases by 0.9 for the Richard-UK formula to 0.974 for the UTCwp20 (Eq. (5)). These relative local scour formulae do not indicate the actual scour depth at the base of the pier.

For example, the intercept is 0.421 in the formula Wilson in Table 4, can be interpreted that without $X = (h_s^0/h)$, there would be $Y = 0.421(h_s^p/h)$ or predicted relative scour depth $h_s^0 = 0.421h$ without actual scour, this makes no sense. Similarly, for other relative scour depths in the Table 4 and dimensional scour depths in the Table 5. However, the dimensional scour depth versus observed scour depths on the field data does not really match the relative scour depth (h_s/h) , correlation coefficient R^2 in Table 5 increases by 0.02 for the Richard-UK formula to 0.493 for the UTCwp20

Table 4 The regression equations of relative local scour depth, $Y = (h_s^p/h)$ versus $X = (h_s^0/h)$ and R^2

The regression equation	R^2	The regression equation	R^2
HEC-18, $Y = 0.641X + 0.18$	0.96	Wilson, $Y = 0.384X + 0.421$	0.92
China-1999, $Y = 1.145X - 0.02$	0.76	Richard-UK, $Y = 0.351X + 0.85$	0.9
Froehlich, $Y = 1.112X + 0.292$	0.94	S-M, $Y = 1.021X + 0.044$	0.94
Russia-95, $Y = 0.731X + 0.284$	0.96	UTCwp20, $Y = 1.27X - 0.067$	0.973
China-02, $Y = 0.952X + 0.074$	0.95		

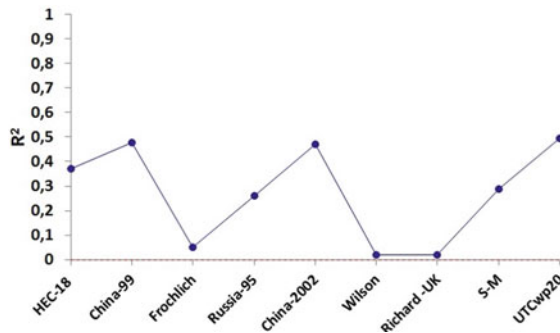
Table 5 The regression equations of dimensional scour depth, $Y = h_s^p$ versus $X = h_s^0$ and R^2

The regression equation	R^2	The regression equation	R^2
HEC-18, $Y = 0.64X + 0.91$	0.37	Wilson, $Y = 0.24X + 2.75$	0.021
China-99, $Y = 2.273X - 4.04$	0.477	Richard-UK, $Y = 0.5X + 4.0$	0.02
Froehlich [8], $Y = 0.322X + 4.5$	0.05	S-M [9], $Y = 0.492X + 2.31$	0.287
Russia-95, $Y = 0.65X + 1.72$	0.26	UTCwp20, $Y = 0.861X + 1.285$	0.493
China-02, $Y = 0.706X + 1.314$	0.47		

Table 6 Descent of the correlation coefficient R of the dimensional scour depths

Formula	UTCwp20	China1999	China2002	HEC-18	S-M2014
R	0.7	0.69	0.685	0.61	0.54
Formula	Russia	Froehlich	Wilson	Richard-UK	
R	0.51	0.22	0.15	0.14	

Fig. 4 Plot of the correlation coefficient R^2 of $Y = h_s^p$ versus $X = h_s^0$



(Eq. (6)). The formula-UTCwp20 has the highest correlation coefficient R compared with the formulas China 1999, China 2002, HEC-18, S-M2014, Russia, Froehlich, Wilson and Richard May of UK in Table 6, respectively (Fig. 4).

4 Conclusion

Dimensionless groups represent proportions of relevant physical phenomena, therefore, the extent of dimensionless groups is more often used to characterize the local scour covered by datasets. However, these relative local scour formulae do not indicate the actual scour depth that designers need to design the elevation to achieve a safe but economical bridge pier foundation. For the circular pier scour formula, the term relative effective flow intensity (V_e / V_d) for live-bed scour to the power 0.055, has a fairly small value, which can be neglected in practice.

It is very difficult to make accurate measurements of flow velocity, flow direction and scour depths during a extreme-velocity flood event. So despite limitations including accuracy of the scour measurement (accuracy = ± 0.3 m), the accuracy of the hydraulic variables, whether the scour has reached equilibrium conditions, bed material variability, etc. In this paper, the method is proposed to predict the local scour depth of circular piers, which can meet the accuracy requirements as shown in Tables 5, 6.

This paper does not claim that any formula is absolutely best in all cases, because the results calculated from the proposed formulas are often larger or smaller than the actual ones. However, with only a few exceptions, the predicted values should not be less than the actual measured values excluding other types of scouring (contraction, degradation, etc.).

References

1. Arneson LA, Zevenbergen LW, Lagasse PE, Clopper PF (2012) Evaluating scour at bridges. Fifth Edition, FHWA-HIF-12-003. Hydraulic Engineering Circular No.18
2. Mueller DS, Wagner CR (2005) Field observations and evaluations of streambed scour at bridges. FHWA-RD-03-052
3. Gao D, Pasada U, Nordin CF (1993) Pier scour equations used in the People's Republic of China. Publication No. FHWA-SA-93-076
4. Chase KJ, Holnbeck SR (2004) Evaluation of pier-scour equations for Coarse-Bed streams. U.S. Geological Survey, Reston
5. Juravlev MM (2022) Local scour at bridge piers. *M. Transport*, 1084-122ps (Russian language)
6. Qi M, Li J, Chen Q (2016) Comparison of existing equations for local scour at bridge piers: parameter influence and validation. *Nat Hazards*. <https://doi.org/10.1007/s11069-016-2287-z>
7. Ettema R, Constantinescu G, Nchrpe BM (2011) Evaluation of bridge scour research: Pier scour processes and predictions. In: National cooperative highway research program. Project 24-27(01)
8. Froehlich DC (1988) Analysis of onsite measurements of scour at piers. In: *Hydraulic engineering, proceedings of the 1988 national conference on hydraulic engineering*. New York, American Society of Civil Engineering, pp 534–539
9. Sheppard DM, Melville B, Demir H (2014) Evaluation of existing equations for local scour at bridge piers. *J Hydraul Eng*. [https://doi.org/10.1061/\(ASCE\)HY.1943-7900.0000800](https://doi.org/10.1061/(ASCE)HY.1943-7900.0000800)
10. Soulsby RL, Whitehouse RJS (1997) Threshold of sediment motion in coastal environments. In: *Proceedings of the 13th Australasian coastal and engineering conference and 6th Australasian port and harbour conference*, Christchurch, pp 7–11

Study on the Effect of Corrugated Webs in Steel I-Girder Bridge



Tran Viet Hung

Abstract The corrugated steel webs are used to allow without continuous stiffeners for the steel and composite bridges. This structure has many advantages compared to steel girder with flat web. A corrugated web steel bridge, corrugated steel webs increase the stability of the girder web, increase the torsional stiffness and reduce the weight of the steel girder. It is many beneficial qualities, such as lower dead-load, increased shear buckling strength and so on. In this article, the advantages and applicability of corrugated steel ribs are presented. The comparison between the behaviors of flat steel I-girder and corrugated web steel I-girder is performed to clearly see the effect of the corrugated webs.

Keywords Corrugated web · Steel bridge · Steel I-girder

1 Introduction

The I-girder structures with corrugated webs are widely used in industrial projects and bridges in many countries around the world. Though corrugated webs used not yet for highway bridges in Vietnam, but they have been constructed at many highway bridges in Europe and Japan [1]. Previous studies have shown that girder with corrugated web have a higher elastic critical moment than those with flat web. A lot of research in corrugated webs is focused on shear strength, and very limited studies have been performed on flange buckling and its influence on flexural behavior. In the case of the steel I-girder bridges with flat webs, most of the cross-sections of the girder's web are very thin, especially in the web of the girders (about 10–20 mm). The

The original version of the chapter has been revised: The author's affiliation the text “/UTC” has been removed. A correction to this chapter can be found at https://doi.org/10.1007/978-981-99-2345-8_83

T. V. Hung (✉)
University of Transport and Communications, Hanoi, Vietnam
e-mail: tranviethung@utc.edu.vn

© The Author(s), under exclusive license to Springer Nature Singapore Pte Ltd. 2024, corrected publication 2024

T. Nguyen-Xuan et al. (eds.), *Proceedings of the 4th International Conference on Sustainability in Civil Engineering*, Lecture Notes in Civil Engineering 344, https://doi.org/10.1007/978-981-99-2345-8_20

slender sections of the steel I-girders are usually sensitive to affected with buckling especially the web of girders subjected to shear stress. Hence to resist the buckling and shear strength of flat web, the corrugated webs was provided. Therefore, it will withstand greater loads on larger spans [2].

Corrugated steel web I-girders are made from sheet steel with a thin-walled corrugated web and the flanges. Under the action of applied loads, the local or global buckling in the web can be controlled depending on the corrugated form. Normally, the corrugated web of I-girder with trapezoidal shape was used. The weight of this type of girder is significantly reduced compared with hot rolled section or welded sections [3]. The buckling failure of web is prevented by the existence of corrugated web. The buckling resistance of corrugated web is comparable to the thickness of smaller flat webs.

Normally, the steel I-girder bridge requires thin webs, but if the web is less thin, the problem of buckling may arise. Thus, this structure can be improved with a new structure type to improve the web instability of the girder, it is corrugations on the web. The main benefit of the corrugated web girder is to increase the stability of the girder against buckling. A corrugated web I-girder provided a new structural system that has excellent load carrying capacity [4]. When comparing beams with bearing capacity, the weight of girders using corrugated web tends to decrease compared to girders using flat web. This reduction value is about 9–13% according to the study of Hamada et al. [5] and about 10.6% according to the study of Chan et al. [6].

However, corrupted web of girder has many advantages compared between corrupted web and flat web. This paper shows a brief of this study on corrugated steel web I-girder, the comparison between the behavior of steel I-girder and corrugated web steel I-girder is performed. From there, helping consulting companies consider applicability to steel I-girder of bridge structures.

2 Applications of Corrugated Web Girders

The scope of application of this type of structure is quite diverse, which can be applied to both steel girder structures as well as composite girder structures. Especially suitable for girder structures subjected to compression and bending such as cable-stayed bridge girders, extradosed bridges. Many types of corrugations were used in which trapezoidal and sinusoidal shapes are more commonly used. A typical profile of a corrugated web is shown in Fig. 1.

Evaluation of the effect of various types of corrugation shapes and parameters has been studied by Zhang et al. [8] and Li et al. [9]. Chan et al. [6] studied the corrugated webs of arc corrugation, which the research was based on I-beams with a length of 500 mm, a flanged width of 75 mm and a depth of 127 mm. Chan et al. [6] shown that the vertical corrugation produces higher strength than the horizontal corrugation and the plane web, at an average range of 1.8–2.1. The shear resistance of the girder is increased when corrugated steel is used. These corrugated irons can be produced from the hot rolled steel process or stamped from sheet steel. Depending on the scope

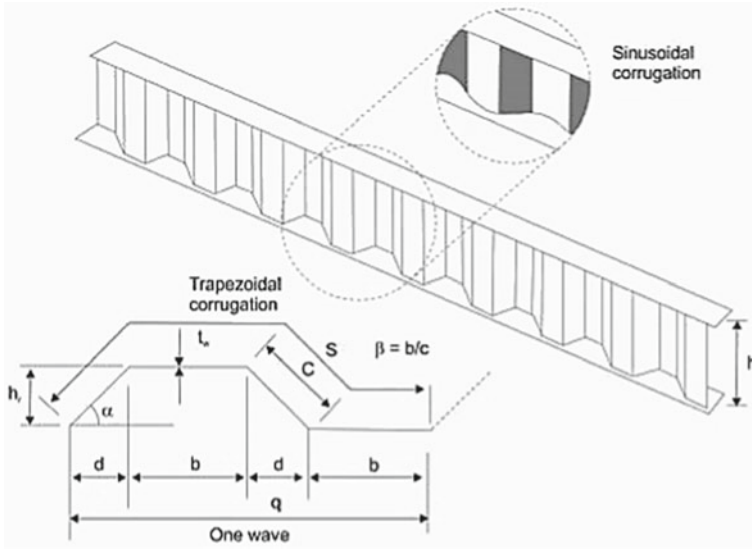


Fig. 1 Profile of I-girder using corrugated web [7]

of application, the dimension of the corrugated web can be changed to match the stability of the girder. Furthermore, reducing the thickness of corrugated web steel for the vertical corrugated webs would reduce more the weight of the girder when compared to the same maximum load between the corrugated web I-girder and the original I-girder.

In this study, to see more clearly the advantages and applicability of corrugated steel girder structure, we analyze two types of girders including a flat web steel I-girder and a corrugated web steel I-girder under the same impact load. From there, consider the effect of using corrugated girder under loading.

3 Structural Behavior of Corrugated Web

The previous studies including theoretical and experimental analysis have shown that the applied shear force is completely resisted by the corrugated steel webs in the I-girder. The bearing capacity and stability of the girder web depends on the height/thickness ratio of the web, the corrugated shape and the effect of defects that may have appeared during the girder's fabrication. In this section, two types of girders are investigated with the parameters of corrugated web as shown in Fig. 2. The parameters of the cross-section's girder are described in Table 1.

In this study, to clearly see the effect of torsion resistance, we use a torque of 10 kN-m/m uniformly distributed around the X-X axis. Then compare the analysis results between the two types of girders.

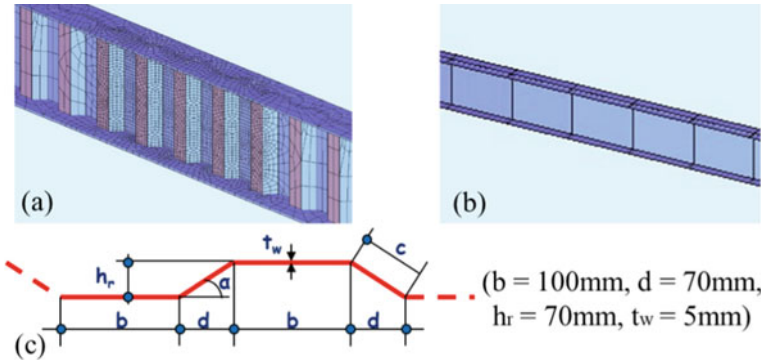


Fig. 2 The geometry of the corrugated web I-girder (a, c) and flat web I-girder (b)

The material properties of steel used for finite element modeling in this study include: Young's modulus E of 200 GPa, the yield stress of 403 MPa and Poisson's ratio of 0.3.

In this study, to see the effect caused by the shearing and torsion effects, three load cases were used to investigate them. The detailed load is described as follows:

- Self-weight, symbol is LC 1.
- Load uniform distributed (10 kN/m), symbol is LC 2.
- Torsion distributed around $X-X$ axis (10 kN·m/m), symbol is LC 3.

The analytical results obtained as shown from Figs. 3, 4, 5, and 6 show that:

- For the load case LC2: The web of the steel I-girder is more bending (with greater stress) than the web of corrugated web steel I-girder, so the flexural resistance (bending stiffness) of the steel I-girder is higher.
- For the load case LC3: The web of steel I-girder is less torsion (with less stress) than the web of corrugated web steel I-girder, so the torsion resistance of corrugated web steel I-girder is larger than steel I-girder.

4 Conclusions

In this study, we initially survey and compare the effects of two types of girders, consist of types of steel I-girder and corrugated web steel I-girder are investigated. This initial study focusing only through finite element analysis showed a relatively good resistance to instability for corrugated web girders. The study results are also consistent with the results of previous studies.

In the coming time, detailed studies combined with experiments will clarify the effectiveness of this type of structure. From there, it will be applied in bridge projects in Vietnam in the future.

Table 1 Comparison between steel I-girder and corrugated web steel I-girder

	Steel I-girder	Corrugated web steel I-girder
Cross-section		
Total weight (tons)	2.746	2.290
Maximum deflection at mid-span due to self-weight-LC 1 (mm)	8	9
Maximum deflection at mid-span due to uniform static load-LC 2 (mm)	61	74
Maximum angular displacement around X-X axis due to torque-LC 3 (mrad)	450	290
Image depicting when cutting 1 m of girders in the middle of span		

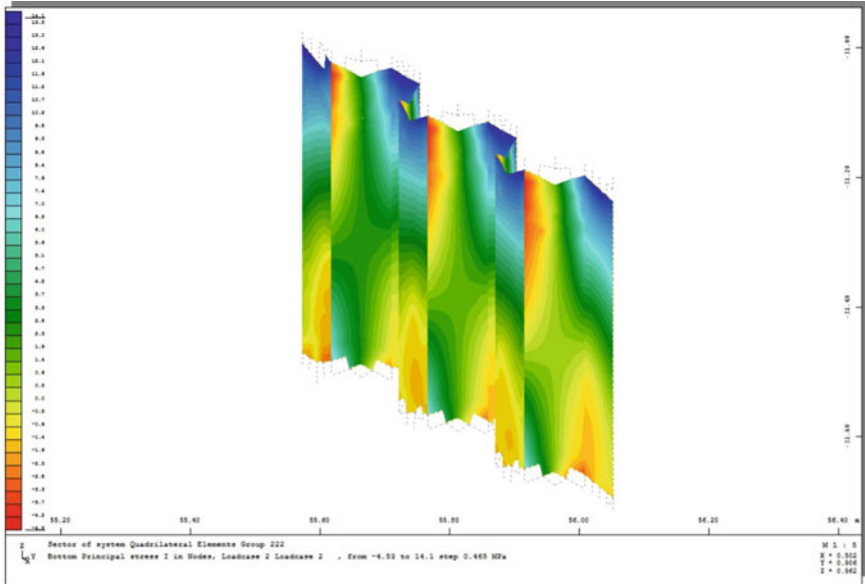


Fig. 3 Stress in web of corrugated web steel I-girder type—in case of LC2 (from -4.53 to 14.1 Mpa)

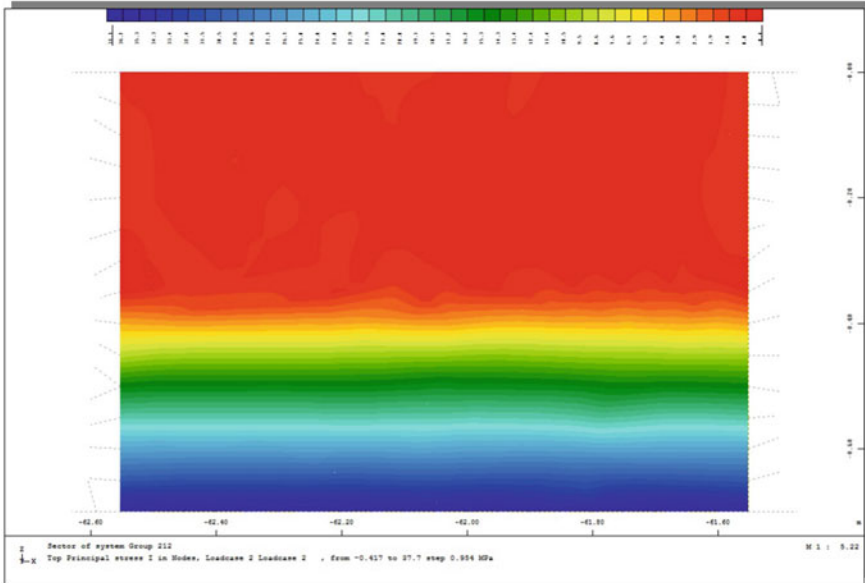


Fig. 4 Stress in web of I-girder type—in case of LC2 (from -0.417 to 37.7 Mpa)

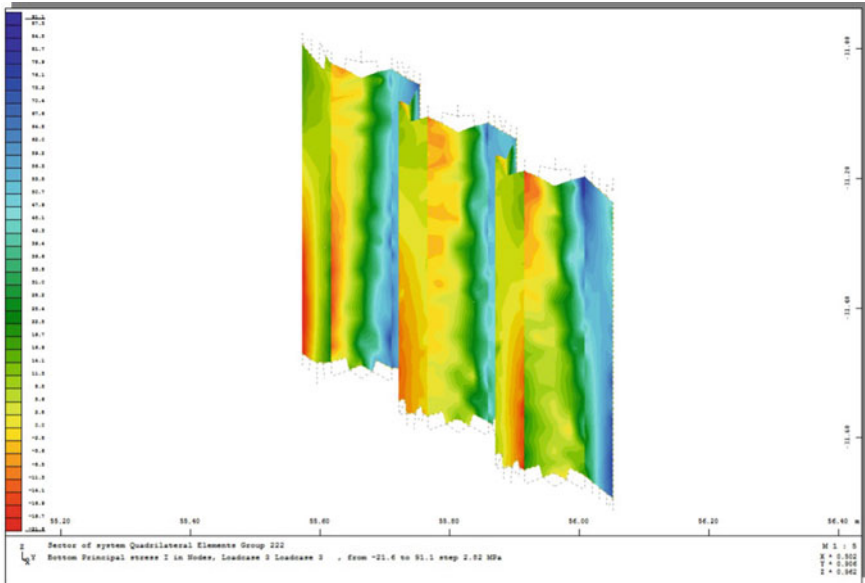


Fig. 5 Stress in web of corrugated web steel I-girder type—in case of LC3 (from -21.6 to 91.1 Mpa)

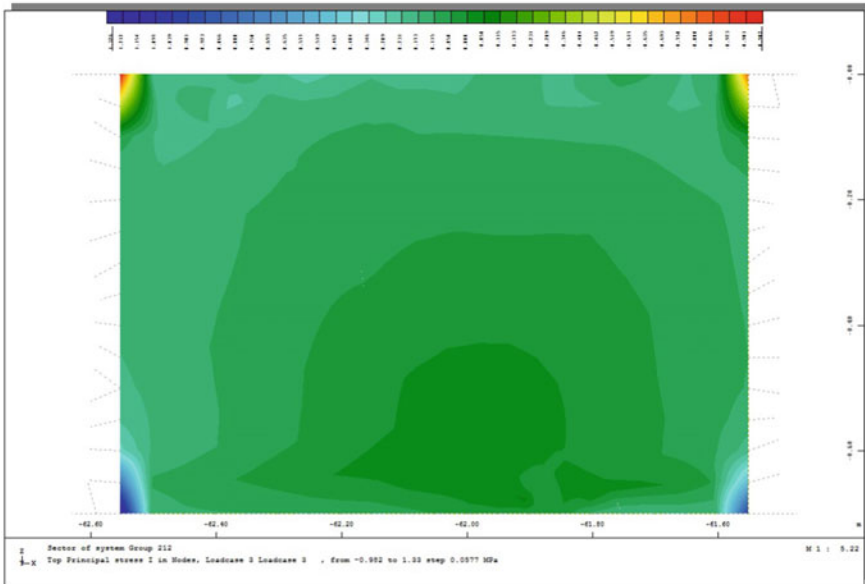


Fig. 6 Stress in web of I-girder type—in case of LC3 (from -0.98 to 1.33 Mpa)

Acknowledgements This research is funded by University of Transport and Communications (UTC) under grant number T2022-CT-001.

References

1. Abbas HH (2003) Analysis and design of corrugated web I-girders for bridges using high performance steel. PhD dissertation, Lehigh Univ., Bethlehem, PA
2. Abdul-Jabbar MS, Baldawi WS, Hamood MJ (2020) A study on the behavior of composite concrete and open web steel joists. *Eng Technol J* 38:869–878
3. Sayed-Ahmed EY (2007) Design aspects of steel I-girders with corrugated steel webs. *Elect J Struct Eng* 7:27–40
4. Yatim MYM et al (2016) Structural performance of corrugated web steel coupling beams. *J Struct Eng* 12:1–10
5. Hamada M, Nakayama K, Kakihara M, Saloh K, Obtake F (1984) Development of welded I-beam with corrugated web. *The Sumitomo search, Tokyo* 29:75–90
6. Chan C, Khalid YA, Sahari BB, Hamouda A (2002) Finite element analysis of corrugated web beams under bending. *J Const Steel Res* 58:1391–1406
7. <https://theconstructor.org/structural-engg/corrugated-webs-in-bridge-girders/13033/>
8. Zhang W, Li Y, Zhou Q, Qi X, Widera GEO (2000) Optimization of the structure of an H-beam with either a flat or a corrugated web. Part 3: development and research on H-beams with wholly corrugated webs. *J Mater Process Technol* 101(1):119–123
9. Li Y, Zhang W, Zhou Q, Qi X, Widera GEO (2000) Buckling strength analysis of the web of a WCW H-beam: Part 2. Development and research on H-beams with wholly corrugated webs (WCW). *J Mater Process Technol* 101(1):115–118

Evaluation of Dynamic Behaviors of Girders in High-Speed Railway Bridges Under Dynamic Impact of Electric Multiple Unit and Push–Pull Trains



Nguyen Duc Thi Thu Dinh

Abstract Due to the demand for the construction of a high-speed railway HSR system in Vietnam, a study on the selection of suitable technology is an important task. Currently, two train technologies, i.e., electric multiple unit (EMU) and push–pull train (PP) are the most feasible options that can be applied in Vietnam. The EMU or PP has its advantages and scope of application. Additionally, the different train technology leads to a difference in related infrastructure, especially bridges, one of the most common structures in HSR lines. Nowadays, the determination of the concordance of bridge span structures considering dynamic effects on HSR routes of trains at the speed over 200 km/h is of interest not only in Vietnam but also in the world. In many recent HSR projects, the applications of box girder bridges become more and more popular. However, one of the major disadvantages of box girders is the large cross-sectional height, which makes the box girder much more expensive in comparison with simple common girders. Hence, this work analyzes the dynamic behavior of several simple girders. Thereafter, the dynamic outcome is compared with that of the box girder bridge with the aim to evaluate the applicability of beams for superstructure railway bridges. Finally, the recommendation of suitable train technology for HSR lines in Vietnam is provided.

Keywords Train technology · Electric multiple unit (EMU) · Push-pull train (PP) · High-speed railways · High-speed train · Girders structures

N. D. T. T. Dinh (✉)
University of Transport and Communications/UTC, Hanoi, Vietnam
e-mail: nguyenthudinh@utc.edu.vn

1 Introduction

Construction of the high-speed railway (HSR) has become one of the most critical requirements for the transportation system of Vietnam due to an increase in traffic demand and operating speed. The selection of train types affects the design of related infrastructures, especially bridges in which two critical factors of trains should be deeply investigated, i.e., the technology and operating speed of the train. In particular, the speed of the train has a great effect on the technical design parameters of bridges such as the horizontal curve radius and longitudinal slope. In Vietnam, two suggested operating speeds of the train for service are 250 and 350 km/h. Actually, the faster the speed the higher investment for infrastructure needs to be provided. Moreover, in terms of train technology, electronic multiple unit (EMU), and push-pull train (PP) are the two main types applied worldwide. The applicability of EMU and PP technologies taking into account the socio-economic efficiency are now being comprehensively examined in Vietnam.

The PP is a dynamic train technology wherein only one tractor (the locomotive) is employed to pull the carriages (trailer carriages). Therefore, the additional carriages can be added or removed without difficulty. The main advantage of PP is the separation between the power supply units and wagons which helps to keep the wagons quiet and obtains low maintenance costs. However, the axial load at the head of the train is large, and only two dynamic wagons with mechanical brakes also lead to rapid wear which are the crucial disadvantages of the PP train. In addition, the effectiveness in saving energy is not achieved because of the use of electric brakes. Up to the present, the PP train has been commonly applied in European countries, e.g., France, Germany, Belgium, and the Netherlands. However, due to these features, the larger the number of trailer wagons and the more the train passes the slope areas, the harder it is to operate the train at such high speed. Consequently, the PP train operation will be limited by several factors such as the total number of wagons, the design slope, and the train's speed.

The EMU is a multi-electric train type with a lot of self-propelled cars, using electricity for motion energy. Unlike the PP, it does not need a locomotive to pull the EMU train. It should be noted that the EMU trains are usually made up of two or more wagons, or only one single self-propelled wagon [2]. Thanks to the advantages, i.e., fast acceleration, almost no pollution, quietness, and much less noise than diesel-engine trains (DMU) and PP, the EMU has become a popular option for serving the railway network connecting major cities. Thus, the EMU train can operate later at night and run at a higher frequency without affecting the population around the railway. In addition, the design of tunnels for EMU trains is less complicated than those for others trains because the problem of train pollution is not a big problem to be solved. Furthermore, among trains, the load from the EMU train is also lighter because it does not need the locomotive, hence, the infrastructure construction cost can be reduced [3].

With the current situation in Vietnam, 70% of the proposed high-speed railway lines are expected to be elevated bridges, thus the cost of constructing HSR lines

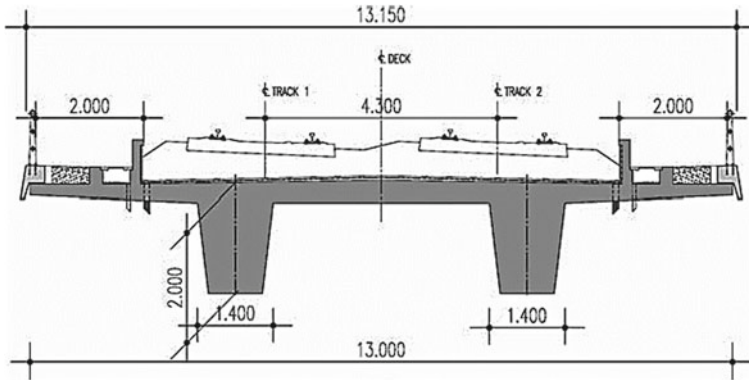
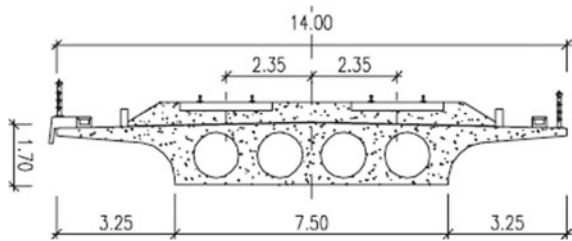


Fig. 1 π (Pi) girders (river Sado, at Alcácer do Sal, Portugal)

Fig. 2 Hollow slab
(Shin-Osaka to Okayama,
Japan)



becomes significantly larger compared to the option of the train on the ground. Therefore, studies to choose the suitable superstructure, pier, and abutment will contribute to reducing the budget for the construction of HSR not only in Vietnam but also in the world.

Figures 1, 2 and 3 show several superstructures of bridges that were utilized for the HSR projects in the world.

The present study analyzes the behavior of several types of superstructures with the aim to determine the advantages and disadvantages of the EMU or PP train that is necessary to suggest the suitable train for the HSR line in Vietnam. Moreover, the analysis can also give recommendations in the selection of train in terms of the operating speed by considering two speeds, i.e., 200 and 350 km/h.

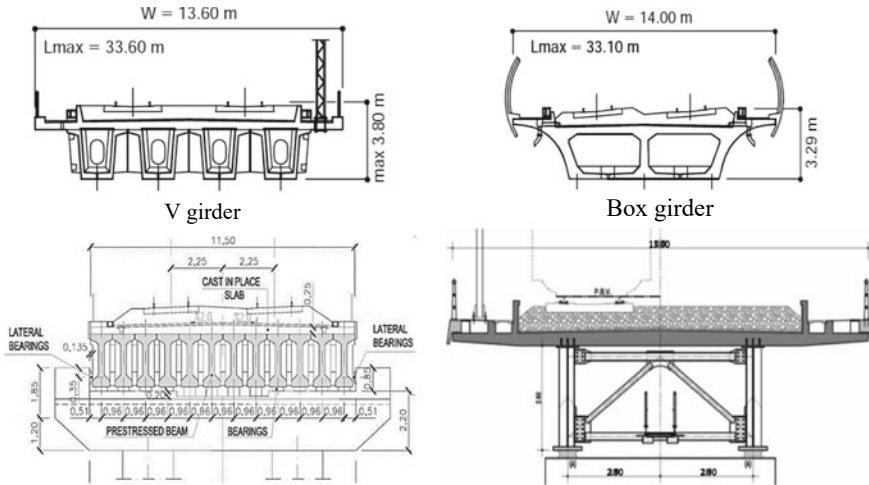


Fig. 3 Concrete I girder and steel I girder on HSR Torino–Milano, Italia [4]

2 Characteristics of EMU and PP High-Speed Trains and Design Load Models

2.1 EMU High-Speed Trains

It is emphasized that rapid acceleration, efficient application of regenerative electric braking, and energy saving are typical characteristics of EMU technology. Additionally, the low axle load of the EMU trains obtains a reduction in investment costs of related infrastructures. In EMU trains, each wagon includes two bogies which are equivalent to four-wheel axles. If the bridge length is longer than that of the train, all train axes locate on and directly impact the bridge. For this case, the deflection at the middle of span becomes moderate. Thereafter, large deflection of girders causes the rail deflection, and deformed track. Consequently, this is the reason leading to an opposite dynamic to the structure.

Cars of an EMU train are commonly divided into four categories, i.e., powered cars, motor cars, driving cars, and hook trailers (non-motorized) in which each car can also take up more than one task. For example, an EMU train car can have both an engine and a cockpit, or it also consists of power and a cockpit at the same time. It is seen that the axle load of the train is determined as the weight of the wagon box whereas the total train weight depends on a huge number of factors such as the type of wagon box, the number of carriages.

In the design standards of HSR bridges in the world, there are two approaches applied for the train’s load: one is a theoretical model and the other is an actual train diagram. Following the Japanese standard, the real train model (Shinkansen train) is entirely employed in the design process. Whereas the model selection for the train

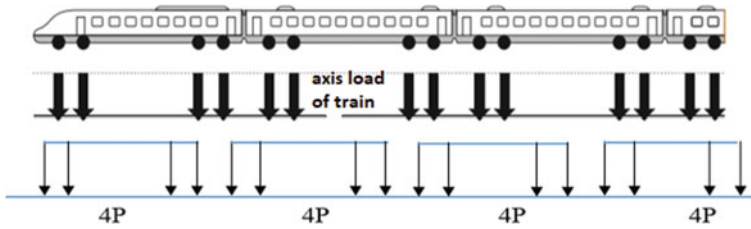


Fig. 4 The diagram load of EMU

load depends on the expected operating speed of trains as suggested in the European standards. Particularly, if the operating speed is smaller than 200 km/h, the design employs the theoretical load model while both the theoretical model and actual train load diagram are utilized if the design speed of the train is higher than 200 km/h. Notably, the European Standard named BS EN 1991-2 specifies the necessity for dynamic analysis of bridge structures for cases of an operating speed above 200 km/h [6]. Thus, the decision-making on the design speed of the train significantly affects not only the design of bridge but also other related infrastructures.

The European Standard EN 1991-2:2003 introduces the design of train load models, including: (1) Load model 71 and model SW/0 for continuous bridges used of mainline railways; (2) Train model SW/2 is heavy train; (3) Model of HSLM passenger train running at high speed > 200 km/h; (4) Model of empty wagon train. When considering the design of a high-speed railway with operating speeds > 200 km/h, the appropriate theoretical models are model 71 and model HSLM [6]. The application of HSLM-A or HSLM-B loads is dependent on the span length, whether the structure is simple or continuous. However, the standard recommends the necessity to employ the real train model for dynamic analyses of bridges.

In the current work, the real train model is examined to determine the dynamic behavior caused by the train running at high speed. The real train load diagram used is the EMU train–Shinkansen train named N700 that consists of a sequence of four, eight, or sixteen carriages. Distributed loads on each carriage are depicted in Fig. 4.

The total weight of the EMU 8-car train N700-I under full passengers is 365 T. The drag force per unit length of the rail on the girder is designed to be 5, 2.5, and 0 kN/m. Technical parameters of several EMU trains are summarized in Table 1.

2.2 PP High-Speed Trains

France and Germany are two countries using PP trains (ICE and AGV). The German ICE3 train entered service in 2000 with a lot of improvements. The ICE4 train applied EMU technology instead of the previous PP trains, i.e., ICE1 and ICE2.

PP train only needs one tractor (locomotive) to pull the wagons which are trailers and can be easily added or removed. Thus, when a large number of carriages pass

Table 1 Technical parameters of several EMU trains [2, 3]

Parameters	Train type		
	E0	E7	ICE3
Maximum weight of axes (T) (E7 = 100%)	16 (140%)	11.4 (100%)	15 (132%)
Type of train	16 M	12M4T	4M4T
The train length (m)	400	400	200
Maximum design speed (km/h)	220	285	330
The outputs energy (KW)	11,840	275	500
Power/weight (KW/T) (100% for E7)	12.2 (66%)	18.6 (100%)	19.6 (105%)
Weight of engine (kg)	876	390	–
The starting year of operation	1964	1999	2000

through steep terrain areas, the operation of the train at a high speed is difficult. Consequently, the train operates under several limitations such the number of cars and the design slope of bridges. Main characteristics of PP trains used in German and French are listed in Table 2.

The PP trains have several typical characteristics, i.e., the use of locomotives at the start and end of the train, the slower acceleration, and the use of the regenerative braking system with the non-motor car only. Furthermore, this train can reduce investigation and maintenance costs, make less noise for passengers, and easily increase or decrease the number of carriages. However, the PP train includes larger axial loads which is the main disadvantage of this system. The train has a small number of axles, so the axle load is large. Therefore, it is suitable for low passenger volume [1].

According to European standard BS EN 1991-2:2003 [5], the design load model is PP wherein the theoretical model or the real train model under the design speed can still be used. The theoretical model and actual train load diagram (considering the dynamic) are recommended to be applied corresponding to the case of the operating speed lesser and larger than 200 km/h. It should be noted that because the load PP

Table 2 Main parameters of some PP train [1, 6]

Parameters	Train type		
	TGV-A	ICE1	ICE2
Maximum weight of axes (T) (E7 = 100%)	17 (149%)	19.5 (171%)	19.5 (171%)
The train length (m)	240	410	205
Maximum design speed (km/h)	300	280	280
The outputs energy (KW)	1100	1200	1200
Power/weight (KW/T) (100% for E7)	18.0 (97%)	10.6 (57%)	11.7 (63%)
Weight of engine (kg)	1450	1980	1980
The starting year of operation	1989	1991	1997

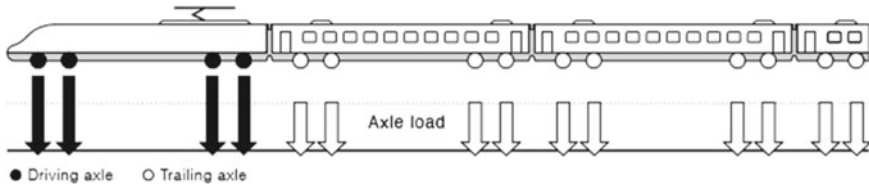


Fig. 5 The diagram load of PP [5]

train with push-pull wagon is quite large, the distribution longitudinal load on bridge requires large concentrated-loads for design (Fig. 5).

2.3 Problems for Dynamic Analysis of High-Speed Railway Bridges

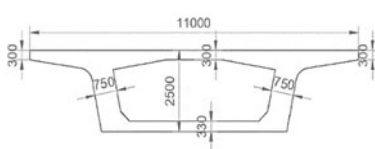
Simpack software is used to analyze the dynamic stability of trains running at different high speeds. The numerical simulation of the train and the railway bridge are conducted, thereafter, the effect of the train’s running speed and the dynamic forces generated at the train’s axes can be considered [7]. The analysis takes into account rails and sleepers, while the bridge span structure is mainly simulated through stiffness and elasticity parameters. The analysis aims to confirm the stability of train dynamics and train safety.

Additionally, Midas Civil, a popular structural analysis software, is utilized to simulate the superstructure of bridges wherein typical girders worldwide applied for HSR lines are examined. This is not a normal analysis but a dynamic analysis. It should be noted that the dynamical forces of the train taken from the Simpact software become the input data for the simulation of the real high-speed train in Midas Civil.

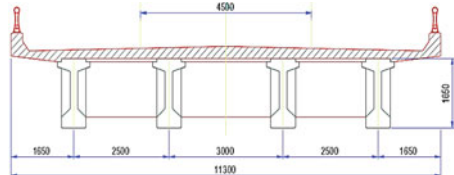
In order to indicate the applicability of types of beams for the superstructure of railway bridges and recommend the suitable train technology for HSR in Vietnam, the dynamic behavior of several simple girders, i.e., T, I are determined and compared with box girder. It should be emphasized that both steel and reinforced concrete are analyzed for two cases consisting of the EMU and PP trains.

The details of input data are shown clearly in Fig. 6 and Table 3. The train is modeled at the location with a limited horizontal curve radius to create the most serious effect (see Table 3). As a result, the horizontal force obtains a large value leading to high horizontal dynamic forces on the structure.

Analyze the behavior of some types of railway bridge span structures such as: simple small span box girder, I girder... under the dynamic impact of high-speed EMU and PP running at a high speed of over 200 km/h, detailed as $v = 200$ km/h, 250 km/h, 300 km/h and 350 km/h that taken from the problem 1.



Case 1: Cross section of prestressing concrete (PC) box girder with span length $l = 50\text{m}$



Case 2: Cross section of prestressing concrete (PC) I girder with span length $l = 33\text{m}$

Fig. 6 Cross-section of girders used for analysis

Table 3 Minimum horizontal curve radius required for bridges on HSR lines

Standard for design	V = 350		V = 300		V = 250		V = 200	
	R _{tt}	R _{min}	R _{tt}	R _{min}	R _{tt}	R _{min}	R _{tt}	R _{min}
European code (Germany)	8.503	4.984	6.247	3.662	4.338	2.543	2.776	1.628
Chinese standard	7.000	5.500	5.000	4.000	3.200	2.800		
Swedish standard	9.800	5.782	7.200	4.248	5.000	2.950	3.200	1.888
Horizontal curve radius (R1)	4900		3600		2500		1600	

Note R_{tt} and R_{min} are the normand value and minimum value, the unit of train speed is km/h

3 The Numerical Analysis Results of Problem Dynamic Analysis of Girders Under EMU and PP Action

In this problem, dynamic forces (horizontal and vertical) are used as input data for structural analysis. Dynamic stability is considered for the case of trains running at a speed of $v = 350\text{ km/h}$. Therefore, this speed is applied for both EMU and PP trains. The dynamic behavior of span structures is analyzed in terms of moments, stresses, vertical displacements, and horizontal displacements. The model of box girder for HSR lines is shown in Fig. 7.

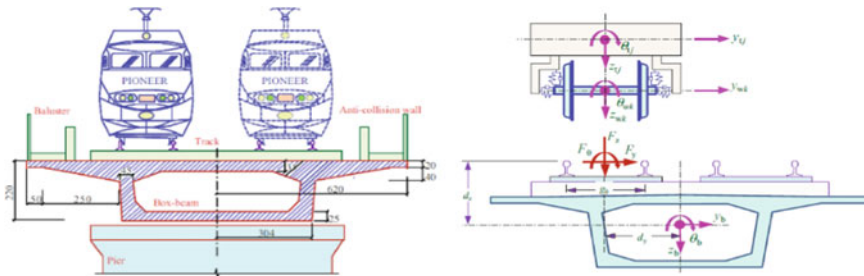


Fig. 7 Problem No1–dynamical analysis of the train on the box girder [3]

Table 4 The maximum dynamical displacement values of reinforced concrete box girder in the cases of EMU and PP trains (at the middle of span)

Girder (m)	Vertical displacement (cm)			Horizontal displacement (cm)		
	EMU	PP	PP/EMU	EMU	PP	PP/EMU
PC box	1.28	1.21	0.94	0.04	0.13	3.12
PC—I	0.49	1.48	3	0.01	0.13	12.45

Table 5 The maximum dynamical moment and stress values of reinforced concrete box girder in the cases of EMU and PP trains (at the middle of span)

Girder (m)	Moment (KN.m)			Stress (KNm/m ²)		
	EMU	PP	PP/EMU	EMU	PP	PP/EMU
PC box	3712.7	5985.2	1.61	0.92	2.632	2.861
PC—I	3710	5067.5	1.366	1.577	16.92	10.73

The maximum values of vertical displacement, horizontal displacement, moment, and stress at the middle of the span are summarized in Tables 4 and 5. It can be seen that all dynamic responses of the girder under PP train are larger than those from the case of EMU train.

3.1 The Horizontal Dynamic Displacement

The train’s horizontal dynamic force on the rail transfers to the superstructure leading to the horizontal dynamic displacement as illustrated in Fig. 8. The conclusions below can be announced:

- The horizontal dynamic deformation of steel beams is approximately 20 times greater than that of concrete girders. This is understandable and explained as the effect of the stiffness of the structure. In particular, the stiffness of reinforced concrete beams (PC) is much higher in comparison with the stiffness of steel beams of the same span length.
- The vibration of the steel girder is still considerably large even after the train comes out of the bridge while this stop quickly and obtains a smaller vibration amplitude in the case of the concrete beam.

When using a I-beam instead of a box girder, the span length of the I-beam is about 60% shorter, but the deformation value of the I-beam is only 0.2% smaller than that of the box girder.

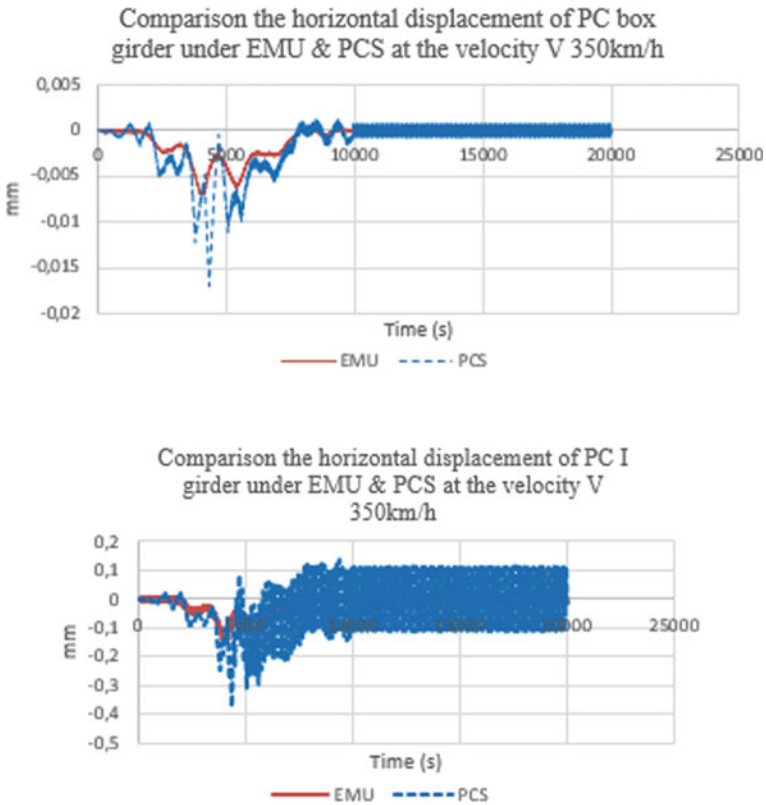


Fig. 8 Horizontal displacement of PC box and PC I girder under EMU and PP (PCS in figure)

3.2 The Vertical Dynamic Displacement

The vertical dynamic displacement of two girders is depicted in Fig. 9. Based on that, several statements can be given as follows:

- Vertical displacements of concrete beams show a different response when different cross-sections are selected. With the box girder cross-section, the behavior is quite similar to that of the steel beam, while for the I-beam, the opposite is true: The beam behavior is large when the train is traveling at high speed within the bridge and low when the train exits the bridge.
- The comparison between the box girder and the I-beam shows that the dynamic vertical displacement of the box girder and the steel I-beam is not much different from each other in value, while the value of the PC box girder is much larger than that of PC I-beam (about 2 times).

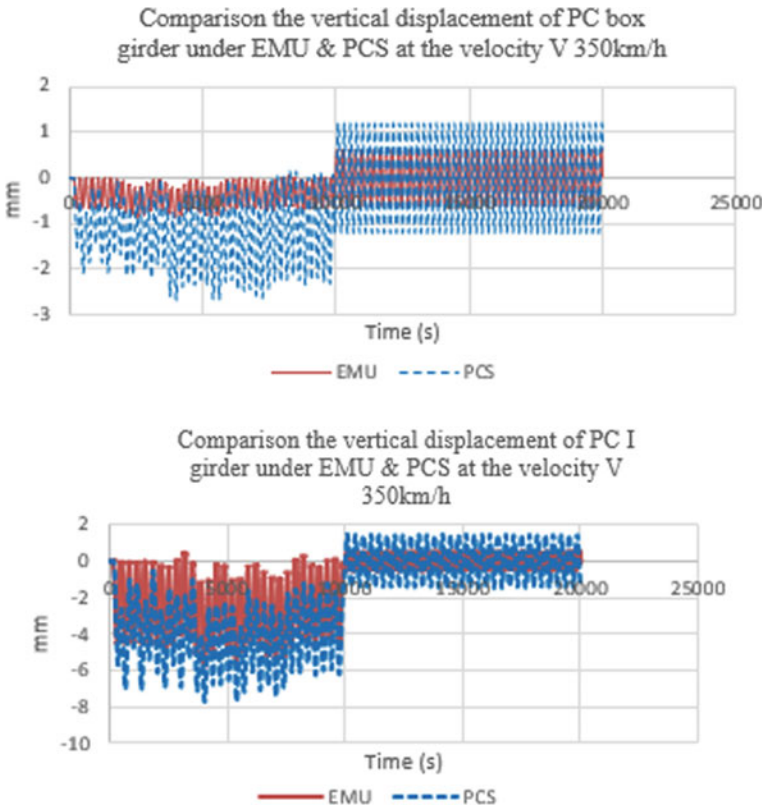


Fig. 9 Vertical displacement of PC box and PC I girder in the cases of EMU and PP (PCS in figure)

3.3 The Dynamic Moment

The dynamic moment of the beams is shown in Fig. 10, it can be seen clearly that the dynamic moment of the beam made of concrete is larger than that of steel. This can be due to the difference between the weight of reinforced concrete (larger) and steel (smaller) girders under the same span length. Additionally, even though the cross-sectional shape is different in the case of steel beams, the moment achieves similar results both in terms of the forms and values. Furthermore, when the train runs in and out of the reinforced concrete bridge, the box girder gets a larger moment in comparison with I-beam. Finally, I-beams will be more feasible and beneficial if the reinforced concrete material is selected.

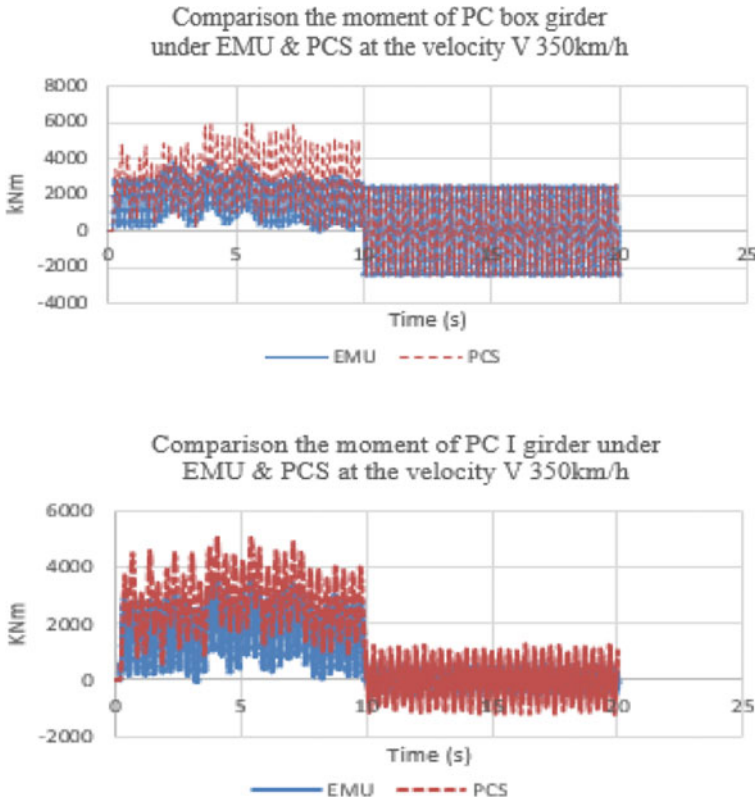


Fig. 10 Dynamic moment of PC box and PC I girder under EMU and PP trains

3.4 The Dynamic Stress

Figure 11 depicts the dynamic stress of girders. It is observed that the dynamic stress of the girder under PP train action is much larger than that due to EMU train wherein the difference depends on the horizontal curve radius. If the radius is changed from 4900 to 2800 m, the ratio between the dynamic stress caused by two trains (PP/EMU) increases from 2 to 7 times.

Moreover, the dynamic stress of the girder under the EMU train impact at a running speed of $V = 350$ km/h indicates: With the same cross-section, the dynamic stress of the reinforced concrete girder is much less than that of the girder fabricated by steel. In addition, when using the same materials but different cross-sections, the steel I-beams with a smaller length span obtain the same dynamic stress as the box girder with a longer length of approximately 66%. However, the stress of the longer concrete box beam (about 26%) is smaller than that of the I-beam.

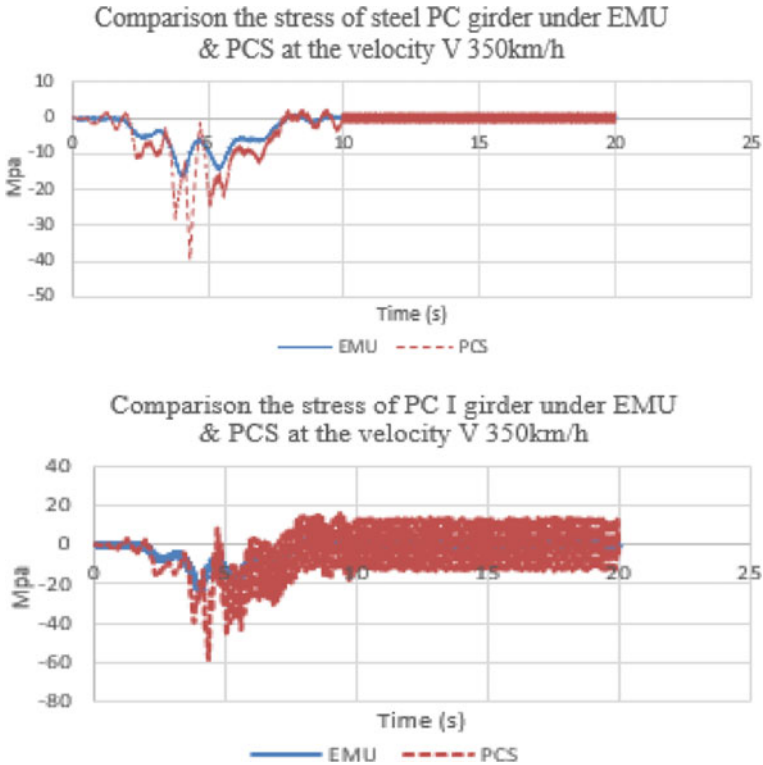


Fig. 11 Dynamic stress of PC box and PC I girder under EMU and PP

4 Conclusions

In the present study, an effort was made to evaluate the dynamic behaviors of several girders with different materials in high-speed railway bridges for two trains, i.e., EMU and PP. From results provided in this work, the following conclusions are given:

Simple girders should be selected for high-speed trains. With a box girder, the span length should be from 30 to 60 m due to the large deformation of the deck. The deformation in this case needs to be tested for the service limit state. Particularly, the maximum deflection at mid-span needs must be less than 1/5600.

When the horizontal curve radius of the span is considered, the effect of the EMU train only act on the bridge at the mid-curve position and turns off quickly after the train exits the curve. The larger variable internal force, the smaller the time interval when the greater speed train operating. On curved route, when the beams are placed straight, the placement of curved rails will cause quite large horizontal displacements.

It is possible to use low-cost simple girders for HSR in Vietnam depending on the selection of the train technology. Furthermore, the use of steel or reinforced concrete

for the bridge girder should be considered. However, if the EMU train is used, the PC girder bridge is more reasonable in terms of bearing capacity.

The vertical and horizontal displacement under the dynamic load of the box girder span is much larger than that of I-beam. Therefore, it is suggested to use only box girders with a length of 30 m so that the deflection and deformation can be reduced. However, based on the construction requirements, the slope of HSR route, the height of 30 m span length must be at least 2.2–2.3 m, which is 35 cm higher than that of I-beam. Finally, a reduction in the height contributes great significance to small vertical bridges, especially to ensure a high operating speed of the train.

References

1. Railway track design, Arema 2003
2. Hagiwara Y, TaNaKa M, Ueno M (2001) Evaluation of advantages of high speed EMUs in the case of series 700 Shinkansen high speed train with IGBT applied traction systems, Central Japan Railway Company, Tokyo, Japan
3. Coleodo R, Delgado R, Campos e Matos A, Gabadon JMGv (2013) Track—bridge interaction on high speed railways, A Balkema book, UK
4. Matsumoto A (2016) Analysis of train—overtun derailments caused by excessive curving speed, Japan Transport Safety Board (JTSB). In: Michitsuji Y, Tobita Y, Ibaraki University, the third international conference on railway technology: research and maintenance meeting, Cagliari, Italy
5. The European Union, Edict of Government, EN 1991–2 (2003) (English): Eurocode1: Actions on structures—part 2: traffic loads on Birdge
6. Muncke M (2008) The effects on the interoperability of the European Railway Traffic of European Standards 15
7. Simpack Release 8.6 (2003) Wheel rail element reference

Application of Mobile Road Profiler for International Roughness Index Monitoring in Hanoi



Hoang Kien Pham and Kazunari Hirakawa

Abstract An essential element of a pavement management system is a means to monitor pavement surface roughness, distress, and other properties. Most pavement management activities include the use of devices that measure longitudinal profile for assessment of surface roughness. The International Roughness Index (IRI) has become one of the major road roughness indexes that is most commonly used. In Japan, a time-stable and user-friendly compact mobile road profiler (MRP) known as STAMPER II has been developed. This system enables frequent, inexpensive, and regular road surface roughness monitoring. In this paper, some results of the first IRI measurement using STAMPER II in the joint research project between Taisei Rotec Corporation and University of Transport and Communications are introduced. The studies also show the applicability and effectiveness of using mobile road profiler STAMPER II for surface roughness monitoring and pavement management in Vietnam.

Keywords IRI · Mobile road profiler · Roughness monitoring · Pavement management

1 Introduction

The International Roughness Index (IRI), developed by World Bank in 1986, has become one of the most common indexes used by road management authorities and researchers worldwide [1, 2]. Along with the development of response-type road roughness measuring systems (RTRRMS), many countries have developed

H. K. Pham (✉)

University of Transport and Communications, Hanoi, Vietnam

e-mail: phkien@utc.edu.vn

Vietnam—Japan Research and Development Center, UTC, Hanoi, Vietnam

K. Hirakawa

Taisei Rotec Corporation, Saitama, Japan

their own road profiling devices for measuring IRI [3, 4]. In Japan, a time-stable and user-friendly compact mobile road profiler (MRP) known as “System with Two Accelerometers for Measuring Profile, Enabling Real-time data collection” (STAMPER II) has been developed by Taisei Rotec Corporation. The STAMPER II not only can easily measure the IRI at relatively low price, it also can construct a road maintenance management system that combines this with the front camera [5, 6]. It is thought that this system will enable frequent, inexpensive, and regular road surface roughness monitoring in Vietnam, where the traffic volume increases fast and pavement damage is difficult to be predicted. For this reason, Taisei Rotec Corporation has signed the joint research with University of Transportation and Communications entitled “Research on the development of pavement management system (PMS) in Vietnam using STAMPER II, simple and compact mobile road profiler”. In order to establish a PMS suitable for road conditions in Vietnam using STAMPER II, measurements are performed semi-annually using STAMPER II, and data is accumulated to understand the form of damage and the speed at which damage progresses, as well as the repair points. We will also consider the selection of repair time and repair method. This paper describes some results of the first measurement of the joint research. The purpose of the first measurement is to understand the service status and damage of the pavement around Hanoi and to accumulate data such as IRI and road surface images. We also examined the adaptability of STAMPER II in Vietnam and the points to be improved for more efficient measurement.

2 Application of STAMPER II for IRI Measurement

Figure 1 shows the configuration of the STAMPER II which has two acceleration converters installed above and below the tire suspension and a GPS receiver installed on the vehicle body to measure not only IRI but also position information and running speed. At the same time as the IRI measurement, the road surface condition can be photographed from the front video camera. The acquired IRI and road surface video data are given the location information acquired by the GPS and can be displayed on an electronic map. As shown in Fig. 2 and Table 1, four types of roads around Hanoi were measured: National Highway, Ring road, Provincial street, and City street. The measurement points were divided into 16 sections according to intersections and road type boundaries. On roads with multiple lanes, measurements were taken for all lanes through which vehicles can pass. Each measurement route name is serial number in the counterclockwise direction starting from the University of Transport and Communications, and the serial number in the road type (if it is the third street C3). In the case of multiple lanes, the number of lanes from the left and whether the travel direction of the measuring vehicle is counterclockwise or clockwise (in the case of clockwise, add “reverse”). There are 49 measurement routes, and as shown in Table 1, the National Highway is 187 km with all 12 lanes, the Ring road is 137 km with all 14 lanes, and the Provincial street is 25 km with all 19 lanes. The City street

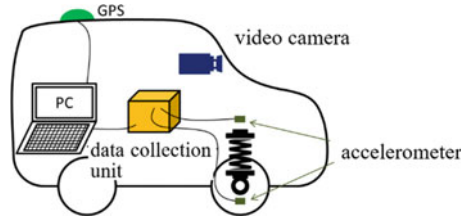


Fig. 1 Mobile road profiler STAMPER II configuration

is 24 km with all 4 lanes. The measurements were taken from October 13, 2018 to November 3, 2018.

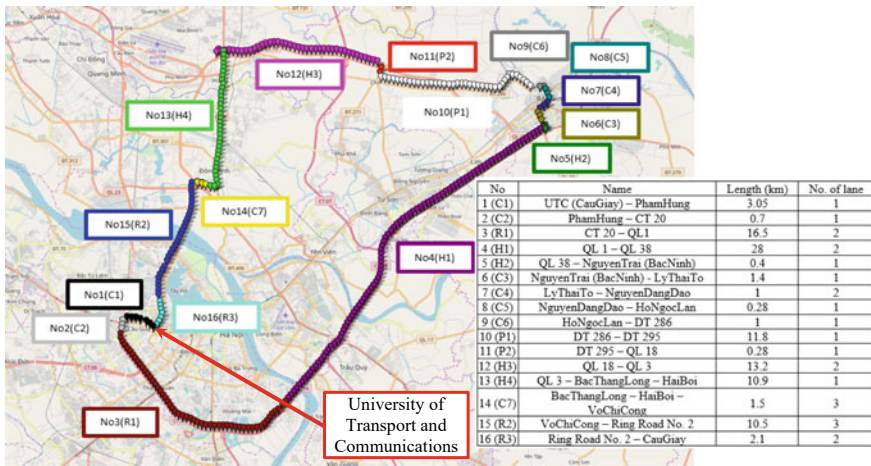


Fig. 2 Measurement routes

Table 1 Extension of measured routes

Kind of road	Total length [km]	Total length of lanes [km]	Number of lane
National highway (H1-4)	53	187	12
Ring road (R1-3)	29	137	14
City street (C1-7)	9	25	19
Provincial street (P1, 2)	12	24	4
Total	103	374	49

3 Measurement Results and Discussion

Since there were many small-scale repair marks and the local damage with longitudinal distance of 10 m or less on the measured line, regarding the specified length of IRI, it was set to 10 m so they could be detected. The measurement results for each road type of IRI10m are shown in Fig. 3 and Table 2. From Table 2, the average values of IRI10m were relatively good at 3.5 and 3.4 for National Highway and Ring road, respectively, and 3.8 for City street and 4.7 for Provincial street, respectively. In addition, according to the “Pavement Management Guidelines based on the Pavement Inspection Guidelines” [7], if IRI is 8 or more, it will be classified in repair stage and it will be necessary to replace the cutting overlay or road base, but appearance rate of IRI10m of 8 or more is National Highway 2.0%, Ring road 1.3%, Provincial street 11.0%, City street 4.4%, Provincial street had the highest percentage of repair’s needs. STAMPER II cannot calculate IRI at speed lower than 20 km/h. In Vietnam, where traffic congestion is frequent, we confirmed how efficiently IRI10m could be obtained using STAMPER II. The results are shown in Table 2. National Highway and Ring road had acquisition rate of 99% or more, Provincial street had acquisition rate of 98% or more, but City street had acquisition rate of 89.1%. Table 3 shows the mean value, standard deviation, ratio exceeding 8, and acquisition rate of IRI10m for each measurement line. The average value of IRI10m on the measurement routes of National Highway and Ring road was about 4 or less. On the other hand, the average values of IRI10m for No.5 and No.5 reverse were as large as 5.6 and 7.0, respectively, but it is thought that this is because No.5 is road connecting national roads and streets, and there were many height differences and joints for bridges. It was confirmed that there are routes with an average IRI10 m close to 5 and measurement routes with value of 5 or more on Provincial street and City street, and there are roads in a relatively poor condition. The data acquisition rate exceeded 90% on all measurement routes on the National Highway and Ring road. On the other hand, there are routes below 90% on Provincial street and City street, and the acquisition rate at No.9 (C6) was 51.6%. The low acquisition rate in No.9 (C6) is because the fact that motorcycles and pedestrians were present in front of the measurement car and car speed could not be maintained at 20 km/h or more, as shown in Fig. 4. Figure 5 shows a specific examples of damage at points where the IRI10m exceeds 8 for the City street road type.

City street No.1 (C1) has an average IRI10m of 6.0, which is one of the worst condition roads measured this time. Typical points where the IRI of No.1 (C1) exceeds 8 are shown in Fig. 5 from ① to ④. In No.1 (C1), there was step around the mass like ① and step at the construction joint part as seen in ② to ④. Since the damage is not considered to be structural damage, cutting overlay can be considered as repair method.

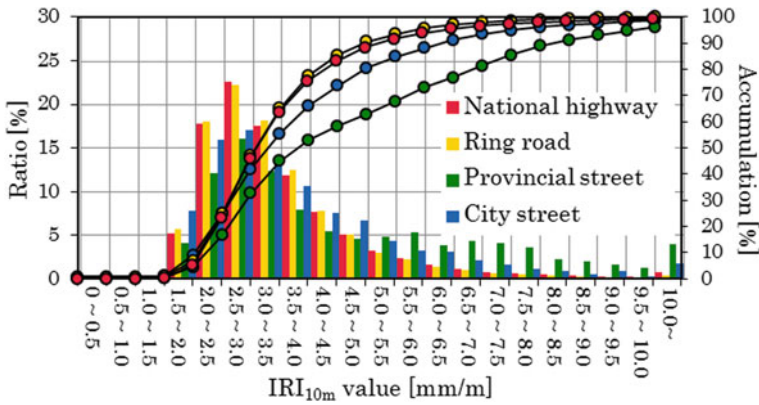


Fig. 3 Histogram of IRI10m by road type

Table 2 Summary of IRI10m

IRI10m				
	Average [mm/m]	Standard deviation [mm/m]	Over 8 [%]	Acquisition rate [%]
National highway	3.5	1.8	2.0	99.5
Ring road	3.4	1.8	1.3	99.0
Provincial street	4.7	2.5	11.0	98.4
City street	3.8	2.4	4.4	89.1
Total	3.6	2.1	2.5	98.6

4 Conclusion

The first measurement was conducted from October 13, 2018 to November 3, 2018, and the total length around Hanoi is about 373 km, of which the National Highway was 187 km, the Ring road was 137 km, the Provincial street was 25 km, and the City street was 24 km. The average value of IRI10m for each road type is 3.5 for the National Highway (standard deviation: 1.8), 3.4 for the Ring road (standard deviation: 1.8), 4.7 for the Provincial street (standard deviation: 2.5), and 3.8 for the City street (standard deviation: 2.4). The ratio of IRI10m exceeding 8 was 2.0% for the National Highway, 1.3% for the Ring road, 11.0% for the Provincial street, 4.4% for the City street, and the Provincial street showed the worst result. Focusing on individual measurement routes, the average IRI10m was close to or less than 4 on the National Highway and Ring road except for No.5 and No.5 reverse, and the ratio of IRI10m of 8 or more was 5% or less. On the other hand, in the Provincial street and City street, there are many lanes with the average IRI10m exceeding 4, and lanes with the IRI10m of 8 or more of 5% or more, and it is considered that there are relatively many points need to be repaired. As the result of looking at specific damage

Table 3 Summary of IRI10m for each measurement line

Kind of road	Lane name	Average [mm/m]	Standard deviation [mm/m]	Over 8 [%]	Acquisition rate [%]
National Highway	No 4 (H1)—LANE1	3.1	1.2	0.9	99.6
	No 4 (H1)—Lane2	3.3	1.3	1.1	99.6
	No 4 (H1)reverse—Lane1	3.1	1.1	0.8	99.6
	No 4 (H1)reverse—Lane2	3.2	1.2	0.7	99.4
	No 5 (H2)	5.6	3.3	16.9	95.1
	No 5 (H2)reverse	7.0	3.0	31.1	91.8
	No 12 (H3)—Lane1	4.1	1.8	3.8	99.7
	No 12 (H3)—Lane2	4.1	1.8	4.5	99.7
	No 12 (H3)reverse—Lane1	3.5	1.5	2.3	99.8
	No 12 (H3)reverse—Lane2	3.8	1.8	3.3	99.8
	No 13 (H4)	3.9	2.3	3.4	98.4
	No 13 (H4)reverse	3.9	1.9	3.7	99.3
	Ring road	No 3 (R1)—Lane1	3.6	1.6	1.7
No 3 (R1)—Lane2		3.7	1.4	1.7	99.8
No 3 (R1)reverse—Lane1		3.5	1.4	1.5	100.0
No 3 (R1)reverse—Lane2		3.9	1.7	3.0	99.7
No 15 (R2)—Lane1		3.2	1.1	0.1	97.1
No 15 (R2)—Lane2		3.1	1.2	0.5	98.8
No 15 (R2)—Lane3		3.1	1.1	0.7	99.0
No 15 (R2)reverse—Lane1		3.2	1.1	0.7	99.1
No 15 (R2)reverse—Lane2		3.2	1.1	0.3	97.5
No 15 (R2)reverse—Lane3		3.1	0.9	0.2	98.9
No 16 (R3)—Lane1		3.1	1.1	1.4	98.1
No 16 (R3)—Lane2		3.1	1.5	2.5	94.4
No 16 (R3)reverse—Lane1		3.1	1.1	1.5	98.1
No 16 (R3)reverse—Lane2	3.3	1.2	0.9	98.3	

(continued)

Table 3 (continued)

Kind of road	Lane name	Average [mm/m]	Standard deviation [mm/m]	Over 8 [%]	Acquisition rate [%]
Provincial street	No 10 (P1)	4.8	2.5	11.6	99.1
	No 10 (P1)reverse	3.7	2.5	11.0	98.6
	No 11 (P2)	3.8	1.3	1.6	96.5
	No 11 (P2)reverse	3.7	1.5	1.4	96.1
City street	No 1 (C1)	6.0	2.9	16.4	89.4
	No 1 (C1)reverse	5.1	2.2	12.3	78.2
	No 2 (C2)	4.0	1.1	6.3	96.3
	No 2 (C2)reverse	4.8	2.1	7.8	94.7
	No 6 (C3)	3.0	1.0	0.0	89.8
	No 6 (C3)reverse	3.2	0.9	0.0	85.7
	No 7 (C4)—Lane1	3.4	1.3	0.0	88.2
	No 7 (C4)—Lane2	3.9	1.8	4.5	90.8
	No 7 (C4)reverse—Lane1	3.6	1.6	3.1	97.0
	No 7 (C4)reverse—Lane2	4.2	1.7	4.5	90.7
	No 8 (C5)	4.7	1.6	3.6	89.4
	No 8 (C5)reverse	4.5	1.7	2.4	84.7
	No 9 (C6)	3.4	1.2	0.0	51.6
	No 14 (C7)—Lane1	2.5	0.8	0.0	100.0
	No 14 (C7)—Lane2	2.5	1.0	0.0	96.2
	No 14 (C7)—Lane3	2.6	0.8	0.0	96.2
	No 14 (C7)reverse—Lane1	2.8	0.8	0.0	96.9
	No 14 (C7)reverse—Lane2	2.7	0.9	0.0	95.9
	No 14 (C7)reverse—Lane3	2.8	0.9	0.0	94.4

with IRI10m exceeding 8 by lane, lanes such as No.13 (H4) and No.10 (P1) reverse where the pavement structure including the roadbed and below may be damaged, and No.16 (R3)—There were lanes where the pavement structure could be sound, such as lane 1 and No.1. From these four lane damage cases, the characteristics of Vietnam's pavement were that there were many pavements without drainage facilities and that there were large steps in the repaired parts and construction joints. Concerning the applicability of STAMPER II, in the first measurement, the overall data acquisition rate was as good as 98.6%. In addition, clear damage was confirmed on road surface images at locations where the IRI10m was 8 or more, confirming the validity of the measurement results.



Fig. 4 Congestion situation of No.9 (C6)

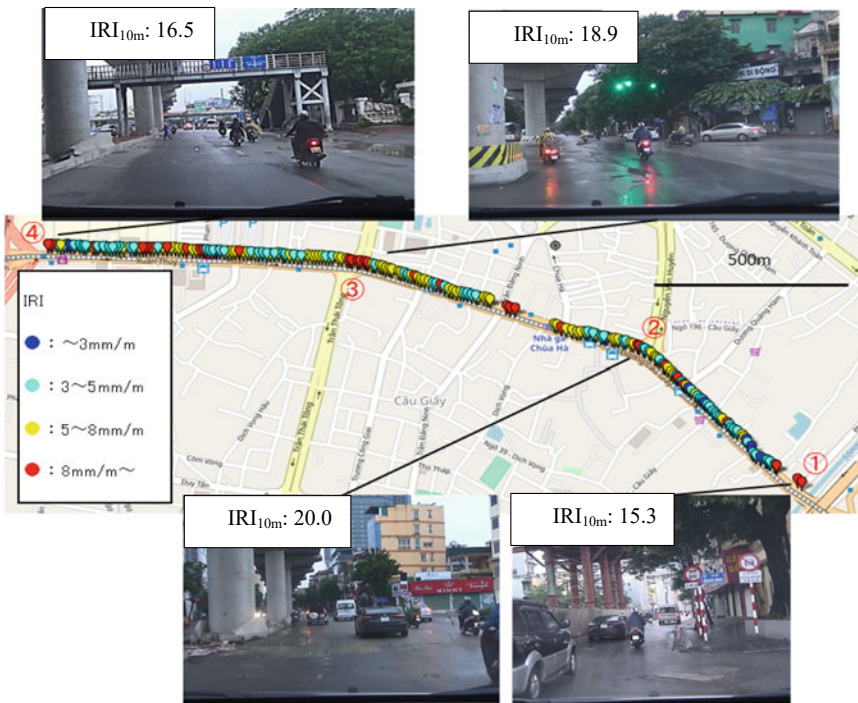


Fig. 5 No.1 (C1) damage example

In the future, it is necessary to continue to monitor the road surface conditions accurately in order to establish a pavement management system, such as determination of diagnostic classification thresholds, determination of repair/repair methods, and formulation of repair/repair plans. In this measurement, the main cause of the poor data acquisition rate was traffic congestion, but there were also the cases where

the vehicle speed could not be maintained at 20 km/h or higher due to the presence of traffic lights and slow vehicles ahead. We plan to improve the measurement system so that IRI can be measured even at 20 km/h or less in order to perform measurement smoothly even under such circumstances. In addition, although the STAMPER II accelerometers and GPS are connected to the interior of the vehicle by cables, we will also make them wireless in order to eliminate the risk of disconnection and to make installation easier.

References

1. Michael WS, Thomas DG, William DOP (1986) Guidelines for conducting and calibrating road roughness measurements. World Bank Technical Paper Number 46, Washington, D.C
2. Steven MK, Thomas DG, Starr DK, Rohan WP (1999) Guidelines for longitudinal pavement profile measurement. Final report NCHRP Project 10–47, University of Michigan Transportation Research Institute
3. Michael WS, Steven MK (1998) The little book of profiling—basic information about measuring and interpreting road profiles. University of Michigan
4. Múcka P (2017) International roughness Index specifications around the world. Road Mater Pavement Design 18(4):929–965
5. Tomiyama K, Kawamura A, Nakajima S, Ishida T, Jomoto M (2012) A mobile Profilometer for Road Surface Monitoring by Use of Accelerometers. SURF0035, Kitami Institute of Technology, Japan
6. Nueraihemaitijiang A, Kawamura A, Tomiyama K, Fujita S (2016) Measuring and evaluating of road roughness conditions with a compact road profiler and ArcGIS. J Traffic Transp Eng 3(5):398–411
7. Japan Road Association (2018) Pavement management guidelines based on the pavement inspection guidelines. Japan

River, Estuary and Coastal Hydrodynamic Engineering

Numerical Simulation of Submarine Landslide-Induced Tsunami Using Two-Layer Extended Boussinesq Equations



Van Khoi Pham, Van Nghi Vu, and Changhoon Lee

Abstract Submarine landslide-induced tsunami, which is caused by earthquakes or volcano eruptions, seriously affects humans' lives and properties. To date, this is a challenging topic for numerical hydrodynamic researchers due to the unpredictable submarine landslide sources. Several researchers assumed the submarine landslide source as the impermeable soil layer and its movement as an elliptic shape. In this paper, the underwater soil surface is porous, water can pass through and then the submarine landslide source becomes a permeable soil layer. The submarine landslide is simulated correctly using the nonlinear shallow water equations (NSWE) and the hybrid finite volume/finite difference (FV/FD) method. To generate tsunami, the time-varying water depths and the porosity inside the submarine landslide are included as the source terms in the two-layer extended Boussinesq equations to generate waves. A high-order FD method is applied to discretize the two-layer Boussinesq equations in time and space. The numerical simulations of submarine landslide-induced tsunami for two-layer case are investigated in a specific porosity. The two-layer and one-layer results are compared and explained by real dynamical phenomena.

Keywords Extended Boussinesq equations · Numerical simulation · Submarine landslide · Tsunami · Two-layer

V. K. Pham (✉)

Vietnam Maritime University, Hai Phong, Vietnam

e-mail: khoipv.ctt@vimaru.edu.vn

V. N. Vu

Ho Chi Minh City University of Transport, Ho Chi Minh City, Vietnam

C. Lee

Sejong University, Seoul, South Korea

1 Introduction

In coastal hydrodynamics computations, landslide-induced tsunami now becomes the most challenging topic for researchers. These complicated phenomena can be composed of landslide movements (lower-layer) and generated water waves (upper-layer). Among many factors that vigorously affect the selection of numerical models, people recognize two inevitable factors, i.e., the computational savings and the discretization of the nonlinear or dispersive consequence of fluid movements [1]. Therefore, the two-dimensional landslide-induced tsunami models [2, 3] are favored models compared to the three-dimensional model [4]. Also, the Boussinesq equations, which include both nonlinear and dispersive terms, are commonly used to generate waves instead of the nonlinear shallow water equations (NSWEs), which included only the nonlinear term. As a result, in the two typical depth-averaged models of landslide-tsunami, the NSWEs-Boussinesq equations are more favored than the NSWEs-NSWEs.

All the landslide-tsunami models until now [2, 3, 5] consider the landslide interface as impermeable bed, not as permeable in which the water can pass through. Moreover, the landslide model often uses the landslide depth perpendicular to the bottom (local coordinate system) of Savage-Hutter NSWEs [6], then it takes time to convert the landslide governing equations to the global coordinate that can connect to the vertical water depth in the water wave equations of [2].

This study introduces a submarine landslide-induced tsunami that imitates soil movement and water wave using the NSWEs and the Boussinesq equations, respectively. The landslide depth using the global coordinate system in this model can be connected easily to the vertical water depth compared to the local landslide depth in the model [2, 3]. Moreover, the porosity of the landslide lower-layer is firstly included in the advanced Boussinesq tsunami model to investigate how the landslide permeable layer affects generated waves.

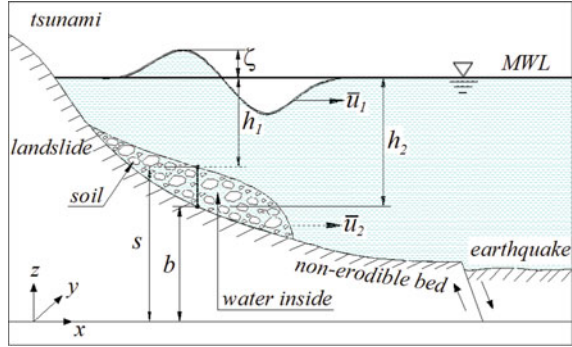
2 Submarine Landslide-Induced Tsunami Model

The schematic of this submarine landslide generated wave is introduced in Fig. 1. This integrated model is composed of the submarine landslide model and the two-layer Boussinesq water wave model. The upper-layer is the water layer, and the lower-layer is the submarine landslide layer, which assumes soil and water movement together.

2.1 Submarine Landslide Model

The governing equations of the submarine landslide model over the non-erodible bed are the NSWEs as

Fig. 1 Schematic of two-layer submarine landslide-induced tsunami model



$$\frac{\partial}{\partial t}(s - b) + \nabla \cdot [(s - b)\mathbf{u}] = 0 \tag{1}$$

$$\frac{\partial}{\partial t}[(s - b)\mathbf{u}] + \nabla \cdot \left[(s - b)\mathbf{u}^2 + \frac{1}{2}g'(s - b)^2 \right] = g'(s - b)(S_0 - S_f) \tag{2}$$

where the variables s and \mathbf{u} are the soil surface elevation and soil depth-averaged velocity, respectively, b is the soil bottom elevation which considers non-erodible bottom, $S_0 = -\partial b / \partial x = \tan \theta$ is the bottom slope term in which θ is the bottom slope angle, $S_f = \frac{n^2 \mathbf{u}|\mathbf{u}|}{(s - b)^{4/3}} + \cos \theta \tan \phi$ is the friction slope term which includes both the bottom surface friction (Manning n coefficient) and the soil internal friction (internal friction angle ϕ), respectively, S_0 and S_f are the non-dimensional source and resistance term, respectively, in landslide movement. It is noticed that the gravitational acceleration g' considers the buoyancy effect in underwater. This value is about 50% of the gravitational acceleration in the air [7]. That's why the submarine landslide is lighter than the subaerial landslide, then it may not cause erosion on the bed when moving. Thus, the non-erodible bed case is used to derive the submarine landslide governing equation in this study.

The hybrid FV/FD method is used to discretize the one-dimensional (1D) landslide governing equations in space. The approximate HLL Riemann solver and the TVD version limiter function are used to solve the advection term to deal with the discontinuity in the domain. While the simple forward FD method solves the slope term in the momentum equations. For solving time derivative of landslide model, the explicit third-order three-stage Runge–Kutta is applied.

2.2 Two-Layer Boussinesq Water Wave Model

The water wave governing equations are the two-layer Boussinesq equations which can simulate accurately the short waves. The continuity equation is given

$$\frac{\partial \zeta}{\partial t} + \nabla \cdot [(h_1 + \zeta) \bar{\mathbf{u}}_1] + \lambda_2 \nabla \cdot [(h_2 - h_1) \bar{\mathbf{u}}_2] + (1 - \lambda_2) \frac{\partial h_1}{\partial t} = 0 \quad (3)$$

As shown in Fig. 1, the water wave domain is composed of the upper-layer and the lower-layer, in which the lower-layer is the submarine landslide layer. Nevertheless, the lower-layer depth and velocity are the submarine landslide depth and velocity, respectively. The upper-layer momentum equation is given

$$\begin{aligned} \frac{\partial \bar{\mathbf{u}}_1}{\partial t} + \frac{h_1^2}{6} \nabla \left[\nabla \cdot \frac{\partial \bar{\mathbf{u}}_1}{\partial t} \right] - \left(\frac{1}{2} + \gamma_1 \right) h_1 \nabla \left[\nabla \cdot \left(h_1 \frac{\partial \bar{\mathbf{u}}_1}{\partial t} \right) \right] = -g \nabla \zeta - \bar{\mathbf{u}}_1 \cdot \nabla \bar{\mathbf{u}}_1 \\ + \gamma_1 g h_1 \nabla [\nabla \cdot (h_1 \nabla \zeta)] + \lambda_2 \frac{h_1}{2} \nabla \left\{ \nabla \cdot \left[(h_2 - h_1) \frac{\partial \bar{\mathbf{u}}_2}{\partial t} \right] \right\} + (1 - \lambda_2) \frac{h_1}{2} \nabla \frac{\partial^2 h_1}{\partial t^2} \end{aligned} \quad (4)$$

where variables ζ and $\bar{\mathbf{u}}_1$ are the water waves surface elevation and the depth-averaged velocity, which is the upper-layer, respectively, γ_1 (equal to 1/15) is the upper-layer tuning parameter which can extend the capability of this model to the deeper waters. g is the gravitational acceleration. Here, h_1 is the upper-layer water depth, which depends on time and space. The relation between upper-layer variation water depth and the submarine landslide surface is given

$$\frac{\partial h_1}{\partial t} = -\frac{\partial s}{\partial t}, \quad \frac{\partial h_1}{\partial x} = -\frac{\partial s}{\partial x} \quad (5)$$

Also, h_2 is the water depth till the bottom of the lower-layer, and then, $(h_2 - h_1) = (s - b)$ is the submarine landslide depth. Finally, $\bar{\mathbf{u}}_2$ and λ_2 are the depth-averaged velocity and the porosity inside the lower-layer, which is the submarine landslide layer, respectively. Here, we assume $\bar{\mathbf{u}}_2 = \mathbf{u}$, i.e., the water velocity inside the submarine landslide and the submarine landslide velocity are moving together.

It can be noticed that the last two terms in the continuity and the upper-layer momentum equations are the wave sources generating the tsunami. The first source terms, $\lambda_2 \nabla \cdot [(h_2 - h_1) \bar{\mathbf{u}}_2]$ and $\lambda_2 \frac{h_1}{2} \nabla \left\{ \nabla \cdot \left[(h_2 - h_1) \frac{\partial \bar{\mathbf{u}}_2}{\partial t} \right] \right\}$, are called the velocity terms, the second source terms, $(1 - \lambda_2) \frac{\partial h_1}{\partial t}$ and $(1 - \lambda_2) \frac{h_1}{2} \nabla \frac{\partial^2 h_1}{\partial t^2}$, are called the interface term. When no porosity is considered ($\lambda_2 = 0$), the submarine landslide surface is impermeable, then the set of Eqs. (3) and (4) are reduced to the one-layer Boussinesq equations [8].

Because the dispersive terms in the Boussinesq governing equations are composed of high-order spatial derivative terms, the high-order FD scheme is applied [9]. The famous Adams–Bashforth/Adams–Moulton predictor–corrector schemes are applied to discretize the governing equations in time. For spatial derivatives, an adaptive FD scheme is used to balance the truncation errors of the non-dispersive and the dispersive terms in the model equations.

3 Preliminary Numerical Results and Discussions

The one-layer numerical model, which is the case of the porosity inside the submarine landslide layer equal to zero, was verified with the experimental data in the one-dimensional domain of [10]. Interested readers can refer to [8] for more detail about the verification test of the one-layer numerical model.

For the two-layer numerical test, we investigate the preliminary numerical simulations of submarine landslide-induced tsunami in application to the 1D domain. Then, we compare the two- and one-layer numerical results and further discuss. To apply this two-layer model, the porosity value of 0.5, which implements the permeable property of the landslide layer, is taken into count in this test. Because of the limited pages in this paper, other details about the numerical domain and landslide parameters can be seen in Fig. 2a and referred to in [8], respectively. Due to submarine landslide triggering, the landslide model generates the landslide velocity (u_2) and the water depth (h_1) changing in time and space by Eq. (5). These parameters are included in the velocity terms and the interface terms in the two-layer Boussinesq governing equations (Eqs. 3 and 4). These source terms generate tsunamis. Figure 2b–d shows numerical results of landslides and tsunami at $t = 1$ s, 10 s and 50 s, respectively. Therein, the solid lines are the water and soil surface elevations, the dashed-dot lines are the initial locations of soil and the dashed lines are the non-erodible bottom elevations. The wave heights are magnified two times in this figure for visualization.

At $t = 1$ s, the landslide slightly moves down on the slope and the water wave immediately responds with a small amplitude of about 5 m. Right after that, at $t = 10$ s, the waves separate into the left- and the right-side components, which belong to the shallow water area and the deep water area, respectively. Further, at $t = 50$ s, the right-side waves move with constant two wave components while the left-side waves move with the increment of three wave components due to shoaling effect in the shallow zones. The wave amplitudes at the right- and left-side are stably about 8 m and 6 m, respectively.

Comparisons of one- and two-layer numerical results for the case of porosity of 0.5 at $t = 1$ s, 10 s and 50 s are shown in Fig. 3. At the starting time, e.g., $t = 1$ s, the two-layer wave amplitude is smaller than the one-layer one. After separating to the left- and right-side components, e.g., at $t = 10$ s and $t = 50$ s, the two-layer wave heights at the right-side are smaller than the one-layer ones, while the two-layer ones at the left-side are larger than the one-layer ones. Those can be mathematically proved by the velocity terms effect in the governing equations. Firstly, there are no velocity terms in the one-layer Boussinesq equations ($\lambda_2 = 0$). Secondly, in the two-layer Boussinesq equations, the velocity terms depend on both the porosity ($\lambda_2 = 0.5 > \lambda_2 = 0$ in the one-layer value) and the landslide depth ($h_2 - h_1$). This landslide depth is changing in time and space, but larger depth at the left-side and smaller at the right-side. That's why the two-layer wave heights decrease at the right-side and increase at the left-side comparing the one-layer ones.

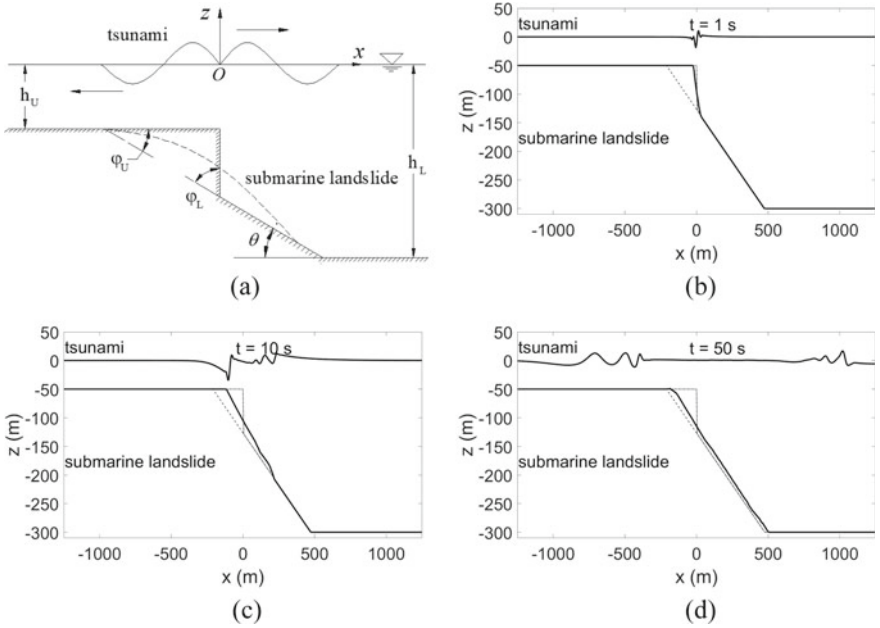


Fig. 2 Numerical simulations of two-layer submarine landslide-induced tsunami for the porosity of 0.5. **a** schematic of the application domain, **b** the numerical simulations at $t = 1$ s, **c** the numerical simulations at $t = 10$ s, **d** the numerical simulations at $t = 50$ s

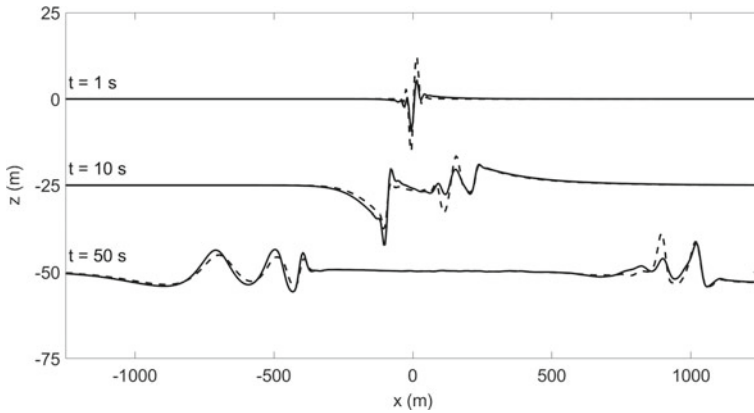


Fig. 3 Comparison of one- and two-layer simulations for the porosity of 0.5 at $t = 1$ s, 10 s, 50 s. The solid lines are the two-layer simulations, the dash lines are the one-layer simulations

4 Conclusion

This paper introduces the submarine landslide-induced tsunami model using two-layer extended Boussinesq equations. In this two-layer model, the lower-layer is defined as the water inside the porous submarine landslide layer and this water takes the submarine landslide velocity. The submarine landslides can be simulated using the NSWEs and a hybrid FV/FD method to deal with the discontinuity problems. The water waves can be simulated using the two-layer Boussinesq equations and the favorite high-order FD method. With the typical porosity value, the preliminary two-layer simulations of submarine landslides and generated water waves are presented together at several time steps to understand the inter-connected phenomena. The water wave elevations are compared with the one-layer results to see how the porosity effect. The differences as well as the explanations of those two results are investigated to understand the mathematical and physical fluid dynamics in realities. The two-dimensional model can be developed to simulate the real field domain of submarine landslide-induced tsunami in the future researches.

References

1. Yavari-Ramshe S, Ataie-Ashtiani B (2016) Numerical modeling of subaerial and submarine landslide-generated tsunami waves—recent advances and future challenges. *Landslides* 13(6):1325–1368
2. Fernández-Nieto ED, Bouchut F, Bresch D, Castro Díaz MJ, Mangeney A (2008) A new Savage–Hutter type model for submarine avalanches and generated tsunamis. *J Comput Phys* 227(16):7720–7754
3. Yavari-Ramshe S, Ataie-Ashtiani B (2017) A rigorous finite volume model to simulate subaerial and submarine landslide-generated waves. *Landslides* 14(1):203–221
4. Ma G, Kirby JT, Hsu T-J, Shi F (2015) A two-layer granular landslide model for tsunami wave generation: theory and computation. *Ocean Model* 93:40–55
5. Paris A, Heinrich P, Paris R, Abadie S (2020) The December 22, 2018 Anak Krakatau, Indonesia, landslide and tsunami: preliminary modeling results. *Pure Appl Geophys* 177(2):571–590
6. Savage SB, Hutter K (1989) The motion of a finite mass of granular material down a rough incline. *J Fluid Mech* 199:177–215
7. Pham VK, Lee C, Vu VN (2019) Numerical simulation of subaerial and submarine landslides using the finite volume method in the shallow water equations with (b, s) coordinate. *J Korean Soc Coast Ocean Eng* 31(4):229–239
8. Pham VK, Lee C, Vu VN (2021) Submarine landslide-induced tsunami model using nonlinear shallow water equations in (b, s) coordinate and extended Boussinesq equations. *J Transp Sci Technol* 40:139–145
9. Wei G, Kirby JT (1995) Time-dependent numerical code for extended Boussinesq equations. *J Waterw Port Coast Ocean Eng* 121(5):251–261
10. Rzakiewicz SA, Mariotti C, Heinrich P (1997) Numerical simulation of submarine landslides and their hydraulic effects. *J Waterw Port Coast Ocean Eng* 123(4):149–157

Selecting Optimal Marina Configuration with Regard to Mooring Safety and Port Area Water Exchange



Izmail Kantarzhi, Alexander Gogin, and L. G. Tran

Abstract The paper considers the configuration of protected port structures and the port gate position as required to ensure the port water area protection from wind waves as well as to provide sufficient water exchange. The object of research is the projected Gelendzhik yacht port located in the Gelendzhik Bay on the north-eastern coast of the Black Sea. Two configurations of protected port structures are compared herein. The wave propagation and water exchange we studied using numerical and physical modeling. The first configuration features the port gates open southeastward. This results in wind waves penetrating the port water area and being capable of forming wave beats which are dangerous for the mooring yachts. The second configuration, a more enclosed one, features the port gates open northeastward. In this case, there is a problem associated with the peculiarities of the wind-wave mode of the area, i.e., the existence of unusually strong offshore winds or “bora”. The paper proposes using SWAN to predict the waves generated by the “bora”. It allows estimating the waves from above. The closeness of the second configuration ensures the protection of the port water area even in “bora” conditions. The port area water exchange differs slightly in the two cases and seems satisfactory. The paper recommends the second configuration based on the results of the presented research.

Keywords Protected port structures · Port gates · Wind waves in the port water area · Water exchange · Numerical studies · Physical modeling

I. Kantarzhi (✉) · A. Gogin
National Research Moscow State University, Moscow, Russia
e-mail: IGKantarzhi@mgsu.ru

L. G. Tran
Vietnam Maritime University, Hai Phong, Vietnam

1 Introduction

The configuration of the port water area determined by many factors. These include wave penetration, port basin resonance, sediment accumulation, and water exchange between the harbor and the sea. In terms of yacht ports, the most important of them is the gate location, which affects the waves in the port and the safety of mooring yachts that are very sensitive to the wave height. Another important factor affecting the choice of the marina water area configuration is the water exchange between the harbor water area and the sea. The two aforementioned factors can often be competing. Indeed, if the gates of a port face the maximum wind direction, the wind currents entering the port and generated directly to the port water area will be maximum and provide intensive water exchange between the water area and the sea. However, such gate orientation maximizes wind entering the port water area and consequently the danger to mooring yachts that the waves can affect. The paper uses composite modeling methods [1–3] to find an optimal configuration of the port water area, providing for the permissible wave regime in the water area and ensuring sufficient water exchange. These methods are based on the balanced use of physical and numerical modeling, as well as field measurements and analytical studies.

Other factors, harbor resonance, and sedimentation are also important, though not addressed in this article. The results of studies into these processes, including those for the marina of Gelendzhik, which is considered in this article as an example, are presented in publications [4, 5]. Physical modeling is used for a local large-scale model and verifies numerical modeling. Examples of such solutions can be found in [6–9]. The main research method used to determine the intensity of water exchange between the port area and the sea is numerical modeling [10–12].

The yacht port in Gelendzhik Bay, the Black Sea has been researched and designed for several years now. The object is located on the Black Sea coast. In Gelendzhik Bay, on its south-western shore of the bay (Fig. 1). The bay is open for south and south-west winds, which are quite strong here. In addition, the bay is subject to a “bora”, a strong northeast wind from the shore. In Gelendzhik its speed reaches 40–50 m/s. The maximum wave height of 4.7 m in the bay according to the observations of the Gelendzhik Hydrometeorological Station were observed from the NE, with the “bora” wind being its generator. Maximum wave heights from the sea were observed from the S and SW directions and amounted to 4.0 m and 4.2 m, respectively.

The initial configuration of the protected structures and the water area of the port is shown in Fig. 2a. Because of the specific shape of the protected moles, this configuration was called “crab claws”. The modified port configuration (2018) is shown in Fig. 2b. The differences of the new configuration of the projected port are primarily that the port gates face the north-east. This solution should protect the port water area from storms of southern and south-eastern directions. However, it is obvious that the waves generated by the bora are becoming more dangerous for the port water area. Naturally, there arises the question of the role this wind plays in the generation of a wave regime in the port water area. The article shows the research methods and presents the results obtained.



Fig. 1 Design area in Gelendzhik Bay

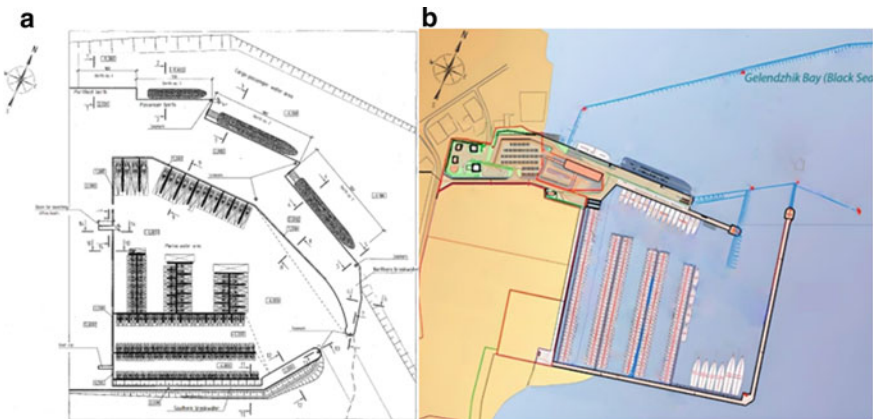


Fig. 2 (a–left) Configuration of the port area, (b–right) proposed configuration

2 Materials and Methods

When implementing projects for scientific and technical support of engineering projects, both the open-source models are used, including the WRF meteorological model, the SELFE oceanographic model, the generation and propagation of wind waves spectral models Wave Watch and SWAN. SWAN is one of the most renowned programs for numerical modeling of wind waves for ports. This software is used in many projects, there is a significant amount of research on verification of wave SWAN simulation results [13–19].

To predict the wave climate in the seaport of Gelendzhik, an open-source wave model ARTEMIS based on the elliptical equation of mild slope was chosen. The ARTEMIS model [20] is based on the equations of mild slope [21, 22]. The model describes the transformation of waves in the coastal zone and is presented in the public domain at the website of the TELEMAC modeling complex [23].

Physical modeling of waves on the model of Gelendzhik seaport was carried out in the shallow water wave basin of the Moscow State University of Civil Engineering (MSUCE). The scale of the simulation was selected based on the planned size of the basin and the size of the simulated port. Since, the dimensions of the basin are $30\text{ m} \times 30\text{ m} \times 1.1\text{ m}$, and the physical model of the port was made in the scale $M = 1:50$.

The hydrodynamic model Semi-implicit Eulerian Lagrangian Finite Element (SELFE) is used. This open-source model for coastal modeling is being developed by an international team of authors [24–27]. Model documentation, sample model applications, and a list of publications using the model are publicly available on the site <http://www.stcmop.org/CORIE/modeling/selfe/>.

3 Results

Wind waves were calculated on four nested rectangular grids. The first grid covers the water area of the entire Black Sea, the last—water area of the projected port (Fig. 3a). To select the strongest storms, wave fields for the entire Black Sea were calculated on the rough grid for 24 years, 1989–2012, as this is the period for which reliable reanalysis data are available. Then the five strongest storms were selected (Table 1) and for them calculations were carried out on three more detailed nested grids.

To construct the extreme wave fields of different exceedance probability, the maximum values of wave heights in nodes of the fourth grid for each year were selected. The so-called generalized extreme-value (GEV) distribution was used. For

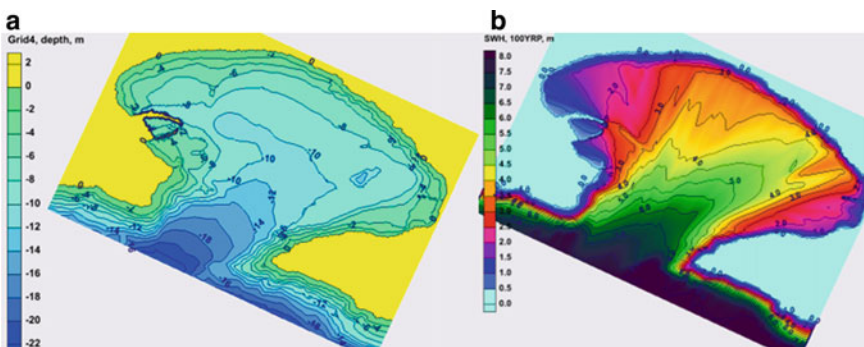


Fig. 3 (a–left) Area of calculation grid No. 4, (b–right) significant waves possible once in 100 years for Gelendzhik Bay

Table 1 Dates of five storm scenarios and parameters of maximum waves on the approach to Gelendzhik Bay

No	Start of the storm	End of the storm	Peak storm	Maximum wave height (m)	Angle of wave approach (deg)
1	2007.11.05	2007.11.16	2007.11.11	8.02	235
2	1989.12.03	1989.12.11	1989.12.07	7.25	240
3	1993.01.16	1993.01.27	1993.01.23	7.15	239
4	2003.01.30	2003.02.06	2003.02.01	7.06	223
5	2001.12.25	2001.12.31	2001.12.30	6.97	232

each point of the grid, the parameters of the Weibull distribution were obtained, according to which the values of the heights of the waves of rare repetition were calculated. The significant waves heights (13%) of the repeatability once every 100 years for Gelendzhik Bay are shown in Fig. 3b.

The bathymetry of the design area of the ARTEMIS model is shown in Fig. 4a. The height of monochromatic waves significantly depends on the direction of the waves approaching the port. So, for calculated waves approaching the port under the direction of 155 deg (SE), the wave heights in the north-western corner of the water area reach 2.4 m—Fig. 4b.

Numerical modeling has shown to fully reproduce the nature of the excitement observed in the physical experiment. The program of experimental studies provided for four experiments on the impact of waves from storms of 5% exceedance probability. The numerical modeling has shown to fully reproduce the nature of the excitement observed in the physical experiment. The large-amplitude excitement at the root of the northern breakwater is registered in the corner of the water area farthest from the entrance to the port. This corresponds to the standing wave observed on modeled by ARTEMIS. Over the physical modeling the overflow of waves through the Northern breakwater was recorded.

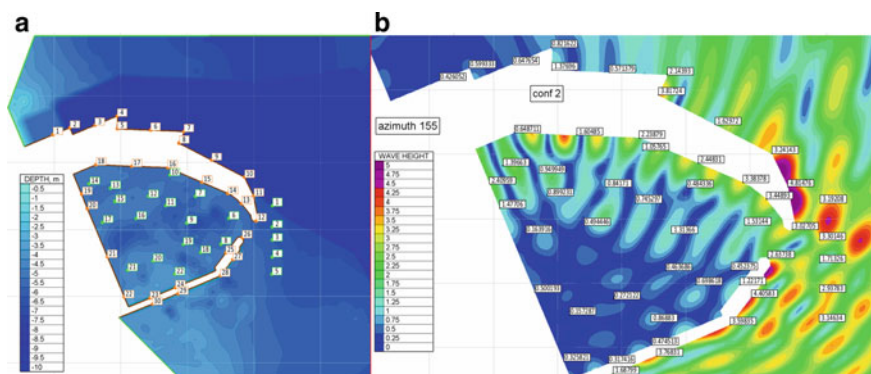


Fig. 4 (a–left) Bathymetry of the design domain of the ARTEMIS model, (b–right) wave heights in the port, calculated for a wave repeatability 1 time in 100 years

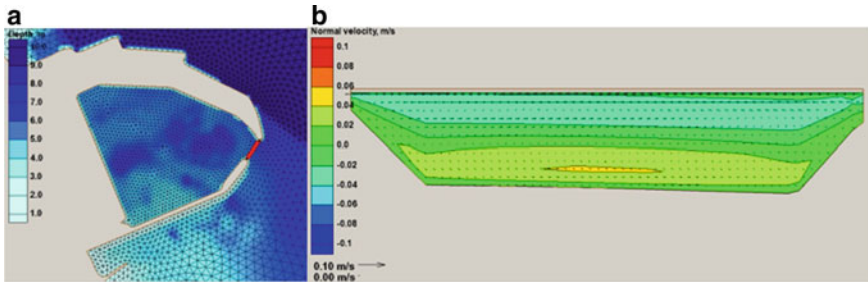


Fig. 5 (a–left) Vertical cross-section for calculation of the water exchange, (b–right) vertical cross-section of normal velocities at the entrance to the port

However, in Gelendzhik Bay, in addition to the waves entering into the bay from the sea, waves can also be generated directly in the bay under the strong northeast wind, called “Nord-ost” or “bora”, typical for this region. Waves generated by bora can be comparable in height with the waves of the highest sea storms entering the bay. To obtain appropriate estimates, the SWAN model conducted a simulation of the wave generation under a northeast wind with speeds of 30 and 35 m/s. It was obtained that height of significant waves generated by bora in the port area can reach 1,38 and 1,71 m, respectively.

The calculations of water exchange were carried out using a hydrostatic version of the SELFE model with a time step of 10 s. At the entrance to the Gelendzhik Bay, radiation conditions were set for the velocities, water level, temperature, and salinity. Based on the analysis of the archive of meteorological data for 1991–2011 from the ERA-interim database, the extremely warm year 2010 was selected for modeling, assuming that meteorological conditions this year are most unfavorable for the water exchange. The water exchange was calculated for vertical cross-section of the port gate, shown by red line in Fig. 5a. Figure 5b shows the example of circulation at the entrance section in the upper layer is directed toward the port, while in the lower layer goes in the opposite direction.

Average water discharge of water exchange, $Q_e = 2.21 \text{ m}^3\text{s}^{-1}$. Water renewal in the port water area time T_e is determined by the flow rate of water exchange Q_e and the volume of water of the port basin V (Eq. (1)).

$$T_e = \frac{Q_e}{V} \quad (1)$$

It is about 3.0 days in summer conditions, characterized by relatively weak wind circulation.

Thus, the results of research show that the proposed configuration of the port ensures acceptable water exchange of the port water with the bay waters. However, the protection of the water area from waves is not ensured. The cargo and passenger berths placed outside of the North mole are also threatened. Therefore, it was proposed to change the configuration of the port protected structures.

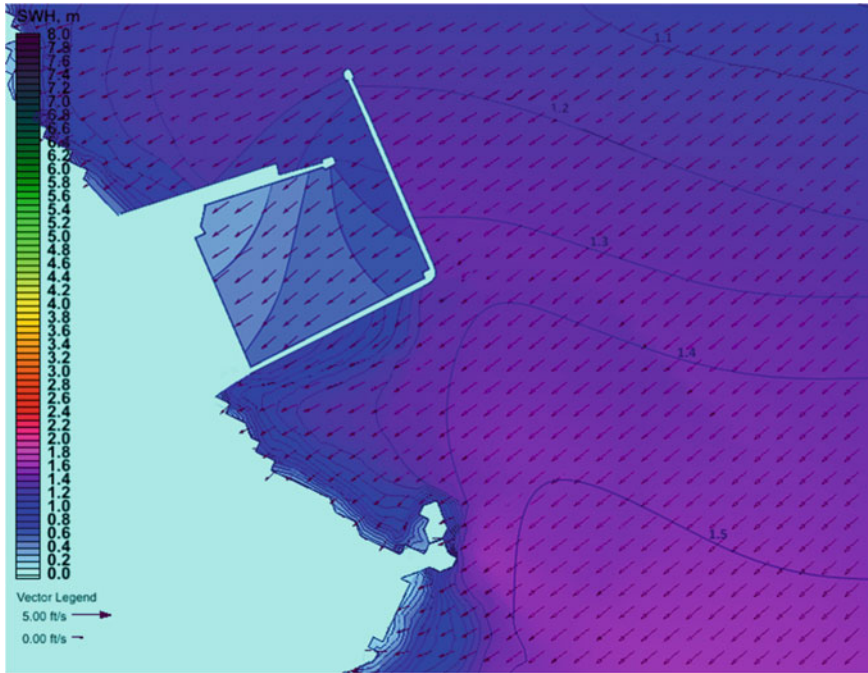


Fig. 6 Wave heights in the seaport of Gelendzhik, the example of simulation

The proposed configuration of the port makes the waves generated by extreme northeast winds (bora) the most interesting. To calculate the waves the author used a SWAN model. The analysis of the simulation results allows concluding that with the new layout, the port water area is sufficiently protected from the waves from the NE direction. Wave fields obtained by numerical simulations demonstrate that the waves enter the port water area only due diffraction (Fig. 6).

In the water area of the port, the waves do not exceed 0.3 m. This allows to conclude that the proposed port configuration allows to reduce the height of waves in the port water area (2.4 m due to strong reflection and standing waves by the first configuration) to 0.3 m by the proposed configuration.

Modeling of the port water exchange in the modified Gelendzhik Bay layout was carried out similarly to that of the initial layout. The calculations were carried out for the selected summer period July–August of 2010, according to the specified values of the meteorological parameters. The average water exchange flow rate, determined by the cross-sectional area of the port gate and calculated input and output flow rates, is $Q_e = 2.8 \text{ m}^3 \text{ s}^{-1}$. The average water exchange time, T_e , equals three days during a summer, characterized by a relatively weak wind circulation. Thus, the intensity of the water exchange for the new layout of the port is nearly the same as the intensity of water exchange for the original layout.

4 Conclusions

The numerical modeling of waves generated by the bora wind shows that classical wind-wave programs such as SWAN are applicable for this and allow at least getting an estimate from above for the waves. The completed studies of the optimal layout of the projected yacht port of Gelendzhik allow selecting a rational solution for the factors of wave height in the port area and the water exchange. The main results of the research are presented in the article. Studies of the final version of the port layout showed that even the waves formed by the “bora” with a sufficiently closed water area do not create dangerous waves in the water area close to the berths. Wave fields obtained by numerical simulations demonstrate that the waves enter the water area of the port only due diffraction. At the same time, the water exchange is sufficient.

References

1. Sutherland J, Barfuss SL (2011) Composite modelling: combining physical and numerical models. In: Proceedings of the 34th IAHR World Congress, Brisbane, Australia
2. Kantarzhi I, Anshakov A, Gogin A (2021) Composite modelling of wind waves in designing of port hydraulic structures. In: Proceedings of the thirty-first international ocean and polar engineering conference, vol 3, pp 2254–2261
3. Hadla G, Anshakov A, Kantarzhi I (2020) Composite modelling in port engineering. In: Proceedings of FORM-2020, IOP conference series: materials science and engineering, vol 7, pp 1–9
4. Kantarzhi I, Zheleznyak M, Sorokin M, Polyakov A (2015) Resonance characteristics of the waters of seaports. *Mag Civil Eng* 5:3–19
5. Kantarzhi I, Zheleznyak M, Kivva S, Kolomiets P, Demchenko R, Sorokin M (2015) Numerical study of coastal processes in Gelendjik Bay, effect of the proposed port. In: Proceedings of the international geographical union regional conference geography, culture and society for our future earth, IGU2015 – 0515, 1333
6. Van Mierlo (2014) Numerical modelling of wave penetration in ports. MSc Thesis. Delft, pp 119
7. Kantardgi IG, Zheleznyak MJ (2016) Laboratory and numerical study of waves in the port area. *Magazine Civil Eng* 6:49–59
8. Kantarzhi I, Zheleznyak M, Sorokin M (2017) Verification of model waves in the port area with laboratory measurements. In: Proceedings of MEDCOAST 17, vol 2, pp 979–990
9. Kantarzhi IG, Mordvintsev KP, Gogin AG (2019) Numerical analysis of the protection of a harbor against waves. *Power Technol Eng* 53(4):410–417
10. Kantarzhi I, Maderich V, Terletskaya E, Brovchenko I, Prokhoda-Shumskikh L (2013) Water quality protection: Grand-Marina, Sochi. In: The proceedings of the global congress on ICM: lessons learned to address new challenges, EMECS 10—MEDCOAST 2013, vol 1, pp 989–1001
11. Kantarzhi I, Maderich V, Sharova V (2015) Water exchange aspects for new seaport in Gelendjik Bay (Black Sea). In: 12th international conference on the mediterranean coastal environment, MEDCOAST, vol 2, pp 657–667
12. Kantarzhi IG, Krukovets AE (2021) The modeling of an emergency fuel spill in a port. *power technology and engineering* 55(3):331–339
13. Booij N, Ris RC, Holthuijsen LH (1999) A third-generation wave model for coastal regions 1. Model description and validation. *J Geophys Res* 104(C4):7649–7666

14. Kantarzi I, Kuznescov K (2014) Field measurements of waves to define the loads on the sea hydraulic structures. *Magazine Civil Eng* 4:49–62
15. Akpınar A, Bingölbali B (2016) Comparison of the calibrated SWAN models' performances forcing with different winds in the black sea. In: *Proceedings of ICSD international conference on sustainable development*
16. Ilic S, van der Westhuysen AJ, Roelvink JA, Chadwick AJ (2007) Multidirectional wave transformation around detached breakwaters. *Coast Eng* 54:775–789
17. O'Donnell AIJ (2018) An assessment of two models of wave propagation in an estuary protected by breakwaters. *J Mar Sci Eng* 6:145
18. Mao M, van der Westhuysen AJ, Xia M, Schwab DJ, Chawla A (2016) Modeling wind waves from deep to shallow waters in Lake Michigan using unstructured SWAN. *J Geophys Res Oceans* 121:3836–3865
19. Cooper AH, Mulligan RP (2016) Application of a spectral wave model to assess breakwater configurations at a small craft harbour on Lake Ontario. *J Mar Sci Eng* 4:46
20. Aelbrecht D (1997) A finite element model for predicting wave agitation in coastal areas and harbours including dissipation. *Trans Built Environ* 27:343–352
21. Berkhoff JC (1972) Computation of combined refraction-diffraction. In: *The Proceedings of 13th coastal engineering conf vol 1*, pp 471–490
22. Berkhoff JC (1976) *Mathematical models for simple harmonic linear water waves, wave diffraction and refraction*. Delft Hydraulic laboratory. Publ. N 163
23. Hervouet JM (1999) TELEMAC, a hydroinformatic system. *La Houille Blanche* 3–4:21–28
24. Zhang Y-L, Baptista AM (2008) SELFE: a semi-implicit Eulerian-Lagrangian finite-element model for cross-scale ocean circulation. *Ocean Model* 21(3–4):71–96
25. Roland A, Zhang YJ, Wang HV, Meng Y, Teng Y-C, Maderich V, Brovchenko I, Dutour-Sikiric M, Zanke U (2012) A fully coupled 3D wave-current interaction model on unstructured grids. *J Geophys Res* 117(C00J33):1–18
26. Bertin X, Oliveira A, Fortunato AB (2009) Simulating morphodynamics with unstructured grids: description and validation of a modeling system for coastal applications. *Ocean Model* 28(1–3):75–87
27. Burla M, Baptista AM, Zhang Y, Frolov S (2010) Seasonal and interannual variability of the Columbia River plume: a perspective enabled by multiyear simulation databases. *J Geophys Res* 115(C00B16)

Wave Reflection from Typical Sloping Dike in the North of Vietnam



Thi Phuong Thao Nguyen

Abstract The sloping revetment and the crest configurations appear to have important effect on wave reflection, especially the presence of crown walls may cause higher reflected wave and might modify the cross-shore current, and eventually affect the sea dike toe scour during storms. In this paper, the degree of wave reflection as well as the distribution of reflected wave are investigated through a series of fix-bed flume model experiments. Based on previous studies, a new spatial autocorrelation function that described the distribution of reflection coefficient in the vicinity of sea-dike structure, has been developed for sloping dike in the north of Vietnam.

Keywords Wave reflection · Sloping dike · Fix-bed model · Crown walls · Overtopping

1 Introduction

The reflected wave from coastal structure cause increased agitation of water in front of structure, and they propagate some distance to become a source of disturbance in area of water. In the north of Vietnam, sea dikes were usually built with crown walls as a measure against wave overtopping is commonly used on low-crested coastal dikes. That may lead to extra scouring of sea-dike toe especially due to high waves during storm. Therefore, the degree of wave reflection as well as the distribution of reflected wave need to be quantified. The coefficient of wave reflection K_r , which is the ratio of reflected wave height to incident wave height, is used to the wave reflection. Reflection coefficients for most structures are usually estimated by mean of laboratory model test. It depends on the slope characteristics, geometrical and configuration structures, incident waves. At reflective structures, the range of K_r vary from 0.05 to 0.2 for case of natural beach and approximate 1.0 for vertical wall [1, 2].

T. P. T. Nguyen (✉)
ThuyLoi University/TLU, Hanoi, Vietnam
e-mail: Thao.n.p@tlu.edu.vn

Seelig [3] has given empirical formula to estimate the reflection coefficient for beaches, revetments, and rubble mound breakwaters depend on Iribaren number ξ_0 :

$$K_r = \frac{a \cdot \xi_0^2}{b + \xi_0^2} \tag{1}$$

In which: a, b are empirical coefficients determined from experiment data, for slope $\cot\beta \leq 6$, suggested coefficients are $a = 1.0$ and $b = 5.0$; a, b coefficients from various sources are listed by Lam [4]. $\xi_0 = \tan / \sqrt{H_{m0}/L_0}$ with $\tan\beta$ is slope of dike, H_{m0} and L_0 are local wave height and deep water wave length.

Zanuttigh [5], based on an extensive database of more than 4000 data, analyzes wave reflection for various types of coastal structures in design conditions, such as smooth, rock and armour unit slopes, and developed the formula that K_r depends not only on Iribaren parameter, but also depends on roughness factor γ_f :

$$K_r = \tanh(a\xi_0^b) \tag{2}$$

$$a = 0.167[1 - \exp(-3.2\gamma_f)]; \quad b = 1.49(\gamma_f - 0.38)^2 + 0.86$$

Zanuttigh [5] also has examined the effect of a low crest on K_r for rock permeable slopes only. The formula is corrected by introducing a proper linear dependence on the relative crest height R_c/H_s : $K_r = K_{r(eq2)} * (0.67 + 0.37R_c/H_s)$ with $-1 \leq R_c/H_s \leq 0.5$.

In which R_c is crest freeboard, H_s is significant wave height.

Van de Meer [6] had done the research on wave transformation and reflection at low-crested structures based on more than 150 tests from four projects, gives a more elaborated formula for rock slopes in the Rock Manual, and proposed the simple relationship for low-crested structures with reduction factor f_r on K_r :

$$f_r = 0.2R_c/H_s + 0.9 \quad R_c/H_s < 0.5$$

$$f_r = 1 \quad R_c/H_s \geq 0.5$$

Another way to defined reflection coefficient is given by Sheremet et al. [7], based on ratio of cross-shore energy fluxes of shoreward and seaward propagating waves:

$$K_r^2 = \frac{F^-}{F^+} \tag{3}$$

The seaward F^- and shoreward F^+ fluxes are determined by the following formula:

$$F^\pm = \int_{f_L}^{f_U} \frac{1}{4} \sqrt{gd} \left[S_{\eta\eta}(f) \pm (2\sqrt{d/g}) S_{\eta u}(f) + \frac{d}{g} S_{uu}(f) \right] df \tag{4}$$

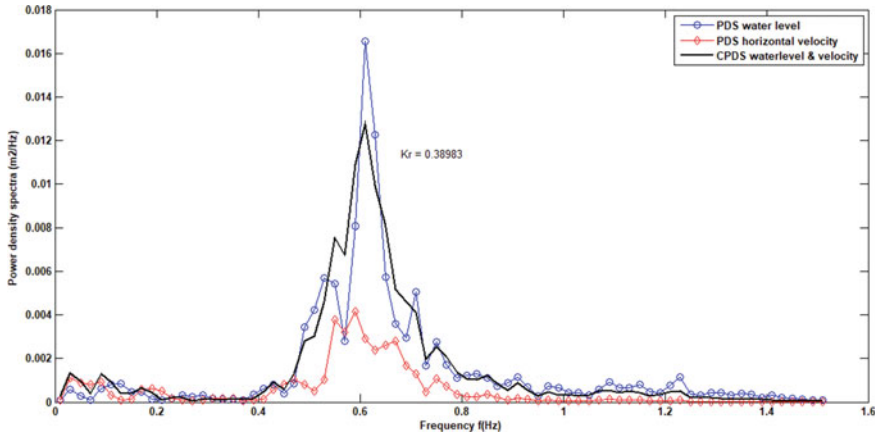


Fig. 1 Power density spectra to calculate reflection coefficient

In which: d is water depth; $S_{\eta\eta}$ and S_{uu} are wave and cross-shore velocity spectral density respectively; $S_{\eta u}$ is the η — u co-spectrum; f is frequency.

The reflection coefficients were obtained from the collocated wave height and cross-shore velocity u time series which are measured in front of structure in experiment tests (Fig. 1).

According to Klopman and Van der Meer [8], ratio between measured and incident wave height at a certain location (x) $H_{m0,x}/H_{m0i,x}$ in the vicinity of reflective structures depends on the reflection coefficient K_r as following:

$$\frac{H_{m0,x}}{H_{m0i,x}} = (1 + 2F_x(x/L)K_{r,0} + K_{r,0}^2)^{0.5} \tag{5}$$

In which $F_x(x/L)$ denotes the spatial autocorrelation function that described the distribution of K_r along the cross-section.

- At $x = 0$ (toe of structure) $F(\frac{x}{L}) = 1$ and $H_{m0}(0) = (1 + K_r)H_{m0i}(x)$
- Far away from structure $F(\frac{x}{L}) = 0$ and $H_{m0}(\infty) = H_{m0i}(x)\sqrt{1 + K_r^2}$

How fast the wave height approaches this limit depends on the form of $F_x(x/L)$, and this function is determined by the shape of incident wave spectrum.

Preceding studies show that a number of formula to define the reflection coefficient were developed based on data from laboratory tests and mostly focus on reflection due to the breakwater and sea wall, the effect of sloping sea dike specially with crown wall on reflected wave are still not considered well yet. Therefore, the reflection coefficient and its distribution in front of sea dike in the north of Vietnam are investigated by setting up experimental wave flume model.

2 Experimental Setup and Program

The objective of experiment is to get data of collocated wave parameters and current at a number of points in front of dike in order to analysis wave reflection according to the approach by Sheremet et al. [7]. The experiments of fix-bed models were carried out based on the following aspects:

- The laboratory conditions at Hydraulic laboratory of ThuyLoi University: The wave flume is 45 m long, 1.2 m height, 1.0 m width and the wave maker is equipped with an automatic system of active reflection compensation (ARC). Random wave with standard JONSWAP spectra can be generated with maximum wave height (H_{m0}) of 0.25 m and peak period (T_p) of 2.5 s.
- The prototype conditions: The beach topography and sea-dike geometrical configuration, testing hydraulic forcing boundary conditions are based on the prototype of Northern Vietnam.
- The model scaling is according to Froude criteria [1]. the dike model dimensions and testing hydraulic conditions are selected in accordance with the model length scale $N_L = 9.0$ and the time scales $N_T = 3.0$.
- The experimental setup is illustrated in Fig. 2. There are three types of geometrical dike model: (1) low dike with crown wall (80 cm dike height combined with crown wall heights of 10 cm); (2) low dike without crown wall (90 cm dike height); (3) very high dike (no wave overtopping and no crown wall). Dike slope is 1/3. Wave overtopping discharges were collected by a tank at the lee side of dike. In order to maintain the still water level during testing, overtopped water was pumped back to the flume at the back side of wave generator.

Goda and Suzuki [2] suggested that the wave gauges are recommended to be located at the distance of more than one wavelength from the test structure. So the collocated wave (WG) sensors and current meters (CG) were positioned at 9 points in front of dike with distance from dike toe: $x = -0.2$ m; 0 m; 0.25 m; 0.5 m; 1.0 m; 1.5 m; 2.0 m; 2.5 m; and 5.0 m. Waves were also measured at the wave board boundary, in middle of the beach, and in front of the dike (five-gauge array).

- Duration of each test was $300 * T_p$.

The test program as the result of various combinations between the dike geometric and hydraulic parameters is summarized in Table 1. Figure 3 presents photos of the

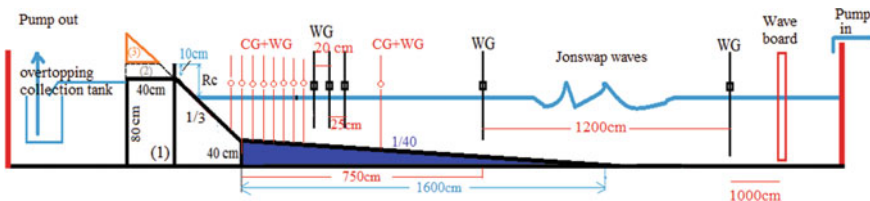


Fig. 2 Experimental setup

Table 1 Summary of tested dike geometrical and hydraulic parameters

N ⁰	Test name	Dike models (slope:1/3)	Crown wall height w(cm)	Wave parameters		Freeboard R _c (m)
				H _{m0} (m)	T _p (s)	
1	KB2	High dike (no overtopping)	0	0.17	1.6	0.25
2	KB3			0.15	1.9	0.2
3	KB4			0.19	1.65	0.2
4	KB5	Low dike (overtopping)	0	0.15	1.9	0.25
5	KB6			0.17	1.6	0.25
6	KB7			0.15	1.9	0.2
7	KB8			0.19	1.65	0.2
8	KB9		10	0.15	1.9	0.25
9	KB10			0.17	1.6	0.25
10	KB11			0.15	1.9	0.2
11	KB12			0.19	1.65	0.2

model dikes as built (1–3). The data of wave height and horizontal velocity were collected by professional software installed in the computer (4).

3 Result Analysis

From collocated wave height and velocity data at nine positions as mentioned above, reflection coefficient K_r is determined by applying the Sheremet et al. [7] formula (3) for 11 tests.

The distribution of reflection coefficients K_r is plotted against the relative distance (x/L) (with L is local wave length) in Fig. 4. The result show reflection coefficient generally decreases as the relative distance increases, especially from water line to position $x/L < 0.75$ and approach a constant at distance $x/L \gg 1.0$. For the degree of wave reflection, the values of K_r in high dike without overtopping tests are smaller than that of low dike cases, and highest for the case of low dike with the presence of crown wall.

In order to reduce the scatter of K_r data, chose K_r at the boundary which it remains constant value and named K_{r0} . K_{r0} is different from each test, depends on the wave parameters and dike geometrical configurations. The ratio between local K_r and K_{r0} are presented in Fig. 5. The changing rules of K_r at vicinity dike structure can be seen more clearly.

Apply the formula Klopman and Van de Meer [8] (Eq. (5) as mentioned above) to calculate the change of ratio between measured total wave height and incident wave height $H_{m0,x}/H_{m0i,x}$ in front of dike. In which $F_x(x/L)$ is function of (x/L), the asymptotical value of this function are:



Fig. 3 Photo of dike models as built

$$\begin{aligned}
 F_x &= 1.0 & x/L &= 0 \\
 F_x &= 0 & x/L &\gg 1 - 2
 \end{aligned}
 \tag{6}$$

(5) combined (6) can be expressed as:

$$\frac{K_{r,x}}{K_{r,0}} = \left(1 + \frac{2}{K_{r,0}} F_x(x/L) \right)^{0.5}
 \tag{7}$$

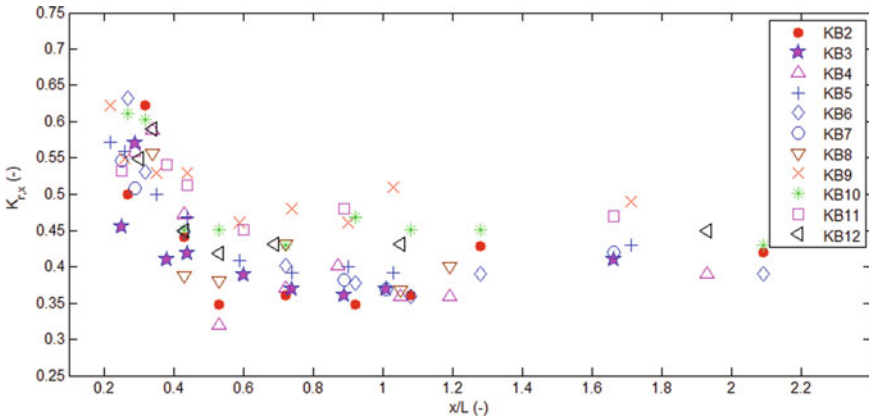


Fig. 4 Distribution of reflection coefficient in front of sea-dike

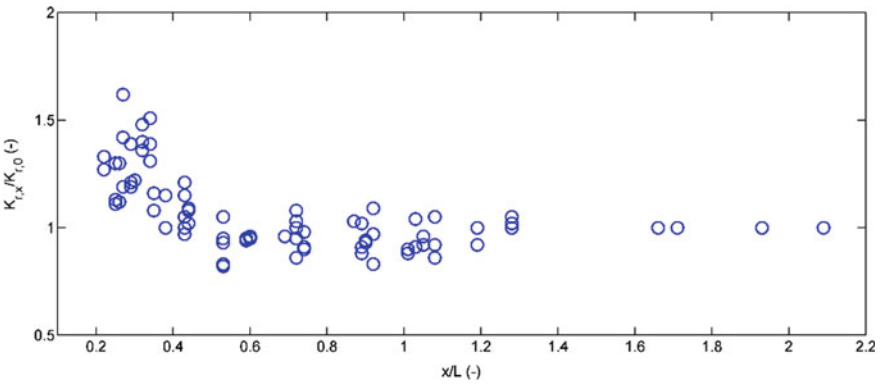


Fig. 5 Distribution of dimensionless reflection coefficient in front of sea-dike

Based on measured data of $K_{r,x}/K_{r,0}$ and reflection coefficient at boundary $K_{r,0}$, the relationship $F_x \sim x/L$ can be determined. The result is shown in Fig. 6. The reflection coefficient changes dramatically from dike toe to a distance $x = 0.6 L$.

Analysis regression function $F_x(x/L)$ with laboratory data and considering the asymptotical value at boundaries gives the result of $F_x(x/L)$ as following ($R^2 = 0.55$):

$$F_x\left(\frac{x}{L}\right) = \exp\left(-6.65\frac{x}{L}\right) \tag{8}$$

The formula (5) combined with Eq. (8) can be used to define $K_{r,x}$ and incident wave height variation in front of sea dike. $K_{r,0}$ is estimated roughly by Eq. (1) or (2). In case of crown wall presence, the equivalent dike slope is used.

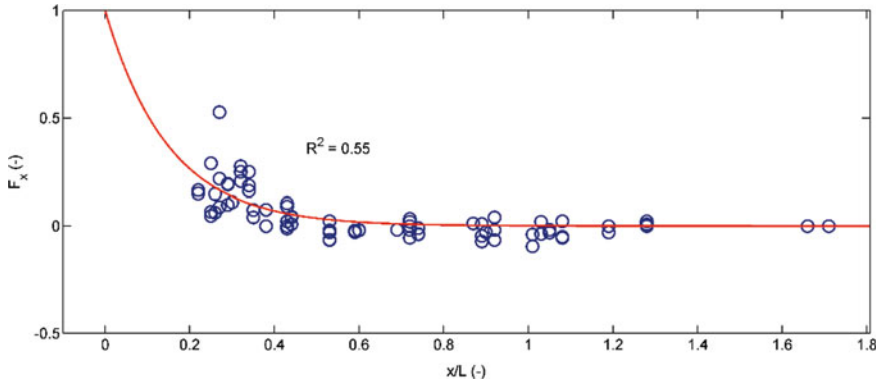


Fig. 6 Result of spatial autocorrelation function $F(x/L)$

4 Conclusions and Remarks

Based on the physical model data for sloping dike in the north of Vietnam, a new simple formula (8) combined with formula from Klopman and Van de Meer [8] (5) has been proposed to predict K_r and incident wave height. That can be used to evaluate the effect of reflected wave on cross-shore current and sea dike toe erosion due to storm waves.

Depending on the geometrical and structural configuration of sea dike as well as hydrodynamic parameters, the variation of wave reflection changes differently in vicinity of structure. Based on Fig. 5, $K_{r,0}$ should be determined at the distance $x \sim 1.3L$. Goda [2] shows that the effects of reflected wave for sea wall vary in the distance $x \sim 1.0 L_0$. Klopman and Van de Meer [8] show that distance is about $0.4 L$ for breakwater. This research shows the result is about $0.6 L$ for sloping dike.

References

1. Hughes S (2005) Physical models and laboratory techniques in coastal engineering, 3rd ed., Singapore: World scientific
2. Goda Y, Suzuki Y (1976) Estimation of incident and reflected waves in random wave experiments. Coastal Eng pp 828–845
3. William S, Ahrén J (1981) Estimation of wave reflection and energy dissipation coefficients for beaches, revetments and Breakwater. U.S. Army Coastal Engineering Research Center, Fort Belvoir, Virginia
4. Lam NT (2020) Sóng gió, Nhà xuất bản Bách Khoa Hà Nội
5. Barbara Z, Van De Meer (2008) Wave reflection from coastal structures in design conditions. Coast Eng
6. Van der Meer JW, Briganti R, Zanuttigh B, Wang B (2005) Wave transmission and reflection at low-crested structures: Design formulae, oblique wave attack and spectral change, Coast Eng, p. 52 (915–929)

7. Sheremet A, RT Elgar, CHerbbers TH (2002) Observations of nearshore infragravity waves: seaward and shoreward propagating components. *J Geophys Res*, pp 107(C8):3095
8. Klopman G, van der Meer J (1999) Random Wave Measurements in Front of Reflective Structures. *J Waterw Port Coast Ocean Eng, ASCE*, 125:1(39). [https://doi.org/10.1061/\(ASCE\)0733-950X](https://doi.org/10.1061/(ASCE)0733-950X).

The Mechanism of Large-Scale Flow Circulation at Asymmetric Sand Spit Inlet: A Case Study in Degi Estuary, Binh Dinh Province



Vu Van Ngoc, Tran Thanh Tung, and Nguyen Quang Duc Anh

Abstract Vietnam's south central coast, from the Quang Ngai province to the Binh Thuan province, is characterized by many asymmetrical inlets with a protruding rocky headland on one side and an elongated sand spit on the other side. The rocky headlands can be located in the North, such as at De Gi inlet and the Tam Quan inlet, or in the South, such as at the My A inlet and the Da Nong inlet. Under certain hydrodynamic conditions, a large-scale flow circulation may emerge at these inlets due to the asymmetrical topography. However, the formation mechanisms and hydrodynamic parameters that drive the evolution of a large-scale flow circulation of asymmetrical sand spit inlet have not been clarified. This paper describes simulated flow patterns at De Gi inlet in the Binh Dinh province under various wave and tide conditions. The findings, based on numerical simulation results, will reveal the mechanism of large-scale flow circulations and their relationship to the physical characteristics of sand spit inlets on Vietnam's South Central Coast.

Keywords De Gi inlet · Large-scale flow circulation · Asymmetrical inlets · Sand spit · South central coast

1 Introduction

Estuaries on Vietnam's south central coast are critical to the region's economic development. Coastal erosion and estuary sedimentation have become severe issues in recent years, posing serious hazards to the safety of residential areas, impeding flood drainage, causing navigation issues, and harming production and socioeconomic

V. Van Ngoc (✉)
Vietnam Academy for Water Resources, Hanoi, Vietnam
e-mail: ngoc_klorce@vawr.org.vn

T. T. Tung · N. Q. D. Anh
Thuyloi University, Hanoi, Vietnam

© The Author(s), under exclusive license to Springer Nature Singapore Pte Ltd. 2024
T. Nguyen-Xuan et al. (eds.), *Proceedings of the 4th International Conference on Sustainability in Civil Engineering*, Lecture Notes in Civil Engineering 344,
https://doi.org/10.1007/978-981-99-2345-8_26

263

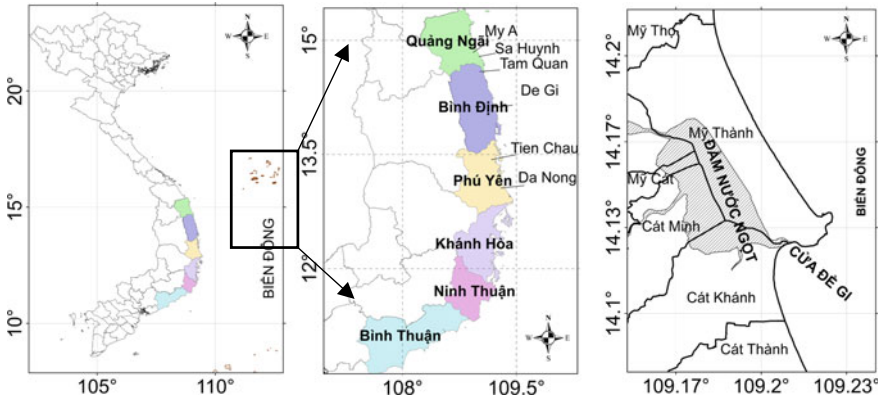


Fig. 1 Vietnam South Central estuaries and De Gi estuary

growth [1, 2]. The estuaries' shapes are diverse due to the topography and hydrodynamic conditions. The most notable example is the asymmetrical estuary, which has a rocky promontory projecting into the sea on one side and an extensive sand spit on the other. There may be a lagoon or bay inside this sort of estuary, such as the Da Nong estuary (in Phu Yen province), My A inlet (in Quang Ngai province), Tam Quan inlet, and De Gi inlet (in Binh Dinh province) [3] (Fig. 1). Because of the interlacing of the asymmetrical estuary's topography and the regulatory works, the estuaries' hydrodynamic and morphodynamic processes have become more intricate. Although complicating hydrodynamic conditions, the efficiency of stabilization structures in asymmetrical estuaries is limited. Eddy flow, which occurs regularly in the estuary's shadow zone, is an essential component that must be carefully studied [3, 4]. Practical observations and the theoretical basis of the cross-sectional boundary layer have been used to explain the formation of local eddy flow in the estuarine region. They have not been confirmed by precise calculations and demonstrated the various characteristics of each specific example compared to the basic principle outlined above. The authors will examine the mechanism of large-scale circulation development and its impact on sedimentation at De Gi Estuary, located in My Chanh Commune and Cat Minh Commune of Phu Cat District, Binh Dinh Province (Figs. 1 and 2).

2 Dataset and Methodology

The data used to carry out this study is inherited from previous studies, as shown in Figs. 3 and 4 [5, 6]. The dataset includes the topography condition, water level, and current characteristics measured at De Gi Estuary in 2012 and 2021. The National Oceanic and Atmospheric Administration provided additional data, such as deep water waves and wind speeds from 1979 to 2021, over a vast spatial domain [7]. De Gi Estuary hydrodynamic regime was studied using the MIKE21SW [8] and

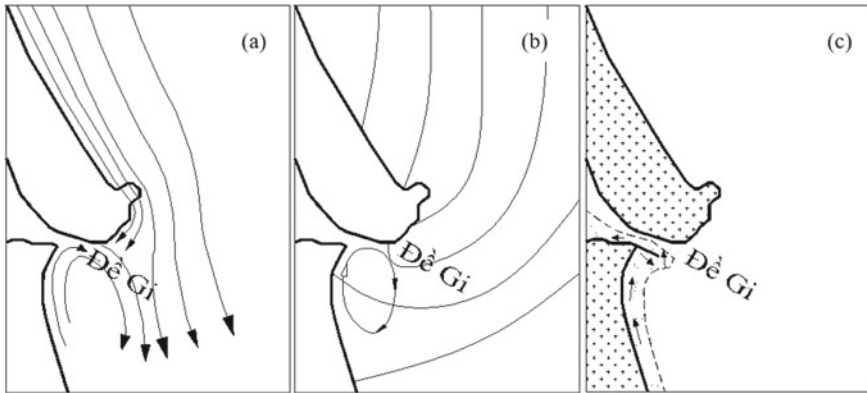


Fig. 2 a Diagram of current lines, b wave diffraction, and c sedimentation in front of protruding headland [3]

MIKE21HD modules [9]. Figure 3 show the domain and the mesh of the hydrodynamic model that was established to a limited extent by the limits to the North (at Vinh Loi beach), the South (Cat Khanh beach), and the East (far about 10 km from the shoreline). In addition, the boundary positions (the red lines) and bathymetry conditions of the model were established for De Gi Estuary, which is based on its topographical data in 2021. Each model’s boundary is around 10 km from De Gi Estuary. The west boundary completely encircles the Nuoc Ngot lagoon. The grid system has a falling resolution of 350 m in the offshore zone to 20 m in the onshore zone. The model’s parameter is inherited from earlier studies, assuring compatibility for the study area. The key model parameters are the temperature of 24 °C, the salinity of 32‰, the roughness coefficient from 32 to 40 m^{1/3}/s, and the wave coefficient of 0.85.

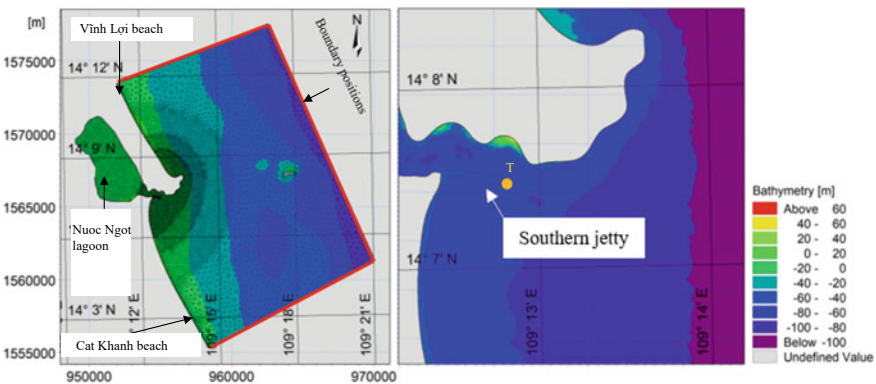


Fig. 3 Boundary positions (red lines), Bathymetry conditions and grid systems of the model

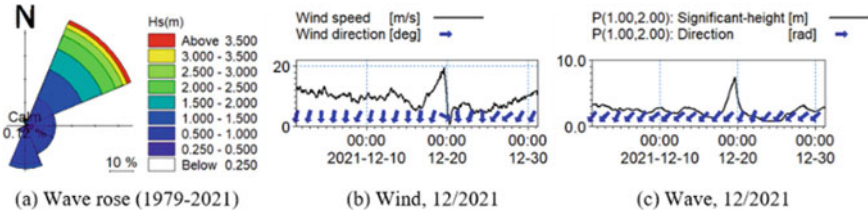


Fig. 4 Wave and wind conditions used in the simulation

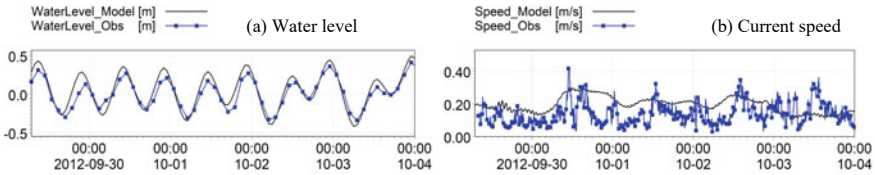


Fig. 5 Compared to water level and current speed between observed and simulated

This study used the surveyed water level and current speed parameters from 30/9 to 05/10/2012 at Point T (307,154.62 m E, 1,562,207.63 m N) to calibrate the hydrodynamic model. The results revealed that the phase and magnitude of the measured and simulated water level and current velocity are similar (Figs. 3 and 5). The Nash coefficients are estimated to be around 0.77 and 0.65 for water level and current speed, respectively. As a result, the parameters are relatively reliable and can be used in the following steps.

3 Scenarios and Results

The authors suggested numerous simulated scenarios using the mean wave height and several wave directions coupled with the tidal parameters during winter time in Table 1 to determine the cause, structure, and mechanism of the eddy flow and large-scale circulations. The features of waves, tides, and simulation data are extracted and analyzed to clarify the location and occurrence of tidal current and wave-induced current in the south of De Gi jetty, as well as causes and mechanisms for flow formation. Large-scale circulation currents are often occurring during the NE monsoon, according to Le Phuoc Trinh et al. [3]. Thus, the simulation scenarios that combined wave and wind conditions during the northeast monsoon in December 2021 were considered in this study.

Figure 6 illustrates the combined flow results during the northeast monsoon season, with the appearance of local large and minor vortices associated with the S1 simulation scenario in Table 1.

Table 1 Simulation scenarios

No	Scenarios	Boundary conditions	Targets
1	S1	The tide, wave, and wind in NE monsoon in December, 2021	Simulation influence of tide, waves, and winds during the NE monsoon
2	S2	Tide condition in December, 2021	Simulation flow regime under the influence of tides
3	S3	Tide condition in December, 2021. H = 1.18 m, T = 7.33 s. North monsoon wave	Simulation influence of tides with average wave following the North direction
4	S4	The tide condition in December, 2021. H = 1.18 m, T = 7.33 s. NE monsoon wave	Simulation influence of tides with mean wave height following the NE direction
5	S5	The tide condition in December, 2021. H = 1.18 m, T = 7.33 s. East monsoon wave	Simulation influence of tides with mean wave height following the East direction
6	S6	The tide in The tide condition in December, 2021. H = 1.18 m, T = 7.33 s. SE monsoon on wave	Simulation influence of tides with mean wave height following the SE direction
7	S7	The tide in The tide condition in December, 2021. H = 1.18 m, T = 7.33 s. North monsoon wave	Simulation influence of tides with mean wave height following the North direction; without the effect of the Nuoc Ngot lagoon

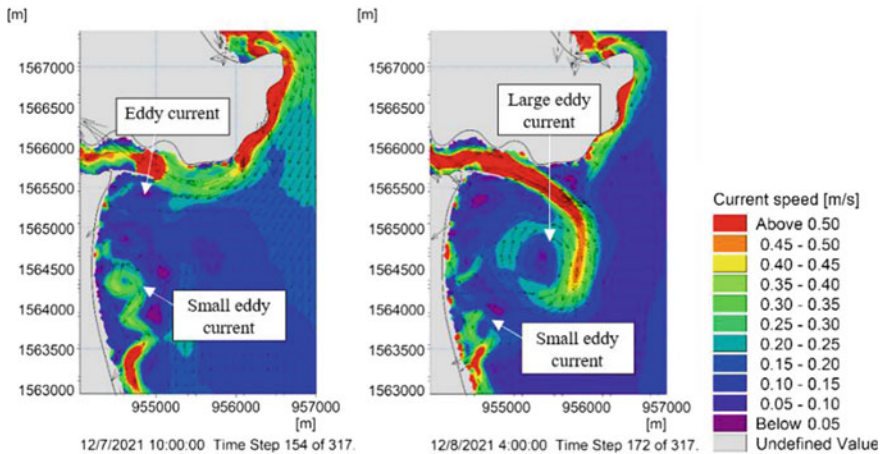


Fig. 6 Overall current speed of flood tide and ebb tide during the Northeast season

In terms of the size, position, velocity, and timing of the formation of eddy flow structures. The major eddy flow area is about 1.5 km south of De Gi estuary, with a radius of about 0.5 km around the edge. At ebb tide, the eddy flow speed at the outside edge is higher than 0.45 m/s. With a velocity of 0.35–0.4 m/s, the local eddy flow area forms during high tide roughly 1.6 km south of De Gi estuary, near to

shore. In the adjacent to the southern jetty region, local eddy flow emerges, and the current rate may reach 0.2–0.3 m/s.

The large eddy flow structure is mainly developed by the ebb-tidal flow from the Nuoc Ngot Lagoon to the sea. During high tide, a minor eddy flow structure close to the shore forms with a current speed of 0.4 m/s. The interaction of waves and terrain may cause eddy flow. Meanwhile, the tidal current is only 0.05 m/s, preventing this eddy flow formation. Similarly, the wave generates eddy flows near De Gi jetty’s southern end. Currents in the vicinity of the jetty always take one main path toward the navigation channel. This current direction is diametrically opposed to the wave and tidal directions. This is a critical stage for the sediment migration trend to fill the navigation channel.

The following steps will highlight the mechanism of eddy flow formation. When subjected to the influence of wave-induced currents, the ebb tide generates a large eddy flow structure, increasing the speed and skewing to the South. The small eddy flow structure is also formed by waves. This section will explain the main features of the aforementioned flow structure using simulation data (Fig. 7) from seven different simulated scenarios, as shown in Table 1.

Figure 7a indicates the flow caused by tidal currents along the channel’s direction, which substantially pulls back to the sea during the ebb tide due to the tidal phase difference between the Nuoc Ngot Lagoon and the sea (corresponding to the simulation scenario S2). The ebb current on either side of the boundary creates two

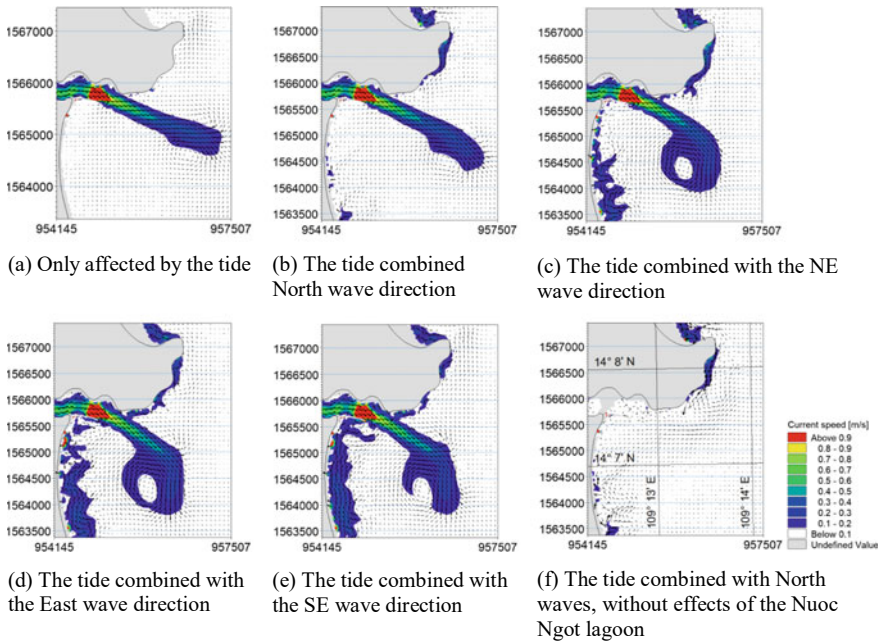


Fig. 7 Current field at ebb tide combined with different wave directions from N to SE

opposing eddy flows. It occurs due to the friction between the strong flow layer along the main channel and the surrounding relatively slow flow layer. As a result, the development of the eddy flow only occurs when current speeds surrounding the main channel are less than 0.1 m/s.

Figure 7b–e demonstrate the flow structure during ebb tide. It is influenced by incoming waves from the N-NE-E-SE directions (corresponding to simulation scenarios S3, S4, S5, and S6). It is possible to conclude that a large eddy flow structure is progressively generated under the impact of waves. The primary flow path along the main channel bends and eventually deviates to the south. The location of the eddy flow shifts to the south and approaches the beach. In contrast, Fig. 7f shows no substantial eddy flow when the flow from the Nuoc Ngot Lagoon is blocked (corresponding to simulation scenario S7).

Figure 7c–e represent small eddy flow configurations in the southern shoreline. The findings indicate that eddy flow is most noticeable when waves influence them in the NE direction (Fig. 7c), which corresponds to simulation scenario S4. When driven by waves in the East direction, the current along the south bank has a regular flowing in the north–south direction (Fig. 7d) and flows in the opposite direction (in the south–north direction) when it is driven by waves in the SE direction (Fig. 7e).

As a result of the findings, the southern circulation is generated primarily by the ebb tide. The main reason is that the ebb current follows along the main channel from the Nuoc Ngot lagoon to the sea, where it is deflected to the south and approaches the shore at high velocity due to wave action.

4 Conclusion and Recommendation

The study simulated the flow structure in De Gi estuary area by generating an asymmetrical shape with a rocky mountain on one side and an elongated sand spit on the other. According to the findings, the structure of large eddy flows that can be seen in NE monsoon is relatively far from the shore (approximately 1.5 km), with a radius of around 0.5 km. A minor eddy flow formation is about 200 m from the shoreline. The appearance of large and minor eddy flows along the navigation channel is highly influenced by the ebb tide. The appearance mechanism of small vortices is created by interacting waves and topographic factors in shallow coastal seas. Small eddies appear more clearly when waves are perpendicular to the shore; the current always tends to withdraw from the beach to the sea, especially nearby the southern jetty.

Acknowledgements This study is funded by the research project “Study on applying sand bypassing system and preventing depositing for estuaries along the Central Coast of Vietnam.” Ministry of Agriculture and Rural Development.

References

1. Duc Anh NQ, Tanaka H, Tam HS, Tinh NX, Tung TT, Viet NT (2020) Comprehensive study of the sand spit evolution at tidal inlets in the central coast of Vietnam. *J Marine Sci Eng* 8(9):722
2. Duc Anh NQ, Hau LP (2015) Efficiency analysis of river entrance construction works in Central Vietnam, presented at the Vietnam-Japan Workshop on Estuaries, Coasts and Rivers 2015, Hoi An, Quang Nam, Vietnam, pp 56–62
3. Trinh LP, Long BH, Mau LD, Trung PB (2021) The specific hydro-dynamical structures created main erosion-accretion points along the southern central Vietnamese coast. *Vietnam J Marine Sci Technol* 03:15–30
4. Trung PB, Mau LD, Trinh LP (2015) The problem of deposition at Sa Huynh (Quang Ngai province), Tam Quan and De Gi (Binh Dinh province) by impact assessment of tidal inlet protection structures. *Vietnam J Marine Sci Technol* 02:1–13
5. Duc DM (2014) Research on scientific and technological solutions to overcome the accretion phenomenon at the navigation channel to storm shelters, a case study in Tam Quan estuary, Binh Dinh province. VNU Hanoi University of Science, p 221. Report No.: 2014–53–211
6. Hao DC (2021) Feasibility study of De Gi Lagoon storm shelter, Binh Dinh province, Institute of Training and Applied Science in Central Vietnam
7. EMC Operational Wave Models. <https://polar.ncep.noaa.gov/waves/index.php>. Last accessed 10 Sept 2012
8. MIKE 21 Spectral Waves FM User guide. DHI, 2017
9. MIKE 21 Flow Model User guide. DHI, 2017

A Mathematical Model of Two-Dimensional Vertical Flow Based on the Dual Approach



The Hung Nguyen

Abstract The mathematical model of two-dimensional vertical flow is commonly constructed using the classic average method by taking the integral from the right to the left riverbank of the three-dimensional Reynolds averaged Navier–Stokes equations. Hence, average quantities obtained from this approach are not generalized in comparison to ones estimated by the dual approach. This paper presents a dual approach to establish the two-dimensional vertical flow equations. The setup model will be more complex than the classic one because the integration can be done locally several times. In this paper, the author performed twice integrals: (i) the first integration is from the right riverbank to the intermediate vertical surface layer between the right bank and the left bank, and then (ii) the second integration is from the right bank to the left bank. The improved two-dimensional vertical flow model received from this dual approach allows the calculation of flow characteristics more accurate than the classical method. In other words, it provides some flexible parameters to adjust based on the field or experimental data.

Keywords Classic average method · Dual approach · Two-dimensional vertical flow · Average quantities

1 Introduction

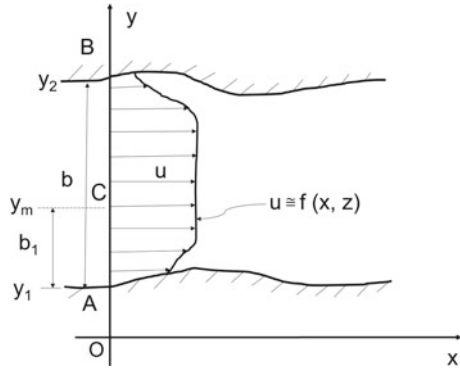
Flow in nature is usually formulated as three-dimensional problems. However, there are cases where it can be considered as two-dimensional vertical flow (such as flow over spillways, flow in deep and narrow bays, flow in narrow and deep rivers with little change in river width, and so on). The three-dimensional flow is described by the three-dimensional (3D) Navier–Stokes equations. Nevertheless, direct solution of this 3D equations encounters many difficulties in terms of numerical calculations, excessive computation time, and lack of actual measured data to verify.

T. H. Nguyen (✉)

University of Science and Technology—The University of Danang, Da Nang, Vietnam

e-mail: ngthung@dut.udn.vn

Fig. 1 Sketch of the construction of 2DV using the dual approach



In order to simplify the problem but still ensure the technical requirements, in many practical cases, the mathematical models are often reduced to simpler forms such as one-dimensional (1D) flow, two-dimensional horizontal (2DH) flow, and two-dimensional vertical (2DV) flow [1–5].

With a 2DV flow model, the horizontal flow velocity (y -axis) is ignored ($v \approx 0$), while the velocities (u, w) in the directions (Ox, Oz) are averaged over the entire river width (see Fig. 1). To derive the 2DV flow mathematical model, the 3D Navier–Stokes system of equations is integrated only once along the river width which is also known as the total integral or classical approach [5]. Average quantities obtained from the classical method are not generalized in comparison to ones received by dual approach [6, 7].

In this paper, the author builds a 2DV model from a system of Reynolds average 3D Navier–Stokes equations by the dual approach.

According to the dual approach, the physical quantities can be integrated many times and can be considered as local and global integrals [6, 7]. In this paper, twice integrals are performed: (i) the 1st integral (also known as local integral), from point A on the right riverbank to the intermediate vertical surface (point C) between the right bank and the left riverbank, (ii) the 2nd integral (called global integration), integrating again from the right to the left riverbank. Based on these integrals, we will receive a new system of differential equations of the 2DV problem according to the dual approach. This approach will be more complicated than the classical method, but in return, we will have better physical quantities in the flow than the classical approach [6, 7].

2 Dual Approach in Construction of 2DV Flow Equation

The Reynolds averaged Navier–Stokes 3D equations system is as follows:

The continuity equation:

$$\frac{\partial u}{\partial x} + \frac{\partial v}{\partial y} + \frac{\partial w}{\partial z} = 0 \tag{1}$$

The momentum equations in the x , y , and z directions:

$$\frac{\partial u}{\partial t} + \frac{\partial(u.u)}{\partial x} + \frac{\partial(u.v)}{\partial y} + \frac{\partial(u.w)}{\partial z} = \frac{1}{\rho} \cdot F_x - \frac{1}{\rho} \cdot \frac{\partial p}{\partial x} + \frac{1}{\rho} \frac{\partial \tau_{xx}}{\partial x} + \frac{1}{\rho} \frac{\partial \tau_{xy}}{\partial y} + \frac{1}{\rho} \frac{\partial \tau_{xz}}{\partial z} \tag{2}$$

$$\frac{\partial v}{\partial t} + \frac{\partial(u.v)}{\partial x} + \frac{\partial(v.v)}{\partial y} + \frac{\partial(v.w)}{\partial z} = \frac{1}{\rho} \cdot F_y - \frac{1}{\rho} \cdot \frac{\partial p}{\partial y} + \frac{1}{\rho} \frac{\partial \tau_{yx}}{\partial x} + \frac{1}{\rho} \frac{\partial \tau_{yy}}{\partial y} + \frac{1}{\rho} \frac{\partial \tau_{yz}}{\partial z} \tag{3}$$

$$\frac{\partial w}{\partial t} + \frac{\partial(u.w)}{\partial x} + \frac{\partial(v.w)}{\partial y} + \frac{\partial(w.w)}{\partial z} = \frac{1}{\rho} \cdot F_z - \frac{1}{\rho} \cdot \frac{\partial p}{\partial z} + \frac{1}{\rho} \frac{\partial \tau_{zx}}{\partial x} + \frac{1}{\rho} \frac{\partial \tau_{zy}}{\partial y} + \frac{1}{\rho} \frac{\partial \tau_{zz}}{\partial z} \tag{4}$$

where: u , v , w are the components of velocity in the x , y , and z directions; F_x , F_y , F_z are the components of the resultant external force in the x , y , and z directions, respectively; p is the average pressure component; τ_{xx} , τ_{yy} , τ_{zz} , τ_{xy} , τ_{xz} , τ_{yx} , τ_{yz} , τ_{zx} , τ_{zy} are the stresses (including both molecular and turbulent effects); ρ is the density of water.

Under certain conditions, we can build a 2DV mathematical model of flow from the Reynolds averaged 3D Navier–Stokes equations [5].

For the 2DV problem, the terms in the Reynolds equations in the y -direction are negligible, and Eq. (3) can be removed from the system of equations.

Building a 2DV mathematical flow model from a 3D mathematical flow model using the dual approach:

Currently, to build a 2DV mathematical model, one only integrates once (called the global integration) of the Reynolds averaged 3D Navier–Stokes equations in the horizontal direction (Oy -axis) from the right riverbank $A(x, z)$ to the left riverbank $B(x, z)$.

- According to the dual approach [6, 7], the problem can be integrated many times (including local and global integrals). In this paper, the author only integrates two times: (i) the first time (called local integral), the integral from the right riverbank $A(x, z, t)$ to any vertical plane $C(x, z, t)$ lying between the right river bank $A(x, z, t)$ and the left bank of river $B(x, z, t)$, (ii) the second time (called global integration), the integral is done from the right river bank $A(x, z, t)$ to the left river bank $B(x, z, t)$.

Boundary conditions of the problem:

Conditions at any plane $C(x, z, t)$ at position y_m between the right riverbank A and the left riverbank B ($v \approx 0$):

$$- \left[u \cdot \frac{\partial y}{\partial x} + w \cdot \frac{\partial y}{\partial z} \right] \Big|_{y=y_m} = - \left[\overline{U} \cdot \frac{\partial y}{\partial x} + \overline{W} \cdot \frac{\partial y}{\partial z} \right] = \frac{\partial y}{\partial t} \Big|_{y=y_m} \tag{5}$$

where: \bar{U} , \bar{W} is the average velocity in the x - and z -direction, respectively.

Building the 2DV continuity equation according to the dual approach

From the continuity equation:

$$\underbrace{\frac{\partial u}{\partial x}}_{I_c} + \underbrace{\frac{\partial v}{\partial y}}_{J_c} + \underbrace{\frac{\partial w}{\partial z}}_{K_c} = 0 \tag{6}$$

Firstly, integrating (local integration) the continuous Eq. (1) from the right bank of the river $A(x, y = y_1, z, t)$ to the vertical plane $C(x, y = y_m, z, t)$ is located somewhere between the right riverbank A and the left riverbank B :

$$T[\text{CQ}] = \int_{y_1}^{y_m} \left(\frac{\partial u}{\partial x} + \frac{\partial v}{\partial y} + \frac{\partial w}{\partial z} \right) \cdot dy = \int_{y_1}^{y_m} \frac{\partial u}{\partial x} \cdot dy + \int_{y_1}^{y_m} \frac{\partial v}{\partial y} \cdot dy + \int_{y_1}^{y_m} \frac{\partial w}{\partial z} \cdot dy = 0 \tag{7}$$

$$T[\text{CQ}] = \int_{y_1}^{y_m} \frac{\partial u}{\partial x} \cdot dy + v(y_m) - v(y_1) + \int_{y_1}^{y_m} \frac{\partial w}{\partial z} \cdot dy = 0$$

Since $v(y_m) = v(y_1) \cong 0$, so we have:

$$T[\text{CQ}] = \int_{y_1}^{y_m} \frac{\partial u}{\partial x} \cdot dy + \int_{y_1}^{y_m} \frac{\partial w}{\partial z} \cdot dy = TI_c + TK_c = 0 \tag{8}$$

Calculate each integral using Leibniz's rule:

$$TI_c = \int_{y_1}^{y_m} \frac{\partial u}{\partial x} \cdot dy = \beta_{1c} \cdot \frac{\partial}{\partial x} (\bar{u} \cdot b_1) - \beta_{2c} \cdot \bar{u} \frac{\partial}{\partial x} (y_m) + \beta_{2c} \cdot \bar{u} \frac{\partial}{\partial x} (y_1) \tag{9}$$

$$TK_c = \int_{y_1}^{y_m} \frac{\partial w}{\partial z} \cdot dy = \delta_{1c} \cdot \frac{\partial}{\partial z} (\bar{w} \cdot b_1) - \delta_{2c} \cdot \bar{w} \frac{\partial}{\partial z} (y_m) + \delta_{2c} \cdot \bar{w} \frac{\partial}{\partial z} (y_1) \tag{10}$$

Adding two expressions (9) and (10) and taking into account the boundary conditions (5), we have:

$$T[\text{CQ}] = TI_c + TK_c = \beta_{1c} \cdot \frac{\partial}{\partial x} (\bar{u} \cdot b_1) + \delta_{1c} \cdot \frac{\partial}{\partial z} (\bar{w} \cdot b_1) + \beta_{*} \cdot \frac{\partial b_1}{\partial t} = 0 \tag{11}$$

Equation (11) itself is the continuity equation of the classical 2DV problem.

Where:

$b_1 = y_m - y_1$ is the distance in the Oy direction from the right riverbank A to the vertical plane through $C(x, z, t)$ at $y = y_m$.

With the correction coefficients in the continuity Eq. (11) as follows:

$$\begin{aligned} \beta_{1c} &= \frac{1}{\frac{\partial}{\partial x}(\bar{u}.b_1)} \cdot \frac{\partial}{\partial x} \int_{Y_1}^{Y_m} u dy \\ \beta_{2c} &= \frac{1}{\bar{u} \cdot \frac{\partial}{\partial x}(b_1)} \cdot \int_{Y_1}^{Y_m} u \frac{\partial}{\partial x} (dy) \\ \delta_{1c} &= \frac{1}{\frac{\partial}{\partial z}(\bar{w}.b_1)} \cdot \frac{\partial}{\partial z} \int_{Y_1}^{Y_m} w dy \\ \delta_{2c} &= \frac{1}{\bar{w} \cdot \frac{\partial}{\partial z}(b_1)} \cdot \int_{Y_1}^{Y_m} w \cdot \frac{\partial}{\partial z} (dy) \end{aligned}$$

$$\gamma_{2c} = (\beta_{2c} + \delta_{2c})/2, \beta_* = (\beta_{2c} + \delta_{2c})/2 \tag{12}$$

The second time, integrating (global integral) the continuity Eq. (1) from the right bank of the river A to the left bank of the river B:

$$T^2[{\text{CQ}}] : \int_{y_1}^{y_2} \left(\beta_{1c} \cdot \frac{\partial}{\partial x}(\bar{u}.b_1) + \delta_{1c} \cdot \frac{\partial}{\partial z}(\bar{w}.b_1) + \beta_* \cdot \frac{\partial b_1}{\partial t} \right) dy = 0 \tag{13}$$

Let's calculate each term of Eq. (13):

$$\begin{aligned} \int_{y_1}^{y_2} \frac{\partial b_1}{\partial t} dy &= \frac{1}{2} \cdot \frac{\partial}{\partial t} (y_2^2 - y_1^2) + \frac{1}{2} \cdot \frac{\partial}{\partial t} (y_1^2) - \frac{1}{2} \cdot \frac{\partial}{\partial t} (y_2^2) = 0 \\ \int_{y_1}^{y_2} \frac{\partial}{\partial x}(\bar{u}.b_1) dy &= \frac{1}{2} (y_2 + y_1) \cdot \left[\frac{\partial}{\partial x}(\bar{u}.b) - \bar{u} \cdot \frac{\partial}{\partial x}(b) \right] \\ &= \frac{1}{2} \frac{\partial}{\partial x} [\bar{u} \cdot (y_2^2 - y_1^2)] - \frac{1}{2} \bar{u} \cdot \frac{\partial}{\partial x} (y_2^2 - y_1^2) \\ \int_{y_1}^{y_2} \frac{\partial}{\partial z}(\bar{w}.b_1) dy &= \frac{1}{2} (y_2 + y_1) \cdot \left[\frac{\partial}{\partial z}(\bar{w}.b) - \bar{w} \cdot \frac{\partial}{\partial z}(b) \right] \end{aligned}$$

$$= \frac{1}{2} \frac{\partial}{\partial z} [\bar{w} \cdot (y_2^2 - y_1^2)] - \frac{1}{2} \bar{w} \cdot \frac{\partial}{\partial z} (y_2^2 - y_1^2)$$

Substituting these terms back into Eq. (13), we receive the continuity equation of the 2DV problem formulated by the dual approach:

$$\begin{aligned} T^2[\text{CQ}] : \quad & \beta_{1c} \frac{\partial}{\partial x} [\bar{u} \cdot (y_2^2 - y_1^2)] - \beta_{1c} \bar{u} \cdot \frac{\partial}{\partial x} (y_2^2 - y_1^2) + \\ & \delta_{1c} \frac{\partial}{\partial z} [\bar{w} \cdot (y_2^2 - y_1^2)] - \delta_{1c} \bar{w} \cdot \frac{\partial}{\partial z} (y_2^2 - y_1^2) = 0 \end{aligned} \quad (14a)$$

If we select the origin of the axis Oy at the right bank of the river $A(y_1 = 0, y_2 = b)$, and taking into account the boundary condition (5), we have:

$$\beta_{1c} \frac{\partial}{\partial x} [\bar{u} \cdot b^2] + \delta_{1c} \frac{\partial}{\partial z} [\bar{w} \cdot b^2] + \gamma_{1c} \cdot \frac{\partial}{\partial t} (b^2) = 0 \quad (14b)$$

where: $\gamma_{1c} = (\beta_{1c} + \delta_{1c})/2$

If $b = \text{constant}$ in the x, z and t , then Eq. (14b) becomes the classical continuity equation of the 2DV problem.

Where: b is the river width; \bar{u} and \bar{w} are the velocity along the Ox and Oz axis which are averaged over the river width b . The coefficients β_{1c}, δ_{1c} are correction coefficients and they are close to 1 ($\beta_{1c} \approx \delta_{1c} \approx 1$). Under ideal conditions such as when velocity u and w are uniformly distributed over the river width b and the depth z , respectively, then these coefficients are equal to 1 ($\beta_{1c} = \delta_{1c} = 1$).

Constructing the 2DV momentum equation by the dual approach in the x direction

First, integrating Eq. (2) from the right bank of the river A to any vertical plane $C(x, y = y_m, z, t)$ located somewhere between the right riverbank A and the left riverbank B :

$$\begin{aligned} T[\text{MEx}] : \quad & \int_{y_1}^{y_m} \left(\frac{\partial u}{\partial t} + \frac{\partial(u \cdot u)}{\partial x} + \frac{\partial(u \cdot v)}{\partial y} + \frac{\partial(u \cdot w)}{\partial z} \right) \cdot dy \\ & = \int_{y_1}^{y_m} \left(\frac{1}{\rho} \cdot F_x - \frac{1}{\rho} \cdot \frac{\partial p}{\partial x} + \frac{1}{\rho} \frac{\partial \tau_{xx}}{\partial x} + \frac{1}{\rho} \frac{\partial \tau_{xy}}{\partial y} + \frac{1}{\rho} \frac{\partial \tau_{xz}}{\partial z} \right) \cdot dy \end{aligned} \quad (15)$$

We integrate each term of Eq. (15):

$$\begin{aligned} T[\text{Ix}] &= \int_{y_1}^{y_m} \left(\frac{\partial u}{\partial t} \right) \cdot dy = \frac{\partial}{\partial t} \int_{y_1}^{y_m} u \, dy - \int_{y_1}^{y_m} u \frac{\partial}{\partial t} (dy) \\ &= \alpha_{1tx} \frac{\partial}{\partial t} (\bar{u}_1 \cdot b_1) - \alpha_{2tx} \bar{u}_1 \left[\frac{\partial y_m}{\partial t} - \frac{\partial y_1}{\partial t} \right] \end{aligned}$$

$$\begin{aligned}
 T[\text{Jx}] &= \int_{y_1}^{y_m} \frac{\partial(\mathbf{uu})}{\partial x} dy = \frac{\partial}{\partial x} \int_{y_1}^{y_m} (\mathbf{uu}) dy - \int_{y_1}^{y_m} (\mathbf{uu}) \frac{\partial}{\partial x} (dy) \\
 &= \beta_{1x} \frac{\partial}{\partial x} (\overline{\mathbf{uu}} \cdot b_1) - \beta_{2x} (\overline{\mathbf{uu}}) \frac{\partial}{\partial x} (y_m) + \beta_{2x} (\overline{\mathbf{uu}}) \frac{\partial}{\partial x} (y_1)
 \end{aligned}$$

$$\begin{aligned}
 T[\text{Lx}] &= \int_{y_1}^{y_m} \frac{\partial(\mathbf{uw})}{\partial z} \cdot dy = \frac{\partial}{\partial z} \int_{y_1}^{y_m} (\mathbf{uw}) \cdot dy - \int_{y_1}^{y_m} (\mathbf{uw}) \cdot \frac{\partial}{\partial z} (dy) \\
 &= \delta_{1x} \frac{\partial}{\partial z} (\overline{\mathbf{uw}} \cdot b_1) - \delta_{2x} (\overline{\mathbf{uw}}) \cdot \frac{\partial}{\partial z} (y_m) + \delta_{2x} (\overline{\mathbf{uw}}) \cdot \frac{\partial}{\partial z} (y_1)
 \end{aligned}$$

$$T[\text{Mx}] = \int_{y_1}^{y_m} \frac{1}{\rho} \cdot F_x \cdot dy = \frac{1}{\rho} \cdot F_x \cdot (y_m - y_1) = \frac{1}{\rho} \cdot F_x \cdot b_1;$$

$$T[\text{Nx}] = \int_{y_1}^{y_m} \frac{1}{\rho} \cdot \frac{\partial p}{\partial x} \cdot dy = \frac{1}{\rho} \cdot \frac{\partial p}{\partial x} \cdot (y_m - y_1) = \frac{1}{\rho} \cdot \frac{\partial p}{\partial x} \cdot b_1$$

$$\begin{aligned}
 T[\text{Fr}_x] &= \int_{y_1}^{y_m} \left(\frac{1}{\rho} \frac{\partial \tau_{xx}}{\partial x} + \frac{1}{\rho} \frac{\partial \tau_{xy}}{\partial y} + \frac{1}{\rho} \frac{\partial \tau_{xz}}{\partial z} \right) \cdot dy = \frac{1}{\rho} \frac{\partial}{\partial x} (b_1 \cdot \tau_{xx}) + \frac{1}{\rho} \frac{\partial}{\partial z} (b_1 \cdot \tau_{xz}) \\
 &\quad - \frac{1}{\rho} \left[\tau_{xx} \cdot \frac{\partial y_m}{\partial x} + \tau_{xz} \cdot \frac{\partial y_m}{\partial z} \right] + \frac{1}{\rho} \left[\tau_{xx} \cdot \frac{\partial y_1}{\partial x} + \tau_{xz} \cdot \frac{\partial y_1}{\partial z} \right] \\
 &= \frac{1}{\rho} \text{div}(b_1 \cdot \vec{\tau})_x - \frac{1}{\rho} \cdot (\vec{\tau} \cdot \vec{n})_x
 \end{aligned}$$

To summarize, after integrating for the second time all the terms of Eq. (15), we have:

$$\begin{aligned}
 T[\text{ME}_x] &: \alpha_{1tx} \frac{\partial}{\partial t} (\overline{u_1} \cdot b_1) + \beta_{1x} \frac{\partial}{\partial x} (\overline{\mathbf{uu}} \cdot b_1) + \delta_{1x} \frac{\partial}{\partial z} (\overline{\mathbf{uw}} \cdot b_1) \\
 &= \frac{1}{\rho} \cdot F_x \cdot b_1 + \frac{1}{\rho} \cdot \frac{\partial p}{\partial x} \cdot b_1 + \frac{1}{\rho} \text{div}(b_1 \cdot \vec{\tau})_x - \frac{1}{\rho} \cdot (\vec{\tau} \cdot \vec{n})_x \quad (16)
 \end{aligned}$$

In which, the correction coefficients are as follows:

$$\alpha_{1tx} = \frac{1}{\frac{\partial}{\partial t} (\overline{u_1} \cdot b_1)} \cdot \int_{Y_1}^{Y_m} \frac{\partial u}{\partial t} dy$$

$$\begin{aligned}
\alpha_{2tx} &= \frac{1}{\bar{u}_1 \cdot \frac{\partial b_1}{\partial t}} \cdot \int_{Y_1}^{Y_m} u \cdot \frac{\partial}{\partial t} (dy) \\
\beta_{1x} &= \frac{1}{\frac{\partial}{\partial x} (b_1 \cdot \overline{uu})} \cdot \frac{\partial}{\partial x} \int_{Y_1}^{Y_m} (uu) \cdot dy \\
\beta_{2x} &= \frac{1}{(\overline{uu}) \cdot \frac{\partial}{\partial x} (b_1)} \cdot \int_{Y_1}^{Y_m} (uu) \cdot \frac{\partial}{\partial x} (dy) \\
\delta_{1x} &= \frac{1}{\frac{\partial}{\partial z} (b_1 \cdot \overline{uw})} \cdot \frac{\partial}{\partial z} \int_{Y_1}^{Y_m} (uw) \cdot dy \\
\delta_{2x} &= \frac{1}{(\overline{uw}) \cdot \frac{\partial}{\partial z} (b_1)} \cdot \int_{Y_1}^{Y_m} (uw) \cdot \frac{\partial}{\partial z} (dy)
\end{aligned} \tag{17}$$

\bar{u}_1 is the average velocity in the x-axis direction, in a reach of width b_1 .

Equation (16) is the momentum equation in the x-direction of the classical 2DV flow problem.

Second, integrating (global integral) the momentum Eq. (2) from the right bank of the river A to the left bank of the river B:

$$\begin{aligned}
T^2[\text{ME}x]: & \int_{y_1}^{y_2} \alpha_{1tx} \frac{\partial}{\partial t} (\bar{u}_1 \cdot b_1) dy + \int_{y_1}^{y_2} \beta_{1x} \frac{\partial}{\partial x} (\overline{uu} \cdot b_1) dy + \int_{y_1}^{y_2} \delta_{1x} \frac{\partial}{\partial z} (\overline{uw} \cdot b_1) dy = \\
& \int_{y_1}^{y_2} \frac{1}{\rho} \cdot F_x \cdot b_1 + \int_{y_1}^{y_2} \frac{1}{\rho} \cdot \frac{\partial p}{\partial x} \cdot b_1 dy + \int_{y_1}^{y_2} \frac{1}{\rho} \text{div}(b_1 \cdot \vec{\tau})_x dy \\
& - \int_{y_1}^{y_2} \frac{1}{\rho} \cdot \tau_{xx} \cdot \frac{\partial b_1}{\partial x} dy - \int_{y_1}^{y_2} \frac{1}{\rho} \cdot \tau_{xz} \cdot \frac{\partial b_1}{\partial z} dy
\end{aligned} \tag{18}$$

We integrate each term of Eq. (18):

$$T^2[\text{I}x] = \int_{y_1}^{y_2} \alpha_{1tx} \frac{\partial}{\partial t} (\bar{u}_1 \cdot b_1) dy = \frac{1}{2} \alpha_{1tx} \cdot \frac{\partial}{\partial t} \{ \bar{u} \cdot (y_2^2 - y_1^2) \} - \frac{1}{2} \alpha_{1tx} \cdot \bar{u} \cdot \left\{ \frac{\partial}{\partial t} (y_2^2 - y_1^2) \right\}$$

$$T^2[\text{Jx}] = \int_{y_1}^{y_2} \beta_{1x} \frac{\partial}{\partial x} (\overline{uw} \cdot b_1) dy = \frac{1}{2} \beta_{1x} \frac{\partial}{\partial x} \{ (\overline{uw}) \cdot (y_2^2 - y_1^2) \} - \frac{1}{2} \beta_{1x} (\overline{uw}) \cdot \frac{\partial}{\partial x} (y_2^2 - y_1^2)$$

$$T^2[\text{Lx}] = \int_{y_1}^{y_2} \delta_{1x} \frac{\partial}{\partial z} (\overline{uw} \cdot b_1) dy = \frac{1}{2} \delta_{1x} \frac{\partial}{\partial z} \{ (\overline{uw}) \cdot (y_2^2 - y_1^2) \} - \frac{1}{2} \delta_{1x} (\overline{uw}) \cdot \frac{\partial}{\partial z} (y_2^2 - y_1^2)$$

$$T^2[\text{Mx}] = \int_{y_1}^{y_2} \frac{1}{\rho} \cdot F_x \cdot b_1 dy = \frac{1}{2\rho} \cdot F_x \cdot (y_2^2 - y_1^2)$$

$$T^2[\text{Nx}] = \int_{y_1}^{y_2} \frac{1}{\rho} \cdot \frac{\partial p}{\partial x} \cdot b_1 dy = \frac{1}{2\rho} \cdot \frac{\partial p}{\partial x} \cdot (y_2^2 - y_1^2)$$

$$T^2[\text{Ox}] = \int_{y_1}^{y_2} \frac{1}{\rho} \text{div}(b_1 \cdot \vec{\tau})_x dy = \frac{1}{2\rho} \text{div}(\vec{\tau}_x) \cdot (y_2^2 - y_1^2) - \frac{1}{2\rho} \cdot \tau_{xx} \cdot \frac{\partial}{\partial x} (y_2^2 - y_1^2)$$

$$\begin{aligned} T^2[\text{Px}] &= - \int_{y_1}^{y_2} \frac{1}{\rho} \cdot \tau_{xx} \cdot \frac{\partial (y_m - y_1)}{\partial x} dy - \int_{y_1}^{y_2} \frac{1}{\rho} \cdot \tau_{xz} \cdot \frac{\partial (y_m - y_1)}{\partial z} dy \\ &= - \frac{1}{2\rho} (\vec{\tau} \cdot \vec{n})_x \cdot (y_2 + y_1) \end{aligned}$$

Summarizing all the terms of Eq. (18) after integrating the second time, we have the equation of motion in the Ox direction according to the dual approach:

$$\begin{aligned} T^2[\text{MEx}] &: \frac{1}{2} \alpha_{1tx} \frac{\partial}{\partial t} \{ \bar{u} \cdot (y_2^2 - y_1^2) \} - \frac{1}{2} \alpha_{1tx} \cdot \bar{u} \cdot \left\{ \frac{\partial}{\partial t} (y_2^2 - y_1^2) \right\} \\ &+ \frac{1}{2} \beta_{1x} \frac{\partial}{\partial x} \{ (\overline{uw}) \cdot (y_2^2 - y_1^2) \} \\ &- \frac{1}{2} \beta_{1x} (\overline{uw}) \cdot \frac{\partial}{\partial x} (y_2^2 - y_1^2) + \frac{1}{2} \delta_{1x} \frac{\partial}{\partial z} \{ (\overline{uw}) \cdot (y_2^2 - y_1^2) \} \\ &- \frac{1}{2} \delta_{1x} (\overline{uw}) \cdot \frac{\partial}{\partial z} (y_2^2 - y_1^2) = \\ &\frac{1}{2\rho} \cdot F_x \cdot (y_2^2 - y_1^2) - \frac{1}{2\rho} \cdot \frac{\partial p}{\partial x} \cdot (y_2^2 - y_1^2) \\ &+ \frac{1}{2\rho} \text{div}(\vec{\tau})_x \cdot (y_2^2 - y_1^2) - \frac{1}{2\rho} (\vec{\tau} \cdot \vec{n})_x \cdot (y_2 + y_1) \end{aligned} \tag{19}$$

Equation (3) is canceled out because for the 2DV problem, the velocity v in the horizontal direction Oy to be negligible.

Constructing the 2DV momentum equation by using the dual approach in the z direction

The first time, integrating Eq. (4) from the right riverbank A to any vertical plane C within the right riverbank A and the left riverbank B :

$$\begin{aligned} T[\text{MEz}] &: \int_{y_1}^{y_m} \left(\frac{\partial w}{\partial t} + \frac{\partial(w.u)}{\partial x} + \frac{\partial(w.v)}{\partial y} + \frac{\partial(w.w)}{\partial z} \right) .dy \\ &= \int_{y_1}^{y_m} \left(\frac{1}{\rho} .F_z - \frac{1}{\rho} . \frac{\partial p}{\partial z} + \frac{1}{\rho} \frac{\partial \tau_{zx}}{\partial x} + \frac{1}{\rho} \frac{\partial \tau_{zy}}{\partial y} + \frac{1}{\rho} \frac{\partial \tau_{zz}}{\partial z} \right) .dy \end{aligned} \quad (20)$$

Integrating each term of Eq. (20).

$$T[\text{Iz}] = \int_{y_1}^{y_m} \left(\frac{\partial w}{\partial t} \right) .dy = \alpha_{1tz} \frac{\partial}{\partial t} (\overline{w_1} . b_1) - \alpha_{2tz} \overline{w_1} \left[\frac{\partial y_m}{\partial t} - \frac{\partial y_1}{\partial t} \right]$$

$$\begin{aligned} T[\text{Jz}] &= \int_{y_1}^{y_m} \left(\frac{\partial(wu)}{\partial x} \right) .dy = \frac{\partial}{\partial x} \int_{y_1}^{y_m} (wu) .dy - \int_{y_1}^{y_m} (wu) . \frac{\partial}{\partial x} (dy) \\ &= \beta_{1z} \frac{\partial}{\partial x} (\overline{wu} . b_1) - \beta_{2z} (\overline{wu}) . \frac{\partial}{\partial x} (y_m) + \beta_{2z} (\overline{wu}) . \frac{\partial}{\partial x} (y_1) \end{aligned}$$

$$\begin{aligned} T[\text{Lz}] &= \int_{y_1}^{y_m} \frac{\partial(ww)}{\partial z} .dy = \frac{\partial}{\partial z} \int_{y_1}^{y_m} (ww) .dy - \int_{y_1}^{y_m} (ww) . \frac{\partial}{\partial z} (dy) \\ &= \delta_{1z} \frac{\partial}{\partial z} (\overline{ww} . b_1) - \delta_{2z} (\overline{ww}) . \frac{\partial}{\partial z} (y_m) + \delta_{2z} (\overline{ww}) . \frac{\partial}{\partial z} (y_1) \end{aligned}$$

$$T[\text{Mz}] = \int_{y_1}^{y_m} \frac{1}{\rho} .F_z .dy = \frac{1}{\rho} .F_z .(y_m - y_1) = \frac{1}{\rho} .F_z .b_1$$

$$T[\text{Nz}] = \int_{y_1}^{y_m} \frac{1}{\rho} . \frac{\partial p}{\partial z} .dy = \frac{1}{\rho} . \frac{\partial p}{\partial z} .b_1$$

$$\begin{aligned} T[\text{Frz}] &= \int_{y_1}^{y_m} \left(\frac{1}{\rho} \frac{\partial \tau_{zx}}{\partial x} + \frac{1}{\rho} \frac{\partial \tau_{zy}}{\partial y} + \frac{1}{\rho} \frac{\partial \tau_{zz}}{\partial z} \right) .dy = \frac{1}{\rho} \frac{\partial}{\partial x} (b_1 . \tau_{zx}) + \frac{1}{\rho} \frac{\partial}{\partial z} (b_1 . \tau_{zz}) \\ &\quad - \frac{1}{\rho} \left[\tau_{zx} . \frac{\partial y_m}{\partial x} + \tau_{zz} . \frac{\partial y_m}{\partial z} \right] + \frac{1}{\rho} \left[\tau_{zx} . \frac{\partial y_1}{\partial x} + \tau_{zz} . \frac{\partial y_1}{\partial z} \right] \end{aligned}$$

$$= \frac{1}{\rho} \operatorname{div}(b_1 \cdot \vec{\tau})_z - \frac{1}{\rho} \cdot (\vec{\tau} \cdot \vec{n})_z$$

To summarize, after integrating all the terms of Eq. (20), we have:

$$\begin{aligned} T[\text{MEz}] : & \alpha_{1tz} \frac{\partial}{\partial t} (\overline{w_1} \cdot b_1) + \beta_{1z} \frac{\partial}{\partial x} (\overline{wu} \cdot b_1) + \delta_{1z} \frac{\partial}{\partial z} (\overline{ww} \cdot b_1) \\ & = \frac{1}{\rho} \cdot F_z \cdot b_1 + \frac{1}{\rho} \cdot \frac{\partial p}{\partial z} \cdot b_1 + \frac{1}{\rho} \operatorname{div}(b_1 \cdot \vec{\tau})_z - \frac{1}{\rho} \cdot (\vec{\tau} \cdot \vec{n})_z \end{aligned} \quad (21)$$

In which, the correction coefficients are as follows:

$$\begin{aligned} \alpha_{1tz} &= \frac{1}{\frac{\partial}{\partial t} (\overline{w_1} \cdot b_1)} \cdot \int_{Y_1}^{Y_m} \frac{\partial w}{\partial t} dy \\ \alpha_{2tz} &= \frac{1}{\overline{w_1} \cdot \frac{\partial b_1}{\partial t}} \cdot \int_{Y_1}^{Y_m} w \cdot \frac{\partial}{\partial t} (dy) \\ \beta_{1z} &= \frac{1}{\frac{\partial}{\partial x} (b_1 \cdot \overline{wu})} \cdot \frac{\partial}{\partial x} \int_{Y_1}^{Y_m} (wu) \cdot dy \\ \beta_{2z} &= \frac{1}{(\overline{wu}) \cdot \frac{\partial}{\partial x} (b_1)} \cdot \int_{Y_1}^{Y_m} (wu) \cdot \frac{\partial}{\partial x} (dy) \\ \delta_{1z} &= \frac{1}{\frac{\partial}{\partial z} (b_1 \cdot \overline{ww})} \cdot \frac{\partial}{\partial z} \int_{Y_1}^{Y_m} (ww) \cdot dy \\ \delta_{2z} &= \frac{1}{(\overline{ww}) \cdot \frac{\partial}{\partial z} (b_1)} \cdot \int_{Y_1}^{Y_m} (ww) \cdot \frac{\partial}{\partial z} (dy) \end{aligned} \quad (22)$$

Equation (21) is the equation of motion in the z direction of the classical 2DV flow problem.

Integrating Eq. (4) for the second time from the right riverbank A to the left riverbank B :

$$\begin{aligned}
T^2[\text{MEz}]: & \int_{y_1}^{y_2} \alpha_{1tz} \frac{\partial}{\partial t} (\overline{w}_1 \cdot b_1) dy + \int_{y_1}^{y_2} \beta_{1z} \frac{\partial}{\partial x} (\overline{w}u \cdot b_1) dy + \int_{y_1}^{y_2} \delta_{1z} \frac{\partial}{\partial z} (\overline{w}w \cdot b_1) dy = \\
& \int_{y_1}^{y_2} \frac{1}{\rho} \cdot F_z \cdot b_1 dy + \int_{y_1}^{y_2} \frac{1}{\rho} \cdot \frac{\partial p}{\partial z} \cdot b_1 dy + \int_{y_1}^{y_2} \frac{1}{\rho} \text{div}(b_1 \cdot \vec{\tau})_z dy - \int_{y_1}^{y_2} \frac{1}{\rho} \cdot (\vec{\tau} \cdot \vec{n})_z dy
\end{aligned} \tag{23}$$

Integrating each term of Eq. (23):

$$T^2[\text{Iz}] = \int_{y_1}^{y_2} \alpha_{1tz} \frac{\partial}{\partial t} (\overline{w}_1 \cdot b_1) dy = \frac{1}{2} \alpha_{1tz} \cdot \frac{\partial}{\partial t} \{ \overline{w} \cdot (y_2^2 - y_1^2) \} - \frac{1}{2} \alpha_{1tz} \cdot \overline{w} \cdot \left\{ \frac{\partial}{\partial t} (y_2^2 - y_1^2) \right\}$$

$$T^2[\text{Jz}] = \int_{y_1}^{y_2} \beta_{1z} \frac{\partial}{\partial x} (\overline{w}u \cdot b_1) dy = \frac{1}{2} \beta_{1z} \frac{\partial}{\partial x} \{ (\overline{w}u) \cdot (y_2^2 - y_1^2) \} - \frac{1}{2} \beta_{1z} (\overline{w}u) \cdot \frac{\partial}{\partial x} (y_2^2 - y_1^2)$$

$$T^2[\text{Lz}] = \int_{y_1}^{y_2} \delta_{1z} \frac{\partial}{\partial z} (\overline{w}w \cdot b_1) dy = \frac{1}{2} \delta_{1z} \frac{\partial}{\partial z} \{ (\overline{w}w) \cdot (y_2^2 - y_1^2) \} - \frac{1}{2} \delta_{1z} (\overline{w}w) \cdot \frac{\partial}{\partial z} (y_2^2 - y_1^2)$$

$$T^2[\text{Mz}] = \int_{y_1}^{y_2} \frac{1}{\rho} \cdot F_z \cdot b_1 dy = \frac{1}{2\rho} \cdot F_z \cdot (y_2^2 - y_1^2)$$

$$T^2[\text{Nz}] = \int_{y_1}^{y_2} \frac{1}{\rho} \cdot \frac{\partial p}{\partial z} \cdot b_1 dy = \frac{1}{2\rho} \cdot \frac{\partial p}{\partial z} \cdot (y_2^2 - y_1^2)$$

$$T^2[\text{Oz}] = \int_{y_1}^{y_2} \frac{1}{\rho} \text{div}(b_1 \cdot \vec{\tau})_z dy = \frac{1}{2\rho} \text{div}(\vec{\tau})_z \cdot (y_2^2 - y_1^2)$$

$$T^2[\text{Pz}] = - \int_{y_1}^{y_2} \frac{1}{\rho} \cdot \tau_{zx} \cdot \frac{\partial (y_m - y_1)}{\partial x} dy - \int_{y_1}^{y_2} \frac{1}{\rho} \cdot \tau_{zz} \cdot \frac{\partial (y_m - y_1)}{\partial z} dy = \frac{1}{2\rho} (\vec{\tau} \cdot \vec{n})_x \cdot (y_2 + y_1)$$

Summarizing all the terms of Eq. (23) after integrating for the second time, we have the equation of motion in the Oz direction based on the dual approach:

$$\begin{aligned}
 T^2[\text{MEZ}]: & \frac{1}{2} \cdot \alpha_{1tz} \frac{\partial}{\partial t} \{ \bar{w} \cdot (y_2^2 - y_1^2) \} - \frac{1}{2} \alpha_{1tz} \cdot \bar{w} \cdot \left\{ \frac{\partial}{\partial t} (y_2^2 - y_1^2) \right\} \\
 & + \frac{1}{2} \beta_{1z} \frac{\partial}{\partial x} \{ (\overline{wu}) \cdot (y_2^2 - y_1^2) \} - \frac{1}{2} \beta_{1z} (\overline{wu}) \cdot \frac{\partial}{\partial x} (y_2^2 - y_1^2) \\
 & + \frac{1}{2} \delta_{1z} \frac{\partial}{\partial z} \{ (\overline{ww}) \cdot (y_2^2 - y_1^2) \} - \frac{1}{2} \delta_{1z} (\overline{ww}) \cdot \frac{\partial}{\partial z} (y_2^2 - y_1^2) \tag{24} \\
 = & \frac{1}{2\rho} \cdot F_z \cdot (y_2^2 - y_1^2) - \frac{1}{2\rho} \cdot \frac{\partial p}{\partial z} \cdot (y_2^2 - y_1^2) + \frac{1}{2\rho} \text{div}(\vec{\tau})_z \cdot (y_2^2 - y_1^2) \\
 & - \frac{1}{2\rho} (\vec{\tau} \cdot \vec{n})_z \cdot (y_2 + y_1)
 \end{aligned}$$

In summary, in this paper, a system of Eqs. 2DV is developed to describe 2DV flow in open channel based on the dual approach as follows:

$$\begin{aligned}
 & \beta_{1c} \frac{\partial}{\partial x} [\bar{u} \cdot (y_2^2 - y_1^2)] + \delta_{1c} \frac{\partial}{\partial z} [\bar{w} \cdot (y_2^2 - y_1^2)] + \gamma_{1c} \cdot \frac{\partial}{\partial t} (y_2^2 - y_1^2) = 0 \\
 \alpha_{1tx} \cdot \frac{\partial}{\partial t} \{ \bar{u} \cdot (y_2^2 - y_1^2) \} & - \alpha_{1tx} \cdot \bar{u} \cdot \left\{ \frac{\partial}{\partial t} (y_2^2 - y_1^2) \right\} + \beta_{1x} \frac{\partial}{\partial x} \{ (\overline{uu}) \cdot (y_2^2 - y_1^2) \} - \\
 \beta_{1x} (\overline{uu}) \cdot \frac{\partial}{\partial x} (y_2^2 - y_1^2) & + \delta_{1x} \frac{\partial}{\partial z} \{ (\overline{uw}) \cdot (y_2^2 - y_1^2) \} - \delta_{1x} (\overline{uw}) \cdot \frac{\partial}{\partial z} (y_2^2 - y_1^2) = \\
 \frac{1}{\rho} \cdot F_x \cdot (y_2^2 - y_1^2) & - \frac{1}{\rho} \cdot \frac{\partial p}{\partial x} \cdot (y_2^2 - y_1^2) + \frac{1}{\rho} \text{div}(\vec{\tau})_x \cdot (y_2^2 - y_1^2) - \frac{1}{\rho} (\vec{\tau} \cdot \vec{n})_x \cdot (y_2 + y_1) \\
 \alpha_{1tz} \frac{\partial}{\partial t} \{ \bar{w} \cdot (y_2^2 - y_1^2) \} & - \alpha_{1tz} \cdot \bar{w} \cdot \left\{ \frac{\partial}{\partial t} (y_2^2 - y_1^2) \right\} + \beta_{1z} \frac{\partial}{\partial x} \{ (\overline{wu}) \cdot (y_2^2 - y_1^2) \} \\
 - \beta_{1z} (\overline{wu}) \cdot \frac{\partial}{\partial x} (y_2^2 - y_1^2) & + \delta_{1z} \frac{\partial}{\partial z} \{ (\overline{ww}) \cdot (y_2^2 - y_1^2) \} - \delta_{1z} (\overline{ww}) \cdot \frac{\partial}{\partial z} (y_2^2 - y_1^2) = \\
 \frac{1}{\rho} \cdot F_z \cdot (y_2^2 - y_1^2) & - \frac{1}{\rho} \cdot \frac{\partial p}{\partial z} \cdot (y_2^2 - y_1^2) + \frac{1}{\rho} \text{div}(\vec{\tau})_z \cdot (y_2^2 - y_1^2) - \frac{1}{\rho} (\vec{\tau} \cdot \vec{n})_z \cdot (y_2 + y_1) \tag{25a}
 \end{aligned}$$

where \bar{u} , \bar{w} are the averaged velocity components along the river width in the Ox, Oz directions respectively; \vec{n} is the boundary normal vector; $(\vec{\tau} \cdot \vec{n})_x$, $(\vec{\tau} \cdot \vec{n})_z$ is the side-wall friction in the Ox and Oz directions, respectively; ρ is the density of water; α_{1tx} , α_{1tz} , β_{1x} , β_{1z} , δ_{1x} , δ_{1z} are correction factors with values close 1.

In the case that the origin of the Oy axis is chosen to coincide with the point A (right riverbank: $y_1 = 0$, $y_2 = b$), the system of Eq. (25a) set up by the dual approach is rewritten as follows:

$$\beta_{1c} \frac{\partial}{\partial x} [\bar{u} \cdot b^2] + \delta_{1c} \frac{\partial}{\partial z} [\bar{w} \cdot b^2] + \gamma_{1c} \cdot \frac{\partial}{\partial t} (b^2) = 0$$

$$\begin{aligned}
& \alpha_{1tx} \cdot \frac{\partial}{\partial t} \{ \bar{u} \cdot (b^2) \} - \alpha_{1tx} \cdot \bar{u} \cdot \left\{ \frac{\partial}{\partial t} (b^2) \right\} + \beta_{1x} \frac{\partial}{\partial x} \{ (\overline{uu}) \cdot (b^2) \} - \\
& \beta_{1x} (\overline{uu}) \cdot \frac{\partial}{\partial x} (b^2) + \delta_{1x} \frac{\partial}{\partial z} \{ (\overline{uw}) \cdot (b^2) \} - \delta_{1x} (\overline{uw}) \cdot \frac{\partial}{\partial z} (b^2) = \\
& \frac{1}{\rho} \cdot F_x \cdot (b^2) - \frac{1}{\rho} \cdot \frac{\partial p}{\partial x} \cdot (b^2) + \frac{1}{\rho} \operatorname{div}(\vec{\tau})_x \cdot (b^2) - \frac{1}{\rho} (\vec{\tau} \cdot \vec{n})_x \cdot (b) \\
& \alpha_{1tz} \frac{\partial}{\partial t} \{ \bar{w} \cdot (b^2) \} - \alpha_{1tz} \cdot \bar{w} \cdot \left\{ \frac{\partial}{\partial t} (b^2) \right\} + \beta_{1z} \frac{\partial}{\partial x} \{ (\overline{ww}) \cdot (b^2) \} \\
& - \beta_{1z} (\overline{ww}) \cdot \frac{\partial}{\partial x} (b^2) + \delta_{1z} \frac{\partial}{\partial z} \{ (\overline{ww}) \cdot (b^2) \} - \delta_{1z} (\overline{ww}) \cdot \frac{\partial}{\partial z} (b^2) = \quad (25b) \\
& \frac{1}{\rho} \cdot F_z \cdot (b^2) - \frac{1}{\rho} \cdot \frac{\partial p}{\partial z} \cdot (b^2) + \frac{1}{\rho} \operatorname{div}(\vec{\tau})_z \cdot (b^2) - \frac{1}{\rho} (\vec{\tau} \cdot \vec{n})_z \cdot (b)
\end{aligned}$$

Comments:

The system of Eq. (25b) has adjustment coefficients α_i and β_i , so it is easy to adjust the calculation results to be closer to reality. In general, all terms of Eq. (25b) have the same order (See Supplementary file) and have terms describing the change in conductivity over time; so, this model allows a general description of flow when there is a deformation in time and space of the conduit.

If the river width b changes slightly in time and space (along the river Ox and the depth Oz), we have:

$$\begin{aligned}
\gamma_{1c} \cdot \frac{\partial}{\partial t} (b^2) \approx 0; \quad \alpha_{1tx} \cdot \bar{u} \cdot \left\{ \frac{\partial}{\partial t} (b^2) \right\} \approx 0; \quad \alpha_{1tz} \cdot \bar{w} \cdot \left\{ \frac{\partial}{\partial t} (b^2) \right\} \approx 0 \quad \beta_{1x} (\overline{uu}) \cdot \frac{\partial}{\partial x} (b^2) \approx 0 \\
\beta_{1z} (\overline{ww}) \cdot \frac{\partial}{\partial x} (b^2) \approx 0; \quad \delta_{1x} (\overline{uw}) \cdot \frac{\partial}{\partial z} (b^2) \approx 0; \quad \delta_{1z} (\overline{ww}) \cdot \frac{\partial}{\partial z} (b^2) \approx 0
\end{aligned}$$

from the system of Eq. (25b), we obtain the system of Eqs. 2DV flow as follows:

$$\begin{aligned}
& \beta_{1c} \frac{\partial}{\partial x} [\bar{u} \cdot b^2] + \delta_{1c} \frac{\partial}{\partial z} [\bar{w} \cdot (b^2)] = 0 \\
& \alpha_{1tx} \cdot \frac{\partial}{\partial t} \{ \bar{u} \cdot (b^2) \} + \beta_{1x} \frac{\partial}{\partial x} \{ (\overline{uu}) \cdot (b^2) \} + \delta_{1x} \frac{\partial}{\partial z} \{ (\overline{uw}) \cdot (b^2) \} = \\
& \frac{1}{\rho} \cdot F_x \cdot (b^2) - \frac{1}{\rho} \cdot \frac{\partial p}{\partial x} \cdot (b^2) + \frac{1}{\rho} \operatorname{div}(\vec{\tau})_x \cdot (b^2) - \frac{1}{\rho} (\vec{\tau} \cdot \vec{n})_x \cdot (b). \quad (26) \\
& \alpha_{1tz} \frac{\partial}{\partial t} \{ \bar{w} \cdot (b^2) \} + \beta_{1z} \frac{\partial}{\partial x} \{ (\overline{ww}) \cdot (b^2) \} + \delta_{1z} \frac{\partial}{\partial z} \{ (\overline{ww}) \cdot (b^2) \} = \\
& \frac{1}{\rho} \cdot F_z \cdot (b^2) - \frac{1}{\rho} \cdot \frac{\partial p}{\partial z} \cdot (b^2) + \frac{1}{\rho} \operatorname{div}(\vec{\tau})_z \cdot (b^2) - \frac{1}{\rho} (\vec{\tau} \cdot \vec{n})_z \cdot (b)
\end{aligned}$$

Linearizing all terms of Eq. (26) with respect to b , as follows:

$$b^2 = b \cdot b \approx b_n \cdot b_{n+1}$$

where b_n and b_{n+1} are river widths at time step n and $n + 1$, respectively; we can easily get the system of 2DV flow equations set up according to the classical method [5].

From the 2DH flow equations derived using the dual approach [3] combined with 2DV flow Eq. (26), we get the system of 1D flow equations built by a dual approach as follows:

$$\begin{aligned} & \frac{\partial H^2}{\partial t} + \frac{\partial}{\partial x}(\alpha_{1c}uH^2) + \frac{\partial}{\partial x}(\beta_{1c}ub^2) = 0 \\ & \frac{\partial}{\partial t}(\alpha_1 \cdot \bar{u} \cdot H^2) + \alpha_{1tx} \cdot \frac{\partial}{\partial t}(\bar{u} \cdot b^2) + \frac{\partial}{\partial x}(\alpha_2 \cdot u^2 H^2) + \beta_{1x} \frac{\partial}{\partial x}(\bar{u} \cdot b^2) = -gH^2 \frac{\partial Z_s}{\partial x} \\ & -g \cdot b^2 \frac{\partial Z_s}{\partial x} + \frac{1}{\rho} \text{div}(\vec{\tau})_x \cdot (H^2) - \frac{1}{\rho} (\vec{\tau} \cdot \vec{n})_x \cdot (H) + \frac{1}{\rho} \text{div}(\vec{\tau})_x \cdot (b^2) - \frac{1}{\rho} (\vec{\tau} \cdot \vec{n})_x \cdot (b) \end{aligned} \tag{27}$$

Formulating the system (27) according to the flow discharge Q and the water level elevation Z_s :

$$\begin{aligned} & \frac{\partial(AH)}{\partial t} + \frac{\partial}{\partial x}(\alpha_{1c}HQ) + \frac{\partial}{\partial x}(\beta_{1c}bQ) = 0 \\ & \frac{\partial}{\partial t}(\alpha_1 \cdot HQ) + \alpha_{1tx} \cdot \frac{\partial}{\partial t}(bQ) + \frac{\partial}{\partial x}(\alpha_2 \cdot \frac{HQ^2}{A}) + \beta_{1x} \cdot \frac{\partial}{\partial x}(Q^2) = -gH^2 \frac{\partial Z_s}{\partial x} - g \cdot b^2 \frac{\partial Z_s}{\partial x} \\ & + \frac{1}{\rho} \text{div}(\vec{\tau})_x \cdot (H^2) + \frac{1}{\rho} \text{div}(\vec{\tau})_x \cdot (b^2) - \frac{1}{\rho} (\vec{\tau} \cdot \vec{n})_x \cdot (H) - \frac{1}{\rho} (\vec{\tau} \cdot \vec{n})_x \cdot (b) \end{aligned} \tag{28}$$

In the system of Eq. (28), the coefficients can be rewritten as follows:

$$\alpha_1 \cong \alpha_{1tx}; \alpha_2 \cong \beta_{1x}$$

More simply, ignoring the effect of the width variation b and $H \gg b$ (See Supplementary file), we receive the system (29) of one-dimensional flow equations set up by the dual approach as follows:

$$\begin{aligned} & \frac{\partial(AH)}{\partial t} + \frac{\partial}{\partial x}(\alpha_{1c}HQ) = 0 \\ & \frac{\partial}{\partial t}(\alpha_1 \cdot HQ) + \frac{\partial}{\partial x}(\alpha_2 \cdot \frac{HQ^2}{A}) = -gH^2 \frac{\partial Z_s}{\partial x} + \nu H \frac{\partial^2 Q}{\partial x^2} - gAHS_f \end{aligned} \tag{29}$$

where:

A is cross-sectional area, H is depth of flow, Q is discharge, Z_s is water surface elevation, ν is kinematic viscosity coefficient, and S_f is frictional slope of the river bed.

Linearizing all terms of Eq. (29) with respect to H : $H \approx H_n$; where H_n is the depth of flow at time step n ; we arrive at a system of classical one-dimensional flow equations [1, 5].

3 Conclusion

The mathematical model of a two-dimensional vertical flow in open channel is developed based on the dual approach (25, 26) which is more general than the one constructed using the classical method. This model also allows a general description of flow when there is a deformation in time and space of the conduit.

The system of one-dimensional flow Eq. (28) is obtained as a direct consequence of building according to the dual approach of the mathematical model of two-dimensional horizontal flow and the mathematical model of two-dimensional vertical flow, it is more general than the classical one-dimensional equations system.

References

1. Nguyen TH (1992) Salinity intrusion in Huong river network and the measure of hydraulic construction. *J Sci Technol (Five University of Technology)* 2:17–21
2. Hung NT (2017) A dual approach to modeling solute transport. In: *The international conference on advances in computational mechanics*, pp 821–834
3. That TT, Nguyen TH, Nguyen DA (2019) A dual approach for model construction of two-dimensional horizontal flow. In: *Proceedings of the 10th international conference on Asian and Pacific Coasts (APAC 2019)* Hanoi, Vietnam, pp 115–120
4. Nguyen The H (2020) A dual approach for modeling two- and one-dimensional solute transport. In: *The international conference on modern mechanics and applications, ICOMMA2020* December 02 - 04, HoChiMinh city, Vietnam, *Lecture notes in mechanical engineering*, pp 1–12, Springer
5. Weiming W (2007) *Computation river dynamics*, Taylor and Francis/Balkema
6. NGUYEN Dong Anh (2012) Dual approach to averaged values of functions. *Vietnam J Mech VAST* 34(3):211–214
7. NGUYEN Dong Anh (2012) Dual approach to averaged values of functions: advanced formulas. *Vietnam J Mech Vast* 34(4):321–325

Analysis on Feasibility Study of PE Material Buoys for Vietnam Inland Waterways and Maritime Channels



Nguyen Xuan Thinh and Bui Minh Thu

Abstract In the modern life, marine structures such as projects for exploiting inland waterways, navigational channels, and transportation types are developing more and more. The research of materials technology for these projects on channels is not only fast but also requires high precision. As a result, aids to navigation play an important role in maritime safety for all marine routes of Vietnam. One of them is buoys which have been improving significantly not only in Vietnam but also around the world. The purpose of this article is given the new improving aids to navigation in modern life. Instead of using steel buoys, new technology buoys will be used for Vietnam maritime channels with the priority of long age and convenient for authorities. At present, new technology buoys latest replacement of steel buoys to low-maintenance quality PE buoys have been installed at Mekong River Commission–Lao PDR, Cambodia, and Vietnam RWS (Lighthouse Authorities)–The Netherlands Port Of Rotterdam–The Netherlands, Maritime Office–Poland DAB VLOOT–Belgium, Nigerian Inland Waterways Administration and Nigerian Port Authorities–Nigeria Australian Maritime Safety Authority–Australia Arabian Maritime and Navigation Aids Services–Oman. In fact, new technology buoys are polyethylene buoys which are rotational molding by a pre-determined quantity of polyethylene powder pre-compounded of required color. Thus, in process of manufacturing PE buoys, rotational molding is a method for manufacturing hollow plastic products with all dimension and shape.

Keywords Polyethylene powder · Rotational molding · PE buoys · Aids to first section

N. X. Thinh (✉) · B. M. Thu
Faculty of Civil Engineering, Vietnam Maritime University/VMU, Haiphong, Vietnam
e-mail: thinhs@vimaru.edu.vn

B. M. Thu
e-mail: thubm.ctt@vimaru.edu.vn

1 Introduction

PE buoy is one of the new technology buoys which have been and are being used popularly on waterways in the world such as England, France, Germany, the Netherlands, Belgium, and so on, and especially they have been installed on the Mekong River, until now according to the Commission of Mekong River, these buoys were still effective and not have to be replaced. Vietnam is a country with the diversity river system, and especially along the coast of Vietnam, there are more than 100 large and small seaports serving domestic and international ships. In addition, there are about 48 bays and over 122 river mouths into the sea [1, 2]. Thus, most of the waterways inland and marine channels are equipped with a lateral buoy system which is mainly steel buoys, and to maintain these steel buoys system in continuous operation on the channels, it is always necessary to manage and supervise the management stations, and maintenance work is continuously checked and reviewed by management units monthly and quarterly. Therefore, this job requires the management unit to have workshops, wharfs, and large specialized vessels. As a result, it takes a lot of labor and equipment for the maintenance and maintenance of steel buoys on the channels. However, with the development of science and technology, PE plastic buoys are currently being researched and tested on a number of waterways Inland in recent years. The advantage of polyethylene (PE) buoy is that the longevity can last 20 years without failure, it is really useful for current maritime and waterway managers about this superiority of polyethylene buoys [3, 4]. Through actual research and evaluation on Vietnam's maritime and waterway channels, because PE buoys are designed according to the assembly between separate parts, so when they are damaged in a collision, it is only necessary to replace that part without having to hoist it, install it, and bring it to the maintenance workshop as steel buoys. Therefore, compared with polyethylene buoys, the research and application of new technology buoys (PE) to assist to upgrade the entire signaling buoys system on navigational and waterway channels superior.

For all types of lateral buoys on waterways and maritime channels in Vietnam, they are installed according to IALA standards as shown in Fig. 1.

2 General Structure of Steel Buoys

Basically, the structure of steel buoys includes four main parts: the steel buoy is made of steel plate with thickness ≥ 8 mm, it is fabricated by electric welding, hollow cylinder form completely sealed to prevent water penetration. Partitions in the float buoy can be designed or not and depending on the type of float. The mast of buoy consists of angle steel bars welded together in the form of a frame, a tower-shaped frame, and this part are placed solar panels, lights, radar reflectors, and protective

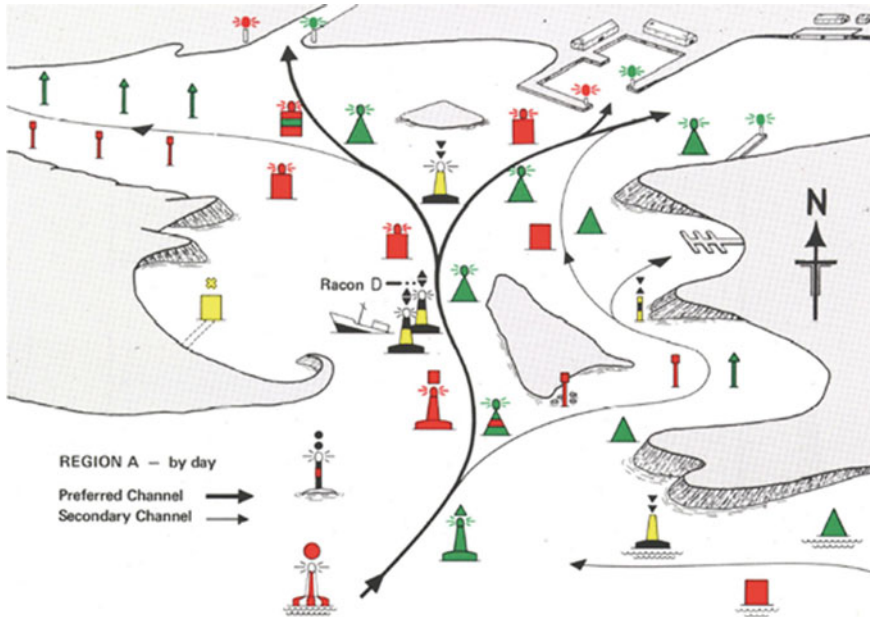


Fig. 1 Installing lateral buoy according to IALA standards (region A) [6]

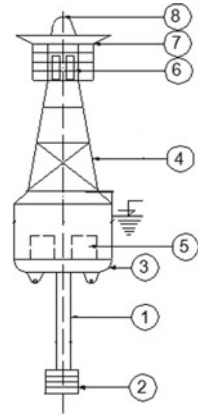
devices for buoys and lights [5]. However, the float tail part is divided into two types as follows:

- Float with tail consists of one round steel tube with small diameter attached to counterweights are cast steel wheels (ballasts). The number of ballasts is more or less, big or small depending on the type of float. The buoy is kept balanced by these ballasts [7].
- Flat bottom buoy: The part of the buoy shell is extended from the bottom, that part must be of sufficient size to catch the ballasts.

The last part of buoy is ballasts, on floats with tails: the ballasts are round cast steel wheels with a scarf-shaped structure as arranged in the lower part of the tail of the float, tightly linked to the tail of the buoy by means of cipher plates. The number and size of ballasts depends on the calculation of each float. And on a flat-bottom buoy, ballasts are cast steel pieces, arranged around the buoy shell, by bolting or riveting, the number and size of ballasts depends on the calculation of each float [9].

Currently, a steel structure placed on waterways and maritime channels. They are designed and installed with eight items as shown in Fig. 2. In addition, this buoyancy system of the buoy will be linked with the anchoring system below the water level to always keep the buoy stable in position on the channel.

- 1—Float tail; 2—Counterweight.
- 3—Float body; 4—Need to brew.

Fig. 2 Steel buoy structure

5—Battery pack; 6—Lights.

7—Lamp protection cage; 8—Peak signal [1, 2].

However, the design calculations comply with the following main contents: Calculating the weight and center of gravity of the buoy, calculating the volume occupied by water, and center of buoyancy. Calculating the height of the center of inclination, determining the period oscillations of the buoy, determining the height of the draft the buoy, and determining the maximum angle of inclination of the buoy. After these main calculation steps, calculating the anchor system including the calculation of the chain link system and the anchor is play an important role in keeping buoy to balance stably on the water level. After the buoy is calculated and designed, it will be verified and put into production to be released on navigational channels and waterways. With the feature that the buoy is made of steel, it is only for a short time that they are easily corroded by the surrounding water environment, and especially every time it is hit by marine and waterway ships, the buoy needs to be replaced, and cranes brought the broken buoys to the workshop for repair and maintenance. With the current use of steel buoys, the management units in Vietnam have to equip a lot of large specialized vessels, large cranes as well as need a lot of workers to maintain and maintain the buoy continuously. This actually consumes a relatively large amount of money for signaling system management units.

3 General Structure of PE Buoys

PE buoys have been produced and applied in the world since the 1990s, with the new technology of using PE plastic to replace the steel buoys [3, 4]. With the diameter from 0.9 to 3 m, they are suitable for both waterways inland and marine channels. All equipment such as marine LEDs lights and lanterns, lanterns and lights support structures in steel, aluminum, PE, etc., monitoring and supervision systems (AIS, Racon, etc.) and lighthouses are placed on PE buoys, see in Fig. 3 [4]. To form the

PE buoy, the plastic powder mixture is molded into the buoy through the centrifugal rotation process, which is the main determining factor in creating each different type of buoy. This process includes filling of the mold with a pre-determined quantity of polyethylene powder pre-compounded of required color, heating and fusion with the mold being bi-axially rotated, until the resin melts and coats the inner mold walls, cooling of the mold to solidify the part, and unloading. The elements of the PE buoy are independent and interchangeable, the materials are carefully selected and tested for critical site conditions, and the floats are assembled around a central structure with a bolting kit [9, 10]. In addition, the PE buoys are designed to be 100% recyclable. They can be repaired and gets a “second life”, and with the main elements of PE, PE buoy achieves a better reserve buoyancy. In case of collision, PE buoys will get back to its original position without being. Because PE buoy is designed by modularity, in case of extreme and violent impact that can damage the hull, then the others quarters float will ensure the buoyancy of the buoy, this is the main advantage of the modularity. Besides, no need to replace the complete buoy, but only the half float or quarter of float damaged by the accident. The selection of plastic mixture to put into production of floats always ensures that a medium density polyethylene quality decisive for each buoy in each different area, as a natural point, it is suitable for Vietnam channels. In particular, virgin pre-compounded polymer powder is also a main element of buoy. Thus, they have high resilience to shocks, with the UV stabilizing additives to reduce color aging. Regarding the mooring line system, for the steel buoy structure being used in Vietnam, they must be calculated selectively for each type to suit each type of buoy in different areas by the design units, while for new technology buoys, the International Association of Lighthouse Authorities (IALA) has endorsed a mooring line calculation software package called CALMAR for all types of plastic buoys. PE buoys on marine and waterways channels are always greatly influenced by the outside environment, such as corrosive water, clinging sea creatures, and especially can be collided ships moving on channels. However, for the PE buoys every time it is damaged, the damaged part will be replaced on the spot at the site. The current new technology buoys, the body of the buoy is usually paired with two float plates, or four panels are assembled together as Figs. 3 and 4 [3, 4].

4 Compare Steel and PE Buoys

In Vietnam so far, the majority of floating signaling systems are steel buoys, and with this steel structure, the useful life of steel buoys is about 08 years to 10 years [3]. However, maintaining these buoys require the manager to have funds, the monitoring unit to maintain their operation on the channels. Besides, the periodic repair of buoys requires regularity and management units to repair them, so this job makes it very easy for managers to miss in regularly checking all buoy systems on channels, most of which can wait for them to be quite broken or have sudden damage before taking them in for repair. This requires a lot of time and money of the administrator [8]. Regarding the production cost of new steel buoys with diameter of 2 m about 200

Fig. 3 PE buoy with two modular

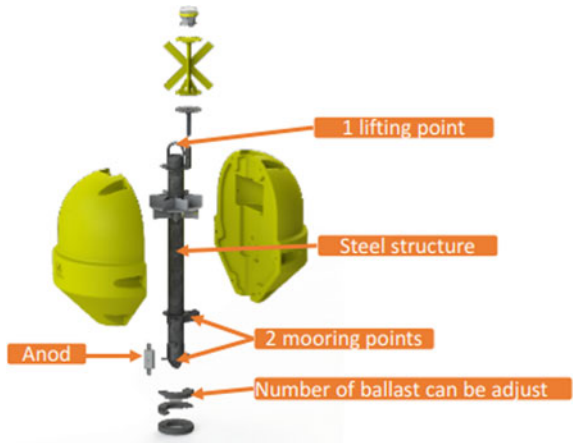
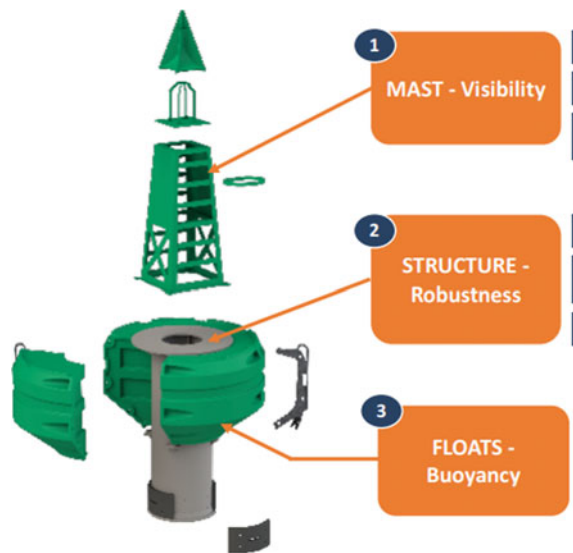


Fig. 4 PE buoy with four modulars



million per buoy, and with the diameter of 2.4 m about 250 million per buoy, these are all popular buoys on Vietnam’s maritime and waterway channels. However, when the steel buoy system is put into use every year, it still requires managers to perform periodic maintenance, painting and repair work [1, 2]. Repairing steel buoy requires managers to incur additional costs even more and complex. At present, according to the maintenance of Vietnam relevant authorities. It is estimated that the cost of maintenance and depreciation in 01 year for steel buoy with the diameter of 2 m and 2.4 m will be about 25 million VND per buoy and buoys with a diameter of less than 2 m will be about 50 million per one. Compared with new technology buoys that have been put into use in countries around the world as well as refer to the price

of some reputable suppliers such as GISMAN, MOBILIS Group and some other suppliers, the cost of buoys is from 200 to 400 million a buoy but with a lifespan of about 20 years. When the channels apply these types of buoys, it is almost only a one-time investment for about 20 years without periodic maintenance or repair like the traditional signaling buoys are steel buoys [7] (Table 1).

Table 1 Comparison of technical elements between steel buoy and PE buoy

Items	Steel buoy	PE buoy
Life expectancy	Average is 10 years	Average is 20 years
Onshore facilities	Steel buoys require heavy lifting facilities for handling and coating system equipment for grit blasting and painting	Large plastic buoys can be modular. Thus, this buoy reduced lifting capacity, and surface storage area. Besides, plastic buoys do not need coating system. As a results, no grit blasting nor painting system
Specialized vessels	Significant servicing vessels (buoys tenders) are required for buoys lifting and deployment operations	Plastic buoys are 50–70% lighter than steel buoys. Therefore, smaller servicing vessels are required for lifting and deployment operations
Intervals between each major maintenance operation onshore	Need a strict corrosion control More site visits The blast cleaning and painting must meet all of the paint manufacturer's requirements: Require the buoy to be brought ashore, so less time at sea on duty	No painting on the hull Plastic materials have better resistance to dense marine fouling The cleaning and maintenance of the hull can be made on station: Thus, PE buoys must be sufficiently robust to withstand weed being scraped off or high-pressure water jetting
Special skills and tools requirements	Operators must be fully trained in using all type of equipment for grit blasting and painting, and for the mix and application of the painting systems	Polyethylene can be easily repaired by trained technicians using hot fusion welding equipment Plastic floats can be modular and consist in 2 or 4 quadrants [10]: this enables changing individual parts and not the entire float when it is damaged or need repairing
Impacts on the environment	Steel components require more intensive maintenance schedule. This leads to more control visits on site, and heavier nautical means (more fuel consumption)	Modular design and reduced weight, this leads to implies smaller logistic and nautical means and less fuel consumption
Labour	Need a lot of workers for the maintenance of steel buoys	Less labor is required for maintenance, mainly for inspection and replacement of damaged modulars

5 Conclusions

In this study, to complete the assessment between steel and PE buoys, data collection, analysis, evaluation, and comparison have been applied to determine the suitability of PE buoys applied to maritime and waterway channels in Vietnam. It can be seen that the PE buoy has outstanding advantages over steel buoys in terms of durability and longevity. Firstly, when using PE buoys for navigational channels, it will help free up workshops for maintenance and maintenance of buoys, which significantly saves human resources for annual maintenance and repair of buoys [8]. Secondly, with the structure of the buoys mainly made of plastic and not fading over time, the maintenance and maintenance of plastic buoys only stops at things like cleaning the buoy or replacing the damaged part directly at the scene. In addition, because these buoys have a lighter structure than steel buoys, the means of transport, cranes for equipment to replace buoys do not require large watercraft like those used for steel buoys. In the world, the application of plastic floats to gradually replace the floats has been applied for a long time, so through the analysis of the results obtained above, the research will assist the application of PE buoys to bring many benefits. More feasibility to use for navigational and waterway channels instead of being tested in some inland waterway channels in Vietnam recently. The use of steel buoys or plastic buoys for navigational and waterway channels in Vietnam requires the close management and supervision of navigational and waterway management units. Especially on the channels in Vietnam where collisions often occur with the aids to navigation on the channel, this collision, whether it is a steel buoy or a polyethylene, will be affected to a certain extent during the operation process to ensure maritime safety and ensure safety of waterways.

Acknowledgements This research is funded by Vietnam Maritime University.

References

1. Information on <https://vinamarine.gov.vn/>. Last accessed 22 Sept 2022
2. Information on <http://viwa.gov.vn/>. Last accessed 22 Sept 2022
3. Information on www.gisman-sa.com. Last accessed 22 Sept 2022
4. Information on <https://mobilis-sa.com>. Last accessed 22 Sept 2022
5. Sealite.com/ Avlite.com/ Star2M.com. Last accessed 22 Sept 2022
6. www.iala-aism.org. Last accessed 22 Sept 2022
7. Thinh NX (2022) Manual of aids to navigation for maritime
8. Thinh NX (2017) Internal magazine of civil engineering, VIMARU
9. Lecture Introduction to the AtoN—Stephen Bennett Vice; IALA World – Wide Academy
10. Park Y, Kim T, Kwak J, Kim I, Park J, Ha K (2016) Design of Korean standard modular buoy body using polyethylene polymer material for ship safety. *J Mater Sci Chem Eng* 4:65–73

Research on Verification of the Pile Types of a Port Structure by Using Impact Vibration Test in Vietnam



Thi Bach Duong Nguyen and Thanh Dat Pham

Abstract The vibration impact test method has been studied very interestingly and is applied to check and evaluate the health status of the pile types of a port structure. The data collection technique for building a theoretical dynamic analysis model depends not only on the influence of the boundary conditions of the passing pile foundation and its load but also on the size of the berth by the scale and port structure classification. The paper reviews and analyzes the research influence of this issue. The paper also presents a simple formula to determine the natural design frequency of the segment of the pile-type port structure through the natural frequency of a typical transverse frame in Vietnam. Calculating the natural design frequency of a typical horizontal frame diagram is simple and quick, even if the original design document has no design records. From this, it is possible to determine the design natural vibration frequency of the whole berth segment and predict the frequency range measured if the pile-type port structure usually works.

Keywords Natural frequency of pile-type port structure · Impact vibration test · Dynamic analysis model · Classification of port structure

1 Introduction

The inspection and early risk detection of the port structures is a concern for port management when they are subject to the influence of global climate change, natural disasters, floods, and erosion. Currently, in the load testing, inspection, and quality control of port infrastructure, it is hard to test the horizontal load capacity caused by ships and anchors in cases of static methods because this method faces many difficulties in implementation with less practical effect, and requires a huge cost.

T. B. D. Nguyen (✉)
University of Transport and Communications/UTC, Hanoi, Vietnam
e-mail: ntbachduong@utc.edu.vn

T. D. Pham
Construction Consultation Joint Stock Company for Maritime Building, Hanoi, Vietnam

© The Author(s), under exclusive license to Springer Nature Singapore Pte Ltd. 2024
T. Nguyen-Xuan et al. (eds.), *Proceedings of the 4th International Conference on Sustainability in Civil Engineering*, Lecture Notes in Civil Engineering 344,
https://doi.org/10.1007/978-981-99-2345-8_29

295

Static methods are also unsafe for people and vehicles when performing measurements in the field (the collision force and anchorage force for ships of 50,000 DWT up to 100 T). The influence of PPS damage relates to construction costs, equipment procurement, repair costs, reducing port operation revenue during the repair period, possible damage to ships, and other problems.

The PPS is built on a sloping roof separating the land and the water area; the lower part is primarily underwater and deep in the ground. This construction site is where the ground is often unstable. Visual inspection of structures is arduous after construction, accidents, and natural disasters, including earthquakes or floods. The consultants in Vietnam usually recalculate if there are irregularities in construction or when operating conditions change, and they also do not mention the deterioration of the structure. If the above measurement results exceed the given requirements, the operability of the pier is in doubt.

Some researchers indicated that the areas with different geologic backgrounds affect the method of determining the dynamic ground coefficient of the dynamic analysis model of the design [1, 3, 5]. PPS in diagnostic applications is verified using an impact vibration test (in the absence of the original measured oscillation frequency). The geology of the port construction has different characteristics between the regions of Vietnam; it is also different from the geological features in Japan. In this paper, it is shown that the natural frequency of port oscillation (theoretical dynamic analysis model) has an inverse relationship with the building grade. In other words, the more important the PPS level, the smaller the natural oscillation frequency. This is not covered under applicable philosophy and guidelines [6]. The article also shows how to determine the natural frequency of the pier in a simple way.

2 Research on Verification of the PPS by Using Impact Vibration Test in Vietnam

2.1 Assessment of Structural Condition of Pile Foundation Type by Impact Vibration Test

The sequence of steps of the impulse test is shown in Fig. 1. The set of indicators for assessing structural health by the impact vibration test (IVT) is in Table 1. The index of assessing structural health (K) is determined by natural frequency measured with the standard natural frequency [6]. The second method is often used to access or determine PPS's technical/health status.

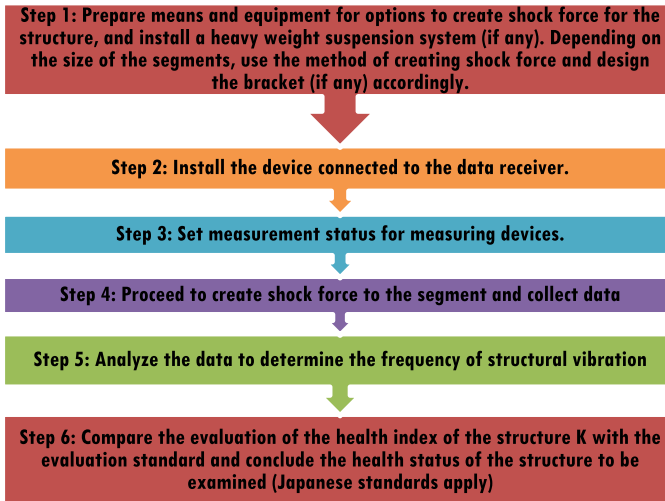


Fig. 1 Sequence of impact vibration test steps

Table 1 Health index

Index of soundness κ	Level	Assessment
$\kappa \leq 0.70$	A1	May cause danger if there is a great external load applied, need to implement other investigations, need to reinforce
$0.70 < \kappa \leq 0.85$	A2	Need to continue to pay attention to the decrement in the natural frequency
$0.85 < \kappa \leq 1.00$	B	There is almost no problem at present
$1.00 < \kappa$	S	The structure is completely healthy at present

2.2 Analysis of the Influence of the Decentralization of Port Facilities on the Port Structure Classification

Circular 06/2021/TT-BXD, dated June 30, on the decentralization of construction works for port facilities is shown in Table 2.

The structure classification affects the determination of the stability coefficient in the calculation of the overall stability of the port facilities in Table 3 (assurance factor

Table 2 Port structure classification

Classification criteria	Specific	I	II	III	IV
Vessel tonnage (thousands of DWT)	> 70	> 40–70	> 20–40	> 5–20	≤ 5

considering the port facilities' importance and the port facilities) and the design life of the port facilities TCVN 11,820–1:2017 Table 4.

Table 1 shows that PPS health index κ is less than 0.7 at the end of design life, for example, 0.6. Assuming that the natural frequency of the structure is equal to the design's natural frequency, then the natural frequency is reduced 0.6, i.e., 1.667 (1/0.6) times.

–According to the importance of port structure:

- Port structure is grade 1, and the natural vibration frequency is reduced to 1.667/1.25 times, i.e., 1.33 times;
- Port structure is grade 2, and the natural vibration frequency is reduced to 1.667/1.2, i.e., 1.38 times;
- Port structure is grade 3, and the natural frequency is reduced to 1.667/1.15, i.e., 1.45 times.

–According to the design age of the port structure:

Assume PPS does not repair and upgrade, then.

- PPS is grade 1 (100 years), the annual natural oscillation frequency is reduced by less than 0.004 times;
- PPS is grade 2 (50 years), the annual natural frequency will be reduced by less than 0.008 times;
- PPS is grade 3 (20 years), the natural frequency of the vibration is reduced by less than 0.02 times.

The set of health indexes considering the importance of port facilities (classification of port facilities) is proposed in Table 5. According to Circular No. 59/2014/TT-BGTVT of the Ministry of Transport, periodic inspection of PPS is every 5 years. Thus, the measured natural frequency should be larger than the original measured natural frequency divided by the value listed in Table 6 (assuming that the measured natural frequency of the structure is equal to the design's natural frequency, the health index at the end of PPS operation time is 0.6).

Table 3 The factor of assurance considering the importance of port facilities k_n

The factor k_n	Grade I	Grade II	Grade III	Grade IV
k_n	1.25	1.2	1.15	1.1

Table 4 Age of the port structure according to the hierarchy of durability and fire resistance

Age (year)	Special/grade I	Grade II	Grade III	Grade IV
Age	> 100	50–100	20–50	< 20

Table 5 Health index of PPS considering the importance of port facilities (classification of port facilities)

Health index/grade	Special/I	II	III	IV
A1	$\kappa \leq 0.87$	$\kappa \leq 0.84$	$\kappa \leq 0.80$	$\kappa \leq 0.77$
A2	$0.87 < \kappa \leq 1.06$	$0.84 < \kappa \leq 1.02$	$0.80 < \kappa \leq 0.98$	$0.77 < \kappa \leq 0.94$
B	$1.06 < \kappa \leq 1.25$	$1.02 < \kappa \leq 1.2$	$0.98 < \kappa \leq 1.15$	$\kappa \leq 1.1$
S	$1.25 < \kappa$	$1.2 < \kappa$	$1.15 < \kappa$	$1.1 < \kappa$

Table 6 The natural frequency of PPS measured according to the age of the structure

Age (year)/grade	Special/I (times)	II (times)	III (times)
10	1042	1087	1250
15	1064	1136	1429
20	1087	1190	1667
30	1136	1316	–
40	1190	1471	–
50	1250	1667	–
100	1667	–	–

3 Case Studies in Vietnam

3.1 Determination of Natural Frequency of PPS in Theory/ Design Dynamics Analysis

The theoretical dynamic analysis to determine the natural frequency (F) of PPS is determined by two methods follow:

The 1st method [5]: Simple method the approximate natural frequency of the type horizontal frame according to Eq. (1).

$$F = \frac{1}{2\pi} \sqrt{\frac{gK}{W}} \text{ (Hz)} \tag{1}$$

where:

- W is the weight of the type horizontal frame with the weight of the upper plate (T)
- g is the acceleration due to gravity 9.8 m/s^2
- K is the coefficient of spring stiffness in the horizontal direction of the structure.

–The 2nd method: Dynamic analysis of PPS using the eigenvalue method is performed in SAP 2000 [1, 2].

Dynamic analysis models of some PPS according to [1, 2, 4] as shown in Figs. 2 and 3.

Fig. 2 Dynamic model of port segment. Grade 3 (Sai Gon Terminal)

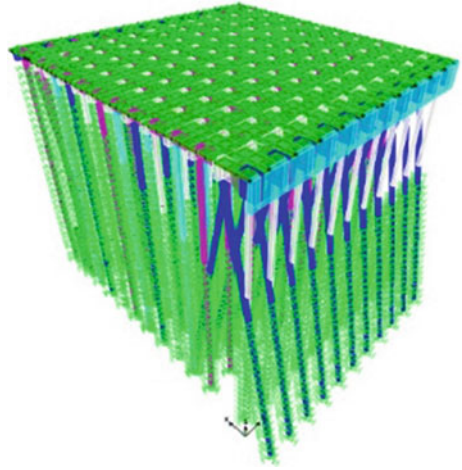
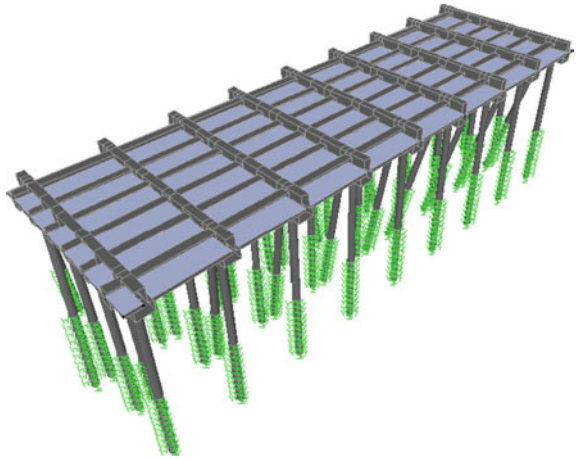


Fig. 3 Dynamic model of port segment. Grade 1 (Binh Thuan Terminal)



3.2 The Results of Design Natural Frequency on Case Studies

According to the previous studies [1, 2, 4], the specific oscillation frequencies of several survey ports by construction level are shown in Tables 4 and 5.

By the 1st method: the K value is determined according to the regression correlation shown in Fig. 4 for the horizontal frame models corresponding to each case.

The natural frequency is shown in Table 7.

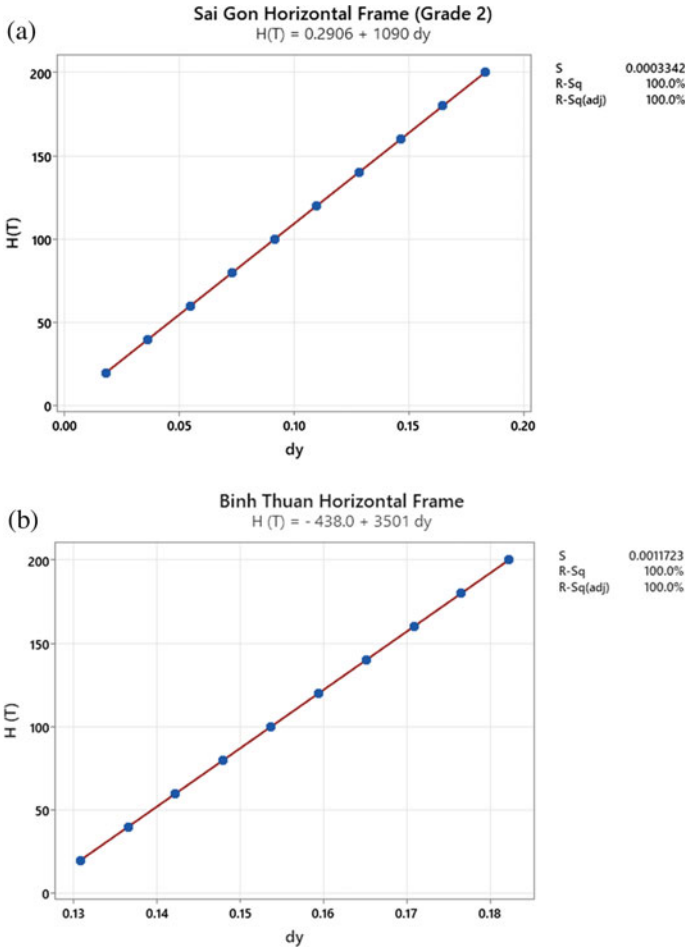


Fig. 4 Relationship between the horizontal force and the horizontal displacement of the type horizontal frame: **a** The frame No. 7 (No. 8) of Sai Gon Terminal (Grade 2); **b** The frame of Binh Thuan Terminal (Grade 1)

3.3 Analysis of the Influence of the Decentralization of Port Facilities

The results of Sect. 3.2 show that ports of regional, national, or regional importance typically serve large vessels. The free height of the pile is significant, and the natural frequency is small. Significantly, the protruding jetties with natural frequency will be smaller than the shore ports. Polynomial regression analysis (Fig. 5) showed that the relationship between the natural frequency of a typical transverse frame (F_{2D}) and the natural frequency of the type pile segment (F_{3D}). F_{3D} is calculated through F_{2D} as shown in Eq. (2).

Table 7 Natural vibration frequency according to grade classification

Grade	Name of port	K	W	Frequency (mode 1)		
				1st method	2nd method	
3	Sai Gon Terminal. port segment No.1	3066	410.89	1.36168	3.09246	
	Sai Gon Terminal. port segment No.2	1090	405.94	0.81684	3.41329	
	Sai Gon Terminal. port segment No.3	1090	405.94	0.81684	4.41299	
2	Sai Gon Terminal. the port structure No.1	1449	427.61	0.91762	2.51166	
	Sai Gon Terminal. port segment No.2	1449	427.61	0.91762	2.5028	
	Sai Gon Terminal. port segment No.3	1449	427.61	0.91762	2.51166	
	Sai Gon Terminal. port segment No.4	4008	447.03	1.49263	2.54728	
	Sai Gon Terminal. port segment No.5	4008	447.03	1.49263	2.54728	
	Sai Gon Terminal. port segment No.6	4008	447.03	1.49263	2.14094	
	Sai Gon Terminal. port structure No.7	1090	299.08	0.95165	1.43891	
	Sai Gon Terminal. port structure No.8	1090	299.08	0.95165	1.54592	
	1	Binh Thuan Terminal. port segment No.1	3501	620.04	1.18451	1.33995
		Binh Thuan Terminal. port segment No.2	3501	620.04	1.18451	1.260
Binh Thuan Terminal. port segment No.3		3501	620.04	1.18451	1.401	

$$F_{3D} = 1.522 - 9.588 \log_{10}(F_{2D}) + 174.5 \log_{10}(F_{2D})^2 - 492.5 \log_{10}(F_{2D})^3 \tag{2}$$

According to Table 7, the natural frequency of vibration of level 1 berth works has a smaller value than that of grades 2 and 3. This is not coincidence with the

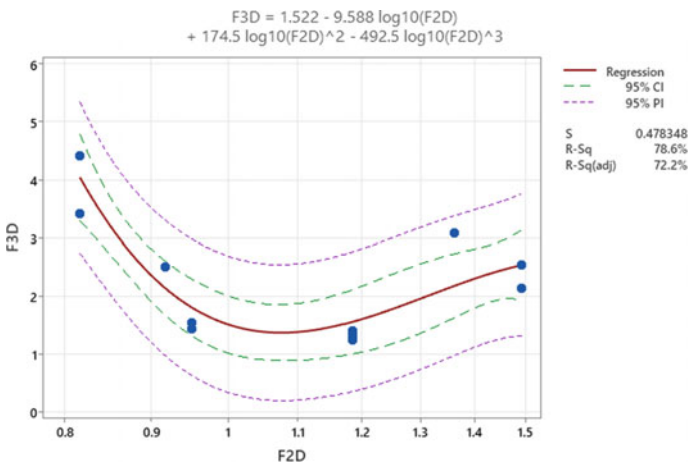


Fig. 5 Relationship between the F_{2D} and F_{3D}

Table 8 The threshold value of measured natural frequencies of some PPS in 2022

Grade	Name of port	Age	F
3	Sai Gon Terminal. the port segment No.1	28	2985
2	Sai Gon Terminal. the port structure No.1	22	2484
	Sai Gon Terminal. the port structure No.5	23	2494
	Sai Gon Terminal. the port structure No.7.8	11	1575
1	Binh Thuan Terminal. the port segment	5	1470

calculation of the frequency of oscillation of a horizontal frame according to method 1.

3.4 *The Measured Natural Frequency on the Age*

The health index at the end of the PPS operation time is 0.6, as the same assumption above (2.2). Before the inspection, the PPS of Saigon Terminal–grade 3 have upgraded to continue operating after 50 years. The measurement frequency must be greater than the value in Table 8 then the PPS ensures the health/technical condition for operation at the time of verification. The value of F in Table 8 is calculated from Table 6.

4 Conclusion–Recommendation

The port structure hierarchical scale or the berth height/depth of the harbor structure affects the determination of natural vibration frequencies. The article has considered the influence of PPS hierarchy in assessing structural health/technical status by IVT as shown in Tables 5 and 6. Table 7 shows that the more important the PPS than the smaller the natural frequency. From there, it is easy to predict the measured value of the natural vibration frequency of the structure in the normal operating condition of PPS (Table 7).

In addition, there is a difference between the formula for determining the horizontal natural frequency of the representative transverse frame and the PPS model according to SAP 2000. Field experiments are usually carried out for the berth segment. The natural design frequency of the PPS can be quickly determined through the horizontal natural frequency of the representative transverse frame by Eq. (2). Calculating the natural design frequency of a typical horizontal frame diagram is simple and quick. Even if the original design document does not include a design file. Thus, the design natural vibration frequency of the PPS segment (especially in case of loss of design/as-built documents) can be determined and the measured frequency range can be predicted if the PPS segment is normally operated. As a

result, the PPS is inspected and can be used as a basis for restoring construction design documents.

Acknowledgements This research is funded by Ministry of Education and Training under grant number B2022-GHA-01.

References

1. Duong NTB et al (2021) Study on dynamic ground reaction coefficients of theoretical dynamic analysis model in health assessment of pier structure by impact vibration test. University of Transport and Communications. Code No. T2020-CT-017 (Leader)
2. Duong NTB, Hung NH, Dan NA (2018) Research on impact vibration test method for port substructure in Viet Nam. Dynamic soil-structure interaction for sustainable infrastructures. Sustainable civil infrastructures ISBN 978-3-030-01919-8 (ISBN 978-3-030-01920-4 (eBook)). ISSN 2366-3405 (ISSN 2366-3413 electronic). <https://doi.org/10.1007/978-3-030-01920-46>. pages 174. Springer Nature Switzerland AG 2019
3. Viet Nam Maritime Administration (2018) TCCS 02/2018/CHHVN: Sea port structure—Audit standard. Hà Nội
4. Saigon Port Joint Stock Company (2020) Dossier of survey design and inspection of piers of Saigon Port
5. The Overseas Coastal Area Development Institute of Japan (2020) Technical Standards and Commentaries for port & Harbour port Facilities. Tokyo—Japan
6. Ministry of Land, Infrastructure, Transport and Tourism of Japan (2007) Structure management and maintenance standard—underground structure and foundation structure. Japan

Prediction of Water Setup and Wave Crest Heights on Submerged Coral Reefs with Steep Slopes



Tao Nguyen Quang, Ha Thi Thu Nguyen, Bau Nguyen Van,
and Cuong Dinh Quang

Abstract Submerged coral reefs develop unique topographic profiles over time. Moving landward from the offshore, they are recognized by a very steep slope with a transition at the algal ridge or reef crest to a large, gentle, or concave region attached to the shore. The water depth of the reef flat is relatively small and often exposed during low tides, in the range of a few to tens meters. The mechanism of wave transformation from offshore to the reef crest and reef flat is complicated. The main distinction in the wave propagation in these geometric profiles is caused by a sudden change of reef topography, from hundreds of meters in deep water depth to a few meters of shallow flat shelves. When waves propagate from deep water to reefs with steep foreshore, the mean sea level (MSL) will significantly increase and be associated with the increased wave crest elevation. Predicting the wave propagation, water setup, and wave crest elevation is crucial in analyzing and designing structures on nearby islands, such as determining the scale of wave height effects, overtopping discharge, etc. This paper predicts the water setup and the increase of wave crests above MSL based on a physical model in a wave flume. The remarkable result shows that the water surface elevation above water level can even reach approximately a wave height offshore due to the resonant phenomenon of wave amplitudes at the shoreline...

Keywords Submerged coral reefs · Steep slope · Water setup · Wave crest height · Physical model

1 Introduction

Vietnam is a tropical coastal country, including thousands of islands and submerged reefs. The existence of these islands plays crucial roles in the socio-economic development, national security, and defense. The topography of the island often divides

T. N. Quang (✉) · H. T. T. Nguyen · B. N. Van · C. D. Quang
Hanoi University of Civil Engineering/HUCE, Hanoi, Vietnam
e-mail: taonq@huce.edu.vn

into patterns based on geographic characteristics, such as soil islands, rock islands, and coral reefs.

The reef corals are commonly found in tropical and subtropical waters, corresponding to latitudes between 30° north and 30° south. There are three reef types: fringing, barrier, and atoll. They all share bio-geographic similarities in their profiles. One of the main topography-related features of the islands or coral reefs is that the reef flat zone is relatively large, which was created by tiny sea animals called corals and associated with small hard coral rocks. Around the coral reef are a reef crest (or algal ridge) and a steep slope zone. The steep region is often divided into two parts. The upper part is a natural fore reef zone where its topography is relatively narrow and connected with submerged coral shelves in a water depth of a few meters to hundreds of meters. Its geography was created by many tiny and individual creatures living and growing in this area. The bottom part is a deep fore reef with a height of thousands of meters, which was created by coral rocks (Figs. 1 and 2).

At the moment, it is necessary to build infrastructures on the island and coral reef in order to ensure the socio-economic requirements. One of the difficult tasks to estimate and build structures in the submerged zone of the island is to determine wave height, water set-up above MSL, and associated with their water surface elevation in this area.

As mentioned above, the coral reef was developed with underwater mountains and associated with a very steep slope laying around. When the wave propagates into a steep-slope bathymetry with a relatively small water depth, the wave certainly breaks. This process often happens complicatedly. The difference in wave transformation on

Fig. 1 Cross-section of a submerged coral reef

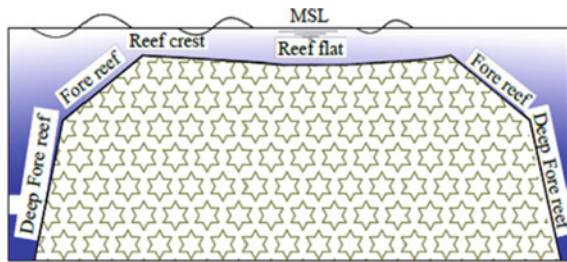
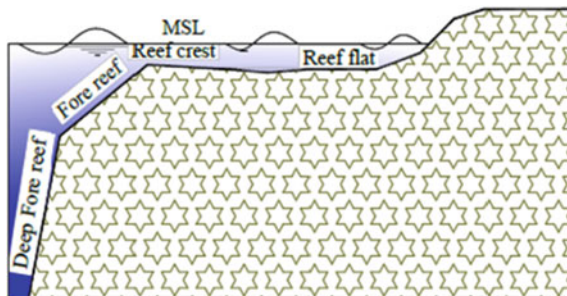


Fig. 2 Cross-section of a coral island



this kind of reef is a sudden change of its topographic profile from hundreds of meters to a few meters in shallow water caused by a wall in the deep fore reef (see Fig. 1). When the deep-water wave propagates into a wall, it often breaks close to the reef crest (if wave height is relatively larger than the corresponding water depth in this area). Consequently, waves dissipate almost their energy and then generate new waves to continue coming into the island.

According to the state-of-the-art in submerged coral reefs worldwide, a variety of studies have been introduced. Jensen [1] conducted experimental test cases of wave transformation over a submerged reef, such as coral reefs or submerged breakwaters. It confirmed that wave energy bunching could be seen at the reef crest, and then the energy dropped quickly and new waves were generated. More importantly, the wave height could reach roughly 0.8 times the water depth of that submerged reef. Buckley et al. [2] illustrated the fringing reef with a similar slope reef of 1/5 and surveyed the wave-reef interaction. They concluded that the wave setup and set-down in the numerical model were both underestimated compared to the laboratory. Based on Wen et al. [3] related wave propagation over the submerged reef with a fore reef of 1/1 and relatively small water depth at the reef compared to the incoming wave height. The substantial increase in water level on this reef could be clearly seen, and the wave height tended to increase in the reef crest, and then decreased quickly. Meantime, the increase of mean sea level was given in this area.

Research on wave propagation over Vietnamese islands is pretty limited. Tuan and Cuong researched the distribution of wave heights on steep submerged reefs [6]. To predict wave height, water set-up, and water surface elevation above MSL are approximately determined. However, it is no longer valid due to the limitations of the guidelines. Based on Vietnamese standards [4], the estimated wave height is not exceeding 78 percent of the water depth (d), and in the basic design stage, the chosen significant wave height can be 0.6 times its water depth. According to the TCVN 8421:2010 about wave loads and actions on a hydraulic structure [5], the breaking wave height on regular slopes can be calculated based on charts by a limited slope of $i = 0.2$.

In this study, the prediction of water surface elevation and water setup will be investigated more detail in order to determine wave impacts on this type of structure.

2 Material and Methods

This section provides the physical model data mentioned in the previous part. The test cases were carried out in a Dutch wave flume at Thuyloi University (Hanoi, Vietnam). The wave flume is 43 m long, 1 m wide, and 1.2 m high with a smooth, impermeable bottom (Fig. 5). The wave generator is equipped with an active reflection compensation (ARC) to absorb the wave incoming from the wave flume and reduce unwanted re-reflections of waves up against the wave board. The wave generator can generate both regular and random waves with a wave height of up to 0.3 m and a wave period of 3.0 s. Capacitance-type wave gauges are used to measure the instantaneous water

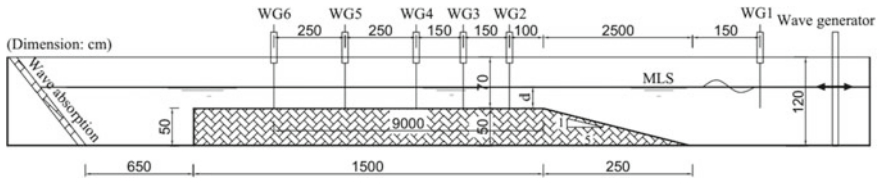


Fig. 3 Sketch of wave flume set-up and wave gauge arrangement

surface elevation with a high accuracy range (in the order of 0.1 mm) and measured frequency of 100 Hz. Six wave gauges are distributed in three regions across the reef, i.e., deep water, the reef crest zone (wave breaking zone), and the reef flat zone (behind the reef crest). The sampling rate was set at 50 Hz for all wave gauges to exactly catch the crest and trough of the wave.

The prototype of the coral reef has a cross-section along the wave direction with a slope is over $1/5$. The deep fore reef can vary from hundreds of meters to about 20 m water depth. The fore reef zone is at a water depth of about 20 m to a gentler submerged area, ranging from $1/5$ to $1/10$, where the physical wave-structure interaction often happens. The reef flat zone (or lagoon area) has more or less the same topographical elevation. Its width varies from hundreds of meters to a few kilometers, but the water depth is relatively shallow, ranging from 5 to 20 m.

Based on the capacity of the wave generator and prototype characteristics, the chosen experimental scale is $1/40$. Based on the Froude scale, the period scale is $1/\sqrt{40}$.

The experimental setup was shown in Fig. 3, where the wave flume's height is 0.5 m to ensure the incoming wave reaches deep water, viz. non-breaking zone. In the previous study of Tuan and Cuong [6], when considering the slope $i = \tan\alpha = 1/5 - 1/10$, the effect of wave transformation on the island is insignificant. Therefore, this research mainly focuses on one representative seaward slope of $i = 1/5$, instead of two. The width of the island is $B = 15$ m, corresponding to 600 m in the prototype, and is covered by a smooth PVC layer. On the island side, a wave absorber is put which is created by rubble armor with a mild slope of $1/6$. A high-resolution video is conducted perpendicular to the wave flume at the outer shelf to record all the movement of waves in the surf zone for all experimental scenarios (Table 1).

3 Results

The water surface elevation of typical scenarios and wave height are provided in Figs. 4, 5, 6 and 7 as follows.

Figures 4, 5, 6 and 7 show that:

- The wave height on the submerged reef does not change significantly when the incident wave height is less than $1/2$ water depth;

Table 1 The scenarios of experimental program

Case	Parameter	Nomenclature	Value	Unit
1	Incoming wave height	Hs	0.05	[m]
	Wave period	Ts	0.9	[s]
	Water depth	d	0.15	[m]
2	Incoming wave height	Hs	0.1	[m]
	Wave period	Ts	1.2	[s]
	Water depth	d	0.15	[m]
3	Incoming wave height	Hs	0.15	[m]
	Wave period	Ts	1.5	[s]
	Water depth	d	0.15	[m]
4	Incoming wave height	Hs	0.20	[m]
	Wave period	Ts	1.7	[s]
	Water depth	d	0.15	[m]
5	Incoming wave height	Hs	0.15	[m]
	Wave period	Ts	1.5	[s]
	Water depth	d	0.2	[m]

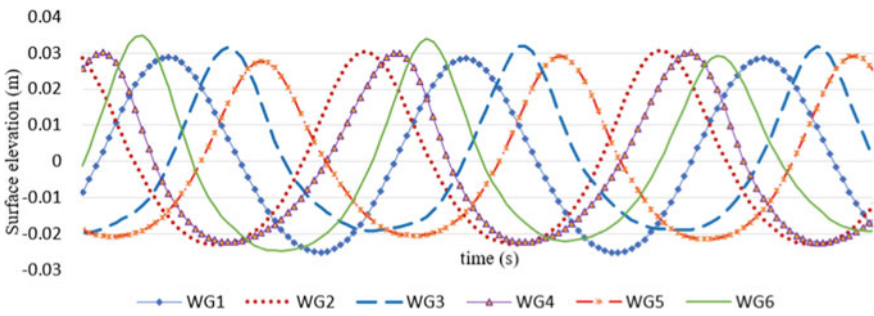


Fig. 4 Water surface elevation of case 1

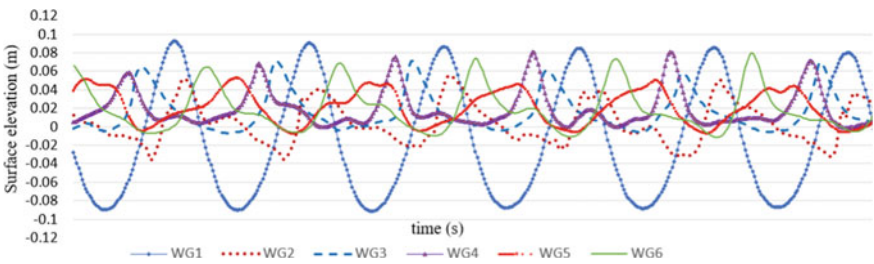


Fig. 5 Water surface elevation of case 3

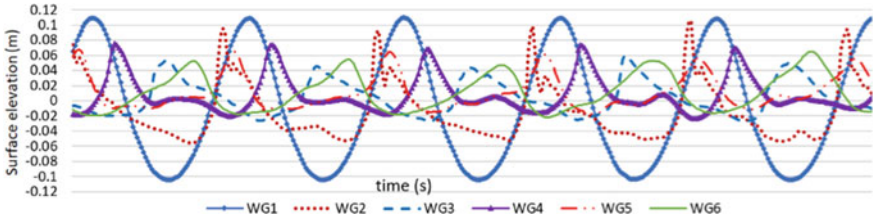


Fig. 6 Water surface elevation of case 4

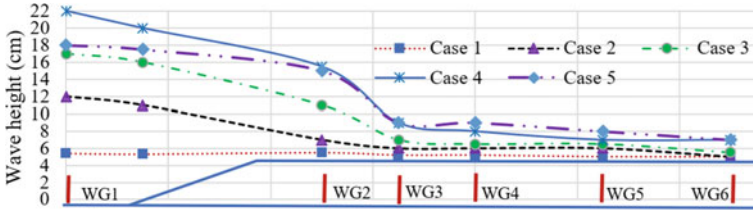


Fig. 7 Wave height at measured points (cm)

- The wave height is reduced gradually in the surf zone (the reef crest zone), and the wave shape already changes quickly. After the WG3 position, the wave shape is reformed and the height is reduced lightly;
- The wave height on the crest zone (surf zone) is able to significantly higher than the water depth of reef flat.

The wave set-up, the ratio between wave crest (as measured from the MSL), and wave height at measured points are provided in Figs. 8 and 9 as followings.

Figures 8 and 9 show that:

- In the landward wave gauges, the mean water surface elevation above MSL is increased significantly.
- When the incident wave height (H_i) is significantly higher than the water depth of the reef flat, the wave distorts strongly. Furthermore, the wave crest (η_{max}) is very large compared to the wave height (H_s). Wave crest can reach up to $0.95 H_s$.

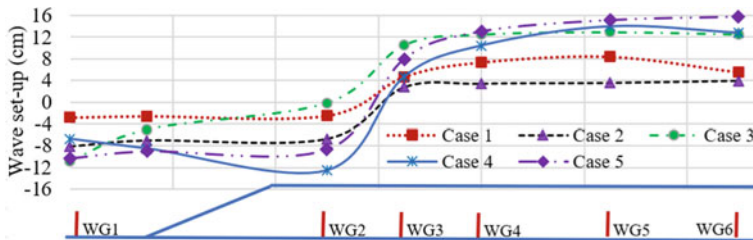


Fig. 8 Water set-up in the submerged reef

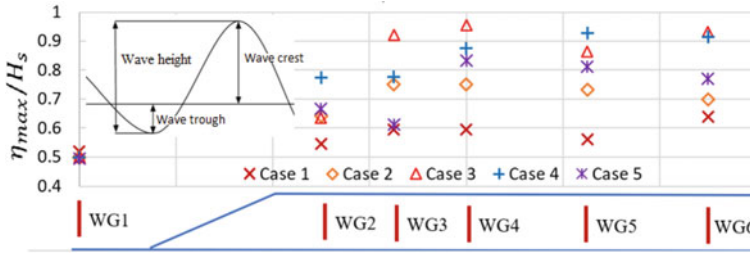


Fig. 9 The ratio between wave crest and wave height at measured points

4 Discussion and Conclusion

Wave transformation from deep water to a steep-slope island is a complicated process of wave height. This process can be influenced by incoming waves and water depth at the submerged reef. In this reef, especially at a distance of a wavelength from the reef crest, the wave height is highly affected due to the resonant phenomenon after breaking the wave. Particularly, the wave height in this surf zone can be even larger than the corresponding water depth of the submerged reef.

When the wave reaches the submerged reef, it can reduce quite fast and its elevation also significantly reduces, compared to the corresponding water depth. Therefore, when designing a structure in this area, it is necessary to bring a suitable solution to determine an appropriate wave height. Clearly, it is incorrect if use 0.78 times the corresponding water depth as an input preliminary wave height to design a coastal structure as the [4].

In the landward, which is far away from the reef crest. The maximum wave height was about 0.55 water depth. This result was also consistent with studies by Nelson based on the experimental data of the model and the surf zone on the flat horizontal bottom [7].

The mean sea level in the submerged reef increases noticeably, and a higher wave crest elevation can be seen, compared with them in a surf zone of a beach. At the distance far from the reef crest, the wave crest is very large compared to the wave height. The wave crest height can reach up to 0.95 times the wave height. At the same time, the water surface elevation changes significantly but non-breaking occurs.

For engineers, it would be better to consider carefully the combination of the water surface phenomenon associated with wave crest elevation.

The research only carrying out of the regular wave need performing more experiments with the irregular wave to accurately determine the wave variability on the reef.

Regarding the numerical model, a free-surface, non-hydrostatic Simulating Waves till Shore (SWASH) can be an appropriate approach to correctly estimate the wave height, water set-up, and water surface elevation [8–10] for this type of structure based on lots of studies about coastal structures, even for islands or coral reefs.

Further studies can examine and validate these values based on the laboratory and the SWASH model.

References

1. Jensen MS (2004) Series paper: Breaking of waves over a steep bottom slope
2. Buckley ML, Lowe RJ, Hansen JE, Dongeren AR (2015) Dynamics of wave setup over a steeply sloping fringing reef. *J Phys Oceanogr*. <https://doi.org/10.1175/JPO-D-15-0067.1>
3. Wen H, Ren B, Wang G, Zhao Y (2018) Numerical simulation of wave breaking over a submerged step with SPH Method. *Int J Ocean Coastal Eng*
4. TCVN 9901:2014 (2014) Hydraulic structures—requirement for sea dike design. Vietnamese version
5. TCVN 8421:2010 (2010) Hydraulic structures—loads and actions of wind-induced and ship-induced waves on structures. Vietnamese version
6. Tuan TQ, Cuong DQ (2019) Distribution of wave heights on steep submerged reefs. (*Ocean Engineering* 189 2019 106409). <https://doi.org/10.1016/j.oceaneng.2019.106409>
7. Nelson RC (1994) Depth limited design wave heights in very flat regions. *Coast Eng* 23:43–59
8. SWASH User Manual (2016) SWASH Version 3.14A; the SWASH Team, Delft, the Netherlands
9. Nguyen TH, Hofland B, Chinh VD, Stive MJF (2020) Wave overtopping discharge for very gently sloping foreshores. *Water* 12(6):1695. <https://doi.org/10.3390/w12061695>
10. Nguyen TH (2022) Wave overtopping process for very mild sloping and shallow foreshores. PhD dissertation. Delft University of Technology, the Netherlands.

A Study of Wave Attenuation Through Vegetation



Phan Khanh Linh, Pham Lan Anh, Truong Hong Son, and Le Hai Trung

Abstract The importance of vegetation in coastal environments is becoming more widely acknowledged. The intricate structure of roots, stems, and canopies of vegetation allows it to absorb external disturbances such as waves and currents. Even though several physical models have been performed, they mostly address the attenuation of regular waves. The influence of wave parameters on vegetation-induced wave height attenuation is not well explored. At the Delft University of Technology, a laboratory mimicking the processes of wave reduction through cylinders was performed. Various tests were carried out, including regular, irregular, broken, and non-broken waves. Moreover, a model imitating the test was built in a non-hydrostatic wave-flow model SWASH, using experimental data to calibrate and validate. The results suggest that the wave attenuation processes inside vegetation strongly depend on the wave characteristic. The numerical model captured very well the processes of the wave height reduction measured in the physical tests. Thus, the rate of wave attenuation was studied as a function of the number of wavelengths and the Ursell number.

Keywords Wave height reduction · Cylinders · Experiment · Numerical model · Ursell number

1 Introduction

As a result of sea level rise, subsidence, and global warming, several coastal locations across the world have been shown to experience rapid erosion [1]. Planting mangrove forests is now one of the good solutions for reducing coastal erosion since mangroves can reduce wave height and therefore increase sediment deposition [2]. Mangroves' intricate roots, stems, and canopy structures allow them to absorb

P. K. Linh (✉) · P. L. Anh · T. H. Son · L. H. Trung
Thuyloi University, Hanoi, Vietnam
e-mail: phankhanhlinh@tlu.edu.vn

external stresses such as waves and currents [3]. Waves travel through a mangrove forest and perform work on vegetation roots, stems, and canopies, thereby losing their energy and reducing their wave height [4]. Therefore, the window of opportunity for sedimentation inside the forest increases.

Several studies have been conducted to investigate the reduction of wave height in vegetation [5]. The reduction of wave height depends on the stiffness, density, and wave characteristics, i.e., the wave height and wave period [6]. However, the influences of wave characteristics on the decreased rate of wave height in vegetation are not completely comprehended. More wave height reduction through vegetation is observed when the approaching wave height in front of the forest increases [7]. However, less wave height reduction is also observed with increasing incoming wave height [8]. It is shown that wave attenuation is substantially influenced by the ratio of stem length to water depth and density [9]. Moreover, high-frequency waves tend to reduce faster than low-frequency waves [10].

Consequently, despite performing several physical models in conjunction with advanced computational models, most studies solely focus on the attenuation of regular waves across a restricted amount of vegetation length in the range of one to four meters. Therefore, this study's main objective is to examine wave characteristics' role on the wave attenuation processes.

2 Method

To achieve the research objective, physical tests and numerical models were selected as the key approaches. The configurations of the physical model are presented in this section. Moreover, a numerical model imitating the experiment was built in the state-of-the-art SWASH model. The model was then calibrated and validated using experimental data sets. Finally, the results of the physical and numerical models were analyzed to investigate the impacts of wave non-linearity on the wave height reduction in the mangrove forests.

2.1 *Physical Model*

A 1D physical model of wave height reduction through cylinder arrays, representing wave decrease processes through a mangrove forest in the Mekong Delta, was built and performed in a wave flume of the Fluid Mechanics Laboratory at the Delft University of Technology. The flume's effective length, height, and width are 40 m, 1 m, and 0.8 m, respectively. The overall experimental setup is given in Fig. 1.

To prevent reflected waves from reflecting back into the flume, a wave generator with an active wave absorption system was positioned at the beginning of the flume. Throughout the experiment, the second-order wave steering was always active. To imitate the processes of shoaling and breaking waves, a steep wooded slope with a

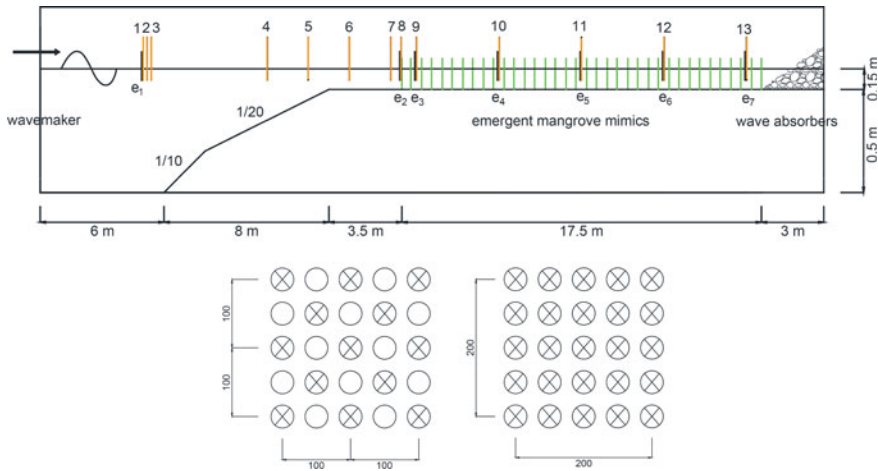


Fig. 1 Representative cross-section of the experimental setup (top panel) and vegetation configuration (lower panel). The depth-averaged velocity and wave height were measured using 13 wave gauges and seven electromagnetic velocity meters (EMS) with a sampling rate of 100 Hz. Representative equipment locations are also included

slope combination of 1/10 and 1/20 was employed. A horizontal bottom was installed with a length of 17.5 m cylinder arrays. The layout of the cylinder arrays examined in the experiment is shown in Fig. 1b. The cylinder array density was determined by the density of the mangroves. Mangrove densities are regarded in two ways: sparse (200 cylinders/m²) and dense (400 cylinders/m²).

The tests were carried out using the described setup for various wave heights and wave period conditions, including regular and irregular, non-broken waves, and broken waves (Table 1). In order to achieve good representative statistical data, the experiments were repeated with varied positions of the equipment to acquire more data inside the plant.

Furthermore, wave height and velocity data were obtained over a long time period, thus at least 100 waves in regular wave situations and 1000 waves in irregular wave scenarios. In the absence of mangroves, the Guza approach was utilized to differentiate incoming and reflected waves from irregular and regular waves [11]. This

Table 1 Experimental scenarios

Vegetation	Wave characteristic	Regular (Re)		Irregular (Ir)	
		H (cm)	T (s)	Hs (cm)	Tp (s)
No vegetation	Broken (type 2)	10	2.0; 2.5; 3.0	10	2.0; 2.5; 3.0
With vegetation	Non-broken (type 1)	1; 2; 3; 4; 5	2.0; 2.5; 3.0	3; 5	2.0; 2.5; 3.0
	Broken (type 2)	7;10	2.0; 2.5; 3.0	7; 9; 10; 13;15	2.0; 2.5; 3.0

approach is based on the collection of surface time series and velocity time series signals at the same locations.

2.2 Numerical Model

A numerical model of the laboratory experiment was constructed in the SWASH model. The SWASH is a state-of-the-art phase-resolving nonlinear shallow water wave model. The governing equations of this model are shallow water equations, in which a non-hydrostatic pressure term is also included [12]. Morrison's equation was used to simulate the presence of plants in SWASH:

$$F_x = \frac{1}{2} \rho C_d h_v b_v N_v u |u| \quad (1)$$

where ρ is gravitational acceleration, C_d is a bulk drag coefficient, h_v is the height of the cylinder, b_v is the diameter of the cylinder, N_v is the number of plants per square meter, and u is the horizontal velocity due to wave motion.

Specific numerical model setups relating to boundary conditions and vegetation characteristics. The model has 4000 active grid points with a minimum grid size of 0.01 m. The number of grid cells per wavelength is about 50–100 grid cells. The time step is 0.001 s. A sponge layer in which there is no wave reflection, a permeable slope mimicking the wave absorber, and an impermeable slope of 1/5 representing a sea dike at the end of the flume are three types of constructions that were applied in the model. The prediction accuracy of the numerical model was assessed using the bias and scatter index SI, which is defined by:

$$\text{bias} = \frac{1}{N} \sum_{i=1}^N (\varphi_{\text{comp}}^i - \varphi_{\text{obs}}^i) \quad (2)$$

$$\text{SI} = \frac{\sqrt{\frac{1}{N} \sum_{i=1}^N (\varphi_{\text{comp}}^i - \varphi_{\text{obs}}^i)^2}}{\frac{1}{N} \sum_{i=1}^N \varphi_{\text{obs}}^i} \quad (3)$$

Here, N is the total number of data points in a particular dataset, φ_{comp}^i denotes the wave parameter computed by SWASH and φ_{obs}^i denotes the corresponding observed wave parameter [12]. The simulation time is 60 min in cases of irregular waves and 20 min in cases with regular waves.

3 Result

In this section, experimental results are introduced relating the influences of the wave non-linearity on the wave height reduction through cylinder arrays.

3.1 Experimental Results

The wave transmission coefficient (K_T), is usually used to investigate the decrease of wave height within vegetation. K_T is the ratio of the transmitted wave height (H_x) to the wave height at the beginning point of the mangroves (H_o at $x = 0$ m). H_x denotes the root mean squared wave height at location x inside the vegetation.

$$K_T = H_x / H_o \tag{4}$$

Figure 2 illustrates the values of the coefficient K_T along the vegetation in different tests of wave conditions and vegetation densities. In cases without vegetation, K_T remains the same along the flume. In regular scenarios, the value of K_T is fluctuated and is larger than one due to the reflection. Bottom friction causes a small reduction in the wave height. The results indicate that vegetation is very effective in reducing wave height. In sparse cases, the wave height is damped by about 60% after the 17.5 m length of cylinder arrays. The wave height attenuation increased by just 10%, despite doubling the density of mangroves from 200 to 400 stems/m².

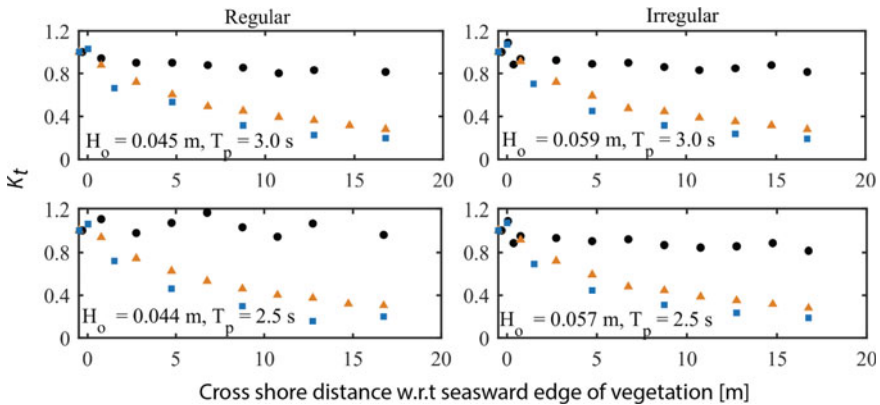


Fig. 2 Distribution of K_T in different scenarios of mangrove densities, including no plants (black circles), sparse vegetation 200 plants/m² (orange triangles), and dense vegetation 400 plants/m² (blue squares). $H_o = 10$ cm, with $T_p = 3.0$ s (upper panels); and $T_p = 2.5$ s (lower panels)

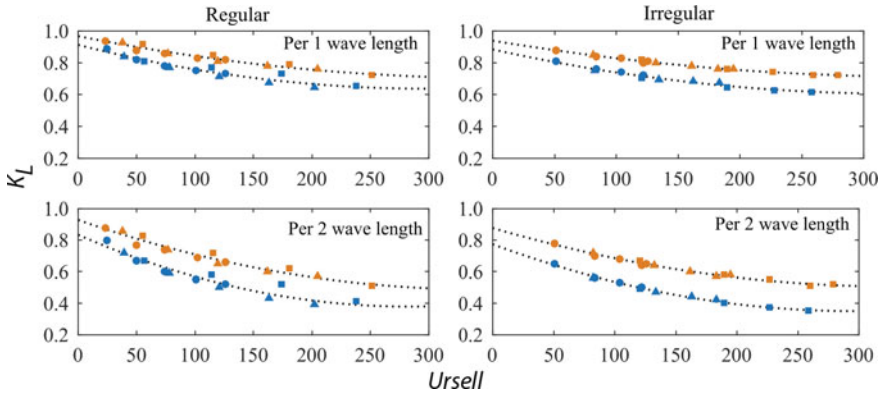


Fig. 3 Relationship between the effective transmission coefficient K_L and Ursell for different wave heights and periods

In this study, to introduce more physics into the analysis of the reduction of wave height through mangroves, a new wave transmission coefficient, namely effective wave transmission coefficient, is defined as:

$$K_L = H_L / H_o \tag{5}$$

The wave height attenuation is described over a relative distance, that is, the number of wavelengths, rather than the length of the mangrove forest. H_L is the root mean squared wave height after a certain number of wavelengths (n) and H_o is the root mean squared wave height at the mangrove edge ($n = 0$). The value of K_L is the value of K_T calculated after every single wavelength. Furthermore, the influence of wave non-linearity on wave damping in mangroves is elucidated through Ursell numbers, given by:

$$\text{Ursell} = H_s L^2 / h^3 \tag{6}$$

The water depth h , the wave length L , and the significant wave height H_s are calculated at the mangrove edge.

Figure 3 displays the connection between K_L , defined as (5) and the Ursell, given in (6) for a different value of n , the number of wavelengths. The results show that as the Ursell increases, K_L decreases, indicating an increase in wave height attenuation.

3.2 Numerical Results

The root-mean-square wave height (H_{rms}) and the mean water level (MWL) measured in the experiment are compared with the results of the numerical model

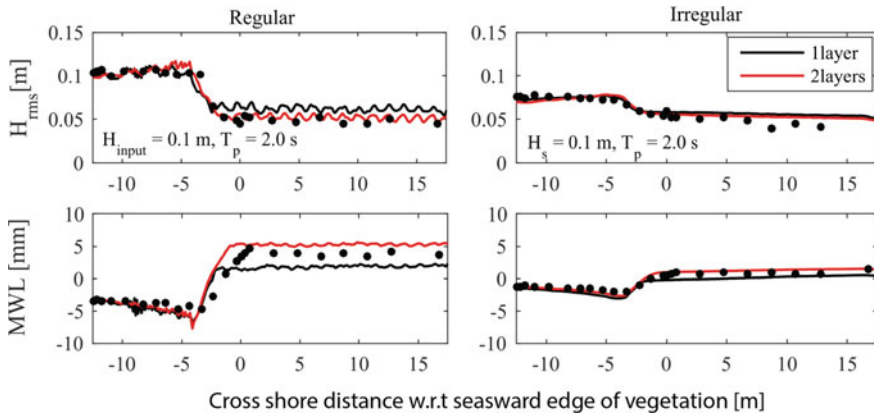


Fig. 4 Comparison H_{rms} and MWL of the numerical model (black and red lines) and measured data (black dots)

(Fig. 4). The results show that increasing the number of layers from 1 to 2 significantly improves the wave setup’s predictive skill. The SI of the wave setup for one layer is 0.62 and for two layers is 0.41. This means that a two-layer model is adequate for this examination. There is a good agreement between the numerical model and the physical model. This implies that the numerical model can reproduce the wave attenuation transformation processes measured in the physical model.

4 Conclusions

Despite the fact that several studies have been published on wave height reduction due to mangroves, the impacts of wave characteristics on this process are still unclear. Consequently, the wave height attenuation rate is usually presented and measured as a function of an absolute length. This paper examined the effect of wave characteristics on the reduction rate of wave height through a new relative length scale, which is the effective wave transmission coefficient (K_L) and include the physic of wave non-linearity through Ursell number (Ursell). It is suggested that the larger the non-linearity of the wave (the larger the Ursell), the stronger the wave height attenuation. Furthermore, a numerical model mimicking the physical test was built within the SWASH model, calibrated, and validated with the measured data. It is suggested that the numerical model can well reproduce the attenuation processes of the wave heights observed in the test. This suggests that the numerical model may be used to increase the attenuation distance of the mangroves in the experiment.

References

1. Truong SH, Ye Q, Stive MJF (2017) Estuarine mangrove squeeze in the Mekong Delta. Vietnam J Coast Res 33(4):747–763
2. Augustin LN, Irish JL, Lynett P (2009) Laboratory and numerical studies of wave damping by emergent and near-emergent wetland vegetation. Coast Eng 56(3):332–340
3. Mork M (1996) Wave attenuation due to bottom vegetation. In: Waves and nonlinear processes in hydrodynamics, Springer, pp 371–382
4. Phan KL, Stive MJF, Zijlema M, Truong HS, Aarninkhof SGJ (2019) The effects of wave non-linearity on wave attenuation by vegetation. Coast Eng 147:63–74. <https://doi.org/10.1016/j.coastaleng.2019.01.004>
5. Mazda Y, Magi M, Ikeda Y, Kurokawa T, Asano T (2006) Wave reduction in a mangrove forest dominated by *Sonneratia* sp. Wetlands Ecol Manage 14(4):365–378
6. Mendez FJ, Losada IJ (2004) An empirical model to estimate the propagation of random breaking and nonbreaking waves over vegetation fields. Coast Eng 51(2):103–118
7. Cavallaro L, Re CL, Paratore G, Viviano A, Foti E (2011) Response of *Posidonia oceanica* to wave motion in shallow-waters-preliminary experimental results. Coast Eng Proc 1(32):49
8. Bradley K, Houser C (2009) Relative velocity of seagrass blades: Implications for wave attenuation in low-energy environments. J Geophys Res: Earth Surf 114(F1)
9. Anderson M, Smith J (2015) Wave attenuation by flexible, idealized salt marsh vegetation. Coast Eng 3:82–92. <http://www.sciencedirect.com/science/article/pii/S0378383913001609> <https://doi.org/10.1016/j.coastaleng.2013.10.004>
10. Phan LK, van Thiel de Vries JS, Stive MJ (2015). Coastal mangrove squeeze in the Mekong Delta. J Coast Res 300:233–243
11. Guza R, Thornton E, Holman R (1985) Swash on steep and shallow beaches. Coast Eng 1984:708–723
12. Zijlema M, Stelling G, Smit P (2011) Swash: an operational public domain code for simulating wave fields and rapidly varied flows in coastal waters. Coast Eng 58:992–1012

Effects of Beach Slope on Wave Characteristics in the Surf Zone Over Fringing Reef



Pham Lan Anh, Phan Khanh Linh, and Truong Hong Son

Abstract Surf zone is an extremely dynamic region which is important to other wave hydrodynamic processes such as non-linear wave interaction, infra-gravity wave formation, wave set-up and decisive in coastal protection work design. This paper presents study on wave characteristics in the surf zone over fringing reef with steep beach slope under monochromatic wave condition conducted in a wave flume at Thuyloi University. Based on cine-photography analysis breaker type, breaker location, breaker wave height, breaker depth and the total surf zone width is determined and discussed. The results show that the relative reef flat submergence (d/H_0 in which d denotes flat depth, H_0 denotes incoming regular wave height) strongly influences on the breaking properties, albeit, the influence of beach slope is of minimal for the case of ten-meter flat width and beach slope $m = 3$.

Keywords Fringing reef · Wave characteristics · Surf zone · Monochromatic waves · Steep beach slope

1 Introduction

Beach morphology is one of the most important factors that controls the wave breaking characteristics. There are numerous research on breaking characteristics on various types of beach profile: plane beach, bar beach, barred beach, and submerged fringing reef. Amongst which wave breaking mechanism on a slightly varying beach slope has been thoroughly studied over 50 years (e.g., Galvin [1]; Komar and Gaughan [2]; Battjes [3]; Goda [4]; Liu et al. [5]). However, there have been few articles on wave breaking on fringing reefs morphology. Smith and Kraus (1990, 1991, 1992) pointed similar deep-water wave characteristics break distinctively on plane beaches and bars/reefs. Gourlay [6] classified the breaker type by a nonlinearity parameter for regular waves transformed on a steep face, F_{co} . Yao [7] demonstrated the reef

P. L. Anh (✉) · P. K. Linh · T. H. Son
Thuyloi University/TLU, Hanoi, Vietnam
e-mail: lananhct@tlu.edu.vn

© The Author(s), under exclusive license to Springer Nature Singapore Pte Ltd. 2024
T. Nguyen-Xuan et al. (eds.), *Proceedings of the 4th International Conference on Sustainability in Civil Engineering*, Lecture Notes in Civil Engineering 344,
https://doi.org/10.1007/978-981-99-2345-8_32

321

flat submergence is more relevant to characterize the breaking features on fringing reef than the common surf-similarity parameter supposed by Battjes [3]. Hence, wave breaking on fringing reef under more specific reef morphology (reef flat with very steep beach slope) has not been fully understood. The purpose of this paper is to determine the breaker type, breaker height, breaker depth, the incipient breaker and ending breaker position for regular waves propagating over fringing reef with beach slope $1/3$. By using Sony Handycam FDR-AX45 recorded images of breaking alongside the wave flume, data of wave breaking are cine-photography analysed to determine the characteristics and comparing them under two conditions: beach slope $m = 3$ and no beach slope.

2 Experiment Set-Up

The experiment was conducted in a wave flume at Thuyloi University in Vietnam. The wave flume effective length is 45 m, width is 1.0 m and height is 1.2 m, which equipped with an automated system of active reflection compensation (ARC) to ensure wave reflection removal at the wave maker and capable of generating both regular and irregular waves up to 0.3 m in height and 3.0 s in period. Wave gauge measurement based on capacitance principle and measure with ± 0.1 mm accuracy. Figure 1 illustrates the setup of laboratory test in which the smooth and impermeable top flat made of plywood is designed 0.5 m above the flume bottom. Because the study focuses on wave breaking characteristics and it is difficult to simulate accurately the bed roughness of coral in small scale, effects of bed friction and porosity are, therefore, disregarded. The length scale selected for the model is $1/20$ which is fully describe the tested wave conditions. The flat width is 10 m sufficiently wide to accommodate both breaking in the surf zone and the transmission behind the surf zone. As the effects of fore reef slope variation is found secondary (Yao [7], Tuan [8]), only one fore reef slope steepness $1/5$ is chosen. Moreover, the effects of beach slope have not been accounted in recent studies of Yao [7]. Normally, reef beach slope varies between $m = 12$ and $m = 3$ up to $m = 1$ (almost vertical). Then a beach slope of $m = 3$ is chosen to consider the influence of beach slope on breaking characteristics. Monochromatic wave condition is applied to better understand the physics of wave features in the surf zone (Table 1).

Six wave gauges were installed in the model with suitable spacing to determine surf zone and post-breaking zone. Wave gauges WG2, WG3 are movable in the surf zone to capture fully wave characteristics. Remain gauges were fixed as illustrated. In the experiment, the surface elevations were registered for 10 min. However, only 5 min after the wave maker starts, data were used to estimate breaking characteristics to gain stable condition. Camera recorded simultaneously and image analysis carried out during last 5 min of wave record. There were three cameras, one of which hanged over the top of flume to catch overall view of breaking process, two others running alongside of flume to catch the incipient and ending position of the surf zone.

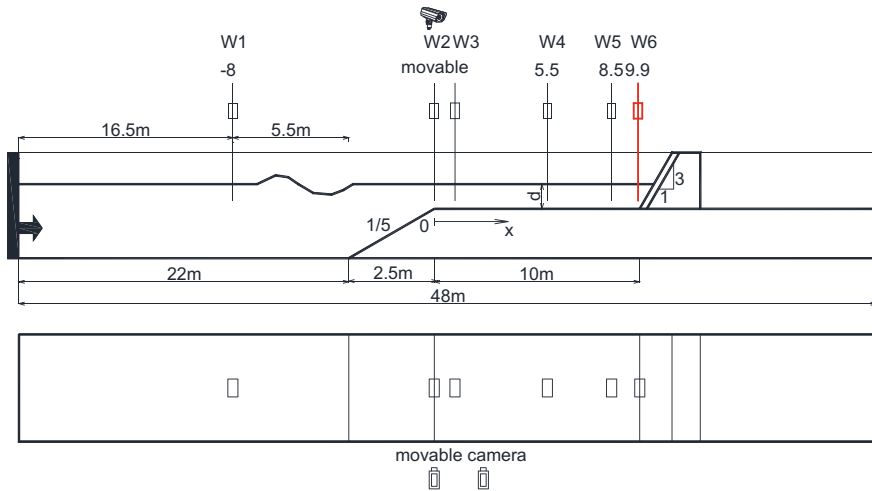


Fig. 1 Experimental set-up of monochromatic wave breaking on the fringing flat

Table 1 Table of experimental scenarios

Monochromatic wave condition (m) (s)	Reef flat depth d (m)				Beach slope
	0.05	0.1	0.15	1/3	
$H_0 = 0.06; T = 1.15$	0.05	0.1	0.15	1/3	No beach slope
$H_0 = 0.06; T = 1.35$	0.05	0.1	0.15	1/3	No beach slope
$H_0 = 0.07; T = 1.13$	0.05	0.1	0.15	1/3	No beach slope
$H_0 = 0.07; T = 1.50$	0.05	0.1	0.15	1/3	No beach slope
$H_0 = 0.09; T = 1.20$	0.05	0.1	0.15	1/3	No beach slope
$H_0 = 0.09; T = 1.40$	0.05	0.1	0.15	1/3	No beach slope
$H_0 = 0.12; T = 1.40$	0.05	0.1	0.15	1/3	No beach slope
$H_0 = 0.12; T = 1.60$	0.05	0.1	0.15	1/3	No beach slope
$H_0 = 0.15; T = 1.55$	0.05	0.1	0.15	1/3	No beach slope
$H_0 = 0.15; T = 1.80$	0.05	0.1	0.15	1/3	No beach slope
$H_0 = 0.17; T = 1.65$	0.05	0.1	0.15	1/3	No beach slope
$H_0 = 0.17; T = 1.90$	0.05	0.1	0.15	1/3	No beach slope

3 Data Analysis

The breaking process on reef face and flat was clearly happened with two types of breakers: plunging breaker and spilling breaker. Spilling breaker criterion is the first appearance of white foam cascading down on the front face (Fig. 2b). The plunging waves starts where a large part of wave front face is vertically erected (Fig. 2c and d). The breaking ends where the white foam totally disappears. The breaker height is the vertical distance from the crest to trough of breaking wave (H_b). The breaker depth

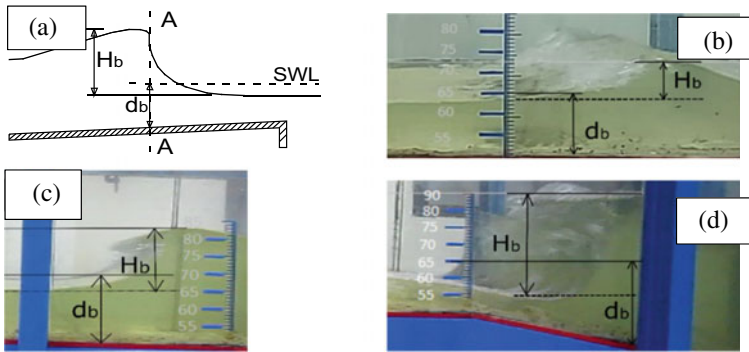


Fig. 2 Different wave breaking type on fringing reef (Battjes [3]) **a** definition sketch **b** spilling breaker **c** plunging breaker on flat **d** plunging breaker on fore reef slope

measured vertically from still water level (SWL) to the bottom at cross section A-A (d_b) (Fig. 2a). The total surf zone width measured horizontally from starting point to ending point of breaking wave (L_b). To validate data collected by cine photography, a comparison between wave height at WG2 and WG3 (movable with the breaking position) and wave height obtained by image analysis is carried out. H_b and d_b were determined from the last 10 waves extracted from time series. The errors between image analysis and time series are under 10% which is acceptable.

4 Results and Discussion

4.1 Breaker Type

According to Battjes [3], there are four types of wave breaking on a slightly sloping beach: spilling, plunging, collapsing and surging. For the situation of abruptly changing topography from very steep slope to very flat reef deck, two mechanisms dominate the breaking process: plunging and spilling. Some other types rank in between of spilling and plunging, or spilling would transform into plunging crest in the form of interference.

The surf similarity indices do not work well on wave breaking on fringing reef (Fig. 3a). Surging and collapsing occurs once $\xi_0 > 3.3$, plunging if $0.5 \leq \xi_0 \leq 3.3$, and spilling if $\xi_0 < 0.5$ (Galvin [1], Battjes [3]) However, in this case, plunging spilling and non-breaking happen for all values of ξ_0 ranging from 1.0 to 1.45. Considering the breaker type due to relative flat submergence, d/H_0 , the dashed lines divide into three separate regions: if $d/H_0 < 1.75$ then well-developed plunging happens; if $1.75 \leq d/H_0 \leq 2.8$ then well-developed spilling happens; if $d/H_0 > 2.8$, there is no breaking. This classification limits fit rather well with the criterion supposed by Gourlay [6] and Yao [7] (Fig. 3b).

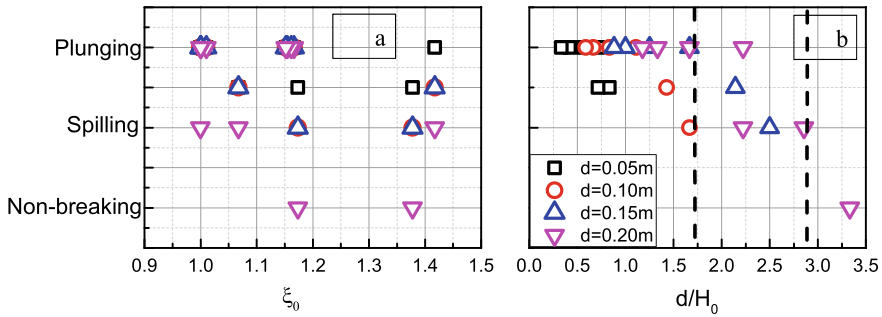


Fig. 3 Breaker type classification **a** dependent on surf similarity parameter **b** dependent on relative reef flat submergence

In order to compare the differences between the situation having beach slope steepness ($m = 3$) and the one without beach slope, all quantities of breaking characteristics are drawn due to changing d/H_0 with red marker denotes for no beach slope and black marker denotes for slope with steepness of $m = 3$ (Fig. 4).

4.2 Breaker Height (H_b) and Breaker Depth (D_b)

The dimensionless breaker height H_b/d characterizes the breaking features once waves shoaling to the nearshore regions and waves will break due the depth restricted. On Fig. 4a, the H_b/d at locations on the reef flat approximates at 0.55, the value supposed by Nelson [9], and far below 0.8, the commonly accepted value proposed by Miche criteria for breaker indices on plane beach. The relative breaker height (H_b/d) increases at high rate for cases $d/H_0 < 1$, which is meant the shallower the flat depth the higher the breaker height is.

The dimensionless breaker depth d_b/H_0 is linearly proportional to reef flat submergence which is meant the deeper the flat depth, the higher the breaker depth is. There are some exceptional points which are unchanged due to the increasing relative submergence. They are breakers occur on the flat at which the breaker depth is accounted from bottom to the still water at the breaking cross section.

There are minimal differences between the case which having beach slope $m = 3$ and without beach slope for both dimensionless breaker height and breaker depth. The presence of back reef slope does not effect on the breaking properties.

4.3 Breaking Locations and Breaking Boundary

On Fig. 4b, wave breaking on fore-reef slope happens for large waves, which are comparable or higher than water depth. Breaking points would translate to the crest

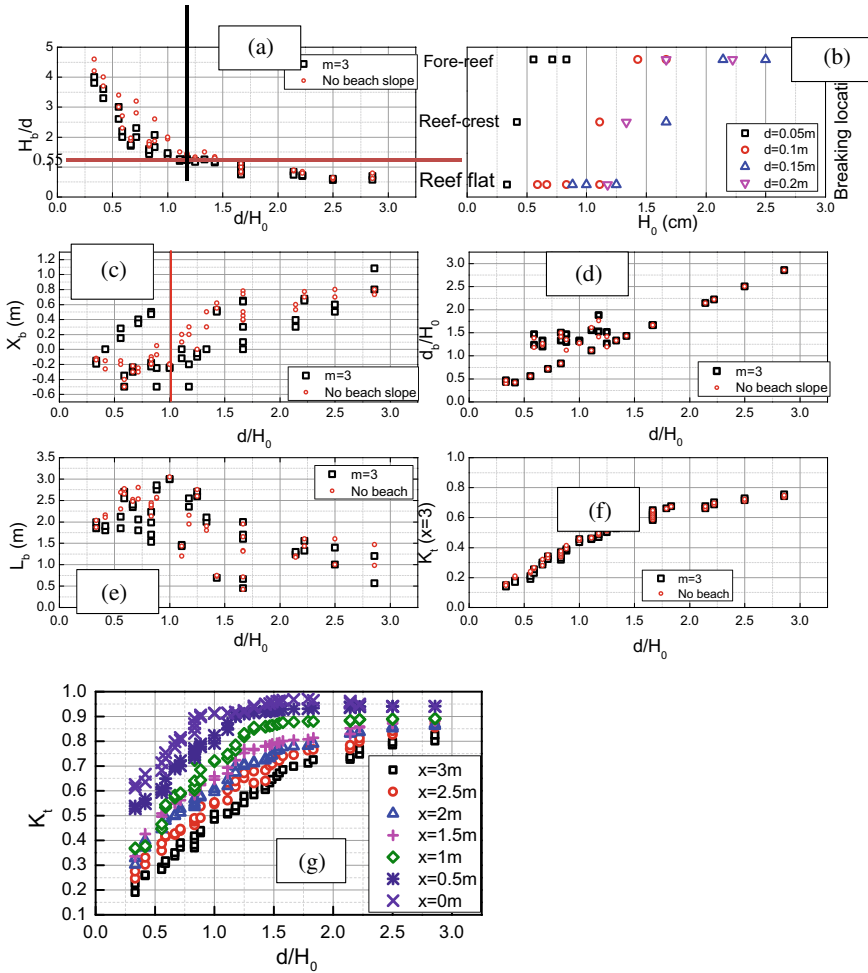


Fig. 4 Measured quantities as a function of d/H_0 **a** dimensionless breaker height H_b/d ; **b** breaking locations; **c** incipient breaking boundary; **d** dimensionless breaker depth; **e** total surf-zone width L_b ; **f** transmission coefficient K_t $x = 3$ m for $m = 3$ and no beach slope; **g** transmission coefficient K_t in the surf zone under beach slope $m = 3$

(on flat) once the smaller waves come. When waves even further decreased, wave breakers happens on the reef flat, and the breaking process would cease. Then waves may be restructured and pass freely on the reef flat.

In Fig. 4c X_b , the incipient breaking locations are in variation with the relative flat submergence. For the case of no beach slope, if $d/H_0 \leq 1$ then $X_b \leq 0$ which is meant the starting point of wave breaking happens on the reef crest and fore reef slope (red markers). For the case of beach slope $m = 3$, there are some scatters for points breaking on the flat when $d/H_0 \leq 1$; and it is hardly to conclude in this situation.

The total surf zone width L_b slightly decreases when the relative flat submergence goes up. However, this dimension depends on the skillfulness of observation to determine the ending point of wave breaking. Hence, there is a need to give detail assessment on surf-zone width.

4.4 The Wave Transmission Coefficient K_t

Wave transmission characteristics for submerged structures are often quantified by transmission coefficient K_t . $K_t = H_x/H_0$; in which H_x is the transmitted wave height at calculated locations; H_0 is the incident wave height in deep water. Based on Fig. 4f, K_t is calculated at position $x = 3$ at the end of breaking boundary. There is no big difference between the case having beach slope $m = 3$ and without beach slope. Wave transmission increased linearly with d/H_0 then it seemed unchanged at certain d/H_0 . However, there is a small difference between reef edge and the end of breaking boundary. At the reef edge ($x = 0, 0.5$), the increase of K_t with d/H_0 is rather steep until $d/H_0 < 1$ then relatively unchanged for larger d/H_0 . At the end of the surf zone boundary, this is mildly risen up ($x = 3$) until the corresponding demarcating ratio $d/H_0 < 1.8$ then unchanged for larger d/H_0 .

5 Conclusion

This study presents on wave breaking characteristics determination (breaker type, breaker location, breaker height, breaker depth, incipient breaker and the total surf-zone width) on fringing reefs with effects of beach slope by using cine-photography analysis. The results show that the relative reef flat submergence (d/H_0 in which d denotes flat depth, H_0 denotes incoming regular wave height) strongly influences on the breaking properties, and value $d/H_0 = 1$ (the transition limit) supposed to assess the breaker indices is totally relevant and consistent with other studies (Gourlay [6]). The study also demonstrates that the influence of beach slope $m = 3$ on the breaking properties on ten-meter flat is minimal. In other words, the breaking process is dominant in the proximity of reef edge, and the back reef slope is sufficiently distant to have little influence on this process. Further study needed for other variation of beach slope steepness and narrower flat width.

References

1. Galvin CJ (1968) Breaker type classification on three laboratory beaches. *J Geophys Res* 73(12):3651–3659
2. Komar PD, Gaughan MK (1973) Airy wave theory and breaker height prediction. In: Proceedings of the 13th international conference on coastal engineering, Vancouver, Canada, ASCE, pp 405–418
3. Battjes JA (1974) Surf similarity. In: Proceedings of the 14th international conference on coastal engineering, Copenhagen, Denmark, ASCE, pp 466–480
4. Goda Y (2010) Reanalysis of regular and random breaking wave statistics. *Coast Eng J* 52(1):71–106
5. Liu Y, Niu XJ, Yu XP (2011) A new predictive formula for inception of regular wave breaking. *Coast Eng* 58:877–889
6. Gourlay (1994) Wave transformation on coral reefs. *Coast Eng* 23:17–42
7. Yao Y (2013) Characteristics of monochromatic wave breaking over fringing reefs. *J Coastal Res* 29:94–104
8. Tuan TQ, Cuong DQ (2019) Distribution of wave heights on steep submerged reefs. *Ocean Eng* 189:1–19
9. Nelson RC (1994) Depth limited design wave heights in very flat regions. *Coast Eng* 23:43–59

A New Framework for Estuarine and Coastal Modeling to Monitor Water Security in a Changing Climate



Truong Hong Son and Phan Khanh Linh

Abstract Managing water resources efficiently, ensuring water quality, and avoiding water resource degradation from adverse effects of climate change and natural disasters are keys to ensuring water security for coastal regions. To propose a comprehensive sustainable approach to address water security challenges, relevant stakeholders need to understand the water-related system, i.e., how and why the system is evolving and how climate change and human interventions may impact that evolution. Therefore, hydraulic engineers, modelers, and managers need expert local knowledge, proof, and some predictive tools. This paper introduces a new framework, summarizes, and describes different mathematical models to simulate, analyze, and understand the changes in the water resources systems, particularly focusing on geomorphodynamics. The techniques discussed range from analytical, conceptual, and dynamic system models and the Monte Carlo method to detailed 2D and 3D numerical models. The principal types of these techniques and some practical examples illustrating how these models can be applied in the water resources engineering field are discussed.

Keywords Water security · Framework · Conceptual model · Dynamic system model · Monte-Carlo simulation

1 Introduction

Models are a substitute for a real-world system. It is usually easier to work with and study “a model” than with the actual system [1]. A formula or an equation describes how sediment is laterally exchanged in harbors; an engineer’s flume, a scientist’s bar, or a graph are all models. These models represent some aspect of a real-world system, for example, a physical process, the attenuation of the wave through vegetation, or an ecological system. These models are useful as they enable

T. H. Son (✉) · P. K. Linh
Thuyloi University, Hanoi, Vietnam
e-mail: truonghongson@tlu.edu.vn

© The Author(s), under exclusive license to Springer Nature Singapore Pte Ltd. 2024
T. Nguyen-Xuan et al. (eds.), *Proceedings of the 4th International Conference on Sustainability in Civil Engineering*, Lecture Notes in Civil Engineering 344,
https://doi.org/10.1007/978-981-99-2345-8_33

329

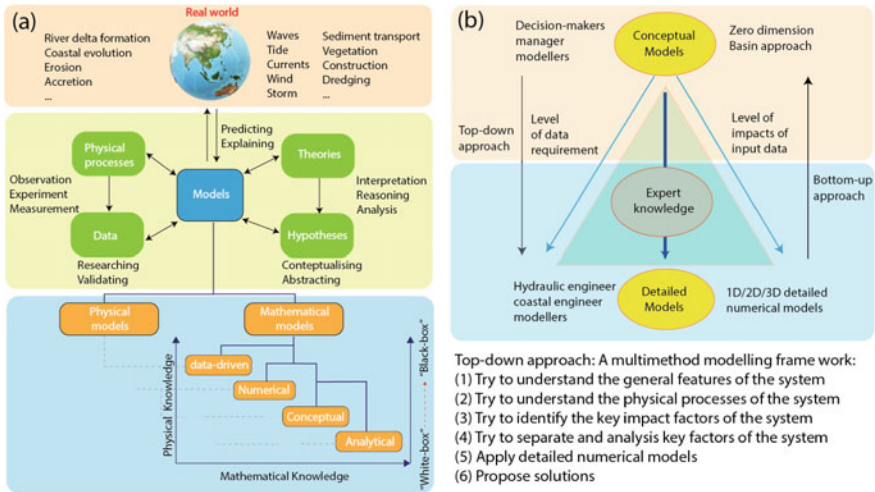


Fig. 1 **a** A representative concept of the model. Different categories of activities that characterize the modeling process and different types of models are also included; **b** typical approach of modeling in the field of water resources engineering. Two main approaches are the top-down approach and the bottom-up approach. These two different approaches require different levels of data input as well as the required knowledge of experts. The level decreases in the direction of the arrow

us to discover or learn something interesting about the systems they represent. The model can be used to simulate the system. The “term simulation” can be interpreted as the process of creating and using “a model” of an existing system to identify and understand the key factors that control the system and to predict the system’s behavior under different scenarios (Fig. 1). Therefore, in order to simulate a system, that system needs to be quantitatively described using rules or equations.

Depending on the complexity of the system, different types of models, including conceptual models, physical models, to numerical models, can be applied to understand the way in which it is likely to evolve, forecast the future behavior of the system, and determine what could be done to influence that future behavior [2]. These models can be static, in which the system does not change with time. These models can also be dynamic models, in which the system changes and evolves with time in response to both external and internal influences. Moreover, the controlling factors, processes, and events in many systems may be poorly understood. If these factors are represented in the model by single values, the simulation is termed a deterministic model. However, if the uncertainty is represented as probability distributions, the simulation is termed probabilistic simulation [1, 2]. It is noted the results of the model based on inputs represented by probability distributions are also a probability distribution.

In estuarine and coastal regions, water resources systems are among the most complex natural system involving different complicated physical processes. For example, the motion of water induced by waves, tides, or water pressure is different through a region of vegetation, near human construction, or in turbulence areas,

which causes an exchange of mass and momentum. The mutual interaction between different components of the system is unclear. These physical processes usually occur at different spatial and time scales. Furthermore, the highly dynamic hydrodynamic and morphodynamic processes are driven by complex interactions between water and terrestrial environments along the coast, resulting in limited representation in predictive models. As a result, the evolution of the whole system related to water resources is governed by a set of higher-order nonlinear differential equations [3].

Estuaries, tidal wetlands, tidal rivers, and shorelines are located at the interface of land and ocean. These areas support a wide range of ecosystem services, including sediment storage, storm and flooding buffering, and aquaculture production, and are home to the most active and diverse ecological system. More than 40% of the world's population is estimated to reside within 100 km of the coast. In addition, coastal regions are the gathering place of the national energy, defense, and industrial infrastructure. These close relationships between the coastal regions and human activities pose a challenge in ensuring water security for coastal regions, especially under the negative impacts of climate change and natural disasters. These water security challenges are managing water resources efficiently, ensuring water quality, and avoiding water resource degradation as urban development and human populations along the coasts continue to rise [2–4].

In order to propose a sustainable approach to address these challenges related to water security in the estuarine and coastal regions, hydraulic/coastal engineers and managers need to make use of a combination of data collection, models, and opinions of experts to inform decision-makers. In other words, data, documentation, models, and knowledge across multiple disciplines need to be translated into a common language, transferred to, and used by decision-makers.

It is noted that there is no single comprehensive model that can capture all hydro-morphological features and ecological processes, as well as the impacts of applying different solutions/policies on economic processes that usually occur in coastal areas at different spatial and temporal scales. Establishing a proper modeling framework in which different types of models across different disciplines are integrated is essential for obtaining a robust, reliable outcome that decision-makers can understand and have confidence in [2, 5]. This paper introduces a new framework for using models and simulation, ranging from conceptual models, physical models, and analytical models to detailed numerical models to study water security challenges in estuarine and coastal areas.

2 A Framework

When starting a new project in coastal areas, detailed numerical models are usually applied right away to study the system. For example, a 2D or 3D shallow water equations solver of Delft3D, Telemac, or Mike21 is often chosen to study a coastal region's hydrodynamic and morphodynamic processes. This way of approach, termed the "bottom-up" approach, is popular in developing countries nowadays. It is noted

that the results of the detailed model are strongly influenced by the quality and the quantity of the input data. In other words, this approach needs a very high level of data inputs, i.e., the accuracy and length of the data series. Moreover, as state-of-the-art numerical models can include many different physical processes, expert judgments are essential to analysis the results of the model, i.e., separating the influences of different processes. Furthermore, without an expert's knowledge, the capability of such a model is usually overrated, leading to inaccurate interpretation of the numerical results. For example, results related to the instantaneous depth-average flow velocity are usually misunderstood as the representative flow field. The presence of circulation flow or vortex structures in a Reynold Averaged Navier Stoke model (RANS model) is usually used to evaluate the erosion/accretion of the river bank or shorelines.

A more appropriate approach can be a top-down approach. Suppose the bottom-up approach begins at the specific and moves to the general. In that case, the top-down approach goes from the general to the specific. In other words, the top-down approach to modeling estuarine/coastal regions usually starts from a conceptual model. Conceptual models represent a system using general descriptive rules, concepts, and relationships. Therefore, it is essential to obtain early agreement on a conceptual/descriptive model of the coastal system and the underlying hydraulic and morphological processes from all the relevant stakeholder groups. Properly understanding the coastal system will lead to the correct choice of predictive methods. In addition, it can enhance confidence in the conclusions from the modeling study. In other words, Conceptual models should be used as the starting point for subsequent detailed numerical modeling [1, 3, 5].

The differences between the top-down and bottom-up approaches are illustrated in Fig. 1 (right panel). It is noted that hydraulic engineers, managers, and decision-makers should choose a general conceptual model to understand the whole system, while modelers and experts are more suitable with a multimethod modeling approach, including conceptual and detailed models. In general, a simplified top-down framework to approach of the problems in coastal regions can be suggested as follows: (1) Try to understand the general features study area in global in regional contexts based on available data (observation, data analysis, compare with similar cases elsewhere); (2) Try to understand the physical processes of the system based on the new measured field data; perform new field measurements if the existing dataset is not sufficient (rules of thumbs models, observation, and data analysis); (3) Try to identify the key impact factors of the system based on general models (conceptual models and analogy models), determine uncertainties, and transformed into a stochastic model (Monte-Carlo simulation) by including input variables with an uncertainty component; (4) Try to control, separate and analysis key factors of the system based on physical models (laboratory experiments, data analysis); (5) Apply detailed numerical models, calibrate and validated or tuning with available data, determine uncertainties, sensitivity study the influences of different parameters (fine tuning, model calibration and validation using field measure data and physical results) (see Table 1); (6) Propose solutions, try to predict and estimate the behavior of the system under

different scenarios, the effects of engineering solutions in the context of climate change and extreme events as well as human interventions using all different models constructed (multimethod modeling).

3 Practical Implementation

Practical examples illustrating how this multimethod modeling can be applied in a complex estuary are illustrated in Fig. 2. Figure 2a illustrates an estuarine region at Tieu estuary with a complex configuration in the Vietnam Mekong Delta. Mangrove forests dominate a wide range of areas from the coastal to the estuary and further upstream. Coastal mangroves are distributed alongshore and are often exposed to waves, and estuarine mangroves are much less exposed to sea waves and storms [4–6].

Estuarine mangroves usually dominate in floodplains, which have gently sloping substrates (2–3%) that are exposed at low tides and flooded at high tides. They can also be flooded by river water. In order to obtain a better understanding of the motion of water around vegetation, a conceptual model (Fig. 2b), physical model (Fig. 2c), analytical model (Fig. 2d), and numerical model (Fig. 2e) were studied, constructed, and developed. The results of a detailed numerical model related to the presence of a large vortex structure in the mixing layer were calibrated and validated based on the knowledge obtained from other models (Fig. 2f). It is suggested that the presence of a large coherent structure at the interface of vegetation and the main channel can contribute up to 90% of the exchange of mass and momentum for the vegetation region and can be captured in a numerical model through a prescribed hybrid eddy viscosity model [4, 5].

Another practical example is the conceptual simulation of a double tidal inlet at the Cua Lo tidal inlet (Fig. 3). The model is calibrated and validated with measured discharge and water level data at Cua Lo tidal inlet using only the discharge coefficient. This simple model (first level of the top-down approach) is able to preliminary evaluate the system's dynamic behavior under the impacts of different solutions, such as reducing the width of the tidal inlets, opening a new channel, or constructing a new port.

4 Conclusions

Different relevant stakeholders, including hydraulic engineers, modelers, and managers, need expert local knowledge, proof, and some predictive tools to propose a comprehensive approach to address water security challenges in the context of climate change and sea level rise. The top-down approach framework should be considered because of its advantages over the bottom-up approach. A new modeling framework ranging from the conceptual model and physical model to the numerical

Table 1 Summary of typical physical processes in the coastal region, key parameters, and available tools and models that can be applied to study the relevant problems

Processes (Estuary and Coast)	Key parameters (Factors that should be considered)	Typical Tools (Existing databases, field data, models)
Geometry and scales of the system	Dimension, the shape of the study area; Bathymetry; Sand dunes, Breaker bars, Slope; Depths of channels; Rates of sedimentation/ erosion patterns for coastlines/ riverbank	Stateline images; Echosounder: Bathymetry as a function of time, Bedform tracking; Model: GIS, GEE
Hydrodynamic: water level, tides, flow, currents, and discharge	Vertical tidal ranges; Peak velocities during the ebb and flood period; Velocity profiles during flood and ebb period; Penetration length into estuary; Mixing layer (for transverse mass and momentum exchange); Residual flow velocity (tide-averaged); Wind-driven currents; Flow patterns in meandering sections; Secondary, Stratified flow; flow velocities; upstream control structures (dam, weirs, barrages, reservoirs); River flood	Water level recordings; Current velocity measured at a fixed location (ADV); Velocity & Discharge measurements (ADCP); Float /dye tracer; Conceptual model: Matlab, Python, Vensim, Any Logic; Physical model: shallow flume, fixed bed models; Numerical model: 1-dimensional model (1D); 2-dimensional-vertical models (2DV); 2 dimensional-horizontal models (2DH) and 3-dimensional models (3D), Software MIKE21, DELFT3D
Wave climate	Dominant wind and wave direction Types of area exposure (open, sheltered, exposed); Significant wave height, Wave period, Wave transformation; Wave spectra density; storms	Wave field data nearshore; Wave measurement sensors; Conceptual models: Theoretical models, governing equations; Physical model: Wave flume; Numerical model: Swan (Delft3D-waves), Swash, Xbeach...
Morphodynamic (Sediment transport)	Types of sediment (sand, mud, silt); profiles of sediment concentration; Bed-load transport; Suspended sediment transport; In-situ settling velocities, Bedforms (types and dimensions)	Types and composition of sand, mud, silt, gravel, Bulk density of bed material; Critical bed-shear stresses for erosion/deposition; Conceptual model: Theoretical models; Physical model: Movable bed engineering models, process models; Numerical models
Other related phenomena	Turbidity maximum; Stratification effects near an outlet (salt wedge); Flood and ebb channel crossings; Migrating of tidal flats and shoals; Migrating mouth bars; Vegetation, ecological system	Field observation and measurement (salinity, migration rate, type of vegetation, vegetation density...); Analytical model, conceptual model, numerical models (2DH & 3D models), detailed Direct numerical simulation (DNS), Large eddy simulation (LES), Smoothed particle hydrodynamics (SPH)... Software including FLOW3D, OpenFOAM, Duals Physics...

(continued)

Table 1 (continued)

Processes (Estuary and Coast)	Key parameters (Factors that should be considered)	Typical Tools (Existing databases, field data, models)
Making decisions	Propose, compare different policies/solutions	Optimization models, GAMS, AHP,...

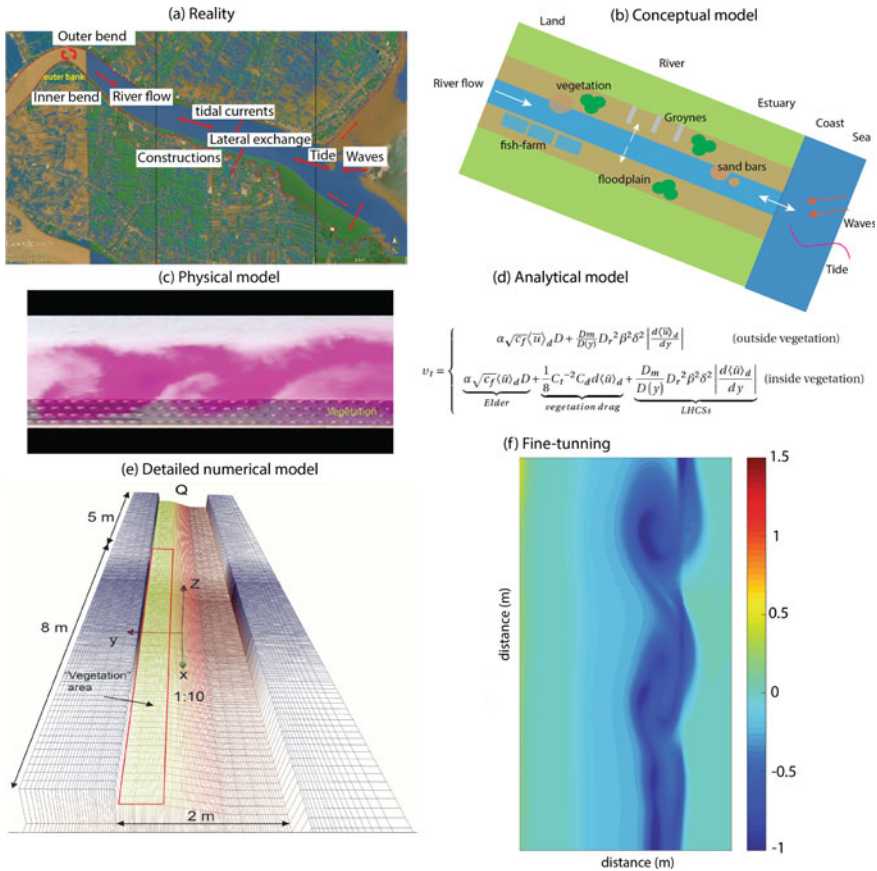


Fig. 2 Tieu estuary (a) and a conceptual model of the system (b), physical model (c) and analytical model (d), numerical model (e) and model results (f)

model can be conducted to obtain a good knowledge of the estuarine and coastal system. The philosophy of these types of models and some practical examples illustrating how these techniques can be applied in the water resources engineering field are introduced.

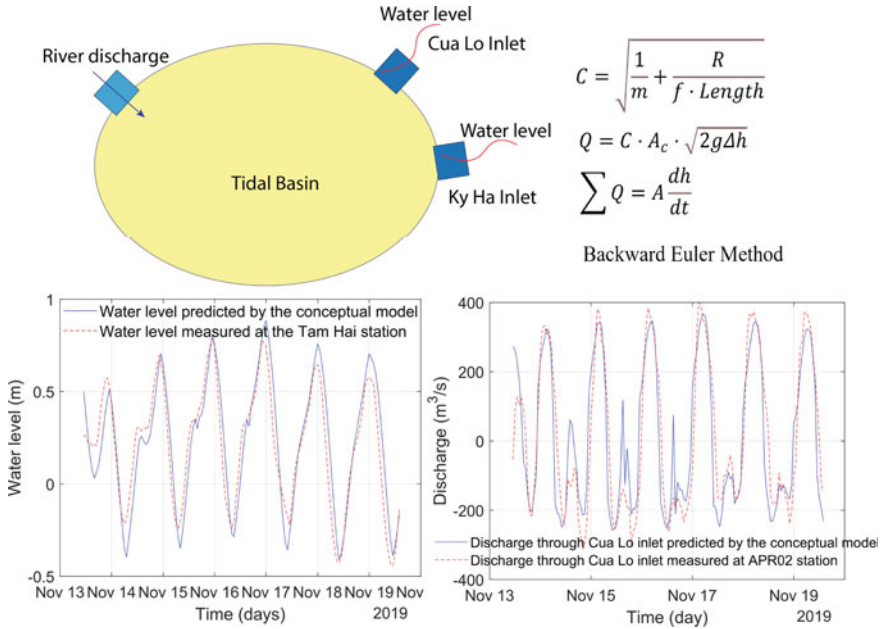


Fig. 3 A conceptual model for the Cua Lo tidal inlet. The model is calibrated and validated using measured data at Cua Lo tidal inlet

References

1. Ford A (1999) Modeling the environment: an introduction to system dynamics models of environmental systems, Book. Island Press, Washington, D.C.
2. Belen LDSRB, Bridget WB, Jonathan S, Alan B, James S, Ben G, Kate J (2019) Coastal morphological modelling for decision-makers, Government report – SC090036/R, p 175
3. van Rijn LC (2005) Principles of sedimentation and erosion engineering in rivers, estuaries, and coastal seas, Book, Aqua Publications, p 609
4. Truong SH, Ye Q, Stive MJF (2017) Estuarine mangrove squeeze in the Mekong Delta. Vietnam J Coast Res 33(4):747–763
5. Truong SH, Uijtewaal WSJ (2019) Transverse momentum exchange induced by large coherent structures in a vegetated compound channel. Water Resour Res (WRR) 55(1):589–612
6. Phan LK, van Thiel de Vries JS, Stive MJ (2015) Coastal mangrove squeeze in the Mekong Delta. J Coast Res 300:233–243

Hydrodynamic Modelling of New Segment Channel to Navigation Channel in Hau River, Vietnam



Nguyen Viet Thanh, Le Vinh An, Thai Thi Kim Chi, Nguyen Dang Phong, Hoang Nam Binh, Nguyen Duy Tien, Bui Vinh Phuc, and Trinh Dinh Lai

Abstract The channel for large vessel to Hau River was completed in January 2016 for vessels of 10,000 DWT full load and 20,000 DWT half load to Can Tho Port. The large vessels from the East Sea to Can Tho port must go through Duyen Hai harbour, then go into Kenh Tat channel, and then go to Quan Chanh Ba channel to enter the Hau River then to Can Tho port. A new segment channel length of 23.9 km consists of three sub-segments such as Offshore, Kenh Tat, and Quan Chanh Bo channels. Kenh Tat channel is a new dredging channel connecting the navigation channel in Quan Chanh Bo channel to the east sea of Vietnam with length of 7.7 km. Duyen Hai harbour was built in 2016, and the harbour basin was protected by two breakwaters. These infrastructures induced an extremely complicated hydrodynamic regime. In this study, the hydrodynamic features were depicted by the numerical model and the result indicated that the hydrodynamic characteristics in the new segment channel to Quan Chanh Bo and Kenh Tat channels depend on the tide and river flows in Dinh An, Kenh Tat estuaries of Hau River and Cung Hau estuary of Tien River.

Keywords Hydrodynamic · Kenh Tat channel · Quan Chanh Bo channel · Estuary · Hau River

N. V. Thanh (✉) · L. V. An · T. T. K. Chi · N. D. Phong · H. N. Binh · N. D. Tien
Faculty of Civil Engineering, University of Transport and Communications, Hanoi, Vietnam
e-mail: vietthanh@utc.edu.vn

B. V. Phuc
Faculty of Basic Sciences, University of Transport and Communications, Hanoi, Vietnam

T. D. Lai
Hanoi University of Civil Engineering, Hanoi, Vietnam

1 Introduction

Mekong River is a famous river in the world and in Vietnam. The Mekong river empty into the East Sea of Vietnam through nine estuaries [1]. Previous studies focused on investigation the characteristics of hydrodynamic, wave transformation and sediment transport in Mekong River's estuaries and showed that the river flows, wave and tidal controlled the hydrodynamic and sediment regime in the estuaries and coastal of Me Kong River Delta. A coupled model included hydrodynamic, spectral wave and sediment transport models for a large scale of the estuaries of Mekong River was established, calibrated and verified by observation data from May 2004 and Sep 2009 [2, 3]. Nguyen and Thanh investigated the influence of climate change on the hydrodynamic and sediment transport of Hau River's estuary. The results shown that the main causes effect on the morphological in Dinh An estuary included river flow, sediment and tide; wave transformation only plays the secondary role in this area. The result also indicated that the hydrodynamic, wave climate and sediment transport in Dinh An estuary and nearby coastal significantly changed which the presented of bypass channel [3]. Recently, Tu et al. indicated that sediment transport is controlled by river discharges and monsoons, and the sand bars formation diverted the direction of current sediment flows and the severe recession of the delta due to human activities [4]. Earlier studies indicated that the Dinh An navigation channel unstable and high back siltation. Therefore, on January 20th, 2016, the navigation channel for large vessels entering the Hau River was completed and took into used for large vessels entrance Can Tho Port. Can Tho port is located in Hau River and far from the East Sea about 120 km. The vessel from East Sea to Can Tho port has to navigable from new segment channel includes offshore, Kanh Tat and Quan Chanh Bo channel to Hau River navigation channel and then to the port (Fig. 1). It is shown that previous studies almost investigated the features of hydrodynamics and sediment transport in estuaries and coastal zone but not focus in new segment channel to Hau River's navigation channel. This study investigates the hydrodynamics of the new segment channel to Hau River's navigation channel by a coupled numerical model.

2 Study Area and Methodology

2.1 Study Area

New segment channel of Hau River navigation channel starts at Dai An mouth to Quan Chanh Bo channel with length of 19 km and then to Kanh Tat channel with length of 9 km and offshore channel with length of 6 km (Fig. 1). The new segment channel connects Hau River to East Sea by new dredging channel called Kanh Tat channel and created new estuary of Mekong River.

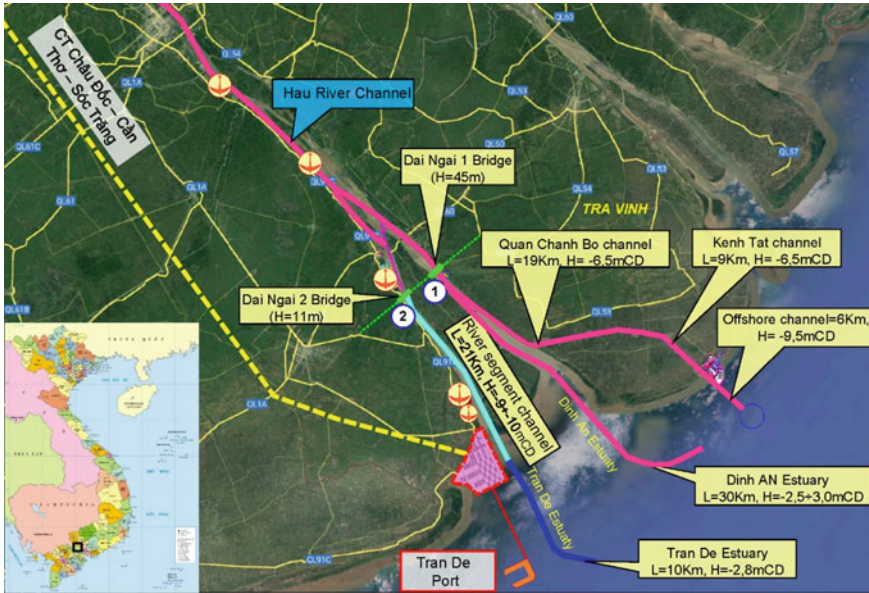


Fig. 1 Location of new segment channel to Can Tho

Dinh An Estuary is average tide estuary and controlled by tide hydrodynamics, freshwater runoff, and sediment transport from the Hau River. The estuary has a high transport with average sediment transport rate of 22 million tonnes a year [5].

The measurement wind data in offshore Tra Vinh coastal indicated that the NE wind prevailing in the winter and changes to SW in the summer. The wind speed reached to 16 m/s and 12 m/s in NE and SW direction, respectively [5].

Offshore wave roses at location of 9.17° N, 107.08° E during period from 1999 to 2008 show that the wave height ranges from 0.88 to 3.58 m and period ranges from 4.3 to 9.6 s in dry season and wave height of 1.29 m and period of 5.8 s has an appearance frequency of 14.7% in flood season (Fig. 2).

The median particle size d_{50} of suspended sediment ranges between 2.5 and 3.9 μm . The bottom sediment is flocculated with flocs size about 40 μm [2, 5].

2.2 Methodology

The coupled model included hydrodynamic, spectral wave and sediment transport models were calibrated and verified by observation data in May and September 2004 by Nguyen [2]. Nguyen and Thanh verified a large scale model by observation data in September 2009 [3]. The coupled model continues verified based on measured data of in September 2017 by Thanh et al. (2021) and based on this coupled model,

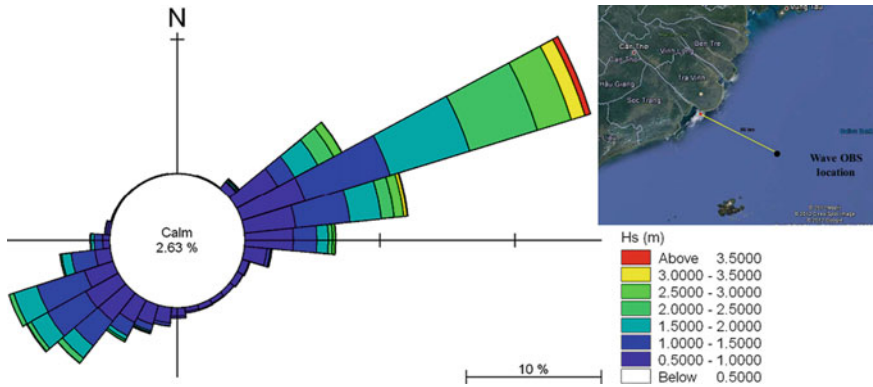


Fig. 2 Wave height rose at offshore of Tra Vinh coastal (1999–2008)

an investigate of hydrodynamic and sediment transport in new segment channel to Hau River and coastal area of Duyen Hai Port will be conducted [6].

3 Results and Discussion

3.1 Hydrodynamics Features at Dai an Mouth

During flood tide, the interaction between the tidal currents from Dinh An estuary and from Quan Chanh Bo channel to Dai An month created a circulation at the Dai An mouth where the Quan Chanh Bo canal begins. In this area, the tide current velocity is very small with ranges of 0.1–0.15 m/s (Fig. 3a). During ebb tide, the ebb tide current tends to empty to the East Sea through the Dinh An estuary, a small tide current occurs in Dai An mouth of Quan Chanh Bo channel. The ebb tide current in Quan Chanh Bo channel increases along the channel from the Dai An mouth to Kenh Tat channel (Fig. 3b). The results in flood and dry seasons indicated that, the current speed in the Dai An mouth almost small, these phenomena may induce the sedimentation in this area. A long the Quan Chanh Bo channel, the highest current speed concentrated in the bending segment of the channel and decreased in two sides of the bending segment. The hydrodynamic model also indicated that, the flood tide current in Quan Chanh Bo channel appeared long time then ebb tide current.

3.2 Hydrodynamics Features in Quan Chanh Bo Channel

Flood tide current field in the tributary of Quan Chanh Bo, Kenh Tat channels and Lang Sac canal plotted in Fig. 4a. It's shown that flood tide current flows from Kenh

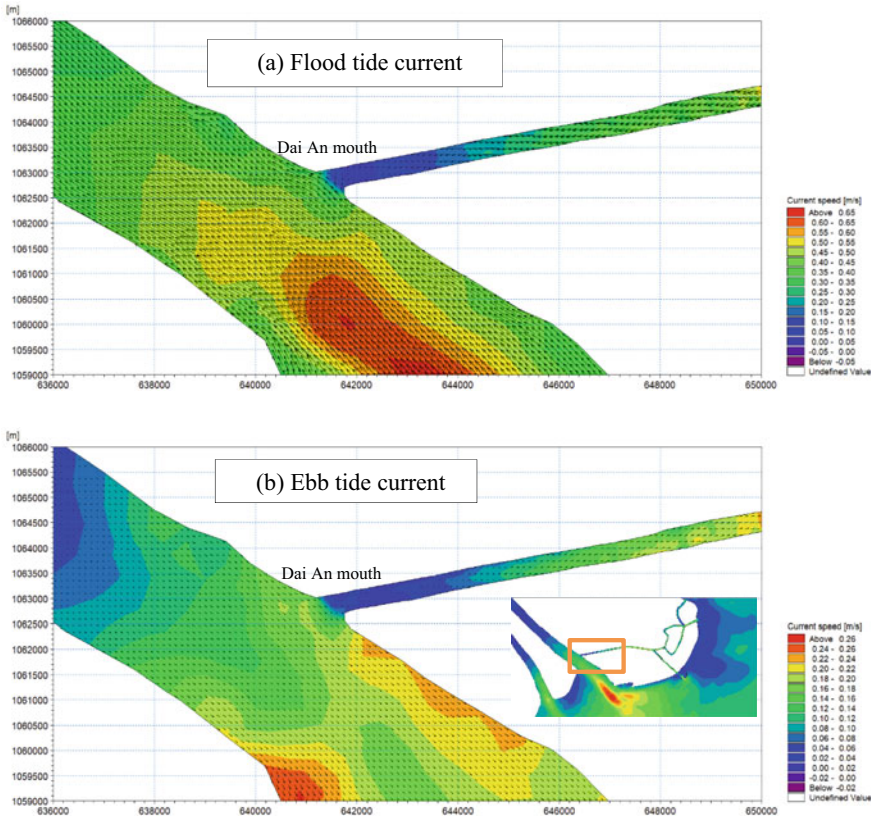


Fig. 3 Flood and ebb tide currents field in Dai An mouth of Quan Chanh Bo channel

Tat channel and Lang Sac Canal to the Quan Chanh Bo channel with speed ranges from 0.1 to 0.4 m/s and the higher flood tidal current speed occur in Quan Chanh Bo channel. The result also indicated that flood tide current in Kenh Tat channel a bit smaller than Lang Sac canal. The current speed varies from 0.1 to 0.3 m/s and from 0.05 to 0.2 m/s in in Kenh Tat channel and Lang Sac canal, respectively. This phenomenon shown that the tidal current from Tien River also has significant influenced to the Quan Chanh Bo channel.

The ebb tide current in the tributary presented in Fig. 4b shown the flow from Quan Chanh Bo channel empty to the sea through Kenh Tat channel and Lang Sac canal. The ebb tide current in Kenh Tat channel with higher speed than in Lang Sac canal and tend to increase to the sea. This phenomenon can be explained by the fact that the Kenh Tat channel is deeper and wider than the Lang Sac canal, and the flows are almost concentrated in the Kenh Tat channel. The tidal current speed in Quan Chanh Bo channel ranges from 0.1 to 0.25 m/s, while the speed in Kenh Tat channel changes from 0.1 to 0.3 m/s.

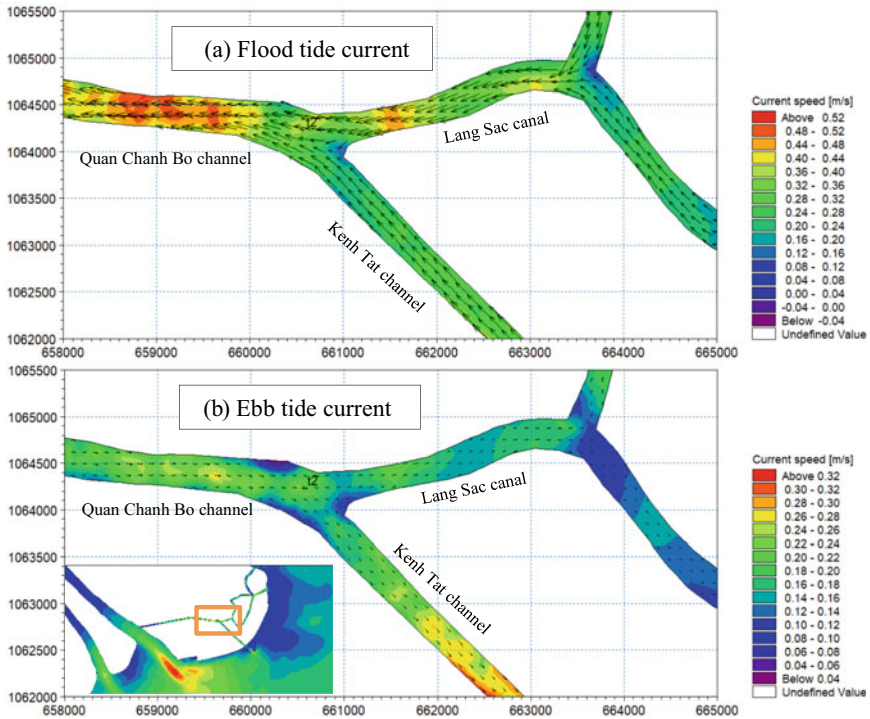


Fig. 4 Flood and ebb tide currents field in the junction of Quan Chanh Bo and Kenh Tat channels

The result also indicated that the ebb tide current is smaller than flood tide current. This result due to the new channel segment is narrow and long, therefore the ebb tide current almost empty to the sea through in Dinh An estuary.

3.3 Hydrodynamics Features in Kenh Tat Channel and Coastal of Duyen Hai Port

Figure 5 is plotted the Kenh Tat channel and coastal of Duyen Hai port. The flood tide current field in the Kenh Tat channels and harbour basin shown that flood tide current flows from Kenh Tat channel and Lang Sac Canal to the Quan Chanh Bo channel with speed ranges from 0.1 to 0.4 m/s, and the higher flood tidal current speed occur in Quan Chanh Bo channel. The result also showed that flood tide current in Kenh Tat channel a bit smaller than Lang Sac canal. The current speed varies from 0.1 to 0.3 m/s and from 0.05 to 0.2 m/s in Kenh Tat channel and Lang Sac canal, respectively. This phenomenon shown that the tidal current from Tien River also has significant influence to the Quan Chanh Bo channel.

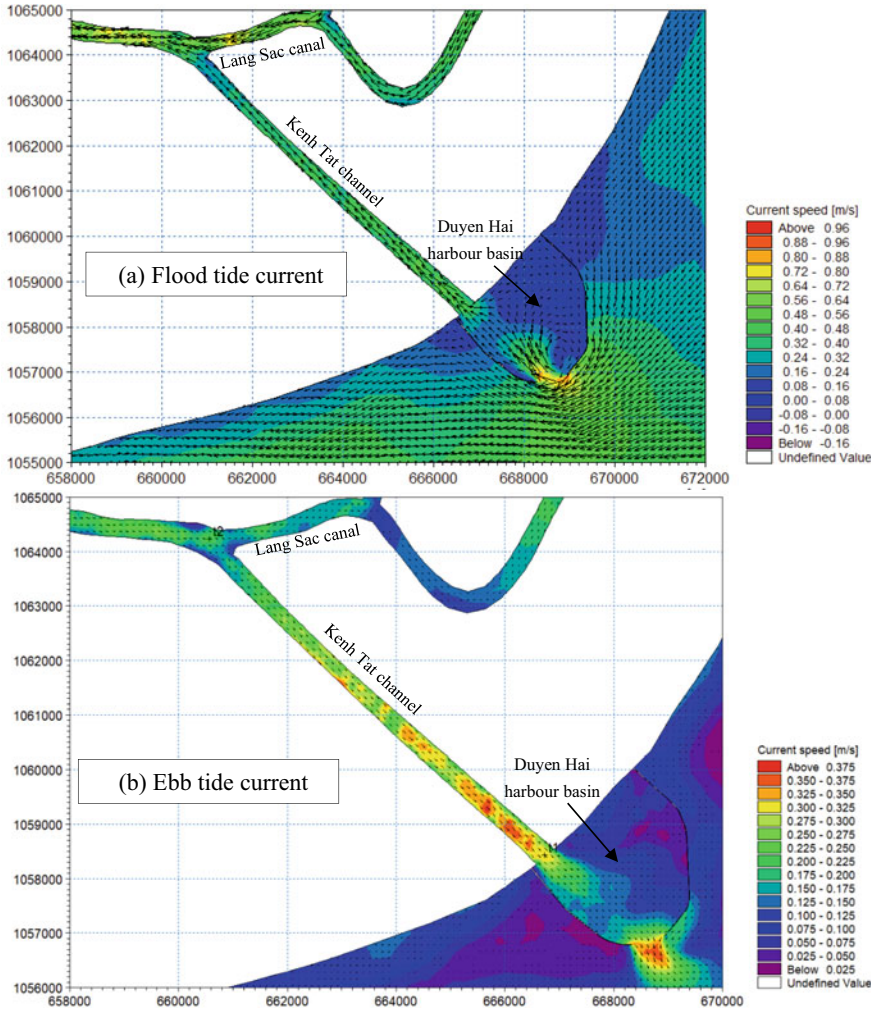


Fig. 5 Ebb tide current in the junction of Quan Chanh Bo and Kenh Tat channels

Flood tide current field in Kenh Tat channel and Duyen Hai harbour basin plotted in Fig. 5a shown that the flood tide through the harbour entrance gate induced remarkably high current speed, reach to 0.8 m/s and the reduced in the basin area. The high current speed increased in coastal segment of Kenh Tat channel then it is decreased at the confluence with the Lang Sac channel into the Quan Chanh Bo channel. Figure 5a also showed the influenced of food tidal current in the Lang Sac canal and from Tien River.

Figure 5b is depicted the ebb tide current field in Kenh Tat channel and Duyen Hai harbour basin. It is shown that the ebb tide current ranges from 0.05 to 0.3 m/s, and it is smaller than flood tide current. In Kenh Tat channel, the ebb tide current

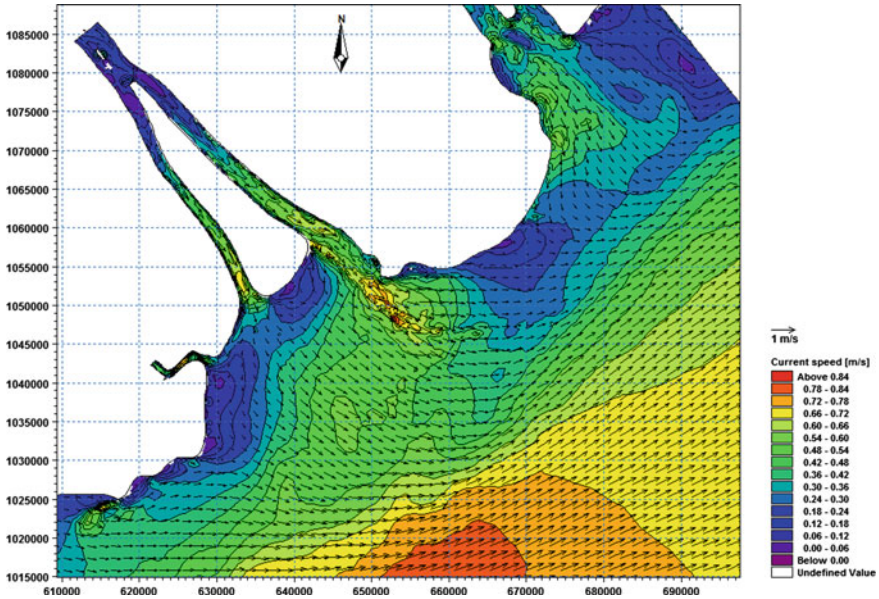


Fig. 6 Nearshore current field before the Duyen Hai harbour built [2]

tends to increase in the direction of discharge to the sea, then decrease sharply in the harbour basin. At the harbour entrance, the ebb tide current is quite strong.

The simulation results also indicated that the presence of Duyen Hai harbour basin has a noteworthy influence on the nearshore current field; two breakwaters protecting the harbour basin induced the high current speed in the harbour entrance, especially in the flood tide. Before Duyen Hai harbour build, Nguyen indicated that the ebb tide current from Dinh An and Cung Hau estuaries results in a low flow area between these estuaries along Tra Vinh coast (Fig. 6) [2].

4 Conclusions

The hydrodynamic modelling results indicated that the flood tide current speed is larger than ebb tide current in the study area, and this result consistent with Nguyen (2012)'s result.

The current in study area controlled by Hau and Tien Rivers's discharges and tide regime in coastal of Tra Vinh province.

The presence of Duyen Hai harbour basin has induced the momentous change of nearshore current.

Acknowledgements This work was supported by the research programme of the Ministry of Education and Training, Vietnam in two research projects, grand number CT.2022.01.GHA.03 and CT.2022.01.GHA.06.

References

1. MRC (2006) Annual flood report 2005, Mekong River Commission 1–82
2. Nguyen VT (2012) Morphological evolution and back siltation of navigation channel in Dinh An Estuary, Mekong River Delta: understanding, modelling and solving. Hohai University: Nanjing 181
3. Nguyen DD, Nguyen VT (2014) Influence of enlargement of Quan Chanh Bo channel on hydrodynamic and sediment transport in Dinh An estuary, Vietnam. In: Proceedings of the 19th IAHR-APD congress 2014, Hanoi, Vietnam: Construction Publishing House
4. Tu LX, Thanh VQ, Reyns J, Van SP, Anh DT, Dang TD, Roelvink D (2019) Sediment transport and morphodynamical modeling on the estuaries and coastal zone of the Vietnamese Mekong Delta. *Cont Shelf Res* 186:64–76. <https://doi.org/10.1016/j.csr.2019.07.015>
5. Nguyen VT, Zheng J, Zhang J (2013) Mechanism of back siltation in navigation channel in Dinh An Estuary, Vietnam. *Water Sci Eng* 6(2):178–188. <https://doi.org/10.3882/j.issn.1674-2370.2013.02.006>
6. Nguyen VT, Hoang NB, Le VA, Nguyen AD, Nguyen DP, Thai TKC (2021) Study on the impact of the bypass channel and the coastal structures of Duyen Hai Thermal Power Center on the change of the flow field and the topographic changes in the coastal area of Tra Vinh province. University of Transport and Communications, Hanoi, Vietnam (in Vietnamese)

Numerical Model of the Impact of Submerged Breakwater on Shoreline Evolution of Bona Beach, France



Vu Minh Tuan and Yves Lacroix

Abstract The Bona beach, one of the beautiful sandy beaches along the eastern Giens double tombolo, is experiencing with severe coastal erosion which menaces its existence as well as many seaside properties on it. Submerged breakwaters (SBWs) are applied to this beach for the purpose of halting or at least limiting coastal erosion, stabilize the shoreline and to promote beach expansion by the formation of salient. SBWs are designated as the most rational measure for beach protection because of a number of outstanding advantages such as not destroying the landscape, not interfering the seaward vision, not reducing beach amenity and minimizing the negative impacts on the surrounding marine environment. These esthetic features are very necessary to maintain the tourist values of sandy beaches. In this study, the one-line numerical model of LITLINE is used to uncover the impact of SBWs on morphological evolution. The numerical results confirm that SBWs have certain effectiveness in protecting the Bona beach in different wave conditions.

Keywords Bona beach · SBWs · Numerical model · Erosion · Accretion

1 Introduction

The Giens double tombolo, located in the southeast coastal area of France, is a unique geomorphological formation in the world (Fig. 1). Its formation is attributed to a combination of several factors, of which the wave diffraction and refraction by the islands are the main causes [1]. The eastern branch of the Giens double tombolo is bounded by the Gapeau estuary to the north and La Badine beach to the south with a width of about 250 m. The beautiful sandy beaches along this branch are very important to the economy of the Provence region with an annual turnover of about 4.6

V. M. Tuan (✉)

Hanoi University of Civil Engineering/HUCE, Hanoi, Vietnam
e-mail: tuanvm@huce.edu.vn

Y. Lacroix

SEATECH, University of Toulon, La Valette du Var, Toulon, France

billion euros, which is one-fifth of the total revenue of the French tourism industry [2]. The Bona beach, one of these nine sandy beaches, extends approximately one kilometer from Hyères port in the north and La Capte port in the south, which bounds the Hyères Bay. It has suffered increasing erosion since the late 1950s as a result of natural causes and human interference, but anthropogenic interventions are still dominant. Specifically, the man-made structures installed along the eastern tombolo, viz. emergent breakwaters, groynes and jetties, have caused a shortage of sediment downstream due to the blockage of main longshore sediment transport [3]. In order to mitigate or prevent coastal erosion, various coastal structures have been implemented to protect sandy beaches and stabilize the shoreline. In 1960, two groynes were first installed at the Bona beach. Moreover, armor stone revetments were installed in the central Ceinturon beach, the southern parts of Hyères port and Gapeau river mouth (1995), while seawalls were established along the La Capte beach (2008) and the Bona beach. Some of these coastal protection measures have been effective in preventing local erosion but have also caused some undesirable adverse effects [4]. Unfortunately, the Bona beach has been undergone the recession due to the attacks of waves and storms, even breaking down amour revetment. The erosion at the toe of seawall is observed in the north part of the Bona beach. Through conducting in situ investigations combined with the use of aerial photographs during the period from 1972 to 2003, Capanni [5] showed that the Bona beach faced a recession with the mean erosion rate of -0.1 m/year. Therefore, a novel solution, which not only protects and stabilizes the shoreline, but also allows the longshore current to flow past as well as does not blot out surrounding the landscape, needs to be required.

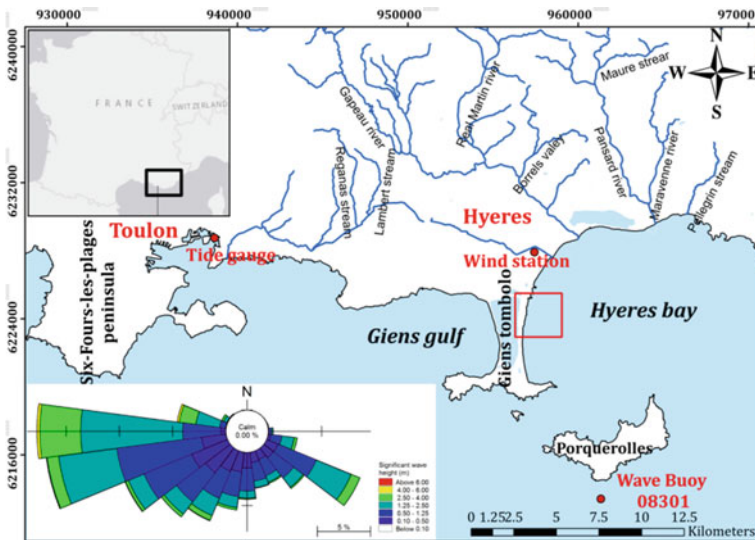


Fig.1 Location of the study area

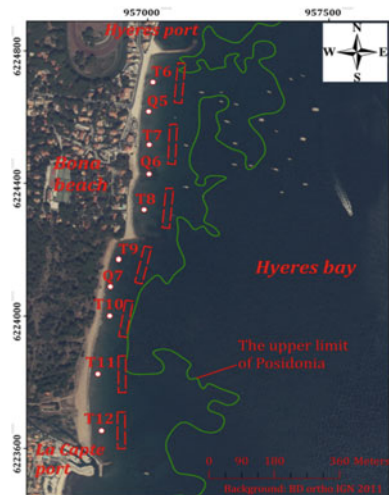
The most effective and sustainable measure in protecting a beach from coastal erosion is to emulate natural defense mechanisms [6]. SBWs (artificial reefs) can produce effects similar to that of natural offshore reefs. The main purpose of designing SBWs is to ensure dynamic balance of the shoreline by reducing hydraulic loads to the required level. They dissipate larger waves and allow milder waves to transmit through [7]. Specifically, these structures force large waves to break right on top of them and so their energy will be reduced before approaching the beach. As a consequence, the reduction of wave energy causes a decrease in flow velocities and promotes sediment accumulation conditions in the leeside of the structure without impeding water exchange and longshore drift [6]. In this work, SBWs are proposed to be applied to limit erosion for the Bona beach and their effects on shoreline evolution are also predicted by using numerical model.

2 Methodology

2.1 Design of SBWs

SBWs are installed within the surf zone and do not encroach on the Posidonia seagrass area, at a distance of 80–90 m from the shore, corresponding to a water depth of 2.5 m (Fig. 2). They are spaced at 60 m intervals and almost parallel to the design shoreline. The length of each SBW is 110–120 m, and the crest width is 20 m. The crest elevation of SBWs is designated to be about 0.4 m under the mean sea level. Both the shoreward and seaward slopes are 1:3. These basic parameters of the SBWs were chosen based on the study results of Vu [8].

Fig.2 Arrangement of the SBWs in the Bona beach



2.2 Numerical Model

LITLINE and LITDRIFT, two main modules of LITPACK model also developed by DHI [9], were used to investigate the position of the shoreline due to the impacts of the storms, seasonal variation and the construction of SBWs in Bona beach. The LITDRIFT calculates the net/gross littoral drift in function of the bathymetry. The results of the LITDRIFT model will be the input to the LITLINE model to describe the coastal behavior to gradients in the process of longshore sediment transport. Specifically, a table of sediment transport rates as functions of water level, surface slope due to wave-induced currents, wave period, wave height and direction is generated by LITDRIFT. The shoreline evolution will be estimated by LITLINE by solving the continuity equations for the coastal sediments. The model also takes into account the effects of structure (jetties and breakwaters), sources and sinks on the wave climate. The coastline position will be calculated based on the wave climate. The one-line model was calibrated by comparing it with the actual shoreline data of the year 2008 extracted from the in situ data of E.O.L [10]. The comparison result between the observed and simulated shorelines of the Bona beach is plotted in Fig. 3. It is clear that the simulated result agrees quite closely with actual field data. The statistical errors include root-mean-squared error (RMSE) of 2.07 m, the R -squared correlation coefficient (R^2) of 0.988 and a scatter index (SI) of approximately 1%. Moreover, Van-Rijn [11] proposed to use the Brier Skill Score (BSS) to evaluate the performance of the models for shoreline evolution. The BSS value of 0.33 can be acceptable. As a result, the goodness of fit between measurement data and the results of model strongly confirms that the numerical model can be employed to simulate the main study scenarios.

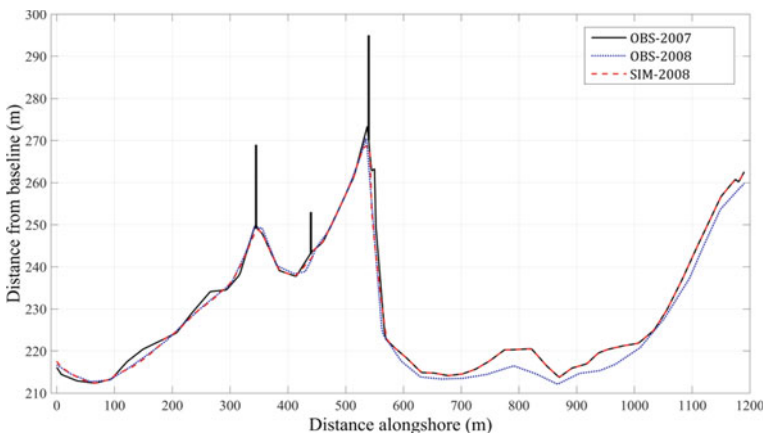


Fig. 3 Comparison of observed (OBS) and simulated (SIM) shorelines of Bona beach for the period from November 2007 to November 2008

Table 1 Simulation scenarios for Bona beach

Case	No SBWs	SBWs
Winter	×	×
Summer	×	×
Decadal storm	×	×
Semi-centennial storm	×	×
Centennial storm	×	×

2.3 Research Scenarios

The impact of SBWs in the study area was clarified and quantified through simulation of different wave conditions, taking into account the seasonal variation and extreme events. Totally, ten cases were modeled as in Table 1.

3 Results and Discussion

3.1 Impacts of SBWs on Shoreline Evolution Under the Seasonal Variation

Figure 4 shows the predicted shoreline change of Bona beach with and without SBWs. If two SBWs were not installed, moderate erosion would be observed in the middle of the Bona beach, corresponding to the position of 100 and 280 m in the x -axis. The landward migration of shoreline reached a maximum retreat of 0.6 m with the total erosion area of about -56.8 m^2 . In addition, slight erosion is also observed in other places. However, slight accretion is found on the downdrift sides of the groynes. In general, without the SBWs, the erosion trend is dominant with the total area loss of about -198 m^2 (Table 2). To reduce the change of the shoreline and prevent coastal erosion, seven SBWs are implemented at the positions of 80 m seaward of the shoreline in the y -axis. The position of erosion and accretion areas reveals that the longshore sediment drift is predominantly from south to north along the coastal area under analysis. It may be the result of the impact of the southeast waves, which is dominant in the winter with the high frequency of 21.3%. With the effect of the SBWs, the shoreline of the Bona beach is almost parallel to the initial shoreline just before the winter. Even, the salient is observed in the rear of the SBWs, viz. the position of 118 and 132 m. The maximum salient amplitude of 2.5 m occurs at the position of 555 m in the x -axis, right the downdrift side of the third groyne. Both of the accretion and erosion areas are decreased significantly to 11.55 m^2 and -117.7 m^2 , corresponding to 17.5% and 59.4%, respectively, comparing to those without the SBWs (Table 2). After the winter, the area losses still exist, but the reduction amount of beach area with the SBWs is much less than that without the

SBWs. Therefore, SBWs promote the effect of shielding and protecting the Bona beach from the impact of winter wave climate.

The summer is also the dry season, so there is no sediment supplied by rivers. As a result, slight accretion is observed in the downdrift side of the third groyne and the northern zone of Bona beach (Fig. 5). Erosion is still found in the middle of Bona beach, viz. at the position of 100 and 180 m in the x -axis. The direct impact of the moderate southeast waves which is dominant in the study area in the summer causes this area loss. Without the presence of the SBWs, the total area loss is estimated approximately $- 134.3 \text{ m}^2$ (Table 2). When the SBWs are established, the shoreline is almost recovered as the initial shoreline before the summer. The small shoreline migration is landward in some places and seaward in other places. The total area loss sharply reduces to 85.41%, corresponding to $- 114.7 \text{ m}^2$, whereas the total advance area also decreases about 73.2%, comparing to those without the SBWs (Table 2). Although there are mostly moderate and low waves in the summer, the simulation results confirm that they are mostly broken and dissipate at the crest of the SBWs.

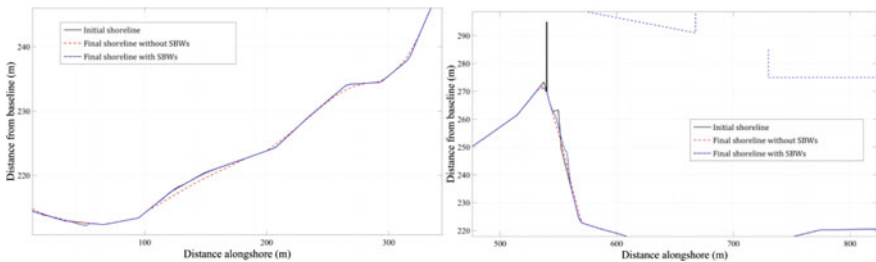


Fig. 4 Bona shoreline changes due to the winter wave climate with/without the construction of SBWs

Table 2 Accretion and erosion area in the Bona beach for different scenarios

Scenario	No SBWs		SBWs		Difference	
	Accretion (m ²)	Erosion (m ²)	Accretion (m ²)	Erosion (m ²)	Accretion (%)	Erosion (%)
Winter	66.03	- 198.00	54.45	- 80.31	17.54	59.44
Summer	18.30	- 134.26	4.90	- 19.58	73.20	85.41
Decadal storm	55.04	- 220.53	35.40	- 40.07	35.68	81.83
Semi-centennial storm	76.48	- 290.71	90.90	- 58.23	- 18.87	79.97
Centennial storm	63.30	- 281.56	41.01	- 41.70	35.21	85.19

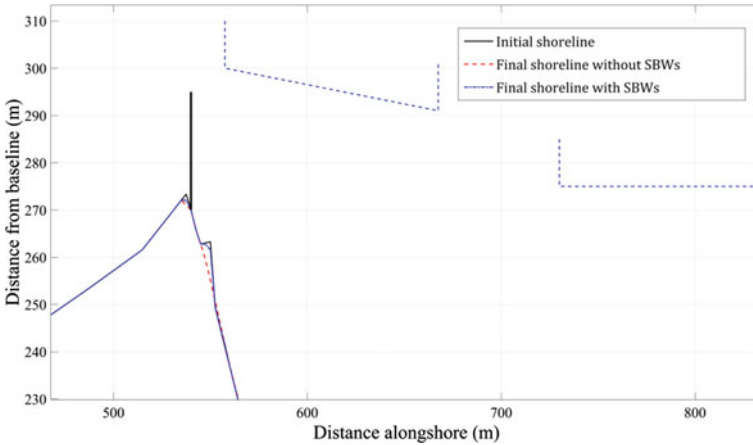


Fig. 5 Bona shoreline changes due to the summer wave climate with/without the construction of SBWs

3.2 Impacts of SBWs on Shoreline Evolution Under Extreme Events

The predicted shoreline changes of Bona beach with and without the SBWs due to the impact of the decadal storm are plotted in Fig. 6. In the case of no SBWs, severe erosion occurs at the positions from 100 to 300 m and from 420 to 450 m in the x -axis. The shoreline has migrated landward with a maximum retreat of 0.6 m at the position of 140 m in the x -axis. In addition, moderate erosion is noticed in the vicinity of the third groyne, corresponding to the position of 520 and 555 m in the x -axis. On the other hand, considerable deposition is found in the northern part of the Bona beach and the downdrift side of the third groyne. These deposited areas coincide with the positions in the reports of E.O.L [10] and Capanni [5]. The presence of seven SBWs results in the minor modification of the shoreline. The overlapping of the initial shoreline and the final simulated shoreline demonstrates this comment (Fig. 6). Even, the small salient is formed in the leeside of the SBWs, viz. the position of 125 and 135 m and the position of 550 and 560 m in the x -axis. The maximum salient amplitude of 1.0 m is reported at the position of 555 m. However, the considerable change of the shoreline is only observed in the gap between the third and the fourth SBWs in the vicinity of the third groyne. The rip currents induced by the breaking waves cause this landward migration of the shoreline. The effect of the SBWs reduces the erosion area from $- 220.5 \text{ m}^2$ down to $- 40 \text{ m}^2$, approximately 81.83% (Table 2). In other words, slight deposition is still found on the downdrift side of the third groyne and in the northern part of Bona beach.

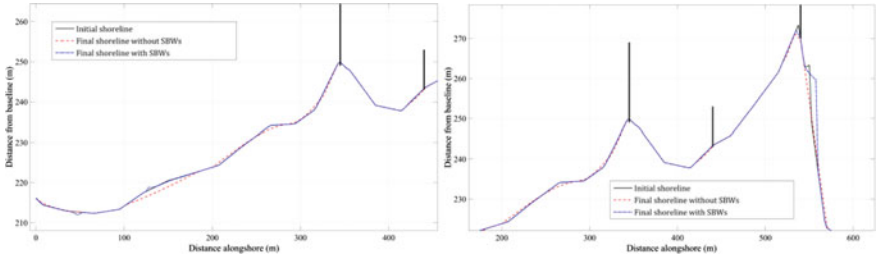


Fig. 6 Bona shoreline changes due to the decadal storm with/without the construction of SBWs

Figure 7 illustrates the changes of the shoreline along the Bona beach in the semi-centennial storm with and without the SBWs. The high waves attacked the beach and caused severe erosion at the position of 100 and 300 m in the x -axis. The highest territorial loss is estimated about -92 m^2 . The shoreline migrates landward with a maximum retreat of 1.5 m at the location of 150 m in the x -axis. In addition, moderate erosion is also reported on the updrift sides of the second and third groynes. Totally, the semi-centennial storm triggers the area loss of about -290.71 m^2 without the SBWs (Table 2). There are some accretion areas of $+76.5 \text{ m}^2$ created after this storm, viz. on the downdrift side of the third groyne, the updrift side of the first groyne and at the position of 0–50 m in the x -axis. With the construction of the SBWs, the area loss is reduced to 80%, in comparison without the SBWs (Table 2). The shoreline not only is stabilized but also slightly migrated seaward on the leeside of the SBWs. In addition, the remarkable salient still occurs on the downdrift side of the third groyne and the northern part of Bona beach, with the maximum amplitude of 4 m at the position of 553 m in the x -axis. It contributes to a significant increase of 18.9% in the accretion beach area, comparing to that without the SBWs. However, moderate erosion is observed till the tip of the third groyne where located in the gap between two segments, corresponding to the position of 535 and 550 m in the x -axis.

A comparison of shoreline positions of the Bona beach in the centennial storm scenario with and without the SBWs is presented in Fig. 8. The moderate erosion predicted by the models occurs in the middle of Bona beach, corresponding to the

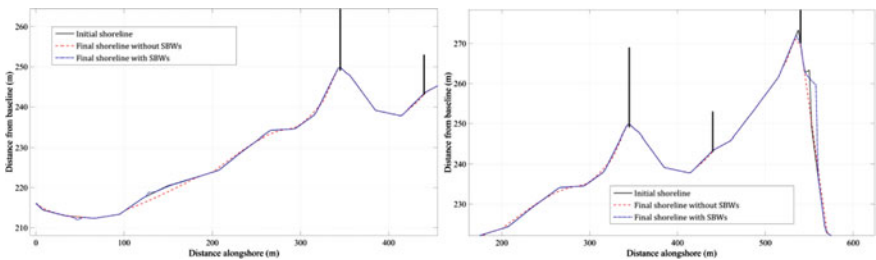


Fig. 7 Bona shoreline changes due to the semi-centennial storm with/without the construction of SBWs

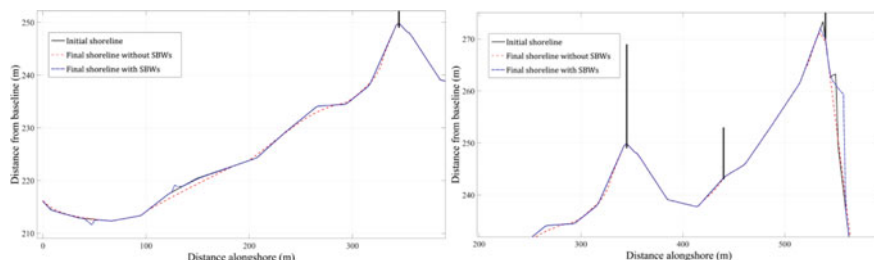


Fig. 8 Bona shoreline changes due to the centennial storm with/without the construction of SBWs

position of 100–300 m in the x -axis. The maximum retreat after the centennial storm without the SBWs was recorded at the position of 150 m in the x -axis, corresponding to about 1.2 m. Moreover, slight erosion is observed on the updrift side of the second groyne, viz. at the position of 410 and 450 m in the x -axis. This erosive area can be attributed to the blockage of littoral sediment drift due to the first groyne and the third groyne. The sediment is trapped and deposited on the upstream of the first groyne and the downstream of the third groyne. Along the Bona beach, the total accretion area is about 63.3 m^2 , while the whole territorial loss is estimated to -281.6 m^2 (Table 2). The results indicate that the decline trend is dominant without the SBWs. With the effect of the SBWs, the final predicted shoreline has changed insignificantly after the centennial storm, except the zone in the gap between the SBWs. The formation of rip currents causes erosion in this zone. The erosion area is reduced from -281.6 m^2 to -41.7 m^2 , corresponding to 85.2%. The salient is observed behind the fourth SBW, viz. the position of 552 and 560 m in the x -axis.

4 Conclusions

With the presence of SBWs in the Bona beach, erosion still takes place in gaps between SBWs, but the total loss amount of beach area due to erosion with SBWs is much less than that without SBWs. Under the highest storms, SBWs still show certain efficiency in reducing wave energy, reducing current speed and sediment transport locally. The presence of SBWs also counteracts the retreat of the shoreline and contributes to beach stabilization. Thus, Bona beach has been protected by SBWs not only in winter stormy conditions but also in stormy conditions.

Acknowledgements The authors are grateful to the 911 Project of Vietnam International Education Development, the Ministry of Education and Training, Vietnam (Grant No. 911), for supporting financially. The authors also sincerely thank the valuable support of EOL, CETMEF, CEREMA, SHOM and REFMAR.

References

1. Blanc JJ (1958) Recherches de sédimentologie littorale et sous-marine en Provence occidentale, Annales de l'Institut Océanographique: Institut Océanographique, Masson et Cie
2. Brunel C, Sabatier F (2007) Pocket beach vulnerability to sea-level rise. *J Coast Res*
3. Jeudy De Grissac A (1975) Sédimentologie dynamique des rades d'Hyères et de Giens (Var). Problèmes d'Aménagements. Université d'Aix-Marseille II: Marseille. 86 + annexes
4. Kliucininkaitė L, Ahrendt K (2011) Modelling different artificial reefs in the coastline of Probstei. *RADOST J 5*
5. Capanni R (2011) Étude et gestion intégrée des transferts sédimentaires dans le système Gapeau/rade d'Hyères. Aix Marseille 1
6. Arnouil DS (2008) Shoreline response for a reef ball submerged breakwater system offshore of Grand Cayman Island, Florida Institute of Technology
7. Pilarczyk KW (2003) Design of low-crested (submerged) structures: an overview. 6th COPEDEC. Int Conf Coastal Port Eng Develop Countries
8. Vu MT (2018) A numerical Approach for the design of coastal protection works in the oriental Tombolo of the Giens Peninsula, Université de Toulon
9. DHI (2014) Coastline evolution-LITLINE USER GUIDE
10. E.O.L (2010) Suivi de l'évolution des plages de la commune Hyères-les-palmiers. Commune de Heres-Les-Palmiers
11. Van Rijn LC, Walstra DJR, Grasmeijer B, Sutherland J, Pand S, Sierra JP (2003) The predictability of cross-shore bed evolution of sandy beaches at the time scale of storms and seasons using process-based profile models. *Coast Eng* 47(3):295–327

Wave Transmission Through Pile–Rock Breakwater to Protect the Mekong Delta Coastal and Develop an Empirical Formula



Nguyen Hai Duong, Dinh Cong San, Nguyen Nguyet Minh, Vu Van Nghi, and Le Duy Tu

Abstract The coastal erosion in the Vietnamese Mekong Delta (VMD) has become a serious problem for many years. Many solutions have been proposed to protect the coasts in many regions. The most popular constructions are pile–rock breakwaters. These structures consist of two rows of centrifugal piles which infilled rock. The wave flume experiments have been applied to build an experimental formula to evaluate wave reduction efficiency of breakwaters. But, there are some limitations of experimental situations, especially in case breakwater width is changed. Therefore, this paper focuses to (1) study the wave reduction ability of pile–rock breakwaters and (2) conduct wave flume experiments which take into account the change of breakwater width to determine the variation of wave spectra in front of and behind breakwaters. Results of experiments show that pile–rock breakwaters performed effectively because the wave transmission coefficients for emerged and submerged breakwaters are both low. Thus, the authors propose an experimental formula to determine the wave transmission coefficient and to be basement to design pile–rock breakwaters in the future.

Keywords Pile–rock breakwaters · Wave transmission · Wave spectra · The Coastal Mekong Delta

N. H. Duong (✉) · V. Van Nghi
Ho Chi Minh City University of Transport, Ho Chi Minh City, Vietnam
e-mail: duong.nguyen@ut.edu.vn

D. C. San · N. N. Minh · L. D. Tu
Southern Institute of Water Resources Research, Ho Chi Minh City, Vietnam

© The Author(s), under exclusive license to Springer Nature Singapore Pte Ltd. 2024
T. Nguyen-Xuan et al. (eds.), *Proceedings of the 4th International Conference on Sustainability in Civil Engineering*, Lecture Notes in Civil Engineering 344,
https://doi.org/10.1007/978-981-99-2345-8_36

357

1 Introduction

In the recent years, the erosion has become a critical phenomenon in the West Coast of the VMD. Several constructions have been implemented for the coastal protection and the mangroves' restoration. One of the most popular solutions is pile–rock breakwaters, which are applied in the coasts of Ca Mau, Kien Giang, Bac Lieu. So far, there has been 70 km of pile–rock breakwaters constructed [1]. At present, there is not much research to evaluate the effect of pile–rock breakwaters. The engineers normally apply the wave transmission coefficient following the instruction of TCVN2014 [2] or TCVN2018 [3] to design the constructions. But, this coefficient has not expressed the nature of the work performed of breakwaters. Therefore, the author would like to build an empirical formula to determine wave transmission coefficient for pile–rock breakwaters based on wave flume experiments. This paper will be divided into five parts: (1) Introduction; (2) Previous research; (3) Methodology and data collection; (4) Results and discussion; and (5) Conclusion and further research.

2 Previous Research

Reference of international and domestic previous researches served the purposes to find unmentioned problems of pile–rock breakwaters in order to propose a new technical solution.

There has been much international research on hollow breakwater, typically Van der Meer and Daemen [4]. The research conducted physical modeling experiments with random waves for narrow crest, trapezoidal, and rubble-mound breakwaters. The study focused on (1) assessing the influence of the permeability of the breakwaters by the nominal diameter of the rock, (2) analyzing the factors affecting the coefficient K_t , and (3) building a formula to determine the coefficient K_t for these breakwaters; following Van der Meer and Daemen are the research of Angremond et al. [5] and Van der Meer et al. [6] that fully consider the main influencing parameters to the wave transmission. These are breakwater crest freeboard, width, and broken wave index representing the interaction between the incident wave and the breakwaters slopes. These parameters have reflected the physical nature of the wave energy dissipation process when waves pass through submerged breakwaters, inclined slope, and narrow crest. Besides, these two studies have built a formula to determine the coefficient K_t for these breakwaters. However, the study only focused on breakwaters with hollow structure, inclined slope, trapezoidal shape, and narrow crest.

There are also many domestic studies on hollow breakwaters, typically Thieu Quang Tuan et al. 2018 [7]. The study (1) conducted physical modeling experiments in wave flumes, and (2) proposed a formula to determine the coefficient K_t through

a non-conventional hollow breakwater with inclined slope and narrow crest. Quang [8], built a formula to calculate the coefficient K_t for the bamboo pile breakwaters in the coast of the VMD. This formula has been applied for vertical bamboo pile structures. This paper can refer to a method for vertical structures. Research by Tu et al. [9] has shown the wave reduction efficiency, the change of wave parameters and developed a formula to determining the coefficient K_t for breakwaters. The type of breakwater that [9] studied is similar to the type of breakwater that the article studied. However, [9] has not assessed how the change in breakwater width leads to the change of the coefficient K_t ; Do Van, Nguyen et al., 2021 [10] overcome the limitation of Nguyen 2014, and Tu et al. 2020, because of taking into account the fluctuation of width breakwater. But Do Van, Nguyen et al., 2021 just built a formula for breakwaters without mentioning the fluctuation of the wave spectra, wave period.

Following previous research, this paper will focus on the wave flume experiments for pile–rock breakwaters. The results of experiments will be used to determine the elements influencing the coefficient K_t and build a formula to design breakwaters in the future.

3 Methodology and Data Collection

The wave flume experiments have been applied to determine wave transmission coefficient for pile–rock breakwaters. The experiments include three stages

3.1 *Input Data Collection*

Input data were collected in the coast of the VMD and put into the experimental model including wave height, wave period, water depth, and dimension of pile–rock breakwaters. The construction was designed in the monsoon condition. The input wave parameters are measured actually and simulated from mathematical models and referred from Ba et al. [11], in which: (1) in the Southwest monsoon condition at the West coast, the incident wave height in front of breakwaters was from 0.25 to 1.00 m and the wave period was from 2 to 5 s, and (2) in the Northeast monsoon condition at the East coast, the incident wave height in front of breakwaters is from 0.5 to 1.5 m and the wave period is from 3 to 7 s. The study used structures with designed height of 3.0 m, pile diameter of 0.3 m, and the distance between two piles of 0.6 m. The crest freeboard height of breakwaters varied from $-H_s$ to $+H_s$ (m). The designed water depth was from 1.6 to 3.5 m, the minimum depth of the flume was 0.2 m, and the maximum water depth in the wave flume was 1.0 m.

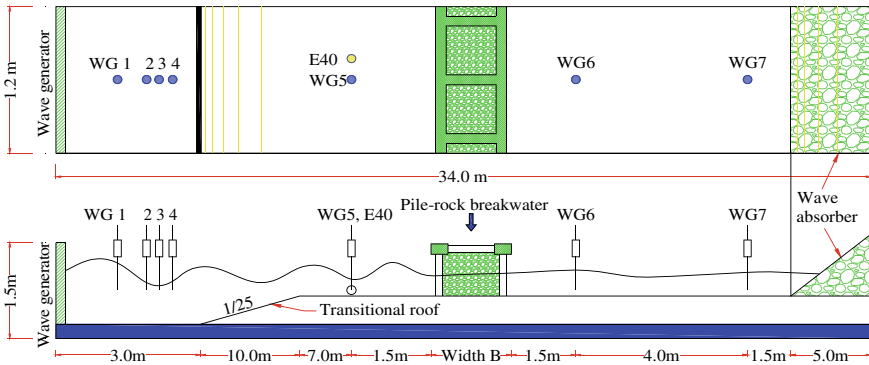


Fig. 1 Experimental layout diagram

3.2 Setting Up Experiment

The wave flume experiments were carried out in the marine hydrodynamics laboratory—Southern Institute of Water Resource Research. The largest scale model was selected based on wave flume capacity and wave parameters, choose $N_L = 7$; $N_t = \sqrt{N_L} = 2.65$; $N_v = \sqrt{N_L} = 2.65$; and $N_m = N_L^3 = 343$. The breakwaters are made of wood with height of 40 cm and pile diameter of 4.2 cm. There are three models designed with three different widths, namely B24, B38, and B52. The rock diameter used in experiments was 4–7 cm. After sieving, the porosity of rock aggregate is $P = 40\%$ according to TCVN 7572:2006. The transitional slope between the deep and shallow water areas is 1/25, and the foot of slope is 3 m from the wave generator. The wave parameters in front of and behind breakwaters are measured by seven wave gauges, in which WG1, WG2, WG3, WG4, and WG5 to measure the wave height in front of breakwaters and WG6, WG7 to measure the wave height behind breakwaters. Particularly, WG1, WG2, WG3, and WG4 are designed to separate the reflected waves and the incident waves in front of breakwaters based on the method of least squares [12]. The boundary condition of wave parameters is simulated by JONSWAP spectra with $\gamma = 3.30$. Each series of experimental data was performed at least for a period of $500 * T_p$. The experimental layout is shown in Fig. 1.

3.3 Scenarios and Experimental Situations

There were 280 experimental situations. The situations are detailed in Table 1. The symbol of wave parameters is described in the glossary.

Table 1 Experimental situations

Scenarios	D (m) và R_c (m)	Wave parameters (m) (s)
Non-construction	$D = 0.2 R_c = + 0.2$	$H_s = 0.12; T_p = 1.51$
B24	$D = 0.25 R_c = + 0.15$	$H_s = 0.12; T_p = 1.89$
B38	$D = 0.3 R_c = + 0.1$	$H_s = 0.12; T_p = 2.27$
B52	$D = 0.35 R_c = + 0.05$	$H_s = 0.12; T_p = 2.65$
	$D = 0.4 R_c = + 0$	$H_s = 0.17; T_p = 1.89$
	$D = 0.45 R_c = - 0.05$	$H_s = 0.17; T_p = 2.27$
	$D = 0.5 R_c = - 0.1$	$H_s = 0.17; T_p = 2.65$
		$H_s = 0.22; T_p = 2.27$
		$H_s = 0.22; T_p = 2.65$
		$H_s = 0.27; T_p = 2.65$

3.4 Output Data Analysis

The results of stage 2 will be analyzed to determine the factors affecting wave transmission and propose a formula to calculate the coefficient K_t for pile–rock breakwaters.

4 Results and Discussion

Tu et al. [9] built a formula based on the wave flume experiments and determined the factors affecting the wave transmission coefficient are $R_c/H_{m0,i}$ and S_{0p} . The formula has the following form:

$$K_t = -0.167 \frac{R_c}{H_{m0,i}} - 4.172 S_{0p} + 0.643 \quad (1)$$

Applying Formula (1), this paper continues to analyze the factors affecting the wave transmission, especially the change of breakwater width (B), thereby building a formula for determining the coefficient K_t for pile–rock breakwaters with various widths.

4.1 Analyzing the Influence of Hydrodynamic Factors on Wave Transmission Coefficient and Building the Formula

Evaluation criteria

According to the principle of conservation of energy, when the waves hit the breakwaters, a part of energy is dissipated, a part is absorbed and reflected in front of

breakwaters, and a part is passed through behind breakwaters. This is a hydrodynamic problem and it is written as an energy balance formula [4]:

$$E_i = E_t + E_r + E_d \tag{2}$$

in which E_i is the incident wave energy, E_t is the transmitted wave energy, E_r is the reflected wave energy, and E_d is the dissipated wave energy. Based on the wave energy transformation Formula [4], Formula (3) can be rewritten as:

$$1 = \left(\frac{H_t}{H_i}\right)^2 + \left(\frac{H_r}{H_i}\right)^2 + \frac{E_d}{E_i} \tag{3}$$

$$1 = K_t^2 + K_r^2 + K_d^2 \tag{4}$$

The influence of hydrodynamic factors on the wave transmission coefficient

a. The influence of $R_c/H_{m0,i}$

$R_c/H_{m0,i}$ depends on factors such as: water height, breakwater height, the wave height in front of breakwaters. The relationship between $R_c/H_{m0,i}$ and the coefficient K_t shown in Fig. 2 is clear when $-1.0 < R_c/H_{m0,i} < 1.0$. This is the distance from the submerged breakwaters to the emerged breakwaters, ($R_c \sim 0$).

b. The influence of the incident wave slope

The relationship between the incident wave slope and the coefficients K_t is based on S_{0p} and S_{0m} (wave slope corresponding to the period of the spectral peak and the period of the spectral average), specifically: S_{0p} is inversely proportional with wave transmission coefficient K_t , but K_t has no significant change as shown in Fig. 3, and S_{0m} is directly proportional with the coefficient K_t , but K_t has no significant change;

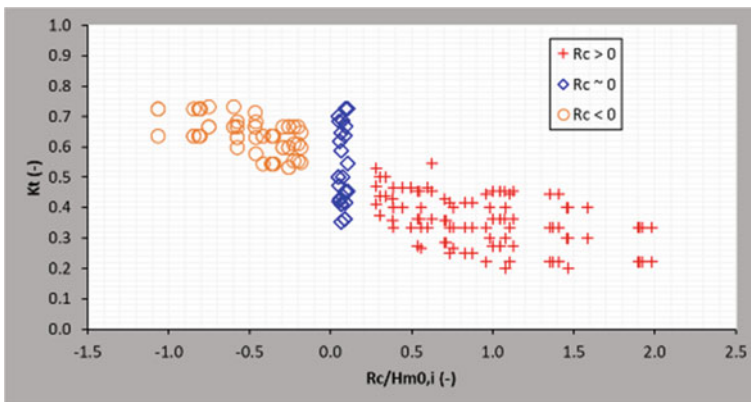


Fig. 2 Correlation between $R_c/H_{m0,i}$ and wave transmission coefficient K_t

the cause is the same as analyzed in Fig. 4. It can be seen that the influence of S_{0p} and S_{0m} on the coefficient K_t is similar. But, the effect on K_t to S_{0p} is more than that of S_{0m} with emerged breakwaters and conversely with submerged breakwaters. This is expressed in the slope $|a|$.

Effect of the comparative breakwater width

Figure 5 shows that B_n/D is inversely proportional to K_t because K_t tends to increase while B_n/D tends to decrease. Similar to Fig. 5, for the emerged breakwaters, K_t is smaller than that of submerged breakwaters. Figure 6 shows that the relationship between $B_n/H_{m0,i}$ and K_t is also similar to the relationship between B_n/D and K_t .

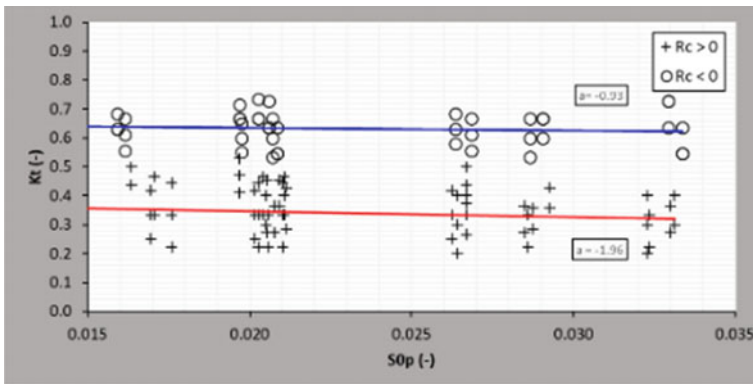


Fig. 3 Correlation between S_{0p} and wave transmission coefficient K_t

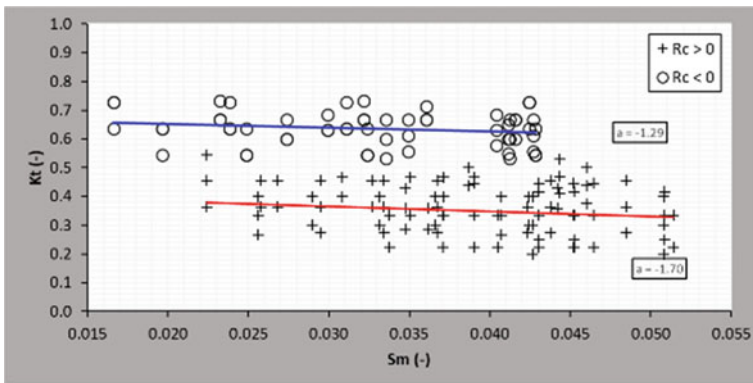


Fig. 4 Correlation between wave slope S_{0m} and wave transmission coefficient K_t

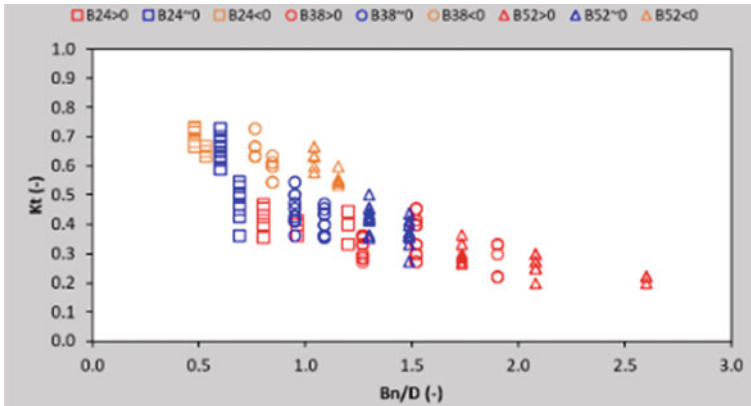


Fig. 5 Correlation between the relative width B_n/D and wave transmission coefficient K_t

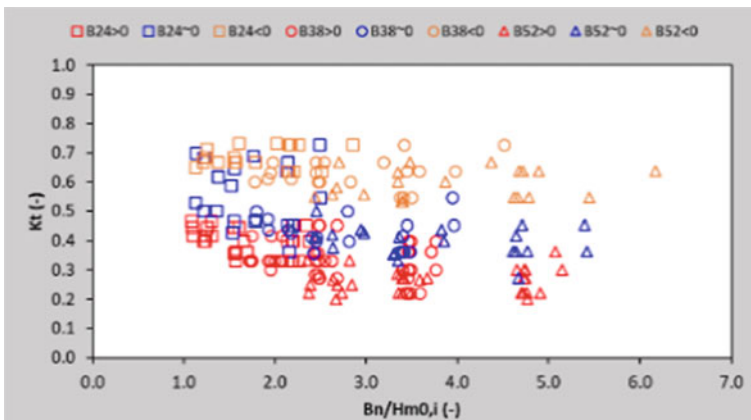


Fig. 6 Correlation between the relative width $B_n/H_{m0,i}$ and wave transmission coefficient K_t

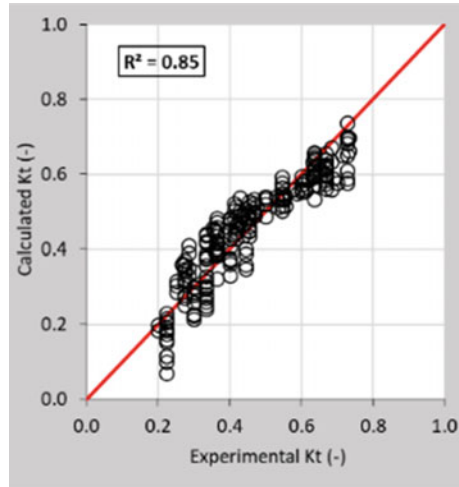
4.2 Experimental Formula

From the above analysis, it can be seen that the coefficient K_t for the pile–rock breakwaters is influenced by parameters such as: $R_c/H_{m0,i}$; $B_n/H_{m0,i}$; B_n/D ; and S_{0p} . Referring to the formula of Tu et al. [9], and Quang et al. [8], the author proposes a general formula to calculate the coefficient K_t as the following:

$$K_t = a \frac{R_c}{H_{m0,i}} + b \frac{B}{H_{m0,i}} + c \frac{B}{D} + d S_{0p} + e \tag{5}$$

in which a , b , c , and d are the typically empirical constants for the respective factors: $R_c/H_{m0,i}$, $B_n/H_{m0,i}$, B_n/D , and S_{0p} . The coefficients a , b , c , d , and e are determined by

Fig. 7 R^2 results from regression analysis



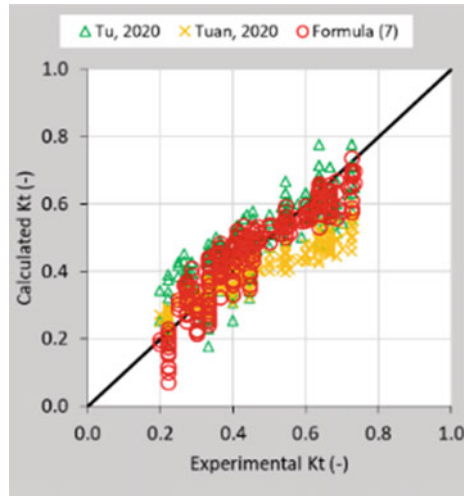
the regression method from the experimental results. The values of $a, b, c, d,$ and e are calculated and chosen so that the correlation coefficient R^2 reaches the maximum value of 0.85 (Fig. 7). The constants $a, b, c, d,$ and e are respectively: $a = -0.117, b = -0.007, c = -0.116, d = -2.420,$ and $e = 0.708$. Based on the results of physical model experiments, we have a formula to determine the coefficient K_t .

$$K_t = -0.117 \frac{R_c}{H_{m0,i}} - 0.007 \frac{B}{H_{m0,i}} - 0.116 \frac{B}{D} - 2.420 S_{0p} + 0.708 \quad (6)$$

The applicable range of (6) is: $-1.068 < \frac{R_c}{H_{m0,i}} < 1.982; -1.086 < \frac{B_n}{H_{m0,i}} < 6.173; 0.48 < \frac{B_n}{D} < 2.6; 0.0086 < S_{0p} < 0.0334; 0.070 < K_t < 0.737$. Applying the collected data into Formula (6) to compare the results of Quang et al. [8] and Tu et al. [9]), shown in Fig. 8.

These comparison results see that the author’s formula is consistent with the formula of Quang et al. [9] and Tu et al. [11] with a high correlation R^2 . But, Formula [9] and Formula [11] have not shown the trend of concentration as the author’s Formula (6). The actual measured K_t and the calculated K_t according to the author’s formula (6) are not much different because this formula has taken into account the influence of the breakwater width.

Fig. 8 Comparison between formula (6) with Tuan’s formula, 2020, and Tu’s formula, 2020



5 Conclusion

The wave transmission through pile–rock breakwaters is affected by the important factors $R_c/H_{m0,i}$, $B_n/H_{m0,i}$, B_n/D , and S_{0p} . The empirical formula for determining the wave transmission coefficient was built with high reliability and quite similar to the previous formula. The new formula can determine the wave transmission coefficient for pile–rock breakwaters in the Mekong Delta without conducting further experiments but still ensuring the applied range of the formula. The foot of breakwaters’ protection solution, the influence of the size of the rock infilled the breakwaters should be carefully considered in the subsequent studies.

Appendix 1

Symbol	Unit	Description
K_t	–	Wave transmission coefficient
K_r	–	Wave reflection coefficient
K_d	–	Wave energy dissipation coefficient
B_n	m	Pile width
B_{24}	m	Model pile–rock breakwater width = 0.24 m, the real width = 1.70 m
B_{38}	m	Model pile–rock breakwater width = 0.38 m, the real width = 2.7 m

(continued)

(continued)

Symbol	Unit	Description
$B52$	m	Model pile–rock breakwater width = 0.52 m, the real width = 3.70 m
$WG1, WG2, WG3, WG4, WG5, WG6, WG7$	–	Wave gauge No. 1, 2, 3, 4, 5, 6, 7
N_L	–	Model length scale
N_t	–	Model time scale
N_v	–	Model speed scale
N_m	–	Model weight scale
H_s	m	Wave height
R_c	m	Crest freeboard
D	m	Depth
P	%	Porosity
$H_{m0,i}$	m	Zeroth moment spectral wave height
T_p	s	Peak wave frequency of the spectrum
$T_{1/3}$	s	Mean of the longest third of the wave period
$T_{m-0,2}$	s	Average wave period
L_m	m	Wave length corresponding to the featured wave spectra period $(g.T_{m-0,2}^2)2\pi$
L_p	m	Wave length at the peak period $(g.T_p^2)\pi$
$B_n/H_{m0,i}$	–	Ratio of pile–rock breakwater width and wave height
B_n/D		Ratio of pile–rock breakwater width and water depth
$R_c/H_{m0,i}$	–	Relative crest freeboard
S_{0p}	–	Slope of mean wave period corresponding to the spectral peak period T_p , $S_{0p} = H_{m0,i}/L_p$
S_{0m}	–	Slope of peak wave period corresponding to the spectral peak period $T_{m-0,2}$, $S_{0m} = H_{m0,i}/L_m$

References

1. VIWAT – KIT review -R1 (2020) Primary proposals of appropriate coastal protection measures from investigation and survey, Prepared by the SIWRR, Vietnam, Reviewed by the KIT-IWG, Germany
2. TCVN 9901 (2014) Hydraulic structures - Requirements for seadike design
3. TCVN 12261 (2018) Hydraulic structures – Coastal protection structures – Design requirements for groin and detached breakwater
4. Meer VD, Daemen (1994) Stability and wave transmission at low crested rubble mound structures. J Waterway, Port Coastal Ocean Eng 1:1–19

5. Angremond K, Van der Meer JW, de Jong RJ (1996) Wave transmission at low-crested structures. In: 25th Coastal engineering proceedings, ASCE, Orlando, USA, pp 2418–2427
6. Van der Meer JW, Briganti R, Zanuttigh B, Wang B (2005) Wave transmission and reflection at low-crested structures: design formulae, oblique wave attack and spectral change. *Coast Eng* 52:915–929
7. Quang TT, San Dinh C, Tu LX, Do Van D (2018) The efficiency of hollow breakwaters on wave flume models. *J Water Resour Sci Technol* 49:95–102
8. Tien NA, Cong Dan T, Quy LP, Tuan TQ (2018) Building a method to calculate wave transmission coefficient through hollow-submerged breakwaters by physical models. *J Water Resour Sci Technol* 46:24–34
9. Quang TT, Trong LM (2020) Monsoon wave transmission at bamboo fences protecting mangroves in the lower Mekong Delta. *Appl Ocean Res* 101:102259. <https://doi.org/10.1016/j.apor>
10. Nguyen NH (2014) Impact assessment of the embankment in the West coast of Ca Mau. *J Water Resour Sci Technol* 17:1–14
11. Le Xuan T, Ba HT, Le Manh H, Do Van D, Nguyen NM, Wright DP, Bui VH, Mai ST, Anh DT (2020) Hydraulic performance and wave transmission through pile-rock breakwaters. *Ocean Eng* 218:1–13
12. Duong DV, Minh NN, Tu LD, Tu LX, San DC, Linh TT (2021) The effect of crest width on the efficiency of pile-rock breakwaters in wave flumes. *J Water Resour Sci Technol* 66:63–73

An Empirical Prediction of $T_{m-1,0}$ on the Reef Flat of Atolls



Thi Thuy Pham, Hai Trung Le, and Thanh Tung Tran

Abstract Among thousands of atolls in the East Sea, some consists of sandy cores emerging from the reef flats. Extreme wind and waves may exert impacts seriously attacking these cores which are usually very small in the area compared to the reef flats. Therefore, the paper explores wave characteristics and how they propagate on the platform of a representative atoll. We conducted experiments in a 50-m-long wave flume at Thuyloi University, Ha Noi, Vietnam. In general, the period of wave spectral $T_{m-1,0}$ would be from one to three times longer than the T_p of deep-water waves. Furthermore, an empirical formula was derived to predict $T_{m-1,0}$.

Keywords Reef flat · Spectral wave period · Infragravity waves · Wave setup · Shallowness

1 Introduction

There are thousands of atolls spreading out over hundreds of thousands of square kilometers of the East Sea. Made of underground mountains at great bathymetry, their upper parts, known as the platforms (reef flat), usually reach the mean sea water level [1]. Among many, several atolls consist of sandy cores that emerge even at high tide. Remarkably, the coral platforms are often expanded much larger than the core. And, water is relatively shallow on this platform, beyond which fore-reef slopes develop continuously into the deep sea (Fig. 1). However, the fore-reef slope changes regarding depth. Deep in the ocean, it shows a very high steepness (from 1/1 to 1/2). Closer to the water surface (from—20 m), the steepness gradually decreases to 1/5 and even 1/10 due to the strong growth of corals.

T. T. Pham (✉)

Thuyloi University and Le Quy Don Technical University, Hanoi, Vietnam

e-mail: thuy39vtl@gmail.com

H. T. Le · T. T. Tran

Thuyloi University, Hanoi, Vietnam

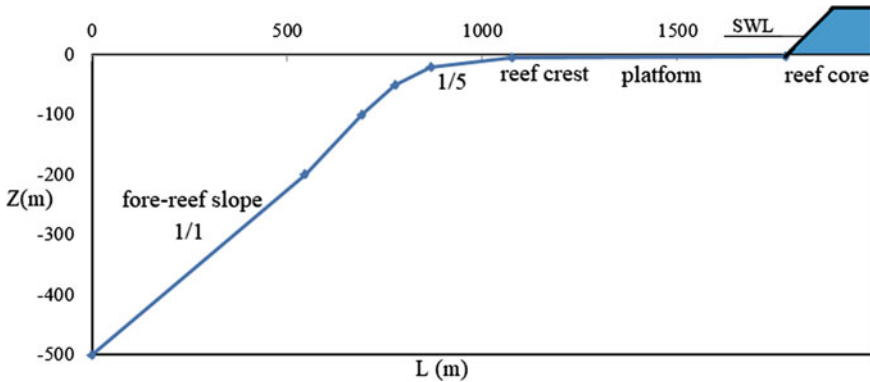


Fig. 1 Topography of a representative coral reef in the study area

Located hundreds of kilometers from the continental, atolls witness complicated hydrodynamic regimes. During storms, extreme wind and extraordinary waves impact that seriously erodes the vulnerable cores. Therefore, how waves propagate on the reef flat and the characteristics of shallow water waves on the platform are essential informations for construction design at any atoll.

Propagating into the reef flat, waves break due to a sudden decrease in water depth; energy and height significantly reduce. The formation and development of infragravity waves become more dominant inward and wave setup raises the water level on the platform [2]. Two factors that govern the wave hydrodynamic regime are the freeboard and the fore-reef slope [2]. In deep water, waves are linear, but when traveling into the areas with limited water depths, the wave spectrum is to be deformed. It is widely accepted to use a significant height H_s and a period T_p to characterize a deep-water wave. In shallow area, the spectral wave height H_{m0} and spectral wave energy periods $T_{m-1,0}$ are usually adopted [2].

There are several empirical approaches being proposed to estimate $T_{m-1,0}$ on either gentle slopes [3] or shallow sea-dike foreshores on mangrove mudflats in the Mekong Delta [4]. However, a formula of the spectral mean wave energy period has not been developed for waves on the reef flat of an atoll. Therefore, the article examines how waves propagate on the platform of an atoll in order to explore theses' characteristics, which are expected to be different from on regular beaches. Based on more than 50 experiments in a wave flume, we attempt to establish a formula to estimate $T_{m-1,0}$ from using the peak period in deep water and the "shallowness" of the reef flat.

2 Experiment Setup

We performed a series of experiments in a 50-m-long wave flume at Thuyloi University, Ha Noi, Vietnam. The flume profile was built up including five areas: a wave maker; a deep water (20 m); a reef edge of 1/5 (2.5 m); a platform (22.5 m); and a core (3 m).

The advanced piston wave generator and active reflection compensation system help to generate regular or irregular waves. The maximum irregular wave height that wave flume can be generated is 0.3 m. Using the JONSWAP spectra wave with the peak enhancement factor $\gamma = 1.25$, as considered the most relevant for the waves in the deep-water areas in the East Sea. Every experiment consisted over 1000 waves to cover the main frequency domain of spectral wave and the statistical characteristics of the wave height are stabilized.

Due to the facility capacity and boundary conditions, a length ratio of $N_L = 15$ and time ratio of $N_t = 3.87$ were selected according to the Froude scaling laws.

Table 1 describes the experimental program consisting of 50 test scenarios, which are 5 water depths (d) \times 5 wave heights (H_s) \times 2 wave periods (T_p).

The experimental configuration was set up as in Fig. 2. The first gauge WG1 measures deep-water waves at about from 2 to 3 times wave lengths in deep water. Four other gauges WG2, WG3, WG4, and WG5 are arranged on the reef flat. The last gauge WG6 measures waves in front of the riprap slope.

In deep water, it is traditional to use a significant height H_s and a period T_p to characterize a deep-water wave. On the platform, the spectral wave heights H_{m0} and the spectral wave energy periods, $T_{m-1,0}$, are usually used [2].

$$H_s \approx 4.004 \sqrt{\int_{f_{\min}}^{f_{\max}} S(f) df} \tag{1}$$

$$T_{m-1,0} = \frac{m-1}{m_0} = \frac{\int_{f_{\min}}^{f_{\max}} f^{-1} S(f) df}{\int_{f_{\min}}^{f_{\max}} S(f) df} \tag{2}$$

where f is the frequency of wave, f_{\max} and f_{\min} are lower and upper frequencies, $S(f)$ is the spectral density, and m is the n -th order spectral moment.

Table 1 Experiment scenarios

Model			Prototype		
d (cm)	H_s (cm)	T_p (s)	d (cm)	H_s (cm)	T_p (s)
14.0	10	1.5; 1.7	2.10	1.50	5.8; 6.6
16.5	12	1.7; 1.9	2.48	1.80	6.6; 7.0
19.0	15	1.8; 2.0	2.85	2.25	7.0; 7.4
21.4	18	1.9; 2.1	3.21	2.70	7.4; 8.1
24.0	20	2.1; 2.3	3.60	3.00	8.1; 8.8

3 Results and Discussion

3.1 Characteristics of Shallow Water Waves on the Reef Flat

When the waves propagate from deep water to shallow water on the reef flat, many physical processes such as reflection, transformation, broken and bottom friction reduce wave energy significantly. Wave energy is dissipated due to the sudden drop in water depth at the top of the reef (reef edge) and because of friction on the platform [5] (Fig. 3).

Shallow water waves are generated on the platform, including short waves (SS) and infragravity waves (IG, with a period of 20–200 s). When propagating on the reef flat, wave energy tends to shift between frequency areas with a movement of the spectrum peak to the left. It means that the high-frequency energy decreases, and infragravity wave energy increases. Longer waves develop in shallower water on the platform. And even the same water level, the higher the incident wave (in deep water), the longer the ones on the reef flat.

As can be seen in Fig. 4, the density spectrum of small wave height, the D66.5H10T170 scenario (water depth 16.5 cm, wave height H_{10} cm, and period $T_{1.7}$). It is noted that the water is relatively deep on the platform, where there are predominantly short waves with frequency (f) of about 0.68 and a spectrum peak period of 1.47 s in model and 5.7 s in prototype.

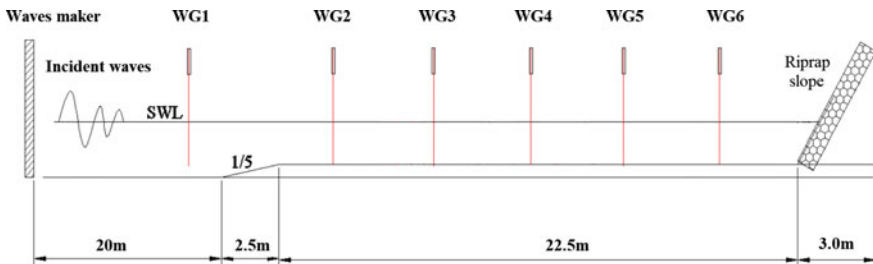


Fig. 2 Experiment setup

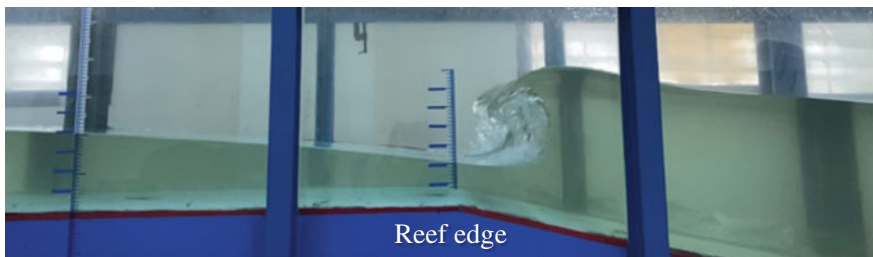


Fig. 3 Wave breaking at the reef edge

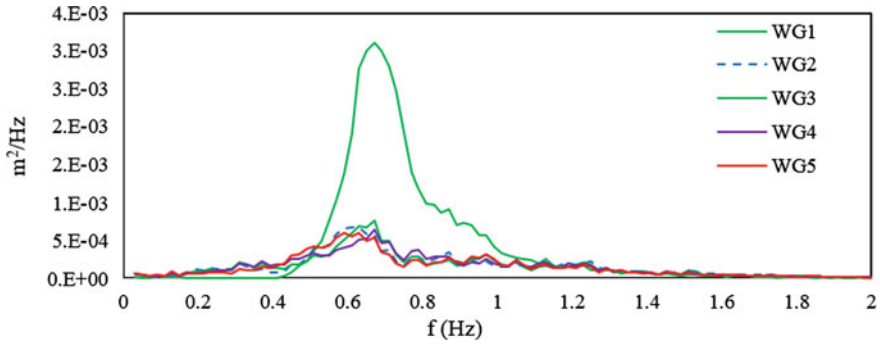


Fig. 4 Variance density spectrum D66.5H10T170

In the case of larger waves coming from deep water and shallower water on the reef flat, short wave energy decreases, and IG wave energy increases. Correspondingly, the peak of wave density spectrum seems to shift to the left toward the low-frequency area. Remarkably, the peak frequency decreases rapidly when traveling toward the core. Illustrating the D64H20T210 scenario (water depth 14 cm, wave height H_{20} cm, and period $T_{2.1}$ s), Fig. 5 graphically depicts a wave frequency of 0.1, i.e., a spectrum peak period of $1/f = 10$ s in the model and 38.7 s in the prototype, much longer than 20 s.

Figure 6 shows a correlation between incident wave heights H_{m0} and wave periods, $T_{m-1,0}$, on the reef flat with limited water depth. The experimental spectral wave periods range from 1.7 to 6.19 s on the platform. It implies that short waves (SSs) are predominant while infragravity ones IG ($T_{m-1,0}$ from 20 to 200 s) are rarely found.

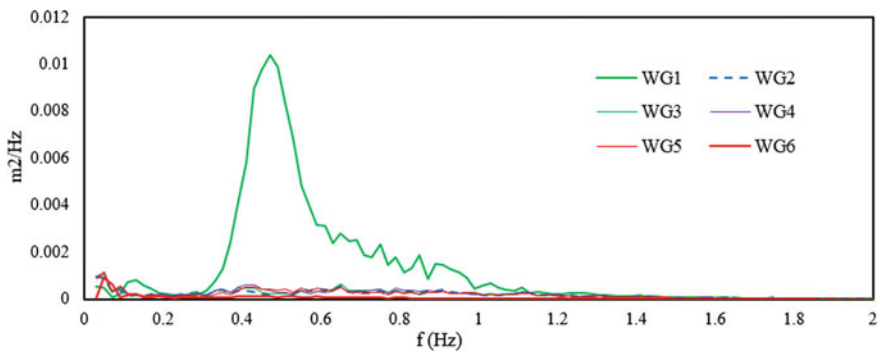


Fig. 5 Variance density spectrum D64H20T210

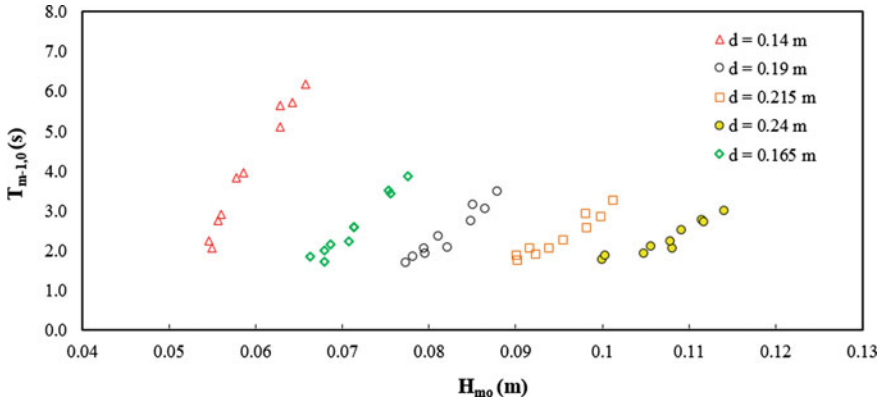


Fig. 6 Correlation of the wave height and the wave period on the reef flat

3.2 An Empirical Formula of $T_{m-1,0}$

It is the fact that the wave height can be measured or estimated by some wave models, but the wave period is difficult to calculate. The most suitable method to estimate the incident characteristic spectral period, $T_{m-1,0}$, regarding the long-period effects is based on practical calculations. Inspired by this, we attempt to derive $T_{m-1,0}$ from data which was measured on the platform. Tuan et al. [4] related the wave period on the reef flat to a parameter O_F representing the “shallowness” of the atoll as follows:

$$S_{om} = \frac{2\pi H_{mo}}{gT_p^2} \text{ and } O_F = \frac{2\pi d}{H_{mo}} \sqrt{S_{om}} \tag{3}$$

where H_{mo} is incoming wave height on the platform, T_p is the peak period at the deep-water boundary, S_{om} represents the wave slope, and d is water depth.

Using data from 50 measurements, we plot the ratio of $T_{m-1,0}/T_p$ against θ_F in Fig. 7. The results show that $T_{m-1,0}$ can be three times larger than T_p when O_F varies in the range of 1.3–2.3. It also shows the differ from in wave characteristics on the shallow water. Furthermore, the ratio of $T_{m-1,0}/T_p$ would be expressed with a function depending on O_F .

$$\frac{T_{m-1,0}}{T_p} = \frac{1}{(b_1 + \ln(1 + b_2 O_F^{b_3}))} \tag{4}$$

where $b_1 = 1.2$, $b_2 = 1.0$, and $b_3 = 1.95$ are coefficients derived from regression analysis.

For construction design at an atoll core, it is convenient and useful to know the wave parameters on the platform. Thanked to advances in GIS and remote sensing, the wave pattern in deep water would be extracted more easily and more precisely. Besides, the topography of an atoll platform can be measured with a considerable

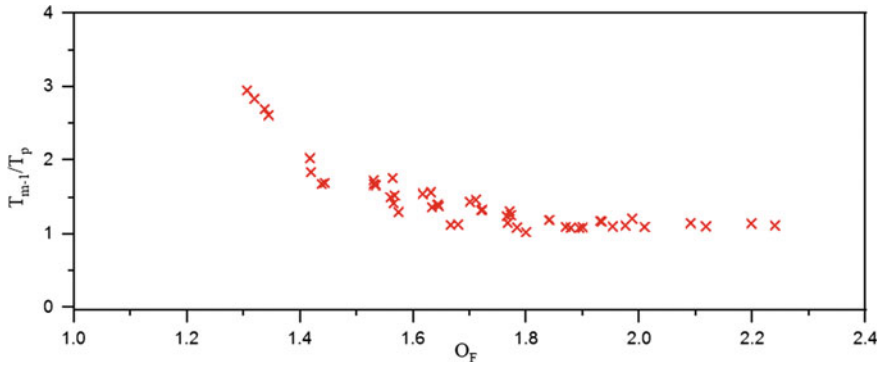


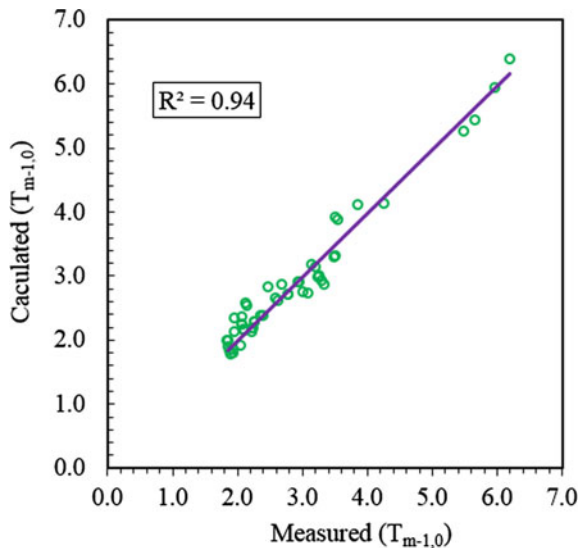
Fig. 7 Transformation of wave periods with regard to the “shallowness” of a reef flat

number of different techniques. As a result, $T_{m-1,0}$ on a reef flat would now be estimated from wave parameters in deep water and the “shallowness” as:

$$T_{m-1,0} = T_p \frac{1}{(1.2 + \ln(1 - O_F^{1.95}))} \tag{5}$$

Figure 8 compares the measured periods against the values of $T_{m-1,0}$ derived from applying Eq. (5) above. In general, the empirical formula owns a relatively high confidence interval with $R^2 = 0.94$.

Fig. 8 Measured and calculated values of $T_{m-1,0}$ in the shallow water of an atoll platform



4 Conclusion Remarks

Presenting a series of experiments performed in a wave flume, the article has explored how wave period transforms on an atoll platform. Experimental results show that the spectral wave periods range from 1.7 to 6.19 s on the platform. It means short waves are predominant while infragravity ones are rarely found. In shallow water, period $T_{m-1,0}$ is about one to over three times longer than period T_p of deep-water waves. A formula predicting $T_{m-1,0}$ on the platform was then proposed refer to T_p in deep water together the shallowness of the platform. A formula predicting $T_{m-1,0}$ emphasizes the effect of long-period waves on the reef flat.

References

1. Thuy PT, Trung LH, Tung TT (2021) Measurements of wave reduction due to artificial reef with varying width on an atoll Environ Sci Proc
2. Tuan TQ, Cuong DQ (2019) Wave transmission across steep submerged reefs. In: International conference on asian and pacific coasts (APAC), Springer, Singapore, pp 687–694
3. Van Gent MR (2001) Wave run up on dikes with shallow foreshores. J Waterway Port Coast Ocean Eng 127(5):254–262
4. Hofland B, Chen X, Altomare C, Oosterlo P (2017) Prediction formula for the spectral wave period $T_{m-1,0}$ on mildly sloping shallow foreshores. Coast Eng 123:21–28
5. Tuan TQ, Luan MT, Cuong LN (2022) Laboratory study of wave damping by porous breakwaters on mangrove mudflats in the Mekong River Delta. Ocean Eng 111846:258

Overview of Coastal Protection Structures in the Mekong River Delta



Le Vinh An, Nguyen Viet Thanh, Pham Van Hai, and Trinh Dinh Lai

Abstract The Mekong River Delta has faced many impacts of climate change, sea level rise, and extreme climate. Besides, the exploitation and use of water resources and sand and gravel lead to serious riverbank and coastal erosion. In recent years, many innovative technologies of coastal protection have been applied to protect coastal erosion. In this paper, based on the results of two field investigations from the coast of Tien Giang province to Ca Mau province, a review of coastal protection also points out some advantages and disadvantages. The results indicated that the applied coastal protection technologies need to be further improved to limit the process of coastal erosion in the Mekong River Delta.

Keywords The Mekong River Delta · Coastal erosion · Coastal protection · Detached breakwater · Groin

1 Introduction

Mekong River Delta (MRD) is the southernmost region of Vietnam, with a coastline of more than 720 km, a prominent position in regional and international trade and freight transport. However, the potential of the region has not been fully exploited due to the influence of natural factors and climate. The coastline in the Mekong Delta has been heavily eroded, affecting production activities and the lives of local people. The coastline of MRD is featured by a dynamic process of erosion and deposition. In some areas, wave attached induced shoreline erosion rate up to 30 m

L. V. An · N. V. Thanh (✉)

Faculty of Civil Engineering, University of Transport and Communications, Hanoi, Vietnam
e-mail: vietthanh@utc.edu.vn

N. V. Thanh · P. Van Hai

Viet Trung R&D Center, University of Transport and Communications, Hanoi, Vietnam

T. D. Lai

Faculty of Hydraulic Engineering, Hanoi University of Civil Engineering, Hanoi, Vietnam

per year, while in other areas land created through deposition can reach up to 64 m per year [1]. Therefore, coastal protection works were also born. Especially, in recent years, a series of new types of structures have been assessed and applied to protect the coastal erosion of the Mekong River Delta. Many kinds of coastal protection have been studied and applied in MRD, but these countermeasures have had limited success in protecting the coastal erosion in MRD. “Nature-based solutions” in a concept for delta management with specific focus on restoring coastal forest and marine ecosystems such as T-shape bamboo fences had been applied for protection of coastal erosion in Kien Giang province in 2009 [1]. However, this countermeasure also limited success. This paper reviews the coastal protection structures applied from Tien Giang to Ca Mau provinces of the Mekong River Delta.

2 Methodology

Two site investigations in the coastal of the Mekong River Delta were conducted from March 31 to April 3, 2022, and from May 9 to 14, 2022 (Fig. 1). The first investigation area included coastal of five provinces such as Ben Tre, Tra Vinh, Soc Trang, Bac Lieu provinces and second investigation in Ca Mau province. In this investigations, flycam was used to record the videos and took the photos and boat visit. The object of these field trips to the breakwater construction sites and mangrove forests to gain insights into the status of the construction progress and implementation conditions as well as the effect of the coastal protection structures. Pictures and video are created by camera and flycam to analyze the present states including the failure and collapse of constructions.



Fig. 1 Site investigation in Nha Mat, Bac Lieu provinces (left), and Ngoc Hien, Ca Mau (right)

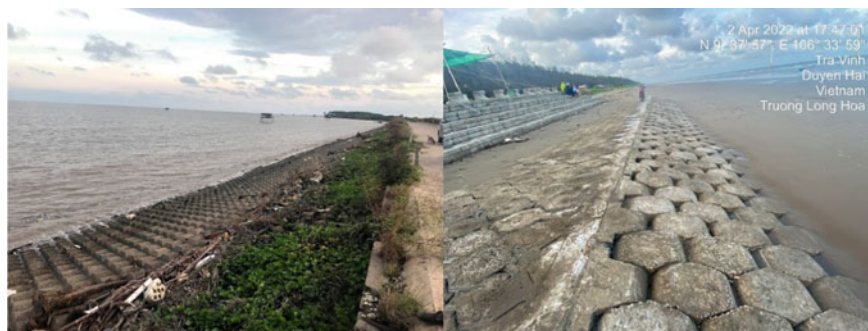


Fig. 2 Sea dike in Tan Thanh, Tien Giang (left), and Ba Dong, Tra Vinh provinces (right)

3 Results and Discussion

3.1 Sea Dike

Sea dike has been applied in many areas in MRD for coastal protection such as Go Cong and Tan Thanh districts, Tien Giang province, Ba Dong district, Tra Vinh province, Nha Mat district, Bac Lieu province and Ca Mau province (Fig. 2).

The sea dike reduces coastal erosion, stability, and easy construction under impact of small wave. However, sea dike is not friendly with environment, due to the hardening of revetment which prevents expansion of the hinterland. One more disadvantage of revetments is limited ability to trap sediment on the shoreline.

3.2 T-shape Fences' Groins

The first T-shape fences' groins were built in Binh Son commune, Hon Dat district, Kien Giang with length of 1400 m to restore mangroves in 2009. Based on the success of this project, the T-fences' groins continued applied in Vinh Tan and Lai Hoa communes, Vinh Chau town, Soc Trang province, with total length of 1400 m, Ca Mau, Bac Lieu, Soc Trang provinces in 2014. The T-fences' groins induced damping of currents and waves and deposition of sediments (Fig. 3).

The T-shape fences' groins are made of two rows of bamboo or wood or coconut piles and filled with twigs and leaf bundles (Fig. 4). The T-fence groins decrease the longshore currents and dampen the incoming wave energy. The fences parallel with the coastline have openings width of 20 m to secure the drainage of the fields. A system of drainage ditches will be created by the natural water flow, enhancing the drainage of the fields, and also supporting the acceleration of the consolidation process.



Fig. 3 T-shaped fence with bamboo poles in Bac Lieu province [1]

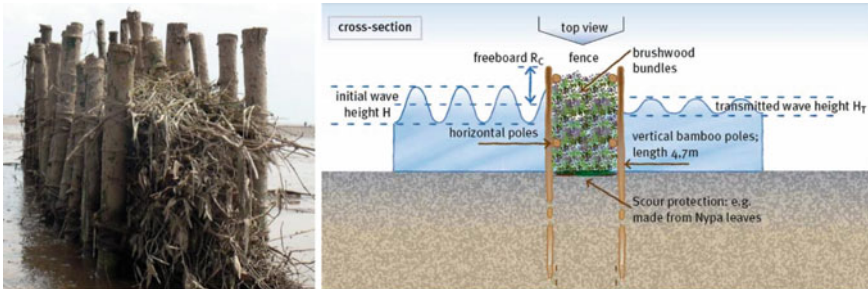


Fig. 4 Cross-section of bamboo T-shape fences' groin [1]

The design parameters of T-shape fences groins systems is as following:

- Crest level: + 1.80 m (National Datum-ND)
- Beam width of groin: 2.7 m
- Length of groin shaft: 130 ÷ 190 m
- Groin head length: 200.35 m
- Spacing between successive groins: 220 m
- Bamboo pile length: 4–4.7 m
- Bamboo pile diameter: 6–8 cm

The advantages of T-shape fence are as following:

- Bamboo materials, bunches of natural twigs are environmentally friendly, are local materials, so they are easy to find and cheap.
- The technique is not too complicated, mainly by hand, fast construction.
- Low construction cost about 3 million VND/m.

The disadvantages of T-shape fence are as following:

- The strength and durability of the material are not high under the influence of waves during the monsoon period, and all kinds of creatures in the seawater, especially shellfish, stick to the tree trunks.
- Project with relatively low life expectancy is prone to damage in high wave conditions, requiring regular monitoring, maintenance, and repair to promptly overcome potential problems.

- The application of bamboo fence is only suitable for small slope beach areas with low wave height. If the construction site is unfavorable (waves, large currents,), maintenance costs will increase significantly before the application becomes effective. Therefore, it can be combined with remote wave reduction works with more solid construction for large wave locations.

3.3 Geotube Structures

Geotube detached breakwaters in Nha Mat, Bac Lieu

The Geotube detached breakwaters were built on the coast of the Nha Mat, Bac Lieu province, with a total length of 1056 m in 2012. This is the first pilot large-scale Geotube detached breakwaters in Mekong River Delta. The design parameters of the Geotubes' detached breakwaters are as follows:

- Length of project: 1056 m
- Crest level: + 1.40 m (± 0.10 m)
- Number of bags: 22 bags
- Length of each bag: 48 m
- Maximum bag height after pumping: ≤ 1.80 m
- Width of bag after pumping: ≥ 4.60 m

After the construction, the crest level satisfied the design requirement of + 1.3 to + 1.4 m, and the average width ranged from 4.7 to 4.9 m (Fig. 5).



Fig. 5 Layout of the Geotube breakwater line at Nha Mat, Bac Lieu

A survey was conducted by South Institute of Water Resources Research on January 12, 2014 (after nearly two years of construction), and the crest level is as follows [2]:

- From + 0.5 to + 0.7 m, accounts for about 65% (accounting for 11/17 sections).
- From + 0.7 to + 1.0 m, account for about 35% (accounting for 06/17 sections).

The project is no longer usable and has been replaced by semicircular breakwater in 2018 (Fig. 6).

Geotube groins in Go Cong, Tien Giang

Three T-shape Geotube groins were built from Rach Bun sluice to Soai Rap estuary in coastal of Go Cong district, Tien Giang province, in December 2016. The T1 groin has length of 140 m and head length of 440 m, the T2 groin has length of 100 m and head length of 440 m, and the T3 groin has length of 140 m and head length of 270 m (Fig. 7). The design crest level of Geotube is + 1.7 m (ND). The gaps between T1 and T2 groin heads are 120 m and T3 and T2 are 40 m. Three groins created accretion area for planting trees to cause forests, to regenerate protective forests that have been eroded before.



Fig.6 Wave-reducing dike by Geotube in Nha Mat, Bac Lieu (2014)

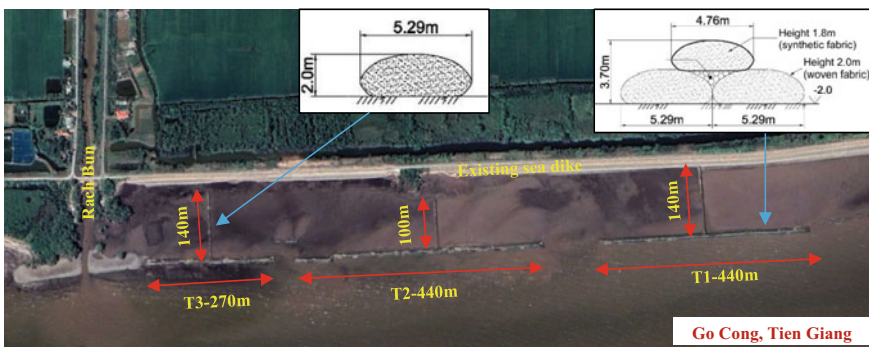


Fig. 7 Construction location of Geotube breakwater in Go Cong, Tien Giang

In 2018, some bags were torn, sand leaked out, and the management unit had to regularly maintain it. In June 2019, the Geotube bags were severely damaged. The Department of Agriculture and Rural Development of Tien Giang province proposed to the Ministry of Agriculture and Rural Development to suspend the pilot implementation of this model in other places (Fig. 8).

Geotube detached breakwater in Tra Vinh province

The first geotube detached breakwaters system were built in Hiep Thanh commune, Dan Thanh district, Tra Vinh province, in 2016 with a length of nearly 2000m, including 13 segments, each segment length ranging from 90 to 140m. The gap between the two detached breakwaters is 20m. Behind the gap is arranged a nearshore geotube bag far from the gap at a distance of 20m to reduce wave height. The crest level after construction is + 1.8 m, and long-term crest level is + 1.1 m (Fig. 9).

To improve the wave attenuation, a “FEN” structure was constructed to reduce the secondary wave with length of 1754 m, the height of the fence above the natural



Fig. 8 Geotube breakwater system in Go Cong, Tien Giang



Fig. 9 Geotube breakwater system in Hiep Thanh, Tra Vinh

ground 2.1 m, the FEN thickness of 0.75 m (Fig. 10). The “PHEN” structure that causes accretion is composed of slats and branches arranged in rows to stimulate sedimentation. A typical cross-section of the coastal protection is shown in Fig. 11.

After construction one year, a stretch of sand bar appeared with crest level ranges from + 2.5 to + 3.5 m, with an average width of 30 m. Compared with the natural level in 2016, the newly appeared sand dunes are 0.5–1.0 m higher. In some locations, the dune width is extended to 50 m. Currently, the construction is unstable, deflected by waves from the original design position, and the Geotube bags have begun to damage, affecting the sustainability of the construction.

Geotube detached breakwaters in Con Nhan, Duyen Hai, Tra Vinh

Due to the southern jetty of Duyen Hai port, the coast of Hiep Thanh commune occurred strong erosion. To protect the coastal erosion, the offshore Geotube detached breakwaters were constructed with total length of 2000 m in 2018. The Geotube was arranged with length of 100 m length, gap distance of 25 m, and crest level of +

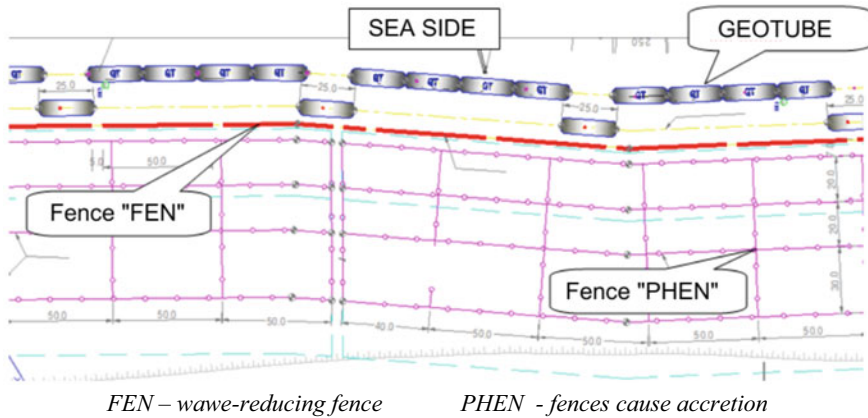


Fig. 10 Layout of the Geotube breakwater in Hiep Thanh, Tra Vinh (excerpt)

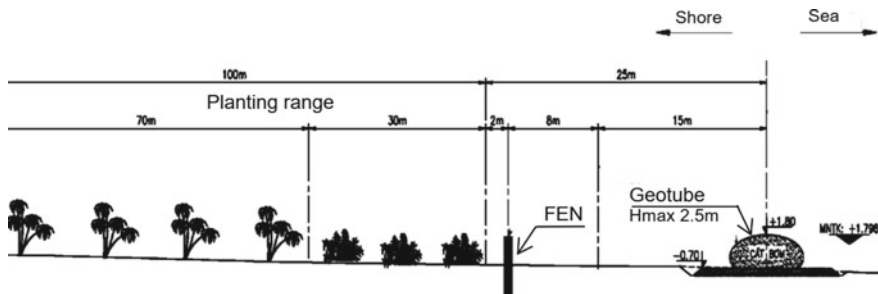


Fig. 11 Cross-section of Geotube breakwater system in Hiep Thanh, Tra Vinh



Fig. 12 Geotube breakwater system in Con Nhan, Tra Vinh

1.4 m. Due to the settlement, the nearshore route with length of 50 m is located behind the gap of the offshore route with a distance of 30 m (Fig. 12).

In September 2019, nearly one year after construction, the nearshore sand bars were formed but not really clear. However, the offshore Geotube detached breakwaters are unstable. The Geotube was displaced and settlement. The nearshore Geotubes' breakwaters were upgraded between the gaps of offshore detached breakwaters to reduce the diffraction wave. However, the breakwater line has almost completely been damaged in the site investigation in April 2022.

Geotube in Ben Tre

A combination of groins and detached breakwaters to reduce waves causing sedimentation protects the coast in Con Bung area of Thanh Phong and Thanh Hai communes, Thanh Phu district, Ben Tre province, with a total length of 1960 m. There are two segments, and the first segment is located on the coast of the Con Bung area, Thanh Hai commune, with a length of 860m, a geotube bag in the form of a groin, the construction line is arranged 15m from the shoreline. Second segment is detached breakwaters arranged along the coast of Thanh Phong commune with length of 1100 m. The project was built in 2018, completed and put into use in 2020, with the task of protecting population, infrastructure, and defense mangrove forests (Fig. 13).

The Geotube structures quickly showed its technical effectiveness. Behind the embankment, there is a large amount of sand accretion, and alluvial deposits are formed with a stable trend, creating conditions for trees to grow. Along with that, the cost of building embankment is quite cheap, about 13 billion VND for one km of embankment. The cost is only about one five compared to the hard embankment solution. However, it can be seen that this solution is only short-term due to the poor durability of Geotube, usually only maintained for 1–3 years according to the conditions in the Mekong River Delta. The impact of waves, currents, and high tides



Fig. 13 Geotube breakwater in Con Bung, Ben Tre

causes the Geotube to be displaced, torn, and deformed. In order to use this method effectively, it is necessary to study reinforcement measures to increase the lifetime of the structure.

3.4 Two Rows Spun Pile–Rock Structure

From the lessons learned with the forms of bamboo fence dikes, the designer replaced the core with stone or the shell with a concrete frame made of two rows of prestressed concrete piles with circular hollow sections (spun pile) and rock filled. Ca Mau province has piloted to apply the new type of breakwater structure in 2010. The detached breakwater with length of 300 m is located far from the sea dike about 150 m. The spun pile length of 12 m and the spacing between the two piles is 15cm. Rock filled into the two rows of spun piles. The crest level ranges from + 1.5 to 1.6 m (Fig. 14).

After one year, the backshore behind the detached breakwater was accreted very quickly, and the mangrove had regenerated. During period from 2011 to 2012, Ca Mau province invested this type of detached breakwater to protect the coastal erosion in the East and West coasts such as: coast of Khanh Tien commune in U Minh district, coast of Khanh Binh Tay commune in Tran Van Thoi district, coast of Tan Hai commune in Phu Tan district, coast of Tan Thuan commune, Dam Doi district, and coast Dat Mui commune, Ngoc Hien district with a total length of more than 8260 m. Up to now, Ca Mau has built more than 50 km of breakwater with this type of structure (Fig. 15).

In Bac Lieu, the spun piles–rock structures are also applied to protect the coastal erosion in Ganh Hao (Fig. 16) and Nha Mat (Fig. 17) of Bac Lieu province.

The spun piles–rock was applied in Con Nhan area, Dong Hai commune, Duyen Hai town, Tra Vinh province, with the goal of protecting the property and lives of more

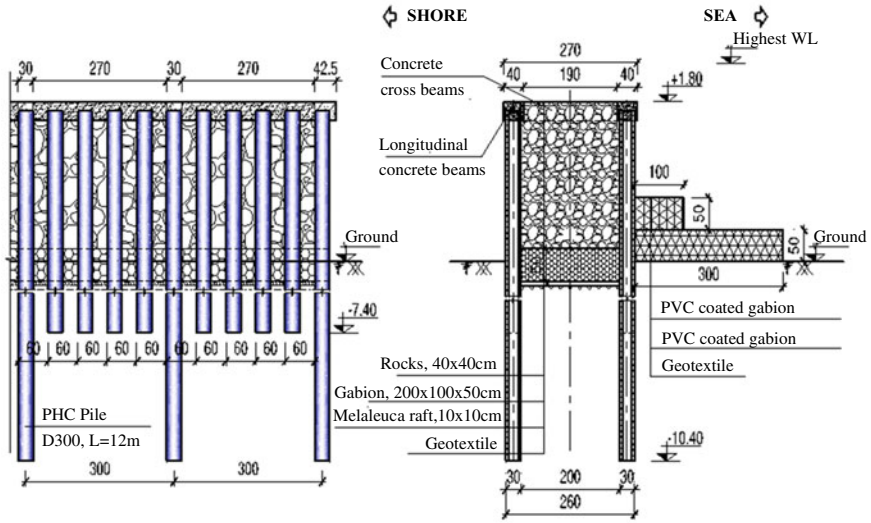


Fig. 14 Typical cross-section of spun piles–rock detached breakwater in Ca Mau



Fig. 15 Spun piles–rock detached breakwaters in the west and east coasts, Ca Mau



Fig. 16 Spun piles–rock detached breakwater in Ganh Hao, Bac Lieu



Fig. 17 Spun piles–rock detached breakwater in Nha Mat, Bac Lieu

than 100 households and more than 200 hectares of crops and forests. Households inside limit the situation of landslides and create the alluvial ground, restoring the area of coastal protection forests. The project was completed in April 2020 with a length of 1100 m and crest level of + 1.5 m (Fig. 18).

Compared with all the solutions currently used to protect against coastal erosion in the Mekong River Delta, Ca Mau’s projects are currently the best solution in terms of technical efficiency (reducing waves, causing sedimentation, creating yards). Construction structure has been evaluated by large waves, high tide is still stable, there are no displacement, breakage, slippage, etc. However, this structural solution has a large construction cost, ranging from 28 to 33 million VND for one meter long. This is a big obstacle to the economic conditions of the coastal provinces of the Mekong River Delta. To reduce construction costs, it is necessary to study solutions to optimize the dike cross-section, including the use of pile types.



Fig. 18 Spun piles–rock detached breakwater in Con Nhan, Tra Vinh

3.5 Modified Semicircular Breakwater

A modified semicircular breakwater is derived from the Japanese semicircular cross-section wave damper, which was used in Miyazaki port in 1993. The first semicircular breakwater was applied in China in Tianjin Port in 1997 with length of 547 m. In Vietnam, the semicircular wave-reducing dike has been studied by Nguyen [3], Nguyen [4, 5] (Fig. 19).

In 2016, the VAWR conducted the pilot project in the West coast of Ca Mau province with a length of 180 m from Vam Da Bac to Vam Kinh Moi in Khanh Binh Tay commune, Tran Van Thoi district. The pilot project was completed in 2017. One segment of semicircular breakwater is about 3 m length, outer diameter is 3.5 m, and the height is 2.6 m. The modified semicircular breakwater has 30 circular holes in seaside and 9 holes in shoreside to reduce waves' height. The bottom plate has a wave-shaped with thickness which ranges from 15 to 30 cm.

At Nha Mat area, Bac Lieu province, the new modified semicircular structure is named DTR304F, with a height of 304 cm, a width of 450 cm, with two tray legs attached to the ground 50 cm, so it can protect the yard at a depth of -1.4 m, higher stability.

DTR304F is an M50-reinforced concrete structure with wave-absorbing holes on the surface (Fig. 20). The offshore side is arranged with 20 holes, the nearshore side is arranged with eight holes, and diameter is 30 cm. The top of the structure is arranged with two round holes Φ 40 cm in diameter to drop stones, and the bottom two sides of the structure are designed with 50 cm stones to prevent slipping. The width of the semicircular breakwater is 4.5 m, the length of a segment is 3 m, and the weight of a segment is about 16 ton (equivalent to 6.5 m^3 of concrete).

The ability to reduce waves from 100 to 150 m from shore can be compared with two rows of spun pile–rock structures. This structure is simple and quick to construct because it is a prefabricated reinforced concrete structure, and the cost is about 22 million VND for one meter, cheaper than the two rows spun piles–rock. However, this solution is only effective for places with low depths, where the water



Fig. 19 Pilot modified semicircular breakwater in Khanh Binh Tay, Ca Mau



Fig. 20 Modified semicircular breakwater-type DTR304F in Nha Mat, Bac Lieu

level is high, the cost will increase greatly. Due to heavy, the settlement occurred after construction.

3.6 BUSADCO Blocks

In 2018, a new type of non-metallic reinforced hollow structure (herein called BUSADCO Block 1) was applied for coastal protection on the west coast of Ca Mau from Vam Da Bac to Vam Kenh Moi, Khanh Binh Tay commune, Tran Van Thoi district with a length of 1.2km and far from the shoreline about 300m (Fig. 21).

The basic parameters of BUSADCO Block 1 are applied in the West Sea with a height of 4.0 m, bottom width of 4.0 m, crest width of 0.52 m, and length of a segment of 1.5 m.

Other BUSADCO Block shown in Fig. 22 with wave-absorbing holes arranged on the front, back, and middle walls of the block (the hole area rate of 32% of total surface area). The size and number of holes to reduce waves are as follows: - Front has 06 elliptical holes arranged in 3 rows of size 50x70cm. - Back side has 02 round



Fig. 21 Installation of BUSADCO Block 1

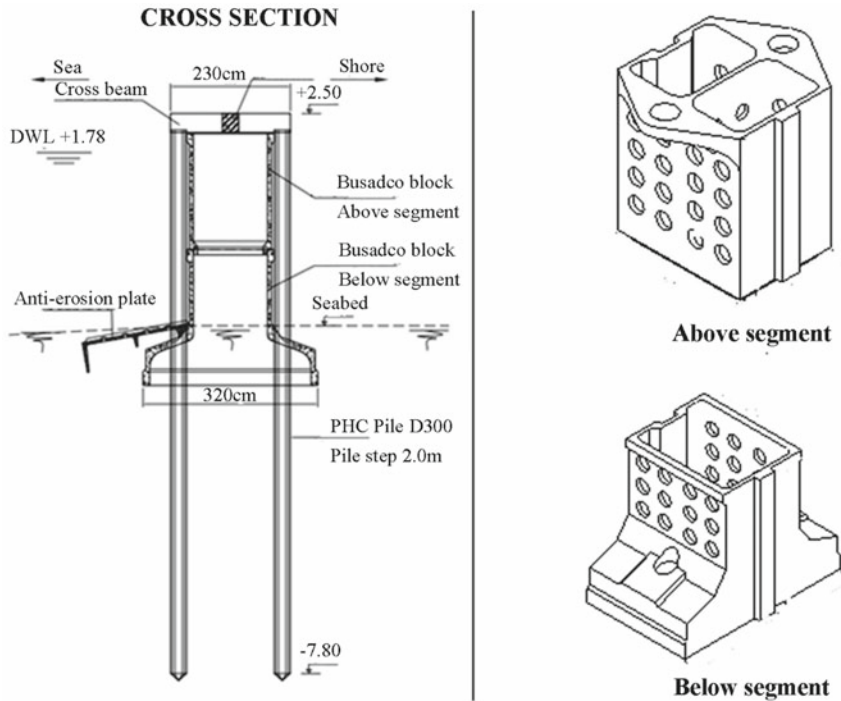


Fig. 22 BUSADCO block applied in Rach Goc, East Sea, Ca Mau province

holes D40, 04 elliptical holes size 50x70cm, 02 round holes D50 arranged in 4 rows. - Middle wall has 27 holes D30 arranged in 8 rows, 14 holes D11 arranged alternately with holes D30.

To fix the block, two rows of spun piles with a diameter of 30 cm, length of 9.0 m, and pile distance of 2.0 m. The pile system is linked together by longitudinal and cross-beams. Longitudinal and cross-beams made of non-metal reinforced concrete and cross-section of 30 × 35 cm. The crest level of the top beam is + 2.50 m. Anti-erosion construction width of 2.0m uses a fiber-reinforced concrete anti-erosion plate, size 2.0 × 0.6 m, thickness of 5.0 cm (Fig. 23).

This detached breakwater was constructed from August 2018 and expected to be completed in January 2019, but the construction has to extension to December 2019. In August 2019, the storm No. 3 knocked down 800 m has been basically completed. After the detached breakwater was damaged, the waves flooded inside, causing landslides of mangrove forest (Fig. 24).

Through recent practical challenges, it was found that BUSADCO’s block is unstable, the components are broken off by waves, wave reduction effect is poor, and big waves still pass through the crest of the breakwater to the shore, causing landslides; it is necessary to study and adjust more for this type of structure.

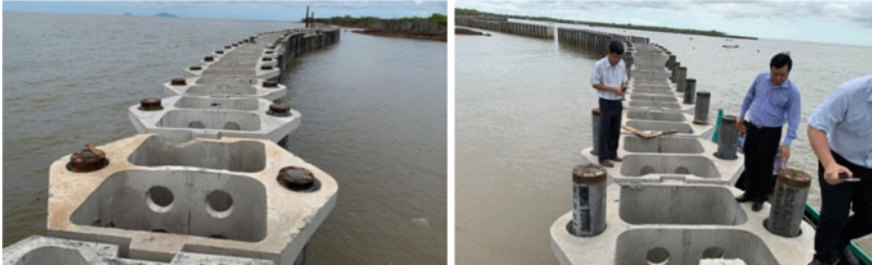


Fig.23 Spun pile system combined with BUSADCO blocks' detached breakwater in East Sea, Ca Mau province



Fig. 24 Reducing wave dike by BUSADCO components in Rach Goc, East Sea of Ca Mau, was destroyed by the storm No. 3 August 2019

For the BUSADCO block in the form of a pyramid, the construction cost is about 18 million VND for one meter, cheaper than the semicircular, but the stability and efficiency of wave reduction are much worse.

With type of BUSADCO block combined with spun piles applied in Rach Goc, Ca Mau, the plan is quite similar to centrifugal concrete pile structure, but the stability is much worse due to the components which are hollow and high; along with that, there is no mechanism to reduce waves, causing obvious sedimentation when many holes are arranged both on the sea side and on the shore. Economically, the construction cost with this type of structure is about 32 million/1 m long, equivalent to the centrifugal concrete pile structure, but the efficiency is obviously much lower.

3.7 Hollow Triangle Breakwater

The hollow triangle breakwater with many holes on both sides is shown in Fig. 25, with the crest height that allows the overflow wave, but the width is small; it can be predicted that the wave reduction effect will not be high, compared to the type of dike dense and protruding. This kind of breakwater applied in Con Cong, Tan Thanh, Tien Giang province.

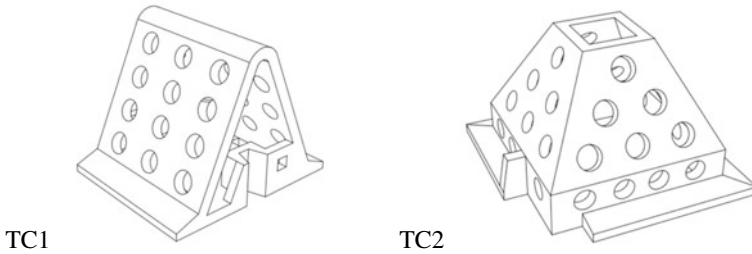


Fig. 25 Block TC1, TC2 of Tu [2]

In June 2020, the detached breakwater with length of 1500 m was constructed to protect the southern area of Tan Thanh tourist area, Tan Thanh commune, Go Cong Dong district, Tien Giang province. Hollow structure TC1 is made by prefabricated reinforced concrete A-shaped M600 member. Each is 250 cm long with a weight of about 9 tons. The structure is placed on the melaleuca rafters and reinforced with rock to prevent foot erosion in front and behind the construction. The gap distance of 10 m, the length of each segment is 200 m, and the distance from the construction to the shore is 100 m (Figs. 26 and 27).

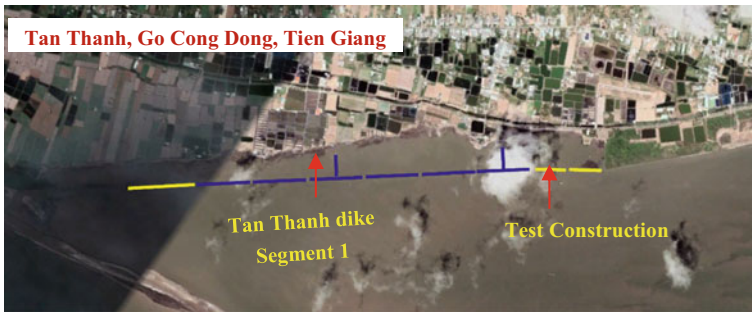


Fig. 26 Layout of detached breakwaters [5]

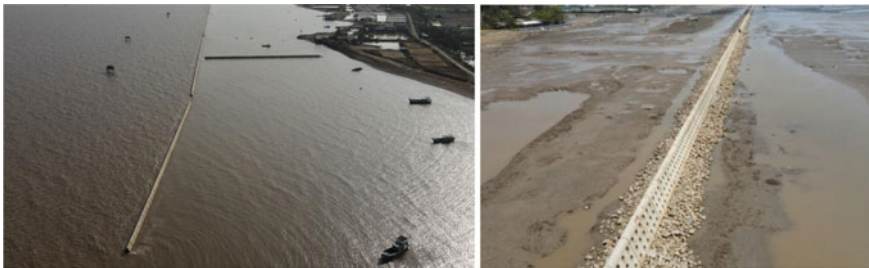


Fig. 27 Detached breakwaters in Tan Thanh, Tien Giang [5]



Fig. 28 Detached breakwaters in Con Cong, Tan Phu Dong, Tien Giang [5]

Con Cong coastal protection project in Phu Tan commune, Tan Phu Dong district, Tien Giang province, was applied TC1 block for detached breakwaters with total length of 1600 m. The project completed and took into use in December 2019 (Fig. 28).

The height of a detached breakwaters is 2.5 m, weight TC1 = 9.05 tons, weight TC2 = 10 tons. Components made of reinforced concrete 40 Mpa. Prefabricated reinforced concrete structures are assembled into lines.

- The number of wave-reducing dikes are 10, length of each section is $L = 135$ m.
- Distance from construction to shore $X = 100$ m, clearance $G = 20$ m.

The wave attenuation efficiency of TC1 and TC2 according to measurement of Tu [5] in December 2020 reached to 60–70%. Behind the detached breakwater appeared alluvial grounds, and young trees grew. Economically, the construction cost is about 18–25 million VND/m depending on the construction location. This price corresponds to hollow cylindrical structure, but it takes more time to verify the effect. The disadvantage of this structure is the same as the hollow cylindrical structure, that is, it is only effective for places with low depth, in places where the water level is high, the structure is larger, leading to higher construction costs (Fig. 29).



Fig. 29 Detached breakwaters in Con Cong area

4 Conclusion

Many types of coastal protection have been introduced, and the advantage and disadvantages also point out as the basis for designers, constructors, and managers when considering future project development.

Most of the coastal protection solutions are still not satisfied to reduce the coastal erosion with the more complex and multi-faceted problem in the Mekong River Delta.

Acknowledgements This work was supported by the research program of the Ministry of Education and Training, Vietnam, in research project, grant number CT 2022.01.GHA.03.

References

1. Albers T, San DC, Schmitt K (2013) Shoreline management guidelines coastal protection in the lower mekong delta, GIZ., Germany. ISBN978-604-59-0630-9.
2. Le Xuan T (2022) Research on reasonable solutions and appropriate technologies to prevent erosion, stabilize the coast and the Mekong estuaries, from Tien Giang to Soc Trang. Vietnam Institute of Water Resources Science (In Vietnamese)
3. Nguyen Thanh T (2007) Research on solutions to correct flat estuaries with sand arrows: application for Nhat Le estuary - Quang Binh province. Master Thesis, National University of Civil Engineering, Hanoi, Vietnam (In Vietnamese)
4. Nguyen Viet T (2014) Semi - circle breakwater - an economic solution for coastal estuary training structures. *Transport J* (11/2014):31–34 (In Vietnamese)
5. Nguyen Viet T (2017) Experiment study on the wave and semi-circular breakwater interaction and propose solution for coastal and harbour protection. Vietnam Maritime Administration Hanoi, Vietnam, p 135 (In Vietnamese)

Geotechnical Engineering

Thermo-Hydro-Mechanical Behavior of the Rock Mass Surrounding Wellbore in Deep Saturated Geological Layer



Nam Hung Tran, Thi Thu Nga Nguyen, Duc Tiep Pham, and Duc Tho Pham

Abstract In case of a wellbore drilled in poro-thermo-elastic rock, the process of wellbore drilling will result in thermic, hydraulic and mechanical phenomena which occur simultaneously and interact with each other. This study presents the analysis of the stress state around the wellbore located in the saturated rock at depth based on a fully coupling thermo-hydro-mechanical behavior model of the rock mass by the finite element method. Two scenarios related to thermal condition at well wall are taken into account, i.e., the drilling fluid temperature is inferior or superior to the temperature of the rock mass corresponding to the cases of “cooling” and “heating” the wellbore. The obtained results indicate that the thermic, hydraulic and mechanical phenomena in interaction with each other occurring in the material produce a large change in the stress state around the wellbore through the cases of cooling and heating. Effect of some thermic and hydraulic parameters of the rock mass on the stress state around the wellbore is also highlighted in this work.

Keywords Wellbore · Deep saturated geological layer · Thermo-hydro-mechanical behavior · Finite element method

1 Introduction

Wellbores are used a lot in fields such as drilling exploration and exploitation of oil and gas, geothermal energy exploitation or underground water extraction, etc. Incidents of wellbore instability in the industries mentioned above cost billions of dollars in remediation worldwide each year [1]. Consequently, the stability assessment of the wellbore system has become an important issue throughout the life cycle of

N. H. Tran (✉) · T. T. N. Nguyen · D. T. Pham
Le Quy Don Technical University/LQDTU, Hanoi, Vietnam
e-mail: tranhung@lqdtu.edu.vn

D. T. Pham
Hanoi University of Mining and Geology/HUMG, Hanoi, Vietnam

wellbore, from drilling and completion of the wellbore to exploitation, maintenance, rehabilitation and enhancement.

At great depth, geological strata are dominated by geothermal phenomena. The temperature of deep geo-materials can be up to several hundred degrees [2]. Besides, the system of interconnected voids and cracks in the rock is often in a state of partially or fully water saturation. During wellbore drilling, mechanically, the drilling process will cause a redistribution of stress–strain field and thereby pore pressure field surrounding the wellbore. In this process, drilling fluid is also injected into the well to increase the stability of the well wall. If the drilling fluid temperature is different from the temperature of the formation, the phenomenon of heat transfer will occur that causes the change of the stresses and interstitial pressure. In turn, the redistribution of pore pressure also affects the stresses and heat transfer in the medium. Thus, the stress state in the rock mass is, at this time, the result of mechanical, thermal and hydraulic phenomena induced simultaneously. Evaluating the influence of temperature changes as well as the influence of drilling fluid pressure on the stress state around the wellbore is necessary to be able to assess the stability of the wellbore in poro-thermo-elastic rock, both in the wellbore design and construction.

In the literature, many studies on the stress field around the wellbore and the stability of the well wall were addressed. Some works focus on analysis of the stress state around the wellbore with consideration only of mechanical phenomena [3, 4]. Based on a hydro-mechanical behavior model of saturated porous rock materials some contributions evaluate stress distribution surrounding the wellbore [5–7]. When the temperature of the rock mass is taken into account, the works of [8–10] relied on the thermo-hydro-mechanical behavior models of anisotropic poro-elastic rocks.

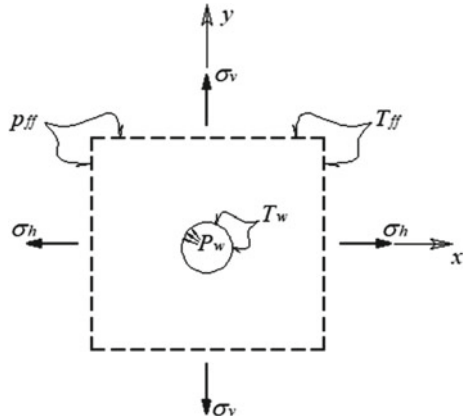
In this work, based on the finite element method, we will present a study on the stress state surrounding a wellbore placed in a homogenous, isotropic, poro-thermo-elastic rock where two cases of that the drilling fluid temperature are inferior and superior to the temperature of the rock mass corresponding to the “cooling” and “heating” to be considered. Moreover, the effect of different parameters (thermal expansion coefficient, permeability) of the rock on the stress state around the well wall is also highlighted.

2 Description of the Problem and Constitutive Equations

2.1 Description of the Problem

Let us consider a horizontal wellbore of radius r_0 drilled in a saturated, homogenous, isotropic rock in a deep geological layer (Fig. 1). The axis of the wellbore is parallel to the z -axis of the Cartesian coordinate system, and its cross-section lies in the x - y plane. As the wellbore is drilled at great depth and/or its diameter is small, one can consider that the wellbore is placed in an infinite medium with a uniform principal

Fig. 1 Horizontal wellbore in saturated hot rock



stress field throughout the medium. The principal stress components include vertical normal stress, horizontal minimum normal stress and maximum horizontal normal stress, σ_v^{ff} , σ_h^{ff} , σ_H^{ff} , respectively, as shown in Fig. 1.

One assumes that the initial temperature and initial pore pressure of the medium are T_{ff} and p_{ff} , respectively; temperature at the well wall where the rock mass is in contact with the drilling fluid is T_w , while drilling fluid pressure is P_w . Since the length of the wellbore is much larger than its diameter, the problem will be studied in the conditions of plane strain in the x - y plane.

2.2 Constitutive Equations

Based on the thermo-hydro-mechanical behavior model, mathematically, all points in the rock mass around the wellbore must satisfy the following equations for the plane strain problem:

- Heat transfer equation and liquid diffusion equation:

The heat transfer within the rock mass obeys Fourier’s law, while the seepage flow occurring in the rock obeys Darcy’s law. For homogeneous and isotropic materials, one has the heat transfer differential equation and pore water pressure diffusion differential equation, respectively, as follows [10, 11]:

$$\frac{\partial}{\partial x} \left(\lambda^T \frac{\partial T}{\partial x} \right) + \frac{\partial}{\partial y} \left(\lambda^T \frac{\partial T}{\partial y} \right) = \rho C_p \frac{\partial T}{\partial \tau}; \quad \frac{\partial}{\partial x} \left(\lambda_w^H \frac{\partial p}{\partial x} \right) + \frac{\partial}{\partial y} \left(\lambda_w^H \frac{\partial p}{\partial y} \right) = \frac{\partial \chi}{\partial \tau} \quad (1)$$

where λ^T and λ_w^T are the thermic and hydraulic conductivities, respectively; ρ is the density of the saturated porous material (rock); C_p is the specific heat of the rock; χ is the change of fluid volume per unit volume of the porous material. The

thermic conductivity of the rock is determined by:

$$\lambda^T = (1 - \phi)\lambda_s^T + \phi\lambda_w^T \quad (2)$$

in which λ_s^T , λ_w^T being respectively diffusion coefficients of solid and liquid phases that depend on the temperature and ϕ is porosity of the rock. The hydraulic conductivity of the rock is determined as follows:

$$\lambda_w^H = K^{\text{int}}/\mu_w \quad (3)$$

in which K^{int} being intrinsic permeability, μ_w being dynamic viscosity of water.

- The thermo-poro-elastic behavior equation [10]:

$$\begin{pmatrix} \varepsilon_x \\ \varepsilon_y \\ \varepsilon_{xy} \end{pmatrix} = \begin{pmatrix} s_{11} & s_{12} & 0 \\ s_{21} & s_{22} & 0 \\ 0 & 0 & s_{33} \end{pmatrix} \left[\begin{pmatrix} \sigma_x \\ \sigma_y \\ \tau_{xy} \end{pmatrix} + \begin{pmatrix} b \\ b \\ 0 \end{pmatrix} p \right] + \begin{pmatrix} \alpha_s \\ \alpha_s \\ 0 \end{pmatrix} T \quad (4)$$

In Eq. (4), α_s is solid thermal expansion coefficient of the material; b is Biot coefficient; T represents the amount of temperature change inside the rock; s_{ij} ($i, j = 1 \div 3$) is compliance coefficients of the material; ε_x , ε_y , ε_{xy} are strain components, and σ_x , σ_y , σ_{xy} are stress components.

- The relationship between the pore pressure and temperature [10]:

$$p = M(\chi - b\varepsilon_v + \beta T); \quad \beta = 3b\alpha_s + (\alpha_f - 3\alpha_s)\phi \quad (6)$$

where M is Biot's modulus; α_f is fluid thermal expansion coefficient.

3 Numerical Example

A wellbore drilled at a depth of 4000 m below the ground surface with a radius equal to $r_0 = 0.1$ m is taken as an example. The properties of the shale [8, 9] used and the values of the calculated parameters as well as the temperature of the drilling fluid are given in Table 1.

Because of the symmetry of the wellbore through two vertical and horizontal axes passing through the center of the wellbore, only $1/4$ wellbore is chosen as the geometry model in numerical simulation. The geometry model and boundary conditions of the problem are imposed as illustrated in Fig. 2a, where Φ_T and Φ_H are thermal flux and hydraulic flux, respectively. The large of the model from the center of the wellbore is 5 m (equal to 50 times the wellbore radius). Figure 2b shows the well wall details with the boundary conditions.

Table 1 Properties of the rock

Parameter	Unit	Value
Young's modulus, E	GPa	24.14
Poisson ratio, ν	–	0.3
Minimum horizontal initial normal stress, σ_h	MPa	– 25
Maximum horizontal initial normal stress, σ_H	MPa	– 34
Vertical initial normal stress, σ_v	MPa	– 30
Initial reservoir temperature, T_{ff}	°C	100
Initial reservoir pore pressure, p_{ff}	MPa	9.8
Solid thermal expansion coefficient, α_s	1/K	18×10^{-6}
Fluid thermal expansion coefficient, α_f	1/K	3×10^{-4}
Solid thermal conductivity, λ_s^T	$W.m^{-1}.K^{-1}$	1.3
Fluid thermal conductivity, λ_w^T	$W.m^{-1}.K^{-1}$	0.586
Solid specific heat, C_s	$J.kg^{-1}.K^{-1}$	768
Fluid specific heat, C_w	$J.kg^{-1}.K^{-1}$	4181
Well wall temperature, T_w	°C	50 (150)
Porosity, ϕ	–	0.10
Hydraulic conductivity, λ_w^H	mD	7.66×10^{-8}
Fluid viscosity, μ	Pa.s	3×10^{-4}
Fluid bulk modulus, K_f	GPa	2.30
Drilling fluid pressure, P_w	MPa	12
Biot coefficient	–	0.76

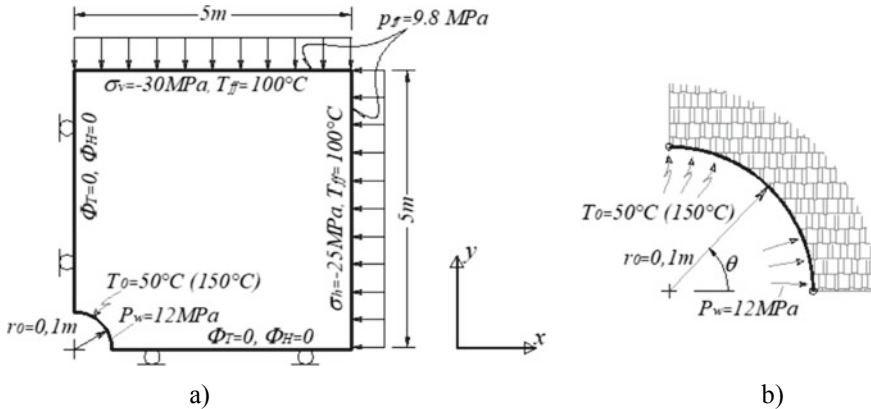


Fig. 2 Geometry model and boundary conditions of problem (a), well wall details (b)

Numerical simulations are performed by the open-source finite element software Code_Aster developed by Electricité de France (EDF). Within the software, a fully thermo-hydro-mechanical behavior model has been developed and validated, and the model has been used for many complicated problems, for example, in calculation of storage of nuclear waste at depth. Readers can see presentation of the development of thermo-hydro-mechanical model within the software in [12]. For numerical simulations, plane strain finite elements of quadratic quadrilaterals of eight nodal points are chosen where a quarter of the well wall is discrete into 50 elements.

In order to evaluate the effect of temperature change on the stress field around the wellbore, two numerical simulation scenarios were conducted. The first case is that the drilling fluid temperature (50 °C) is inferior to the initial medium temperature (100 °C) corresponding to the cooling. The second one considers that the drilling fluid temperature (150 °C) is superior to the initial medium temperature corresponding to the heating.

4 Results and Discussion

4.1 *Evaluation of Effect of the Cooling and Heating the Wellbore on the Stress Distribution Around the Well Wall*

Figure 3 shows the change in temperature and pore pressure of the rock mass surrounding the wellbore over time for the two scenarios. It is straightforward to observe in the first case that, because the temperature of the drilling fluid is smaller than the initial temperature of the rock mass, the temperature around the well decreases gradually. In the latter case, when the drilling fluid temperature is greater than the initial medium temperature, the temperature of the rock mass around the well increases gradually. For the pore pressure, it decreases strongly at early time in the vicinity of the well wall and increases gradually by the time in the first scenario, whereas this tends to be the opposite for the second scenario. It can be noted that a region of excess pore pressure occurs around the well wall due to the increase of temperature and the very low permeability of the formation, i.e., the pore pressure does not dissipate in time under the influence of high temperature. This could result in change of stresses between the two simulation scenarios.

Figure 4 shows the radial, tangential and axial stresses on the vertical edge passing through the center of the wellbore with time.

It can be seen from Fig. 4 that the radial compressive stress does not change much, while the tangential and axial stresses vary greatly through the two cases. For the cooling case, a zone of tangential and axial tensile stress occurs in the vicinity of the well wall (≈ 8 MPa). This could cause well wall instability, i.e., an initiation of cracks occurs herein, due to the small tensile resistance of rock material. Meanwhile, for the case of heating, the tangential and axial compressive stresses increase to a

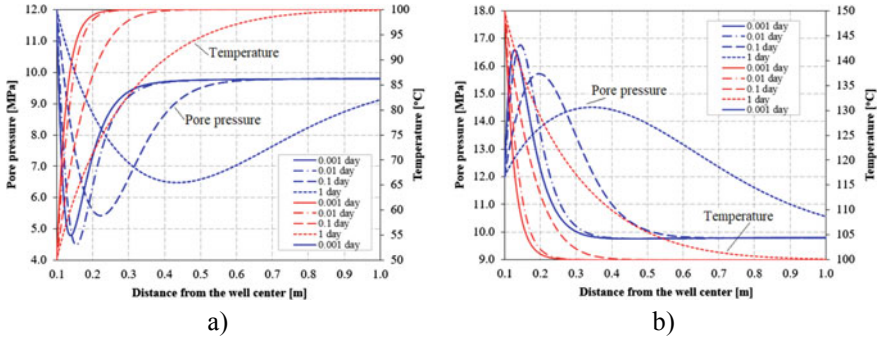


Fig. 3 Temperature and pores pressure evolutions over time for two cases: cooling case (a) and heating case (b)

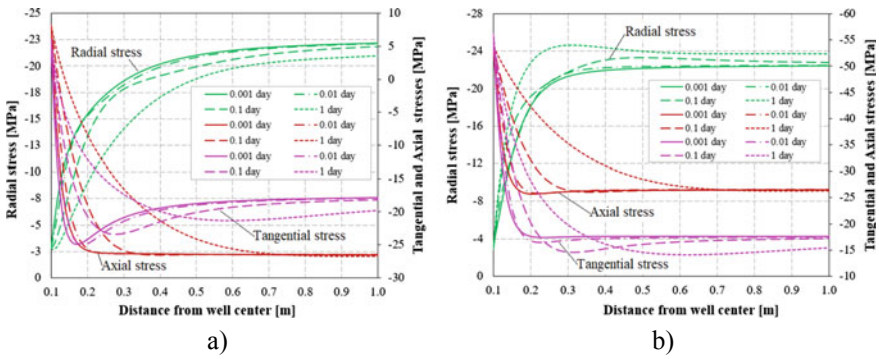


Fig. 4 Radial, tangential and axial stresses corresponding to cooling (a) and heating (b)

high level ($\approx 54 \div 57$ MPa) in the same area around the well wall. If the rock has low compressive strength, it could cause well wall collapse.

4.2 Evaluation of the Effect of Hydraulic and Thermic Parameters on the Stress Field Around the Wellbore

For the purpose of investigation of the effect of hydraulic and thermic parameters on the stress state around the wellbore, one changes the parameters including the permeability and thermal expansion coefficient of the rock mass. Once changing a parameter, the others are kept the unchanged. For each scenario, the permeability is increased by 1000 times, while the thermal expansion coefficient is increased by 20% from the values given in Table 1.

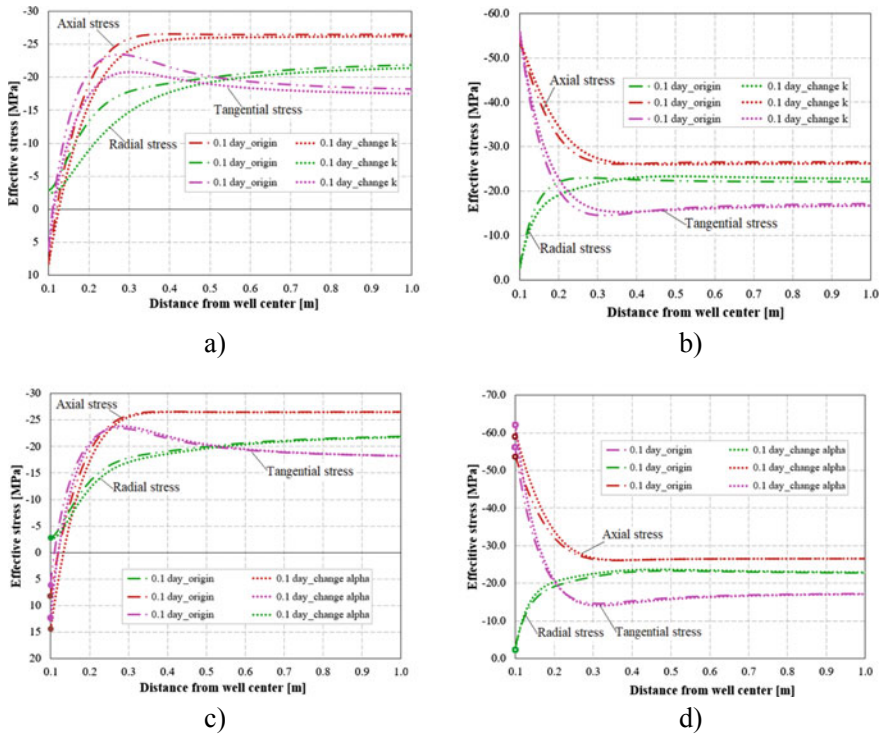


Fig. 5 Comparison of radial, tangential and axial stresses for the cases of changes in permeability: **a** and **b**; in coefficient of thermal expansion: **c** and **d** with the original case for the two scenarios

Figure 5 presents results of the parametric study for the permeability (noted k) and the solid thermal expansion coefficient α_s (noted *alpha*) compared with the original case (noted *origin*). Figure 5a and b show that, with increasing permeability, all the radial, tangential and axial stresses do not change much in the vicinity of the well wall. These quantities can vary widely at locations far from the well wall, for example, the region from 0.1 to 0.3 m away from the well wall for the cooling case. However, the tangential and axial stresses are sensitive to the thermal expansion coefficient that increase strongly in the vicinity of well wall (Fig. 5c and d). This is also not the case of the radial stress.

5 Conclusion

This study presents the analysis of the stress state around the wellbore located in the saturated rock at depth based on a fully coupling thermo-hydro-mechanical behavior model of the rock mass. The two scenarios of cooling and heating wellbore related

to thermal condition at well wall are taken into account. The following main conclusions can be drawn: a larger difference of stress field occurs around the wellbore between the cooling and heating cases; a tensile region of tangential and axial stresses occurs around the well wall in the case of cooling, while a region of high compressive of tangential and axial stresses occurs around the well wall in the case of heating. This suggests for the evaluation of wellbore stability based on the characteristics of tensile and compressive strength of each rock. The parametric analysis shows that the stress state around the wellbore is sensitive to the solid thermal expansion coefficient, while this is not the case for the permeability of the rock.

Acknowledgements This research is funded by Vietnam National Foundation for Science and Technology Development (NAFOSTED), under grant number 105.99-2020.21.

References

1. Sayers C, Dewhurst D (2008) Introduction to this special section - Shale geophysics. *Lead Edge* 27(6):736–737
2. Zhu Z, Wang C, Guan Z, Lei W (2021) Thermal characteristics of borehole stability drilling in hot dry rock, ACS Omega, ACS Publications, pp 19026–19037
3. Bradley WB (1979) Failure of inclined boreholes. *J Energy Resour Technol Trans AIME* 102:232–239
4. Aadnoy BS, Ong S (2003) Introduction to special issue on borehole stability. *J Petrol Sci Eng* 38:79–82
5. Kanfar MF, Chen Z, Rahman SS (2015) Effect of material anisotropy on time-dependent wellbore stability. *Int J Rock Mech Min Sci* 78:36–45
6. Do DP, Tran NH, Hoxha D, Dang HL (2017) Assessment of the influence of hydraulic and mechanical anisotropy on the fracture initiation pressure in permeable rocks using a complex potential approach. *Int J Rock Mech Min Sci* 100:108–123
7. Tran NH, Do DP, Vu MN, Nguyen TTN, Pham DT, Trieu HT (2022) Combined effect of anisotropy and uncertainty on the safe mud pressure window of horizontal wellbore drilled in anisotropic saturated rock. *Int J Rock Mech Min Sci* 152(105061):1–20
8. Ghassemi A, Diek A (2002) Porothermoelasticity for swelling shales. *J Pet Sci Eng* 34:123–135
9. Kanfar MF, Chen Z, Rhaman SS (2016) Fully coupled 3D anisotropic conductive-convective porothermoelasticity modeling for inclined boreholes. *Geothermics* 61:135–148
10. Abousleiman Y, Ekbote S (2005) Solutions for the inclined borehole in a porothermoelastic transversely isotropic medium. *J Appl Mech* 72:102–114
11. Roland WL, Perumal N, Seetharamu KN (2004) Fundamentals of the finite element method for heat and fluid flow, vol 3. John Wiley & Sons
12. Granet S (2014) Modelings THHM. Gen Inf Algorithms. https://code-aster.org/V2/doc/default/en/man_r/r7/r7.01.10.pdf

Numerical Study on Behaviors of EPS Geofoam Embankment on Soft Ground



Quoc-Bao Truong, Anh-Tuan Vu, Hoang-Kien Pham, and Duy-Canh Nguyen

Abstract In 1972, expanded polystyrene (EPS) geofoam was first utilized as a lightweight fill material for constructing roads in Oslo, Norway. The use of EPS geofoam in civil engineering has been applied widely for over four decades in various countries throughout the world. Especially, the EPS construction method was applied to reduce the deformation of soft ground for the highway embankment. In this study, numerical modeling of the EPS geofoam embankment using the Finite Element Method (FEM) through Plaxis 2D software was carried out. In the analyses, the hardening soil model (HS) was also used to model the grounds and EPS geofoam. Additionally, the interface elements were used to simulate the slippage between the blocks of EPS geofoam with two distinct densities, i.e., 0.2 and 0.35 kN/m³. The analyzed results indicated that EPS geofoam is an effective method to diminish the settlement influence of highway embankments on soft ground.

Keywords EPS geofoam · Numerical study · Soft ground · Settlement reduction

1 Introduction

In road construction, embankments constructed over soft soils induce a significant load over an immense area and are always a challenge for geotechnical engineers to ensure stability depending on the nature of the soil. A lot of ground improvement techniques have been applied widely for over 40 years and cannot be underestimated in this field. An effective method would be to use innovative lightweight material

Q.-B. Truong · A.-T. Vu (✉)
Le Quy Don Technical University, Hanoi, Vietnam
e-mail: vuanhtuan@mta.edu.vn

H.-K. Pham
University of Transport and Communications, Hanoi, Vietnam

D.-C. Nguyen
Ngo Quyen Technical University, Binhduong, Vietnam

(e.g., EPS geofabric) to diminish consolidation settlement of highway embankments on soft ground, as advanced technology has been implemented by state transportation agencies throughout the world [1]. In addition, EPS geofabric was first used as a material for an embankment foundation in Oslo, Norway, in 1972 [2]. It has long been used in numerous geotechnical applications as it is lightweight and durable [3]. EPS with the unit weight of only 1–2% compared with rock or concrete but can withstand relatively large compressive stresses, is molded into standard-sized blocks in the factory [1, 4]. Compared to the other soil improvement methods, EPS geofabric blocks are not only easily handled but also do not require special machinery, which speeds up construction procedures. In Vietnam, where construction on soft soil of low bearing capacity is ineluctable, it is necessary to study the applicability in civil engineering. In this study, numerical modeling of the EPS geofabric embankment with two distinct densities, i.e., 0.2, 0.35 kN/m³. In the analyses, the hardening soil model (HS) was used to model the grounds and EPS geofabric. Additionally, the interface elements were used to imitate the slippage between the blocks of the EPS geofabric. The analyzed results indicated that EPS geofabric is an effective method to diminish the settlement influence of highway embankments on soft ground.

2 Numerical Model

2.1 Finite Element Model

In two cases, a numerical model was developed on Plaxis 2D for the EPS embankment using the same geometry, boundaries, and loading conditions. A typical embankment of 4.0 m crest width with 1.5:1 side slopes has been chosen for this study, with a bottom length of 16.08 m loaded on the soft ground including three layers, as shown in Fig. 1. The height of the embankment is 3.9 m, and the construction time of the embankment is 16 days. Due to the symmetric condition of the studied case, only half of the road embankment and the ground were modeled in the numerical analysis. Figure 2 illustrates an example of finite element mesh in which the dimensions of the model are indicated.

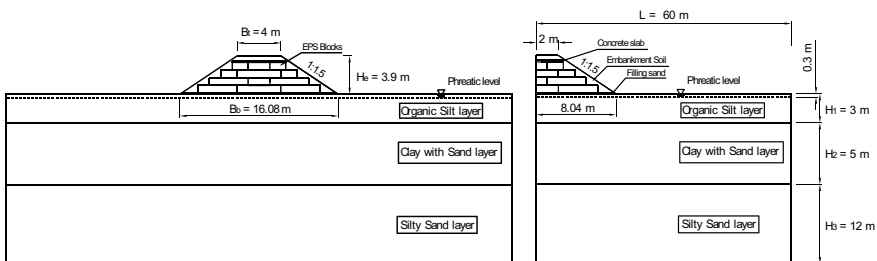


Fig. 1 EPS embankment on soft soil ground

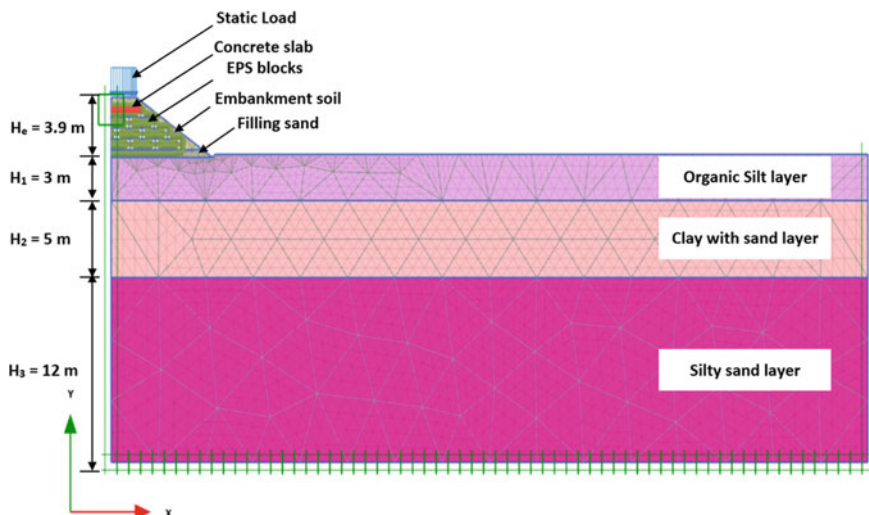


Fig. 2 Typical mesh generation

2.2 Material Model

The EPS embankment consists of two different densities of 0.2 (EPS 20) and 0.35 (EPS 35) kN/m^3 in (Fig. 3), EPS block with an overall size of $2.0 \text{ m} \times 1.0 \text{ m} \times 0.7 \text{ m}$ [5] as a replacement for conventional compacted soil embankments for roadways (Fig. 3). The HS constitutive model was used to imitate EPS geofoam material as shown in Table 1. EPS parameters for the HS model were based on measurements from other studies [6, 7], and foundation soil has been modeled using the HS model. The physical properties of the soil layer and embankment soil layer are presented in Table 2 [8–10].

The EPS embankment consists of geofoam blocks with a load distribution slab and a soil cover above it (Figs. 1 and 2). A plate element as a load distribution slab on top of the EPS blocks was used and imitated with the linear elastic model. The plate parameters are summarized in Table 3. Additionally, static load as per 22TCN 262-2000 specification is applied on the embankment with an equivalent load, $q = 15.38 \text{ kN/m}^2$ [11].

Interface elements of EPS–EPS and EPS with various materials were applied as shown in Fig. 3. The interface parameters employed in this study were based on the static direct shear tests from other studies [6, 12–14]. A reduction factor of the interface was applied as 0.6 according to the suggestion of Plaxis 2D.

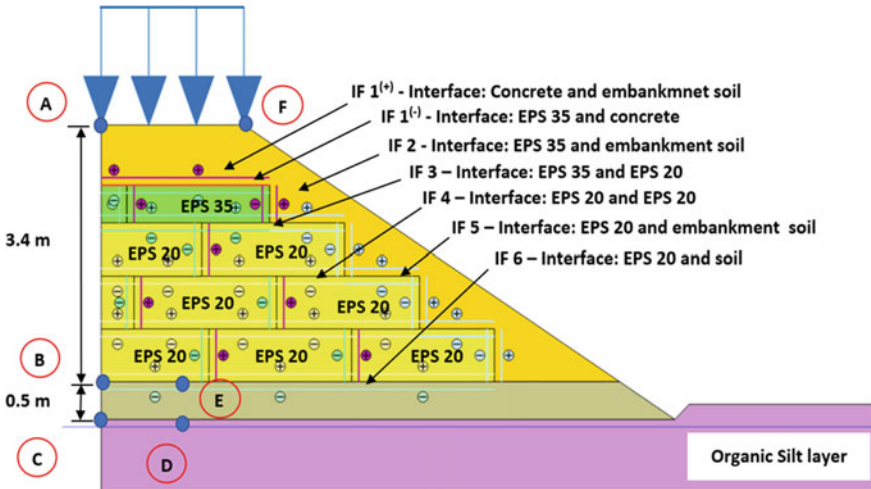


Fig. 3 Numerical model geometry for EPS embankment and soil embankment

Table 1 EPS properties are utilized in the numerical model of EPS embankment

Constitutive model	Hardening soil (HS)	
	γ (kN/m ³)	0.35
Cohesion, c (kPa)	84	12
Friction angle, ϕ (°)	35	33
Dilatancy angle, ψ (°)	6	0
Initial stiffness, E_0 (kPa)	4924	2357.9
Secant stiffness, E_{50} (kPa)	4672	2357.9
Poisson's ratio, ν	0.20	0.20
Interface reduction factor, R_{inter}	0.60	0.60

3 Results and Discussions

3.1 Effect on Settlement

Figure 4 shows the settlement of ground due to the construction of embankments in the cases of soil and EPS embankments. It is obvious to see that the consolidation settlement in the case of EPS embankment is significantly reduced compared with that of soil embankment. In the case of soil embankment, the maximum settlement at the centerline is about 250 mm. Meanwhile, the maximum settlement in the case of EPS embankment is only 50 mm. It is worth noting that the difference in the maximum settlement was reduced by about 80% when using EPS blocks. Figure 5 shows settlement vs. time at point C in soil and EPS embankment cases. The maximum settlement value of two embankments is less than the allowable value [11]. As for

Table 2 Soil parameters of the embankment soil

Item	Embankment soil	Filling sand	Organic silt	Sandy clay	Silty sand
Internal friction angle, φ , (deg.)	30	41	3.78	23.6	0
Dilatancy angle, ψ (deg.)	0	11	0	0	0
Cohesion unit, c , (kN/m ²)	0.5	2	15.7	41.05	24.47
Secant stiffness, E_{50} , (kN/m ²)	12,000	20,000	1091.74	3498.26	7624.18
One-dimensional stiffness, E_{oed} , (kN/m ²)	12,000	20,000	873.39	2798.61	6099.34
Unloading/reloading stiffness, E_{ur} , (kN/m ²)	36,000	60,000	4792.98	7668.2	22,872.5
Nonlinear factor, R_f	0.9	0.85	0.9	0.7	0.8
Stress dependency parameter for stiffness, m	0.5	0.5	1	1	0.5
Poisson's ratio	0.2	0.25	0.2	0.2	0.2
Reference stress, p_{ref} , (kN/m ²)	100	100	100	100	100

Table 3 Plate element properties are utilized in FE analysis

Item	Concrete	Unit
EA	8.50E + 06	kN/m
EI	1.59E + 04	kNm ² /m
w	1.8	kN
ν	0.15	–

soil embankment, the settlement obtained a stable value at the time of about 120 days from the beginning of construction. In the case of the EPS embankment, only after 30 days from the beginning of construction, the settlement obtained a stable value. Using EPS blocks reduced the consolidation time by about 75% compared with that of soil embankment.

3.2 Effect on Vertical Stress

Figure 6 shows the vertical stress in the ground due to the dead load of the embankment in the cases of soil and EPS. The external stress in the ground due to the soil embankment is considerably larger than that due to the EPS embankment, affecting the depth of settlement influence. The results in Table 4 indicate that the depth of settlement influence in the case of EPS is only 3.8 m which is much smaller than that in the case of soil embankment (8.63 m), about 56%. It is the reason why the geological survey depth in the case of EPS embankment is considerably smaller than that in the case of soil embankment.

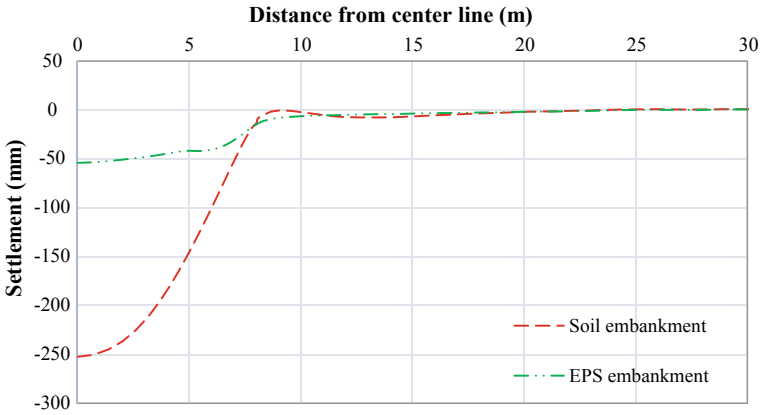


Fig. 4 Settlement curve of embankments

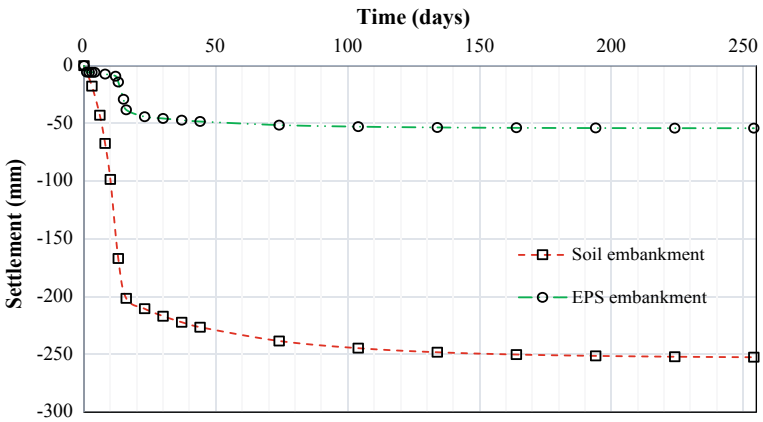


Fig. 5 Settlement versus time at point C

Fig. 6 Vertical stress by dead load

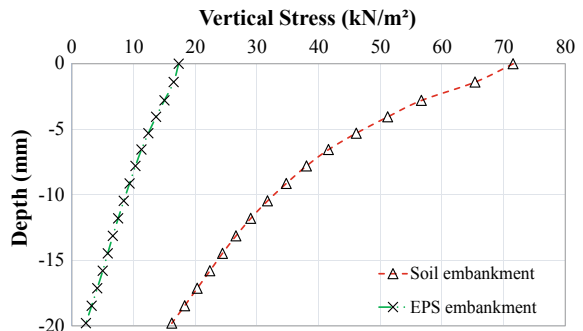


Table 4 Depth of settlement influence with two embankments

Type	EPS embankment	Soil embankment	Differential depth
[Stress (self-weight) = 0.2*Dead load stress]			
	(m)	(m)	(m)
(1)	(2)	(3)	(4) = (3) – (2)
Depth	– 3.8	– 8.63	4.83

Table 5 Safety factor of two embankments [M_{sf}]

No	Phases/types	EPS embankment	Soil embankment
1	After constructing	1.61	1.10
2	After 8 months	1.74	1.10

3.3 Effect on Stability

Table 5 shows the safety factor of two embankments. The numerical analyses indicated that the safety factor in the case of EPS embankment is larger than that in the case of soil embankment. Using EPS blocks increased the safety factor of stability after 8 months compared with that of soil embankment by about 58.2%. The safety factor of the stability value of EPS embankment is larger than the allowable value [M_{sf}] = 1.5 [5]. EPS geofoam is also an advanced method over traditional backfilling in road embankment construction.

4 Conclusions

The authors carried out a numerical study on the behaviors of EPS embankment compared with soil embankment. It is derived from the particular study that:

- The settlement in the case of EPS is significantly reduced by about 80% compared with that of soil embankment. Also, the time to obtain the stable settlement value in the case of EPS is reduced by about 75% than that in the case of soil.
- The depth of settlement influence in the case of EPS is considerably reduced by about 56% than that in the case of soil embankment.
- Using EPS blocks increased the safety factor of stability after 8 months compared with that of soil embankment by about 58.2%.

References

1. Thompsett DJ, Walker A, Radley RJ et al. (1995) Design and construction of expanded polystyrene embankments. Practical design and methods as used in the United Kingdom. *Const Build Mater* 9(6):403–411
2. Stark TD, Arellano D, Horvath JS, Leshchinsky D (2004) Geofoam applications in the design and construction of highway embankments. In: NCHRP project 24-11, transportation research board of the national academies, Washington D.C., USA
3. Aabøe R (1985) 13 years of experience with expanded polystyrene as a lightweight fill material in road embankments. In: The 1st international conference on EPS geofoam blocks in construction applications, Oslo, Norway
4. Aabøe R (2011) 40 years of experience with the use of EPS geofoam blocks in road construction. In: The 4th international conference on geofoam blocks in construction applications, EPS 2011, Lillestrøm, Norway
5. EPS Development Organization (2019) EDO-EPS Construction method—standard plan of design and construction and quality control
6. Abdel Salam SS, Jama RA, Salah MA (2019) EPS inclusion to reduce vertical stresses on shallow tunnels. *Geosynthetics Int.* <https://doi.org/10.1680/jgein.18.00042>
7. AbdelSalam SS, Azzam SA, Abdel-Awad AS (2015) Laboratory characterization and numerical modeling of EPS geofoam. In: International conference on advances in structural and geotechnical engineering, ICASGE'15
8. Phan V, Nguyen HS (2020) Analysis of some solutions to calculate embankment on soft ground to stabilize of the river bank. In: Anthology of science and technology results 2019–2020. Southern Institute of Irrigation Science, Vietnam
9. Phan V, Nguyen KLT (2020) The analysis of the wall stability is based on the standard penetration test. In: Anthology of science and technology results 2019–2020, Southern Institute of Irrigation Science, Vietnam
10. Fukkan and Minami Consultant Co., Ltd (2019) Factual report on soil investigation for small scale experimentation for EPS solution project, Location: Phuoc Hoa Ward, Tan Thanh District, Ba Ria – Vung Tau Province, Vietnam
11. 22TCN 262-2000 (2000) Design survey process of highway foundation the weak ground
12. Bartlett SF, Lawton EC (2008) Evaluating the seismic stability and performance of freestanding geofoam embankment. In: Keever M, Mesa L (eds) Proceedings of the sixth national seismic conference on bridges and highways, Charleston, SC, MCEER, Buffalo, NY
13. AbdelSalam SS, Azzam SA (2016) Reduction of lateral pressures on retaining walls using geofoam inclusion. *Geosynthetics Int.* <https://doi.org/10.1680/jgein.16.00005>
14. AbdelSalam SS, Anwar MB, Eskander SS (2018) Long-term behavior of EPS geofoam for road embankments. Meguid M, Guler E, Giroud J (eds) *Advances in geosynthetics engineering, GeoMEast 2018, Sustainable civil infrastructures*. Springer, Cham. https://doi.org/10.1007/978-3-030-01944-0_8

Investigation of Slope Protection Using Vegetation: A Case Study in Ninh Thuan Province, Vietnam



Tuan-Nghia Do and Lan Chau Nguyen

Abstract This study investigates slope protection using vegetation in the area of soil with high disintegration characteristics. The investigated site was a downstream slope (1:2.5) of a dam at the Song Trau lake, Thuan Bac district, Ninh Thuan province. A grass seed mat was employed to cover the slope surface, which could help to activate the development of grass. Eroded soil and the developing height of grass were recorded during watering time with the volume of water, which was calculated from precipitation conditions at the site. In addition, three small-scale flumes ($0.5 \times 0.5 \times 1.5$ m) were made to cultivate grass with different slope angles (1:1, 1:1.5, and 1:2.5) using the same grass seed mat. The eroding rainfall intensity was employed at 50 mm/2 h, 80 mm/2 h, 100 mm/2 h, and 150 mm/2 h. Results showed that the eroded soil weight after using the grass seed mat reduced 8 times as much as that before using the mat. The developing rate of grass in the site was the same as in the flumes, which was 1 cm/day in average. Finally, the soil strength was increased after the development of grass. In particular, cohesion and friction angle of soil were increased to 56% and 43%, respectively.

Keywords Slope protection · Grass seed mat · Soil disintegration · Eroding · Rainfall

1 Introduction

The application of vegetables (plant cultivation) to slope protection is called as the bioengineering method. In essence, during the growth of vegetables, they will serve as the protection layer of slope and activate the transforming between the air above

T.-N. Do (✉)
Thuyloi University/TLU, Hanoi, Vietnam
e-mail: dotuannghia@tlu.edu.vn

L. C. Nguyen
University of Transportation and Communications/UTC, Hanoi, Vietnam
e-mail: nguyenchaulan@utc.edu.vn

and land. Root of vegetables helps water vapor in air to penetrate into subsoil with the penetrating depth depending on the length of root system. Therefore, root of vegetables will affect the water flow to river, lake, underground, and water table. The other parts of vegetables above the ground surface, such as stem, leaf, can absorb partially runoff water and reduce the wind velocity so that they can prevent the eroding procedure of topsoil. On the other hand, the existence of root beneath the ground surface will increase the strength of topsoil and therefore reinforce the shallow stability of slope. Since the vegetable cover makes the protected slope green, the application of bioengineering method is so-called a green solution. This solution is more stable than the structural ones using reinforced concrete elements (i.e., diaphragm wall) because the vegetable cover can re-grow up after each of plant life cycles and does not generate CO₂ emission. The green solution is also cheaper than the structural ones at most cases. The mechanism and technical procedure to apply the biological method have been presented firstly by Gray and Leiser [1]. Kraebel [3] has applied the biological method in USA using the vegetable strips to protect slopes along the Angeles Crest expressway in South California.

Recently, the grass cultivation using vegetation mats has been widely applied (i.e., products by the Rontai company). A vegetation mat is usually composed of five layers: (1) grass seed and fertilizer layer; (2) green paper layer; (3) moisture absorber layer; (4) nonwoven geotextile layer; and (5) outer net layer. In principle, when a raindrop falls down to the vegetation mat, the nonwoven geotextile layer will reduce kinetic energy of the raindrop. Then, the raindrop is stored in the moisture absorber layer, causing the swelling of this layer, which presses the mat onto the slope and reduces the initial eroding impact of the raindrop. Water stored in the moisture absorber layer will be used to bring up grass seeds. A mature grass layer can help to prevent eroding of the slope surface from runoff water and wind and strengthen the topsoil through the root system. The green color of grass creates a beautiful landscape for the slope. Jesus et al. [2] have investigated the anti-eroding capacity of a geotextile accompanied with grass layer as applied to slopes in Spain. The slope angles in this study were 45° and 60°, respectively. The employed geotextile was 3D polyester one. The cultivated plants contain 75% grass and 25% legume. Results showed that the growing probability of seeds was the key factor that controlled the penetration of runoff water into ground. On the other hand, the soil retention capacity of the geotextile strongly affected the growing procedure of seeds. Many researchers have studied on this field such as Mahmud et al. [4] and Shao et al. [5].

This study aims to investigate the slope protection probability of vegetation mats in high disintegration soil in Ninh Thuan province, Vietnam. Grass cultivation was performed both on a downstream slope (1:2.5) of a dam at the Song Trau lake, Thuan Bac district, Ninh Thuan province and in the experimental flumes. Data on the eroded soil weight, grass height, and the increase in shear strength of soil would be collected and analyzed.

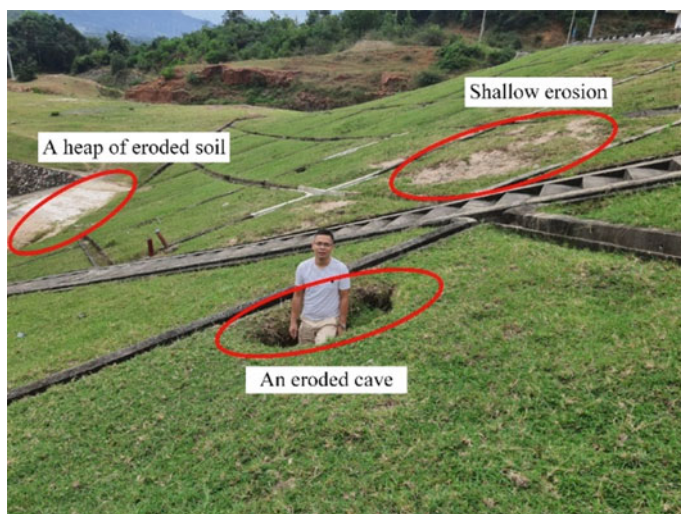


Fig. 1 Eroding failure at the downstream slope of a dam at the Song Trau lake

2 Site Characteristics

2.1 Eroding Failure

The studied area is a downstream slope (1:2.5) of a dam at the Song Trau lake, Thuan Bac district, Ninh Thuan province. Soil in this area is highly disintegrated. During the operation of the dam, there are two unfavorable phenomena as follows: (1) the vegetable layer grows slowly so that it cannot cover whole the slope and (2) the eroded topsoil cumulates at the slope toe and eroding of soil within the slope body generates large caves with the depth of 1 m as shown in Fig. 1.

2.2 Soil Properties

Properties of topsoil at the downstream slope of a dam at the Song Trau lake are summarized in Table 1. This is gray clayey sand. Moisture content of remolded sample is 11.6%. Specific gravity of topsoil is 2.68. Moisture and saturated unit weights are 1.92 g/cm^3 and 2.08 g/cm^3 , respectively. At initial state, cohesion and friction angle of soil are 0.196 kg/cm^2 and $17^\circ 31'$, whereas at saturated state, they are 0.196 kg/cm^2 and $17^\circ 31'$. Based on results of standard proctor tests, optimal moisture content and maximum dry unit weight of soil are 11.6% and 1.81 g/cm^3 . pH index of soil is 8.05.

Table 1 Properties of topsoil

No.	Properties	Symbol	Unit	Name
				Topsoil
1	Specific gravity	G_s		2.68
2	Moisture unit weight	ρ	g/cm ³	1.92
3	Dry unit weight	ρ_d	g/cm ³	1.72
4	Degree of saturation	S_r	%	55.6
5	Porosity	n	%	35.9
6	Initial void ratio	e_0		0.559
7	Liquid limit	W_L	%	19.8
8	Plastic limit	W_P	%	14.4
9	Plastic index	I_P	%	5.3
10	Initial cohesion	c	kg/cm ²	0.196
11	Initial friction angle	ϕ	°	17° 31'
12	Saturated cohesion	c_{sat}	kg/cm ²	0.074
13	Saturated friction angle	ϕ_{sat}	°	6° 16'
14	Coefficient of permeability	K	cm/s	7.23E-05
15	Optimal moisture content	W_{op}	%	11.6
16	Maximum dry unit weight	$\rho_{d\ max}$	g/cm ³	1.81
17	Description	Gray clayey sand		

2.3 Rainfall Data

Rainfall data were collected from the rain gauge station in the site from 2019 to 2021. The accumulated rainfall in 2019, 2020, and 2021 was 901.6 mm, 1171 mm, and 1557.1 mm, respectively. Figure 2 plots the rainfall data in these years by month. As shown in Fig. 2, the maximum rainfall often took place in September, October, and November with the maximum magnitude of 628.1 mm. On the other hand, in January, February, and March, the recorded rainfall was usually very low, sometimes no rain. The maximum daily rainfall event data are plotted in Fig. 3 by month. As shown in the figure, the largest daily rainfall events were recorded at 72.85 mm, 211.93 mm, and 175.37 mm in 2019, 2020, and 2021, respectively, with an average value of 153.3 mm. Based on data by QCVN 02:2009/BXD [6], the rainfall event often occurs from 1 to 3 h. Therefore, the representative rainfall event, which was adopted in this study, was 80 mm within 2 h.

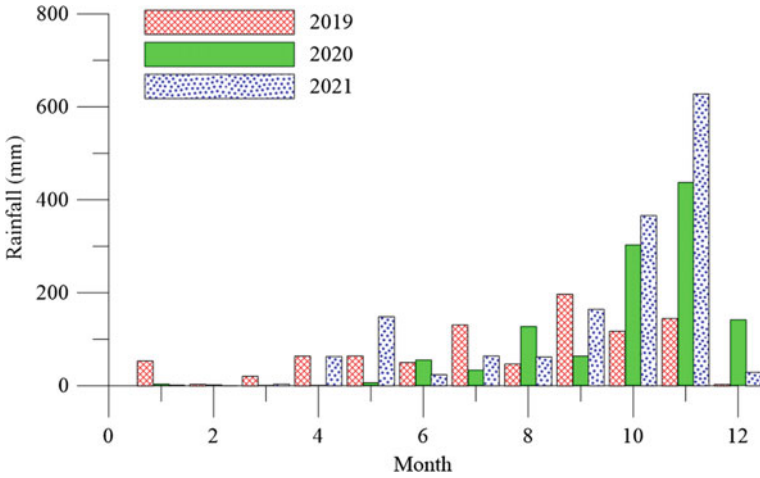


Fig. 2 Rainfall data at the Song Trau lake by month

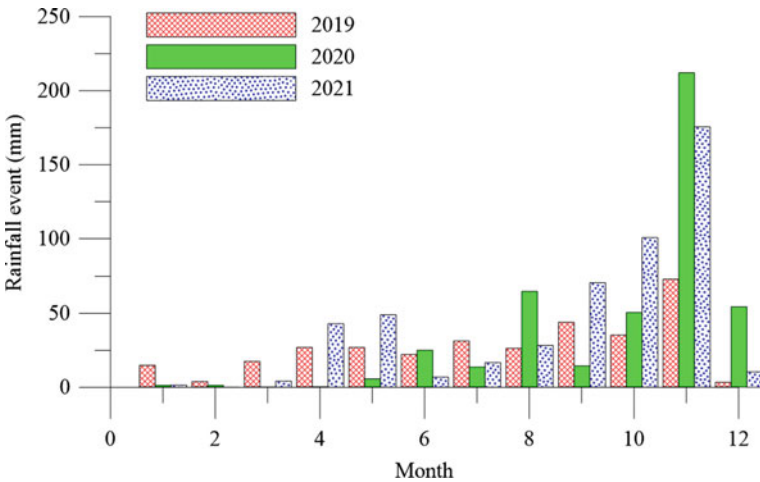


Fig. 3 Daily rainfall event data at the Song Trau lake by month

3 Small-Scale Model and Test Procedure

3.1 Small-Scale Model

The topsoil at the downstream slope of a dam at the Song Trau lake was taken to cultivate grass and perform eroding tests in small-scale models. Three flumes were adopted in this study, whose dimensions were $50 \times 150 \times 50$ cm, as shown in Fig. 4a. These flumes were set at different slopes of 1:1.0, 1:1.5, 1:2.5 (Fig. 4b). The density

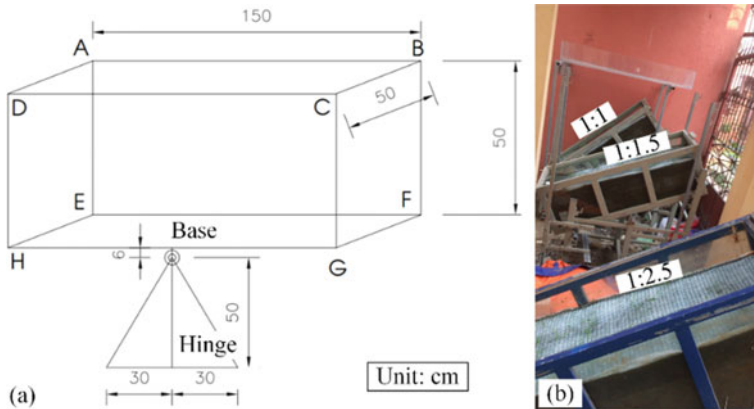


Fig. 4 Small-scale model: **a** dimension and **b** slope

of remolded soil was adopted at K95, at which the dry density of soil was equal to 95% the maximum one.

During eroding test, rainfall simulator was a top flume, which was located at 1 m above the slope in average. This top flume included a number of holes with 0.5 mm in diameter, which was distributed in a network of 3×3 cm. The adopted eroding rainfall events were 50, 80, 100, and 150 mm within 2 h when the slope was bare and 80 mm within 2 h when the slope was covered by grass.

For grass cultivation, a grass seed mat was employed. Grass seeds were composed of four types, including Bermuda, K280, Ruzi, and Stylo. These types of grass were selected based on the contribution to soil strength due to the development of root systems and providing nutrition to soil for next developing cycle. Grass height was gathered every 3 days within 3 months. The daily amount of water used for cultivation was equal to the average daily rainfall event recorded in the site from 2019 to 2021.

3.2 Field Test

The downstream slope of a dam at the Song Trau lake was covered by grass seed mats. The tested area was 7×7 m. The slope was 1:2.5. The amount of water used for cultivation was taken the same as that in small-scale test. Also, grass height was gathered every 3 days within 3 months (Fig. 5).

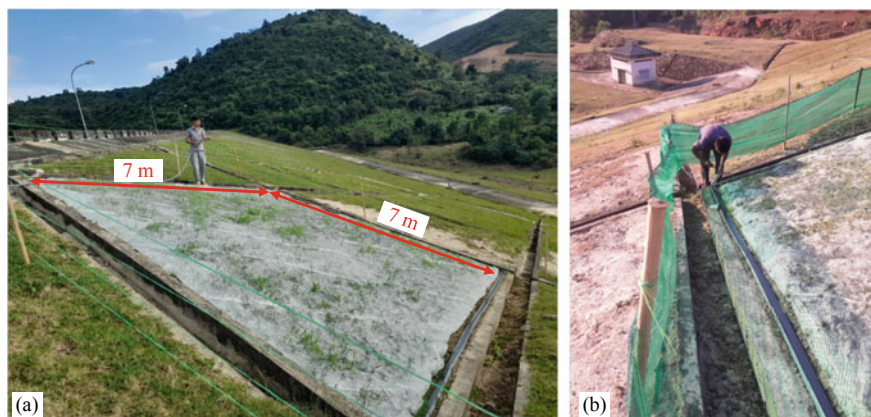


Fig. 5 Grass cultivation at the Song Trau lake: **a** watering and **b** gathering eroded soil

4 Results and Discussions

4.1 Eroded Soil

Figure 6 plots the eroded soil before and after performing grass cultivation in small-scale test. Note that amount of eroded soil was divided by tested area and the eroding rainfall event was 80 mm within 2 h. As shown in the figure, before grass cultivation, eroded soil weight increases with the slope, from 400 to 700 g/m² corresponding to the slopes of 1:2.5 and 1:1. Besides, when the eroding rainfall increases, the eroded soil weight also develops. For example, with the slope of 1:1.5, when the eroding rainfall changes from 50 to 150 mm within 2 h, the eroded soil weight was retrieved from 400 to 600 g/m². After grass cultivation, the eroded soil weight decreases 8 times as much as before grass cultivation, at which the eroding rainfall remains at 80 mm within 2 h. Although the eroded soil weight is keep increasing with the slope, it is reduced with the cultivating time. The reduction of eroded soil weight is due to the soil retention capacity of the geotextile layer in the grass seed mat. The geotextile layer can also reduce the kinetic energy of rain as hitting the slope surface. In addition, the grass layer serves as a mattress with many layers of leaves to reduce the velocity of rains and transport them to soil through stems. The existence of root systems can increase soil shear strength and decrease soil eroding due to runoff water.

Figure 7 shows the eroded soil weight after performing grass cultivation in the site. Results show that the maximum eroded soil weight is 1.6 g/m², which is very small as compared with that retrieved from the slope of 1:2.5 in small-scale test. It may be due to the different rainfall generating procedures between field test and small-scale test (the amount of used water is the same, but the watering time is different).

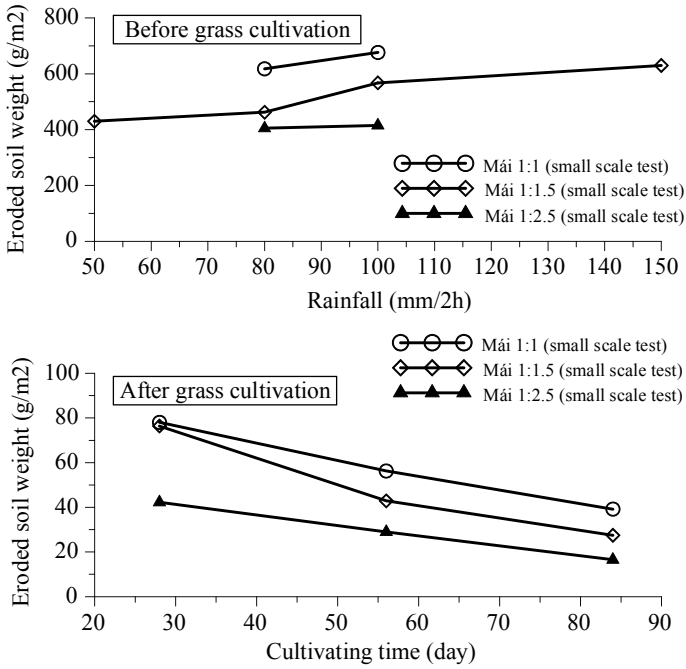


Fig. 6 Eroded soil weight at small-scale test: a before grass cultivation and b after grass cultivation

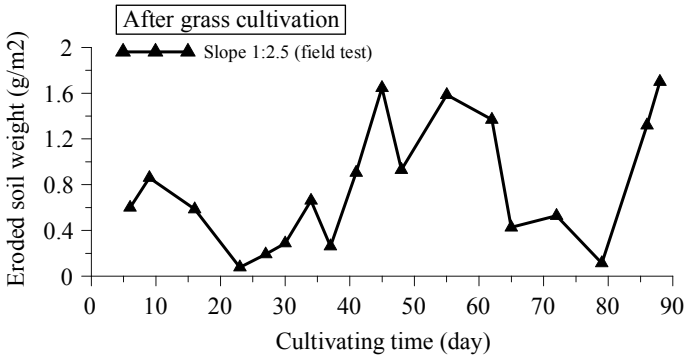


Fig. 7 Eroded soil weight at field test after grass cultivation

4.2 Grass Height

Grass height data recorded from small-scale test and field test are plotted in Fig. 8 with time. As shown in the figure, grass height increases 1 cm/day in average, at which that in field test develops similarly to that in small-scale test. It proves that

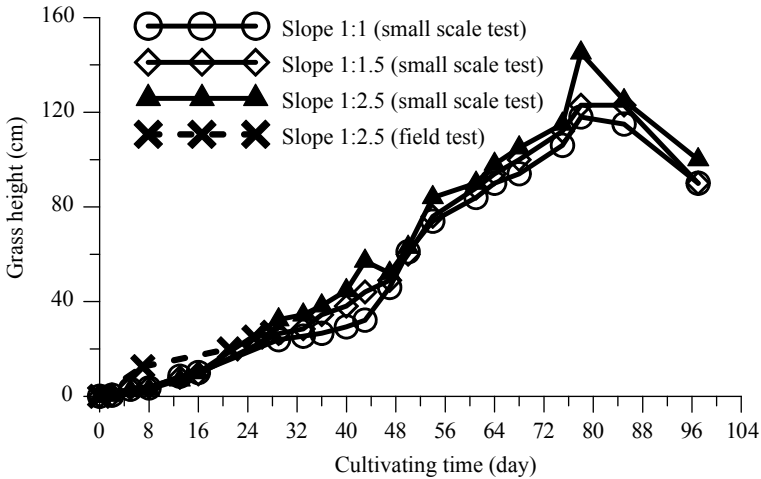


Fig. 8 Grass height with time

grass used in this study can grow well under the weather condition at the Song Trau lake, Thuan Bac district, Ninh Thuan province.

4.3 Soil Shear Strength

After the development of grass in the site, soil samples were taken to perform direct shear test, which could estimate strength parameters of soil after treatment. Results showed that $c = 30.5$ kPa and $\phi = 25.0^\circ$ which were 56% and 43% higher than those before grass cultivation ($c = 19.6$ kPa and $\phi = 17.5^\circ$), respectively. It is clear that the existence of root system has improved significantly soil shear strength.

5 Conclusions

Based on results of this study, some conclusion could be drawn for topsoil at the Song Trau lake, Thuan Bac district, Ninh Thuan province as follows:

- i. Eroded soil weight increased with the slope angle and could reduce 8 times as much as compared with that before grass cultivation.
- ii. Grass height grew with time with 1 cm/day in average and the developing velocity of grass in small-scale test was similar to that in field test.
- iii. Soil shear strength was increased after grass cultivation. Particularly, cohesion and friction angle of soil increased 56% and 43%.

Acknowledgements The authors would like to thank Rontai company (<https://rontaivietnam.com/>) for your financial aid and technical support related to grass seed mats.

References

1. Gray DH, Leiser AT (1982) Biotechnical slope protection and eroding control. Van Nostrand Reinhold, New York
2. Jesus AM, Abad E, Gimenez R, Campo MA, Goni M, Arive M, Casali J, Diez J, Diego I (2014) Evaluation of eroding control geotextiles on steep slopes. Part 2: influence on the establishment and growth of vegetation. CATENA 121:195–203
3. Kraebel CJ (1936) eroding control on mountain roads. USDA circular no. 380. U.S. Department of Agriculture, Washington, DC
4. Mahmud MM, Chowdhury NH, Elahi MM, Rashid MH, Hasan MK (2012) Mitigation of soil eroding with jute geotextile aided by vegetation cover: optimization of an integrated tactic for sustainable soil conservation system (SSCS). Glob J Res Eng Civ Struct Eng 12(2):1–7
5. Shao Q, Gu W, Dai QY, Makoto S, Liu Y (2014) Effectiveness of geotextile mulches for slope restoration in semi-arid northern China. CATENA 116:1–9
6. Vietnam Building Code QCVN 02:2009/BXD (2009) Natural physical and climatic data for construction. Ministry of Construction

Rockfall Mitigation for Highway in Vietnam: A Case Study on the Hoang Sa Road, Da Nang City



Cho Thu Thu Naing, Lan Chau Nguyen, and Tien Dung Nguyen

Abstract This paper presents a study on mitigating the impacts of rockfall on the Hoang Sa road, a coastal route to Son Tra peninsula, Da Nang city. Son Tra peninsula is very well-known for tourist attraction places. The Hoang Sa road is located in mountainous terrain. Rockfall events had occurred along this highway several times in the past. As a result, it affected the tourism sector and damaged the road infrastructure in Da Nang city. In this study, UAV was used to investigate the rockfall-prone area. According to the field survey, there were many large tectonic fractures and unstable blocks on the rock cliff along the Hoang Sa road. This paper focused on the mechanism of rockfall in a high-risk rockfall area on the Hoang Sa road and determined a suitable barrier location and height using parameters such as run-out distance, bounce height, velocity, and kinetic energy of the falling rock blocks with the RocFall software. The numerical analysis indicated that the appropriate barrier location and height for this area were at 14.5 and 5 m, with a kinetic energy of 590 kJ.

Keywords Rockfall mitigation · Slope stability · RocFall · Flexible barrier

1 Introduction

Rockfalls are one of the geological hazards and the fastest type of landslide that happen mainly in the mountainous region. Rockfall means the amount of stone freely falling from the high point of the terrain. The falling of large blocks of rock is the main issue for humans and the transportation sector because these blocks cause

C. T. T. Naing (✉) · T. D. Nguyen
Infrastructure Engineering Program, VNU Vietnam Japan University, Hanoi, Vietnam
e-mail: 21117070@st.vju.ac.vn

T. D. Nguyen
e-mail: nt.dung@vju.ac.vn

L. C. Nguyen
University of Transportation and Communications/UTC, Hanoi, Vietnam
e-mail: nguyenchaulan@utc.edu.vn

© The Author(s), under exclusive license to Springer Nature Singapore Pte Ltd. 2024
T. Nguyen-Xuan et al. (eds.), *Proceedings of the 4th International Conference on Sustainability in Civil Engineering*, Lecture Notes in Civil Engineering 344,
https://doi.org/10.1007/978-981-99-2345-8_42

delays for the moving vehicles on the highway along the mountainous area and threaten people's lives and the environment [1]. In mountainous areas, the reasons for rock slope failures depend on the following factors: rainfall, natural hazards, seepage, weak rock properties, the free-thaw process, and soil erosion.

With the development of infrastructure in Vietnam, rock slope failures are also frequently encountered along roads No. 1A, 12, 4C, 4D, 4E, 16, etc., in Vietnam [2]. Recently, rockfall occurred along the Ha Long–Van Don highway in the northern area of Vietnam and concrete barriers were damaged [2]. The Hoang Sa road, which is the study area, is constructed in a mountainous area that passes through many road cuts and high-slope sections. The Hoang Sa road has two lanes for motor vehicles and two lanes for rudimentary vehicles, and the roadway width is 10.5 m. Several rockfalls have occurred along the Hoang Sa road. For example, in 2007, rockfall events happened on the Hoang Sa road due to Typhoon No. 9. The large rock blocks rolled down on the Hoang Sa route and damaged road infrastructure, as well as impacted traffic flow on the entire route [3]. Moreover, the phenomenon of rolling stones and areas at risk of landslides was observed on the Hoang Sa route in April 2022. There were six places at risk of accidents on the Hoang Sa road, the section on Son Tra peninsula. Thus, these locations need to be handled with an appropriate protection method. A flexible barrier is a useful method for protection against landslides, mostly debris flow or rockfall, because it can catch and stop falling material, such as boulders or debris [4]. Hence, a flexible barrier is easy and rapid to install and easy to maintain [5]. Therefore, the author proposed a flexible barrier as a mitigation method for rockfall protection in the study area.

2 Study Area

Son Tra peninsula is located to the east of Da Nang city in the middle of Central Vietnam. It is a well-known place in Vietnam for tourists, with beautiful panoramas of majestic mountains and seas in downtown Da Nang. The Hoang Sa road on Son Tra peninsula is the main route leading to Linh Ung pagoda. The study area is a tropical monsoon zone with a temperate and equable climate. It has an average humidity of 83.4%, temperatures ranging from 26 to 30 °C, and an average rainfall of about 2505 mm between October and November. There are two seasons in Da Nang: the wet from August to December and the dry season from January to July.

The study area lies from 16° 06' 10" to 16° 06' 36" north latitude and from 108° 16' 12" to 108° 16' 92" east longitude. Based on the field investigation at the Hoang Sa road, the dip angle of this high-risk rockfall area ranges between 70 and 85°. Geologically, Son Tra area rocks are principally granite which belong to the Hai Van complex (γ_a , T_3 , h_{v1}). The geological feature of Son Tra area is mainly granite rock covered by sandy soil with a depth of 3–10 m (Fig. 1).

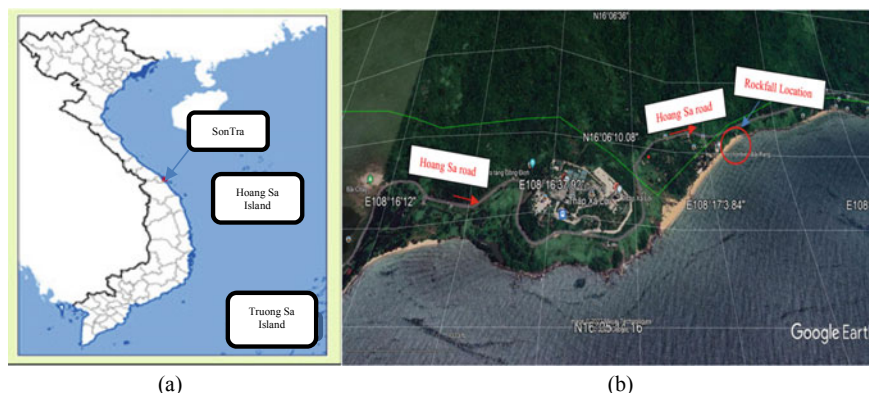


Fig. 1 a Location of study area. b Hoang Sa road and place where rockfall happened

3 Methodology

The field survey was carried out on rock slope failure conditions along the Hoang Sa road in August 2022 by taking photos, manually measuring, and using an unmanned aerial vehicle (UAV). The location of potential rock falls can be determined based on UAV surveys. Furthermore, UAV can be used to generate the DEM (Digital Elevation Model). This technology is a quick and safe tool for collecting detailed topographic surface data that is used as a reference for the design of barriers [6]. DEM with small, medium, or large pixel sizes has also been used for rockfall detection. RocFall is a useful computer program that uses a mathematical model based on the laws of motion and the theory of collision. RocFall software simulates the rockfall trajectories, bounce height, and velocity after defining the geometry and parameters of the slope and the quantity, shape, and position of the rock falling [7]. In addition, this software estimates the impact force at selected analysis points along the slope profile. The result can be used for the design of rockfall protection measures (to select the location and size of structures), i.e., catchment benches or ditches, fences, or walls. In this research, RocFall software (V.4.0) was used to analyze rockfall mechanisms along the terrain slope with and without a flexible barrier.

3.1 RocFall Geometry for Rockfall Analysis

Rockfall simulation was carried out using the rigid body method with the RocFall software to determine the mechanism of rockfall in this research. The sources of falling rocks were specified based on field investigation and a site video recording. Based on the field survey data, the model was divided into three parts: the first part is a terrain, the second is a retaining wall, and the final part is an asphalt road, as shown in Fig. 2. The material of the terrain is bedrock (weathered granite). The shape of a

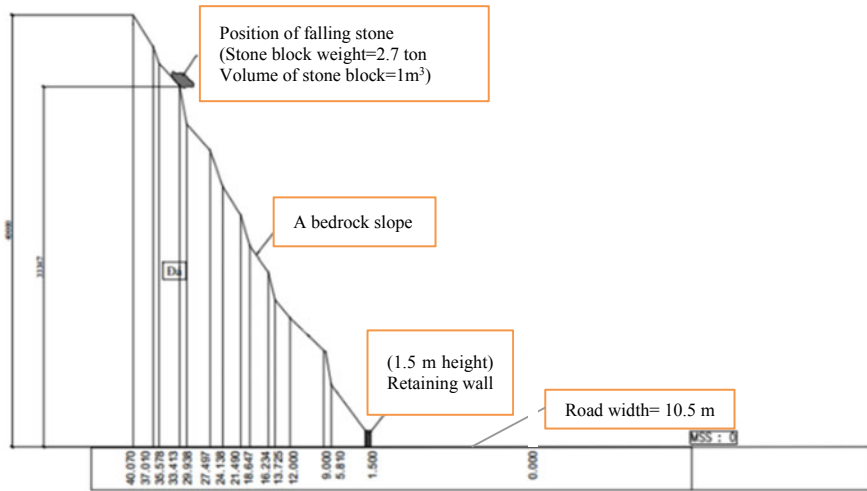


Fig. 2 RocFall geometry for rockfall analysis

falling stone is hexagonal for rockfall model analysis. According to a video recorded on site, the largest size of the fallen block was 2.7 tons, falling speed was 5 m/s, and the stone dropped from a height of 30 m.

3.2 Input Parameter for RocFall Software

Physical properties of rock material, size and shape of blocks, geological profile, roughness, velocity, and hardness of material along the profile are input parameters. For this research, the software mainly requires normal and tangential restitution coefficients, friction angle, velocity, and rock mass density. The coefficient of restitution (COR) is an important parameter for the analysis of rockfall. The normal coefficient of restitution (R_n) can be obtained from in situ experiment or provided by Rocscience. The value of tangential COR (R_t) can be taken from the COR table provided by Rocscience [8]. Based on the in situ condition of material on the surface and the recommended value from Rocscience, input parameter values for RocFall software are shown in Table 1.

Table 1 Input material values of rock slope on the Hoang Sa road

Material type	Normal coefficient of restitution (R_n)		Tangential coefficient of restitution (R_t)		Friction angle ($^\circ$)		Slope roughness
	Mean	Standard deviation	Mean	Standard deviation	Mean	Standard deviation	Standard deviation
Bedrock	0.35	0.04	0.85	0.04	30	2	0
Retaining wall	0.5	0.03	0.5	0.03	30	0	0
Asphalt road	0.4	0.04	0.9	0.04	30	2	0

4 Results and Discussions

4.1 Field Survey Results

The field surveys were conducted at two locations on the Hoang Sa road: the first is from the electric poles nos. 174 to 186, and the second is from the electric poles nos. 53 to 69. The first section has a retaining wall that is on top of a rolling stone screen with a height of 1 m. Although a retaining wall exists in this section, it has not prevented rocks from falling onto the terrain. Therefore, 1 m³ of orphaned stones dropped onto the road that damaged the steel mesh, broke the cable, warped the steel poles, as well as caused traffic insecurity as shown in Fig. 3. Consequently, gabion walls and stone retaining nets were rusted and damaged quite badly. The locations of the electric poles ranged from no. 174 to no. 186, where the rock slope failures occurred, as shown in Fig. 4a. Therefore, this section was necessary to apply long-term stable measures according to field investigation.

The second section has 1.5 m height retaining wall. The slope in this portion is high, with a slope height range of 30–70 m. According to the field survey, the high-risk rockfall area has slightly weathered rock and an intrusive large formation and is normally granite, quite homogeneous lithologically. Moreover, the surface is an inert rock and has a few shrubs. Additionally, many rock locations within the second section are unstable blocks due to their collision, as shown in Fig. 3. Hence, landslide and rockfall cases mostly happen in this area.

4.2 UAV Results

Figure 5 shows that the topography of the rockfall area was investigated using an UAV mounted with a high-megapixel camera. Figure 5a shows UAV results in rock slope failure on the terrain along the Hoang Sa road in Da Nang city. The DEM model can be generated using UAV images and Agisoft PhotoScan software. Figure 5b describes DEM model for the Hoang Sa road. There are many rockfall cases along

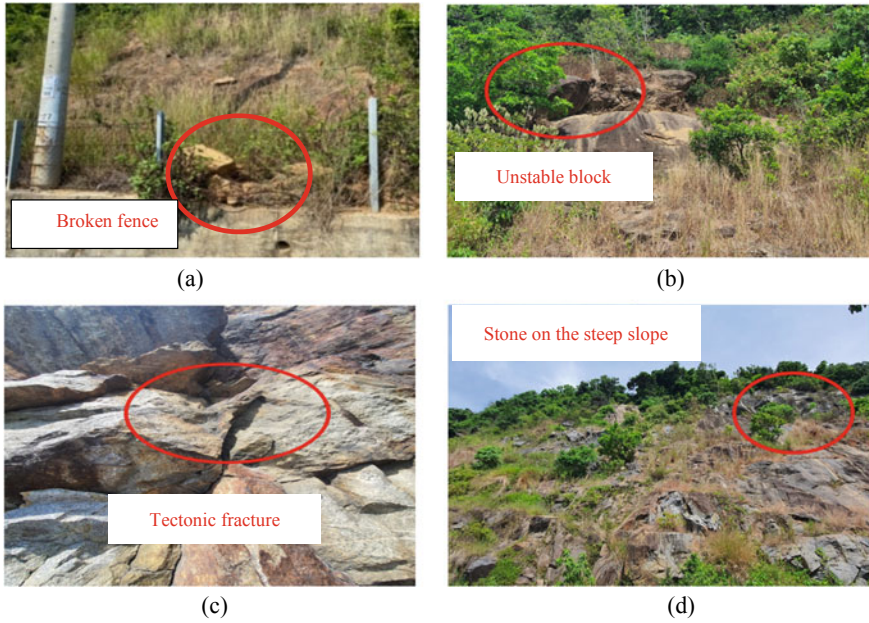


Fig. 3 Phenomenon of rockfall on the Hoang Sa road. **a** Broken posts, cables, and fence. **b** Unstable block. **c** Weathered rock and cracked surface. **d** Stone on the steep slope



Fig. 4 **a** Falling rock happened in July 2022. **b** Falling rocks occurred in May 2022

the Hoang Sa road. A high-risk rockfall event of about 500–600 m length happened on the Hoang Sa road in April 2022. The high-risk rockfall location is described in Fig. 5a.

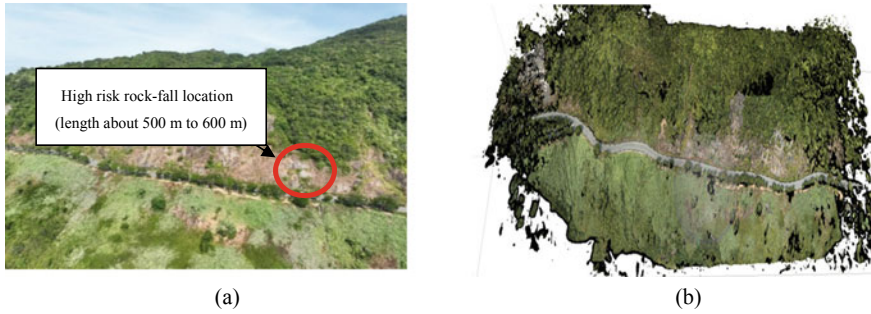


Fig. 5 **a** Image of rocks with a high risk of rockfall taken by UAV on the Hoang Sa road in 2022. **b** DEM model from UAV pictures

4.3 Numerical Results for Rock Slope Without a Barrier

The maximum bounce height was 9.69 m at 13.5 m of run-out distance (horizontal distance), as shown in Table 2 and Fig. 6. The maximum values of total kinetic energy and translational velocity were about 612 kJ and 21 m/s at a 14.5 m of horizontal distance, as shown in Table 2. Damaged capacity levels for all locations were in the high-intensity zone because their total kinetic energy values were greater than 300 kJ, as shown in Table 2 [9] (Fig. 7).

The energy of blocks is lost after the first impact, causing the fragmentation of blocks into smaller pieces on impact. Consequently, blocks are bouncing and rolling along their trajectories before stopping on the asphalt road. As a result of the rockfall analysis (without a barrier), rock blocks reached the asphalt road, causing damage to the road infrastructure and harm to commuters on the Hoang Sa road. Hence, this research used flexible barriers to catch the falling rock blocks on the road.

Table 2 Parameters obtained from RocFall model (without a barrier)

Horizontal distance (m)	Bounce height (m)	Total kinetic energy (kJ)	Translational velocity (m/s)	Intensity level zone
9.45	7.93	312	15	High
10.80	9.60	385	17	High
12.15	9.07	463	19	High
13.50	9.69	562	20	High
14.50	7.95	612	21	High

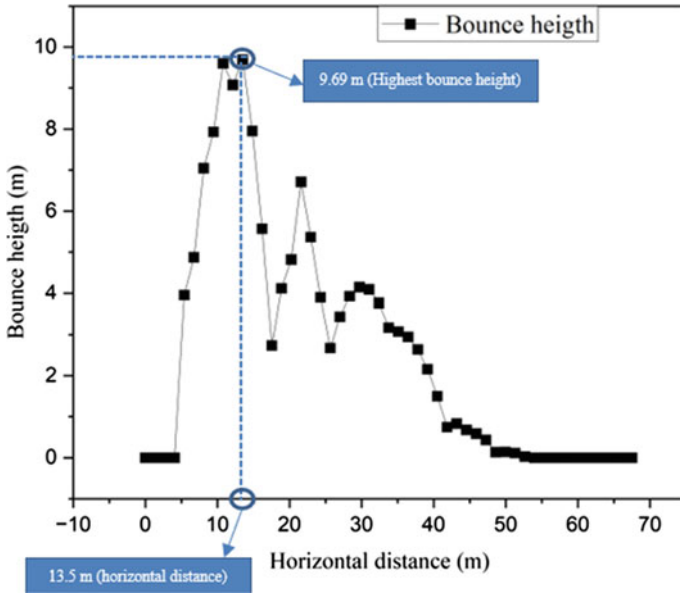


Fig. 6 Bounce height result (without a barrier)

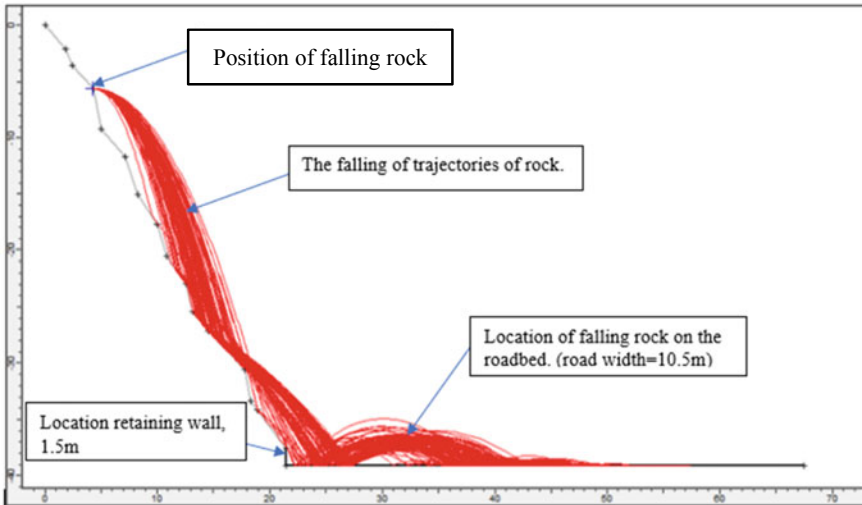


Fig. 7 Rock trajectories' result (without a barrier)

4.4 Numerical Results for Rock Slope with a Barrier

At 13.5 m of horizontal distance, which was the horizontal moving distance of the falling rock, it had the highest bounce height compared with the others, as shown in Fig. 6 and Table 2. Thus, a horizontal distance of 13.5 m was considered as a barrier location in the RocFall model. And then, trajectories, run-out distance, bounce heights, translational velocity, and total kinetic energy were calculated with various barrier heights (3, 4, 5, and 6 m). The RocFall model was considered as a flexible barrier type using high-strength steel wire mesh fencing with a 3000 kJ capacity of kinetic energy. Figure 8 describes falling trajectories and their endpoints. Their trajectories are based on the characteristics of the barrier height. According to Fig. 8, although 3 and 4 m of barrier height were applied, rockfall failures have also happened in this area. In addition, a 5 m barrier height was not a safe design for rockfall mitigation because it had not fully caught the rock blocks. Only a 6 m barrier height at a 13.5 m barrier location can be capable of preventing blocks from rolling on the terrain, as shown in Fig. 8.

When a barrier was installed at a horizontal distance of 14.5 m with various barrier heights (3, 4, 5, and 6 m), the software calculated rock trajectories, as shown in Fig. 9. For a 14.5 m barrier location, the result showed that a barrier height of 3 m was not enough to protect blocks from rolling rocks. Rocks have been moving to the ground according to Fig. 9. Starting at a 5 m barrier height, it can protect the rock rolling on the cliff (Fig. 9). Table 3 shows the maximum values of translational velocity and total

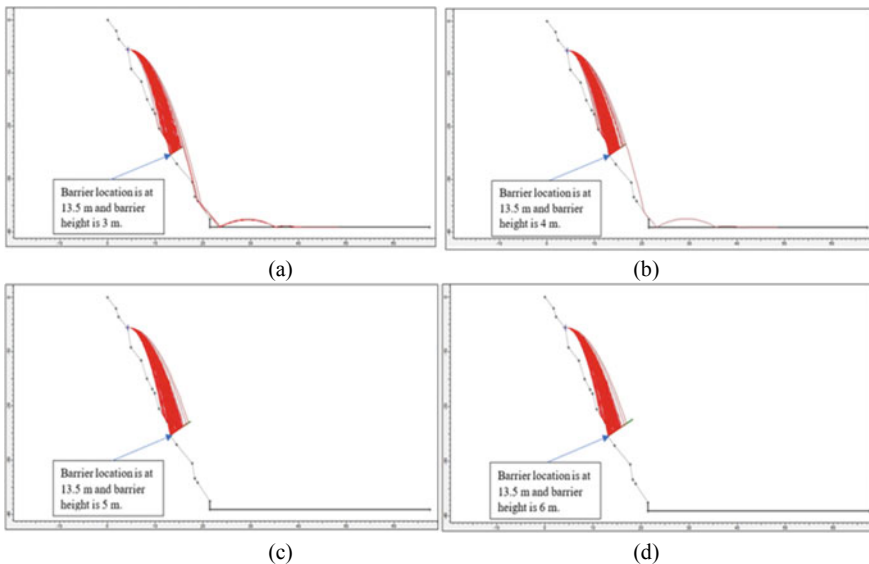


Fig. 8 Rock trajectories at a 13.5 m barrier installed with different barrier heights **a** 3 m barrier height. **b** 4 m barrier height. **c** 5 m barrier height. **d** 6 m barrier height

kinetic energy. At four different heights (i.e., 3, 4, 5, and 6 m), both the maximum translational velocity and the maximum kinetic energy were observed at a barrier height of 3 m, as shown in Table 3. An impact barrier means that the value gives the maximum total kinetic energy and velocity within the barrier location. Even though the barrier height varies, maximum total kinetic energy and translational velocity values of the impact barrier have not changed significantly based on the barrier height. As an analysis result, the reasonable height of the barrier to protect rock fragments from rolling was 5 m for the case of a 14.5 m barrier location.

At a 14.5 m run-out distance (horizontal distance), bounce height values were 7 m, 4 m, 3.6 m, and 2 m, with 2 m, 4 m, 5 m, and 6 m barrier heights, respectively, in Table 4. Figure 10 illustrates the result of bounce height and horizontal location based on four types of barrier heights (2, 4, 5, and 6 m). It can be seen that a 2 m barrier height has the highest bounce height among other barrier heights, and the lowest trend is at a 6 m barrier height. As shown in Fig. 10, bounce height values of 4 and 5 m of

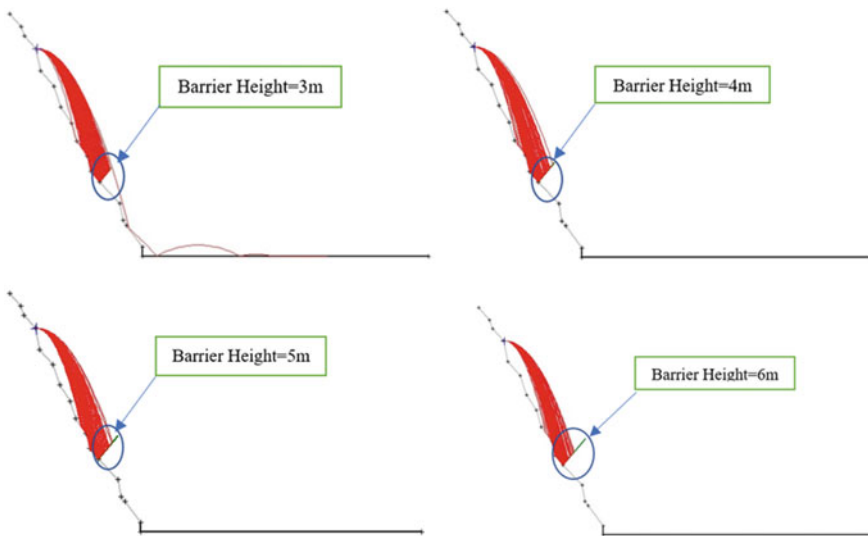


Fig. 9 Rock trajectories at a 14.5 m barrier installed with various barrier heights

Table 3 Parameters at a 14.5 m of horizontal location obtained from RocFall model (with a barrier)

No.	Barrier height (m)	Max. total kinetic energy (kJ)	Max. translational velocity (m/s)	Impact barrier (max. total kinetic energy) (kJ)	Impact barrier (max. translational velocity) (m/s)
1	3	780	24	599	21
2	4	590	21	599	21
3	5	590	21	599	21
4	6	591	21	599	21

Table 4 Bounce height results in different barrier heights at a 14.5 m of horizontal location

Horizontal distance (m)	Bounce height (m)			
	2 m barrier height	4 m barrier height	5 m barrier height	6 m barrier height
14.5	7	4	3.6	2

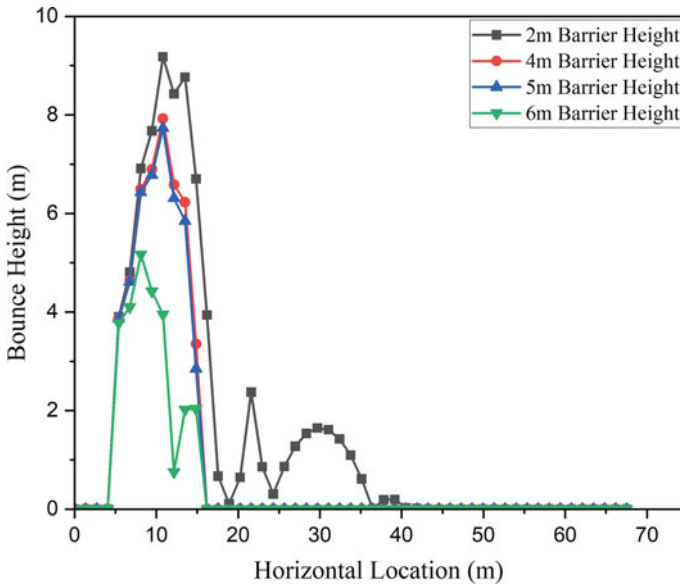


Fig. 10 Bounce height result with various barrier heights

barrier height are insignificant, but Fig. 9 clearly describes that a 5 m barrier height can protect rocks from rolling down on the road. Previous researchers have carried out rock trajectory, end location, bounce height, translational velocity, and kinetic energy calculations based on various sizes and shapes of rock blocks by using the RocFall software [10]. Another researcher in the literature has conducted relations between different rock sizes and mechanisms of rockfall that include calculations of run-out path, bounce height, kinematic energy, and velocity with RocFall [9].

5 Conclusions

The study was carried out to assess the rock mechanisms and propose a mitigation method for the study area. The result from the RocFall model found that this study area had a high-intensity level and rock run-out paths extended beyond the edge of the roadway if a flexible barrier was not applied for this area. Thus, rockfall protection is needed for the mitigation of rockfall events based on the results of rock trajectories.

Compared with the rockfall analysis results of two barrier locations (13.5 and 14.5 m horizontal locations), a 5 m barrier height at a 14.5 m barrier location can catch boulders, whereas a 5 m barrier height at a 13.5 m location cannot protect, and boulders are still bouncing and rolling onto the road.

Regarding rock simulation results after treatment, the RocFall model proved that a flexible barrier is a mitigated solution for rockfall hazards. It is concluded that a 5 m barrier height at a 14.5 m barrier location is a suitable design approach to protect against rock rolling due to the rock failure of the Hoang Sa road.

References

1. Budetta P (2004) Assessment of rockfall risk along roads. *Nat Hazards Earth Syst Sci* 4
2. Duong-Ngo H, Do-Tuan N, Nguyen-Chau L (2020) Retaining system against rockfall near a highway in Vietnam—a case study. In: *Lecture notes in civil engineering*, vol 62. Springer, pp 865–869. https://doi.org/10.1007/978-981-15-2184-3_112
3. Phan T, Khanh LB (2015) Analysis of highway slope failure at Hoang Sa highway, along Son Tra peninsula, Da Nang city: causes and solutions. In: *APSEC 2015 & ACEC 2015 conference*
4. Volkwein A, Schellenberg K, Labiouse V, Agliardi F, Berger F, Bourrier F, Dorren LKA, Gerber W, Jaboyedoff M, Bourrier F (2011) Rockfall characterisation and structural protection—a review. *Nat Hazards Earth Syst Sci* 11:2617–2651. <https://doi.org/10.5194/nhess-11-2617-2011>. HAL Id: insu-00844897. <https://hal-insu.archives-ouvertes.fr/insu-00844897v2>
5. Richard Andrew AD, Bartingale R, Hume H, Haramy K, DeMarco M, Surdahl R, Mohamed K, Barrows R, Anderson S, Siel B, Greer M, Ortiz T (2011) Context sensitive rock slope design solutions 13. Type of report and period covered final report. <http://www.cflhd.gov>
6. Alptekin A, Çelik MÖ, Yakar M, Çelik Ö, Doğan Y. Mapping of a rockfall site with an unmanned aerial vehicle. Development of geographic data model for protected areas of immovable cultural property view project. In: *Advanced engineering days view project*. Mersin Photogramm J. <https://dergipark.org.tr/tr/pub/mephoj>
7. Dadashzadeh N, Duzgun HSB, Yesiloglu-Gultekin N, Bilgin A (2014) ARMA-2014-7177, 01 June 2014. <https://onepetro.org/ARMAUSRMS/proceedings-abstract/ARMA14/All-ARM A14/ARMA-2014-7177/123430>
8. Verma AK, Sardana S, Sharma P, Dinpuia L, Singh TN (2019) Investigation of rockfall-prone road cut slope near Lengpui Airport, Mizoram, India. *J Rock Mech Geotech Eng* 11(1):146–158. <https://doi.org/10.1016/j.jrmge.2018.07.007>
9. Sazid M (2019) Analysis of rockfall hazards along NH-15: a case study of Al-Hada road. *Int J Geo-Eng* 10(1). <https://doi.org/10.1186/s40703-019-0097-3>
10. Tuan NQ (2021) Analysis of rock slope failure and rockfall for preliminary hazard assessment of the cliff at Chau Thoi quarry. In: *Lecture notes in civil engineering*, vol 108. Springer Science and Business Media Deutschland GmbH, pp 230–249. https://doi.org/10.1007/978-3-030-60269-7_12

Volume Loss During the TBM Construction of Metro Line 1, Ho Chi Minh City, Monitoring Data Assessment and New Analytical Model for Prediction



Nguyen Phuong Duy, Nguyen Thach Bich, and Tran Duc Nhiem

Abstract During the TBM construction, volume loss occurs and should be well controlled. This is considered the most critical tunneling factor affecting the movement and ground surface settlement. The empirical method with analytical equations or numerical methods is based essentially on that factor for evaluating the surface settlement trough. This factor, however, depends on different TBM parameters and operation experiences and is sometimes difficult to estimate accurately. Through an assessment of the monitoring data acquired during the construction of metro line 1, Ben Thanh—Suoi Tien of Ho Chi Minh City, this paper proposes an analytical equation for evaluating the volume loss factor based on some basic TBM parameters. A good correlation between the calculation results using this new equation and the in situ monitoring data proves the efficiency of the mathematical model for future prediction in Ho Chi Minh City for example.

Keywords Volume loss · Settlement monitoring · TBM construction · Underground metro

1 Introduction

The volume loss causing by the operation of the TBM construction is considered as the most critical parameter which affects to the ground surface movement. At the design stage, this parameter should be well evaluated in considering the TBM parameters and actual ground conditions. During the construction stage, the volume loss should then be closely controlled to avoid any potential risk of excessive settlement and surrounded building damages. On another hand, the empirical and numerical methods for evaluation of the surface settlement are both considered this value as an

N. P. Duy (✉) · N. T. Bich · T. D. Nhiem
University of Transport and Communications/UTC, Hanoi, Vietnam
e-mail: npdud@utc.edu.vn

© The Author(s), under exclusive license to Springer Nature Singapore Pte Ltd. 2024
T. Nguyen-Xuan et al. (eds.), *Proceedings of the 4th International Conference on Sustainability in Civil Engineering*, Lecture Notes in Civil Engineering 344,
https://doi.org/10.1007/978-981-99-2345-8_43

439

important input parameter. In general, the defining of this parameter is more qualitative based on experiences of the designer and contractor. The accurate values are hard to determine.

The volume loss (V_L) is generally expressed as a percentage of the excavated circular area (V_s) of the tunnel.

$$V_s = V_L \frac{\pi D^2}{4}. \quad (1)$$

It is well known that the surface settlement trough causing by the tunneling excavation maybe approximated by a Gaussian distribution curve as proposed first by Peck [1]:

$$S_x = S_{\max} \exp\left(\frac{-x^2}{2i_x^2}\right); \quad S_{\max} = \frac{V_s}{i_x \sqrt{2\pi}}, \quad (2)$$

where S_x is the vertical surface settlement at the distance x from the tunnel axis. S_{\max} is the maximum surface settlement at tunnel axis. D is the tunnel diameter. i_x is the distance on the ground surface from tunnel axis to the inflection point of the settlement trough. V_L is the volume loss caused by the tunneling process. Equation (2) is later completed by other auteurs: O'Reilly and New [2], Attewell and Woodman [3], Mair and Taylor [4], but volume loss (V_L) is always considered as the most important input value.

Numerical method, usually used to simulate the complex interaction between the tunneling operation and the existing surface structure, is also required V_L factor as an important input parameter. A contraction is generally applied on the contour of the tunnel lining to simulate the volume loss effect due to the tunnel excavation [5].

This paper presents a new proposal analytical equation to evaluate the volume losses caused by Earth Pressure Balanced (EPB) tunneling machine operation during the construction of the first underground metro line in Ho Chi Minh City. The equation is based on a regression process of the surface settlement monitoring data. Different TBM parameters such as face pressures, backfilling grout volume, and pressure were taken into consideration and discussion for potential improvement of the volume loss values determination.

2 TBM Construction for Underground Metro

2.1 Project Background

During the construction of the underground metro of Ho Chi Minh City line 01 between Bason station and Opera House station (Fig. 1), the volume loss is successfully controlled under the contractual limit value of 1%. The surface settlements and

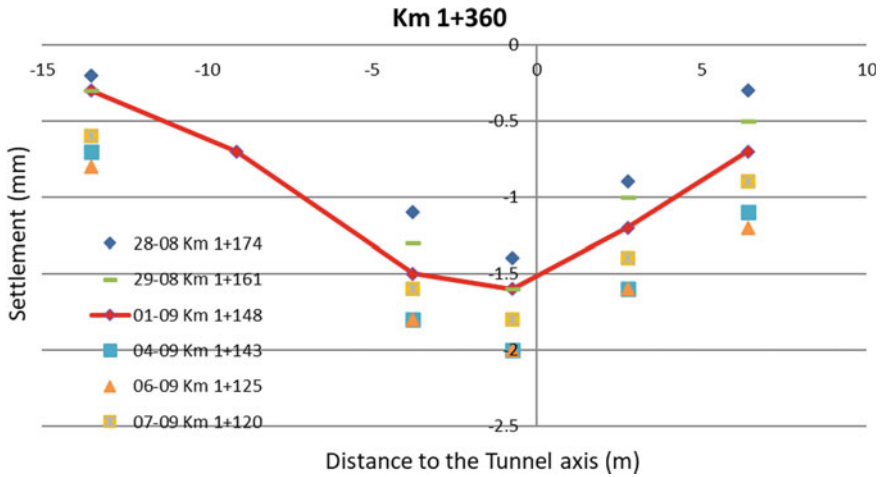


Fig. 3 Typical monitoring data at cross-section Km1 + 360

Table 1 Geotechnical data of the underground section

Layer No.	Depth (m)	Thickness (m)	SPT (N)	Description
1	- 7	7-12	< 10	Alluvium marine clay
2	- 17	7-8	10-18	Alluvium silty fine sand layer 1
3	- 25	8-9	20-22	Alluvium sand layer 2
4	- 33	7-8	20-40	Alluvium sand layer 3
5	N/A	N/A	> 40	Alluvium hard clayey silt

Due to the complexity of the bi-tunneling interaction, only the first tunneling monitoring data had been used for this study (Eastbound track—from Bason to Opera House).

The geotechnical data of that underground section consist of four alluvium sand layers based on a hard-clayed layer. The resume is presented in Table 1.

3 TBM Operation and Volume Loss Measurement

In design practice, the volume loss (V_L) is generally proposed between 0.2 and 0.5% for modern TBM operation. This parameter is the complex combination result of different TBM parameters such as backfill grouting volume and pressure, effective diameter of the cutting wheel, conveyor rotation speed, and then face pressure.

As the tunnel rings were installed behind the TBM tail skin, the tail void created around the segment should be immediately filled with grout material to help prevent

the volume loss annulus and then surface settlement. This operation is called backfill grouting and is carried out simultaneously with the TBM advancement. Both grouting pressure and grouting volume were controlled and recorded during the TBM operation [6].

The tail clearance, which is the space between the outer diameter of the tunnel linings and the inner diameter of the TBM tail skin, is sealed by three rows of wire brushes [6]. During the TBM advancement, the gap between each row of brushes shall be kept full of tail seal grease to prevent grout, groundwater, and soil infiltration into the TBM tail skin and help to protect the tail seals from damage.

Other than backfill grouting and tail skin sealing controlling, the soil removal through the crew conveyer and the cutting wheel rotation were the operations that can affect a lot the front surface pressure but also the volume loss value. The screw conveyor is used to discharge excavated material from the cutting wheel chamber into the sludge pump. The rotation speed of the screw and the opening amount of the gate of the screw conveyor were adjusted to maintain earth pressure in the cutting chamber and excavated face during the TBM drive. The rate of discharge of excavated material from the screw conveyor should be balanced by the rate that excavated material is entering the cutting chamber. During the operation of the tunnel line between Bason station and the Opera House station, the discharged volume and the face pressures were monitored and recorded for controlling [7]. If the indicated earth pressure becomes too low, the rotating speed of the screw conveyor or the amount of the gate opening shall be decreased to increase the pressure being exerted by the TBM.

By accepting that the surface settlement trough may be approximated by a Gaussian distribution curve “Eq. (2)”, the area of the settlement trough can be expressed as a product of maximum surface settlement and the width of the settlement trough.

$$V_L \frac{\pi D^2}{4} = S_{\max} \cdot (i_x \sqrt{2\pi}). \quad (3)$$

Based on the surface settlement monitoring data during the TBM construction and “Eq. (3)”, the volume loss values then can be calculated and presented in Table 2.

4 Prediction

4.1 TBM Parameters

The monitored and recorded surface settlements of the TBM parameters [8] such as the cutting wheel chamber pressures (P_s) and the backfill grouting pressures (P_a) are presented in Table 2. The measured volume loss (V_L) is also calculated by “Eq. (3)” and presented.

Table 2 TBM parameters and surface settlement recorded during the tunneling [8]

Chainage (m)	Depth Z_0 (m)	S_{\max} (mm)	Trough width (m)	Face pressure P_s (MPa)	Grout pressure P_a (MPa)	Vertical stress σ_z (MPa)	Measured V_L (%)
1483	- 14.99	- 5.6	17.0	0.24	0.25	0.309	0.14
1462	- 15.43	- 5.7	20.0	0.22	0.25	0.320	0.16
1420	- 15.98	- 5.0	18.0	0.23	0.27	0.342	0.13
1400	- 17.08	- 4.0	20.0	0.23	0.27	0.352	0.12
1380	- 18.47	- 5.7	22.0	0.22	0.30	0.370	0.18
1360	- 19.34	- 1.8	20.0	0.30	0.31	0.387	0.05
1325	- 20.86	- 2.4	18.0	0.27	0.31	0.417	0.06
1304	- 21.77	- 2.5	17.0	0.27	0.30	0.435	0.06
1284	- 21.87	- 2.2	15.0	0.30	0.33	0.437	0.05
1264	- 21.97	- 1.6	17.0	0.32	0.34	0.440	0.04
1243	- 22.08	- 1.9	17.0	0.30	0.33	0.442	0.05
1203	- 22.28	- 2.5	20.0	0.27	0.33	0.446	0.07
1183	- 22.44	- 3.0	16.0	0.27	0.33	0.449	0.07
1163	- 22.61	- 6.1	18.0	0.22	0.29	0.452	0.16
1123	- 22.94	- 5.0	22.0	0.23	0.33	0.459	0.16
1063	- 23.43	- 4.1	18.0	0.25	0.34	0.469	0.11
1043	- 23.43	- 3.9	20.0	0.25	0.34	0.472	0.11
1003	- 23.92	- 3.6	21.0	0.24	0.30	0.478	0.11
980	- 24.23	- 5.3	20.0	0.23	0.30	0.485	0.15
965	- 24.44	- 7.0	16.0	0.22	0.25	0.489	0.16
945	- 24.71	- 4.1	20.0	0.24	0.30	0.494	0.12
925	- 24.98	- 4.5	18.0	0.24	0.30	0.500	0.12
900	- 25.32	- 4.1	20.0	0.24	0.30	0.506	0.12
890	- 25.39	- 6.6	22.0	0.21	0.27	0.508	0.21
860	- 25.60	- 1.7	22.0	0.27	0.34	0.512	0.05
842	- 25.37	- 1.3	26.0	0.28	0.35	0.507	0.05
828	- 25.19	- 1.7	20.0	0.28	0.35	0.504	0.05
815	- 25.02	- 3.8	20.0	0.24	0.35	0.500	0.11

4.2 New Proposal Equation for Prediction

We propose a new equation to evaluate the value of volume loss (V_L) as a function of the cutting wheel chamber pressure (P_s), the backfill grouting pressure (P_a), and the backfill grouting volume (V) with the form as below:

Table 3 Proposed new analytic model parameters

K	β_1	β_2	β_3
31.6×10^{-3}	2.3	0.8	0.7

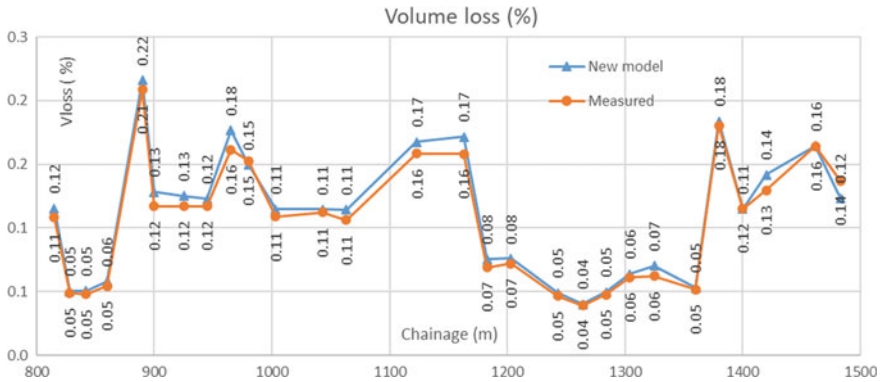


Fig. 4 Volume loss (%) measured versus new equation results

$$V_L = K \cdot \left(\frac{1}{P_s - K_0 \sigma_z} \right)^{\beta_1} \left(\frac{1}{\sigma_z - P_a} \right)^{\beta_2} \left(\frac{1}{V} \right)^{\beta_3} \tag{4}$$

Using the linear regression function process on the logarithm of the three elements, we found the values of K , β_1 , β_2 , and β_3 , respectively, presented in Table 3.

Equation (4) then can be expressed as:

$$V_L = \frac{31.6 \times 10^{-3}}{(P_s - K_0 \sigma_z)^{2.3} (\sigma_z - P_a)^{0.8} V^{0.7}} \tag{5}$$

The volume losses calculated using the new proposal equation at different monitored sections suit very well the in situ measured values proving the efficiency of the new analytic model. The comparison is presented in Fig. 4.

5 Conclusion and Discussion

The volume loss induced by the tunneling is considered as an important parameter which may cause surface settlement and damage to the surrounding buildings. Analytical and numerical methods for evaluating the surface settlement during the TBM construction are both considered volume loss as the important input data. This value, however, is determined qualitatively based on the experiences of the designers and contractors. Their values are about 0.2–0.5% for modern TBM.

During the construction of the underground metro line 1 of Ho Chi Minh City, the section between the Bason station and Opera House station, the surface settlement but also the EPB TBM parameters such as face pressure, backfill grouting pressure, and volume had been monitored and recorded. An assessment of those data allows calculating the measured volume loss. It is clear that all the measured values are successfully well controlled below the contractual limit of 1%.

A new analytical equation is also proposed in order to determine the values of volume loss as a function of the tunnel depth, the face pressure, backfill grouting pressure and volume. Then, the results of volume loss evaluation are compared to the measurement values. This quality concordance proves the efficiency of the new proposal equation and can be applied for future project in similar working and geotechnical conditions.

References

1. Peck RB (1969) Deep excavation and tunnelling in soft ground. In: Proceedings of the 7th international conference on soils mechanics and foundation engineering. State of the art, Mexico City, pp 225–290
2. O'Reilly MP, New BM (1982) Settlements above tunnels in the United Kingdom—their magnitude and prediction. In: Jones MJ (ed) Tunnelling'82. London, pp 173–181
3. Attewell PB, Woodman JP (1982) Predicting the dynamic of ground settlement and its derivatives caused by tunnelling in soil. *Ground Eng* 15(8):13–36
4. Mair RJ, Taylor RN (1997) Bored tunnelling in the urban environment. In: Proceedings of the 14th international conference on soil mechanics and foundations engineering, vol 4. Balkema, Hamburg, pp 2353–2385
5. Wang XT, Schmettow TV, Chen XS, Xia CQ (2022) Prediction of ground settlements induced by twin shield tunnelling in rock and soil—a case study. *Undergr Space* 7:623–635
6. Shimizu-Maeda J-O (2014) Proposed construction method statement—Ho Chi Minh City urban railway construction project. In: Tech 17, Hanoi
7. Shimizu-Maeda JO (2019) Ground and building monitoring report for shield tunnel (TBMS). UMR11-CP1b-TBMS-MON-RPT-00568-A. Ho Chi Minh City
8. Bich NT, Le LT, Duy NP (2020) Numerical analysis of the influence of shield-gap pressure on the volume loss and surface settlement of the TBM tunneling. In: Proceedings of the 3rd international conference on sustainability in civil engineering. Lecture notes in civil engineering. Springer, pp 222–228

Proposing an Analytical Equation to Evaluate the Maximum Surface Settlement Due to TBM Construction Based on the Monitoring Data from Ho Chi Minh City Metro Construction



Nguyen Thach Bich, Nguyen Phuong Duy, and Tran Duc Nhiem

Abstract The most concerns during the underground metro construction by TBM method is the ground movement and surface settlement which may cause the damages to the surrounded buildings. The maximum surface settlement should then be monitored and controlled by setting the different alarming levels. The prediction of the maximum surface settlement is in the critical important. Analytical or numerical method could be used for the evaluation of the value. In this paper, throughout the acquired monitoring data of the maximum surface settlement during the construction of the Ben Thanh-Suoi Tien, underground metro section of Ho Chi Minh City, an analytical prediction equation was proposed. A very good correlation between the calculation results using this new equation and the site monitoring data proves the efficiency of the mathematical model for future prediction in very similar condition. The influences of different operation parameters are then discussed.

Keywords Maximum settlement · TBM construction · Settlement monitoring · Underground metro

1 Introduction

During the construction of the underground section of Ho Chi Minh metro line 1 between Bason station and Opera House station, surface settlement occurred due to the operation of the Earth Pressure Balance Tunnel Boring Machine (EPB TBM) was successfully controlled under the contractual limit value of 20 mm. At the design stage, the ground movement needs to be evaluated in order to prevent or avoid any possibility of excessive surface settlement and/or surrounding buildings damage. The

N. T. Bich · N. P. Duy (✉) · T. D. Nhiem
University of Transport and Communications/UTC, Hanoi, Vietnam
e-mail: npduy@utc.edu.vn

© The Author(s), under exclusive license to Springer Nature Singapore Pte Ltd. 2024
T. Nguyen-Xuan et al. (eds.), *Proceedings of the 4th International Conference on Sustainability in Civil Engineering*, Lecture Notes in Civil Engineering 344,
https://doi.org/10.1007/978-981-99-2345-8_44

447

estimated values of maximum surface settlement allow also to setup the alarming thresholds to follow-up during the TBM operation.

The surface settlement caused by TBM construction has generally the origin from ground disturbance ahead the cutting wheel, voids created between the cutting wheel and the protection shield, and between the inside of tail skin and the permanent linings. These voids space needs to be immediately fill with grout material to help to prevent the movement of surrounding ground toward the gap which is the cause of the surface settlement. This action is to reduce the void space created during the TBM operation or the volume loss.

With the EPB machine such as the one used in Ho Chi Minh City for the metro line 1, the screw conveyor is used to discharge excavated material from the cutting wheel chamber into the sludge pump. The volume loss (V_L) then depends on the rotation speed of the screw and the opening amount of the gate of the screw conveyor.

Based on the ground movement monitoring data such as the ground surface settlements and the volume loss but also different TBM operation geometries including the tunnel diameter (D), surcharge on the surface (Q), unit weight of the soil (γ) and the Young modulus (E) of ground acquired during the tunnel construction, this paper proposes a new analytical equation for evaluating the maximum surface settlement (S_{\max}). The comparison between the in-situ measurement data in Ho Chi Minh City with the calculation results using the new equation shows a very good concordance proving the efficiency of the new analytical model.

2 Surface Settlement Evaluation

For evaluating the surface settlement due to the TBM construction, the traditional analytical method is considered as the most practical approach. Many researchers have attempted to develop and improve the different analytical models. The method is essentially based on the on-site observation of the sharp of the surface settlement trough and field measurement [1, 2]. The first mathematical model (Eq. 1) to describe the curve of the surface settlement was proposed by Peck [2] and Schmidt [3]. This is based on the assumption that the surface movement induced by a single tunnel construction can be represented by a Gaussian distribution. The curve is later on confirmed by many site measurements.

$$S_x = S_{\max} \exp\left(\frac{-x^2}{2i_x^2}\right); \quad S_{\max} = \frac{V_L \cdot A_s}{i_x \sqrt{2\pi}} \quad (1)$$

where S_x is the settlement at the distance x from tunnel axis. V_L is the volume loss, determined in percentage of the tunnel excavation area A_s . i_x is the distance at ground level from the tunnel axis to the inflection point of the curve.

Table 1 Different analytical model to predict the maximum surface settlement S_{max}

Researcher (year)	Equation for S_{max}	Inflection point	Remarks
Peck (1969) [2]	$S_{max} = \frac{V_L \cdot A_s}{i_x \sqrt{2\pi}}$	$i_x = K Z_0$	Based on the observation and measurements
Attewell (1977) [7]	$S_{max} = \frac{V_L \cdot A_s}{i_x \sqrt{2\pi}}$	$\frac{i_x}{R} = \alpha \cdot \left(\frac{Z_0}{2R}\right)^n$	Based on real cases observation in England
Atkinson and Potts (1977) [5]	$S_{max} = \frac{V_L \cdot A_s}{i_x \sqrt{2\pi}}$	$i_x = 0.25(Z_0 + R)$	Based on the real case observation and experimental model
Clough and Schmidt (1981) [6]	$S_{max} = \frac{V_L \cdot A_s}{i_x \sqrt{2\pi}}$	$\frac{i_x}{R} = \alpha \cdot \left(\frac{Z_0}{2R}\right)^n$	Based on the real cases observation in United States
O'Reilly and New (1982) [3]	$S_{max} = \frac{V_L \cdot D^2 \cdot \sqrt{2\pi}}{8 \cdot i_x}$	$i_x = 0.43 Z_0 + 1.1$	Based on real cases observation in England
Mair and al. (1993) [4]	$S_{max} = 1.252 \frac{V_L \cdot R^2}{i_x}$	$i_x = 0.5 Z_0$	Based on full scale monitoring data and centrifuge model

The determination of the S_{max} is later on proposed by many researchers for improvement the results based on fields observation and measurements. Some published [2–6] works are presented in Table 1.

It's evident that the analytical approach is generally simple and cannot accommodate all construction parameters or considering complex ground/building interaction. However, the approach is very useful for quick evaluation of the short-term ground movement at the early design stage and field construction. The main parameters are considering as most influenced on the maximum settlement and appeared on the prediction models: tunnel diameter, depth of the tunnel, volume loss, and the distance to inflexion point of the settlement curve.

3 Monitoring Data

3.1 Ben Thanh–Suoi Tien Underground Metro Section

The underground section of Ben Thanh–Suoi Tien metro line consists of two segments: the TBM segment between Opera House and Ba Son stations with the total length of 781 m and the cut and cover segment from Ba Son station. At the Ba Son station, the two metro tubes are horizontally arranged in parallel when at Opera House station, they are vertically arranged in parallel (Figs. 1 and 2).

The geotechnical condition of the underground section is dominated by four (04) layers of alluvium sand all basing on the hard clayed (Table 2).

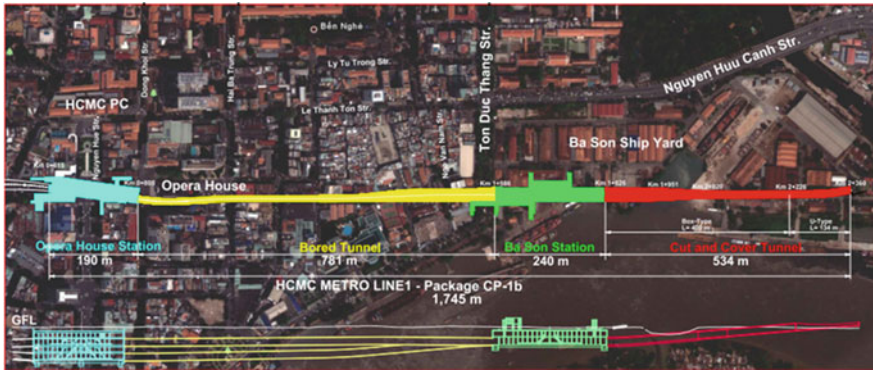


Fig. 1 Underground section between Bason station and Opera House station, Ho Chi Minh City metro line 1

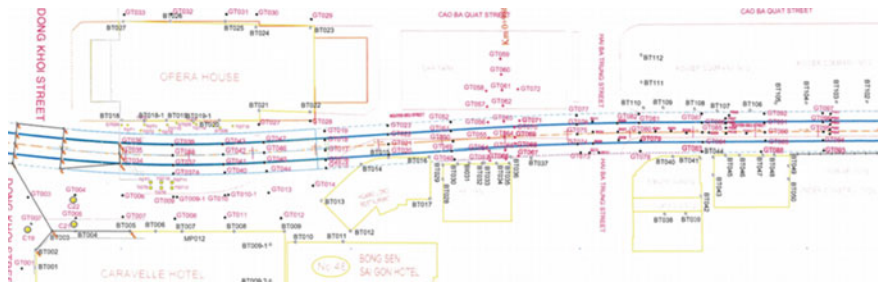


Fig. 2 Surface settlement monitoring layout near the Opera House station [8]

Table 2 Geotechnical data of the underground section

Layer No.	Depth (m)	Thickness (m)	SPT (N)	Description
1	- 7	7-12	< 10	Alluvium marine clay
2	- 17	7-8	10-18	Alluvium silty fine sand layer 1
3	- 25	8-9	20-22	Alluvium sand layer 2
4	- 33	7-8	20-40	Alluvium sand layer 3
5	N/A	N/A	> 40	Alluvium hard clayey silt

3.2 Monitoring Data Assessment

The monitored and recorded maximum surface settlement (S_{max}), also the TBM geometrical parameters like cutting wheel diameter (D), surcharge (Q), unit weight of ground (γ), and the volume loss (V_L) are presented in Table 3.

Analytical models were then used for comparing with the monitoring data, and the results are present in Fig. 3 on a typical cross section. Figure 4 presents the calculated

Table 3 TBM parameters recorded during the operation and advancement

Chainage (m)	Depth Z_0 (m)	S_{max} (mm)	Trough width (m)	Volume loss V_L (%)	γ (kN/m ³)	Q (kN/m)	D (m)
1483	- 14.99	- 5.6	17.0	0.14	20	10	6.65
1462	- 15.43	- 5.7	20.0	0.16	20	10	6.65
1420	- 15.98	- 5.0	18.0	0.13	20	10	6.65
1400	- 17.08	- 4.0	20.0	0.12	21	10	6.65
1380	- 18.47	- 5.7	22.0	0.18	21	10	6.65
1360	- 19.34	- 1.8	20.0	0.05	21	10	6.65
1325	- 20.86	- 2.4	18.0	0.06	21	10	6.65
1304	- 21.77	- 2.5	17.0	0.06	21	10	6.65
1284	- 21.87	- 2.2	15.0	0.05	19	10	6.65
1264	- 21.97	- 1.6	17.0	0.04	19	10	6.65
1243	- 22.08	- 1.9	17.0	0.05	19	10	6.65
1203	- 22.28	- 2.5	20.0	0.07	19	10	6.65
1183	- 22.44	- 3.0	16.0	0.07	20	10	6.65
1163	- 22.61	- 6.1	18.0	0.16	20	10	6.65
1123	- 22.94	- 5.0	22.0	0.16	20	10	6.65
1063	- 23.43	- 4.1	18.0	0.11	20	10	6.65
1043	- 23.43	- 3.9	20.0	0.11	20	10	6.65
1003	- 23.92	- 3.6	21.0	0.11	20	10	6.65
980	- 24.23	- 5.3	20.0	0.15	20	10	6.65
965	- 24.44	- 7.0	16.0	0.16	20	10	6.65
945	- 24.71	- 4.1	20.0	0.12	20	10	6.65
925	- 24.98	- 4.5	18.0	0.12	20	10	6.65
900	- 25.32	- 4.1	20.0	0.12	20	10	6.65
890	- 25.39	- 6.6	22.0	0.21	21	10	6.65
860	- 25.60	- 1.7	22.0	0.05	21	10	6.65
842	- 25.37	- 1.3	26.0	0.05	21	10	6.65
828	- 25.19	- 1.7	20.0	0.05	21	10	6.65
815	- 25.02	- 3.8	20.0	0.11	21	10	6.65

maximum settlement in the longitudinal direction of the tunnel in comparing to the measured values. We observe that existing analytical models seem overestimated the ground surface settlement and the maximum settlement measured during the EPB TBM construction of the Ho Chi Minh metro line 1 underground section.

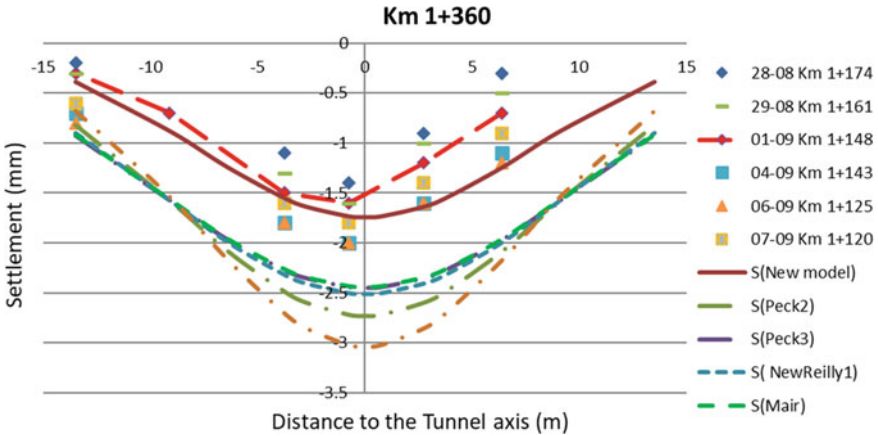


Fig. 3 Measured surface settlement and prediction using different analytic model

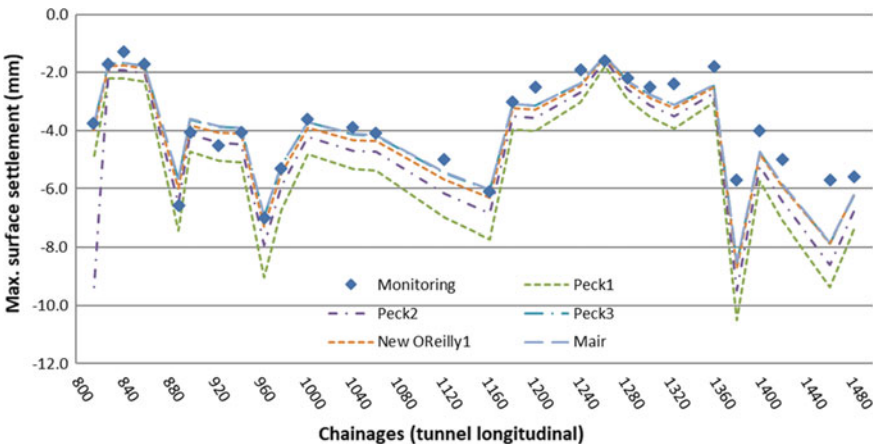


Fig. 4 Results from different available analytical models comparing to the monitored maximum surface settlement

4 New Equation Proposal

We propose a new equation to evaluate the value of maximum settlement (S_{max}) as a function of the volume loss (V_L), the tunnel excavation diameter (D), the depth of the tunnel axis (Z_0), unit weight of soils (γ), Young modulus of the ground and surface loading (Q), with the form as below:

$$S_{max} = (V_L)^{\beta_1} \left(\frac{D \cdot Q}{Z_0} \right)^{\beta_2} \left(\frac{E}{\gamma} \right)^{\beta_3} \tag{2}$$

Table 4 Proposed new analytic model parameters

β_1	β_2	β_3
0.96	1.65	1.7

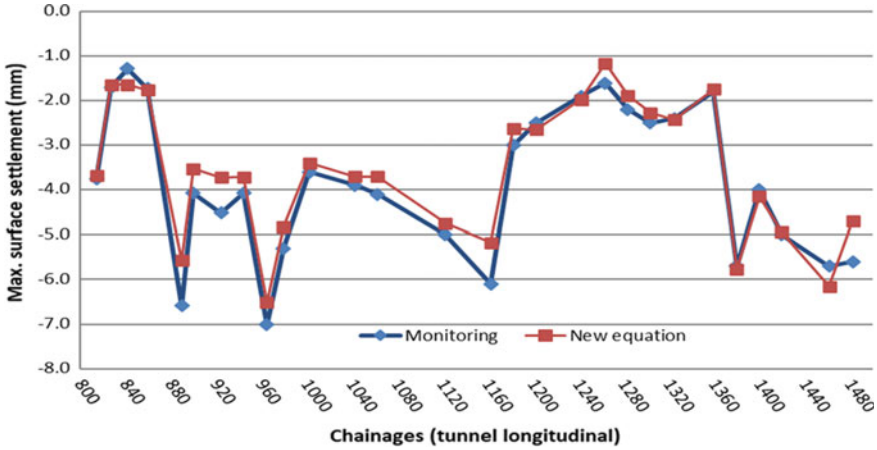


Fig. 5 Comparison between the monitoring data and the new proposal analytical model for predicting the maximum surface settlement

Using the linear regression function process on the logarithm of the three elements, we found the values of β_1 , β_2 , and β_3 , respectively, presented in Table 4.

Equation (3) then can be expressed as:

$$S_{\max} = (V_L)^{0.96} \left(\frac{D \cdot Q}{Z_0} \right)^{1.65} \left(\frac{E}{\gamma} \right)^{1.7} \tag{3}$$

The maximum settlement (S_{\max}) calculated using the new proposal equation at difference monitored sections suite very well to the in-situ measured values proving the efficiency of the new analytic model. Average error is about 2.99%. The comparison is presented in Fig. 5.

5 Conclusion and Discussion

The surface settlement induced by the TBM construction is considered as the critical important which may damage the surrounding buildings. Analytical and numerical methods are both available for evaluating the surface settlement during the TBM construction. Analytical approach, however, is considering as the most useful in

engineering practice. Many researchers had attempting to develop different mathematical models to predict the settlement based on field observation and measurement data.

During the construction of the underground metro line 1 of Ho Chi Minh City, section between the Bason station and Opera House station, the surface settlement and volume loss had been monitored and recorded. Different geometrical parameters of the TBM construction had been measured.

Based on the monitoring data and the measured geometrical parameters, a new analytical equation is proposed to evaluate the values of maximum surface settlement. The results of the new equation are then compared to the monitoring data. The very good concordance proves the efficiency of the new proposal equation and can be apply for future project in similar working and geotechnical conditions.

References

1. Martos F (1958) Concerning an approximate equation of the subsidence trough and its time factors. In: International strata control congress, Leipzig, pp 191–205
2. Peck RB (1969) Deep excavation and tunnelling in soft ground. In: Proceedings of the 7th international conference on soils mechanics and foundation engineering. State of the art, Mexico City, pp 225–290
3. O'Reilly MP, New BM (1982) Settlements above tunnels in the United Kingdom—their magnitude and prediction. In: Jones MJ (ed) Tunnelling'82, London, pp 173–181
4. Mair RJ, Taylor RN, Bracegirdle A (1993) Subsurface settlement profiles above tunnels in clays. In: *Geotechnique* (43), issue 2, pp 315–320
5. Atkinson JH, Potts DM (1977) Subsidence above shallow tunnels in soft ground. In: *Journal geotechnical engineering division, ASCE, Vol: GT4*, pp 307–325
6. Clough GW, Schmidt B (1981) Design and performance of excavations and tunnels in soft clay. In: *Developments in Geotechnical Engineering*, 20, pp 567–634
7. Attewell PB (1977) Ground movements caused by tunneling in soil. In: *Conference on Large Ground Movements and Structure*. Wiley, New York, pp 812–948
8. Shmz-Maeda JO (2019) Ground and building monitoring report for shield tunnel (TBMS). UMRLT1-CP1b-TBMS-MON-RPT-00568-A. Ho Chi Minh City

EPS Geofam Embankment on Soft Ground—A Full-Scale Test



Quoc-Bao Truong, Hoang-Kien Pham, Anh-Tuan Vu, Satoshi Kobayashi,
and Duy-Canh Nguyen

Abstract Expanded polystyrene (EPS) geofam has been applied widely to diminish consolidation settlement of highway embankments on soft ground for over four decades in various countries throughout the world. With the advantage of being a lightweight fill material, whose weight is only 1–2% compared with rock or concrete with the same volume but can withstand relatively large compressive stresses, is molded into standard-sized blocks in the factory. However, the EPS geofam is quite new and has not been widely used in Vietnam. In this study, an experimental study was conducted to compare an EPS embankment on the soft ground with a soil embankment through full-scale field measurements at Ba Ria-Vung Tau Province, Vietnam. The study results indicated that the settlement of EPS embankment is significantly reduced comparing with that of the soil embankment.

Keywords EPS geofam · Embankment · Soft ground · Settlement · Full-scale test

1 Introduction

Fills and embankment structures resting on the soft soil of low bearing capacity frequently suffer from excessive settlement and instability problems caused by imposed self-weight. A lot of ground improvement techniques have been used

Q.-B. Truong · A.-T. Vu (✉)
Le Quy Don Technical University, Hanoi, Vietnam
e-mail: vuanhtuan@mta.edu.vn

H.-K. Pham
University of Transport and Communications, Hanoi, Vietnam

S. Kobayashi
Okasan Livic Co. Ltd., Tokyo, Japan

D.-C. Nguyen
Ngo Quyen Technical University, Binhduong, Vietnam

feasible and effective to diminish consolidation settlement such as vacuum consolidation by vertical drains beneath circular embankments [1], geotextile-encased granular columns supporting test embankments on soft deposit [2], geosynthetics and pile walls [3], geotextile-encased granular columns [4], lightweight fill material [5–8]. Also, EPS geofom was invented during the second half of the twentieth century with the advantage of being a lightweight fill material, and is molded into standardized blocks in the factory [9, 10]. EPS blocks were first used as a material for an embankment foundation in Oslo, Norway in 1972 [11]. The EPS method has been applied widely to diminish consolidation settlement of highway embankments on soft ground for over four decades in various countries throughout the world. Especially, developing countries like Vietnam are facing challenges with infrastructure projects on soft ground in the immense areas of the highway embankments. On the other hand, the EPS geofom is quite new and has not been widely used in Vietnam. The method of constructing embankments using EPS geofom is necessary to study the applicability in civil engineering in Vietnam conditions. In this study, an experimental study on EPS embankment on the soft ground using two different densities of 0.2 (D-20) and 0.24 (DX-24H) kN/m³ compared with a soil embankment through full-scale field measurements in the long term.

2 Description of Full-Scale Tests

The full-scale tests for the EPS embankment (assembling by EPS geofom blocks) and the soil embankment (filling by soil) were constructed at Ba Ria-Vung Tau Province, Vietnam. The soft ground includes four layers as shown in Table 1.

A soil embankment of 4.0 m crest width with 1.5:1 side slopes and the EPS embankment have been chosen to compare the consolidation settlement of two embankments during and after filling up to the final level, as shown in Fig. 1. The material properties of the EPS embankment summarised in Table 2. The height of the two embankments is 3.4 m, and the construction time of the embankment is 30 days in Table 3. Monitoring is divided into two phases: testing with short-term

Table 1 Geotechnical parameters for the soft ground

No.	Layer	Thickness (m)	γ (kN/m ³)	e_0	C_c	C_s	P_c (kPa)	SPT N -value
1	Filling sand	0.5	19.0					1/30
2	Organic silt	3.4	15.4	1.848	0.720	0.123	46.4	0.3/30
3	Clay with sand	4.8	19.8	0.667	0.147	0.045	187.75	7.5/30
4	Silty sand	11.4	20.0					12/30

and long-term monitoring. In the long-term monitoring, the settlement and deformation of the embankment during the construction phase are measured for 8 months. The frequency of measurements was conducted four times per month. Figure 2 shows the pictures of the full-scale test. In the short term, we conducted two measurement times from position 0 to 11 and vice versa on the EPS embankment. The dump truck (20 metric tons) stopped for 1 min per measurement position when the truck’s rear axle was at the measurement position. The truck moved to every point, stopped, and turned off the engine until a stable measurement result is obtained. To investigate the effectiveness of settlement and stress with a live load (20 metric tons), the short-term vehicle loading was only conducted on the EPS embankment in this full-scale test.

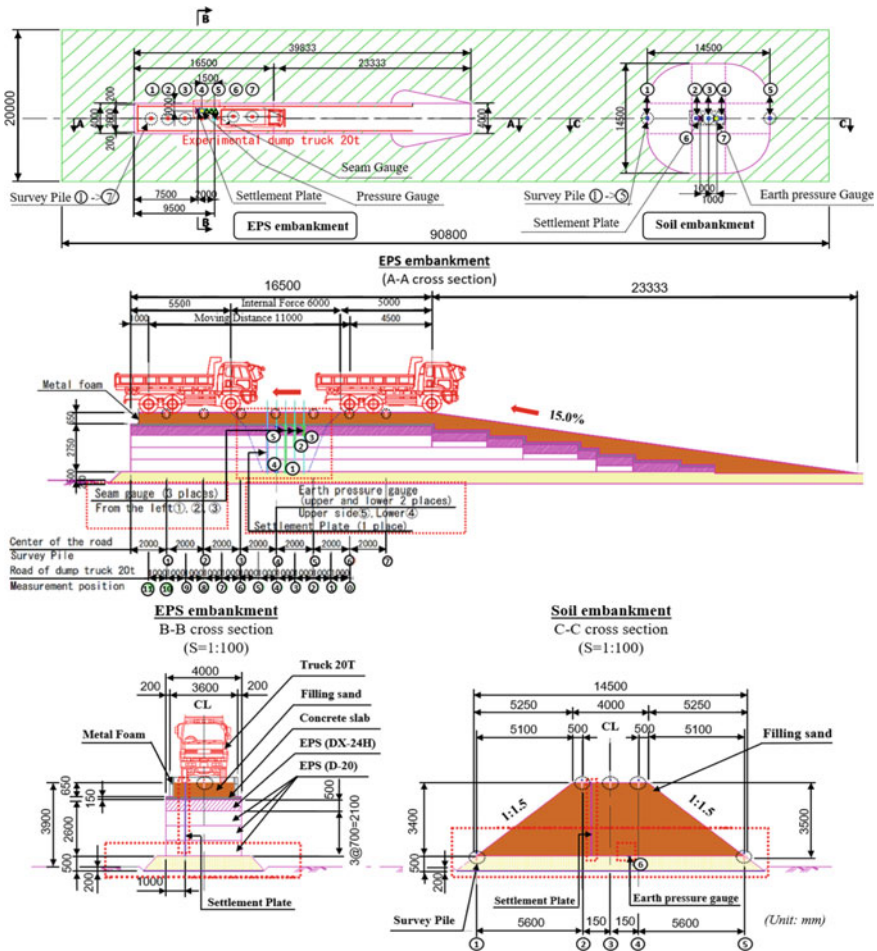


Fig. 1 Layout of the full-scale embankment test with monitoring devices

Table 2 Design parameters for embankment material

Layer	Filling sand	Soil	Concrete	EPS block (D-20)	EPS block (DX-24H)	Sand
<i>H</i> (m)	3.4	0.65	0.15	2.1	0.5	0.5
γ (kN/m ³)	19.0	19.0	24.0	0.20	0.24	19.0

Table 3 The period of the construction phase

EPS embankment			Soil embankment		
No.	Phase	Time (days)	No.	Phase	Time (days)
1	Laying sand and gauge installment	15	1	Laying sand and gauge installment	15
2	Install EPS blocks	4	2	Filling soil to a height of 1.5 m	6
3	Cast concrete	5	3	Filling soil to a height of 2.5 m	7
4	Filling soil	6	4	Filling soil to a height of 3.5 m	1
			5	Filling soil to a height of 3.9 m	1
	Total	30		Total	30



Fig. 2 Full-scale test of embankments and monitoring equipment at Ba Ria-Vung Tau province, Vietnam

3 Results and Discussions

3.1 Short-Term Vehicle Loading

The short-term vehicle loading was conducted on the EPS embankment 3 months after the construction phase. The frequency of measurements was conducted when the truck had moved forward every 1 m, and the moving distance of the truck was 11 m, as shown in Fig. 3.

Figure 4 shows the results of the short-term vehicle loading on the EPS embankment. It is obvious to see that the deformation insignificantly occurred with the maximum value at position 4 in the seam gauge 1 (deformation of four layers of EPS) of about only 1.7 mm. Also, it was observed from the test that the compressive strain completely returns to the value 0 when unloading.

Figure 4b presents the variation of vertical pressure in EPS blocks when the position of the applied load (truck 20 T) changes. The maximum value of vertical pressure due to live load at the upper level (gauge 5) and the lower level (gauge

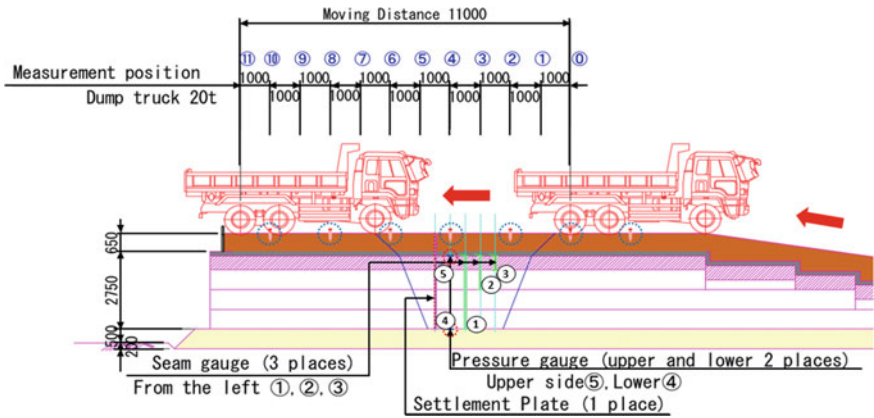


Fig. 3 Layout and method of conducting vehicle loading

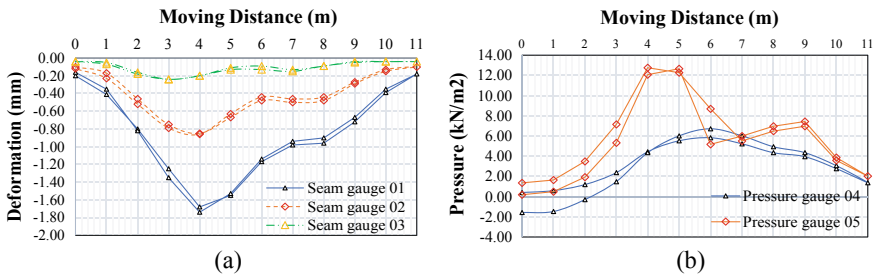


Fig. 4 Deformation of EPS block and vertical pressure in a short-term load test

Table 4 The maximum value of deformation

	Experimental value (mm)			Design value (mm)		
	Gauge 1	Gauge 2	Gauge 3	Gauge 1	Gauge 2	Gauge 3
Dead load	8.8	4.9	1.8	7.7	3.1	0.8
Live load	1.7	0.9	0.2	6.4	3.3	1.0
Total	10.5	5.8	2.0	14.1	6.4	1.8
Strain (%)	0.40	0.48	0.40	0.54	0.53	0.36

4) is at 12.76 kN/m^2 , and 6.72 kN/m^2 , respectively. These values are much smaller compared with the maximum value of the design vertical pressure of EPS geofoam material (19.92 kN/m^2). Similarly, Table 4 presents the comparison between the maximum value of experimental deformation and the design value. The measured value of the strain caused by the live load is less than the design value. In addition to the absolute deformation, the relative strain is also calculated and shown in Table 4. Note here that the strain value of the EPS blocks measured from the load test is less than 0.5%. These values are much smaller compared with the elastic limit of EPS geofoam material (normally 1%). From the experimental values of both strain gauges and pressure gauges, it is seen that both strain and stress obtained in the EPS embankment are within the design value. Thus, EPS material is fully functional to be used as embankment material. The experimental results also indicate that the design is safe enough.

3.2 Long-Term Monitoring

Figure 5 shows the results of the long-term test on the soil embankment and the EPS embankment. It is clear to see that the final settlement of the EPS embankment (38 mm) was significantly reduced compared with that of the soil embankment (261 mm), indicating the high effectiveness in diminishing the settlement of EPS in road embankment construction on soft ground. Also, it is interesting to see in Fig. 5b that the pressure acting on the natural ground (under the embankment) in the case of EPS is much smaller than that in the case of soil.

Figure 6 shows the deformation of the EPS during the long-term test. The deformation of EPS increases steadily during the construction phase and attains the maximum value at the end of the construction phases (in 30 days). Then, the deformation of EPS remains stable until the end of the long-term test.

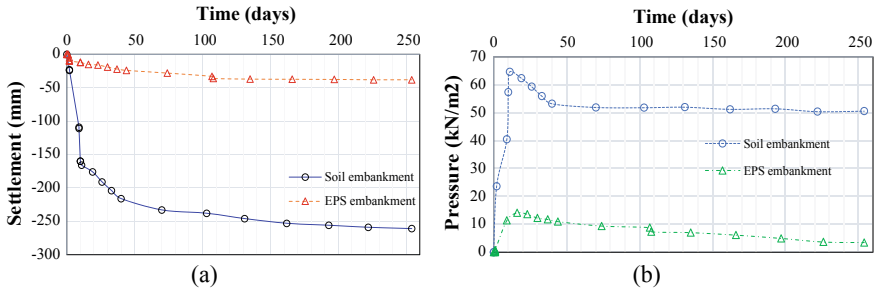


Fig. 5 The curves of settlement and vertical pressure during the long-term

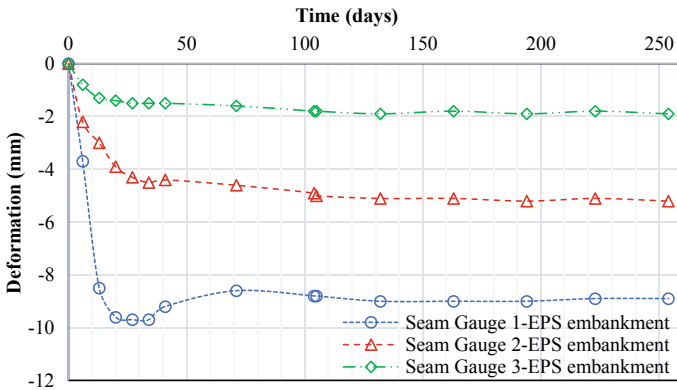


Fig. 6 Deformation of the EPS during the long-term test

4 Conclusion

Full-scale tests of EPS and soil embankments were conducted to investigate the effectiveness in diminishing the settlement of EPS compared to traditional backfilling in the long term. The testing results indicated that the settlement of EPS embankment was significantly reduced compared with that of soil embankment, and both strain and stress in the EPS were in the range of allowable values.

References

- Indraratna B, Kan ME, Potts D, Rujikiatkamjorn C, Sloan SW (2016) Analytical solution and numerical simulation of vacuum consolidation by vertical drains beneath circular embankments. *Comput Geotech* 80:83–96

2. Almedia MSS, Hosseinpour I, Riccio M, Alexiew D (2014) Behavior of geotextile-encased granular columns supporting test embankment on soft deposit. *J Geotech Geoenviron Eng* 141(3):04014116
3. Zheng JJ, Chen BG, Lu YE, Abusharar SW, Yin JH (2009) The performance of an embankment on soft ground reinforced with geosynthetics and pile walls. *Geosynth Int* 16(1):1–10
4. Hosseinpour I, Almedia MSS, Riccio M (2015) Full-scale load test and finite-element analysis of soft ground improved by geotextile-encased granular columns. *Geosynth Int* 22(6):428–438
5. Baykal G, Edincliler A, Saygili A (2009) Highway embankment construction using fly ash in cold regions. *Resour Conserv Recycl* 42:209–222
6. Yoon S, Prezzi M, Siddiki NZ, Kim B (2006) Construction of a test embankment using a sand-tire shred mixture as fill material. *Waste Manage* 26:1033–1044
7. Umashankar B, Mouli S, Hariprasad C (2015) Settlement of embankment constructed with geofoam. In: Iskander M, Suleiman MT, Anderson JB, Laefer DF (eds) *Proceedings of the international foundations congress and equipment expo 2015*. American Society of Civil Engineers, pp 161–170
8. Horvath JS (1994) Expanded polystyrene (EPS) geofoam: an introduction to material behavior. *Geotext Geomembr* 13(4):263–280
9. Aabøe R (1985) 13 years of experience with expanded polystyrene as a lightweight fill material in road embankments. In: *The 1st international conference on EPS geofoam blocks in construction applications*, Oslo, Norway
10. Aabøe R (2011) 40 years of experience with the use of EPS geofoam blocks in road construction. In: *The 4th international conference on geofoam blocks in construction applications*, EPS 2011, Lillestrøm, Norway
11. Alfheim S, Flaate K, Refsdal G et al (2011) The first EPS block road embankment—1972. In: *The 4th international conference on geofoam blocks in construction applications—EPS 2011*, Lillestrøm, Norway, 6–8 June 2011

Earthquake Resistance of Caisson-Type Quay Wall Renovated by Grouting and Deepening: Geo-Centrifuge Test



Anh-Dan Nguyen and Young-Sang Kim

Abstract This study introduced a solution to renovate a caisson-type gravity quay wall by grouting and deepening and investigated its dynamic behavior using the geo-centrifuge test. The experiments were conducted for both existing and renovated quay walls. During the tests, the acceleration and caisson displacements were recorded. The results indicated that both models increased acceleration from the base to the surface. However, the increase in the renovated quay wall was lower than that of the existing case. The deformed shape of the caissons was different between the two cases. In the case of renovated quay wall, the caisson slipped horizontally, while in the existing case, it rotated to the seaside. The displacements of the caisson significantly decreased after renovation, implying that damage resistance increased.

Keywords Earthquake · Renovated quay wall · Centrifuge test · Grouting · Deepening

1 Introduction

Caisson-type quay wall is a common type of gravity quay wall which consists of large hollow cellular concrete elements with filling material inside placed on a foundation, including a layer of gravel or rubble on top of each other [2]. The study on the earthquake performance of caisson-type gravity quay walls has been mentioned in various previous papers. Al-Homoud and Whitman [1] compared the tilting of the gravity quay wall determined by the finite element model and centrifuge test to suggest a suitable model used in the numerical analysis. In addition, sensitivity analyses were performed for an experimental case to clarify the change in boundary

A.-D. Nguyen (✉)

Faculty of Civil Engineering, University of Transport and Communications, Hanoi, Vietnam
e-mail: nadan@utc.edu.vn

Y.-S. Kim

Department of Civil Engineering, Chonnam National University, Gwangju, South Korea
e-mail: geoyoskim@jnu.ac.kr

conditions and rotational stiffness of the wall. Shiozaki et al. [7] studied the seismic response of hybrid caisson-type quay walls using an underwater shaking table test and finite element simulation. The study concluded that the hybrid caisson-type quay wall design using the current standard has sufficient seismic stability for the level of design earthquake. Miura et al. [6] performed a shaking table test and finite element simulation to clearly understand the damage mechanism of the quay walls under earthquake loading. They found that the liquefaction in the backfill soil affected the damage to the quay walls. In the case of non-liquefied backfill, the earth pressure fluctuated opposite to the inertial force acting on the wall.

In some countries, many caisson-type quay walls were constructed decades ago. Nowadays, most of them have become obsolete, and the renovation of the existing quay walls also was an effective option. However, the literature mentioned above indicated that almost all previous researchers were mainly interested in considering the behavior of normal quay walls but did not pay much attention to the study about renovated quay walls. Therefore, this study first proposed a solution to extend the performance of the caisson-type quay walls by increasing the water depth in front of the wall. The grout was injected to solidify the rubble mound beneath the front toe of the caisson before a part of the rubble in front of the wall was removed. Secondly, we performed centrifuge model tests on both the existing and renovated quay walls. Based on test results, some dynamic properties of renovated quay wall, such as the acceleration, caisson displacements, and rotation, were analyzed and compared to those of the existing case. These results were also compared to the criteria value proposed in the standards to clarify the advantages of the renovation technology.

2 Case Study

The cross section of the caisson-type quay wall before renovation examined in this study is shown in Fig. 1a. This design was based on the example provided by the Korean standard [5]. The quay wall consists of a caisson having 17.5 m height and 10 m width resting on a 10-m-thick rubble mound foundation. The structure was constructed on the bedrock ground and filled with sand. The front water depth was 13.5 m, and it could receive 40,000 DWT tonnage ships.

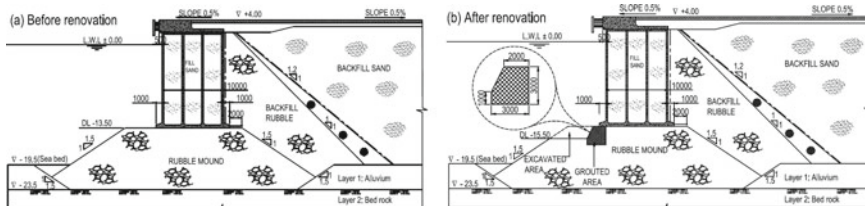


Fig. 1 Cross sections of the quay wall studied in this paper

To enhance the performance of the port, the quay wall was deepened to increase the front water depth by removing the rubble in front of the wall. The rubble mound under the caisson front toe was improved by grouting before excavation. As shown in Fig. 1b, after renovation, the front water depth of the quay wall increased to 15.5 m. Its performance also increased significantly, and 70,000 DWT tonnage ships could berth [5].

3 Geo-Centrifuge Test

The test was conducted at the Korea Advanced Institute of Science and Technology. The earthquake simulator could experiment with 100 g centrifuge acceleration. The base shaking acceleration can reach a maximum value of 20 g at 40 g centrifugal acceleration with a maximum payload of 700 kg [4]. The equivalent shear beam (ESB) container was used in the tests to reduce the effect of the container wall boundary. The tests were performed with a scaling factor of 1/120 with the two-scaling theory suggested by Iai et al. [3]. Table 1 calculates the scaling factors in detail.

Figure 2a, b shows the model cross sections for the existing quay wall and renovated quay wall used in the centrifuge tests, respectively (model scale). The location and type of measuring sensors were also plotted in each figure. Figure 3 illustrates some pictures of the renovated quay wall model.

Figure 4 presents the earthquake excitation used in the centrifuge tests on the prototype scale. This motion included six consecutive earthquake waves designed by using the acceleration time history of the Hachinohe earthquake and multiplied with different factors.

Table 1 Scaling factors of various variables in centrifuge model test [3]

Quantity	Partitioned				Scaling factor (prototype/physical model)	
	Virtual 1 g field		Centrifugal field		Equation	Value
Length	μ	3	η	40	$\mu\eta$	120
Density	μ_ρ	1	1	1	μ_ρ	1
Time	$(\mu\mu_\epsilon)^{0.5}$	2.280	η	40	$(\mu\mu_\epsilon)^{0.5}\eta$	91.180
Acceleration	1	1	$1/\eta$	0.025	$1/\eta$	0.025
Displacement	$\mu\mu_\epsilon$	5.196	η	40	$\mu\mu_\epsilon\eta$	207.846
Strain	$\mu_\epsilon = \mu^{0.5}$	1.732	1	1	μ_ϵ	1.732

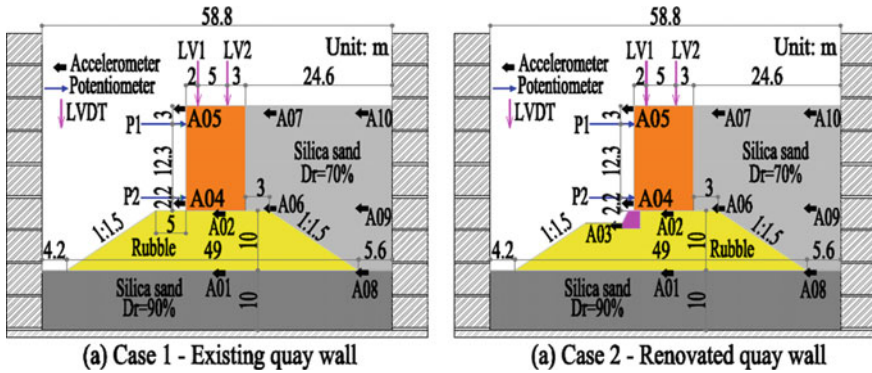


Fig. 2 Cross sections of the models used in the centrifuge test

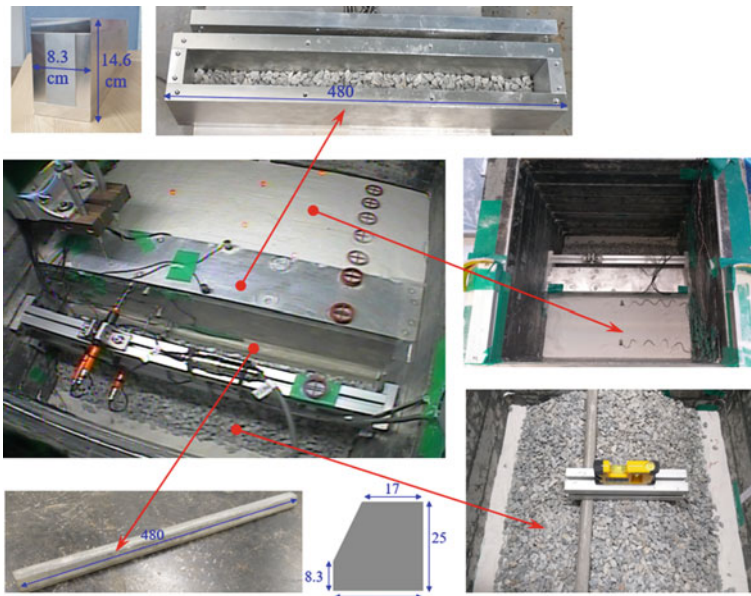


Fig. 3 Setup of centrifuge model test (renovated quay wall model)

4 Results and Discussion

4.1 Propagation of Wave in the Models

The comparison of PGAs at the model surface (points A05, A07, and A10) between two cases for all cases is summarized in Table 2. The values in the brackets are interpreted for the renovated quay wall. The results indicated that the accelerations

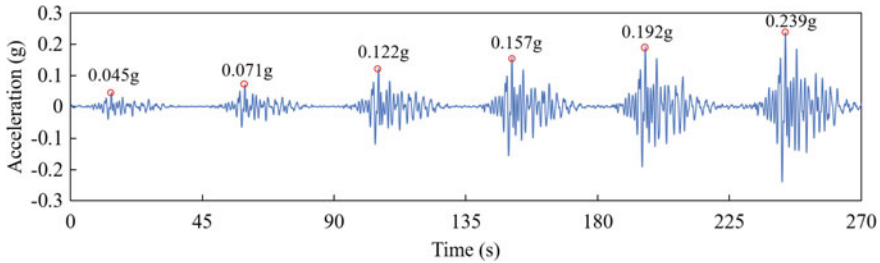


Fig. 4 Earthquake excitation used in the experiments

Table 2 Comparison of PGAs at the model surface for two cases

	Step 1	Step 2	Step 3	Step 4	Step 5	Step 6
A05	0.086 (0.080)	0.125 (0.121)	0.211 (0.194)	0.306 (0.254)	0.370 (0.312)	0.424 (0.373)
A07	0.080 (0.070)	0.118 (0.110)	0.180 (0.177)	0.257 (0.221)	0.311 (0.274)	0.369 (0.350)
A10	0.075 (0.068)	0.120 (0.110)	0.190 (0.178)	0.251 (0.239)	0.298 (0.283)	0.335 (0.345)
Input motion	0.045	0.071	0.122	0.157	0.192	0.239

recorded on the caisson were larger than those in the backfill, especially in the existing quay wall model. Besides, the accelerations measured on the renovated quay wall were lower than those of the existing case. Compared to PGAs of input motions at the base, the PGAs at the top of the existing quay wall increase 1.8 and 1.6 times on the caisson and backfill, respectively, whereas for the renovated quay wall, these values were 1.6 and 1.5 times, respectively.

4.2 Deformed Shape of the Quay Walls

Figure 5a shows the horizontal displacement of the caisson in the case existing at the end of each step measured by potentiometers P1 and P2. Similarly, the result for the renovated quay wall is depicted in Fig. 5b. As can be seen, in the case of the existing quay wall, the horizontal displacement at level P1 was larger than that of P2.

A similar trend was also received from vertical displacement measured by LVDT sensors, as shown in Fig. 6. The downward movement was defined as negative. For the existing case, the vertical displacements at LV1 were about 1.5–3 times as large as at LV2, while the renovated quay wall showed a similar settlement at LV1 and LV2.

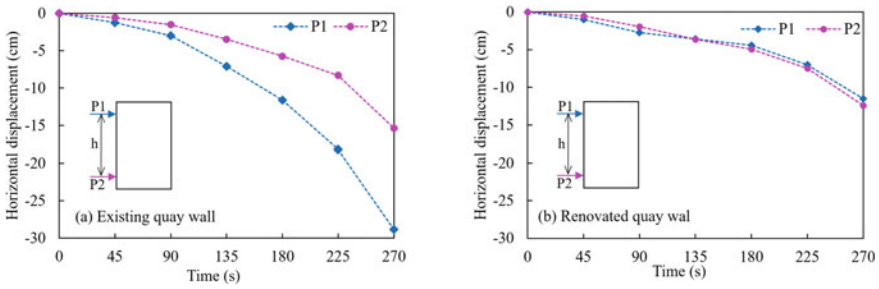


Fig. 5 Horizontal displacement of caisson at P1 and P2

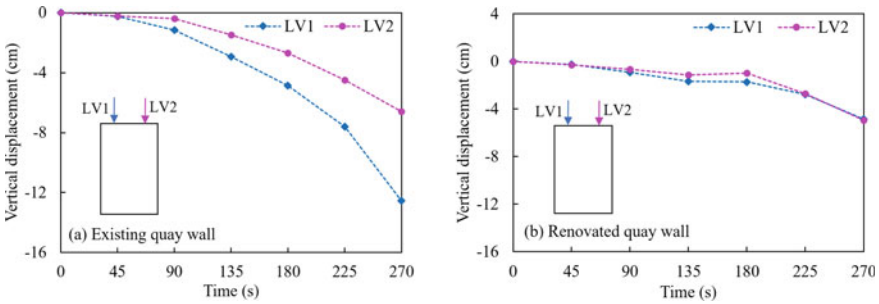


Fig. 6 Vertical displacement of caisson at P1 and P2

The results measured by the potentiometers and LVDT sensors showed a clear difference in displacement and deformation trends of the caisson before and after renovation. The existing caisson had larger displacements and tilted toward the sea. In comparison, the displacements of the upgraded caisson were lower and slipped horizontally to the sea. This difference was investigated in detail by comparing the rotation angle of the caisson between the two cases, as depicted in Fig. 7. As can be seen, the rotation angle of the caisson in the case of the existing quay wall increased after each step. In the case of renovated quay wall, the rotation angle of the caisson was approximately 0° regardless of time and earthquake magnitude increasing.

4.3 Assessment of Damage Resistance of Quay Wall

The Korean standards [5] suggested that if the displacement of the wall top was lower than $1.5\% H$ (H is the height of the quay wall), most structures were classified into “Damage Level I” and no damage was found in the main body. Figure 8 depicts the horizontal displacements at the top left of the caisson (Point A) for both existing and renovated quay walls after each step and compares them to allowable displacement. The allowable displacement was calculated as $1.5\% \times 1750 = 26.25$ cm. As can be

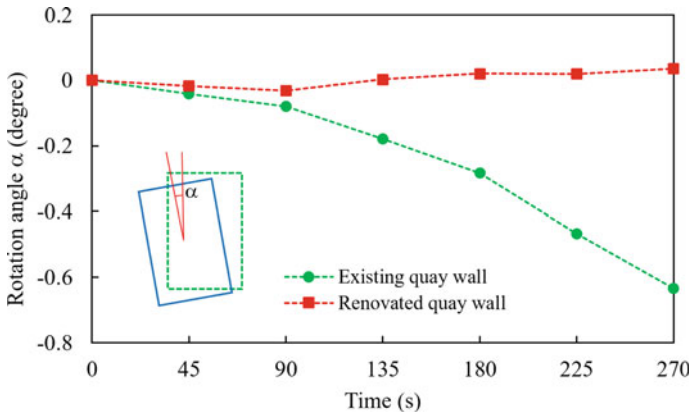


Fig. 7 Comparison rotation angle of caisson between existing and renovated quay walls

seen, the displacements of renovated quay wall were significantly lower than those of the existing case. At the end of shaking, the existing quay wall was classified as “Damage Level II”, while renovated quay wall was located in “Damage Level I”. These results demonstrated that the renovation could significantly reduce the damage potential of the quay wall.

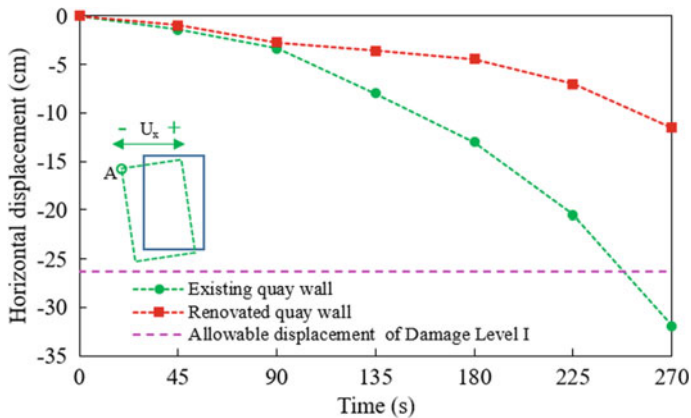


Fig. 8 Horizontal displacement at the top of the quay wall

5 Conclusions

The experimental results indicated that the dynamic resistance of the quay wall increased significantly after renovation. Based on these results, some conclusions were reached:

- (1) Both existing and renovated quay walls exhibited a similar trend of wave propagation. The acceleration increased significantly from the base to the top of the model. However, the increase in the case of the renovation was lower than in the existing case. In the case of the existing quay wall, the PGAs at the top of the caisson increased around 1.8 times compared to input motion, whereas the PGAs at the backfill surface raised 1.6 times. In the case of the renovated wall, the PGAs at the caisson top and backfill surface were about 1.6 and 1.5 times as large as the input motion, respectively.
- (2) The deformed shape of the caisson changed after renovation. In the case of the existing quay wall, the horizontal displacement at the caisson top was larger than that of the bottom. The vertical displacement at the seaside also was larger than the port side. Meanwhile, the renovated case exhibited a similar horizontal displacement at the top and bottom of the caisson. The vertical displacement was also the same at the seaside and port side. This indicated that the caisson of the existing quay wall rotated to the seaside, while for renovated case, it slipped horizontally.
- (3) Both permanent horizontal and vertical displacements at the top left of the caisson of renovated quay wall were lower than those of the existing case. After renovation, the horizontal displacement decreased by approximately 20–60%, whereas the reduction of vertical displacement was approximately 40–70%.

Acknowledgements This research was a part of the project titled “Development of Design Technology for Safe Harbor from Disasters” (No. 20180323), funded by the Ministry of Oceans and Fisheries, Korea.

References

1. Al-Homoud AS, Whitman RV (1995) Comparison between FE prediction and results from dynamic centrifuge tests on tilting gravity walls. *Soil Dyn Earthq Eng* 14(4):259–268
2. de Gijt J, Broeken ML (2005) *Handbook quay walls*. Taylor & Francis
3. Iai S, Tobita T, Nakahara T (2005) Generalised scaling relations for dynamic centrifuge tests. *Geotechnique* 55(5):355–362. <https://doi.org/10.1680/geot.2005.55.5.355>
4. Kim DS, Kim NR, Choo YW, Cho GC (2013) A newly developed state-of-the-art geotechnical centrifuge in Korea. *KSCE J Civ Eng* 17(1):77–84. <https://doi.org/10.1007/s12205-013-1350-5>
5. Ministry of Ocean and Fisheries—Korea (2020) *Harbor and fishing port design standard*
6. Miura K, Kohama E, Inoue E, Ohtsuka N, Sasajima T, Hayashi T, Yoshida N (2000) Behavior of gravity type quay wall during earthquake regarding dynamic interaction between caisson and backfill during liquefaction. In: *Proceedings of the 12th world conference on earthquake engineering*

7. Shiozaki Y, Sugano T, Yamamoto S, Tanaka T, Koji S (2000) Experimental study of the behavior of hybrid caisson type quay walls during earthquakes using an under water shaking table. In: Proceedings of the 12th world conference on earthquake engineering

Remedy Solutions for a Deep-Seated Landslide on Road No. 155, Section Km 12 + 667.85–Km 12 + 711.57, Sapa Town, Lao Cai Province, Vietnam



Thu Zar Aung, Lan Chau Nguyen, and Tien Dung Nguyen

Abstract Landslide hazards are geological disasters caused by heavy rainfall and debris flow, mainly occurring in mountainous regions. This paper presents remedy solutions for a deep-seated landslide on Road No. 155, section Km 12 + 667.85–Km 12 + 711.57, near a new Mong Sen bridge in Sapa town, Lao Cai province. In October 2020, two deep-seated landslides occurred in this area with some serious cracks. The landslide area was divided into two zones: zones 1 and 2, and up to date, these two zones have still been under reinforcement. While these two zones were reinforced with the retaining structure, soil nails, and grounded anchor system, a landslide (named Zone 3) happened in the area between Zones 1 and 2, where soil erosion and water erosion appeared serious because of heavy rainfall and cutting slopes. In this study, geological investigations, laboratory tests, topographical features, hydrological features, and stability analysis (Geo-Slope/W software) were studied and analyzed to understand the failure mechanism. Then, mitigation solutions such as the retaining wall with the ground anchors, drainage pipe, and soil nails were proposed for the reinforcement. The analysis results showed that the sliding surface of the entire landslide body and the behavior of the new cut slope, with and without reinforcement structures, were based on the numerical analysis by Geo-Slope/W software.

Keywords Landslides · Heavy rainfall · Cutting slopes · Geo-Slope/W · Ground anchor

T. Z. Aung (✉) · T. D. Nguyen
Infrastructure Engineering Program, VNU Vietnam Japan University, Hanoi, Vietnam
e-mail: 21117068@st.vju.ac.vn

T. D. Nguyen
e-mail: nt.dung@vju.ac.vn

L. C. Nguyen
University of Transportation and Communications, UTC, Hanoi, Vietnam
e-mail: nguyenchaulan@utc.edu.vn

1 Introduction

A landslide is one of the most common geological disasters that occurs in mountainous regions and coastal areas. Landslides can be caused by complex geological conditions and heavy rainfall. Vietnam has a large mainland area, of which 75% is mountainous and hilly area. The other remaining area is located on the eastern margin of the Indo-Chinese peninsula, which is a coastal area. Therefore, landslides, soil erosion, flash flood hazards, typhoons, and tropical depressions have occurred every monsoon season in Vietnam [20]. In the 1961–2010 period, Vietnam faced 12 typhoons per year, which brought heavy rainfall and floods [5]. These disasters can affect the lives of human beings and infrastructure. Most of the landslide disasters occurred along the national North–South railway and national highways, such as the Ho Chi Minh route and the northern mountainous province, Lao Cai, Sapa town, near the Sapa Ancient Rock Field in Hau Thao commune, Vietnam [8, 11, 13].

In July 2018, a deep-seated landslide occurred, the biggest one in terms of its debris volume and sliding surface depth on the Ha Long-Van Don expressway, Quang Ninh province [15]. The main cause is the downslope movements caused by the heavy rainfall while slope cutting [14]. Landslides occurred several times in 1990, 1994, 1996, 1998, 2000, 2001, 2002, 2010, 2019, 2020, and 2021 due to heavy rainfall, continuous rainfall, cutting slope, and complicated geological conditions in the old Mong Sen bridge, Sapa town, Lao Cai province [4, 6, 7, 13, 22]. Among them, provinces such as Lai Chau, Lao Cai, Ha Giang, Yen Bai, Son La, Hoa Binh, Thanh Hoa, and Nghe An have the most frequent landslide-causing locations [21]. Especially, landslides and slope failures occurred in Lao Cai province [17–19].

Recently, in October 2020, two deep-seated landslides happened near the New Mong Sen bridge while excavating the slope and constructing the new road [6]. That landslide case was specified as having two zones: Zone 1 and Zone 2. Ground anchors and soil nails were used as remedy solutions in two zones. At the moment, these zones have stable slopes. Despite the fact that these slopes are stable, a new landslide occurred between zones 1 and 2, where new soil erosion areas appeared seriously again as a result of the cutting slope and heavy rainfall caused by the construction of a retaining system for zones 1 and 2. It has also partly lost the balance of soil and rock gravity, changed the natural flow, and increased the surface water collection zone, and the increase in ground surface displacement was partially attributed to the dynamic load of the drilling machine due to the installation of ground anchors and soil nails, thereby increasing the landslides. Moreover, this landslide area is located near the new Mong Sen bridge, where many landslides have been recorded [6, 7]. Therefore, Provincial Road 155 from Lao Cai city to Sapa town, new construction section: Km 12 + 667.85–Km 12 + 711.57, is a new remedy solution. In this paper, this new section is specified as “landslide Zone 3”.

This paper aims to study the slope failure mechanism and mitigate the collapsed area based on the topography and geologic features, geotechnical investigation, laboratory testing results, and numerical analysis data for the Zone 3 landslide case. This

numerical analysis has estimated the stability of the slope with countermeasures by using limit equilibrium methods.

2 Methodology

In this paper, to study the topography, geologic features, and hydrological conditions of the sliding surface area, as well as the climate and rainfall data, field survey work was performed after the landslides and soil erosion occurred. A borehole investigation was conducted to determine the geological structures of the slope. From the geological survey data, soil properties were estimated from physical tests to apply a numerical analysis model. In this study, a numerical analysis model was used to determine the failure surface's stability or instability. In addition, the sliding surface along cross sections 3-3 (Zone 3 landslide) of the entire landslide body and the behavior of the new cut slope with and without reinforced structures were analyzed using a numerical analysis model with the Geo-Slope/W program (Geo Studio 2018).

3 Geological Investigation and Numerical Results for Zone 3 Landslide

3.1 Climate and Rainfall

In Vietnam, the rainy season begins in May and lasts until October, when it collects 80% of the total annual rainfall. According to the recorded 2021 monthly rainfall data, the average rainfall is 220 mm/month, the maximum rainfall is 460 mm in October, and the least rainfall is 60 mm/month. According to 2022 data, the average rainfall is 150 mm/month, the maximum rainfall is 350 mm in May and August, and the least rainfall is 70 mm/month. Sometimes hail occurs in February, March, and April. In Northern Vietnam, from May to October, it is a hot, humid, and rainy summer. Figure 1 indicates monthly rainfall data and accumulative data from 2021 to 2022. This information was obtained from the Sapa Meteorological Station. Based on this recorded data, landslides happened mainly in October 2021 and May and August 2022 compared with other periods.

3.2 Field Investigation Results

On October 27, 2020, the biggest landslides occurred near the new Mong Sen bridge, Sapa town, Lao Cai province. These two deep-seated landslides happened due to road

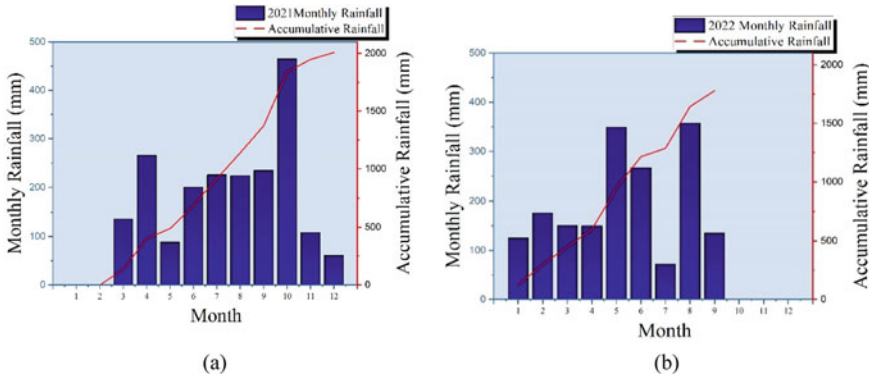


Fig. 1 Monthly rainfall and accumulative rainfall data. a 2021 and b 2022

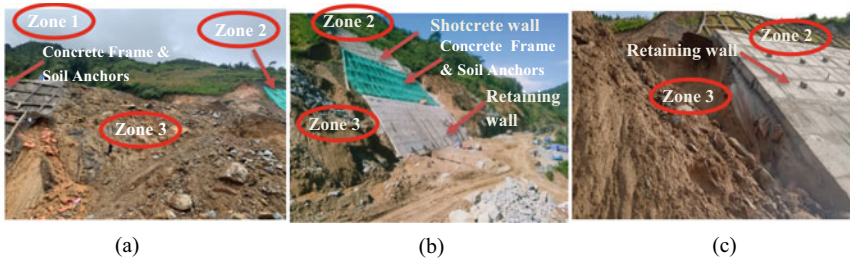


Fig. 2 Slope collapsed area between Zone 1 and Zone 2 (Zone 3 area)

construction that included cutting slopes and retaining structures. During the under-construction of two zones, Zone 3 landslides (i.e., a new landslide area) appeared again, as shown in Fig. 2. According to the site investigation data, soil erosion and water dissipation were seen from the terrain within the landslide Zone 3 area during the heavy rainfall. The retaining structure construction on both sides of the Zone 3 landslide area was almost finished. Therefore, the Zone 3 area is weaker than the Zone 1 and Zone 2 areas. They are removing the original green vegetation cover, cutting the toe slope, and excavating to construct the retaining structure. Besides, this area is a heavy rainfall area. These phenomena are the main reason for causing the Zone 3 landslide.

3.3 Topography and Geologic Features

The new Mong Sen landslide case appeared in the Trung Chai commune, Sapa town, Lao Cai province, Vietnam, which is located at 22° 25' 1.68" N and 103° 54' 18.03" E, approximately 0.6 km away from the new Mong Sen bridge as presented in Fig. 3.

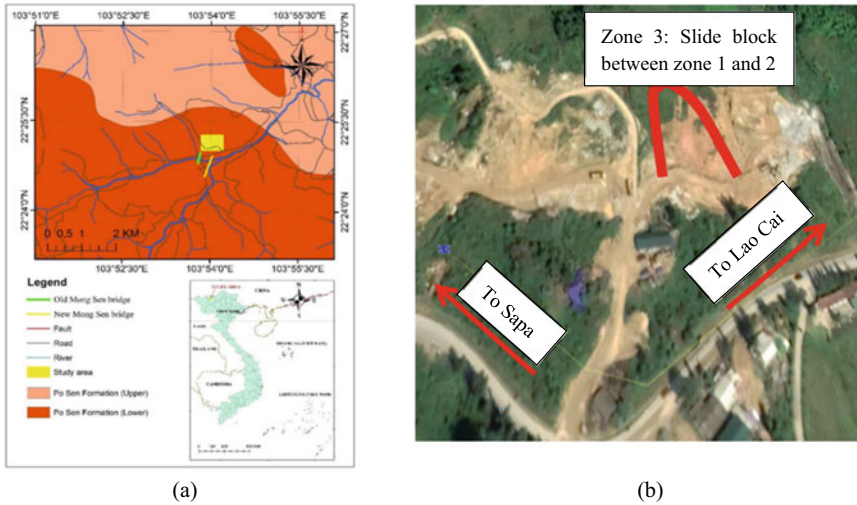


Fig. 3 **a** Geological map and location of the new Mong Sen landslide. **b** Location of landslide new section Zone 3

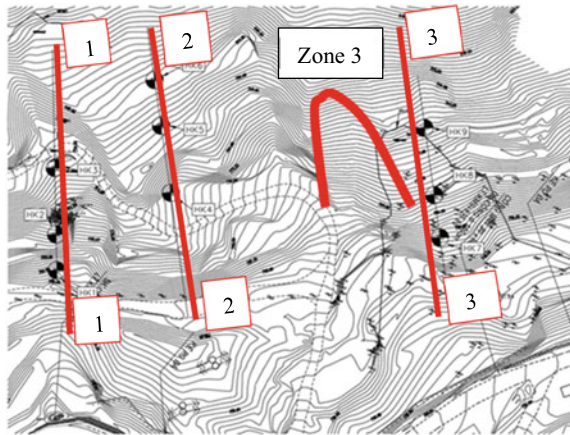
The slope angle in this area was about 25°. It is not steep terrain, and this location is mostly strongly weathered soil and rock layers. Moreover, this area is located in the Posen formation with intrusive rocks including diorite, granodiorite, and granite. Thus, along with the Mong Sen bridge, a new Mong Sen bridge on the Lao Cai–Sapa expressway was suggested to avoid landslide hazards. However, a new landslide occurred at the new Mong Sen bridge, Trung Chai commune, Sapa town, Lao Cai province, in 2020 [6]. As a result, the completely weathered zone becomes soil with a high dust or sand content that is irregularly distributed, causing surface erosion, scour grooves and erosion holes, local erosion, and very complex landslides, and the topography is influenced by complex hydrological conditions.

National Highway 4D is the survey route in the direction from Lao Cai city to Sapa town. The topography of the area has a cross section in the shape of a V, with the bottom of the valley being the Dum stream and Mong Sen stream. Dum stream starts from Sapa village–Sapa town, intersects with Mong Sen stream at Mong Sen bridge, and then flows downstream and empties into the Red River in Lao Cai city. In the direction of upstream to downstream, the survey route goes along the mountainside to the left of the valley.

3.4 Geological Drilling and Investigation

Zone 3 is near borehole cross sections 3-3. It was investigated in three boreholes: 7, 8, and 9. Standard penetration tests (SPT) were performed for each borehole, and soil samples were taken to test in the laboratory (Fig. 4).

Fig. 4 Geological borehole cross section for Zone 3 landslide



There are five layers in cross sections 3-3 for the Zone 3 landslide. The first layer is a yellow/brown medium sandy clay mixed with 40% boulder (ML). Its thickness changes from 5 to 15 m with uncorrected $N_{spt} = 15-50$. The fourth layer is yellow/brown medium sandy clay mixed with gravel (ML). Its thickness varies from 4 to 10 m, with an uncorrected $N_{spt} = 12-20$. This layer is also a landslide layer. The fifth layer is yellow/dark medium to hard sandy clay mixed with gravel (ML). This layer, with a thickness of 5–15 m and an uncorrected SPT value of $N_{spt} = 20-50$, is distributed across all sites. The ninth layer is gray, strongly weathered rock. This layer has a total core recovery (TCR) = 40–50% and a rock mass quality (RQD) = 30–40%. Its thickness varies from 3 to 10 m. The tenth layer is gray weathered rock. This layer has TCR = 60–70% and RQD = 50–60%. Its thickness is very large. The rock layers are found at a depth of 10 m, 30 m, and 15 m, respectively.

From SPT field tests, data was collected from both sieving and hydrometer tests. Stratigraphy and physical–mechanical properties of soil layers were determined from laboratory tests, as given in Table 1. The friction angle and cohesion of soil were examined in both natural and saturated conditions using direct shear tests.

3.5 Numerical Analysis Results

3.5.1 Proposed Countermeasure for Zone 3 Landslide

According to the landslide mechanism, the results of field investigation, and laboratory tests, countermeasures have been proposed to retain the failure slope surface and protect against future hazards. In general, the remedy solutions are topsoil excavation, reinforced concrete walls, ground anchors, earth nails, underground drainage pipes, and concrete spraying to prevent erosion. In principle, it is possible to reduce

Table 1 Soil properties from laboratory tests

Properties	First layer	Fourth layer	Fifth layer
USCS	ML	ML	ML
Water content (%), w	27.3	27.6	23.5
Natural unit weight (kN/m^3), γ	19.3	18.9	19.2
Dry unit weight (kN/m^3), γ_d	15.1	14.9	15.6
Specific gravity, G_s	2.69	2.69	2.68
Porosity (%), n	43.7	44.8	41.9
Void ratio, e	0.78	0.81	0.72
Degree of saturation (%), S_r	94.7	91.7	86.8
Liquid limit (%), LL	36.0	36.1	35.1
Plastic limit (%), PL	25.6	24.6	24.6
Plasticity index (%), PI	10.4	11.5	10.5
Coefficient of compressibility (a_{v1-2} kPa)	0.00036	0.00042	0.00033
Cohesion at natural state (kPa), c'	21.80	22.00	22.90
Friction angle at natural state ($^\circ$), ϕ'	20.0	16.2	22.5
Cohesion at saturated state (kPa), c'	20.2	19.8	19.2
Friction angle at saturated state ($^\circ$), ϕ'	16.2	14.2	17.9

the impact of causing landslides, terrain adjustment, slope reduction, and deep reinforcement of the rock mass to increase the shear resistance of the soil and create a pre-compression zone of the soil mass (earth nails). Firstly, the topsoil of the slope was partially removed, and the cutting slope was excavated at 1:1.5. Secondly, the reinforced concrete wall was applied. Thirdly, three rows of ground anchors with a total length of 20 m were installed. Fourthly, three rows of earth nails with a total length of 11.7 m were arranged. Fifthly, two rows of underground drainage pipes with a total length of 20 m and an underground drainage drilling distance of 6 m were installed. Finally, shotcrete spraying was applied to protect the surface from erosion [3, 9, 16].

3.5.2 Numerical Analysis

A numerical analysis model was analyzed on the computer software Geo-Slope/W Program to examine the sliding surface of the landslide. In this study, the stability of the slope was simulated using the limit equilibrium slope stability analysis method (Bishop: 1955 Simplified Method). The soil properties of each layer were obtained from the laboratory tests as given in Table 1, and the soil input parameters are as presented in Table 2. According to the geological investigation results, the fourth layer (sandy clay mixed with gravel, ML) is a landslide layer. It was assumed that the existing groundwater table significantly increased the water dissipation in that layer. Thus, the initial groundwater table (piezometric line) was specified within the

Table 2 Input parameters of soil and rock for Geo-Slope/W model for Zone 3

S. No.	Soil type	Natural state			Saturation state		
		γ	c	ϕ	γ	c	ϕ
		kN/m ³	kPa	°	kN/m ³	kPa	°
1	First layer: sandy clay mixed with 40% boulder	19.5	21.8	20.05	19.6	20.2	16.33
	Fourth layer: sandy clay mixed with gravel	18.96	22.2	16.28	19.5	19.8	14.25
	Fifth layer: medium to hard sandy clay mixed with gravel	19.0	22.9	22.5	19.2	19.2	17.9
	Ninth layer: strongly weathered rock	26.9	50	30	27.0	50	30
	Tenth layer: weathered rock	26.9	100	30	27.0	100	30

fourth layer, alternatively above the weathered rock layer in the numerical model. Additionally, the range of entry and exit lines for the slip surface was specified at the crest and toe of the slope, respectively. Saturation parameters were used for soil layers below the groundwater table, and natural parameters were taken for soil layers above the groundwater table. In this numerical analysis, rock layer parameters are based on the analysis results from Rock Lab software. Previous research has been published utilizing Geo-Slope/W software [2, 10, 12].

3.6 Geo-Slope/W Analysis Result

The failure surface was determined automatically by numerical analysis, as illustrated in Figs. 5 and 6. These figures evaluated the sliding surface plane of the entire slide body and the behavior of slope failure with and without reinforcement structures. Figure 5 shows the results of the predicted failure surface and the critical factor of safety before the mitigation. Before the mitigation system was installed on the slope, the critical factor of safety in the analysis is 1.016, which is the instability of the slope according to the Vietnamese standard [1]. There are many mitigation systems, such as retaining walls, MSE walls, and ground anchors. Retaining walls have a wall height limitation and are unsuitable for high slopes. The MSE wall needs to be cut through the large soil area to install the geogrid and compaction. The ground anchor method necessitates only a small amount of soil cutting and can be extended sufficiently deep into the soil to benefit a wide range of shallow and deeply seated potential failure surfaces with insufficient safety factors. The anchor forces act on these potential slip surfaces to ensure they have an acceptable factor of safety. It is relatively faster to install than conventional pre-drilled anchors and saves time and money on the construction site. Thus, in this paper, it was decided to use ground anchors as the mitigation solution for landslide areas. Besides, the ground anchors provided the highest safety factor when compared with the other methods.

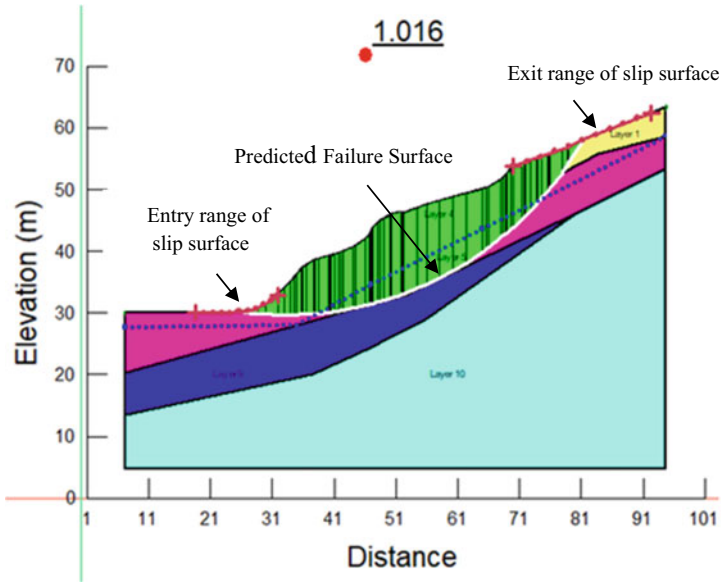


Fig. 5 Stability analysis without reinforcement system

As shown in Fig. 6, after the mitigation system that was applied to the reinforced wall and ground anchor to stabilize the slope, the predicted failure surface and the critical safety factor is 1.565, which is greater than the allowable coefficient of sliding stability value of 1.25 in the Vietnamese standard [1], and that is the stability of the slope after treatment.

4 Discussions and Recommendations

This paper describes the deep-seated landslide that happened on Road No. 155, section Km 12 + 667.85–Km 12 + 711.57, near the new Mong Sen bridge, on the Lao Cai–Sapa expressway, in Sapa town, Lao Cai province. The landslide area is the middle area of the under-construction Zone 1 and Zone 2 retaining structures. Based on the field investigation data and the deep-seated failure mechanism, the characteristics of landslides were observed during the under-construction of the retaining structure, as presented in Fig. 2. This landslide area has a very thick topsoil that is composed of clay, sand, gravel, and small rocks. This topsoil is easy to erode and reduces the shear strength during heavy rainfall, as well as the groundwater runoff and saturated soil observed from the surface. On the other hand, the shape of the failure surface and the factor of safety were predicted by the stability analysis in Fig. 5. According to the investigation data and analysis results, heavy rainfall and a cutting slope were the major trigger factors for this Zone 3 landslide.

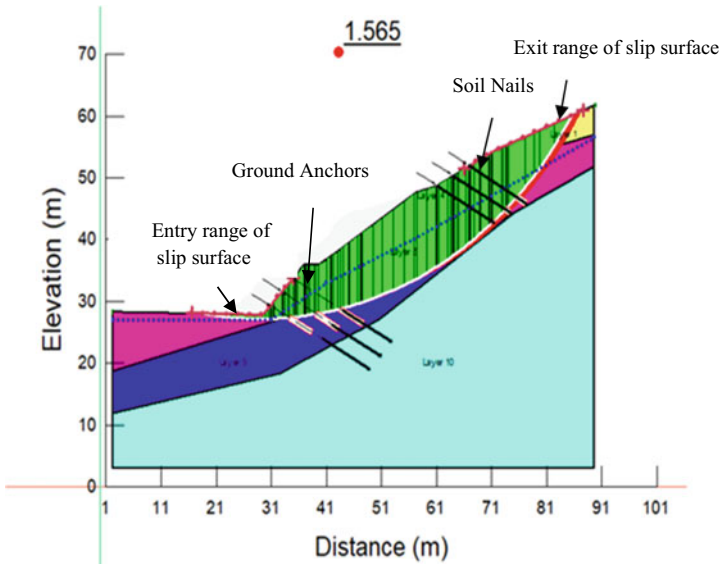


Fig. 6 Stability analysis with reinforcement system

This study carried out the topography and geological features and collected the climate and rainfall data, hydrologic characteristics, and borehole investigations to predict the failure mechanism of the slope and the critical factor of safety. Based on observation data and analysis results, they investigated the remedy solutions for the landslide's causes. The remedy solutions were suggested by the two methods.

The first solution was to excavate the topsoil on unstable terrain to reduce the soil weight, and the second solution was analyzed using the installation of ground anchors, soil nails, underground drainage pipe, and shotcrete based on the numerical analysis. Utilizing ground anchors and soil nails was an effective way to stabilize the slope. In this paper, the stability of the critical safety factor was obtained at 1.565, which is larger than the required value of 1.25 after applying the countermeasures analysis. The comparison with the other studied papers indicated that the critical safety factor is between 1.27 and 1.201 [6, 10].

References

1. 22 TCN 171-87. Soil investigation procedure and design of stabilizing method for road embankment in area vulnerable to landslide (in Vietnamese)
2. Abbas JM, Mutiny ZA (2018) Slope stability analysis for earth dams using (Geo-Slope/W). *Diyala J Eng Sci* 11(1):70–81. <https://doi.org/10.26367/DJES/Vol.11/No.1/12>
3. American Association of State Highway and Transportation Officials (2012) AASHTO LRFD bridge design specifications, customary U.S. units. American Association of State Highway and Transportation Officials

4. Anh LTL, Anh BT, Sang GX, Dat TTH, Huong HT, Thanh ND, Thuy LTB (2019) A study on vegetative propagation of *Huperzia serrata* by cuttings in Sa Pa, Lao Cai. TAP CHI SINH HOC 41(3). <https://doi.org/10.15625/0866-7160/v41n3.13921>
5. Cong NC, Binh NQ, Phuoc VND (2020) Landslide susceptibility mapping by combining the analytical hierarchy process and regional frequency analysis methods: a case study for Quangngai province (Vietnam). In: APAC 2019—proceedings of the 10th international conference on Asian and Pacific coasts, pp 1327–1334. https://doi.org/10.1007/978-981-15-0291-0_180.
6. Do TN, Nguyen LC, Nguyen QD (2022) Characteristics and remedy solutions for a new Mong Sen deep-seated landslide, Sa Pa town, Vietnam, 1st edn, vol 1
7. Duan NB, Duc Vu M (2011) Studying to determine reasons of landslide in the area of the Mong Sen bridge, Lao Cai province (in Vietnamese). <https://www.researchgate.net/publication/332240494>
8. Duc DM (2013) Rainfall-triggered large landslides on 15 December 2005 in Van Canh district, Binh Dinh province, Vietnam. Landslides 10(2). <https://doi.org/10.1007/s10346-012-0362-4>
9. FHWA (2015) Soil nail walls reference manual developed following: AASHTO LRFD bridge design specifications, 7th edn
10. Gian QA, Tran DT, Nguyen DC, Nhu VH, Tien Bui D (2017) Design and implementation of site-specific rainfall-induced landslide early warning and monitoring system: a case study at Nam Dan landslide (Vietnam). Geomat Nat Hazards Risk 1978–1996
11. Luong LH, Miyagi T, van Tien P, Loi DH, Eisaku H, Abe S (2017) Landslide risk evaluation in central provinces of Vietnam. In: Advancing culture of living with landslides. Springer International Publishing, pp 1145–1153. https://doi.org/10.1007/978-3-319-53498-5_130
12. Mishal U, Khayyun T (2018) Stability analysis of an earth dam using geo-slope model under different soil conditions. Eng Technol J 36:532–532
13. Nguyen DM, Tran QH (2020) Features of large-scale landslide at Hau Thao area, Sa Pa town, Lao Cai province. In: Lecture notes in civil engineering, vol 62. Springer, pp 917–922. https://doi.org/10.1007/978-981-15-2184-3_119
14. Nguyen LC, Tien PV, Do TN (2020) Deep-seated rainfall-induced landslides on a new expressway: a case study in Vietnam. Landslides 17(2):395–407. <https://doi.org/10.1007/s10346-019-01293-6>
15. Pham VC, Nguyen CL, Do TN, Pham VT (2020) Multiple solutions to stabilize a deep-seated landslide. In: Lecture notes in civil engineering, vol 62. Springer, pp 859–864. https://doi.org/10.1007/978-981-15-2184-3_111
16. Sabatini PJ, Pass DG, Bachus RC (1999) Geotechnical engineering circular no. 4, ground anchors and anchored systems
17. Tran TV, Hung HV, Pham HD, Sato G, Vu HH (2021) A non-linear, time-variant approach to simulate the rainfall-induced slope failure of an unsaturated soil slope: a case study in Sapa, Vietnam. J Disaster Res 16(4):512–520. <https://doi.org/10.20965/jdr.2021.p0512>
18. Tran TV, Pham HD, Hoang VH, Trinh MT (2021) Assessment of the influence of the type of soil and rainfall on the stability of unsaturated cut-slopes—a case study. Int J GEOMATE 20(77):141–148. <https://doi.org/10.21660/2020.77.66560>
19. Tran TV, Alvioli M, Hoang VH (2022) Description of a complex, rainfall-induced landslide within a multi-stage three-dimensional model. Nat Hazards 110(3):1953–1968. <https://doi.org/10.1007/s11069-021-05020-0>
20. Van Tien P, Luong LH, Duc DM, Trinh PT, Quynh DT, Lan NC, Thuy DT, Phi NQ, Cuong TQ, Dang K, Loi DH (2021) Rainfall-induced catastrophic landslide in Quang Tri province: the deadliest single landslide event in Vietnam in 2020. Landslides. <https://doi.org/10.1007/s10346-021-01664-y>
21. Van Tien P, Luong LH, Nhan TT, Duc DM, Quynh DT, Lan NC, Phi NQ, Hao DC, Ha NH, Thuy DT, Thao VB (2021) Secondary processes associated with landslides in Vietnam. In: Lecture notes in civil engineering, vol 108. Springer Science and Business Media Deutschland GmbH, pp 192–209. https://doi.org/10.1007/978-3-030-60269-7_10

22. Yamasaki T, Sato G, Kimura T, Hung HV, Manh ND, Ozaki T, Yokoyama O, Tosa S, Wakai A (2021) Landslide process revealed by mineralogical properties of landslide deposits in the Sapa district, Vietnam. *J Disaster Res* 16(4):556–560. <https://doi.org/10.20965/JDR.2021.P0556>

Water Resource and Environment Engineering

Uses Field-Scale Data to Modify the HEC-18 Scour Model



Huy Quang Mai and Nghien Dinh Tran

Abstract The lowering of the river bed elevation near bridge piers caused by the flow washing away the material flowing downstream is known as local scour. Accurate estimation of maximum local scour depth around piers is essential for the safe and efficient design of bridge foundations. To estimate local scour depths around single piers, prevailing methods rely on empirical formulae developed mostly from laboratory studies. To improve the predictability of the HEC-18 scour model, this paper presents the modified equation for prediction of local scour depth around circular piers in non-cohesive soil condition, developed by using field scale data and nonlinear regression. This modified equation already has a determination coefficient (R^2) calculated to be 0.95.

Keywords Local scour · Bridges · Piers · HEC-18 · Field data

1 Introduction

The lowering of the river bed elevation near bridge piers caused by the flow washing away the material flowing downstream is known as local scour. This is a continual process with both natural and anthropogenic factors. River sediment erosion is increased by local acceleration in river velocity. Local accelerations are caused by bridge pier constructions during river crossings. If enough silt is removed from the riverbed near the bridge pier, the bridge may become unstable, increasing the risk of failure. The Federal Highway Administration estimates that approximately 600,000 bridges in the United States necessitate some type of scouring mitigation [1]. According to the statistics provided by the Department of Transportation of the United States of America [2], 383 bridges were destroyed all by themselves in the United States in 1973. Shirhole and Holt [3] found that about 60% of bridge collapses in the United States were caused by hydraulics. To maintain safety, the

H. Q. Mai (✉) · N. D. Tran
University of Transport and Communications/UTC, Hanoi, Vietnam
e-mail: mqhuy@utc.edu.vn

© The Author(s), under exclusive license to Springer Nature Singapore Pte Ltd. 2024
T. Nguyen-Xuan et al. (eds.), *Proceedings of the 4th International Conference on Sustainability in Civil Engineering*, Lecture Notes in Civil Engineering 344,
https://doi.org/10.1007/978-981-99-2345-8_49

487

final scour depth is often overstated due to ambiguity in existing scour prediction algorithms. Moreover, the stretching of the piles may be feasible for short bridges crossing narrow streams, they might be prohibitively expensive for longer bridges with many spans [4]. Reduced unpredictability in scour depth calculation methods may help save the total investment without affecting the stability of the structure [4].

Scour research has been dominated by statistical and physical modeling over the last several decades, with the primary objective being to find a correlation between hydrodynamics, geometry, and sediment data and scour depth. At this current time, the state of the field is dominated by empirically determined scour prediction equations. These equations are mostly obtained from experimental flume data utilizing cohesiveless sediment. The most typical approach to identifying factors that affect pier scour is to utilize experimental results as a data source [5]; however, this method does not adequately depict the sophistication of bridge scour as a result of scaling difficulties [6, 7]. Many times, silt of a comparable size to that which is found in the field is used in scaled-down versions of the physical models. Cohesive properties of sediment make it difficult to scale the sediment, and the existence of bed formations is controlled by particles' dimensions in terms of the thickness of the viscous layer [5]. Scaling sediment is challenging. The variety of the different factors within which the formulas may be solved are often variables, which is another source of uncertainty [8]. Because it is difficult to accurately measure complicated distribution of velocity and field depth measurement, these equations also come with a significant amount of uncertainty attached to them. For the purpose of predicting scour for individual foundation components, the standard procedure that is currently followed depends on empirical data and simplified one-dimensional (1D) design equations found in Hydraulic Engineering Circular Number 18 (HEC-18, Arneson et al. 2012) [9]. These equations assume that the layer of soil being characterized by d_{50} is uniform. Because of this, the scour design can turn out to be more traditional. The present HEC-18 scour calculation places a significant amount of emphasis on flow parameters, but it ignores the geotechnical qualities of the multilayered soils near the bridge foundations. The current HEC-18 equation is able to provide predictions about the maximum pier scour depths for circular cylinder and round-nose piers that are aligned with flow:

$$\frac{y_s}{y_1} = 2.0 \left(\frac{a}{y_1} \right)^{0.65} Fr^{0.43} \quad (1)$$

where: y_s —scour depth; y_1 —flow depth directly upstream of the pier; a —pier diameter (or width) in the direction of flow; Fr_1 —Froude number directly upstream of the pier, $Fr = V_1/(gy_1)^{1/2}$; V_1 —mean velocity of flow directly upstream of the pier; g —acceleration of gravity.

It is advised to use the HEC-18 pier scour equation (Eq. 1) for both live-bed and clear-water pier scour. This equation was developed on the basis of research carried out at Colorado State University (and is commonly referred to as the CSU equation). At very high Froude Numbers, the ratio of y_s/a may approach the value of 3. As a

result, it is suggested that the maximum value of the ratio be set at 2.4 for Froude numbers that are less than or equal to 0.8 and at 3.0 for Froude numbers that are more than 0.8. Only round nose piers that are perpendicular to the direction of flow are subject to these limiting ratio values.

The ability to determine the maximum local scour depth around the bridge piers based on the field data has been the subject of a great number of research. Johnson made the observation that numerous equations are not appropriate for the design because the estimated results are lower than the field measurements. On the other hand, several equations give overprediction with a large positive bias, which results in an increase in the cost of construction [8].

This study summarizes the findings of an assessment that was done to determine whether or not it is possible to forecast the maximum local scour depth around the bridge piers using the HEC-18 equation based on field observations. The precision of the HEC-18 formula used in the design process may be improved thanks to this study finding, which serves as a platform for improvement.

2 Development of Scour Prediction Equation in the Form of HEC-Equation

In this section, the use of field scour depth data is presented in combination with exponents applied to the normalized width and Froude number to increase the accuracy of the scour depth estimation formula. That is to say, no effort is made to establish a causal relationship between key physical factors and an alternative functional form. The computation makes use of field data for the pier in the rivers from sources like Mueller and Wagner/US, Gao et al./China, and Juravlev/Russia found in the literature [5, 10, 11]. Table 1 provides the ranges of field data utilized to describe the local scour.

Due to the fact that the approach velocity is higher than the critical velocity, the dataset in question is a live bed scour. The critical velocity may be determined by using the equation for Laursen's critical velocity, which can be found in Eq. 2:

$$V_{c,50} = 6.19y_1^{1/6}d_{50}^{1/3} \quad (2)$$

When compared to the critical velocity, the ratio of the average velocity to the critical velocity might range anywhere from 1.27 to 7.21. A nonlinear regression analysis was used to re-derivate the HEC-18 pier scour equation in order to generate an equation that uses scour field data as their summary in Table 1. The re-derived or modified HEC-18 equation for pier scour, which has a determination coefficient of 0.95, is as follows:

$$\frac{y_s}{y_1} = 2.6 \left(\frac{a}{y_1} \right)^{0.69} Fr^{0.76} \quad (3)$$

Table 1 Scour field statistics [5, 10, 11]

Description	Scour depth, y_s (m)	Water depth, y_1 (m)	Pier diameter, a (m)	(y_s/y_1)	a/y_1	y_s/a	d_{50} (mm)	a/d_{50}	V (m/s)	Froude number Fr
Max	5.6	16.55	5.03	0.52	4.0	1.8	1.53	23,300	3.2	0.78
Min	1.62	0.9	3.05	0.145	0.302	0.37	0.165	3268	1.02	0.11

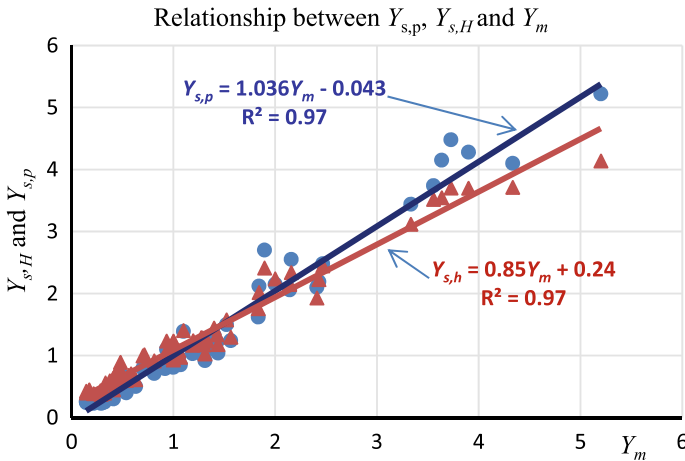


Fig. 1 Improved version of the relative HEC-18 pier-scour equation for live-bed scour circumstances

Figure 1 presents a comparison of the scour depths that were actually observed with those that were estimated using Eqs. 1 and 3.

Equations 1 and 3 are evaluated in terms of scatter index (SI), standard deviation of relative error (RES D), and the sum of errors squared (SSE). These parameters are defined as follows:

- For modified HEC-18-Eq. 3:
 - Scatter index (SI):

$$SI = \frac{RMSE}{\bar{Y}_m} \tag{4}$$

- Root mean-square error (RMSE):

$$RMSE_p = \sqrt{\frac{1}{N-1} \sum (Y_p - Y_m)^2} \tag{5a}$$

where $\bar{Y}_m = \frac{1}{N} \sum Y_m$; $Y_p = \frac{y_{s,p}}{y_1}$ is defined as the relative modified scour depth; $Y_m = \frac{y_{s,m}}{y_1}$.

- For current HEC-18-Eq. 1:

$$RMSE_H = \sqrt{\frac{1}{N-1} \sum (Y_H - Y_m)^2} \tag{5b}$$

where $y_{s,p}$ —the depth of the scour as calculated by Eq. 3; $y_{s,H}$ —the predicted scour depth using Eq. 1; $y_{s,m}$ —the measured scour depth, \bar{Y}_m is the arithmetic

mean of the measured scour depth values; $Y_H = y_{s,H}/y_1$ is defined as the relative current HEC-18 scour depth.

The relative error values of modified HEC-18 Eq. 3 is:

$$RE_{s,p} = (Y_{s,p} - Y_m) / Y_m \tag{6a}$$

And for current HEC-18 Eq. 1:

$$RE_{s,H} = (Y_{s,H} - Y_m) / Y_m \tag{6b}$$

The standard deviation of relative error values was applied to measure and check the dispersion of the relative error of the proposed scour depth, and current HEC-18 scour depth values are:

$$RES_{D_{s,p}} = \sqrt{\frac{1}{N-1} \sum (RE_{s,p} - \overline{RE}_{s,p})^2} \tag{7a}$$

$$RES_{D_{s,H}} = \sqrt{\frac{1}{N-1} \sum (RE_{s,H} - \overline{RE}_{s,H})^2} \tag{7b}$$

The sum of errors squared is used to calculate the amount of difference that exists between the scour depth that was actually measured and the scour depths that were estimated using Eqs. 1 and 3:

$$SSE_{s,p} = \frac{\sum (Y_{s,p} - Y_{s,m})^2}{\sum Y_{s,m}^2}$$

and

$$SSE_{s,H} = \frac{\sum (Y_{s,H} - Y_{s,m})^2}{\sum Y_{s,m}^2} \tag{8}$$

Scatter index (SI) values of modified HEC-18 (Eq. 3) and current HEC-18 (Eq. 1), the relative error (RE), the standard deviation of relative error values (RES_D), and the sum of errors squared (SSE) for both Eqs. 1 and 3 are given in Table 2.

Table 2 Comparative indices of Eqs. 1 and 3

Equation	RMSE	SI%	RE		RES _D %	SSE%
Current HEC-18	0.25	22	Max	Min	46.94	2.1
Modified HEC-18	0.22	17	+ 0.79	- 0.3	17	1.7

3 Discussion and Conclusion

Scour around bridge piers is notoriously difficult to predict. This complicated behavior precludes the employment of a single design relationship or approach, despite the numerous advancements that have been achieved in the sector over the course of the last 40 years. Chiew and Melville [12] observed that the scour depth is proportional to the flow depth up to a limiting value of y_s/a , beyond which the flow depth has no impact on the scour depth anymore. As the flow depth increases, the interference decreases until there is no longer any noticeable influence when y_s/a is less than 3. Scour depths measured in the laboratory had a tendency to overestimate more than those measured in the field when the flow depth was increased. The researchers Raudkivi and Ettema [13] came to the conclusion that the scour depth was unrelated to y/a when the a/d_{50} ratio was at high levels. For a particular value of a/d_{50} , however, it did not seem that the scour depth would cease growing at $y/a = 6$. The current HEC-18 equation for circular cylinder and round-nose piers aligned with flow, in this study, does not satisfy live-bed scour in practice because the comparative indexes of Eq. 1 have large deviations from Eq. 3 as given in Table 2 (SI: 22% > 17%, RE_{\max} : + 1.97 > + 0.79, RESD: 46.94% > 17% and SSE: 2.1% > 1.7%). In addition, they are also shown in the slope and constant of the equation as indicated in Fig. 1:

$$Y_H = \frac{y_{s,H}}{y_1} = 0.85 \left(\frac{y_{s,m}}{y_1} \right) + 0.24 \quad (9)$$

where Y_H is defined as the relative current HEC-18 scour depth; $y_{s,H}$ —the predicted scour depth using Eq. 1; y_1 —flow depth directly upstream of the pier; and $y_{s,m}$ —the measured scour depth.

For cylinder diameters greater than 3.05 and less than 5.03, with $0.25 < y_1/a < 3.31$, the modified HEC-18 pier-scour Eq. 3 matches the field data under the live-bed condition as shown in Table 1 and Fig. 1. This equation is suitable for the research of Chiew and Melville [12] and Raudkivi and Ettema [13]. According to the results of the calculation, the sum of squared errors (SSE) is 1.7%, which demonstrates that the suggested equation is statistically consistent. The suggested modified HEC-18 pier-scour equation is also assessed in terms of the determination coefficient (R^2) and the scatter index (SI), both of which were estimated to be 17% and 0.95, respectively. Both of these values were determined using the equation. These data further illustrate the dependability of the equation that was provided.

References

1. Nassif H, Ertekin AO, Davis J (2002) Evaluation of bridge scour monitoring methods. United States Department of Transportation, Federal Highway Administration, Trenton

2. U.S. Department of Transportation (1993) Evaluating scour at bridges. Hydraulic Engineering Circular No. 18. Report No. FHWA-IP-90-017. Federal Highway Administration (FHWA), Washington, DC
3. Shirhole AM, Holt RC (1991) Planning for a comprehensive bridge safety assurance program. *Transp Res Rec* 1290:137–142
4. Calappi T, Miller CJ, Carpenter D, Dahl T (2012) Developing a family of curves for the HEC-18 scour equation. Civil and Environmental Engineering Faculty Research Publications. <https://doi.org/10.4236/ijg.2012.32031>
5. Mueller D, Wagner CR (2005) Field observations and evaluations of streambed scour at bridges. United States Department of Transportation, Federal Highway Administration, Mclean
6. Hopkins GR, Vance RW (1980) Scour around bridge piers. Washington, DC
7. Ettema R, Melville BW, Barkdoll B (1998) Scale effect in pier-scour experiments. *J Hydraul Eng* 124(6):639–642. [https://doi.org/10.1061/\(ASCE\)0733-9429\(1998\)124:6\(639\)](https://doi.org/10.1061/(ASCE)0733-9429(1998)124:6(639))
8. Johnson P (1995) Comparison of pier-scour equations using field data. *J Hydraul Eng* 121(8):626–629. [https://doi.org/10.1061/\(ASCE\)0733-9429\(1995\)121:8\(626\)](https://doi.org/10.1061/(ASCE)0733-9429(1995)121:8(626))
9. Federal Highway Administration, Lagasse PF, Zevenbergen LW, Spitz WJ, Arneson LA, Clopper PE (2012) Evaluating scour at bridge. Hydraulic Engineering Circular No. 18, 5th edn, FHWA-HIF-12-003 HEC-18. U.S. Department of Transportation Federal Highway Administration, Washington, DC
10. Gao DG, Pasada U, Nordin CF (1993) Pier scour equations used in the People's Republic of China. Publication No. FHWA-SA-93-076, Sept 1993
11. Juravlev MM (1984) Local scour at bridge piers. Transport, Moscow, 1984-122ps (Russian language)
12. Chiew YM, Melville BW (1987) Local scour around bridge piers *Journal of Hydraulic Research* 25(1):15–26. <https://doi.org/10.1080/00221688709499285>
13. Raudkivi AJ, Ettema R (1983) Clear-water scour at cylindrical piers. *J Hydraul Eng* 131:338–350

Identifying the Reasonable Rainfall Intensity Formula and Intensity–Duration–Frequency Curve for Tan Son Hoa Station, Ho Chi Minh City



Dong Nguyen Dang and Thi Hoa Binh Le

Abstract Determining the relationship between rainfall intensity–duration–frequency (IDF) is primarily required for the design and management of any city’s drainage system worldwide. In recent years, Ho Chi Minh City has had to face to climate problems such as growth in the extreme rainfall events which resulted in rising serious floods and inundation. This city’s drainage system and flood defense structures were designed based on outdated input criteria, which may no longer be suitable for recent situation. This paper presents updated information on the rainfall IDF curve for Ho Chi Minh City. Moreover, the reasonable rainfall intensity formula-based IDF curves for frequencies of 2, 5, 10, 50 and 100 years are proposed. The results are able to support the local government in designing or upgrading drainage systems.

Keywords Rainfall intensity · The IDF curve · Drainage systems · Flood inundation · Tan Son Hoa station

1 Introduction

The drainage systems play a crucial role in urban areas since they mostly convey the runoff during rainfall events. The capacity of a drainage system is mainly based on the rainfall characteristics of the local urban areas in which intensity–duration–frequency (IDF) curves are normally selected for design purpose as a convenient form of rainfall information. In urban areas, natural land surfaces have commonly been replaced by artificial surface. As a result of this, the direct runoff increases, which may put more pressure on the drainage systems. As such, the performance of drainage systems may no longer meet the requirements and thereafter results in

D. N. Dang (✉) · T. H. B. Le
Thuyloi University, Hochiminh City, Vietnam
e-mail: nguyendd@tlu.edu.vn

water-loggings or inundations. Besides, rainfall characteristics have been changed, especially increasing in extreme rainfall events, due to global warming [1–3], which are now significantly contributing in exacerbating inundation in urban areas.

Ho Chi Minh City (HCMC) is known as the biggest economic city of Vietnam. This coastal city is also at the highest risk of floods and inundation [4, 5]. Located in low-lying lands of the Sai Gon–Dong Nai River basin with a complex river network, HCMC is easily affected by different flood sources [6–8]. During rainy season, the inundation in HCMC is more frequently due to a long rainy period from May to November. The average cumulative rainfall is about 2000 mm per year with approximately 160 rainfall events. Obsolete and accomplished sewer systems, together with a heavy rainfall, could make the city highly on inundation, traffic jam and paralysis. This situation may become worse and effect more citizens in the future because of the ongoing rapid population and rising in extreme rainfall [7]. Viet [9] investigated the change in rainfall intensity due to the global climate and urbanization by using Wenzel formula. The author reported that HCMC witnessed a significant increase in rainfall intensity during the period of 1955–2007. In another study on HCMC's rainfall, Nguyen et al. [10] developed the rainfall IDF curve for HCMC using rainfall data from 1980 to 2015. The result showed that the generalized extreme value (GEV) distribution is appropriate for modeling extreme rainfall corresponding to different durations. Similarly, there are several studies on the rainfall IDF curve for HCMC [11, 12]. However, in the authors' knowledge, the suggestion of a reasonable rainfall intensity formula with local parameters for HCMC could not be found in previous papers so far. Hence, the aim of this research is to provide the updated information on the rainfall IDF curve for HCMC. Besides, the reasonable empirical formula-based IDF curves for frequencies of 2, 5, 10, 50 and 100 years are also proposed to assist the local government in planning or upgrading the drainage systems in urban areas.

2 Data and Methodology

The methodology adopted for this research is presented in Fig. 1. Verified sub-hourly rainfall data from Tan Son Hoa station is used in the present analysis. The data is provided by the National Hydro–Meteorological Service (NHMS) of Vietnam. The time series span through 64 years from 1952 to 2015 and was checked carefully for quality.

There are several probability distributions in the literature that can be used for frequency analysis of extreme value. For comparison purpose, the Normal, Log-Normal (LN), Pearson III (P3), Log-Pearson III (LP3), Gumbel, GEV distributions are used for frequency analysis in this study. The probability distribution functions employed in this paper are shown in Table 1.

The best-fit probability distribution is selected by the Akaike information criterion (AIC) [13] and Bayesian information criterion (BIC) [14]. The distribution with the lowest AIC and BIC values is supposed to be the most appropriate. The forms of AIC and BIC are shown by Eqs. 1 and 2:

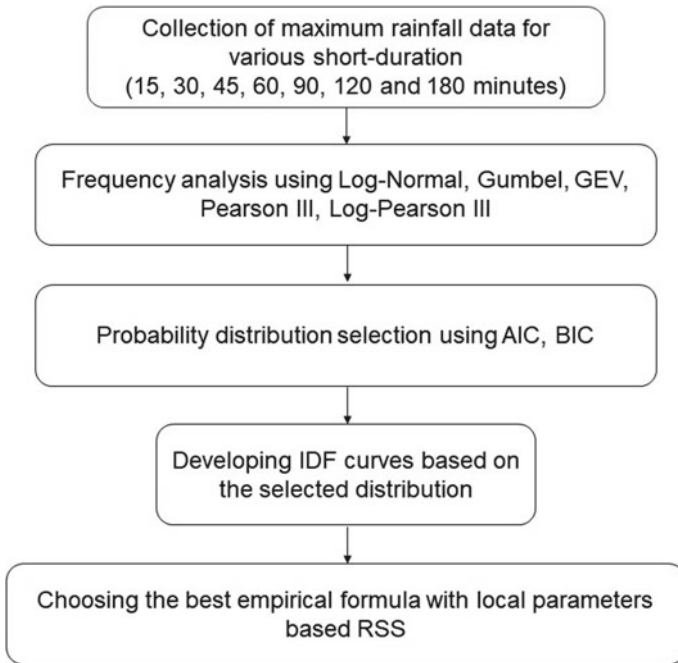


Fig. 1 Employed research methodology

$$AIC = -2 \log L(\theta|X) + 2k \tag{1}$$

$$BIC = -2 \log L(\theta|X) + k \ln(n) \tag{2}$$

where n is the sample size, k is the number of parameters in a given model, $-\log L(\theta|X)$ is the minimized negative log-likelihood function.

Since the best-fit probability distribution is found out, the T -year return level Z_T can be calculated. Then, the rainfall IDF curves can be represented as a graph, in which rainfall intensity is placed on the vertical axis, rainfall duration is placed on the horizontal axis and the curves display the return period.

In order to easily use the results of rainfall IDF curves in practical applications, the present study uses some empirical formulas to describe these IDF curves, including Sherman (1931), Bernard (1932) and Wenzel (1982) formulas.

Sherman: $I = \frac{a}{(T_d+b)^c}$

Bernard: $I = \frac{a}{T_d^n}$

Wenzel: $I = \frac{c}{T_d^e+f}$

where I is rainfall intensity, T_d is rainfall duration and a, b, c, e, n and f are local parameters.

Table 1 Description of probability distribution functions

Dist.	Probability density function	Range	Parameters
Normal	$f(x) = \frac{1}{\sigma\sqrt{2\pi}} \exp\left[-\frac{1}{2}\left(\frac{x-\mu}{\sigma}\right)^2\right]$	$-\infty < x < +\infty$	μ = mean σ = standard deviation ($\sigma > 0$)
LN	$f(x) = \frac{\exp\left[-\frac{1}{2}\left(\frac{\ln(x)-\mu}{\sigma}\right)^2\right]}{(x)\sigma\sqrt{2\pi}}$	$\gamma < x < +\infty$	σ = scale parameter μ = shape parameter
P3	$f(x) = \frac{1}{x\beta\Gamma(\alpha)} \left(\frac{x-\gamma}{\beta}\right)^{\alpha-1} \exp\left(-\frac{x-\gamma}{\beta}\right)$	$0 < \gamma < x$ $\alpha > 0, \beta > 0$	α = shape parameter β = scale parameter γ = location parameter
LP3	$f(x) = \frac{1}{x\beta\Gamma(\alpha)} \left(\frac{\ln(x)-\gamma}{\beta}\right)^{\alpha-1} \exp\left(-\frac{\ln(x)-\gamma}{\beta}\right)$	$0 < x < +\infty, \beta < 0$ $e^\gamma \leq x \leq +\infty, \beta > 0$	α = shape parameter β = scale parameter γ = location parameter
GEV	$f(x) = \begin{cases} \exp\left\{-\left[1 + \xi\left(\frac{x-\mu}{\sigma}\right)\right]^{-1/\xi}\right\} \\ \exp\left\{-\exp\left[-\left(\frac{x-\mu}{\sigma}\right)\right]\right\} \end{cases}$	$1 + \xi\left(\frac{x-\mu}{\sigma}\right) > 0$ $\sigma > 0, \xi \neq 0$ $\sigma > 0, \xi = 0$	μ = location parameter σ = scale parameter ξ = shape parameter When $\xi = 0$, the GEV distribution converts into the Gumbel distribution

To select the most suitable empirical formula with its local parameters for representing the rainfall IDF curves, the residual sum of square (RSS) is used. The empirical with the lowest value of RSS is considered as the suitable formula to describe the rainfall IDF curves.

$$RSS = \sum_{i=1}^n (y_i - f(x_i))^2 \tag{3}$$

where y_i is the i th value of the variable to be estimated, x_i is the i th value of the explanatory variable and $f(x_i)$ is the estimated value of y_i .

3 Results and Discussions

The AIC and BIC values between various probability distributions are shown in Table 2. The lowest value of AIC and BIC for each duration is bold. It can be seen that LN distribution shows its superiority over others. Hence, LN distribution is used for calculating return levels and developing IDF curves.

Table 3 presents the values of rainfall intensity corresponding to different rainfall durations and return periods. The IDF curve developed by LN distribution is shown in Fig. 2. It is clear that, in the same rainfall duration, rainfall intensity increases corresponding to higher return period. In the same return period, the rainfall intensity decreases when the duration increases. For example, for the 100-year return period, the value of precipitation intensity is 139.60 mm/h corresponding to duration of 30 min, meanwhile this value is 48.00 mm/h for the duration of 180 min.

In comparison with research of Nguyen et al. [10], our results show that the values of rainfall intensity are higher than those values for the duration of 15 min. For instance, the value of rainfall intensity is 228.05 mm/h corresponding to duration of 15 min, meanwhile this value in the study of Nguyen et al. [10] is about 190.00 mm/h for the 100-year return period. For longer durations (e.g., 60 and 180 min), the rainfall intensity values in our study are not significantly different from those values of the previous study [10].

Table 4 shows the most suitable empirical formula for describing IDF curves corresponding to different return periods. It can be noted that the selected empirical formula is chosen based on the RSS value. It can be seen from Table 4 that the

Table 2 AIC and BIC values between various distributions

Rainfall duration (min)	Model selection	Distributions				
		LN	P3	LP3	GEV	GUMBEL
15	AIC	643.9	641.4	640.9	641.4	642.8
	BIC	648.2	647.9	647.4	647.9	647.1
30	AIC	558.1	558.3	558.8	558.9	556.9
	BIC	562.4	564.8	565.2	565.4	561.2
45	AIC	547.2	548.5	548.3	547.9	549.6
	BIC	551.5	555	554.8	554.4	553.9
60	AIC	542.1	542.7	542.4	542.6	544.4
	BIC	546.4	549.1	548.9	549.1	548.7
90	AIC	510.1	509.2	508.3	508.3	512.4
	BIC	514.4	515.7	514.8	514.8	516.7
120	AIC	479.2	479.2	479.3	479.3	481.2
	BIC	483.5	485.7	485.8	485.8	485.5
180	AIC	432.3	434	434	434	433.5
	BIC	436.6	440.5	440.5	440.5	437.8

Table 3 Values of rainfall intensity (mm/h) corresponding to different rainfall duration and return period

Duration (min)	Return period (years)				
	2	5	10	20	100
15	92.33	128.06	151.94	174.98	228.05
30	83.94	100.90	111.09	120.27	139.60
45	74.32	89.95	99.39	107.93	125.97
60	63.98	79.17	88.50	97.03	115.31
90	47.09	59.00	66.39	73.17	87.83
120	37.22	46.57	52.36	57.68	69.15
180	25.90	32.38	36.38	40.06	48.00

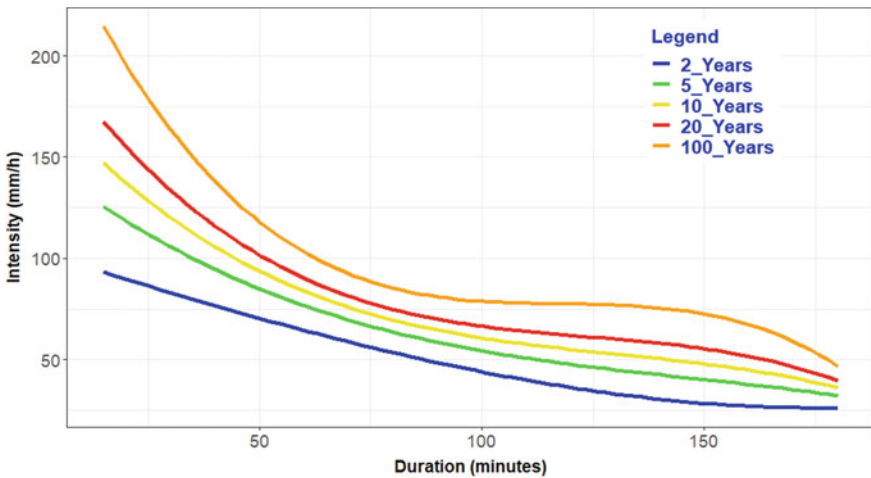


Fig. 2 Rainfall IDF curve

Wenzel formula is suitable for simulating IDF curves of 2, 10 and 20-year return period. Meanwhile, the Sherman formula is considered as the most suitable empirical formula for describing IDF curves of 5 and 100-year return period. Besides, the values of local parameters corresponding to selected empirical formulas are also shown in Table 4.

Table 4 Values of local parameters of the selected empirical formula

Return period (year)	Selected empirical formula	RSS	Local parameter				
			<i>a</i>	<i>b</i>	<i>c</i>	<i>e</i>	<i>f</i>
2	Wenzel	6.83			109,200	1.56	1105
5	Sherman	27.73	109,800	92.62	1.45		
10	Wenzel	91.44			7320.32	0.97	35.18
20	Wenzel	173.30			3557.48	0.81	11.59
100	Sherman	425.30	910.31	− 1.38	0.53		

4 Conclusion

This study has built the IDF curve for Tan Son Hoa rainfall station in the period 1952–2015 by applying the LN probability distribution function which is considered as the most suitable distribution for frequency analysis of rainfall intensity. The results from this study provide the values of rainfall intensity corresponding to different periods and frequency. Especially, short-duration rainfall (under 180 min) is considered to be quite important information in finding solutions to cope with waterlogging due to extreme rainfall in HCMC.

In addition, the local parameters of the characteristic of the IDF curve are also determined. This data can be useful to build the design hyetograph from the IDF curve and can be easily use in engineering design applications, such as serving the planning and designing of urban infrastructure projects.

References

1. Trenberth KE, Dai A, Rasmussen RM, Parsons DB (2003) The changing character of precipitation. *Bull Am Meteorol Soc* 84:1205–1217
2. Groisman PY, Knight RW, Easterling DR, Karl TR, Hegerl GC, Razuvayev VN (2005) Trends in intense precipitation in the climate record. *J Clim* 18:1326–1350
3. Milly PC, Betancourt J, Falkenmark M, Hirsch RM, Kundzewicz ZW, Lettenmaier DP, Stouffer RJJS (2008) Stationarity is dead: whither water management? *Science* 319:573–574
4. Hanson S, Nicholls R, Ranger N, Hallegatte S, Corfee-Morlot J, Herweijer C, Chateau J (2011) A global ranking of port cities with high exposure to climate extremes. *Clim Change* 104:89–111
5. Storch H, Downes NK (2011) A scenario-based approach to assess Ho Chi Minh City's urban development strategies against the impact of climate change. *Cities* 28:517–526
6. Lasage R, Veldkamp T, De Moel H, Van T, Phi H, Vellinga P, Aerts J (2014) Assessment of the effectiveness of flood adaptation strategies for HCMC. *Nat Hazards Earth Syst Sci* 14:1441–1457
7. Asian Development Bank. <https://www.adb.org/publications/ho-chi-minh-city-adaptation-climate-change-summary-report>. Accessed 01/09/2022
8. The World Bank. <https://documents.worldbank.org/en/publication/documents-reports/documentdetail/866821468339644916/climate-risks-and-adaptation-in-asian-coastal-megacities-a-synthesis-report>. Accessed 01/09/2022

9. Viet LV (2009) Anh huong cua su phat trien do thi, bien doi khi hay toan cau den gia tang cuong do mua va viec xay dung bieu do mua thiet ke cho thanh pho Ho Chi Minh. Tap chi Khi tuong thuy van 8:24–30
10. Nguyen TQ, Pham TTN, Dao NK (2017) Xay dung duong cong IDF mua cuc doan cho tram Tan Son Hoa giai doan 1980–2015. Tap chi phat trien Khoa hoc va Cong nghe 20:73–81
11. Van Khiem M, Truong Minh H, Nhat Linh L (2017) Impact of climate change on intensity-duration-frequency curves in Ho Chi Minh City. *Clim Change Sci* 3:40–48
12. Trong Quan N, Thi Thao Nhi P, Nguyen Khoi D (2017) Danh gia anh huong cua bien doi khi hau den moi lien he cuong do-chu ky-tan suat cua mua cuc doan tai tram Tan Son Hoa. *Khi tuong thuy van* 10:7–14
13. Akaike H (1974) A new look at the statistical model identification. *IEEE Trans Autom Control* 19:716–723
14. Schwarz G (1978) Estimating the dimension of a model. *Ann Statist* 461–464

Use of Disdrometer Dataset to Detect Kinetic Energy Expenditure and Rainfall Intensity Relationships



Linh Nguyen Van, Xuan-Hien Le, Giang V. Nguyen, Minhho Yeon, Younghoon Kim, and Giha Lee

Abstract Soil is a vital component for supporting life on Earth and is substantially responsible for the operation of any ecological system. Soil erosion is a global problem because it has resulted in the destruction of agricultural land. Raindrops contacting the soil surface may cause soil separation. This process may be identified by assessing the rainfall kinetic energy (KE). Since direct measurements of KE are challenging, statistical formulas are often employed as an alternative option to estimate the KE using rainfall intensity (RI), which significantly influences soil erosion and is very simple to detect. In this study, we collected a rainfall dataset using a laser-based device (OTT Parsivel² optical disdrometer) between June 2020 and December 2021 in Sangju City (Korea) to analyze the property of KE-RI relationship. A total of 37 rainfall events were selected and used for the formation of KE-RI equations. We derived three KE-RI equations in each group based on the three different rainfall intensity groups. Power-law, linear, and polynomial models were used to link KE to RI, and the best correlation between KE and RI was determined using a power-law form.

Keywords OTT Parsivel² disdrometer · Rainfall kinetic energy · Korea

1 Introduction

Soil is an indispensable component for organisms on Earth and is primarily responsible for the operation of every ecological environment. Globally, water-driven soil erosion has been recognized as the leading cause of soil deterioration [1]. Therefore, it is necessary to comprehend the mechanisms that lead to soil erosion.

L. N. Van · X.-H. Le · G. V. Nguyen · M. Yeon · Y. Kim · G. Lee (✉)
Kyungpook National University, Sangju, Korea
e-mail: leegiha@knu.ac.kr

X.-H. Le
Thuyloi University, Hanoi, Vietnam

Soil erosion caused by water involves two main steps. First, rainsplash separates soil particles from the topsoil surface. Then, surface runoff carries the detached soil particles away. When rain particles land on the ground, they generate rainfall kinetic energy (KE), which sends soil particles traveling [2]. In past decades, a number of scholars have devised numerous methods for estimating the KE of rainfall. For instance, direct measurements of raindrop impact have been attempted [3]; however, the related devices are costly and complex to use. Consequently, empirical equations are an option for predicting KE from rainfall intensity (RI), which is readily obtainable. In soil erosion models, for example, the surface soil erosion model (S-SEM) [4], the KE is a crucial parameter for describing the erosivity of raindrops. Equations (1) and (2) employ power-law [5] and linear correlations [2] to link KE to IR.

$$KE = a \times IR + b \quad (1)$$

$$KE = c \times IR^d \quad (2)$$

where a , b , c , and d are empirical parameters.

The primary objective of this research is to determine the optimal KE–RI connection in Sangju City (Korea) and maybe in other Sangju regions with comparable climate circumstances. To do this, a database of raindrop sizes and terminal velocities (collected from June 2020 to December 2021) compiled by a laser optical disdrometer constructed at Kyungpook National University was used to in this investigation. Our results should help the development of improved physics-based models of soil erosion.

2 Area Description and Measurement Instruments

Sangju is situated in central Korea (the North Gyeongsang Province) and has an inland climate (Fig. 1).

The OTT Parsivel² disdrometer was installed atop a Kyungpook National University building. Beginning in June 2020, the disdrometer was used to monitor rainfall characteristics. The Parsivel is an optical sensor that creates a 30-mm wide, 180-mm long, and 1-mm high laser beam, and the measurements are conducted according to the following method. (1) If no raindrop crosses the laser beam, the receiver creates the highest voltage. (2) Rain particles obstruct a portion of the laser beam proportional to their diameter as they travel across the beam; the resulting decrease in output voltage determines the particle size. (3) The duration of the signal determines the particle's velocity. A signal is created when a raindrop enters the light strip and is terminated when the raindrop completely departs the light strip.



Fig. 1 Parsivel disdrometer located inside the Kyungpook National University campus

3 Methodology

Different criteria were used to sort the suitable rainfall events for the study (Table 4) [6–8]. After the data were processed, they were carefully looked over for anomalies in the distribution of rainfall intensity. Lim et al. noted that when raindrops hit the disdrometer’s safety covers and combine with other drops, they may cause disturbance in the laser zone, which makes the raindrops bigger [7]. During storms, it is feasible for two raindrops to pass through the sensor at the same time, giving an overstated, unusually high intensity recording [8]. Consequently, data with unexpectedly high intensity values were recognized outliers and deleted.

RI (mm/h), the most important indicator for soil loss, was found by using the below formula:

$$RI = 3.6 \times 10^{-3} \left(\frac{\pi}{6}\right) \left(\frac{1}{\Delta t \times A_b}\right) \sum_i^{32} N_{D_i} D_i^3 \tag{3}$$

where $A_b = 0.0054 \text{ m}^2$, $\Delta t = 10 \text{ s}$, and N_{D_i} = number of raindrops corresponding to diameter D_i .

Equation (4) constitutes the rainfall erosivity indices [namely time-related kinetic energy (KE_{exp} ; $\text{J m}^{-2} \text{ h}^{-1}$)] that was employed in this investigation.

Table 1 Description of the evaluation criteria used in this research

Name	Equation	Limitation	Best value
RMSE	$\sqrt{\frac{1}{n} \sum_{i=1}^n (O_i - F_i)^2}$	0.0 to $+\infty$	0.0
MAE	$\frac{1}{n} \sum_{i=1}^n O_i - F_i $	0.0 to $+\infty$	0.0
R^2	$\frac{[\sum_{i=1}^n (O_i - \bar{O})(F_i - \bar{F})]^2}{\sum_{i=1}^n (O_i - \bar{O})^2 \sum_{i=1}^n (F_i - \bar{F})^2}$	0.0 to 1.0	1.0

O_i observations, F_i forecasts; \bar{O} mean of observed values, \bar{F} mean of forecasted values, n number of samples

$$KE_{exp} = 3.6 \times 10^3 \left(\frac{\pi}{12}\right) \left(\frac{\rho}{\Delta t \times A_b}\right) \sum_i^{32} N_{D_i} D_i^3 V_i^2 \tag{4}$$

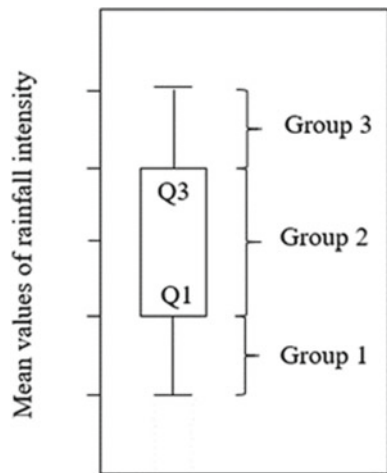
where V_i = raindrop velocity (m/s) corresponding to diameter D_i .

Multiple statistical metrics including RMSE, MAE, and R^2 , were employed to evaluate the observed and predicted KE values that were forecasted by KE-IR equations (Table 1).

4 Results and Discussion

We established the relationship between RI and KE_{exp} using three rainfall event groups (Fig. 2). The required empirical parameters were calculated using the least square method in MATLAB to reduce the standard estimation error.

Fig. 2 Details on the categorization of each kind of group. Group 1 includes events 3, 8, 9, 10, 11, 20, 29, 35, and 37, while group 3 contains events 1, 13, 17, 21, 23, 24, 26, 27, and 33. The rest rainfall events compose group 2.



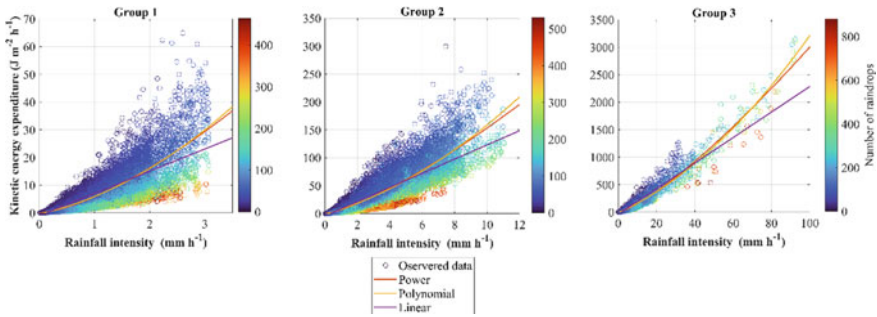


Fig. 3 Scatter plots of KE_{exp} –IR points were analyzed by three mathematical equations corresponding to each rainfall event group

Table 2 KE_{exp} –RI equations corresponding to the three different rainfall event groups

	Power-law	Linear	Polynomial
Group 1	$5.83 \times RI^{1.47}$	$8.02 \times RI - 1.01$	$1.90 \times RI^2 + 4.42 \times RI - 0.42$
Group 2	$7.12 \times RI^{1.33}$	$12.70 \times RI - 3.99$	$0.76 \times RI^2 + 8.43 \times RI - 1.45$
Group 3	$7.97 \times RI^{1.29}$	$23.22 \times RI - 36.69$	$0.16 \times RI^2 + 15.87 \times RI - 13.31$

Figure 3 depicts the connections between KE_{exp} and RI for the three categories of precipitation events. Table 1 presents the fitting formulas for each rainfall event group, whereas Table 2 summarizes the statistical results in comparison with the observed data. We see that the KE_{exp} –RI values in group 1 display less dispersion than those in the other groups, resulting in similar trends for all three equations; nevertheless, the R^2 values in group 1 (0.77–0.79) are less than those in group 2 (0.83–0.85) and group 3 (0.91–0.95). In every rainfall event group, the power-law models excelled over the others, producing the greatest R^2 and the lowest MAE and RMSE (Table 3).

5 Conclusions

The most typical soil erosion models use the KE of rainfall as an erosivity parameter, whereas direct KE observations are rare. Thus, empirical relationships between RI and KE are used as an alternative option in soil erosion models to characterize erosivity. Here are some of our main conclusions:

- (1) The KE_{exp} values typically fall within a constrained range.
- (2) The power-law model found the most accurate match between KE_{exp} and RI.

Table 3 Statistical analysis of the relationship between KE_{exp} and RI corresponding to the three rainfall event groups

	Function	R^2	RMSE ($J m^{-2} h^{-1}$)	MAE ($J m^{-2} h^{-1}$)
Group 1	Power	0.79	2.14	0.90
	Polynomial	0.79	2.14	0.84
	Linear	0.77	2.25	0.99
	Power	0.85	8.58	4.02
Group 2	Polynomial	0.85	8.63	4.16
	Linear	0.83	9.16	5.17
	Power	0.95	42.17	16.15
Group 3	Polynomial	0.94	43.63	20.47
	Linear	0.91	55.16	33.90

Funding This work was supported by the National Research Foundation of Korea (NRF) grant funded by the Korean government (MSIT) (No. 2020R1A2C1102758).

Appendix

See Table 4.

Table 4 Information on the selected rainfall events

Event	Date (dd/mm/yy hh:mm)	Duration	Number of raindrops	Number of outliers	Intensity (mm/h)				
					Max	Mean	Median	Std. dev	Skewness
1	10/06/2020 20:51	09 h 30 min	307,808	119	17.87	4.70	4.00	4.26	0.87
2	13/06/2020 19:54	13 h 42 min	385,208	431	7.4	1.36	0.21	1.85	1.49
3	24/06/2020 12:45	26 h 31 min	347,936	1573	1.22	0.20	0.10	0.24	2.37
4	12/03/2021 10:40	06 h 01 min	95,761	93	3.95	1.44	1.31	0.87	0.65
5	27/03/2021 13:25	14 h 04 min	359,840	117	5.01	1.61	1.47	1.14	0.60
6	03/04/2021 10:20	21 h 06 min	714,019	314	5.20	1.35	0.98	1.24	1.02
7	12/04/2021 11:53	13 h 36 min	223,265	202	4.73	1.30	1.08	1.12	0.92
8	01/05/2021 12:32	17 h 09 min	61,303	1088	0.5	0.13	0.10	0.08	2.89
9	04/05/2021 16:31	09 h 32 min	182,322	326	3.07	0.65	0.39	0.69	1.41
10	10/05/2021 07:26	25 h 33 min	188,754	1156	2.05	0.35	0.10	0.47	1.94
11	16/05/2021 18:15	13 h 23 min	512,393	525	2.55	0.51	0.24	0.57	1.50
12	20/05/2021 09:37	14 h 49 min	743,031	188	4.38	1.19	0.96	1.04	0.90
13	28/05/2021 11:49	2 h 39 min	92,003	68	18.24	5.96	4.75	3.92	1.02
14	30/05/2021 22:25	7 h 04 min	51,022	151	4.71	0.94	0.10	1.22	1.37
15	03/06/2021 10:01	16 h 13 min	484,004	251	5.68	1.31	0.90	1.31	1.03
16	10/06/2021 20:06	11 h 45 min	149,679	131	4.34	1.13	0.83	1.04	0.98
17	22/06/2021 19:45	52 min	17,647	22	32.48	7.37	3.37	8.29	1.35
18	03/07/2021 13:17	15 h	371,419	305	7.65	1.66	0.76	1.90	1.28
19	05/07/2021 19:18	9 h 04 min	196,799	75	4.75	1.23	0.82	1.17	1.05
20	06/07/2021 17:13	24 h 40 min	210,285	1704	0.37	0.12	0.10	0.05	3.15

(continued)

Table 4 (continued)

Event	Date (dd/mm/yy hh:mm)	Duration	Number of raindrops	Number of outliers	Intensity (mm/h)				
					Max	Mean	Median	Std. dev	Skewness
21	08/07/2021 01:29	4 h 16 min	149,756	99	19.50	5.71	4.42	4.71	1.05
22	10/07/2021 19:08	03 h 58 min	52,814	208	4.93	0.70	0.10	1.13	2.06
23	11/07/2021 19:06	40 min	43,737	36	53.55	14.22	12.40	11.54	1.28
24	27/07/2021 19:33	01 h 01 min	81,024	7	92.52	26.08	21.43	23.14	0.82
25	01/08/2021 15:47	07 h 15 min	167,090	318	10.04	1.90	1.15	2.14	1.45
26	08/08/2021 13:55	01 h 21 min	36,583	78	30.97	4.29	1.24	7.25	2.32
27	10/08/2021 09:54	01 h 13 min	31,325	30	36.20	6.31	0.78	9.59	1.52
28	23/08/2021 09:09	27 h 49 min	578,908	659	8.47	1.99	1.40	1.98	1.16
29	25/08/2021 16:20	07 h 34 min	137,149	339	2.87	0.47	0.1	0.69	2.00
30	27/08/2021 08:59	8 h 17 min	118,828	138	8.33	1.55	0.19	2.22	1.41
31	01/09/2021 02:48	13 h 21 min	286,138	404	11.05	2.09	0.73	2.59	1.34
32	06/09/2021 16:38	21 h 54 min	290,235	837	3.72	0.65	0.11	0.88	1.66
33	16/09/2021 23:06	13 h 25 min	320,541	173	11.13	2.45	1.23	2.72	1.11
34	21/09/2021 07:01	4 h 06 min	86,537	38	9.40	2.32	1.58	2.25	0.94
35	11/10/2021 02:20	40 h 37 min	695,308	561	2.20	0.50	0.29	0.49	1.15
36	15/10/2021 16:26	14 h 19 min	210,792	419	2.79	0.75	0.57	0.64	1.19
37	30/11/2021 07:22	16 h 04 min	158,070	406	3.07	0.62	0.17	0.76	1.43

References

1. Panagos P, Borrelli P, Meusburger K, Yu B, Klik A, Jae Lim K, Yang JE, Ni J, Miao C, Chatterpadhyay N et al (2017) Global rainfall erosivity assessment based on high-temporal resolution rainfall records. *Sci Rep* 7:4175
2. Torres DS, Salle SC, Creutin JD, Delrieu G (1992) Quantification of soil detachment by rain-drop impact: performance of classical formulae of kinetic energy in Mediterranean storms. In: *Proceedings of the Oslo symposium on erosion and sediment transport monitoring programmes in river basins*
3. Madden LV, Wilson LL, Ntahirpera N (1998) Calibration and evaluation of an electronic sensor for rainfall kinetic energy. *Phytopathology*® 88:950–959
4. Lee G, Yu W, Jung K (2013) APIP catchment-scale soil erosion and sediment yield simulation using a spatially distributed erosion model. *Environ Earth Sci* 70:33–47
5. Park SW, Mitcell JK, Bubenzer GD (1980) An analysis of splash erosion mechanics
6. Fornis RL, Vermeulen HR, Nieuwenhuis JD (2005) Kinetic energy-rainfall intensity relationship for central Cebu, Philippines for soil erosion studies. *J Hydrol* 300:20–32
7. Lim YS, Kim JK, Kim JW, Park BI, Kim MS (2015) Analysis of the relationship between the kinetic energy and intensity of rainfall in Daejeon, Korea. *Quat Int* 384:107–117
8. Petan S, Rusjan S, Vidmar A, Mikoš M (2010) The rainfall kinetic energy-intensity relationship for rainfall erosivity estimation in the Mediterranean part of Slovenia. *J Hydrol* 391:314–321

Evaluating the Performance of Light Gradient Boosting Machine in Merging Multiple Satellite Precipitation Products Over South Korea



Giang V. Nguyen, Xuan-Hien Le, Linh Nguyen Van, Sungho Jung, Chanul Choi, and Giha Lee

Abstract Precipitation information with high accuracy plays a crucial role in hydrology and water resources management. With the advance in technology, satellite precipitation products (SPPs) provide an unprecedented opportunity for monitoring the spatial and temporal variation of precipitation from space. However, SPPs still present a low performance with high uncertainty. To overcome this problem, the current study aims to produce a new reanalysis of precipitation data by integrating information from observation data with multiple SPPs over South Korea under the aid of a fast and high-performance machine learning-based, namely a light gradient boosting machine. In addition, other statistical merging methods were also carried out to highlight the robustness of the machine learning-based algorithm. To examine the accuracy of merging precipitation products, observed data from 64 automated synoptic observation system rain gauge stations were collected and compared with merging precipitation products. A high agreement between merging precipitation data generated from the machine learning-based approach with observation was witnessed through several continuous criteria and categorical indicators. The results from this study point out that light gradient boosting machine not only has the capability in merging multi-sources precipitation but also it could provide extraordinary rainfall information for the region of interest, especially in areas with low observed station density.

Keywords Satellite precipitation · Merging · Machine learning · Light gradient boosting machine

G. V. Nguyen · X.-H. Le · L. N. Van · S. Jung · C. Choi · G. Lee (✉)
Kyungpook National University, Sangju, South Korea
e-mail: leegiha@knu.ac.kr

X.-H. Le
Thuyloi University, Hanoi, Vietnam

1 Introduction

Variations of precipitation in spatial and temporal have concrete influences on water resources, such as floods and droughts [1]. For that reason, information regarding the variability of precipitation is extremely important. Recently, there are three-main channel sources that provide precipitation information: rain gauges, weather radar, and satellite precipitation products (SPPs) [2]. High accuracy is the main advantage of rain gauge-based data. However, sparse and uneven distribution [3] is one of the disadvantages of this method for presentation variability of precipitation in terms of spatial [4]. Weather radar-based is considered an alternative solution for mitigating the limitation of gauge-based estimation by providing highly spatiotemporal resolution precipitation data [5]. Unfortunately, there is ample evidence pointing out that the quality of precipitation data estimated from weather radar-based still unsatisfactory with several requirements [6, 7]. With the developments in the remote sensing area, SPPs provide invaluable data sources for monitoring precipitation from space on a global scale [3]. Notwithstanding, low accuracy in both rainfall intensity estimation and capability in detecting rainfall events becomes the major challenge of SPPs for further application in hydrological and water resources management [2]. To meet requirements for further studies, various approaches were proposed for improving the performance of SPPs, especially in the regions, that suffer from the absence of observed data [2]. One of the typical methods is merging multiple precipitation data sources together. This method is based on the assumption, each precipitation source has its own merits and drawbacks [8], and the merging process tries to inherent advantages from the each data source to generate new higher accuracy precipitation product. In addition, the effect of topography as well as the geographical similarity should be take account in merging precipitation product (MPP). Onwing to they have concrete influence on spatial distribution of rainfall [2]. So that this make merging process which becomes more complicated.

Nowadays, machine learning (ML) has become more popular and widely utilized in many fields. For hydrological studies, ML models are increasingly proving to have more advantages than the traditional model [2, 9]. The previous studies also proved that ML could effectively map the non-linear relationship in the merging process [8, 10]. Zhang et al., demonstrated that the integration of two ML algorithms for merging could generate a higher accuracy product compared to using only one algorithm. This originates from the fact that the decision-making by many experts will be better rather than relying on only one person and also the primary mechanism of ensemble machine learning algorithms. Recently, an ensemble algorithm, namely light gradient boosted machine (LGBM), received more attention due to its characteristics, and the result achieves from LGBM which generally presents better than the other method [11].

With the aim generate a new precipitation product in this study, which has high accuracy over South Korea, the LGBM algorithm was adopted to take advantage of multiple precipitation data sources. In addition, two other statistical merging methods were also applied for comparison purposes.

2 Methodology and Study Area

2.1 Methodology

Light Gradient Boosting Machine

An LGBM (Fig. 1) is a fast gradient boosting framework proposed by Microsoft Research Asia in 2017 [12, 13]. It belongs to the decision tree-based ensemble model, and LGBM is demonstrated to be superior in terms of computation performance and predicting accuracy [14]. Two novel techniques, which include gradient-based one-side sampling and exclusive feature bundling, were proposed to improve computation speed in LGBM. In addition, the leaf-wise growth strategy was adopted in LGBM to lighten the computation burden in the training process instead of using a level-wise growth method like in gradient boosting or other boosting paradigms, which is the main cause to make significantly increased memory consumption [13]. In the LGBM, the number of the tree ($n_{estimators}$), the boosting learning rate ($learning_rate$), and the maximum tree deep for base learners (max_depth) are the main hyperparameters that need to be tuned. In this study, a trial and error strategy was utilized to achieve the best hyper-parameters, and the final values of $n_{estimator}$, $learning_rate$, and max_depth are 100, 0.01, and 4 which were set, respectively.

Statistical Merging Method

In the current study, two statistic-based methods (namely one-outlier-removed average (OAR) and inverse error variance weighting (IEVW)) were also conducted for merging multiple SPPs. The formulation of each approach was presented as the following:

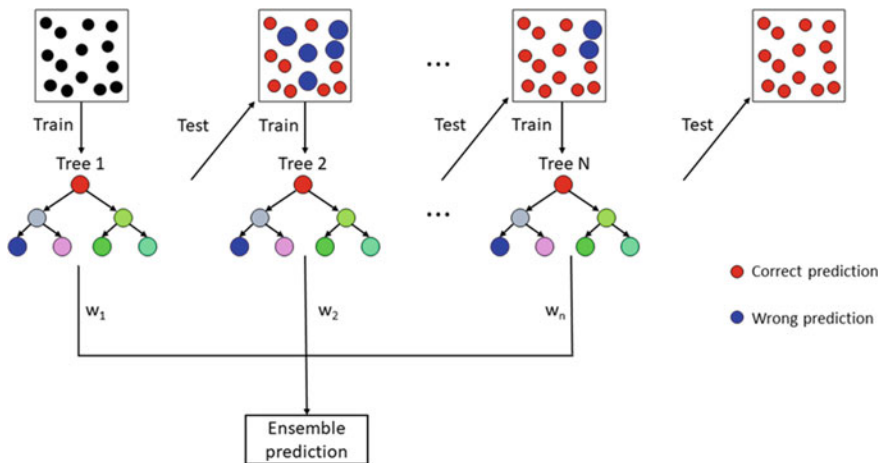


Fig. 1 Schematic of light gradient boosting machine

Table 1 Evaluation indices are used for measuring performance

Continuous indices	Categorical indices
$CC = \frac{\sum_{i=1}^N (S_i - \bar{S})(O_i - \bar{O})}{\sqrt{\sum_{i=1}^N (S_i - \bar{S})^2} \sqrt{\sum_{i=1}^N (O_i - \bar{O})^2}}$	$POD = \frac{Hit}{Hit+Miss}$
$MAE = \frac{\sum_{i=1}^N O_i - S_i }{N}$	$FAR = \frac{False}{Hit+False}$
$RMSE = \sqrt{\frac{1}{N} \sum_{i=1}^N (O_i - S_i)^2}$	$CSI = \frac{Hit}{Hit+Miss+False}$

$$P_{OORA} = \frac{1}{N} \sum_{i=1}^{N-1} S_i \tag{1}$$

$$P_{IEVW} = \frac{1}{\sum_{i=1}^N 1/e_i^2} \sum_{i=1}^N \frac{1}{e_i^2} S_i \quad \text{with } e = \frac{1}{\sigma_i^2} \tag{2}$$

where P_{OORA} and P_{IEVW} are the merging precipitation product achieved from OORA and IEVW, respectively. N is the number of the SPPs, S_i is the i th SPP, e is the error variance, and σ is the error square between SPP and observed data. The OORA method (Eq. 1) belongs statistical-based. First, SPPs compared with observation data by error index (e.g. root mean square error in this study), and then, the SPP with highest error was excluded from the merging process. Meanwhile, in the IEVW (Eq. 2) method, observation data in the study area will be collected and utilized to estimate error variance. After that, the weight of each precipitation product will be determined based on its performance.

To investigate the performance of merging precipitation products from the LGBM algorithm as well as original SPP data, several continuous indices including correlation of coefficient (CC), mean absolute error (MAE), and root mean squared error (RMSE) were utilized. Simultaneously, the three categorical, namely probability of detection (POD), false alarm rate (FAR), and critical success index (CSI), were exploited to measure the capability detection of rainfall events at different rainfall intensities, including no rain ([0, 1) mm/d), light rain ([1, 5) mm/d), moderate rain ([5, 20) mm/d), heavy rain ([20, 40) mm/d), and violent rain (≥ 40 mm/d). The formulation of these indices was presented in Table 1.

where S_i stands for estimated precipitation, O_i presents for precipitation obtained from ground-based data. Whilst *Hit*, *Miss*, and *False* values are determined from the contingency Table 2.

2.2 Study Area

South Korea is located in the northern part of Asia, between 33–39°N and 124–130°E, with a total area is approximately 99,373 km². Owing to its position and

Table 2 Contingency table was used to measure the categorical indices

Satellite product	Observation data		
	Yes	No	Total
Yes	Hit (H)	False alarm (F)	$H + F$
No	Miss (M)	Correct negative (C)	$M + C$
Total	$H + M$	$F + C$	$N = H + F + M + C$

geographical characteristic, South Korea suffers from many storms moving from the sea to the mainland. Consequently, a lot of severe damage to people and property. Moreover, the topography in South Korea is very complicated, which has a significant impact on the rainfall distribution and climate in this region. Furthermore, the country is mainly mountainous, with small valleys and narrow coastal plains. So that reason, obtaining the observation data in a remote area or at high altitudes is frequently tricky [4].

The data from three SPPs, which include Climate Hazards Group InfraRed Precipitation with Station data (CHIRPS), Global Satellite Mapping of Precipitation (GSMaP), and Tropical Rainfall Measuring Mission (TRMM) at a daily scale, were combined with observation data from Automatic Weather Stations (AWS). In addition, an independent dataset was collected from another system, namely Automated Synoptic Observation System (ASOS), which was used for validation purposes. All aforementioned data were collected from 2003 to 2017. The geographical information about the region of interest and the distribution of rainfall stations in the current study was presented in Fig. 2

As can be observed in Table 3, since the spatial resolution of SPPs is heterogeneous, this study firstly applied a simplification but efficient method, namely nearest neighbour interpolation, to resample all SPPs to identical spatial resolution. In addition, the data from digital elevation model (DEM) and the similarity between stations which were calculated based on euclidean distance (ED) also used as input data for the LGBM model. The information from 384 AWS stations was then exploited to extract the precipitation from resampled precipitation data, DEM, and ED information at corresponding locations for creating training data for the LGBM model. It should be noted that statistical merging approaches only use SPPs data corresponding to AWS stations for estimating the weight values of each SPPs, and DEM and ED information are excluded from these methods.

Fig. 2 Map of South Korea's position and observation data used in this study

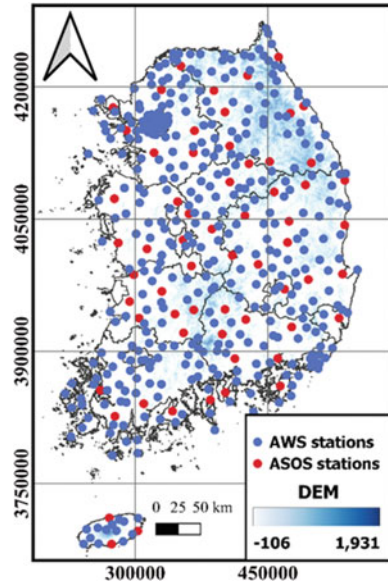


Table 3 Basic information satellite-based precipitation products

Data	Resolution		
	Spatial	Temporal	Spatial coverage
CHIRPS	0.05	Daily	50° S–5° N
GSMaP	0.10	Daily	6° S–60° N
TRMM	0.25	Daily	5° S–5° N

3 Results and Discussion

The density scatter plots in Fig. 3 presented the correlation between estimated precipitation and ground-based data during the period from 2003 to 2017. As presented in Fig. 3, most of the precipitation obtain from satellite-based shows a reasonable correlation with ground-based data. However, SPPs tend to be underestimated precipitation when there is the presence of extreme events. There are several reasons that could be explained why SPPs show poor skill for precipitation estimation. SPPs generally show high error in mountainous areas or in high-altitude regions [2]. Although South Korea is primarily composed of mountains, the limited agricultural lowlands that exist are sandwiched between successive mountain ranges. So that SPPs in South Korea normally come with low performance. The correlation of three MPPs against observation data was presented in Fig. 3d–f. Obviously, merging multiple precipitation products offer new precipitation data, which indicates higher performance in comparison with the original or single precipitation product. CC of precipitation products from the OORA and IEVW methods is 0.535 and 0.549, respectively. The results

achieved from the statistical method also indicated that precipitation estimates from the merging process could shorten the differences against observation data. Figure 3f shows an impressive performance of the LGBM for merging multi-sources precipitation with the value of CC being 0.944. It has been proved unequivocally that the LGBM model can enhance the accuracy of SPPs.

Table 4 summarizes the performance of SPPs and MPPs in two error statistic indicators. The primary SPPs exhibit relative biases over the region of interest in this study. For instance, the values of MAE vary from 3.96 to 4.65 mm/d, and the values of RMSE span from 12.25 to 13.83 mm/day for precipitation information at a daily scale achieved from SPPs.

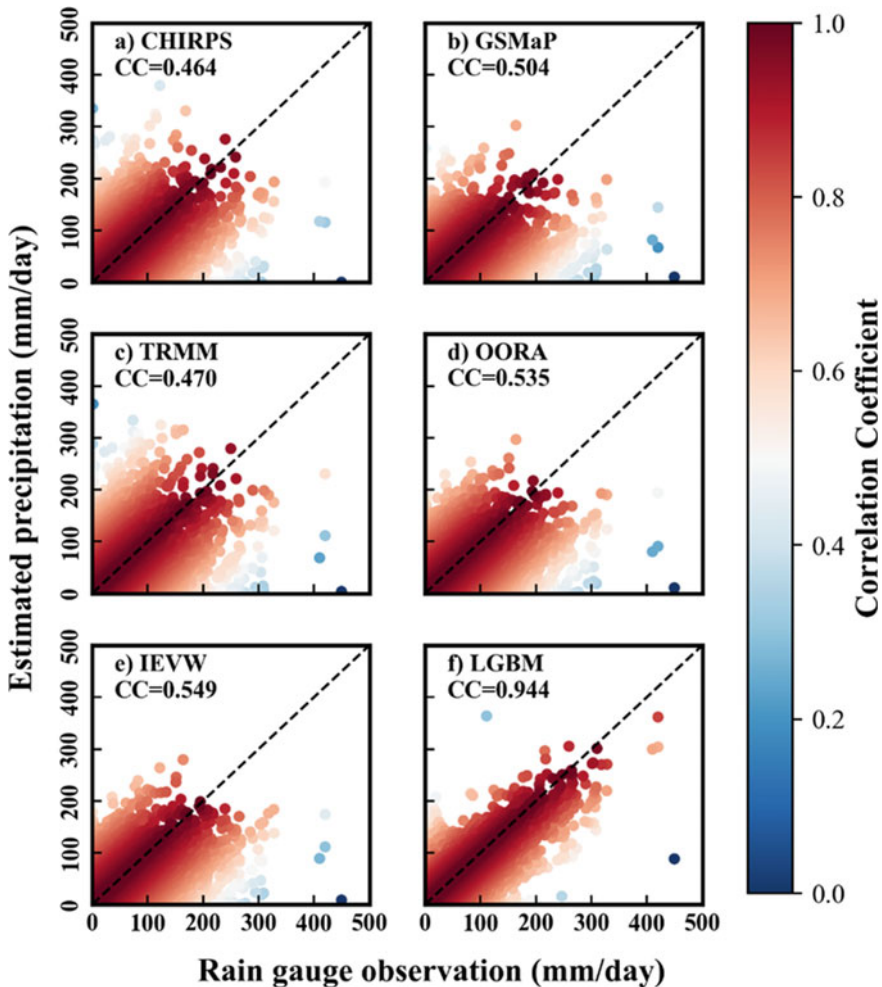


Fig. 3 Correlation between observation data and a CHIRPS, b GSMaP, c TRMM, d OORA, e IEVW, and f LGBM

Table 4 Error statistics in terms of MAE and RMSE of four precipitation products on a daily scale from 2003–2017

	CHIRPS	GSMaP	TRMM	OORA	IEWV	LGBM
MAE (mm/d)	4.65	3.96	4.51	4.06	4.04	1.18
RMSE (mm/d)	13.83	12.25	13.73	12.11	11.71	4.55

The CHIRPS has the worst performance in the SPPs group, with a median MAE of 4.65 mm/d, followed by the TRMM (median MAE of 4.51 mm/d). The GSMaP seems to be more accurate than the two aforementioned products; as can be seen, the median MAE and RMSE values of GSMaP are 3.96 mm/d and 12.25 mm/d, respectively. The information in Table 3 also demonstrated the robustness of the LGBM algorithm for producing high-quality precipitation, the best proof of that is the difference between precipitation obtained from the merging process by the LGBM, and the observed data have been significantly decreased compared with errors of the original SPPs. By comparing with the CHIRPS product, the accuracy of precipitation from the LGBM approximate increases three times with MAE and RMSE which are 1.18 (mm/d) and 4.55 (mm/d), respectively.

For further investigating the accuracy of SPPs as well as MPPs, current research also conducted an evaluation based on categorical indices to elucidate the rainfall event detection of precipitation products.

Figure 4 demonstrates quantitatively how MPPs differ from SPPs in terms of rainfall event detection capability at five rainfall intensities. Generally, all precipitation products present the best performance at no rain events ($[0, 1)$ mm/d) detection, and the ability detection becomes worst at high rainfall intensity. The intercomparison between original SPPs points out that satellite-based precipitation could be provided reasonable accuracy (POD, CSI) with acceptable error (FAR) in the detection of rain and non-rain events. With the rainfall intensity range in $[0, 1)$ mm/d interval, comparative performance is witnessed by CHIRPS, GSMaP, and TRMM with the value of POD 0.902, 0.876, and 0.881, respectively. The categorical indices in Fig. 4 also reveal that all SPP is still unable to capture the rainfall events at higher rainfall intensity, especially for light rainfall events. Except for MPP from the LGBM model, the average value of FAR of remaining precipitation products is over 0.8. Figure 4 also demonstrated that at higher rainfall intensity, where satellite-based is clearly indicated the highest error and the results from statistical-based merging methods also have poor performance, the LGBM offers a new precipitation product that has remarkable capability in rainfall events detection with the mean values of POD and CSI for light rainfall event which are 0.636 and 0.429. Meanwhile, the mean value of FAR is approximately decreased two times when compared with others products at similar rainfall intensity. Investigating the performance of different precipitation products (e.g., SPPs and MPPs in this study) strengthens the fact that the LGBM could be considered an effective method for merging multi-precipitation data sources.

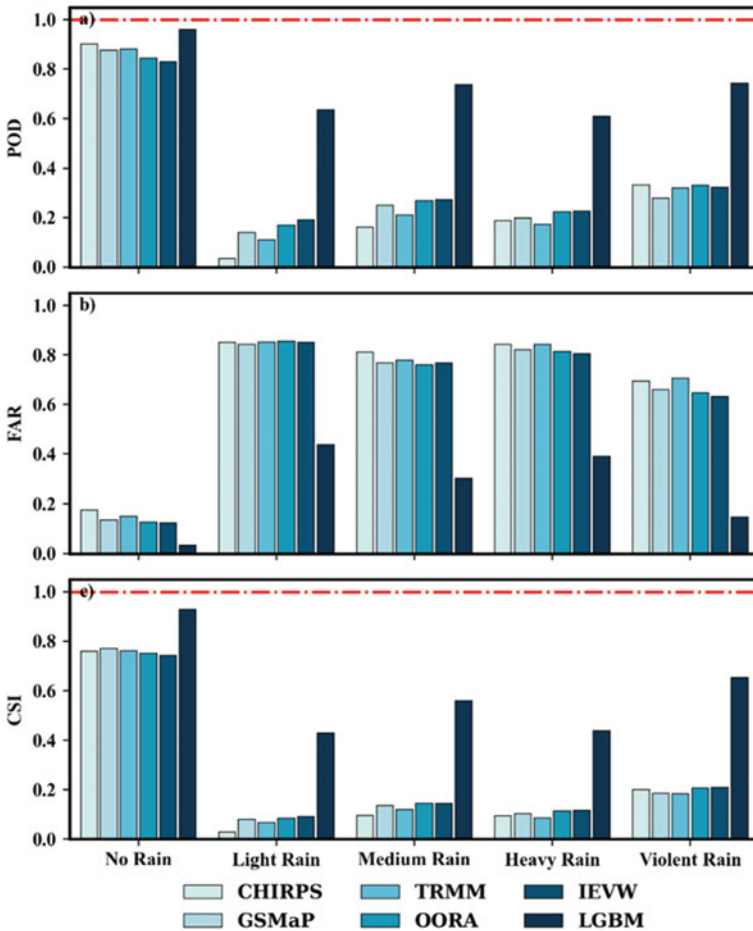


Fig. 4 Categorical indices of a CHIRPS, b GSMaP, c TRMM, and d LGBM at five rainfall intensities

4 Conclusion

With the aim of producing a novel precipitation product with high accuracy by leveraging the robustness of the ML-based model and the advantages of multi-data sources precipitation, the LGBM has been successfully exploited by merging all sources together in this study. The high accuracy of the result achieved from the merging process which was conducted by the LGBM indicated that the LGBM algorithm could consider an effective tool for integrating multiple data sources with a CC value increase of approximately two times when compared with the original data (CC value of merging product from LGBM is 0.944, whilst the highest CC value of original data is 0.504 for GSMaP). In addition, the statistical merging method could

be reduced the error of SPPs. However, the improvement is insignificant. The finding in our research is completely applicable to other regions of the world, specifically in the region with sparsely observed stations.

Declaration of Competing Interest The authors declare no conflict of interest.

Acknowledgements This work was supported by the National Research Foundation of Korea (NRF) grant funded by the Korea Government (MSIT) (No. 2020R1A2C1102758).

References

1. Bennett B, Leonard M, Deng Y, Westra S (2018) An empirical investigation into the effect of antecedent precipitation on flood volume. *J Hydrol* 567:435–445
2. Nguyen GV, Le X-H, Van LN, Jung S, Yeon M, Lee G (2021) Application of random forest algorithm for merging multiple satellite precipitation products across South Korea. *Remote Sensing* 13(20):4033
3. Beck HE, Vergopolan N, Pan M, Levizzani V, Van Dijk AI, Weedon GP, Brocca L, Pappenberger F, Huffman GJ, Wood EF (2017) Global-scale evaluation of 22 precipitation datasets using gauge observations and hydrological modeling. *Hydrol Earth Syst Sci* 21(12):6201–6217
4. Kim J, Han H (2021) Evaluation of the CMORPH high-resolution precipitation product for hydrological applications over South Korea. *Atmos Res* 258
5. Voormansik T, Cremonini R, Post P, Moisseev D (2021) Evaluation of the dual-polarization weather radar quantitative precipitation estimation using long-term datasets. *Hydrol Earth Syst Sci* 25(3):1245–1258
6. Rico-Ramirez M, Liguori S, Schellart A (2015) Quantifying radar-rainfall uncertainties in urban drainage flow modelling. *J Hydrol* 528:17–28
7. Villarini G, Krajewski WF (2010) Review of the different sources of uncertainty in single polarization radar-based estimates of rainfall. *Surv Geophys* 31(1):107–129
8. Baez-Villanueva OM, Zambrano-Bigiarini M, Beck HE, McNamara I, Ribbe L, Nauditt A, Birkel C, Verbist K, Giraldo-Osorio JD, Xuan Thinh N (2020) RF-MEP: A novel Random Forest method for merging gridded precipitation products and ground-based measurements. *Remote Sens Environ* 239
9. Mao G, Wang M, Liu J, Wang Z, Wang K, Meng Y, Zhong R, Wang H, Li Y (2021) Comprehensive comparison of artificial neural networks and long short-term memory networks for rainfall-runoff simulation. *Phys Chem Earth Parts A/B/C* 123:103026
10. Zhang L, Li X, Zheng D, Zhang K, Ma Q, Zhao Y, Ge Y (2021) Merging multiple satellite-based precipitation products and gauge observations using a novel double machine learning approach. *J Hydrol* 594
11. Zhong J, Zhang X, Gui K, Wang Y, Che H, Shen X, Zhang L, Zhang Y, Sun J, Zhang W (2021) Robust prediction of hourly PM_{2.5} from meteorological data using LightGBM. *Nat Sci Rev* 8(10):nwaa307
12. Ke G, Meng Q, Finley T, Wang T, Chen W, Ma W, Ye Q, Liu T-Y (2017) Lightgbm: a highly efficient gradient boosting decision tree. *Adv Neural Inf Process Syst* 30
13. Cui Z, Qing X, Chai H, Yang S, Zhu Y, Wang F (2021) Real-time rainfall-runoff prediction using light gradient boosting machine coupled with singular spectrum analysis. *J Hydrol* 603:127124
14. Wei J, Li Z, Pinker RT, Wang J, Sun L, Xue W, Li R, Cribb M (2021) Himawari-8-derived diurnal variations in ground-level PM_{2.5} pollution across China using the fast space-time light gradient boosting machine (LightGBM). *Atmos Chem Phys* 21(10):7863–7880

Multiple Methods for Homogeneity Analysis of Precipitation Series in Vinh Phuc Province



Phan Manh Hung and Chien Pham Van

Abstract This paper presents multiple statistical methods consisting of cumulative deviations (Cd), Bayesian (Ba), Worsley's likelihood ratio (Wo), and von Neumann's ratio (vN) tests that can be applied to the homogeneity analysis of precipitation series. Vinh Phuc province, an adjacent area of the economic triangle named Ha Noi—Hai Phong—Ha Long in North Vietnam, is used for demonstrating the methods. The series of daily rainfall in the long period between 1/1/1975 and 31/12/2021 at eight meteorological locations in the province are applied. The results depict that the Cd , Ba , and Wo value changes in the permitted range. In detail, the Cd value ranges from 0.23 to 4.34, while the Ba value changes between 0.17 and 2.63, and the vN value varies from 0.16 to 3.51. The Wo showed that almost rainfall series at the studied locations are homogeneity, with the Wo value ranging from 0.13 to 2.66. The series of rainfall at almost locations illustrates homogeneity, and thus, these data can be used for assessing rainfall variability, trend analysis, and for input data in relevant calculations. The Cd , Ba , and vN tests showed similar homogeneity results.

Keywords Rainfall homogeneity · Bayesian test · Cumulative deviations test · Worsley's ratio test · Von Neumann's ratio test

P. M. Hung

Vinh Phuc Department of Agriculture and Rural Development, Vinh Phuc, Vietnam

C. P. Van (✉)

Thuyloi University, 175 Tay Son, Dong Da, Hanoi, Vietnam

e-mail: Pchientvct_tv@tlu.edu.vn

1 Introduction

Rainfall is an important quantity in water bodies, hydrological cycles, water balance, drought, floods, and inundation in river basins. Rainfall series are often assumed to be homogeneous, stable, and independent. On the other hand, when rainfall is measured for a long time, there are many potential reasons and errors for the non-homogeneity of data records, e.g., errors in monitoring and measurements, change of measuring methods, change of measuring devices, and errors in corrections and assimilations. Thus, assessment of rainfall quality in both space (at different monitoring locations) and time is crucial necessary before it is used in relevant studies and calculations.

Different statistical methods are available for homogeneity analysis of the time series of data and precipitation series. Buishand [2] used the von Neumann ratio (vN), cumulative deviations (Cd), Bayesian (Ba), and Worsley's likelihood (Wo) tests to examine the homogeneity of annual rainfall over 30 years in the four regions of the Netherlands. Talaei et al. [4] applied the Ba , Cd , and vN tests for the assessment of the reliability and quality of historical precipitation at forty-one locations over the period from 1966 to 2005 in Iran. Ahmed et al. [1] used different statistical methods mentioned above for the homogeneity assessment of annual and monthly series of precipitation in Pakistan. These examples demonstrate that the above multiple statistical methods can be used to examine the homogeneity of precipitation series in a given domain of interest.

The present study aims to investigate the homogeneity of rainfall at eight locations in Vinh Phuc using multiple statistical methods, named cumulative deviations, Bayesian, von Neumann's ratio, and Worsley's likelihood tests. The daily rainfall data over the long period 1975–2021 for eight stations throughout the domain of interest are used for investigation and analysis purposes.

2 Studied Area and Data Collection

Vinh Phuc is known as the adjacent area of the economic triangle (Ha Noi—Hai Phong—Ha Long) in North Vietnam. The area of the province is about 318.60 km², including different typical topographies such as (i) plain characteristics in the central province with the elevation ranging from 6 to 30 m, (ii) midland properties in the northwest where the elevation changes from 6.4 to 74.6 m, and (iii) mountainous terrain whose the slope varies between 8 and 150‰ (Fig. 1). The province is characterized by the tropical monsoon and humid, with the rainy season from April to November, while the dry remains from December to March.

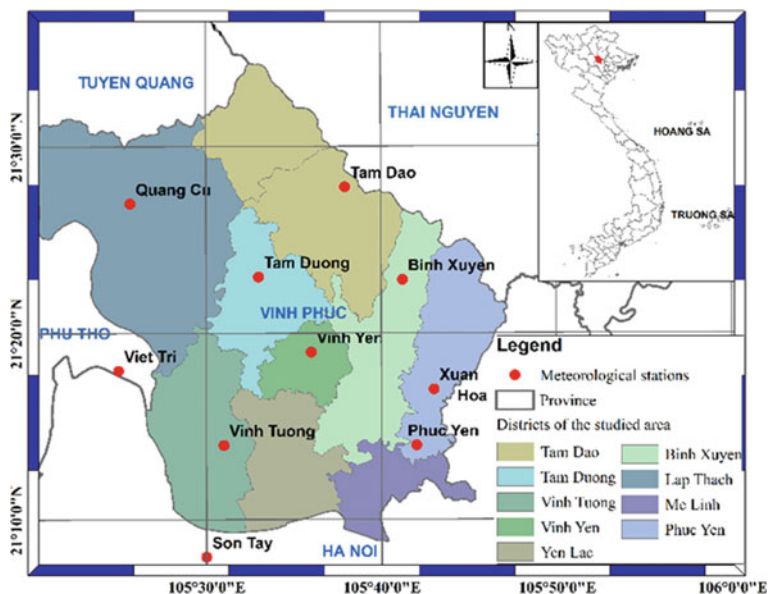


Fig. 1 Study area together with meteorological stations

In recent years, parallel socio-economic development has been the process of renovating and upgrading existing and new urban centers and building industrial parks. Along with the development of urban, the population has increased significantly, revealing a sudden increase in the amount of domestic and industrial wastewater. This amount of wastewater has been directly discharged to receiving sources (e.g., rivers, lakes, and canals) that have not been treated, making the quality of water greatly reduced. Indeed, the rainwater drainage system is still inadequate for urbanization, creating an increasingly serious threat that may impact the sustainable development of the province.

Daily rainfall observations over the Vinh Phuc province are used for investigating multiple statistical methods in analyzing and assessing the homogeneity of rainfall time series. The collected meteorological stations are shown in Fig. 1, while the detailed collective period for each station is summarized in Table 1. The daily rainfall data over the period 1975–2021 for eight stations throughout the province are obtained from the Vietnam National Center for hydro-meteorological forecasting.

Table 1 Collected period of daily rainfall time series at eight stations in the domain of interest

No	Name	Station		Collected data period
		Longitude (°)	Latitude (°)	
1	Binh Xuyen	105°39'00''	21°16'00''	1975–2017
2	Phuc Yen	105°42'00''	21°15'00''	1975–2017
3	Quang Cu	105°29'30''	21°31'10''	1990–2021
4	Tam Dao	105°39'00''	21°28'00''	1975–2021
5	Tam Duong	105°57'00''	21°28'10''	1975–2017
6	Vinh Tuong	105°29'30''	21°15'10''	1975–2017
7	Vinh Yen	105°35'00''	21°18'00''	1975–2021
8	Xuan Hoa	105°28'00''	21°25'10''	1991–2017

3 Method

Four tests, named *Cd*, *Ba*, *Wo*, and *vN*, are chosen in the present study because these tests are widely used in different applications (e.g., [1, 2, 5]). General information on these tests is introduced in this section.

3.1 The *Cd* Test

The *Cd* test is based on the maximum value of a ratio between cumulative deviations from the mean S_k^* and the standard deviation D_x , under the form:

$$Cd = \max \left| \frac{S_k^*}{D_x} \right|, \quad \text{with } 0 \leq k \leq n \tag{1}$$

where the cumulative deviations and standard deviation are calculated as [2]:

$$S_k^* = \sum_{i=1}^k (x_i - \bar{x}), \quad D_x = \frac{1}{n} \sum_{i=1}^n (x_i - \bar{x})^2, \quad \text{with } 1 \leq k \leq n \tag{2}$$

herein, x_t is the observed value, \bar{x} is the mean value of the time series, and n is the number of records in the time series. Note that the maximum value of the *Cd* depicts the non-homogeneity. A critical value of about 1.27 is used for the cumulative deviations test at a 95% confidence level [1, 2].

3.2 The νN Test

The νN test is a non-parameter test that is often applied to investigate the non-homogeneity of series in times. According to von Neuman [5], the νN test is defined as

$$\nu N = \frac{\sum_{i=1}^{n-1} (x_i - x_{i+1})^2}{\sum_{i=1}^n (x_i - \bar{x})^2} \quad (3)$$

A time series is measured as homogeneous or non-homogeneous when the νN value is equal to or below 2, respectively. As pointed out in the previous studies (e.g., [1, 5], a critical νN value equals 1.54 for the time series of the quantity of interest varying between 41 and 57 years at a 95% confidence level.

3.3 The Ba Test

The Bayesian test statistic Ba is defined as [1]:

$$Ba = \sum_{k=1}^{n-1} \left[\frac{\{k(n-k)\}^{-0.5} S_k^*}{D_x} \right]^2, \quad \text{with } 1 \leq k \leq n \quad (4)$$

A large value of the Ba depicts the departure from homogeneity [2]. The critical value of 2.48 for the Ba is identified at a 95% confidence level.

3.4 The Wo Test

Another method, which is widely applied to assess the homogeneity of a time series, is known as Worsley's test denoted as Wo . The Wo is defined as

$$Wo = \frac{\sqrt{n-2}V}{\sqrt{1-V^2}} \quad (5)$$

where V is an indicator that is computed as

$$V = \max |Z_k^{**}|, Z_k^{**} = \frac{1}{\sqrt{k(n-k)}} \frac{S_k^*}{D_x}, 1 \leq k \leq n-1 \quad (6)$$

If the value of W_0 is smaller than the critical value of 3.16 at a 95% confidence level, the time series of interest is considered to be homogeneous [1, 2].

4 Results and Discussion

Table 2 summarizes the results of the homogeneous tests for the monthly rainfall time series at eight meteorological stations (i.e., Binh Xuyen, Phuc Yen, Quang Cu, Tam Dao, Tam Duong, Vinh Tuong, Vinh Yen, and Xuan Hoa), while the detailed values of Cd , vN , Ba , and W_0 versus the critical value at each are shown in Figs. 2, 3, 4 and 5, respectively.

The values of Cd at eight considered stations vary in a range from 0.23 to 4.34, while the vN values range between 0.16 and 3.51. The Ba values for all considered stations change from 0.17 to 2.63, while the W_0 values vary between 0.13 and 2.66. In addition, the monthly series of rainfall at most locations shows a homogeneous (except for a few months at given stations) when the cumulative deviations test is used. This result consists of the results achieved from the Ba and vN tests (see Figs. 2, 3 and 4). When the W_0 test is applied, the monthly series of rainfall is found to be homogeneity.

Among the four considered methods, the Worsley likelihood ratio test statistic shows that there are not any non-homogeneous for every monthly rainfall in a year at eight studied stations. When the three remaining methods are applied, there is at least one month of non-homogeneous in a year. The main reason for the discrepancy between the Worsley likelihood ratio test and the others is due to the use of a large critical value (of 3.16) in the Worsley likelihood ratio test.

Figure 6 shows an example of a radar plot for twelve monthly rainfall time series at Tam Dao station. Note that both critical and calculated values from each method are represented together to compare between four studied methods as well as to identify which methods are most similar. At Tam Dao station, the Cd test is more sensitive to monthly rainfall time series in January, February, and December, in which the values of Cd are greater than the critical value. Besides that, most methods result in consistent homogeneous static for monthly rainfall time series. These results suggest that the rainfall time series can be used for other investigations related to spatial analysis of rainfall trends or long-term variations of rainfall in the domain of interest.

Table 2 Values of Cd , vN , Ba , and Wo for monthly series of rainfall at eight stations

Station	Method	Jan	Feb	Mar	Apr	May	Jun	Jul	Aug	Sep	Oct	Nov	Dec
Binh Xuyen	Cd	1.35	0.99	1.07	1.12	1.00	0.61	1.41	0.93	1.08	0.64	0.42	0.87
	vN	1.35	0.67	0.84	1.07	0.61	1.16	0.94	1.41	1.04	1.05	0.41	0.39
	Ba	0.94	1.12	0.74	1.24	0.64	1.00	1.21	0.79	0.77	0.85	0.45	0.98
	Wo	1.08	0.89	0.73	1.40	0.52	0.83	1.00	1.02	1.00	0.64	0.67	0.89
Phuc Yen	Cd	1.12	2.08	2.04	1.39	1.60	1.99	1.59	1.74	1.65	2.16	2.11	2.38
	vN	1.41	2.06	2.04	1.47	2.13	2.17	2.12	1.98	2.25	1.20	2.27	2.46
	Ba	2.22	2.40	2.20	1.90	1.96	1.95	1.60	1.89	2.63	1.92	2.23	1.79
	Wo	1.91	2.01	2.09	1.48	1.86	2.20	1.72	1.83	1.79	1.72	2.05	2.23
Quang Cu	Cd	4.04	1.84	0.91	1.07	1.18	0.37	4.34	2.14	2.15	0.65	0.28	1.57
	vN	2.80	0.95	0.99	3.04	0.34	2.00	1.69	3.51	1.89	2.33	0.27	0.33
	Ba	0.91	1.74	0.95	2.19	0.48	1.36	1.72	1.41	0.67	1.38	0.32	1.32
	Wo	1.89	1.03	0.66	1.71	0.35	1.28	2.20	2.54	1.63	1.07	0.44	1.11
Tam Dao	Cd	3.00	2.28	1.32	0.82	0.47	0.23	0.39	0.27	0.37	0.29	0.26	2.16
	vN	1.68	1.20	0.67	0.59	0.23	0.35	0.20	0.33	0.32	0.47	0.16	0.45
	Ba	1.20	1.80	0.76	0.94	0.36	0.39	0.38	0.25	0.32	0.34	0.32	1.71
	Wo	2.02	2.35	0.85	1.18	0.30	0.32	0.42	0.32	0.50	0.27	0.51	1.99
Tam Duong	Cd	0.75	1.34	0.69	1.04	0.75	0.64	1.06	0.82	0.57	0.92	0.53	0.56
	vN	1.39	0.60	0.99	0.99	0.49	1.05	0.68	1.09	0.77	0.93	0.56	1.01
	Ba	0.82	1.13	0.83	1.24	0.77	1.08	0.47	1.17	0.82	0.72	0.81	0.87
	Wo	1.22	1.01	0.80	0.94	0.75	0.91	0.68	1.13	1.07	0.54	0.65	0.60
Vinh Tuong	Cd	1.68	2.04	2.06	2.07	2.14	2.20	1.21	2.08	2.03	1.81	2.19	2.38
	vN	1.37	1.97	1.64	1.45	1.95	2.12	1.99	1.63	2.14	1.22	2.14	2.07
	Ba	1.44	2.08	2.07	1.68	1.97	2.21	2.06	1.85	2.37	1.91	1.89	2.43
	Wo	1.69	1.38	1.87	2.49	1.89	2.16	1.62	1.72	1.98	1.71	2.39	2.61
Vinh Yen	Cd	1.49	3.42	0.56	0.85	0.69	0.33	1.74	1.09	0.74	1.08	0.40	0.38
	vN	2.58	0.54	1.13	2.07	0.35	1.71	0.73	1.89	0.78	2.01	0.34	1.61
	Ba	2.00	1.98	0.92	1.64	0.71	1.51	0.43	2.57	1.03	0.62	1.08	1.12
	Wo	2.66	1.26	0.56	2.07	0.77	1.42	1.13	2.36	1.63	0.53	0.36	0.59
Xuan Hoa	Cd	1.54	2.64	0.63	0.73	0.39	0.24	0.40	0.27	0.29	0.36	0.29	1.15
	vN	1.84	1.16	0.87	0.69	0.24	0.30	0.17	0.29	0.25	0.27	0.31	1.48
	Ba	1.44	2.61	0.92	0.82	0.40	0.32	0.17	0.36	0.35	0.30	0.56	1.80
	Wo	1.41	1.79	0.53	0.42	0.21	0.23	0.13	0.21	0.42	0.16	0.27	0.67

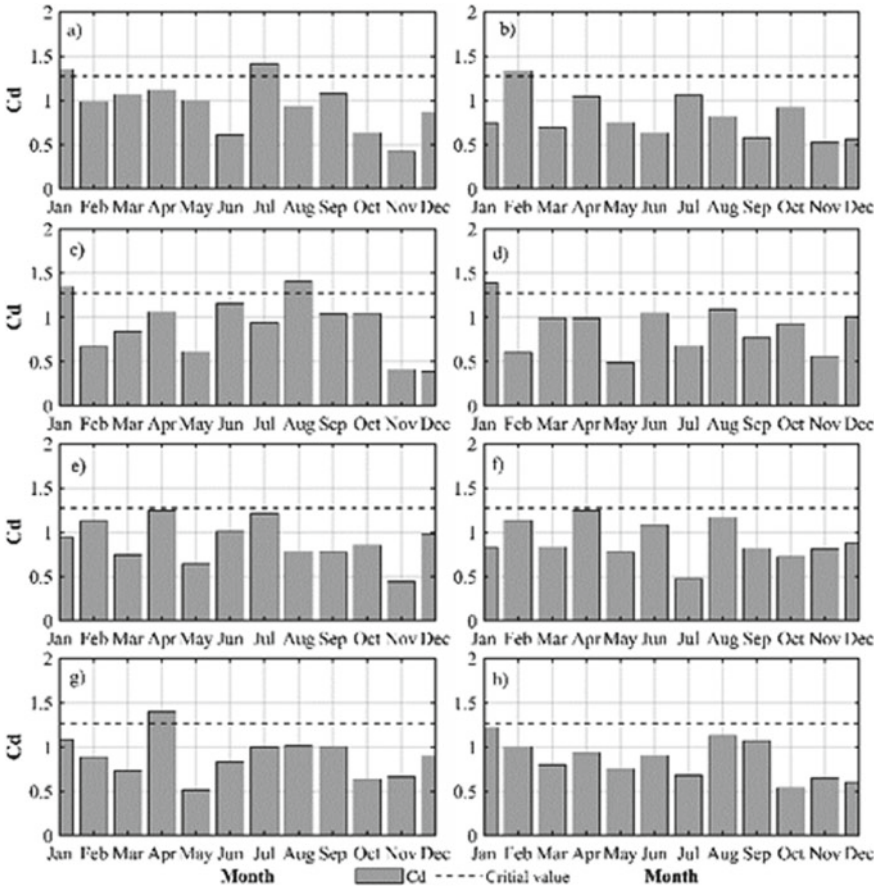


Fig. 2 Calculated values of Cd , at: a) Binh Xuyen, b) Phuc Yen, c) Quang Cu, d) Tam Dao, e) Tam Duong, f) Vinh Tuong, g) Vinh Yen, and h) Xuan Hoa

5 Conclusion

Based on the multiple statistical tests, named Cd , Ba , Wo , and vN , rainfall series in the period 1975–2021 at Vinh Yen, Phuc Yen, Tam Dao, Quang Cu, Tam Duong, Vinh Tuong, Binh Xuyen, and Xuan Hoa stations in Vinh Phuc province were found to be homogeneity. In addition, the Cd , Ba , and vN tests, among the four selected methods, showed similar results.

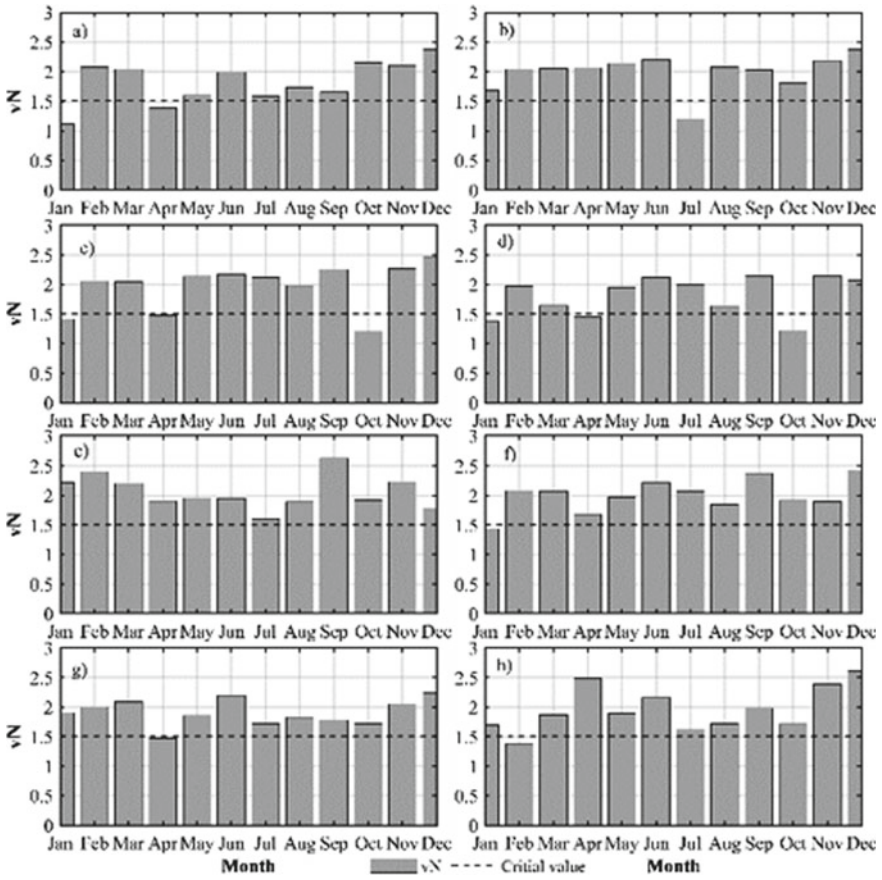


Fig. 3 Calculated values of vN , at: a) Binh Xuyen, b) Phuc Yen, c) Quang Cu, d) Tam Dao, e) Tam Duong, f) Vinh Tuong, g) Vinh Yen, and h) Xuan Hoa

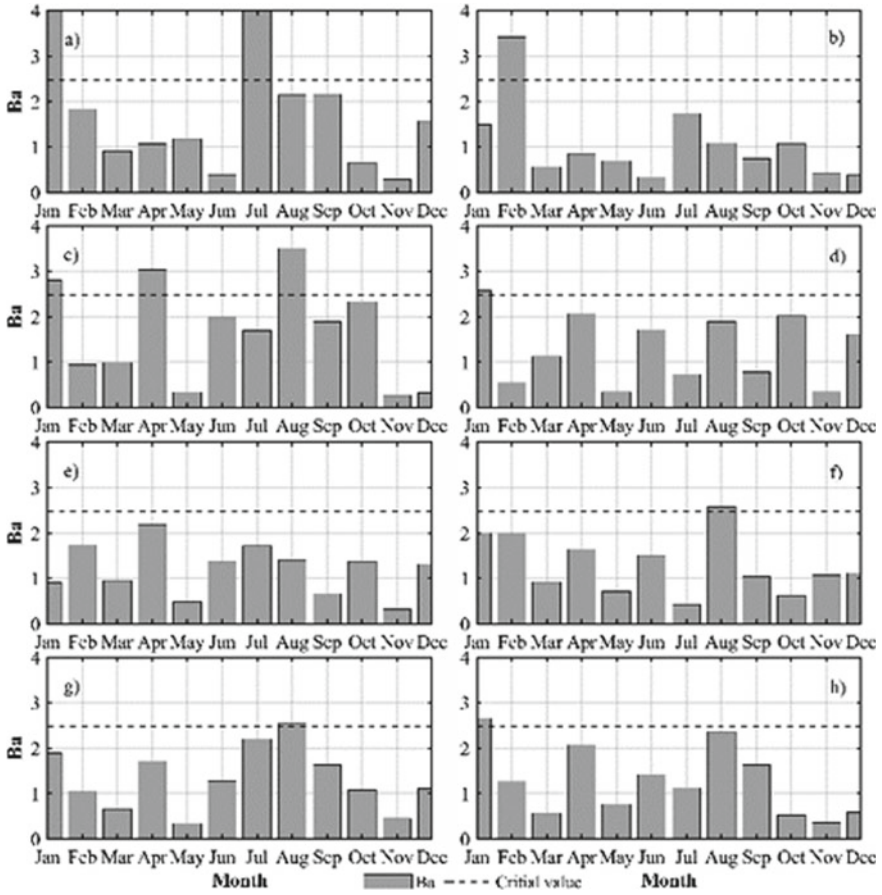


Fig. 4 Calculated values of Ba , at: a) Binh Xuyen, b) Phuc Yen, c) Quang Cu, d) Tam Dao, e) Tam Duong, f) Vinh Tuong, g) Vinh Yen, and h) Xuan Hoa

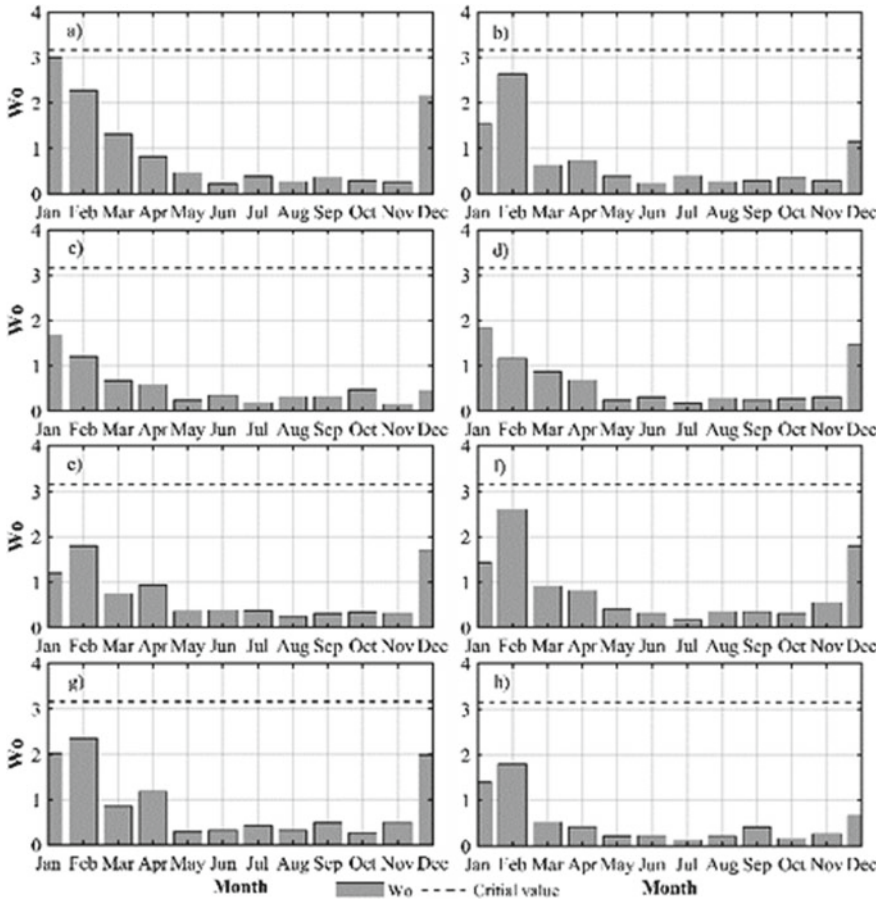


Fig. 5 Calculated values of W_0 , at: a) Binh Xuyen, b) Phuc Yen, c) Quang Cu, d) Tam Dao, e) Tam Duong, f) Vinh Tuong, g) Vinh Yen, and h) Xuan Hoa

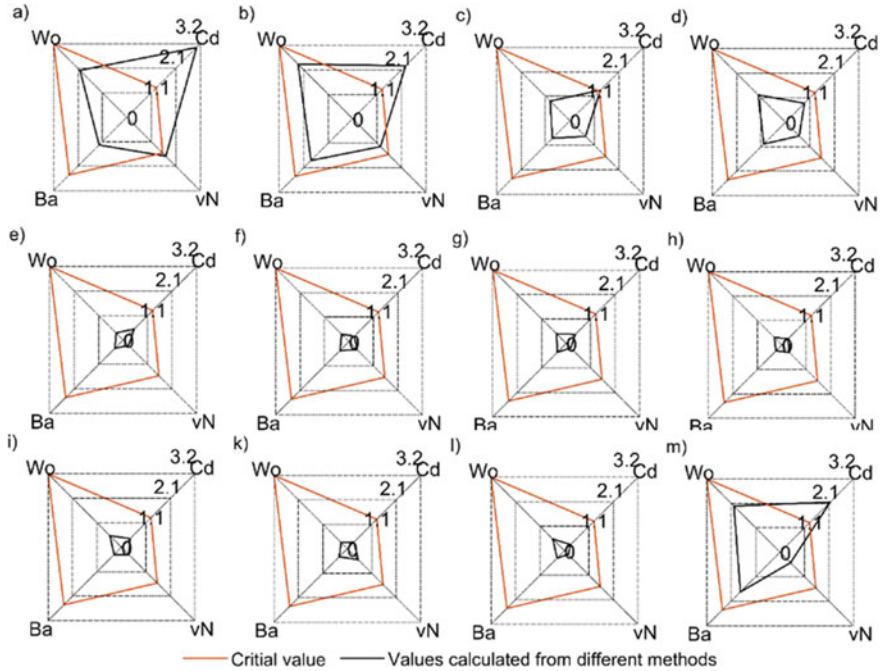


Fig. 6 Values calculated from different methods at Tam Dao station, for monthly rainfall time series on: **a** January, **b** February, **c** March, **d** April, **e** May, **f** June, **g** July, **h** August, **i** September, **k** October, **l** November, and **m** December

References

1. Ahmed K, Shahid S, Ismail T, Nawaz N, Wang XJ (2018) Absolute homogeneity assessment of precipitation time series in an arid region of Pakistan. *Atmosfera* 31(3):301–316
2. Buishand TA (1982) Some methods for testing the homogeneity of rainfall records. *J Hydrol* 58:11–27
3. Machiwal E, Jha MK (2008) Comparative evaluation of statistical tests for time series analysis: application to hydrological time series. *Hydrol Sci J* 53(2):353–366
4. Talaee PH, Kouchakzadeh M, Some'e BS (2014) Homogeneity analysis of precipitation series in Iran. *Theor Appl Climatol* 118(1–2):297–305
5. von Neumann J (1941) Distribution of the ratio of the mean square successive difference to the variance. *Ann Math Stat* 12:367–395

Impacts of the Threshold Value of the Enhanced Vegetation Index on Surface Water Area and Extent in MODIS Imagery



Chien Pham Van

Abstract Impacts of enhanced vegetation index (EVI) on the monitoring of surface water from the MODIS imagery are presented for the lowland region of the Mekong River consisting of the Tonle Sap Lake and its tributaries, the Tonle Sap channel, the Mekong River from Kraite to Tan Chau, and the Bassac River. Records of 839 MODIS images and daily water elevation at ten locations in the domain of interest are collected in the period from 2000 to 2019. A wavelet-based filter algorithm is applied for detecting the water surface. Using the relation between observed water elevation and surface water area and extent, a sensitivity analysis of EVI is performed to determine and classify the non-flood, mixture, and flood pixels in MODIS images. The results showed that the EVI affects significantly correlation coefficients. A value of 0.95 is obtained for the magnitude of the correlation coefficient at most studied locations when appropriate values of 0.30 and 0.45 are used for classifying non-flood, mixture, and flood pixels in MODIS images. Spatio-temporal variation of surface water area and extent associated with different flow conditions is also discussed.

Keywords MODIS · Tonle Sap · Surface water area · Enhanced vegetation index

1 Introduction

In river basins, surface water area and extent (SWAE) resulting from different hydro-meteorological conditions is an important characteristic that can be used for different applications such as mapping and monitoring of water bodies and assessments of water quality [1]. Indeed, data on SWAE in general, and flood inundation in particular, is commonly used to assess the magnitude and extent of floods as well as to calibrate and validate hydraulic models. Yet, due to the complex topography,

C. P. Van (✉)

Thuyloi University, 175 Tay Son, Dong Da, Hanoi, Vietnam

e-mail: Pchientvct_tv@tlu.edu.vn

hydro-meteorological alternations, hydropower, infrastructure, etc., it is not straightforward to extract from the complicated spatio-temporal varying flow characteristics the features that are relevant for understanding water extent and related physical processes in the long period of time. Thus, accurate monitoring of SWAE in a long-term period and a large scale of lowland regions is crucial for evaluating interactions between human activities, environmental behaviors, and hydro-meteorological conditions [1].

Besides hydrodynamic models, SWAE can be measured by using different kinds of remote sensing imagery such as Landsat, MODIS [1–4], and SAR imagery like RADARSAT [2]. Among these, MODIS imagery is still one of the most widely applied moderate-resolution optical sensors since they are provided free for users. The results from the previous studies also demonstrated that MODIS imagery can be used to monitor spatio-temporal SWAE in lowland regions of river systems.

Regarding the downstream region of the Mekong River (located from Kraite in Cambodia to the coastal region in Vietnam), different studies have been performed to investigate spatio-temporal flood inundation using MODIS images. Sakamoto et al. [1] examined the characteristics of flood inundation within the Mekong River (MR) basin in Vietnam and Cambodia using the wavelet-based filter for detecting the spatio-temporal changes in flood inundation (WFFI) and time series of MODIS images collected in the period from 2000 to 2004. Using the same WFFI algorithm and studied domain, Pham-Duc et al. [3] investigated the monthly variations of water storage during the period between 2003 and 2009 using MODIS images and water level maps. Vichet et al. [4] explored spatio-temporal flood inundation in Cambodia, using MODIS images in the period 2002–2013 and the WFFI algorithm. Note that the threshold value of the enhanced vegetation index (EVI) is a key indicator in the WFFI algorithm because it is used for classifying non-flood, mixture, and flood pixels in MODIS images. The use of different threshold values of EVI will result in different SWAE. This quantity, however, has not yet been considered and investigated in detail in the previous studies.

The present study aims at investigating a sensitivity analysis of the threshold value of EVI when monitoring SWAE from MODIS images. The MODIS images and daily water elevation at ten locations in the domain of interest are collected in the period from 2000 to 2019. Indeed, the correlation coefficient between observed water elevation and estimated surface water area and extent is also calculated for analysis purposes. The main difference between the present study and the previous studies [1, 3, 4] is that impacts of the threshold value of EVI for classifying non-flood, mixture, and flood pixels in MODIS images were investigated in detail for different flow conditions in the long period from 2000 to 2019.

2 Material and Method

2.1 Studied Area and Data Collection

The domain of interest in the present study is the downstream region of the MR located mostly in Cambodia. It consists of the Tonle Sap Lake (TSL) and its tributaries, the Tonle Sap channel, the MR from Kraite to Tan Chau, and the Bassac River (Fig. 1). The studied area is the dominant crop and fishery production region as well as cultural and economic development, environmental protection, and biodiversity conservation [5, 6]. However, the domain of interest is facing different problems, e.g., hydro-meteorological alternations, impacts of hydropower, and infrastructure [7, 8]. This is likely to accelerate the massive loss of arable land for agriculture and make the region to be one of the most at-risk and vulnerable regions on Earth under global warming. Therefore, accurate estimations of SWAE associated with different flow dynamics in the domain of interest are critical for proposing appropriate measures in the region while safeguarding its environment [8].

The daily observed water elevation at 10 locations (Table 1) is collected in the period from 01–01–2000 to 15–08–2019. These data are then used for calculating the correlation coefficient between water elevation and SWAE determined from the MODIS images. Note that the MODIS images (with land surface reflectance 8-day and 500 m spatial resolution) are used to estimate SWAE over the entire domain of interest. Indeed, MODIS images are collected in the period from 13–03–2000 to 22–10–2019, resulting in 893 images.

2.2 Method

To determine the SWAE from MODIS images, the methodology proposed by Sakamoto et al. [1] is used. Figure 2 depicts the flow diagram to estimate the SWAE from MODIS images used in the present study. Note that enhanced vegetation index (EVI), land surface-water index (LSWI), and different value between EVI and LSWI (DVEL) are used for classifying non-flood and water-related pixels in each image. These quantities are computed as

$$\text{EVI} = 2.5 \times \frac{\text{NIR} - \text{RED}}{\text{NIR} + 6 \times \text{RED} - 7.5 \times \text{BLUE} + 1} \quad (1)$$

$$\text{LSWI} = \frac{\text{NIR} - \text{SWIR}}{\text{NIR} + \text{SWIR}} \quad (2)$$

$$\text{DVEL} = \text{EVI} - \text{LSWI} \quad (3)$$

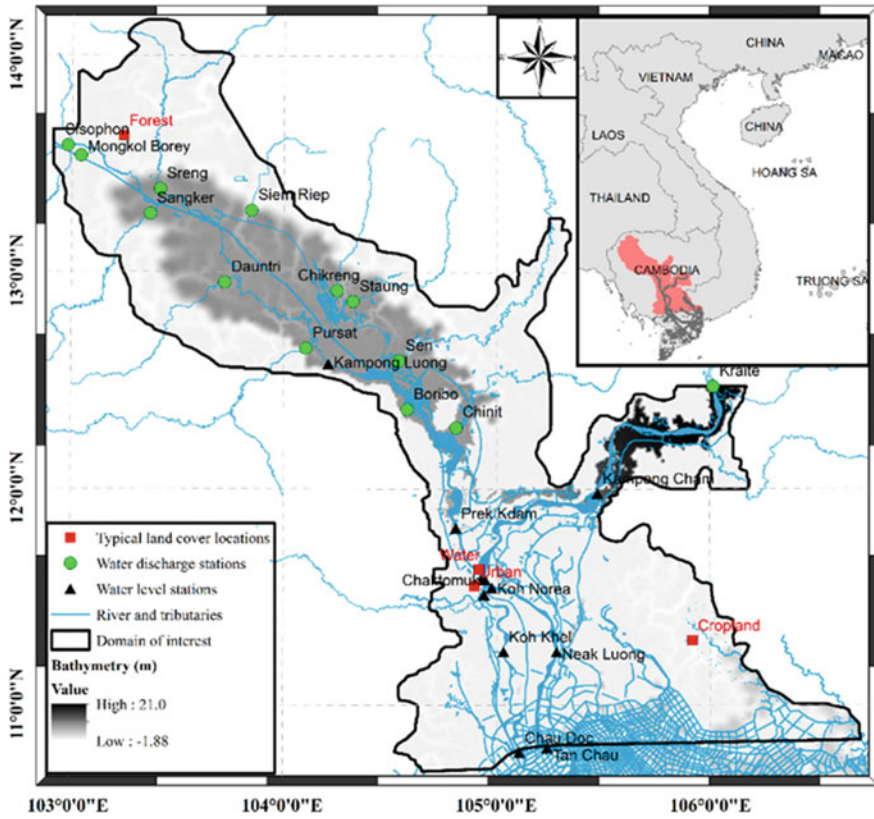


Fig. 1 Map of the studied area together with water level stations

Table 1 Water level stations in the domain of interest, together with collected data period

No	Station	River	Location		Period	Abb
			Latitude (°)	Longitude (°)		
1	Kraite	Mekong	12.240	105.987	2000–2019	KR
2	Kongpong Cham		11.909	105.388	2000–2019	KC
3	Bassac Chaktomuk		12.240	105.987	2006–2019	BC
4	Phnom Penh Port	Tonle Sap	11.575	104.923	2000–2019	PP
5	Neak Luong	Mekong	11.045	105.248	2006–2019	NL
6	Koh Khel	Bassac	11.046	105.000	2006–2019	KK
7	Prek Kdam	Tonle Sap	11.813	104.804	2000–2019	PK
8	Kompong Luong		12.575	104.215	2000–2019	KL
9	Tan Chau	Mekong	10.803	105.243	2000–2019	TC
10	Chau Doc	Bassac	10.707	105.133	2000–2019	CD

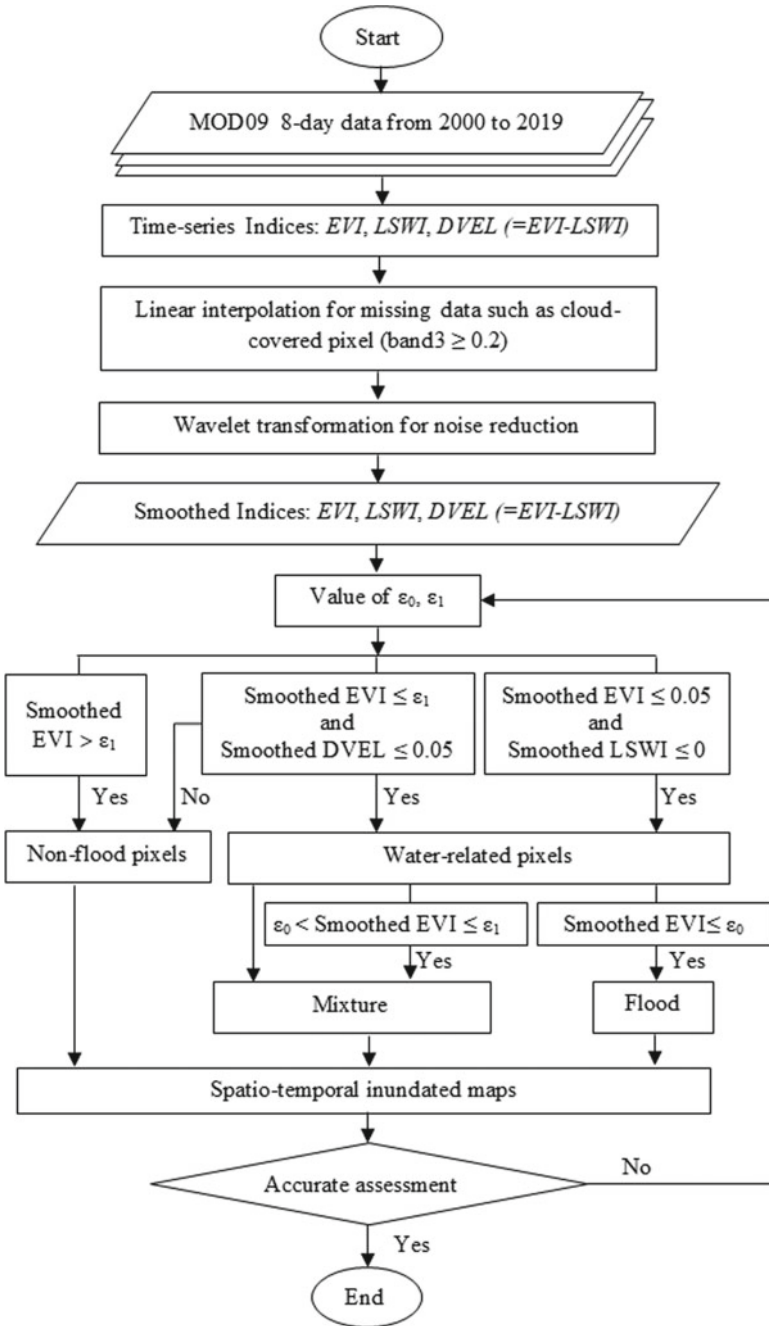


Fig. 2 Flow diagram to estimate the SWAE from MODIS images in the present study. Modified after [1]

where NIR is the surface reflectance value of near-infrared Band 2 (841–876 nm), RED is the visible Band 1 (RED, 620–670 nm), BLUE is the visible Band 3 (BLUE, 459–479 nm), and SWIR is the short-wave infrared Band 6 (1628–1652 nm).

As shown in Fig. 2, the coefficient ε_1 is used firstly for classifying non-flood and water-related pixels in MODIS images. Then, to separate mixed or full flood pixels from water-related pixels, a threshold value of the EVI (denoted by ε_0) is applied. In this study, different values of ε_0 and ε_1 are investigated. In addition, the correlation coefficient between SWAE and observed water level at 10 locations is calculated to quantitatively assess the impacts of EVI on estimated SWAE. Figure 3 shows an example of the time series of the EVI, LSWI, and DVEL for water, forest, urban, and cropland locations.

Different values of ε_0 ($= 0.05, 0.08, 0.10, 0.12, 0.15, 0.20, 0.23, 0.30, \text{ and } 0.40$) and ε_1 ($= 0.08, 0.10, 0.15, 0.20, 0.25, 0.30, 0.40, 0.45, 0.50, \text{ and } 0.55$) are tested to investigate impacts of EVI on estimating water surface area and extent, resulting 67 test cases from combining these values. In each test case, given values of ε_0 and ε_1 are used to classify the water, non-water, and mixture pixels in MODIS images. Then, the SWAE is calculated based on the classification of water, non-water, and mixture pixels. Finally, the correlation coefficient between SWAE and observed water

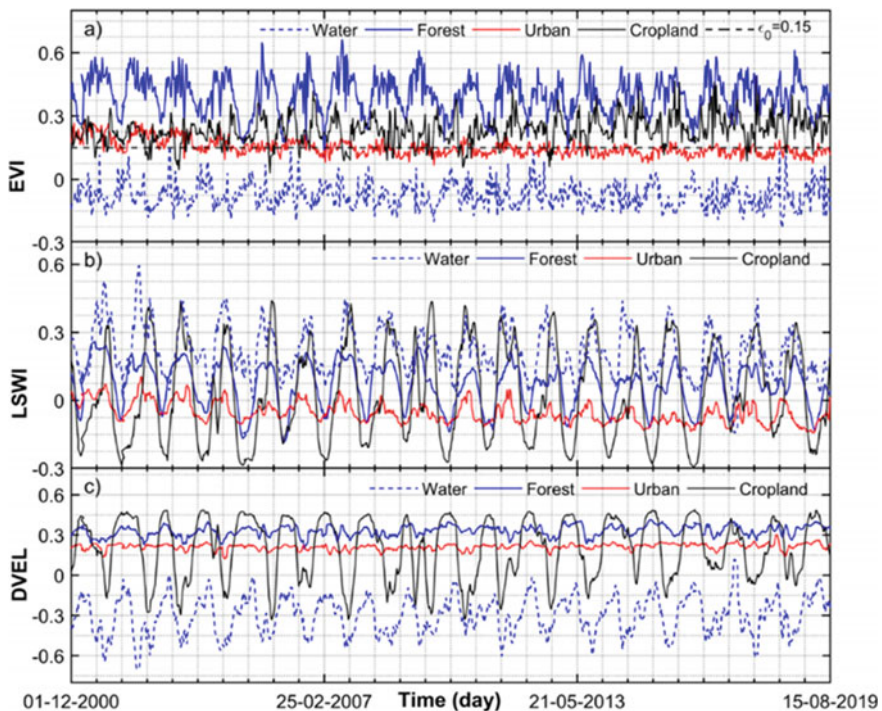


Fig. 3 Time series of: **a** EVI, **b** LSWI, and **c** DVEL at the permanent water, forest, urban, and cropland locations (see Fig. 1)

elevation at 10 locations is computed. Note that only full water pixels are considered in calculating the SWAE in the present study to render the investigation of EVI impacts as simple as possible.

3 Results

Figure 4 depicts the correlation coefficient between SWAE and observed water elevation at 10 locations of interest for the collected series of 893 MODIS images. It is observed that the correlation coefficient varies significantly when ϵ_0 ranges from 0.05 to 0.40 and ϵ_1 changes from 0.08 to 0.55. At seven locations (i.e., BC, PP, NL, KK, PK, TC, and CD), the correlation coefficient ranges from 0.90 to 0.96, revealing a close link between water elevation and SWAE in the studied domain. At the KR, KC, and KL locations, a smaller value of the correlation coefficient is achieved, ranging between 0.77 and 0.90. Figure 5 shows an example of SWAE versus water elevation at different locations for the case $\epsilon_0 = 0.15$ and $\epsilon_1 = 0.25$. At all studied locations, the plot of SWAE versus water elevation shows apparent scatters, depicting that there is a non-linear relationship between water elevation and SWAE in the studied domain.

Figure 6 shows the temporal variation of the SWAE during the collected period for different given values of ϵ_0 and ϵ_1 . In each year from 2000 to 2019, large values of SWAE are obtained in flood seasons, where high water elevation is inherently presented as shown in Fig. 6a. In contrast, low values of the SWAE are achieved in dry seasons. In the other words, the variable trend of the SWAE is consistent with the variable trend of the water elevation at different locations (e.g., Phnom Penh Port, Neak Luong, and Tan Chau). In the Vietnamese Mekong Delta, the tide can propagate up to the Tan Chau location, especially in low-water elevation situations (see Fig. 6a). However, the impact of the tide on the SWAE in the domain of interest is not depicted because the studied area locating in the upstream region of the Tan Chau location.

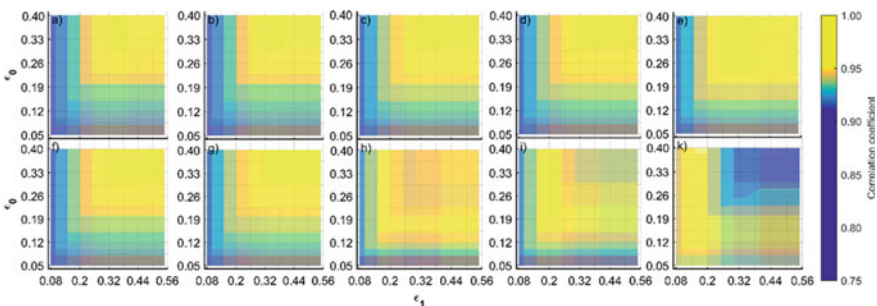


Fig. 4 Correlation coefficient r between observed water level and estimated water extent, at: **a** KR, **b** KC, **c** BC, **d** PP, **e** NL, **f** KK, **g** PK, **h** KL, **i** TC, **k** CD

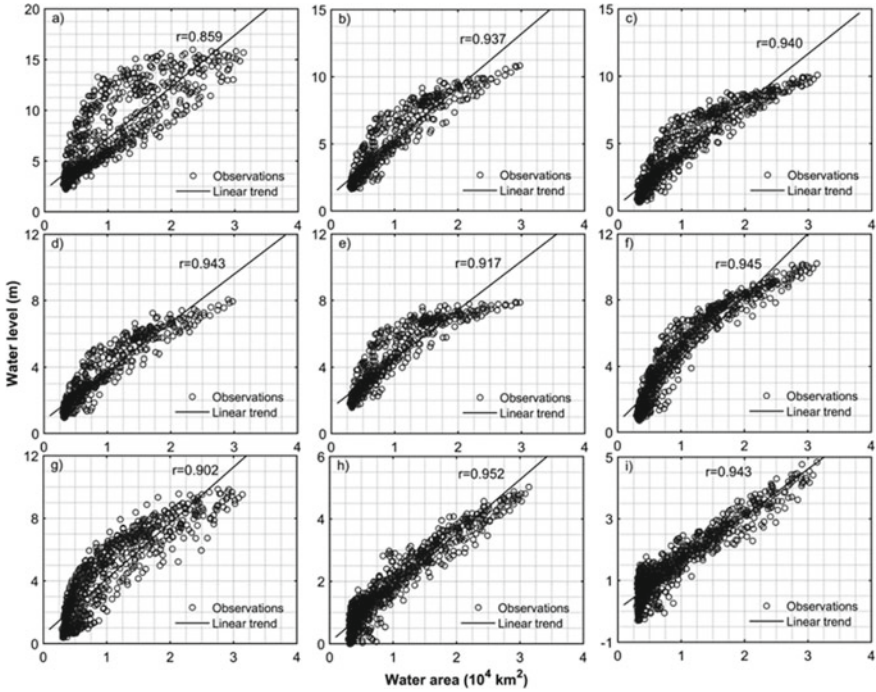


Fig. 5 Surface water area and extent versus water elevation, at: **a** KC, **b** BC, **c** PP, **d** NL, **e** KK, **f** PK, **g** KL, **h** TC, **i** CD when using $\varepsilon_0 = 0.15$ and $\varepsilon_1 = 0.25$

Figure 7 illustrates an example of the spatial distribution of water, mixture, and non-water areas in the studied domain when using $\varepsilon_0 = 0.15$ and $\varepsilon_1 = 0.25$. It is observed that the SWAE from the selected MODIS image varies significantly depending on bathymetry and positions. In addition, even for the given pair of ε_0 ($= 0.15$) and ε_1 ($= 0.25$), the spatial distribution of surface water extent clearly shows that a wide extent of surface water is also obtained in years such as 2000, 2002, 2002, 2011, and 2018. These results are consistent with the historical floods observed in the downstream region of the MR system.

Sakamoto et al. [1] used $\varepsilon_0 = 0.10$ and $\varepsilon_1 = 0.30$ for classifying non-flooded, mixture, and flooded pixels in MODIS images when investigating annual flooding in the downstream region of the MR. Vichet et al. [4] investigated spatio-temporal flood inundation based on $\varepsilon_0 = 0.08$ and $\varepsilon_1 = 0.10$. These previous studies, however, mainly focused on investigating spatio-temporal inundation due to floods, without considering the relations between SWAE and water level in detail.

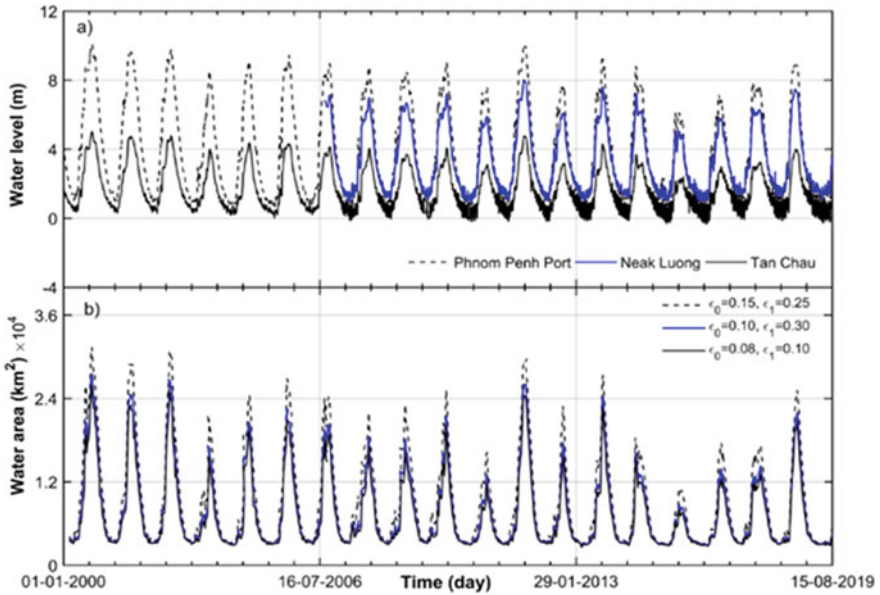
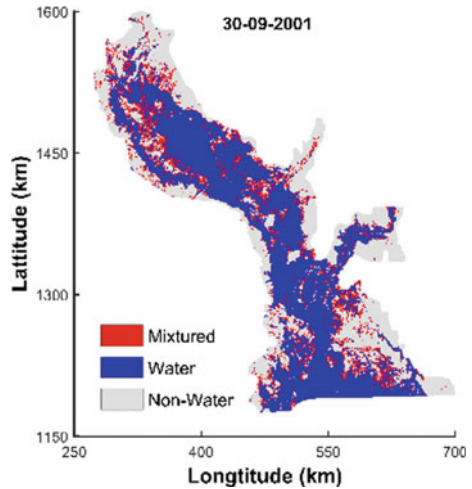


Fig. 6 Series of: **a** water level and **b** SWAE using different values of ε_0 and ε_1

Fig. 7 Example of the estimated mixture, water, and non-water areas



4 Conclusion

A sensitivity analysis of EVI impacts on classifying non-flood, mixture, and flood pixels in MODIS images was performed for the downstream region of the MR using 839 MODIS images and daily observed water elevation at ten locations in the period

from 2000 to 2019. The main remarks from the results are as follows: The threshold values of the EVI affected significantly correlation coefficients between SWAE and water elevation. The correlation coefficients were close to unity at most studied locations if appropriate threshold values (e.g., 0.30 and 0.45) were used for classifying non-flood, mixture, and flood pixels in MODIS images. There is a close link between water elevation (at ten locations) and SWAE in the domain of interest, even though only full water pixels were taken into account in calculating the SWAE.

References

1. Sakamoto T, Van Nguyen N, Kotera A, Ohno H, Ishitsuka N, Yokozawa M (2007) Detecting temporal changes in the extent of annual flooding within Cambodia and the Vietnamese Mekong Delta from MODIS time-series imagery. *Remote Sens Environ* 109:295–313
2. Islam AS, Bala SK, Haque MA (2010) Flood inundation map of Bangladesh using MODIS time-series images. *J Flood Risk Manag* 3:210–222
3. Pham-Duc B, Papa F, Prigent C, Aires F, Biancamaria S, Frappart F (2019) Variations of surface and subsurface water storage in the lower Mekong basin (Vietnam and Cambodia) from multi-satellite observations. *Water* 11:75
4. Vichet N, Kawamura K, Trong DP, On NV, Gong Z, Lim J, Khom S, Bunly C (2019) MODIS-based investigation of flood areas in Southern Cambodia from 2002–2013. *Environments* 6:57
5. Masumoto T, Pham TH, Shimizu K (2008) Impact of paddy irrigation levels on floods and water use in the Mekong River basin. *Hydrol Process* 22:1321–1328
6. Fuji H, Garsdal H, Ward P, Ishii M, Morishita K, Boivin T (2003) Hydrological roles of the Cambodian floodplain of the Mekong River. *Int J River Basin Manage* 1:253–266
7. Mekong River Commission (2015) Annual mekong flood report 2011 72
8. Darby SE, Hackney CR, Leyland J, Kummu M, Lauri H, Parsons DR, Best JL, Nicholas AP, Aalto R (2016) Fluvial sediment supply to a mega-delta reduced by shifting tropical-cyclone activity. *Nature* 539:276–292

Extracting Water Depth from Landsat-8 Multispectral Satellite Imagery in Coastal Waters



Tran Duc Phu

Abstract Bathymetric data generates nautical charts, seafloor profiles, biological oceanography, etc. Water depth is collected using active sensors like sonar, lidar, or using passive multispectral imagery. Determining the bathymetry for a large area using sonar and LiDAR is very expensive. At the same time, a multispectral satellite can effectively determine the water depth and cost savings, especially for shallow water areas. In the coastal region, the nature of the bottom is very dynamic, and water is primarily turbid, which degrades the accuracy of satellite-derived bathymetry assessment. This study focuses on extracting water depth in Hai Phong's coastal region (Viet Nam) by applying the ratio transform algorithm on Landsat-8 satellite imagery bands. The result shows a good correlation between the algorithm-derived and the sounding values.

Keywords Bathymetry · Water depth · Landsat-8 · Multispectral satellite imagery · Coastal waters

1 Introduction

The underwater bathymetric data provides essential information for the planning of coastal facilities. In coastal areas, bathymetry data is crucial to determine the underwater topographic surface and sediment movement, avoid stranding during nautical navigation, and simulate high tides and waves for scientific purposes. The primary measurement methods for bathymetry are sonar and airborne lidar. Sonar measurements from a vessel could face a risk of stranding [1]. Airborne lidar bathymetry (ALB) is costly, and the survey area must be flight-capable. Consequently, in coastal areas which are inaccessible by ships or airplanes, insufficient water depth has been collected.

D. P. Tran (✉)
Vietnam Maritime University, Hai Phong, Vietnam
e-mail: phutd.ctt@vamaru.edu.vn

Remote sensing technology is a vital source for determining the depth of the seabed in coastal areas [2]. Using analytic methods to obtain depths from multispectral satellite images which are called satellite-derived bathymetry (SDB) has been necessary for hydrographic surveyors worldwide.

Many empirical algorithms [3] and analytical algorithms [4–6] are available to determine the seabed depth in the literature. For the application of the analytical method in building a database of topographic seabed maps, input parameters including pressure, atmospheric characteristics and bottom material, etc., are needed to collect. Determining the depth of the seabed is complicated. Meanwhile, the comparative empirical method only requires simple parameters and can easily map the depth.

This study applies light spectrum analysis techniques of multispectral satellite images to determine water depth in optically complex waters and to understand the applicability of remote sensing image data. The author used the ratio algorithm to analyze Landsat-8 multispectral satellite image data to determine the seawater depth of the Hai Phong area. The procedure was executed in the open-source software QGIS.

2 Data Collection and Study Method

2.1 Study Area and Sources of Study Data

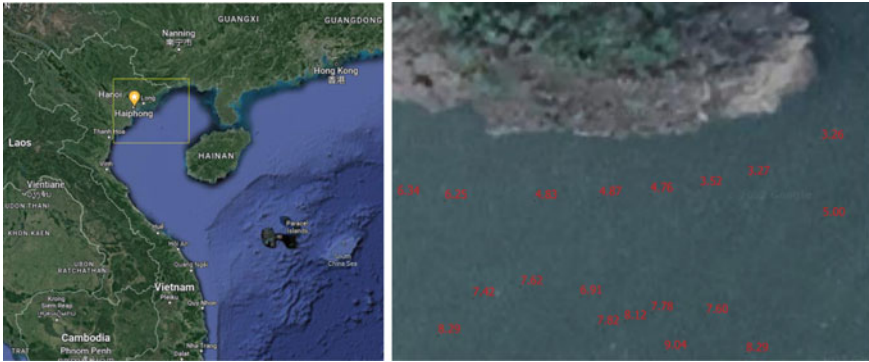
The study used the survey data collected from a single-beam echosounder at the Do Son and Cat Ba sea area (Fig. 1) of the Hai Phong water region (Viet Nam) and images captured on December 09th, 2021 by the Landsat-8. The echo depth measurements are in meters and refer to the Vietnamese national elevation system, with the elevation datum being the mean sea level (MSL) in the Hon Dau area. The study analyzes the data to generate a water depth estimation model based on the Landsat-8 multispectral images for the Hai Phong water region.

2.2 Method

2.2.1 Bathymetric Inversion Models for Optical Multispectral Imagery

Retrieving bathymetric data from optical satellite images is based on the attenuation of light when passing through water [7]. Consequently, the more deep water the darker appearance of the optical remote sensing images. The distribution of the upwelling radiance (L_t) in the images includes four components:

$$L_t = L_b + L_v + L_s + L_p \quad (1)$$



(a) Map of the Hai Phong water region (b) Sample sounding points collected by sonar

Fig. 1 Location map of the Hai Phong water region and sample sounding points

where L_b is the path radiance of the bottom surface, L_v is the subsurface volumetric radiance, L_s is the specular radiance, and L_p is the path radiance of the atmosphere [7].

Based on the Lambert–Beer law, the attenuation of light’s intensity is exponential with water’s depth [7]. Lyzenga [4–6] and [8] proposed a model of radiative transfer that could be applied in shallow waters:

$$L = L_\infty[1 - e^{-gz}] + A_d e^{-gz} \tag{2}$$

where $L = L_b + L_v$ is the measured radiance after correcting the effect of atmospheric and sunglint; $L_\infty = L_v$ is the deep water radiance; A_d is the bottom’s upwelling spectral radiance, also called bottom albedo; g is the diffusion attenuation coefficients’ function [3]; z is the water depth [7].

2.2.2 Ratio Algorithm

For the reduction of the number of parameters, the ratio transform (RT) algorithm [3, 9, 10] selects two spectral bands to estimate the seawater depth. The coastal water depths of greater than 25 m could be retrieved by the algorithm. The ratio of the drop of bottom albedo between the two bands leads to the difference in depth. Since the distribution of both channels is equal, the error that occurs because of the effects of the atmosphere, pressure, or seafloor could be neglected. Based on a log-transformed band ratio, a non-linear bathymetric inversion model is proposed to determine the depth of seawater [3]:

$$Z = ax + b \tag{3}$$

where the corresponding pixel value $x = \frac{\ln(k \cdot L(\lambda_i))}{\ln(k \cdot L(\lambda_j))}$ is obtained from the two channels i and j of the multispectral image, called satellite-derived bathymetry (SDB); a is a tunable constant for scaling the ratio to depth values; b is a constant to offset a depth from 0 m. The fixed value of k in Eq. (3) is chosen to guarantee the positive values of logarithms [3].

3 Results and Discussion

3.1 Results

To reduce depth estimation errors of bathymetric inversion models, the study uses the least attenuation wavelength channels. Lights of different wavelengths have a variety of water penetration [11]. The penetration of blue light (with a spectral from 440 to 540 nm) could reach a 30 m depth so it could be used to extract water depth. The longer wavelengths, the more rapid attenuation in water. Maximum penetration in the clear water of green light (500–600 nm) is 15 m, while red light (600–700 nm) and near-infrared (700–800 nm) are 5 m and 0.5 m, respectively [11].

In Fig. 2a, it is apparent that the near-infrared (NIR) reflects the water dark and the land bright. Therefore, there are two modes of water and land in the NIR images. The water is represented by the smooth surface with radiative values of around 6000 while the land has higher fluctuated values, see Fig. 2b. As a result, we use the 6000-threshold-value to divide the water from the ground and to subtract the speckle noise in the blue (λ_i) and green (λ_j) channels of Landsat-8 imagery.

The RT algorithm is applied to identify constants of Eq. (3) from overlaid values of the hydrographic survey data and that in the satellite image. The elevation is collected from single-beam echo sounders and referred to the Vietnamese national elevation system. The pixel values are derived from satellite imagery at corresponding sounding points. Based on Eq. (3), the parameters a and b are estimated from the scatterplot of more than 10,000 water depths in Fig. 3, where $a = -2441$ and $b = 2460.5$. Therefore, water depth could be obtained from a Landsat-8 multispectral

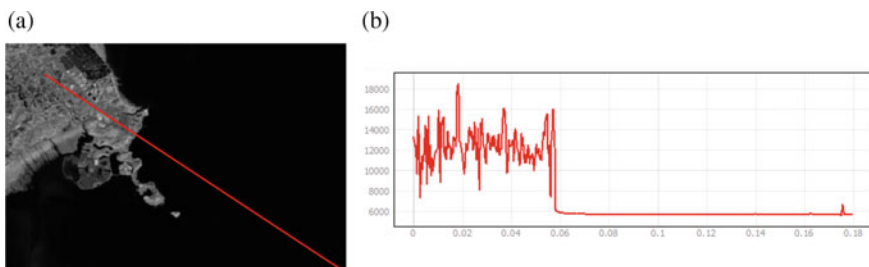


Fig. 2 a NIR band imagery of study area. b Corresponding profile graph of NIR band

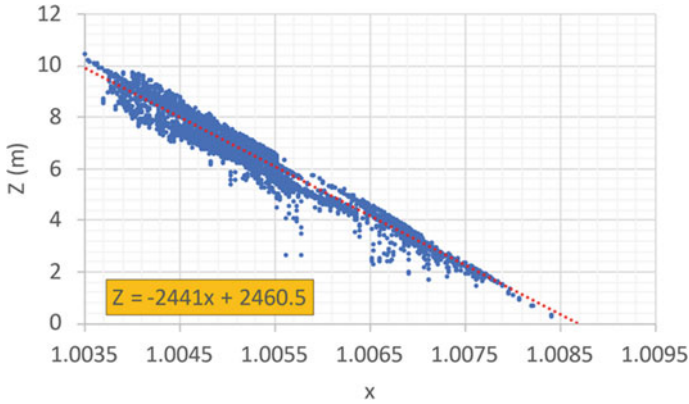


Fig. 3 Correlation between satellite-derived bathymetry pixel values (SDBV) and water depth collected by single-beam echo sounders

image based on the following formula:

$$Z = -2441x + 2460.5 \tag{4}$$

3.2 Discussion and Validation

For validating the model, the study calculates statistical indexes, including mean absolute error (MAE), root mean square error (RMSE), and coefficient of determination (R^2), between the algorithm-derived and observed sounding values. The results are illustrated in Table 1 where 0.225 m are the model’s root mean square error (RMSE), the mean absolute error (MAE) is 0.193 m, and the coefficient of determination (R^2) is 0.952.

The R^2 refers to the prediction ability of a model. A good prediction model should have a R^2 value close to 1. Hence, the model’s coefficient of determination demonstrates that Eq.’s non-linear bathymetric inversion model is very well-predicted.

The RMSE reflects how much difference between predicted depth values and observed water depths. Similarly, the MAE is the average of the errors in a set of depth predictions without direction consideration. A reliable model should have small RMSE and MAE values.

Table 1 Statistical indices value of validating the model

Statistical indices value	RMSE (m)	MAE (m)	R^2
Ratio transformation algorithm	0.255	0.193	0.952

Table 2 Depth measurement precision of hydrographic survey based on IHO’s standard

Depth’s range (m)	MAE	Accuracy order	Error limitations for depth accuracy
0–5	0.276	1	$m = 0.5 m; k = 0.013$
5–10	0.399	1	$m = 0.5 m; k = 0.013$
> 10	0.680	1 2	$m = 0.5 m; k = 0.013$ $m = 1.0 m; k = 0.023$

In Table 1, the MAE and RMSE for water depth estimation using Eq. (4) met International Hydrographic Standards for accuracy of order 1 [12], in which the error limits for depth accuracy are $\pm\sqrt{m^2 + (k \times z)^2}$, where m is the independent error of water depth, k is the depth-dependent error’s factor.

From Table 2, it can be seen that water depth estimation using Eq. (4) could be applied in the examination of nearshore coastal areas before performing high-resolution hydrographic surveys using costly equipment like multi-beam depth gages, etc.

4 Conclusions

The statistics obtained in this study estimated a formula based on the ratio transform algorithm to retrieve depth from multispectral satellite image data. Determining depth from satellite images met IHO’s standards for hydrographic surveys and could be a convenient tool to examine nearshore coastal areas before performing high-resolution hydrographic surveys with costly equipment. The results of this study could support marine surveyors to assess changes in depth and decide to update the existing seafloor topographic map data if there are less reliable factors. Environmental conditions such as water clarity and cloud coverage level should be considered in determining depth using satellite images since they could reduce the depth estimation accuracy.

Acknowledgements The author is grateful to the Vietnam Maritime University (VMU) for providing the necessary research facilities during this study.

References

1. Sagawa T, Yamashita Y, Okumura T, Yamanokuchi T (2019) Shallow water bathymetry derived by machine learning and multitemporal satellite images. *Int Geosci Remote Sens Symp* 8222–8225. <https://doi.org/10.1109/IGARSS.2019.8899043>
2. Colak TI, Senel G, Goksel C (2019) Coastline zone extraction using Landsat-8 OLI imagery, case study: Bodrum Peninsula, Turkey. *Int Arch Photogramm Remote Sens Spat Inf Sci ISPRS Arch* 42:101–104. <https://doi.org/10.5194/isprs-archives-XLII-4-W12-101-2019>
3. Stumpf RP, Holderied K, Sinclair M (2003) Determination of water depth with high-resolution satellite imagery over variable bottom types. *Limnol Oceanogr* 48:547–556. https://doi.org/10.4319/lo.2003.48.1_part_2.0547
4. Lyzenga DR (1978) Passive remote sensing techniques for mapping water depth and bottom features. *Appl Opt* 17:379. <https://doi.org/10.1364/ao.17.000379>
5. Lyzenga DR (1981) Remote sensing of bottom reflectance and water attenuation parameters in shallow water using aircraft and landsat data. *Int J Remote Sens* 2:71–82. <https://doi.org/10.1080/01431168108948342>
6. Lyzenga DR, Malinas NP, Tanis FJ (2006) Multispectral bathymetry using a simple physically based algorithm. *IEEE Trans Geosci Remote Sens* 44:2251–2259. <https://doi.org/10.1109/TGRS.2006.872909>
7. Su H, Liu H, Heyman W (2008) Automated derivation of bathymetric information from multi-spectral satellite imagery using a non-linear inversion model. *Mar Geod* 31:281–298. <https://doi.org/10.1080/01490410802466652>
8. Philpot WD (1989) Bathymetric mapping with passive multispectral imagery. *Appl Opt* 28:1569. <https://doi.org/10.1364/ao.28.001569>
9. Caballero I, Stumpf RP (2021) On the use of Sentinel-2 satellites and lidar surveys for the change detection of shallow bathymetry: the case study of North Carolina inlets. *Coast Eng* 169:103936. <https://doi.org/10.1016/j.coastaleng.2021.103936>
10. Caballero I, Stumpf RP (2019) Retrieval of nearshore bathymetry from Sentinel-2A and 2B satellites in South Florida coastal waters. *Estuar Coast Shelf Sci* 226:106277. <https://doi.org/10.1016/j.ecss.2019.106277>
11. Green E, Mumby P, Edwards A, Clark C (2000) Remote sensing handbook for tropical coastal management
12. IHO (2020) International hydrographic organization standards for hydrographic surveys

The Novelty of Extreme Natural Drought Trend Using the Statistical Approach



Tuong Vo

Abstract This study presents a method to estimate the trend of natural drought. The trend was evaluated based on the natural drought index from 1981 to 2016. Total of 6 types of Mann-Kendal models and regression models was utilized to explore the trend of natural drought for whole South Korea. The spatial characteristic of natural drought was analyzed with zonal statistical model. Various spatial statistics such as mean, variance, and extreme was investigated to find the spatial change at each zone. In addition, diverging temporal scale monthly, seasonally, and annually trend of drought was analyzed. Results show monthly temporal scale of mean zonal NDI values which is increasing or trend drought decreasing. Because the smaller NDI values, the more severe drought is. The variance zonal drought is increasing. The extreme drought is increasing in 1- and 6-months temporal scales of NDI. In the west season (summer), drought has an increasing trend. For annual temporal scale, drought has an increasing trend in the North-East of South Korea. In short, the integrated approach of regression model and geo-statistical model gives the comprehensive estimate of natural drought at various temporal scales.

Keywords Natural drought index · Zonal statistic · Spatial–temporal drought analysis

1 Introduction

Drought, the most challenging natural phenomenon to comprehend due to the influence of meteorology, hydrology, environment, and human activities [1]. It leads to difficult for drought prediction accuracy. To less uncertainty of drought prediction, computing the trend of drought is important in the water management. Several studies have been conducted to find the trend of drought. The change of drought frequency was compared by the standardized precipitation index (SPI), the Palmer

T. Vo (✉)

Ho Chi Minh City Open University, Ho Chi Minh City 700000, Vietnam

e-mail: tuong.vq@ou.edu.vn

drought severity index (PDSI), and dry spells (DS), which is based on average daily temperature and precipitation, and takes into account the length of a spell [2].

Byakatonda et al. [3] used SPI and SPEI with various temporal scales 1-, 3-, 6-, 12-, 18-, and 24- months to estimate drought for period 1960–2016. The trend of drought was estimated by Mann-Kendall, and Sen’s slope was able to detect the historical drought events. Results show the effectiveness of drought trend with climate index such as El Nino and ENSO.

Beside Mann-Kendall and Sen’s slope, the “pre-whitened” methods are used to remove the serial correlation in drought trend prediction [4]. Using various temporal scales of SPI has been analyzed. The linear slope and invert distance weight have been used to determine drought trend in both spatial–temporal characteristics.

From the previous studies, Mann-Kendall is a popular method for determining drought trend. The most studies focus on the trend of single catalog drought such as SPI and SPEI. There is a little study main in the integrate drought index. Therefore, this study proposal estimates drought trend by Mann Kendal and natural drought index.

2 Methodology

Extreme drought assessment using natural drought index (NDI) and spatial distribution using statistical indicators conducted according to Fig. 1.

The meteorological and topographical data includes precipitation, temperature, wind speed, the digital elevation (Dem), land use, and soil characteristics which were analyzed to get the simulated runoff and soil moisture. Then, simulated runoff and soil moisture were combined to observational precipitation as input for computation of NDI.

NDI was computed from precipitation, runoff, and soil moisture using principal component analysis.

Then, calculate the correlation matrix Eq. (1).

$$R = \frac{1}{n-1} X X^T \quad (1)$$

where n is the number of years of this month, in this case, $n = 45$, X is matrix consisted of 3monthly precipitation, runoff, and soil moisture for each month, X^T is the transpose matrix of X . In the next step, determine the eigenvalue, eigenvector for R with Eq. (2). The eigenvector represents principal component, and eigenvalue represents explanation of variance for each principal component.

$$R v_k = \lambda_k v_k \quad (2)$$

where v_k is eigenvector, or it is principal component. λ_k is an eigenvalue. Then, the principal component score (PC’) was calculated with Eq. (3).

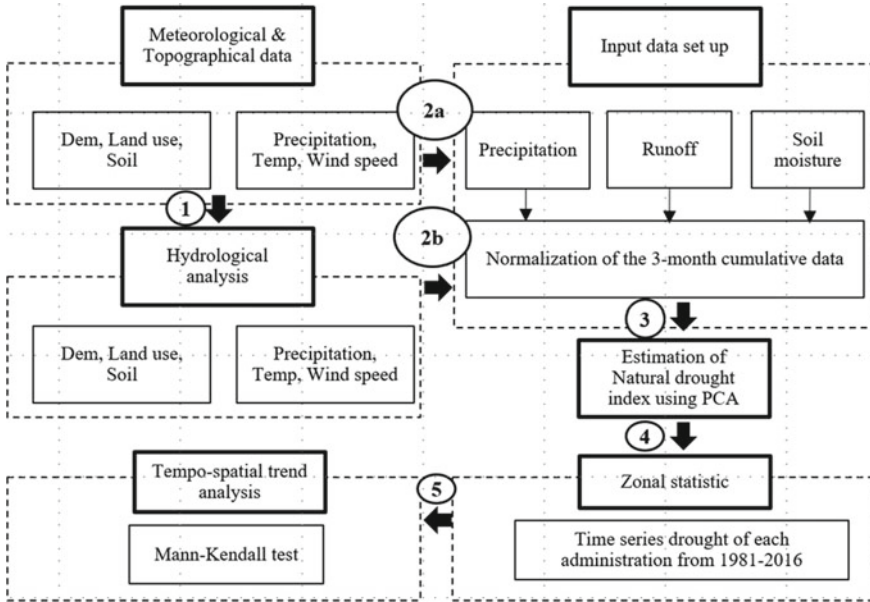


Fig. 1 Flowchart of natural extreme drought trend assessment

$$PC' = v_1^T X \tag{3}$$

where v_1^T is the first principal component vector. Then, determine the standard deviation σ'_{PC} and calculate the standardized principal component score PC with Eq. (4).

$$PC = \frac{PC'}{\sigma'_{PC}} \tag{4}$$

Another principal component score for an additional observation data period was calculated with Eq. (5).

$$PC'_{new} = v_1^T X_{new} \tag{5}$$

where X_{new} is matrix of 3monthly precipitation, runoff, and soil moisture in the additional period. Standardized principal component score for an additional period was calculated with Eq. (6).

$$PC_{new} = \frac{PC'_{new}}{\sigma'_{PC}} \tag{6}$$

Finally, to calculate the NDI, we used the Kernel probability density estimation method. P is standardized cumulative probability according to standard Gaussian distribution and corresponding to gamma distribution to determine the NDI follows the empirical method by Markovic (1965).

In case: $0.0 < P \leq 0.5$:

$$t = \sqrt{\ln\left(\frac{1}{P^2}\right)} \tag{7}$$

$$\text{NDI} = -\left(t - \frac{c_0 + c_1t + c_2t^2}{1 + d_1t + d_2t^2 + d_3t^3}\right) \tag{8}$$

In case: $0.5 < P \leq 1.0$:

$$t = \sqrt{\ln\left(\frac{1}{(1-P)^2}\right)} \tag{9}$$

$$\text{NDI} = \left(t - \frac{c_0 + c_1t + c_2t^2}{1 + d_1t + d_2t^2 + d_3t^3}\right) \tag{10}$$

where $c_0, c_1, c_2, d_1, d_2,$ and d_3 are empirical constant numbers, c_0 is 2.515517, c_1 is 0.802853, c_2 is 0.010328, d_1 is 1.432788, d_2 is 0.189269, and d_3 is 0.001308.

From 59 NDI time series at 59 ASOS location, the invert distance weight method was used to interpolate surface of NDI with spatial resolution at 0.1° or 10 km. The IDW predicts observational values based on the distances of observational data.

The zonal statistical model was used to determine the statistical values of each zone. In another words, it was determining the zones boundary of objective to be considered the drought trend.

A nonparametric Mann-Kendall family of the trend test was used to determine the trend for each zone which various temporal scale. We considered the changes of drought for monthly, seasonally, and annual. Homogeneous test for trend using Mann-Kendall equations from Eqs. (11)–(15):

$$Z_R = \frac{R - \frac{2N_1N_2}{N_1+N_2} + 1}{\sqrt{\frac{2N_1N_2(2N_1N_2-N)}{N^2(N-1)}}} \tag{11}$$

where Z_R is run homogeneous test result, R is run number, N_1 is number of values lower than medium, N_2 is number of values higher than median. If Z_R value corresponds to 5% significance level or below, then the data is non-homogenous. Only homogeneous data is used to determine trend conditions.

Mann-Kendall test was computed which Eqs. (2)–(5).

$$Z_{MK} = \left\{ \begin{array}{l} \frac{S-1}{V(S)} \text{ for } S > 0 \\ 0 \text{ for } S = 0 \\ \frac{S+1}{V(S)} \text{ for } S < 0 \end{array} \right\} \tag{12}$$

$$V(S) = \frac{n(n-1)(2n+5)}{18} \tag{13}$$

$$S = \sum_{k=1}^{n-1} \sum_{j=k+1}^n \text{sgn}(x_j - x_k) \tag{14}$$

$$\text{sgn}(x_j - x_k) = \left\{ \begin{array}{l} +1 \text{ if } (x_j - x_k) > 0 \\ 0 \text{ if } (x_j - x_k) = 0 \\ -1 \text{ if } (x_j - x_k) < 0 \end{array} \right\} \tag{15}$$

The Z_{MK} has positive value which means increasing trend, negative value means the decreasing trend, and zero value means no trend. $V(S)$ is the variance, and S is the Kendall statistic. The difference between each consecutive value is computed as positive (+1), negative (-1), and neural (0). x_j and x_k are value of time series at time j , at time k of n observational values. The trend is considered significant if Z_{MK} is more than the significant levels. For instance, confidence 90% has $\alpha = 10\%(Z_{MK} \geq Z_{\alpha/2} = \pm 1.645)$.

3 Results and Discussion

3.1 Study Area

The study area covers South Korea’s latitude (33.0–39.0 N) and longitude (125.0–131.0 E), a country with complex topography. South Korea is in a monsoon area. The country has suffered droughts in times of an absolute shortage of summer rainfall. The total study area is around 100,210 km². We used data from the automated synoptic observing system (ASOS) network. The data spanned more than 30 years. Each station provided nine observed climate variables (daily precipitation, maximum temperature, minimum temperature, average air temperature, dew point temperature, average wind speed, maximum wind speed, average humidity, and minimum humidity).

Fig. 2 Location of typical zone



3.2 Results and Discussion

Monthly, seasonally, and annual trend was demonstrated with the regression which show the increasing drought trend or decreasing NDI values as Chungju15 we analyzed various temporal scaled (Figs. 2, 3 and 4).

Drought trend using Mann-Kendall test was examined with 1-, 3-, and 6-months scales. Several characteristics of zones such as standard deviation, average value, and extreme value at 10 percentiles were analyzed to figure out adequate drought properties (Figs. 5 and 6).

Six types of Man Kendall family test were examined in this study: (a) Original Mann-Kendall Test [5, 6], (b) Hamed and Rao Modified MK Test Hamed and Ramachandra Rao [7], (c) Yue and Wang Modified MK Test [8], (d) Pre-Whitening [9], (e) Multivariate MK, (f) Test Hirsch, et al. [10] proposed Seasonal MK Test [10] (Table 1).

Based on the assumptions of each model, the trend could be various. Yue and Wang Modified MK Test (c) is the most sensible trend test. It is detective the most number zones trend compared to other models.

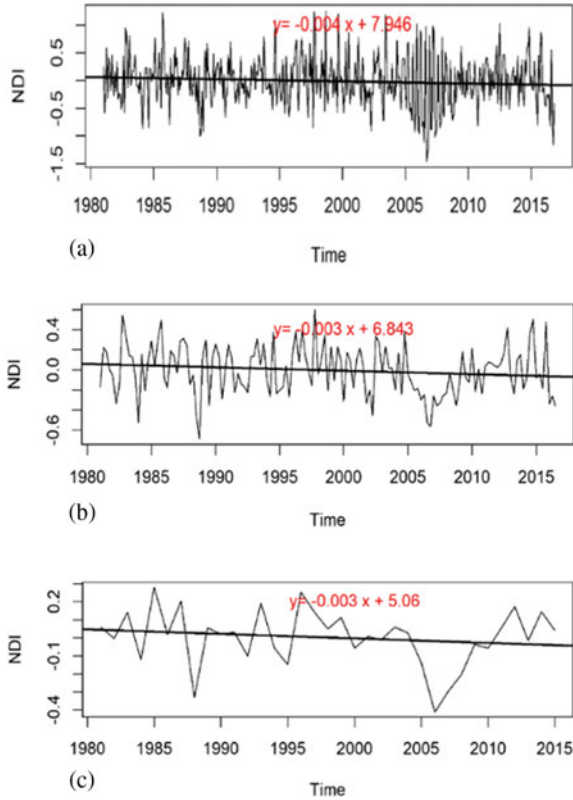


Fig. 3 Monthly (a), seasonably (b), annual (c) scale trend

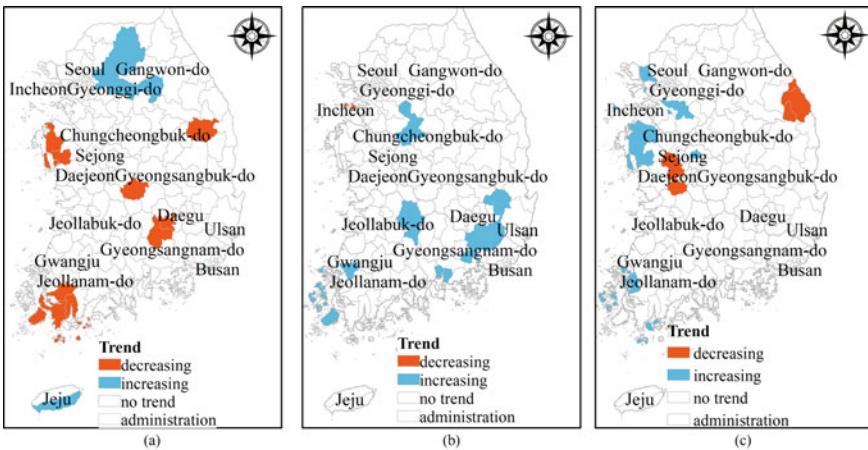


Fig. 4 Trend of zonal statistic average NDI 1-month (a), NDI 3-months (b), and NDI 6- months temporal scales

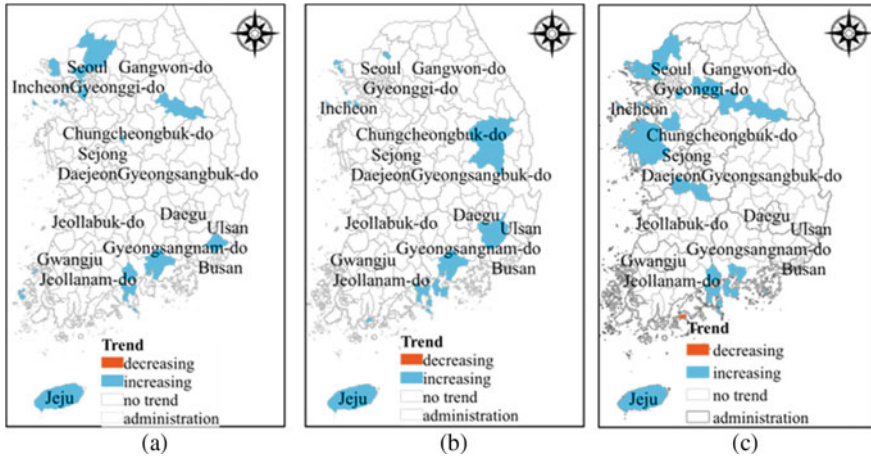


Fig. 5 Trend of zonal statistic standard deviation NDI 1-month (a), NDI 3-months (b), and NDI 6-months temporal scales

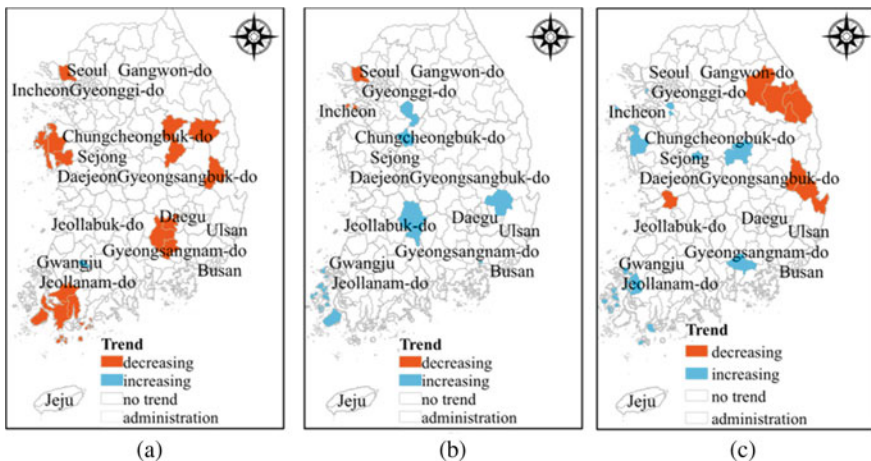


Fig. 6 Trend of zonal statistic extreme (10 percentile) NDI 3-month (a), NDI 3-months (b), and NDI 6-months temporal scales

Table 1 Result from six types of Man Kendall family test for 5 sub-districts

Station	(a)	(b)	(c)	(d)	(e)	(f)
Andong106	No trend	No trend	Increasing	No trend	No trend	No trend
Ansan75	No trend	No trend	Increasing	No trend	No trend	No trend
Ansoeng76	No trend	No trend	Increasing	No trend	No trend	No trend
Anyang77	No trend	No trend	Increasing	No trend	No trend	No trend
Asan25	No trend	No trend	Increasing	No trend	No trend	No trend

4 Conclusion

The long-term drought trend was analysis for South Korea which shows diverge of drought in various temporal scales. It is a natural drought trend with assuming the trend does not change for specific period. The trend can be divided into short-range assessment. This can lead to the complicated trend of this study area.

Various drought indices, such as SPI, have been employed to assess the drought patterns in South Korea. The consensus among these studies indicates an increasing trend in drought, suggesting that NDI can effectively capture drought trends. However, it is noted that our findings did not incorporate the influences of climate phenomena, such as El Nino and La Nina. These factors could provide valuable insights into the link between drought trends and global climatic conditions.

This study provided the trend of drought with several models and temporal scale. Monthly temporal scale of mean zonal NDI values is increasing or trend drought decreasing. The variance zonal drought is increasing. The extreme drought is increasing in 1- and 6-months temporal scales of NDI. Drought has an increasing trend in the summer. For annual temporal scale, drought has an increasing trend in the North-East of South Korea. Results show that the trend of drought at various temporal scales. It shows the complicated and difficulty of drought trend prediction. The trend varies not only based on temporal scale and spatial scale, and it also depended on the assumptions of testing models.

References

1. Wilhite DA (2016) Droughts: a global assesment. Routledge
2. Krysanova V, Vetter T, Hattermann F (2008) Detection of change in drought frequency in the Elbe basin: comparison of three methods. *Hydrol Sci J* 53(3):519–537. <https://doi.org/10.1623/hysj.53.3.519>
3. Byakatonda J, Parida BP, Moalafhi DB, Kenabatho PK (2018) Analysis of long term drought severity characteristics and trends across semiarid Botswana using two drought indices. *Atmos Res* 213:492–508. <https://doi.org/10.1016/j.atmosres.2018.07.002>
4. Gumus V, Simsek O, Avsaroglu Y, Agun B (2021) Spatio-temporal trend analysis of drought in the GAP Region, Turkey. *Nat Hazards* 109:1759–1776. <https://doi.org/10.1007/s11069-021-04897-1>
5. Kendall M (1975) Rank correlation measures. Charles Griffin, London, p 220
6. Mann HB (1945) Nonparametric tests against trend. *Econometrica* 13(3):245. <https://doi.org/10.2307/1907187>
7. Hamed KH, Ramachandra Rao A (1998) A modified Mann-Kendall trend test for autocorrelated data, (in en). *J Hydrol* 204(1–4):182–196. [https://doi.org/10.1016/S0022-1694\(97\)00125-X](https://doi.org/10.1016/S0022-1694(97)00125-X)
8. Yue S, Wang C (2004) The Mann-Kendall test modified by effective sample size to detect trend in serially correlated hydrological series, (in en). *Water Resour Manage* 18(3):201–218. <https://doi.org/10.1023/B:WARM.0000043140.61082.60>
9. Yue S, Pilon P, Phinney B, Cavadias G (2002) The influence of autocorrelation on the ability to detect trend in hydrological series, (in en). *Hydrol Process* 16(9):1807–1829. <https://doi.org/10.1002/hyp.1095>
10. Hirsch RM, Slack JR, Smith RA (1982) Techniques of trend analysis for monthly water quality data, (in en). *Water Resour Res* 18(1):107–121. <https://doi.org/10.1029/WR018i001p00107>

Proposed Adaptation Measures for Saltwater Intrusion in the Vietnamese Mekong Delta



Nguyen Phuong Mai, Sameh Kantoush, Sumi Tetsuya, and Tang Duc Thang

Abstract The Vietnamese Mekong Delta (VMD) plays an extremely important and central role in the country's food security. The influences of the upstream dam's development, sea-level rise, and complicated tidal regime in the dry season have caused barriers and constraints for local agricultural activities in VMD. Once these causes combined climate change, the salinity intensity is more severe, and intrusion length is likely further in seven Mekong estuaries. The purpose of this study to propose mitigation and adaptation measures for saltwater intrusion (SI) for sustainable agricultural development in the Mekong estuary areas. The relationship between $Q \sim S$ and $Q \sim L$ has been built to predict the S and L along five of seven branches. Also, the boundary between freshwater—brackish—saltwater zone also was proposed for planning the land use and water use. Moreover, the location of salinity monitoring stations, as well as the kinds of saltwater control works, is also discussed to serve the operation of saline control works based on analysis of field measurement data. The study will be very meaningful for local farmers to select crops that are adaptable with the different saltwater values or change land use and cultivation models for higher yields.

Keywords Saltwater intrusion · Upstream dams · Sea-level rise · Tidal regime · Vietnamese Mekong Delta

N. P. Mai (✉)

Faculty of Civil Engineering, Dongda District, Thuyloi University, 175 Tayson Street, Hanoi City, Vietnam

e-mail: maiswru@tlu.edu.vn

S. Kantoush · S. Tetsuya

DPRI, Kyoto University, Goka-Sho, Uji-Shi 611-0011, Japan

T. D. Thang

VietNam Academy for Water Resource, Dongda District, 171 Tayson Street, Hanoi City, Vietnam

© The Author(s), under exclusive license to Springer Nature Singapore Pte Ltd. 2024

563

T. Nguyen-Xuan et al. (eds.), *Proceedings of the 4th International Conference on*

Sustainability in Civil Engineering, Lecture Notes in Civil Engineering 344,

https://doi.org/10.1007/978-981-99-2345-8_57

1 Introduction

The Mekong River flows through 6 countries with total length of about 4800 km from Tibetan Plateau China to Vietnam and total basin area of 795,000 km². The Vietnamese Mekong Delta (VMD) is located at the lowermost of MR with total area of 39,000 km² from Vietnam-Cambodia border to the East Sea. The MR is divided into two branches flowing into Tien River and Hau River in Vietnamese territory. Firstly, Tien River carries of the majority of the flow (85%) and later convert to Hau River through VamNao linking channel. After MyThuan and CanTho, TienRiver and Hau River flow into the East Sea of Vietnam through eight estuaries such as Tieu, Dai, HamLuong, CoChien, CungHau, DinhAn, and TranDe (Fig. 1).

VMD has been facing with so many critical problems such as flooding, river and coastal erosion, subsidence, drought, and salinity intrusion. Specially, salinity

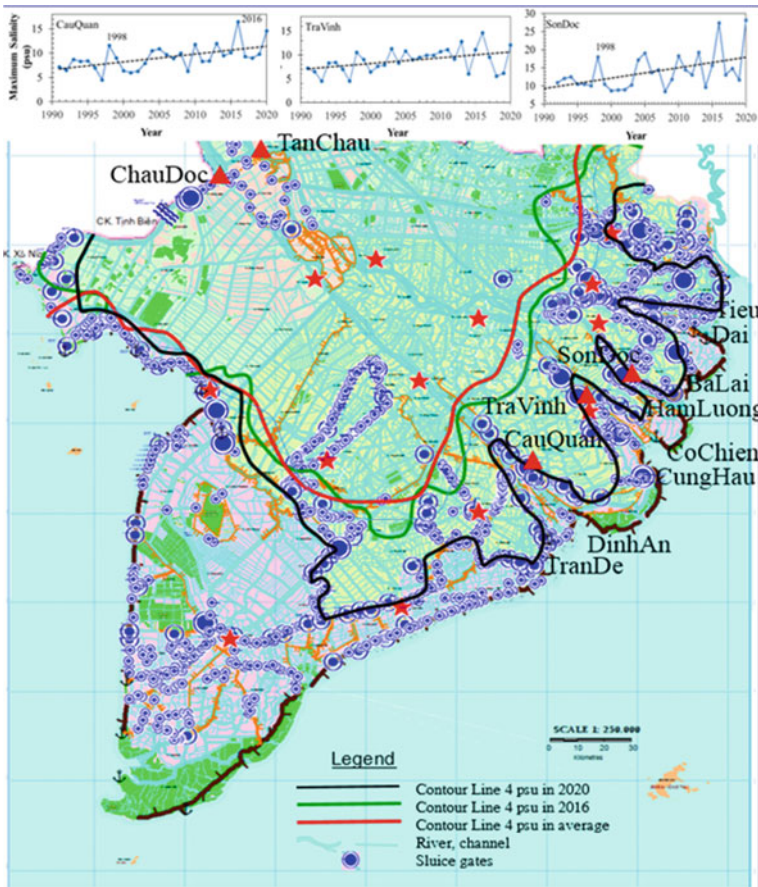


Fig. 1 Map of study area and salinity intrusion contour in mean average years, 2016 and 2020

intrusion in 2016 and 2020 was a most severe over 90 years in the delta. Figure 1 shows the trend of salinity concentration more complicated and serious with maximum concentration increasing for 30 years. The intrusion length of 4 psu in 2020 is 78, 68, and 65 km on HamLuong, CoChien, and Hau Rivers, 5, 3, and 5 km deeper than 2016 and 35, 24 and 24 km deeper than the average 26 years, also on all three estuaries of HamLuong, CoChien and Hau Rivers. That affected on 52.7% areas of the VMD with a total economic loss approximate US\$360 million because the salinity impacted on over 405,139 ha of rice field, 28,457 ha of fruit free areas, 194,163 ha of aquaculture area, and over 389,831 household have been faced water shortage [1]. So, understanding the causes and the mechanism of salinity intrusion was very necessary to propose the solutions, the mitigation, and adaption measures.

Saltwater intrusion (SI) is a natural phenomenon occurring in the estuary and coastal areas where tidal influence is observed.

The previous studies have shown factors affecting saline intrusion, including river flow, topography, morphology, river bed slope, water use, precipitation, sea level, tidal regime, wind direction, wind speed, and human activities.

The recent studies have concluded that sea-level rise and upstream flow changes have significantly impact on salinity concentration (S) and intrusion length (L). For example, the results show that the S increases 2.5 psu and L increases from 10 to 20 km in the main river and 20–35 km in the paddy field under 20–45 cm of sea-level rise [2]. One of the main causes, up to 2016, over 56 upstream dams was completed, so the total dry flow has an increasing trend by 5.1% due to shifting water from the wet season to the dry season, and the S will be reduced by 11.6% at 28 km from the river mouth [1]. But the total dry flow was unevenly flowing distribution during 6 months of the dry season. The flow has increased from March to May, while it has decreased from November to February. Hence, the S raised from November and maintained a high concentration from December to February and reached the peak value in February [1]. That was causes of maximum S occurred earlier and more severely in recent years.

Besides, the upstream dams do not only store water but also trap the sediment inside the reservoir, causing the flood peak, the frequency of floods, and the amount of sediment to be significantly reduced downstream, especially in the VMD area. Such as since 1993, when large upstream dams were built and over 56 hydropower dams have been completed in 2016, the Mekong dams have caused large-scale morphology changes in VMD. In the building dam period of 1993–2011, the annual sediment load decreased by 64.1% (59.7 Mt) and by more than 74.6% (42.3 Mt) in the completed dam period 2012–2016 [1]. This is the main cause of erosion or incision of the bottom topography of the Hau and Tien Rivers in VMD. A comparison of the riverbed elevation data between 2009 and 2017 shows that the mean incision rate from ChauDoc to CanTho (0.22 m/year) is more than 3 times that of CanTho to the DinhAn estuary (0.07 m/year). Also, the maximum incision rate in the lower part is 0.22 m/year so 0.22 m/year of riverbed incision is used for the whole Hau River for simulation, while the mean incision rate in the upper and lower part of Tien (CoChien branch) is 0.34 m/year and 0.19 m/year, respectively [1].

The reduction of upstream flow and sediment may cause many related environmental issues, such as riverbank erosion and the lowering of riverbed elevation, a reduction in nutrient-rich sediment transference into floodplains, and increased salt-water intrusion. In addition to human-induced factors, sea-level rise and tides are also threats to the VMD.

As a result, these issues have changed farming practices by intensifying the use of agrochemicals and affecting the livelihoods of people in the VMD. These issues may lead to serious challenges for the Vietnamese government in terms of food security and environmental sustainability. Therefore, setting up operation rules for the upstream reservoir and proposing suitable water resources management solutions to ensure sustainable socio-economic development downstream are needed.

2 The Mitigation and Adaptation Measurement on SI

2.1 Mitigation Measures for Mekong River Basin (MRB)

Based on analyzing the changes of upstream flow regime into the downstream region, especially in the VMD and its related environmental issues, this study proposed some measures to enhance sustainable socio-economic development in the downstream, especially in the VMD by reducing adverse impacts of upstream dam development. Therefore, it is needed to maintain environmental flow and sediment flow and to ensure a water demand in the downstream region which could support people's livelihoods, farming practices, and ecosystem services.

In extreme cases, reservoir operation rules should be appropriately adjusted to mitigate extreme drought events in the downstream regions, which may minimize transboundary impacts. For example, if the upstream reservoirs have suitable operation rules (such as releasing water one or two months earlier than usual) during extreme drought events in dry seasons of 2016 and 2020, the VMD would have avoided severe socio-economic losses. So, it is very necessary to set up and improve the monitoring system and sharing hydrology data and operation rules among countries for proactive preparedness to face extreme events and make a future plan. Moreover, strategic collaboration among riparian countries and different geographical regions is crucial to share the benefits from the Mekong River.

2.2 Mitigation and Adaptation Measures for Vietnam Mekong Delta (VMD)

It was noted that saltwater intrusion processes (SI) in the VMD in recent years have been very complicated, especially in 2016 and 2020. SI has caused 389.831 households to lack fresh water, and over 405.139 ha of rice crops were affected so

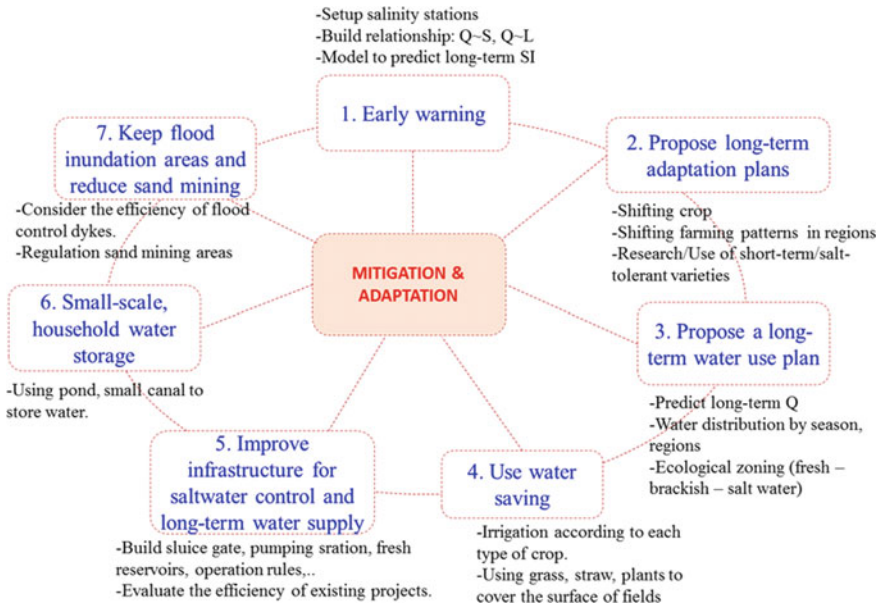


Fig. 2 Long- and short-term measures for mitigation and adaptation with SI in VMD

short-term and long-term solutions need to be considered. Therefore, both structural and non-structural measures are needed for mitigating the risks of saltwater intrusion.

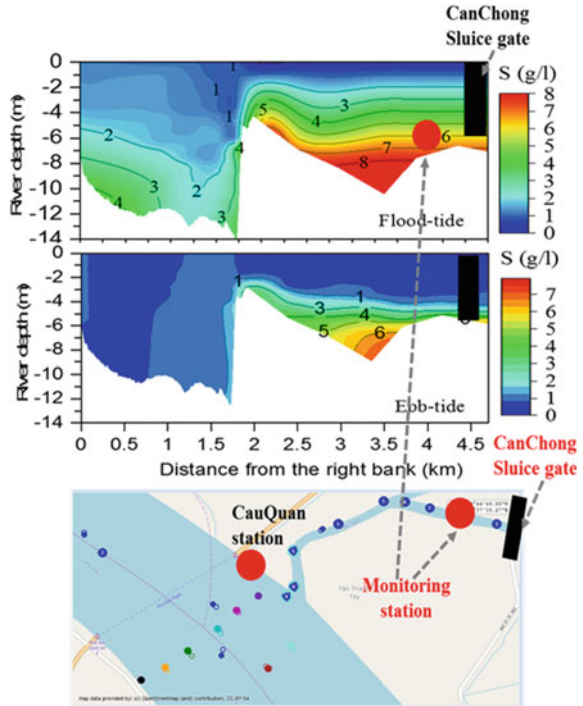
The comprehensive solutions were proposed in Fig. 2 to prevent and mitigate the impact of drought and salinity intrusion in short (such as days, weeks, months, seasons, or years) and long-time frames (many years). This diagram includes seven solutions, including four non-structural solutions and three structural solutions.

2.2.1 Early Warning

Until 2020, there have been about 81 salinity monitoring stations located along 13 main tributaries of the VMD. Thirty-nine monitoring stations of them in the seven estuaries of the Mekong River have been installed to service the operation of over 130 sluice gates located along seven MR estuaries and 122 salinity control sluices in the delta. Most of the manual stations only monitor from January to May with an interval time of 2 h so the results were less correct. So, it is necessary to set up automated monitoring stations and share salinity data to be more proactive with the intake of fresh water and prevent seawater intrusion to reduce the damage of the latter.

The location of salinity monitoring station has been suggested that at the intersection of the river and the canal, it is advisable to incorporate monitoring stations on the main river upstream of these tributaries which have saltwater control sluices

Fig. 3 Vertical distribution of salinity at one cross section of the Hau River and 2.5 km long of CauQuan River in front of the CanChong sluice gate



and a single station in front of the sluice gates if those sluices are located far from the main river.

Because salt concentration in the main rivers and canals is quite different due to the riverbed elevation of the tributary and the main canal. This is due to the retention of saltwater along the river bottom.

Figure 3 shows that S_{max} in the mainstream is 4 psu, while S_{max} in the front of the sluice gate is 6 psu in the flood tide. In the ebb tide, the S_{max} in the mainstream is less than 1 psu but the gate still close because the S_{max} in the canal still high about 3–4 psu. So, the gate could not intake fresh water from the mainstream.

In addition to automatic salinity monitoring, it is easy to estimate salinity concentration in the VMD by using the relationship curve between $Q_{TC+CD} \sim$ salinity by historical data (Fig. 4a) and $Q \sim L$ intrusion length in the main estuaries (Fig. 4b) by numerical model.

2.2.2 Proposed Long-Term Adaptation Plans and Water Use Plans

To prevent serious impacts of salinity drought in the VMD, it is very important to develop an adaptation plan which considers the changes of water sources from upstream regions. Then, make the production calendar according to the river flow such as shifting the rice crops or shifting the farming patterns in some regions

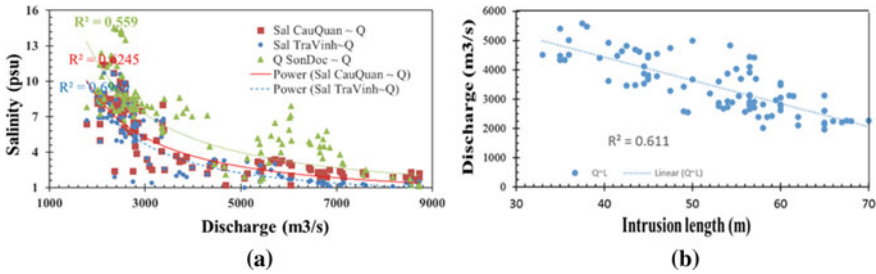


Fig. 4 a, b Relationship between discharge at TanChau + ChauDoc and salinity concentration at three stations and intrusion length

according to the salt-tolerant crops. For example, in coastal areas where the salinity concentration is frequently higher than 6 psu during the six-month of dry season, the most reasonable solution is to change the land use purpose. Converting land for rice cultivation, green flowers into aquaculture or a combination of shrimp-rice rotation model. In the rainy season, it is possible to combine rice cultivation with freshwater fish, while in the dry season with high salinity value, shrimp and crab can be cultured.

Figure 5 divides the ecological zoning according to the saltwater value, such as freshwater (< 1 psu: saltwater tolerance of plants), brackish (1–16 psu), and saltwater (> 16 psu: saltwater threshold which is suitable shrimp farming). To have a basis for dividing water use and corresponding production zoning, the author uses the numerical model results for the baseline scale to partition the VMD into 3 parts according to the above saline boundary [1].

2.2.3 Saving Water Use

Alternating wetting drying (AWD) method was recommend to apply for saving water for irrigation. This method is very developed and widely used in Asia because it can save 30% of water use depending on the type of soil so the local farmers can apply to reduce their irrigation water consumption in rice fields without decreasing its yield [3].

2.2.4 Improve Infrastructure Systems for Saltwater Control and Long-Term Water Supply

The hydraulic work systems of over 880 small-large sized sluices, 450 km sea-dike, 1290 km of river dikes, and 7000 km ring dikes in high salinity areas have received investment but have not yet been completed (closed), so there is still pollution of water sources [1]. Also, the environment and construction work efficiency are not high. The sea dike, river dike, and sluices at TranDe, DinhAn, and Cung Hau estuaries have been closed, but the height of the dikes is still low and needs to be upgraded.

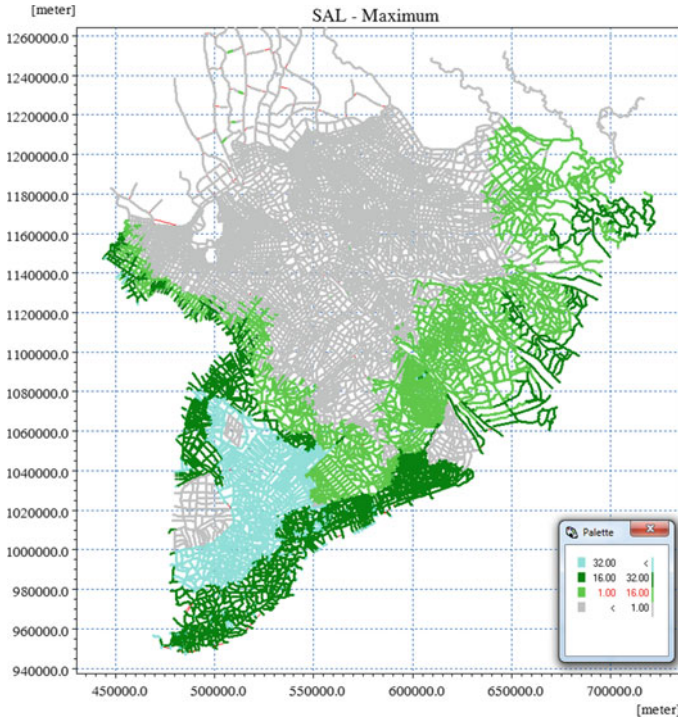


Fig. 5 Saltwater results by three partitions as above (freshwater < 1 psu, brackish water: 1–16 psu)

Along the left bank of the CoChien and HamLuong Rivers, the dikes system has been completed, but the sluice system has not been closed, so the whole province of BenTre is affected by the 4 psu salinity line.

So, it is necessary to create a new land use plan in coastal areas, scheduled seasonally to develop effective operating procedures for sluices and pumping stations. The land use should be shifting from agriculture to aquaculture in areas always faced with high salinity concentration to increase income and adapt with the changing of flow regime conditions. However, aquaculture farming practices must be friendly to the environment and systems. When the estuary is aquatic, the sluices located along 15–20 km from the estuary should not closed in the dry season, so saltwater will not intrude deeper upstream. However, it is necessary to build small sluice systems at the boundary of aquaculture and rice cultivation so that salt water does not penetrate deep upstream of the tributary canal. If the *L* increases in the mainstream when all the sluices are closed, we should propose constructing new sluice gates along the main rivers toward upstream. Furthermore, re-evaluation of existing structures is needed to assess the location and operation routines and propose suitable new operations.

Furthermore, needs to propagate to raise people’s awareness for saving water use, strengthen measures to store fresh water in each household, comply with land use

plans for each area, and support local people from finance to technology during the process of livelihood transformation.

3 Conclusion

Salinity trends are increasingly complex and adversely affect agriculture, fisheries, and livelihoods. So, salinity adaptation measures are necessary. Mitigation measures from MRB are collaborative and call for action. So, to minimize the effect of salinity intrusion in VMD, the seven mitigation measures mentioned above need to conduct simultaneously and immediately. The results show the relationship between $Q \sim S$ and $Q \sim L$ for short salinity prediction and propose the location of salinity monitoring for sluice gates operations and location of new sluices along the boundary of rice field and aquatic field. The results also propose three ecological zones according to the saltwater value from 1 to 16 psu, suggest raising people's awareness for saving water use, and strengthen measures to store fresh water in each household.

References

1. Mai NTP (2022) Study on assessment and adaptation to saltwater intrusion under the impacts of tide, sea-level rise flow and morphological changes in the Vietnamese Mekong delta. Kyoto University, Japan
2. Duong TA, Hoang LP, Minh BD, Peter R (2018) Simulating future flows and salinity intrusion using combined one- and two-dimensional hydrodynamic modelling—the case of Hau River Vietnamese Mekong Delta. MDPI Water J 10(897):1–21
3. Richards M, Sander BO (2014) Alternate wetting and drying in irrigated rice. CGIAR research program on climate change, agriculture and food security. Copenhagen, Denmark (CCAFS)

Structural Modelling and Analysis

Evaluation of Partial Safety Coefficients in the Concrete Tank Design by a Semi-Probabilistic Approach



Hocine Hammoum, Karima Bouzelha, and Amar Aliche

Abstract Traditionally, the optimization of civil engineering structures is conducted by a deterministic approach based on global safety coefficients recommended by the dimensioning codes, such as the Algerian seismic code and the Eurocodes. These coefficients are applied to take into account the uncertainties related to live loads in order to protect the structures against unpredictable variations in the mechanical performance of the materials. In reality, the use of these safety factors still do not lead to an optimal solution, as they can lead to an over-dimensioning of the structure when it does not lead to a lack of robustness. This approach gives to the dimensioning a reliability without having to perform a reliability analysis. The use of these coefficients aims to introduce a sufficient margin of safety in order to increase the safety of the structure design and to reduce the role of the uncertainties on the performances of the optimized structure. This research aims to evaluate the partial safety factors associated with the internal tensile stress developed in the upper beam of a tank, as well as its resistance. The evaluation of the partial safety factors is presented with a semi-probabilistic calculation. Two random variables were considered, the live load, as well as the compressive strength of concrete, modeled by distribution normal laws. In addition, the target reliability index is taken in a range of performance of the civil engineering structure.

Keywords Tank · Safety coefficients · Reliability index · Semi-probabilistic approach

1 Introduction

A semi-probabilistic approach is a method which is based on the notions of limit states and safety coefficient, this approach is used in many design codes, notably the Eurocodes. The ultimate limit states correspond to the collapse of the structure [1].

H. Hammoum (✉) · K. Bouzelha · A. Aliche
Department of Civil Engineering, Mouloud Mammeri University, 15000 Tizi-Ouzou, Algeria
e-mail: hocine.hammoum@ummto.dz

The serviceability limit state corresponds to conditions beyond which the service aptitude requirements are no longer met (deflection, crack opening for a tank, etc..) [2].

The semi-probabilistic approach consists to make sure that the calculation values respect the safety margin defined by the limit state. The partial coefficients approach is qualified as semi-probabilistic because it combines, within the same limit state, statistically estimated values and deterministic values, while adopting a deterministic formalism. This approach offers a good compromise between ease of implementation and information on data dispersions. The semi-probabilistic approach with limit states will apply to all materials as it was already the case for concrete through the Eurocodes [3].

The principle of the semi-probabilistic approach is to limit the failure probability of the structures to a value low enough to be accepted. The failure probability is the probability that the stresses of the structure are greater than its resistance. This probability is determined from the probability laws, the effects of the loads and strengths which are considered as random variables. In the international literature, different calculation methods can be found to assess a partial safety factor of a resistant component of a structure.

The developed approach in this study aims to propose, on the basis of probabilistic results conducted by first-order reliability method approximation (FORM) and confirmed by Monte Carlo method, values for the partial safety factors applied to materials and loading in the calculation of the upper belt of a RC tank placed on the ground. The present study covers a wide range of coefficients of variation (COV), which reflects the dispersion of the values of the live load applied to the roofing dome as well as the hazard on the values of the characteristic resistance of the concrete, considered as the two random variables adopted in this study.

2 Evaluation of Partial Safety Coefficients

Traditionally, the dimensioning rules are associated with coordinate failure scenario (R, S) defined in most cases by [1, 4]:

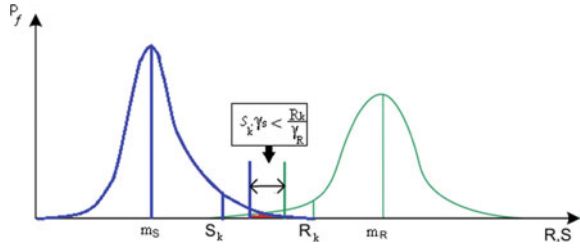
$$G(R, S) = R - S \quad (1)$$

In the current dimensioning codes, the failure evaluation conducted by a probability calculation is replaced by the verification of a criterion involving the characteristic values of R and S denoted R_k and S_k or of the design values R_d and S_d and partial safety coefficients (γ_s, γ_R), expressed by the following relation [5] (Fig. 1):

$$S_d - R_d < 0 \Rightarrow S_d = \gamma_s S_k \leq \frac{R_k}{\gamma_R} = R_d \quad (2)$$

where the coefficients are given by

Fig. 1 Characteristics values and partial coefficients



$$\gamma_R \leq \frac{R_k}{R_d} \text{ and } \gamma_s \leq \frac{S_d}{S_k} \tag{3}$$

The value assigned to the global safety coefficient is given by the product [5]:

$$\gamma_G = \gamma_R \cdot \gamma_s \tag{4}$$

3 Practical Application

We focus in this section in the safety coefficients evaluation of the upper beam of a circular concrete tank of capacity 250 m³ (see Fig. 2). The geometrical characteristics of this structure are mentioned in Table 1. The tank placed on ground is located in Ain El Hammam at an altitude of 1400 m, in Tizi-Ouzou region, classified as snow zone A by snow and wind standard (DTR99) [6].

The limit state function considered in this study is linked to the strenght of the upper beam under the dead and live loads applied on the cover dome. The limit state function of tensile stress induced in the beam can be written as follows:

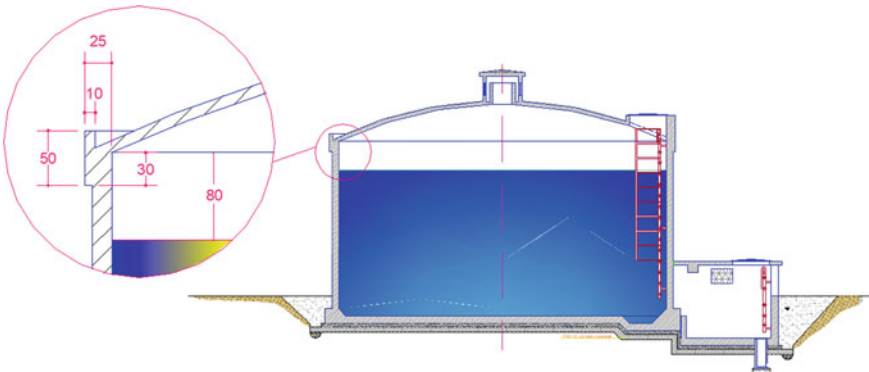


Fig. 2 Cross section of the tank placed on ground

Table 1 Geometrical characteristics of the tank

Designation	Notation	Values	Units	Observations
Internal diameter	D	9,00	m	Deterministic
Dome arrow	f	1,00	m	Deterministic
Dome radius of curvature	R_c	10,63	m	Deterministic
Dome surface	S_c	66,76	m ²	Deterministic
Compressive strength of concrete after 28 days	f_{c28}		Mpa	Random
Live load	Q		KN	Random

$$G(x_1, x_2) = T_R - T_S \tag{5}$$

The previous relation can be written after linearization by

$$G(x_1, x_2) = aX_1 - bX_2 \tag{6}$$

In this last equation which defines the criterion of tensile stress developed in the upper beam, the variable X_1 is mainly composed of the physico-mechanical characteristics of the element studied, while the variable X_2 denotes the loading. Only two variables are considered in this study as random (see Table 1), which are the compressive strength f_{c28} and the live load Q , recognized as the source of uncertainties linked to this tank component with [7]:

$$a = 0.8.A.10^6 \tag{7}$$

$$b = \left(\frac{S}{\pi D} \right) (R - f) \tag{8}$$

$$X_1 = \sqrt{n.(0.6 + 0.06 f_{c28})} \tag{9}$$

$$X_2 = Q + G \tag{10}$$

The calculation parameters are mentioned in Table 2.

In the absence of precise values or samples of live loads, we cannot attach values to coefficient of variation (COV) and the standard deviation. For this purpose, we propose to analyze the variability effect of the reliability index, evaluated by applying

Table 2 Statistical parameters of the random variables

Parameter	Unit	Distribution type	Mean value	CV	Standard deviation value
f_{c28}	Mpa	Normal	29.90	0.12	2.65
Q	N/m ²	Normal	1459.80	–	–

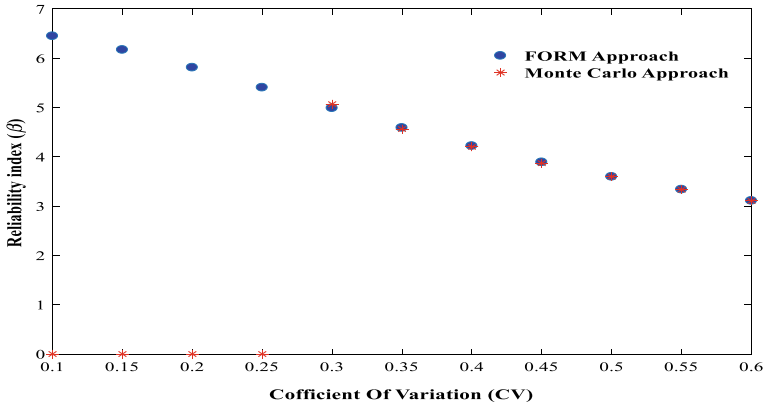


Fig. 3 Reliability index as a function of the coefficient of variation

the FORM method, as a function of (COV). The obtained results are shown in Fig. 3 and are compared with those resulting from the Monte Carlo simulation method.

As the tank is classified «Reliability Class 2 (RC2)», the admissible value of the reliability index ($\beta = 4.75$) is reached for values of COV lower than 35%. So for ($COV < 35\%$), the distribution law of the live load is tight around the mean value, which indicates better control of the live load. On the other hand, for ($COV > 35\%$), the distribution law is spread out, which will result in uncertainties linked to the live load value. We note that the results of the reliability index calculated from the two methods (FORM and MC) are confused beyond the value of the COV of 30%.

The parameters used for the variables X_1 and X_2 introduced in the calculations are given in the Table 3. The results presented in the Fig. 3 highlight that the reliability index of the beam is influenced by the coefficient of variation of the live load distribution law. We note that the results of the reliability index calculated from the two methods (FORM and MC) are confused beyond the value of the CV of 30%.

Table 3 Identification of the parameters of variables X_1 and X_2

Designation	Notation	Values	Units
Concrete strength at 28 days	f_{c28}	29.9	Mpa
Coefficient of variation of live load	COV	0.2	
Live load	Q	1459.8	N/m ²
Target reliability index	$\bar{\beta}$	4.75	
Mean of the variable X_1	m_{X1}	1.95	Mpa
Mean of the variable X_2	m_{X2}	4697.1	N/m ²
Standard deviation of the variable X_1	σ_{X1}	0.391	MPa
Standard deviation of the variable X_2	σ_{X2}	939.42	N/m ²

Table 4 Results of the design values

Designation	Parameter	Results	Units
Design value of strength	T_R^d	33 609.00	N
Design value of load	T_S^d	164 080.00	N

Table 5 Results of the characteristic values

Designation	Parameter	Values	Units
p -fractile of strength	P_R	5%	
p -fractile of load	P_S	95%	
Characteristic value of strength	T_R^k	104 600.00	N
Characteristic value of load	T_S^k	141 860.00	N

Table 6 Results of the safety coefficients

Safety coefficients	Values
γ_R	3.11
γ_S	1.15
γ_G	3.60

The design values (T_R^d and T_S^d) for a target reliability index β_{target} corresponding to a target failure probability $P_{f-target}$ (Table 4).

The characteristic values (T_R^k, T_S^k) for the p -fractile of resistance (P_R) and stress (P_S) are taken equal to 5% and 95%, respectively (Table 5).

The partial safety coefficients γ_R and γ_S as well as the global safety coefficient γ_G are presented in Table 6.

The evolution of the global safety coefficient γ_G depending of the reliability index for different values of the coefficient of variation is shown in Fig. 4.

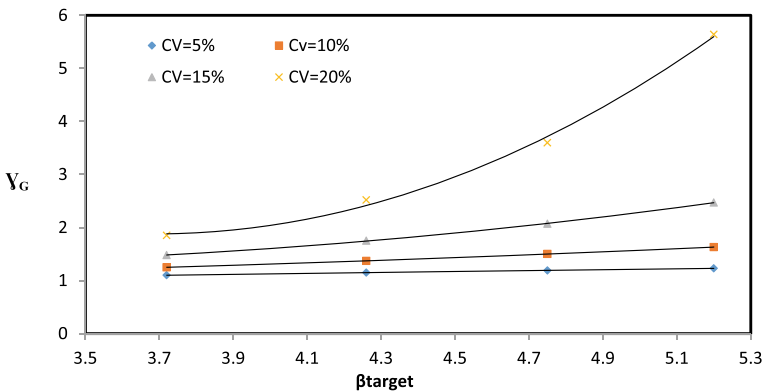


Fig. 4 Evolution of the global safety coefficient γ_G depending on the reliability index β

Table 7 Characteristics of the $\gamma_G(\beta)$ curves

	CV = 5%	CV = 10%	CV = 15%	CV = 20%
<i>a</i>	-0.0025	0.0344	0.1942	1.6227
<i>b</i>	0.1092	-0.0493	-1.0665	-11.964
<i>c</i>	0.7283	0.9573	2.7623	23.932
R^2	0.9996	1	0.9998	0.9967

We notice that whatever the value of CV, the coefficient γ_G increases as a function of the reliability index β and follows a linear law, that is:

$$\gamma_G = a\beta^2 + b\beta + c \tag{11}$$

The coefficients *a*, *b*, and *c* as well as the correlation coefficient R^2 are given in Table 7.

4 Conclusion

This semi-probabilistic approach of partial safety coefficients is based on the dispersion evaluation of certain parameters from statistical studies which are integrated as characteristic values. We retain generally as characteristic value a fractile of the measured sample distribution. It is admitted to choose a probability value of 5% for strength and a probability value of 95% for load. The case study examined in this study showed the interest of this approach in the calculation of safety coefficients. These safety partial coefficients depend of the target reliability and the coefficients of variations which are expressed physically by the degree of control of the uncertainties linked to the live load. It has been demonstrated that for a coefficient deviation of live load around 0.1, it does not need to penalize the live load value, for a target reliability index. Conversely for a coefficient of variations of live load around 0.3, the penalization of the live load becomes important. This justifies the values of the coefficients codified by the regulations. The civil engineer, in his design, must use the semi-probabilistic method to choose the adequate safety coefficients according to the available data at his level (CV, β).

Acknowledgements The authors wish to thank the Algerian Ministry of higher education and scientific research for funding the University education research project (PRFU—N° A01L02UN150120220004) with Tassili Project (PHC—18MDU121). Without forgetting to thank African Geosystem Company (<http://www.agc-dz.com>) that provided the documentation for the practical example.

References

1. Eurocode (2000) Basis of structural design. The European Union Per Regulation
2. Breysse D (2009) *Maîtrise des risques en génie civil*, 3^{end} edn. Lavoisier Ed, Paris. ISBN 9782746224438
3. Aliche A, Hammoum H, Bouzelha K (2019) Mecano-reliability analysis applied to RC tank under seismic loads according to the Algerian seismic standard. *Asian J Civil Eng* 20(3):395–408. <https://doi.org/10.1007/s42107-018-00113-x>
4. Ditlevsen O, Madsen HO (1996) *structural reliability methods*. Wiley, New York. ISBN 0471960861
5. Lemaire M, Châteauneuf A, Mitteau JC (2009) *Structural reliability*. Wiley, New York. ISBN 978-1-84821-082-0
6. DTR B-C. 2–4.7 (1999) *Règlement neige et vent (RNV 1999)*, Ministère de l’habitat, Alger
7. Fascicule 74 (1998) *texte officiel, Construction des réservoirs en béton—cahier des clauses techniques générales*, Ministère de l’équipement des transports et du logement, Paris

Multi-Criteria Optimization of the Quality Indicators of Steel Foundry Ladles, Based on Priorities and Weighting Coefficients of the Indicators



Dimitar Borisov

Abstract In the present study, the significance of the quality indicators of “Fosuk” type driving masses used for the monolithic construction of the walls of the steel foundry ladles used in steel production was determined by rank correlation method. Six quality indicators of driving masses were studied: linear changes, open porosity, compressive strength, beginning of deformation, 4% deformation and 40% deformation. The three most significant indicators of driving masses “Fosuk” type have been determined. A multi-criteria optimization was performed, using a genetic optimization algorithm, the set of fifty Pareto-optimal solutions (Pareto-front) were found in the two-dimensional space of the control parameters within their range limits. A multi-criteria analysis was done by using fractional-rational generalized functions of usefulness in order to determine the optimal content of clay substances (Al_2O_3) and the temperature of heat treatment of the inner lining of the steel foundry ladles.

Keywords Driving masses · Quality indicators · Multi-criteria optimization · Pareto-optimal solutions · Fractional-rational generalized functions of usefulness

1 Introduction

The steel foundry ladles (presented on a Fig. 1) are used for transportation of the molten steel from the furnaces at temperature between the range of 1500 and 1700 °C to the casting process or supply of molten steel to an ingot mold. Steel companies need high-quality refractory solutions for the refractory linings of ladles that achieve maximum productivity at the lowest cost. The improvement of the quality indicators of the refractory materials is mainly determined by the improvement of the

D. Borisov (✉)

University of Chemical Technology and Metallurgy/UCTM, Sofia, Bulgaria

e-mail: shtain@uctm.edu

Fig. 1 Steel foundry ladle

technological processes or increasing the productivity by increasing the temperatures, which requires a higher resistance of the refractory linings. This is usually achieved by improving the thermo-mechanical properties, corrosion and erosion resistance of refractory materials. These linings must have excellent resistance to steel and basic slag corrosion, as well as high thermal shock and oxidation resistance. The main properties of refractories, affecting their performance are: compressive strength, MPa; temperature of onset of deformation (beginning of deformation), °C; apparent density, %; specific density, t/m^3 ; thermal expansion upon heating and cooling leading to irreversible polymorphic transformations, %; the thermal resistance at a certain number of heat exchanges and refractoriness °C.

The main objectives of the present study are quality indicators priority evaluation based on a rank correlation approach and multi-criteria optimization through finding a set of Pareto-optimal solutions and by fractional-rational generalized functions of usefulness using.

2 Priorities and Weight Coefficient Determination

Optimal decision making in the presence of many objective parameters is an incorrect task because it does not have a single solution. The difficulties in choosing an optimal decision are increasing with the increase in the number of objective parameters and the subjective contradictions that arise between the stakeholders during a specific decision making. The number of objective parameters can be reduced by removing the parameters with a low priority or by studying the linear correlation between the objective indicators and removing some of them.

In order to find compromise solutions for the optimal technological parameters in the quartz driving masses production, it is necessary to evaluate the priorities of the quality indicators of the driving masses [1]. Based on the study of expert opinions, the importance of degree of concordance between them was determined. The enquiry card is presented in Table 1.

According to a proposed methodology [2, 3], the coefficient of concordance for non-repeating ranks w_k was determined by following procedure:

Table 1 Enquiry card for quality indicators priority determination

Quality indicator	Objective parameter	Rank
Linear changes (%)	Y_1	
Open porosity (%)	Y_2	
Compressive strength (MPa)	Y_3	
Beginning of deformation (°C)	Y_4	
4% deformation (°C)	Y_5	
40% deformation (°C)	Y_6	

Average sum of all ranks is calculated.

$$S_{\text{aver}} = \frac{R(m+1)}{2} = 35 \quad (1)$$

where

R number of enquired experts ($R = 10$);

m number of quality indicators ($m = 6$).

The Kendall coefficient of consent is calculated [2].

$$w_k = \frac{12 \sum_{j=1}^m \Delta_j^2}{R^2(m^3 - m)} = 0.562 \quad (2)$$

where

Δ_j is the deviation of the sum of the ranks for each indicator $\sum \alpha_{ij}$ by the average sum S_{aver} .

The statistical significance of the coefficient of concordance w_k is proved by Z-criterion [3] because the number of quality indicators is less than 7 ($m < 7$).

$$Z_{\text{calc}} = \frac{1}{2} \ln \frac{w_k(R-1)}{1-w_k} = 1,224 \quad (3)$$

With an accepted level of significance $\alpha = 0.05$ (confidential probability $\beta = 0.95$) the tabular value $Z_{\text{tabl}}(\alpha; \nu_1; \nu_2)$ is obtained from statistic tables [2, 3].

$\nu_1 = m - 1 - \frac{2}{R} = 4.8 \approx 5$; $\nu_2 = \nu_1(R - 1) = 43.2 \approx 43$, rounded to the nearest integer number.

The coefficient of concordance w_k is considered as a significant because:

$$Z_{\text{calc}} = 1.224 > Z_{\text{tabl}}(0.05; 5; 43) \approx 0.445.$$

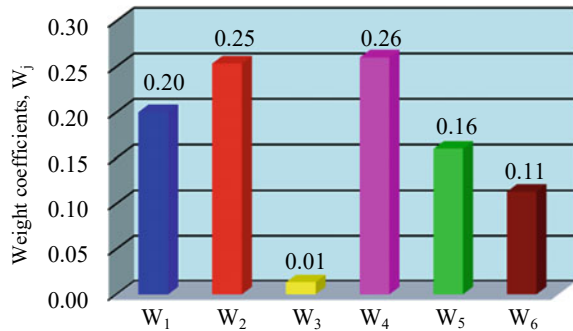
The results are summarized in Table 2.

Table 2 Matrix of ranks of the quality indicators of ceramic driving masses

Quality indicator → Expert ↓	Y_1	Y_2	Y_3	Y_4	Y_5	Y_6
1	3	2	5	1	4	6
2	2	3	6	1	4	5
3	1	3	6	2	5	4
4	5	3	6	4	2	1
5	2	1	6	3	4	5
6	3	2	6	1	5	4
7	4	2	6	1	3	5
8	3	1	5	2	4	6
9	4	1	6	5	3	2
10	3	4	6	1	2	5
$\sum \alpha_{ij}$	30	22	58	21	36	43
Δ_j	-5	-13	23	-14	1	8
V_j	0.6	0.76	0.04	0.78	0.48	0.34
W_j	0.20	0.25	0.013	0.26	0.16	0.113
Rank	3	2	6	1	4	5

The most important criterion is Y_4 ($W_4 = 0.26$), followed by criteria Y_2 ($W_2 = 0.25$) and Y_1 ($W_1 = 0.20$). The weight coefficients are graphically presented on Fig. 2.

Fig. 2 Weight coefficients of the quality indicators of the “Fosuk” type driving masses



3 Multi-Criteria Optimization

A multi-criteria optimization of the three quality indicators with the highest ranks is done by using the software product QStatLab [4, 5]. Fifty Pareto-optimal solutions, randomly distributed in the feasible region of the compromise solutions were determined and presented in Table 3.

The graphical interpretation of the results is presented on Fig. 3. The Pareto-front, i.e., the entire set of solutions is presented on Fig. 3a. The Pareto-optimal solutions are presented in pairs Y_1 – Y_2 (Fig. 3b), Y_1 – Y_4 (Fig. 3c) and Y_2 – Y_4 (Fig. 3d).

Table 3 Pareto-optimal solutions for the quality indicators

N ^o	X ₁	X ₂	Y ₁	Y ₂	Y ₄	N ^o	X ₁	X ₂	Y ₁	Y ₂	Y ₄
-	Al ₂ O ₃ , %	°C	%	%	°C	-	Al ₂ O ₃ , %	°C	%	%	°C
1	6.37	200	0.21	24.99	1355	26	6.51	200	0.18	24.80	1348
2	5.48	200	0.30	25.87	1412	27	7.20	1571	1.60	21.54	1457
3	5.80	201	0.27	25.63	1388	28	7.20	1443	1.40	23.59	1420
4	7.20	1358	1.28	24.73	1398	29	7.20	1462	1.43	23.30	1425
5	7.20	1395	1.33	24.25	1407	30	7.20	1431	1.39	23.75	1417
6	6.92	200	0.12	24.20	1334	31	7.20	1322	1.23	25.18	1389
7	7.20	1557	1.58	21.79	1452	32	7.20	1452	1.42	23.45	1422
8	7.20	1577	1.61	21.43	1459	33	7.20	1389	1.32	24.34	1405
9	5.97	200	0.26	25.44	1377	34	7.20	1519	1.52	22.42	1441
10	7.20	1535	1.55	22.16	1446	35	6.24	200	0.22	25.14	1361
11	7.20	1285	1.18	25.59	1381	36	7.20	1507	1.50	22.61	1438
12	7.20	1420	1.37	23.92	1413	37	5.02	201	0.34	26.15	1452
13	7.20	1307	1.21	25.35	1386	38	6.02	200	0.25	25.39	1374
14	5.59	200	0.29	25.79	1403	39	7.20	1385	1.32	24.39	1404
15	5.21	201	0.32	26.06	1434	40	6.54	200	0.18	24.76	1347
16	6.10	200	0.24	25.31	1369	41	6.99	200	0.11	24.10	1332
17	7.20	1527	1.53	22.28	1443	42	7.20	1490	1.48	22.87	1433
18	7.20	1414	1.36	24.00	1412	43	7.20	1590	1.63	21.20	1463
19	7.20	1502	1.49	22.70	1436	44	7.20	1439	1.40	23.65	1418
20	7.20	1294	1.19	25.49	1383	45	6.40	200	0.20	24.94	1353
21	7.20	1548	1.57	21.94	1450	46	6.16	200	0.23	25.24	1366
22	7.20	1563	1.59	21.68	1454	47	7.20	1478	1.46	23.06	1429
23	7.20	1539	1.55	22.09	1447	48	7.20	1448	1.41	23.52	1421
24	7.20	1472	1.45	23.16	1427	49	7.20	1330	1.24	25.08	1391
25	7.20	1585	1.62	21.30	1461	50	7.20	1374	1.30	24.54	1402

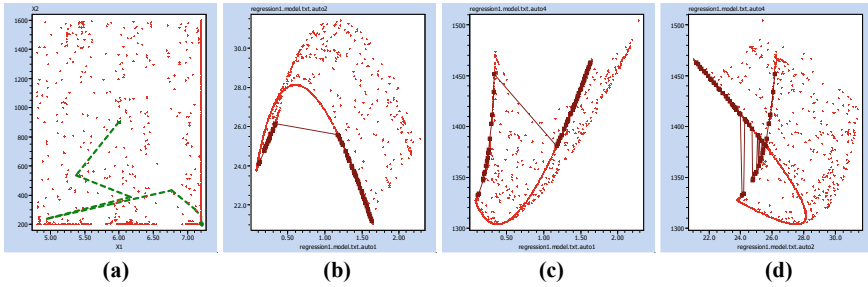


Fig. 3 Pareto-front and Pareto-optimal solutions

4 Multi-Criteria Optimization by Fraction-rational Generalized Functions Usefulness

A multi-criteria study using fractional-rational generalized functions (FRGF) of usefulness was done [6, 7]. In order to eliminate the influence of the different dimensions of the objective indicators (technological, physical, economic, etc.), they are normalized as usefulness coefficient $\eta_j(\mathbf{X}), j = 1, 2$ and 4 in the limits $(0 \div + 1)$, taken as absolute values [6].

$$\eta_j(\mathbf{X}) = \left| \frac{Y_j(\mathbf{X}) - Y_j^{pes}(\mathbf{X})}{Y_{j,max}(\mathbf{X}) - Y_{j,min}(\mathbf{X})} \right|, \quad j = 1, 2 \text{ and } 4 \tag{4}$$

where

$Y_j(\mathbf{X})$ is the natural value of each objective parameter, $j = 1, 2$ and 4;

Y_j^{pes} is the worst value of each objective parameter;

$Y_{j,max}$ and $Y_{j,min}$ are the maximum and minimum values for each objective parameter.

A 0.5% reduction of the maximum and minimum values depending on the requirements of the relevant objective parameter is used in the present article (Table 4).

Three FRGF of usefulness were studied [7]:

Fractional-rational generalized arithmetic mean objective function of usefulness

$$F - 1 \equiv F_{am}^p(\eta(\mathbf{x}), \mathbf{x}) = \frac{\frac{1}{m_1} \sum_{j_1=1}^{m_1} \eta_{j_1}(\mathbf{x})}{\frac{1}{m_2} \sum_{j_2=1}^{m_2} \eta_{j_2}(\mathbf{x})} = \frac{\eta_4}{\frac{\eta_1 + \eta_2}{2}} \tag{5}$$

Fractional-rational generalized geometric mean objective function of usefulness

Table 4 Usefulness coefficients for the quality indicators

N ^o	$\eta_1 \downarrow$	$\eta_2 \downarrow$	$\eta_4 \uparrow$	N ^o	$\eta_1 \downarrow$	$\eta_2 \downarrow$	$\eta_4 \uparrow$
1	0.9359	0.2346	0.1742	26	0.9495	0.2727	0.1240
2	0.8714	0.0559	0.6075	27	0.0199	0.9317	0.9541
3	0.8903	0.1061	0.4257	28	0.1499	0.5163	0.6678
4	0.2309	0.2862	0.5020	29	0.1303	0.5754	0.7094
5	0.1956	0.3835	0.5729	30	0.1608	0.4839	0.6448
6	0.9927	0.3942	0.0131	31	0.2651	0.1968	0.4354
7	0.0349	0.8810	0.9198	32	0.1404	0.5445	0.6876
8	0.0134	0.9539	0.9690	33	0.2018	0.3662	0.5604
9	0.9030	0.1427	0.3426	34	0.0737	0.7533	0.8327
10	0.0573	0.8066	0.8692	35	0.9251	0.2042	0.2212
11	0.2991	0.1127	0.3714	36	0.0858	0.7145	0.8060
12	0.1721	0.4507	0.6212	37	0.8507	0.0050	0.9141
13	0.2793	0.1610	0.4084	38	0.9066	0.1530	0.3195
14	0.8779	0.0739	0.5417	39	0.2058	0.3549	0.5522
15	0.8579	0.0184	0.7809	40	0.9522	0.2802	0.1151
16	0.9131	0.1708	0.2825	41	0.9950	0.4149	0.0050
17	0.0653	0.7805	0.8514	42	0.1024	0.6618	0.7696
18	0.1777	0.4344	0.6095	43	0.0050	0.9950	0.9950
19	0.0911	0.6974	0.7942	44	0.1537	0.5049	0.6597
20	0.2904	0.1338	0.3876	45	0.9392	0.2436	0.1615
21	0.0441	0.8504	0.8990	46	0.9181	0.1849	0.2554
22	0.0285	0.9028	0.9345	47	0.1143	0.6244	0.7436
23	0.0532	0.8202	0.8784	48	0.1449	0.5311	0.6782
24	0.1212	0.6033	0.7288	49	0.2573	0.2170	0.4506
25	0.0060	0.9793	0.9861	50	0.2163	0.3260	0.5312

* The arrows in the header indicate the direction of the desired values of the objective parameters

$$F - 2 \equiv F_{gm}^p(\eta(\mathbf{x}), \mathbf{x}) = \frac{\sqrt[m_1]{\prod_{j_1=1}^{m_1} \eta_{j_1}(\mathbf{x})}}{\sqrt[m_2]{\prod_{j_2=1}^{m_2} \eta_{j_2}(\mathbf{x})}} = \frac{\eta_4}{\sqrt[2]{\eta_1 \cdot \eta_2}} \tag{6}$$

Fractional-rational generalized harmonic mean objective function of usefulness

$$F - 3 \equiv F_{hm}^p(\eta(\mathbf{x}), \mathbf{x}) = \frac{m_1}{\sum_{j_1=1}^{m_1} \frac{1}{\eta_{j_1}(\mathbf{x})}} / \frac{m_2}{\sum_{j_2=1}^{m_2} \frac{1}{\eta_{j_2}(\mathbf{x})}} = \frac{1}{\frac{1}{\eta_4} / \frac{1}{\eta_1} + \frac{1}{\eta_2}} \tag{7}$$

The results and the ranks for the FRGF are presented in Table 5 and on Figs. 4, 5 and 6.

Table 5 Results for the fractional-rational generalized functions

№	$F - 1$	R	$F - 2$	R	$F - 3$	R	№	$F - 1$	R	$F - 2$	R	$F - 3$	R
1	0.2977	45	0.3718	45	0.4644	45	26	0.2029	47	0.2437	47	0.2927	47
2	1.3101	37	2.7521	18	5.7811	14	27	2.0051	17	7.0013	5	24.4469	5
3	0.8545	39	1.3849	39	2.2448	30	28	2.0046	18	2.4004	23	2.8744	24
4	1.9414	30	1.9526	35	1.9638	37	29	2.0104	11	2.5909	20	3.3391	21
5	1.9786	26	2.0919	29	2.2116	31	30	2.0004	22	2.3118	25	2.6717	26
6	0.0189	49	0.0209	49	0.0232	49	31	1.8853	32	1.9063	38	1.9275	38
7	2.0083	13	5.2421	8	13.6827	8	32	2.0079	14	2.4867	21	3.0797	22
8	2.0035	19	8.5581	4	36.5566	4	33	1.9731	27	2.0614	30	2.1535	32
9	0.6552	40	0.9543	40	1.3898	40	34	2.0138	5	3.5342	13	6.2025	13
10	2.0122	8	4.0430	11	8.1234	11	35	0.3917	44	0.5089	44	0.6611	44
11	1.8041	35	2.0234	32	2.2693	29	36	2.0144	3	3.2562	14	5.2635	15
12	1.9946	23	2.2303	26	2.4937	27	37	2.1365	1	14.0162	2	91.9505	2
13	1.8551	33	1.9258	36	1.9993	36	38	0.6030	41	0.8577	41	1.2200	41
14	1.1383	38	2.1266	28	3.9730	18	39	1.9696	28	2.0432	31	2.1195	33
15	1.7823	36	6.2208	6	21.7119	6	40	0.1868	48	0.2229	48	0.2659	48
16	0.5213	42	0.7154	42	0.9818	42	41	0.0071	50	0.0078	50	0.0085	50
17	2.0131	7	3.7711	12	7.0644	12	42	2.0141	4	2.9561	16	4.3388	17
18	1.9913	24	2.1935	27	2.4161	28	43	1.9900	25	14.1067	1	100.00	1
19	2.0144	2	3.1504	15	4.9268	16	44	2.0033	20	2.3683	24	2.7997	25
20	1.8278	34	1.9668	34	2.1163	34	45	0.2731	46	0.3376	46	0.4174	46
21	2.0100	12	4.6411	9	10.7162	9	46	0.4630	43	0.6198	43	0.8296	43
22	2.0071	15	5.8308	7	16.9392	7	47	2.0131	6	2.7829	17	3.8471	19
23	2.0115	10	4.2039	10	8.7861	10	48	2.0065	16	2.4448	22	2.9788	23
24	2.0122	9	2.6959	19	3.6120	20	49	1.9002	31	1.9071	37	1.9141	39
25	2.0017	21	12.9010	3	83.1462	3	50	1.9588	29	2.0002	33	2.0425	35

For the fractional-rational generalized geometric mean and the harmonic mean functions, the highest rank has Pareto-optimal solution №43, followed by solutions №37, №25 and №8. For the fractional-rational generalized arithmetic mean function, the highest rank has Pareto-optimal solution №27. Fractional-rational generalized arithmetic mean function has the least sensitivity regarding to the results compared to the fractional-rational generalized geometric mean and harmonic mean functions. The greatest sensitivity has fractional-rational generalized harmonic mean function. The following five Pareto-optimal solutions №43, №37, №25, №8 and №27 have the highest priority and are proposed for further studies.

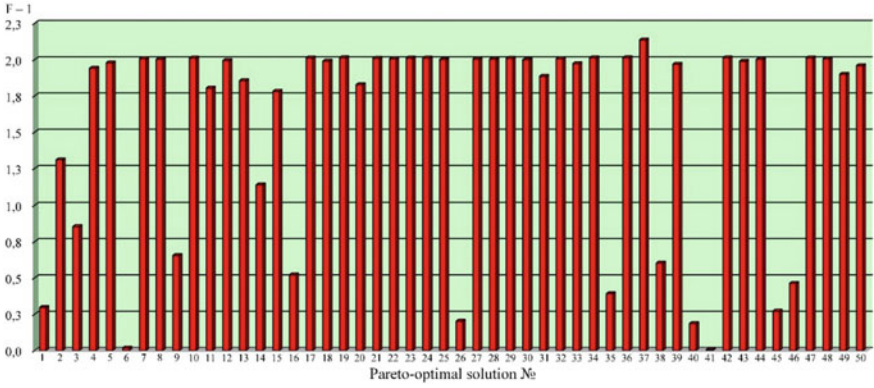


Fig. 4 Results for the fractional-rational generalized arithmetic mean function

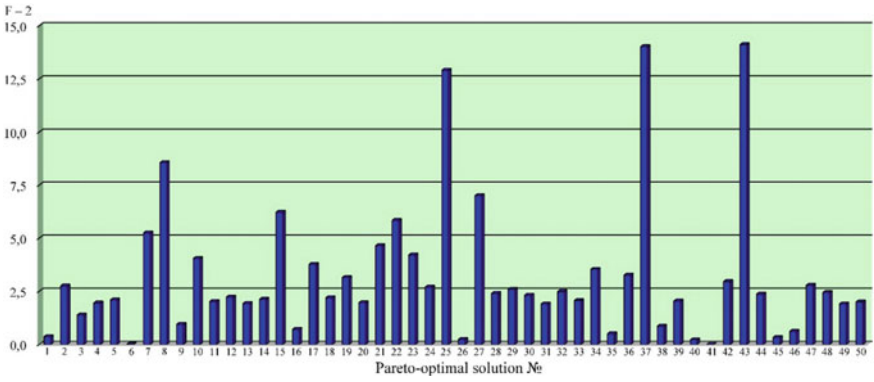


Fig. 5 Results for the fractional-rational generalized geometric mean function

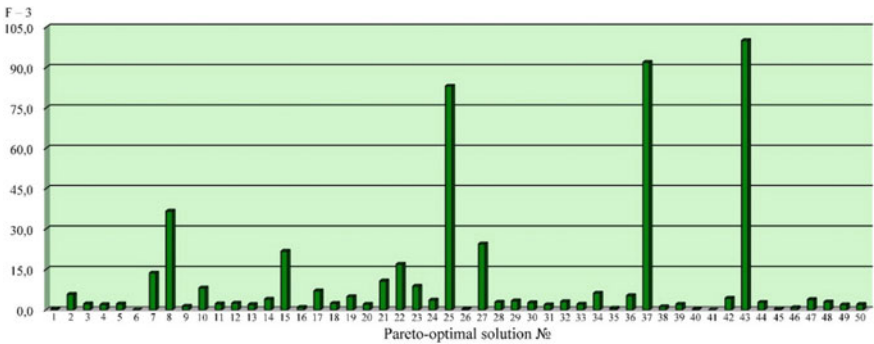


Fig. 6 Results for the fractional-rational generalized harmonic mean function

5 Conclusions

- (a) The use of subjective opinions and the objective evaluation of their concordance are proposed for ranking the priorities of the quality indicators in multi-criteria decision making problems.
- (b) Three kinds of strategies are proposed to create FRGF of usefulness from arithmetic, geometric and harmonic type are proposed and investigated using real practical problem as an example.
- (c) The efficiency of the strategies and their sensitivity has been studied for multi-criteria optimal decision making. Five Pareto-optimal solutions with the highest priority are proposed for further studies and optimal decision making about the process control variables.
- (d) The results of investigation of the strategies show that the arithmetic type of FRGF has the lowest sensitivity in respect to the obtained values of the generalized functions of usefulness.
- (e) The deviations of the values of generalized functions of usefulness between Rank 1 and Rank 5 for the proposed three strategies are: 0.122 for the strategy *F-1*; 14.6 for the strategy *F-2* and 75.56 for the strategy *F-3*.

References

1. Marinov M, Stoyanov S (1986) Experimental-statistical mathematical modeling of the “Fosuk” driving mass ceramic indexes. Works Iron Steel Res Inst 17(3):31–42
2. Kendall MG (1957) Rank correlation methods. Griffin, London
3. Vuchkov I (2007) Statistical methods for process control. Technics, Sofia
4. Stoyanov S (1993) Optimisation of technological processes. Technics, Sofia
5. Computer Program Package QStatLab. V 4.1. <http://www.qstatlab.co.uk>
6. Stoyanov S (2008) Customer satisfaction and decision making in healthcare organization, publ. EC Print, Sofia. ISBN 978 954 465 014-8
7. Borisov D (2021) Comparative analysis of generalized objective functions used in multicriteria optimization. J Inf Innov Technol (JIIT) 2(3):35–42. ISSN: 2682–9517 (print) ISSN: 2683–0930 (online)

Research on Construction of Prefabricated Precast Concrete Columns Combined with S-VRO Foam Core Slab



Thang Hoang Duc

Abstract Solutions of precast components and prefabricated construction are increasingly widely used for civil and industrial construction with the advantage of fast-track and material-saving implementation, good quality components which are less damaged by subjective factors and weather. A S-VRO foam core slab is a flat reinforced concrete slab with a hollow foam core in the middle which reduces the weight of the slab, but still maintains the same stiffness beneficial to fast-track and material-saving implementation, long-span structure, heat and sound insulation increase. The combination of the prefabricated S-VRO slab and prefabricated column components opens the new way for Vietnam's construction industry in the future, promisingly brings high quality construction works in extremely short time. This research paper will study advantages and disadvantages of the construction process using precast concrete columns combined with prefabricated S-VRO compared to conventional construction methods.

Keywords A S-VRO flat slab · Precast components/structure · Prefabricated construction · Precast concrete columns · Long-span flat slab

1 Introduction

Precast S-VRO foam core slab is a reinforced concrete flat slab type including mushroom and S-VRO panels. Mushroom panels are connected with precast concrete columns via joints and made in blocks. S-VRO panels are connected with mushroom panels via steel hook anchors (see Fig. 1).

The S-VRO panels have 3D spatial structure with inserted hollow cores occupying the concrete space in the neutral zone and the connecting hook between the panels. Precast S-VRO slabs are divided into two types, one-way slabs and two-way slabs (see Fig. 2).

T. H. Duc (✉)

Hanoi University of Civil Engineering, 55 Giai Phong, Hanoi, Vietnam
e-mail: vrojsc@gmail.com

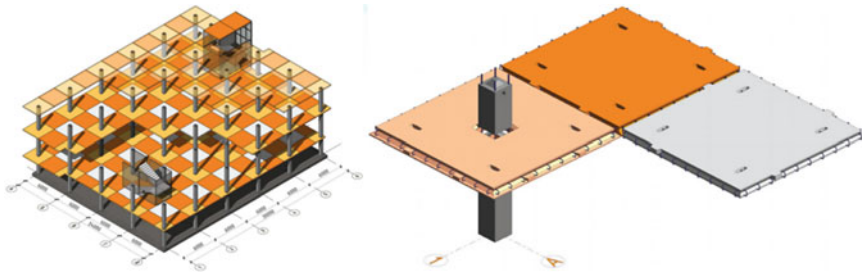


Fig. 1 Combination of S-VRO slab and precast concrete columns

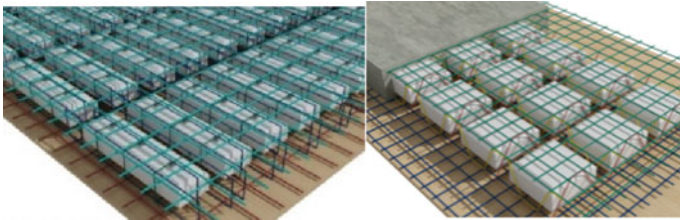


Fig. 2 Two types of precast S-VRO flat slabs

Precast concrete column (wall) is a column structure that is precast in the factory or at the construction site, consisting of a body and two connecting ends. Based on column head connection, precast concrete columns are composed of two kinds: fixed connection (see Fig. 3) and jointed connection [3]. In the paper, the author will focus on researching joint connected columns combined with prefabricated VRO flat slab.

The combination of precast prefabricated S-VRO foam core slab and precast concrete columns and walls will open a new way for civil and industrial construction implementation. It allows construction works to be executed much faster while taking advantage of the superior functions of the foam core slab, which meets many quality criteria for the project. Although this construction method has many advantages compared to the traditional construction solution, it still faces many obstacles such as not many people deeply understand the work of hollow core slab structures; plenty of design contractors, construction organizers and supervisors do not have enough expertise and experience in prefabricated construction of a flat slab and precast

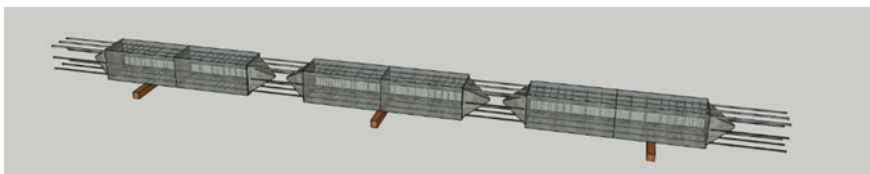


Fig. 3 Precast reinforced concrete columns

columns to ensure works' quality; a few documents instruct flat slabs' calculation and prefabricated construction in Vietnamese; hesitation of domestic users in applying new things. The introduction of precast prefabricated S-VRO slab erection solution combined with precast concrete columns helps engineers have more appropriate choice when applying design calculations and investors have more effective solution for the project. Then this superior solution gradually delves into domestic users' subconscious.

2 Calculation Method of a S-VRO Flat Slab and Erection Process of the Precast S-VRO Slab Combined with Precast Concrete Columns

2.1 Calculation Method of Precast S-VRO Flat Slab

S-VRO flat slab consists of S-VRO panels with a hollow structure in the middle zone which has relatively small stress when the slab is subjected to bending. Remaining concrete part can be calculated as consecutive I-beams linked together at flange plate. With slabs bearing simple load (slabs with regular column grid and uniformly distributed load), we can separate flat horizontal flexural I-beam components (see Fig. 4).

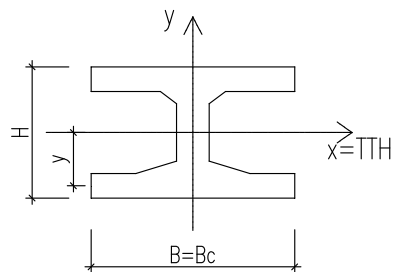
Then we can use material strength formulas to calculate stress (1) and deformation of a flat hollow core slab (2):

$$\sigma_z = \frac{M_x}{I_x} y \quad \tau_{zy} = \frac{Q_y S_x^c}{I_x b_c} \tag{1}$$

$$\varphi(z) = \int -\frac{M_x}{EI_x} dz + C \quad y(z) = \int \left(\int -\frac{M_x}{EI_x} dz + C \right) dz + D \tag{2}$$

However, in reality, works usually have a complex column grid structure, concentrated or unevenly distributed load. Nowadays, finite molecular models have become indispensable tools to save time and give accurate results. Among many S-VRO slab

Fig. 4 Cross-section of flat horizontal flexural I-beam



modeling methods introduced [4], in this paper, the author will use the equivalent flat slab method.

The equivalent flat slab method uses the conversion from hollow slabs to solid slabs which have the same stiffness and weight to use the popular Etabs software. This method is very close to the solid model by Ansys software [5].

In the simulation of a flat S-VRO slab (see Fig. 5): Mushroom panels are simulated by solid slab panels which are linked to precast concrete columns (simulated by beam molecules) via point connections. S-VRO panels simulated by solid slabs are linked to mushroom panels via joint connections (see Fig. 6).

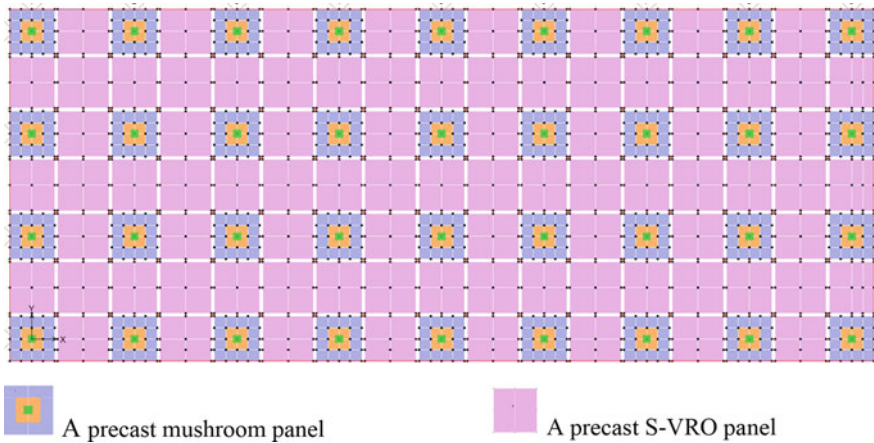


Fig. 5 Layout plan and panel connection in Etabs software



Fig. 6 Simulation of panels with joint connections

2.2 Construction Process of a Precast Prefabricated S-VRO Flat Slab in Combination with Precast Prefabricated Concrete Columns

Erection process of precast concrete columns

In order to make the best use of the construction (the truck crane’s responsiveness, joint minimization, waiting time), columns are usually divided into 3 sections corresponding to 3 levels (see Fig. 3). The process of erecting columns includes:

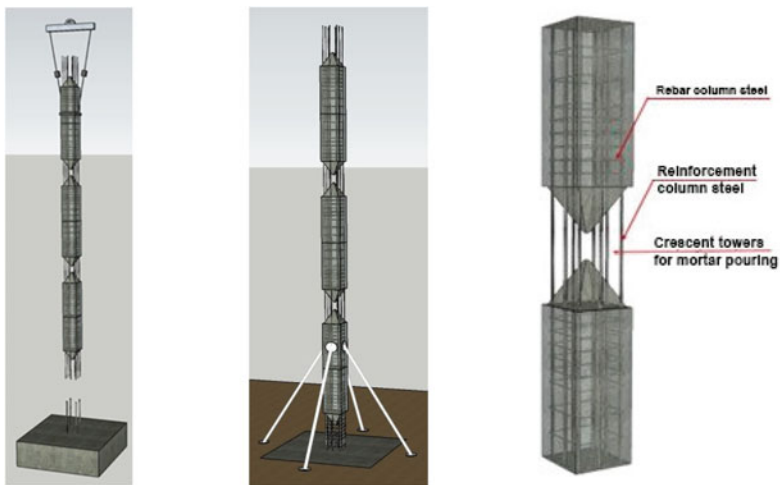
The crane moves the column sections into erection position, aligns steel joints waiting for connectors as described in Fig. 7a.

Fix the column with a frame, a turnbuckle and a strut as shown in Fig. 7b.

Weld starter steel and connecting steel, pile formwork and pour non-shrinkage mortar to fill up crescent towers at the waiting segments of the columns as Fig. 7c.

Erection process of a precast prefabricated S-VRO slab mounted on the erected columns

Prefabricated flat S-VRO slabs are divided into 2 types: mushroom panels and S-VRO panels with the advantage of light weight (due to removing foam of neutral axis), hence the quantity of S-VRO panels will be divided more than that of mushroom panels to make sure their weights are similar to ease the operation of cranes. The installation process of precast S-VRO slab is as follows:



a. Crane columns to the right position

b. Fix columns

c. Structure of column segment

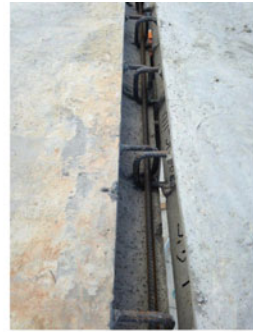
Fig. 7 The process of erecting precast concrete columns



a. Install column shackles



b. Install mushroom panels using cranes



c. Form column segments



d. Install S-VRO panels



e. Pour concrete into connecting lines

Fig. 8 Construction process of a precast S-VRO slab mounted on erected columns

Erect all scaffolds including shackles on columns and struts at the remaining corners as shown in Fig. 8a, b.

Sort the panels and crane them into position (install mushroom panels first) as shown in Fig. 8b.

Weld mushroom panel on starter steel at the column segment.

Continue to crane to place a S-VRO panel on a mushroom panel, align and install connecting steel among panels as shown in Fig. 8c, d.

Pour concrete into connecting lines among panels and into waiting towers where columns and mushroom panels are connected as shown in Fig. 8e.

Complete erection installation of the remaining two slabs (a column structure consists of 3 segments which are respectively installed for 3 slabs to reduce the waiting time compared with traditional column construction). After completion, continue to erect the 3-segment column and repeat the process.

3 Example and Discussion

3.1 Example for Applying Calculation

Input specification

Application to calculate a hotel project A with 6 floors, total floor area ~ 1400 m² (24m×59m) (Tables 1, 2 and 3).

Result and discussion

According to internal force results in Fig. 9, negative moments are mainly concentrated on mushroom panels with values ranging from -1 Tm to -16 Tm. The closer it is to the column, the more moment value is increasing. The S-VRO panel creates positive moment in the belly band, in each direction fluctuated around the value of 1.8 Tm (Fig. 9a, b); negative moment in the S-VRO panels connected with the mushroom panels in the opposite direction fluctuated around the value -1 Tm. These internal force values cannot be compared with those of a traditional slab because structure is basically different. Therefore, they will be evaluated via the amount of distributed material like concrete and steel when referring to them with the same evaluation criteria such as the same transposition and deflection.

Table 1 Dimensional specifications of column structure and floor [6]

Size (m)	S-VRO panel's size (mm)	Mushroom panel's size (mm)	Column segment height (m)	Column size (mm)
7 × 7	200	200 and 300	3.1	500 × 500

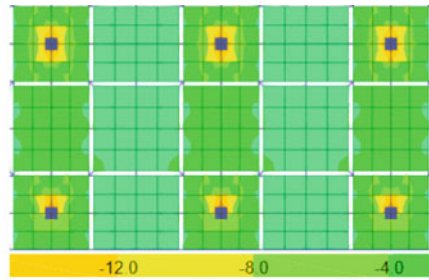
Table 2 Material specification [1]

Material	Tensile strength (Rs) (Mpa)	Compressive strength (Rb) (Mpa)	Shear strength (Rsw) (Mpa)	Elastic module E (Mpa)
Concrete B40	1.4	22		36,000
Steel CB300-V	260	260	210	210,000
Steel CB400-V	350	350	280	200,000

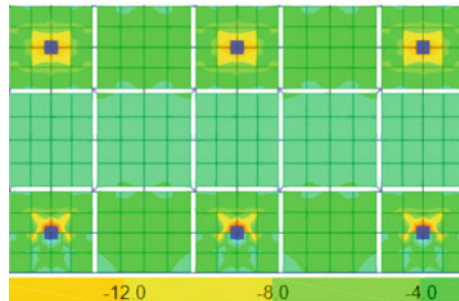
Table 3 Basic active load

Static load (kg/m ²)	120
Dynamic load (kg/m ²) [1]	150; 200
Load of bearing wall (kg/m ²)	400
Wind pressure (daN/m ²) [2]	95

Fig. 9 Internal force result of a precast S-VRO slab combined with a precast column model



a. Moment M11



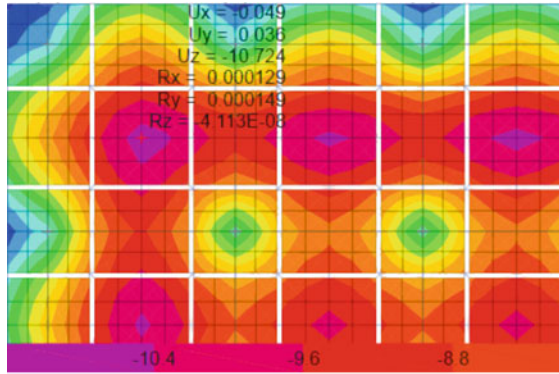
b. Moment M22

Figure 10 shows S-VRO slab with a long-term deflection of 10.7 mm met TCVN, considering the same deflection with a traditional slab (Fig. 10b), we get the basic specifications of the traditional slab (the main beam connecting columns: 30×70 cm, secondary beam: 22×50 cm, slab thickness at 13 cm). Details of economic efficiency and construction progress will be further analyzed in Sect. 3.2.

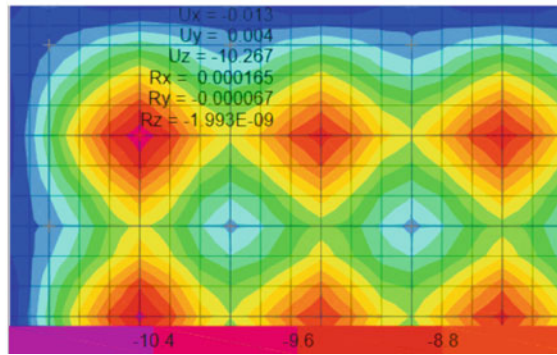
3.2 Performance Comparison of the Prefabricated S-VRO Slab with Precast Column and Traditional Options

Construction progress

The conventional construction is a continuous construction, so it takes time to wait for installing columns on each floor finished before proceeding with slab. With the option of precast columns and prefabricated S-VRO slab (S-VRO slab), it is possible to simultaneously do columns constructing and S-VRO slab erecting. The method helps shorten construction time, every 3 floors will save 8 days of column construction (9 days for traditional columns and 1 day of erection for precast columns), kindly see more in Fig. 11.



a. Long-term transposition of a S-VRO slab using Safe software



b. Long-term transposition of a traditional slab using Safe software

Fig. 10 Long-term transposition of 2 different slabs (a S-VRO and a traditional slab)

Under normal conditions, the conventional construction of a beam slab will take 7 days to complete one floor and 2 days to wait for columns finished while prefabricated S-VRO slab only takes 3 days and 1/3 day to wait for columns. From there, the difference time for 6 floor construction is 50 days, see more in Fig. 11c.

Economic efficiency

Considering a slab (1/6 slab), according to Fig. 12, we can see the amount of material used for a S-VRO slab is smaller than that of a traditional slab. In which, 11% less concrete quantity comes from the advantage of a S-VRO slab, specifically optimizing concrete material by removing unnecessary concrete in the neutral zone (for example: the main beam of conventional method has excess concrete in the neutral zone). Reinforcement steel is 22.8% less used due to slab’s lighter weight and optimal moment distribution (this is only optimal when the traditional slab is designed and constructed according to total material diagram). Formwork is up to 67% less for the

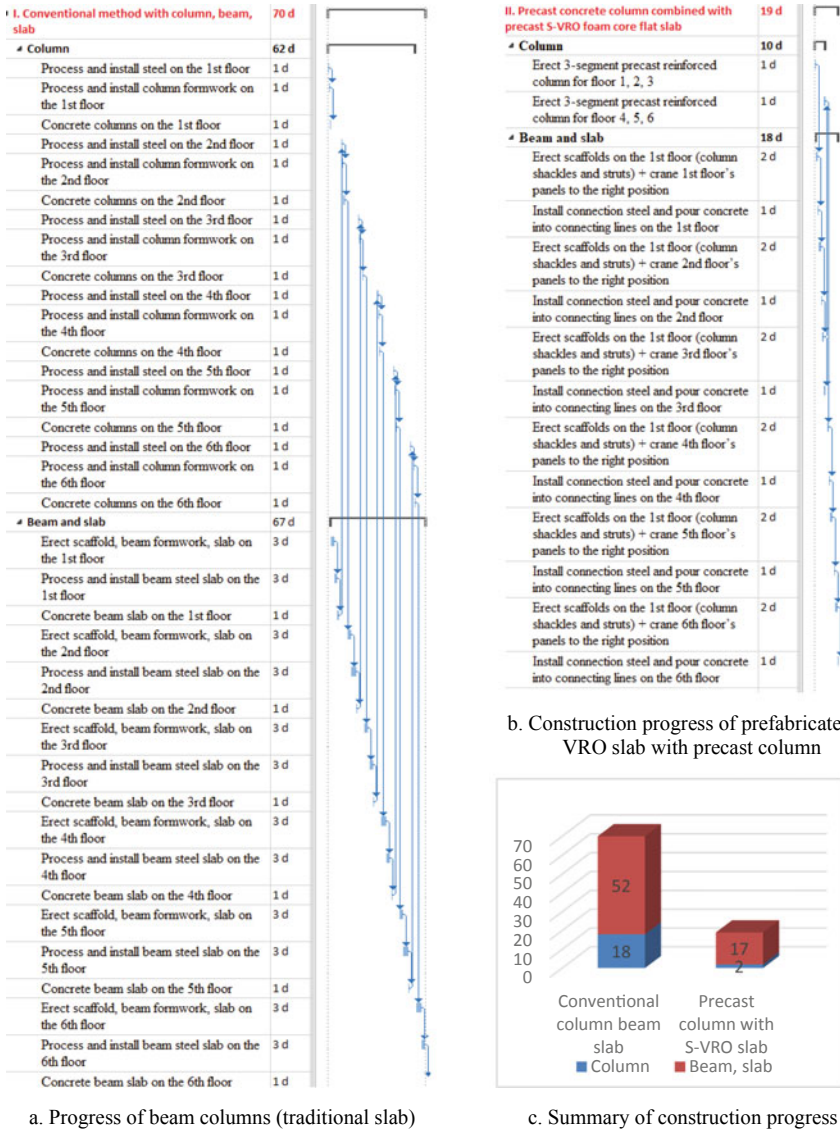


Fig. 11 Summary of construction progress of the two options

reason that S-VRO slab uses formwork only at the bottom, not in high beams and secondary beams.

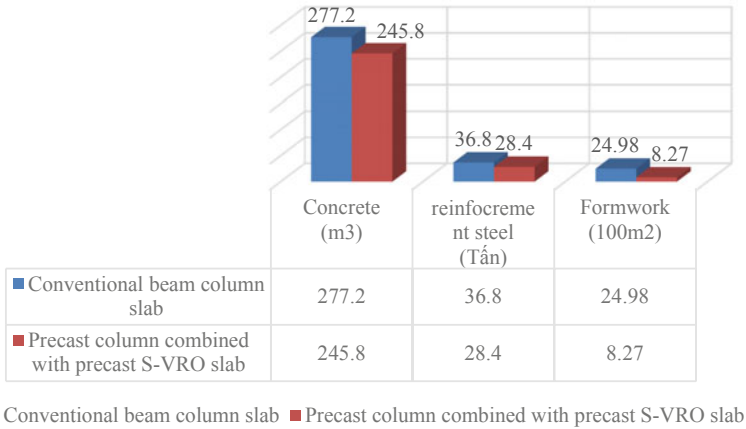


Fig. 12 Comparison of material quantity used for a S-VRO slab and a traditional slab

4 Conclusions

The solution of precast concrete columns combined with precast prefabricated S-VRO slabs introduced in this research paper has clearly shown the superiority of prefabricated construction structures, which helps to save building time (an average reduction of ~ 8 days/ floor) and material cost (a reduction of 10–25%). Shortening time and saving materials help reduce human force, hence increase works’ quality and the economic efficiency of the whole project.

However, within the scope of the study, the author has not mentioned:

In the construction theory, the author has not mentioned the contractor’s capacity, but has estimated the volume in accordance with the capacity of construction machinery on the market.

The detailed calculation theory for panel-to-panel, panel-to-column and column-to-column connections can pay the way for future research topics.

Acknowledgements The author sincerely thanks the financial support of Hanoi University of Civil Engineering for project "Research on construction of precast prefabricated concrete columns combined with S-VRO foam core slabs", code no. 62-2021/KHXD.

References

1. Institute of Construction Science and Technology (2018) Design of concrete and reinforced concrete structures, TCVN 5574–2018
2. Institute of Construction Science and Technology (1995) Loads and impacts, TCVN 2737–1995
3. Thang HD, Nam BN (2020) Research, manufacture, and construct foam core flat slab concreted on site with precast concrete columns. Department of Infrastructure and Construction of Marine & Coastal Works, Faculty of Marine & Petroleum Engineering, 93–2020/KHXD.

4. Thang HD, Nam BN (2021) Stress research in hollow core plat slab and applications. Springer, pp 895–902
5. Thang HD, Nam BN (2019) Study of stresses in hollow core flat slabs, provide calculation methods and applications. Department of Infrastructure and Construction of Marine & Coastal Works, Faculty of Marine & Petroleum Engineering, 109–2019/KHXD
6. S-VRO Catalogue (2022). <https://vro.vn/wp-content/uploads/2022/01/SVRO-catalogue-2022.pdf>

Influence of Cohesive Interface on the Flexural Behavior of Textile-Reinforced Concrete



Nguyen Thi Thu Nga, Dang Thi Thu Hien, and Tran Nam Hung

Abstract Textile-reinforced concrete (TRC), which is known as a combination of textiles or fibers embedded in fine-grained concrete and concrete, is a form of reinforced concrete. Recently, TRC is becoming more and more interesting because of many advantages, such as good mechanical properties, durability to external agents and performance at failure. In addition, the TRC applications in structures results in lightweight, high speed of execution, flexibility and durability. Besides, the combination of TRC and high-performance concrete (HPC) can improve significantly the flexural behavior of this composite structure. The cohesive interface between fine-grained concrete and concrete is one of the key factors affecting the flexural behavior of the material. In this study, numerical simulations of three-point bending tests were carried out at different rigidities of the interface to examine the flexural performance. The results show that the flexural behavior of TRC depends strongly on the strength of textile layer. In addition, the contact between two layers of materials should be increased to avoid premature failure such as fiber slip or premature detachment. Furthermore, good bonding enhances the flexural strength, thus enhances the properties of the reinforcing material.

Keywords Textile-reinforced concrete · High-performance concrete · Flexural behavior · Interface · Three-point bending test

1 Introduction

Nowadays, building civil and military structures need to improve their sustainability especially in the marine environment. One of the key strategies is using sustainable materials with best properties.

N. T. T. Nga (✉) · T. N. Hung
Le Quy Don Technical University/LQDTU, Hanoi, Vietnam
e-mail: nguyennga@lqdtu.edu.vn

D. T. T. Hien
University of Transport and Communications/UTC, Hanoi, Vietnam

© The Author(s), under exclusive license to Springer Nature Singapore Pte Ltd. 2024
T. Nguyen-Xuan et al. (eds.), *Proceedings of the 4th International Conference on Sustainability in Civil Engineering*, Lecture Notes in Civil Engineering 344,
https://doi.org/10.1007/978-981-99-2345-8_61

605

Textile-reinforced concrete (TRC), a composite material, consists of two different materials, non-metallic reinforcement and cementitious matrix (fine-grained concrete or mortar). The non-metallic reinforcement is the grid-like one with impregnated yarns which have thousands of filaments. The fibers can be made of carbon, glass, aramid, basalt, polymeric materials as well as inorganic materials in which carbon and alkali resistant glass are the most common [1].

High-performance concrete (HPC) is one type of concrete that has higher properties in terms of workability, strength, modulus of physical property, density, dimensional stability and resistance to chemical attack than conventional concrete. As an example of compressive strength, this concrete has a high compressive strength of 55 MPa or greater. In terms of high performance, HPC has ease of placement, long-term mechanical properties, high initial strength, high toughness and more durability in severe environments. Because of these better features, HPC is more and more commonly used in the industrial or high-corrosion constructions. The efficiency of such material in strength, toughness and durability characteristics has been evaluated by experimental analysis [1, 2]. Regarding the combination of HPC with other materials in bending structures, a number of works have been completed, for example HPC and fiber reinforced concrete [3, 4]. The adding of TRC to high-performance concrete can improve the flexural behavior of the composite structure. However, so far there is not much experimental or numerical data for this combination. Besides, the main advantages of the used material in some cases would be wasted due to the interface between HPC and other materials [3].

Experimental studies showed that debonding can occur at the interface due to differences between the materials. To simulate the interface, there are two micromechanical models. The first one is discrete model following the irregular Signorini, regular Newton–Euler or Coulomb’s law. It shows interconnected classes but it requires lot of parameters in numerical simulations. The second one is a continuous model which supposes a new zero thickness layer characterized by normal and tangential stiffnesses C_N , C_T [5]. In addition, the fine-grained concrete in TRC has an adhesion performance that may be sufficient enough to safely transfer the tensile loads from the TRC to another layer of material, i.e., HPC [6]. Studies on HPC-TRC composite are still limited in literature. This material has not been used yet in engineering applications, and require further understanding.

For all the aforementioned reasons, the main objective of this paper is to study the influence of cohesive interface on the flexural behavior of textile-reinforced concrete which is known as a combination of textiles or fibers embedded in fine-grained concrete and HPC. For the purpose, a dynamic mechanical analysis of 3-point bending mode is used with a series of rigidity of the interface. In this study, for the sake of simplicity, the continuous model of interface with zero-thickness interface elements is used for the simulations. Based on the flexural stress–strain response of the material, the effect of cohesive interface on the flexural behavior will be evaluated.

Table 1 Mix proportions of the HPC-TS C60 and TRC fine-grained concrete substrate

Material	Symbol/unit	HPC-TS C60 (10%)
Cement VICEM PCB40	C(kg/m ³)	414
Silica fume	SF(kg/m ³)	46
Basalt 5/10 mm	Đ(kg/m ³)	1085
Fracturing sand 0.05/2 mm	CV(kg/m ³)	261
Crushed sand 0.05/5 mm	CN(kg/m ³)	485
Superplasticizer (GPS-5000)	SP(l/m ³)	7
Water	W(l/m ³)	155
Water/binder ratio	W/(C + SF)	0.34

2 Materials and Methods

2.1 Materials

The composite concrete consists of two materials, HPC and TRC. The HPC mixture compositions are given in Table 1. The material data for HPC is as follows: The elastic modulus $E = 32.7$ GPa; the compressive stress $f_n = 70$ MPa and the tensile limit stress $f_t = 3$ MPa. For the TRC, fine-grained concrete substrate also has a compressive strength of 70 Mpa, an elastic modulus $E = 32.7$ MPa and a Poisson ratio $\nu = 0.20$. Carbon fiber is assumed to have an average tensile strength of from 140 to 6000 MPa and the elastic modulus in tension is from 3 to 600 GPa. In this study, TRC is considered a homogeneous linear elastic material by using one of homogenization techniques, for example, a multi-stage homogenization method to determine the effective properties of layered materials presented in [7]. The effective properties of TRC are characterized by elastic modulus and Poisson ratio, with $E = 58$ GPa ÷ 580 GPa, $\nu = 0.2$. Obviously, the elastic modulus of TRC is about from 2 to 20 times as high as that of HPC.

2.2 Three-Points Bending Test

The HPC–TRC beam with dimensions of 60 mm × 20 mm × 10 mm has prefabricated crack with length of 1 mm. The spacing between two support cylinders $L = 40$ mm [8]. The TRC layer of 2 mm thickness was applied on the middle surface of HPC as shown in Fig. 1b.

An imposed strain at the center point of the span is supported and the fixed rate is equal to 0.05 mm/min according to the ASTM D2344 standard. Several other rates

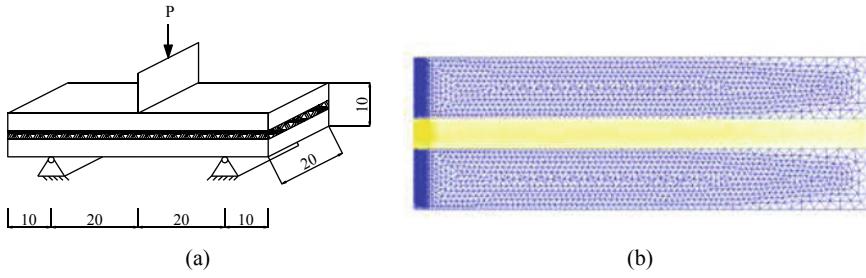


Fig. 1 Three-point bending test on the specimen (a) and finite element model of a haft of the beam in Cast3M code (b)

are also investigated (0.5, 0.005 and 0.0005 mm/min) to examine the effect of TRC on overall performance of the structure. Computations are driven in plane-stress with the finite element code Cast3M-2000. Figure 1b shows the finite element mesh used for the analysis where the specimen is simulated in 2D by three-node solid element.

The bending strength of non-reinforced beam can be calculated according to the classical beam theory:

$$\sigma = \frac{P_{\max} L}{4W} \tag{1}$$

where $W = bh^2/6$ is bending section modulus of the specimen; b , h are width and thickness of the specimen; L is the span of the beam length or the distance between end-supports ($L = 40$ mm).

2.3 Interface Element Constitutive Law

The continuous model of interface with zero-thickness interface elements is used in this study. The contact element will have stiffnesses $C_N = \lim_{e \rightarrow 0} \frac{\bar{C}_{3333}}{e}$, $C_T = \lim_{e \rightarrow 0} \frac{\bar{C}_{1313}}{e}$ (normal and tangential stiffnesses) depending on the material with a lower elastic modulus, where \bar{C}_{3333} , \bar{C}_{1313} are the components of the effective stiffness tensor \bar{C} of the lower material (i.e., HPC), see [5] for more details.

2.4 Fracture Energy

In this study, fracture in the middle of the beam of length l embedded into an elastic medium is considered. The fracture energy G_c is supposed to be 61 N/m, [9]. Driving force of propagation F reads:

$$F = \frac{1}{E} \frac{9\pi l P^2 L^2}{4h^4 T^2} g(l/h)^2 \quad (2)$$

where $g(X) = \frac{1.99 - X(1-X)(2.15 - 3.93X + 2.7X^2)}{\sqrt{\pi(1+2X)(1-X)^{3/2}}}$ is a function of the ratio of crack length l to beam height h when $h/L = 1/4$, P is the applied load, T is the beam thickness, L is the beam span. If the driving force F reaches a threshold G_c , the fracture propagates:

$$F < G_C \Rightarrow \text{non propagation}; \quad F = G_C \Rightarrow \text{propagation} \quad (3)$$

Twelve types of specimens with different interface laws, different rate of loadings and different strength of textile layers were produced that are given in Table 2. Different rigidities of the interface will also be examined including perfect bonding between two layers of materials, i.e., no slip and no detachment at the contact between layers. Three cases of non-reinforced beam were studied (CAS01, CAS02, CAS03). The effective properties of TRC were supposed to be 58–580 GPa. All the textile layer (TRC) are set in the middle of the specimen.

3 Results and Discussion

As can be seen in the Fig. 2, the crack at the middle of the beam propagated until the specimen completely failed (CAS01 and CAS02). Maximum force value P_{\max} in all cases of imposed strain is 206 (N). Using Eq. (1), the bending strength of non-reinforced beams is 6.18 MPa. The crack propagation began early, at the rate of 0.005 mm/min.

Figure 3 shows that the strength of textile layers strongly influences the behavior of the specimen. The bending failure has no intermediate fracture when the beam has TRC reinforcement (CAS21, CAS11). At rate of 0.05 mm/min, only CAS01 has definitely failure while CAS11 and CAS21 are still in state of partial-propagation, i.e., crack propagation occurs only in the bottom HPC part of the beam. Besides, increasing the strength of TRC increased the load-bearing capacity of the specimen as well as the corresponding displacement.

In Fig. 4, when TRC has $E = 58.0$ GPa and $\nu = 0.2$ (about two times as high as that of HPC) then $P_{\max} = 941$ (N) and therefore, the bending strength of the specimens increases at a value of 28.2 MPa, or 4.5 times as high as non-reinforced beam. The failure mode of the specimens observed in bending failure should be investigated. For the specimen without interface law at the two different layers (perfect contact—CAS11, CAS13, CAS21, CAS23), no interlayer failure can be observed. Sometimes, interfacial debonding between TRC and HPC matrix is observed as a small detachment. Therefore, three cases of specimen accounting for interface law are considered (CAS11a, CAS13a, CAS21a, see Table 1).

Figure 5 shows the load–displacement curves divided into two periods. In the first half of the first period, the load increases quasi linearly with displacement. In

Table 2 Properties of specimens

Specimen number	Strength of textile layer		Interface law	C_N [GPa]	C_T [GPa]	Rate of loading [mm/min]	Strength of HPC		State propagation
	E_2 [GPa]	ν					E [GPa]	ν	
CAS01	-	-	-	-	-	0.05	32.7	0.2	Pro
CAS02	-	-	-	-	-	0.005	32.7	0.2	Pro
CAS03	-	-	-	-	-	0.0005	32.7	0.2	N,Pro
CAS11	58.0	0.2	Perfect	-	-	0.05	32.7	0.2	N,Pro
CAS13	58.0	0.2	Perfect	-	-	0.5	32.7	0.2	Pro
CAS21	580.0	0.2	Perfect	-	-	0.05	32.7	0.2	N,Pro
CAS23	580.0	0.2	Perfect	-	-	0.5	32.7	0.2	N,Pro
CAS11a	58.0	0.2	Imperfect	64.44	24.16	0.05	32.7	0.2	N,Pro
CAS13a	58.0	0.2	Imperfect	64.44	24.16	0.5	32.7	0.2	N,Pro
CAS13b	58.0	0.2	Imperfect	35.55	13.33	0.5	32.7	0.2	N,Pro
CAS21a	580.0	0.2	Imperfect	3555	1333	0.05	32.7	0.2	N,Pro
CAS21b	580.0	0.2	Imperfect	35.55	13.33	0.05	32.7	0.2	N,Pro

Fig. 2 Case of non-reinforced beam: load–displacement of the beam under different rate of imposed strains

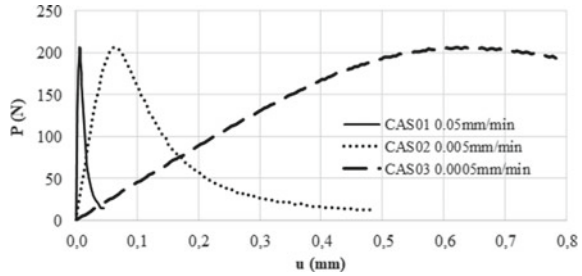


Fig. 3 Perfect interface, E_2 changes: load–displacement of CAS11 ($E_2 = 58$ GPa) and CAS21 ($E_2 = 580$ GPa) at the rate of 0.05 mm/min in comparing with CAS01

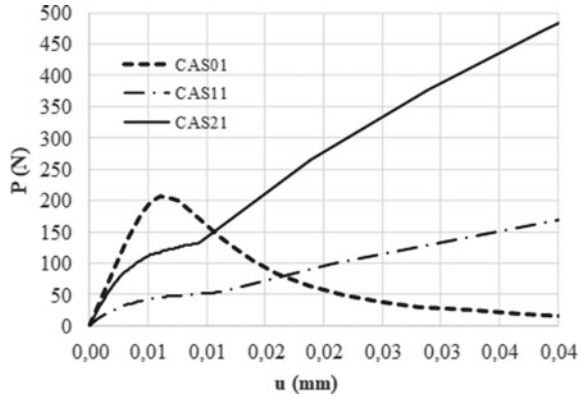
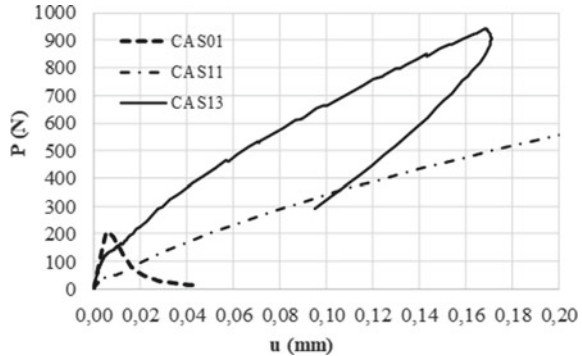
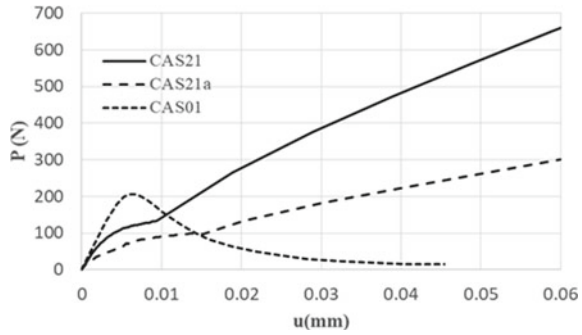


Fig. 4 Load–displacement at different rate of imposed strain: CAS11 (0.05 mm/min) and CAS13 (0.5 mm/min). The strength of textile layer is constant ($E_2 = 58$ GPa)



the second half, the load increases more slowly while the displacement increases rapidly. The second phase of the curve goes up quasi linearly to the maximum load with smaller slope than that of the first stage. In general, the specimen completely would be failed at a large displacement. Specimens with TRC predict a failure at large displacements. The results are also observed in the literature, see [9] for example.

Fig. 5 Load–displacement of CAS21 (non-interface) and CAS21a (with interface) at rate of 0.05 mm/min in comparing with CAS01 (non-reinforcement)



In Fig. 6, the normal and tangential stiffnesses C_N and C_T of the interface increase from one time (CAS11b, CAS21b) to 2 times (CAS11a) and 100 times (CAS21a) and reaches the maximum value (perfect contact–CAS11 and CAS21).

The strength decreases or increases strongly depending on the interface law and the strength of TRC. If the strength of TRC is low (see Fig. 6a), the load–displacement curves of CAS11b and CAS11a coincide and much lower than that of CAS01 (non-reinforced beam). This result indicates that when the strength of TRC is low and the adhesion between two layers of materials is not perfect, the reinforcement effect is absent, it even reduces the bending strength of the beam. Therefore, the flexural behavior of textile-reinforced concrete plate depends strongly on the strength of textile layer.

As can be seen in Fig. 6b, when the strength of TRC is high, the reinforcement effect only can be seen if the adhesion is strong (CAS21a) or perfect (CAS21). Thus, the contact between two layers of materials should be increased to avoid premature failure that may cause by fiber slip or premature detachment.

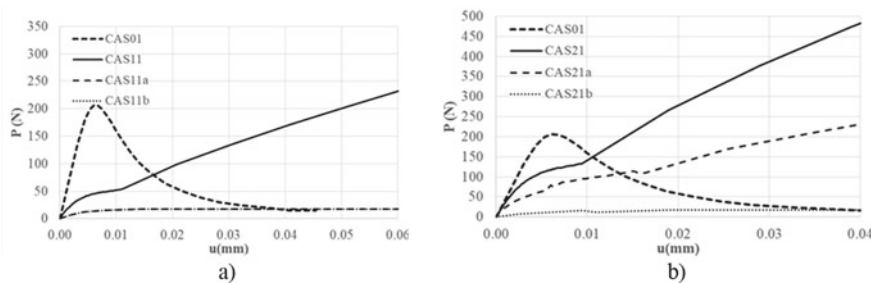


Fig. 6 Load–displacement curves with different stiffnesses of the interface. Strength of TRC is low (a) and high (b)

4 Conclusions

This study investigated the influences of the cohesive interface on the flexural behavior of textile-reinforced concrete where two cases of the strength of TRC were considered. The results showed that the flexural behavior of TRC depends strongly on the strength of textile layer. Even if the effective properties of TRC is not great (almost 2 times HPC), crack development has been prevented that occurs only in the bottom HPC part of the beam. When the strength of TRC increases, the load-bearing capacity is improved significantly and predict a failure at larger displacements.

A good bonding enhanced the flexural strength, thus enhanced the properties of the reinforced beam. Low cohesive interface should be avoid for both cases to get reinforcement effect. Furthermore, perfect bonding gave the best results even if the reinforcement was not very strong. Therefore, it is recommended to make perfect bonding when the reinforcement is set in the middle of the section of specimen.

References

1. Venigalla SG, Nabilah AB, Mohd Nasir NA, Safiee NA, Abd Aziz FNA (2022) Textile-reinforced concrete as a structural member: a review. *Buildings* 12(4):474
2. Vejmilkova E, Pavlikova M, Keppert M, Keršner Z, Rovnaníková P, Ondráček M, Černý R (2010) High performance concrete with Czech metakaolin: experimental analysis of strength, toughness and durability characteristics. *Const Build Mater* 24(8):1404–1411
3. Travush VI, Konin DV, Krylov AS (2018) Strength of reinforced concrete beams of high-performance concrete and fiber reinforced concrete. *Mag Civil Eng* 1(77):90–100
4. Rigaud S, Chanvillard G, Chen J (2012) Characterization of bending and tensile behavior of ultra-high performance concrete containing glass fibers. In *high performance fiber reinforced cement composites*, vol 6. Springer, Dordrecht, pp 373–380
5. Nguyen TTN, Tran NH (2020) Modeling of contact interface between two material layers in hybrid structures. *Tạp chí Khoa học Giao thông vận tải* 71(4):419–430
6. Thanh MBT, Huy CN, Dang QN, Huu TD (2020) Experimental study on flexural and shear behaviour of sandwich panels using glass textile reinforced concrete and autoclaved aerated concrete. *Tạp chí Khoa học Giao thông vận tải* 71(1):18–26
7. Nguyen TTN, Tran NH (2021) A multi-stage homogenization method for determining the effective elastic properties of layered materials. *J Sci Techn Sect Special Constr Eng* 4(02):140
8. Li WQ, Zhu JH, Chen PY, Xing F, Li D, Su M (2019) Evaluation of carbon fiber reinforced cementitious matrix as a recyclable strengthening material. *J Clean Prod* 217:234–243
9. Nguyen ST, Jeannin L, Dormieux L, Renard F (2013) Fracturing of viscoelastic geomaterials and application to sedimentary layered rocks. *Mech Res Commun* 49:50–56

Nondestructive Mechanical Characterization by Small Punch Test and Statistical Fractography for the Determination of the Residual Lifetime of Old Steel Bridges



Bholah Bhimal, Delgado Julien, Depale Bruno, Auvray Nicolas, and Ponson Laurent

Abstract The purpose of this work is to present an innovative method of structural integrity assessment dedicated to steel bridges. According to the European Commission, at least 30% of steel bridges are more than 100 years, and most of them were not designed to support today's increased traffic intensity. However, this cyclic solicitation gives rise to fatigue induced damage of vital bridge elements that ultimately may lead to their failure. The structural integrity assessment of these elements by fracture mechanics requires the mechanical properties of the material aged by environmental and mechanical conditions. However, destructive sampling for conventional testing is seldom not viable. A patented technology based on the statistical fractographic analysis of the surface of a millimetric fractured punch test specimen opens new perspectives to address this issue. It provides the fracture properties (toughness, cohesive strength...) of a material in a "quasi-nondestructive" manner, and it can be combined with the determination of the elastoplastic properties through the analysis of the force versus displacement response of the punch test specimen. Such a procedure provides a full characterization of the residual mechanical properties of an aged material that can then be used as input data for predictive fracture mechanics-based models of residual lifetime. We believe that such original approach may help local authorities involved in assessment of fatigue-prone bridges to take appropriate decisions.

Keywords Small punch test · Statistical fractography · Fracture mechanics · Structural integrity · Bridge elements

B. Bhimal · D. Julien · D. Bruno (✉)
Centre Technique Des Industries Mécaniques, Senlis, France
e-mail: depale.bruno@cetim.fr

A. Nicolas · P. Laurent (✉)
Tortoise, 231 Rue Saint-Honoré, 75001 Paris, France
e-mail: laurent.ponson@tortoise.io

1 Introduction

One of the main degradation mechanisms of steel bridge components leading to failure is fatigue, corrosion, and deformation due to shocks [1]. Sheer reported that at least 26% of failure cases he studied were caused by such shock-related incidents [2]. Risk assessment of old bridges aftershocks-related events is hence important but is confronted to the difficulty of getting accurate materials parameters for technical assessment. A significant number of bridges constructed in the early nineteenth century were made of cast iron and latter with wrought iron with little traceable standards. According to a study conducted by Aesson, most civil structures failures are due to false assumptions, material defects, poor supervision, and disregard of fatigue and instabilities [3].

Fatigue failure is a critical and harmful phenomenon for most structures submitted to cyclic loading over the course of their designed lifetime and may be aggravated by mechanical shocks on critical components. The two main stages of fatigue life can be separated in a portion spent to localize damage until a crack initiates followed by a portion of the lifetime spent in propagating the said crack till an unstable structural failure occurs [4]. The magnitude of the maximum stress that applies to the bridge component over their lifetime is usually below the yield strength, σ_y , of the material. However, it does not protect them from fatigue failure, as the fatigue limit of steels can be as small as a half of the yield strength. On top of it, generalized corrosion due to weathering and air pollution may speed up fatigue failure by reducing the thickness of loaded components and consequently increasing the stress through their sections. Localized corrosion near weldments may also build up high stress levels in site with large concentration factors, leading ultimately to early crack initiation.

In some cases, the failure of bridge components may be tolerated when the load can be redistributed to other components after its failure. However, regulatory authorities then require a complete assessment of the risk of failure of such degraded bridges. This is also the case when bridges are damaged by mechanical shocks. To evaluate the risk of failure of such structures, the accurate knowledge of the material mechanical properties of the critical structural parts of the bridge is then necessary.

Metallic alloys composing structures such as bridges components are characterized by two sets of mechanical properties that are both relevant to evaluate the failure risk (see Fig. 1). First, metallic alloys are characterized by their elastoplastic properties that describe how the material deforms under the action of mechanical loads. The Young's modulus describes the ability of the material to deform within its linear elastic regime, while the yield strength provides the elastic limit of the material. A third quantity of particular interest for evaluating the risk of failure is the hardening exponent, n , that describes the material deformation beyond its elastic limit. In the Hollomon description, it corresponds to the exponent of the power law relating the strain to the stress (see Fig. 1a). A large value of n (corresponding to a high material ductility) requires a larger stress level before a crack can initiate.

A second set of mechanical properties describes the ability of metallic alloys to resist to crack propagation. Under monotonic loading conditions, a high resistance

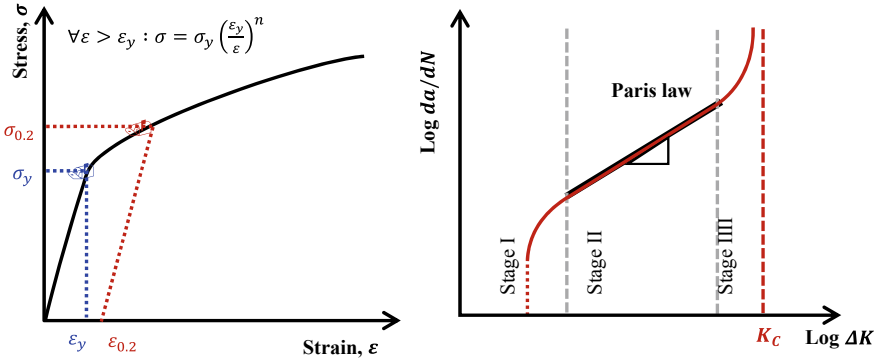


Fig. 1 (Left) Elastoplastic response of structural steel in traction as described by Hollomon model, (right) the so-called Paris' law [5] that provides the crack speed as a function of the applied stress intensity factor in the fatigue regime

to crack growth corresponds to a high fracture toughness, K_c , (see Fig. 1b). Within the theoretical framework of fracture mechanics, a cracked structure under a given mechanical load is characterized by a stress intensity factor K that corresponds to the crack driving force—note that K generally increases with the crack length. If K is below the material toughness K_c , the structure is safe while failure takes place when K reaches K_c . In practice, such a failure criterion provides a critical crack length a_c beyond which catastrophic failure takes place. Under cyclic loading conditions, the approach is different: We introduce the so-called Paris' law that provides the crack speed as a function of the cycle load amplitude ΔK (see Fig. 1b). Using fracture mechanics, we can then predict the lifetime of a bridge component that can be expressed in terms of number of cycles before the critical crack length (and so catastrophic failure) is reached.

In the following, we describe a methodology that provides both the elastoplastic properties and the fracture properties of metallic alloys from a small millimetric sample. These material properties are then used as inputs of a fracture mechanics model that predicts the lifetime of a structure component.

2 Determination of the Elastoplastic Properties by Small Punch Test

The small punch test, originally developed in the 80's [6] for the determination of post-radiation mechanical behavior, has now gain interest for a wider range of applications including power generation systems [7], piping engineering [8], and more recently in powder metallurgy [9] or for assessing hydrogen embrittlement of metals [10].

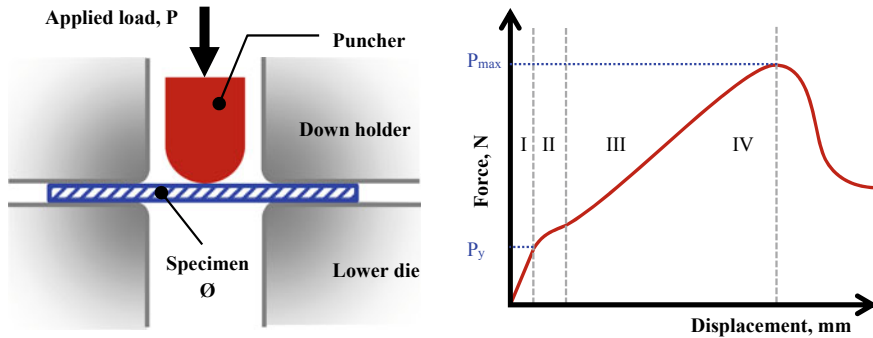


Fig. 2 Measurement of elastoplastic properties by small punch: (left) schematic of the mechanical test. (Right) Typical load–displacement response of the small punch test specimen

The small punch test consists in forcing a puncher into a small cylindrical specimen, as shown in Fig. 2. The specimen gradually deforms until failure takes place by ductile shear. The load–displacement response of the specimen displays several regimes that can be used to determine the elastoplastic properties of the material (see Fig. 1).

The regime I, governed by the elastic response of the specimen, provides the material young’s modulus. The transition between regime I and II results from the yielding of the specimen. As a result, the yield strength can be inferred from the transition force between these both regimes. Finally, the regime III is reminiscent of the hardening of the material so that the slope of the force–displacement curves in this regime informs about the hardening exponent. The last regime IV that displays softening results from the shear failure of the specimen.

In practice, small punch test requires a mm thick cylindrical specimen of 8 mm diameter. As a result, it can be cut out from a small sample (typically 20 mm diameter and 2 mm thick) extracted by scoop sampling directly from the bridge component. The elastoplastic properties are measured locally, so that several sampling on different locations of a same component and/or on different components might be required to assess the representativity of the measurement.

Interestingly, the small punch test is a European standard (BS EN 10371:2021). However, it is limited to the measurement of the elastoplastic properties of a material. To determine its fracture properties like its toughness K_c , we propose here to analyze the fracture surface of the failed punch test specimen using statistical fractography.

3 Determination of the Residual Fracture Properties by Statistical Fractography

Statistical fractography is a recently developed engineering technique which extracts the failure properties of a material from the scan and the analysis of the topography of its fracture surface [11–13]. This approach is nowadays applied to metallic alloys but also to brittle solids like rocks and ceramics. In this section, the steps involved in the determination of fracture properties are presented using the example of an aged metallic part from which a microsample has been extracted.

The technique is implemented in several steps. First, the roughness of the fracture surface of the punch test is scanned with a profilometer that provides its topographic map with a micrometric resolution (see the upper left panel of Fig. 3). This topographic map is then transformed into another map of the same size that provides the local slope of the fracture surface (see the upper right panel of Fig. 3). This so-called damage map displays some features that correspond to steep cliffs reminiscent of the ductile cavities involved at the microscale during crack growth, the size of which is called ξ .

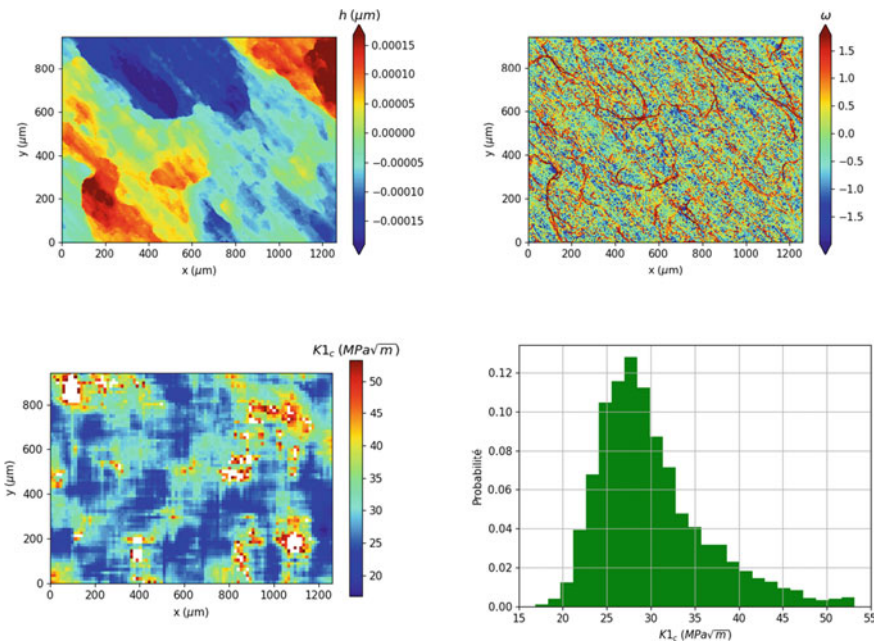


Fig. 3 Determination of the fracture properties of a metallic alloy by statistical fractography. (Upper left) Height map of the fractured surface. (Upper right) Damage field derived from height map. (Lower left) Fracture toughness map inferred from damaged field. (Lower right) Statistical distribution of local fracture toughness values. The overall toughness measured by statistical fractography $K_{c\text{ fracto}} = 29.6 \text{ MPa m}^{1/2}$ compares well with the one $K_{c\text{ test}} = 30.1 \text{ MPa m}^{1/2}$ obtained by standard (destructive) mechanical test

Finally, the field of local toughness K_c (see the lower left panel of Fig. 3) is computed from the local value of ξ and the elastoplastic properties of the material using a micromechanics model. These elastoplastic properties have been determined by the punch test methodology, see Sect. 2.

This procedure can be applied on a height map of typically $200 \times 200 \mu\text{m}^2$. As a result, the analysis of a $1 \times 1 \text{ mm}^2$ height map does not provide a single toughness value, but instead a distribution of toughness as well as a toughness map describing the variations of toughness within the mean fracture plane, as shown in the bottom panels of Fig. 3. The overall material toughness is then defined as the average of the local values of toughness. In this example, the fracture toughness obtained by statistical fractography is $K_c^{\text{fracto}} = 29.6 \text{ MPa m}^{1/2}$, a value that is compatible with $K_c^{\text{test}} = 30.1 \text{ MPa m}^{1/2}$ obtained by standard mechanical test on the same material.

As a result, statistical fractography provides a simple and reliable mean to determine the fracture properties of a metallic alloy without having to cut large ($\sim 10 \text{ cm}$) notched specimens, paving the way for a nondestructive method of material characterization and ultimately of predictive maintenance, as discussed below.

4 Prediction of the Residual Lifetime from Fracture Mechanics

Now, the residual mechanical properties of the material are known, and fracture mechanics can be used to predict the harmfulness of cracks present in structure components. The critical crack length a_c at failure is predicted from the material toughness (determined by statistical fractography, see Sect. 3) and the structural parameters. The failure of the bridge component is then inferred from the comparison of the (theoretically predicted) crack length with a_c , as discussed below.

The approach adopted to predict the residual lifetime of a structure component is the following. Strictly speaking, the methodology described before does not provide the Paris' law of the material, as the one presented in Fig. 1b. However, Paris' law is bounded by the toughness value (see Fig. 1b). As a result, knowing K_c allows for a reasonably accurate determination of the Paris' law that can be crossed checked with literature data. Fracture mechanics provide then the cycle amplitude ΔK from the structural parameters and the traffic parameters (i.e., the characteristic weight of the vehicles crossing the bridge), from which the crack speed da/dN as a function of the crack length a is inferred using Paris' law (see Fig. 1b). Integrating the equation $da/dN(a)$, one obtains the theoretically predicted crack length $a(N)$ as a function of the number of cycles N . The comparison of $a(N)$ with the critical crack length a_c at failure provides the residual lifetime N_c where $a(N_c) = a_c$. Note that the residual lifetime expressed here in terms of number N of vehicles can also be expressed in terms of month, if the traffic density over the bridge is known.

5 Conclusions

In this work, a novel method based on small punch test and statistical fractography was presented. It evaluates the structural integrity of aged and cracked steel structures, such as bridges. Failure risk assessment requires two sets of material parameters: the elastoplastic properties and the residual fracture properties. The small punch test, which is a European standard, is used to obtain the elastoplastic parameters from representative millimetric samples from onsite structural components. Statistical fractography which is based on the statistical analysis of the roughness of the resulting fractured surface can be used to obtain the fracture properties. Hence, the residual mechanical properties of a metallic component of an aged structure can be assessed through a quasi-nondestructive approach. Once the fracture properties are known, the residual lifetime of critical components can be estimated for a known load spectrum using fracture mechanics. The application of this novel technique can increase the safety of old infrastructures and help setting up adapted plan of predictive maintenance.

References

1. Kühn MHB, Lukić M, Nussbaumer A, Günther H-P, Helmerich R, Herion S, Kolstein ÖB, Walbridge S, Androic B, Dijkstra O (2008) Assessment of existing steel structures: recommendations for estimation of the remaining fatigue life. <http://eurocodes.jrc.ec.europa.eu/doc/background/EUR23252EN.pdf>. Accessed 20 Dec 2021
2. Scheer J (2010) Failed bridges: case studies, causes and consequences, p 307. <https://www.wiley.com/en-ie/Failed+Bridges%3A+Case+Studies%2C+Causes+and+Consequences-p-9783433029510>. Accessed 08 Oct 2022
3. Åesson B (2014) Understanding bridge collapses. CRC Press, New York
4. Lawn B (1993) Fracture of brittle solids. Cambridge University Press, Cambridge
5. Paris PC, Gomez MP, Anderson W (1961) A rational analytic theory of fatigue. Trends Eng. <https://typeset.io/papers/a-rational-analytic-theory-of-fatigue-4tutowfpeb>. Accessed 11 Oct 2022
6. Manahan MP, Argon AS, Harling OK (1981) The development of a miniaturized disk bend test for the determination of post irradiation mechanical properties. J Nucl Mater 104:1545–1550. [https://doi.org/10.1016/0022-3115\(82\)90820-0](https://doi.org/10.1016/0022-3115(82)90820-0)
7. Bulloch JH (2002) A review of the ESB small punch test data on various plant components with special emphasis on fractographic details. Eng Fail Anal 9(5):511–534. [https://doi.org/10.1016/S1350-6307\(01\)00034-6](https://doi.org/10.1016/S1350-6307(01)00034-6)
8. Cuesta II, Alegre JM (2011) Determination of the fracture toughness by applying a structural integrity approach to pre-cracked small punch test specimens. Pergamon. <https://doi.org/10.1016/J.ENGFRACMECH.2010.09.004>
9. Krizik P, Balog M, Nagy S (2021) Small punch testing of heat resistant ultrafine-grained Al composites stabilized by nano-metric Al₂O₃ (HITEMAL®) in a broad temperature range. J Alloys Compd 887:161332. <https://doi.org/10.1016/J.JALLCOM.2021.161332>
10. de Almeida LFM, Oliveira SAG, Paes MTP, Ramos Neto FF, Franco SD, Arencibia RV (2021) Effect of test velocity on the tensile strength of high strength steels using the small punch test in a hydrogen environment. Int J Press Vessel Pip 194:104552. <https://doi.org/10.1016/J.IJPVP.2021.104552>

11. Ponson L (2016) Statistical aspects in crack growth phenomena: how the fluctuations reveal the failure mechanisms. *Int J Fract* 201(1):11–27. <https://doi.org/10.1007/S10704-016-0117-7>
12. Vernède S et al (2016) Ponson, Procédé de caractérisation du mécanisme de fissuration d'un matériau à partir de sa surface de rupture. Brevet français FR3026843 (2014). Method for characterizing the cracking mechanism of a material from the fracture surface thereof. International Patent WO2016/050871
13. Auvray N, Negi N, Trancart S, Ponson L (2019) L'analyse statistique des faciès de rupture: la science de la donnée au service de l'analyse de défaillance. *Traitements Matériaux* 459:47–51

Evaluating Damping Model Applied for Cable Tension of Cable-Stayed Bridge



An Huynh-Thai, Toan Pham-Bao, Hung Nguyen-Quoc,
and Luan Vuong-Cong

Abstract Urban development has recently got the attention of the supervisor and inspector of construction. The researcher must find a method to assess the structural situation. The cables of the cable-stayed bridge are simplistically modeled to evaluate the cable tension that have been defined in this report, through the Euler beam theory of the cables with viscous damping. Owing to simplified assumptions of boundary conditions, the tension of cables and viscous damping coefficient has been found through measured frequencies. The proposed method is experimented with by a cable of the Phu My cable-stayed bridge over the Saigon River in Vietnam.

Keywords Cable-stayed bridge · Cable tension · Natural frequency · Viscous damping · Flexural rigidity

1 Introduction

Through construction development, tensile cables have been popular in civil works and bridge operations because of their flexibility, toughness and lightweight. However, they are easily excited vibration by the dynamics effects of wind, storm and traffic because of low damping properties. Most of the operational time, these excitations exert great tension on the cables and give damage in cable structures. Thus, it is essential to determine the tension of cables in ambient excitations through damped vibration.

In bridge structure, for large span overpasses, the cable-stayed bridge and suspension bridges are the most used structures with cable mooring systems in the tower and girders to support the deck system [1]. The cable tension has a significant role in monitoring conditions as well as an indicator for the maintenance of cable-stayed bridges. Currently, the technical method for assessing cable tension includes a primarily

A. Huynh-Thai · T. Pham-Bao (✉) · H. Nguyen-Quoc · L. Vuong-Cong
Laboratory of Applied Mechanics (LAM), Faculty of Applied Sciences, Ho Chi Minh City
University of Technology (HCMUT), VNU-HCM, Ho Chi Minh City, Vietnam
e-mail: baotoanbk@hcmut.edu.vn

direct method and an indirect method using vibration frequencies. Cable tension can be determined directly and accurately by hydraulic jacks costly and difficult to perform [2]. Vibration measurement methods, an indirect solution, are economical and feasible. The accuracy of this indirect method depends on the geometry and material properties of the cable such as mass, length, sag, flexural rigidity and damping.

There are a few kinds of research on cable vibration of a cable-stayed bridge. In 1999, Cunha and Caetano [3] used an interferometry laser system for measuring vibration on cables of cable-stayed bridges. Dynamic analysis of cables with variable flexural rigidity was performed by Zhong [4]. A method with the asymptotic equation for cable used for a large range of flexural rigidity with the sag-to-span ratio is proposed to assess the cable tension of the Phu My cable-stayed bridge in Vietnam [2]. Huang et al. [5] established unified practical formulas from the taut string theory with different boundaries to calculate cable tension by applying correction coefficients. Because of the difficulty of determining low frequencies, Shimada [6] proposed to use of high-frequency modes for estimating cable tension considering the effect of the sag, flexural rigidity and inclination of the cable. In addition to the influence of above parameters, the damping parameter of a general cable was analytically considered inaccurate asymptotic formulas [7]. However, the damping of the cable is rarely considered in calculating tension. Therefore, this study proposed that cable tensions in case damping vibration have been determined by measured frequencies.

2 General Equations of the Cables

To expand the string model of cable, a beam model with a finite flexural rigidity EI and length L considering damping has been used. The differential equation of the cable vibration with response $u(x, t)$

$$EI \frac{\partial^4 u(x, t)}{\partial x^4} - N \frac{\partial^2 u(x, t)}{\partial x^2} + \rho \frac{\partial^2 u(x, t)}{\partial t^2} + c \frac{\partial u(x, t)}{\partial t} = 0 \tag{1}$$

where ρ , c , N , E and I are mass density, the damping coefficient, cable tension, Young’s modulus and area moment of inertia, respectively.

In the vibration analysis, the response u of the beam [8] is found in the form of separation of variables: $u(x, t) = W(x) \cdot T(t)$

$$\begin{cases} W(x) = C_1 e^{s_1 x} + C_2 e^{-s_1 x} + C_3 e^{s_2 x} + C_4 e^{-s_2 x} \text{ (a)} \\ T(t) = D_1 e^{\frac{t}{2}(\sqrt{k^2 - 4\lambda} - k)} + D_2 e^{\frac{t}{2}(\sqrt{k^2 - 4\lambda} + k)} \text{ (b)} \end{cases} \tag{2}$$

where the C_1 , C_2 , D_1 and D_2 are the constants, determined from the homogeneous boundary conditions. The value of s_1 , s_2 are given by

$$s_1; s_2 = \sqrt{\frac{N}{2EI} \pm \sqrt{\left(\frac{N}{2EI}\right)^2 + \frac{4\rho\pi^2 f_n^2}{EI}}} \quad (3)$$

where f_n is the natural frequency of the n th mode shape.

With simply supported boundary conditions at both ends, the deflection $W(x)$ and the curvature $W''(x)$ are zero. Then, Eq. (3) yields the tension equation of cable through natural frequency, as shown

$$N = \rho \left(\frac{2Lf_n}{n} \right)^2 - EI \left(\frac{n\pi}{L} \right)^2 \quad (4)$$

The damping ratio is determined by viscous damping divided by critical damping, as desired

$$\zeta_n = \frac{c}{4\pi f_n \rho} \quad (5)$$

According to the underdamped vibration, the measured frequency is assumptively damping frequency f_{dn} . It is necessary to change the damping frequency f_{dn} to the natural frequency f_n by using Eq. (5) to show the desired formula, as below:

$$f_{dn} = f_n \sqrt{1 - \zeta_n^2} \quad (6)$$

According to Eq. (6), natural frequency f_n can be determined by using a couple of damping frequencies f_{di} and f_{dj} ($i \neq j$), as follows:

$$f_n = n \sqrt{\frac{f_{di}^2 - f_{dj}^2}{i^2 - j^2}} \quad (7)$$

It is necessary to apply these calculating formulas for structural health monitoring, determined cable tension and compare with designed technical standard.

3 Calculating Application

In early march 2022, the cable of Phu My Bridge is investigated. The cable was excited by traffic, and vibration response was recorded by the accelerometers. The fundamental purpose of the inspection is to evaluate the cable tension from natural frequency to propose the calculating procedure of tension cable with viscous damping; moreover, the studied result can be used for structural health monitoring of the cable-stayed bridge. The properties of the cable C2115 (Fig. 1), given in

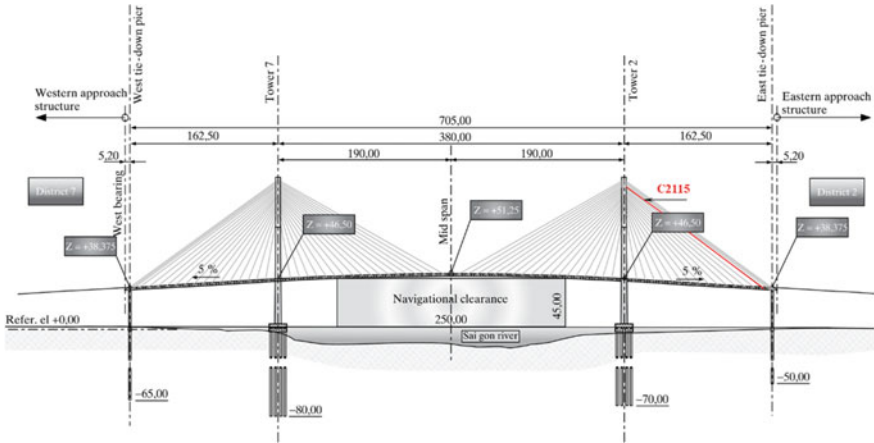


Fig. 1 Phu My Bridge sketch [9]

Table 1 Cables’ properties [2]

Cable no	Outer diameter (m)	Cable weight (kg/m)	Inertia (m ⁴)	Length (m)	Young’ modulus (N/m ²)
C2115	0.200	60.18	2.468×10^{-5}	177.1652	1.97×10^{11}

Table 1, are chosen to analyze. The result of cable tension from this study has been shown and compared with Shimada’s solution.

The first step, measured damping frequencies in power spectral density (PSD) are determined in ten vibration measures of cable C2115 (Fig. 2). Then, natural frequencies are calculated from Eq. (7) by using the minimum and maximum pair of damping frequencies in each measures. Finally, Eq. (4) is used to estimate cable tensions. In addition, the viscous damping ratios for cables are also determined in Table 2 by using Eq. (6).

Repeating the process to evaluate the tension cable. The cable tensions have been performed in Fig. 3, as shown.

The average tension for each cable, compared to the method which using regression to determining tensions without damping (Shimada et al.) [2], was given in Table 3.

With the higher mode and the less highly effective viscous damping, the effect of viscous damping on vibration isn’t outstanding. The difference between the two methods, which is damping, has been studied and calculated. The method of the study gives a more stable value of cable tension than the method of Shimada.

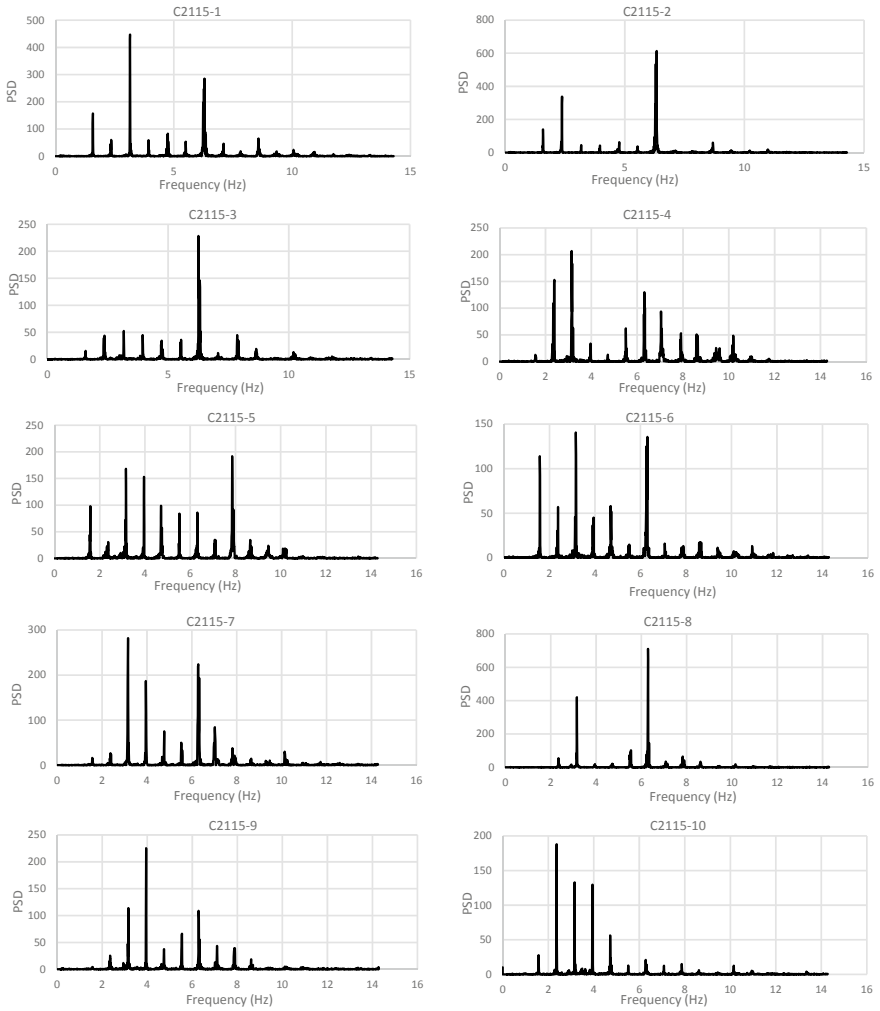


Fig. 2 Spectrum of C2115 cable in 10 measurements

Table 2 Viscous damping ratio for cable C2115

Repeat	Mode 1	Mode 2	Mode 3	Mode 4	Mode 5	Mode 6
1st	0.5642	0.0966	0.0363	0.1417	0.0542	0.1284
2nd	0.5616	0.1330	0.1332	0.1520	0.1331	0.1578
3rd	0.5454	0.0624	0.0554	0.0629	0.0171	0.0558
4th	0.5520	0.1489	0.1287	0.0798	0.1173	0.0679
5th	0.5620	0.1344	0.1345	0.1128	0.1345	0.0174
6th	0.5591	0.0707	0.1251	0.1015	0.0845	0.0955
7th	0.5547	0.1411	0.1088	0.0806	0.0871	0.1377
8th	0.5557	0.3802	0.1247	0.0855	0.0916	0.0386
9th	0.5575	0.0599	0.0837	0.1194	0.0999	0.1193
10th	0.5477	0.0688	0.0345	0.0228	0.0511	0.0907

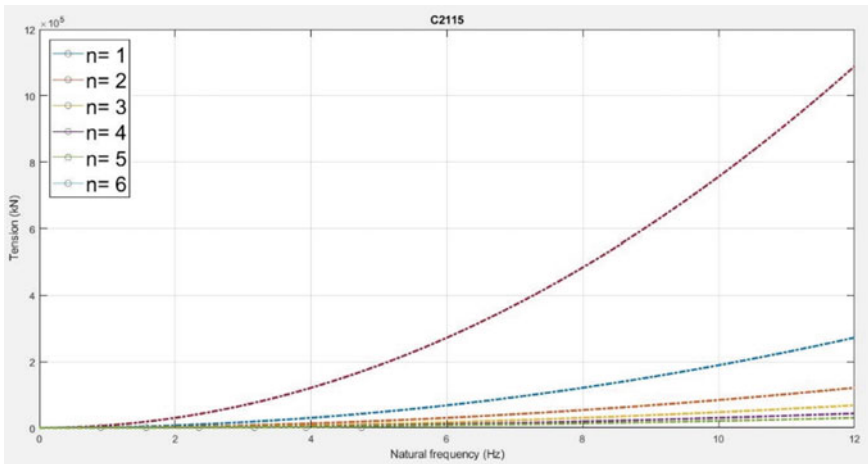


Fig. 3 Relationship between cable tension–natural frequencies for cable C2115

Table 3 Tension of cable C2115

No	Tension (kN) by study	Tension (kN) by Shimada [6]
1st	4619.1302	4609.2449
2nd	4629.6365	4857.3329
3rd	4693.6441	4371.9923
4th	4667.6746	4396.6426
5th	4628.0029	4539.7602
6th	4639.1865	4348.0507
7th	4656.7789	4661.4854
8th	4652.9971	4465.0441
9th	4645.7013	4621.9174
10th	4684.7409	4271.5685

4 Conclusion

A simplified vibration model of cable is developed to evaluate damping and tension. The governing equation of the cable vibration is simplistically derived from the fourth order partial differential equation of the beam model considering axial tension. Therefore, a new method is proposed to define tension and damping from the value of measured frequencies. The proposed procedure has been performed by vibration data of cable in the monitoring process of Phu My Bridge in Vietnam. The results indicated that the method of study fits to evaluate tensions for cables indirectly.

Acknowledgements We acknowledge Ho Chi Minh City University of Technology (HCMUT), VNU-HCM for supporting this study.

References

1. Ni YQ, Ko JM, Zheng G (2002) Dynamic analysis of large diameter sagged cables taking into account flexural rigidity. *J Sound Vibr* 257(2):301–319
2. Nam H, Nghia NT (2011) Estimation of cable tension using measured natural frequencies. *Proced Eng* 14:1510–1517
3. Cunha A, Caetano E (1999) Dynamic measurements on stay cables of cable-stayed bridges using an interferometry laser system. *Exp Techn* 23(3):38–43
4. Zhong M (2003) Dynamic analysis of cables with variable flexural rigidity. Doctoral dissertation, University of Hawaii at Manoa
5. Huang YH, Fu JY, Wang RH, Gan Q, Liu AR (2015) Unified practical formulas for vibration-based method of cable tension estimation. *Adv Struct Eng* 18(3):405–422
6. Shimada T (1994) Estimating method of cable tension from natural frequency of high mode. *J Jpn Soc Civil Eng* 50(1–29):163–171
7. Fujino Y, Hoang N (2008) Design formulas for damping of a stay cable with a damper. *J Struct Eng ASCE* 134(2):269–278
8. Rao SS (2019) *Vibration of continuous systems*, 2nd edn. John Wiley & Sons Ltd., New York
9. Moir G, Edmonds C, Walser P, Romberg M (2010) Construction engineering of Phu My cable-stayed bridge, Vietnam. *Struct Eng Int* 20(3):331–337

Investigating Seismic Response of Container Crane Subjected to Near-Field Ground Motions



Van Bac Nguyen and Van Hung Nguyen

Abstract In this paper, the seismic response of a container crane subjected to near-field ground motion was studied via using a shake table testing on a 1/20 scale container crane. The 1/20 scale model was designed and manufactured based on the theory of similitude laws. Three independent quantities as geometric length, acceleration, and elastic modulus were selected as fundamental parameters to design the 1/20 scale model. Two near-field ground motions were chosen as input ground motions to investigate the seismic response of the 1/20 scale container crane at the Seismic Research and Test Center, Pusan National University, Yangsan Campus. The results show that the maximum moment occurs on the location of the top of the lower seaside leg.

Keywords Container crane · Shake table testing · Seismic response · Near-field ground motions · Strain gauges

1 Introduction

Container cranes are special equipment widely utilized in seaports to transfer containers between ships and harbors. Despite having an important role in freight, they were the most vulnerable part of the harbor during the past moderate earthquake. In the past study, buckling and plastic hinges of portal frames were a typical failure mode under seismic excitation [1–4] but detailed causes and location of damages were not shown in those studies. This paper analyzed a container crane stationed

V. B. Nguyen (✉) · V. H. Nguyen

Faculty of Civil Engineering, VNU Hanoi, University of Engineering and Technology, 144 Xuan Thuy, Cau Giay, Hanoi, Vietnam

e-mail: bacnguyenvan@vnu.edu.vn

at Gwangyang port to find the riskiest location of the portal frame when subjected to seismic excitations by employing shake table testing on its 1/20 scale container crane. In order to accurately describe the seismic response of the prototype container crane, the 1/20 scale crane was designed according to the theory of similitude law [5]. It means that the data between the prototype crane and the scale crane must be converted by scale factors. The past work on another structure, for example, a cable-stayed bridge [6], low-rise shear walls [7], and concrete gravity dams [8] showed that near-field ground motions affected on seismic response of their structures more than far-field ground motions. Grimaz and Malisan [9] showed that near-field and far-field motions have a difference based on intensity, nature, and typology, and suggested scale factors for near-field and far-field ground motions. In this paper, two original near-field ground motions, Pohang and Gazli USSR Iran earthquakes, were matched to the elastic response spectrum in South Korea, then acceleration time history was applied along the trolley boom direction to analyze the seismic response of the 1/20 scale container crane.

2 Model Establishment

2.1 A 1/20 Scale Container Crane

A container crane stationed at Gwangyang port was used to be a prototype container crane to design its 1/20 scale container crane in this testing. The crane has typical information as follows: the total height from the ground to the top of crane was 78 m, the length of trolley boom girder was 136 m, the height of a portal beam was 17.5 m, and the total mass was about 1,175 tons. In order to design the 1/20 scale container crane, the scale factors (see Table 1) were calculated based on the theory of similitude law, cross-sections of each part of the scale crane were designed based on a scale factor of the moment of inertia. The scale factors for converting from prototype container crane to the 1/20 scale container crane were determined by Eq. (1).

$$S_i = \frac{\text{Quantities of prototype crane}}{\text{Quantities of scale crane}} \tag{1}$$

The 1/20 scale container crane is shown in Fig. 1, the total mass of the 1/20 scale container crane converted by the scale factor of mass was 2,939 kg, but the

Table 1 Scale factors for manufacturing the 1/20 scale container crane

Quantities	Symbol	Scale factor	Quantities	Symbol	Scale factor
Geometric length, l	S_l	20	Mass, m	S_m	400
Elastic modulus, E	S_E	1	Time, t	S_t	4.472
Acceleration, a	S_a	1	Moment of inertia, I	S_I	160,000

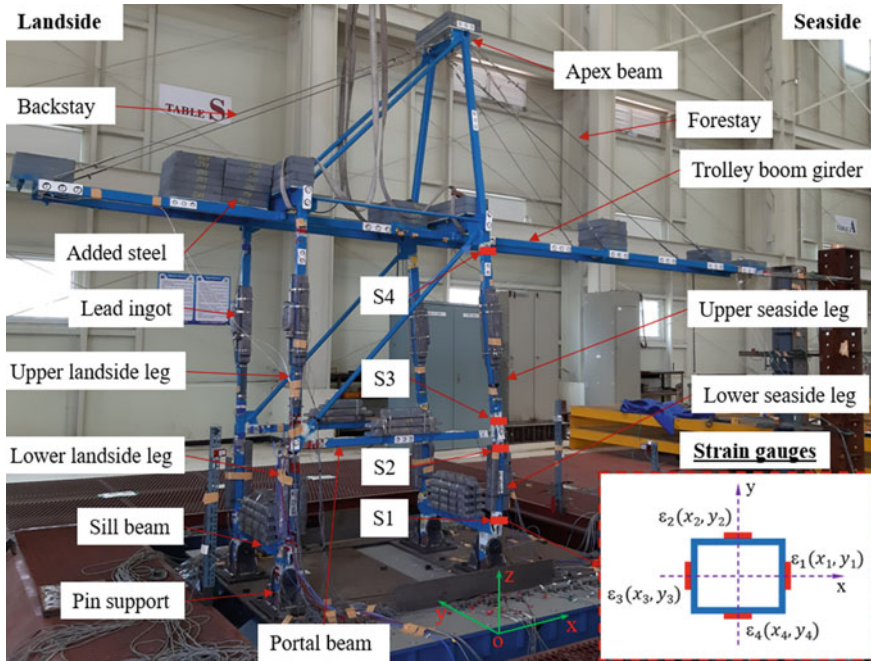


Fig. 1 1/20 scale container crane

self-frame mass of the scale crane was only 235.5 kg. Hence, additional masses of 2703.5 kg were attached to frames of the 1/20 scale container crane: the added steels were attached to the trolley boom girders and apex beam; while the lead ingots were attached to the upper landside and seaside legs, the lower landside and seaside legs, portal beams, and sill beams. Details of the 1/20 scale container crane could be seen in a previous study [2]. Internal forces along the seaside leg were determined via strain gauges that were attached to frames to find the most disadvantaged location.

2.2 Near-Field Ground Motions

Near-field ground motions are generally known to be qualified within an epicentral distance of about 25 km from an epicenter [10]. In this paper, two ground motions were Pohang and Gazli USSR Iran earthquakes as shown in Table 2. To characterize the elastic Korean design standard [11], two ground motions were matched to the

Table 2 Original near-field ground motions

Earthquake	Year	Magnitude	Epicentral distance (km)	Peak ground acceleration (PGA) (g)
Pohang	2017	5.4	9.0	0.27
Gazli USSR Iran	1976	6.8	12.82	0.61

elastic response spectrum Z1S4_2400, zone 1, soil type S4, and the return period of 2400 years. Then, acceleration time histories were scaled down by using the scale factors of time ($S_t = 4.472$) and acceleration ($S_a = 1$) to make input ground motions of the shaking table test. Figure 2a shows the response spectrum of two earthquakes: original response spectrums and response spectrum matched to the target response spectrum (Target Z1S4_2400). Figure 2b, c shows the acceleration time history of earthquakes: original and matched acceleration time history, scaling down matched acceleration time history for shake table testing.

3 Results and Discussions

The moments M_y about Y -axis (perpendicular to trolley boom direction) and M_x about X -axis (along to trolley boom direction) were calculated based on four strain gauges on each section. Equations for determining the moments M_x and M_y could be seen in previous studies [3, 4]. The measured locations were shown in Fig. 1, in which four locations were noted as S1–S4, and each location has four strain gauges. Due to input motions applied along X -axis, the moment M_x (see Fig. 3a) was lower than the moment M_y (see Fig. 3b), and the fundamental mode of container crane was vibration along X -axis as a discussion of Nguyen et al. [2]. Figure 4 shows the moment of location S2 based on time, it is clearly seen that Moment M_y (blue line) was larger than moment M_x (orange line). Figure 3b shows the M_y of the seaside leg, the maximum value occurred at location S2, while the minimum value appeared at location S4. In detail, the maximum moments of location S2 were 80 and 123 kN-cm, while the values of location S4 were only 10 and 17 kN-cm for Pohang and Gazli USSR earthquakes, respectively. Location S3 was lower with moments of 58 and 95 kN-cm than location S2. Therefore, the top of the lower legs (S2) was an adverse location under seismic excitation. In spite of matching two response spectrums to the target response spectrum, as can be seen in Fig. 2 the matched PGA of Gazli USSR earthquake (0.34 g) was lower than that of Pohang earthquake (0.55 g), the seismic response of the Gazli USSR earthquake was still larger than that of the Pohang earthquake, the maximum value M_y of the Gazli USSR earthquake was one and a half time the maximum value M_y of the Pohang earthquake.

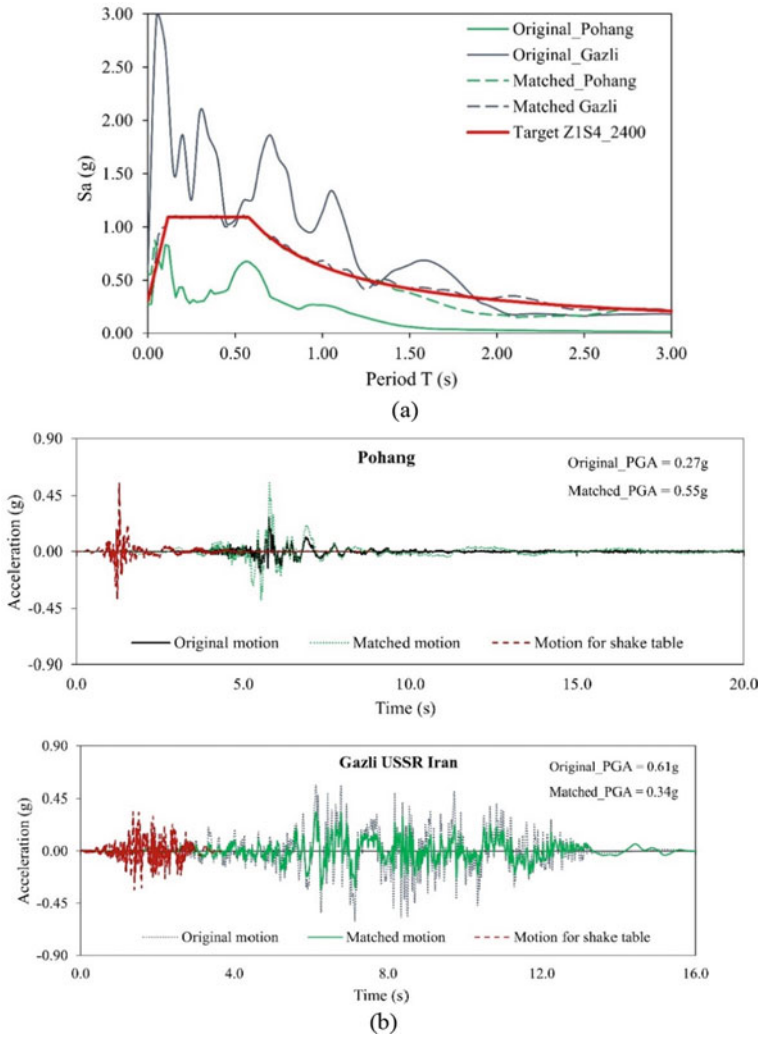
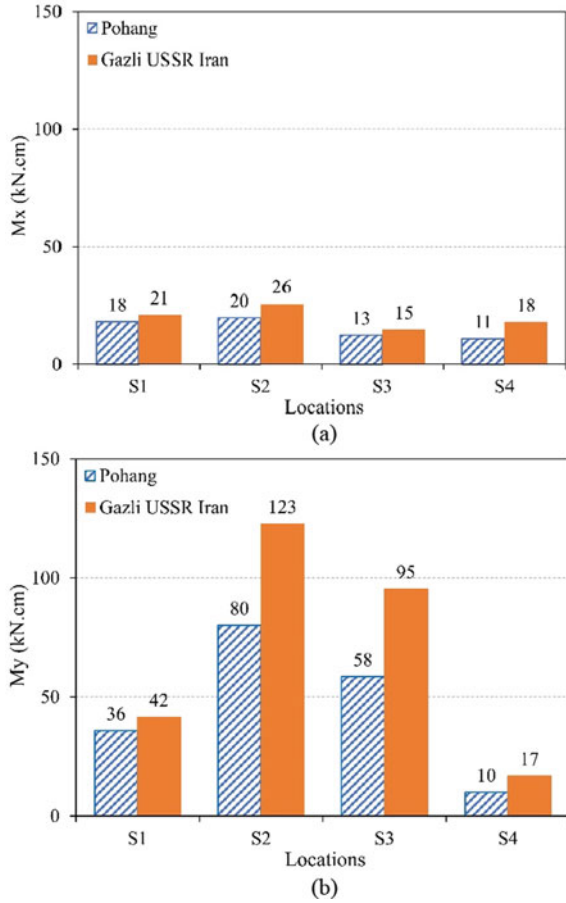


Fig. 2 Input ground motions: a response spectrum; b acceleration time histories

Fig. 3 Maximum moment of the lower–upper seaside leg: **a** moment about *X*-axis; **b** moment about *Y*-axis



4 Conclusions

The seismic response of the container was investigated by using shake table testing on its 1/20 scale crane. The 1/20 scale container crane was designed according to the theory of similitude law, in which the cross-section of each part was designed owing to the scale factor of the inertial moment, and artificial masses were added to satisfy the total mass of the 1/20 scale container crane as demanding of the similitude law. Two original near-field ground motions were selected and matched to the elastic response spectrum (Z1S4_2400), which were applied along the trolley boom direction to the 1/20 scale container crane. The results indicated that the maximum moment value

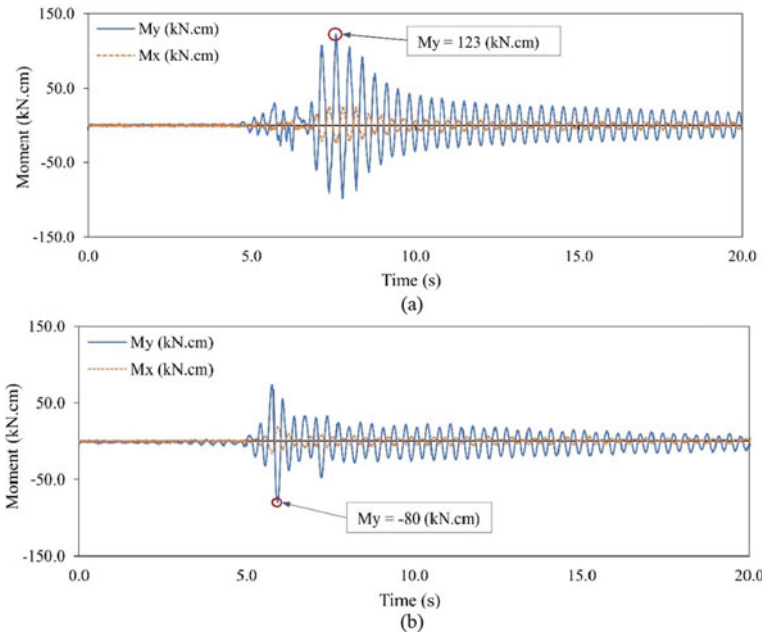


Fig. 4 Moment time history of location S2: **a** Gazli USSR earthquake; **b** Pohang earthquake

of seaside leg occurred at the top of the lower leg: the maximum moment M_y were 80 and 123 kN.cm for Pohang and Gazli USSR earthquake. Therefore, the location around the portal frame, especially the top of the lower leg, was the most disadvantage of the container crane.

References

1. Kanayama T, Kashiwazaki A, Shimizu N, Nakamura I, Kobayashi N (1998) Large shaking table test of a container crane by strong ground excitation. *Seism Eng* 14:243–248
2. Nguyen VB, Seo J, Huh J, Ahn J, Haldar A (2021) Seismic response investigation of 1/20 scale container crane through shake table test and finite element analysis. *Ocean Eng* 234:109266
3. Nguyen VB, Huh J, Meisuh BK, Tran QH (2021) Shake table testing for the seismic response of a container crane with uplift and derailment. *Appl Ocean Res* 114:102811
4. Nguyen VB, Huh J, Meisuh BK, Kim J, Park I (2021) Seismic response of container crane under near-field and far-field ground motions. *Appl Sci* 11:1–16
5. Moncarz PD, Krawinkler H (1981) Theory and application of experimental model analysis in earthquake engineering. Stanford University, Stanford, CA
6. Tochaei EN, Taylor T, Ansari F (2020) Effects of near-field ground motions and soil-structure interaction on dynamic response of a cable-stayed bridge. *Soil Dyn Earthq Eng* 133:106115
7. Brun M, Reynouard JM, Jezequel L, Ile N (2004) Damaging potential of low-magnitude near-field earthquakes on low-rise shear walls. *Soil Dyn Earthq Eng* 24:587–603
8. Gorai S, Maity D (2019) Seismic response of concrete gravity dams under near field and far field ground motions. *Eng Struct* 196:109292

9. Grimaz S, Malisan P (2014) Near field domain effects and their consideration in the international and Italian seismic codes. *Boll Geofis Teor Appl* 55:717–738
10. Yadav KK, Gupta VK (2017) Near-fault fling-step ground motions: characteristics and simulation. *Soil Dyn Earthq Eng* 101:90–104
11. Korean Design Standard (KDS 17 1000) (2018) Korea institute of civil engineering and building technology. <http://www.kcsc.re.kr>

Structural Damage Detection and Health Monitoring

Mechanical Reliability Analysis of an RC Storage Tank Considering Pitting and Uniform Corrosion



Karima Bouzelha, Nassima Miloudi, Hocine Hammoum, Lysa Benaddache, and Serine Bennabi

Abstract The lifetime of a reinforced concrete (RC) storage tank depends strongly on the aggressiveness degree of its environment (presence of chlorides and carbon dioxide). The aggressiveness of these agents leads to corrosion of steel reinforcements. To understand the evolution in time of this corrosion pathology, the engineer uses corrosion models in deterministic calculation of RC structures. However, this deterministic approach, using average values of input variables, leads to an unreliable representation of the reality. Similarly, the loads applied to the structure are not always perfectly known. It is why the civil engineer uses probabilistic analysis to take into account the uncertainties marring these parameters. This paper is dedicated to mechanical reliability analysis of the RC tank upper beam, taking into account pitting corrosion and uniform corrosion of its steel reinforcements. The influence of chloride ion concentration and carbon dioxide content on the evolution of corrosion is studied in order to determine the evolution, as a function of time, of the residual section of its steel reinforcements. The reliability analysis is performed with the Monte Carlo method.

Keywords Concrete tank · Pitting corrosion · Uniform corrosion · Steel reinforcement · Reliability · Monte Carlo method

1 Introduction

Corrosion of steel reinforcements in concrete can be initiated by carbonation of concrete cover in contact with atmospheric carbon dioxide (CO_2) (uniform corrosion) or by penetration of chloride ions (Cl^-) present in the environment (pitting corrosion). Many models have been developed from Fick's law to predict the progress of carbonation front in function of CO_2 concentration, concrete porosity, and relative humidity; we mainly cite the models of DuraCrete [1], Task Group 5.1 of CEB1, and

K. Bouzelha · N. Miloudi · H. Hammoum (✉) · L. Benaddache · S. Bennabi
Department of Civil Engineering, Mouloud Mammeri University, 15000 Tizi-Ouzou, Algeria
e-mail: hocine.hammoum@ummto.dz

Oxand [2]. The kinetics of chloride ions diffusion is conditioned by concentration of chloride ions, relative humidity, and temperature. The penetration of these ions in the concrete is described by several models such us Duracrete model, Li model, and the Francy model [2]. In addition, to estimate the cross-section loss of steel reinforcements, induced by corrosion in concrete, several models have been proposed to express the uniform corrosion current (Li and Lawanwisut model, Gonzales, coll and Tuutti model...) [3] and the pitting corrosion current (Liu and Weyers model, Vu and Stewart model, Vu et al. model, Gonzales et al. model, Tuutti) [3]. In this research, we are interesting in reliability analysis of an underground water tank, implanted in marine environment and urban area, in the department of Jijel (Algeria). The diagnosis of this tank revealed the degradation of its upper beam by the corrosion of its steel reinforcements. To quantify this corrosion, the two models proposed by Gonzales, coll and Tuutti [3] for the uniform and pitting corrosion are used. In addition, the effect of the chlorides concentration and carbon dioxide will be analyzed. Finally, the failure probability of the tank upper beam is calculated using the Monte Carlo method. The random variable considered is the live load.

2 Deterministic Model of the Tank Upper Beam

The necessary section of steel reinforcements in tank upper beam is calculated as a ring submitted to an internal pressure H_1 . This pressure is induced by a compression effort N_1 , acting in the meridian axis of the dome (Fig. 1).

The horizontal component H_1 induces an horizontal tensile effort T , as follows:

$$T = H_1 \cdot \frac{D}{2} \tag{1}$$

where D is the internal diameter of the tank.

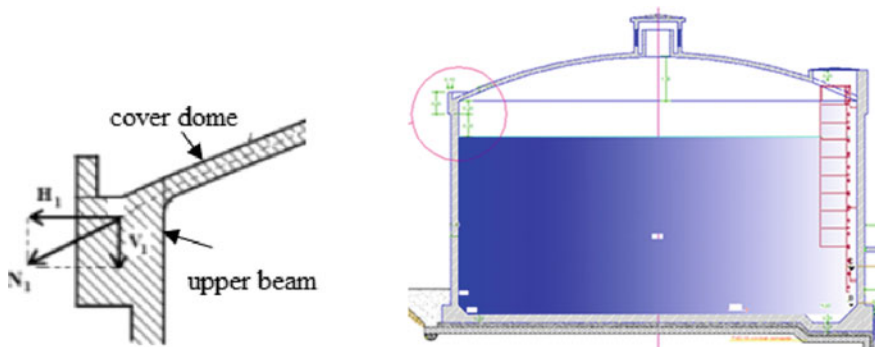


Fig. 1 Cross-section of the tank placed on ground and the upper beam

This effort (T) will be fully taken up by the steel reinforcements of the upper beam. These steel reinforcements are determined at the serviceability limit state “Eq. (2),” by considering the opening cracks at very damaging state.

$$A_s \geq \frac{T}{\sigma_{st}}, \quad (2)$$

where σ_{st} is the steels limit stress.

Furthermore, to introduce the corrosion effect (pitting and uniform), we evaluate the residual section of the steel reinforcements as a function of time as follows:

$$A_r(t) = n_b \cdot A_{ri}(t), \quad (3)$$

where $A_{ri}(t)$ is the residual section of a steel bar after an effective corrosion period of t years, and n_b is the number of the reinforcements (bar).

2.1 Pitting Corrosion

The residual section of steel reinforcements $A_{ri}(t)$, after corrosion, is given by the relation of Duprat [4]

$$A_{ri}(t) = \begin{cases} \frac{\pi d_0^2}{4} - A_1 - A_2 i f p(t) \leq \frac{d_0}{\sqrt{2}} \\ A_1 - A_2 i f p(t) \leq d_0 \\ 0 \text{ if } p(t) > d_0 \end{cases} \quad (4)$$

The maximum pitting depth $p(t)$, due to the penetration of chloride ions at time t , is given by “Eq. (5)” [5]

$$p(t) = 0.0116\alpha \int_{t_{ini}}^t i_{corr} dt \quad (5)$$

The initiation time of pitting corrosion t_{ini} (years) is obtained from the second law of Fick. For current corrosion by pitting i_{corr} ($\mu A/cm^2$), we retain, in our case, the model of Gonzales, coll and Tuutti [3].

2.2 Uniform Corrosion

The residual section of a steel reinforcement as a function of time $A_{ri}(t)$ is calculated in function of its residual diameter which is function of its initial diameter d_0 , as expressed by “Eq. (6)” of Rodriguez [3]

$$d(t) = d_0 - 0.023 \int_0^t I_{\text{corr}} dt \quad (6)$$

The uniform corrosion current is expressed by Gonzales coll and Tuutti model [3], and the initiation time for uniform corrosion is defined by a Portuguese method LNECE465 [3].

3 Practical Application

3.1 Structure Presentation

The studied structure is an underground water storage tank, made of reinforced concrete. Geometric characteristics of the tank and materials characteristics are listed in Table 1. The steel reinforcements section is calculated for the different load combinations taken from Fascicule 74 [6] and BAEL 99 [7]. The most unfavorable reinforcement of the upper beam is obtained for the load combination at serviceability limit state. The section of steel reinforcements adopted is 21. 98 cm² corresponding to 7 bars of ϕ 20 mm.

The diagnosis of the tank revealed that the space above the cover dome was transformed into a parking area for the management company’s vehicles, and that the steels reinforcements at level of the upper beam are stripped and have undergone

Table 1 Characteristics of the structure and materials [8]

Parameter	Symbol	Value	Unit
Tank capacity	V	500	m ³
Internal diameter of tank	D	15	m
width of tank upper beam	B	30.00	cm
Height of tank upper beam	H	30.00	cm
Section of the tank beam	A	900.00	cm ²
Nuance of steels	Fe	400.00	Mpa
Tensile strength of concrete at 28 days	fc28	25	Mpa
Steels limit stress	σ_{st}	161.31	Mpa

oxidation [8]. Their corrosion, aggravated by the salty atmosphere of the marine environment, led to a strong reduction in the cross-section of the steel reinforcements.

3.2 Evaluation of Corrosion Effect on Steel Reinforcements Section

The curves of evolution as a function of time of residual section of steel reinforcements show that the initiation time at corrosion increases with the decrease of chloride ions concentration (Fig. 2), from an environment with extreme aggressiveness to an environment with low aggressiveness and also with the decrease of CO₂ content (Fig. 3). We also notice that, in the same order of aggressiveness, corrosion is initiated more quickly in the case of pitting corrosion. It should also be noted that the residual reinforcement section reaches the necessary section more quickly in the case of pitting corrosion.

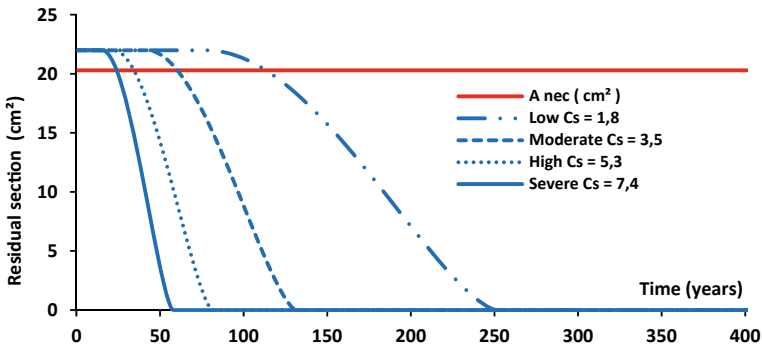


Fig. 2 Evolution of the steel reinforcements section for different concentration of chloride ion

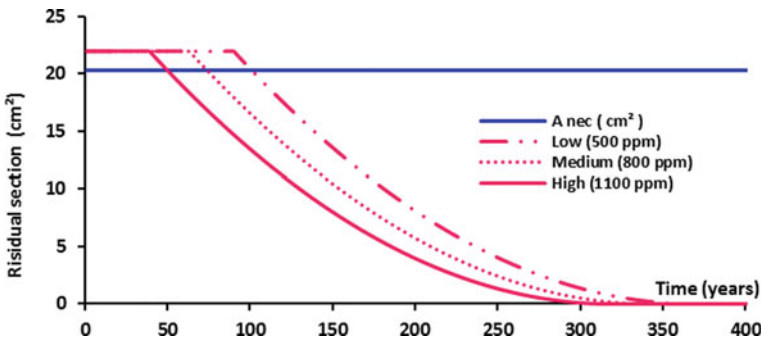


Fig. 3 Evolution of steel reinforcements section for different contents of CO₂

4 Probabilistic Analysis of Tank Upper Beam

To quantify the failure risk of the tank upper beam, it is necessary to define the limit state function $G\{X\}$ induced by the corrosion of its steel reinforcements. The justification criterion compared to this limit state is to check that the residual reinforcement section « A_r » is greater than the necessary section of reinforcements « A_s ».

$$G(\{X\}) = A_r(\{X\}) - A_s(\{X\}) \tag{7}$$

$\{X\}$ is a random vector constituted of random variables x_i .

The components of the deterministic model are affected by many uncertainties. In this study, we are interested in the live load variable Q . The variability of this external action is due to the use attributed to the surface above the upper beam tank. The random variable Q is generated by a normal distribution law according to the literature. The two parameters of this distribution law are the mean and the standard deviation linked by the following relation:

$$\text{mean} = CV * \text{standarddeviation} \tag{8}$$

The analytical assessment of the probability of failure of upper beam tank is carried out using the Monte Carlo simulation method [5], for its simplicity and the accuracy of its results.

The evolution of the probability of failure as a function of time, taking into account pitting corrosion show that, for the values of coefficient of variation $CV > 10\%$, the admissible probability of failure for civil engineering structures ($P_f = 10^{-3}$) is reached at the first year. Furthermore, for $CV < 10\%$, the tank lifetime is extended beyond 50 years (Fig. 4). This shows the sensitivity of the live load on the behavior and durability of the tank. We notice that same observations are made for uniform corrosion.

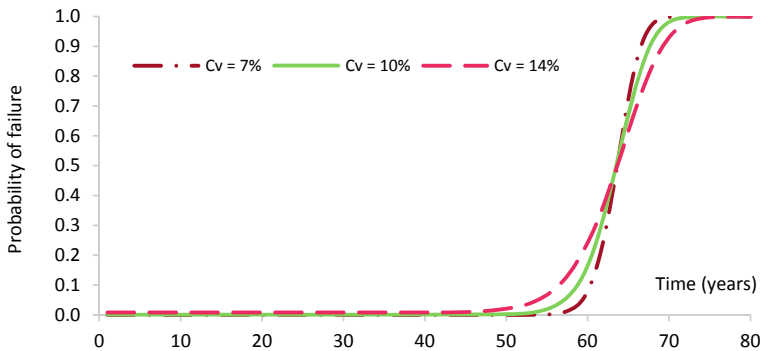


Fig. 4 Failure probability in function of time, for different CV (pitting corrosion)

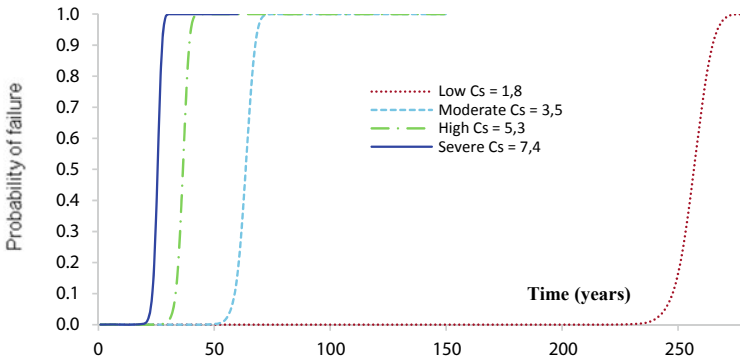


Fig. 5 Probability of failure as function of time for different environments (pitting corrosion)

We have varied the CV from 5 to 20%. For readability reasons and clearness of the curves in Fig. 4, we present only three curves which CV are respectively 7, 10, and 14.

To estimate the influence of the environment aggressiveness on probability of failure of the upper beam of the tank, we represent its evolution over time for different concentrations of chloride ions and for coefficient of variation $CV = 10\%$ (Fig. 5). We note that the admissible probability of failure for civil engineering structures ($P_f = 10^{-3}$) is reached at 17 years in extreme aggressiveness environment, at 25 years in high aggressiveness environment, at 47 years in an average aggressiveness environment and beyond 200 years in low aggressive environment, which greatly exceeds the life of the tank. At same, the influence of concrete carbonation on probability of failure of tank upper beam studies in time for three contents of CO_2 (low, medium, and high) and for $CV = 10\%$. The results show that the admissible probability of failure ($P_f = 10^{-3}$) is reached at 90 years in environment of low content of CO_2 , at 58 years in environment of medium content of CO_2 and at 40 years in the environment of strong content of CO_2 .

5 Conclusion

In this research, results have highlighted the influence of chloride ions concentration and carbon dioxide content on the initiation and propagation of corrosion phenomenon and revealed that pitting corrosion is more dangerous than uniform corrosion. However, it should know that in reality both corrosions (pitting and uniform) can occur simultaneously because the carbonation has also a releasing effect of the chloride ions trapped in the cement matrix, which accentuates corrosion phenomenon. Currently, studies on coupling of the two corrosion phenomena “carbonation and penetration of chloride ions” are initiated and are the subject of reflection and research.

Furthermore, the assessment of the probability of failure for a tank upper beam, considering the corrosion of its reinforcements showed that the no mastering of live load variability leads to the reduction of the tank lifetime.

Acknowledgements The authors wish to thank the Algerian Ministry of higher education and scientific research for funding the University education research project (PRFU—No A01L02UN150120220004) with Tassili Project (PHC—18MDU121). Without forgetting to thank African Geosystem Company (<http://www.agc-dz.com>) that provided the documentation for the practical example.

References

1. DuraCrete (2000) Statistical quantification of the variables in the limit state functions. The European Union-Brite EuRam III-Contract BRPR-CT95-0132-Project BE95-1347/R9
2. Perlot C, Capra B, Rougeau P (2007) Mieux maîtriser la durabilité des bétons par l'approche probabiliste. Rapport du centre d'études et de recherches de l'industrie du béton (CERIB). Ed. du CERIB réf. 75 E
3. Petre-Lazar I (2011) Evaluation du comportement en service des ouvrages en béton armé soumis à la corrosion des aciers. Thèse de doctorat, Université Laval Quebec
4. Duprat F (2006) Reliability of RC beams under chloride-ingress. Construction and Building Materials, Toulouse
5. Aoues Y, Bastidas-Arteaga E (2011) Conception optimale des structures en béton armé soumises à la pénétration d'ions chlorure. XXIXe Rencontres Universitaires de Génie Civil, Tlemcen
6. Fascicule 74 (1998) Texte officiel, construction des réservoirs en béton - cahier des clauses techniques générales, Ministère de l'équipement des transports et du logement, Paris, p 261
7. B.A.E.L. (2000) 91 modifiées 99. Règles techniques de conception et de calcul des ouvrages et constructions en béton armé suivant la méthode des états limites. Edition Eyrolles
8. Hammoum H, Bouzelha K, Hannachi NE (2012) Analyse d'un scenario de vieillissement de deux réservoirs jumelés par un calcul aux états limites. Ann BTP 5:51–60

Study to Apply Artificial Neural Network for Establishing Displacement Models of a Cable-Stayed Bridge



Thuy Linh Nguyen and Van Hien Le

Abstract Establishing a displacement model of a cable-stayed bridge plays an important role in the operating process of structures in order to assess the structural health conditions, detect damages to structures, and suggest recommendations for maintenance. This paper studies to application of Artificial Neural Network (ANN) for establishing the displacement models along to X , Y , and Z directions of the center main span point of a cable-stayed bridge. The strategy of the building displacement model includes three steps. Firstly, Structural Health Monitoring systems (SHMs) data of a cable-stayed bridge were acquired in long-term monitoring which includes Global Navigation Satellite System (GNSS) displacement data in 3D of the center main span point, air-temperature data, windspeed, and stress data. The acquired data were de-noised and then assessed the correlation between the GNSS displacement data and other influencing factors such as air-temperature, windspeed, and stress data. Secondly, the displacement models were established by applying the ANN method for the long-term monitoring data. Finally, the establishing models were then assessed for their precision by some criterions such as Root Mean Square Error (RMSE), the determination coefficient (R^2), and making comparisons between the real GNSS measurement data and the predicting data. The results show that the displacement models have high precision and reliability with the $RMSE$ less than ± 3 mm and R^2 over 0.96.

Keywords Displacement model · ANN · Cable-stayed bridge · SHMs · GNSS

1 Introduction

A long-span cable-stayed bridge is a lightweight supperstructure that is sensitively affected by many factors during its operation such as the live weight of vehicles and environmental loads. SHMs have been applied worldwide to monitor the health

T. L. Nguyen (✉) · V. H. Le
University of Transport and Communications/UTC, Hanoi, Vietnam
e-mail: linhnt@utc.edu.vn

© The Author(s), under exclusive license to Springer Nature Singapore Pte Ltd. 2024
T. Nguyen-Xuan et al. (eds.), *Proceedings of the 4th International Conference on Sustainability in Civil Engineering*, Lecture Notes in Civil Engineering 344,
https://doi.org/10.1007/978-981-99-2345-8_66

649

of a superstructure in order to define the status conditions of structures and any damage detection. Then, SHMs long-term monitoring data can be processed to predict structural health in the future.

Establishing a displacement model in order to predict the accurate displacements of structures during their operation plays an important role in monitoring works. A displacement model can provide the detail of structural displacements and then make alarm some unusual events or predict damages in the future. Establishing a displacement model for a real cable-stayed bridge is a complicated work that combines many nonlinear effect factors such as live weight, windspeed or air-temperature change, and so on. In the world, there were some studies focusing on applying ANN for the prediction of eigenfrequency change of suspension bridges [1, 2]. Kaloop and Hu [2] studied to apply ANN for detecting the damage location of a cable-stayed bridge using acceleration monitoring data. Zhou et al. [1] studied to apply the ANN method for predicting the oscillation frequency change due to the effect of air-temperature change. Moreover, Mazurov et al. [3] applied the ANN method to build displacement models along horizontal and lateral directions of the tower points of a suspension bridge using GNSS monitoring data. Moon et al. [4] studied to apply the ANN method to model the vertical displacement of a simulated bridge using some assumptions of live loads of vehicles. It can be seen that ANN is an effective method for studying to establish a displacement model of a bridge [4]. However, there were not any studies working on applying the ANN method for establishing the displacement model of a real cable-stayed bridge with long-term monitoring data.

In Vietnam, applications of Global Navigation Satellite System-Real-Time Kinematic (GNSS-RTK) for SHMs monitoring of cable-stayed bridges were studied in some studies. Nguyen et al. [5] studied the application of GNSS-RTK for SHMs monitoring of the Can Tho cable-stayed bridge, and this study showed that the GNSS-RTK technique assures the accuracy and reliability of monitoring task. Otherwise, some researchers studied to apply the ANN method for subsidence prediction of hydroelectricity [6]. In the previous studies, the authors applied the ANN method to interpolate the GNSS missing data in bridge monitoring and predict the vertical displacements due to environmental effects [7, 8]. This study focuses on establishing displacement models for the center main span of a cable-stayed bridge using the ANN method.

2 Theory of Artificial Neural Network—ANN

ANN is a mathematical model that is built based on biological neurons. An ANN model includes a group of neural (nodes) that connect to others by an appropriate weight.

2.1 Multi-layer Perceptron—MLP

In this algorithm, an artificial neuron is trained to learn from the input factors for building an accurate model, then it gives output results. A neural network is arranged by three components including input layers, hidden layers, and output layers. The input layer is used for input factors which may be constants, time series data, or an output of another neural network. The input factors are calculated by carrying weight (w_{ij}) in neurons of the hidden layer. The input layer was then processed by activating functions such as sigmoid or tan-hyperbolic functions in the hidden layer, then the updated weight w_{jk} is calculated to transform to the output layer. The connective between the hidden layer and input and outputs imitate better the nonlinear correlation. The learning process of the ANN model is done by training algorithms such as Back Propagation (BP).

2.2 Back Propagation Algorithm

An ANN model creates a relationship between an input vector X_i ($i = 1-m$) and an output vector Y_k ($k = 1-n$). For an ANN model with a hidden layer, neuron H_j is defined as below [9]:

$$H_j = f \sum_{i=1}^n X_i w_{ij} + b_j. \quad (1)$$

Then, the output \widehat{Y}_k (estimation) is calculated as below:

$$\widehat{Y}_k = f \left(\sum_{j=1}^q H_j w_{jk} + b_k \right) = f \left(\sum_{j=1}^q f \left(\sum_{i=1}^n X_i w_{ij} + b_j \right) w_{jk} + b_k \right). \quad (2)$$

For an observation t ($t = 1-T$), the output estimation is $\widehat{Y}_{k,t}$, the corresponding measurement is $Y_{k,t}$, thus the difference between $\widehat{Y}_{k,t}$ and $Y_{k,t}$ is called error. The objective of model estimation is to define the weights w_{ij} and w_{jk} allowing the condition of the minimum square summation of errors. The objective function $E(w)$ is calculated by

$$E(w) = \frac{1}{2} \sum_{k=1}^n (Y_{k,t} - \widehat{Y}_{k,t})^2. \quad (3)$$

The basic concept of the Back Propagation algorithm is that when w changes then $E(w)$ changes. And, there is a set of w which allows the value of $E(w)$ is minimum. In order to estimate the weight w , a set of w is assigned value to estimate the $E(w)$

function. Then, the value of w is adjusted to get the minimum value of $E(w)$. This process is called Gradient Descent. The value of w is adjusted by

$$\Delta w = w_{r+1} - w_r = -\eta \frac{\partial E}{\partial w} \quad (4)$$

$$\Delta b = b_{r+1} - b_r = -\eta \frac{\partial E}{\partial b}. \quad (5)$$

Here, r is the iteration step; η is a learning constant. The learning process is iterated until getting the minimum value of Δw .

3 Experiment Analysis

3.1 Data Preparation

3.1.1 Data Acquisition

SHMs monitoring data of the Can Tho cable-stayed bridge in Vietnam are acquired for the experiment in this study. The objective study is to establish displacement models in 3D of the center main span using the ANN method. The length of the bridge is 2750 m, the width is 26 m, the main span length is 550 m, and the height of the tower is 170 m. The main span has 210 m in the middle which is made of concrete. The SHM system of the Can Tho Bridge includes many kinds of sensors located in specific positions. There is a GNSS system used to monitor the displacements of some specific locations such as on the top of towers, center main span, quarter main span, and some piers. For observing the effects of the environment, there are temperature sensors, windspeed, wind direction, etc. There are also eight strain gauges located at the center main span for measuring the stress of structures. The monitoring data are observed in real time and stored at some kinds of average data such as 1, 10 min, 1 h, and 1 day [10]. In this study, the acquisition data were extracted in 1 week in a 10-min average format. The study data include GNSS displacements in 3D of the center main span point and top of tower points, air-temperature data, windspeed data, and stress data at the center main span.

3.1.2 Pre-processing Data

The typical abnormal data here is the missing data that need to interpolate. Statistically, there are about 90% missing cases that occurred in less than five continuous data [11]. Therefore, the Moving Average (MA) is applied to interpolate the missing data and de-noise of all study data (Fig. 1).

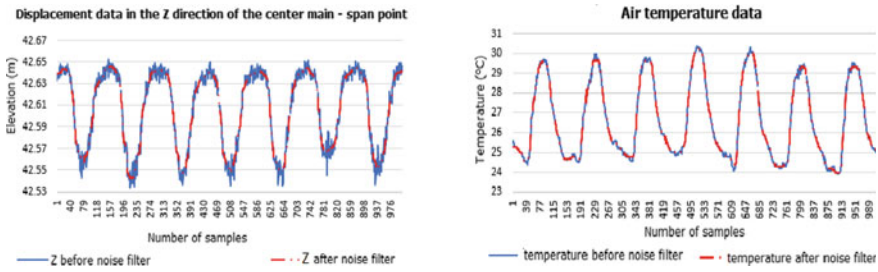


Fig. 1 Pre-processing data

3.1.3 Correlation Analysis

The correlation between GNSS data of the center main span and influencing factors such as air-temperature, windspeed, and stress data is studied. The factors have a high correlation with the GNSS data which are selected to be the input factors in the ANN model. Table 1 explains the correlated coefficients between GNSS displacements of the center main span, the tower points, and environmental effect factors, while Table 2 shows the correlated coefficients between GNSS displacement data and the stress data [12, 13]. The correlated coefficients are larger than 0.5 or less than -0.5 which are concerns to analyze.

It can be seen that the Z displacement direction of the center main span has a high correlation with the air-temperature and the X displacement direction of the tower points. Otherwise, the X-direction of the center main span has a correlation with the

Table 1 Correlated coefficients between the center main span point with the tower points, and the environmental factors

Center main span point	Correlated coefficients							
	Temp	Windspeed	North tower point			South tower point		
			X	Y	Z	X	Y	Z
X	0.58	0.25	0.54	-0.08	1	0.24	-0.13	0.08
Y	0.07	0.02	0.52	0.65	0.29	-0.50	0.67	-0.10
Z	-0.93	-0.05	-0.67	0.29	-0.05	0.77	0.36	-0.31

Table 2 Correlated coefficients between the center main span point and the stress data

Center main span point	Correlated coefficients							
	Sensor 1	Sensor 2	Sensor 3	Sensor 4	Sensor 5	Sensor 6	Sensor 7	Sensor 8
X	0.08	0.12	0.10	0.19	0.50	0.38	0.32	0.50
Y	0.69	0.69	0.66	0.68	0.50	-0.14	-0.25	0.13
Z	-0.14	-0.20	-0.17	-0.33	-0.93	-0.71	-0.60	-0.88

air-temperature and the X -direction of the North tower point, while the Y -direction has a correlation with both X - and Y -directions of all tower points.

Table 2 shows that the Z -direction has a correlation with sensors 5–8, while the Y -direction has a correlation with sensors 1–5, and X -direction has a correlation with sensors 5 and 8. Overall, stress data at sensors 5 and 8 and X displacement at the North tower are selected as influencing factors for establishing the displacement model of the X -direction of the center main span. The stress data at sensors 1–5 are chosen to input to the ANN model for establishing the Y -direction displacement model. For the Z -direction displacement model, the air-temperature, X displacements of tower points, and stress data at sensors 5–8 are selected for the training model.

3.2 Establishing the Displacement Models

3.2.1 Designing the ANN Model for the Target Point

The ANN with the BP algorithm is taken to establish the displacement models. The training function is sigmoid, and supervised training is adopted. The ANN is designed with an input layer, one hidden layer, and an output layer. To select the number of neurons in the hidden layer, train the network with the number of neurons increasing from 1 to 40. The number of neurons selected will have the smallest $RMSE$. With the above determination, the number of neurons in the hidden layer are respectively 30, 7, and 4 for X -, Y - and Z -directions. The acquisition data are divided into two data sets: The training data set includes 864 data in 6 days; the other data set includes 144 data in 1 day which are used for establishing displacement models. The training data set is divided into three parts including 70% for training, 15% for validation, and 15% remaining data for the testing step.

3.2.2 Training the ANN Model

The designed ANN model was trained to get the most appropriate model with the results coming out as given in Table 3. It can be seen that the MSE value in all directions is very small, and the R^2 value is much closed to 1. It can be concluded that the training model is highly accurate and reliable.

Table 3 Results of the raining network

Displacement direction	R^2	MSE (m^2)
X	0.962	5×10^{-7}
Y	0.995	4×10^{-7}
Z	0.997	5×10^{-6}

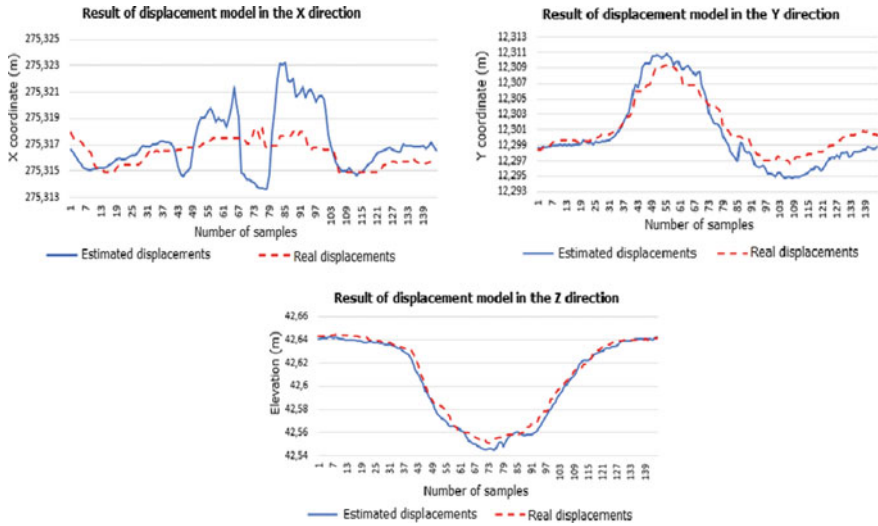


Fig. 2 Comparing estimated displacement and actual one

3.2.3 Establishment of the Displacement Models

After the training process, the displacement models in 3D of the center main span were established by using 1 day of monitoring data. The output displacements were then assessed by comparing them to the real monitoring data and assessing the *RMSE* criterion. Figure 2 shows the comparison between the real observation data and the estimated displacements in three directions. It can be seen that there is a good coincidence between estimated displacements and the real data along to *Y*- and *Z*-directions, especially in the trend of displacements. However, there is a difference between the estimated displacement and the actual one along to *X*-direction. This can be understood that the target bridge is a symmetric structure, thus the displacement of the *X*-direction of the center main span is very small (equal to 0 in theory), and displacement model along the *X*-direction is not necessary to build.

To evaluate the accuracy of the bridge displacement models, calculate the *RMSE* values in the *X*-direction by ± 0.002 (m), *Y*-direction by ± 0.002 (m), and ± 0.003 (m) in the *Z*-direction. It means that the displacement models have high accuracy.

4 Conclusion

- Pre-processing data is an important step for actual monitoring data to clear the abnormal data in order to get higher accuracy in establishing the displacement models.

- The ANN model showed its effectiveness in establishing displacement models. Furthermore, correlation analysis is important to define the correct impact factors on the target data. The displacement models established by using the ANN model have high accuracy and reliability. Especially, the displacement model along to Z-direction of the cable-stayed bridge has high accuracy even though its displacement amplitude is very large as compare to other directions.

References

1. Zhou HF, Ni YQ, Ko JM (2010) Constructing input to neural networks for modeling temperature-caused modal variability: mean temperatures, effective temperatures, and principal components of temperatures. *Eng Struct* 32:1747–1759
2. Kaloop M, Hu JW (2015) Optimizing the de-noise neural network model for GPS time-series monitoring of structures. *Sensors* 15(9):24428–24444
3. Mazurov B, Zarzoura F, Hassan M (2017) Study of suspension bridge deformation using neural network. *Act Issues Mech Eng AIME* 133:490–494
4. Moon HS, Ok S, Chun P, Lim YM (2012) Artificial neural network for vertical displacement prediction of a bridge from strains (Part 1): girder bridge under moving vehicles. *Appl Sci* 9(14):2881
5. Nguyen TL, Ho TLH, Le VH (2018) Study to evaluate the accuracy of vertical cable-stayed bridge movement monitoring data by GPS-RTK measurement technique. *Transp Commun Sci J* 67:41–48
6. Pham QK (2019) Research on application of artificial neural network to predict settlement of hydropower works. *J Mining Earth Sci* 60(4):59–65
7. Nguyen TL, Ho LTH, Nguyen HH (2019) Research and application of artificial intelligence (AI) to build a model to predict vertical displacement of cable-stayed bridges. *Transp Commun J* 14:72–77
8. Nguyen TL, Ho LTH, Nguyen HH, Le VH (2021) Research on application of neural network to recover GNSS data in cable-stayed bridge displacement monitoring. *Transp Commun J* 140:67–71
9. Science and Technology Publishing House (2009) Huu Duc Duc Pham: neural networks and applications in automatic control. Science and Technology Publishing House, Hanoi
10. Nippon Koei Co. LTD, Chodai Co, LTD & Tedi South (2010) Summary of technical report on design of Can Tho bridge structure monitoring system
11. Van Le H, Nishio M (2015) Time-series analysis of GPS monitoring data from a long-span bridge considering the global deformation due to air temperature changes. *J Civil Struct Health Monit* 5(4):415–425
12. Ho LTH, Le VH (2017) Research on the correlation between wind, temperature and displacement of some locations on can Tho bridge. *Transp Commun Sci J* 54:36–42
13. Le TD, Le HV, Nguyen LT, Nguyen TKT, Le DT (2020) Application of correlation and regression analysis between GPS-RTK and environmental data in processing the monitoring data of cable-stayed. *J Mining Earth Sci* 61(6):59–72

Filtering Outliers in GNSS Time Series Data in Real-Time Bridge Monitoring



Ngoc Quang Vu and Van Hien Le

Abstract Real-time GNSS data plays a crucial role in structural health monitoring and early warning in bridge displacement monitoring. Outliers in the range of observations may lead to wrong assessments and maintenance plans. However, outliers are un-avoiding in GNSS time series data caused by various reasons and need to remove for further steps of analysis. The paper studies the ability to filter outliers of two algorithms, including moving average and moving median with different sizes of moving windows. At the same time, the paper also compares the sensitivity of both algorithms with the same set of data and moving windows. The study uses real-time displacement data from P5U GNSS devices of the CHC navigation brand in Dachongyong Bridge, Naning province, China. The results show that these two algorithms can be applied for filtering outliers, and the sensitivity is compared together as well.

Keywords Filtering · Outliers · Time series data · GNSS data · Monitoring

1 Introduction

The development of global navigation satellite systems leads to an increase in the number of satellites in the sky. Therefore, a rover can get data from 40 to 50 satellites for each epoch [1]. Along with that combined processing techniques have also been significantly improved to increase the accuracy of the positioning results, and expand the GNSS applications [2, 3]. Regarding the monitoring field, a range of GNSS applications had been listed in the work [4] including displacement monitoring of dams, landslides, towers, chimneys, high-rise buildings, or long-span bridges [4–6]. GNSS plays a key role in assessing the safety status of the bridge [6, 7]. If the results

N. Q. Vu (✉)
University of Transport Technology/UTT, Hanoi, Vietnam
e-mail: quangvn@utt.edu.vn

V. H. Le
University of Transport and Communications/UTC, Hanoi, Vietnam

© The Author(s), under exclusive license to Springer Nature Singapore Pte Ltd. 2024
T. Nguyen-Xuan et al. (eds.), *Proceedings of the 4th International Conference on Sustainability in Civil Engineering*, Lecture Notes in Civil Engineering 344,
https://doi.org/10.1007/978-981-99-2345-8_67

657

consist of big errors, operation, and maintenance schedules will be impacted [2] and lead to huge consequences for the economy and society. The first requirement for further analysis and assessment steps is a “clean” data set. Generally, time series data may include linear displacement, cyclic displacement (periodic displacement), and consist of noises (white and color noises), and (jump values) [8]. GNSS technology will be the main solution for determining linear displacement, and accelerometer sensors are the main method to determine periodic displacement. However, linear and periodic displacement always consists of various noises, and combining GNSS and sensors is a good choice for structural health monitoring [9].

For the accuracy analysis and assessment of the structure, the first requirement is detecting and removing outliers in the range of observation. Outlier definition depends on the assumptions regarding data structure and the detecting method applied [10–12]. Thus, outliers are the observations that differ from the rest of the data. There is no hard standard for the static threshold for all data sets in the geodesy field. Instead, the magnitude of the threshold is determined by several criteria including data characteristics, required accuracy, and data processing scenarios [13]. When the data set is big enough, the range of observations will follow the bell curve. In this model, the lower threshold the more observations will be removed.

Based on the above analysis and the reality of using GNSS technology for real-time bridge monitoring, the study research, and approaches outliers filtering with moving average and moving median algorithm to assess the ability to detect outliers, and their sensitivity as well. This is the first step to producing a clean data file for further analysis such as determining frequency, interpolating, or extrapolating, and predicting displacement trends.

2 Sliding Window and Algorithms

The concept of the sliding window is defined in the study [10], for time series data in T time and M length, subsequences can be extracted using a sliding window of n size over T . This can be explained as follows: From a range of the original data, by selecting a window size and an applied threshold for filtering outliers, a subrange of observations can be created, and a clean data set then is obtained. This is fundamental for selecting moving window sizes in GNSS time series data. The moving average and moving median were applied in some studies and predictions in which data have seasonal and trending characteristics. These two algorithms were applied for filtering outliers with TEC data, the sliding window size was 30, and the threshold was 2.5 at Bako IGS station. The results showed that the sliding median algorithm has a better sensitivity [8].

The moving average algorithm is as follows:

$$\bar{Y}_i = \frac{y_n + y_{n-1} + \cdots + y_{M-(n-1)}}{M}, \quad (1)$$

where

n the number of observations

M Sliding window size.

The moving median algorithm: Moving median is one of the nonlinear non-recursive outlier filtering. For a range of observations and each sliding window M , the observations will be rearranged [13], and the center measurement is the median like the following.

$$x = [48 \ 55 \ 35 \ 51 \ 60 \ 47 \ 75 \ 55 \ 76 \ 66 \ 87 \ 102 \ 90 \ 135 \ 168].$$

This series is now sorted in increasing order to determine the median value. This operation is a nonlinear one because the ordering of the data are interchanged. The newly sorted list looks like $x_{\text{sort}} = [35 \ 47 \ 48 \ 51 \ 55 \ 55 \ 60 \ 66 \ 75 \ 76 \ 87 \ 90 \ 102 \ 135 \ 168]$.

For both algorithms, the *standard deviation* will be used for detecting outliers.

3 Data and Result Analysis

3.1 Data

The study uses GNSS monitoring data of the Dachongyong river bridge, Naning province, the total length of the bridge is 888 m, with three main spans, designed with a high and a low tower, concrete cable-stayed bridge. The Northern tower is 138 m, and the Southern tower is 103.5 m. GNSS monitoring technology is used to monitor the surface displacement of the bridge in real time and determine the deformation status and geometric alignment, which provides data support for the analysis of the study of the relationship between the pylon displacement and environmental changes (such as temperature and wind), structural health and safety status of the bridge. Meanwhile, this project will provide a data source for displacement monitoring of cable-stayed bridge in main channels, and it will monitor the safety of the bridge structure in real time to provide early warning. DCQ01 is on the Northern tower. Data were extracted over 105 days from March 2, 2022, to the end of June 14, 2022, with 1646 observations for each monitoring point (Fig. 1).

3.2 Result Analysis

Based on the above theory, the real-time GNSS monitoring data were filtered outliers by self-developed software using moving average and median algorithms. The outliers are marked on the line graph (Figs. 2 and 3).



Fig. 1 Monitoring point on Dachongyong (CHC permission)

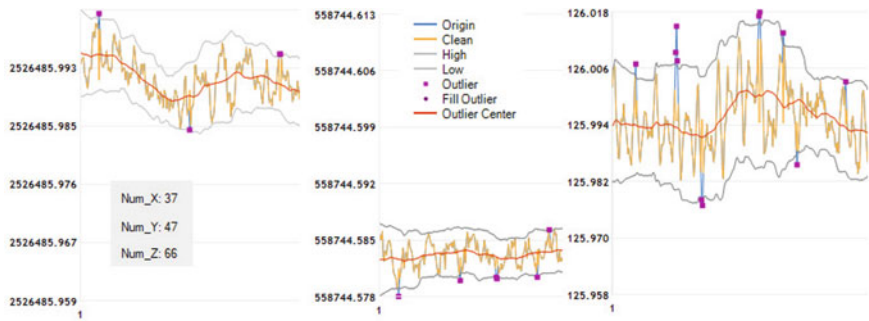


Fig. 2 X, Y, Z outliers of DCQ01—moving average

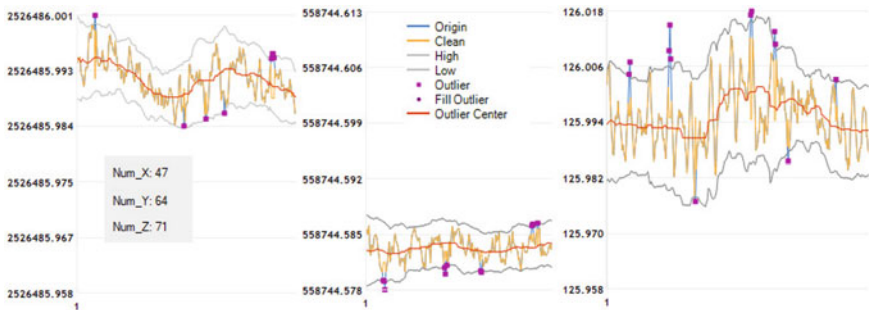


Fig. 3 X, Y, Z outliers of DCQ01—moving median

Taking a look at Figs. 2 and 3, the number of outliers in the X, Y, and Z time series data of the DCQ01 monitoring point detected by the moving median is more than the moving average with the same threshold 2 and same sliding window size 24 (the number of observations in a day/sample interval is 01 h). At the same time, clean

data sets will be created, and the displacement of the clean data set will be compared to the original displacement (Figs. 4, 5, 6, 7, 8 and 9).

Figures 4, 5, 6, 7, 8 and 9 display the variation amplitude of three components X, Y, Z and compare them to the original displacement. For better observation, the max and min values are in Table 1.

The range between the max and min values of the moving average and the moving median is smaller than the original data. The difference between the moving average and moving median is small. However, the moving median is more sensitive than the moving average base on the number of detected outliers.

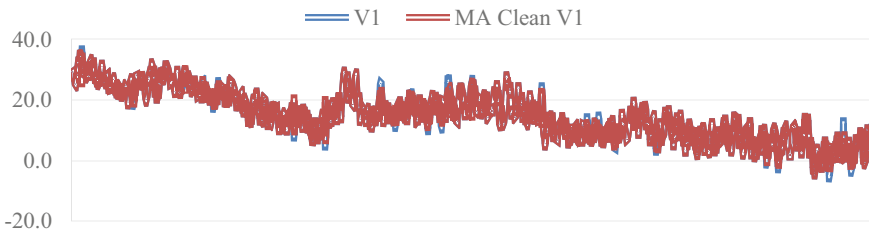


Fig. 4 Original data and MA clean data (X)

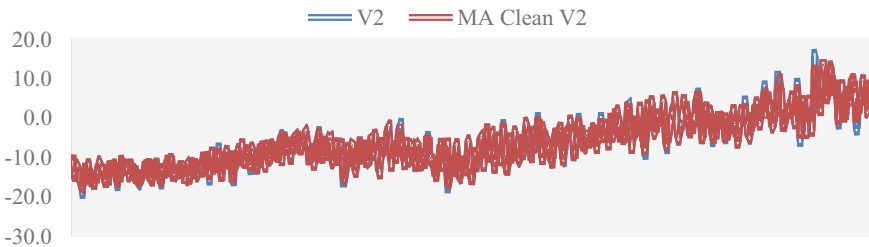


Fig. 5 Original data and MA clean data (Y)

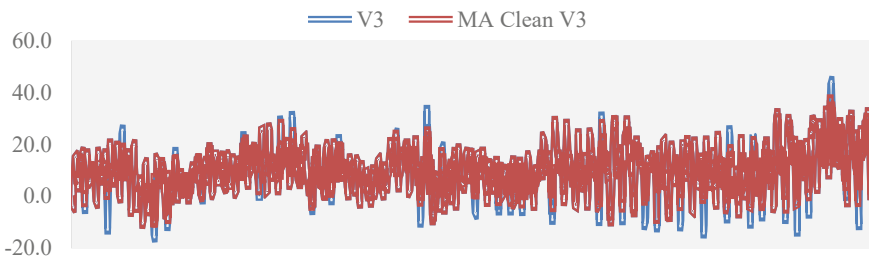


Fig. 6 Original data and MA clean data (Z)

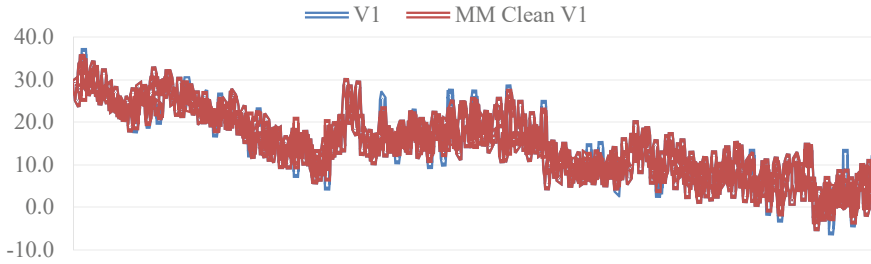


Fig. 7 Original data and MM clean data (*X*)

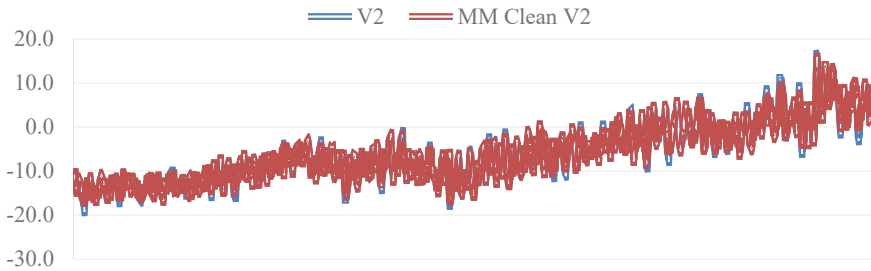


Fig. 8 Original data and MM clean data (*Y*)

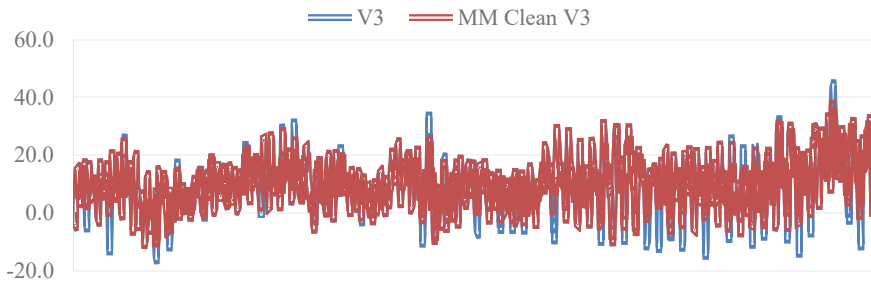


Fig. 9 Original data and MM clean data (*Z*)

Table 1 Compared to the original data

	Original			Moving average			Moving median		
	<i>X</i>	<i>Y</i>	<i>Z</i>	<i>X</i>	<i>Y</i>	<i>Z</i>	<i>X</i>	<i>Y</i>	<i>Z</i>
Max	36.0	16.0	44.1	34.5	14.1	37.1	34.5	15.4	37.1
Min	- 5.2	- 18.9	- 15.6	- 4.2	- 17.8	- 10.3	- 4.2	- 16.7	- 10.3

4 Conclusions and Discussion

The paper investigated two outlier filtering algorithms including the moving average and moving median algorithm to apply for GNSS time series data in the bridge monitoring field. The initial results are basic toward real-time outliers filtering in displacement monitoring using time series data.

The results show that the moving median is a robust statistic and more sensitive than the moving average in outlier filtering while the moving average is affected by noise in time series data.

Two algorithms in the study need to be compared with other algorithms and conducted with different sample intervals, sliding window sizes, and thresholds.

References

1. Yu J, Meng X, Yan B, Xu B, Fan Q, Xie Y (2019) Global navigation satellite system-based positioning technology for structural health monitoring: a review. *Struct Control Heal Monit* 27:1–27
2. Xi R, Xiaolin M, Jiang W, He Q, An X (2019) Performance analysis of bridge monitoring with the integrated GPS, BDS and GLONASS 15–17
3. Vũ ĐC, Vũ NQ, Lương ND, H ăng HT, Đình Trọng T (2021) Nghiên cứu các phương án xử lý kết hợp số liệu của nhiều hệ thống định vị vệ tinh trong mạng lưới GNSS. *Tạp chí Khoa học Công nghệ Xây dựng* 15:156–166
4. Im SB, Hurlebaus S, Kang YJ (2013) Summary review of GPS technology for structural health monitoring. *J Struct Eng* 139:1653–1664
5. Stiros SC (2021) Gns (Gps) monitoring of dynamic deflections of bridges: structural constraints and metrological limitations. *Infrastructures* 6:1–14
6. Roberts GW, Brown CJ, Ogundipe O (2010) Monitoring bridges by GNSS. In: *Proceedings of the XXIV FIG international congress 2010 facing challenges: building capacity*, pp 11–16
7. Wang X, Zhao Q, Xi R, Li C, Li G, Li L (2021) Review of bridge structural health monitoring based on GNSS: from displacement monitoring to dynamic characteristic identification. *IEEE Access* 9:80043–80065
8. Thi NL, Männel B, Jarema M, Seemala GK, Heki K, Schuh H (2021) Selection of an optimal algorithm for outlier detection in GNSS time series. *EGU Gen Assem* 2021:5194
9. Yunus MZM, Ibrahim N, Ahmad FS (2018) A review on bridge dynamic displacement monitoring using global positioning system and accelerometer. *AIP Conf Proc* 1930:2–8
10. Yu Y, Zhu Y, Li S, Wan D (2014) Time series outlier detection based on sliding window prediction. *Math Probl Eng* 2014:1–14
11. Blázquez-García A, Conde A, Mori U, Lozano JA (2021) A review on outlier/anomaly detection in time series data. *ACM Comput Surv* 54:1–31
12. Ben-Gal I (2005) *Outlier detection. Data mining and knowledge discovery handbook: a complete guide for practitioners and researchers*. Kluwer Academic Publishers, New York, pp 1–16
13. Charles DG, Paul RW (2006) *Adjustment computations*. John Wiley & Sons, INC., Amsterdam

Safety Warnings for Technical Status of Port Structure by Automatic Monitoring in Vietnam



Thi Bach Duong Nguyen, Van Hien Le, and Duc Cong Tran

Abstract The GNSS–RTK technique has been studied and applied to monitor the displacement of buildings in structural health monitoring systems (SHMs), especially with large-scale works such as super high-rises or bridges with long spans and special construction structures. Monitoring data obtained, including short-term and long-term (continuous), can be used to study, analyze the health status of the structure, detect damage, and predict future structural displacements. In port construction monitoring or maritime safety, the structural displacement or stability monitoring system has also been researched and initially applied by authors. However, the studies are still local, focusing on a few specific objects in a short observation period, not to mention the automatic warning of the risk level. In other words, people must also continuously monitor the data to detect risks when detected promptly. The article delves into the experiment of automatic safety warning monitoring of harbor works with whistles/lights or messages to solve the above problems. This is a new solution suitable for the 4.0 technology revolution era. Primarily, it is a valuable solution to monitor, evaluate/diagnose the stability of the port structure in case the construction is different from the design, in terms of operation and maintenance, to develop the port sustainably, safely, and effectively and minimize environmental impact.

Keywords Automatic monitoring · GNSS–RTK techniques · Stability condition of a port structure · Damage detection · Port structure displacement

1 Introduction

Nowadays, the methods of field experimentation, laboratory testing for quality assessment, and assessment of the stability of port structures are few, instantaneous, and not automatically proactive. Some previous research studies on monitoring of reinforced concrete wharves, such as using Structural Health Monitoring System

T. B. D. Nguyen (✉) · V. H. Le · D. C. Tran
University of Transport and Communications/UTC, Hanoi, Vietnam
e-mail: ntbachduong@utc.edu.vn

© The Author(s), under exclusive license to Springer Nature Singapore Pte Ltd. 2024
T. Nguyen-Xuan et al. (eds.), *Proceedings of the 4th International Conference on Sustainability in Civil Engineering*, Lecture Notes in Civil Engineering 344,
https://doi.org/10.1007/978-981-99-2345-8_68

665

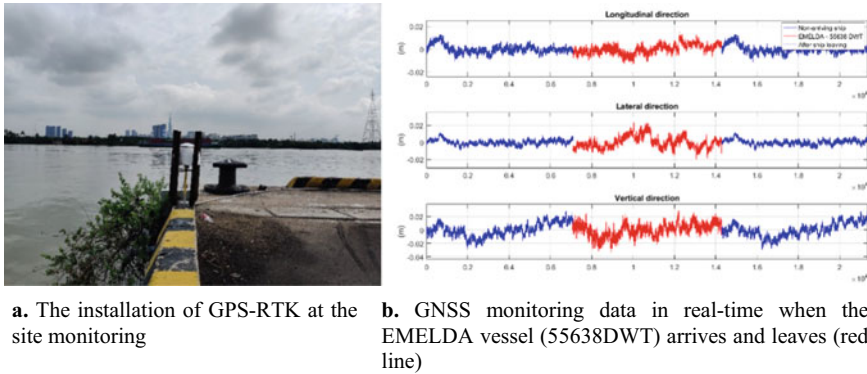


Fig. 1 Example of real-time monitoring displacement of a wharf

(SHMs) and material testing to assess port structures [1], using inclinometers to monitor factors of high-pile port structures to detect damage [2], establishing a real-time monitoring system for landing pier-type port structure by using some FBG sensors [3]. However, no research is working on global displacement monitoring of port structures using the GNSS-RTK technique. The GNSS-RTK system is a method of regularly monitoring and measuring the displacements of the construction structure to ensure the general stability conditions and the technical condition of the works [4]. Previous studies on applying the GNSS-RTK system have not shown automatic warnings of the risk level (see Fig. 1). In other words, people must always continuously monitor the data for timely detection [4–6]. The following section dives into constructing a real-time data collection management program using mobile devices and directly processes the collected data to warn of risky situations automatically. This application helps ports to monitor safety when operating in adverse conditions due to natural disasters, incidents, or receiving large ships to reduce load. The GNSS-RTK system, when integrating risk situations and threshold displacement, will ensure timely automatic warnings by sound, light, and even messages via the Zalo application. It is supported to prevent and Assurant sustainable development of the environment. The research topic is also a premise for developing and applying artificial intelligence (AI) technology in construction monitoring, ensuring safety and benefits for operators and observers in all cases.

2 Requirements of Monitoring System Establishment for Assuring Port Safety

The principle of GNSS technology is to observe satellite signals from space. Thus, the location of GNSS points needs to contain some requirements such as clearing sight to the space and avoiding electrical stations. In the Structural Health Monitoring

field, GNSS-RTK is applied to get displacement measurements of specific points that GNSS sensors need to operate 24 h daily and daily. Therefore, in the case of port automated monitoring, there are some requests following for setting up a GNSS system:

- Inspecting on the port side to investigate the locations of monitoring points, for instance, locations that have a high risk of movement or cracking by loading effects, not be affected by exploiting equipment on the port site, and so on.
- The installation location is airy and has sufficient viewing angle to space according to the satellite positioning measurement requirements.
- Each GNSS location point needs to be supplied power for operating 24 h per day.
- GNSS sensors need to be safe during their operation.

3 Integrated Program for Data Management and Processing

The integrated program to manage the reception and processing of signals for automatic warning in case of structural risks consists of four separate modules:

- Acquiring GNSS signals from all points and transfer to saving on the server.
- Processing and transferring data
- Web data viewing and alert setting
- Online warning module.

Figure 2 shows the integrated program which expresses how each module works. Here, modules (1) and (2) are common modules of the GNSS-RTK program in GNSS measurement survey. Modules (3) and (4) are the integrated modules that created for automated monitoring of port.

4 Hypothetical Warning Test Scenario

The integrated program of the GNSS monitoring system is then tested on the warning case. A GNSS monitoring system is created, including a base station and two other rover stations. Warning equipment was created to connect to the monitoring system via a wireless connection such as Wi-Fi or 3G/4G. The integrated program is run on a website that can be accessed by computer or mobile. Figure 3 shows a real port doing the warning test in case a large ship arrives, and Fig. 4 shows the warning equipment arranged on the port site. Figure 5 shows the warning configuration for real-time observation, and Fig. 6 shows the real-time observation on the computer. Furthermore, when the displacements of the monitoring point observed by the GNSS receiver move over the threshold, then the warning signals come out by a light and a sound. Figure 7 shows the warning messages sent to the Zalo account so that the

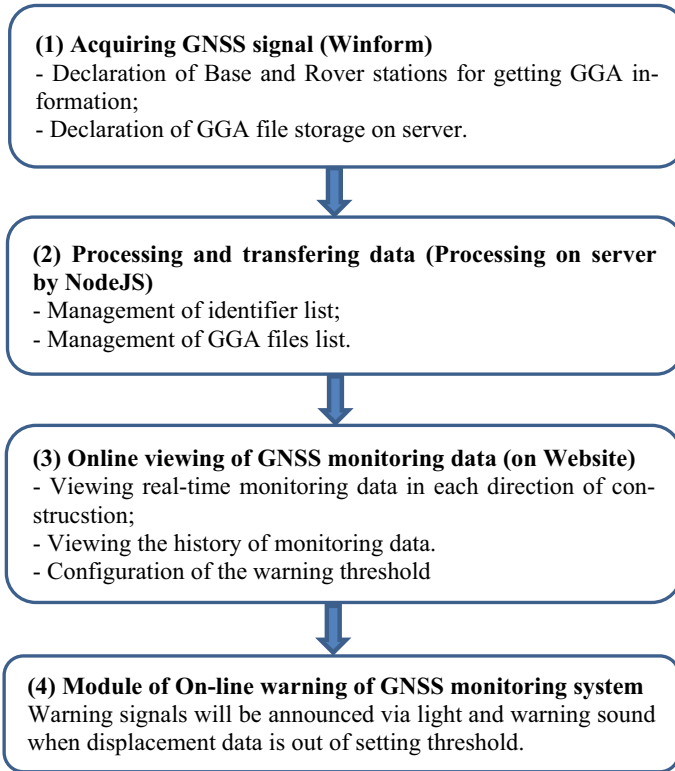


Fig. 2 Strategy of the integrated program for data management and processing

manager can get a warning signal from the system even if not in the monitoring office. And Fig. 8 shows the real-time observation on a mobile phone.

Overall, Fig. 9 expresses sample monitoring data of a real port with 1 Hz sampling frequency, and Fig. 10 shows a warning case of a test by an effect of crane loading. When data comes out of the given threshold, the system makes a warning immediately by light and whistle.

5 Conclusion—Recommendation

A GNSS–RTK monitoring system is a tool for application in monitoring displacement and stability of wharf structure with accurate results. It is a valuable tool for monitoring the stable conditions of the berth and checking the quality of the pier structure. Users can monitor regularly and continuously. The cost of equipping the GPS-RTK system is low and easy for new or under-construction projects. It is entirely feasible to apply to ports in Vietnam. The above-integrated management program

Fig. 3 Real port for a testing warning system

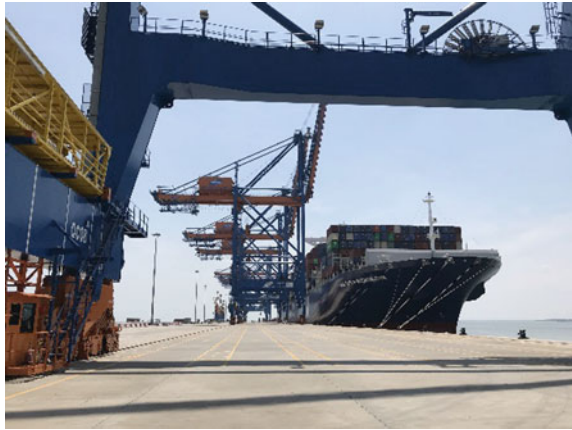


Fig. 4 Warning equipment



Fig. 5 Setting the warning configuration

helps to automatically alert by sound, light, and message directly to the mobile. It helps port businesses and state management units proactively respond in adverse situations caused by natural disasters or incidents or receive large ships to reduce the load in and out of the port. The hypothetical warning test program shows the feasibility of the system.

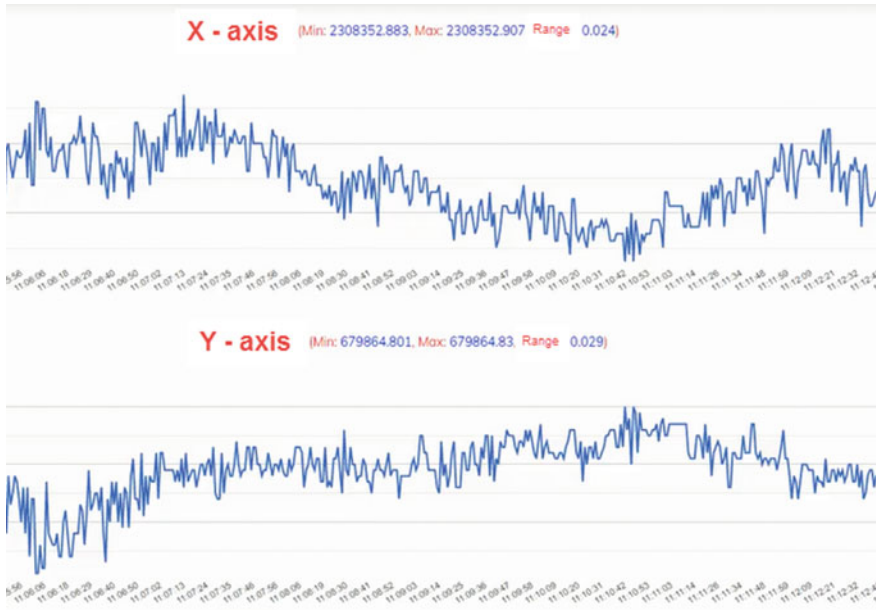


Fig. 6 Observing GNSS monitoring data in real time on PC

Fig. 7 Messages on Zalo app (mobile)

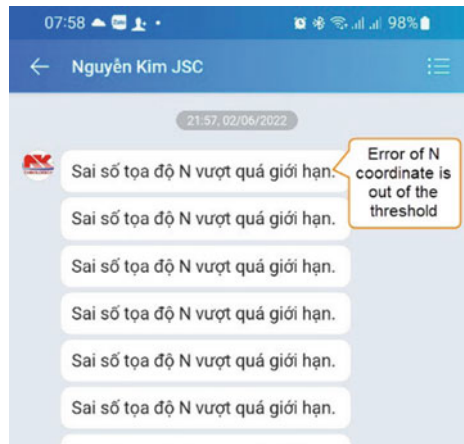


Fig. 8 Real-time observation on mobile

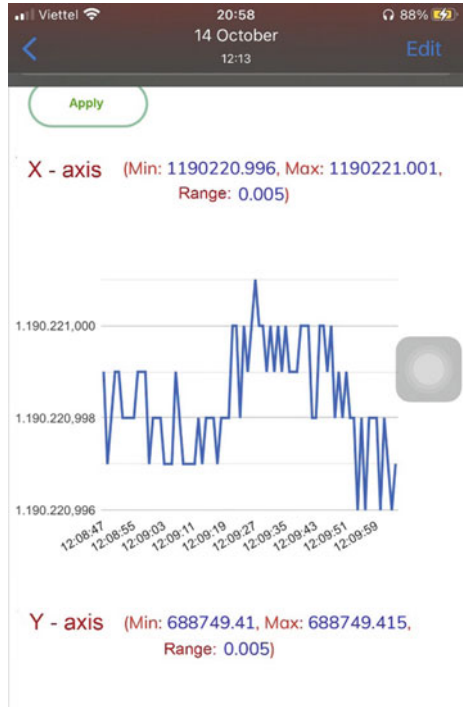


Fig. 9 Sample monitoring data

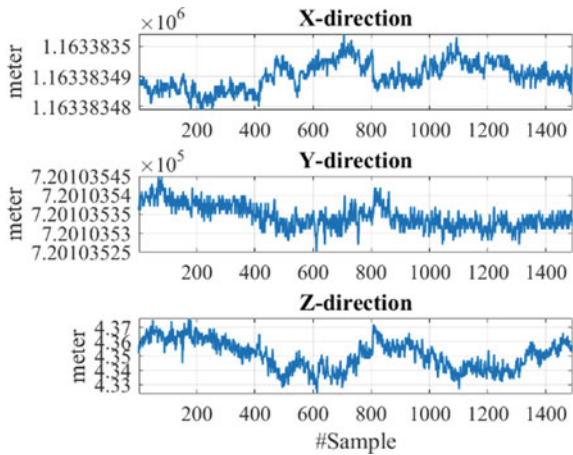
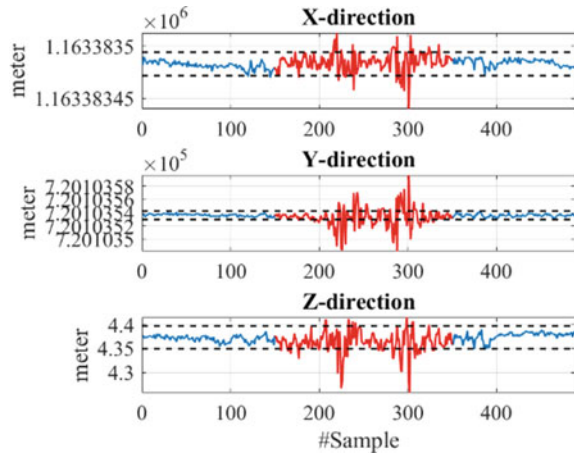


Fig. 10 Warning case of a test by an effect of loading: the red line is under loading; the blue line for non-loading; and the dash-dark lines are the threshold



References

1. Yann L et al (2019) Monitoring of a reinforced concrete wharf using structural health monitoring system and material testing. *J Mar Sci Eng* 7(4):84. <https://doi.org/10.3390/jmse7040084>
2. Zhang H, Jiang Q, Lai L, Shi X (2011) Case based structural health monitoring analysis of Chun Xian wharf in Hangzhou. In: Proceedings of the 2011 international conference on electric technology and civil engineering (ICETCE). <https://doi.org/10.1109/ICETCE.2011.5775795>
3. Jo BW, Jo JH, Kim JH, Khan RMA (2018) Development of real-time condition assessment method for landing pier-type wharf structure monitoring system. *IOSR J Mech Civil Eng* 15(1):01–07. <https://doi.org/10.9790/1684-1501040107>
4. Bach DNT, Van HL, Duc CT (2020) Research on automated monitoring to access the port structure inspection in operating offloading vessel test. *Lecture Notes in Civil Engineering (LNCE, volume 145)*, ISSN 2366-2557 (ISSN 2366-2565: electronic), ISBN 978-981-16-0052-4 (ISBN 978-981-16-0053-1 eBook). Springer Nature Singapore Pte Ltd, New York. <https://doi.org/10.1007/978-981-16-0053-1>
5. Duong NTB, Hoan ND (2016) Research on overview of structure, evaluation and maintenance solutions for ports in Hai Phong fairways, Viet Nam, bridge maintenance, safety, management, life-cycle sustainability and innovations, ISBN: 9780429279119, p 2059
6. Le HV, Nishio M (2015) Time-series analysis of GPS monitoring data from a long-span bridge considering the global deformation due to air temperature changes. *J Civil Struct Health Monit* 5(4):415–425

Opportunities and Challenges of Digital Twins in Structural Health Monitoring



Minh Quang Tran, Hélder S. Sousa, Nhung Thi Cam Nguyen,
Quyet Huu Nguyen, and José Campos e Matos

Abstract Digital twin (*DT*) is one of the most modern and promising technologies in realizing smart manufacturing and implementing Industry 4.0. *DT* offers opportunity to integrate the physical world with digital world with a seamless data source. Civil engineering industry, in general, is facing many challenges in the process of digital transformation to improve efficiency and technology to meet the current growth rate of the economy. *DT* technology has the potential to transform and improve the exploitation and management of infrastructure in civil engineering, especially in the service phase. Based on *DT* model, managers and maintenance operators can test different scenarios, improve efficiency, and make accurate decisions in maintenance of the structure, leading to reduction of management and other regular monitoring costs, as well as accurate prediction of risks during the lifespan of the infrastructure. This study presents advances in digital twin implementations in structural health monitoring. This presents the opportunities and challenges of the digital twin in structural health monitoring with current technologies and future directions.

Keywords Digital twin · Structural health monitoring · Opportunities and challenges of *DT*

1 Introduction

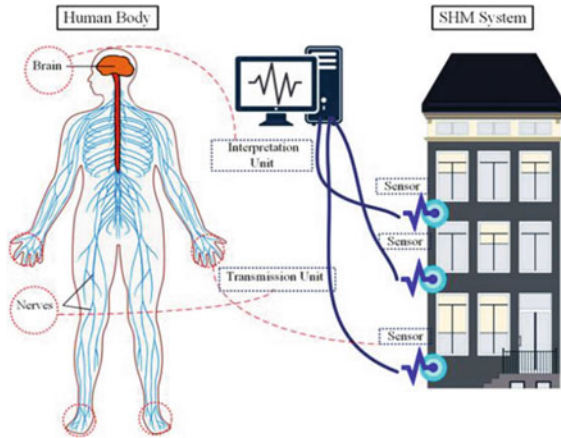
Early warnings, regular maintenance, inspection, and emergency response plans are essential to ensure safety throughout the lifecycle of critical infrastructure. Stemming from the above requirements, structural health monitoring (*SHM*) systems have been widely deployed and received much attention from researchers in the field of civil engineering around the world. Through the data collected during the operation of the

M. Q. Tran (✉) · H. S. Sousa · J. Campos e Matos
Department of Civil Engineering, ISISE, University of Minho, Guimarães, Portugal
e-mail: minhtq@uct.vn

N. T. C. Nguyen · Q. H. Nguyen
University of Transport and Communications, Hanoi, Vietnam

© The Author(s), under exclusive license to Springer Nature Singapore Pte Ltd. 2024
T. Nguyen-Xuan et al. (eds.), *Proceedings of the 4th International Conference on Sustainability in Civil Engineering*, Lecture Notes in Civil Engineering 344,
https://doi.org/10.1007/978-981-99-2345-8_69

Fig. 1 Comparison between the human body and the *SHM* system [9]



infrastructure by sensors, the change in the properties of the constructions will serve as the basis for diagnosing the structural health [1–4].

In the past, when sensor technology was not yet developed, *SHM* was often performed based on geodetic engineering and machinery [5–8]. *SHM* is based on the characteristics of geometrical factors such as settlement, deformation, and displacement, among others of structures.

Monitoring the response of structures and detecting possible failures to improve their performance and reduce maintenance costs are considered to be a main goal in *SHM*. From the modern point of view, the foundation of *SHM* includes existing techniques for damage identification, diagnosis, and prediction of possible risks to the structure using advanced automated techniques, smart sensors, and artificial intelligence. Speckmann and Henrich suggested that *SHM* could be described through an analogy with the human nervous system (Fig. 1) [9].

SHM is an inverse problem in which damage is identified through data collected from sensors (Fig. 2). *SHM* is a technology to automate the inspection process in order to assess and evaluate the health condition of structures in real-time or at specified time intervals. There are four different sequential levels: detection, identification, quantification, and prediction. The higher levels of *SHM* are, the more complicated *SHM* technology. The levels of *SHM* have been studied and classified as follows:

- Level 1: Identification: determine the existence of damage on the whole structure.
- Level 2: Locate: find out the damaged part and location.
- Level 3: Evaluation: determine the damage level of various components
- Level 4: Assess the life and durability of the structure on the basis of detected damage.

Currently, research often focuses on goals at levels 1–3. Yan et al. [4] propose a wavelet-based method of the free vibrational responses of structures to accurately determine the location of the damage. The digital twin with many advantages being

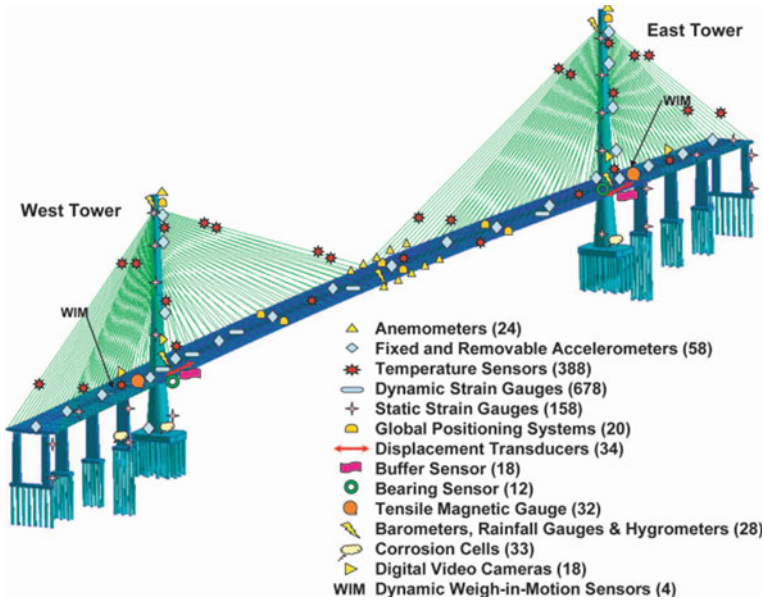


Fig. 2 SHM monitoring system in Stonecutters Bridge [10]

able to integrate the physical world with the virtual world is one of the potential techniques for development, covering all levels of SHM. The DT is capable of accurately reflecting the behavior of the real object and continuously updating throughout its lifecycle. As a result, the digital twin has great potential in the field of SHM.

2 Digital Twins

2.1 Digital Twin Concept

DT insight was first introduced in 2003 by Michael Grieves as a concept for Product Lifecycle Management [11]. However, at that time, DT only consisted of a physical object, virtual counterpart, and connection, with no specific description and exploration. The importance of DT is increasingly recognized by both academia and industry. According to Gartner [12], digital twins is the leading strategic technology trend in the Hype Cycle for Emerging Technologies (Fig. 3).

The digital twin must have a physical system with a digital representation or virtual model of that system, and the digital model reflects the physical system. Reflection and interoperability can only be achieved through data exchange, which requires sensors to be installed on the physical system to collect and transmit these

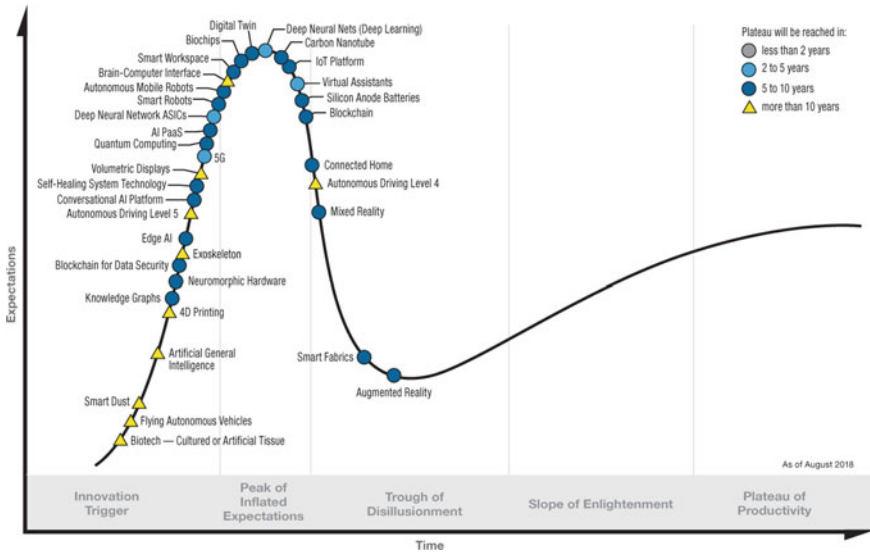


Fig. 3 Hype cycle for emerging technologies [12]

data through the network to the virtual model. Figure 4 presents a general theoretical framework of DT.

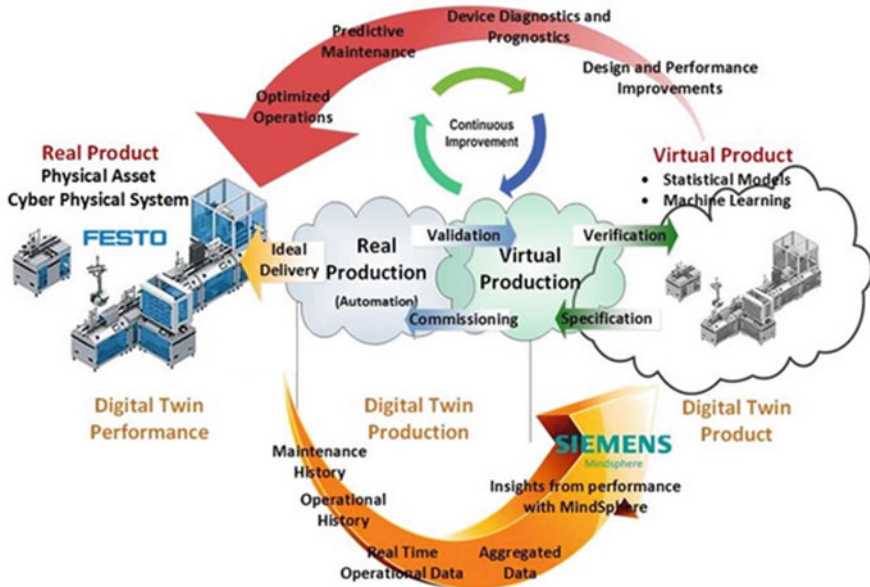


Fig. 4 General framework of a DT

2.2 Properties of Digital Twin

There are many views on the components of the digital twin expressed under various definitions. However, essentially digital twin must consist of five parts: (i) the physical part, (ii) the virtual part, (iii) the connections, (iv) the data, and (v) the services (Fig. 5).

One of the main parts of a digital twin is the real part of the object (the physical part). The physical part includes all the physical entities that appear in the real world. The physical objects in the digital twin are capable of perceiving the outside world. In other words, like the human senses, the real part of the digital twin is equipped with sensor systems to get real data. These sensors generate data about various aspects of a physical object’s activity, such as energy output, temperature, weather conditions, and more. These data are then forwarded to a processing system and applied to the digital twin.

The virtual part of the digital twin is virtual models created by digital transformation that are reflected by the real object. The virtual part is often built and simulated through finite element programs that incorporate information management using other tools. Different from conventional simulation models, this model contains all the information about reality. The virtual part is always updated and changed according to the physical part.

The connection and data flow between the real part and the virtual part form a closed loop. In there, the real data are transmitted from the sensor to the virtual part to help the model continuously update attributes. The virtual model also provides predictive cases and possible scenarios, affecting human decisions in the real part. Two parallel data flows coexist, interact, and complement each other. It can be said that the digital models are like a photograph, while the digital twin is like a movie about the whole working process of the real object (Fig. 6).

Reviews show that digital twins can have applications in many areas. Digital twins allow the integration of the real world into the virtual world. In the virtual world, people can perform tasks that are impossible in the real world. Destructive experiments, texture response perceptions, or full lifecycle reviews of an object can be visualized in the virtual world. Not only that, supporting important decisions greatly affects the real audience.

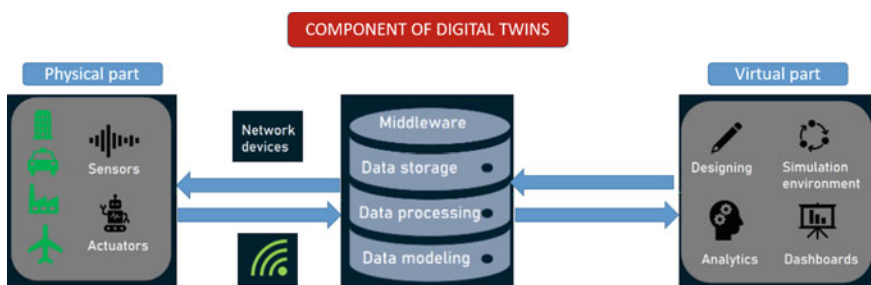


Fig. 5 Components of digital twins

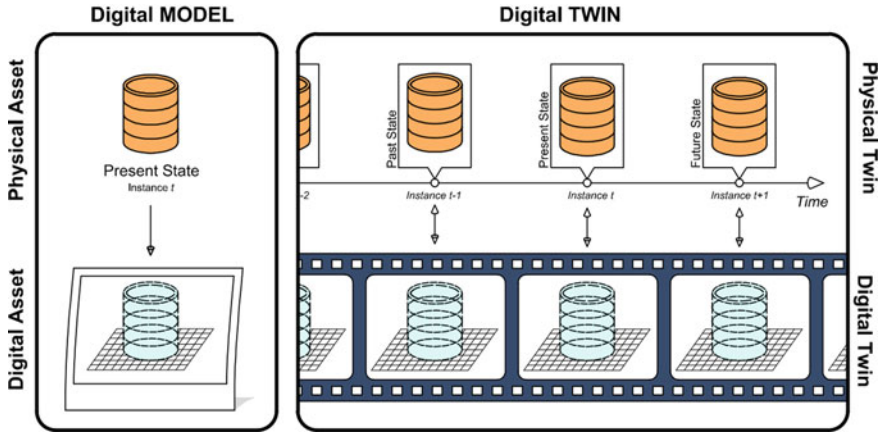


Fig. 6 Distinguishing between digital models and digital twins

3 Opportunities and Challenges of Digital Twins in Structural Health Monitoring

3.1 Opportunities of Digital Twins in Structural Health Monitoring

Digital twin technology is a virtual digital model of an object, but unlike conventional digital simulations, this digital object is very intelligent and has the ability to acquire and analyze large data sources and a variety of actual objects. There is a data flow between the virtual and the actual object, and through the sensors on the actual system, the virtual part is updated so that the system’s state can be monitored in real time. In other words, digital twin technology integrates Artificial Intelligence, Machine Learning and analyzes software with data to create a living digital simulation model that updates and changes as physical objects change. A digital twin continuously learns and updates from multiple sources to describe its near-real-time status, working conditions or location, thereby helping to make accurate diagnoses about the status of the device, and object when any abnormal changes occur. Digital twin helps improve decisions made on real-world objects (such as optimizing aircraft and automobile designs, or automating and increasing production line productivity), thereby improving the actual object itself. At the same time, DT improves itself based on new data collected from real subjects.

Physical objects are an integral part of *DT* because they are data sources from the real world. Technologies implemented in the physical object make the *DT* aware of data such as geometrical shape, physical properties, and mechanical precision. Currently, sensor and measurement technologies deployed for *DT* include *IoT* sensing technology, reverse engineering, image recognition metrology, and particle sensing technology.

The high-fidelity digital twin model contains a lot of complex information. Some must be stored intact; some are just a small part of the process. The data is very large. Therefore, data construction and management technology are quite important in *DT*. Nowadays, in data storage frameworks a large amount of data can be sorted and used correctly (such as *MySQL* database, *HBase* database, and *NoSQL*, among others). In *MySQL*, data are stored as a table. Many rows and columns form a form, and several forms create a database. *HBase* employs the Hadoop Distributed File System (HDFS) as its file storage system, and Hadoop *MapReduce* provides *HBase* with high-performance computing power.

Virtual modeling technologies allow users to visualize specific objects in the *DT*, while helping to manage information about geometry and texture response. Currently, there are many Computer-Aided Design (*CAD*) software that can display the geometric information of a physical object, such as *UG*, *AutoCAD*, *SolidWorks*, and *Creo*. Many physics-based theories/models have been established to reveal the mapping relationship between input and behavior, such as computational fluid dynamics models (*CFD*), finite element modeling (*FEM*) [13].

The available data transmission methods include wired transmission and wireless transmission. Currently, transmission methods using coax cables are being widely used. However, wireless transmission methods including Zig-Bee, Bluetooth, Wi-Fi, ultra-wideband are gradually replacing and becoming more modern. A series of application program interfaces (*APIs*) are commonly used to exchange data between different software to perform data transfer at the software level. Recently, 5G technology can be applied to meet the demand for high data rates, high reliability, high coverage, and low latency.

3.2 Challenges of Digital Twins in Structural Health Monitoring

Currently, building the *DT* framework for structural health monitoring (*SHM*) is incomplete: Although the digital models have been accurate and minimize the difference to the real structure by updating the model based on real data, this model is only a reflection of the actual structure at a moment of the object (similar to a picture in a movie clip). The update over time has not been thoroughly implemented due to the lack of transmission and storage methods. In fact, all things and phenomena in real life are subjected to change over time. These objects are uncertain, constantly changing in physical space. Building digital models in virtual space to reflect realities with high fidelity is a fundamental problem. When there is no consistency between virtual models and real objects, how to define and update them appropriately is very difficult.

The connections between the virtual model (virtual part) and the real part have not been made. Because of the lack of connectivity, the implementation of tasks such as real-time-based control, continuous updating is still difficult. The virtual

structural model uses real-time data of physical entities, and the analysis results are used to guide physical entities in real time. Due to a large amount of data, network latency, and model analysis time, it is difficult for *DT* in structural health monitoring to achieve real-time, bidirectional connectivity.

There have yet to be any standards to assess the reliability of digital twins. Therefore, research directions are scattered. This poses a challenge to a unified standards framework. Although Artificial Intelligence technologies have been integrated (through machine learning algorithms), this is not enough to create breakthroughs in the self-updating of the system. Deploying too many sensors on the structure leads to very expensive. More optimization is needed in data generation and prediction. The data transmission is also one of the problems to be solved in structural health monitoring. Data transmission methods also have a delay. Solutions for deep learning, direct data processing need to be developed. The storage space of *DT* in structural health monitoring is currently not interesting. Most of the raw data collected from real textures after a while become huge and get erased. Solutions for data optimization and noise filtering need to be developed. In *DT* in general, the data seem to be very large, multidimensional, multisource, and heterogeneous. In structural health monitoring, although the data source has been reduced, this is still a challenge for research and application of *DT* in structural health monitoring. The actual data source is too large to be collected on a daily basis. It requires an optimized method, and the raw data need to be converted to filter noise and processed quickly. To ensure reliable and real-time simulation analysis results, we need to develop some fast data analysis methods with high accuracy.

4 Conclusions

This paper presents the opportunities and challenges of digital twins in structural health monitoring. With the explosion of information technology, modern sensor technologies, 5G techniques, and digital transformation, the development potential of digital twins in structural health monitoring is huge. However, there are also many challenges posed in developing a comprehensive digital twin. Integrating and applying new technologies to the digital twin in structural health monitoring will bring many benefits to managers, help sustainable development, and reduce maintenance costs. At the same time, it helps to make accurate decisions based on the scenarios predicted by the digital twin.

Acknowledgements The authors acknowledge the financial support of the project research “B2022-GHA-03” of the Ministry of Education and Training. This work was partly financed by FCT/MCTES through national funds (PIDDAC) under the R&D Unit Institute for Sustainability and Innovation in Structural Engineering (ISISE), under reference UIDB/04029/2020. The first author acknowledges the funding by MIT Portugal Program (MPP) through the MPP2030-FCT Research Grants. The second author acknowledges the funding by FCT through the Scientific Employment Stimulus—4th Edition. Nguyen Huu Quyet was funded by the Master, Ph.D. Scholarship Programme of Vingroup Innovation Foundation (VINIF), code VINIF.2022.ThS.075.

References

1. Kralovec C, Schagerl M, Review of structural health monitoring methods regarding a multi-sensor approach for damage assessment of metal and composite structures. *Sensors* 20(3):826. <https://doi.org/10.3390/s20030826>
2. Salawu O (1997) Detection of structural damage through changes in frequency: a review. *Eng Struct* 19(9):718–723. [https://doi.org/10.1016/S0141-0296\(96\)00149-6](https://doi.org/10.1016/S0141-0296(96)00149-6)
3. Ren W-X, De Roeck G, Structural damage identification using modal data. I: simulation verification. *J Struct Eng.* [https://doi.org/10.1061/\(ASCE\)0733-9445\(2002\)128:1\(87\)](https://doi.org/10.1061/(ASCE)0733-9445(2002)128:1(87))
4. Yan G, Duan Z, Ou J, De Stefano A, Structural damage detection using residual forces based on wavelet transform. *Mech Syst Sig Process.* <https://doi.org/10.1016/j.ymsp.2009.05.013>
5. Encardio-Rite Group, A guide on geodetic survey and monitoring. <https://www.encardio.com/blog/a-guide-on-geodetic-survey-and-monitoring/>
6. Beshr AAA, Structural deformation monitoring and analysis of highway bridge using accurate geodetic techniques. *Engineering* 07(08):488–498. <https://doi.org/10.4236/eng.2015.78045>
7. Nhung NTC, Minh TQ, The effects of ground vibration induced by construction activities of urban railways in Hanoi. *J Mater Eng Struct (JMES)*. [Online]. Available: <https://revue.ummto.dz/index.php/JMES/article/view/2591>
8. Nhung NTC, Minh TQ, Campos e Matos J, Sousa HS, Research and application of indirect monitoring methods for transport infrastructures to monitor and evaluate structural health. Presented at the 2nd international conference on structural health monitoring and engineering
9. Speckmann H, Henrich R, Structural health monitoring [SHM]—overview on technologies under development. [Online]. Available: https://www.ndt.net/article/wcndt2004/pdf/aerospa/563_henrich.pdf
10. Wong K-Y, Design of a structural health monitoring system for long-span bridges. In: *Structure and infrastructure engineering: maintenance, management, life-cycle design and performance.* <https://doi.org/10.1080/15732470600591117>
11. Grieves MW (2003) Virtually intelligent product systems: digital and physical twins. In: *Complex systems engineering: theory and practice*, pp 175–200. <https://doi.org/10.2514/5.9781624105654.0175.0200>
12. Costello K, van der Meulen R, Gartner identifies five emerging technology trends that will blur the lines between human and machine
13. Tuegel EJ, Ingrassia AR, Eason TG, Spottswood SM (2011) Reengineering aircraft structural life prediction using a digital twin. *Int J Aerosp Eng.* <https://doi.org/10.1155/2011/154798>

Damage Detection in Structural Health Monitoring Using a One-Dimensional Convolutional Neural Network—The Z24 Bridge Case Study



Hieu Nguyen-Tran, Dung Bui-Ngoc, Dung Pham-Tuan, Lan Ngoc-Nguyen, Hoa Tran-Ngoc, and Thanh Bui-Tien

Abstract Recently, one of the most significant study areas in civil engineering has been the application of machine learning (ML) to structural damage identification. Traditional statistical pattern recognition methods, such as artificial neural networks (ANNs), are limited to detecting minor damage to bridges. Deep learning algorithms (DLs) extract complicated high-level abstractions, such as data representations, through a hierarchical learning process. Based on comparatively simpler abstractions created at the preceding level of the hierarchy, complex abstractions are learnt at some level. Similar to standard deep learning algorithms, convolutional neural networks (CNNs) are feed-forward ANNs with alternating convolutional and subsampling layers. The main idea is to use the time-series data from the output-only approach as inputs to the one-dimensional convolutional neural network (1DCNN) processing system. A significant benefit is that 1DCNNs have recently been proposed to provide instant monitoring performance at the forefront of structural condition monitoring. The proposed method is validated with the reference data of the Z24 bridge to classify the damage scenario. The results show that the proposed 1DCNN methods exhibit structural defects with excellent accuracy.

Keywords Damage detection · 1D convolutional neural network · Z24 bridge · Time-series analysis

D. Pham-Tuan · L. Ngoc-Nguyen · H. Tran-Ngoc · T. Bui-Tien
Faculty of Civil Engineering, University of Transport and Communications, Hanoi, Vietnam

H. Nguyen-Tran · D. Bui-Ngoc (✉)
Faculty of Information Technology, University of Transport and Communications, Hanoi, Vietnam
e-mail: dnbui@utc.edu.vn

1 Introduction

Monitoring structural degradation is crucial for preserving the priceless life span of structures used in civil engineering. Massive progress has been achieved in the field of vibration-based damage detection techniques, which use a supervised system's vibration response to evaluate its health and find structural problems. The extraction of manual attributes is necessary for both parametric and nonparametric vibration-based damage diagnosis techniques employing conventional ML algorithms [1]. To discover the combination that best describes the structural damage, many characteristic/classifier combinations were investigated. However, there is no assurance that a specific set of features and classifiers will be appropriate for all categories of civil engineering projects and structural damage at once.

A large amount of computing time and effort is also required by techniques usually employed to extract handcrafted features. In order to create cutting-edge vibration-based damage detection methods that do not require human feature extraction, researchers have just lately started to apply new DL algorithms [2]. Recent research has demonstrated that without data preprocessing or the extraction of manually created characteristics, two-dimensional (2D) convolutional neural networks and 1DCNNs are more effective at identifying structural damage from the raw vibration data. For handling one-dimensional (1D) vibration signals, 1DCNNs are chosen over their two-dimensional counterparts because they are simpler to train and have less computing complexity [3].

Abdeljaber has introduced 1DCNN to detect vibration-based real-time damage. The 1DCNN configuration used in all the tests consists of (10, 10) neurons in two fully linked latent layers and (64, 32) neurons in two possible convolutional layers. From damaging specific joints of Qatar Grandstand truss structure simultaneously, the author generated a database of vibration signals to develop a neural network. Each link in the proposed model was trained separately, and the resulting classification accuracy was nearly flawless [4]. Zhang utilized the 1DCNN's computing capability to find changes in structural characteristics like stiffness and mass. The proposed methodology achieves a mean classification accuracy of 98% using *T*-shaped steel beams, short steel girder bridges, and long steel girder bridges as the three separate structural elements for data collection and model validation [5]. In a recent study, Azimi and Pekcan investigated the idea of learning transfer in vibration measurements. When applied to similar infrastructure, training one type of structure while evaluating a different kind of structure, transferred learning is particularly effective. For numerical training, the authors employed a four-level IASC-ASCE SHM model. Using the reference building and the Qatar University Grandstand simulator, the suggested model was tested in experimental investigations with 90–100% accuracy [6]. Recently, Sharma and Sen demonstrated the capability of 1DCNN to detect damage to steel structures. The study looked at how localized damage to building structures might be relevant. A 2D steel framework with various damage sites and levels of severity underwent experimental validation. The technique demonstrated the ability to recognize various damage scenarios, and the false positive rate

was evaluated and found to be within acceptable bounds [7]. Liu also conducted a study that combined the capabilities of neural networks and conventional Fourier transform (FT) techniques. The authors successfully identified damage to the ASCE SHM reference framework using a transfer function-based 1DCNN. In comparison with time series and frequency domain data based on a rapid Fourier transform, the proposed method was examined by several writers; FT signals demonstrated more severe damage sensitivity and higher stability in the presence of excitation interference [8, 9].

In this research, we used 1DCNN as the primary method for detecting damage. The proposed method is used in the Z-24 bridge case study to validate the ability to detect damage. The results show that 1DCNN can accurately detect structural damage.

2 Proposed Methodology

2.1 1DCNN

Convolutional neural networks (CNNs) are a particular kind of feed-forward neural network model created to approach a function $y = f(x; \theta)$. The model associates an input or entry with a category for the classification of the function y . The parameter θ is learned by a gradient descent optimization algorithm to best fit a given set of teaching data [10]. The most popular model of CNN is a 2DCNN, which is utilized in the field of computer vision for tasks like classifying pictures from tables (in 2D matrices). A more straightforward variant of CNN called 1DCNN uses vector inputs in 1D format, which often represents time-series data. 1DCNN is used widely in various problems requiring sequential signal processing, such as speech recognition [11]. In recent years, 1DCNN has become more and more popular in its application for SHM over the main family of 2DCNN because it requires the straightforward application of arrays and shallow networks, thus resulting in simpler and more effective computation.

Figure 1 depicts the conventional 1DCNN architecture utilized in the article. It comprises one or more completely linked levels, an input level (time series), and a number of alternating convolutional and pooling layers. The input x in the time series of the input layer is transformed as you move to the hidden levels, and the softmax output layer generates the class label y . This architecture is known as a profoundly convolutional neural network if there are many hidden layers. One of CNN's core components is the convolutional layer. A set of learnable kernels specified by a kernel length (m) make up the parameters for each convolutional layer. Convolutional layers have fewer parameters than fully linked layers since the weight of the spatial input positions is shared by a single kernel. The convolution process is shown in Eq. (1) [10] as follows:

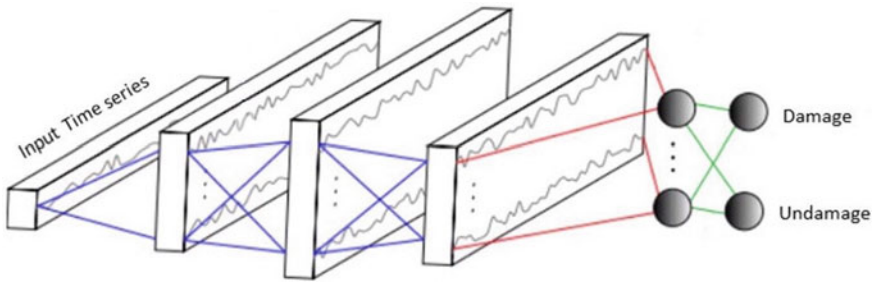


Fig. 1 Typical 1D CNN for time-series classification architecture

$$y(n) = f(x(n) \otimes h(m)), \tag{1}$$

where $x(n)$ is the input vector of length n , and $h(m)$ is the kernel of length m . \otimes represents the conventional 1D convolution between the two signals, and it is defined in Eq. (2):

$$x(n) \otimes h(m) = \sum_{k=0}^n x(k)h(n - k). \tag{2}$$

An activation function f is a nonlinear transformation that is typically used in a conventional 1D convolution. The network can learn intricate mappings between the input signal and class labels thanks to nonlinear activations. The network can learn intricate mappings between the input signal and class labels thanks to nonlinear activations. In this study, we employ Rectified Linear Unit (ReLU, see Fig. 2) as an activation function that, by lowering negative values to zero, essentially removes them from the activation map. A pooling layer is added after the convolution layer to subsample the convolution output. The pooling feature makes a given map smaller, emphasizing noteworthy features and assisting in the elimination of duplication. Max pooling requires that the highest number be chosen in the input map’s scrolling window. In Fig. 1, the max-pooling layer has reduced the size of each convolution output dimension. The output layer’s choice of activation mode is influenced by the output’s kind. In this case, it is best to enable the sigmoid function (representing the two states damage/undamaged) as shown in Eq. (3).

$$\sigma(x) = \frac{1}{1 + e^{-x}}, \tag{3}$$

where x is the input to the function.

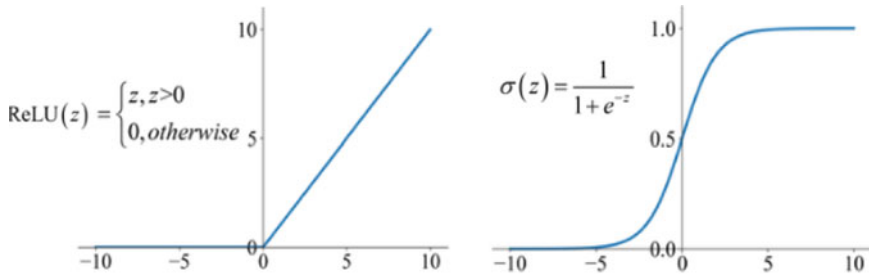


Fig. 2 ReLU (left) and sigmoid (right) function

2.2 Proposed Method

This paper uses a typical 1DCNN for time-series classification architecture to identify the damaged or undamaged state. There is nothing special about the network structure or chosen hyperparameters. Here, the measured data has a large length and wide amplitude, so it will not achieve high accuracy when fed to the training CNN. The reason that the result is not high is that the objective function is not working properly. So we do some preprocessing steps like scaling to normalize data, optimize layers and kernel size, and pooling size for best results. In Table 1, the network structure is displayed. Two convolution layers, a global average pooling layer to minimize the size of the feature map and a fully linked layer with a sigmoid activation function are all present in the network. Besides, in order to avoid overfitting, we use two dropout layers to ignore some nodes in the training phase in this network.

Table 1 1DCNN architecture

Layer	Layer	Size
1	Convolution-ReLU	3 × 3 for 128 filters
2	Convolution-ReLU	3 × 3 for 64 filters
3	Dense	32
4	Pooling	3 × 3
5	Fully connected	256
6	Sigmoid	2 (damaged/undamaged)

3 Case Study

3.1 Details of the Z24 Bridge

A real database for the Swiss bridge Z24 from the BRITE-EURAM BE96-3157 System Identification to Monitor Civil Engineering Structures (SIMCES) project [12] serves as the basis for the structure suggested in this section. The road that connects Bern and Zurich is crossed by the prestressed Z24 bridge. Figure 3 depicts the bridge, which has three spans with a combined length of around 60 m.

Due to the need to construct a new bridge with a greater side span for the new railway alongside the highway, the old bridge was destroyed in late 1998. Several scenarios of progressive failures were generated a month before the bridge was completely demolished, including lowering, lifting of the piers, concrete spalling, the collapse of the anchor heads, and rupture of prestressed tendons. During the destruction of the bridge, a sensor system was strategically positioned along it to gauge its structural reactions to the Progressive Damage Test (PDT). The progressive failure scenarios occurred within a month; just before the bridge was officially demolished during the damage tests, a report on intact conditions was created. Different progressive damage measurements were conducted for different damage scenarios of the bridge. Nine test configurations were performed for each PDT, and 33 acceleration time series were collected from different sensors for each configuration. The accelerometers were placed in different bridge spans, as shown in Fig. 4. The data

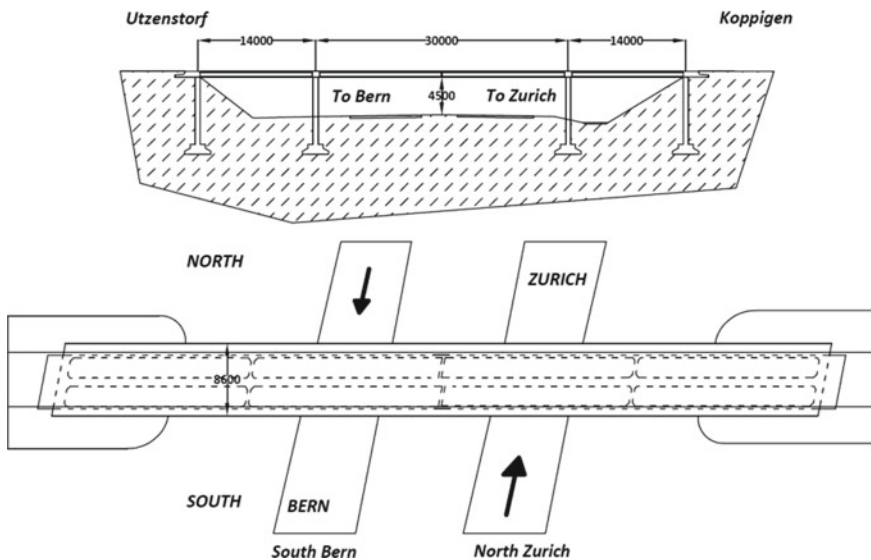


Fig. 3 Schematic of the Z24 bridge

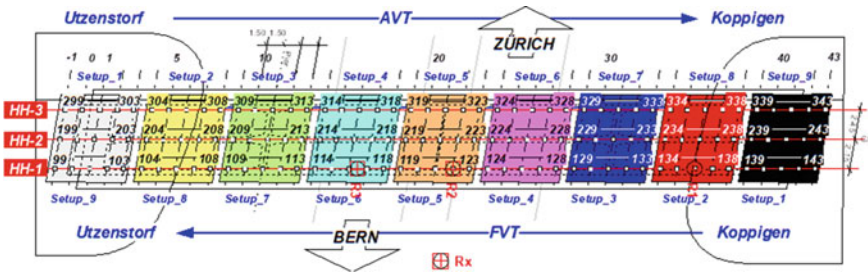


Fig. 4 Locations of sensors are in the Z24 bridge

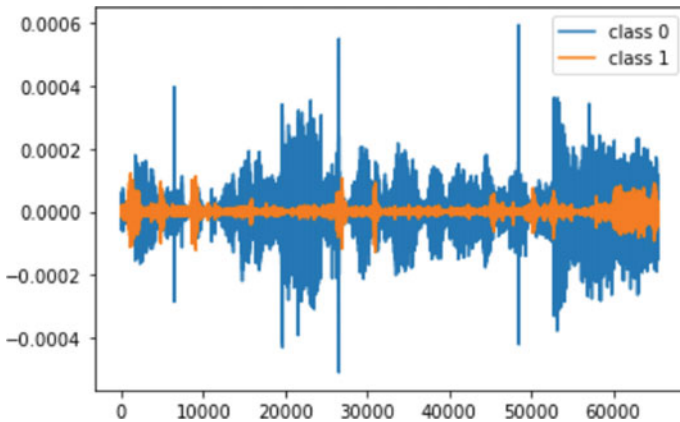


Fig. 5 Data for class 1 (undamaged) and class 0 (damaged)

was sampled at 100 Hz, and a total of approximately 65,500 samples were taken [13].

August 4, 1998, saw the collection of unharmed data, and August 31, 1998, saw the introduction of damage to the bridge. The aforementioned datasets for class 1 (undamaged) and class 0 (damaged) are shown in Fig. 5.

The lowering of the 276-pier dataset has 1056-time series, while the rupture of tendon dataset has 1231-time series (i.e., vibration signals). A time series has 65,530 samples in total. To prevent the model from overfitting, both datasets 277 are divided into three sets of train-validation-test as 60–20–20% of the original suite of time series.

3.2 Obtained Results from the Proposed Method

At first, raw time-series signals known as input multivariate time series are put into the preprocessing stage. The main task of this layer is to rescale data from the original

range to new values that are within the range of 0 and 1. Then, the data is fed as an input to two convolutional layers with the ReLU activation function. The first convolutional layer has 128 filters with a size of 3×3 ; the second one is 64 filters by a size of 3×3 . Next step, to downsample the detection of features in feature maps, we use dense and pooling layers. In order to identify the data as damaged or undamaged, the output layer's activation function uses the sigmoid function and fully connected layers that are equivalent to the layers of a standard Multi-layer Perceptron (MLP). The framework of the proposed method is shown in Fig. 6.

Figure 7 displays the effectiveness of the network's training and testing process.

The core idea of positive and negative detection is used to evaluate prediction accuracy through a series of tests. The more accurate the model forecast is, the higher the accuracy score. An accuracy score is a valuable tool for improving the predictive success of unbalanced classes. The convocation score shows how accurately the model can predict positive and fundamental aspects. In contrast, the accuracy of the model is determined by counting how many positive predictions there are for every positive prediction. The precision and recall scores are used to determine the *F1* score. It is frequently utilized as the single metric that gives crucial details about a model's construction quality. The accuracy score is formulated as:

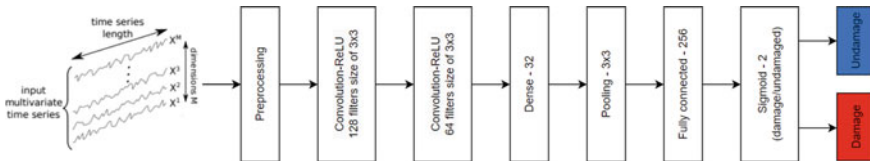


Fig. 6 Workflow of the proposed method

Fig. 7 Accuracy of training and testing

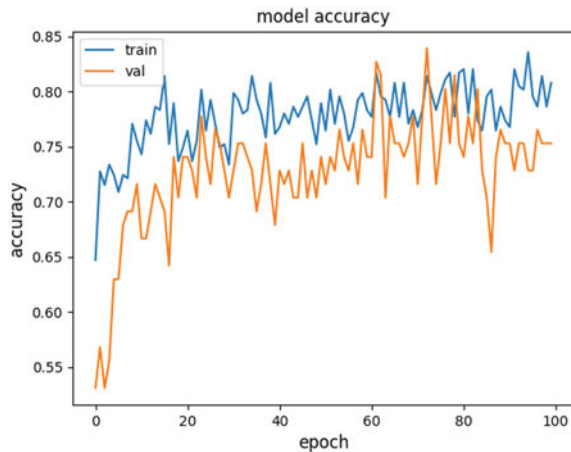


Table 2 Confusion matrix

	Undamaged (predicted)	Damage (predicted)
Undamaged (actual)	True Positive (TP = 78)	<i>False Negative (FN = 17)</i>
Damage (actual)	<i>True Positive (FP = 27)</i>	True Negative (TN = 52)

Bold and Italics represents True positive (TP) is the value of the predicted positive label and is the actual true label. True Negative (TN) is the value of the predicted negative label and is true negative

$$\text{Accuracy_Score} = \frac{(\text{TrueNegative} + \text{TruePositive})}{(\text{TrueNegative} + \text{FalsePositive} + \text{TruePositive} + \text{FalseNegative})} \tag{4}$$

$$\text{Precision_Score} = \frac{\text{TruePositive}}{(\text{FalsePositive} + \text{TruePositive})} \tag{5}$$

$$\text{Recall_Score} = \frac{\text{TruePositive}}{(\text{TruePositive} + \text{FalseNegative})} \tag{6}$$

$$\text{F1_Score} = \frac{2 * \text{Precision_Score} * \text{Recall_Score}}{(\text{Precision_Score} + \text{Recall_Score})} \tag{7}$$

Table 2 displays the confusion matrix for the proposed approach. The suggested method’s accuracy is expressed as a percentage of correctly identified samples out of all samples.

According to the method’s performance, the technique’s accuracy in the training phase was 82% and in the test phase, 75%. In addition, Table 2’s perplexing matrix shows that there are 174 total samples, 95 of which are undamaged samples and 79 of which are damaged. Seventy-eight samples were successfully detected for undamaged detection, whereas 17 samples were incorrectly classified. There were 52 damaged samples discovered in a damaged state for damage detection, and 27 samples were incorrectly classified. Our findings are 0.74, 0.82, and 0.78 for the accuracy, recall, and *F1* scores, respectively. The outcome implies that 1DCNN techniques can be used to analyze the altered vibration data.

4 Conclusions

The 1DCNN model is used by the authors of this research to provide a damage identification approach. Time series are used as 1DCNN inputs in this model. The technique can be utilized to overcome issues with damage detection, according to experimental data. The case study results indicate that the proposed method has created a high level of accuracy in the structure’s damage detection. This technique can be further enhanced in subsequent studies to quantify the degree of damage to the structure in addition to categorizing it.

Acknowledgements Dung Pham Tuan was funded by the Master, Ph.D. Scholarship Programme of Vingroup Innovation Foundation (VINIF), code VINIF.2022.ThS.015.

Furthermore, we really want to thank Katholieke Universiteit Leuven, who supports the Z24 data that is available at <https://bwk.kuleuven.be/bwm/z24>.

References

1. Avci O, Abdeljaber O, Kiranyaz S, Hussein M, Gabbouj M, Inman DJ (2021) A review of vibration-based damage detection in civil structures: from traditional methods to machine learning and deep learning applications. *Mech Syst Sig Process* 147:107077
2. Bui-Ngoc D, Bui-Tien T, Nguyen-Tran H, Wahab MA, De Roeck G (2020) Structural health monitoring using handcrafted features and convolution neural network. In: SDMA 2020, the 1st international conference on structural damage modelling and assessment
3. Avci O, Abdeljaber O, Kiranyaz S (2021) An overview of deep learning methods used in vibration-based damage detection in civil engineering. *Dyn Civ Struct CPSEMS* 2:93–98
4. Abdeljaber O, Avci O, Kiranyaz S, Gabbouj M, Inman DJ (2017) Real-time vibration-based structural damage detection using one-dimensional convolutional neural networks. *J Sound Vib* 388:154–170
5. Zhang Y, Miyamori Y, Mikami S, Saito T (2019) Vibration-based structural state identification by a 1-dimensional convolutional neural network. *Comput Aided Civ Infrast Eng* 34(9):822–839
6. Azimi M, Pekcan G (2020) Structural health monitoring using extremely compressed data through deep learning. *Comput Aided Civ Infrast Eng* 35(6):597–614
7. Sharma S, Sen S (2020) One-dimensional convolutional neural network-based damage detection in structural joints. *J Civ Struct Health Monit* 0123456789 (2020)
8. Liu T, Xu H, Ragulskis M, Cao M, Ostachowicz W (2020) A data-driven damage identification framework based on transmissibility function datasets and one-dimensional convolutional neural networks: Verification on a structural health monitoring benchmark structure. *Sensors (Switz)* 20(4):1–25
9. Dang HV, Tran-Ngoc H, Nguyen TV, Bui-Tien T, De Roeck G, Nguyen HX (2021) Data-driven structural health monitoring using feature fusion and hybrid deep learning. *IEEE Trans Autom Sci Eng* 18(4):2087–2103
10. Bui-Ngoc D, Nguyen-Tran H, Nguyen-Ngoc L, Tran-Ngoc H, Bui-Tien T, Tran-Viet H (2022) Damage detection in structural health monitoring using hybrid convolution neural network and recurrent neural network. *Focuss Steels Compos Eng Struct* 59:461–470. <https://doi.org/10.3221/IGF-ESIS.59.30>
11. Kiranyaz S, Avci O, Abdeljaber O, Ince T, Gabbouj M, Inman DJ (2019) 1D convolutional neural networks and applications: a survey, pp 1–20. Retrieved from <http://arxiv.org/abs/1905.03554>
12. Maeck J, Peeters B, De Roeck G (2001) Damage identification on the Z24 bridge using vibration monitoring. *smart materials and structures*. *Mech Syst Sig Process* 10(3):512
13. Reynders E, De Roeck G (2009) Continuous vibration monitoring and progressive damage testing on the Z24 bridge. In: Boller C, Chang FK, Fujino Y (eds) *Encyclopedia of structural health monitoring*. Wiley, New York, pp 2149–2158

The Effect of the Cut on the Power Spectral Density of the Beam



Toan Pham-Bao and Luan Vuong-Cong

Abstract Cracks are one of the causes of the decline in the bearing capacity of beams. Crack studies often use the natural frequencies as a parameter to identify the occurrence and growth of cracks. However, for a small crack, the natural frequency does not change significantly, and thus, it is not useful for the early damage identification. In this study, the shape change of the power spectral density (PSD) is proposed as a novel feature more sensitive to cracking. This feature is represented by the centroids of the PSD (C-PSD) of the beam under moving load with different levels of cuts.

Keywords Power spectral density (PSD) · Beams · Damage · Moving load · C-PSD

1 Introduction

The problem of damage identification (DI) of some structures like beams, shells, frames, and pillars has been presented in many studies. Structural degradation is often simulated into different types of damage, especially cracks. The authors [1–3] describe damage as any change related to one of two factors: the material or the geometrical state of the system. According to Rytter [4], the problem of DI is divided into four levels: damage existence, damage location, damage severity, and remaining life of the structure. The power spectral density (PSD) is a popular and effective tool in assessing the health condition of a structure [5]. In Ref. [6], Liberatore and Carman also proposed a method to determine and locate the damage of beams based on the change in amplitude and shape of the PSD. Kumar [7] uses PSD's peak change to locate damage. However, for small-scale damage, this parameter proved ineffective. Some authors [8–10] try to use other features such as the curvature of

T. Pham-Bao (✉) · L. Vuong-Cong
Laboratory of Applied Mechanics (LAM), Ho Chi Minh City University of Technology (HCMUT), VNU-HCM, Ho Chi Minh City, Vietnam
e-mail: baotoanbk@hcmut.edu.vn

the PSD from acceleration signal. The reason for the disadvantage of these studies may be that separated components of the PSD are used without the overall changes of the PSD. Besides that, some other studies proposed to use statistical properties of PSD of different vibration signals such as displacement [11], bending moment [12]. The limitation of these studies is that the levels of damage identification were only performed based on numerical simulations without verifying with real structures. In general, the DI still remains the unsolved problem and attractiveness to researchers. The PSD contains a lot of potential information for DI but has not been exploited most effectively. Therefore, in this study, the change of the PSD is continuously investigated by tracking statistical moments of PSD in each frequency band.

2 Methodology

According to Euler–Bernoulli beam theory, the differential equation of motion of beams with length l under moving load $f(t)$ with speed a is as following:

$$EJ(x)\frac{\partial w^4(x,t)}{\partial x^4} + \rho\frac{\partial w^2(x,t)}{\partial t^2} + c\frac{\partial w(x,t)}{\partial t} = \delta(x-at)f(t), \tag{1}$$

in which: x is location of points on beams, ρ is mass density per unit of length, c is damping coefficient, E is Young’ modulus, J is inertial moment of area.

The solution of Eq. (1) can be found in general forms as following:

$$w(x,t) = \frac{2}{\rho l} \sum_{j=1}^{\infty} \frac{\phi_j(x)}{\omega_{dj}} \int_0^t h_j(t-\tau) f(\tau) \sin j\omega_a t \, d\tau, \tag{2}$$

where ω_{dj} , ϕ_j , and h_j are damping frequency, mode shape, and impulse function of j^{th} normal mode and $\omega_a(=\pi a/l)$ is speed frequency of load.

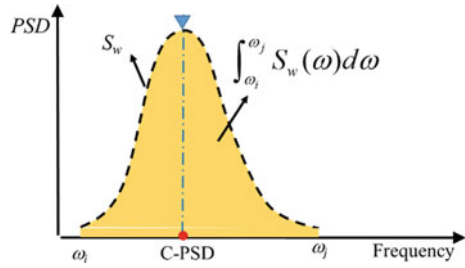
If $f(t)$ is assumed as a white noise with constant spectral amplitude S_f , autocorrelation function R_w of vibration response is determined by:

$$R_w(x,t) = \frac{8\pi S_f}{\rho^2 l^2} \sum_{j=1}^{\infty} \phi_j^2(x) \int_0^t h_j^2(t-\tau) \sin^2(j\omega_a \tau) \, d\tau. \tag{3}$$

And, PSD of vibration response is Fourier transform of R_w as follows:

$$S_w(x,\omega) = \frac{1}{2\pi} \int_{-\infty}^{\infty} R_w(x,t) e^{-i\omega\tau} \, dt = \frac{4\pi S_f}{\pi \rho^2 l^2} \sum_{j=1}^{\infty} \phi_j^2(x) |H_j(\omega)|^2 \int_{-\infty}^{\infty} \sin^2(j\omega_a t) e^{-i\omega\tau} \, dt \tag{4}$$

Fig. 1 Centroid of PSD



with $H(\omega)$ is frequency response function (FRF) of j^{th} normal mode. If ω_{0j} is natural frequencies of j^{th} normal mode, FRF is determined as following:

$$H_j(\omega) = \frac{1}{\omega_{0j}^2 - \omega^2 + c\omega i} \quad \text{with } \omega_{0j} = \frac{\int_0^l E J(x) \left[\frac{d^2\{\phi_j(x)\}}{dx^2} \right]^2 dx}{\int_0^l \rho [\phi_j(x)]^2 dx}. \quad (5)$$

Generally, PSD of response $S_w(x, \omega)$ depends not only on material properties (E) and geometry (J) but also mode shape (ϕ). When damage (crack or cut) occurs in structures, the variation of J and ϕ will make PSD change. To access the change of PSD, centroid of power spectral density (C-PSD) in Fig. 1 is defined by

$$\text{C-PSD} = \frac{\int_{\omega_i}^{\omega_j} \omega S_w(\omega) d\omega}{\int_{\omega_i}^{\omega_j} S_w(\omega) d\omega}. \quad (6)$$

3 Experiment and Result

The experimental model was created at the Faculty of Applied Science, Ho Chi Minh City University of Technology, as shown in Fig. 2. The main components of the model include: experimental beam, moving load, speed control, data logger, data acquisition, and four vibration sensors evenly distributed in positions K1, K2, K3, and K4 of the beam.

The experimental model is a simply supported beam with dimension $100 \times 10 \times 1.5$ (cm). Material of the beam is medium-density fiberboard (MDF). In order to reduce the friction between the beam and the support, there is a rubber base at the contact position. The speed of load is controlled by an inverter.

In this study, we used cuts instead of cracks to facilitate control of crack extent (Fig. 1). The cuts are made in the middle of the beam by a CNC machine, with a width of 3 mm, distributed over the entire girder width (10 cm), and the depth is given in Table 1.

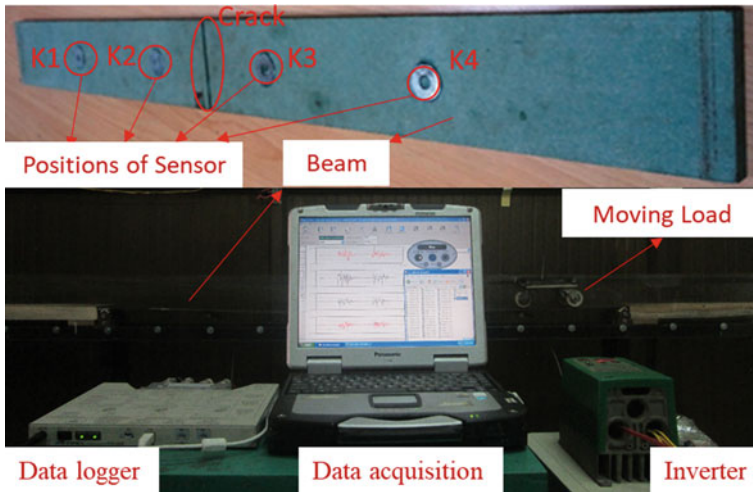


Fig. 2 Experimental setup

Table 1 Parameters of the cuts

Sign	Parameters of the cuts	
	Length (mm) × Width (mm)	Depth (mm)
H0	100 × 3	0
H1		4
H2		8
H3		12

With the effect of the cuts, the shape of the spectrum changes leading to the movement of the centroid of the power spectral density. In this study, we only investigate the movement of the centroid along the frequency axis. The vertical line passing through the centroid is determined based on Eq. (6). The movement of this line represents the movement of the centroid of spectrum. To investigate the change of the spectrum more efficiently, we use seven centroids instead of only one, so there are seven vertical lines passing through them for each spectrum. These lines are determined according to the following procedure:

- Step 1: The fourth centroid and the vertical line through it (line 4) are determined by Eq. (5). This line divides the spectrum into two equal areas (Fig. 3a).
- Step 2: For each area, the centroids (and the line passing through it) are determined. It is the second centroid (line 2) and sixth centroid (line 6). Line 2 passes through the centroid of the left area, while line 6 passes through the centroid of the right area in Fig. 3a. Three lines (lines 2, 4, and 6) divide the spectrum into four equal areas (Fig. 3b).

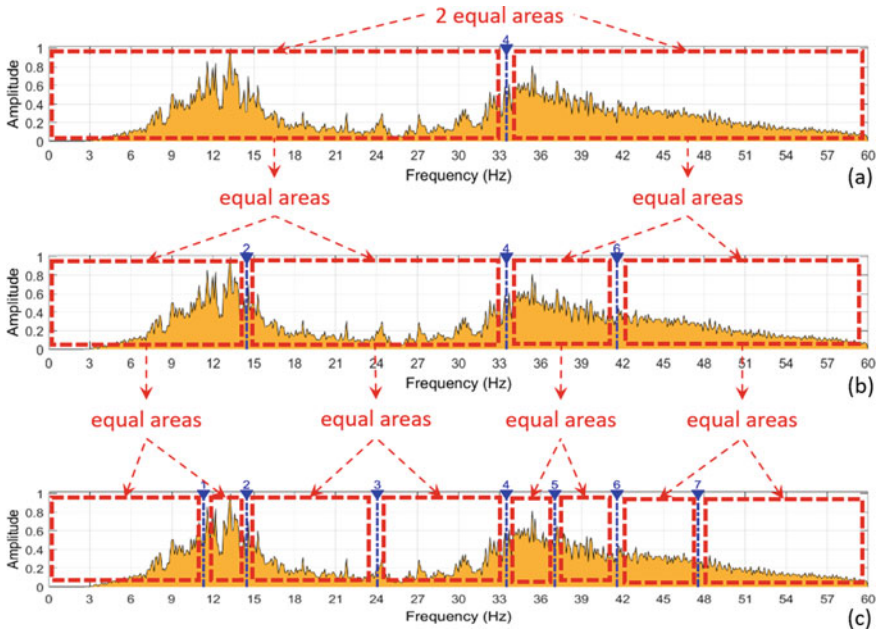


Fig. 3 Procedure to determine the seven centroids of the power spectrum density

- Step 3: The centroids of each area (and the line passing through it) are determined similarly to step 2. They are the first, third, fifth, and seventh centroids (with the lines 1, 3, 5, and 7) (Fig. 3c).

As a result of the above procedure, there are seven vertical lines passing through seven centroids, numbered in order from left to right which divides the spectrum into eight parts of equal area. To study the change of the power spectral density, the position of these lines will be investigated.

When the cut increases in degree from H0–H3, the centroids of the power spectrum of a beam are shown in Fig. 4.

To make it simpler and more intuitive, a line chart is used to represent this change. Symbols ▼ and ▲ are also included to show respectively the increase and decrease of the center coordinate value compared to the previous state. Considering four responses in different positions of the beam, the results of C-PSD are shown in Fig. 5.

The results from the four positions show that when the depth of the cut increases, most of the seven centroids move to the left.

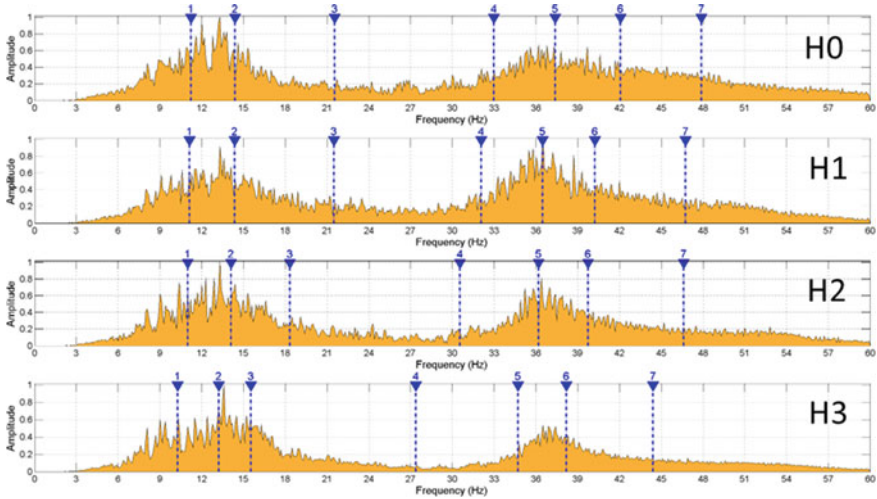


Fig. 4 Movement of the seven centroids due to the increasing depth of cut

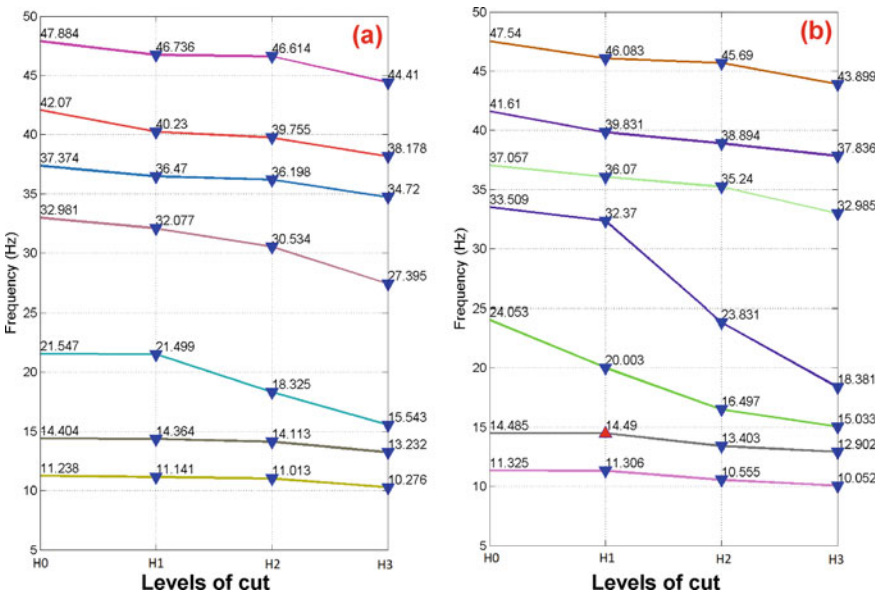


Fig. 5 Change of the seven centroids in different positions due to the increasing depth of cut a K1; b K2; c K3; d K4

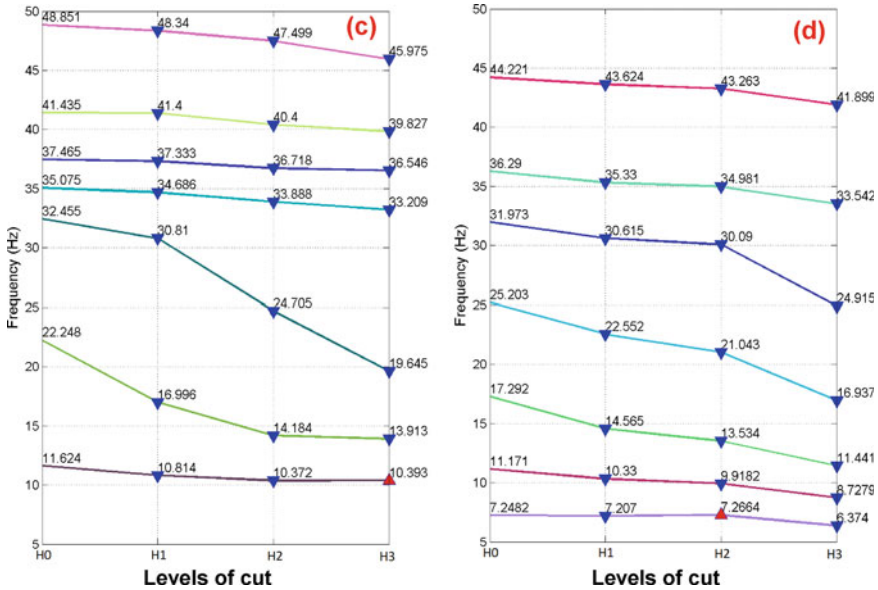


Fig. 5 (continued)

4 Conclusion

A PSD-based method of DI is proposed in this study. The experimental results show that the C-PSD is more sensitive than specific natural. Therefore, C-PSD is a novel index for early damage detection. In addition, the distribution of this value allows to determine the degradation of the beam-like structure at many distinct locations. This characteristic may be used for the location of damage. By using seven centroids, the variation of the PSD is investigated more comprehensively than using only a region or even a peak (natural frequency). The feasibility of the above feature is verified by the wooden beam model and shows the potential for application to other materials and to real structures.

Acknowledgements This research is funded by Vietnam National University Ho Chi Minh City (VNU-HCM) under grant number C2021-20-05. We acknowledge Ho Chi Minh City University of Technology (HCMUT), VNU-HCM, for supporting this study.

References

1. Bhardwaj G, Singh IV, Mishra BK (2015) Stochastic fatigue crack growth simulation of interfacial crack in bi-layered FGMs using XIGA. *Comput Methods Appl Mech Eng* 4:186–229

2. Kunin B (2013) Stochastic model of brittle crack growth under cyclic load. *Int J Pure Appl Math* 84(3):163–174
3. Yu H, Wu L, Guo L, Wu H, Du S (2010) An interaction integral method for 3D curved cracks in nonhomogeneous materials with complex. *Int J Solids Struct* 47:2178–2189
4. Rytter A (1993) Vibration based inspection of civil engineering structures. Ph.D. thesis. University of Aalborg, Denmark
5. Lutes LD, Sarkan S (2003) Random vibrations: analysis of structural and mechanical systems. Butterworth-Heinemann
6. Liberatore S, Carman GP (2004) Power spectral density analysis for damage identification and location. *J Sound Vib* 274(3–5):761–776
7. Kumar RP, Oshima T, Mikami S, Miyamori Y, Yamazaki T (2012) Damage identification in a lightly reinforced concrete beam based on changes in the power spectral density. *Struct Infrastruct Eng* 8:715–727
8. Beskhyroun S, Oshima T (2005) A numerical study of structural damage detection using changes in the curvature of power spectral density. *J Struct Eng* 51:38–49
9. Beskhyroun S, Oshima T, Mikami S, Tsubota Y (2006) Damage identification of steel structures based on changes in the curvature of power spectral density. In: Proceedings of the 2nd international conference on structural health monitoring of intelligent infrastructure. Shenzhen, China, pp 791–797
10. Beskhyroun S, Oshima T (2005) Structural damage identification algorithm based on changes in power spectral density. *J Appl Mech* 8:1–12
11. Bayissa WL, Haritos N (2007) Structural damage identification in plates using spectral strain energy analysis. *J Sound Vib* 307:226–249
12. Bayissa WL, Haritos N (2007) Damage identification in plate-like structures using bending moment response power spectral density. *Struct Health Monit* 6:15–24

Building Information Modelling and AI in Civil Engineering

Application of FARO Focus 3D S350 Terrestrial Laser Scanner in Building 3D Models of Potential Areas of Landslides and Rocks—Case Study in Ha Giang Province, Vietnam



Hanh Hong Tran, Hung Quoc Vu, and Anh Van Tran

Abstract Morphology and topographic factors are closely related to soil and rock characteristics, tectonic activities, and endogenous and exogenous processes such as flash floods, landslides, and rocks. The aim of this paper is to present the application possibility of the FARO Focus 3D S350 Terrestrial Laser Scanner (TLS) in building 3D models in the potential case study of landslides and rocks—the Na Chi commune, Xin Man district, Ha Giang province. The FARO Focus 3D S350 TLS uses the phase-shift technology to determine the distance, the measuring range of 350 m, the measurement speed of up to 976,000 points/second, and the accuracy of ± 2 mm. The results show that the FARO Focus 3D S350 TLS fully meets the accuracy and is highly applicable for building the 3D point-cloud models in the landslide and rock areas. This research will be useful to local managers as well as geologists.

Keywords Terrestrial laser scanner · FARO focus 3D S350 · 3D model · Areas of landslides and rocks · Ha Giang

1 Introduction

The 3D Terrestrial Laser Scanning (TLS) technology is a technique to collect field data in digital form, using laser light to scan the object surface from fixed points (control points). Then, the size and spatial relationship between objects are recorded. It is a dramatic change in field data collection for three-dimensional applications [1]. After completing a data collection cycle, the laser scanners will form point clouds. They represent completely images of the objects that the laser has scanned.

H. H. Tran (✉) · A. Van Tran
Hanoi University of Mining and Geology, Hanoi, Vietnam
e-mail: hanhtranvub@gmail.com

H. Q. Vu
Hanoi University of Civil Engineering, Hanoi, Vietnam

Depending on the scanner models and manufacturers, the scanning distance to actual objects can range from a few hundred meters to several kilometers. The point data obtained is less than 5 mm accurate with data acquisition speed from several tens of thousands to million points per second. Scanning speed depends on the scanning point density requirements of each application [2]. When the objects are larger than one scan, we have to use multiple stations at different angles, then connect these stations together to form a complete point cloud. As soon as the 3D point cloud is established, the data is ready to be applied. It is possible to conduct direct measurements, build 3D models, calculate the volume and volume of objects with any shape.

The 3D TLS technology is applied in many fields such as large industrial zones, nuclear power plants, offshore oil and gas, mining, transportation, topography, cartography, urban planning, cultural works, conservation [3]. Many studies related to the 3D TLS technology were studied, for example, [4–7]. Andrea Biasion et al. studied that the 3D TLS is very useful for natural hazards and risk assessment where morphological investigation is a starting point to evaluate stability properties, to acquire and monitor emergency situations [4]. The TLS method measured modification in the mine roadway surface profiles including pillar displacements, roof movements, floor heave, and other dynamic phenomena [5]. Terrain and non-terrain objects applications were researched and compared the similarities and differences between the uses of 3D TLS technology [6]. Architecture, engineering, and construction using 3D TLS were studied in details by Wu et al. [7]. The advantage of TLS is measuring many points in a short time with a density up to several millions points/second. Meanwhile, one point is only measured in the traditional method, and it is difficult to assess the accuracy of many locations.

2 FARO Focus 3D S350 Terrestrial Laser Scanner and the Process

2.1 The FARO Focus 3D S350 Terrestrial Laser Scanner

The assessment of the TLS system is based on the following technical characteristics [8]: accuracy of measuring distances; horizontal and vertical angles; maximum resolution when scanning; maximum scanning distance; scanning speed and scanning angles; dispersion of the laser beam; safety level of laser use; lightweight, easy to handle, and transport. The TLS equipment is classified based on the following functions [9]: angle measuring equipment; length measuring equipment; height measuring equipment; integrated measuring equipment; specialized equipment (vertical projection, construction, etc.); auxiliary equipment: centerpiece, target, reflector, etc. (Fig. 1)

FARO Focus S350 is a long-range scanner of FARO's Focus series. There are many advantages of this device. It is one of the high-quality scanners with protection

Fig. 1 Picture of the FARO Focus S350 [10]



mechanism that adapts to the harsh environment such as narrow, dusty, or wet areas, in rain or direct sunlight. Moreover, it is equipment with the outstanding data collection. It allows optimizing data quality in the field. The integration of GPS and GLONASS receivers leads to the easy positioning. HDR images and HD resolution ensure the scanning results with high data quality.

It is an equipment that uses the phase-shift technology [10]. The measuring range is from 0.6 to 350 m. The High Dynamic Range (HDR) is $2 \times / 3 \times / 5 \times$. The measurement speed is up to 976,000 points per second. The accuracy is about ± 2 mm in the current versions. The angle accuracy is 19 arcsecs for vertical/horizontal angle. Waterproof design meets IP54. On-site compensation. The sensor system includes GPS, compass, height sensor, and dual-axis compensator. The TLS is controlled via the touch screen and WLAN. The camera has the HD mode. It has the resolution of up to 70 megapixels. The size is $240 \times 200 \times 100$ mm. The weight is 5.2 kg.

2.2 Characteristics of the Case Study

The case study is Na Chi, a commune located in the southwest of Xin Man border mountainous district in the Ha Giang province. The geographical coordinates of the Na Chi commune are $22^{\circ} 31' 34''$ N and $104^{\circ} 28' 21''$ E. The administrative boundary of the Na Chi commune is bordered to the North by Lao Cai province and Nam Dan commune, the East borders Quang Nguyen and Khuon Lung communes, the South borders Lao Cai province and Khuon Lung commune, and the West borders Lao Cai province (Fig. 2).

The Na Chi commune has an area of 81.34 km². The population in 2019 is 4,674 people [11]. The population density reaches 48 people/km². The Na Chi commune is divided into 13 groups, villages, and hamlets.

The commune area has two main topographical forms low/medium and high mountainous terrain. The first one account for over 60% of the total natural area of the commune and has a slope from 200 to 250 m. The latter accounts for over 30% of the total natural area, mainly forest land, and has a slope of over 250 m.

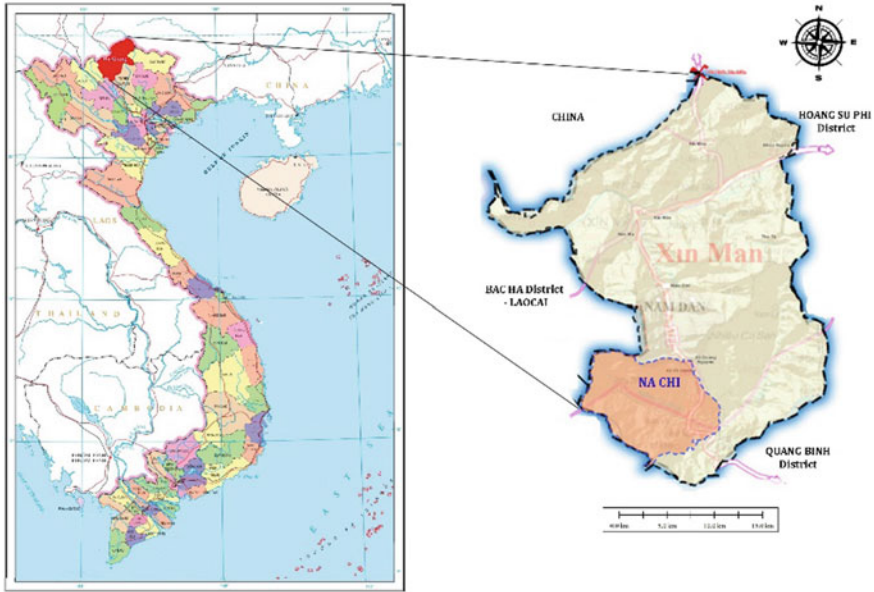


Fig. 2 Location of the Na Chi commune of Xin Man district in the Ha Giang province

In the case study, landslides are concentrated mainly in the thick weathered crust or on the slopes. However, in fact, the phenomenon of natural landslides is rare, but mostly due to human impacts such as cutting slopes to build terraced fields, house, and roads. The Na Chi markets and its inhabitants are located on sliding blocks with thick weathered crust, which is also the landslide areas with the above characteristics.

2.3 Process of the Study

The process is shown in Fig. 3. There are many steps in the process. Data was entered into the Faro Scene software. Data was exported to e57 format, then was imported into Autodesk Recap software for simpler display or extraction of measurement points at the necessary locations for monitoring of volatility. The e57 format is a standard format that allows the original scan files to be unformatted, keeping the locations of the stations. To read data in the Autodesk software, data was converted from e57 into Autodesk Recap software in Recap project (RCP) format.

Data was conducted and collected in early 2018, in the middle of 2019, and in the middle of 2020. The determination basis is the calculation of the various measuring point displacements, then comparing with the DEM. The control checking points were located in the locations where there is little or no risk of movement. These locations were fixed throughout the survey periods and were committed not to remove

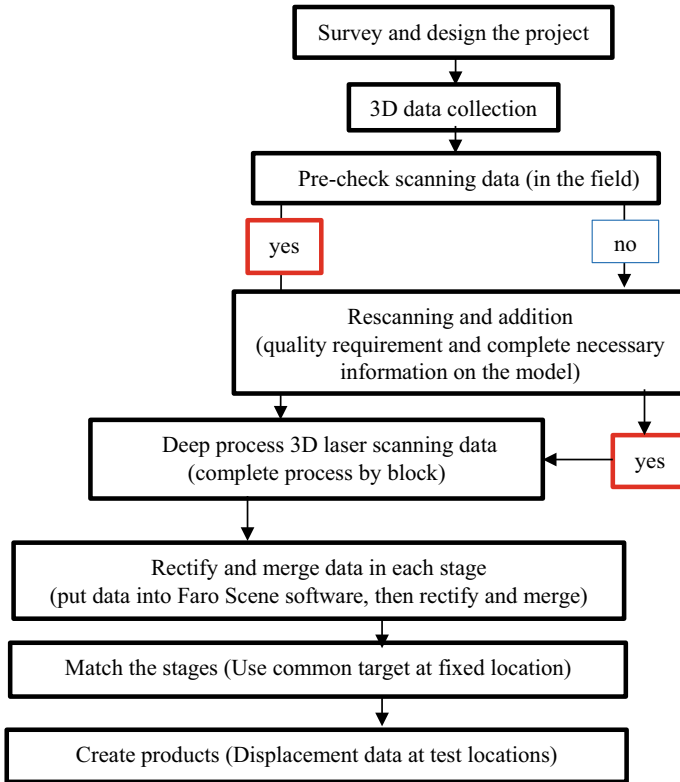


Fig. 3 Process of study

the landmarks. The results include the monitoring status of different periods, then comparing those periods in order to find the potential areas of landslides and rocks.

3 Results and Discussions

Figure 4 shows the instance of the point-cloud data and the case study area image after the first scanning in 2018. The 3D point-cloud models of the potential areas of landslides and rocks of the case study—the Na Chi commune in Ha Giang province—were built and extracted (Fig. 5).

The images of the above point-cloud models can be clearly observed the potential areas of landslides and rocks in the experimental area. These models were created from the 3D laser scanner as we reproduce 100% of reality at the 1:1 scale. All data has been established in complete 3D space. The whole process of measuring and editing was carried out on this 3D model with very high accuracy (up to mm) without having to go out to set up the device or pull the tape measure.

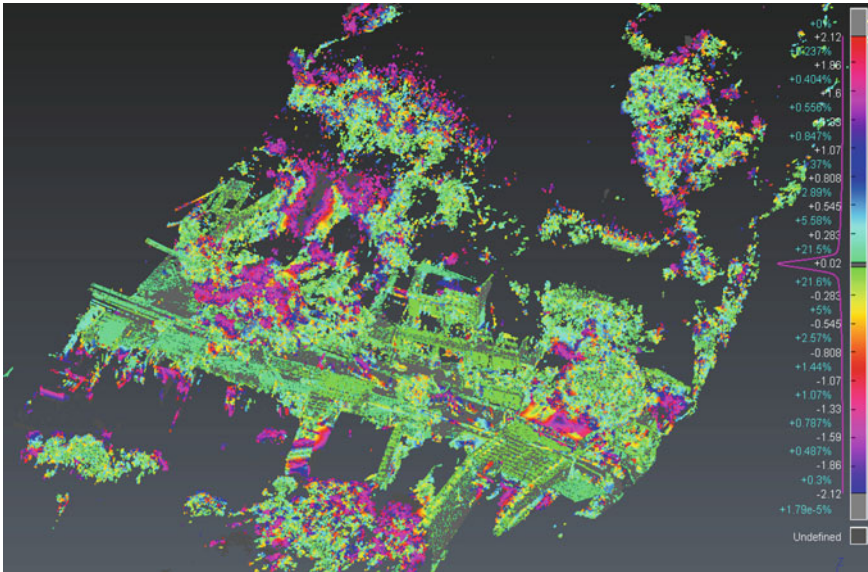


Fig. 4 Point-cloud data and the case study area image after the first scanning in 2018

The preprocessing check step of data in the field data will ensure the optimal quality. Besides, it will not leave any ‘white space’ on the point-cloud model later on. There are many factors that can affect and decrease the accuracy of laser measurement in practice, for example, temperature, humidity, air turbidity, scanning distance, locations, and angles of the laser with the scanned objects in the field (right angle, inclined one, etc.).

The accuracy achieved in this study is ± 2 mm. The 2 mm accuracy is the precision of the scanning device which has been tested and checked for quality. This accuracy is calibrated within 100 m from the measuring objects to the instrument. The accuracy of ± 2 mm can only be got with a prerequisite that the scanning distance between consecutive scanning stations is only within the range of 10–15 m. However, shortening the scanning distance between consecutive stations also means that the number of scanning stations increases and the data collection time will be longer.

There are many advantages of using TLS technology in researching the potential areas of landslides and rocks. For instance, status survey data ready as a complete 3D model; the detailed level of the survey data is extremely high; the data accuracy reaches mm and is homogeneous in the whole case study; full information of all components present in the case study; measure and extract floor plans accurately and quickly; convert to 3D solid model for design; visually test different change repair models; measure and determine distance, area, and volume directly on the model; continuous monitoring during construction. However, the cost of this survey method can be higher than traditional methods.

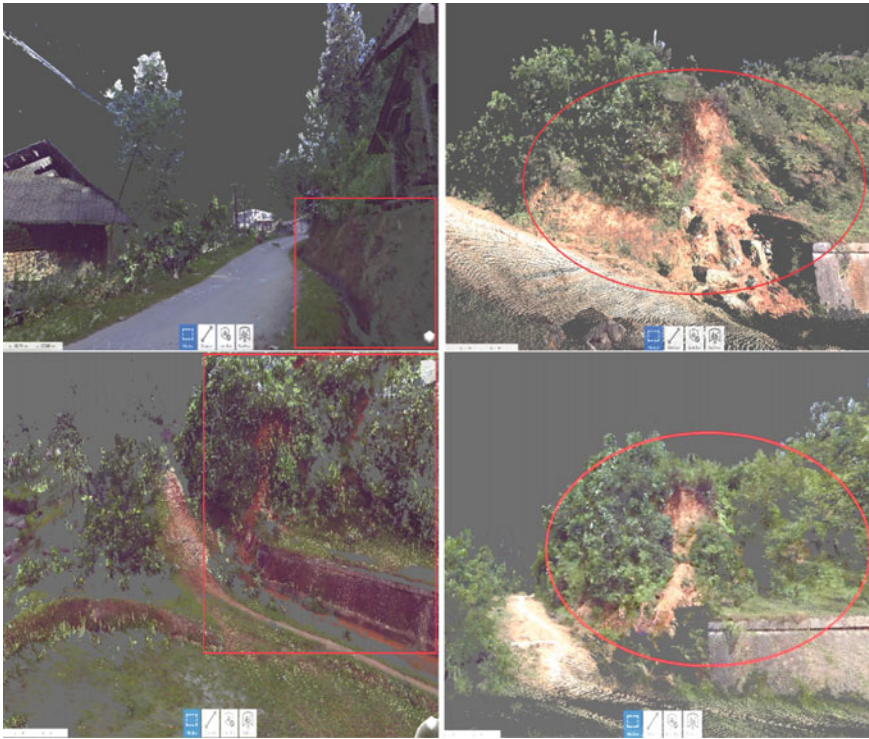


Fig. 5 Three-dimensional point-cloud models of the potential areas of landslides and rocks in the Na Chi commune, Ha Giang province

4 Conclusions

The 3D TLS affirms the superiority compared to other traditional technologies. It contributes to strengthening and modernizing the survey, mapping, and geographic information. The results show that the FARO Focus 3D S350 Terrestrial Laser Scanner is one of the modern devices, which fully meets the accuracy (± 2 mm). It is highly recommended for building the 3D point-cloud models in the landslide and rock areas with the high-quality point clouds. This research will help the local authorities for management and geologists for researching.

References

1. Mostafa E (2016) 3D laser scanners: history, application, and future. LAP LAMBERT Academic Publishing, UK
2. Historic E (2018) 3D laser scanning for heritage, 3rd edn. Historic England, UK

3. Bernd B (2014) 25 years of high definition 3D scanning: history, state of the art, outlook. In: Electronic workshop in computing (electronic visualisation and the arts). London, UK, 8–10 July 2014, pp 262–266
4. Andrea B, Leandro B, Fulvio R (2005) Laser scanning applications on disaster management. geo-information for disaster management, pp 19–33
5. Radovan K, Vlastimil K, Petr W, Jan N (2016) Use of 3D laser technology to monitor coal pillar deformation. In: Coal operator’s conference COAL. Wollongong, Australia, pp 109–117
6. Hanh HT, Cuong SN, Anh VT (2021) Application comparison of 3D terrestrial laser scanning between terrain and non-terrain objects. In: The 38th Asian conference on remote sensing (ACRS). Can Tho, Vietnam, 22–24 Nov 2021
7. Chao W, Yongbo Y, Yang T, Boquan T (2022) Application of terrestrial laser scanning (TLS) in the architecture, engineering and construction (AEC) industry. *Sensors* 22(1):265, 1–32
8. Sanna K (2014) Change detection of tree biomass with terrestrial laser scanning and quantitative structure modelling. *Rem Sens* 6(5):3906–3922
9. Ngo C (2022) Research on terrestrial laser scanning technology in terrain and non-terrain fields in Vietnam. Ph.D. thesis. Hanoi, Vietnam
10. FARO website. <https://www.faro.com>. Last accessed 09 Sept 2022
11. Ha Giang Province Statistics Office (2019) Statistical yearbook

Risk Identification and Prediction for Highway Bridge Projects Using an Artificial Intelligence Model



Dao Duy Lam, Le Duc Anh, Luu Truong Giang, and Hoang Ha

Abstract The risk management is quite important for the highway bridge projects due to the complicate structures and technologies influenced by site conditions, environment, service condition, etc. The risks in these projects are sometime unavoidable, so the identification and prediction of risk are required to ensure the high requirements of safety, quality, longevity and to optimize the management and maintenance activities. Technical risks of bridge in Vietnam have identified and analyzed by some authors with initially proposing of effective models and solutions to control and limit the risks. However, the risk factors in bridge projects are comparatively fuzzy, random and complicatedly connected to each other. Hence, there are some disadvantages of these proposed models and methods in solving the complex and multi-risk problems and the prediction has not been well done. In this paper, an Artificial Intelligence model for technical risk identification and prediction in highway bridge projects will be constructed based on the previous investigation results during the bridge construction and operation in Vietnam, the ensemble methods with Random Forest algorithm will be discussed and be used to obtain better risk predictive performance, and then, the application for real projects is intended.

Keywords Risk identification · Risk prediction · Artificial intelligence model · Random forest algorithm · Highway bridge

D. D. Lam (✉) · H. Ha
University of Transport and Communications/UTC, Hanoi, Vietnam
e-mail: daoduylam@utc.edu.vn

L. D. Anh
Ministry of Transport/MOT, Hanoi, Vietnam

L. T. Giang
Department for Expressway of Vietnam—MOT, Hanoi, Vietnam

1 Introduction

Among transport infrastructures, highway bridges always play a key role, and the excessive destruction of a bridge can cause harmful consequences for the management in general. Bridge risks refers to any hazard or uncertain event that could obstruct its goal achievement, and the stakeholders' expectations and the occurrence of the consequences are sometime unavoidable so the identification and prediction of risk are required to ensure the high requirements of safety, quality, longevity and to optimize the management and maintenance activities. By classifying, a list of risks of the highway bridge project can be given as the output of the process, which often includes: technical, external, environmental, organizational, project management, construction, regulatory risks, etc. The risk management is quite important for the highway bridge projects due to the complicate structures and technologies, and a risk management plan is considered as an attempt of analyzing risks that can enrich the decision-making process and provide additional arguments to support choosing the optimal variant using multiple approaches [1, 2].

Numerous techniques are available to facilitate risk identification, techniques commonly used in risk identification are: brainstorming; scenario planning; expert interviews; nominal group methods; Delphi methods; Crawford slip methods; influence or risk diagramming. The risk factors in bridge projects are comparatively fuzzy, random and complicatedly connected to each other. Hence, there are some disadvantages of these mentioned above techniques in solving the complex risk management problems. Most of the multi-hazard risk assessment models are based on traditional probabilistic approaches such as based on questionnaires. Recently, some authors such as Clark-Ginsberg [3], Andric [4], Zio [5], Chen [6] have introduced new approaches, more effective tools for risk identification than the traditional probabilistic approach.

Researchers on risk management in transport construction projects in Vietnam such as Anh and Tuan [2] have applied Monte Carlo for risk analysis during construction phase. Trung [7] studied risk management of bridge, Son [2] studied risks in the form of public-private partnership to develop road transport infrastructure projects in Vietnam which has summarized 51 specific risks. Chau and Toan [8] researched and managed technical risks of road construction in Vietnam, Lam and Anh [2, 9–11] research on identification and management of technical risks of expressway bridges, etc.

Artificial Intelligence (AI) in Construction Management was defined by Clavero [12] as an amount of information that the human mind can process which is limited by time and space. However, AI arrests a big quantity of data to analyze the information for patterns and trends. In essence, AI uses the computer power to model the human natural intelligence. The machine learning (ML) is used in AI to solve problems and accomplish tasks with high speed and precision that have been developed since the 1970s and 80s. The combination of ML with Monte Carlo simulation can help risk managers to improve the assessment and prediction of risk. Fuzzy logic is used for assessing risks in construction projects [12]. Anon, in 2016, stated

that the ML tools are mostly used in the business field. Moreover, it was stated that just some machine learning models are capable to compete or even accompany conventional civil engineering techniques of design in: predicting demand depending on economic indicators, predicting delays depending on progress toward existing schedule, assessing the subcontractors and suppliers' performances, understanding when scheduling is optimistic, etc. [13]. Furthermore, the ML has been utilized in the highway construction as it provides efficient use of materials, reduces losses, and offers uniform results. Whether it is only enhancing operational life cycles or even avoiding over compacting, decision-making is improved by Artificial Intelligence and ML. Based on the previous review, there is a shortage of studies on the applying of machine learning for risk management of highway bridge construction.

In this paper, an Artificial Intelligence model for technical risk identification and prediction in highway bridge projects will be constructed based on the previous investigation results during the bridge construction and operation in Vietnam, the ensemble methods with Random Forest algorithm (a supervised machine learning algorithm used for classification and regression problems in ML) will be discussed and be used to obtain better risk predictive performance, and then, the application for real projects is intended.

2 AI Model for Risk Identification and Prediction of Highway Bridge

2.1 Model Construction

AI model is built using the machine learning with the following main steps:

- Collecting datasets of risks on highway bridges.
- Building Artificial Neural Networks (ANN model).
- Building a feature extractor using Random Forest (RF) algorithm.
- Building an ANN risk prediction model using RF (AI model).

Collecting datasets will be presented in Item 2.2.

ANN, flexible mathematical structures that are capable of identifying complex nonlinear relationships between input and output datasets, was constructed for this model in using multi-layer perceptron's (MLPs) structure [6], and the neurons are grouped into four layers: the first and last ones are called input and output layers, respectively, which represent the dataset's attributes (inputs) and risk scores (outputs) of the overall network for risk model; the remaining ones are hidden layers.

The Random Forest algorithm is one method for determining the importance of a feature in a dataset [14]. A RF is simply a set of decision trees [14, 15]. The features for any decision tree are chosen by partitioning the training set into pure subsets (minimum cross-entropy). A decision tree then generates a list of steps to partition the data most efficiently and quickly. As a result, the features at the top of the tree

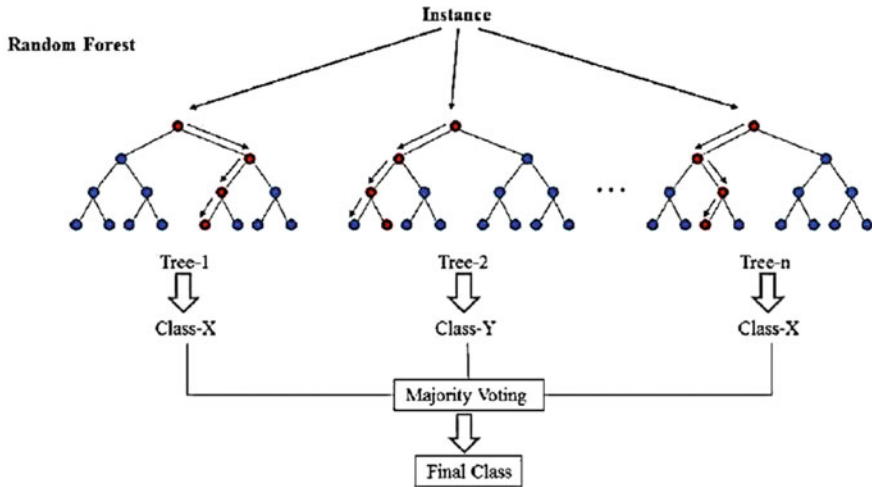


Fig. 1 Random forest algorithm

(closest to the root node) are the most important. The general flow of this algorithm is depicted (see Fig. 1).

The advantage of RF is that the tree is built without branching from different sub-datasets, but rather with the boosting technique with replacement, resulting in trees with low-bias error. Furthermore, by randomly constructing feature subspaces, the correlation relationship between decision trees is minimized. As a result, combining the outcomes of a large number of low-bias, high-variance independent decision trees will assist RF in achieving both low bias and low variance. The predictive quality of the decision trees and the degree of correlation between the decision trees determine the accuracy of RF.

To model risk assessment of highway bridges, we use a multi-layer straightforward neural network with input of important features extracted from the RF algorithm.

The expert opinion survey is necessary to make the AI model more objective when evaluating quantitatively biased attributes in the dataset. We proceed to build a survey questionnaire that includes information about various types of technical parameters. We conduct a survey with technical parameters including factors that have little influence on the risk level of the bridge after running the Random Forest algorithm.

2.2 Dataset and Investigation

In this paper, we use the dataset taken from the Department for Roads of Vietnam [16]. The data include a lot of information such as bridge structure type, girder structure type, span structure type, year of operation, average traffic volume, and especially,

Table 1 Number of bridges in dataset

Road management zone	I	II	III	IV	Departments of transport of provinces	Total
Number of bridges	901	988	890	1393	7008	11,180

risk index to assess damage level of a bridge at the survey time by experts. There are 59 attributes collected for each bridge. This information is very valuable for us to analyze and build risk models for different types of highway bridges. We collected a total of 11,180 data samples of bridges in the country which include many different types of bridges as in Table 1.

For data samples with adequacy of more than 80%, we use technique of replacing missing values with the average value of attributes with full data. For attributes with values less than 20%, we use the method of removing that attribute from the dataset.

After conducting the data preprocessing steps, we proceed to divide the dataset into training dataset and test dataset.

2.3 Scenario for Testing and Error Estimation

Experiments were conducted according to the following two scenarios:

Using AI model without feature extraction: a test run on the dataset without feature extraction step but with support of investigation of expert.

Using AI model with important attributes: AI model with important feature extraction by Random Forest algorithm.

To build an important set of attributes with the Random Forest algorithm, there are several hyperparameters that need to be selected such as *n_estimator*, *criterion*, *max_depth*, *max_samples*, *max_features*. The choice of values of these hyperparameters will affect the efficiency of the Random Forest algorithm. However, finding some optimal parameters is a difficult and time-consuming task. It usually requires the knowledge and experience of the modeler. For each scenario, the neural network using Gradient Descent was launched [6, 17], and its effectiveness was measured with mean squared error (MSE) defined as follows:

$$MSE = \frac{1}{n} \sum_{i=1}^n (Y_i - \bar{Y})^2, \tag{1}$$

in which X_i and Y_i are actual value and calculated value; \bar{X} , \bar{Y} : the average value.

These parameters are measured per epoch of the training process with both the training dataset and the test dataset. The best evaluation results are obtained at the time when the model has the MSE value on the smallest test set.

3 Risk Identification of Real Bridges by AI Model

As mentioned in Item 1, to facilitate risk identification in bridge projects, numerous techniques are available. For the case using AI model without using feature extraction even with support of some expert investigation, the model falls into the overfitting phenomenon [16–18], i.e., being overfitted into the training dataset without the ability to generalize to the test dataset. This problem is clearly shown in Fig. 2. Obviously, this method is not effective because the neural network architecture only learns well on the training dataset without generalization on the test set. The best MSE loss value of the model on the training set is 0.0022 and on the test set is 0.037.

For the case where the RF algorithm is used for feature extraction, the AI model works more stably, as the loss on the training set and the test set both decreases quite smoothly and has the ability to generalize to the data on the test set. This proves that feature extraction has helped the model to remove information that is not related to the level of risk. This makes the model simpler and avoids being fitted with outliers in the dataset. The best MSE loss value of the model on the training set is 0.0009 and on the test set is 0.0018, which is much better than the first case (see Fig. 2).

For risk factors' identification, we proceed the dataset into the RF algorithm to predict the importance of the collected 59 attributes in Item 2.2, some observations as follows:

- The factors that have the most influence on the risk level of a bridge: average traffic volume, service load, service speed, year of operation, common running objects. This is understandable because these attributes will represent the actual exploitation and use of the bridge and also the data collected directly during the actual mining process on many other bridge samples, so they will show the generalization level of the models.
- The factors that have less influence on the risk levels (in this dataset) related to the technical characteristics of the bridge such as wearing coat, bearing structure material, cross-beam. These factors proved to have little effect on the risk levels of the bridge. Meanwhile, factors in the specifications of a bridge will certainly have an influence on the level of risk. To overcome this situation and increase the

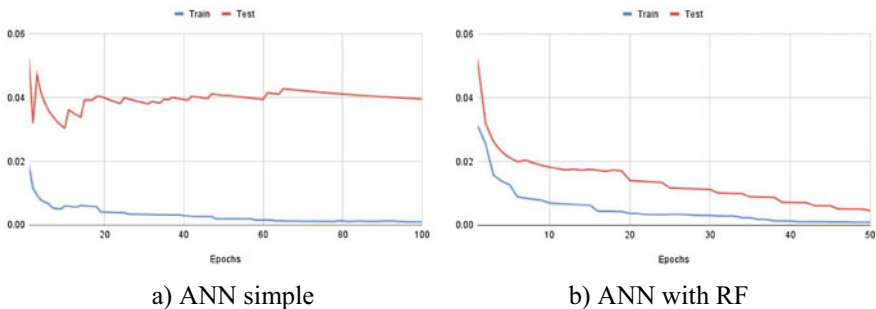


Fig. 2 MSE index of AI model

objectivity of the research, we conducted also a survey of experts about the actual influence of these attributes on the risk score of bridges and the identification results will be continued to discuss in our next paper.

4 Risk Prediction by AI Model

For risk prediction illustration, we selected 11 real data samples from the test dataset, including actual highway bridges collected from the VBMS dataset [19] and site survey [2]. Details are described in Table 2, in which we have representative and the most influencing factors such as Service Year—Number of service years of the bridge, Average speed—average service speed, Average Load—Average Service Load of Vehicle, Average Traffic Volume—Average Service Traffic Volume, Score—Risk Score assessed through the expert survey [19], Predicted Score—the risk score assessed by the proposed AI model.

A lower risk score represents a higher level of risk, calculated on a 100-point scale. It means that if the score is small, the risk is higher. In Table 2, we can find that the old bridge with big traffic volume has more risk with the low score, but a new bridge with high traffic volume may also have a not high score. In this case, it shows the important impact of traffic volume in risk prediction. The speed will also an important impact as well and should be considered later in other paper.

Table 2 Prediction results by AI model

No.	Service years	Average speed (km/h)	Average traffic volume	Risk score	Predicted score
1	20	60	30,000	60	61.4
2	20	50	15,000	69	70.2
3	20	50	2000	90	91.2
4	15	50	100,000	48	49.3
5	15	50	20,000	72	71.2
6	15	50	5000	83	83.4
7	10	50	100,000	50	50.4
8	10	50	35,000	65	66.2
9	10	50	2000	90	89.3
10	5	55	100,000	52	51.2
11	5	50	1000	99	98.2

5 Conclusion

In this paper, an AI machine learning models was built based on the data of 11,180 bridges, collected from the Department for Roads of Vietnam to train and test with the MSE index. The risk factors can be identified by Random Forest algorithm, and the most important five ones were found from the 59 attributes at the beginning. The use of AI model for prediction shows the advantages and gives accurate results in comparison with the exist ones of expert survey, so it can be improved to overcome current limitations in risk identification and prediction when the database is missing. However, the accuracy of the AI model depends heavily on the quality of the data, which is also a limitation in predictive analysis, and adding input data from investigation to retrain the AI model is one solution to help the model more accurate. The risk identification and prediction AI model, in the Fourth Industrial Revolution (4.0), will be a good tool to support design, verification, and management of technical design stage, construction and operation stages with the combination of all the big and fuzzy input data, so it needs to be fully promoted.

Acknowledgements The authors would like thank to Department for Roads of Vietnam and University of Transport and Communications, Vietnam, for their kind support in our research.

References

1. Deco A, Frangopol DM (2011) Risk assessment of highway bridges under multiple hazards. *J Risk Res* 14:1057–1089
2. Lam DD, Anh LD, Dong NT (2019) Report of scientific and technological research project of Ministry of transport. In: Research on identification and management of technical risks of expressway bridges (in Vietnamese)
3. Clark-Ginsberg A, Abolhassani L, Azam Rahmati E (2018) Comparing networked and linear risk assessments: from theory to evidence. *Int J Disaster Risk Reduct* 30B:216–224
4. Andric JM, Lu D (2016) Risk assessment of bridges under multiple hazards in operation period. *Saf Sci* 83:80–92
5. Zio E (2018) The future of risk assessment. *Reliab Eng Syst Saf* 177:176–190
6. Chen Z, Li Z, Huang C, Zhang G, Yu H (2018) Safety assessment method of bridge crane based on cluster analysis and neural network. *Proc Comput Sci* 131:477–484
7. Trung NV, Tam DC (2011) Risk analysis and management in bridge construction. *Civil Construction Public House* (in Vietnamese)
8. Chau NV (2016) Researching and managing technical risks in road construction in Vietnam. Ph.D. thesis. University of Transport and Communications (in Vietnamese)
9. Anh LD, Lam DD, Dong NT (2019) Identification of technical risks for bridges on the highway in Vietnam. *Transp J* 12:40–44 (in Vietnamese)
10. Lam DD, Anh LD, Dong NT (2021) Risk management of expressway bridge projects in Vietnam: current status and future researches. In: Proceedings of the tenth international conference on bridge maintenance, safety and management (IABMAS 2020), 1st edn, pp 1962–1965
11. Lam DD, Trung NV, Huy NQ (2019) Solution pour améliorer la maintenance des ponts. *Acad J Civ Eng* 36

12. Clavero J (2018) Applications for artificial intelligence in construction management. Retrieved from <https://esub.com/applications-artificial-intelligenceconstruction-management/>
13. Anon (2016) How machine learning meets construction industry. Retrieved from <http://ai.business/2016/12/15/how-machine-learningmeets-construction-industry>
14. Jia H, Lin J, Liu J (2019) An earthquake fatalities assessment method based on feature importance with deep learning and random forest models. *Sustainability* 11:2727–2748
15. Kira K, Rendell LA (1992) A practical approach to feature selection. *Mach Learn Proc* 1992:249–256
16. Van der Aalst WMP, Rubin V, Verbeek HMW, Van Dongen BF, Kindler E, Gunther CW (2010) Process mining: a two-step approach to balance between underfitting and overfitting. *Softw Syst Model* 9:87–111
17. Gonzalez Zelaya CV (2019) Towards explaining the effects of data preprocessing on machine learning. In: *IEEE 35th international conference on data engineering (ICDE)*, pp 2086–2090
18. Hawkins DM (2004) The problem of overfitting. *J Chem Inf Comput Sci* 44:1–12
19. Department for Roads of Vietnam: data from bridge management system. <http://www.vbms.vn>

Integrating Terrestrial Laser Scanning Technology and Unmanned Aerial Vehicles in Establishing a Database for the Preservation of Ancient Constructions



Do Van Manh, Le Quang, and Vu Ngoc Phuong

Abstract Nowadays, ancient buildings with cultural and historical value are in danger of being completely destroyed by natural disasters, climate change, and even war. It isn't easy to restore buildings of this type without the necessary databases. Therefore, generating 3D models is the most convenient method to establish databases of constructions for maintenance and preservation purposes. Hence, this study aims to integrate terrestrial laser scanning technology and unmanned aerial vehicles (UAV) in establishing a 3D model where all the detailed information about the ancient building can be stored for the preservation of the unique intangible cultural values of each country.

Keywords Unmanned aerial vehicles (UAV) · 3D-models · Digital modeling · Terrestrial laser scanning · Ancient buildings

1 Introduction

Nowadays, there are a variety of causes for the deconstruction of historically significant and culturally significant buildings, such as fire [1–4], war [2, 5–7], traffic roads [8], the construction of public works new construction, or illegal construction. The restoration of these works is extremely difficult because of the lack of detailed data and documents on the structure of the work (Fig. 1).

Many solutions have been offered, such as building models, creating the database from the construction of detailed structures using ground laser scanners, or backing up detailed data on structures as designed drawings or digital files [10–12]. The weakness of the above solutions is that the landscape around the work cannot be obtained, so the restoration will be limited.

D. Van Manh (✉) · L. Quang · V. N. Phuong
University of Transport and Communications/UTC, Hanoi, Vietnam
e-mail: manhdv@utc.edu.vn

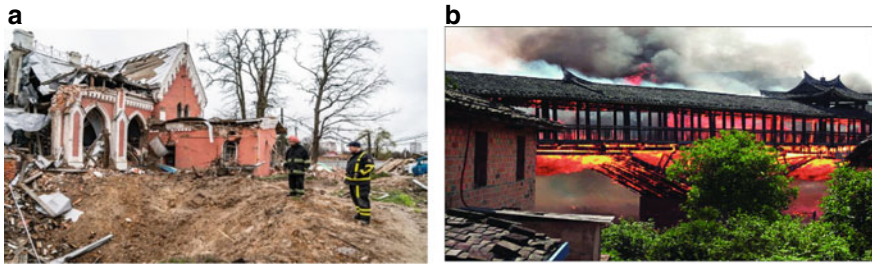


Fig. 1 Important cultural sites were destroyed or damaged by war and fire. **a** The Historical Chernihiv Library, located in a residential area of the city, was heavily damaged by bombing during the Russian invasion on April 16, 2022 (<https://www.forbes.com>). **b** The Yuqing Bridge was destroyed by fire in 2011, one of over 60 lost in recent years [9]

Therefore, this study aims to provide a solution that integrates terrestrial laser scanning (TLS) and unmanned aerial vehicle (UAV) technology to create 3D models of construction projects for reconstruction purposes. It can support the restoration of ancient buildings, such as churches, temples, roads, bridges, and skyscrapers that were damaged by natural disasters, fire, and war.

2 Methodology

2.1 *The Process of Integrating Laser Terrestrial Laser Scanning (TLS) and Unmanned Aerial Vehicles (UAV)*

First, establish a geodetic control network (Fig. 2).

The horizontal control network and leveling control network are established as the basis for determining the coordinates of the center of the image, the control points of the image, and the control points used to convert the coordinate system of the scanning station.

- The deployment of UAV technology:

- Design UAV photography:

Selecting the flying altitude for photography, design flight routes, horizontal coverage, vertical coverage, and bevel angle when taking photos. It may be necessary to fly multiple times at different angles and directions of experimental areas.

- Fly and take pictures with the UAV:

The subject is photographed from the UAV at both vertical and oblique angles, and the coordinates of the center of the image are determined simultaneously during flight and ground photography.

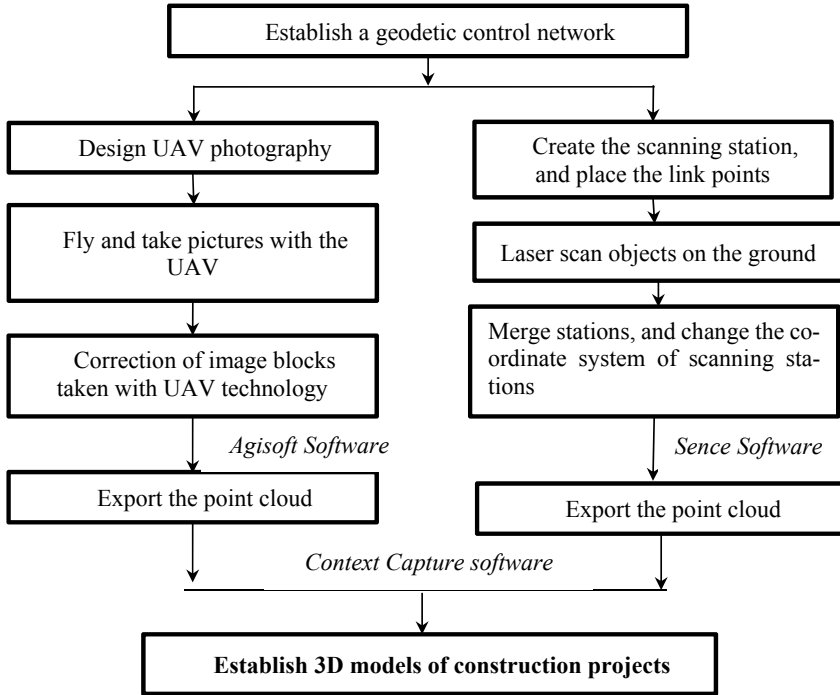


Fig. 2 The process of integrating TLS and UAV

- Correction of image blocks taken with UAV technology by Agisoft Software:

The image blocks are linked, and the adjustment is calculated based on the coordinates of the image control points, and the coordinates of the shooting centers.

- The deployment of TLS:

- Design scanning station, and location of link points:

Design the scan station position to optimize the number of stations. To link the scanning stations, it is necessary to select the location of the link points between the measuring stations appropriately.

- Laser scan objects on the ground:

Objects are scanned from ground stations at various locations to ensure detail and completeness. There should also be an overlap between consecutive stations.

- Merge stations, and change the coordinate system of scanning stations by Sence software:

Scanning stations are combined into blocks based on common points, then transform the object space coordinate system based on control points.

- Finally, export the point cloud to generate 3D model Context Capture software:

The image blocks and scanning stations, after being processed and returned to the object space coordinate system, will be output to the point cloud. These two point clouds are paired together by the same control points (geodetic control network) or the same clear objective points on two models as the basis for building 3D models of objects.

2.2 Assessing the Accuracy of the 3D Model

The accuracy of the 3D model is evaluated according to the following steps.

- Step 1: Mark the overlapping points in the empirical area and on the 3D model
- Step 2: Use the robust tool to measure the distance between 2 points on the model (by software support tools) and in the empirical area (by using a total station or a steel ruler)
- Step 3: Compare the distance measured on the model and the distance in the field
- Step 4: Conclusion about the accuracy.

3 Implementation

The experiment was carried out at Hoang An Pagoda area, Tay Ho district, Hanoi with an area of about 2.5 ha. Taking pictures of 785 images from UAV including a straight shot and a shot with a 30° bevel, the coordinates of the center of the image were determined by global positioning systems-Post processed kinematic (GPS-PPK) method. Then creating the digital elevation model (DEM) of the empirical area (Fig. 3).

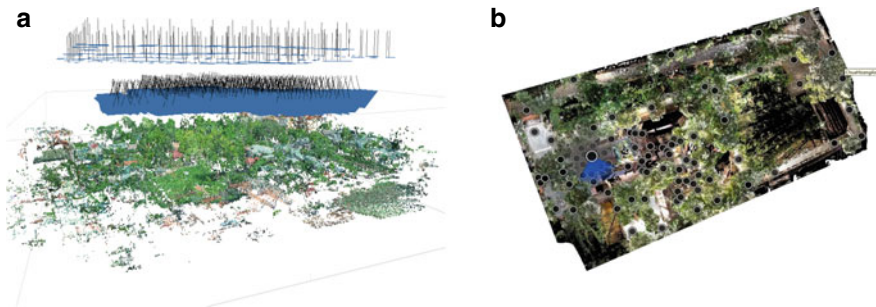


Fig. 3 The empirical area. **a** Creating the digital elevation model (DEM) of the empirical area. **b** 91 stations were conducted to scan both the outside and the inside of this ancient temple

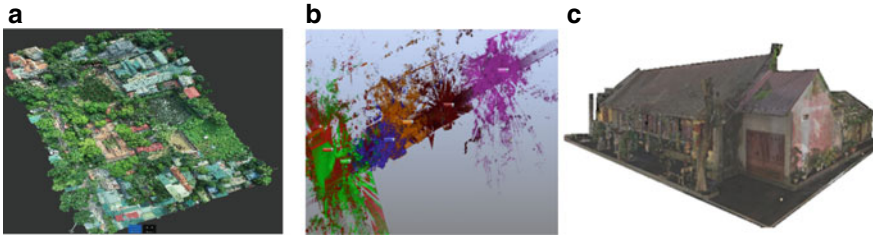


Fig. 4 The experimental results at Hoang An Pagoda. **a** The point cloud of UAV. **b** The point cloud of laser scanning. **c** 3D of Hoang An Pagoda

On the ground, 91 stations were conducted to scan both the outside and the inside of this ancient temple. Scanning stations are performed by a laser scanner named Faro Focus S350, between stations using common points to link. The coordinates of the control points used to convert the coordinate system of the scanning station are measured by the total station. The results after processing are shown in (Fig. 4).

4 Conclusions and Remarks

There are two sources of error in the accuracy of the 3D model due to the UAV image processing and the error caused by the processing of TLS. After testing some distances on the natural ground and the 3D digital model, the average error of the lengths of 10 typical measuring distances is $M_D = \pm 12$ (cm). The details of the test, how to test, and how to improve accuracy will be published in the next publication of this study.

In establishing 3D models, the ground laser scanning method gives high detail in the ground and the details inside the building, but it is difficult to obtain with the overhead structures of the building. The research has provided a basis for combining images taken from an auxiliary UAV for the ground laser scanning method to build a complete and effective 3D model.

Currently, the establishment of 3D models of architectural works, and historical sites, has been done quite a lot. However, it is necessary to have standards in the construction of 3D models to have a basis for making accuracy requirements for each stage or a basis for evaluating the accuracy of methods.

References

1. Amriddinovich AD et al (2021) Architecture of historical cities of Uzbekistan. Acad Int Multidisc Res J 11(12):443–445
2. Bevan R (2016) The destruction of memory: architecture at war-second expanded edition. Reaktion Books

3. Martinho E, Dionísio A (2018) Assessment techniques for studying the effects of fire on stone materials: a literature review. *Int J Arch Herit* 14(2):275–299
4. Okubo T (2016) Traditional wisdom for disaster mitigation in history of Japanese architectures and historic cities. *J Cult Herit* 20:715–724
5. Brosché J et al (2017) Heritage under attack: motives for targeting cultural property during armed conflict. *Int J Herit Stud* 23(3):248–260
6. Stiros SC (2020) Monumental articulated ancient Greek and Roman columns and temples and earthquakes: archaeological, historical, and engineering approaches. *J Seismolog* 24(4):853–881
7. Themistocleous K (2017) Model reconstruction for 3D visualization of cultural heritage sites using open data from social media: the case study of soli, cyprus. *J Archaeol Sci Rep* 14:774–781
8. Cherkas B et al (2019) Search of authenticity in sacral architecture in the territory of Western Ukraine. *IOP Conf Ser Mater Sci Eng* 603(2):022078
9. Zhou H et al (2018) China's unique woven timber arch bridges. *Proc Inst Civ Eng Civ Eng* 171(3):115–120
10. Edl M, Mizerák M, Trojan J (2018) 3D laser scanners: history and applications. *Acta Simul Int Sci J Simul* 4:4–5
11. Sepasgozaar SM, Shirowzhan S, Wang CC (2017) A scanner technology acceptance model for construction projects. *Proc Eng* 180:1237–1246
12. Wang C et al (2018) Semantic line framework-based indoor building modeling using backpacked laser scanning point cloud. *ISPRS J Photogramm Remote Sens* 143:150–166

Pavement Crack Segmentation Using an Attention-Based Deep Learning Model



Hieu Dao, Tung Khuc, Quan Truong, Cang Dinh, and Andy Nguyen

Abstract It has been observed that cracks, the most common sign of deterioration happening on the pavement, are difficult to detect at an early stage. Although the U-net-based model has detected well-established cracks, it shows some limitations when working with low-quality pavement images that are automatically captured by moving pavement-inspection vehicles. In this study, the attention technique is applied to the U-net model to enhance the results of pavement crack detection under some difficult pavement image conditions. Attention gates (AGs) are deployed at the skip connections of the U-net model to remove irrelevant regions by setting attention weights for each image part. This procedure helps the U-net model learn how to eliminate extraneous regions in the input image. Therefore, the technique minimizes the computational resources by ignoring wasted irrelevant operations and enhances crack segmentation results. The proposed model is verified using a real-life image packet of pavement. The performance of the attention U-net model illustrates better outcomes compared to the ones from the U-net model.

Keywords Deep learning · Attention gate · U-net · Pavement crack detection

1 Introduction

The development of digital image technologies and data processing algorithms makes it possible to detect and identify the deterioration of civil engineering projects and structures [1]. Due to the constant direct load of vehicles, the pavement surface requires regular monitoring and early detection of damage before it becomes severely damaged. Vision-based methods have been introduced in pavement surface maintenance, starting with images pictured by cameras mounted on a survey vehicle. Then,

H. Dao · T. Khuc (✉) · Q. Truong · C. Dinh

Faculty of Bridge and Road Engineering, Hanoi University of Civil Engineering, Hanoi, Vietnam
e-mail: tungkd@huce.edu.vn

A. Nguyen

School of Engineering, University of Southern Queensland, Springfield Central, QLD, Australia

© The Author(s), under exclusive license to Springer Nature Singapore Pte Ltd. 2024

727

T. Nguyen-Xuan et al. (eds.), *Proceedings of the 4th International Conference on*

Sustainability in Civil Engineering, Lecture Notes in Civil Engineering 344,

https://doi.org/10.1007/978-981-99-2345-8_75

classical image processing algorithms were applied to detect cracks that yielded potential results [2]. Although these methods can detect cracks, their accuracy is still very limited. Since the algorithms are still developed with manually inputting parameters, their results will depend on the experience of monitoring and analysing engineers. Moreover, these methods are commonly less effective with automatically collected images, which always contain a lot of noise.

Recently, a new approach attracted the research community to apply deep learning techniques [3]. An initial study conducting the deep learning algorithm in crack detection has been developed by Kelvin Wang's group based on 3D laser images of pavement surfaces [4]. Majidifard uses Google's application programming interface (API) in street view to propose a method of pavement crack detection [5]. Early CNN-based models for pavement crack detection can only detect cracks at the image or block level. In order to detect the shapes and dimensions of pavement cracks, subsequent studies have proposed methods of pixel-level detection based on decode-encode networks of deep learning. One of the most well-known decode-encode algorithms named U-Net is used by Ju et al. [6] to propose a model called CrackU-net that can detect pavement cracks on images collected by vehicle-mounted smartphones. Chen et al. [7] used the SegNet model, a more minimalist model than the U-Net model, for real-time detection due to the outperformance of SegNet's calculating optimizations. Another study focuses on combining several deep learning models to improve pavement crack detection performance [8]. Image datasets used by those studies are CrackForest [9], CrackTree200 [10], or designed by their own groups [6, 11]. As it is seen that designing and preparing labelled images for pixel-level crack detection are laborious, augmentations are commonly applied [12].

1.1 Motivation and Research Objective

Although the U-net-based model has detected well-established cracks, the main challenge of the algorithm is the inaccurate crack detection outcomes when the pavement images are of low quality due to the movement of the pavement-inspection vehicle. In this study, the attention technique is proposed to overcome that problem. By implementing attention gates (AGs) at skip connections of the U-net model, the irrelevant regions are ignored by placing attention weights on each part of the image. This mechanism will improve the performance of the conventional U-net model and increase the ability to recognize pavement cracks in noisy and low-quality pavement images. Several studies applied attention U-Net to available datasets and showed its effectiveness in pavement crack segmentation [13, 14]. The common point of these studies is that they all use purpose-built datasets generated by still images, which significantly eliminates the noise that the real-life monitoring images may have. Therefore, in this research, image datasets captured by a pavement-inspection vehicle at a real-life highway are labelled and enhanced based on pavement image engineering properties to increase network training performance. Using a dataset that has been applied in real-life monitoring work, the research contribution is to

reduce the workload by improving the automatic pavement crack detection with the attention U-net model. The accuracy metrics are calculated that demonstrated the effectiveness of the proposed method.

2 Dataset

Pavement surface images are collected by two cameras mounted at the rear of a pavement-inspection vehicle. Due to being captured when the vehicle is moving, the image quality is significantly affected. Some popular imaging problems are blurring and having less contrast, which always influences the training effectiveness of deep learning models. To enhance the image quality, a contrast-based method is applied to increase the difference between light and dark parts of images [15]. Data labelling is also a challenge because the labelled image accuracy requires expert intervention, which leads to the number of labelled images is limited. Since a deep learning model always needs large enough datasets, several augmentation techniques are implemented to generate more images. Figure 1 presents the process of image enhancement and augmentation to develop datasets for the training model.

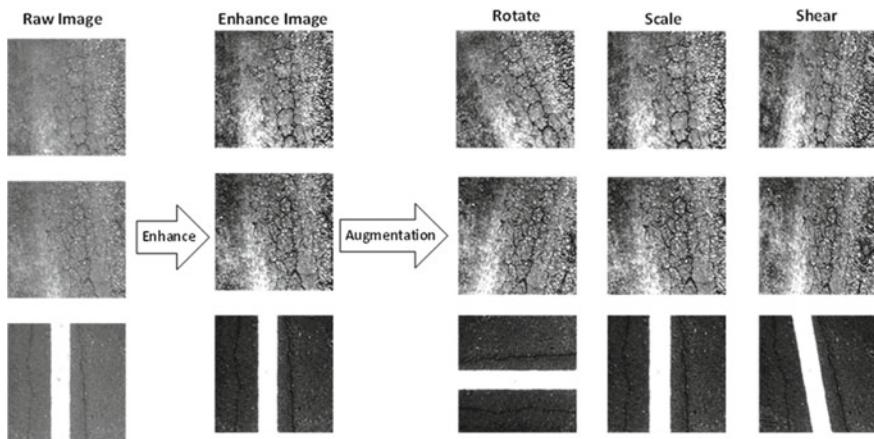


Fig. 1 Image enhancement and augmentation

3 The Attention U-Net Deep Learning Model

3.1 The U-Net Deep Learning Model

An advantage of the U-Net model is that the model can be trained with few images in the dataset. Moreover, the U-Net is a type of pixel classification algorithm, so it has potential for the application of pixel-level crack detection [16]. This model is a symmetric network consisting of two main parts called the encoder and decoder branches (Fig. 2). In this study, the input data are 480×480 grayscale images, and the output data are same-size binary segmentation maps. The main component is the convolutional block including a convolutional layer, a batch normalization and a ReLU activation function. The encoder branch is a conventional convolution network. After every two convolutional blocks, a 2×2 max-pooling layer with a stride of 2 is arranged to halve the feature map dimension. Since the feature map dimension is halved, the kernel's numbers in convolutional layers are twice as large as those in the previous layer.

In the decoder branch, the max-pooling layer is replaced by the up-sample layer with 2×2 kernels to double the dimension of previously feature maps. Since the encoder branch aims to filter, highlight and extract image feature maps, the decoder branch tries to reconstruct those extracted features to map with labelled images for training. The skip connection links the feature maps from the encoder branch to its counterpart in the decoder branch. This mechanism intends to enhance the accuracy of the feature locations for reconstructing images. The sigmoid activation is located at the end of the network to calculate the probability of each of the classes, which are cracks or background pixels in pavement surface images.

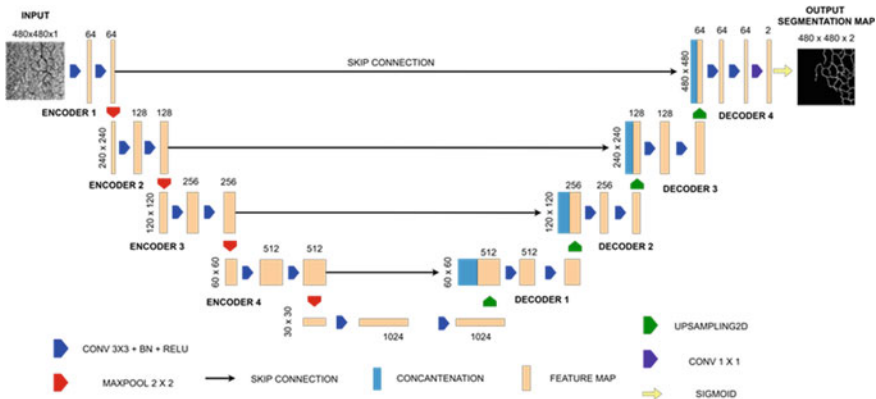


Fig. 2 Architecture of U-net model—modified from a figure in [16]

3.2 Attention Gates (AGs)

Two types of attention are studied: hard attention and soft attention. For hard attention, the relevant region is highlighted by cropping the image, so it only focuses on one region of an image at a time. It means that hard attention deep learning model has only two choices of either paying attention to a relevant region or not. Therefore, this attention type is non-differentiable and could not apply standard backpropagation for the training model as in deep learning methods. On the other hand, soft attention sets weights on each pixel in the image. These attention weights are learnable and are assigned high values to regions of salient feature. Due to this deterministic property, it can be differentiable and applied with standard backpropagation for training [17]. Figure 3a presents the attention U-Net model architecture used in this study. AGs are added to the skip connections and are calculated from the encoder and decoder up-sampling features.

Figure 3b explains the attention gate operation, where the input includes up-sampling feature s in the decoder and encoder feature f from the encoder. The up-sampling feature s is taken from the deeper layer and located before the output layer of the attention gate. Encoder feature f is the output of the layer in the encoder branch at the location of the corresponding attention gate. Because the dimensions of these features are not equal, the feature s has to go through a transposed convolution layer to double its dimensions. When the dimensions of feature s and f are the same, they are summed creating the resultant feature map. This map is then passed through two activation functions and resampled to get the attention coefficient map by using trilinear interpolation. Finally, the attention coefficient map is multiplied by the original feature f and results in the attention weight map [18].

By applying the attention gate, the U-net model takes an additional step to remove the irrelevant and focus on the regions that need attention. Figure 4 shows the original image, the enhanced image and their attention coefficient map. In Fig. 4c, the magnitude of the attention coefficient is represented in the brightness colour fashion. The coefficients at the crack region are clearly shown with the high brightness colour, while the coefficients in the background are assigned almost zero. However, the regions far away from the cracks also have high attention coefficients. This could be explained that the enhanced image still contains noise, and the attention gate cannot be clearly identified and eliminated. The identification and elimination of these regions could be done in the deeper layers of the U-Net model.

4 Experiment and Evaluation

As described in the previous section, a dataset of 20 pavement images was augmented for training two deep learning models: a conventional U-net and an attention U-net. The augmented image dataset consists of 320 images including 288 images for training and 32 images for testing. The deep learning networks were written by Python

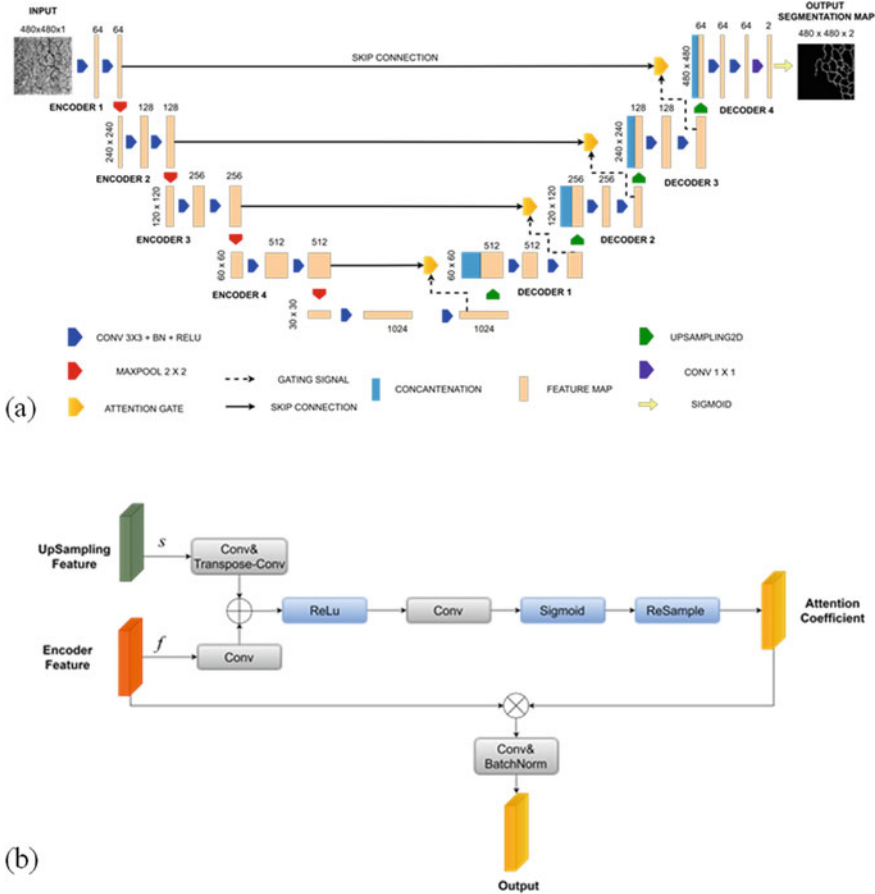


Fig. 3 **a** Architecture of the attention U-net model. **b** Schematic of the attention gate (AG)—modified from figures in [18]

(v3.7) in the Google Colaboratory (Google Colab) environment. This environment allows users to program Python through a web browser and performs tasks in a cloud environment provided by Google. The configuration provided by Google Colab in this research is GPU NVIDIA Tesla T4 and 25 Gb RAM. The image data in this study were processed by using the Albumentation library, a Python-based computer vision toolbox [19]. Figure 5 shows the training accuracy and loss of the attention U-net model after 50 epochs. The last values of accuracy and loss are 0.9923 and 0.1341, respectively.

After training, the last model (at the final epoch) was evaluated with Recall, Precision and F1-score:

$$\text{Recall} = \frac{\text{TP}}{\text{TP} + \text{FN}} \tag{1}$$

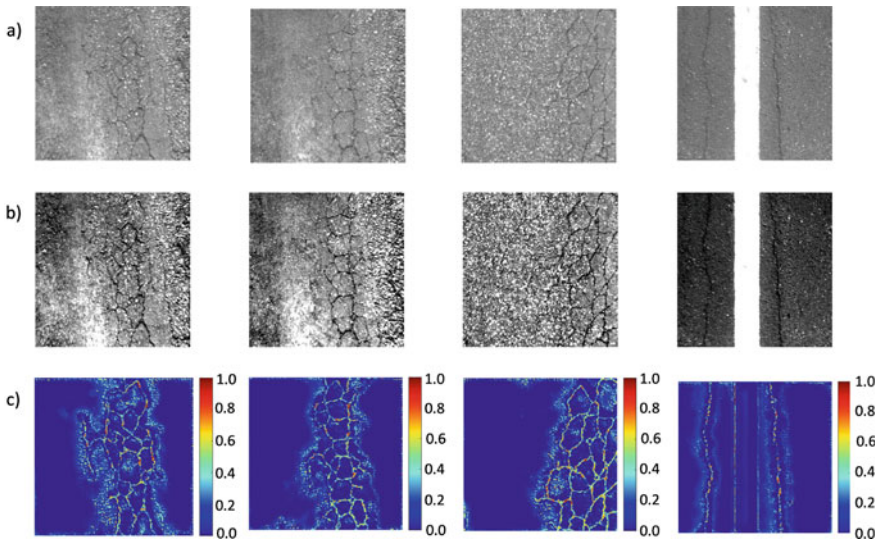


Fig. 4 **a** Original image; **b** enhanced image; **c** the attention coefficient map of the corresponding enhanced image

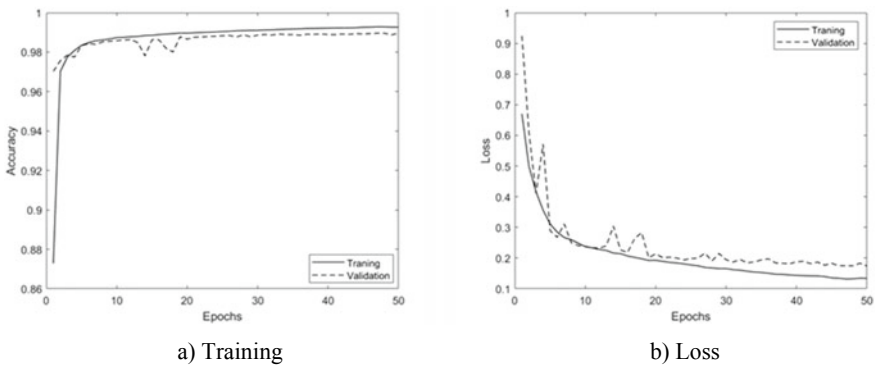


Fig. 5 Model accuracy and loss during the training process

$$\text{Precision} = \frac{TP}{TP + FP} \tag{2}$$

$$F1 - \text{score} = \frac{2 * \text{Precision} * \text{Recall}}{\text{Precision} + \text{Recall}}, \tag{3}$$

where TP is the true positive (pixels that correctly match the labelled crack region); TN is the true negative (non-defected pavement pixels are correctly detected by the trained model); FP is the false positive (defective pixels are detected incorrectly);

Table 1 Comparison of metrics and running time between the U-net model and attention U-net model

	Precision	Recall	F1-score	Time (seconds)
U-net	0.829	0.817	0.823	3244
Attention U-net	0.893	0.892	0.892	4162

FN is the false negative (defective pixels are not detected by the trained model); Precision is the proportion of correct crack pixels in the detection results; Recall is the proportion of correct crack pixels that are not ignored by the deep learning model, and *F1*-score is the harmonic mean of both Precision and Recall.

Table 1 presents the metric results of each model determined based on absolute pixel accuracy without using tolerance margin. It is seen that the resulting metrics of the attention U-net are better than the U-net model outcomes. Results of the attention U-net model achieve Precision = 0.893 and Recall = 0.892 that outperform the U-net model's values with Precision = 0.829 and Recall = 0.817. It means that the attention U-Net model is capable of sufficiently and accurately detecting the crack shape better than the U-Net model.

Figure 6 includes the original image taken from the pavement surface dataset, the enhanced image, the manually labelled image as ground truth and the detected result image from U-Net and the attention U-Net model. The cracks predicted by both models are almost completely compared to the labelled data. However, the identification results from the attention U-Net are more accurate because the detected crack lines are not as broken as those of the U-Net model. Figure 7 shows more clearly the difference between the detection pixel results of the two deep learning models. In these images, the white pixel represents the crack correctly detected, and black pixels are detected as undamaged pavement background. Green pixels are those that the model did not identify as cracks, but were labelled as damaged. In addition, purple pixels were recognized by the model as cracks, but in the labelled image those pixels were not labelled as cracks. Although the results from both models still have some false detections in the crack edge regions, the purple pixels in the attention U-Net model results are significantly reduced. In the U-Net model, green pixels represent some parts of the crack that are completely ignored, which can be detected precisely with the attention U-Net model.

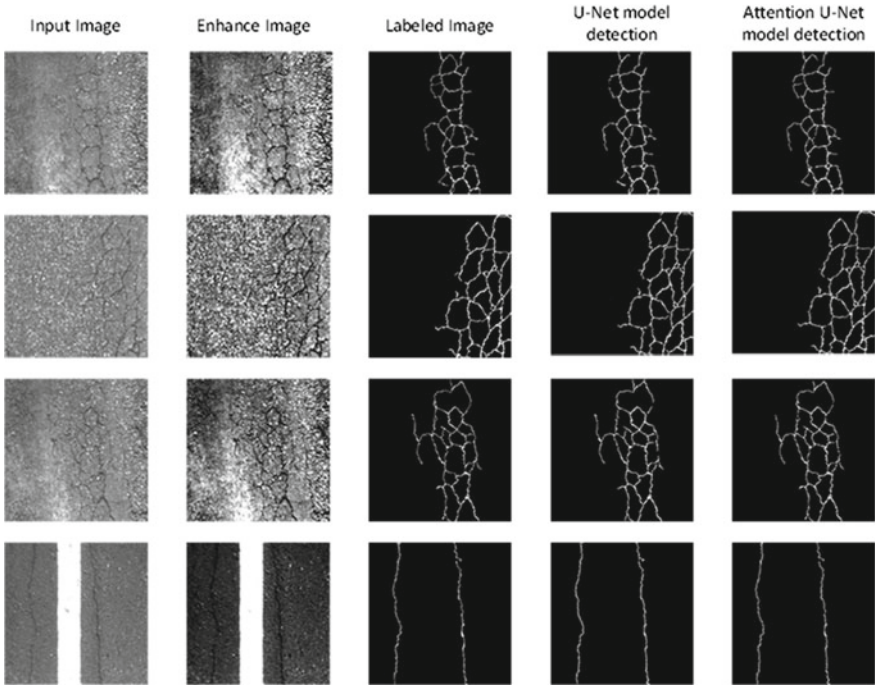
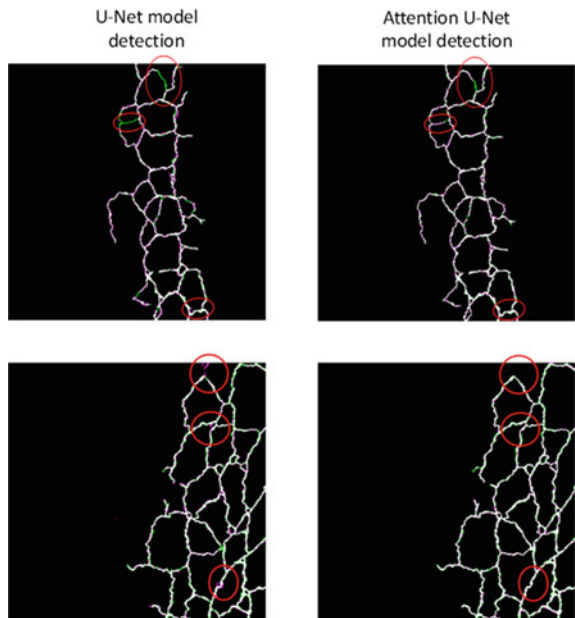


Fig. 6 Comparison of the models' performances

Fig. 7 The crack detection pixel results of the U-Net model and the Attention U-Net model



5 Conclusion

In this study, an attention U-Net-based deep learning model is studied for automatically detecting pavement cracks. The proposed model has the ability to accurately detect the crack shape and dimension better than a conventional U-net performance. By adding the attention gates to the U-net model, the cracks in pavement surfaces can be detected more accurately. The proposed approach has been evaluated using the pavement surface dataset at a real-life expressway and achieving some potential results. The model's detection results are $Precision = 0.893$ and $Recall = 0.892$, which is a higher rate of detection compared to previous studies. The results show that the attention U-net model is suitable for real-life crack detection tasks, which can replace human labour.

Acknowledgements This research is funded by Hanoi University of Civil Engineering (HUCE) under the grant number of 10-2022/KHXD-TĐ.

References

1. Khuc T, Catbas FN (2018) Structural identification using computer vision-based bridge health monitoring. *J Struct Eng* 144:04017202
2. Wang KC, Li Q, Gong W (2007) Wavelet-based pavement distress image edge detection with a trous algorithm. *Transp Res Rec* 2024:73–81
3. Brisolin J, Nguyen A, Ullah F, Bourke A, Khuc T, Nsanabo V (2022) Smart automated fault detection for improved road maintenance planning in Australia
4. Wang KC, Zhang A, Li JQ, Fei Y, Chen C, Li B (2017) Deep learning for asphalt pavement cracking recognition using convolutional neural network. *Airfield Highway Pavements* 2017:166–177
5. Majidifard H, Jin P, Adu-Gyamfi Y, Buttlar WG (2020) Pavement image datasets: a new benchmark dataset to classify and densify pavement distresses. *Transp Res Rec* 2674:328–339
6. Huan J, Li W, Tighe S, Xu Z, Zhai J (2020) CrackU-net: a novel deep convolutional neural network for pixelwise pavement crack detection. *Struct Control Health Monit* 27:e2551
7. Chen T, Cai Z, Zhao X, Chen C, Liang X, Zou T, Wang P (2020) Pavement crack detection and recognition using the architecture of segNet. *J Ind Inform Integ* 18:100144
8. Lau SL, Chong EK, Yang X, Wang X (2020) Automated pavement crack segmentation using u-net-based convolutional neural network. *IEEE Access* 8:114892–114899
9. Shi Y, Cui L, Qi Z, Meng F, Chen Z (2016) Automatic road crack detection using random structured forests. *IEEE Trans Intell Transp Syst* 17:3434–3445
10. Qu Z, Mei J, Liu L, Zhou D-Y (2020) Crack detection of concrete pavement with cross-entropy loss function and improved VGG16 network model. *IEEE Access* 8:54564–54573
11. Zhang K, Zhang Y, Cheng H-D (2020) CrackGAN: pavement crack detection using partially accurate ground truths based on generative adversarial learning. *IEEE Trans Intell Transp Syst* 22:1306–1319
12. Huang Z, Chen W, Al-Tabbaa A, Brilakis I (2022) NHA12D: a new pavement crack dataset and a comparison study of crack detection algorithms. *arXiv preprint [arXiv:2205.01198](https://arxiv.org/abs/2205.01198)*
13. König J, Jenkins MD, Barrie P, Mannion M, Morison G (2019) A convolutional neural network for pavement surface crack segmentation using residual connections and attention gating. In: *Proceedings of the 2019 IEEE international conference on image processing (ICIP)*. IEEE, pp 1460–1464

14. Wu Z, Lu T, Zhang Y, Wang B, Zhao X (2020) Crack detecting by recursive attention U-Net. In: Proceedings of the 2020 3rd international conference on robotics, control and automation engineering (RCAE). IEEE, pp 103–107
15. Negi SS, Bhandari YS (2014) A hybrid approach to image enhancement using contrast stretching on image sharpening and the analysis of various cases arising using histogram. In: International conference on recent advances and innovations in engineering (ICRAIE-2014). IEEE, pp 1–6
16. Ronneberger O, Fischer P, Brox T (2015) U-net: Convolutional networks for biomedical image segmentation. In: International conference on medical image computing and computer-assisted intervention. Springer, New York, pp 234–241
17. Jetley S, Lord NA, Lee N, Torr PH (2018) Learn to pay attention. arXiv preprint [arXiv:1804.02391](https://arxiv.org/abs/1804.02391)
18. Oktay O, Schlemper J, Folgoc LL, Lee M, Heinrich M, Misawa K, Mori K, McDonagh S, Hammerla NY, Kainz B (2018) Attention u-net: learning where to look for the pancreas. arXiv preprint [arXiv:1804.03999](https://arxiv.org/abs/1804.03999)
19. Buslaev A, Iglavikov VI, Khvedchenya E, Parinov A, Druzhinin M, Kalinin AA (2020) Albumentations: fast and flexible image augmentations. Information 11:125

Hindrances to the Application of Building Information Modeling (BIM) in the Construction Field in Vietnam



Nguyen Tai Duy

Abstract In recent years Building Information Modeling (BIM) has been introduced and gradually adopted in the Vietnamese construction field. It has received simultaneously the increasing attention of stakeholders in construction projects because BIM could bring benefits to the stakeholders. However, the adoption of BIM, in reality, has faced many difficulties and has not achieved the desired results. This paper aims to explore the factors that hinder BIM adoption in the Vietnamese construction field. To achieve the aim, interviews were carried out to collect qualitative data from six practitioners in the Vietnamese construction sector. After that, the deductive content analysis technique was employed to analyze the data. The results indicate that the hindrances to the adoption of BIM in Vietnam are in four main groups including legal, technology and information security, financial, and perspective and culture. Stakeholders can utilize these research findings to make decisions to help the adoption of BIM become more favorable.

Keywords Building information modeling · Barrier · Hindrance · BIM

1 Introduction

Building Information Modeling (BIM) is an advanced technology and is gradually being widely applied in the world. Some countries such as the US, China, the UK, France, and Singapore are leading in implementing BIM to gain potential benefits. The benefits which BIM can bring to stakeholders are the provision of an intuitive view and support of the process of choosing investment options and design

The original version of the chapter has been revised: The author's affiliation the text "/UTC" has been removed. A correction to this chapter can be found at https://doi.org/10.1007/978-981-99-2345-8_83

N. T. Duy (✉)
University of Transport and Communications, Hanoi, Vietnam
e-mail: ntduy@utc.edu.vn

© The Author(s), under exclusive license to Springer Nature Singapore Pte Ltd. 2024, corrected publication 2024
T. Nguyen-Xuan et al. (eds.), *Proceedings of the 4th International Conference on Sustainability in Civil Engineering*, Lecture Notes in Civil Engineering 344, https://doi.org/10.1007/978-981-99-2345-8_76

739

options; minimization of downtime and waiting for unintended conflicts arising from design errors or inconsistencies between design and construction; decrease in errors in the implementation from design drawings to construction in practice; support for detecting and anticipating difficulties in the construction process right from the stage of accessing design documents; reduction in the time of researching and approving permit documents as well as effective support for the inspection and inspection of construction works because the information of the works is presented logically, fully, and intuitively, etc. [1]. In order to catch up with the world trend and reap these benefits, the Prime Minister of Vietnam approved the Scheme on the application of BIM in construction and operation management activities in Decision No. 2500/QD-TTg on 22/12/2016 [2]. However, so far the BIM application in the construction sector in Vietnam is still in the early stages, faces many difficulties and does not always bring the desired benefits to stakeholders participating in construction projects. The paper will clarify the hindrances that stakeholders face when they apply BIM in Vietnam.

2 General Background Information on BIM

2.1 Introduction and Definition of BIM

In recent decades, the construction industry is increasingly interested in using BIM because BIM can bring many benefits and save resources in the process of planning, design, and construction of new infrastructure or buildings. In the 1970s, in several industries, 3D modeling began to be developed based on computer-aided design (CAD) efforts. Although several industries initiated object-based parametric modeling and integrated analysis instruments (this is the basic BIM concept), the construction field has still been limited to 2D traditional design for quite a long time. The introduction of BIM model in pilot construction projects in the early 2000s was to support engineers and architects' design. As such, the main research trends at the period focused primarily on improving planning, design, conflict detection, visualization, cost estimation, and data management. Until recently, specialized tools for designers, architects and engineers have been developed to provide other primary functions such as scheduling, structural analysis, site safety, energy analysis, and progress tracking.

According to Decision 348/QD-BXD of the Ministry of Construction, BIM is defined as “the use of advances in information technology to digitize the information of the building expressed through the three-dimensional (3D) to support the process of design, construction, management and operation of works” [3]. BIM is usually object-oriented programs and comprises parametric objects that represent the components of a building. These parametric objects could contain non-geometric or geometric characteristics related to semantic, functional, or topological information [4].

BIM could be viewed from a narrow or wide angle. From a narrow perspective, BIM is a design model that only contains the information to represent drawings on

a unified view. At this time, BIM plays the role of improving 2D design tools that contain information about dimensions or descriptions of components. From a broad perspective, BIM is seen as a unified process of creating, managing, and exploiting information for the entire life cycle of a project. From this perspective, BIM not only provides information about the dimensions of the structures, but also contains other information about progress, cost, work efficiency, and management methods [4].

2.2 Development Levels of BIM

To ensure that the levels of supporting standards and expected competence are distinguished for contracts and projects, and BIM development is divided into four levels [5]. Those levels are described as follows.

BIM level 0: 2D CAD software is commonly used to create information. 2D CAD drawings have not been specified or standardized to a certain standard. The data and information are stored and exchanged mainly in the form of paper documents. Stakeholders and project participants are limited to sharing information [6].

BIM level 1: the software is used to create information for the project through 2D drawings, which can be combined with 3D models. Drawings are subject to certain common standards, formats, and data structures. Project participants exchange data separately. These exchange data are in the form of paper documents or electronic files which are shared on cloud services such as Google Drive, Dropbox, One Drive. Although the participants may receive the data in one shared environment, the environment is only used to store files. These files are not combined to form a shared model that is used for unified management of all aspects of the project. In other words, the files are fragmented, there is no coordination, or information exchange with other disciplines, low level of consistency, and many difficulties in checking and tracking [6].

BIM level 2: characterized by collaborative work among stakeholders. The determination of how information is exchanged among stakeholders is an extremely important feature of the level. Participants employ different 3D CAD models. Stakeholders use a common file format to share design information, so they can incorporate this data into their data to build a linked BIM model. Then stakeholders can check, monitor and manage the information on this BIM model [7].

BIM level 3: demonstrates close collaboration across all disciplines utilizing one single shared model. This project model is stored in a concentrated online data repository. All project participants could access, share, edit, and store project model information from a single source throughout the life of the project. This can help eliminate the risks associated with information conflicts. This BIM model is called the open BIM model [7].

3 Research Design

This study used the qualitative research design to identify hindrances to the application of BIM in the construction sector in Vietnam. The advantage of the qualitative design is that it allows for an in-depth study of hindrances to the application of BIM that are still not well known in the context of Vietnam. Elo and Kyngäs [8] suggested that existing concepts or theories that are applied in a new context should be revised by analyzing qualitative data collected from the field. This study used the interview to collect qualitative data to conduct an in-depth and in-breadth examination of research problems [9]. The interview is the most commonly utilized technique in qualitative research due to its flexibility to gain valuable insights. Interviewees have the opportunity to expand their ideas and explain their views that can help identify hidden factors. Semi-structured interviews were adopted in this research since they allow the interviewer to clarify doubts, modify the questions and rephrase questions to help the participants fully understand them. Moreover, they are suitable to explore the interviewees' perceptions about complex issues, and allow clarification of answers [10].

Purposive sampling, which is a popular non-random sampling and more appropriate than random sampling for qualitative studies [11], was used in this research. Purposive sampling refers to identifying and intentionally selecting individuals who have suitable experience or qualities related to research problems. This technique helps reduce the time and costs and increase the likelihood of discovering appropriate people for the interviews [12]. The participants in this study required at least general familiarity with BIM in the Vietnamese construction industry.

The interviews comprised two main sections. The first section consisted of background information about the participants' work experience and general information about BIM. The second section concentrated on hindrances to the application of BIM.

There is no consensus about the sample size of interviews. However, Marshall et al. [13] suggested that the number of interviews can be approximately six. Additionally, data saturation, which depends on the richness of data, the nature and purposes of the study, and informational needs, may be a criterion to show the optimal sample size and can occur with six interviews [14]. Consequently, six interviews conducted in the study were considered an acceptable sample size. The participants had different positions in their organizations. Among the six participants, four were managers, two others were an engineer and a lecturer. The work experience of the interview participants ranged from 5 to 20 years in the construction industry.

The face-to-face interview is an acceptable way to collect qualitative data in this study. The research objectives were introduced to the interviewees at the beginning of each interview session. When the researcher was sure that the interviewees fully understood the ideas related to BIM, the relevant questions were asked and discussed. The length of the interviews varied from 15 to 45 min.

Content analysis was employed in this study to analyze the qualitative data. Content analysis refers to a research technique employed to categorize oral or written

data as themes with similar meanings [15]. The deductive content analysis approach is suitable for research that aims to test an incomplete existing theory or retest existing concepts in a new context [8]. The approach is appropriate for the aim of the study, so it was selected to analyze the qualitative data from the interviews.

4 Hindrances to the Application of BIM

The analysis results show that the hindrances in the process of BIM application in Vietnam can be divided into four main groups: legal, technology and information security, financial, and perspective and culture. These hindrance groups were acknowledged by other authors [5, 16, 17].

4.1 Legal Hindrances

Although the government has been gradually introducing policies to encourage BIM application, currently the guiding documents have not reached the acceptable level of completeness and synchronization to enable smooth BIM application. Circular No. 12/2021/TT-BXD, although allowing to the cost estimation of BIM application, has not yet provided specific estimate norms or how to calculate proportional cost norms. This makes it difficult to determine the cost of applying BIM in construction investment consultation cost. In addition, the documents do not give specific information about the project participants who will own the BIM model during development and after completion. Stakeholders will create their intellectual products in the process of completing the BIM model, but there is no rule to clearly define the rights, obligations, and ownership of these intellectual properties. The Ministry of Construction has just issued basic guidelines on information exchange between disciplines in the process of applying BIM, while national standards for information sharing among stakeholders have not yet been established. If technical errors occur during the cooperation of the parties to apply BIM, the issue related to the project participants, who solve these errors, has not been clarified yet.

4.2 Technical and Information Safety Hindrances

File format compatibility between BIM software packages is still not at an acceptable level. Currently, many different software packages on the market allow BIM implementation, each of these packages is aimed at many clients and has different advantages and disadvantages. Stakeholders often choose software according to their criteria and the ease of deployment for each field. Therefore, when files that are

exported from different software are imported into a single shared BIM model, there is a possibility that the entire data cannot be synchronized.

The interface, user manual, and official support from BIM software companies are still mainly in English. Many Vietnamese engineers have a low level of English. As a result, these engineers often can only handle previously trained situations. If new situations arise or engineers encounter errors during their use, it often takes a long time to resolve and causes delays in the work process.

Integrating new modules according to Vietnam's regulations into BIM software is still difficult. BIM software is usually commercial and closed-source software. While the cost estimation, payment settlement, project management, etc. are carried out according to the regulations of the Vietnamese government. The integration of these new modules into BIM models is often unfavorable.

Information security in the process of sharing and exchanging between stakeholders in the project is still not guaranteed. In the process of applying BIM, project members need to cooperate comprehensively and share information through online platforms. These online platforms allow parties to share data from a variety of programs. The security of online information, when it is illegally accessed from the outside or under cyberattacks, has not been appreciated in the current situation.

4.3 Financial Hindrances

Consulting and construction companies often consider the benefits and costs regarding the adoption of BIM when the number of projects applying BIM is small. The costs related to BIM application are still quite high for Vietnamese small and medium enterprises, including software costs, hardware costs, and human resource training costs. Software costs include costs to initially purchase and install software and costs to periodically update the software. Hardware costs to upgrade existing computers or buy new computers are expensive because BIM software packages often require higher powerful computers to handle complex information compared to 2D design software packages. In addition to these two costs, businesses need to spend money on training employees to be able to use the BIM software package effectively for work because the approach and information processing in the BIM package has many different points in comparison with traditional software.

4.4 Hindrances of Perspective and Culture

Many businesses are still not ready for BIM adoption. Leaders of some companies have yet to see the possible benefits of BIM. While 2D models still bring benefits and are the main source of revenue for businesses, businesses still do not appreciate the extra cost and time to convert from 2D models to 3D models. Adopting BIM means changing the way they work. Therefore, some employees believe that they

have not received sufficient training to switch to the BIM model. This often happens to several older engineers when they have a high level of expertise but are afraid to interact and familiarize themselves with new technologies. In addition, the culture of information sharing and comprehensive cooperation is still not widespread in the construction sector.

5 Conclusion

BIM application is an inevitable trend in the world and Vietnam due to the benefits of BIM for project participants. The Vietnamese government has gradually introduced policies and documents to encourage, guide, and stimulate BIM adoption in construction projects. Nevertheless, the application of BIM has faced many difficulties in the construction field. The paper pointed out four main groups of hindrances that stakeholders often encounter when implementing BIM. These four groups of hindrances include legal, technical and information security, financial, perspective and culture. On the basis of these groups of hindrances, policymakers and company leaders can propose appropriate solutions to help the adoption of BIM become more widespread.

Acknowledgements This research is funded by University of Transport and Communications (UTC) under grant number T2022-QLXD-002.

References

1. Nguyen LH, Le TT, La NM (2022) Economics and management in construction field. Transportation Publishing House, London
2. Prime Minister of the Vietnamese government (2016) Decision No. 2500/QĐ-TTg, decision approving the project of building information modeling (BIM) application in construction activities and construction operation management
3. Ministry of Construction (2021) Decision No. 348/QĐ-BXD dated April 2, 2021 on the publication of general guidelines for the application of building information model (BIM)
4. Volk R, et al (2014) Building information modeling (BIM) for existing buildings: literature review and future needs. *Autom Const*
5. Georgiadou MC (2019) An overview of benefits and challenges of building information modelling (BIM) adoption in UK residential projects. *Const Innov*
6. <https://bccd-blog.com/cac-cap-do-phat-trien-bim/>. Accessed 26 Oct 2022
7. Burgess G, Michael J, Kathryn M (2018) BIM in the UK house building industry: opportunities and barriers to adoption. University of Cambridge, Cambridge
8. Elo S, Kyngäs H (2008) The qualitative content analysis process. *J Adv Nurs* 62:107–115
9. Fellows RF, Liu AMM (2015) *Research methods for construction*, 4th edn. Wiley, Chichester
10. Denscombe M (2014) *The good research guide: for small-scale research projects*, 5th edn. McGraw-Hill Education, Maidenhead
11. Neuman WL (2014) *Social research methods: qualitative and quantitative approaches*, 7th edn. Pearson Education Limited, Boston

12. Etikan I, Musa SA, Alkassim RS (2016) Comparison of convenience sampling and purposive sampling. *Am J Theor Appl Stat* 5:1
13. Marshall B, Cardon P, Poddar A, Fontenot R (2013) Does sample size matter in qualitative research? A review of qualitative interviews in is research. *J Comput Inform Syst*
14. Elo S, Kääriäinen M, Kanste O, Pölkki T, Utriainen K, Kyngäs H (2014) Qualitative content analysis: a focus on trustworthiness. *SAGE Open*, New York
15. Cho JY, Lee E-H (2014) Reducing confusion about grounded theory and qualitative content analysis: similarities and differences. *Qual Rep*
16. Ma X et al (2020) An empirical analysis of barriers to building information modelling (BIM) implementation in construction projects: evidence from the Chinese context. *Int J Const Manag* 22:3119–3127
17. Saka AB, Chan DWM (2020) Profound barriers to building information modelling (BIM) adoption in construction small and medium-sized enterprises (SMEs). *Const Innov* 12:3710

AI Solutions for Innovation of Pavement Crack Analysis on Images Taken from Specialized Road Surface Survey Vehicles in Vietnam



Thao Dinh Nguyen and Nhung Thi Hong Nguyen

Abstract In today's world, innovation is not only the application of new technologies, but also the continuous improvement of existing technologies based on new scientific and technological achievements. The article presents the efforts of the authors in researching to improve the technology of road surface survey by specialized road surface survey vehicles, which have been widely used in Vietnam in recent years. On the basis of the road surface image dataset collected during previous surveys, the authors have applied machine learning algorithms to build models to automatically detect pavement cracks on the collected images instead of conventional method of manual detection. Initial efforts using machine learning techniques such as: support vector machines (SVMs), machine learning, especially the combination learning algorithm Boosting (Adaboost) and deep learning (DL) had demonstrated the feasibility of the new solution alternative to manual analysis. The next research at a higher challenging level, a deep architecture using convolutional neural network (CNN) for crack segmentation on gray scale images has been developed for much better improvement of the current technology in terms of pavement crack detection.

Keywords Road survey · Pavement crack detection · Crack segmentation · Machine learning · Deep learning

1 Introduction

The noticeable development of the road network in Vietnam after the Doi Moi or renovation (1980) has posed a need to change the approach in road maintenance from passive to active and planned. According to this new approach, establishing and forming databases and the application of road maintenance planning systems are indispensable to replace the traditional methods of working on hard-copies of

T. D. Nguyen (✉) · N. T. H. Nguyen
University of Transport and Communications, Hanoi, Vietnam
e-mail: nguyendinhthao@utc.edu.vn

© The Author(s), under exclusive license to Springer Nature Singapore Pte Ltd. 2024
T. Nguyen-Xuan et al. (eds.), *Proceedings of the 4th International Conference on Sustainability in Civil Engineering*, Lecture Notes in Civil Engineering 344,
https://doi.org/10.1007/978-981-99-2345-8_77

747

documents and paper drawings as well as visual-based evaluation of road conditions and experience-based maintenance proposing.

In the early stages, the database and planning software systems introduced for use were all ready-made commercial software such as Rosy Road Systems for data registration and The Highway and Development Management Series (HDMs) for planning [1]. In terms of hardware, the collection of road surface condition data is recommended using the devices; however, it is performed by separate measurements which leads to time consuming, costly and concerns of safety and traffic accident while performing at sites.

After more than a decade of transitioning to the new approach to road asset management, two major problems have been identified, including: (i) poor customization of ready-made systems and (ii) non-optimized and manual pavement condition survey technology [2]. These irreparable limitations led to the decision to: (i) develop a new customized pavement management system for road management in Vietnam; (ii) applying new pavement condition survey by specialized road surface survey vehicles. These innovations have shown remarkable effectiveness: in a short time, many national roads in Vietnam have been surveyed using the above technology to create a database that helps maintenance planning to be supported effectively by the newly developed planning system.

However, the fact of using the technology also demands for improvement the current practices of pavement crack analysis from manual detection to automatic detection by AI technology.

In 2019, the authors completed a research project for the Ministry of Transport to develop a machine learning model for pavement crack automatic detection system [3]. Realizing that raw data of pavement cracking is in very detailed and, if fully exploited, it can be effectively extended to pavement management at the project level. Therefore, the authors continue to expand the research to automatic detection of pavement crack feature on images taken from specialized road surface survey vehicles.

2 Current Practice of Pavement Crack Analysis on Images Taken from Specialized Road Surface Survey Vehicles in Vietnam

In an effort to innovate the evaluation of road surface conditions, pavement survey technology by specialized road surface survey vehicles was first introduced in Vietnam in 2012 [1]. In 2014, the road authority in Vietnam had taken over the first survey vehicle granted by Japan International Cooperation Agency (JICA). On the basis of effective application of this technology, the road authority equipped one more vehicle in 2018 (Fig. 1).

As soon as it was introduced into Vietnam, the pavement survey technology by specialized road surface survey vehicles has clearly demonstrated its benefits thanks

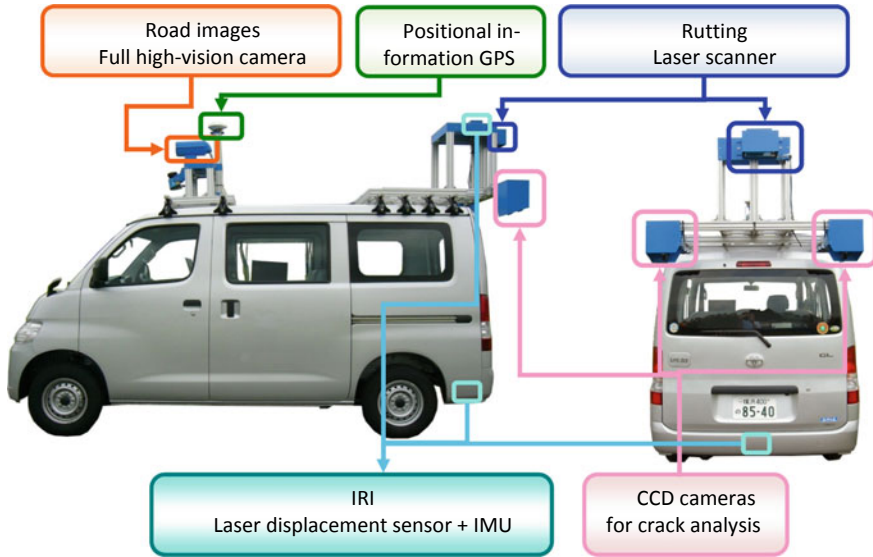


Fig. 1 Overview image of the pavement survey vehicle [4]

to the integration of technologies and equipment on survey vehicles that allow simultaneous collection of pavement indicators and relevant information about the pavement conditions when the vehicle is running normally on the road. All indicators are collected with high accuracy and detail with short intervals of data recording: interval of one meter for recording detailed surface cross-sections to determine rutting depth by rutting laser scanner, interval of ten centimeters for recording vertical displacements from laser displacement sensor to the pavement surface to calculate pavement roughness IRI [4].

Because the road surface has many image disturbances or noises such as dark or shiny images or existence of objects of branches, water streaks, rubber gum, shadow in the images, etc., it is not suitable to automatically determine the cracking condition when the vehicle is running on the road. Instead, detailed images of the road surface are captured when the vehicle is running and sent to the office for analysis using software that supports displaying of road surface images with the square grid 0.5×0.5 m. The technicians must determine for himself the type of crack in each square: (i) type 1 for square without cracks; (ii) type 2 for square with one crack; (iii) type 3 for square with two or more cracks. With the convention that the pavement crack area of the types of cracks: type 1, type 2, type 3 is 0, 60% and 100% respectively, the system will calculate the pavement crack ratio in percentage of the specific analysis area or homogeneous sections of 100 lane-meters long as the common segment [5] (Fig. 2).

It is no doubt about the high level of detail of the current practice of pavement crack analysis on images taken from specialized road surface survey vehicles in Vietnam. However, productivity is the concern. Based upon the actual implementation of the

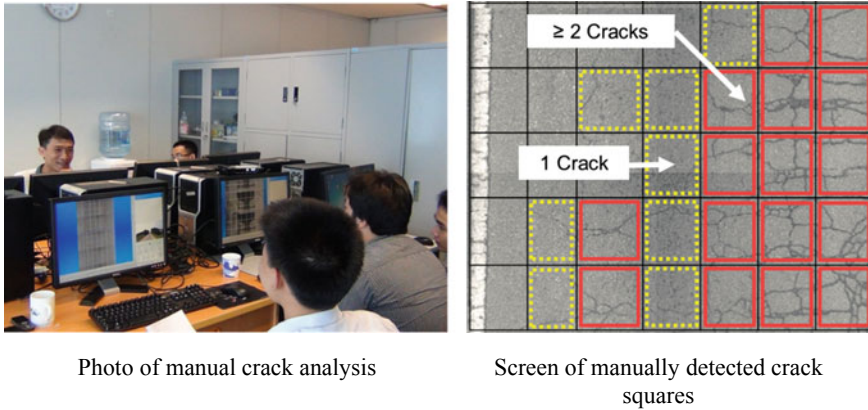


Fig. 2 Manual detection of pavement crack on images taken from specialized road surface survey vehicle

manual pavement crack analysis, to complete manual crack analysis for image data collected in one-shift surveying at the site, it requires eight working shifts or eight technicians working in one shift [1]. Not only time consuming but also costly is the disadvantage of the current practice. Budget allocation for manual cracking analysis accounts for approximately 50% of the total survey cost comprising both in-situ survey and in-door analysis work items.

Finding solutions for the problem of the current practice of pavement crack analysis on images taken from specialized road surface survey vehicles in Vietnam is objective of authors' researches recently since 2017.

3 AI Solutions for Innovation of Pavement Crack Analysis on Images Taken from Specialized Road Surface Survey Vehicles in Vietnam

3.1 Crack Areas Detection

AI has been used in transport field in many different ways. In this section, we present an application of AI in detection crack areas on road pavement images.

The purpose of crack area detection is automatically highlighting all regions containing cracks on pavement images. These regions (areas) are not overlap with the common size of 50×50 cm in reality corresponding to resolution of $150 \text{ pixels} \times 150 \text{ pixels}$ on pavement images. Our research focused on using machine leaning in a trainable network and produce a model to auto-detect the crack areas. The machine learning algorithms can be a traditional algorithm such as Adaboost, or a modern method such as a deep learning network. Our experiments using Haar-like features

in an Adaboost model [6, 7] to classify crack and non-crack areas, the final F1 score is around 80% (Fig. 3).

However, in the case of images with noises or artifacts, the accuracy rate is not high as the result of wrong detection by simple boosting learning algorithm (Fig. 4). For the better improvement of the crack detection, the authors developed a new model using deep learning algorithm with convolutional neural networks to work on real datasets containing noises and artifacts [3]. The F1 score from deep learning method is higher than that from Adaboost method, and it is about 90% (Fig. 5).

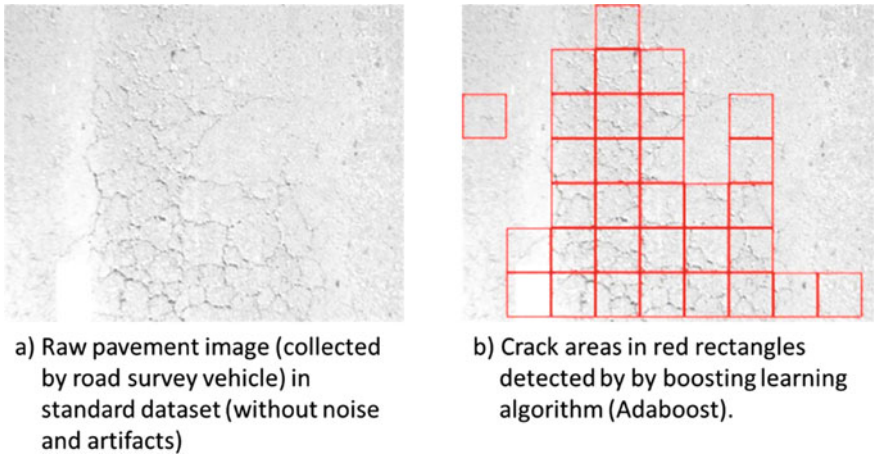


Fig. 3 Automatic detection of pavement crack areas on road surface images by boosting learning algorithm on selected images without noise and artifacts

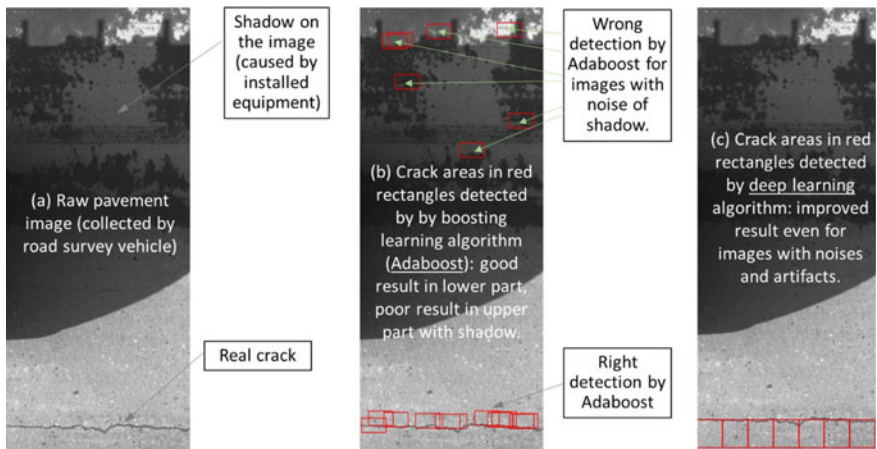


Fig. 4 Automatic detection of pavement crack areas on road surface images by boosting learning algorithm and deep learning algorithm

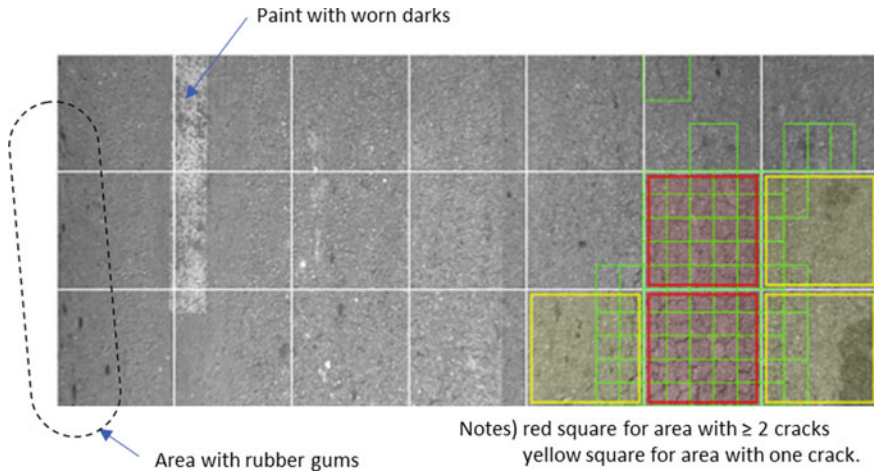


Fig. 5 Automatic detection of pavement crack areas on road surface images by deep learning algorithm on real datasets containing noise and artifacts

3.2 Crack Segmentation

Based upon the good results from our initial researches, the authors conducted a following research to investigate further feature of the cracks on pavement images with the focus on crack segmentation.

In the research, a deep neural network to train a model for crack segmentation has been formulated. The network architecture contains several layers of convolutional neural network following by max-pooling layers and activation layers. The input of the training phase comprises of pavement crack image samples, and their ground truth prepared by road experts. The output of the training phase is a reusable model for crack segmentation. In the testing phase, the input is gray scale images that need to segment, and the output is binary images that contain cracks only. Figure 6 shows two examples of crack segmentation (Fig. 6).

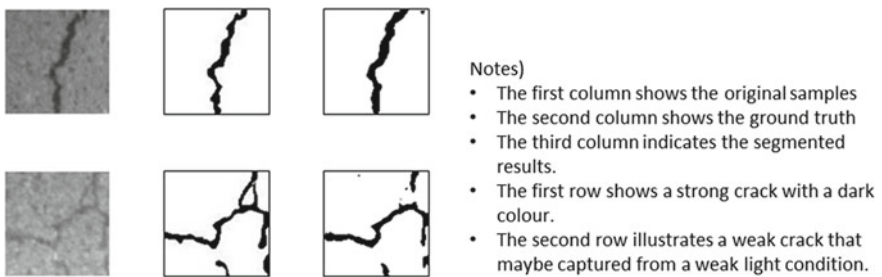


Fig. 6 Examples of crack segmentation

4 Conclusion

This paper introduces some application of AI in road pavement asset management. Within initial efforts, automatic detection system of crack areas on pavement images had been developed with high accuracy to support road management at network level. The following research helps to expand the crack detection to crack segmentation that is beneficial for road management and maintenance at both network and project levels. In the next step, the authors will deepen the research to determine more specific features of pavement cracks such as crack length, crack width and crack classification based on the results from crack segmentation. Online detection and segmentation of pavement cracks from arbitrary sources such as smart phone or other cameras will be our next target also.

Acknowledgements We would like to express our very great appreciation to University of Transport and Communications, the donor for our research coded T2021-CT-009TĐ.

References

1. Japan International Cooperation Agency (2014) Technical cooperation project for capacity enhancement in road maintenance. Final report
2. Thao ND, Aoki K, Kato T, Nam Toan T, Kobayashi K, Kaito K (2015) A practical process to introduce a customized pavement management system in Vietnam. *J JSCE* 3(1):246–258
3. Ministry of Transport (2019) Research project code DT184047 “Development of pavement crack automatic detection system by machine learning model”. Final report
4. PASCO Corporation (2012) Instruction book of real-mini
5. PASCO Corporation (2012) Pavement survey manual
6. Nhung NTH, Cong DC, Thao ND (2016) Crack detection on captured pavement images by new approach of advanced image processing. In: Proceedings of transport sector conference for young researchers
7. Nhung NTH, Thao ND, Cong DC (2017) Crack detection on captured pavement images by new approaches. *Transp J*

Traffic Engineering, Transportation and Logistics Engineering

An Investigation of Cargo Handling Equipment Performance in Vietnam Container Terminals



Pham Huy Tung and Nguyen Luong Hai

Abstract Cargo handling equipment (CHE) plays an essential role in ensuring the proficiency and effectiveness of a container terminal. This study aims to examine the performance of CHEs using the overall equipment effectiveness technique (OEE) based on specific data obtained from questionnaires collected from 159 respondents working in container terminals in Vietnam. The findings reveal that the performance of the quay cranes group (HS1) and the performance of the lift on/off vehicles group (HS3) contribute to improving the OEE. In addition, the performance of the lift on/off vehicles group (HS3) acts as a mediator of the potential effects of the performance of the yard cranes group (HS2), while the performance of the quay cranes group (HS1) and the performance of lift on/off vehicles group (HS3) acts as mediators of the potential effects of the performance of yard tractors group (HS4). The CHEs' OEE in Vietnam container terminals is generally estimated below design capacity due to their old technologies and poor management mechanism. Therefore, the study findings provide evidence to propose some strategies to improve the CHEs' performance, thereby enhancing container terminals' performance in Vietnam.

Keywords Cargo handling equipment · Equipment performance · Exploitation · Effectiveness · Container terminal

1 Introduction

In recent years, shipping containerization has been identified as a major development in the global transport industry. The expansion of large-tonnage container shipping has put significant pressure on container terminals to increase throughput and remain competition in the global market [1–3]. Although container shipping companies

P. H. Tung
Vietnam Maritime University, Hai Phong City, Vietnam

N. L. Hai (✉)
University of Transport and Communications, Ha Noi City, Vietnam
e-mail: hainl@utc.edu.vn

© The Author(s), under exclusive license to Springer Nature Singapore Pte Ltd. 2024
T. Nguyen-Xuan et al. (eds.), *Proceedings of the 4th International Conference on Sustainability in Civil Engineering*, Lecture Notes in Civil Engineering 344,
https://doi.org/10.1007/978-981-99-2345-8_78

757

have taken full advantage of the massive catch-up demand from the development, the container transport industry has faced disruptions due to various factors, such as container shortages, the impact of the COVID-19 pandemic, port delays, and a lack of docworkers and truck drivers. This has caused massive congestion in many container terminals worldwide, resulting in reduced capacity in the container market. In Vietnam, the container shipping industry has experienced significant growth, becoming the third-largest container throughput in the ASEAN region, following Singapore and Malaysia. The annual container throughput at Vietnam's container terminals has increased by an average of 9.2% during the period from 2013 to 2020, which is the highest growth rate among eight Southeast Asian countries [4]. Despite the many viable advantages in the development of container shipping, Vietnam's container terminals face various challenges related to terminal planning, equipment performance, and operational management.

Although container terminals in Vietnam have been improving their capacity annually and are expected to increase by 10–20% compared to their design capacity [5], there are still a large number of issues related to poor performance of CHEs due to inadequate technologies and management aspects. As a result, the poor performance of CHEs reduces the overall productivity of container terminals. This study is aimed to examine the empirical performance of the CHEs from the perspective of the overall equipment effectiveness (OEE) approach [6, 7].

2 Methodology of CHEs' Performance in a Container Terminal

The CHE includes a group of vehicles and equipment that serve the movement of containers within terminals. Generally, CHEs are classified based on their technical specialization and working area. They include the group of quay cranes (QC/Liebherr...), the group of yard cranes (RTG/RMG), the group of lift on/off vehicles (REACH STACKER, STADDLE CARRIER, Top Loader/Lifting), and the group of yard tractors.

From the perspective of the Total Productive Maintenance (TPM) methodology, equipment performance loss is a major cause of waste in total productivity. The overall equipment effectiveness (OEE) technique, which is a commonly-used standard in measuring the productivity and efficiency of a production system [8–10], is based on TPM. The application of OEE allows for the examination of the performance of the production process, recognition of problems in the operation of the equipment system and estimation of maintenance schedules, and tracking the progress of the problems—solving. An OEE with 100% or a higher level characterizes perfect performance, indicating no downtime, and smooth and fast production. Therefore, tracking the performance of CHE during operation can help analyze the productivity

in exploiting the CHE. The OEE index is built by indices of availability, performance, and quality:

- *Availability of a CHE group (A)*: The ratio of the total actual operating time of the group of CHE and the total theoretical operating time of the group of CHE.
- *Performance of a CHE group (P)*: The performance of a CHE group (*P*) is determined by the ratio of the total actual throughput achieved during the operating time of the CHE group and the total design actual throughput by job step (maximum working vehicle/equipment; nominal lifting load) according to the theoretical operating time of the CHE group.
- *Quality of a CHE group (Q)*: The quality of the CHE group is determined by the ratio between the total actual throughput by operational option ensuring the required time and the total actual throughput by operational option of the CHE group.

3 Materials and Methods

The study conducted a survey of 159 respondents, with 132 respondents working in container seaports in the northern region of Vietnam, 16 respondents from container seaports in the central region of Vietnam, and the 11 respondents from the container seaports in the southern of Vietnam. The distribution of professional experience among the respondents shows that the majority of respondents have more than 10 years of professional experience (49.7%), followed by 35.2% with 5 - 10 years of experience, and 15.1% with 1–5 years of experience. This distribution is reasonable and ensures the reliability of the collected survey data.

Structural equation modeling (SEM) was used to test the research hypotheses. The SEM technique is the most commonly applied to examine the interactive impact among variables in a regression model and the degree of independent variables in the goodness of fit model.

4 Results and Discussion

The analysis results in Table 1 and Fig. 1 demonstrate statistically significant relationships between the pairs of observed variables:

- (1) Performance of yard cranes group (HS2) and performance of quay cranes group (HS1) ($\beta = 0.557, p < 0.000$),
- (2) Performance of yard cranes group (HS2) and performance of lift on/off vehicles group (HS3) ($\beta = 0.220, p < 0.05$),
- (3) Performance of quay cranes group (HS1) and OEE (HS5) ($\beta = 0.325, p < 0.000$),

Table 1 The results of regression analysis

Hypotheses	Coef	VIF	R-square	Adjusted R-square	P-value	Note
Performance of yard cranes -> Performance of quay cranes	0.557	1.348	0.400	0.385	0.000	Supported
Performance of yard cranes -> Performance of lift on/off vehicles	0.220	1.348			0.007	Supported
Performance of yard cranes -> OEE	0.278	1.907			0.996	Not supported
Performance of quay cranes -> OEE	0.325	1.815			0.001	Supported
Performance of lift on/off vehicles -> OEE	0.445	1.756			0.000	Supported
Performance of yard tractors -> Performance of quay cranes	0.159	1.348			0.019	Supported
Performance of yard tractors -> Performance of lift on/off vehicles	0.497	1.348			0.000	Supported
Performance of yard tractors -> OEE	0.219	1.770			0.623	Not supported

- (4) Performance of lift on/off vehicles group (HS3) and OEE (HS5) ($\beta = 0.445, p < 0.000$),
- (5) Performance of yard tractors group (HS4) and performance of quay cranes group (HS1) ($\beta = 0.159, p < 0.05$),
- (6) Performance of yard tractors group (HS4) and performance of lift on/off vehicles group (HS3) ($\beta = 0.197, p < 0.0000$).

This result supports the research hypothesis that the performance of quay cranes group (HS1) and the performance of lift on/off vehicles group (HS3) have a direct and statistically significant influence on the OEE (HS5). However, the analysis results show that there is no direct influence from the performance of yard cranes group (HS2) and the performance of yard tractors group (HS4) to the OEE (HS5). Specifically, the performance of yard cranes group (HS2) and the OEE (HS5) ($\beta = 0.278, p > 0.05$), the performance of yard tractors group (HS4) and OEE (HS5) ($\beta = 0.219, p > 0.05$). The analysis results show that the performance of yard cranes group (HS2) indirectly affects the OEE (HS5) through the performance of lift on/off vehicles group (HS3); meanwhile, the performance of yard tractors group (HS4) indirectly affects the OEE (HS5) through the bridge of the performance of quay cranes group (HS1)

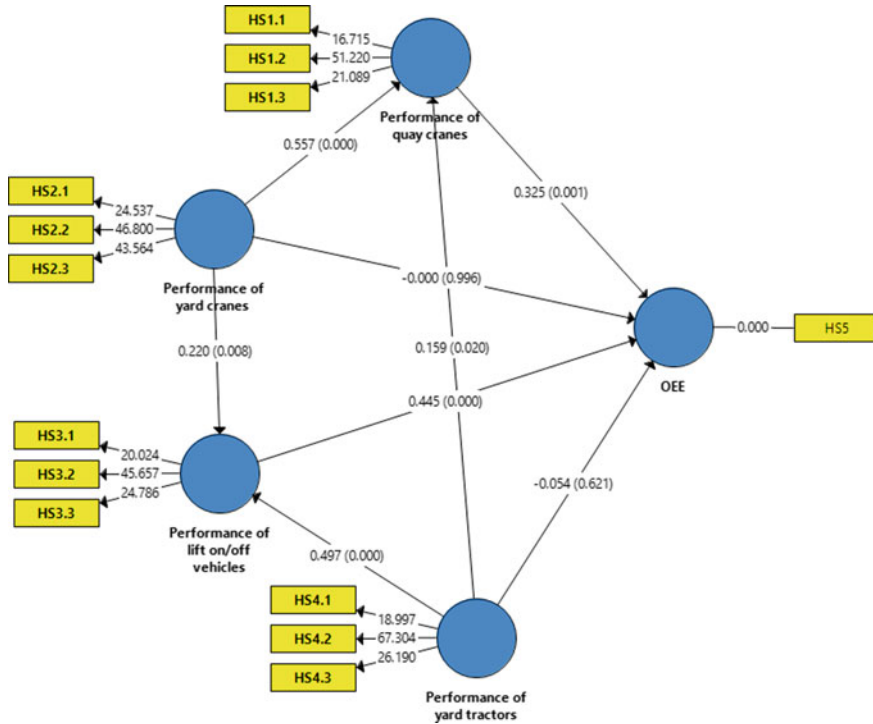


Fig. 1 Performance of CHE groups and OEE

and the performance of lift on/off vehicles group (HS3). At the same time, Variable Inflation Factors (VIF) values were checked to observe the multicollinearity between predictor variables in the analyzed model. The results show that the maximum VIF value (1.907) is all less than the threshold of 10, which clarifies that there is no multicollinearity among the predictors. The robust model can explain 38.5% of the statistically significant difference in the overall operating efficiency of the CHE.

It is noted that the individual groups of the CHEs in container terminals significantly influence the overall equipment effectiveness of the CHE and the container terminal as a whole. However, the findings also reveal that the operating cycle of each group of equipment depends not only on the individual cycle but also on the coordination among other groups in the CHE system. For each group, the process of each operation is related to the equipment’s mechanical cycle and container position. However, the empirical findings indicate that the quay cranes group and the lift on/off vehicles group are central to the CHE operation, with the yard cranes group and yard tractors group operating in these core operating cycles. This may infer that the operating indicators of the CHE are not compatible with the premeditated capacity. Thus, the container terminals can periodically evaluate the CHE’s performance and make reasonable adjustments to the operating factors. In addition, it is relevant to design

a reasonable plan that helps allocate the CHEs, thereby meeting the cargo handling needs and ensuring the productivity of the CHEs' capacity.

5 Conclusions

The study conducted an empirical investigation in container terminals in Vietnam, revealing that the performance of the equipment groups has a significant impact on the overall performance of the CHE, either directly or indirectly. These findings suggest that the designed capacity of the equipment groups has not been fully utilized. Old equipment and inefficiency in the use and maintenance of CHEs have been identified as the main causes of the ineffectiveness. The analyses of the effectiveness of CHEs and container terminals in the study scope may infer that the operating performance of the CHEs has a great influence on the OEE and the performance of the container terminals. Therefore, it is necessary to invest in the CHE system and design effective management of CHEs to maintain the capacity and high performance, as consequently, enhance the container terminals' productivity.

References

1. VILAS (2022) Efficiency of transporting goods by container. <https://vilas.edu.vn/hieu-qua-cua-viec-van-chuyen-hang-hoa-bang-container.html>
2. Transport MO (2021) The international container fleet is increasingly "huge" in size. <https://www.mt.gov.vn/vn/tin-tuc/77462/doi-tau-container-quoc-te-ngay-cang--khung--ve-kich-co.aspx>
3. Saxon S, Stone M (2017) Container shipping: the next 50 years. Travel, Transport & Logistics: McKinsey & Company, London
4. Kuo K-C, Lu W-M, Le M-H (2020) Exploring the performance and competitiveness of Vietnam port industry using DEA. *Asian J Shipp Logist* 36(3):136–144
5. Administration VM (2019) Project to improve the efficiency of management and operation of the existing Hai Phong seaport and Lach Huyen port area. Vietnam Maritime Administration, Hanoi
6. Lanza G et al (2013) Measuring global production effectiveness. *Proc CIRP* 7:31–36
7. Paris AD (2016) Overall equipment effectiveness-OEE: necessário, mas não suficiente: uma análise integrando o OEE e a data envelopment analysis-DEA
8. Team NPE (2018) Maintain overall device performance—TPM: basic content and application guidelines. Hồng Đức: Hồng Đức
9. CMMS W (2022) Overall equipment effectiveness. <https://winmaincmms.com/phan-mem-quan-ly-bao-tri-hieu-suat-toan-dien/>
10. VU LE TECHNOLOGY CO., L (2019) Importance of OEE equipment overall performance. <https://vuletech.com/tam-quan-trong-cua-hieu-suat-tong-the-thiet-bi-oe/>

Assessment of Traffic Safety Between Pedestrians and Vehicles Using Traffic Conflict Technique



Tuan Thanh Nguyen and Phuong Thao Cao

Abstract This paper presents a method to assess pedestrian safety, the traffic conflict technique was used to detail potential hazards or collisions with pedestrians at crosswalks. We use two parameters of this technique to describe the conflict process including the time to conflict (TTC) and post-encroachment time (PET), which have been proven effective in the evaluation of pedestrian traffic safety. In addition, the conflicting data will be classified through the K-means classification algorithm to identify the danger level of the conflicting points and areas, thereby proposing the appropriate solution to minimize conflict areas, which have a high risk to traffic safety.

Keywords Traffic safety · Conflict parameter · K-means

1 Introduction

In recent years, road traffic accidents in Vietnam have decreased in a number of accidents, deaths, and injuries. According to statistics from the National Traffic Safety Committee, in 2020, traffic accidents decreased significantly in all three criteria. Specifically, there were 12,985 traffic accidents, making 6048 people dead and injuring 9652 people. Compared to the same period in 2019, the number of traffic accidents decreased by 2900 cases (−18.26%), the number of deaths decreased by 927 people (−13.29%), and the number of injured people decreased by 2492 people (−20.52%). According to traffic police department statistics, there were 321 traffic accidents (2.2%) involving pedestrians in 2020, making 144 people dead (2.1%) [1]. Although traffic accidents have decreased, they are still higher than in other countries with the same socio-economic conditions. Also, the traffic accidents with pedestrians are not large, however, pedestrians are vulnerable objects in the traffic system, so the

T. T. Nguyen · P. T. Cao (✉)
University of Transport and Communications, Hanoi, Vietnam
e-mail: thaocp@utc.edu.vn

probability of death in an accident is very high. Therefore, it is necessary to have a solution to support and protect pedestrians when participating in traffic.

The currently proposed solutions are mainly based on the analysis and subjective assessment of traffic experts or on the history of traffic accidents [2]. However, it is difficult to collect traffic accident data at intersections, especially accidents related to pedestrians. Besides, there are inadequacies in intersection geometry, traffic organization, and behavior of traffic participation which are also causes of potential conflicts. Therefore, it is necessary to have studies and diagnoses on traffic safety as well as perform traffic simulations with appropriate traffic conditions and behavior for each city. Through collected image data and visual traffic simulation, we can see safety problems so that we can propose solutions and evaluate the effectiveness of solutions, thereby improving the safety of pedestrian traffic. Currently, advances in image processing and collision techniques allow collection and analysis of conflict data, specifically the collisions between pedestrians and vehicles. The researchers in have shown the possibilities of image analysis, specifically based on vehicle trajectory data, to calculate parameters for vehicle-to-vehicle collisions, or vehicles-to-pedestrians collisions. Especially for mixed traffic, when the vehicles are independent and flexible like traffic in Vietnam, it is much more difficult to describe the conflict. Therefore, choosing the appropriate conflicting parameters is an important requirement before analyzing the traffic flow on the image.

Normally, traffic conflict studies are conducted in crowded areas such as schools, shopping malls, stations, and pedestrian crossings. Ni et al. [2], He et al. [3] have studied road traffic safety and assessment based on a classification algorithm. He et al. [3] researched potential conflicts between left-turn vehicles and pedestrians at signalized intersections. Also, Ren et al. [4] have modeled the danger of conflicts between pedestrians and vehicles at signalized intersections. In addition, studies on conflict simulation parameters, data classification, and the relationship between conflicts and actual accidents are also being developed [5, 6]. In this paper, image processing techniques and collision parameters combined with data classification are used to evaluate traffic safety between pedestrians and vehicles.

2 Methodology

2.1 Conflict Parameters (PET, TTC)

T_{c1} and T_{c2} are the time vehicles take to enter and leave the conflict area. T_{p1} and T_{p2} are the time when pedestrians enter and leave the conflict zone, t_0 is the time at which evasive action is taken, i is the point time of conflict, $d_c(i)$ is the distance from the vehicle to the extrapolated line drawn from the vehicle's trajectory i and $d_p(i)$ is the distance from the pedestrian to this outline, $v_c(i)$ and $v_p(i)$ are the speeds of the vehicle and the pedestrian at the time i , respectively, and l and w are the length and

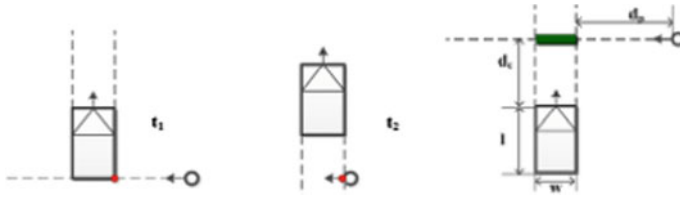


Fig. 1 Description of an example of basic parameters

width of the vehicle, respectively [4, 8]. The method of calculating PET and TTCmin is calculated as follows (Fig. 1):

- (1) Post-encroachment Time (PET)
 - If a pedestrian passes first

$$PET = T_{c1} - T_{p2} \tag{1}$$

If a vehicle pass first

$$PET = T_{p1} - T_{c2} \tag{2}$$

- (2) Time to Collision (TTC)

If a pedestrian passes first

$$TTC(i) = \max\left(\frac{d_p(i) + w}{v_p(i)}, \frac{d_c(i)}{v_c(i)}\right) \tag{3}$$

If a vehicle pass first

$$TTC(i) = \max\left(\frac{d_p(i)}{v_p(i)}, \frac{d_c(i)}{v_c(i)}\right) \tag{4}$$

2.2 Applying K-Means Classification Model

The K-means data classification algorithm is implemented to find the center point of each group when the input data, and the number of classes are divided, thereby creating groups of data with related characteristics [10]. The algorithm is presented as below:

Assume there are n data points of the pattern $X = [X1, X2, \dots, Xn]$ and $K < N$ is the number of classes to divide. Find the center coordinates m_1, m_2, m_3, m_k , and the label of each data point needs to be implemented [10, 11]. Set y_i as the label vector

for each point x_i , and if x_i falls into class k , then $y_{ik} = 1$ and $y_{ij} = 0$. As a result, there will only be one vector element with the value $y_i = 1$ (indicating the class of x_i), and all others will be zero. This encoding of the label is called “one-hot representation”. The y_i constraint can be written in the following form:

$$y_{ik} \in \{0, 1\}, \sum_{k=1}^K y_{ik} = 1 \quad (5)$$

m_k is the central point of a data class, and all the points to be estimated in this class is implied x_{ik} , then the deviation between the selected point and the center will be $(x_i - m_k)$. For a point to be in the class, this deviation must reach a minimum value, which means

$$\|x_i - m_k\|_2^2 \quad (6)$$

Moreover, x_i is classified as belonging to data class k , so $y_{ik} = 1$ and $y_{ij} = 0$. The expression will then be revised as follows:

$$y_{ik} \|x_i - m_k\|_2^2 = \sum_{j=1}^K y_{ij} \|x_i - m_j\|_2^2 \quad (7)$$

In summary, optimizing the following issue is required

$$Y, M = \arg \min \sum_{i=1}^N \sum_{j=1}^K y_{ij} \|x_i - m_j\|_2^2 \quad (8)$$

3 Experimental Results

The traffic conflict elements are obtained through data processing of the video recorded by the camera. The duration of the survey is 30 min, it happened during the peak hour with relatively large pedestrian traffic in two main directions, including from the An Hung urban area to the opposite side of the market and from The Pride building to the park in the An Hung urban area. By the survey, the number of conflicts is gained by 138 points. The data of TTCmin and PET parameters are presented in an excel sheet and are demonstrated according to the cumulative frequency distribution graph below (Figs. 2 and 3).

Besides, K -means approach has been adopted to categorize severity levels for the dataset including 138 events extracted. The final result of this algorithm is to find center points that are present for clusters. There are 3 center points found after dataset analysis with K -means as TTCmin and PET traffic conflict elements including

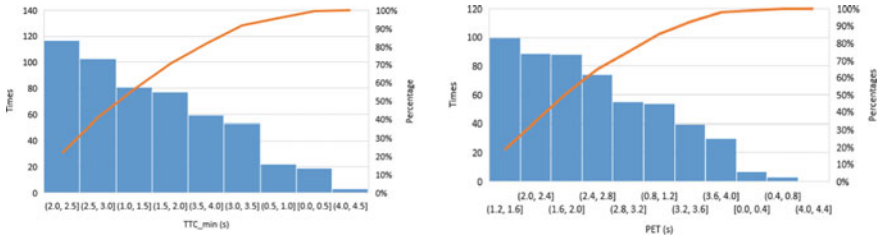


Fig. 2 Graph of TTCmin and PET cumulative frequency



Fig. 3 Camera location and survey area at Thanh Binh intersection

[TTCmin, PET]: [0.93, 0.80], [1.5, 2.2], [2.8, 3.3]. Besides, there are also three severity levels of conflict including critical conflict event, less serious conflict, and safe passage corresponding to the center points of the conflict indicator calculated above. Ten first points in the dataset are presented in Table 1.

According to calculation results, level 2 conflicts occur the most frequently (43%), followed by level 1 conflicts (38%) and level 3 conflicts (19%). This outcome is consistent with the survey team’s opinion that high-danger conflicts—Level 1—occur often, particularly those involving motorbikes and pedestrians. The survey’s findings also demonstrate that confrontations constantly happen in the investigated regions during peak hours with heavy vehicle traffic and that 1-way conflicts are particularly common. These conflicts mostly involve people and vehicles turning left from the urban area to Thanh Binh Street on the opposite side of the local market. The result indicates that better traffic control measures are required at the

Table 1 Safety assessment of the first 10 recorded conflict points in the project dataset

STT	Conflict point time	Time to collision TTCmin (s)	Post-encroachment time PET (s)	Level 1	Level 2	Level 3	Level of conflict point
1	5:23:28 PM	1.72	2.51	0	1	0	II
2	5:25:37 PM	1.53	1.82	0	1	0	II
3	5:26:03 PM	2.50	2.87	0	0	1	III
4	5:26:12 PM	2.17	1.95	0	1	0	II
5	5:28:18 PM	0.92	0.85	1	0	0	I
6	5:28:42 PM	0.88	1.02	1	0	0	I
7	5:29:37 PM	1.32	2.21	0	1	0	II
8	5:29:40 PM	1.01	1.17	1	0	0	I
9	5:33:46 PM	2.10	1.97	0	1	0	II
10	5:34:42 PM	2.52	2.12	0	1	0	II

intersection of the urban areas of Thanh Binh and An Hung, giving preference to pedestrians (particularly in attractive spots) during regular daytime hours.

4 Conclusion

Traffic safety has been an issue of concern to society, including pedestrian traffic. The current approach is applying the traffic conflict method to safety assessment studies is a trend and is used in almost traffic safety research, video processing, to analyze the features of confrontations between pedestrians and automobiles to provide effective solutions. The article presents research results by making the application of video processing to identify conflict point between vehicles and pedestrians to calculate the parameters conflict TTCmin and PET. By using a clustering algorithm, severity levels of conflict points will be divided, from which to identify the places with the frequency of the sites of conflict dangerous conflict hide that may cause traffic accidents to implement prompt, consistent improvement solution.

Acknowledgements This research is funded by University of Transport and Communications (UTC) under grant number T2022-MT-002.

References

1. WHO (2018) Global status report on road safety 2018: summary. World Health Organization, Geneva, pp 2018 (WHO/NMH/NVI/18.20). Licence: CC BY-NC-SA 3.0 IGO). Accessed 19 Jan 2019
2. Ni N, Wang M, Sun J, Li K (2016) Evaluation of pedestrian safety at intersections: a theoretical framework based on pedestrian-vehicle interaction patterns. *Accid Anal Prevent* 96:1486
3. He Y-L, Li R-T, Li L, Schwebel DC, Huang H-L, Yin Q-Y, Hu G-Q (2019) Left-turning vehicle-pedestrian conflicts at signalized intersections with traffic lights: benefit or harm? A two-stage study. *Chin J Traumatol*
4. Ren G, Gu C, Lu L, Zhou Z, Ding C (2012) Modeling risk degree of conflicts between crossing pedestrians and vehicles at signalized intersections. *J Transp Syst Eng Info Technol* 12(5):76–78
5. Zheng L, Ismail K, Meng X (2014) Traffic conflict techniques for road safety analysis: open questions and some insights. NRC Research Press, Ottawa
6. Santhosh D, Binhdhu BK, Koshy BI (2020) Evaluation of pedestrian safety in unsignalized *T* and *X*—Intersections through comparison of the frequency and severity of pedestrian conflicts. *Case Stud Transp Policy*
7. Salamati K, Schroeder B, Roupail NM, Cunningham C, Long R, Barlow J (2011) Development and implementation of conflict-based assessment of pedestrian safety to evaluate accessibility of complex intersections. *Transp Res Rec J Transp Res Board* 2264:148–155
8. Ni Y, Wang M, Sun J, Keping J (2016) Evaluation of pedestrian safety at intersections: a theoretical framework based on pedestrian-vehicle interaction patterns. *Accid Anal Prev* 96:118–212
9. Ismail K, Sayed T, Saunier N, Lim C (2009) Automated analysis of pedestrian-vehicle conflicts using video data. *Transp Res Rec J Transp Res Board* 2140:44–54
10. Proyanka A, Rjayakarthishik D (2018) Road safety analysis by using *K*-means algorithm. *Int J Pure Appl Math* 119(10):253–257
11. Kim K, Yamashita EY (2005) Using a *k*-means clustering algorithm to examine patterns of pedestrian involved crashes in Honolulu. Hawaii. *J Adv Transp* 41(1):69–89

Vehicle Speed Analysis Toward Traffic Safety at School Zones Considering Roadside Activities—Case Study in Vietnam



Dang Minh Tan and Vu Quang Huy

Abstract In Vietnam, school traffic accident is an urgent problem that needs mitigation solutions. Schools such as primary and secondary schools are located in the roadside of streets/roads, national highways, and provincial roads. School children who usually walk, ride a bicycle, or taken by their parents by motorbikes going to school are considered as vulnerable road users. Meanwhile, solutions for traffic organization and traffic safety in these areas have not really ensured traffic safety. Motor vehicles often use high speed through schools, causing traffic safety problems. On that basis, this paper conducts observations and evaluates the speed of motor vehicles when passing through the school areas. Three sites (schools) with different levels of roadside activities in Pleiku city, Vietnam, were selected for observation and analysis. An image processing method is used for collecting speed data. It is found that there is a relationship between the free-flow speed of vehicles and roadside activities. The results of the paper help to provide solutions for improving traffic safety for school children.

Keywords Traffic safety · School zone safety · School children · Roadside activities

1 Introduction

In recent years, traffic accidents in Vietnam still remain high with more than 8000 deaths per year with the information announced by the country [1]. Meanwhile, according to organizations such as World Bank, WHO, this number can be estimated as higher than 20,000 fatalities. Children are particularly vulnerable with 1900 children's fatalities on Vietnam's roads each year. Road crashes are the second leading cause of death for Vietnamese children between the ages of 5 and 14 [2].

D. M. Tan · V. Q. Huy (✉)
University of Transport and Communications, Ha Noi, Vietnam
e-mail: vuquanghuy@utc.edu.vn

There have been many studies around the world on traffic safety in school areas [3–7]. In general, these studies have spent efforts to assess traffic safety or speed at school gate areas, thereby suggesting solutions to improve traffic safety. The solutions proposed in these studies focus on reducing the accessibility of motor vehicles and reducing the speed in school areas. Sun et al. [3] found that by reducing speed limits from 50 to 30 kph at school zones can contribute to the significant reduction of fatal and injury collisions. However, in another study, Hidayati et al. [4] conducted a study in the Indonesia case and found that the School Safety Zone, which is a time-dependent speed control zone, does not reduce the speed of vehicles.

In Vietnam, schools are often located near the streets or even close to the roadside of busy streets, provincial highways, or national highways. In fact, there is a lack of reasonably protective measures and legal provisions to deal with traffic safety issues. Sidewalks/walking paths and crossing facilities on major roads or busy streets as well as other traffic regulation facilities that require drivers to slow down around schools are not adequately or properly arranged. Road traffic safety issues cause deep concern and worry for parents. Therefore, most parents will have to take their children to school, instead of letting them walk to school on their own. This even contributes to a negative impact on traffic safety, and even causes chaos and traffic jams when parents come to school to pick up and drop off students. With the goal of focusing on reducing the traffic accident of school children, the study aims to conduct an analysis of the speed of vehicles running through school zones with some specific cases in Vietnam. The study quantifies the relationship between roadside activities and vehicle speed, and that will help to find appropriate solutions to improve safety at schools in Vietnam.

2 Methodology and Results

2.1 Data Collection

The data to be surveyed includes two data types: road geometry and roadside activities and traffic data (type and speed of vehicles). Roadside activities that are considered in the study include some major factors such as the development of residential housing in the area around schools (high- or low-developed area), availability of sidewalks, and level of roadside trading. In this study, it is focused on free-flow vehicles on the interaction with those general roadside activities. This study does not focus on analyzing each specific activity such as cases of vehicles making U-turns, pedestrians crossing, vehicle parking, etc.

An image processing tool [8] is used to get data at measurement sites to analyze vehicle speed passing through the analyzed cross sections. Videos are then inputted into the image processing tool, through which spot speed data is collected. The method to get speed data in the image processing tool is a basic method that is calculated based on the distance and time a vehicle passing through two given points.

Three sites corresponding with three primary schools in Pleiku city, Vietnam, are selected for the study.

Three schools are located on the roadside of different streets with different levels of roadside activities (Table 1). At each site, two cross sections were selected for collecting vehicle speed data (spot speed data). These two cross sections include as follows: Cross section 1 locates in front of the school gate, and Cross section 2 locates at a distance of 200 m from the cross section 1 (before the speed limit zone). The analysis direction will be the vehicles moving in the direction from cross section 2 to cross section 1. The choice of the location of the second cross section is based on the conditions of the road through school and within the effective distance of the speed limit sign that can be provided (Fig. 1).

The survey was conducted in Pleiku in April 2022 (just after the lockdown duration of Covid pandemic). The video data was collected in one day (on weekdays) for each site. Time survey was conducted at each school with four time frames/day, including:

Table 1 Basic information of the survey sites

Site	Name of school	Carriage-way width (m)	No. of lane	Roadside activities
NVT	Nguyen Van Troi Primary School	10.0	2	High-developed area, sidewalk available, low level of roadside trading
NDC	Nguyen Duc Canh Primary School	9.3	2	Low-developed area, sidewalk not available, very low level of roadside trading
CCL	Cu Chinh Lan Primary School	7.0	2	High-developed area, sidewalk available, high level of roadside trading

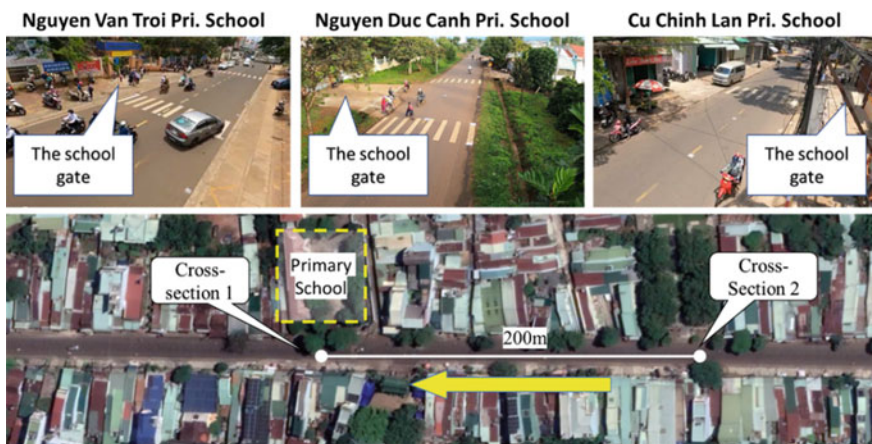


Fig. 1 Relative position of two cross sections

from 6:00 to 7:00, from 10:30 to 11:15, from 12:15 to 13:00, and from 16:30 to 17:30, and these are the times when students go to school or come back home. Speed limits in these school zones are 30 kph, but the speed is only limited during the above four time frames.

In this study, vehicles with free-flow speed were selected for analysis while crossing the analyzed cross sections. A certain number of samples are randomly selected at each time frame. However, because the number of data is limited, this analysis does not separate each time frame, but aggregates into a dataset for each cross section. Moreover, in this analysis due to the low traffic volume of cars (passenger cars, buses, trucks, etc.), statistical results of vehicle speed are aggregated into two categories: motorbikes and cars, regardless of car types. The number of samples is attempted to be as large as possible to warrant the presentation of statistical distributions.

2.2 Data Analysis, Results, and Discussion

The analysis results are shown from Figs. 2, 3, 4, 5, 6 and 7; Tables 2 and 3. Figures 2 and 3 show the histogram and the cumulative frequency distribution of vehicle speeds at cross sections 1 and 2 of the Nguyen Van Troi site (NVT). Figures 4 and 5 show the histogram and the cumulative frequency distribution of vehicle speeds at cross sections 1 and 2 of Nguyen Duc Canh site (NDC). Figures 6 and 7 show the histogram and the cumulative frequency distribution of vehicle speeds at cross sections 1 and 2 of Cu Chinh Lan site (CCL). Tables 2 and 3 show statistical values of vehicle speed at cross sections 1 and 2 at all observed sites corresponding with Figs. 2, 3, 4, 5, 6 and 7.

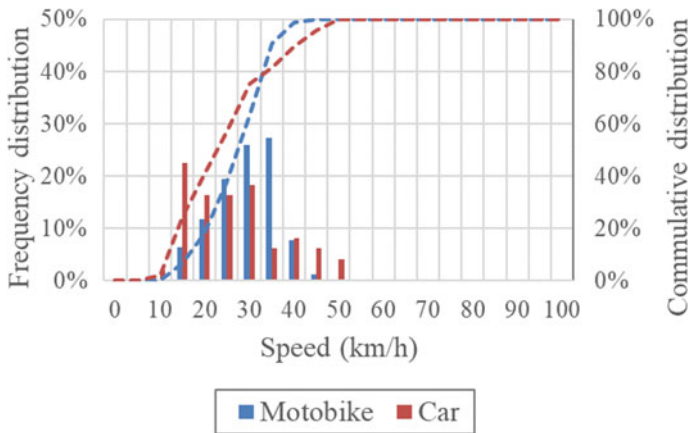


Fig. 2 Histogram and cumulative frequency distribution of vehicle speed at cross section 1—site NVT

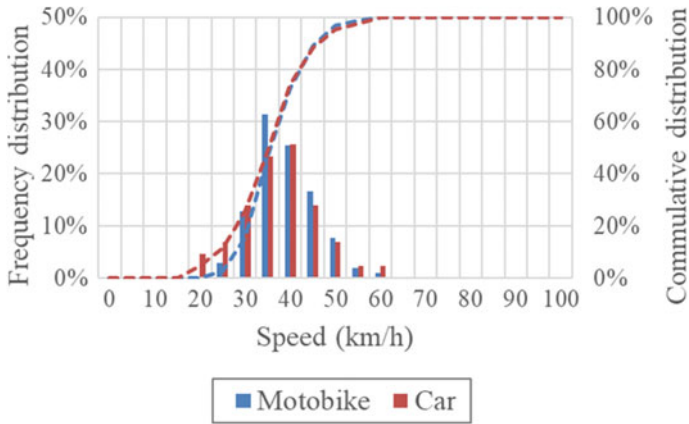


Fig. 3 Histogram and cumulative frequency distribution of vehicle speed at cross section 2—site NVT

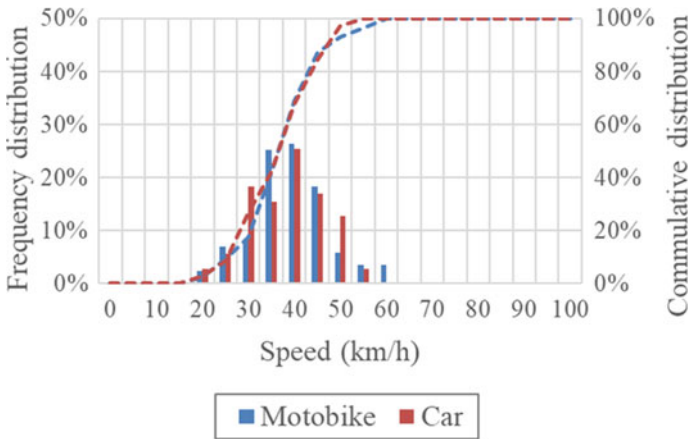


Fig. 4 Histogram and cumulative frequency distribution of vehicle speed at cross section 1—site NDC

The results show that at all three road segments, vehicle speed decreases when passing through the school gate (from cross section 2 to cross section 1). The results also indicate that vehicles have greater speeds and higher variation when the width of the road segment is wider and the speed of vehicles in the street with low roadside activities is higher than in roads with higher roadside activities. Moreover, there are differences between the speed of cars and motorbikes, but not clear at all sites. At cross section 2, the highest 85% speed is found at the NDC site with low roadside activities (51.62 kph for cars and 45.80 kph for motorbikes), and the lowest 85% speed is at the CCL site with high roadside activities (33.59 kph for cars and 36.07 kph for motorbikes). This similarity can be seen at cross section 1. Although

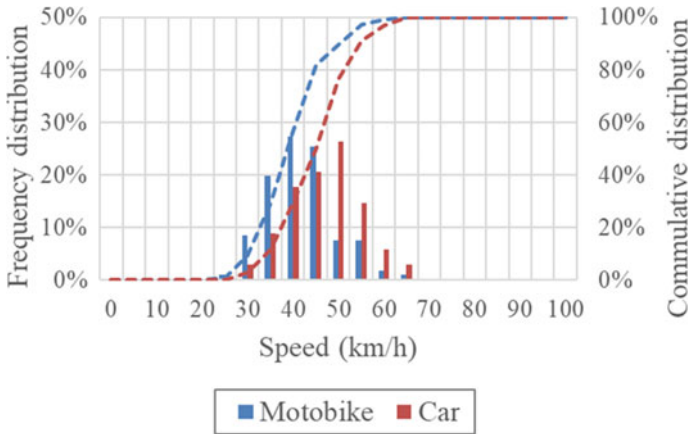


Fig. 5 Histogram and cumulative frequency distribution of vehicle speed at cross section 2—site NDC

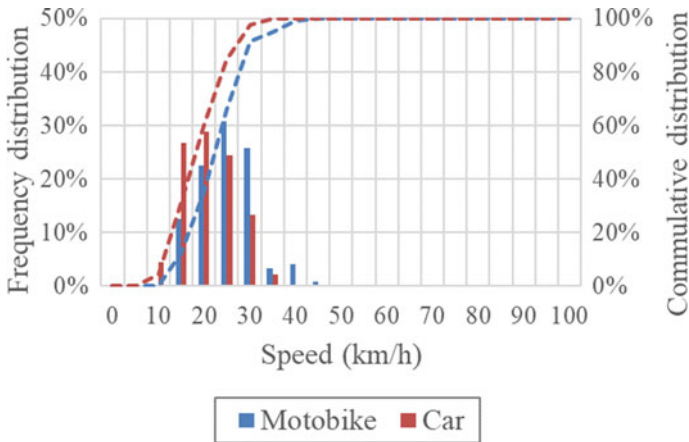


Fig. 6 Histogram and cumulative frequency distribution of vehicle speed at cross section 1—site CCL

vehicles tend to slow down when going through the school gate, it is still higher than the 30 kph speed limit. Especially with the NDC site, the vehicles were still running at 85% speed higher than 40 kph, especially, there were some vehicles running with speed higher than 50 kph at the cross section 1.

Although there are speed limit zones in existence on these streets, however, the effectiveness is not so high. Some of the reasons that vehicles still maintain high speeds can be mentioned as follows:

- Generally, the behavior of road users is not so good. The reality of participating in traffic on the road shows that many road users do not fully comply with traffic

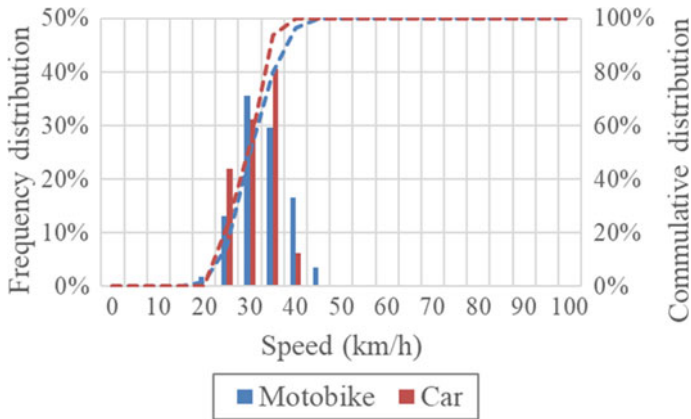


Fig. 7 Histogram and cumulative frequency distribution of vehicle speed at cross section 2—site CCL

Table 2 Statistic values of vehicle speed at cross section 1

Statistic index	Unit	Cross section 1					
		Motorbike			Car		
		NVT	NDC	CCL	NVT	NDC	CCL
Maximum	kph	43.57	59.84	40.94	48.83	51.64	32.32
85%	kph	33.35	43.34	28.37	36.44	44.64	24.89
Average	kph	26.72	36.72	22.60	24.40	36.22	18.76
15%	kph	18.67	29.05	16.47	13.61	27.53	13.58
Minimum	kph	12.28	18.89	10.73	9.72	16.07	7.44
Stdev		6.86	8.33	6.14	10.22	8.06	5.67
No of sample		77	87	120	49	71	45

Table 3 Statistic values of vehicle speed at cross section 2

Statistic Index	Unit	Cross section 2					
		Motorbike			Car		
		NVT	NDC	CCL	NVT	NDC	CCL
Maximum	kph	55.27	61.97	42.14	55.33	60.24	36.96
85%	kph	43.36	45.80	36.07	43.09	51.62	33.58
Average	kph	36.27	39.21	30.35	34.92	44.20	28.78
15%	kph	29.92	31.12	25.24	26.82	37.32	23.55
Minimum	kph	22.61	23.06	18.59	17.26	29.15	21.19
Stdev		6.60	7.41	5.15	8.47	7.38	4.44
No of sample		102	106	115	43	34	32

laws. The traffic police patrol can contribute to improve the efficiency of law enforcement; however, it is difficult to carry out in a large area. Local road users are familiar with road activities, and when they know the rules of traffic police activities, they may avoid the control of the authorities.

- Solutions for speed limit signs according to four time frames are complicated and also make it difficult for road users to recognize and comply.
- The social isolation period of the Covid epidemic has reduced traffic volume, and schools are not working. While the survey was carried out just right after the isolation time of the Covid pandemic, students just started going to school, so traffic users still have a subjective mentality, not complying with speed limit solutions.
- Other speed reduction countermeasures such as rumble strips, road making, and road signs have not been used effectively.

3 Conclusion

In general, the study is a part of a topic for traffic assessment at school zones. In this paper, it is focused on the analysis of the speed of free-flow vehicles running on three streets through school zones in Pleiku, Vietnam. The observed streets have different levels of roadside activities. An image processing tool is used for getting speed data. It is found that there is a reduction of speed of vehicles running through the school gate. Vehicle speed is higher at wider streets and lower levels of roadside activities. The difference in speed between cars and motorbikes is not really clear. However, the speed limit zones of 30 kph are not so effective in reducing speed. Many vehicles still run with speeds of over 50 kph, even over 60 kph.

For further study, it is necessary to focus on analyzing the conflicts between road users, especially school children and motor vehicles in the vicinity of schools, from which more specific solutions can be found to improve traffic safety for pedestrians.

References

1. GRSF (2022) Vietnam's road safety country profile. <https://www.roadsafetyfacility.org/country/vietnam>. Accessed 25 Sep 2022
2. National Traffic Safety Committee (2022) Mỗi năm Việt Nam có 1.900 trẻ em tử vong vì ATGT. <http://antoangiaothong.gov.vn/den-do/moi-nam-vn-co-1900-tre-em-tu-vong-vi-tngt-78657.html>. Accessed 25 Sep 2022
3. Sun D, El-Basyouny K, Ibrahim S, Kim AM (2018) Are school zones effective in reducing speeds and improving safety? *Can J Civil Eng* 45(12):1084–1092
4. Hidayati N, Liu R, Montgomery F (2012) The impact of school safety zone and roadside activities on speed behaviour: the Indonesian case. *Proc Soc Behav Sci* 54:1339–1349
5. Rahman MH, Abdel-Aty M, Lee J, Rahman MS (2019) Enhancing traffic safety at school zones by operation and engineering countermeasures: a microscopic simulation approach. *Simul Model Pract Theory* 94:334–348

6. Renard A, Novacko L, Babojelic K, Kožul N (2022) Analysis of child traffic safety near primary school areas using UAV technology. *Sustainability* 14(3):1144
7. Putri LD, Soehardi F, Saleh A (2017) A review of vehicles speed on school safety zone areas in Pekanbaru city. In: IOP conference series: earth and environmental science, vol 97. IOP Publishing, Bristol, p 012019
8. Tan DM (2018) A smoothing method to reduce data noise: a functional analysis od speed profile of road users. In: Conference proceedings, ICSCSE 2018 international conference, ISSN-2354-0818

Impact of COVID-19 on the Inland Waterways and Review Recovery Solutions



Nguyen Viet Thanh, Nguyen Dinh Thao, Dang Tuyet Ly, and Pham Van Hai

Abstract The COVID-19 pandemic caused by the SARS-CoV-2 virus has appeared in Vietnam since January 2020. The pandemic has spread to all 63 provinces and cities in Vietnam. In this paper, based on the volume of freight and passenger transport of inland waterway transport (IWT) in 2020 and 2021, the impact of COVID-19 was investigated. The result indicated that the passenger transport decreased from 8.3% in 2020 and 27% in 2021 where the total volume of freight increased 19% in 2020 but decreased 6% in 2021. To promote the inland waterway transport, several recovery solutions for IWT are proposed and conditions for implement are also presented.

Keywords COVID-19 · Inland waterway transport · Volume of freight · Passenger transport · Recovery solutions

1 Introduction

The first case of COVID-19 was infected in Vietnam on January 23, 2020 [1]. In 2020, Vietnam had quite a well-controlled pandemic, with the number of confirmed deaths for the entire year only 35 people. However, in 2021, the pandemic situation has become more severe with the number of COVID-19 cases and the number of deaths spike. Ho Chi Minh City has a total of 501,258 infections and 19,389 deaths (as of December 27, 2021) [2]. The Civil Aviation Authority of Vietnam estimates that aviation revenue will be lost at about VND 25,000 billion [3], the aviation industry has fallen into the “worst” situation in its 60-year history of the development, and

N. V. Thanh (✉) · N. D. Thao
Faculty of Civil Engineering, University of Transport and Communications, Hanoi, Vietnam
e-mail: vietthanh@utc.edu.vn

D. T. Ly
Transport Researcher, Hanoi, Vietnam

N. V. Thanh · P. Van Hai
Viet Trung Research and Development Center, University of Transport and Communications,
Hanoi, Vietnam

all flight routes have been suspended. According to the Hanoi Tax Department, in the first 2 months of the year, more than 2600 business households were dissolved, and 6400 business households stopped doing business; the state budget lost revenue from 4200 to 16,600 billion VND [4]. The resort and transport industries lost revenue due to the social isolation policy. The number of international tourists in the first three months of the year was only 3.7 million people and a decrease rate of 18.1% over the same period in 2019. The domestic and international tourism markets are “almost completely frozen” [5]. Migrant workers in cities are unemployed and their incomes decrease due to social distancing at home. Ho Chi Minh City reported 600,000 unemployed people as of the end of March [6]. Khanh Hoa had about 17,000 unemployed people in the first quarter [7]. On April 21, 2021, the General Statistics Office said that 5 million workers are unemployed or on rotational leave due to the impact of the epidemic, and this is the rate of underemployment of working age at the highest level in the past 5 years [8]. The pandemic has significant on all sectors and the human living where the inland waterways’ transport faced any difficulties due to epidemic control measures. The supply chains were interrupted and broken due to isolation and society distance. In this paper, based on the statistics data of volume of freight and passenger transport by IWT, the effect of COVID-19 is presented and analyzed.

2 Overview of Inland Waterway Transport Before and After the COVID-19 Pandemic

According to the report on master plan of inland waterway infrastructures for the period 2021–2030, vision to 2050, by the end of 2019, the whole country has: 293 inland waterway ports, including 218 cargo ports, 12 passenger ports, 02 general ports, and 63 specialized ports (national inland waterway has 266 ports, local inland waterway has 27 ports); 8199 inland waterway berths, of which 6497 berths have been licensed to operate, reached to 75% (national inland waterway has 3137 berths, local inland waterway has 3360 berths); 1702 unlicensed berths (national inland waterway 1297 berths, local inland waterway 405 berths); 2526 passenger berths across the river, of which 2058 licensed berths reached 81.5% [9].

Annually, inland waterway transport transports about (18–22)% of freight tons, (5–6.8) % of passengers in the total transport volume of the whole transportation flied; the average growth rate is from 8 to 12%/year with many advantages: low investment, low freight, can carry oversized and super heavy goods, minimal impact on the environment, high socialization. Inland waterway transport is currently concentrated in two areas in the North and in the South, each with its own characteristics.

Volume of freight of inland waterway transport in 2019 reached 266 million tons (up 5.6% compared to 2018) and volume of freight traffic reached 63.3 billion tons-km (up 22.9% compared to 2018), accounting for a market share of 12.51% for general freight transport and 26.8% for inter-provincial inland freight transport. IWT

passenger transport in 2019 reached 241.7 million passengers (up 5.5% compared to 2018), and passenger rotation reached 3.99 billion passengers.km (up 7.5% compared to 2018), which holds a market share of 5.03% for all passenger transport and 6.76% for domestic passenger transport. The volume of goods transported by VR-SB vessels through the seaport from the opening of the route (from June 2014) to the end of April 2019 reached 85 million tons of goods with more than 81,500 turns of vessels entering and leaving the seaport [10].

In 2020, the volume of freight by IWT reached 337.1 million tons, accounting for 19% of the whole industry. Cargo turnover reached 68.9 billion tons-km, accounting for 20.3% of the whole industry. Inland waterway passenger transport reached 191.5 million passengers, down 8.3% in rotation to 3.4 billion passengers-km, down 18.7% over the same period last year [11].

In 2020, the volume of VR-SB and Vietnam-Cambodia cross-border transport with the number of tons of goods through is 10,046,724.8 tons; 374 inland waterway vessels are licensed to operate waterway transport between Vietnam and Cambodia. The IWT port authorities have conducted procedures for 6026 VR-SB vessels [11].

In 2021, passenger and cargo transports on IWT were estimated to reach about 165 million passengers and 316 million tons, respectively. Passenger transport is down 27% compared with 2020, and rotation reached 2.73 billion passengers-km, down 26% compared with 2020. The cargo transport was estimated at 316 million tons, down a rate of 6%, and in terms of rotation, reached 67.6 billion tons-km, down a rate of 2%. The volume of freight through seaports by inland waterway vessels reached 198 million tons, down 3% over the same period in 2020 [12].

In which, VR-SB (combined river-coastal) transport is increasing and effective. In recent years, the transport of goods by VR-SB vessel on the coastal transport route has been increasing. The IWT and coastal transport have been promoting positive effects in increasing the market share of inland waterway and coastal transport and contributing to reducing pressure on road traffic. In 2021, coastal transport by VR-SB vessel is estimated to reach more than 50,000 turns of vessels mooring ports and berths, with a cargo volume of 78.5 million tons, an increase of more than 9 times compared to 2015 (the first year of opening the route). The volume of freight through the seaport by VR-SB vessels reached 58 million tons, an increase of 57% compared to 2020, accounting for 29% of the total volume of freight through inland waterway transport.

Container transport by IWT is increasing. Specifically, at Hai Phong seaport, the volume of container transported by IWT in 2020 is 73,518 TEU, accounting for 1.4%. In 2021, it is estimated to reach 83,223 Teus, accounting for 1.8%. Seaport in Ho Chi Minh City, in 2020 it reached 849,000 Teus, accounting for about 11%, and in 2021 it is estimated to reach 670,301 Teus, accounting for about 10%. Ba Ria-Vung Tau seaport, container transported by IWT in 2020 reached more than 3 million Teus, accounting for about 72% of the total volume of containers through the port, and in 2021 it is estimated to reach more than 3 million Teus, accounting for about 77% [12].

3 Evaluation of the COVID-19 Pandemic Impact on the Inland Waterways

3.1 General Impact

Inland waterways' transport has a close relationship with all sectors of the economy of our country. The following will summarize the impacts of COVID-19 on economic sectors including both inland waterway and maritime transport.

Vietnam's economy since 2020 has suffered a strong shock from the COVID-19 pandemic from both the supply side and the demand side. From the supply side, production and business faced difficulties due to epidemic control measures. The supply chain was interrupted and broken due to almost main input materials to Vietnam (such as China and Korea) taking measures to block the border to control the COVID-19 Pandemic. From the demand side, COVID-19 causes demand to decline for several reasons: moving and working lockdown measures reduce consumer demand, decrease consumer income, and enterprises cut off investment due to reduced economic expectations and stagnant production. The main impact trends show on the following aspects:

- (1) **Disrupting the growth trend:** Actual data show that our country's economy has been significantly affected by the COVID-19 crisis. Vietnam's GDP growth in 2020 is only reach to 2.91%, a sharp decrease compared to the 6.5–7% forecasted before the COVID-19 crisis and down to 4.1% points compared to the previous achieved growth rate in 2019 (7.02%). GDP growth in the first 6 months of 2021 reached 5.64%, lower than the target set by the Government in Resolution No. 01/2021/NQ-CP of 0.58 percentage points (6.22%) and lower than 1.55 percentage points compared to the Government's forecast updated in the first quarter of 2021 (7.19% due to the impact of the epidemic that broke out again in April in many localities). GDP in the third quarter of 2021 and is the deepest decline ever. The general estimate of GDP growth in 2021 is only about 2%.
- (2) **The service sector is heavily affected:** The service sector growth decreased by 4.96 percentage points (from 7.3% in 2019 to 2.34% in 2020). In 2021, the decline will continue, reducing the overall growth of the service sector and the entire economy. In the first nine months of 2021, the service sector's growth will decrease by 0.69%, of which the first 6 months of 2021 will increase by 3.96% and the third of 2021 will decrease by 9.28%.
- (3) **The processing and manufacturing industry dropped sharply due to the disruption of supply chains and the decline of market demand:** In 2020, the industry and construction sector still maintained a strong recovery and a driving force for growth for the whole economy with a growth rate of 3.98%, in which the processing and manufacturing industry played a key role with an increasing rate of 6.82%. However, in 2021, the impact of the COVID-19 pandemic will become clearer. Industrial production in the first 9 months of 2021 will be severely affected, especially in big cities and provinces where many industrial

parks, key economic zones are concentrated. The growth rate of the industrial and construction sector will be at 3.57% for the first nine months of 2021 (in which, the third of 2021 will decrease by 5.02%). The processing and manufacturing industry spent an increase of 6.05 percent in the first nine months of 2021.

- (4) ***Agriculture, forestry, and fisheries (AFF) play a significant role in supporting growth:*** Although the export demand for many AFF products decreased sharply and was affected by salinity intrusion in the Mekong Delta. AFF products maintained a good growth rate of 2.68% in 2020, even higher than in 2019 (2.01%). In nine months of 2021 reached 2.74% and played the role of a “supporting platform” to support growth for nonagricultural activities.
- (5) ***On the demand side, economic activities declined due to weak domestic consumption and world demand:*** In 2020, a final record consumption lowest growth was recorded. Spending increased by 1.06% over the same period in 2019. It is the first-time total retail sales of consumer goods and services decreased by 1.2% over the same period. In 2021, there is a decrease rate of 7.1% in the first nine months compared to the same period in 2020.

3.2 Impact on Transportation Enterprise

Vietnamese enterprises faced many difficulties and challenges caused by the pandemic in 2021. In the first 11 months of 2021, the indexes on the number of newly established enterprises, capital, and additional jobs all decreased sharply compared to the same period in 2020; the number of enterprises shutting down and temporarily closing increased. The epidemic has forced enterprises to restructure and change business models to suit the new situation. Negatively affected enterprises tend to change their strategies, production, and business models, restructure their service portfolio, find new suppliers and markets, apply digital technology, and diversify sales and service provision to maintain operations instead of moving to other fields or industries.

Inland waterway enterprises cannot avoid the above-mentioned difficulties. Facing the complicated situation of the COVID-19 pandemic, many localities across the country must comply with instruction of Direction No. 16/CT-TTg dated on March 31, 2020, of the Prime Minister on the implementation of urgent measures for prevention and control of COVID-19. Accordingly, localities must implement social isolation, not gathering more than 2 people outside of offices, hospitals, schools, and public places; suspending business and service establishments. Businesses dealing in essential goods and services are allowed to operate but must strictly implement anti-epidemic measures, etc. Therefore, activities of the supply chain have been minimized throughout the country. This has had a significant impact on inland waterway and maritime transport throughout the country. COVID-19 has disrupted the supply chain to serve the essential needs of people and businesses. Goods at seaports as well as inland ports and berths are congested and unable to be delivered to customers on



Fig. 1 Container trucks are stuck on the way to Cat Lai New Port

time as planned. Typically, the cargo congestion at Cat Lai New Port from July to August 2021 is due to social distancing. According to Instruction No. 19, many factories and enterprises reduce production or suspend operations. Regarding the volume of imported containers at the port facilities, the ICD increased rapidly, affecting the receipt, exploitation, and flow of import and export goods. The congestion at Cat Lai New Port has caused great impacts on society as follows:

- Causing traffic jams on Dong Van Cong road, the congestion also spread to many surrounding roads such as Mai Chi Tho, the Eastern Belt, Nguyen Thi Dinh, inter-provincial road 25B (Fig. 1).
- Increased logistic costs because shipping lines have unilaterally applied 5–7 types of fees (depending on shipping lines), such as loading and unloading fees at the port (about 130–135 USD/40-ft container), air conditioning of empty containers, unbalanced fee for container (about 30 USD/40 ft container). It has just added a “congestion fee” at 100 USD/40 ft container.
- To manage this problem, it is necessary to involve relevant agencies including the National Assembly, the Government, the Ministries, City, and neighboring provinces.

The number of inland waterway vessel through Vietnam’s seaport system reached more than 206,900 times in the first 7 months of 2021 go down with a rate of 6% compared with the same period in 2020. VR-SB vessel reached more than 24,400 times decrease with rate of 30% compared to the same period in 2020. The sharp decrease in the number of vessels also made the volume of goods through the seaport by inland waterway transport in the first seven months only 123.6 million tons, a

decrease of 11%. However, the volume of goods through VR-SB still maintained its growth rate with an increase of 64% over the same period last year, reaching 34.8 million tons (28% of the total volume of goods through the inland waterways). The causes induced the decreasing of the number of vessel and the total of goods transported by inland waterway transport are social distancing, which has caused the production and business of many manufacturers to decrease. Machines, factories are stopped or temporarily interrupted. As a result, the demand for freight also declines.

4 Recovery Implemented Solutions

4.1 *Marco Solutions*

The direction of the Ministry of Transport is shown in the following guiding documents.

- Decision No. 1589/QD-BGTVT dated August 27, 2021, of the Minister of Transport promulgated the temporary guidance on traffic organization and epidemic control for maritime transportation activities during the COVID-19 epidemic prevention and control period.
- Notice No. 367/TB-BGTVT dated September 17, 2021, of the Minister of Transport on the conclusion of Minister Nguyen Van The at the meeting (online) on facilitating inland waterway and maritime transportation, and logistic services in the prevention and control of COVID-19, the Ministry has requested provinces and cities to implement the following solutions:
 - Reviewing procedures and conditions for replacement of crew member at seaports, with regulations and guidelines in the direction of creating all favorable conditions for sailors to be replaced quickly and safely.
 - Prioritize vaccination against COVID-19 as soon as possible for vehicle drivers, crew members, and participants in the provision of transport services related to import and export of goods at seaports.
 - Create all favorable and quick conditions for people and vehicles to participate in import, export, and circulation of goods. Do not allow traffic jams or congestion of goods at ports related to the operation of inspection and control checkpoints.

Notice No. 374/TB-BGTVT dated September 24, 2021, of the Minister of Transport on the conclusion of Deputy Minister of Transport Le Dinh Tho at the briefing (online) on September 22, 2021, on freight transport associated with the prevention and control of the COVID-19 epidemic. Accordingly, the Deputy Minister assigned the Vietnam Inland Waterway Administration (VIWA) to continue to coordinate with localities closely and effectively with favorable conditions in inland waterway transport and coastal transportation to promote intra-provincial and inter-provincial transportation of goods and passengers.

The “Green waterways” solution is given in the temporary guidance on traffic organization and epidemic control for transport by car during the time of COVID-19 prevention and control according to Decision No. 1570/QĐ-BGTVT August 24, 2021, of the Minister of Transport which is a clear demonstration of the transport industry’s ability to apply 4.0 technology. There are a series of modern technologies which have been thoroughly applied to make it convenient for people and businesses to access, as well as disease control to become effective, practical, and quick. Transport management and regulation are prominent in a series of applied technologies and organizations that receive registration and issue electronic passports with QR codes for businesses and transport units.

The enterprises that stay at home can be registered the “Green Waterways”. Many services are implemented according to the model of a one-stop electronic portal, receiving, and returning results online. People with QR codes are given priority to go through a separate, faster route because they have declared in advance, updated enough information on business conditions and goods carried on the vehicle. The officer at the quarantine checkpoints uses the mobile phone to scan the QR code on the identification paper to check information and give priority to the fastest passing vehicle.

Implementing Resolution No. 128/NQ-CP dated October 11, 2021, of the Government promulgating the temporary regulation “Safely adapting, flexibly, effectively controlling the COVID-19 epidemic”, the Ministry of Transport has issued Decision No. 1812/QĐ-BGTVT dated October 6, 2021, of the Minister of Transport on organization of transport activities in five fields (road, inland waterway, maritime, railway, and aviation) safe, flexible response, and effective control of the COVID-19 epidemic.

4.2 Business Support Solutions

Notice No. 367/TB-BGTVT dated September 17, 2021, of the Minister of Transport on the conclusion of Minister Nguyen Van The at the meeting (online) on facilitating maritime transportation and logistics services in the prevention and control of COVID-19 epidemic, the Ministry of Transport has proposed the Ho Chi Minh City’s government to consider extension time of infrastructure’s fee collection; request Hai Phong City People’s Committee to consider and reduce infrastructure fees.

Circular No. 90/2019/TT-BTC dated December 31, 2019, regulate to apply of low fees for all levels of inland waterway vessels, free shipping insurance fees, and free mooring fees for ships with VRH-III registration class engaged in domestic maritime activities with a total tonnage of less than 500 GT entering and leaving the maritime area until the end of the day December 31, 2024. It also regulates fee exemption and reduction to reduce costs for enterprises and encourage fair and equal competition between inland waterway vessels of VR-SB, VRH-III, and seagoing vessels less than 500 GT for cargo transportation on Vietnam’s domestic routes.

Free of charge of quarantine and isolated ships applies from August 27, 2021, and in the future. The port authority is the agency assigned to take the lead and coordinate activities between specialized state management agencies at seaports according to regulations of Articles 120, 121, Decree No. 58/2017/ND-CP dated May 10, 2017, of the Prime Minister on the detailing of articles of the Vietnam Maritime Law.

4.3 Solutions from Specialized Management Agencies

In 2020 and 2021, the VIWA has issued more than 100 directing documents, requesting units under the VIWA, local Inland Waterway Administrations, transport enterprises, enterprises operating of inland waterway ports and berths, facilities for training crew member, and drivers of inland waterway vessels; Departments of Transport of provinces and cities carry out COVID-19 epidemic prevention and control, focusing on inland waterway passenger transport, and propose solutions and recommendations to remove difficulties for enterprises who are affected by the COVID-19.

Organize propaganda of Directive No. 15/CT-TTg dated March 27, 2020, of the Prime Minister on recommendations of health authorities on disease prevention and remind passengers to wear facemasks on public transport vehicles or public places and limit the movement of people in passenger transport vehicles. Minimize the gathering of more than 20 people in a room, do not gather more than ten people out of the office, or school, and implement a limited distance between people in public places.

5 Discussions

The leadership and direction are drastic, timely, in the right direction, comprehensive and effective, initiative-taking, and flexible, suitable to the actual situation of the inland waterway industry.

The Government has introduced strong epidemic prevention and control measures early in order to promptly prevent the spread and reduce the impact of the pandemic on people's health, the health system, and the economic development of society. Therefore, the impact on shipping activities in Vietnam has been minimized.

The Government and relevant agencies have consistently provided professional and technical solutions, while proactively and flexibly taking solutions in tracing, testing, isolating, and treating in accordance with the actual situation, especially the testing strategy to detect and quickly remove the infections from the community. This has helped the trade activities of the inland waterway industry to be maintained synchronously and effectively.

Communication work requires a high consensus in the whole society. Promote propaganda of good examples, good examples, good practices in epidemic prevention

and control, and promptly prevent bad, untrue, and fake information that adversely affect the psychology of the force. Fight against the epidemic and cause confusion and worry for people. This is a remarkably effective solution to help officials in the inland waterway transport industry confidently trust the direction of all levels to perform their assigned tasks during the epidemic season. This has also contributed to improving the exploitation efficiency of the inland waterway industry.

The COVID-19 pandemic has put the Vietnamese economy as well as the inland waterway industry before enormous challenges. However, this is also an opportunity to accelerate the process of digital transformation and the basis for the application of the results of the Fourth Industrial Revolution in the management and exploitation of the inland waterway industry.

6 Conclusions

COVID-19 has major influence on the IWT, and the volume of freight decreased 6% in 2021.

The Vietnamese Government and related authorities have issued many policies to promote inland waterway transport. Several recovery solutions for IWT are proposed, and conditions for implementation.

In the field of inland waterway transport, the widespread application of information technology has limited contact, helping to control the epidemic situation to ensure safe exploitation.

References

1. Coleman J (2020) Vietnam reports first coronavirus cases. The Hill, Washington, DC
2. Thanhnien (2022) Ho Chi Minh City restricts vehicles from entering the city until the end of April 15. Thanhnien online. Accessed 27 June 2022
3. People (2020) Enterprises join hands to deal with the Covid-19 epidemic. People. Accessed 4 March 2022
4. Linh A (2022) Hanoi: Covid-19 caused 3400 households to go bankrupt, the budget lost 16,000 billion VND. Dan Tri. Accessed 14 March 2022
5. VnExpress (2020) What scenario for Vietnam tourism? VnExpress.vn. Accessed 18 June 2020
6. Tung M (2022) 600,000 people in Ho Chi Minh City lost work due to Covid-19. VnExpress. Accessed 27 March 2022
7. Labor (2022) 17,000 workers have been cut of work, what is Khanh Hoa's government worried about? Labor. Accessed 24 April 2022
8. Ngoc B (2022) Nearly 5 million labors job loss, job loss, job relaxation, rapid increase in unemployment. Tuoi tre online. Accessed 24 April 2022
9. Investment Magazine (2022) Descendants of Vinashin fight. Investment Magazine. Accessed 28 June 2022

10. TEDI-TEDIWECCO-TDSI (2021) Master plan of inland waterway infrastructures period from 2021 to 2030, vision to 2050
11. VIWA (2019) Report summarizing work in 2019, implementing the 2020 task plan
12. VIWA (2020) Report summarizing work in 2020, implementing the 2021 task plan

COVID-19 Impact on the Operations of Road Transport Enterprises and Green Recovery Solutions



Thao Dinh Nguyen, Ly Tuyet Dang, and Quyen Van Nguyen

Abstract Since early 2020, the acute pneumonia pandemic caused by a novel corona virus (COVID-19) has left negative impacts on every sphere of human life, economy, and society globally. The pandemic also took a heavy toll on the business sector; however, its impacts on each industry and field of enterprises in Vietnam varied greatly by the nature, scope, and characteristics of their production and business activities. Road transport enterprises, whose business models are apparently associated with the travel needs of passengers and freight transport, are directly and deeply affected. Among good results, one interesting finding in this research had been clarified: although transport enterprises have experienced many difficulties over the past period, they are very determined to maintain their business with better awareness of risks and adaptability.

Keywords COVID-19 · Road transport · Adaptation measures · Green recovery

1 Introduction

This thematic research was conducted with the common goal of assessing the impact of COVID-19 on the operations of road transport enterprises, thereby identifying major issues and putting forward recommendations for effective recovery, advancing sustainability, and environmentally friendly transport with extra adaptability.

T. D. Nguyen (✉)
University of Transport and Communications, Hanoi, Vietnam
e-mail: nguyendinhthao@utc.edu.vn

L. T. Dang
Transport Researcher, Hanoi, Vietnam

Q. Van Nguyen
Vietnam Automobile Transportation Association, Hanoi, Vietnam

In order to achieve these common and specific goals, this thematic research was carried out with the main contents: (i) in-depth investigation and survey; (ii) quantitative analysis and expert assessment. Scope of the research: the road transport sector across Vietnam with the focus on enterprises [1] having at least ten business vehicles in 2019 [2].

The subject of the research: road transport operations of road transport enterprises, is focusing on the two periods: (i) before the COVID-19 pandemic and (ii) after the COVID-19 pandemic. The total number of survey respondents for the road transport is 87 enterprises.

2 Assessment of the COVID-19 Impact on Road Transport Enterprises

2.1 Impact on Total Revenue

The survey results revealed a relatively comprehensive picture of the COVID-19 impact on road transport enterprises. During the COVID-19 period, 95% of respondents confirmed a decrease in revenue compared to 2019. Specifically, the average decrease in revenue commonly fell within the range of 25–50% (49% of total enterprises), followed by a drop of about 25% in revenue (23% of total enterprises); 13% of enterprises suffered a revenue decline of 50–75%; particularly, 10% of enterprises experienced a reduction of more than 75% in revenue. Only a very small number of enterprises (5%), which are mainly freight transport enterprises, experienced an increase in revenue.

A more detailed analysis of the implication of revenue reduction by forms of transport business (the right chart) indicated that:

- Passenger transport was hardest hit, followed by general transport. Particularly, only these two forms of businesses suffered a revenue reduction of 50% or above.
- The COVID-19 pandemic also caused revenue reduction to freight transport enterprises, but the impact was of a less severe scale compared to passenger transport enterprises: Only a few enterprises experienced a 25–50% decrease in revenue, and the rest reported a slight drop in revenue of <25%.
- Only a small number of freight transport enterprises enjoyed growth in revenue by a margin that has gone up no more than 50%.

2.2 Impact on Operating Costs of Enterprises

The COVID-19 impact on the production and business activities of transport enterprises will be adequately assessed when the decrease in revenue is reviewed in conjunction with the decline in operating expenses of enterprises. Thirty-one percent

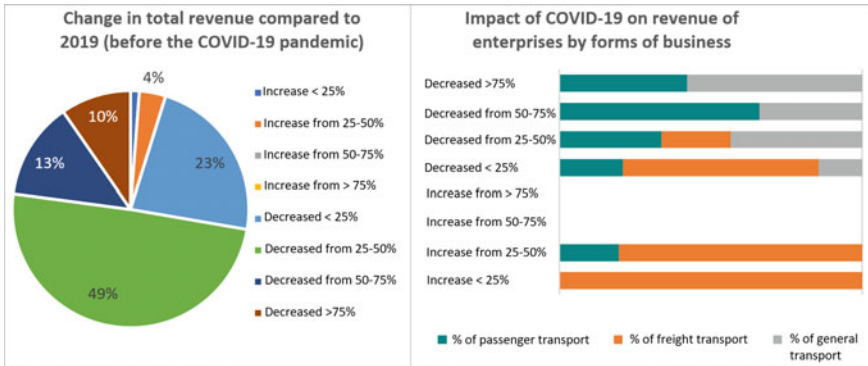


Fig. 1 Change in total revenue of road transport enterprises compared to 2019 (before the COVID-19 pandemic)

of enterprises recorded an operating cost surge, while the other 69% recorded an operating expense drop. While a rise of <25% in operating costs was common, a fall of <25% in this indicator was reported by nearly half of the respondents.

The survey results revealed that the transport market reached a deadlock during the COVID-19 period due to a demand drop or even stagnation, which showed a correlation between the downward trend in revenue and the descending trend in operating costs.

The problem, however, is that the rates of this decline vary considerably; meanwhile, the common revenue fall was 50% (Fig. 1), and the common operating cost drop was <25%. As a consequence, a great number of road transport enterprises have incurred losses due to the COVID-19 pandemic.

In addition, although some enterprises (mainly freight transport enterprises) recorded an increase in transport activities and revenues during the COVID-19 period compared to those in 2019, the revenue growth was much lower than the surge in expenses. Among 11% of enterprises with operating costs reduced by more than 50%, there is no full freight company.

2.3 Impact on Overall Production and Business Activities

In general, transport enterprises experienced a shrinkage in production and business activities (experienced by over 90% of respondents) with the most common decrease in the range of 25–50% (corresponding to 51% of enterprises), followed by a drop of <25% (corresponding to 19% of enterprises) and over 50%, which was also suffered by a large proportion of enterprises (corresponding to 25% of respondents).

Among these enterprises, the groups that suffered a sharp decrease of more than 50% were passenger transport or general transport enterprises (right figure). For

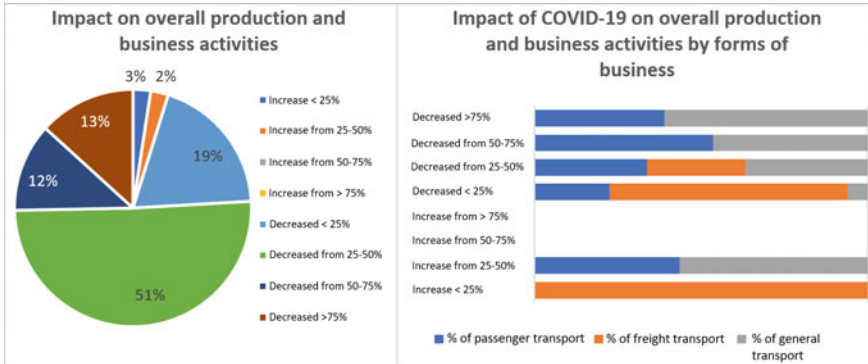


Fig. 2 Change in overall production and business activities of road transport enterprises compared to 2019 (before the COVID-19 pandemic)

freight transport enterprises, the common reduction was <25%. A few freight transport enterprises recorded a growth in production and business activities during the COVID-19 period, but the growth rate was <25% (Fig. 2).

2.4 Impact on Labor Size and Employee Income

The sharp revenue decline and the losses incurred by enterprises would certainly exert an immediate impact on the employees. Employee retrenchment among transport enterprises was undesirable, but it did happen in over 90% of respondents. As indicated in the above analysis, although transport enterprises experienced a significant revenue drop by an average of about 50% and suffered from losses, the percentage of employee cuts recorded in these enterprises was generally <10% (10–20% in just some enterprises). The number of enterprises with greater employee layoffs only accounted for a small percentage.

Despite many difficulties, the reduction in labor size was much lower than the decrease in revenue. This partly showed that enterprises had good faith in their rebound and the determination to maintain production and business activities in the transport sector to wait for recovery opportunities.

Revenue decline, stagnation of production, reduced business activities, and employees’ insufficient working days directly resulted in income reduction. The survey results demonstrated that the reduction in employee income occurred in most of road transport enterprises with the most common income reduction percentage being <25%, followed by a decrease of 25–50%, as confirmed by many enterprises.

2.5 Impact on the Efficiency of Transport Activities

The efficiency of transport activities is evaluated based on the capacity utilization rate (for passenger transport) and the average load factor (for freight transport).

These are the most important factors based on which the efficiency of transport activities is determined. According to the calculations, expert experience as well as opinions of enterprises, for passenger transport enterprises, the capacity utilization rate of 70% or more must be achieved to earn a profit.

Some common points could be observed through the survey results as follows:

- **Passenger transport:**

The capacity utilization rate in passenger transport went down sharply during the COVID-19 period compared to 2019. Specifically, all groups of passenger transport vehicles saw a decrease by 40–50% in the capacity utilization rate in 2021 compared to 2019; large passenger buses suffered the biggest decline in this indicator, and passenger buses with more than 46 seats experienced a drop of over 70% to an average of 33% in 2021; passenger transport enterprises incurred heavy losses for two consecutive years.

- **Freight transport:**

On average, the percentage of empty trips was also on the rise from 2019 to 2021 (with a rise of 3–9%, depending on the groups of vehicles); the group of vehicles of under 2 tons and from 2–7 tons suffered the highest increase of no-freight trips (by 9%); and container trucks experienced the lowest increase (3%).

3 Assessment of the Resilience and Adaptability of Road Transport Enterprises to the COVID-19 Pandemic Toward Green Recovery

The COVID-19 pandemic has caused many unprecedented immense impacts. Apart from negative aspects, the pandemic can be viewed as an opportunity for enterprises to review their business and management models for adjustments, reforms, and restructuring not only during the immediate recovery period but also during the long-term and sustainable adaptation period with better risk management capacity. The activities of transport enterprises are also placed in a more inclusive context, such as environment and climate change.

This research also initially surveys and evaluates the resilience and adaptability of road transport enterprises through the following four topics.

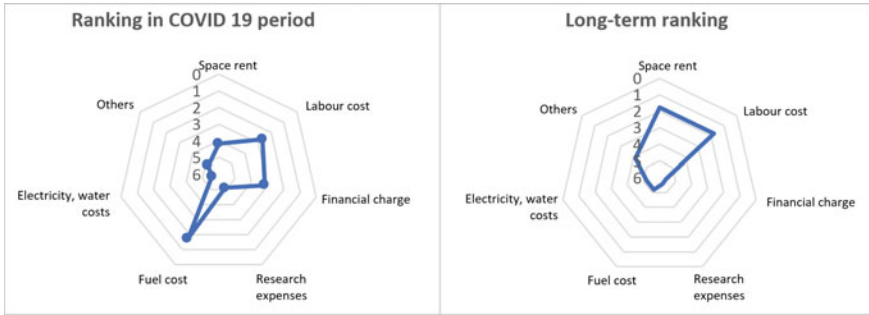


Fig. 3 Ranking of cost burdens to enterprises during the COVID-19 time and in the long term

3.1 Understanding of Operating Costs

The efficiency of production and business activities is a decisive factor in the existence of enterprises. Hence, it is critical to accurately identify the cost factor affecting production and business operation, thereby approaching appropriate cost reduction measures.

The survey in this research was also conducted to collect the opinions of road transport enterprises on the classification of expense burdens during the COVID-19 time and in the long term on a scale of 1–6 (with level 1 as the heaviest burden and level 6 as the lightest one). Both during the COVID-19 time and in the long term, a majority of enterprises considered fuel cost the heaviest burden, followed by the salary cost for employees.

According to the evaluation by enterprises, during the COVID-19 time, in addition to the fuel costs being the biggest burden, followed by the salary costs for employees, the financial costs (interest payment) are also considered a great pressure.

In the long term, enterprises also acknowledged that the space rent and labor costs will be a great burden for them. The remaining costs shared the same rank during the assessment process (Fig. 3).

3.2 Fuel Efficiency Management Effort

For passenger transport enterprises, the survey revealed that only 11% of enterprises recorded an increased fuel consumption rate, while 89% of enterprises confirmed decreased fuel consumption rate. This is a reflection of the general trend of reducing costs and enhancing business efficiency and competitiveness in enterprises.

Of the total number of surveyed passenger transport enterprises, 39% of enterprises achieved quite impressive fuel efficiency (a reduction of 5–10% in fuel consumption rate); 36% of enterprises reported a reduction of about 5% in fuel

consumption rate. Particularly, about 11% of enterprises applied a variety of measures and achieved an effective reduction of the rate by more than 20%.

The survey results also showed that about 11% of enterprises did not achieve fuel efficiency but recorded a rise in the rate of about 10% compared to the previous 5 years.

For freight transport enterprises, by analyzing the survey results in the same way as for passenger transport enterprises, it also indicated that most of the enterprises achieved the reduction target of fuel consumption rate: 73% (27% of enterprises failed to reach the goal of improving fuel efficiency). Specifically, the common percentage of reduction in fuel consumption rate was <10% (confirmed by 54% of surveyed enterprises).

In a macro-context, transport fuel efficiency improvement helps to reduce logistics costs, maintain export competitiveness, achieve the common goal of low-carbon transport, and move toward carbon neutrality.

3.3 Approach to Adaptation Measure

This research also surveyed the evaluation of how road transport enterprises will manage their production and business activities in the event that the COVID-19 pandemic persists for a long period of time in the scenarios of another 1, 2, and 5 years.

The longer the COVID-19 pandemic persists, the more difficult it is for transport enterprises, especially passenger transport ones, to ensure stable operations. In the short term, the popular ad-hoc measure chosen and applied by the enterprises was the reduction in production and business scale. In the longer term, this would not be the preferred measure; instead, the enterprises should focus on new and long-term adaptation measures. As the percentage of enterprises considering bankruptcy or dissolution was tiny (<5%), it suggested that although transport enterprises have experienced many difficulties over the past period, they are very determined to maintain their transport operations which play an important role in the economy. More importantly, most enterprises are well aware of the risks and are gradually developing and improving their adaptability (Fig. 4).

3.4 The Premise for Digital Transformation

Digital transformation is considered one of the breakthroughs in the transport sector. For transport enterprises, digital transformation plays a crucial role in improving production and business efficiency as well as managing and adapting to risks in a greater manner.

The survey results pointed out that among the main operations, including GPS tracking, management of fuel consumption, management of vehicle maintenance

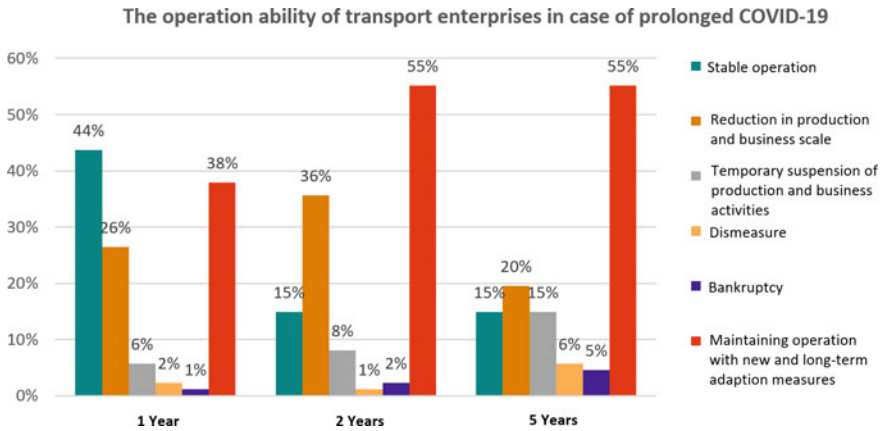


Fig. 4 Evaluation of operation ability of transport enterprises in case of prolonged COVID-19

processes, driver management and transaction management, most of the surveyed enterprises applied IT and deployed application software. Although the degree of application remained sporadic, a full application could be found in some operations, especially in GPS tracking. The majority of road transport enterprises use social media platforms (Facebook, Zalo, Viber, etc.) as a channel to connect with their customers. Meanwhile, the development of websites and especially of private applications for an online connection with customers was limited to large enterprises.

4 Conclusions

COVID-19 took a heavy toll on the transport sector in general and road transport enterprises in particular. In addition to extreme measures such as labor layoffs, salary cuts, allowing employees to take unpaid leave, and suspension of operations, the enterprises synchronously implemented such adaptation measures as downsizing of production and business scale, reduction in operating costs, allowing employees to take time off from work or apply for leave in rotation, and renegotiation with parties to the contract.

In addition to ad-hoc measures, the survey and analysis results suggested optimism about the resilience and adaptability to COVID-19 of road transport enterprises. This proved that the enterprises paid serious attention to the implications of the efficiency of the road transport business, identified the core factors for risk management, proactively performed risk management, implemented digital transformation, and premises for digital transformation.

References

1. Vietnam Automobile Transportation Association (2021) List of road transport enterprises
2. Vietnam Register (2021) Datasheet of national means of transport

Correction to: Proceedings of the 4th International Conference on Sustainability in Civil Engineering



Tung Nguyen-Xuan, Thanh Nguyen-Viet, Thanh Bui-Tien,
Tuan Nguyen-Quang, and Guido De Roeck

Correction to:

T. Nguyen-Xuan et al. (eds.), *Proceedings of the 4th International Conference on Sustainability in Civil Engineering*, Lecture Notes in Civil Engineering 344, <https://doi.org/10.1007/978-981-99-2345-8>

In the original version of chapters 20 and 76, the following belated correction has been incorporated.

In chapters 20 and 76, in the author's affiliation the text "/UTC" has been removed and the affiliation in these chapters has been changed from "University of Transport and Communications/UTC, Hanoi, Vietnam" to "University of Transport and Communications, Hanoi, Vietnam".

The correction chapters and the book has been updated with these changes.

The updated version of these chapters can be found at
https://doi.org/10.1007/978-981-99-2345-8_20,
https://doi.org/10.1007/978-981-99-2345-8_76